NASA CR-168211

R83AEB503



National Aeronautics and
Space Administration

# Energy Efficient Engine

## Integrated Core/Low Spool Design and Performance Report

by

Aircraft Engine Business Group
Advanced Technology Programs Dept.
Cincinnati, Ohio 45215



Prepared for
National Aeronautics and Space Administration



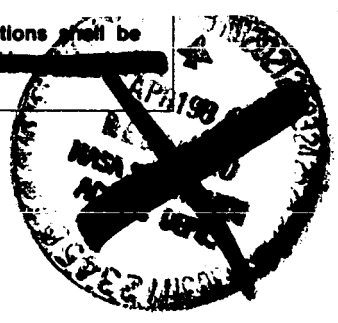

NASA Lewis Research Center
Contract NAS3-20643

## FOREWORD

This report presents an overview of the design and the results of testing the Integrated Core/Low Spool test vehicle of General Electric's Energy Efficient Engine ($E^3$). This work was performed for the National Aeronautics and Space Administration (NASA), Lewis Research Center, under Contract NAS3-20643 as part of the Aircraft Energy Efficiency Program and Energy Efficient Engine Project. Mr. Carl C. Ciepluch is the NASA $E^3$ Project Manager and Mr. Peter G. Batterton is the NASA Assistant Project Manager. Mr. Roger Chamberlin is the NASA Project Engineer responsible for the effort associated with the design and test reported here. Mr. Donald Y. Davis is manager of the $E^3$ Project for the General Electric Company. This report was prepared by Mr. E. Marshall Stearns and the General Electric $E^3$ staff.

TABLE OF CONTENTS

TABLE OF CONTENTS (Continued)

TABLE OF CONTENTS (Concluded)

## LIST OF ILLUSTRATIONS

## LIST OF ILLUSTRATIONS (Continued)

LIST OF ILLUSTRATIONS (Continued)

LIST OF ILLUSTRATIONS (Continued)

LIST OF ILLUSTRATIONS (Continued)

LIST OF ILLUSTRATIONS (Continued)

LIST OF ILLUSTRATIONS (Continued)

## LIST OF ILLUSTRATIONS (Continued)

LIST OF ILLUSTRATIONS (Continued)

LIST OF ILLUSTRATIONS (Continued)

## LIST OF ILLUSTRATIONS (Continued)

LIST OF ILLUSTRATIONS (Continued)

LIST OF ILLUSTRATIONS (Continued)

LIST OF ILLUSTRATIONS (Continued)

## LIST OF ILLUSTRATIONS (Concluded)

## LIST OF TABLES

## LIST OF SYMBOLS, ABBREVIATIONS, AND ENGINE STATION DESIGNATIONS

| Symbol or Abbreviation | Definition |
|---|---|
| A | Area, $cm^2$ ($in^2$) |
| ACC | Active clearance control |
| Accel | Acceleration |
| AGB | Accessory gearbox |
| Amb | Ambient pressure |
| AMAC | Advanced multistage axial flow core compressor |
| bhp | Brake horsepower |
| Btu | British thermal unit |
| CAFD | Circumferential average flow determination computer program |
| CDP | Compressor discharge plane, compressor discharge pressure |
| CF6-50 | General Electric commercial turbofan engine family |
| CRT | Cathode-ray tube |
| CO | Carbon monoxide |
| cps | Cycles per second |
| D | Diameter, m or cm (in.) |
| Decel | Deceleration |
| DOC | Direct operating cost |
| DMS | Data management system |
| DS | Directionally solidified |
| D/A | Double annular |
| $E^3$ | Energy Efficient Engine |
| EI | Emissions index |
| F | Force, N (lbf) |
| f/a | Fuel-air ratio |
| FADEC | Full authority digital electronic control |
| FAR 36 | Federal Noise Compliance |
| FHV | Fuel heating value |
| $F_N$ | Net thrust |
| FOD | Foreign object damage |

| Symbol or Abbreviation | Definition |
|---|---|
| FPS | Flight Propulsion System (refers to the fully developed configuration of the energy efficient engine which would be suitable for airframe installation) |
| G-Idle | Ground idle |
| h | Heat transfer coefficient, [$W/m^2 °C$ (°F)] |
| Δh | Energy extraction, kJ/kg (Btu/lbm) |
| HC | Hydrocarbon |
| HCF | High cycle fatigue |
| HIP | Hot isostatic pressure |
| hp | Horsepower |
| HP | High pressure |
| HPC | High pressure compressor |
| HPT | High pressure turbine |
| ICLS | Integrated core/low spool (the complete turbofan test configuration of the $E^3$) |
| IGV | Inlet guide vane |
| KE | Kinetic energy |
| L | Length, m (in.) |
| LP | Low pressure |
| LPT | Low pressure turbine |
| LCF | Low cycle fatigue |
| M | Mach number |
| MXCR | Maximum cruise operating point |
| MXCL | Maximum climb operating point |
| N | Speed, rpm |
| $NO_x$ | Oxides of nitrogen |
| OGV | Outlet guide vane (compressor or turbine) |
| P | Pressure, Pa (psi) |
| PE | Potential energy |
| PLA | Power lever angle (throttle position) |
| P/A | Force/area (stress), kPa (ksi) |
| PTO | Power takeoff |
| rpm | Revolutions per minute |

| Symbol or Abbreviation | Definition |
|---|---|
| RNI | Reynolds number index |
| sfc | Specific fuel consumption, kg/N°hr (lbm/lbf°hr) |
| SLTO | Sea level takeoff |
| SRTC | Start range turbine cooling |
| S/A | Single annular |
| T | Temperature, K (°R) |
| U | Rotor tangential velocity of the mean radius, m/s (ft/s) |
| V | Velocity, m/s (ft/s) |
| W | Weight flow, kg/s (lbm/s) |
| $\Gamma$ | Turbine exhaust swirl, degrees |
| $\eta$ | Efficiency |
| $\Theta$ | Blade tip shroud angle, degrees |
| $\sigma$ | Solidity |
| $\phi$ | Assembled pretwist rotation angle of blade tip shroud, degrees; Unit of fuel flow/unit of compressor discharge pressure, pph/psi |

Subscripts

| | |
|---|---|
| a | Air |
| C | Coolant, compressor |
| DT | Dovetail |
| g | Gas |
| h | Hub |
| P | Pitch |
| t | Tip |
| S,s | Static |

The General Electric mixed-flow engine station designation system is used in this report. Engine station nomenclature is defined in Figure 1.

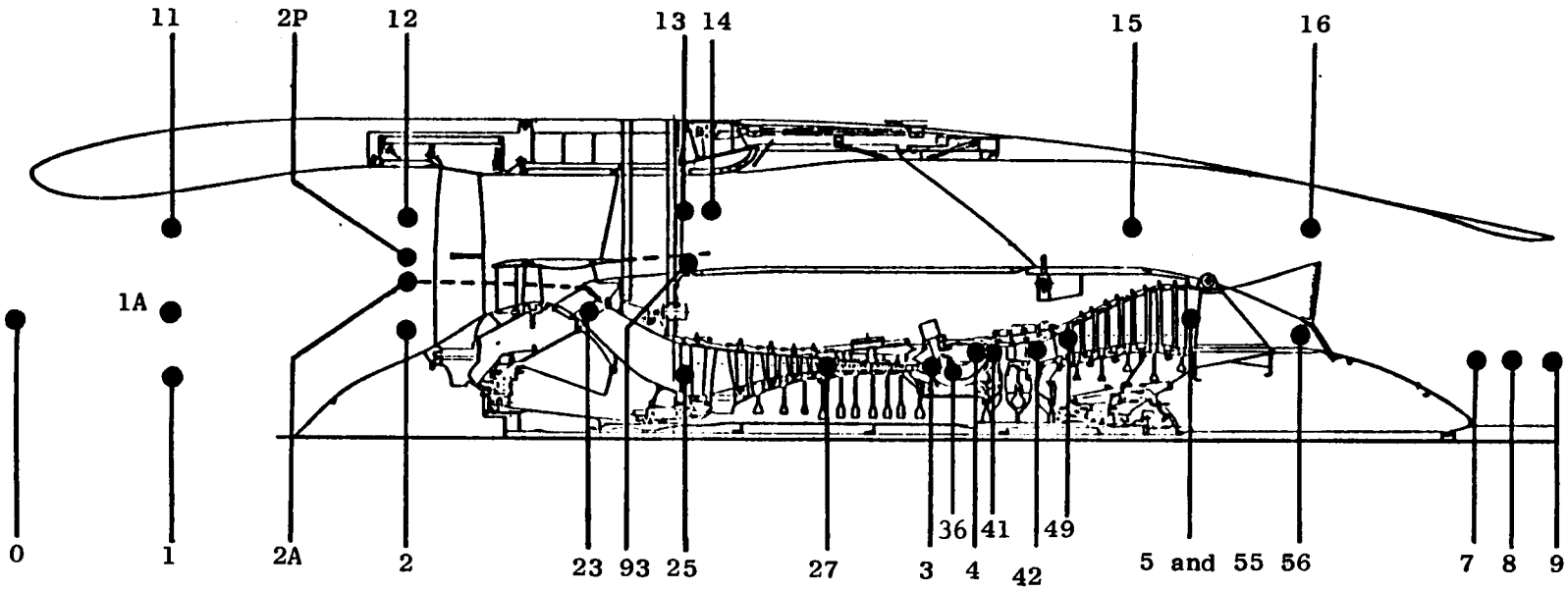


0 Ambient
1 Inlet Discharge at Fan Hub
1A Flow-Weighted Average at Inlet/Engine Interface
11 Inlet Discharge at Fan Tip
12 Fan Inlet at Tip
13 Fan Tip OGV Discharge
14 Bypass Duct Inlet
15 Bypass Duct Exit
16 Bypass Stream Mixing Plane
2 Fan Inlet at Hub
2A Flow-Weighted Average for Total Engine Flow at the Fan Face
2P Flow-Weighted Average for Total Bypass Flow at the Fan Face
93 Fan Hub Discharge That Goes to the Bypass Duct
23 Fan Hub Discharge That Goes to the Compressor Inlet
25 Compressor Inlet
27 Compressor Interstage Bleed Port (5th Stage)
3 Compressor Discharge
36 Combustor Inlet
4 HP Turbine First Stage Nozzle Inlet
41 HP Turbine First Stage Nozzle Discharge
42 HP Turbine Discharge
49 LP Turbine First Stage Nozzle Discharge
5 LP Turbine Discharge
55 Core Duct Exit
56 Core Duct Exit and Core Stream Mixing Plane
7 Exhaust Nozzle Inlet
8 Exhaust Nozzle Throat
9 Exhaust Nozzle Discharge

Figure 1. $E^3$ Station Designation.

## 1.0 SUMMARY

The Integrated Core/Low Spool (ICLS) vehicle provided a test evaluation of the NASA/General Electric Energy Efficient Engine ($E^3$) design. The $E^3$ program created fuel-saving technology for transport aircraft engines which would be introduced into service in the late 1980's and the 1990's. The mechanical, material, aerodynamic, and system technologies in the ICLS vehicle were advanced beyond current production engine state of the art.

The ICLS test vehicle completed 64 hours and 50 minutes of testing on June 15, 1983. The objective of these tests was to demonstrate the readiness of the advanced technologies incorporated in ICLS.

The ICLS test vehicle was an undeveloped technology research engine, designed as a practical flight engine. Advances in propulsion technology have been enhanced by the use of these types of vehicles. High risks can be taken at low cost without jeopardizing a major production engine program. A primary purpose of technology research vehicles is to provide an opportunity to demonstrate the practicality of innovative designs and technical concepts in a reasonable period of time and at a reasonable cost. Additionally, they afford the advantage of evaluating the operation of advanced components in realistic environments. The ICLS demonstrated the readiness of the advanced technologies incorporated in the vehicle.

The measured sea level static standard day specific fuel consumption (sfc) at rated thrust was 0.0332 kg/hr°N (0.326 lbm/hr°lbf) as tested.

The test sfc could be reduced to 0.0327 kg/hr°N (0.321 lbm/hr°lbf) for the current test configuration by correcting an inlet bellmouth misalignment, correcting nacelle leaks, and repairing cowling panels which protruded into the airstream.

The fully corrected ICLS sea level static standard day (sfc) at rated thrust was 0.0316 kg/hr°N (0.310 lbm/hr°N) with the diagnostic instrumentation

removed, with the areas of first stage nozzles of both turbines and the exhaust area properly rematched, with cooling flows properly set, and with 100% ram recovery (an ideal inlet standard used for quoting performances). The uninstalled maximum cruise sfc at 10.67 km (35,000 ft), M0.8, is projected to be 0.0561 kg/hr°N (0.550 lbm/hr°lbf). These values represent $E^3$ technology existing at the time of the first engine to test.

The $E^3$ Flight Propulsion System is projected to have an installed (isolated nacelle) maximum cruise sfc of 0.0561 kg/hr°N (0.551 lbm/hr°lbf) at 10.67 km (35,000 ft), M.8.

The ICLS achieved a static corrected takeoff thrust of 16,971 kg (37,415 lbf), 2.5% above design thrust. The mechanical performance of the ICLS was nearly perfect, with nothing inhibiting the planned testing.

The following is a brief summary of the design and the conclusions drawn from ICLS testing, for each component and system:

Noise reduction features were designed into the fan and low pressure turbine. A full length fan duct with mixer reduced noise levels. Bulk absorber was incorporated into the nacelle and exhaust system. Based on test measurements, ICLS exceed the program goals with an average 5 EPNdB margin.

A full fan stage, plus a quarter stage booster under an untrapped island, made up the fan design. The fan blades were solid titanium with 50% span shrouds. Fan outlet guide vanes were integral with the fan frame.

Fan bypass stream efficiency was 0.886 and fan hub and booster core stream efficiency was 0.901. These exceeded the respective goals by 0.4% and 1.4%. (Efficiency levels in this discussion correspond to maximum cruise engine operation.)

The compressor was designed to achieve a very high pressure ratio, 23:1, on a single spool in only 10 stages. Compressor efficiency was 0.856,

exceeding its goal by 0.5 points. No stalls were experienced. Performance and successful operation of this advanced compressor was demonstrated.

The combustor used a double annular arrangement to achieve very low emissions over the full operating range and still retain a short length. A pilot dome operated during starting and at low power. Both pilot and main domes were used at higher power. Combustor efficiency slightly exceeded goal status at high power. Start ignition, staging from single to double annular combustion, and all operational characteristics were smooth and trouble free. No smoke was observed. Emissions of hydrocarbons and carbon monoxide were better than the goal, while those of oxides of nitrogen were slightly over goal.

The high pressure turbine used two stages. The aerodynamic design was a significant departure from prior state of the art. Mechanical design was structurally very clean to achieve very high life at the high rotational speeds inherent in the $E^3$ core spool. High pressure turbine efficiency was 0.925, exceeding the goal by 0.6%. This marks a major advancement over prior state of the art.

The low pressure turbine was a higly loaded design close coupled to the high pressure turbine without a midturbine frame. Low pressure turbine efficiency was about 0.7% below the goal and 1.0 to 1.5 points below the level measured in rig tests of this design. The deviation from rig performance levels was not expected and, as yet, is unexplained.

A mixer was incorporated to combine the fan and core streams prior to their being discharged through a single exhaust nozzle. Mixer effectiveness was 8% better than expected from model tests. Analytical modeling has since been changed to reflect the information learned from engine testing.

ICLS used a simply arranged two-sump, five-bearing system. A thrust and roller bearing carried the forward end of the fan shaft and a roller bearing carried the aft end. The forward end of the core rotor was carried by

a thrust bearing which was spring mounted from the front frame and was squeezed film damped. The aft end was spring mounted from the fan shaft.

Engine system vibrations were well behaved, demonstrating the effectiveness of the spring mounted and squeeze film damped core bearing arrangement. All engine operating temperatures and airfoil vibration characteristics were well within acceptable levels.

Active clearance control was used for the compressor, high pressure turbine, and low pressure turbine. Its use on the high pressure turbine was restricted, however, because the clearance control system had been modified to correct a rotor-to-casing eccentricity.

An on-engine Full Authority Digital Electronic Control (FADEC) provided the engine control functions and additionally incorporated features for test operation flexibility in both manual and automatic modes. The FADEC performed very well. Failure Indication and Corrective Action (FICA) demonstrated that the control can replace failed single and double engine sensor signals with its own calculated values and continue to control the engine.

Automatic starts were trouble free, with starts of 44 seconds being achieved with no stall and no bleed required. During starts and fast transients, no aerodynamic, thermal or aeromechanical problems were encountered.

## 2.0 INTRODUCTION

The objective of the $E^3$ Program is to develop the technology to improve the energy efficiency of propulsion systems for subsonic commercial aircraft introduced in the late 1980's and early 1990's. The need for the $E^3$ Program was established by shortages of petroleum-based fuels. Since the $E^3$ Program was launched, escalated fuel prices have made improved energy efficiency essential. The $E^3$ Program is a major element of the NASA Aircraft Energy Efficient Program (ACEE).

The following technical goals were established by NASA for the fully developed Flight Propulsion System (FPS):

- Fuel Consumption - Minimum 12% reduction in installed sfc compared to a CF6-50C at maximum cruise thrust, M = 0.8 at 10.67 km (35,000 ft) altitude on a standard day.
- Noise - Comply with FAR 36 (1978), with provisions for growth.
- Emissions - Comply with EPA Proposed (1981) Standards for new engines.
- Performance Retention - A 50% reduction in the rate of performance deterioration in-service as compared to the CF6-50C.

To meet and demonstrate the NASA Aircraft Project goals, the $E^3$ Project has four major technical tasks structured as follows:

### TASK 1 - PROPULSION SYSTEM ANALYSIS, DESIGN, AND INTEGRATION

This task addresses the design and evaluation of the $E^3$ Flight Propulsion System (FPS), the propulsion system designed for commercial service. The FPS is executed only through the design phase. Task 1 also establishes the component design and performance requirements to be executed and tested in subsequent tasks. The initial function of Task 1, establishment and evaluation of the FPS design, has been completed. However, it is periodically upgraded and modified as the technology evolves, as new ideas develop, and as test results become available.

TASK 2 - COMPONENT ANALYSIS, DESIGN, AND DEVELOPMENT

This tasks consists of the design, fabrication, test, and post-test analysis of the components and includes supporting technology efforts. Task 2 has been completed.

TASK 3 - CORE TEST

This task consists of the design, fabrication, test, and post-test analysis of the core test vehicle which consists of the compressor, combustor, and high pressure turbine. Task 3 has been completed.

TASK 4 - INTEGRATED CORE/LOW SPOOL (ICLS)

This task consists of the design, fabrication, test, and post-test analysis of the ICLS turbofan ground-test vehicle. The core and low pressure components are combined in this vehicle. The ICLS design differs from the FPS in that it does not use a flight design gearbox, controls, nacelle, or fan frame. Task 4 is the subject of this report.

Testing of the $E^3$ ICLS had two general purposes: First, provide for the evaluation of engine components operating in the turbofan engine environment. Second, evaluate the performance of the complete turbofan system.

This report describes the ICLS design and test and presents the ICLS test results.

## 3.0 HARDWARE DESCRIPTION

The General Electric $E^3$ Flight Propulsion System (FPS) achieves high propulsive efficiency by using a low fan pressure ratio and a mixer that combines the fan and core streams prior to discharging them through a common exhaust nozzle. Higher thermal efficiency is achieved by using a higher engine pressure ratio, higher high pressure turbine (HPT) inlet temperature (T41), and improved component performance compared to the CF6-50C. The engine was sized for 162 kN (36,500 lbf) takeoff thrust at sea level static standard day conditions. Characteristic cycle parameters are given in Table I.

The FPS mechanical layout is compact, thereby contributing to decreased deterioration, allowing simple frame and bearing arrangements, and making the full length fan duct/mixer arrangement practical. The aerodynamic and mechanical designs, the materials, and manufacturing techniques are advanced beyond current production engine technology. The major features of the engine are shown in a sectional view in Figure 2. A cross section of the engine, including the integrated nacelle, is shown in Figure 3. The FPS design is described in References 1 and 2.

The Integrated Core/Low Spool test vehicle (ICLS), the subject of this report, was a complete full-scale turbofan engine built for ground testing. FPS design hardware was used throughout the engine except for the gearbox, control, nacelle, and fan frame. These were non-flight type designs used for their lower cost, more ready availability, and, for the control, special capabilities needed for exploratory testing. A thrust reverser was not included, and a static test inlet configuration was utilized. Details on the component designs and hardware will be given in the subsequent sections. The upper and lower halves of the ICLS test vehicle are shown in Figure 4. The assembled ICLS test vehicle is pictured in Figure 5.

Table I. $E^3$ FPS Cycle Characteristics.

| | |
|---|---|
| Cycle Pressure Ratio at Max Climb[1] | 38 |
| Bypass Ratio at Max Climb[1] | 6.8 |
| Fan Pressure Ratio at Max Climb[1] | 1.65 |
| Turbine Rotor Inlet Temperature at Sea Level Static Warm Day[2] Takeoff Power | 1343°C (2450°F) |
| Specific Fuel Consumption at Max Cruise[3], Bare Engine | 0.0553 kg/(N°hr) [(0.542 lbf/(lbm°hr)] |
| Specific Fuel Consumption at Max Cruise[4], Installed Engine | 0.0575 kg/(N°hr) [(0.564 lbf/(lbm°hr)] |

(1) Max climb is the aerodynamic design point, M = 0.8/10.67 km (35,000 ft), standard day plus 10°C (18°F).

(2) Sea level static warm day refers to a standard +15°C (27°F).

(3) Max Cruise is the performance evaluation point, M = 0.8/10.67 km (35,000 ft), standard day.

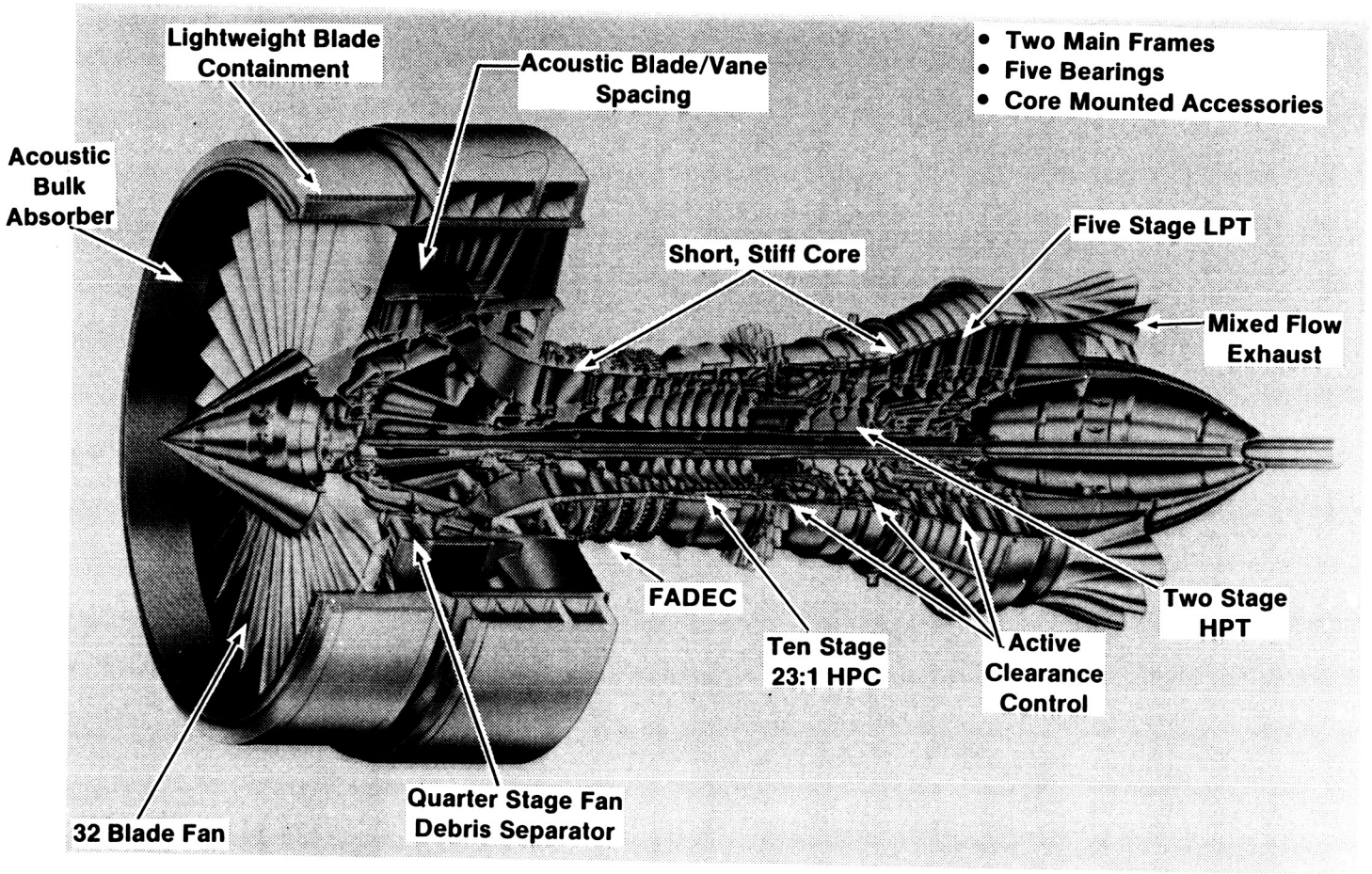


Figure 2. $E^3$ Flight Propulsion System (FPS) Major Features.

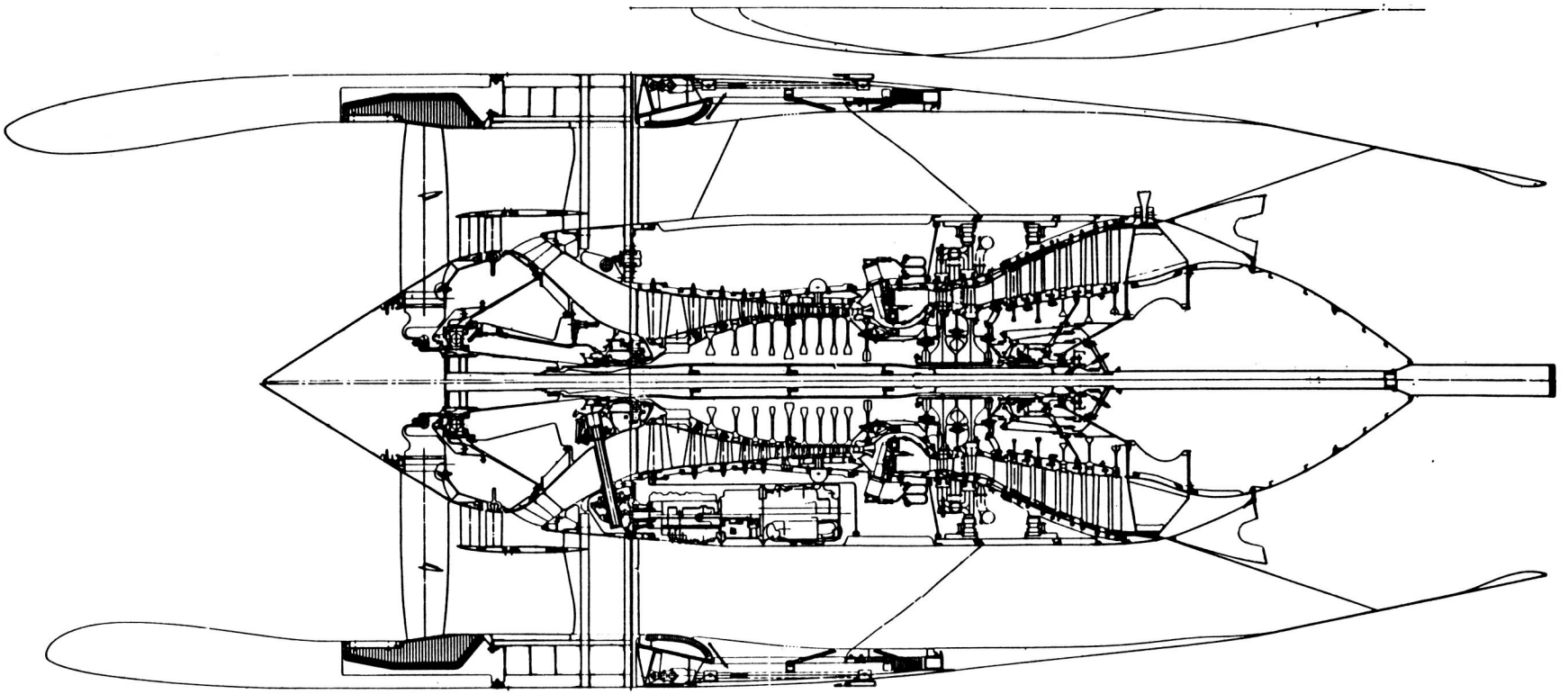

Figure 3. $E^3$ Flight Propulsion System Cross Section.

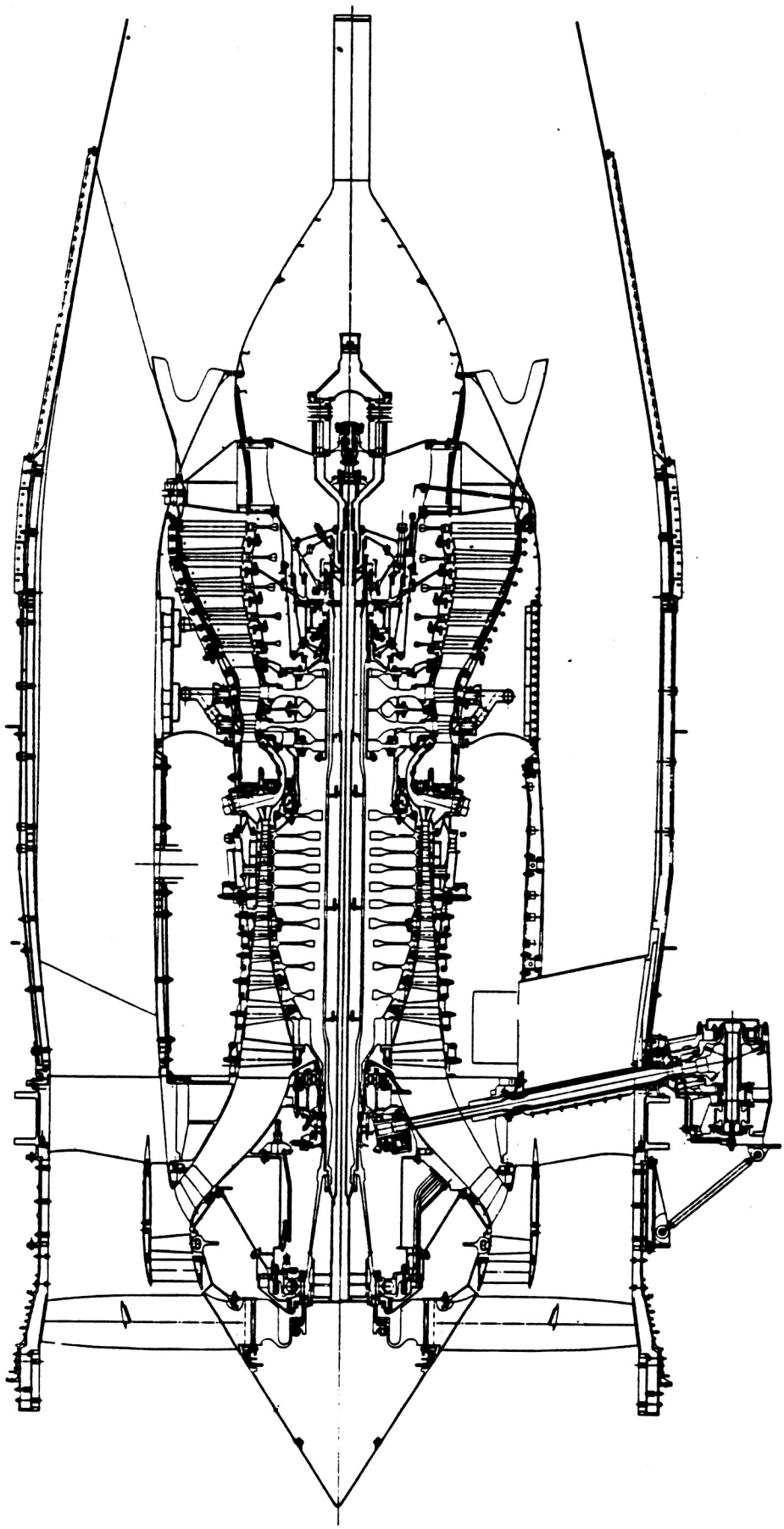

Figure 4. ICLS Cross Section

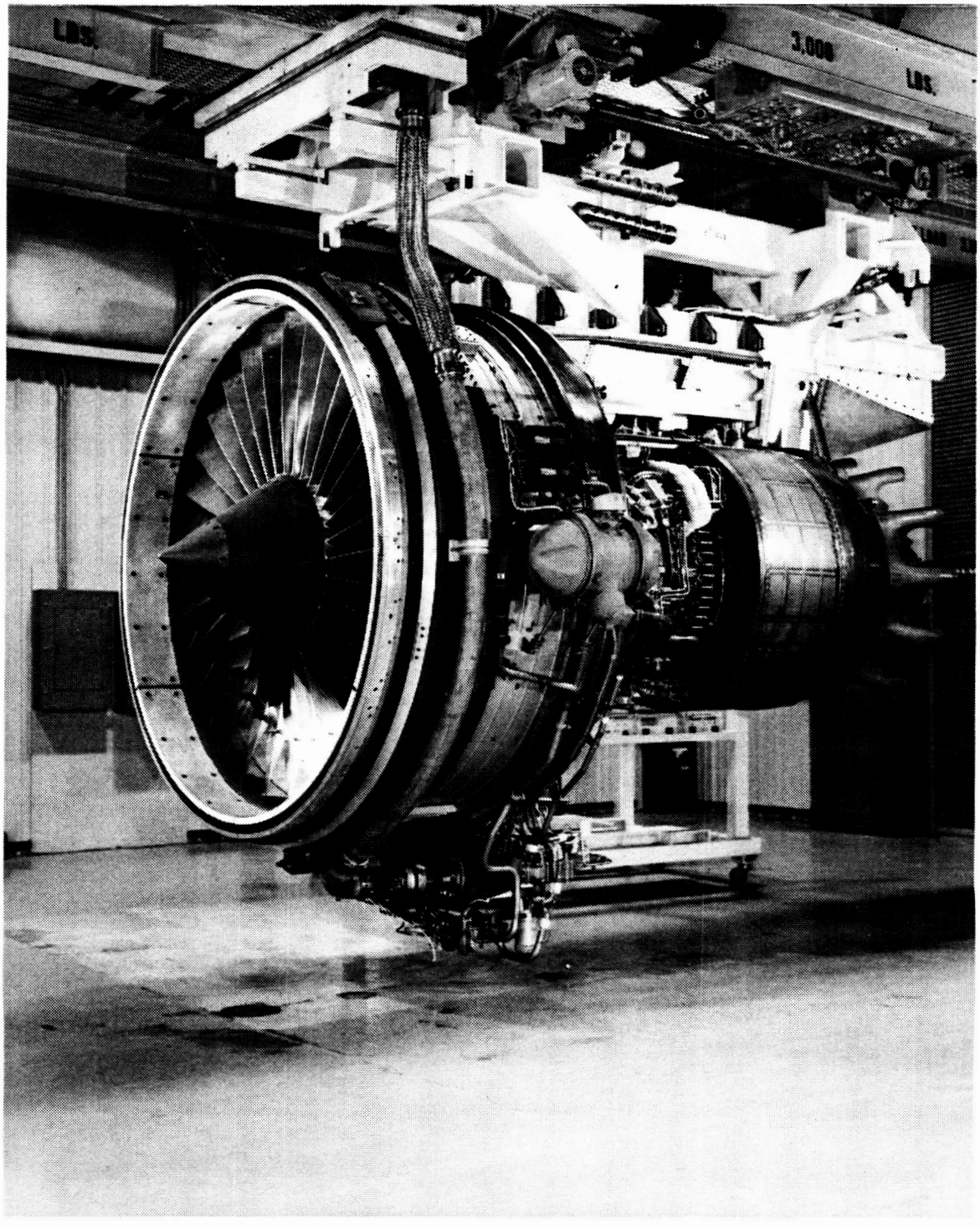


Figure 5. $E^3$ Integrated Core/Low Spool Test Vehicle.

## 3.1 ACOUSTIC SYSTEM DESCRIPTION

The ICLS system incorporated several advanced acoustic technology concepts (reference Figure 6). All of these concepts were successfully demonstrated during testing.

### Fan Rotor - Integral Vane Frame Design

The fan rotor and stator design was developed with a "cut-on" fan having large rotor-stator spacing. The blade counts of the fan rotor and the integral vane frame were selected for mechanical and performance reasons such that the corresponding interaction acoustically propagates from the duct. This penalty was alleviated by increasing the spacing between the fan rotor and the integral vane frame, weakening the generated strength of the blade passing frequency and harmonics.

### Low Pressure Turbine Design

The low pressure turbine, which required tight spacing for high efficiency, had to be designed with the vane-blade count of the next to last stage selected for interaction tone "cut-off." An increased vane to blade spacing was also used in that stage. Tone levels generated in the earlier stages were attenuated by propagation through the blade rows and over the bulk absorber treatment in turbine centerbody nacelle.

### Bulk Absorber Treatment Description

The bulk absorber treatment used in the nacelle are summarized below:

Inlet Suppression:
- Area = 7.15$m^2$ (77 $ft^2$)
- Density = 112 and 64 $kg/m^3$ (7 and 4 $lb/ft^3$) kevlar
- L/D = 0.516

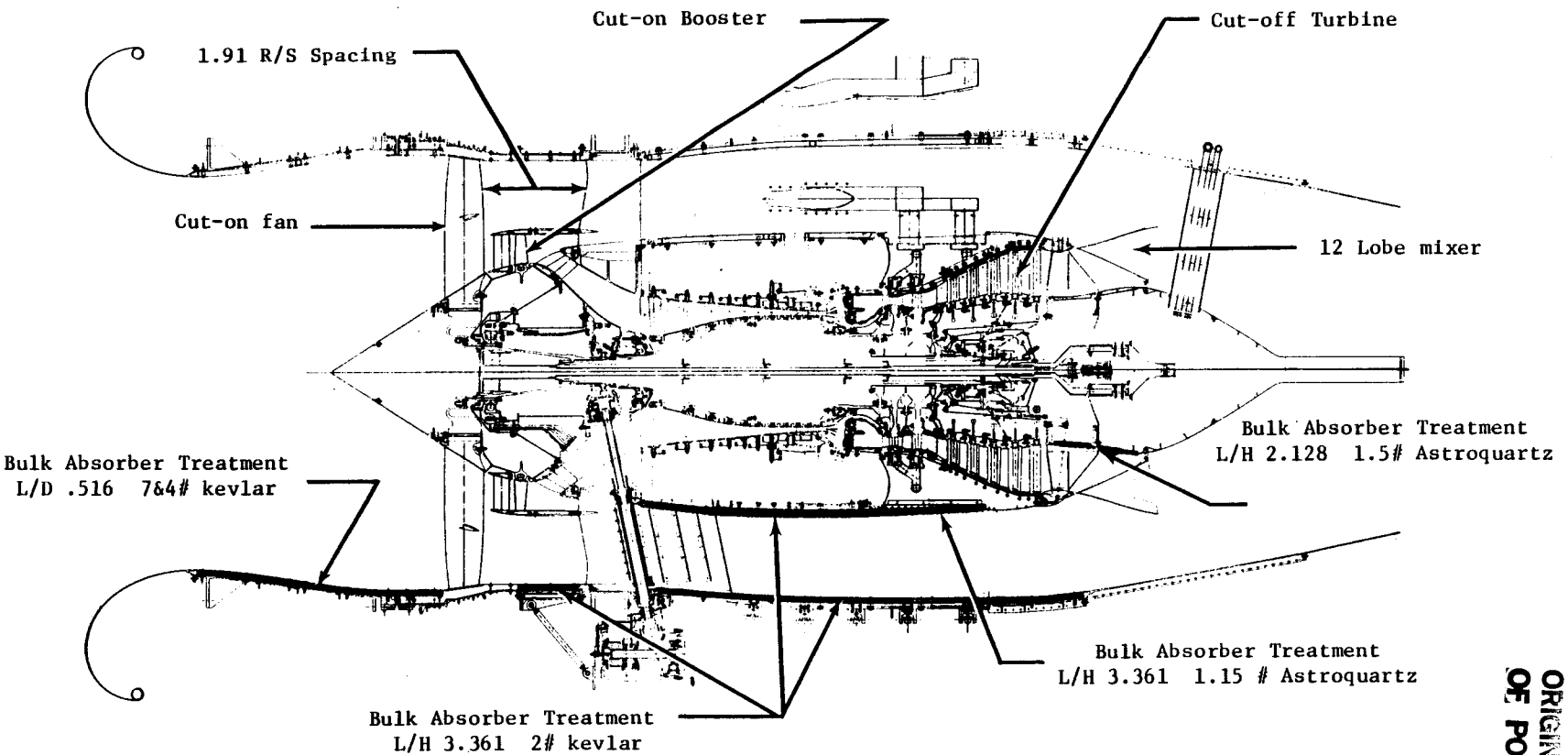


**Figure 6. ICLS Test Vehicle Acoustic Features.**

Fan Exhaust Suppression:

| | | |
|---|---|---|
| Outer Wall: | Area | = 9.48$m^2$ (102 $ft^2$) |
| | Density | = 32 $kg/m^3$ (2 $lb/ft^3$) kevlar |
| Inner Wall: | Area | = 3.81 $m^2$ (41 $ft^2$) |
| | Density | = 32 $kg/m^3$ (2 $lb/ft^3$) kevlar |
| Core Cowl: | Area | = 1.94$m^2$ (20.9 $ft^2$) |
| | Density | = 18.4 $kg/m^3$ (1.15 $lb/ft^3$) Astroquartz |
| | L/H | = 3.361 |

All face sheets 30% open

High Bypass, Mixed Flow Jet Nozzle

Noise generated by turbulent mixing in the jet plume was reduced because the mixer reduced peak exhaust temperature and therefore peak plume velocity.

## 3.2 INLET DESCRIPTION

### 3.2.1 Inlet Aerodynamic Design

The ICLS engine was tested with two different inlet bellmouths: a performance bellmouth and an aero-acoustic inlet/bellmouth. A schematic of the two inlets is presented in Figure 7. The performance bellmouth is the same hardware that was used for the full scale fan component test and was installed on the engine for all ICLS performance tests. The performance bellmouth was designed to provide high flow measurement accuracy and to be compatible with the full-scale fan test facility and test requirements. The inlet lip and contraction section were designed based on CF6 engine bellmouth experience. A 41.91 cm (16.5 inch) low Mach number cylindrical section provided a high accuracy flow measurement station. A schematic of the bellmouth and several key dimensions are shown in Figure 8.

The aero design of the aero-acoustic inlet, used exclusively during noise measurement tests, was established primarily by acoustic testing

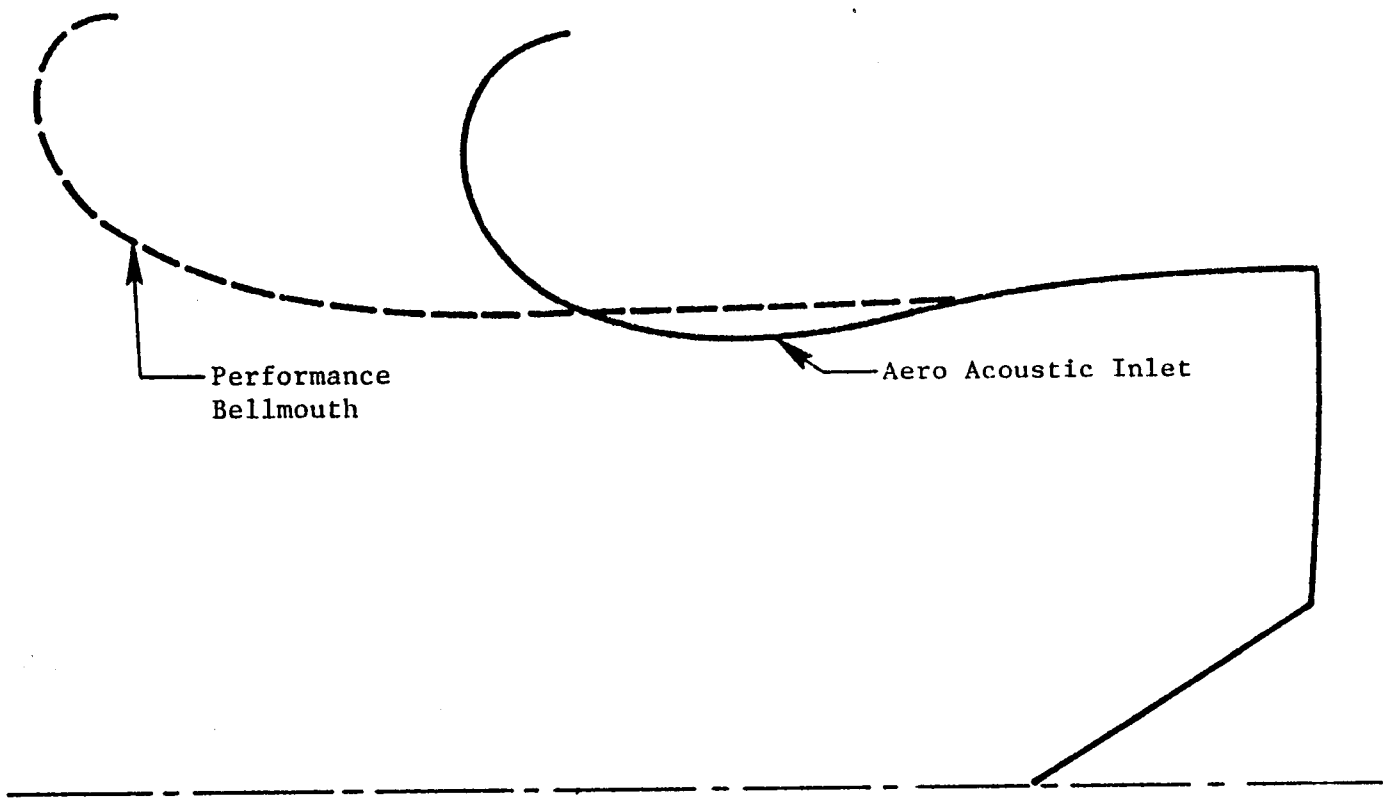


- Performance Bellmouth Used for Fan Component Test and all ICLS Performance Tests; High Flow Measurement Accuracy.
- Aero-Acoustic Inlet Used for ICLS Noise Tests.

**Figure 7. ICLS Inlet Configurations.**

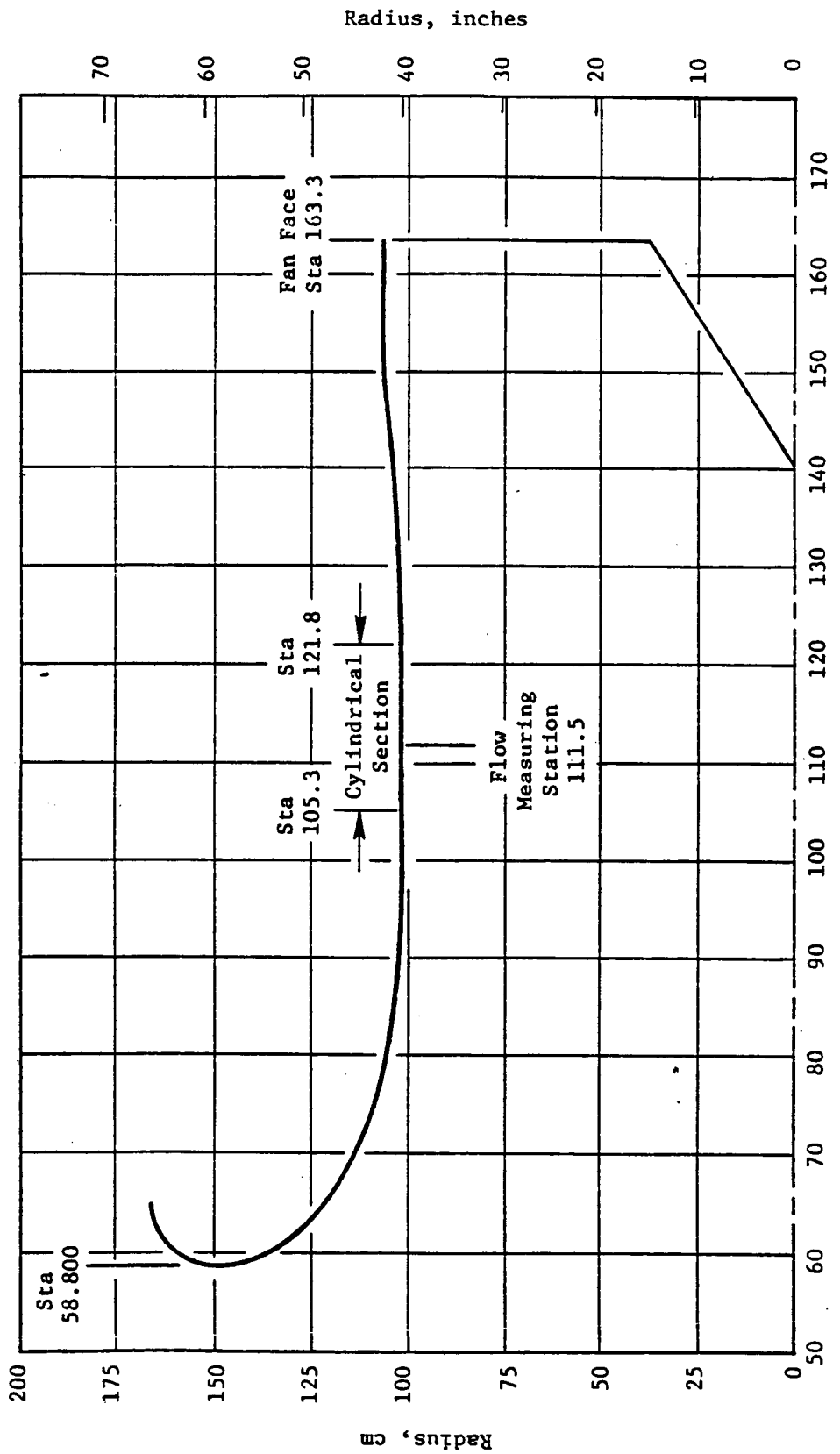


Figure 8. ICLS Performance Bellmouth.

requirements. To ensure the proper acoustic environment, the inlet was designed to provide the same diffuser wall and throat Mach number distribution at SLS max power operating conditions as the real FPS inlet at the takeoff noise rating point. To achieve this requirement, the inlet diffuser flowpath was made identical to the FPS inlet, undropped. This provided the same inlet acoustic treatment area and met the same inlet diffusion criteria as the FPS inlet. The bellmouth/lip contour was defined using CF6 bellmouth design experience to provide a uniform flow field acceleration to the throat with no flow separation. Figure 9 summarizes the aero-acoustic inlet bellmouth description.

An analytical study of the aero-acoustic inlet was conducted using the GE Streamtube Curvature (STC) potential flow program. The bellmouth was analyzed at SLS max power conditions and compared to the FPS inlet analysis at the takeoff noise rating point. Results, shown in Figures 10 and 11, indicate that the wall and throat Mach number distributions are nearly identical for each inlet, particularly the important wall Mach number where noise attenuation is achieved.

The ICLS inlets were not directly mounted to the engine/fan casing. Rather, it was "soft-mounted" with a flexible seal between the inlet and engine. At high power settings, relative motion occurred between the engine and inlet. This relative displacement was measured with potentiometers to determine its magnitude and to calculate any expected change in inlet recovery.

### 3.2.2 Inlet Mechanical Design

The aero-acoustic inlet, shown in Figure 12, consisted of a diffuser section with a flowpath identical to the undrooped FPS inlet and a bellmouth/lip structure to provide uniform flow acceleration. This structure was all slave hardware and was supported from the test facility and soft mounted to the engine.

The bellmouth/lip structure was a one piece separable assembly which was of a honeycomb sandwich type structure utilizing aluminum honeycomb and

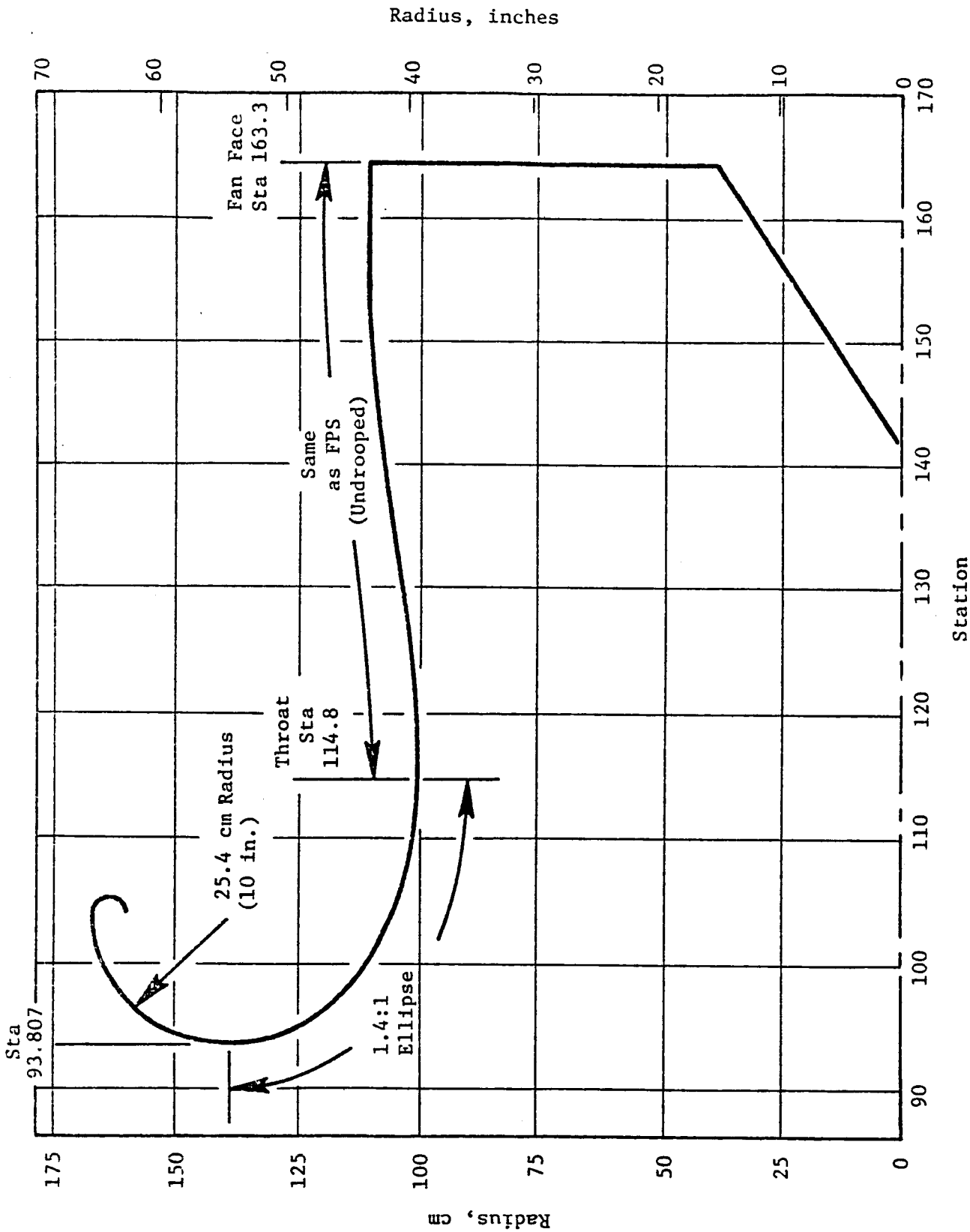


Figure 9. ICLS Aero-Acoustic Inlet Bellmouth.

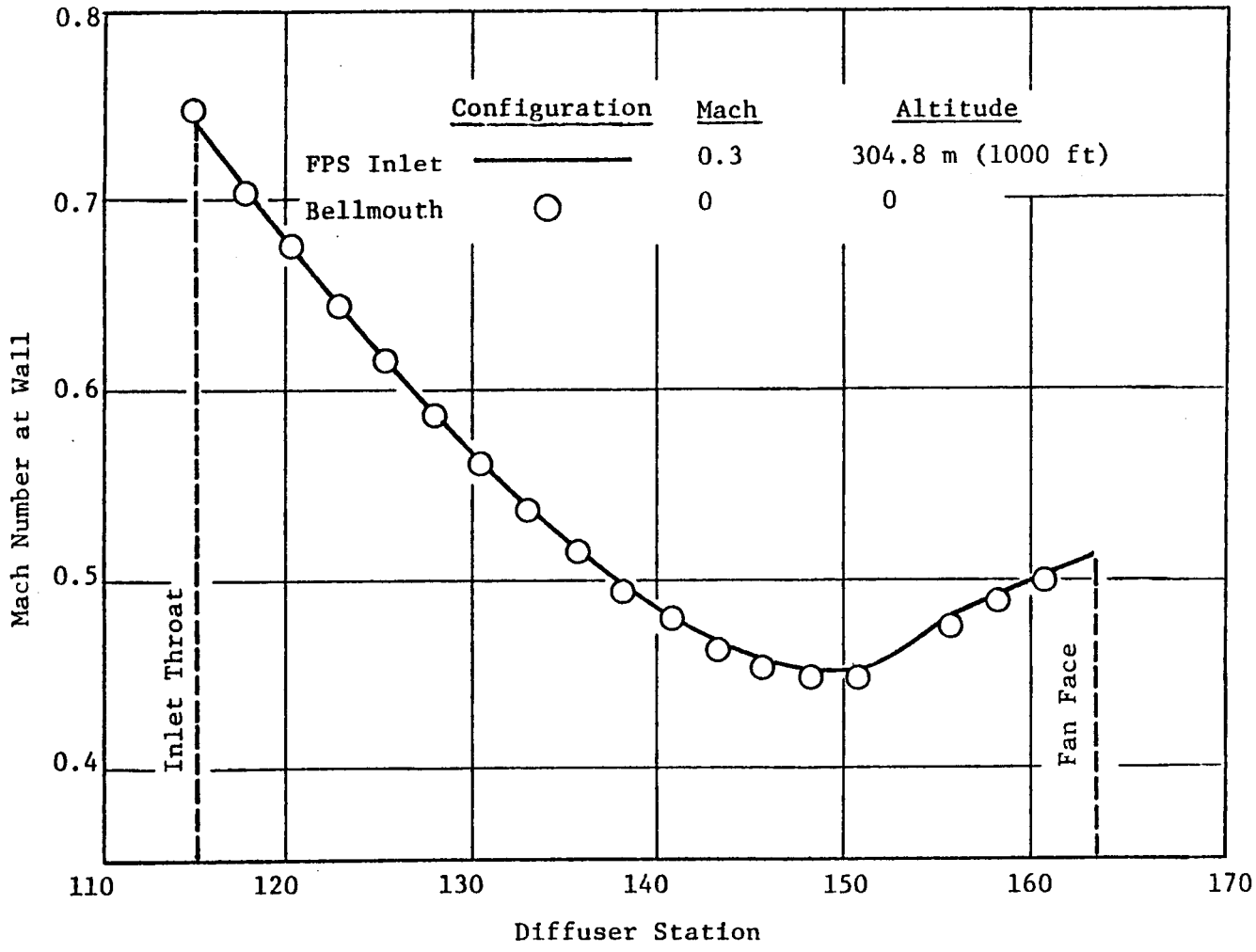


Figure 10. ICLS Aero-Acoustic Inlet - Stream Tube Curvature (STC) Analysis of Mach Number Along Diffuser Wall.

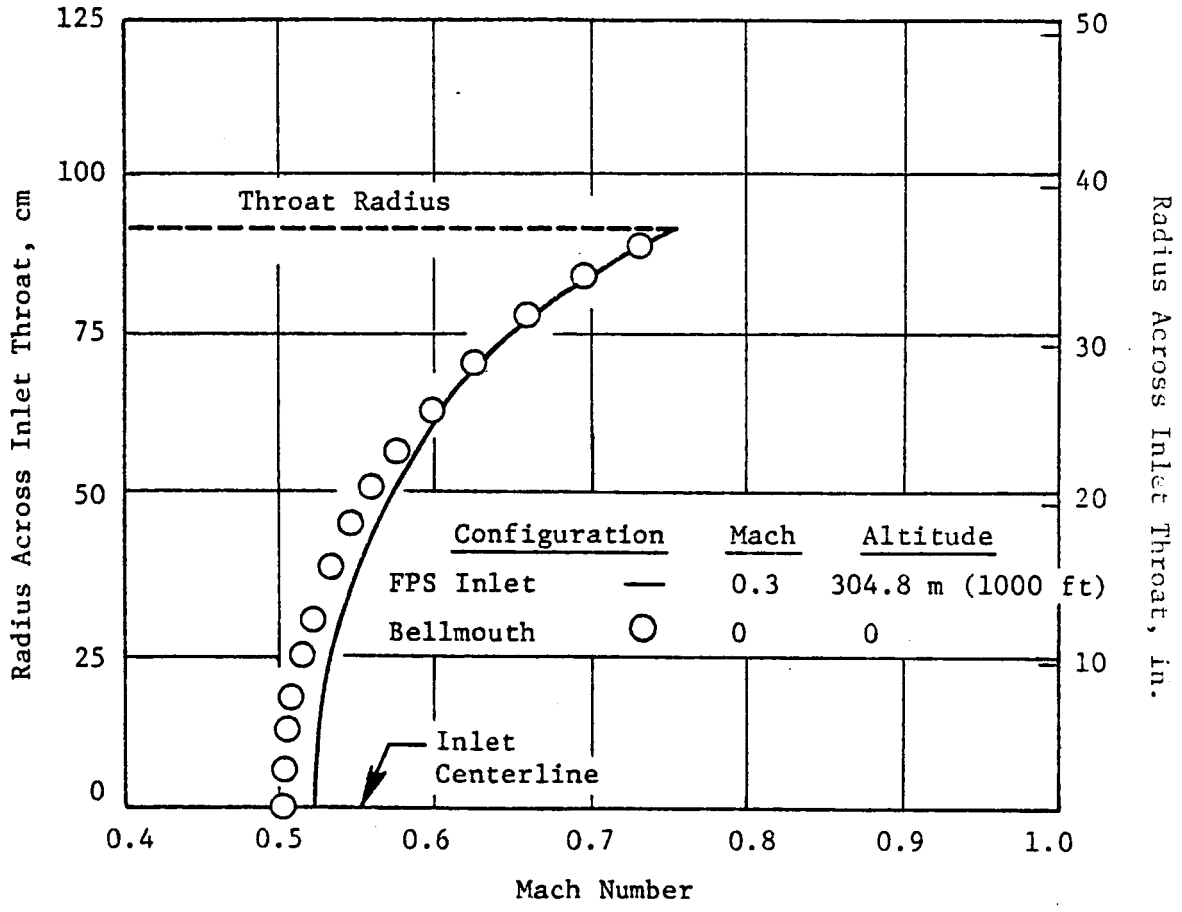


Figure 11. ICLS Aero-Acoustic Inlet - Stream Tube Curvature (STC) Analysis of Mach Number Across Inlet Throat.

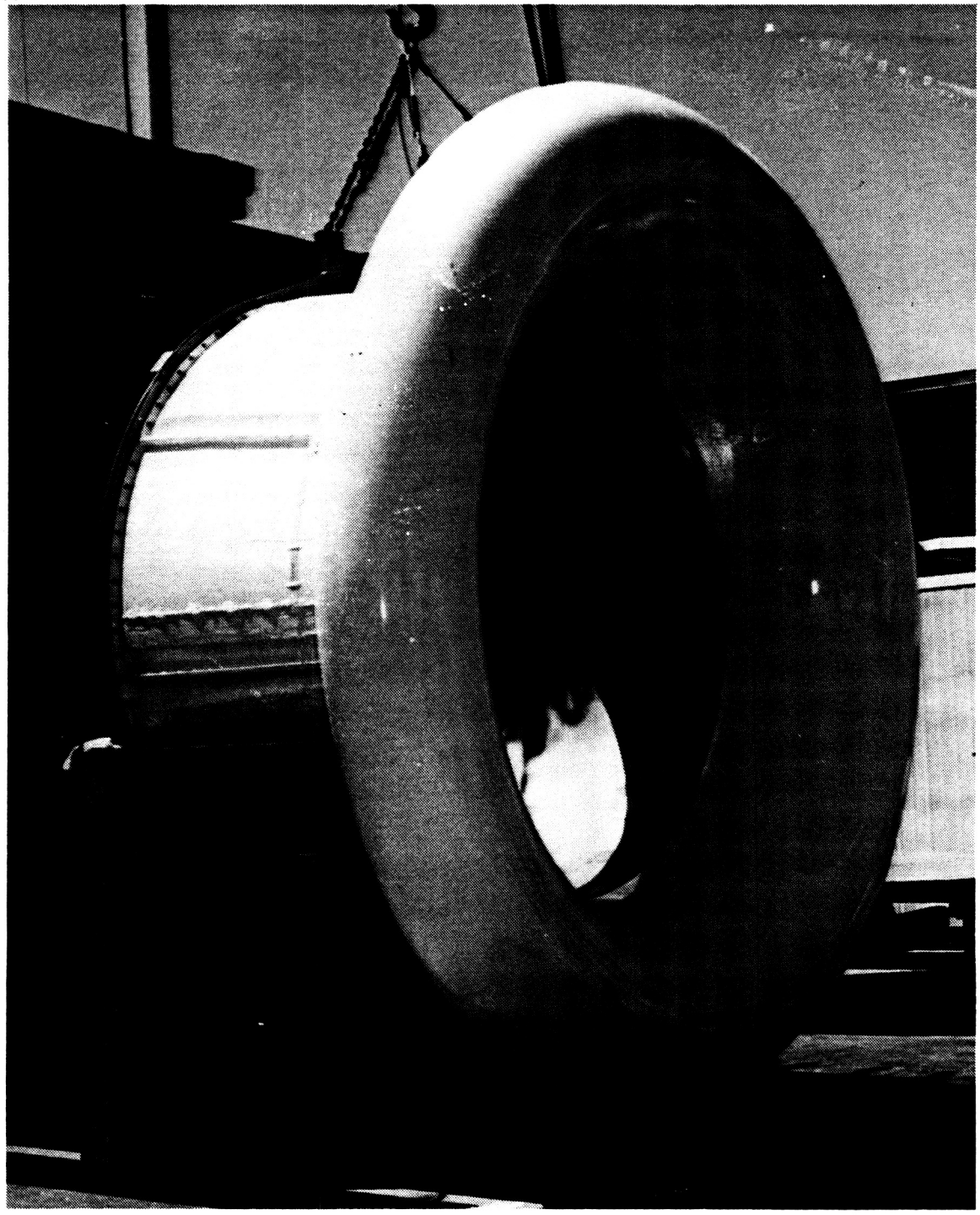

Figure 12. ICLS Aero-Acoustic Inlet.

fiberglass face sheets. The lip was reinforced by a built-in steel ring, and the aft flange consisted of an aluminum ring which was both bonded and mechanically fastened to the basic sandwich structure.

The inlet diffuser was a fiberglass face sheet/honeycomb core structure with integrated acoustic treatment. In order to reduce tooling costs, the diffuser was made in nine circumferential sections which were bolted together to form the 360° structure. The acoustic treatment was applied to the flowpath side of the structural sandwich. Perforated aluminum sheet was formed into pan shape structures which were filled with Kevlar felt bulk absorber material. These pans were bonded and mechanically fastened to the ends and sides of the structural sandwich prior to the assembly of the sectors into the 360° structure. Steel interface rings were bolted to each end of the diffuser.

The performance inlet bellmouth was designed for use on both the full-scale fan test rig and on ICLS. It used fiberglass and honeycomb construction. A box-shaped ring built into the bellmouth carried the mount loads from the facility mount.

## 3.3 MOUNT SYSTEM DESCRIPTION

The engine mount system used seven links as shown in Figure 13. The four front mount links connected to mount brackets attached to the aft side of the fan frame. Two links carried vertical and side loads while the other pair of links carried the thrust load. The aft three link system attached to the turbine rear frame. The short lateral link provided roll and side load restraint while the pair of links carried vertical loads. All links were mounted in uniballs.

The engine mount system was designed to minimize the engine backbone bending and circular distortions that result from the engine vertical, side, and thrust loads. Circular distortions in the engine (compressor) casing are generated by the vertical and thrust (axial) load reaction at the forward

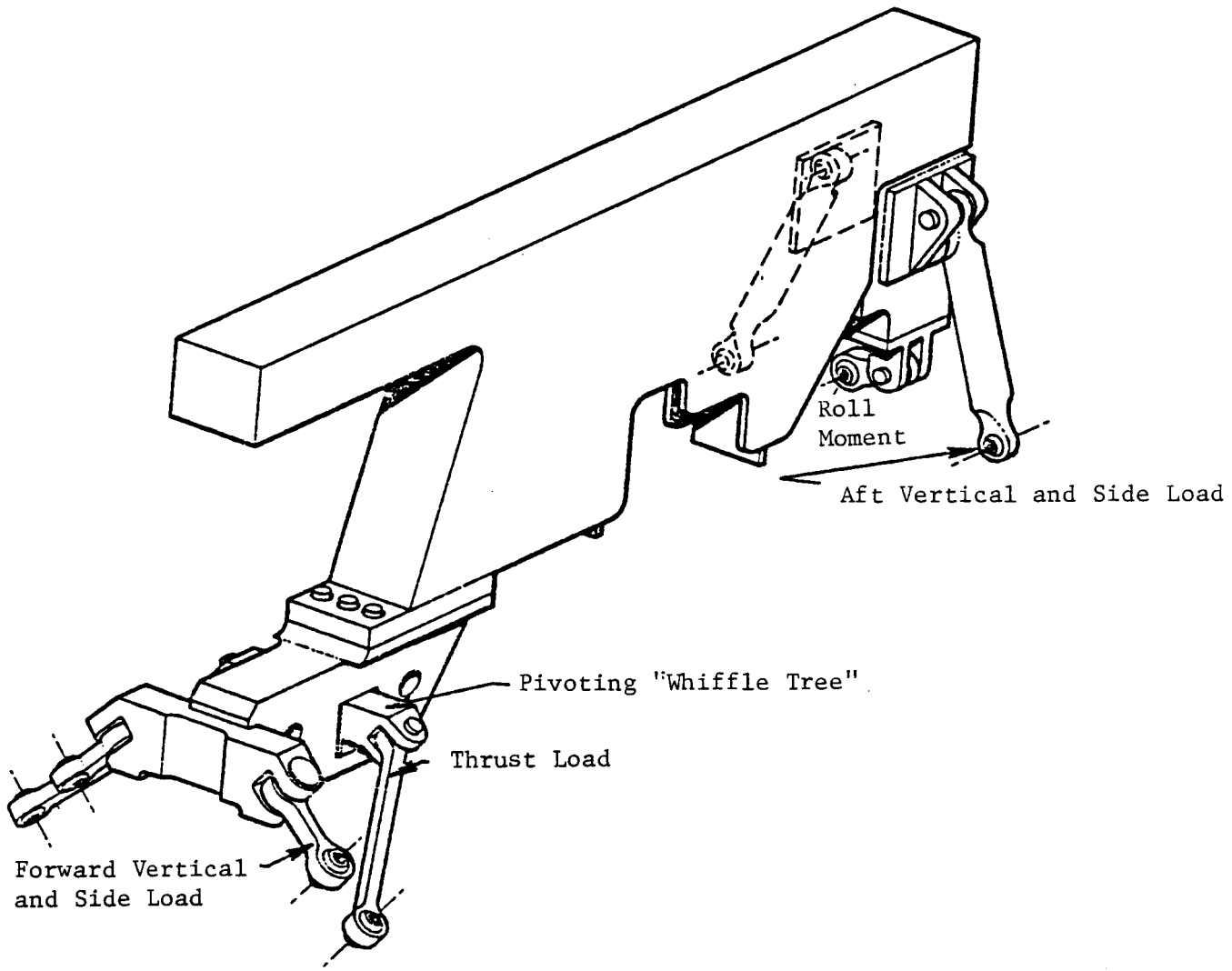


**Figure 13. $E^3$ Mount Schematic.**

mount location (fan frame). Analytical studies have shown that the major component of the circular distortion in the engine casings due to the thrust load reactions at the forward mount can be minimized by reacting the thrust load at two points separated by 90°. The $E^3$ ICLS thrust mounts were located at ±45° from the top vertical. Figure 14 shows the location of the forward mount brackets on the aft side of the fan frame.

All forward links were located under the core compressor cowling aft of the fan frame. The aft lateral link was located within the pylon. The aft vertical links were streamlined and extend through the fan stream from the pylon to the turbine rear frame.

## 3.4 FAN DESCRIPTION

The fan design for the General Electric/NASA Energy Efficient Engine was selected following an extensive preliminary design study of alternate fan configurations. The selected fan configuration (Figures 15 and 16) used a quarter-stage booster to provide the required core supercharging. This design was chosen over a single-stage rotor with a higher tip speed and a more highly loaded hub due to its higher core-stream efficiency potential and an easier growth path for future engine development. The fan bypass stream also had a higher efficiency potential by reason of the lower fan speed. Additionally, the quarter-stage island arrangement provided an excellent means for separating foreign objects from the core flow. The flowpath was made to be nearly optimum for the flight propulsion cycle, with some provisions to accommodate a potential growth application. The aerodynamic design point corresponded to the maximum climb power setting at Mach 0.80 and 10.67 km (35,000 feet) altitude.

The rotor structure features an aluminum nonstructural spinner, a titanium high-bore ring disk for coupled blade-disk mode stiffness and internal fan-structure accessibility, a one-piece titanium quarter-stage spool, and a steel fan shaft arrangement that allows for disassembly of either the shaft, the entire fan rotor, or the fan module (rotor and stator) from the high pressure compressor forward face.

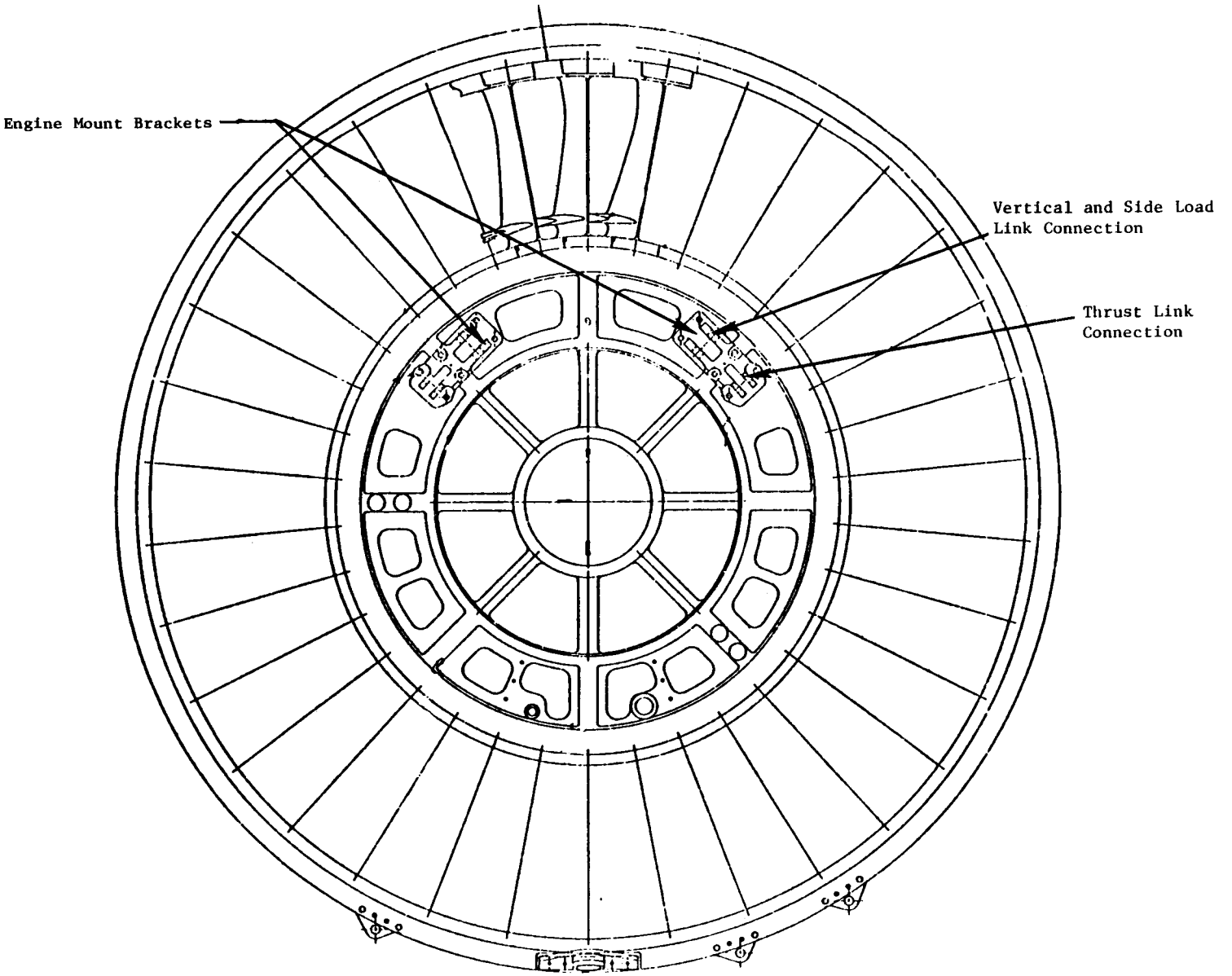


Figure 14. Forward Mount Brackets - Fan Frame.

ORIGINAL PAGE IS
OF POOR QUALITY

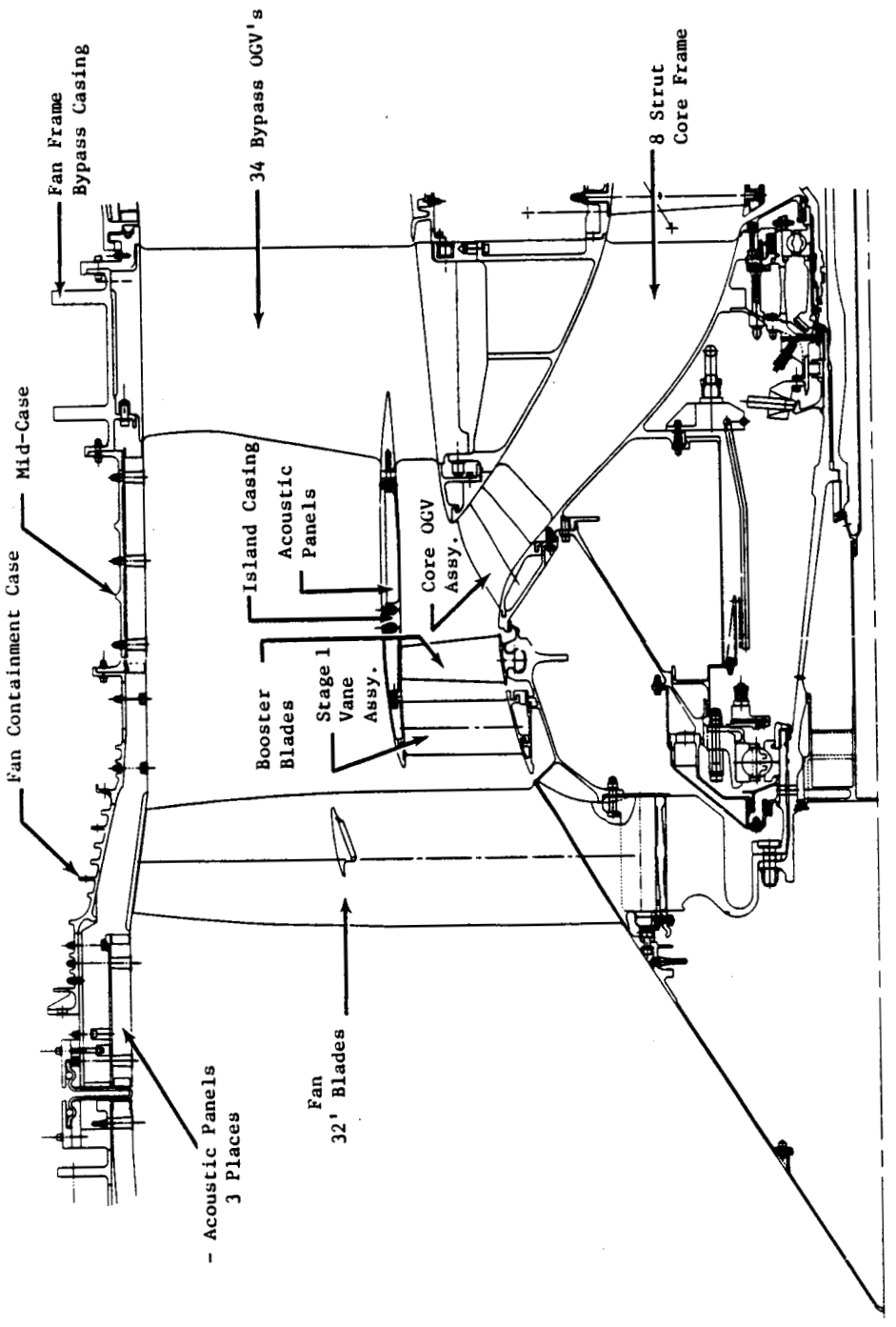


Figure 15. ICLS Fan Configuration.

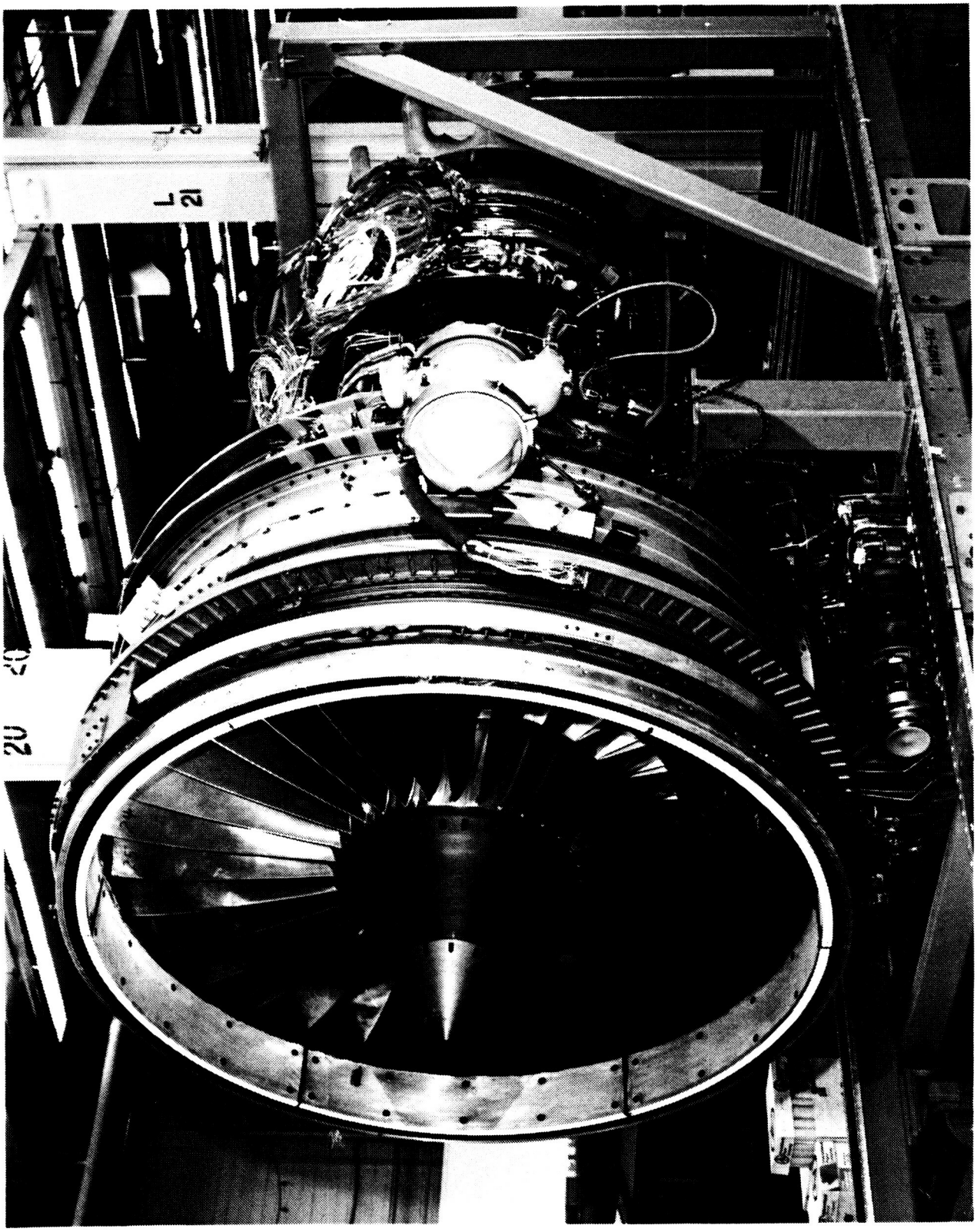


Figure 16. ICLS Fan Component Assembly

The axial spacing between the fan rotor trailing edge and the bypass outlet guide vanes (which also serve as the fan frame structural members) was approximately 1.8 rotor-tip chords, and made large in order to minimize fan noise generation.

The airfoils and rotor structure have been designed for a service life of 36,000 missions with two stress cycles per mission. The fan structure is designed to be capable of sustaining stalls with no mechanical damage, and there are no coupled-mode resonances predicted between the rotor and fan cast in the operating-speed range.

### 3.4.1 Fan Aerodynamic Design

#### Vector Diagram Design

The principal aerodynamic characteristics of the fan at three key operating points are shown in Table II. The aerodynamic design point coincided with the maximum climb condition of the Flight Propulsion System (FPS) cycle. The selected flowpath is shown in Figure 17 with the pertinent aerodynamic design parameters indicated. The fan tip diameter at the rotor inlet was 2.108 meters (83 inches) and the inlet hub-to-tip radius ratio was 0.342. The fan operated at a flow rate per design tip speed of 411.5 m/sec (1,350 ft/sec) with a specific rotor inlet annulus area of 208.9 kg/sec-$m^2$ (42.8 lbm/sec-$ft^2$). A quarter stage, or booster, was added to increase the fan hub pressure ratio and help separate foreign objects for the core flow. The fan rotor has 32 medium-aspect-ratio blades with a part-span shroud at 55% blade height based on the stacking axis. The spinner cone half angle was 32°, and the slightly contoured fan hub approximately followed that angle.

The total fan flow was split by the quarter-stage island with 22.3% of the flow passing under the island and supercharged by the quarter-stage rotor. Before entering the core duct, the flow was further split with approximately 42% of the quarter-stage flow reentering the bypass stream. The flow that entered the core duct had a total pressure ratio of 1.67. After

Table II. FPS Fan Aerodynamic Design Requirements.

| | Maximum Climb | Maximum Cruise | Takeoff |
|---|---|---|---|
| Corrected Tip Speed, m/sec (ft/sec) | 411.5 (1350) | 399.6 (1311) | 365.2 (1198) |
| Corrected Airflow, kg/sec (lbm/sec) | 643.6 (1419) | 634.1 (1398) | 577.9 (1274) |
| Flow/Annulus Area, kg/sec-$m^2$ (lbm/sec-$ft^2$) | 209.0 (42.8) | 206.0 (42.1) | 187.0 (38.4) |
| Bypass Stream Pressure Ratio | 1.65 | 1.61 | 1.50 |
| Bypass Stream Adiabatic Efficiency, % | 87.9 | 88.7 | 90.0 |
| Core Stream Pressure Ratio | 1.67 | 1.63 | 1.51 |
| Core Stream Adiabatic Efficiency, % | 88.5 | 89.2 | 89.7 |
| Bypass Ratio | 6.8 | 6.9 | 7.3 |

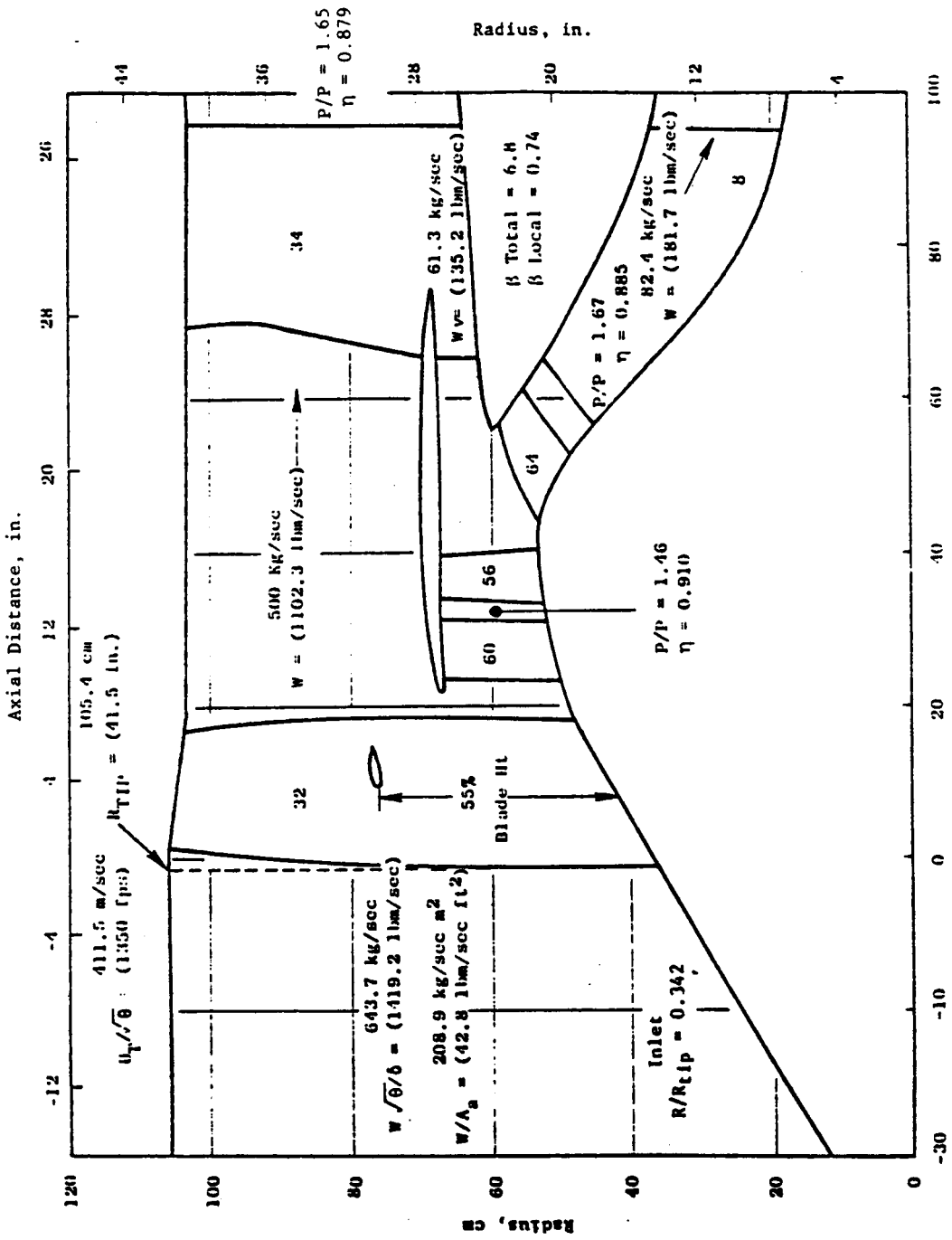


Figure 17. Selected Fan Configuration Flowpath.

1.8% duct pressure loss was sustained, the flow entered the core compressor with a corrected airflow of 54.4 kg/sec (120 lbm/sec). The airflow that passed over the upper surface of the island rejoined the flow that was spilled from the quarter stage to give an average total-pressure ratio of 1.65 at the bypass vane-frame exit plane. The total bypass ratio was 6.8 at the aerodynamic design point.

The total pressure ratio profile for the FPS fan is shown in Figure 18. The rotor exit profile as well as the stage exit profiles are shown. The booster rotor turned the tip-strong pressure coming out of the fan hub to the radially constant pressure ratio value of 1.683.

Fan Rotor Blade Design

The aerodynamic design of the fan rotor at the maximum climb cycle condition included the definition of airfoil sections which were transonic in the outer region and subsonic near the hub. The fan rotor blade airfoil shapes were specifically tailored for each streamline section using General Electric's Streamsurface Blade Section computer program. In general, the airfoils were shaped in an attempt to minimize shock losses since the inlet Mach numbers were subsonic for all streamlines above the quarter-stage island. Below the island streamline location, the Mach number ranged from 1.02 at 78% flow value to 0.70 at the hub streamline. The airfoils on the hub streamline were patterned after other advanced fan hub airfoil shapes that have shown excellent performance.

Quarter-Stage Rotor and Stator 1

The quarter-stage rotor and stator 1 airfoils were specified similar to the design of the fan rotor blade using the streamline section and cascade analysis computer programs. The vector diagrams were defined for several streamlines at axial stations including the leading edge, trailing edge, and intrablade region. Airfoil sections were defined for each streamline by specifying the thickness and meanline angle distributions.

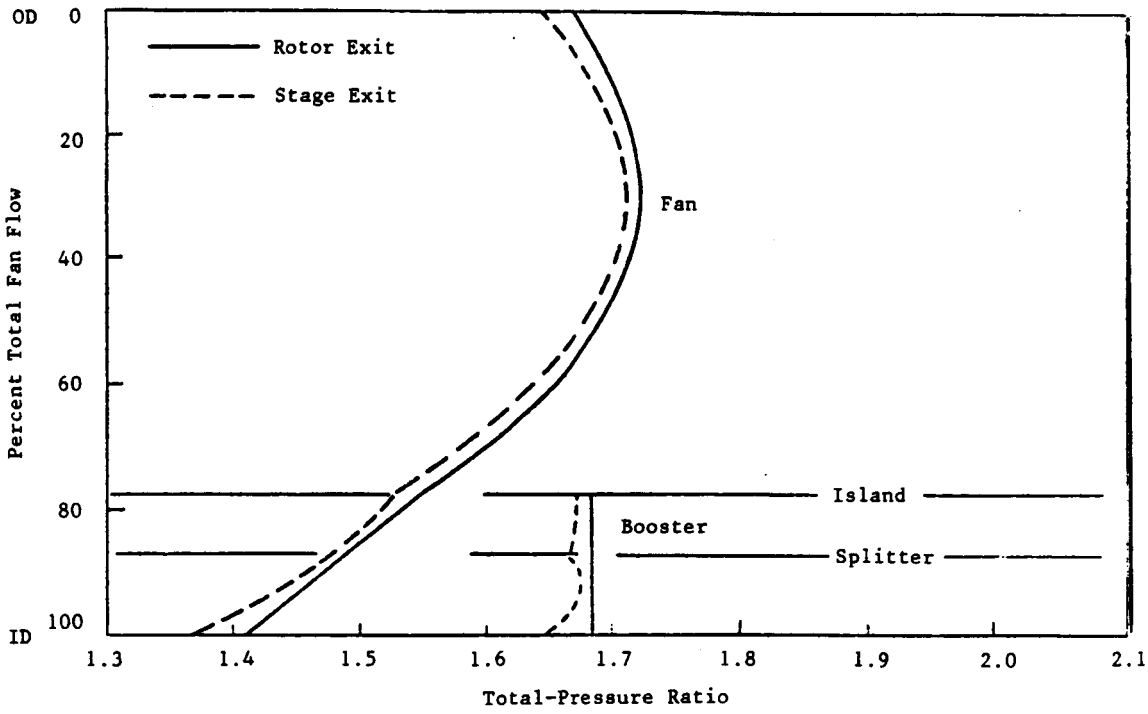


**Figure 18. Aerodynamic Design Point Total-Pressure Ratio.**

Inner OGV

The inner outlet guide vane (OGV) blade row was designed to remove the swirl received from the booster rotor and direct the flow into the core duct. To do this efficiently, the 64 vanes were swept aft and leaned with the pressure side facing the fan axis of rotation. The aerodynamic design of this blade row was performed using a procedure that consisted of cutting the airfoil along streamlines and viewing the sections along the blade axis. The blade axis was a curved line in space, swept aft by 60° from a radial line and leaned circumferentially in an amount that varies from 0° (no lean) at the OD to 20° at the ID. The stacking axis for viewing the cascade projection and for defining manufacturing sections was a straight line between the intersection of the blade axis with the OD flowpath and the intersection of the blade axis with the ID flowpath. The sweep angle (60°) of the stacking axis was selected to be compatible with the shape of the flowpath in the region entering the core duct. The degree of lean was chosen primarily to control and minimize the level of Mach number in the hub region as the flow entered the core duct.

Bypass OGV Vane-Frame

The aerodynamic design of the bypass vane-frame was complicated by the presence of a pylon having a maximum thickness of 40.6 cm (16 in) and located at the top of the engine (0°) just downstream of the vane trailing edges. In addition, the overall engine system design required the botton (180°) vane or strut to be substantially thicker than the rest of the vanes to provide space for a radial drive shaft and accessory pipes. The presence of these bodies relative to the rotor and OGV planes set up a non-axisymmetric flow field which required circumferentially nonuniform airfoil geometry to be defined using a special analysis. The vanes were grouped into five sets, each of a different camber angle.

### 3.4.2 Fan Rotor Mechanical Design

The fan rotor was a two-stage design consisting of a 32-bladed first stage and a 56-bladed quarter stage. Both stages of blades were made of titanium 6-4 forgings and were assembled to titanium 6-4 disks. The stage 1 disk was a ring-type design with axial dovetail slots staggered 10°. The quarter-stage disk was a spool-type design with a circumferential dovetail slot. Both rotors were assembled to a forward shaft made of 4340 stainless steel (Reference Figure 15).

The stage 1 blade rotor was shrouded at 55% span, had a tip diameter of 2.108 meters (83 in), a radius ratio of 0.342, and an aspect ratio of 2.6. The design tip speed was 411.5 m/sec (1,350 ft/sec).

The quarter-stage blade rotor was cantilevered, had a tip diameter of 1.337 meters (52.66 in), a radius ratio of 0.782, and an aspect ratio of 2.12. Its function was to supercharge the flow that fed the core (approximately 22% of total flow). Additionally, the quarter-stage island arrangement provided an excellent means for separating foreign objects from the core flow.

### 3.4.3 Fan Stator Mechanical Design

The mechanical design of the $E^3$ ICLS fan stator included the design of the fan frame, the fan containment and mid-case, the stage 1 vane assembly and flow splitter island, and the core OGV assembly. Figure 19 identifies the components of the ICLS Fan Stator assembly. The fan stator assembly utilized non-flight type materials and hardware designs to reduce the program costs. For example, the fan bypass vanes and bypass casing were made from solid low cost steel for the Full-Scale Fan Test rig and ICLS configurations. The FPS configuration is based on a hollow composite bypass vane integrated with an outer casing/nacelle structure. The ICLS fan containment features a modified CF6-50 steel casing to also reduce the hardware costs. The containment case design for the FPS is similar to current production engine containment case

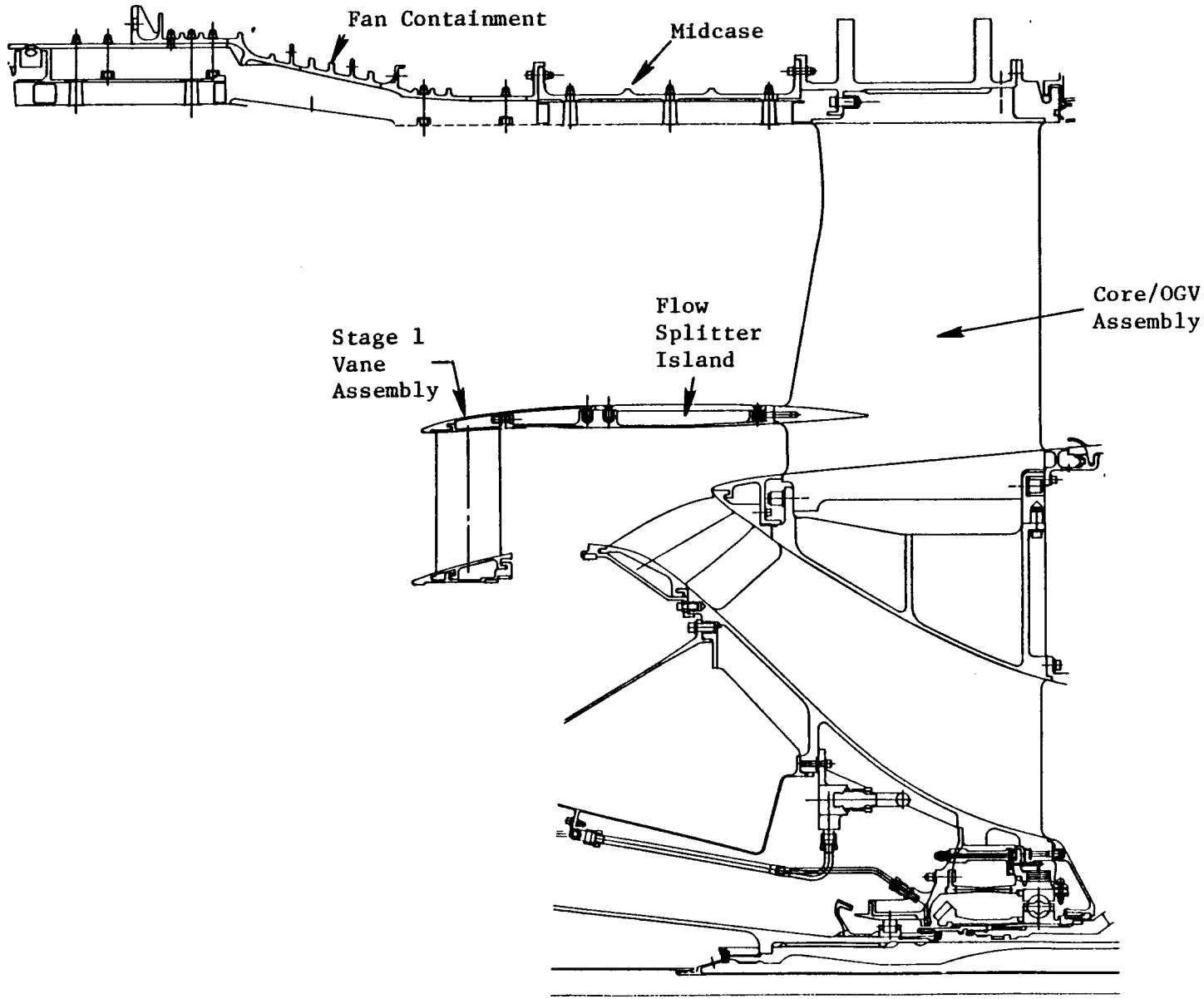


Figure 19. $E^3$ ICLS Design Performance

designs (CF6-80, CF34) which features a lightweight steel/honeycomb/kevlar structure.

The fan frame hardware (core frame and bypass vanes) used for the ICLS engine is the same hardware used for the Full Scale Fan Test (FSFT) program with some changes and additions. The fan frame configuration features an integral vane frame design in which the outer bypass vanes provide both the aerodynamic and structural function. The integral vane frame design uses five different bypass vane configurations in the vane row to correct for circumferential flow distortions caused by the proximity of the engine pylon structure to the frame. In the FSFT, the fan frame was mounted to the test facility at the outer bypass case. For the ICLS engine test, the forward engine mount brackets were located on the aft side of the core frame structure between the core and bypass flowpaths at $\pm 45°$ from 12 o'clock. In addition, to accommodate the fan-mounted gearbox required for the ICLS engine configuration, mount brackets were located on the outer fan frame casing. While provisions were made in the FSFT frame configuration for the gearbox driveshaft, additional hardware was required for the incorporation of the driveshaft interface with the frame for the ICLS configuration. Figure 20 shows the engine mount and gearbox mount locations on the fan frame and the bottom fan bypass vane assembly to accommodate the radial driveshaft to the gearbox and to accommodate the engine service lines. Figure 21 shows the modifications to the bypass vanes adjacent to the bottom bypass vane assembly for the gearbox driveshaft and service lines.

The fan casings including the containment case were unchanged from the FSFT configuration to the ICLS engine configuration. The removable panels in the containment case (forward of the fan) and in the mid-case were changed from hardwall used in the FSFT to acoustic (perforated plate face sheet with Kevlar bulk absorber as acoustic treatment material) for the ICLS engine configuration.

The vane assemblies for the Stage 1 vane and the core outlet guide vane (OGV) were the same for both fan stator configurations. These vane assemblies were geometrically representative of flight-type hardware and used lightweight

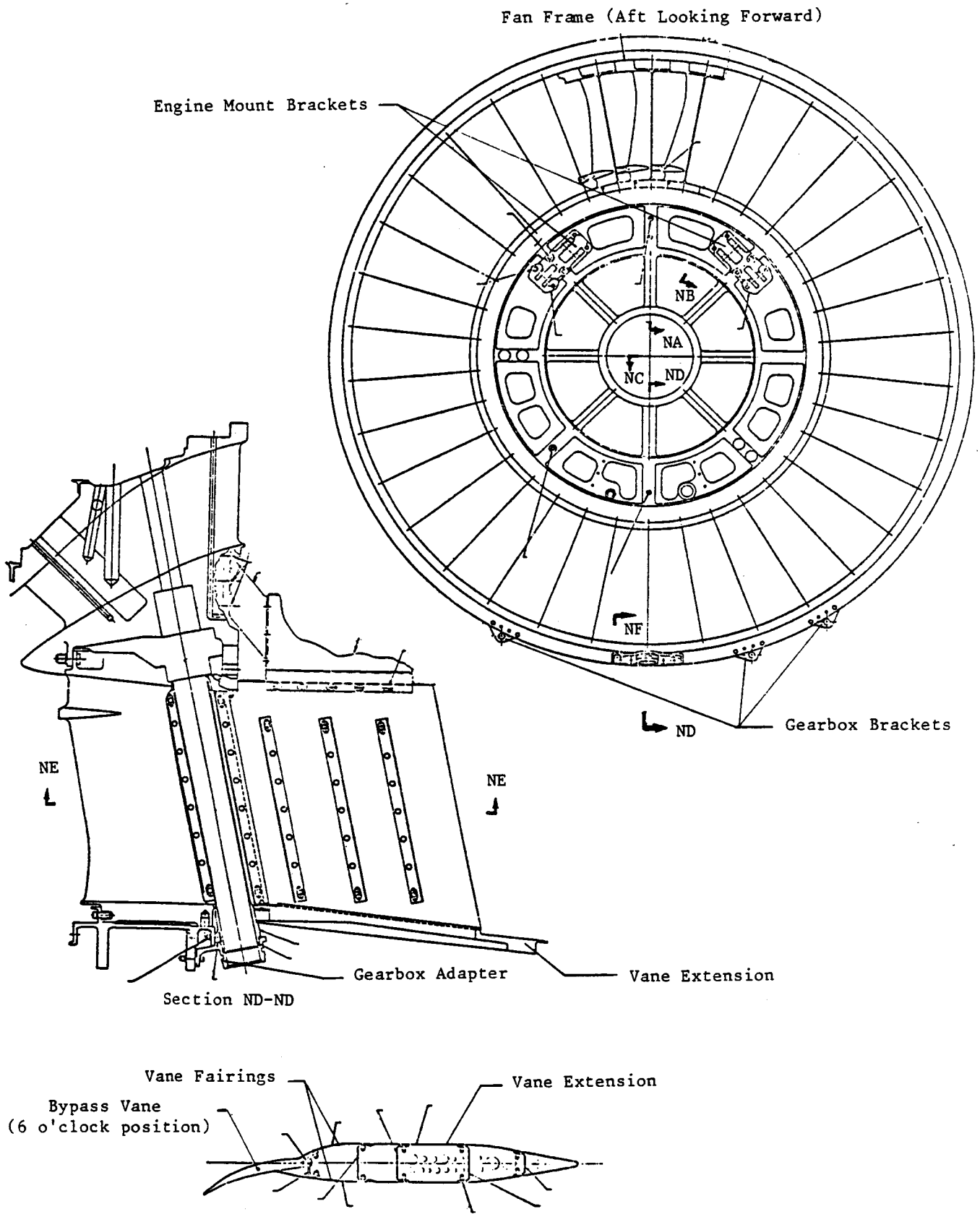


Figure 20. Fan Frame Modifications for ICLS Configuration

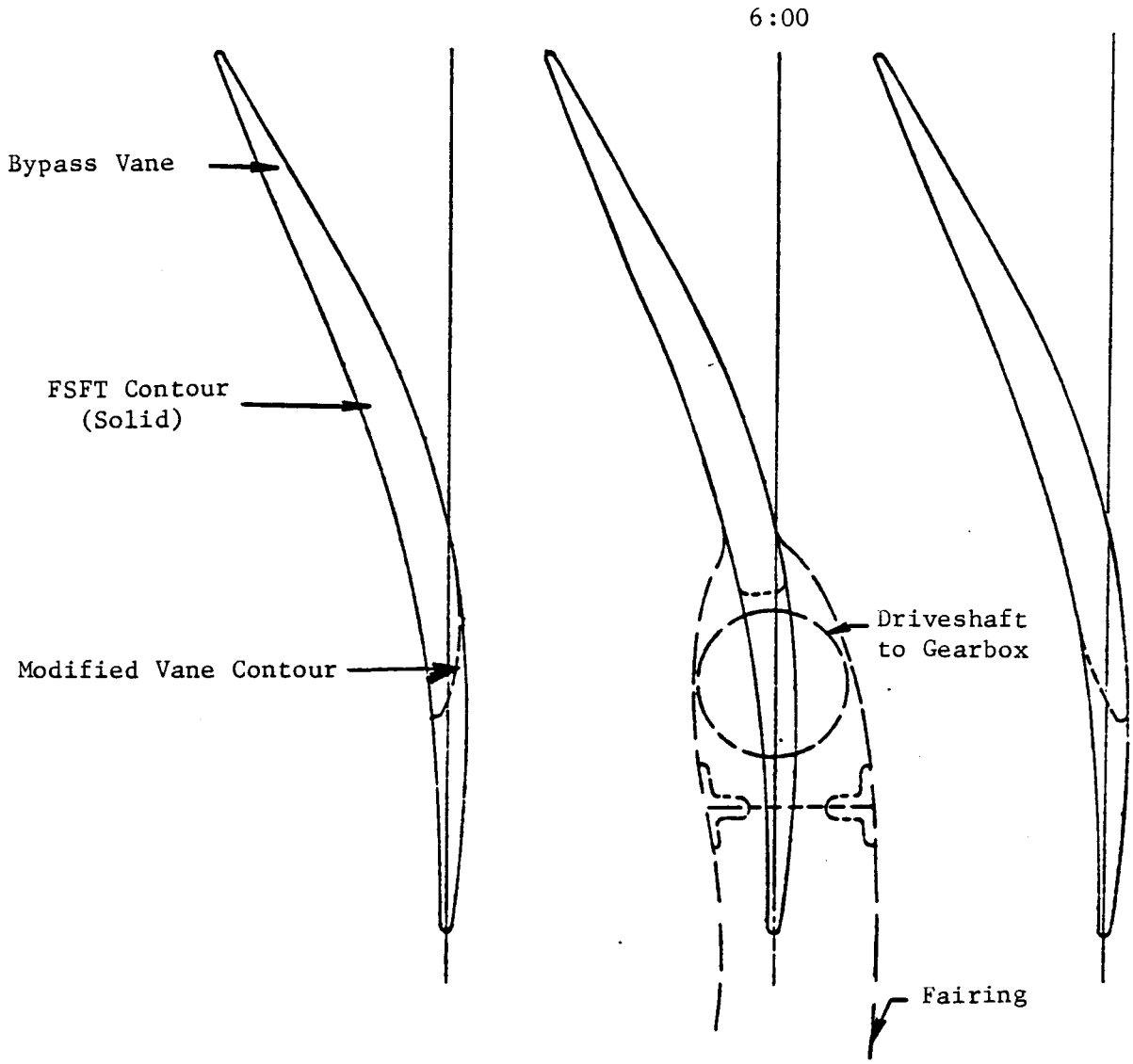


**Figure 21. Bypass Vane Modifications for ICLS Driveshaft and Fairings.**

materials where possible. In the Stage 1 vane assembly the flow splitter casing was aluminum with 403SS used in the vanes for cost reasons. (Ti 6-4 is used for the FPS design.) The inner shroud and outer fairing were steel for foreign object damage protection during the development tests but aluminum will be utilized where possible in the FPS configuration for weight reduction. The core OGV assembly utilized 7075 Al in the vanes and 6061 Al for the inner and outer shrouds.

## 3.5 CORE DESCRIPTION

The core, consisting of the high pressure compressor, combustor, and high pressure turbine, was tested as a separate vehicle in 1982. The core test vehicle is shown in Figure 22. The core was incorporated into the ICLS vehicle without having been disassembled. Design of the core components is presented in detail in the Core Design and Performance Report in Reference 3. This section provides an overview of the design of the core components.

### 3.5.1 Compressor Aerodynamics Design

The core compressor was an advanced technology, 10-stage unit designed to produce an operating line total-pressure ratio of 23 at a design corrected tip speed of 456 m/sec (1,495 ft/sec). Because of the high speed, pressure ratio, and aerodynamic loading, it is one of the most technically challenging designs that General Electric has built.

Core compressor aerodynamic design requirements were established primarily for the maximum-climb-thrust power setting at a flight condition of Mach 0.8 at 10.67 km (35,000 ft) altitude on a +10°C (+18°F) day. This operating condition placed the core compressor at maximum corrected speed, corrected airflow, and total pressure ratio, and was therefore defined as 100% design corrected speed. Compressor efficiency requirements, however, were most important at altitude cruise. Performance requirements for these operating conditions as well as requirements for sea level takeoff are listed in Table III. The operating line pressure ratios listed are for zero customer

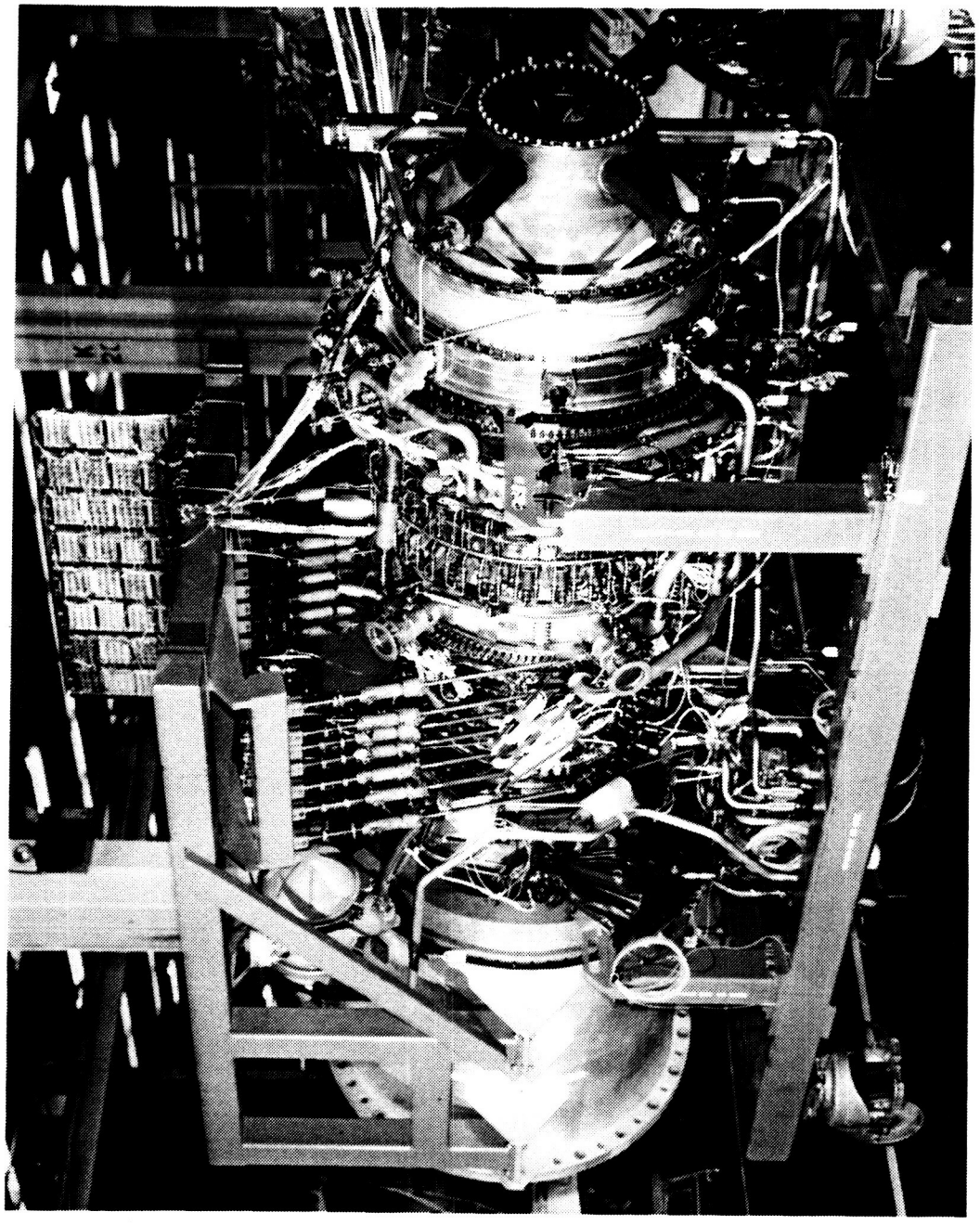

Figure 22. Core Test Vehicle.

Table III. FPS Compressor Aerodynamic Operating Requirements.

| Parameter | Max. Climb | Max. Cruise | Takeoff |
|---|---|---|---|
| Corrected Speed, % Design | 100.0 | 99.5 | 97.7 |
| Corrected Airflow, kg/sec (lbm/sec) | 54.4 (120.0) | 53.5 (118.0) | 49.3 (108.7) |
| Total-Pressure Ratio | 23.0 | 22.4 | 20.1 |
| Adiabatic Efficiency | 0.857 | 0.861 | 0.865 |
| Polytropic Efficiency | 0.903 | 0.905 | 0.908 |
| Inlet Temperature, K (°R) | 304.0 (547.9) | 301.4 (542.5) | 327.8 (590.1) |
| Inlet Pressure, $N/m^2$ ($lb/in.^2$) | 59,641.8 ( 8.65) | 58,055.9 ( 8.42) | 150,586.8 (21.84) |

bleed air and zero power extraction. The performance goals in Table III are for the fully developed FPS. The efficiency goal for the core and ICLS engines is one point lower than the FPS goal, reflecting current $E^3$ technology rather than the expected 1986-1990 technology of the fully developed FPS product engine.

The aerodynamic design of the airfoils for the $E^3$ core compressor included the design of both transonic and subsonic rotor blades, subsonic stator vanes, and an inlet guide vane. Fundamentally, the approach utilized for all blade and vane designs was one of tailoring stream surface blade shapes to produce specific airfoil surface velocity distributions. The first four rotors were transonic blade rows and were designed utilizing techniques employed for the advanced fan stages. The remaining six stages of rotor blades and all stages of stator vanes operate in a subsonic flow environment. Figure 23 shows Stator 6, representing a typical stator. The airfoil section is shown, as well as the unique stagger angle distribution used for the stator vanes.

A casing port for customer bleed and compressor active clearance control (used subsequently for low pressure turbine cooling and purge) was located at rotor 5 exit. Another casing port for starting bleed and high pressure turbine cooling air was located at Stage 7 exit. Start bleed capability was deleted from ICLS. The IGV and Stators 1 through 6 were variable. However, the ICLS Stators 5 and 6 were locked in place, conforming to the FPS compressor.

The original aerodynamic design of the core compressor was completed in the second quarter of 1979. Three component tests were conducted: the front six variable-stator stages were tested in the first quarter of 1980; the full 10-stage compressor was tested for the first time during the first quarter of 1981; and a second version of the full 10-stage compressor was tested in early 1982. Various design refinements made as a result of the data obtained during these experimental evaluations were incorporated into the final version of the compressor which was first tested in the $E^3$ core engine. The same hardware

was used in the ICLS turbofan engine. A new fully-ganged variable stator actuation system was added to the ICLS engine compressor for control of the IGV and Stators 1 through 4. No other changes were made; therefore, the ICLS engine compressor was aerodynamically identical to the core engine compressor.

### 3.5.2 Compressor Mechanical Design

Design requirements for the production engine called for an installed service life of 18,000 hours without engine removal and a total useful life of 36,000 hours. With the exception of some items that were reworked for instrumentation, all components of the core compressor met these requirements.

A cross section of the 10-stage HP compressor rotor is shown in Figure 24. Unique features contributing to the design objectives of producing a lightweight, rugged, efficient rotor are denoted. Note the use of a single bolt joint at midrotor in order to yield a short, stiff structure. A photograph of the rotor is shown in Figure 25. The use of low aspect ratio airfoils produces a high tolerance to FOD and stalls. Sealing the blade dovetails and polishing the airfoils provide an increase in compressor efficiency. Utilization of fan discharge air to cool the rotor bores helps to optimize rotor-stator clearances, thus providing additional efficiency gains. The rotor materials selected to achieve a high strength, cost effective design are shown on Figure 26.

The compressor stator cross section is shown in Figure 27. Unique features of the design are denoted. The titanium fire prevention requirement was met by the use of nontitanium casings and vanes. To improve compressor cruise performance, the aft case was designed to provide active control of rotor-stator clearances. This was accomplished by isolating the casing structure from the hot flowpath gases and then bathing the structural rings with cooler Rotor 5 discharge air to shrink the casing closer to the rotor blade tips. This cooling air was collected in the annulus over Rotor 10, then was ported through the forward case and was piped aft where it was used to cool the LPT and rotor cavity (Reference Figure 28). The flow of air was controlled by a fuel-activated valve.

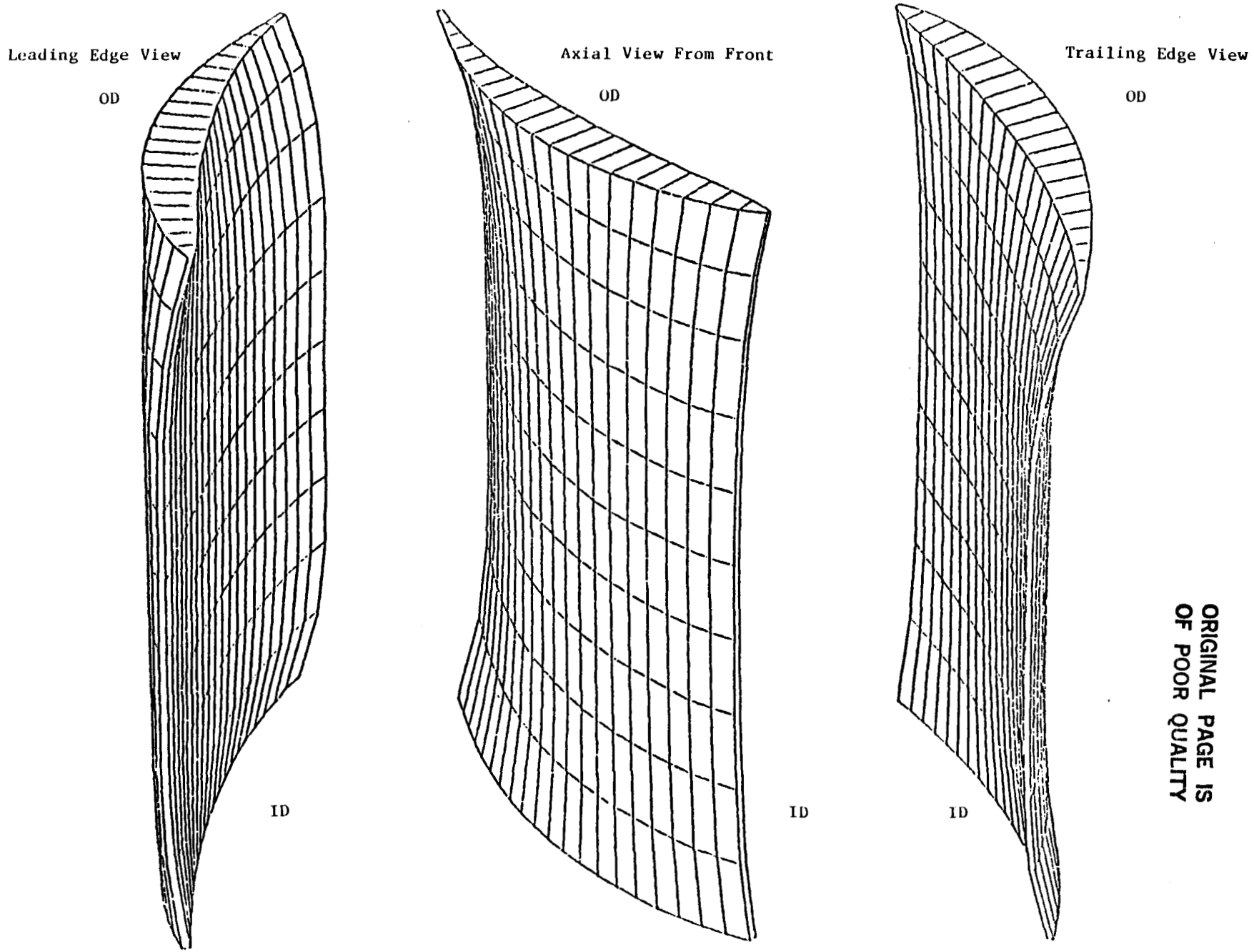


Figure 23. Three-Dimensional Sketch of Stator 6.

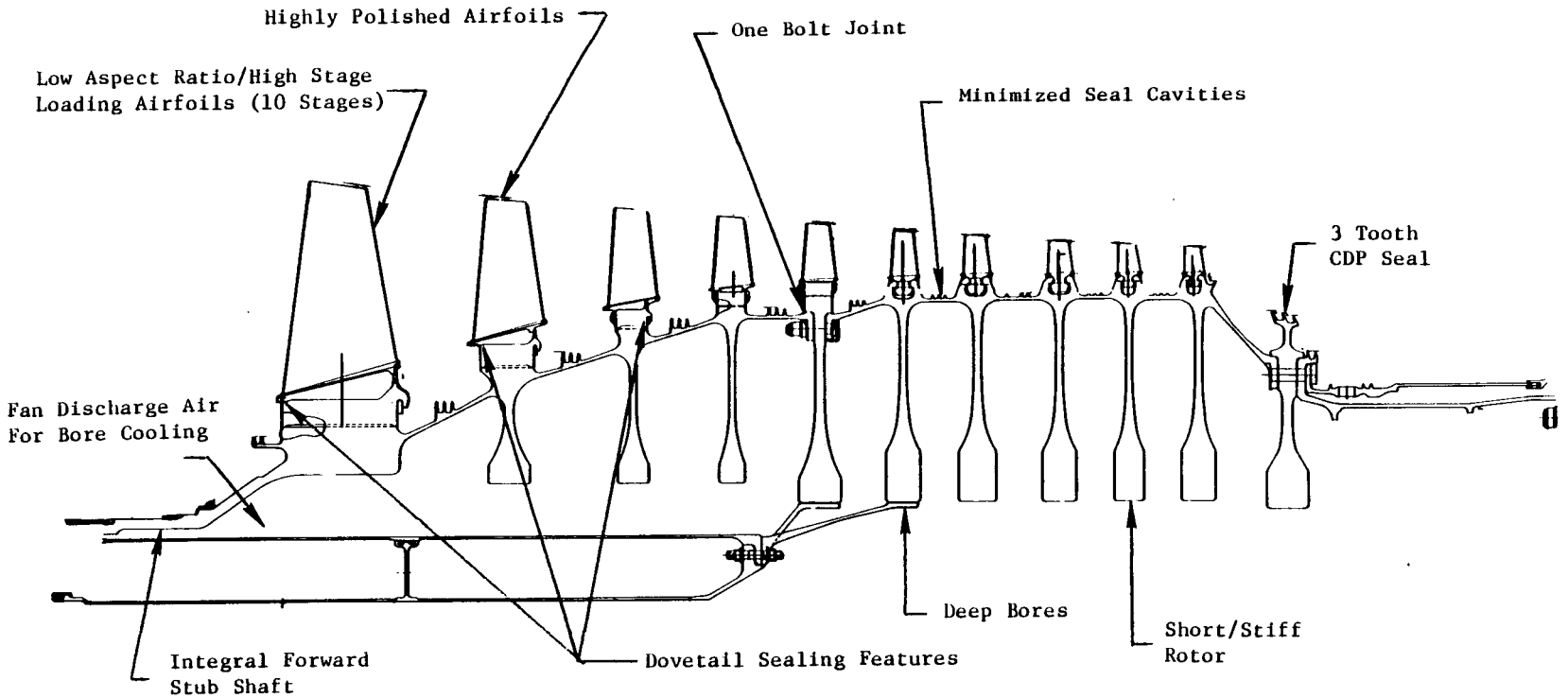


**Figure 24. Compressor Rotor Design Features.**


Figure 25. Compressor Rotor Hardware

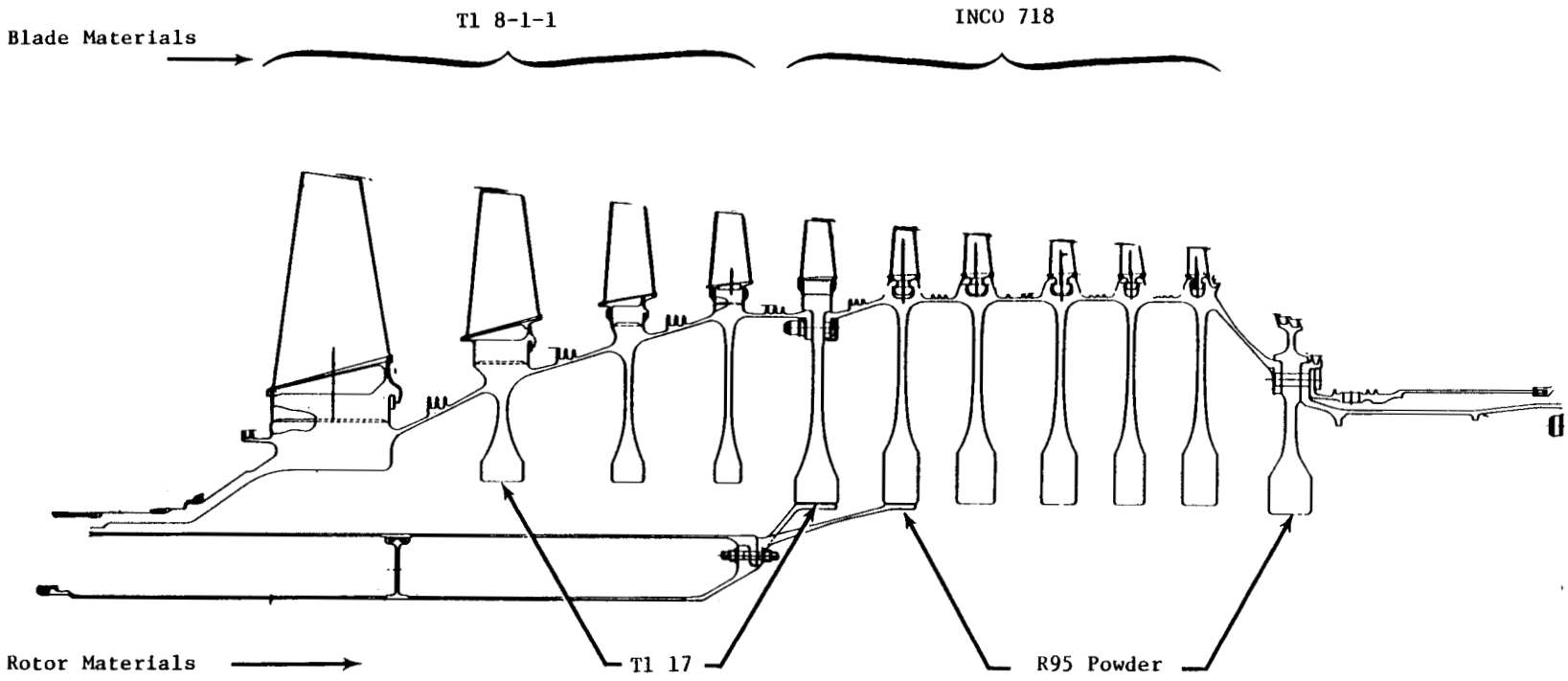


Figure 26. Core and ICLS Compressor Rotor Materials.

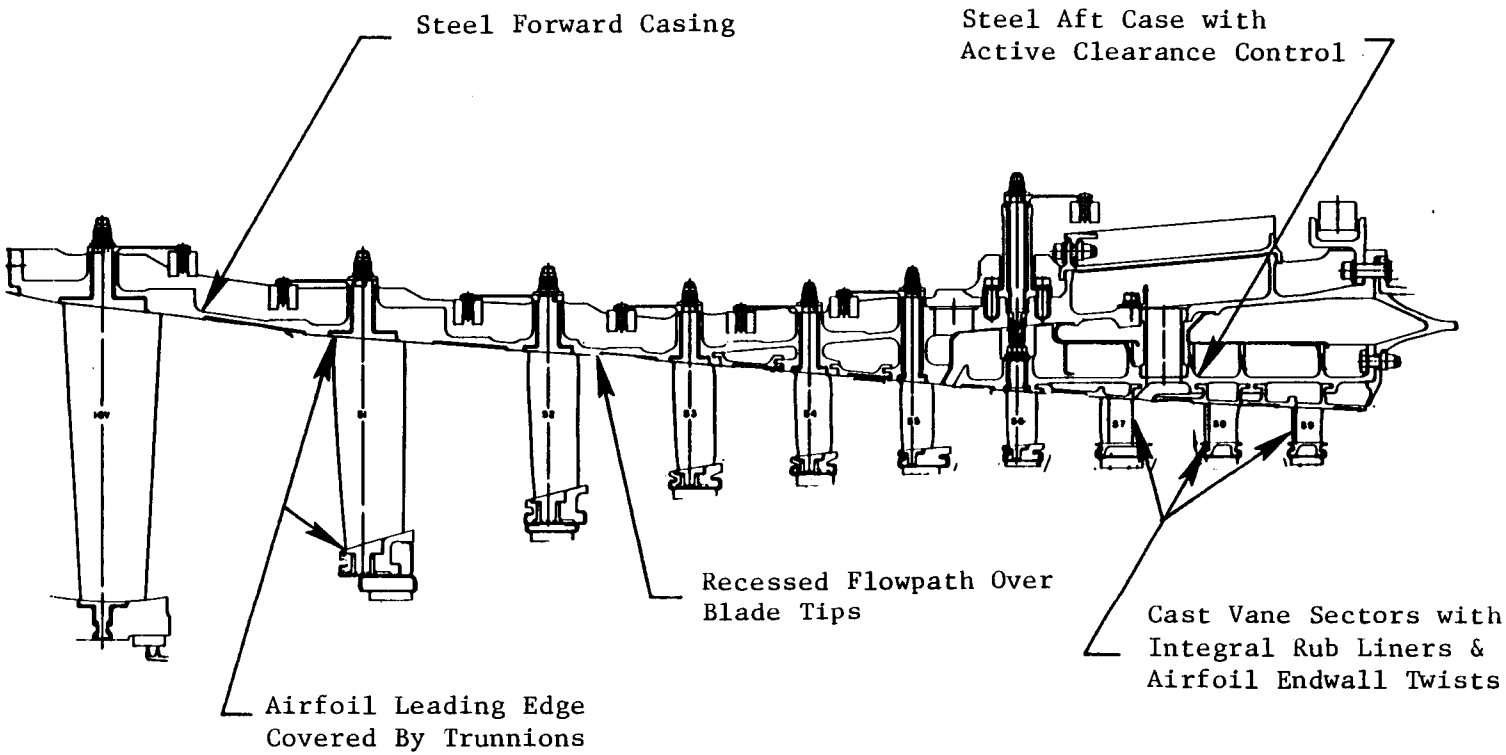


**Figure 27. Compressor Stator Design Features.**

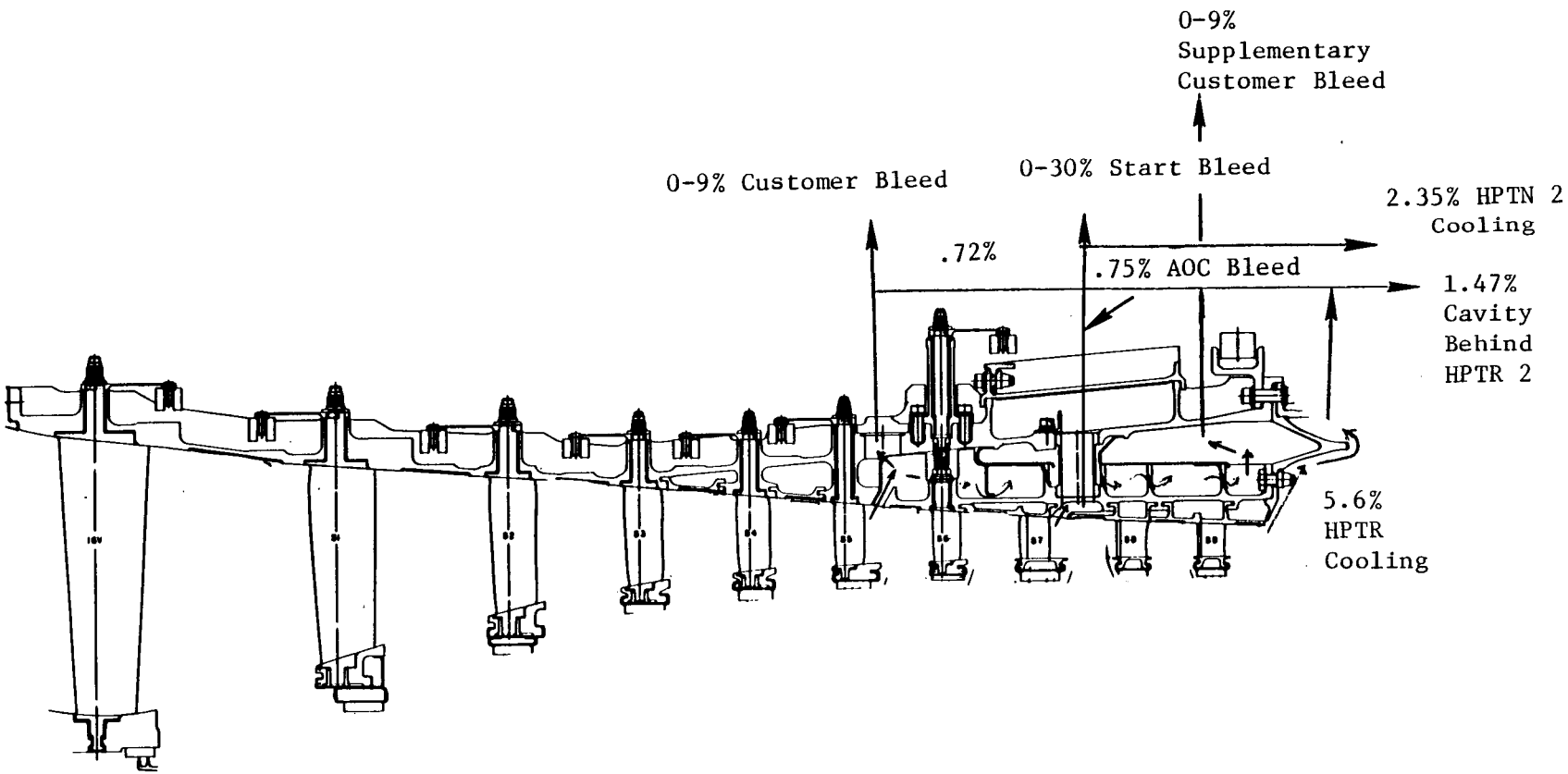


**Figure 28. Compressor Cooling Flow (Bleeds).**

Variable vane leading edge tip were covered by the OD/ID trunnions to prevent circumferential crossflow, thereby enhancing performance. Internal GE research tests have shown that small performance gains can result from recessing the flowpath over the blade tips, a feature incorporated on the $E^3$ compressor. End-wall losses were reduced by uniquely contouring the airfoil ends. Because of the end-wall contouring, the fixed geometry vanes could not be fabricated by ordinary methods but had to be cast.

The compressor diffuser discharge, shown in Figure 29, was a unique cast structure featuring a flowpath that was split into two annular passages and supported by hollow struts. A portion of the air exhausting at the splitter island was ducted inboard through the hollow struts to provide cooling for the HP turbine. The geometry of the diffuser was so complex that it required an advancement in the state of casting technology in order to be produced. In the early designs, it was planned that the outlet guide vane (OGV) ring would be cast integrally with the diffuser. However, the successful welding of the OGV ring to the diffuser for the core engine has proved this to be a more workable approach.

Inlet guide vanes through Stator 6 were variable on the compressor test rigs, on the core engine and on the ICLS engine to allow for complete performance mapping over the operating range. It was originally intended that Stators 5 and 6 would be fixed in the product engine; it was demonstrated during the core and ICLS tests that this is acceptable.

The ICLS compressor featured a variable stator vane (VSV) torsion bar actuation system which had the capability of providing nonlinear vane angle variability on a stage-to-stage basis. The system consisted of two torsion bars located 180° apart, each driven by a hydraulic actuator. Motion was transmitted to each VSV actuation ring through links and adjustable turn buckles (Figure 30).

Compressor stator materials are listed in Figure 31. The M152 steel alloy was chosen for the casings because its coefficient of expansion closely matched that of the rotor structure, making clearance control easier. Rotor

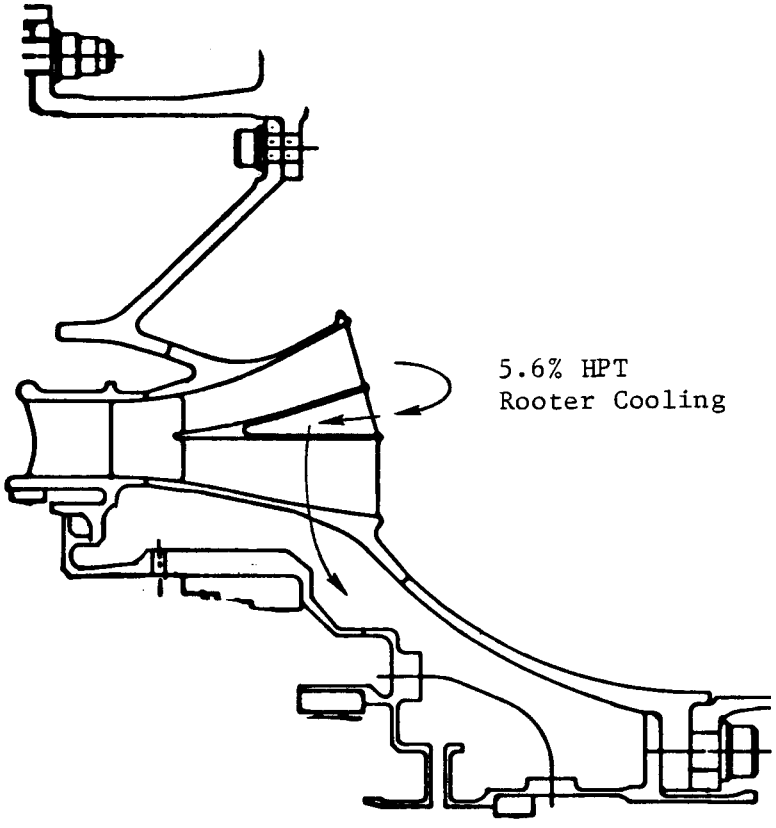


**Figure 29. Compressor Diffuser Discharge.**

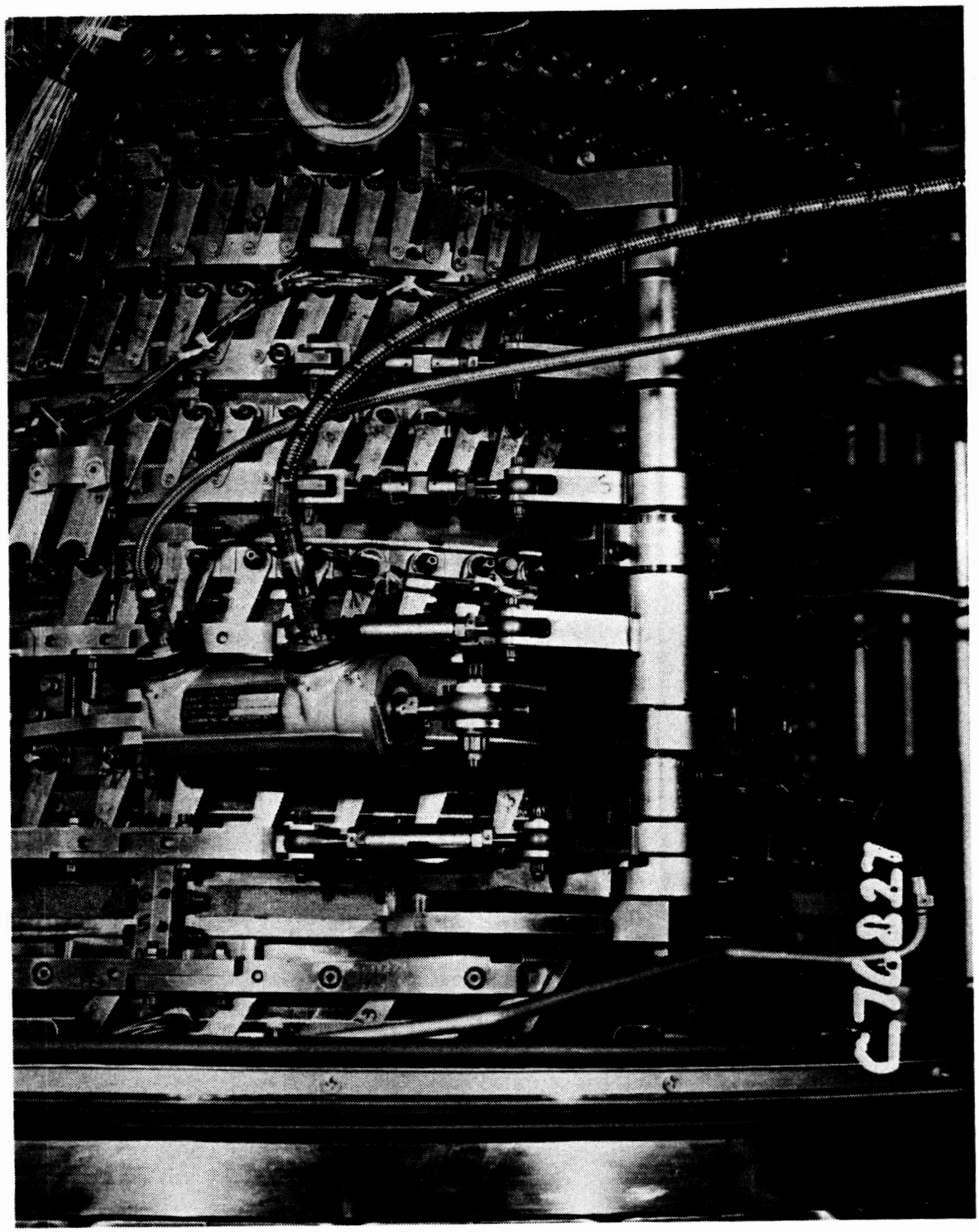


Figure 30. Compressor Variable Stator Actuation.

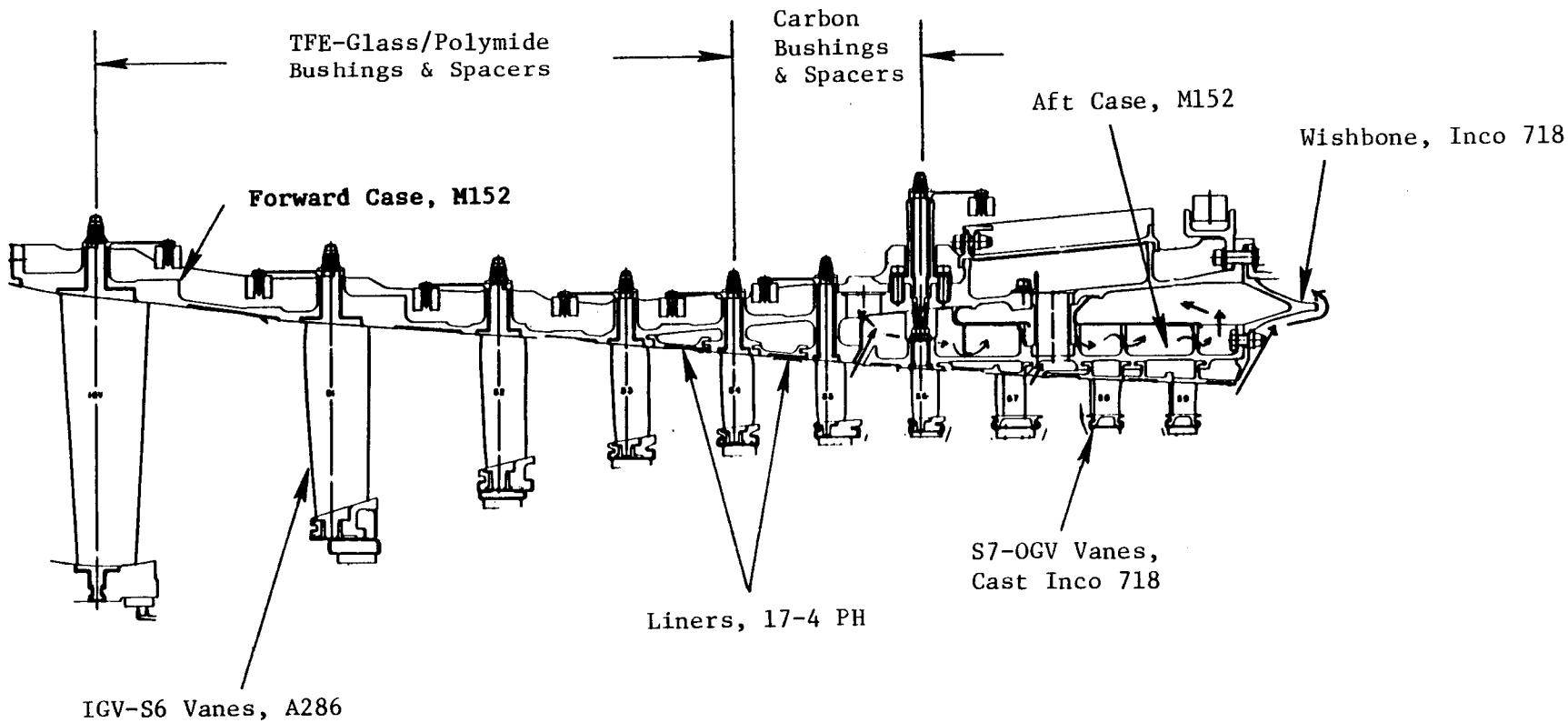


| Rub Material | Honeycomb | Shrouds | Interstage Seals |
|---|---|---|---|
| Stages 1 - 4, Al-Br-Ni-Cg | Hastelloy X | IGV and S1, 6061-T6 | Inco 600 |
| Stages 5- 10, Metco 443 Ni-Cg | | S2 - S4, 17-4 PH | |
| | | S5 - S6, Inco 718 | |

**Figure 31. Compressor Stator Materials.**

rub lands were coated with current, proven production-engine materials. Variable stator vane bushing materials were chosen after extensive development and test programs to assure they would meet engine life requirements.

Compressor bleeds, their quantities and uses, are summarized in Figures 28 and 29. During the initial design phases, one area of concern was the starting of a high pressure ratio engine. Provisions were made to bleed up to 30% of Stage 7 air to aid in starting. A portion of the core test was dedicated to investigating engine start characteristics. As a result of these tests, it was determined that the engine could be started without the use of compressor bleed.

### 3.5.3 Combustor Aerodynamic Design

The $E^3$ combustor was a short length, double annular design shown in Figure 32. The double annular feature was used to provide low emissions over a wide range of power levels. Only the outer pilot zone was used at low power levels, and it was tuned for low fuel-air ratios. At higher power levels, both zones were used. The inner main zone was tuned for higher fuel-air ratios.

The $E^3$ combustor used dual cone nozzles for fuel injection. Compressor discharge airflow was directed to the combustor by a split duct prediffuser. Forty-eight percent of the air flowed through the outer passage of the prediffuser toward the pilot stage dome, and the remaining 52% was directed toward the main stage dome by the inner passage of the prediffuser. The dome cups of the pilot stage and the main stage were each comprised of axial primary and counterrotating radial secondary airflow swirlers. The liners were of double wall construction and used impingement plus spent-film cooling on the segmented (shingle) section adjacent to the hot gas stream.

Fuel injection for each $E^3$ combustor dome was provided by duplex-type fuel pressure atomizing nozzle tips mounted on a single stem. Each of the two tips had a low-fuel-flow primary system for good atomization at low power

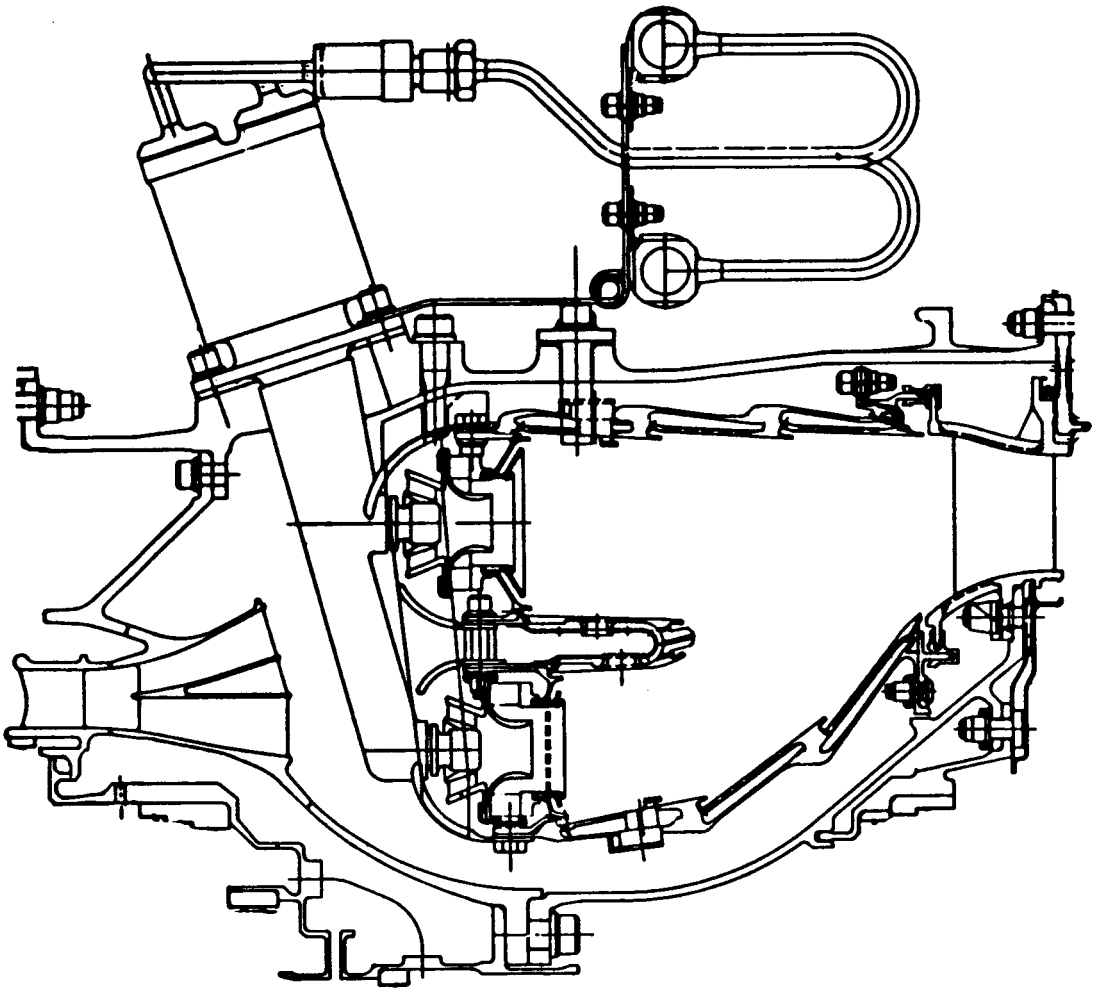

Figure 32. Combustor Cross Section.

operating conditions and a high-fuel-flow secondary system to achieve the required fuel flow levels at high power. Fuel flow was supplied to the fuel nozzles by an annular manifold system. Fuel nozzle inlet check valves were intended to keep the manifold full and pressurized during shutdown to prevent fuel leakage into the combustor and to reduce start times. Fuel flow to the duplex nozzle tips was controlled by each of two scheduling valves (one for each tip) located in the housing above the stem. The fuel nozzle stem was encased in a heat shield to insulate the fuel from hot compressor gas temperatures. Each fuel-carrying tube within the stem was surrounded by a clearance gap to provide additional insulation. The fuel nozzles were arranged in the combustor to provide the most uniform fuel distribution based on the results of flow calibrations.

### 3.5.4 Combustor Mechanical Design

The $E^3$ combustor with the materials selection called out is illustrated in Figure 33. Photographs of the assembly are shown in Figures 34 and 35. A centerbody structure separated the outer diameter pilot zone from the inner main zone of the combustor. The double annular dome design consisted of 60 identical swirl cups. Fuel was injected into the combustor through 30 dual-tip fuel nozzle assemblies. Each nozzle featured independent fuel metering. The combustor utilized a double-wall shingled liner design to provide long life. The combustor assembly was supported at the forward end by 30 support pins positioned radially to transmit all loads from the liners to the outer combustor casing. The combustor-to-stator interface was sealed with fishmouth seals which accommodate axial and radial thermal expansion and assembly clearance stackups between the components.

The outer casing supported the combustor assembly, fuel nozzles, fuel delivery system, and ignition system. Ports were provided in the casing for borescope inspection, compressor bleed, and instrumentation leadout.

The liner assembly consisted of three axial rows of shingles in the pilot and main zones which were installed in outer/inner support liners. Each

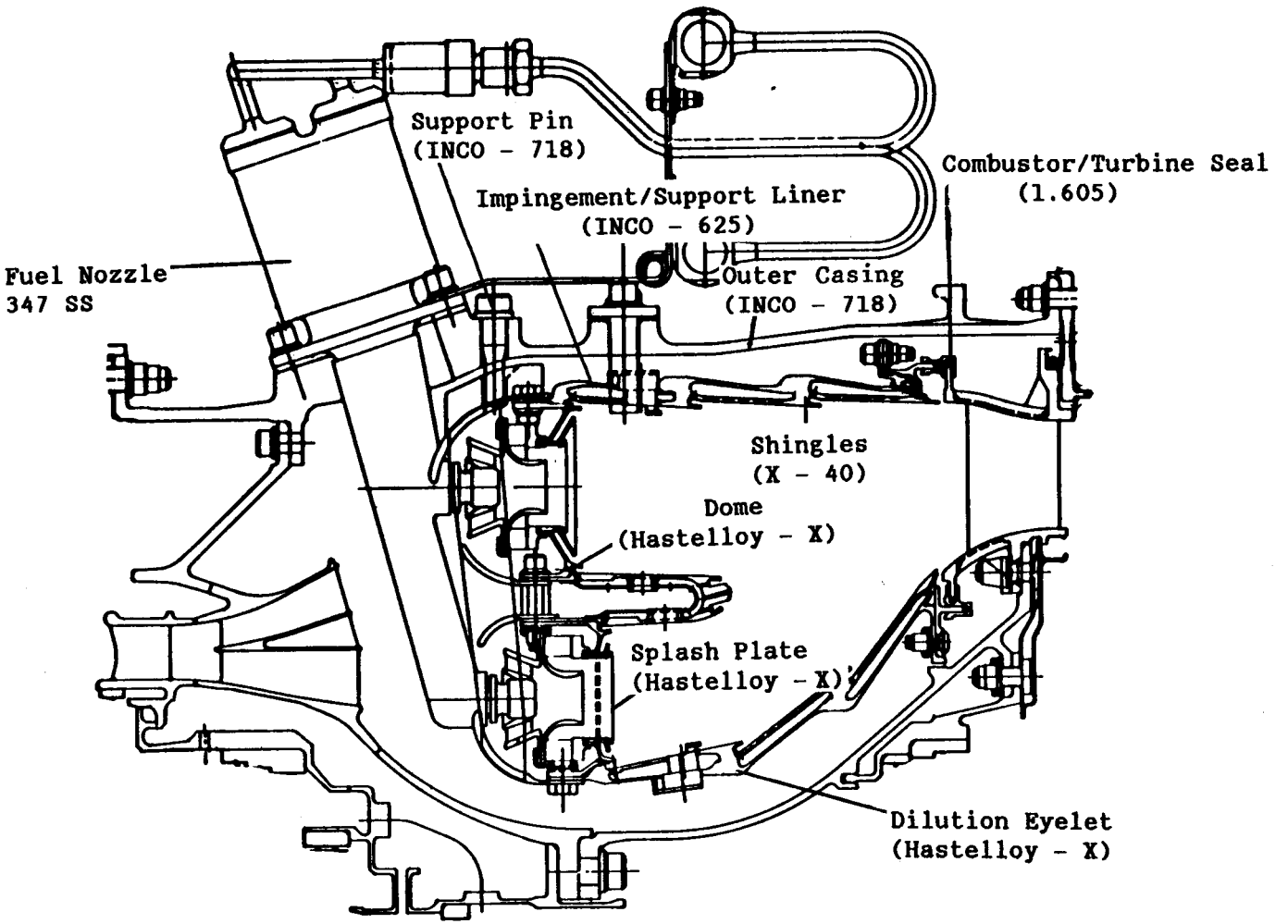


Figure 33. Combustor Materials Selection.

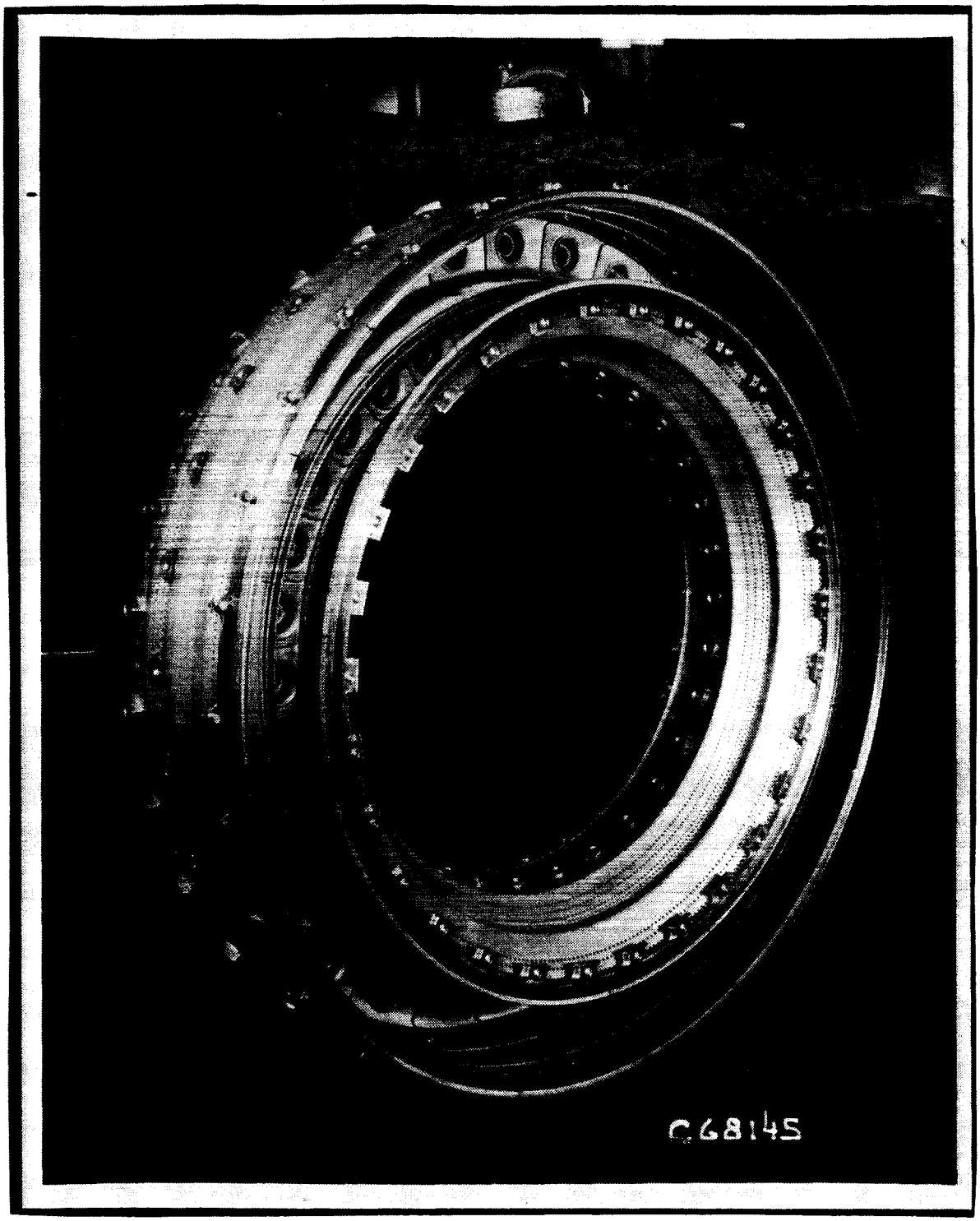


Figure 34. Combustor Liner/Dome Assembly - Aft Looking Forward

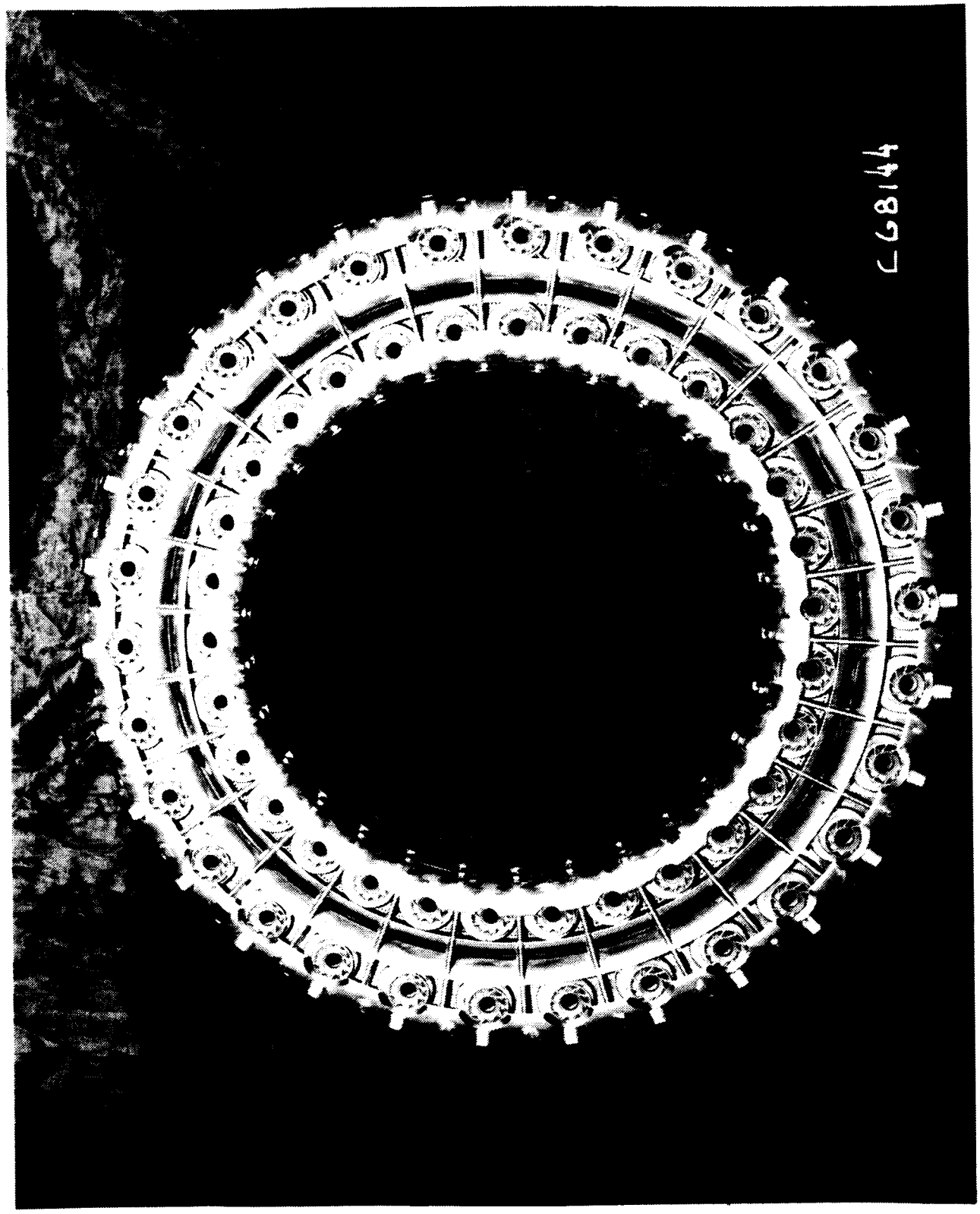


Figure 35. Double Annular Dome and Cowling - Forward Looking Aft

row of shingles formed an annular impingement cavity with the support liner. The impingement and dilution holes were laser drilled into the support liners which were machined from forgings.

### 3.5.5 High Pressure Turbine Aerodynamic Design

To meet cycle requirements and goals of the program, a two-stage turbine of moderate loading was selected. The aerodynamic design point was chosen to be the maximum climb condition at Mach 0.8 and 10.67 km (35,000 ft). This point was determined to be the most stringent, based on a comparison of ICLS and FPS requirements.

Following completion of the turbine aerodynamic design, early compressor rig testing of the first six stages indicated the potential for a stall margin deficiency relative to pretest prediction. In an effort to reduce this stall margin deficiency, the flow area of the first stage stator of the high pressure turbine was increased by 4%. This was accomplished by rotating the vane airfoils to the desired throat area.

The significant turbine operating point data are summarized in Table IV. The efficiencies presented in this table represent the goals of the program. Note that the open Stage 1 stator flow area is intended only for core and ICLS use.

### 3.5.6 High Pressure Turbine Mechanical Design

The description of the high pressure turbine (HPT) is covered in detail in the $E^3$ Core Design and Performance Report, Reference 1. A cross section of the HPT is shown in Figure 36. The Stage 1 nozzle assembly, Stage 2 nozzle assembly, and rotor assembly are shown in Figures 37, 38, and 39, respectively.

A few modifications were made after completion of the core engine test and before completing the buildup of the ICLS engine. Otherwise the HPT tested in the ICLS engine was identical to the core engine. The HPT was not disassembled between the core and ICLS engine tests.

Table IV. HPT Aero-Thermodynamic Design Requirements.

| Parameter | Units | ICLS | | FPS | | |
|---|---|---|---|---|---|---|
| | | Max. Climb | Max. Climb + 4% $A_{41}$ | Max. Climb | Max. Cruise | Sea Level Takeoff + 27°F |
| Inlet Temp, $T_{41}$ | K | 1588 | 1591 | 1557 | 1515 | 1618 |
| | ° R | 2858 | 2863 | 2802 | 2728 | 2913 |
| Energy, $\Delta h/T$ | J/kg·K | 353.4 | 353.4 | 355.5 | 353.4 | 354.6 |
| | Btu/lbm/° R | 0.0844 | 0.0844 | 0.0849 | 0.0844 | 0.0847 |
| Speed, $N/\sqrt{T}$ | rad/sec·√K | 33.19 | 33.78 | 33.56 | 33.68 | 34.22 |
| | rpm/√°R | 236.2 | 240.4 | 238.9 | 239.7 | 243.6 |
| Corrected Flow, $W\sqrt{T}/P$ | g√K/sec·Pa | 0.8648 | 0.8913 | 0.8643 | 0.8638 | 0.8628 |
| | lbm√°R/sec·psi | 17.65 | 18.19 | 17.64 | 17.63 | 17.61 |
| Efficiency, $\eta_T$ % | | 91.9 | 91.9 | 92.4 | 92.4 | 92.1 |

ORIGINAL PAGE IS
OF POOR QUALITY

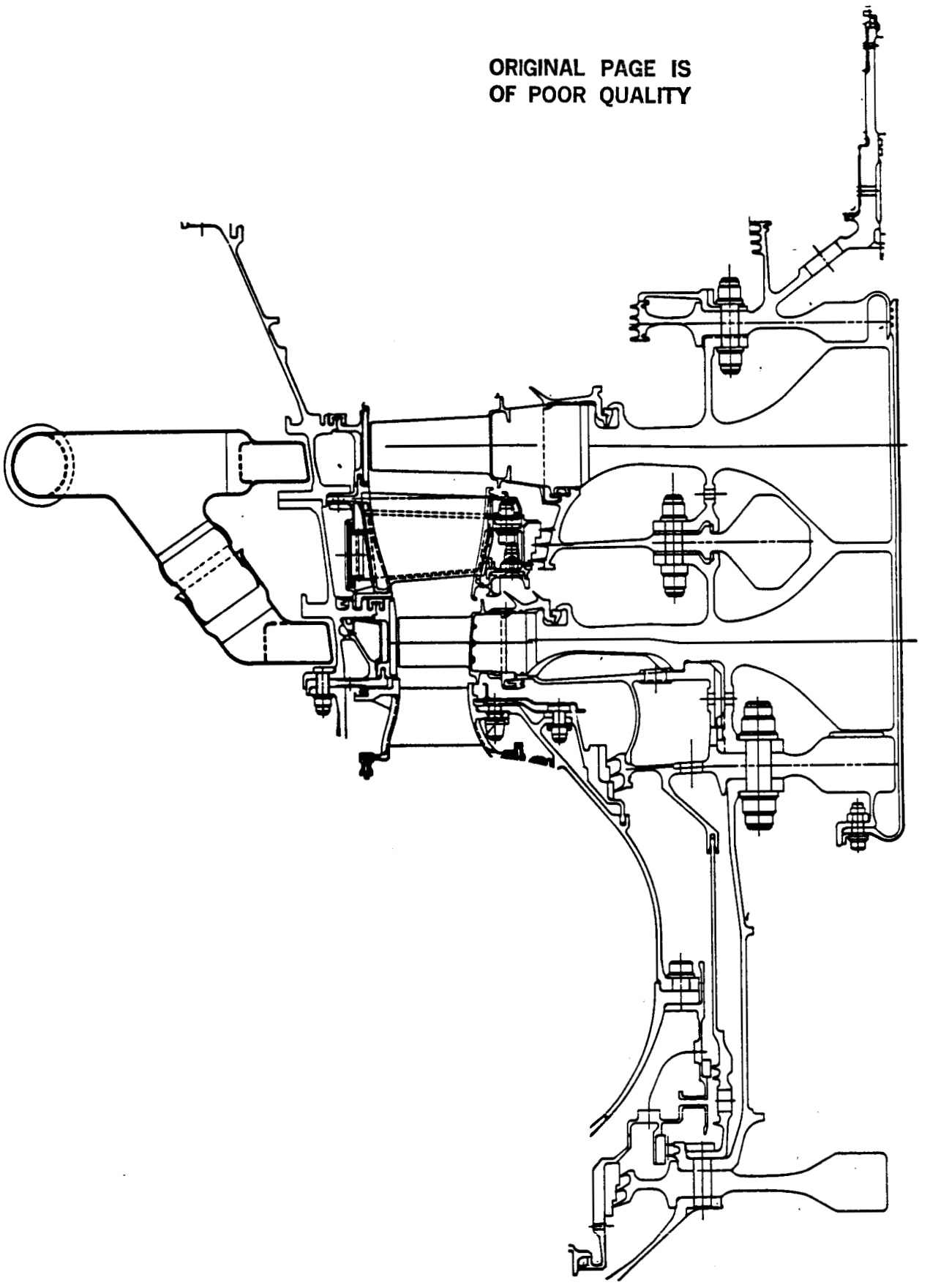

Figure 36. High Pressure Turbine (HPT) Cross Section.

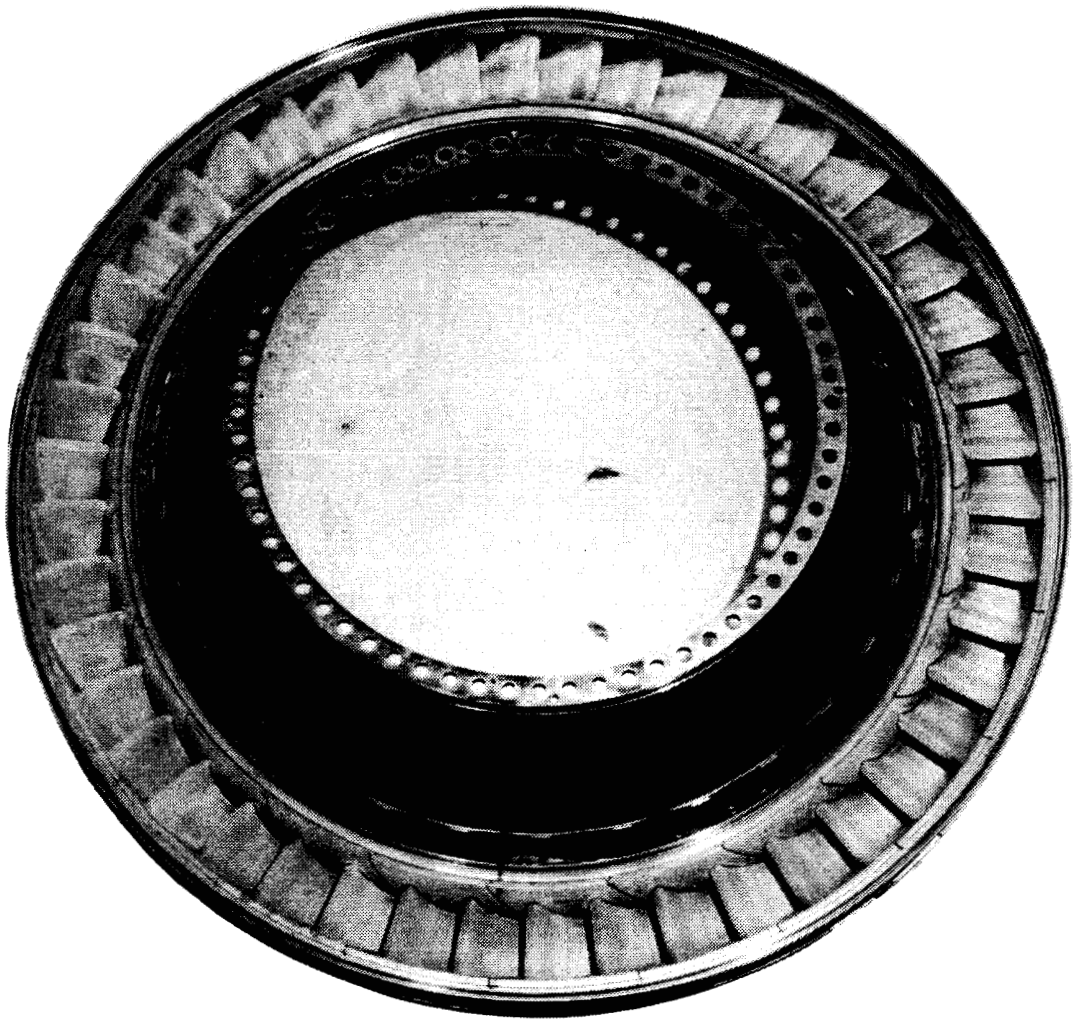

Figure 37. HPT Stage 1 Nozzle Assembly

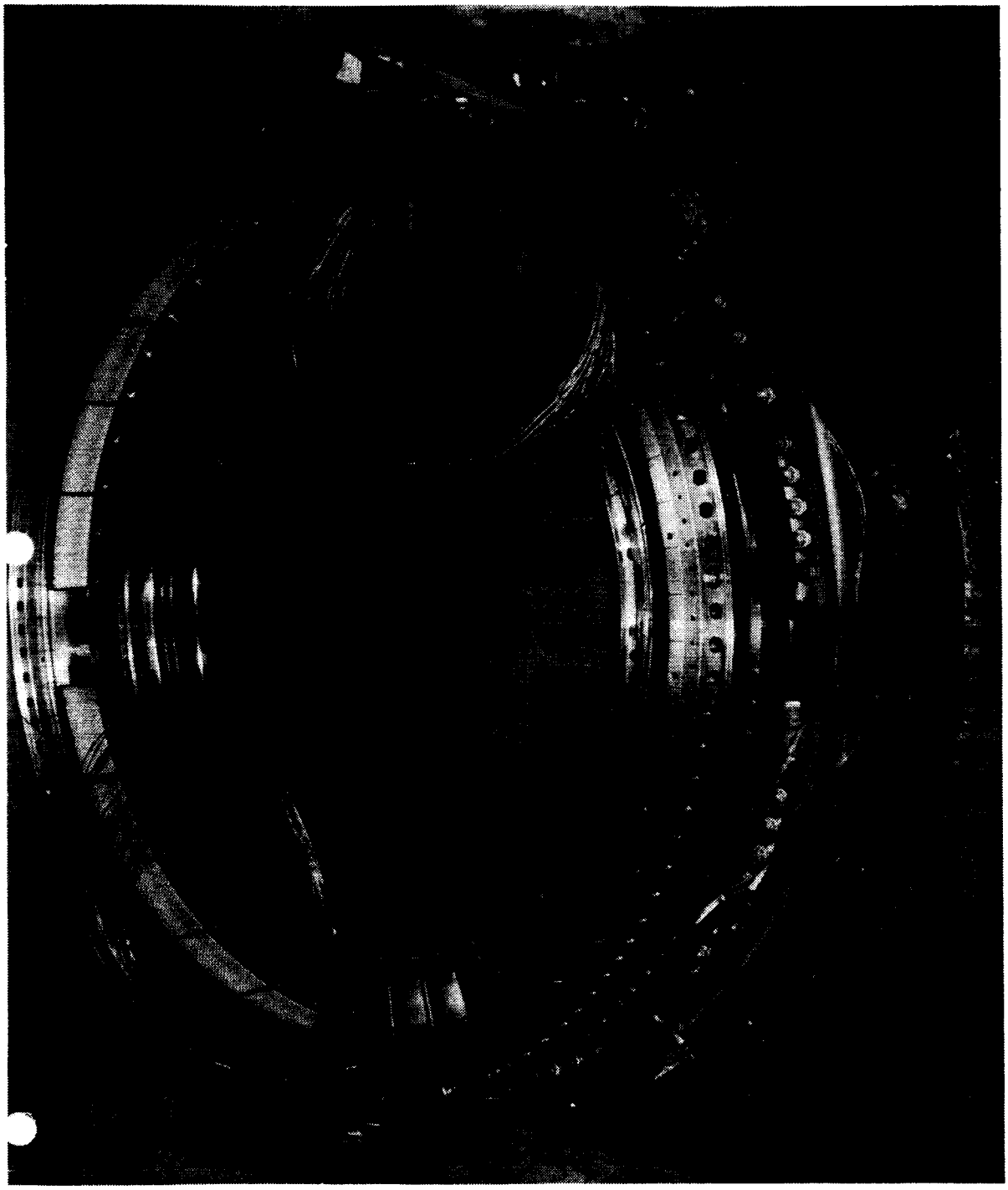

Figure 38. HPT Stage 2 Nozzle Assembly.

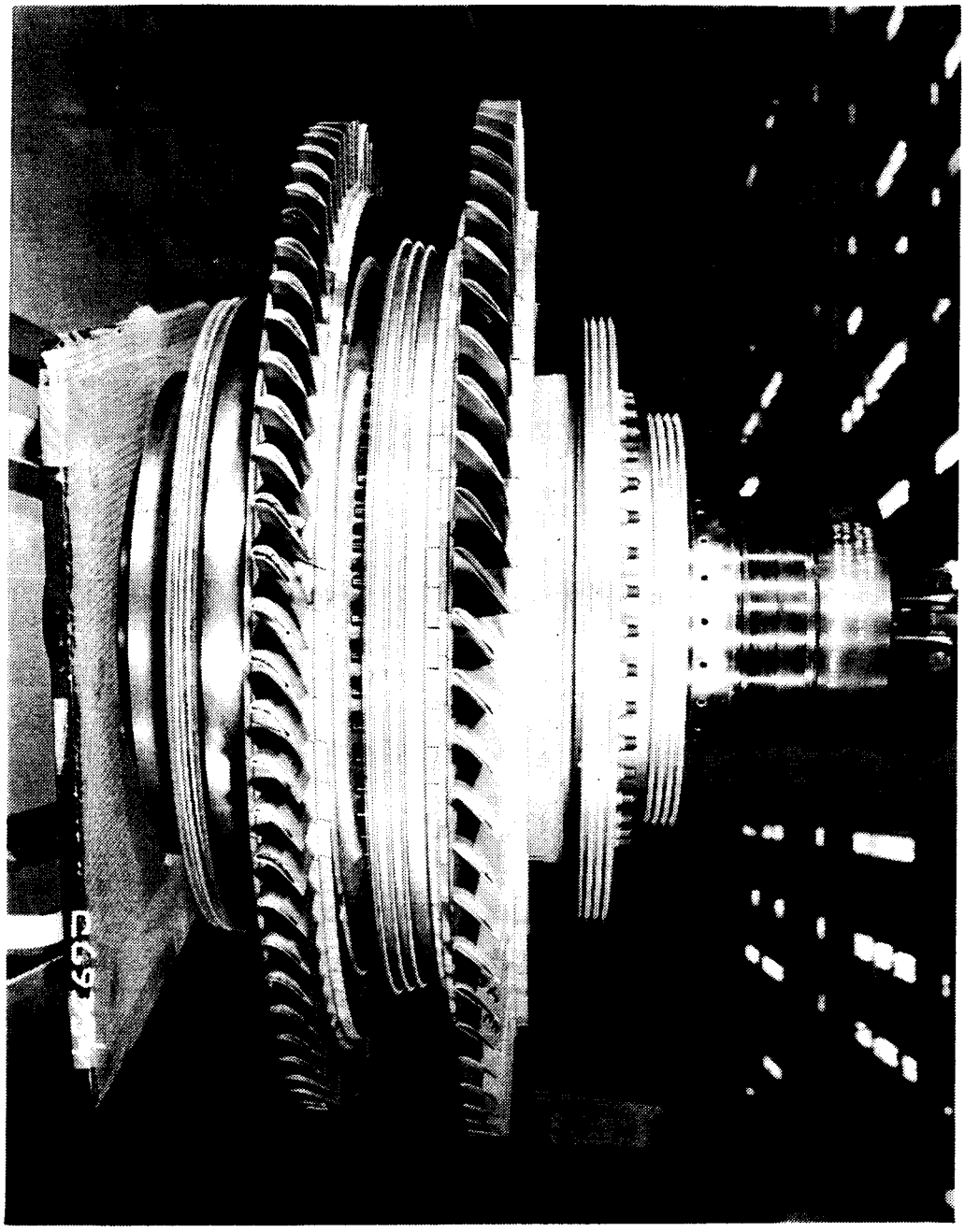

Figure 39. HPT Rotor Assembly.

The changes consisted of adding impingement holes to all four sectors of the ACC cooling air manifold as shown in Figures 40 and 41. These holes were added to the same manifolds used for the core engine tests and were flow-checked prior to assembly for the ICLS test. The holes were added to improve the amount of radial clearance closure capability relative to the levels obtained during the core tests. The total increase in fan bleed air due to the addition of these holes was 50% relative to the non-reworked manifolds.

The "E" seal (shown in Figure 42) located between the aft face of the Stage 2 shroud and the LP turbine outer liner was unintentionally left out during the core assembly. The purpose of the "E" seal is to minimize hot gas ingestion into the cavity formed between the liner and shroud and also to minimize the Stage 5 bleed air from leaking into the flowpath. The "E" seal was subsequently assembled for the ICLS tests.

## 3.6 LOW PRESSURE TURBINE DESCRIPTION

The low pressure turbine (LPT) is a five-stage, highly loaded, low through-flow design with a high outer wall slope (25°). It is close coupled to the HPT via a 7.6 cm (3 in) axial length transition duct. The casing is a 360° (nonsplit) structure. Blade tip and seal clearances are controlled by an active clearance control (ACC) casing cooling system. Figure 43 presents the LPT flowpath. The ICLS low pressure turbine represents an earlier FPS design. The flowpath of the current FPS LPT is different in that it has the outward slope of both the outer wall and inner wall continued through the last two stages.

### 3.6.1 Low Pressure Turbine Aerodynamic Design

Table V presents LPT cycle data for the ICLS max-climb aerodynamic design point and, for comparison, data for the FPS maximum climb, maximum cruise, and sea level takeoff points. Note the relatively small differences between climb and cruise for the FPS. Note further that the ICLS has been

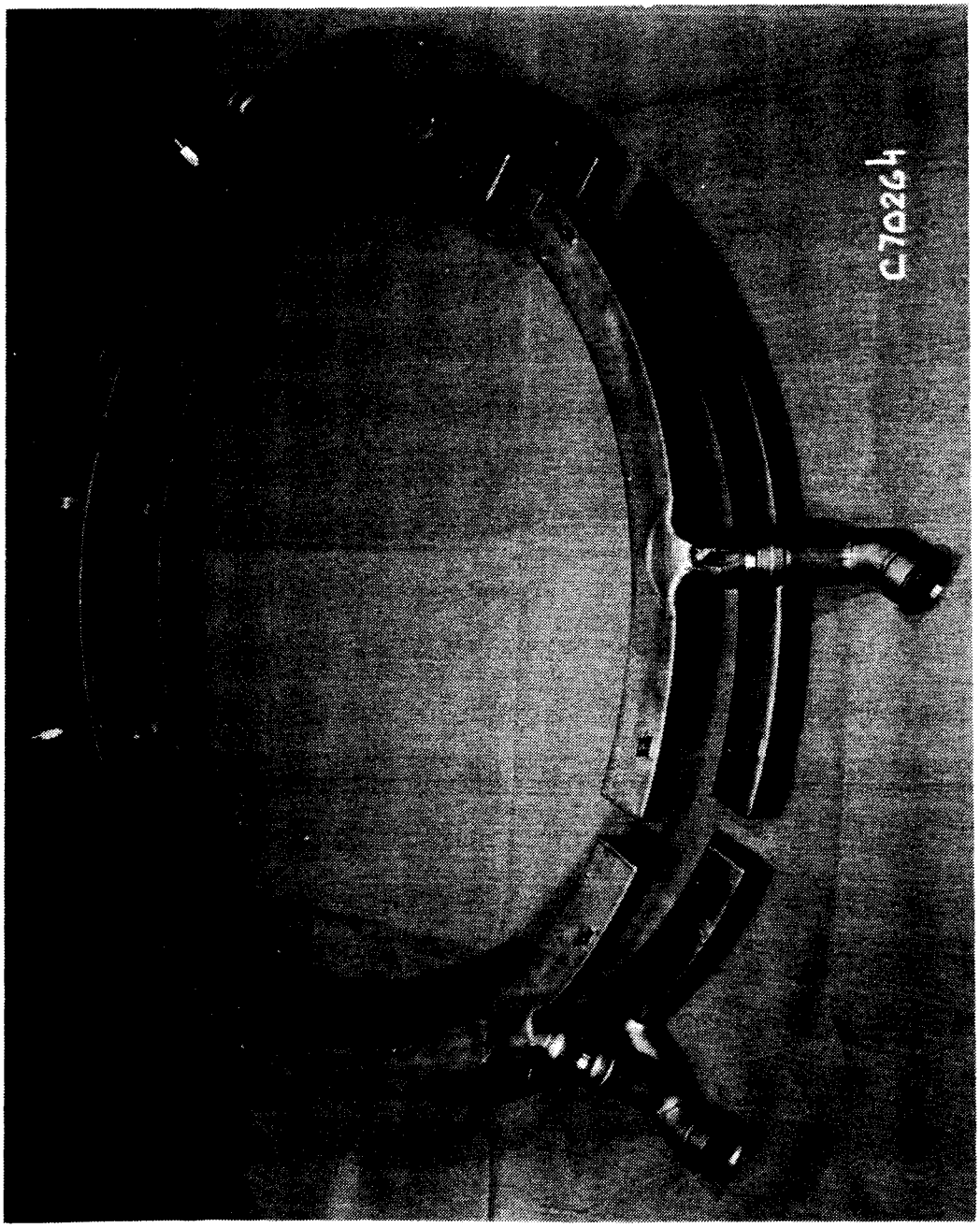


Figure 40. HPT Active Clearance Control (ACC) Manifolds.

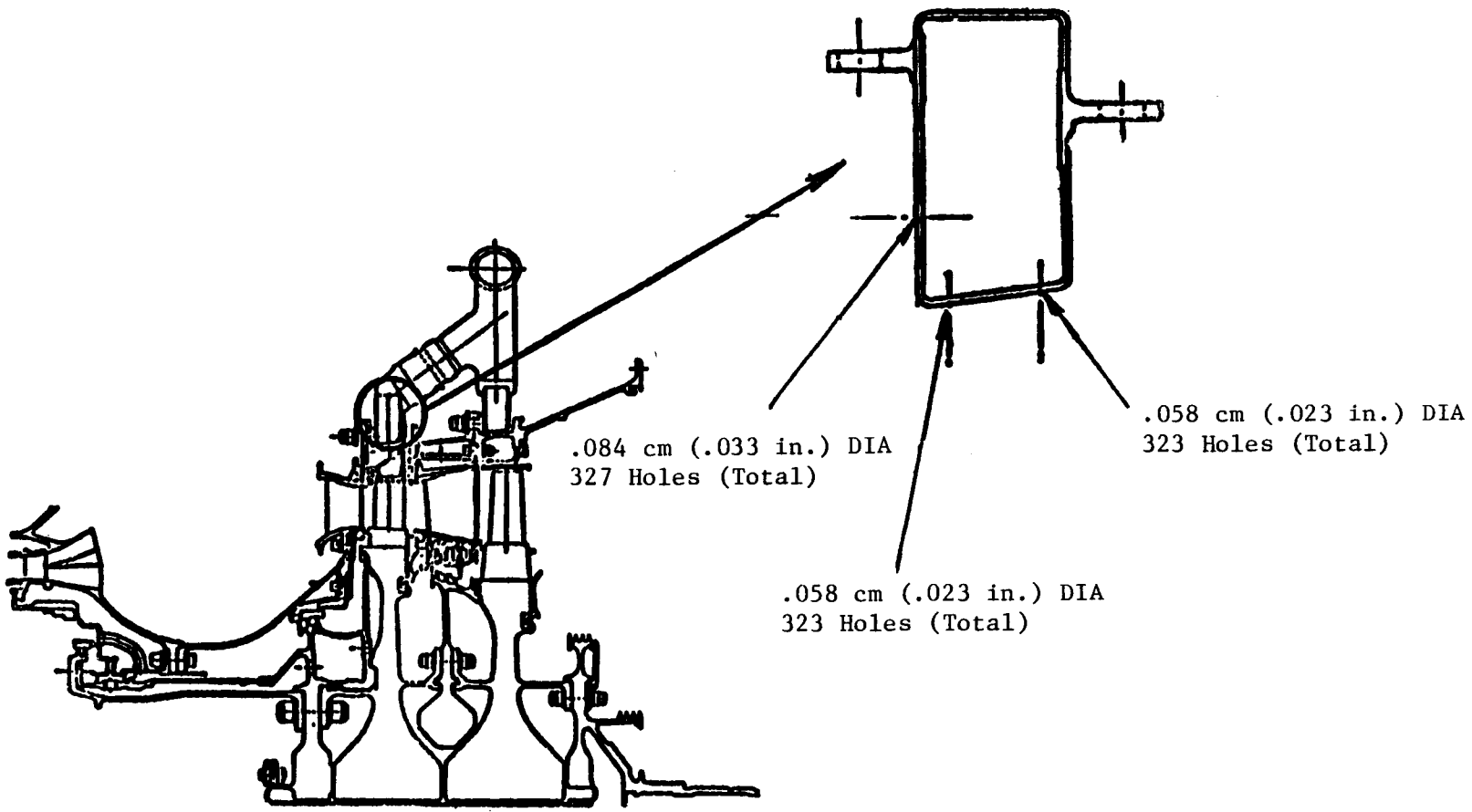


Figure 41. Rework on HPT Stage 1 Active Clearance Control Manifolds.

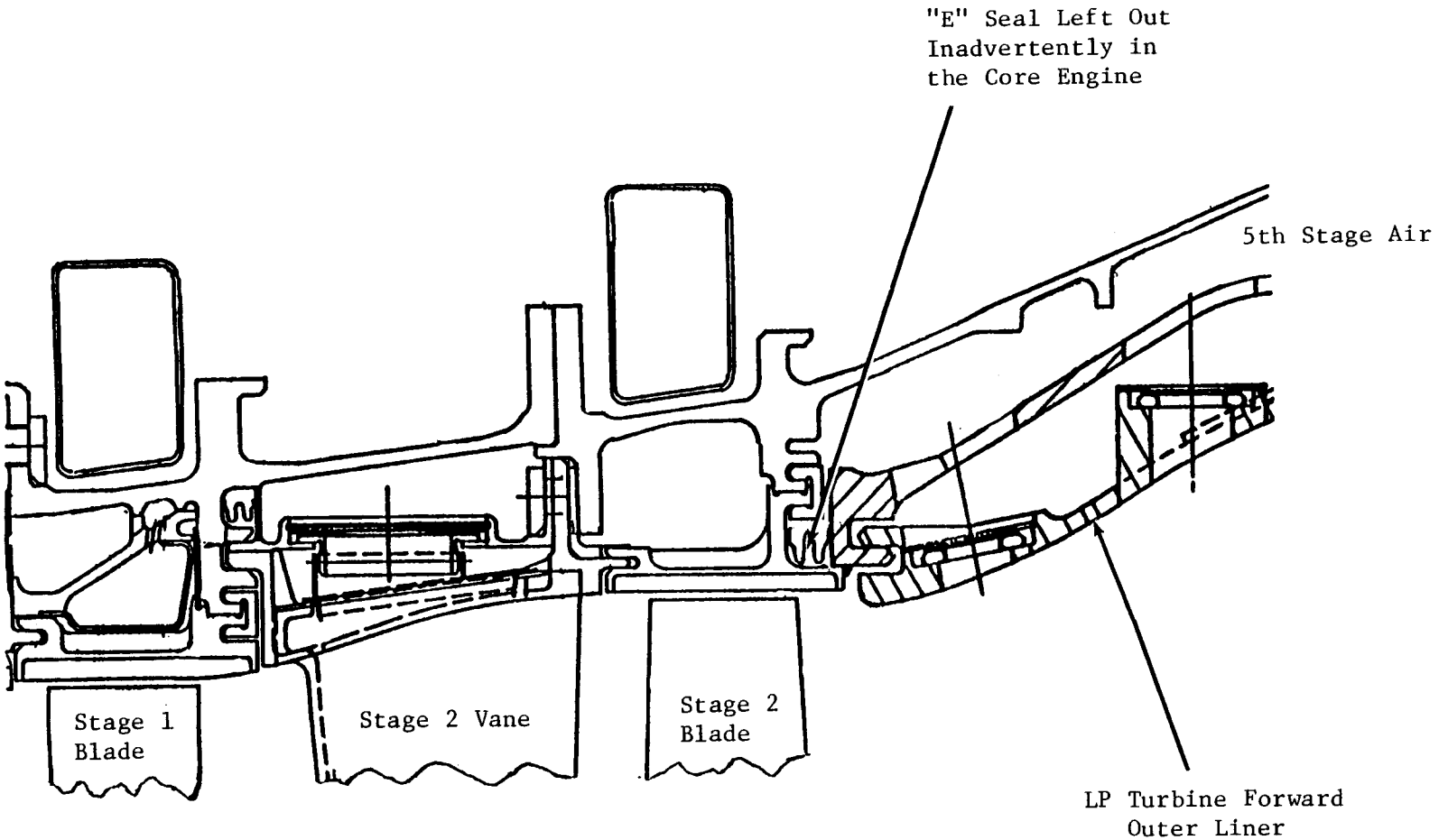


**Figure 42. Location of "E" Seal Used to Reduce 5th Stage Air Leakage.**

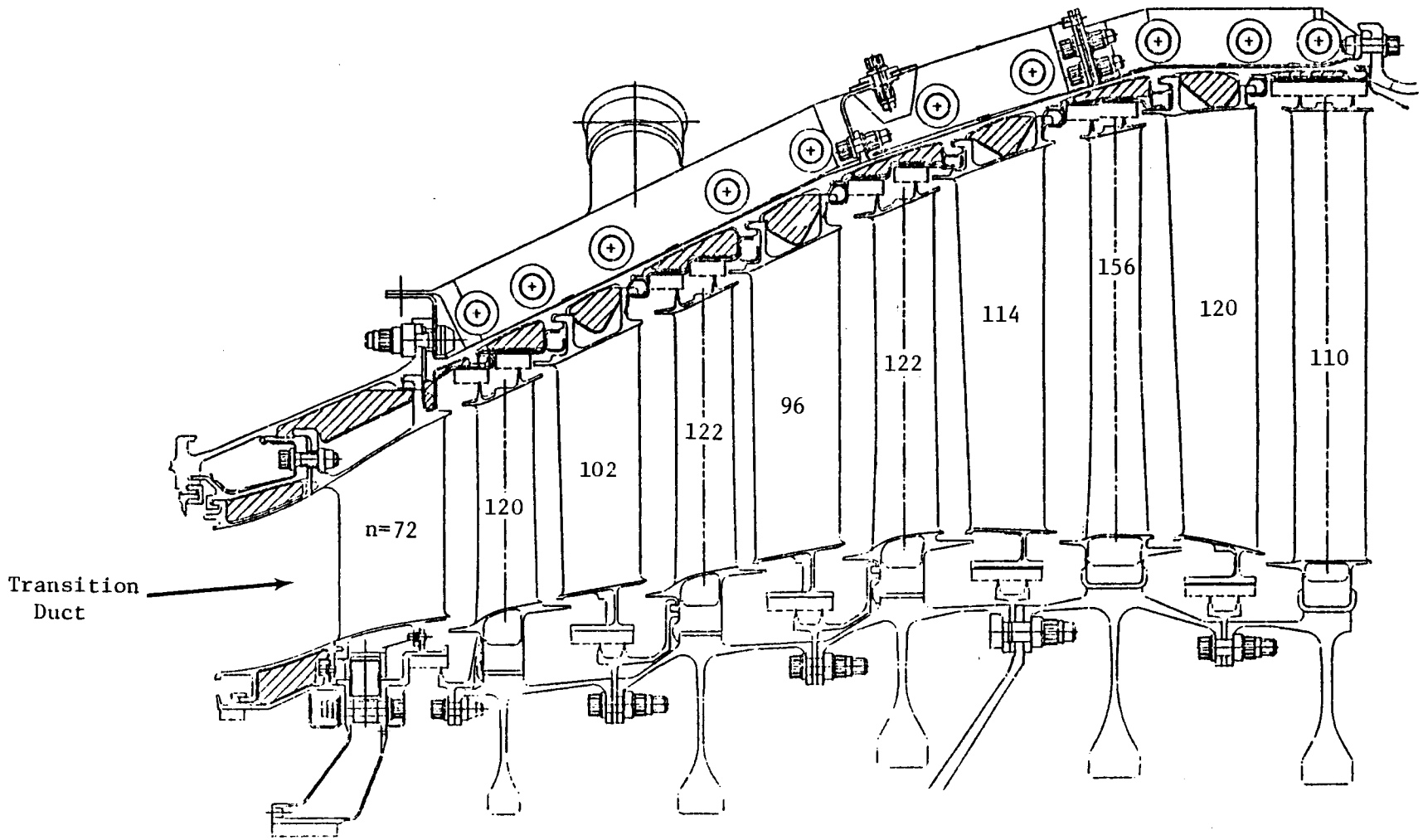


**Figure 43. Low Pressure Turbine (LPT) Flowpath.**

Table V. Critical LPT Operating Point Data.

| | | ICLS | FPS | | |
|---|---|---|---|---|---|
| Parameter | Units | Max. Climb | Max. Climb | Max. Cruise | Sea Level Takeoff +27°F |
| Inlet Temp, $T_{49}$ | K | 1099.8 | 1083.2 | 1054.6 | 1128.7 |
| | ° R | 1979.7 | 1949.8 | 1898.2 | 2031.6 |
| Energy, $\Delta h/T$ | J/kg/K | 318.1 | 326.5 | 322.3 | 306.3 |
| | Btu/lbm/° R | 0.07597 | 0.07798 | 0.07697 | 0.07315 |
| Speed, $N/\sqrt{T}$ | rad/sec√K | 11.07 | 11.26 | 11.08 | 10.61 |
| | rpm/√°R | 78.82 | 80.14 | 78.86 | 75.53 |
| Corrected Flow, $W\sqrt{T}/P$ | g√K/sec·Pa | 4.098 | 3.936 | 3.947 | 3.967 |
| | lbm√°R/sec·psi | 83.57 | 80.27 | 80.33 | 80.90 |
| Efficiency, $\eta$ | | 0.911 | 0.917 | 0.916 | 0.921 |



C-2

designed to a flow function approximately 4% higher at climb than the FPS. This reflects the derated component efficiencies and estimated instrumentation losses in the ICLS.

Cooling requirements have been minimized so that only the Stage 1 nozzle employs controlled purge air from the fifth-stage compressor bleed for seal blockage and disk rim purge.

The Stage 4 rotor-to-stator spacing employs a wide gap (1.4 blade chord lengths) to minimize turbine noise.

Efficiency goals at Mach 0.8/10.67 km (35,000 ft) maximum climb are 0.911 (or 91.1%) for the ICLS and 0.917 (91.7%) for the FPS.

The selection of a five-stage configuration for the $E^3$ LPT was based in part on results obtained during the IR&D-funded Highly Loaded Fan Turbine (HLFT) technology development program and also on $E^3$ system studies aimed at minimizing direct operating cost (DOC). These system studies evaluated the impact of turbine loading, weight, and cost on DOC and indicated a relative optimum at loading level attainable in five stages. Further, significant performance gains at this loading level had been demonstrated in the HLFT program, indicating that the ICLS goal could be met with a five-stage turbine.

The five-stage flowpath was defined during the design phase through an iterative technique whereby a candidate outer-wall contour was selected (within the limitations on wall slope and exit diameter), and the inner wall contour and stage energy distribution were iterated concurrently to yield acceptable levels of loading ($gJ\Delta h/2u^2$) and flow coefficient ($V_z/u$) for each stage. The best candidate flowpaths were selected based on a stage-by-stage efficiency estimate which accounted for the effects of loading, flow coefficient, tip slope, aspect ratio, and clearance.

The detailed vector diagram analysis was accomplished using a calculation procedure that solves the full, three-dimensional, radial-equilibrium equation for axisymmetric flow accounting for (1)

streamline slope and curvature, (2) the effects of radial-component blade force due to airfoil sweep and dihedral, and (3) airfoil blockage and radial gradient of flow properties. Calculations were made with radial gradients of blading losses to simulate end-loss effects. The calculation model for the $E^3$ LPT showing meridional streamlines and intrablade-row calculation stations is shown on Figure 44.

The airfoil aerodynamic design process was initiated by generating approximate airfoil shapes using a numerical procedure which applied a thickness distribution to a mean camber line as a function of flow angles and appropriate input coefficients. These preliminary airfoil shapes were analyzed by a procedure that calculates the compressible flow along the stream surfaces determined from the through-flow analysis which accounted for the variation in stream tube thickness.

The undesirable features of the resultant surface-velocity distributions were corrected, and modified surface Mach number distributions were input to the analysis procedure which, in turn, made the necessary modifications to airfoil shapes in order to produce the desired velocity distribution.

An assessment of the performance of the LPT has been made based on a series of scaled air-turbine tests divided into two phases: Block I and Block II. The transition duct and the first two stages of the turbine were evaluated during the Block I phase from March through August 1979. The full five-stage scale model, representing the final ICLS design and incorporating redesigns of Stages 1 and 2 based on Block I data analysis, was tested as Block II in June through September 1981.

The five-stage rig flowpath (a 0.67 geometric scale of the ICLS flowpath) is shown in Figure 45. The test map for the rig is shown in Figure 46. Efficiency and flow function characteristics over the matrix are shown in Figures 47 and 48, respectively.

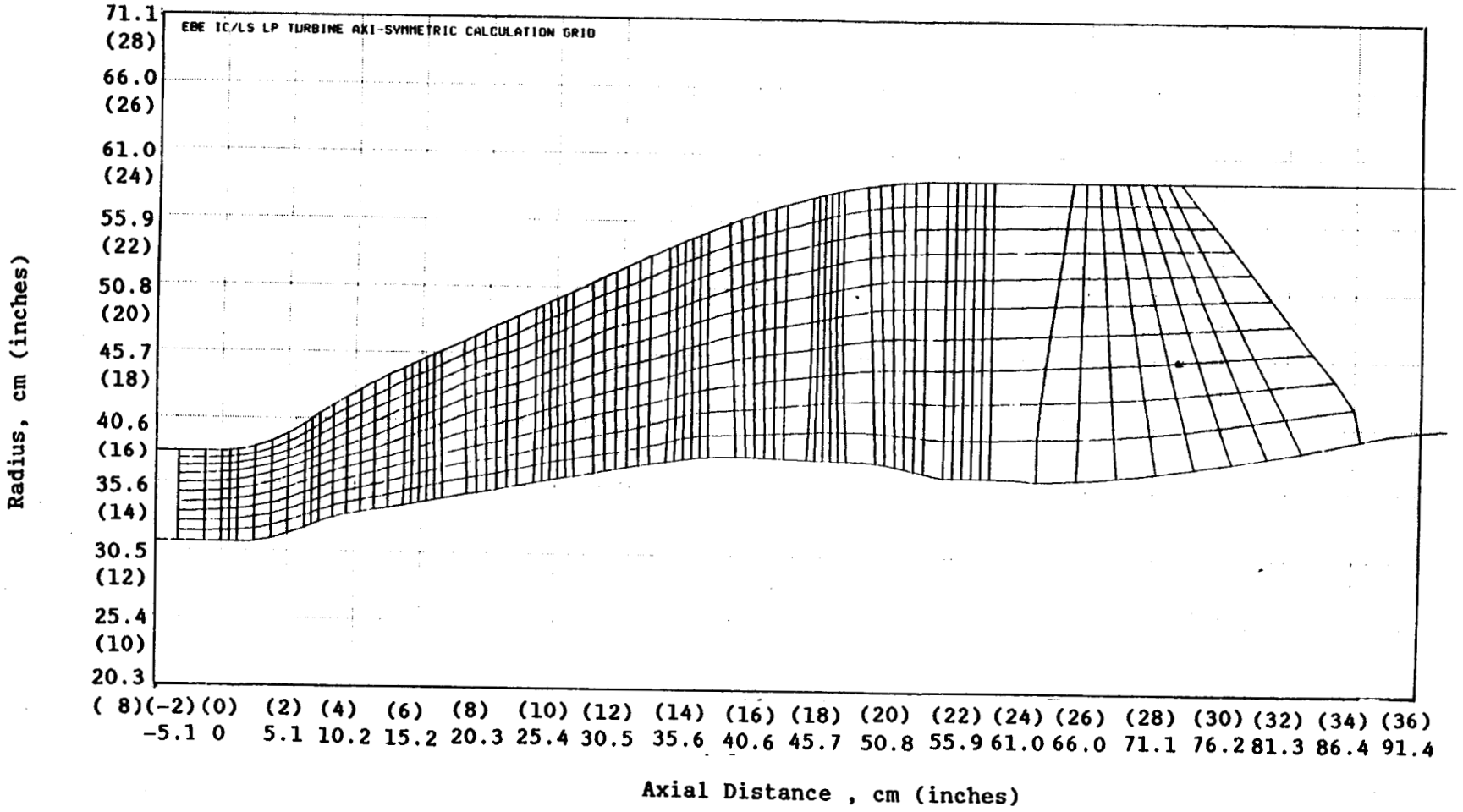


Figure 44. LPT Axisymmetric Vector Calculation Model.

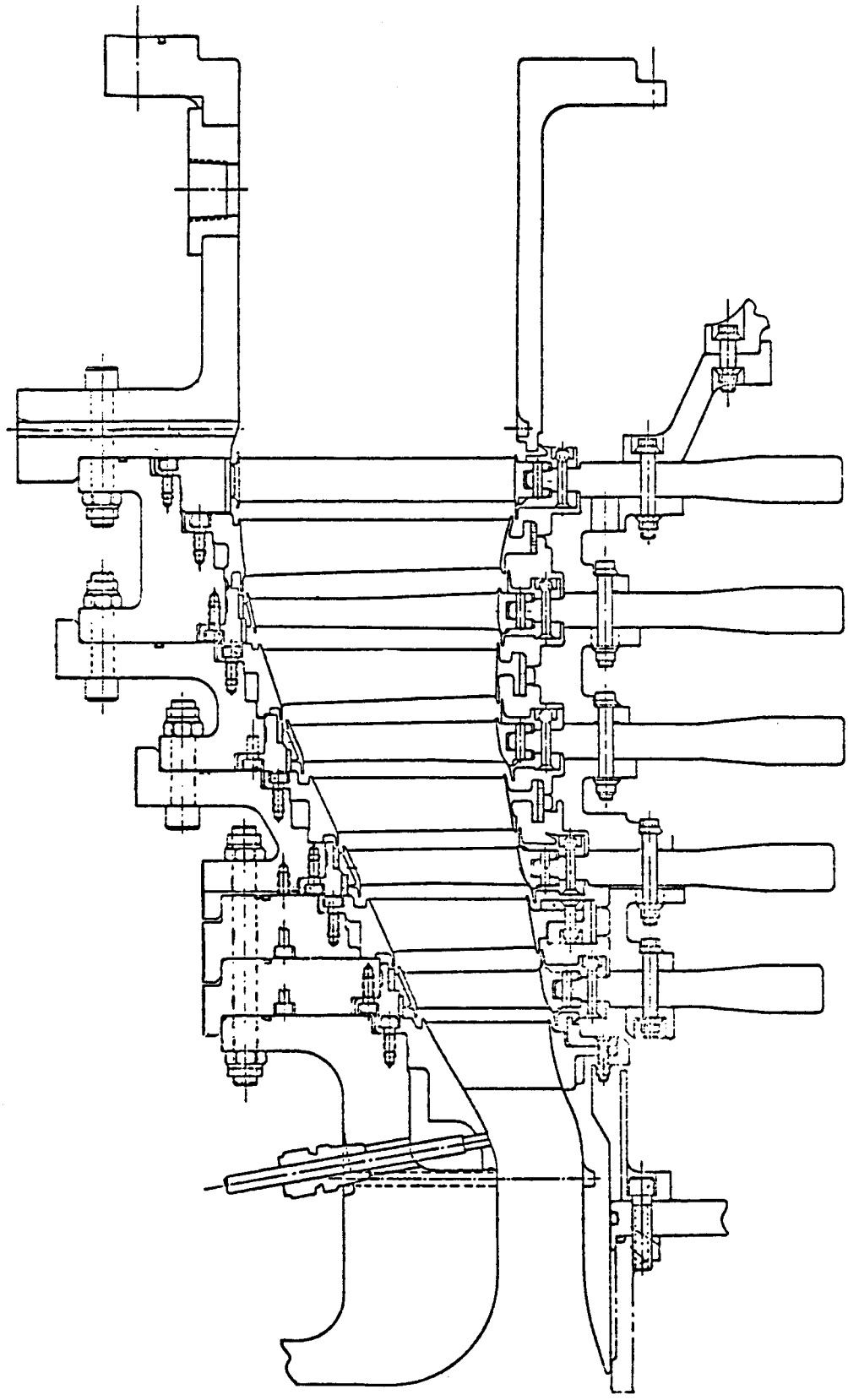

Figure 45. Scaled Turbine Test Vehicle, Five-Stage Configuration.

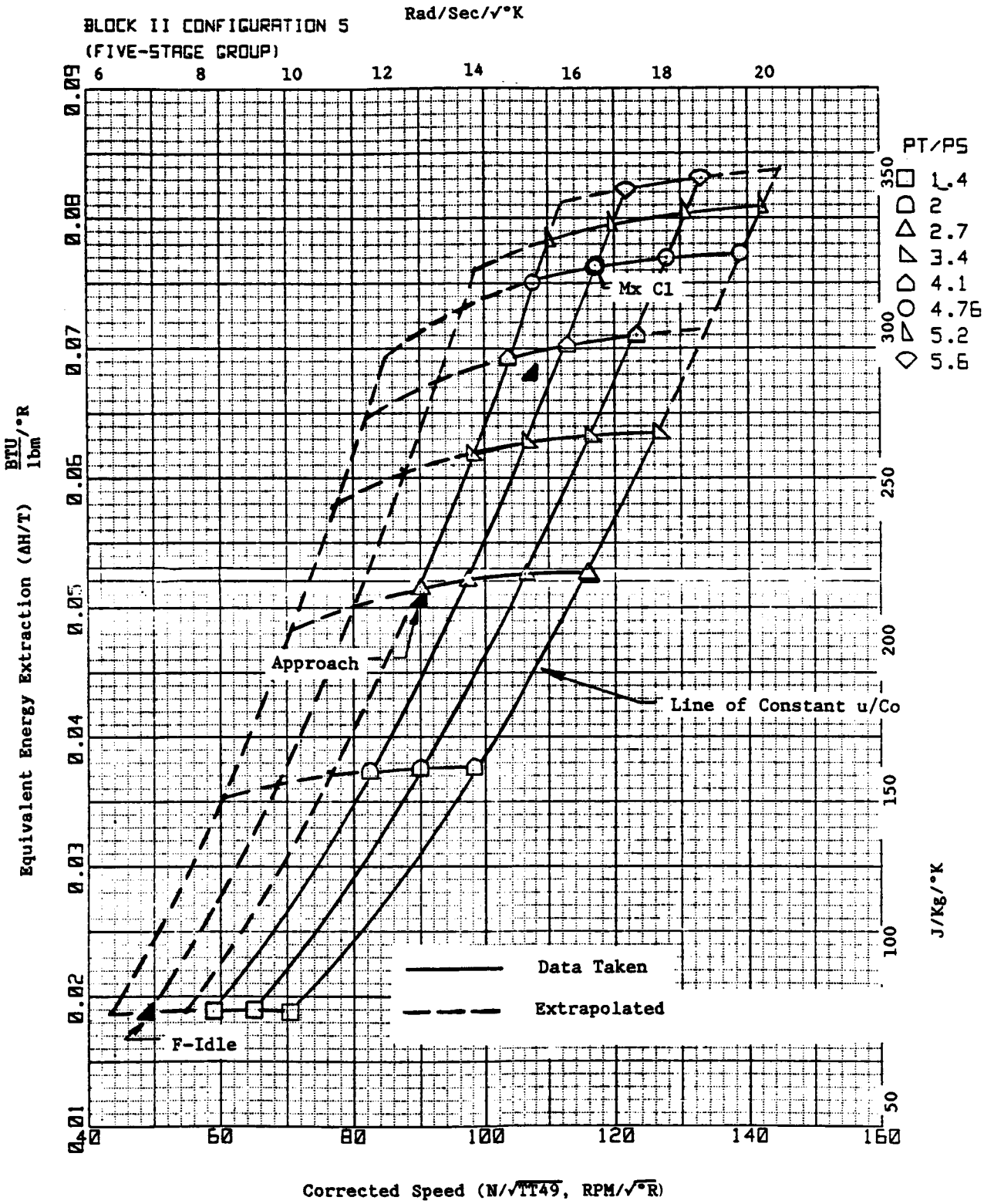


Figure 46. Low Pressure Turbine Map - Speed-Energy.

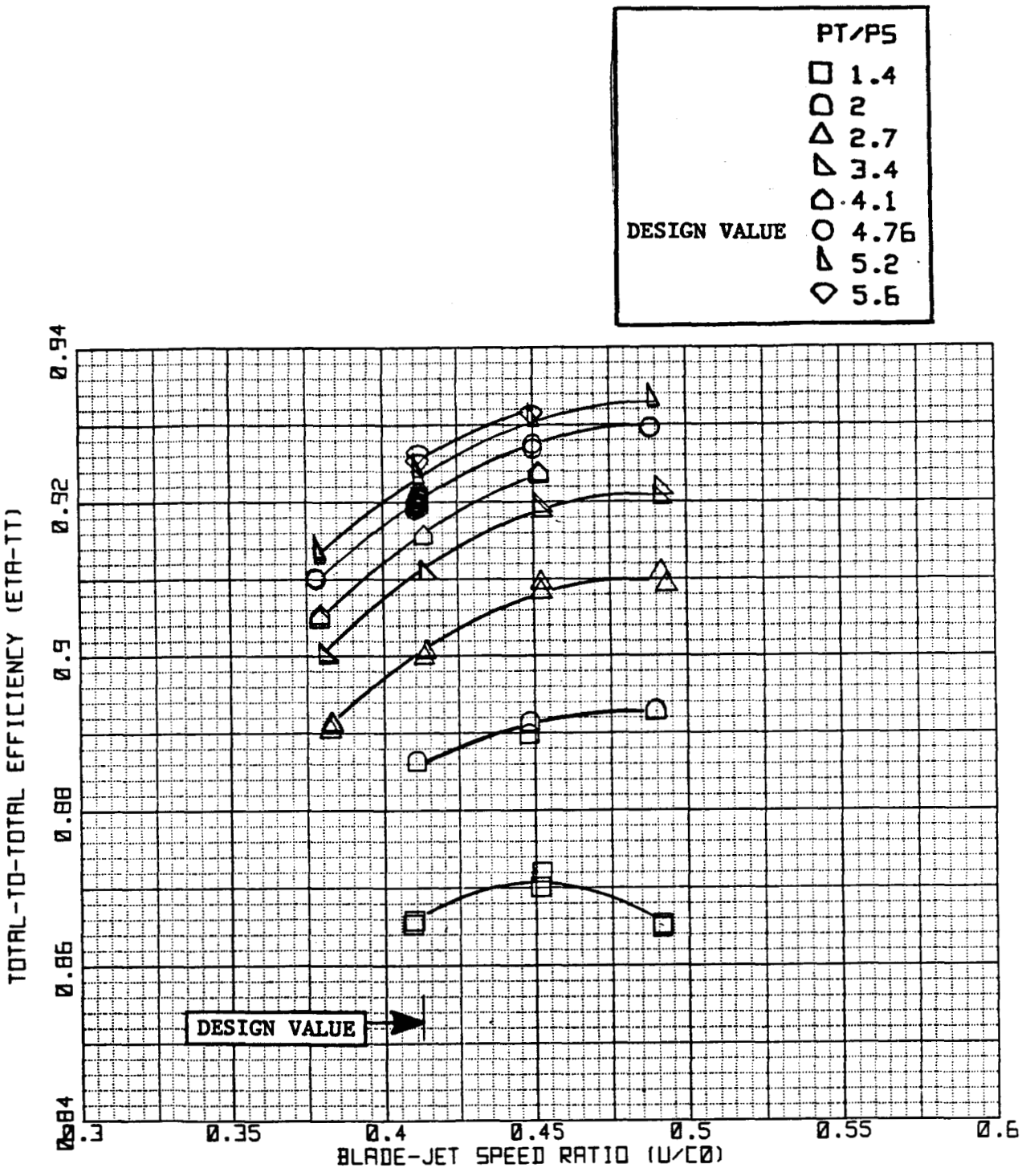


Figure 47. LPT Map - Efficiency vs. Blade Jet Speed Ratio.

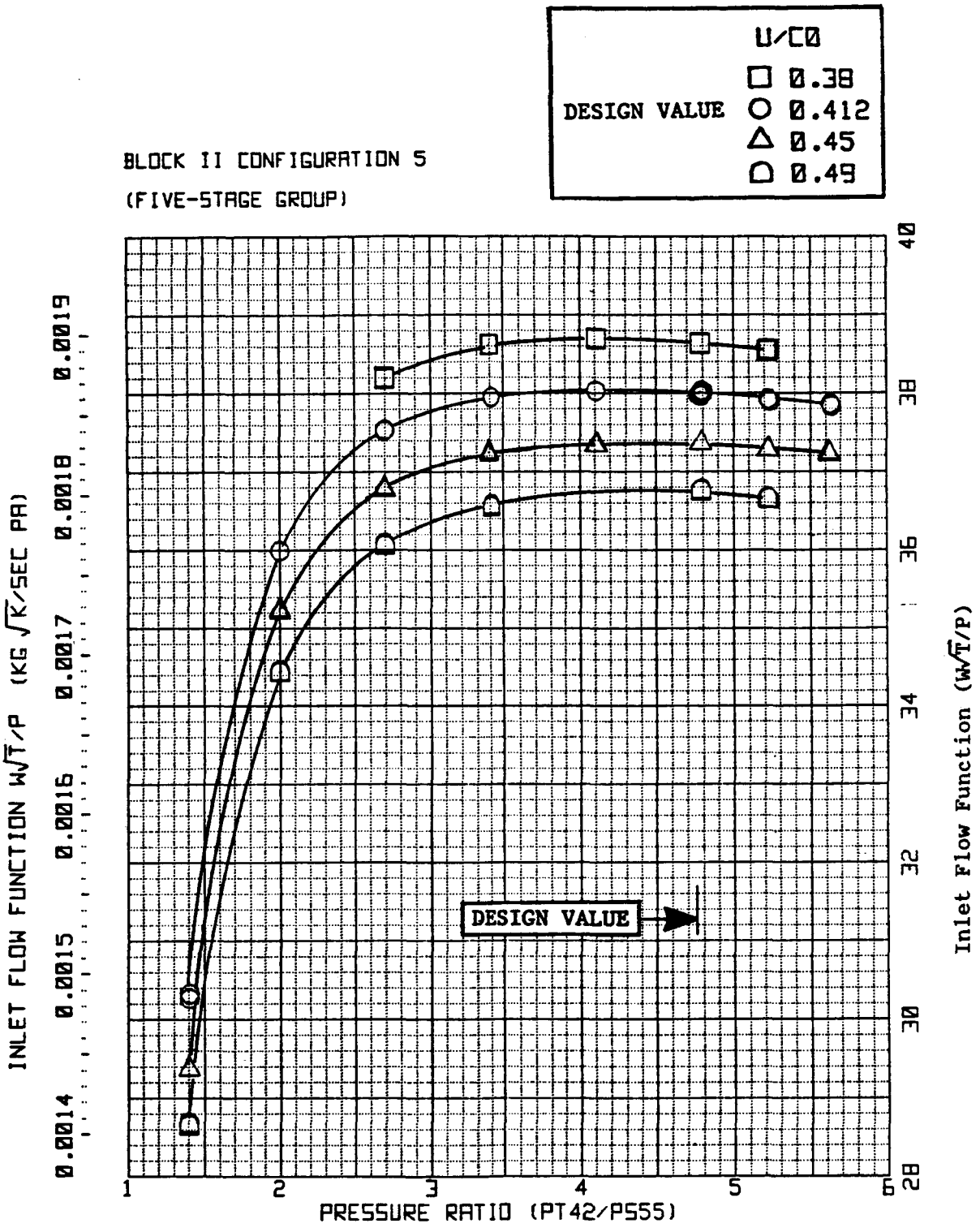


Figure 48. LPT Map - Flow Function vs. Pressure Ratio.

Based on the rig design point efficiency of 92.0%, the predicted performance of the ICLS LPT at the M 0.8/10.67 km (35,000 ft.) max climb design point was established as follows:

| Item | Magnitude |
|---|---|
| Rig at Design Point | 92.0 |
| Edge Blockage Correction | + 0.1 |
| Purge Air | + 0.1 |
| Reynolds Number | - 0.7 |
| Installed $\eta_{TT}$ at M0.8/10.67 km (35,000 ft) | 91.5% |

This is relative to goals of 91.1% for the ICLS and 91.7% for the FPS.

The correction for edge blockage accounts for the fact that all Block II rotor blades were received from the vendor with trailing edge diameters which were, on the average, 25% oversized relative to design intent.

The correction for purge air is based on the calculated net availability of a total of just over 1% of air which will enter the engine flowpath at the inner wall after the stage one vane. This flow was not modelled in the rig.

Based on rig test results then, the Block II design for the ICLS LPT was expected to satisfy system requirements for both flow capacity and efficiency.

### 3.6.2 LPT Purge and Cooling System Design

The LPT cooling air requirements for the ICLS engine are presented in Figure 49. The major portion of the rotor purge air is defined by the estimates of the seal clearances and the required flow to block the seals and prevent the flowpath gases from being injected into the rotor cavity. To

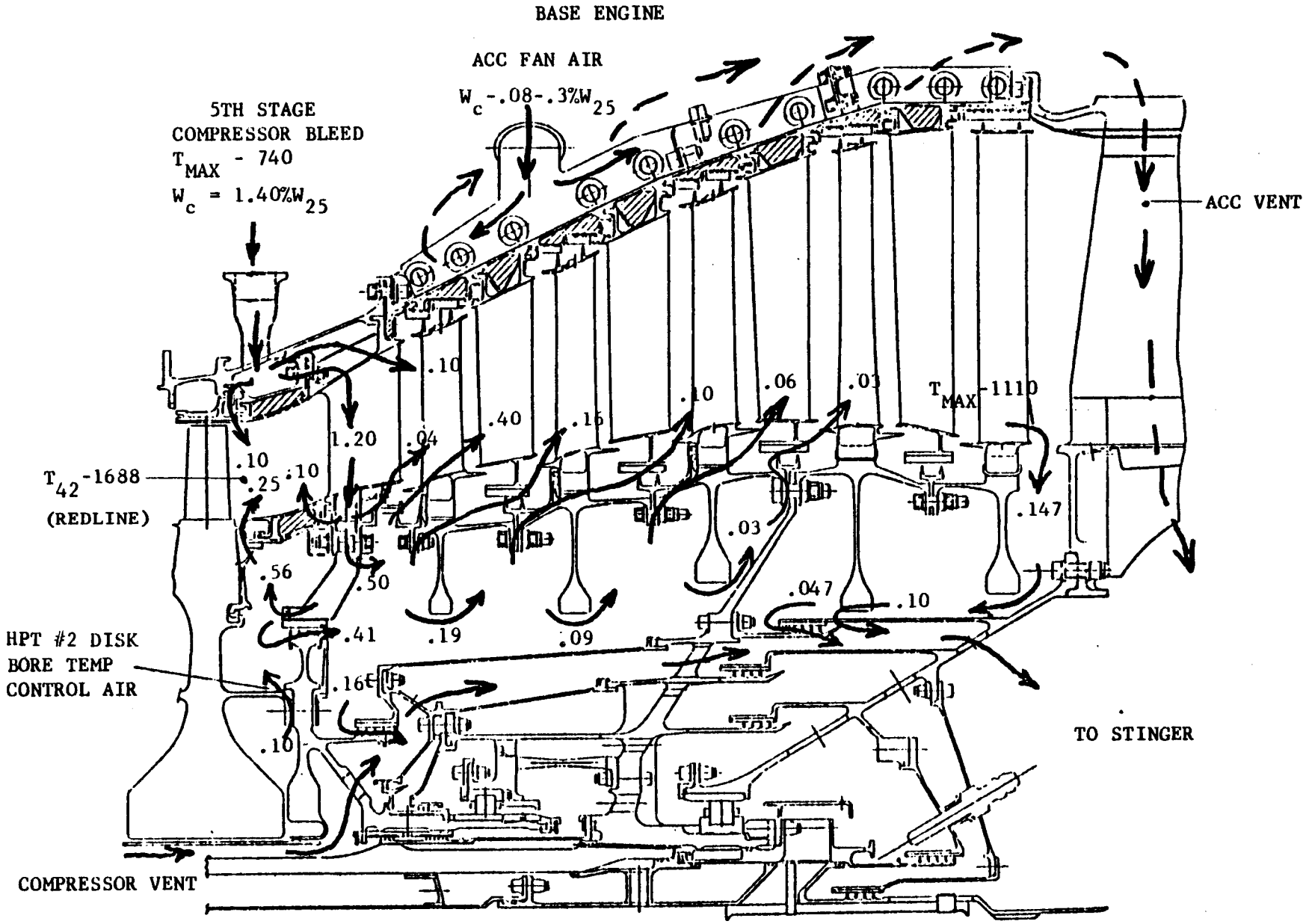


Figure 49. LPT Cooling Air Supply System.

accomplish this, 1.40% of 5th stage compressor bleed air was used to purge the outer and inner band of the Stage 1 nozzle, cool the vane approximately 56°C (100°F), block the HPT rotor balance seal, and purge the LPT rotor cavity. A small portion of the rotor purge air leaked into the sump purge cavity and eventually exited through the stinger at the back-end of the engine. The majority of the flow returned to the LPT flowpath. The flow through the Stage 1, 2, and 3 rotor spacer arm flanges was determined by the required spacer arm temperatures.

The aft rotor cavity was cooled with the LPT exhaust gas. This was a significant change from the preliminary design where 5th stage compressor bleed air was used to purge the cavity. The prime reason for purging the cavity with warm air was to improve the ICLS performance and reduce thermal gradients in the rear frame hub and in the rotor disks on Stages 4 and 5. This system allowed a reducton in 5th stage bleed air by 0.1% $W_{25}$ and provided better temperature matching within the frame hub and between the bore and rims of the disks.

The outer casing was kept within the design objective metal temperatures of 704°C (1,300°F) by impingement cooling with fan air. The ACC and the casing impingement cooling scheme were combined into one system. The cooling of the casing required an 0.08% $W_{25}$; this was increased to 0.3% for maximum cooling in order to achieve the greatest clearance reduction.

### 3.6.3 Low Pressure Turbine Mechanical Design

The General Electric $E^3$ low pressure turbine represents advanced technology in a balanced design with stron emphasis on high efficiency and performance while retaining good maintenance features and low cost.

The mechanical configuration represents a combination of the best features to achieve high efficiency through a blend of technology disciplines which include aerodynamics, heat transfer, metallurgy, mechanical design, manufacturing, and test evaluation. These features are shown in Figure 50

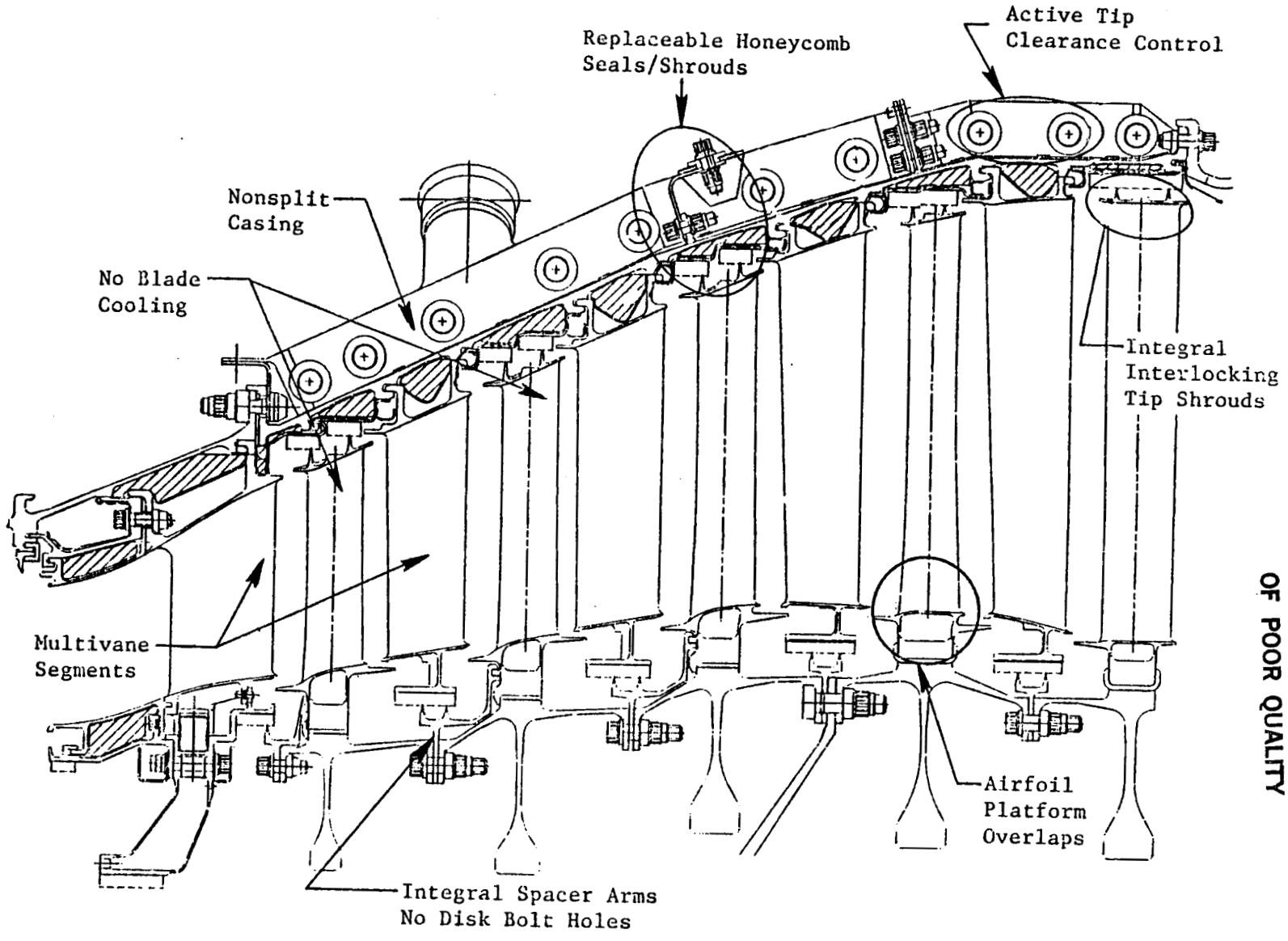


Figure 50. Low Pressure Turbine Features.

(LPT cross section) and Figures 51 through 53 with the material selections shown in Figure 54.

The LPT rotor was an uncooled design comprising disks with integral spacer arms and bolted joints between each stage. The main support cone extended from the sump between the HPT and LPT rotors and attached at the LPT spool between the Stage 3 and 4 disks. LPT blading was a proven cast design with tip shrouds and multi-tang dovetails. The large quantity of stage 4 blades and the oversized axial gap (Stage 4 blade to Stage 5 nozzle) were incorporated to provide acoustic improvement. Inner stage seals of the LPT spool were repairable, two-tooth designs and were attached at the bolted flange joints between the disk spacer connections. They provided good performance (low leakage) and easy replacement.

In the LPT stator assembly, the casing was a continuous, no-split-flange design with wall insulation and local impingement cooling for improved clearance control. The Stage 1 nozzle was a conventionally cast four-vane segment attached by a hooked tang at the outer flowpath. Stages 2 through 5 nozzle vanes were cast multivane segments attached by hook tangs to the outer-case supports. Outer honeycomb seals were brazed to sheet metal backing strips that hook into the outer casing and assist in the radial retention of the Stages 2 through 5 nozzles. The inner diameters of these vanes had integral seals which consisted of honeycomb brazed to the cast vane seal support. Interlocks were built into the integral seals to provide torsional stiffness and restraint without the need for separate bolted restrained pieces. A full-ring inner seal was bolted to the Stage 1 vane and consisted of three sections of honeycomb brazed to a sheet metal structure.

The ICLS rotor hardware incorporated additional life margin beyond FPS requirements by being designed for "growth engine" speeds and temperatures.

An active clearance control system was incorporated which utilized fan air to thermally shrink the casing at selected operating points, thus improving seal clearances.

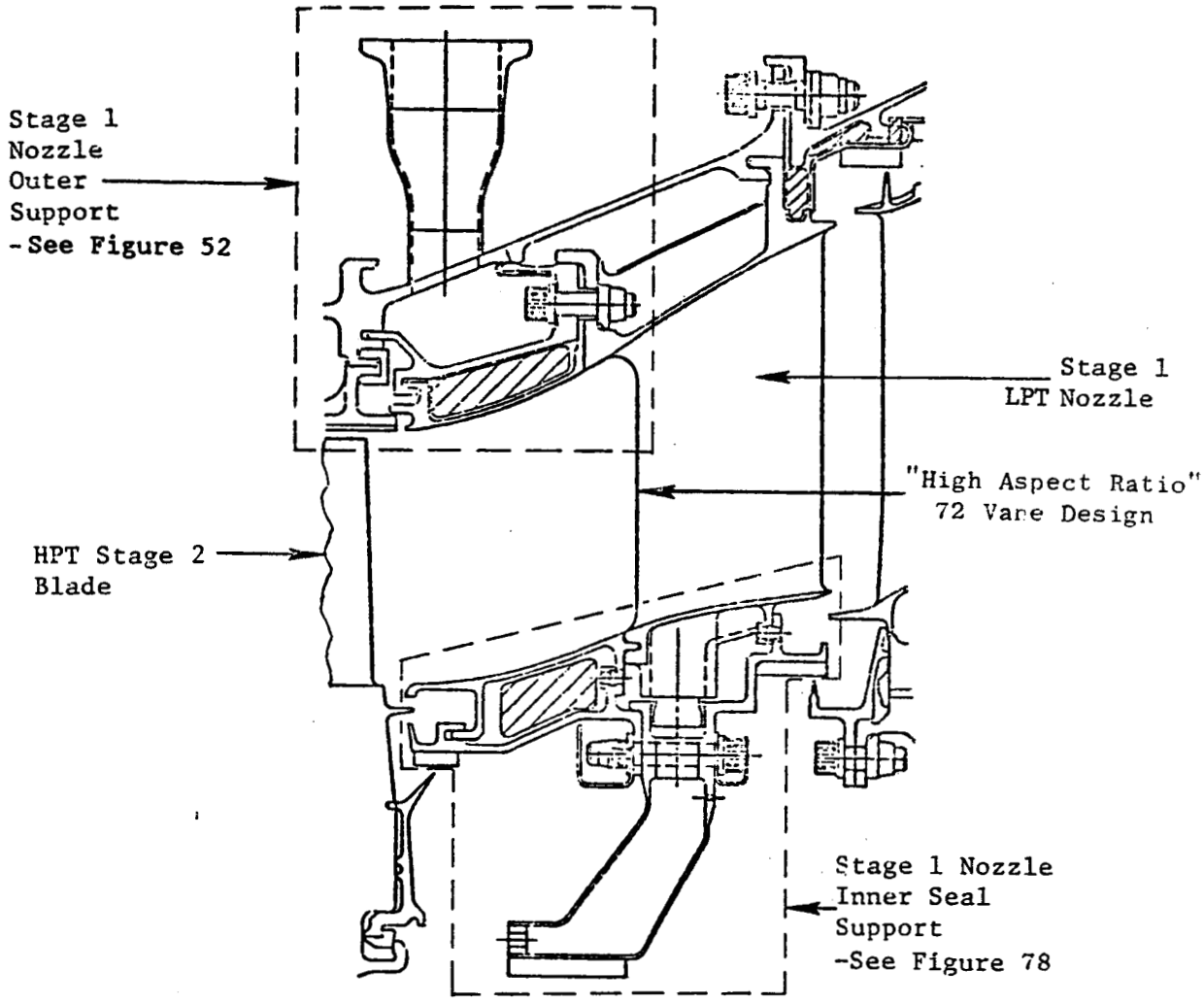


**Figure 51. LPT Stage 1 Nozzle Assembly.**

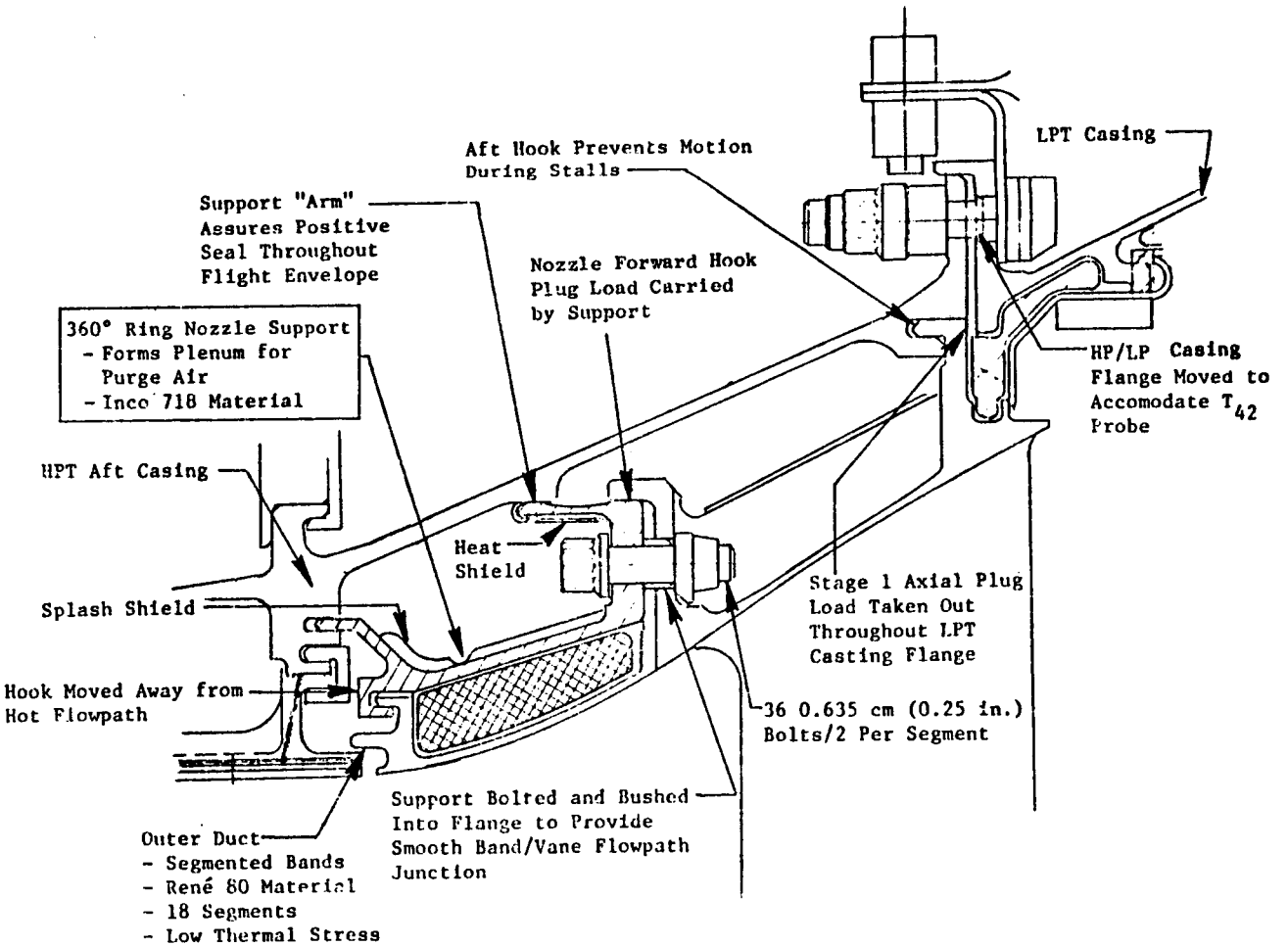


Figure 52. LPT Stage 1 Vane/Support Features.

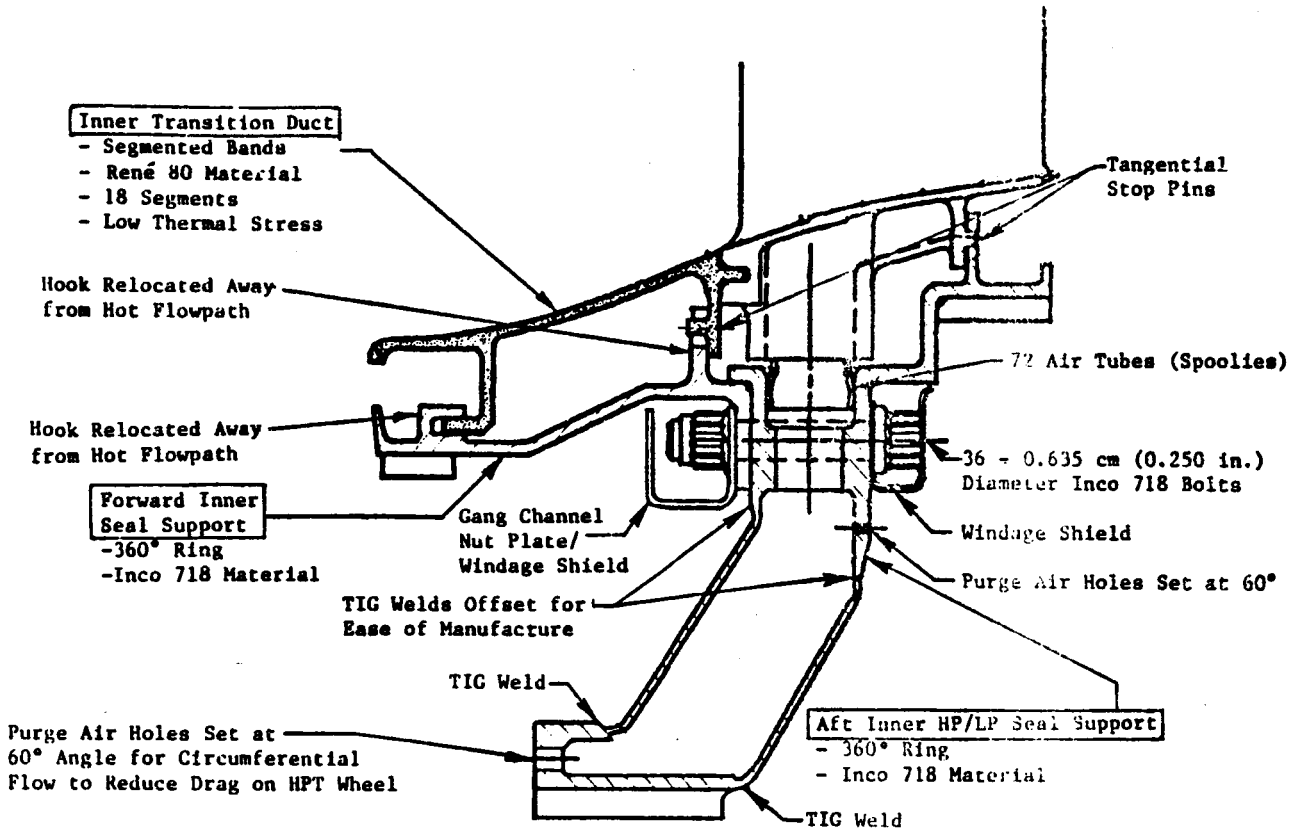


Figure 53. LPT Stage 1 Nozzle Inner Seal Support.

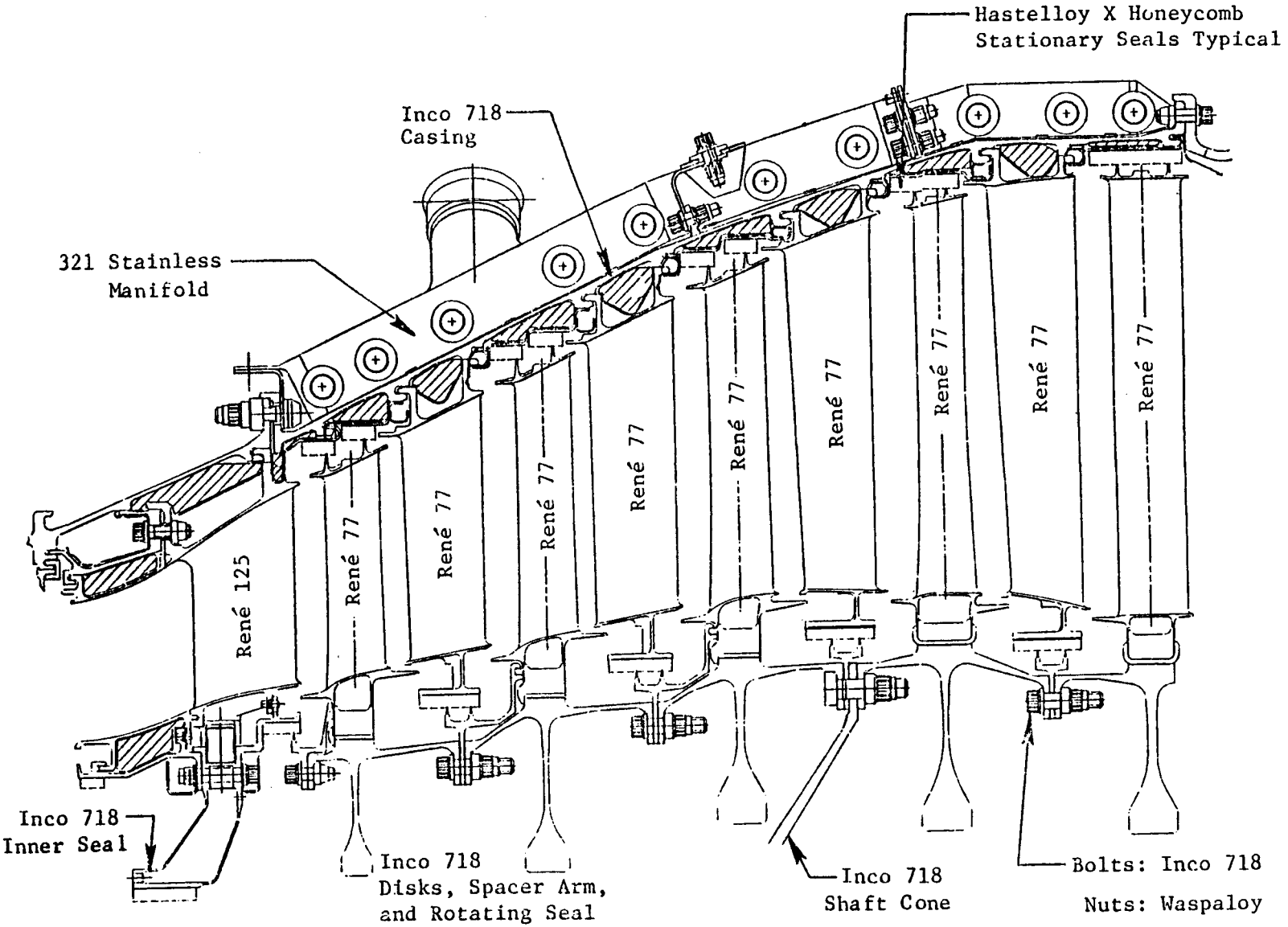


**Figure 54. Low Pressure Turbine Materials.**

Rework of blades, nozzles, disks and casing for ICLS instrumentation reduced component lives to varying extents but posed no concern for ICLS test requirements.

Major LPT components were photographed at various points during engine assembly and are shown as follows: The Stage 1 nozzle with outer support and main seals attached is shown in Figure 55. The Stage 3 rotor with blades assembled into the disk is representative of the other stages as well and is shown in Figure 56. One of the four quadrants which comprised the LPT active clearance control manifold is shown in Figure 57. Engine level final assembly of the LPT module is shown in Figure 58 (forward end showing the stage 1 rotor leading edge).

## 3.7 TURBINE FRAME DESCRIPTION

Figure 59 is a photograph of the turbine rear frame. Its primary functions were to maintain alignment of the rotor system within the static structure, transmit loads across the gas flowpath, provide engine structure spring elements, and help maintain airfoil top clearances. In addition, this frame had been designed for removing residual turbine swirl, support of the centerbody, mixer and the No. 5 bearing housing. Also, it had provisions for three engine mounts and ground handling features. The turbine frame contained acoustic panels to reduce engine noise, was used to route sump lube lines across the gas flowpath, and provided a path to vent engine Active Clearance Control (ACC) air to ambient pressure.

The turbine frame construction is illustrated in Figures 60 and 61. The material was INCO 718. For this one-of-a-kind piece, the strut ends and hub rings were machined, while the struts and strut extensions were made from formed sheet metal. The basic design features of this frame included 12 radial struts, mount lugs located on the top three struts, a variable thickness polygonal outer casing, and thermal expansion control features.

Radial struts were used in order to achieve the required high spring rate of 1,751,181 N/cm (one million pounds per inch) from the bearing to the

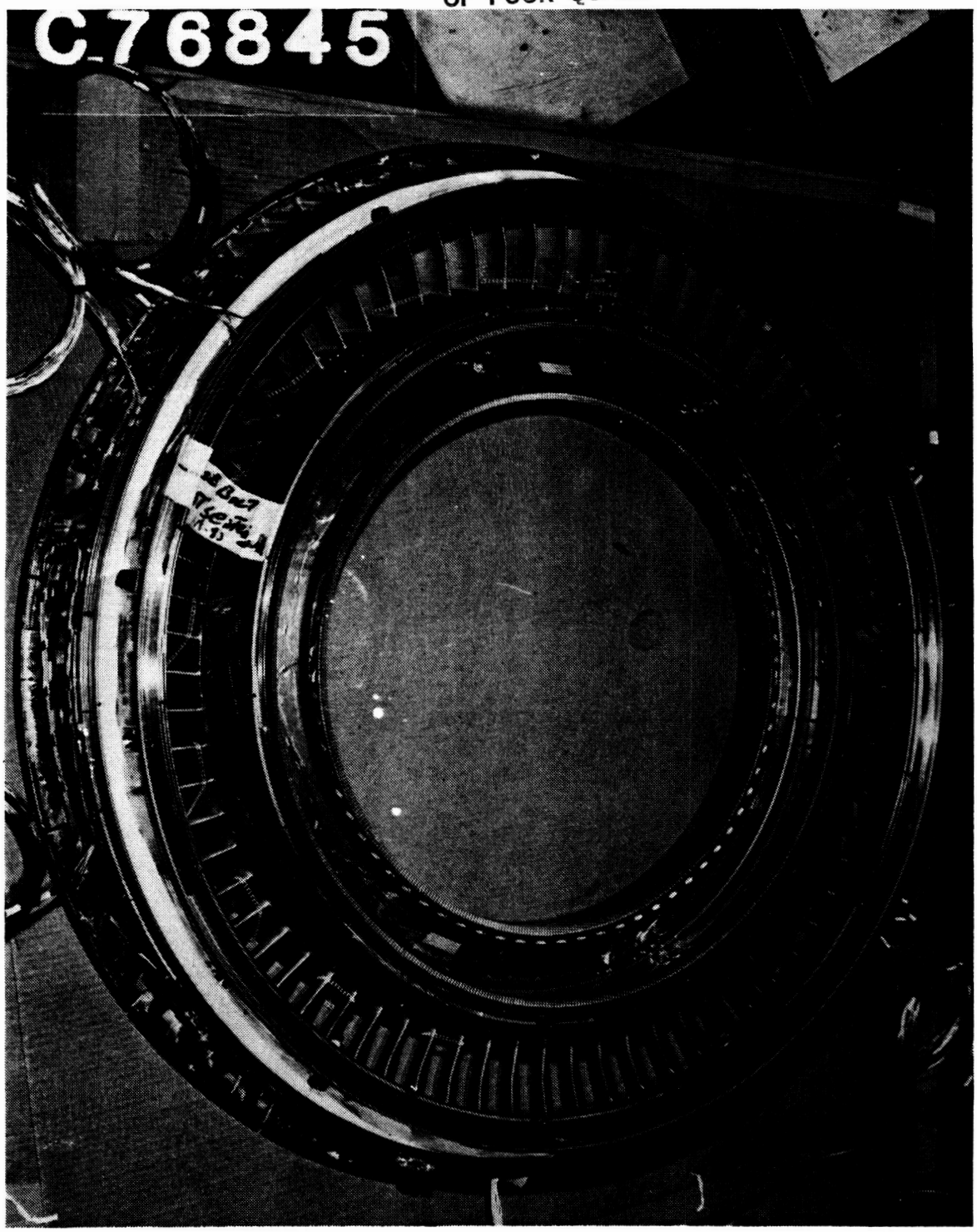


Figure 55. LPT Stage 1 Nozzle Subassembly (Forward Side).

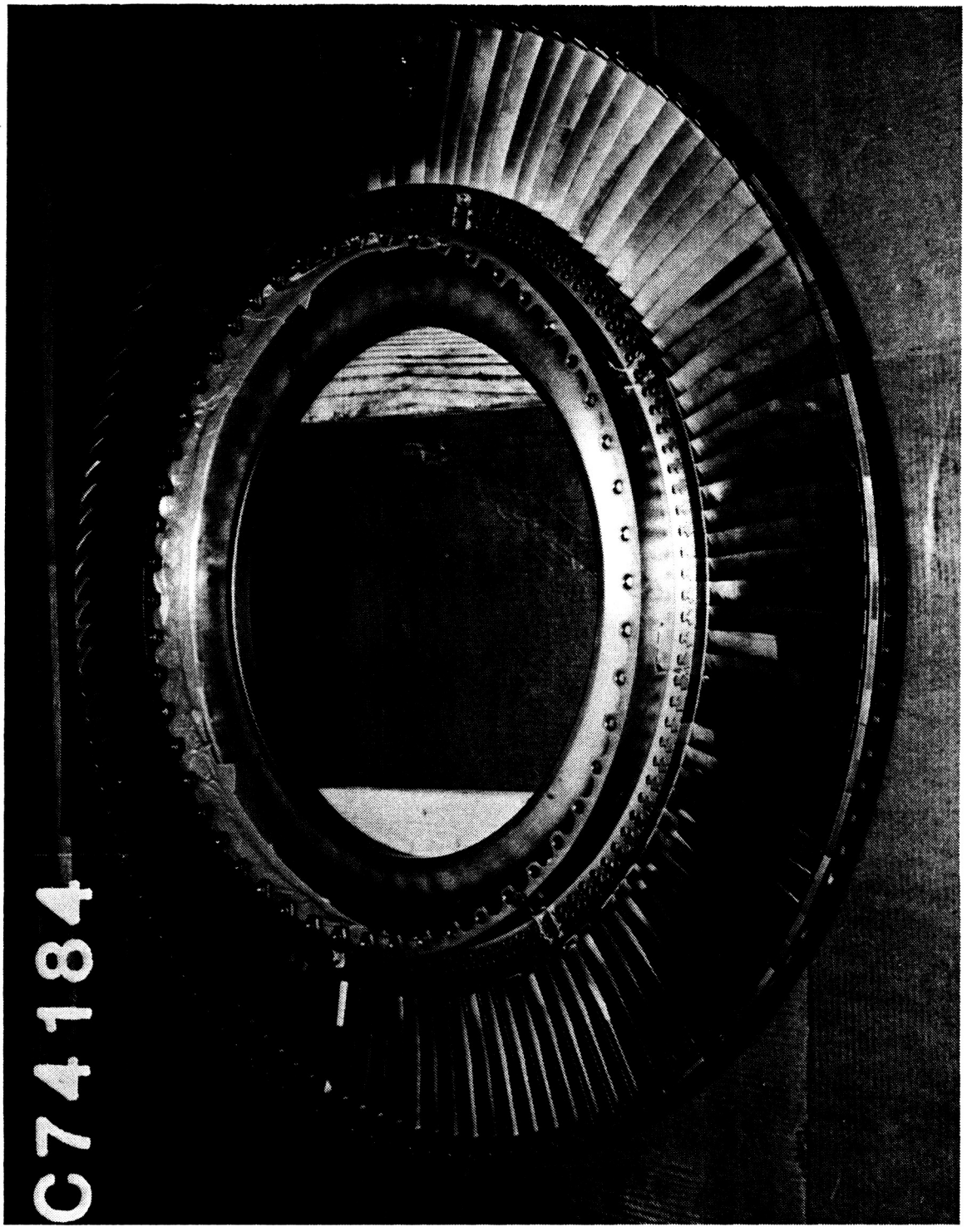


Figure 56. LPT Stage 3 Rotor Assembly (Aft Side).

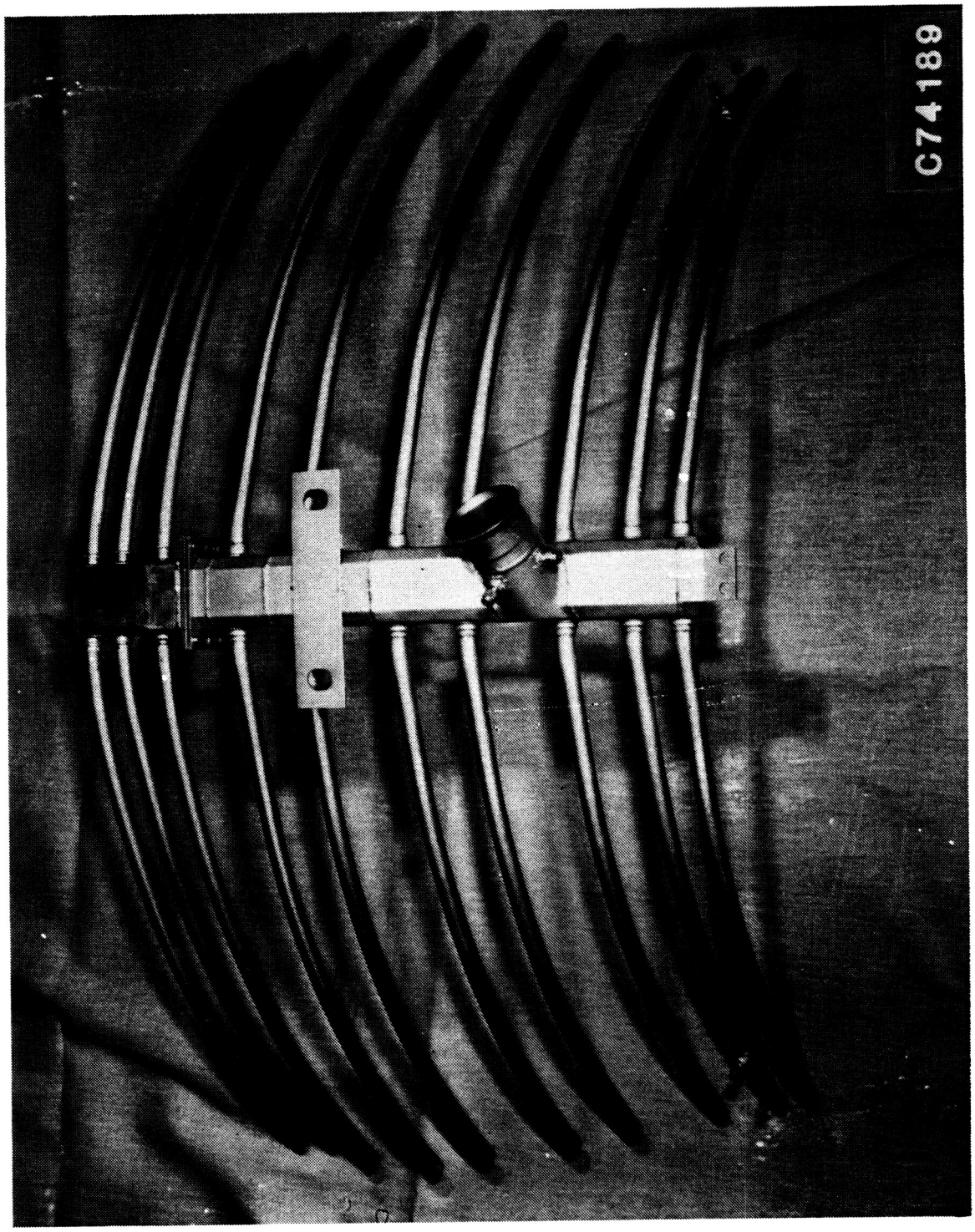


Figure 57. LPT ACC Manifold Quadrant.


Figure 58. LPT Stage 1 Module Assembly.

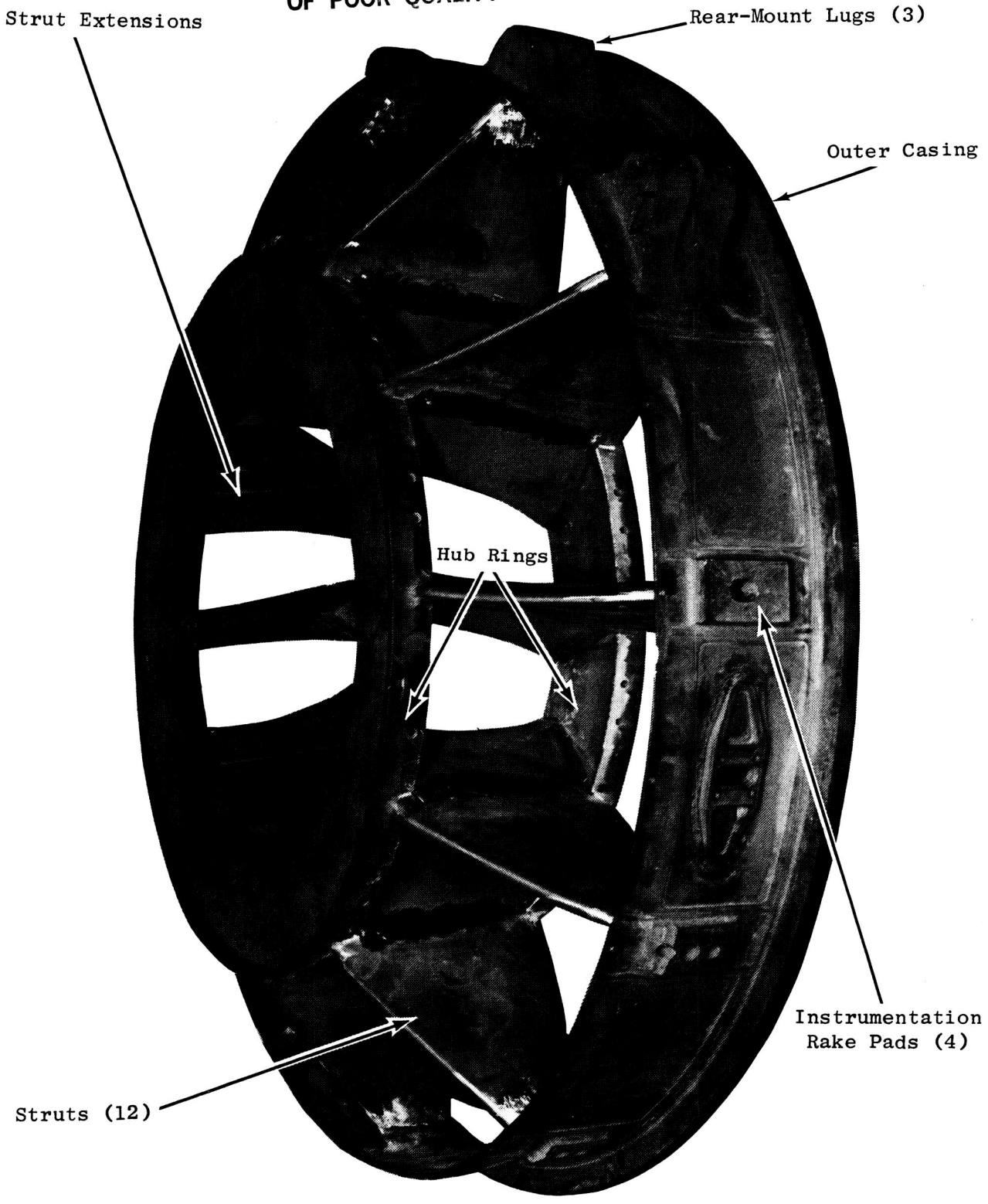


Figure 59. Turbine Rear Frame.

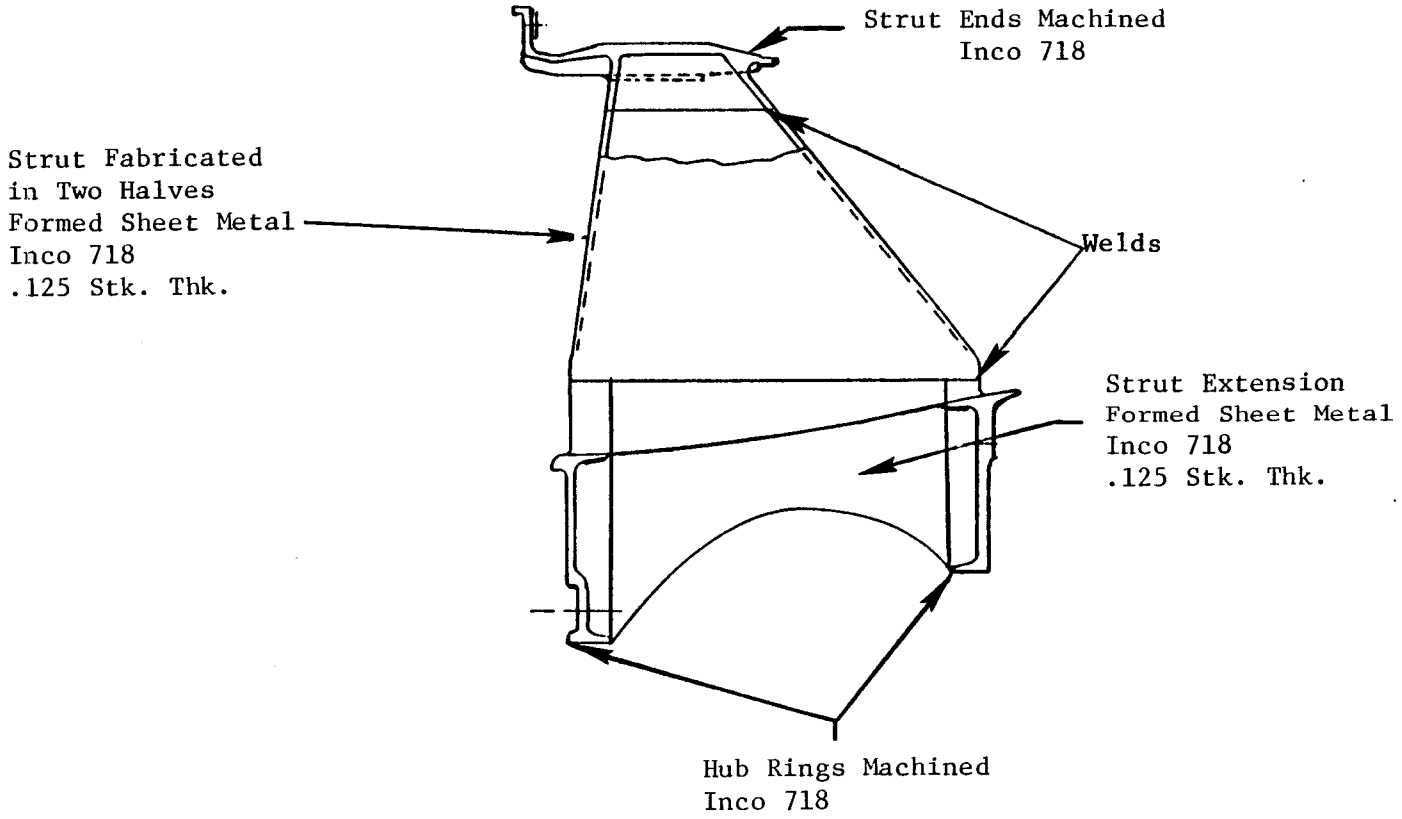


**Figure 60. Turbine Frame Construction.**

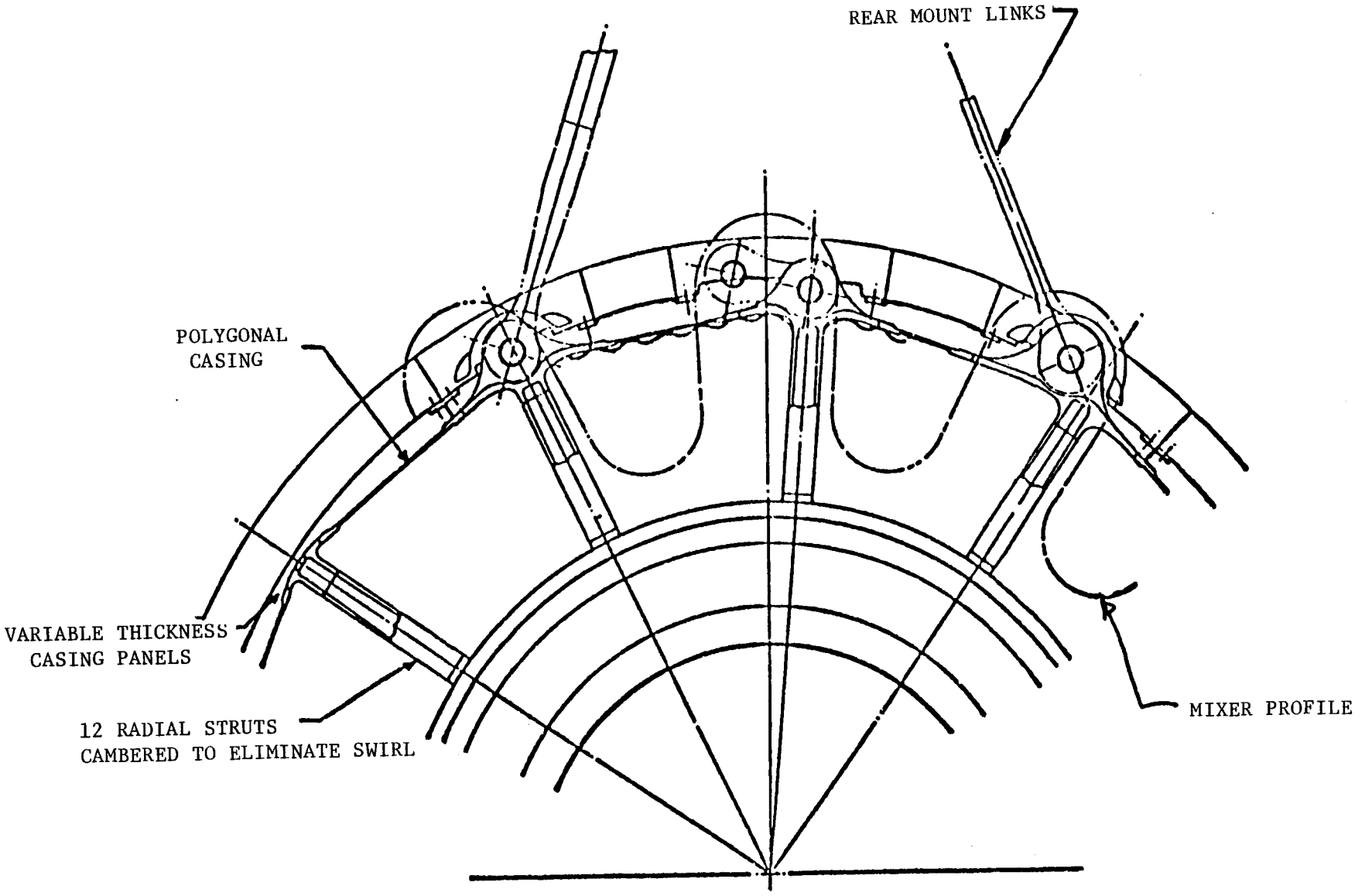


**Figure 61. Turbine Frame Features.**

strut plane at the casing. The radial struts were stiffer than semitangential because they were shorter, which also results in a lower strut weight. In addition, the struts have been cambered to remove residual turbine swirl.

The polygonal outer casing carried point loads more efficiently than a conventional cylindrical casing. That is, with radial loads reinforced by the struts, a polygonal casing loaded up uniformly in tension or compression, while a cylindrical case would be subject to high bending stresses at the strut ends. The polygonal case was also stiffer, due to its lower flexibility under the imposition of radial loads at the struts.

The polygonal panels were chem-milled between strut ends to reduce the stock thickness, as shown in Figure 62. This produced preferential strain distribution in the casing. By thinning the panel in the center, more straining took place in the panel center than at the ends where the welds were located. These panels were made of wrought sheet material and could withstand higher stress levels than can cast strut ends.

In order to reduce the maximum thermal expansion difference between the frame major components, two thermal expansion control features were incorporated into the design. One feature was a sheet metal heat shield on the outer casing as shown in Figure 63. This liner served as a radiation shield and both decelerates the thermal response of the casing during transient operation and effects a lower steady state casing operating temperature. The other feature concerns convectively heating the frame hub with flowpath gas, also shown in Figure 63. The forward hub ring was heated by means of bleeding flowpath gas radially inward between the last stage of the low pressure turbine and the frame hub. The aft hub ring was heated by bleeding hot gas radially inward between a sheet metal baffle and the aft hub ring. Bleeding the flowpath gas radially inward was possible because the entire cavity inside the frame hub, including the aft centerbody, was vented to ambient through the center vent tube. The relatively large mass comprising the frame hub usually results in a hub thermal response which lags the other frame components and therefore results in large thermal expansion differences during transient operation. Convectively heating the hub accelerated its

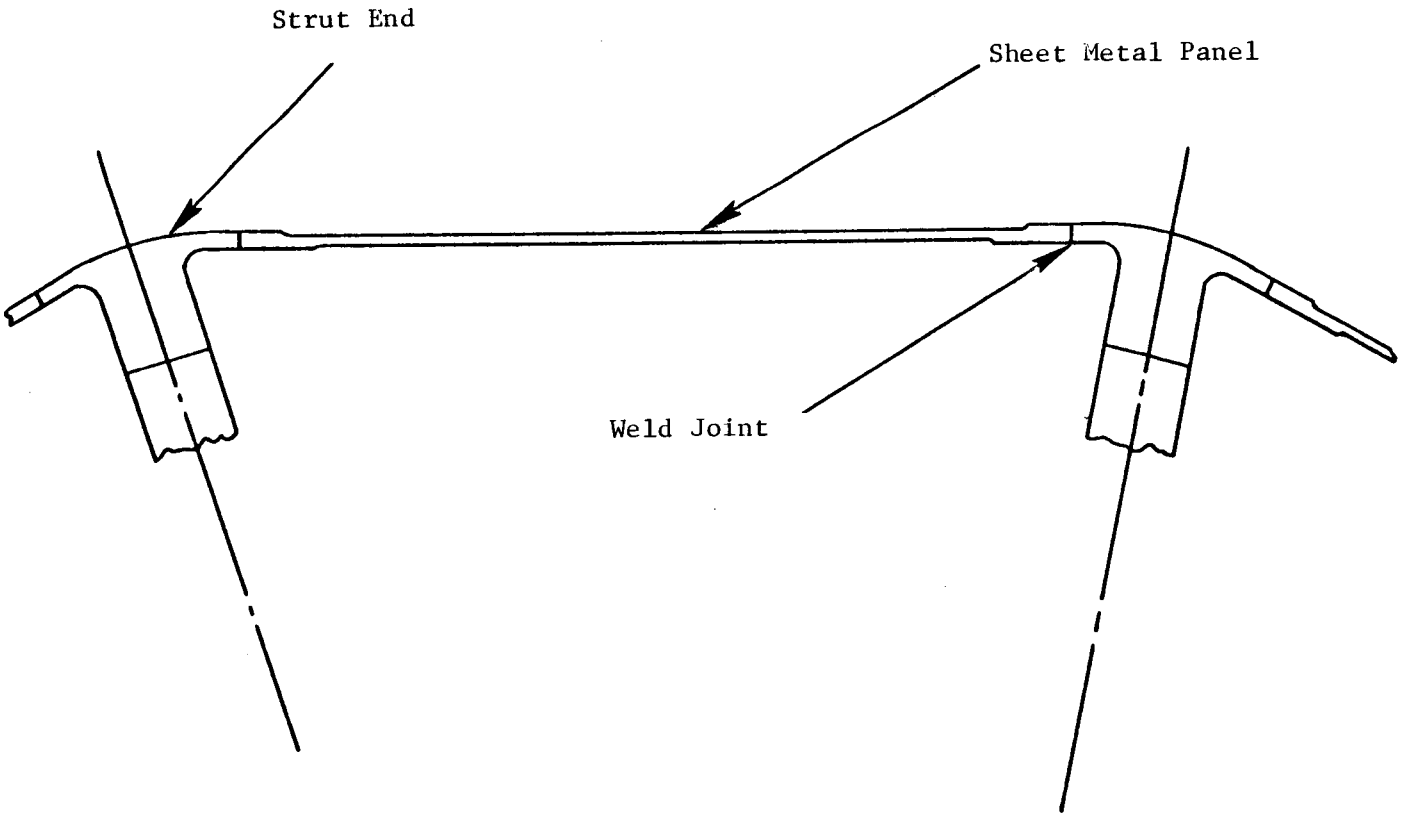


**Figure 62. Turbine Frame Casing Panel Chem Milled to Reduce Stock Thickness Between Strut Ends.**

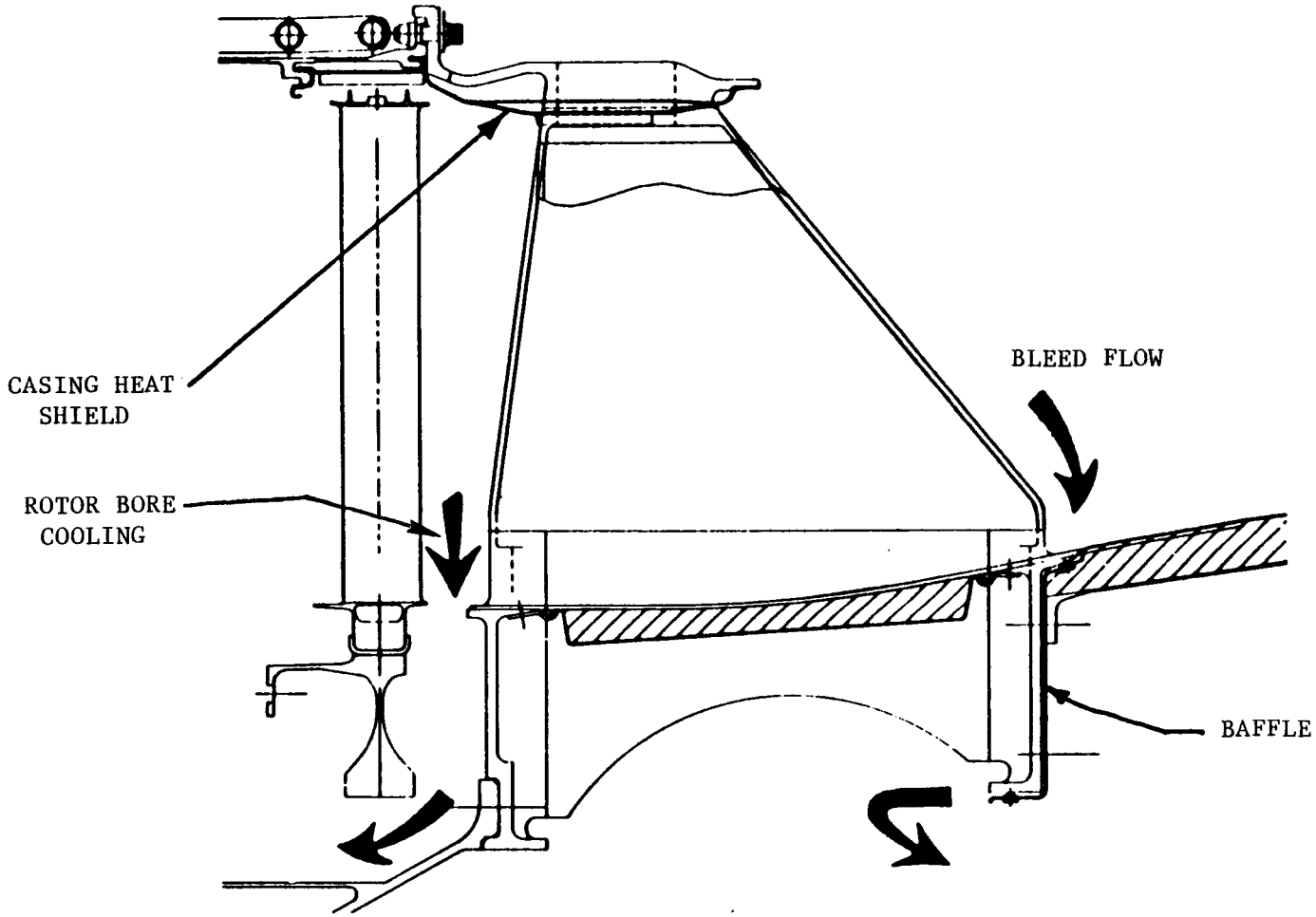


**Figure 63. Turbine Frame Thermal Expansion Control Features.**

thermal response and again reduced the thermal expansion differences which can exist during both transient and steady state operation. The hot gas used to heat the hub had a low impact on performance since it was reinjected into the gas stream at the center vent tube exhaust.

Acoustic treatment panels were placed beneath the shear cylinder between the struts. The panels contained Astroquartz with nominal density of 25.63 $kg/m^3$ (1.6 pounds per cubic foot) and are 1.27 cm (0.5 inch) deep. The shear cylinder portions above these panels were perforated with 0.158 cm (0.062 inch) diameter holes in a standard staggered pattern with 30% open area.

## 3.8 EXHAUST SYSTEM DESCRIPTION

The ICLS engine used a full length duct to carry fan discharge air to a mixer. The mixer combined the fan and core streams prior to being discharged through a single exhaust nozzle. A centervent tube extended from the tailcone, located ahead of the exhaust plane, out through the center of the nozzle. This tube vented purge and leakage air from the aft sump and turbine frame cavities.

### 3.8.1 Exhaust System Aerodynamic Design

The major components of the ICLS exhaust system flowpath include the fan exhaust duct, the pylon, the exhaust nozzle, and the mixer/centerbody. The aerodynamic design of these flowpaths have been developed through a combination of analytical studies and scale model performance test to provide a high performance exhaust system compatible with a lightweight, low drag nacelle.

The fan exhaust duct has been designed for low Mach numbers to minimize duct pressure losses and at the same time to be compatible with (1) a thrust reverser for a low drag FPS nacelle, (2) a core-mounted gearbox for an FPS nacelle, and (3) the mixer flowpath. An analytical study of the duct at cruise operating conditions indicated the desired low Mach numbers were

achieved as shown in Figure 64. Typical Mach numbers for separate flow nacelle fan ducts range from 0.45 to 0.50 whereas the $E^3$ fan duct ranges from below 0.40 to 0.45 for most of the duct. The fan duct flowpath has been included in all the scale model mixer performance tests, and results have verified a low pressure loss design.

The pylon cross section flowpath, shown in Figure 65 has been designed with two major considerations. The forward, or nose, portion of the pylon was designed to assure aerodynamic compatibility with the fan by proper selection of nose angle and axial location relative to the fan OGV's. The aft portion of the pylon from the maximum width to the trailing edge was designed to be aerodynamically compatible with the mixer and to provide low pressure loss. The pylon has been simulated in the scale model mixer development tests, and back-to-back testing with and without the pylon verify pressure losses even lower than predicted. The engine aft mount links were positioned over the turbine frame as shown in Figure 66 to minimize drag and to eliminate any potential interaction/impact on the mixer. These links were also tested in the scale model mixer development program and were shown to have both low drag/pressure loss and no effect on the mixer aerodynamics.

The ICLS engine was tested with two exhaust nozzles as shown in Figure 67. The basic performance nozzle is a conical nozzle designed to provide area trim capability for optimizing the engine cycle area match. The exit survey nozzle was used during the exhaust nozzle exit survey tests and initially had a 5% larger exit area at an exit station of 348.3 to account for estimated exit survey rake blockage. As a result of the nozzle flow coefficient identified from the scale model tests, the performance nozzle was cut back to station 339.4 to provide the desired ICLS effective area cycle match. Since the scale model mixer test was conducted with a nozzle exit station of 344.7, it was decided to cut the survey nozzle to that station to provide a more exact comparison of mixing effectiveness with the scale model. Combined with a higher flow coefficient for the survey nozzle because of the shallower half angle, the effective area of the survey nozzle was approximately 2.5% smaller than the performance nozzle without rake blockage. The survey rake had a projected area of blockage of 7% of the nozzle area.

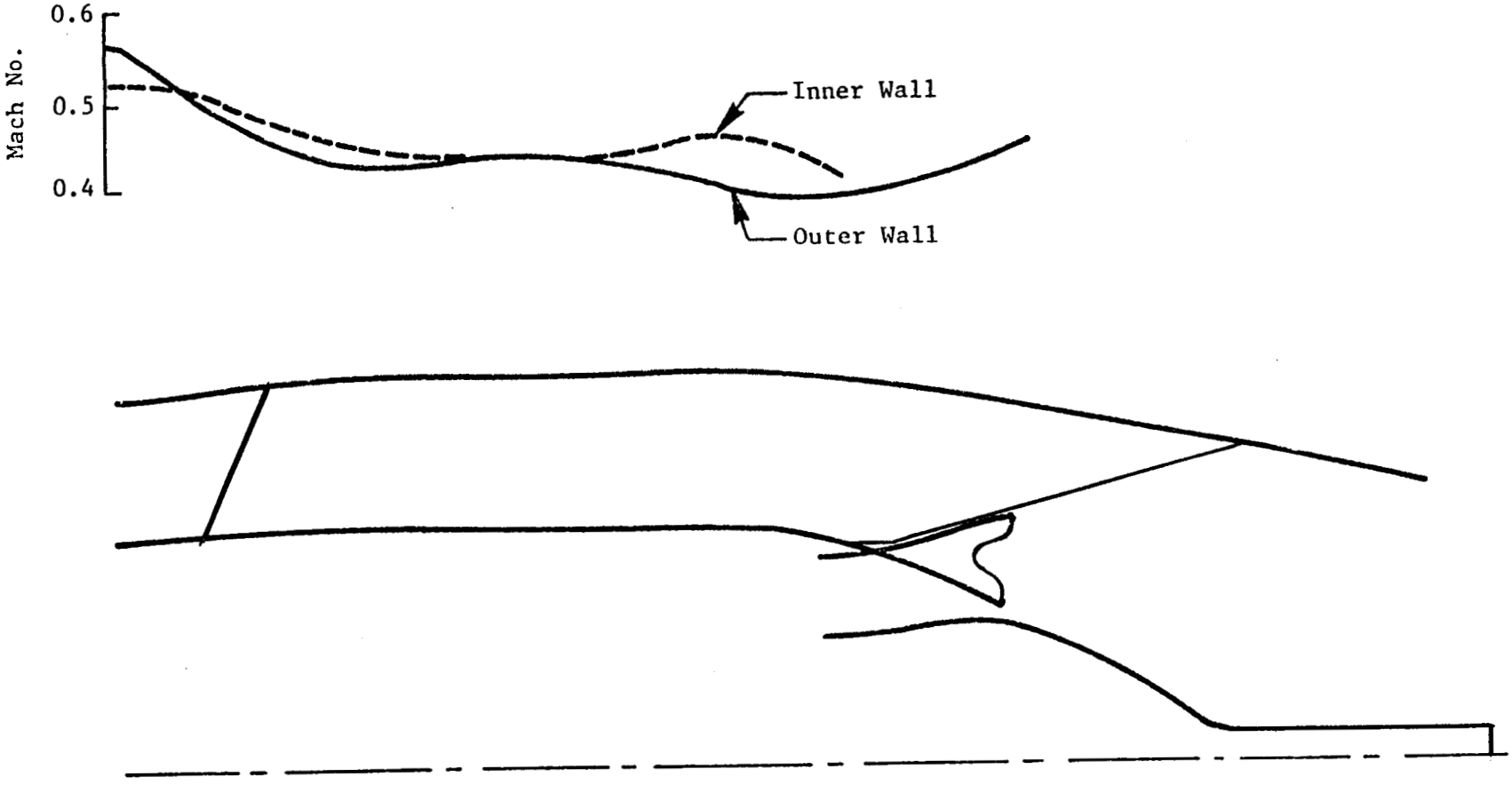


Figure 64. Fan Duct STC Analysis (Altitude Cruise Condition).

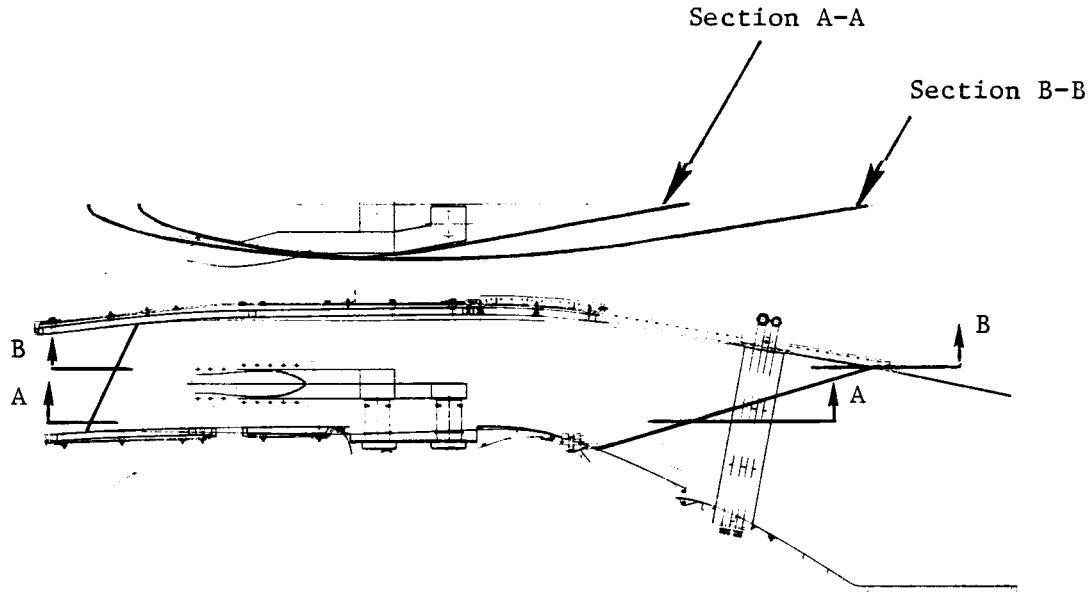


**Figure 65. Pylon Cross Section.**

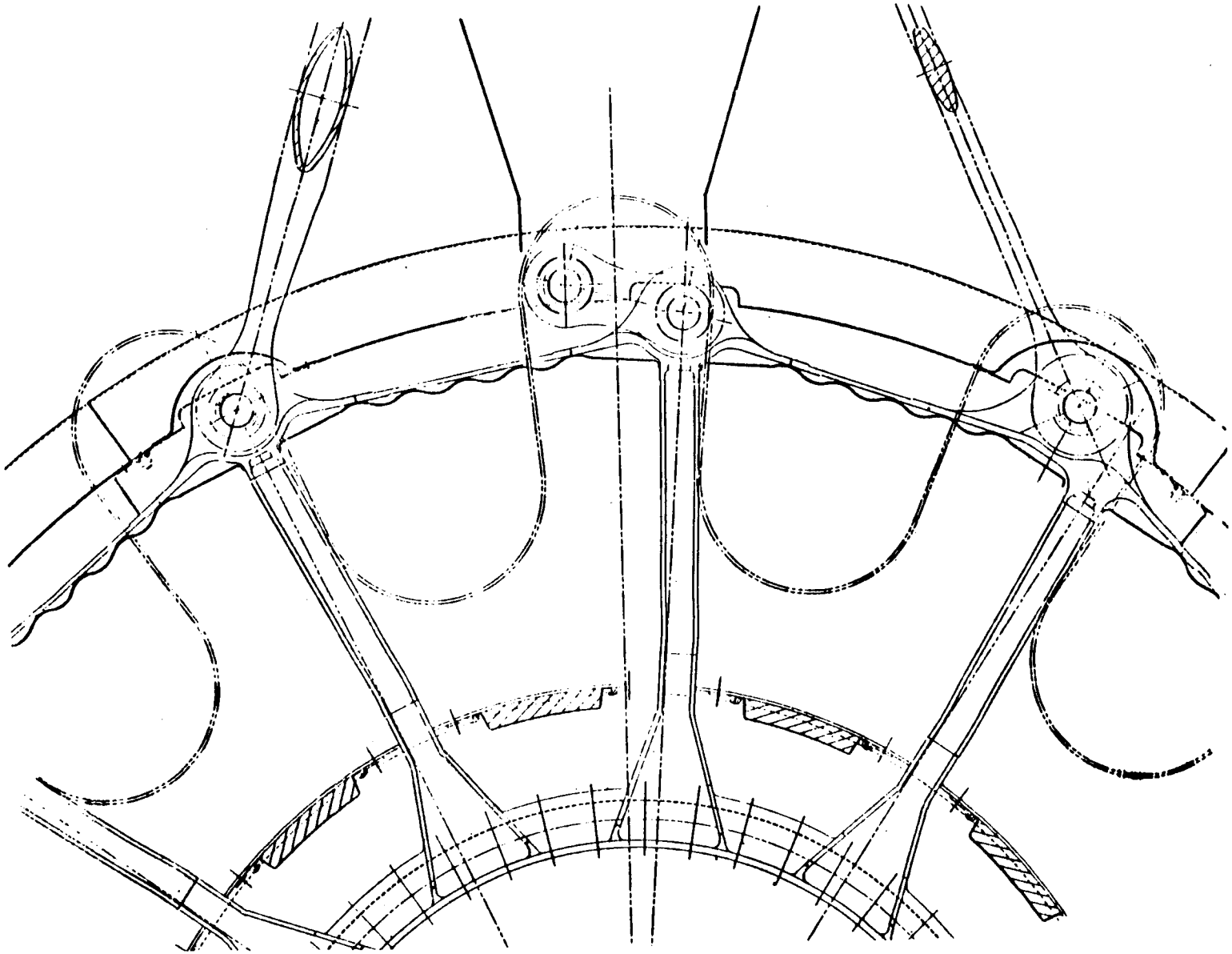

Figure 66. Mixer/Pylon/Aft Mount Integration.

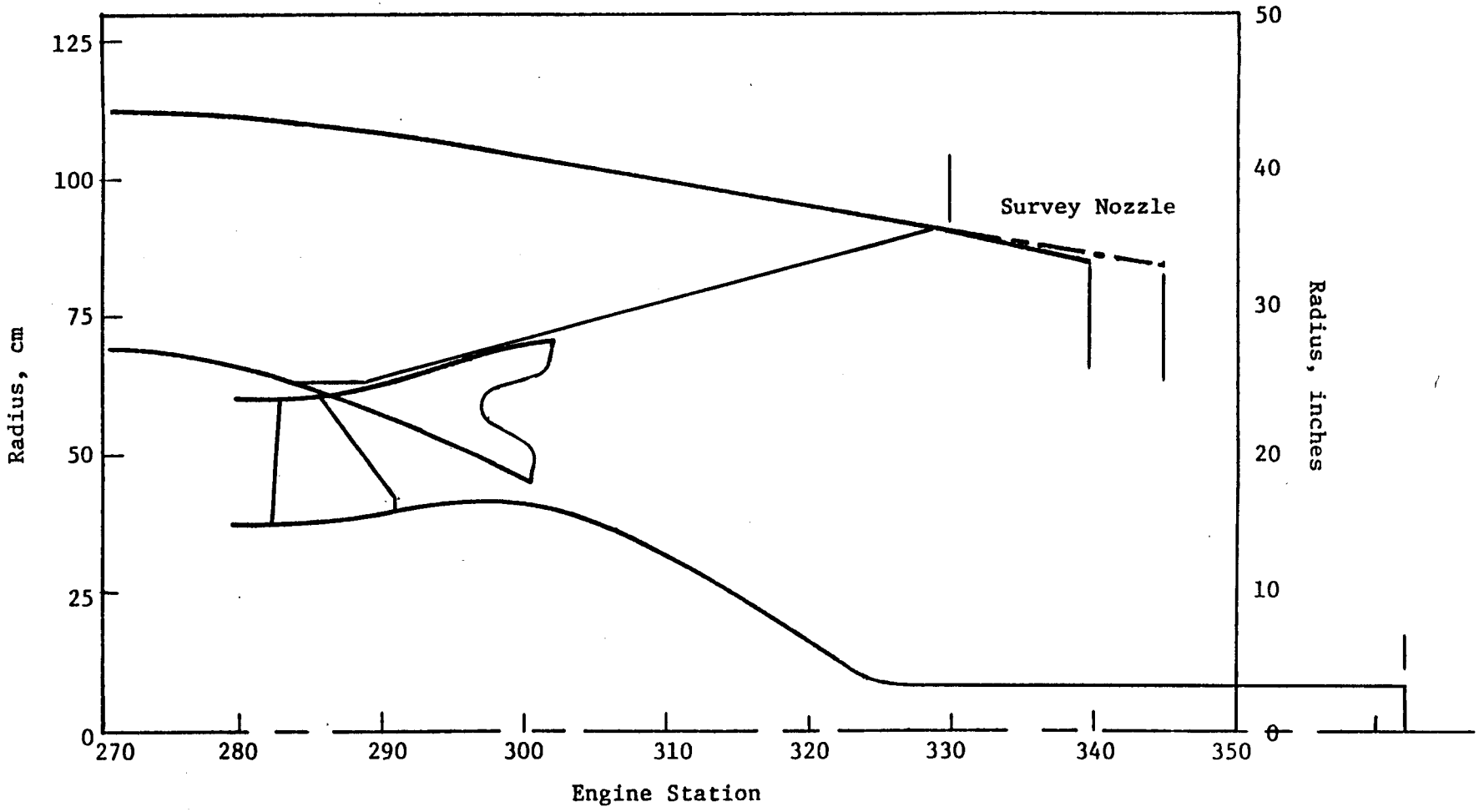


Figure 67. ICLS Exhaust Nozzle Aero Design.

The selected mixer and exhaust system design for the ICLS engine is shown schematically in Figure 68 along with a tabulation of major geometric features. The ICLS configuration was derived from the analysis and application of results from the scale model test experience. The mixer had 12 lobes with scalloped, radial sidewalls to promote mixing.

The mixer penetration was selected to be 43% and the tailpipe length from the mixing plane to the nozzle exit was 111.8 cm (44 inches) giving an L/DMP ratio of 0.55. Both parameters were selected by optimizing total system performance using the scale model test results. The trade studies conducted for this optimization are shown in Figure 69. Tailpipe length variations investigated in the model tests were used to determine effects of length on sfc at the M0.8/10.67 km (M0.8/35 K) MX cruise design point relative to a base tailpipe length of 88.9 cm (35 inches). The sfc curve in Figure 69 includes the estimated increase in external drag as well as the internal benefit due to mixing. With increasing tailpipe length, both engine and aircraft weight increase. The weight increases and sfc gains were combined to obtain the net system performance variation with tailpipe length in terms of percent fuel burned. This curve, also shown in Figure 69 indicates a peak near 119.38 cm (47 inches). It was decided to select the 111.8 cm (44 inch) length which is essentially near the peak. Using mixing effectiveness and pressure loss trends versus penetration developed from the model tests, a trade study of performance gain versus mixer penetration was also conducted. In this case, the sfc gains were strictly internal and the weight effects were very small. The sfc improvements were made relative to a baseline 39% penetration mixer. As expected based on earlier preliminary studies, there is not a significant change in net performance for the mixer in the 40 to 50% penetration range; in that range the increase in mixing effectiveness is offset by the increase in mixer pressure loss for the $E^3$ cycle. Even though the gain was small, it was decided to select the 43% penetration mixer for ICLS to maximize the performance gain potential.

The ICLS exhaust system flowpath differs from the FPS design because of changes in the mixer design to improve performance. Because of ICLS hardware

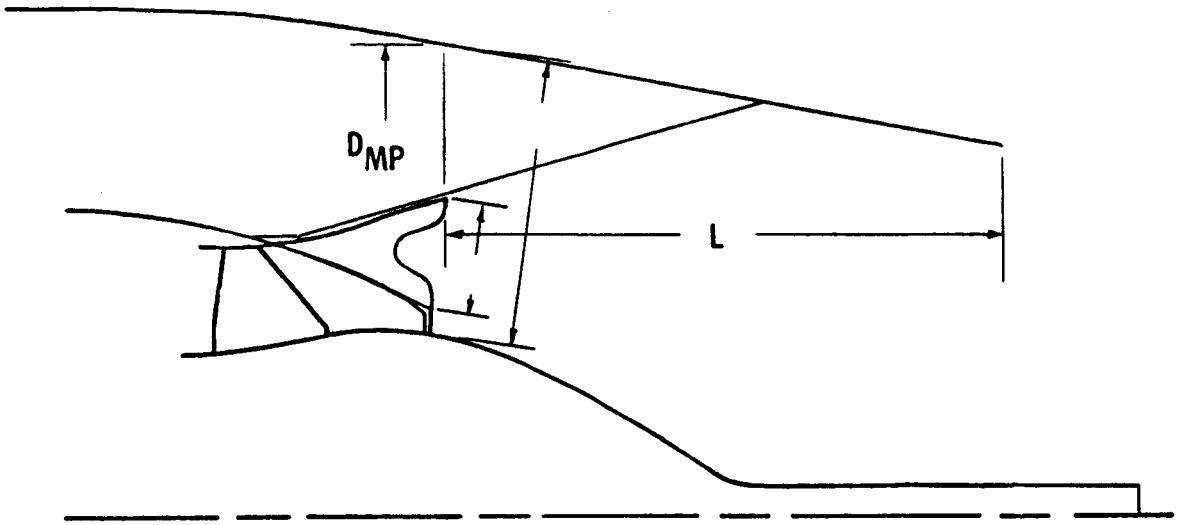


- 12 Lobes
- Scalloped Radial Sidewalls
- 43% Penetration
- 44 Inch Tailpipe Length, $L/D_{MP}$ = .55
- Integrated With Pylon and Aft Mount

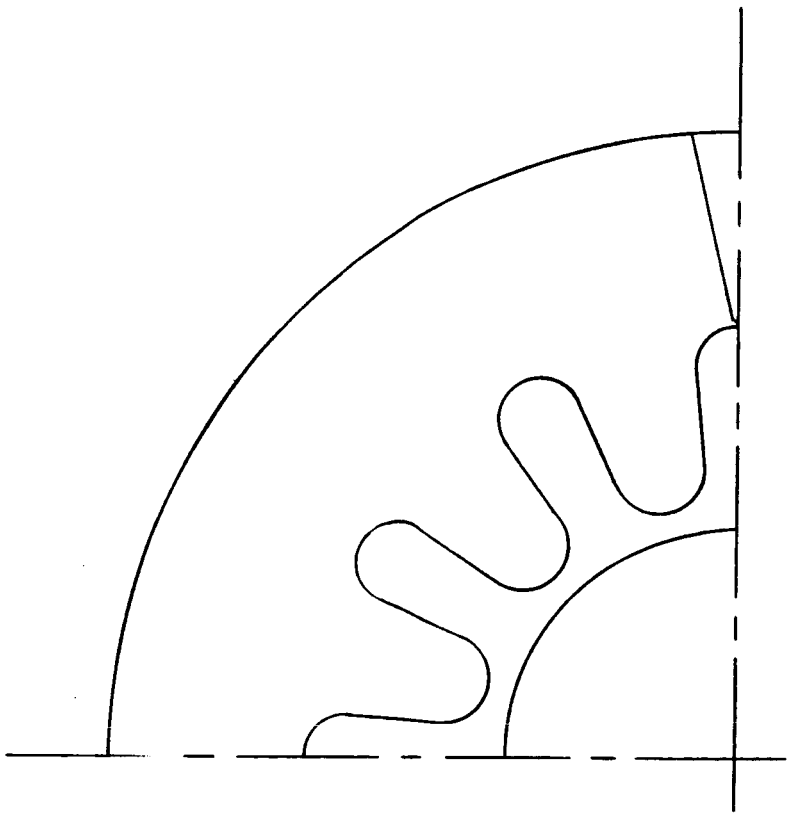

**Figure 68. ICLS Mixer Aero Design.**

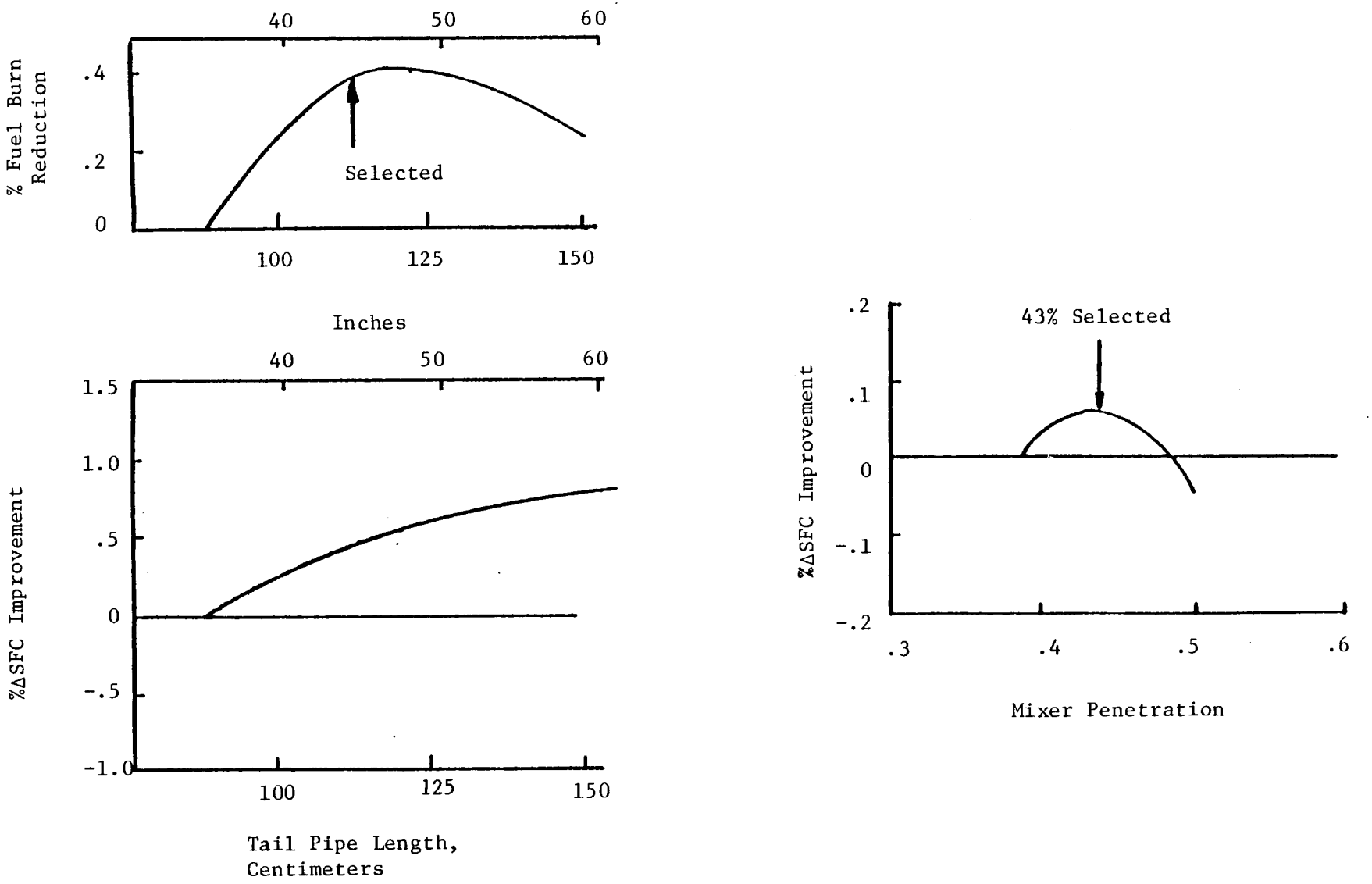


Figure 69. Mixer/Exhaust System Trade Studies.

detail design and procurement schedules, the ICLS design had to be selected prior to completion of the scale model performance tests. Thus, the ICLS mixer represents an interim design for $E^3$. Continued scale model testing following the ICLS mixer selection identified an improved mixer design which altered the exhaust nozzle flowpath and was included in the FPS design.

An overall comparison of the ICLS and FPS exhaust system flowpaths is shown in Figure 70. Forward of the turbine frame, the two flowpaths are identical. Aft of the turbine frame, the ICLS exhaust nozzle geometry differs from the FPS to match the ICLS mixer flowpath previously described. The FPS design has a larger centerbody and a mixer which is larger in diameter; consequently, the FPS exhaust duct diameter must be increased in the region of the mixing plane to maintain mixing plane areas and Mach numbers. This change in the FPS design, designated the flared turbine flowpath, was incorporated to improve performance as noted in Figure 70. Based on the scale model mixer tests, the flared turbine/mixer flowpath combined with mixer lobe design changes improved mixing effectiveness by 7% and reduced mixer pressure loss by 0.1% resulting in an sfc improvement of 0.4% at max cruise. Additionally, the increased diameter of the last two LPT stages was estimated to improve LPT efficiency resulting in a further 0.16% sfc gain.

The exhaust nozzle shape near the nozzle exit is also different between FPS and ICLS. The FPS has a low area ratio, converging-diverging nozzle for desired takeoff-to-cruise nozzle flow coefficient characteristics. This type of nozzle is not amenable to area trimming and would, for a typical engine development program, be sized for production based on substantial engine development testing. Since the ICLS engine is a single engine technology program and will only be tested at SLS conditions, it was concluded that the exhaust nozzle should be a simple, conical/convergent nozzle to provide area trim capability as previously discussed. This nozzle difference can be seen in Figure 70.

In addition to the basic exhaust system flowpath differences, there are several differences in flowpath pressure loss between ICLS and FPS. These

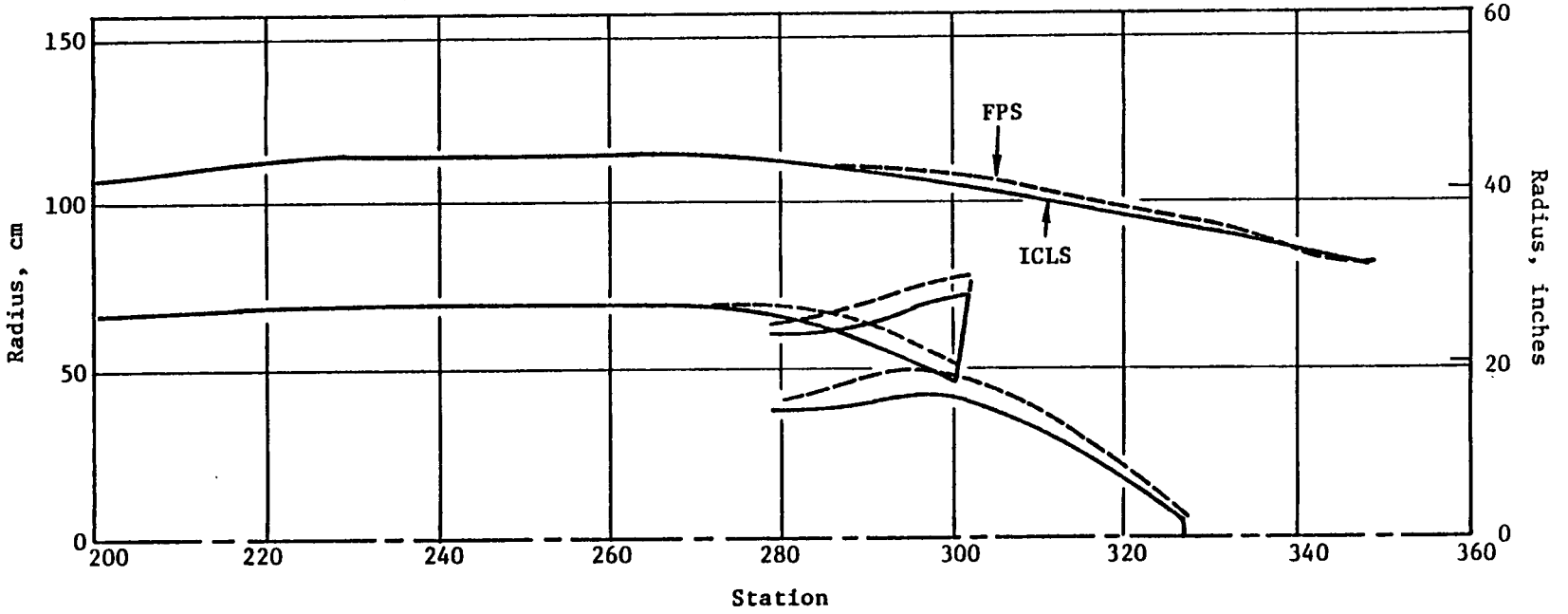


- Flared Turbine Flowpath Provides:
  - Improved Mixing Effectiveness
  - Potential for Reduced Mixer Pressure Loss } 0.2% SFC Estimated
  - Improved LPT Efficiency 0.16% SFC Estimated
- Analysis and Conclusions too Late (June 1980) for Incorporation into ICLS

Figure 70. Flared Turbine Flowpath.

differences are listed in the following table along with an estimate of the change in duct pressure loss. Figure 71 shows the location of several of these items.

Differences from FPS

- Differences in flowpath pressure loss items include:
  - No steps and gaps associated with reverser (+0.12% ΔPT)
  - No drain mast at bottom centerline (+0.01% ΔPT)
  - No precooler scoop (+0.05% ΔPT)
  - Instrumentation strut at 75° in exhaust nozzle (-0.10% ΔPT)
  - Lower pylon behind fan frame for ICLS gearbox (-0.05% ΔPT)

### 3.8.2 Exhaust System Mechanical Design

#### Fan Cowl

The fan cowling extended from the aft outer ring of the fan frame aft to the end of the fan nozzle. The structure was divided into the fan cowl doors, mid fan cowl, aft fan cowl, and fan exhaust nozzle. All of this structure was slave hardware which provided the proper internal aerodynamic lines and acoustic treatment but had no aerodynamic outer surface. No attempt was made to provide a flight weight design, therefore the most economical materials were used which would provide the necessary structural characteristics. An overall view of the ICLS fan cowling, attached to the mount beam, is shown in Figure 72.

The fan cowl doors were hinged to the facility mount beam structure at six hinge points at the top and latched together with five latches at the bottom. For the ICLS these doors did not contain the reverser structure that would be included in an FPS design. The basic structure of the doors consisted of a ring-stiffened aluminum shell. The doors had a forward aluminum ring which had a tongue which engaged a groove on the aft side of the fan frame. Since doors were supported from the facility and not the engine,

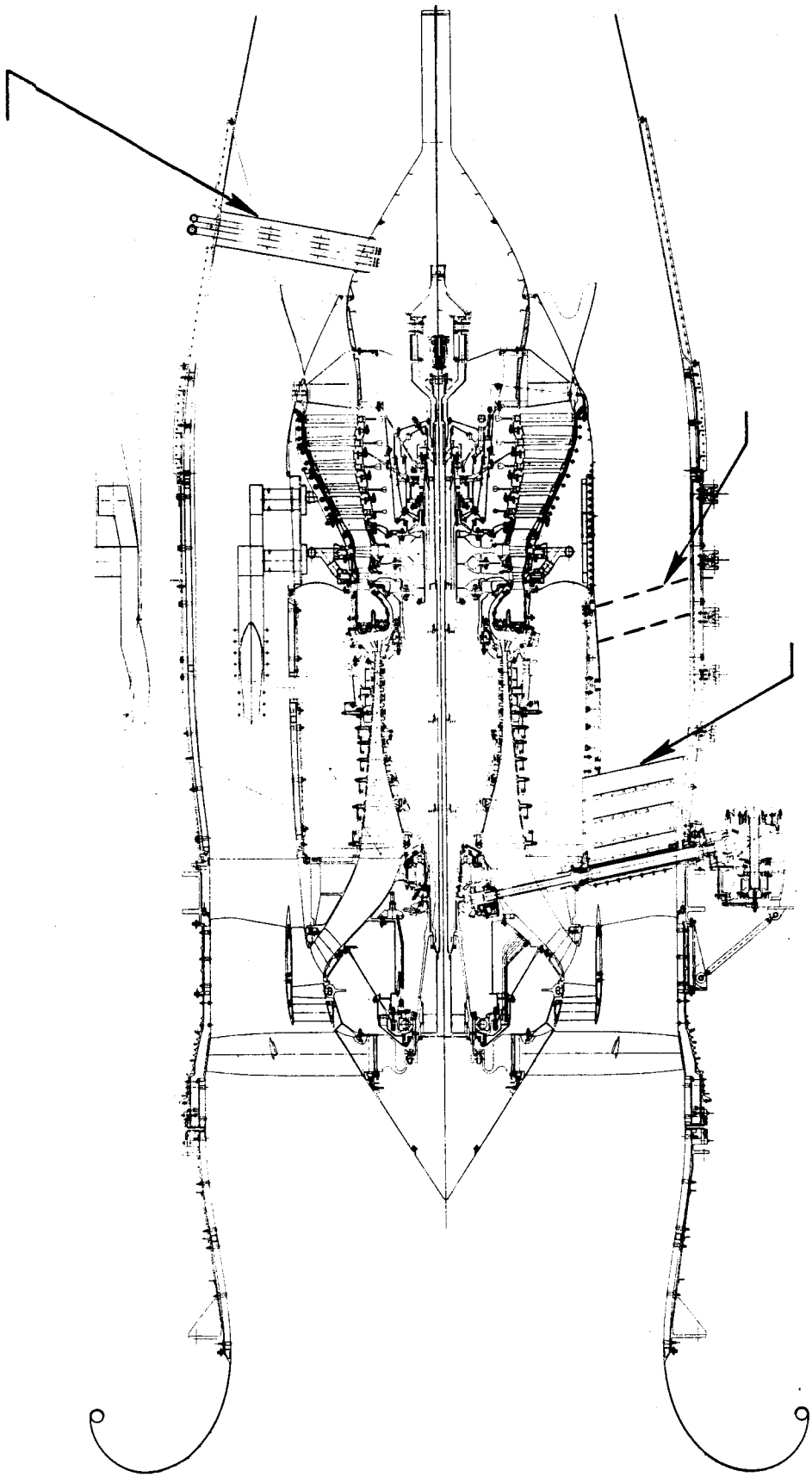

Figure 71. Pressure Loss Items.

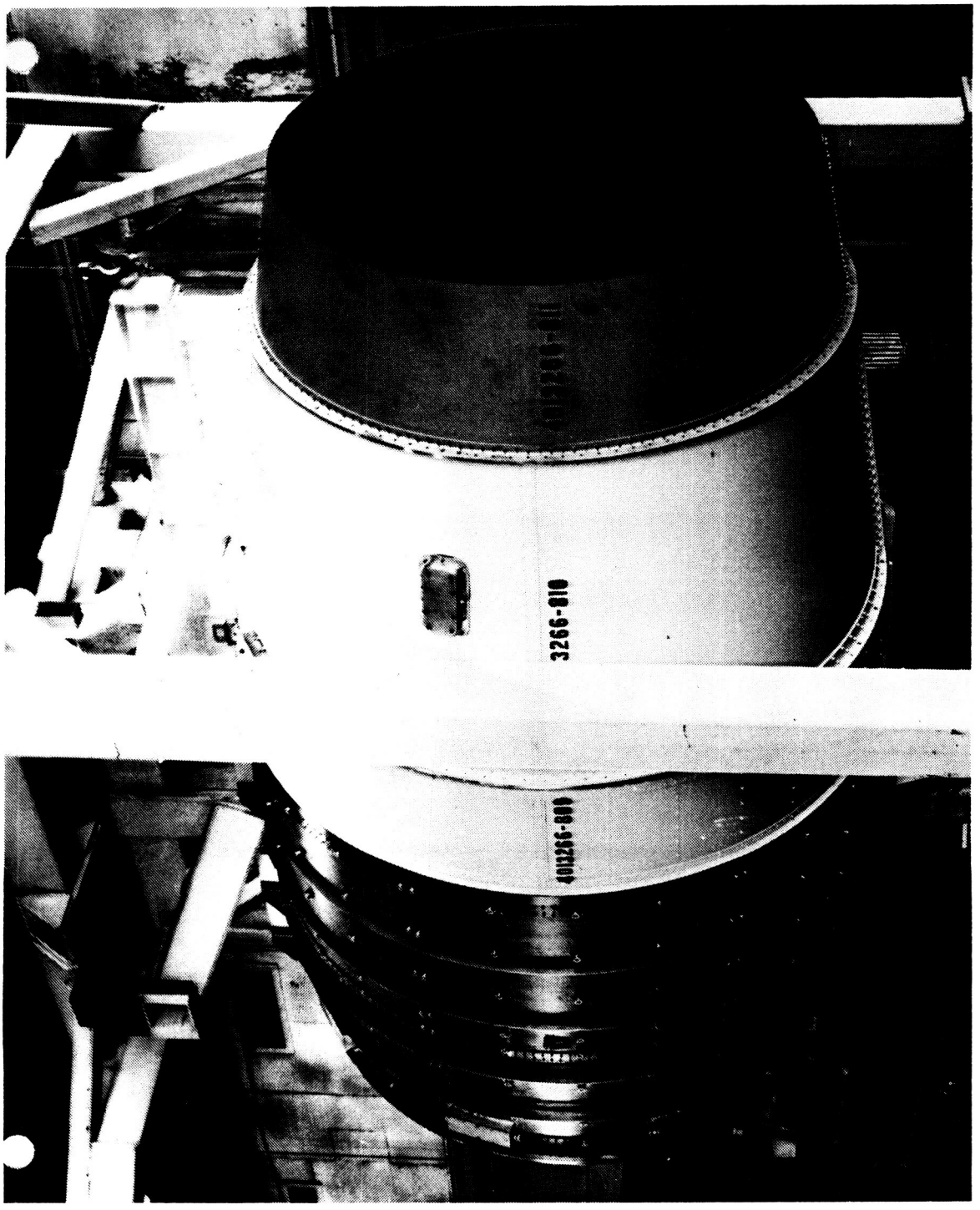


Figure 72. ICLS Fan Cowling.

the fit of the tongue into the fan frame groove was very loose so as not to transmit any load through this joint. The aft ring on the doors was also a tongue and groove arrangement with the tongue fitting into a groove in the mid fan cowl. This joint was a tight fit to make it a load carrying attachment. The bulk absorber type acoustic treatment was contained in replaceable felt-filled aluminum panels which were bolted to the flowpath side of the structure.

The mid fan cowl was an all-aluminum structure with integral bulk absorber type acoustic treatment. This structure was made in two halves which were bolted together at the bottom and bolted to the engine mount beam at the top. The outer skin was stretch-formed and attached to rolled "Z" rings at each end. These "Z" rings were, in turn, attached to machined interface rings. The forward interface ring incorporated the groove for the tongue and groove attachment to the outer cowl doors while the aft interface ring bolted to a similar ring on the aft fan cowl. A perforated aluminum skin was attached to the inner legs of the rolled "Z" rings, and the cavity thus formed was filled with Kevlar felt to provide the acoustic treatment.

The aft fan cowl was a simple aluminum shell and contained no acoustic treatment. It was made in two halves and was attached to the mount beam at the top centerline and to itself at the bottom. There are two manufacturing splices on the horizontal centerline. Machined interface rings were mechanically attached to each end. The forward interface ring was bolted to a similar ring on the mid fan cowl and the aft ring was attached to, and supported, the fan nozzle.

The ICLS vehicle utilized a conical nozzle rather than the converging/diverging nozzle designed for the FPS. Two of these nozzles were available for use with the ICLS. Each nozzle was made from two pieces of rolled AISI 321 stainless steel sheet bolted together with a splice plate at the top and bottom to form a 360° conical structure. A steel ring was attached to the forward edge of this 360° cone to provide the interface attachment to the aft fan cowl. The two nozzles vary slightly in length and

cone angle in order to obtain different exit areas. The smaller exit area nozzle was used during basic engine performance testing while the other nozzle was used when evaluating mixer effectiveness.

Core Cowl Doors

The forward core cowl was 115.25 cm (43.37 inches) long and varied from 121.92 cm (48 inches) to 129.54 cm (51 inches) in diameter. This cowling consisted of two doors which were hinged to a floating apron structure at the top and latched at the bottom. When closed, the doors were supported from a ring on the back of the fan frame. The doors extended back over the forward edge of the fixed aft core cowl. There was a slight circumferential gap between these two structures to permit exhausting the core cowl purge air back into the fan stream. This purge air was obtained by scoops on the fan frame support ring which led to the under cowl cavity.

The basic structure of the doors consisted of rolled 321 stainless steel plate to which the hinges and latches were fastened. Even though the ICLS utilizes a fan-mounted gearbox, the expanded flow lines in the lower portion of the core cowl necessary to accommodate a core-mounted gearbox were incorporated into the ICLS design. The steel front flange contained a machined tongue which fit into a groove in a ring on the back of the fan frame. The doors were latched together at the bottom centerline except at the forward edge where they were latched to the fan frame to provide circumferential continuity in the area of the lower pylon which required a cut-out in the lower forward portion of the doors. Stand-offs were welded to the steel shell to provide mounting points for the acoustic panels. The basic structure described above is shown in Figure 73.

The doors each contained four large acoustic panels. These panels consisted of an aluminum framework with an aluminum back sheet and a perforated aluminum sheet on the flow surface. This structure was also filled with Kevlar felt for bulk absorber acoustic treatment. These panels were bolted to the basic steel structure. Figure 74 shows one complete and one partially completed panel installed on one core cowl door.

Figure 73. Core Cowl Doors - Basic Structure.

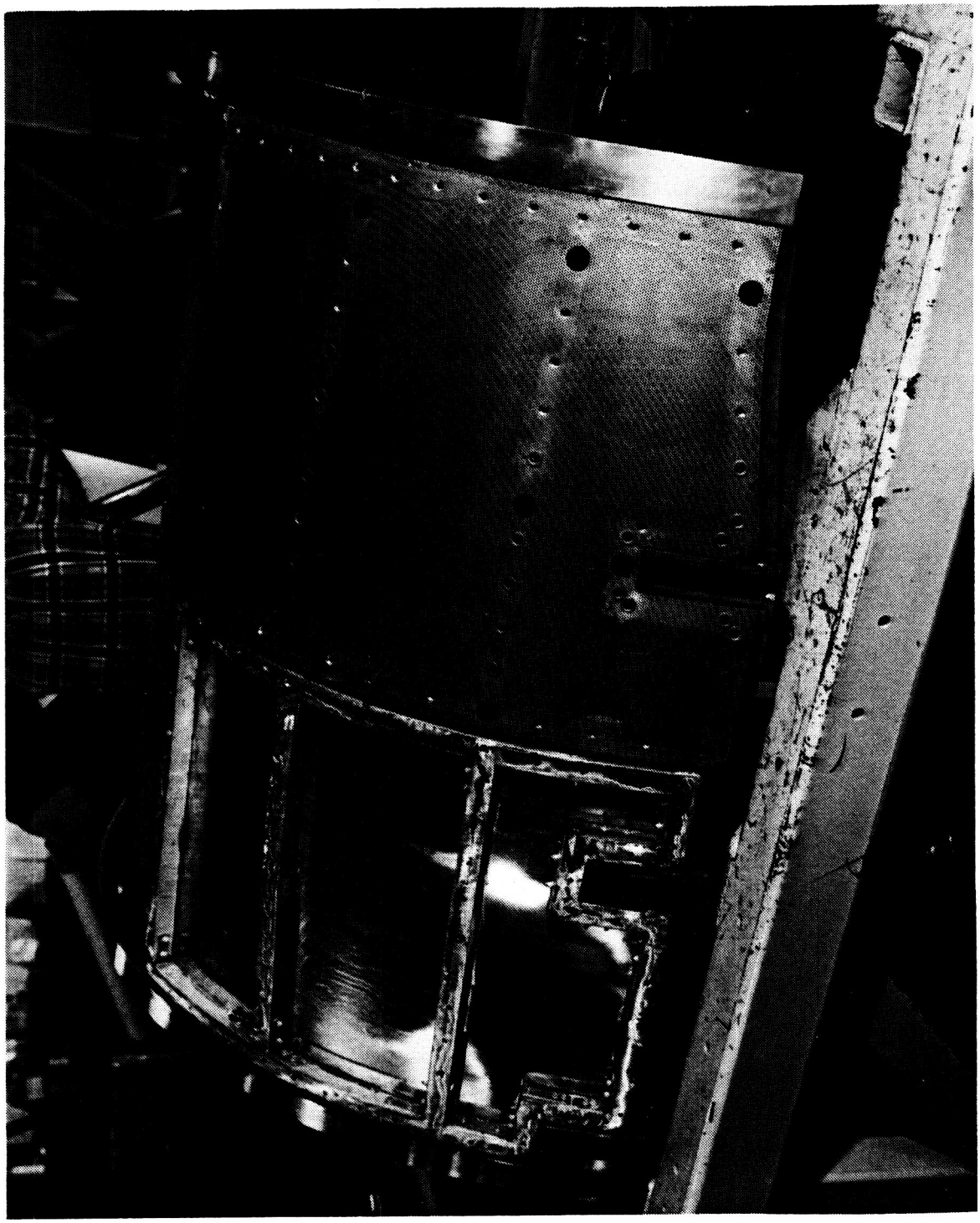

Figure 74. Core Cowl Door Partially Complete

## Pylon

The pylon structure housed the mount structure, various services, and the scoop and plenum serving the active clearance control system. In addition, a considerable amount of test instrumentation was routed up the pylon. The pylon leading edge was a fabricated structure bolted to the forward edge of the mount beam. The sidewalls consisted of a number of separate removable panels attached through bulkheads to the side of the mount beam. The pylon sidewalls were sealed against both the outer and inner cowl aprons. The pylon internal pressure was therefore ambient until just aft of the active clearance control plenum where a firewall was located in the mount beam/pylon structure. Aft of this point the pylon sidewalls were sealed to the mount beam and the aft fan duct and the internal pressure was the same as in the fan duct. The aft panels of the pylon were steel due to the mixed exhaust gasses in that area. The rest of the pylon was aluminum. The pylon structure, assembled to the mount beam and dummy engine, is shown in Figure 75.

## Centerbody

The centerbody cross section is shown in Figure 76 in relation to the other exhaust components. Its primary function was to provide a flowpath for the core air stream. In addition, this centerbody contained acoustic treatment panels, provisions for engine instrumentation leadout, and support for the mixer. It was designed as two axial pieces for ease of assembly. The material selected was INCO 625. The acoustic treatment panels were made as separate, removable boxes of 321 stainless steel. The boxes were 1.27 cm (0.5 inch) deep and filled with Astroquartz at a nominal density of 25.63 $kg/m^3$ (1.6 pounds per cubic foot). The panel face exposed to the core flow contained a hole pattern of 0.158 cm (1/16 inch) diameter hole in a standard staggered pattern with 30% open area.

The centerbody cavity was vented to ambient by means of the center vent tube in order to provide a sink pressure for the spent clearance control air.

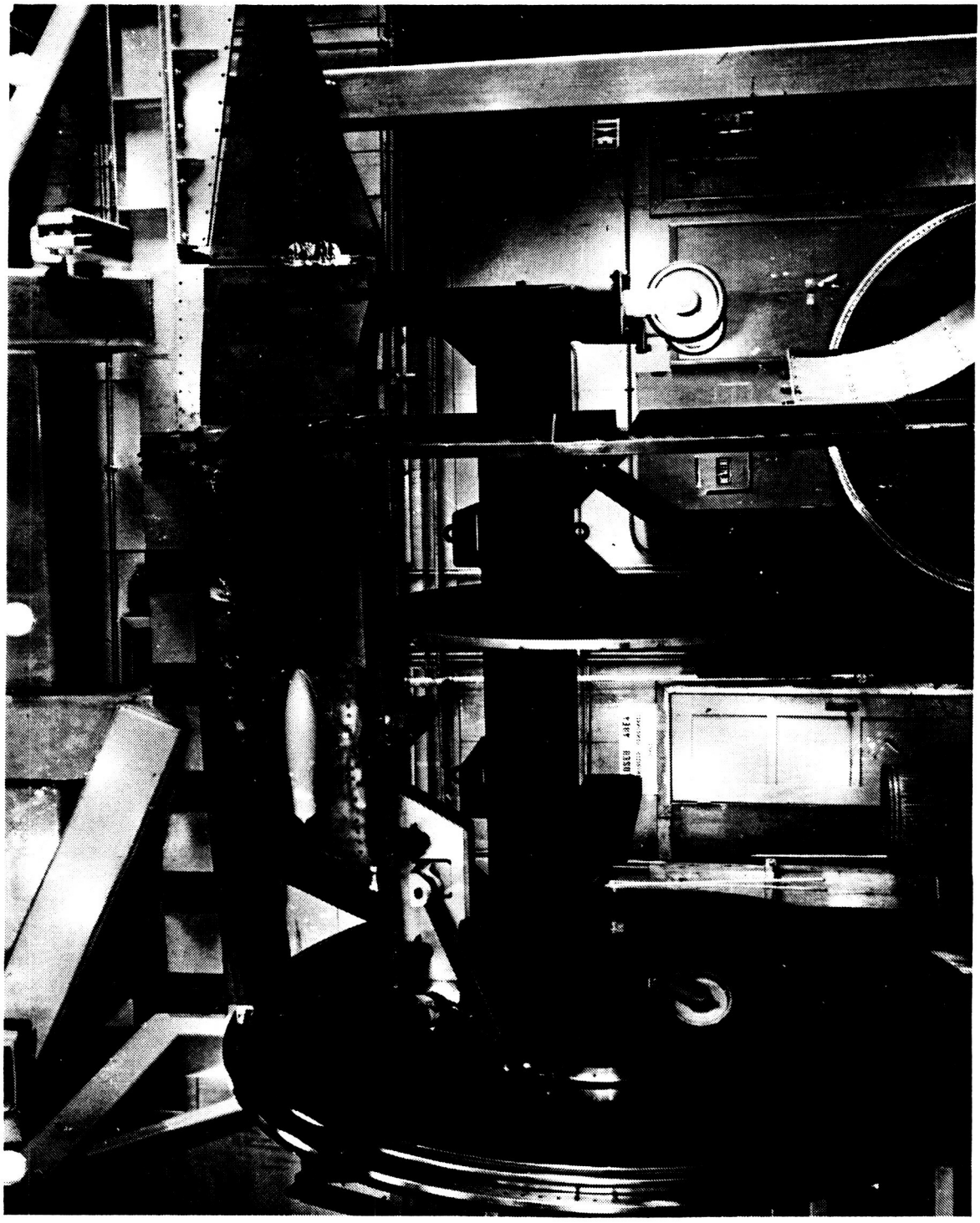

Figure 75. Pylon Structure.

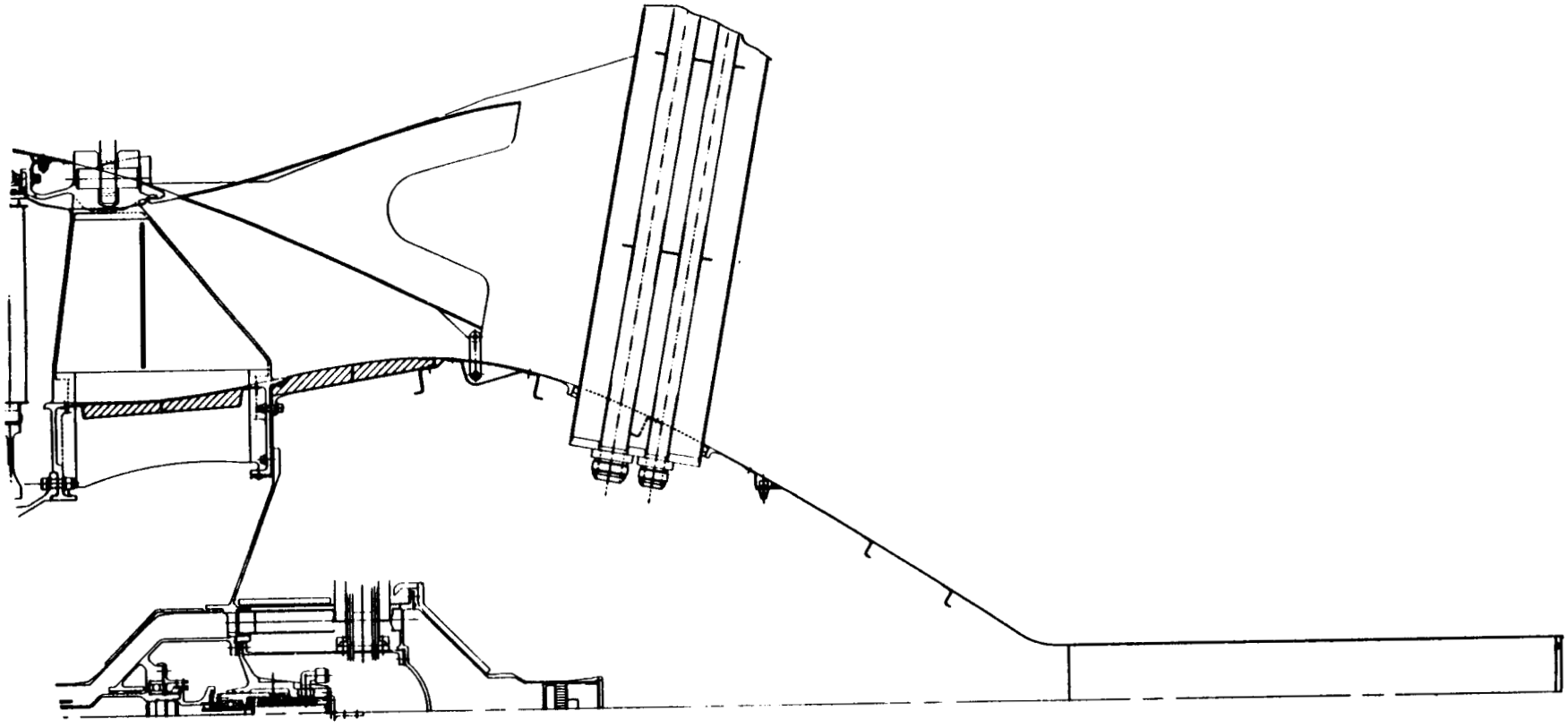

Figure 76. Centerbody Cross Section.

The spent air flowed through the turbine frame struts into the centerbody and then flowed out the center vent tube to ambient.

Aft Inner Core Cowl

The aft inner core cowl made up the inner fan flowpath immediately forward of the turbine frame. Its main design features are shown on Figure 77. Its secondary functions included routing the Active Clearance Control (ACC) air from the pylon to both the high and low pressure turbine casings, providing surface area for acoustic treatment, and providing structural support for the clearance control air actuation system and a significant portion of the test instrumentation. The core cowl is shown in Figure 78.

The cowl was designed as three parts; two sides with the portion situated beneath the pylon made into a separate piece by means of axial flanges on either side. This allowed removal of both sides of the cowl without disturbing the instrumentation leads or the clearance control air valves which are mounted on this plate. It also permitted removal of the cowl without removal of the pylon fairing. A third split flange located at the bottom of the cowl allowed both sides to be easily removed for access to the turbine casings.

The structural shell of the cowl was made of 321 stainless steel. This was covered by a 2.54 cm (one inch) thick layer of Astroquartz acoustic bulk absorber material [density of 25.63 $KS/m^3$ (1.6 pounds per cubic foot)], which in turn was held in place by a sheet of 321 stainless steel, perforated with the same hole pattern used on the frame and centerbody. The perforated sheet was bolted on to allow access to the bulk absorber if necessary.

On the inner side of the structural shell were welded two circumferential manifolds which routed the ACC air to the self-aligning ducts which interfaced with the turbines' ducting systems. These manifolds were also constructed of 321 stainless steel.

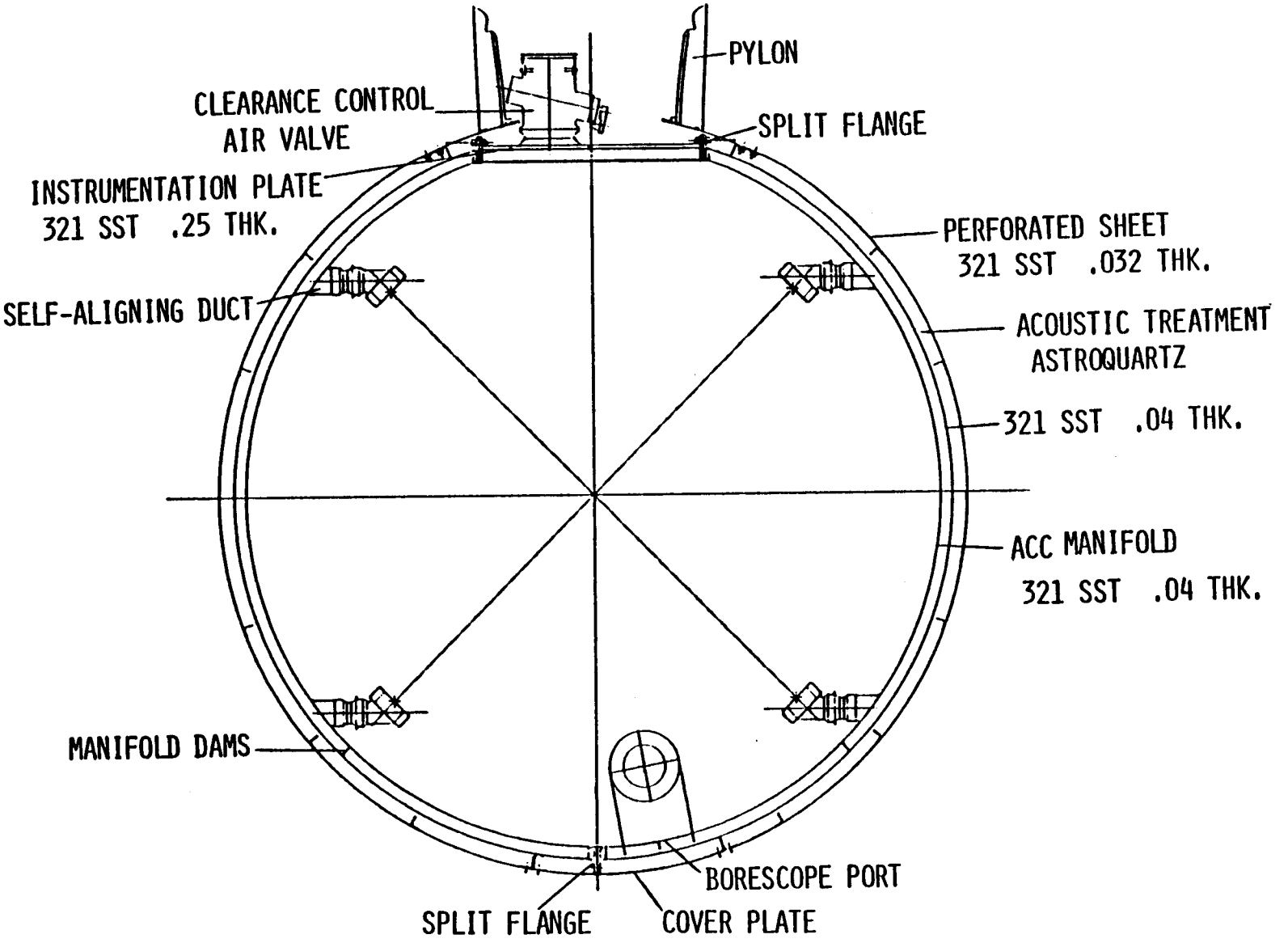


Figure 77. Aft Inner Core Cowl Description.

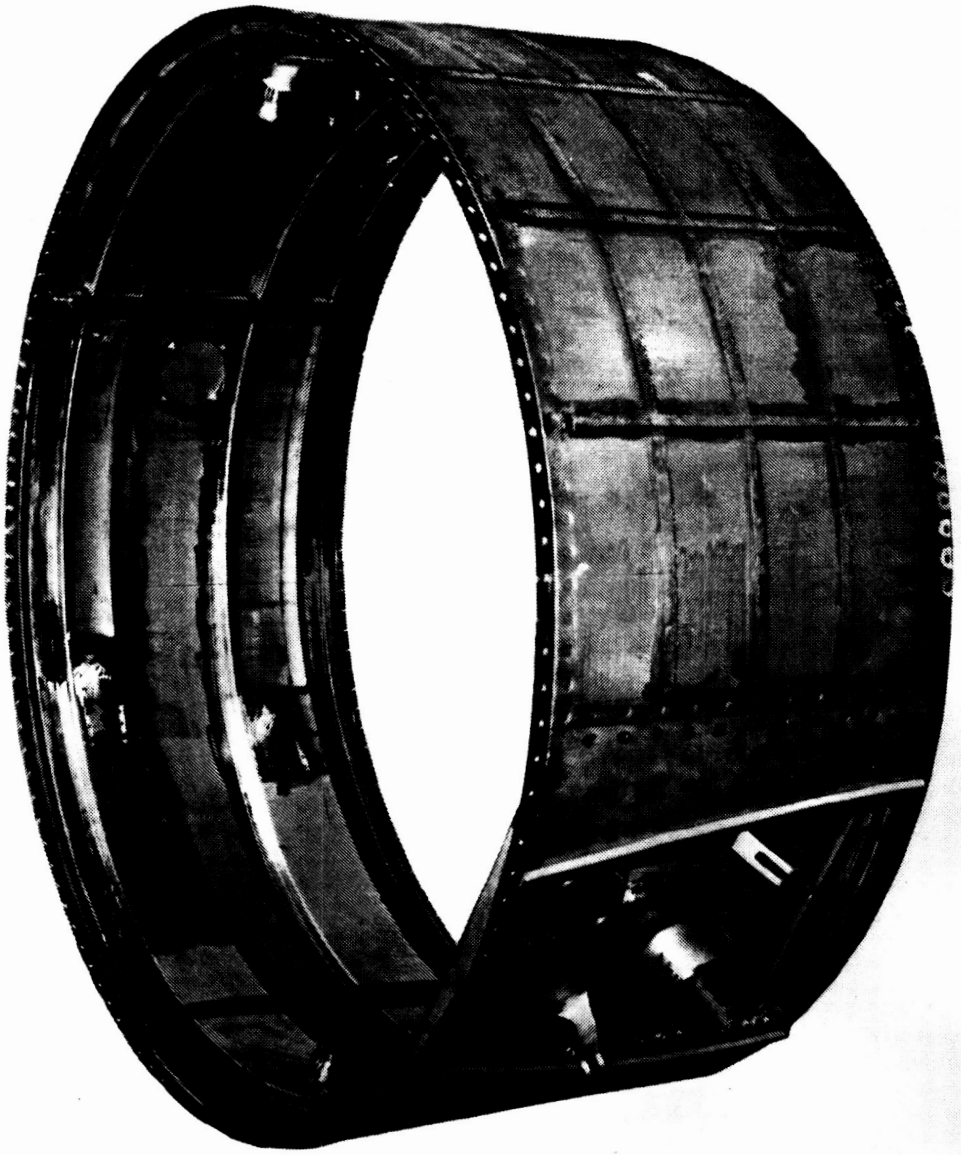

Figure 78. Core Cowl Assembly.

Mixer

The mixer was a twelve lobe, scalloped design. A cross section of the design is shown in Figure 79. For the ICLS engine, the mixer was constructed of 321 stainless steel. It was fastened to the centerbody by pinned links at each lobe, to the frame at the frame/low pressure turbine flange, and to the aft inner core cowl at the cowl's aft edge.

The depth of the mixer scallop was investigated to assure that the hot chute natural frequency fell outside the engine operating range. As is illustrated in Figure 80, the selected geometry had a natural frequency out of the maximum fan speed range.

The inner portion of the fan flowpath aft of the core cowl was an integral part of the mixer. This section of the mixer shroud contained fairings for the aft engine mount lugs which penetrated into the fan stream, removable doors for access to the sump service lines, and a borescope port for inspection of the last stages of the LPT. The portion of the mixer shroud located under the pylon had been designed as a separate piece which gave additional room for instrumentation lead out and simplified removal of the mixer, since the mount link covers and the pylon fairing could remain in place.

### 3.8.3 Core Cowl Purge System Design

The core cowl purge is divided into two zones. The forward zone contains the fuel supply manifold and the aft zone contains both the HPT and LPT active clearance control system. The two zones are separated by the fire safety wall which also acts as a pressure bulkhead so that the HPT/LPT ACC air can discharge to a lower pressure.

The forward core cowl cavity is purged with 0.3% $W_{25}$ of fan air that is extracted from the fan duct. The air enters the core cowl cavity through metering holes ahead of the core cowl doors. This air flows aft around the core engine and fuel manifold. The air re-enters the fan stream through slots

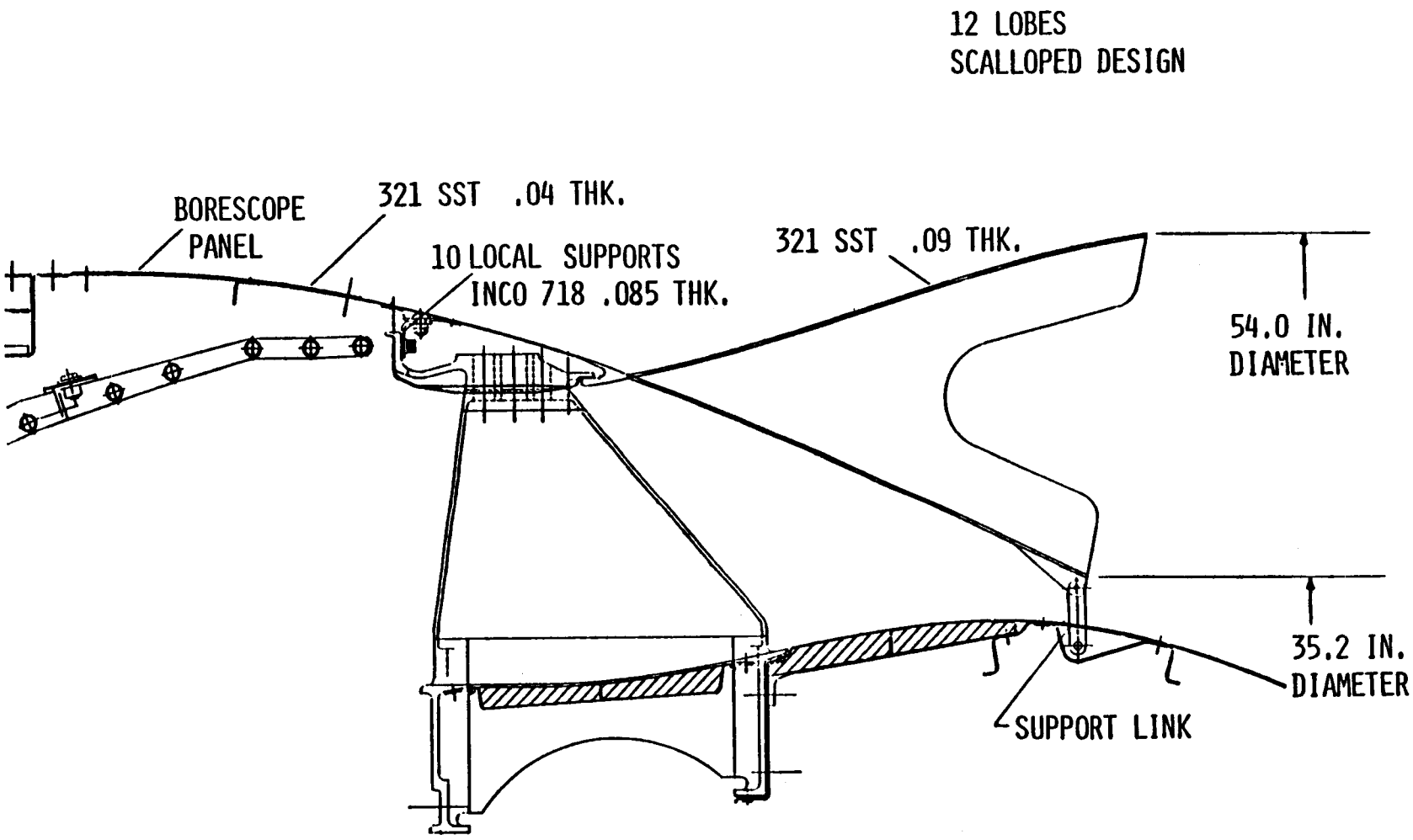


Figure 79. Mixer Cross-Sectional Description.

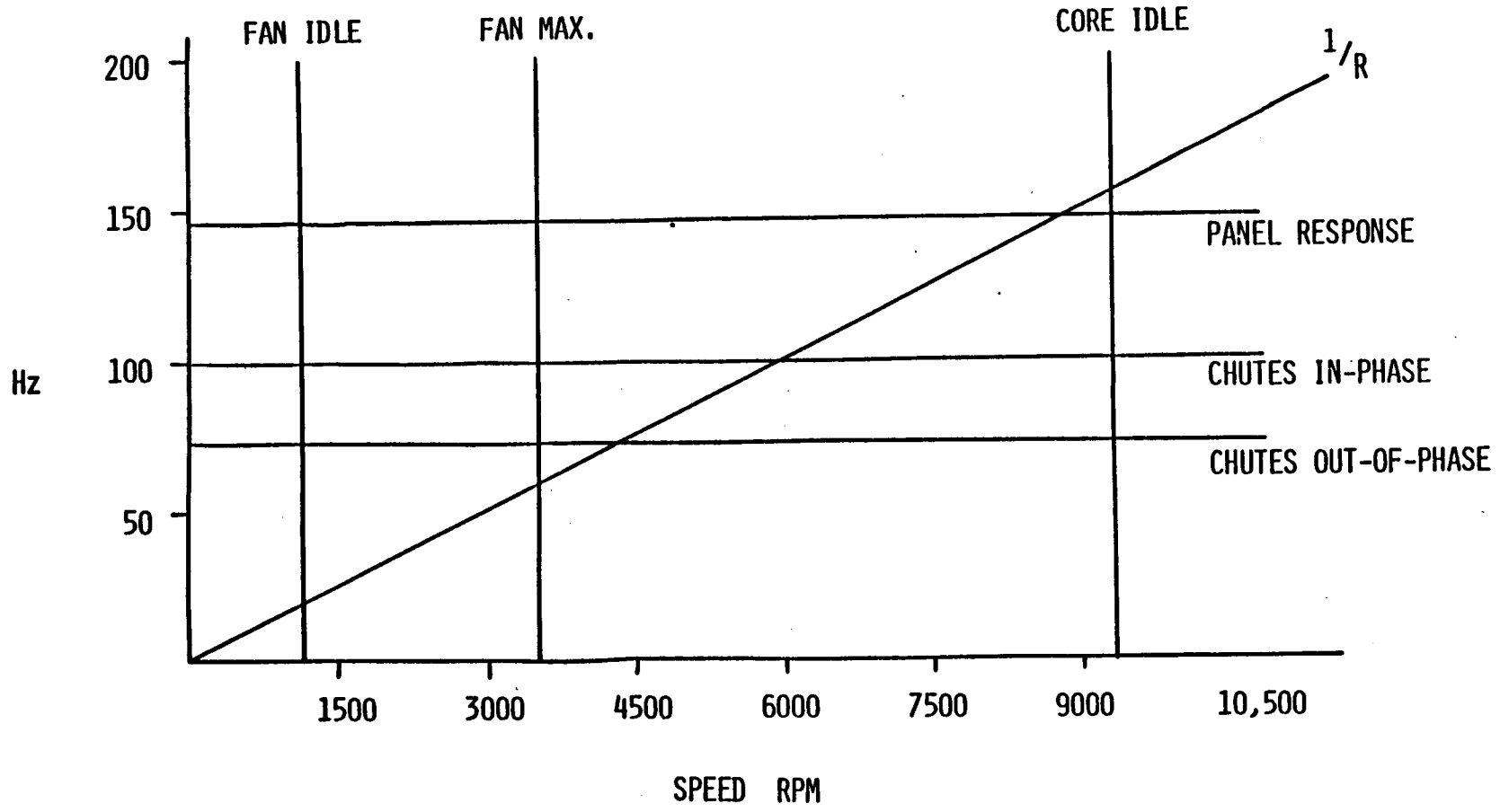


Figure 80. Mixer Campbell Diagram.

on the aft side of the core cowl door. The 0.3% $W_{25}$ is sufficient flow to keep the core cowl air temperatures below 232°C (450°F) at max power conditions. It is intended that the flow be sufficient to keep the air temperature low enough so that spontaneous combustion will not occur if a fuel leak occurs.

The aft core cowl cavity is not purged on a continuous basis like the forward core cowl cavity since there is no fuel manifold within. The fire safety wall acts as a pressure bulk head so that the aft core cowl cavity pressure level can be dropped below the fan stream static pressure. The purpose in dropping the aft core cowl pressure below fan stream static pressure was to allow the fan stream flow to be used as impingement air to cool the HPT and LPT casing.

In order to accomplish this, the sink pressure for the impingement system had to be dropped below the fan stream static pressure. Once the air impinges it is vented through the rear frame to the stinger. The stinger discharge pressure was close enough to ambient that the satisfactory impingement flow of approximately 0.65 $W_{25}$ of HPT and LPT ACC air could be vented.

During the core engine test an inadvertent HPT blade tip rub occurred when the start bleed CDP air supply valve failed in the open position and caused a pipe failure.

Since there was no tear down of the HP turbine after the core engine test and no opportunity to replace blades, the decision was made to enhance the HPT active clearance control system. This would reduce the clearance back to the expected level of the FPS design. The method of enhancing the ACC system was to supply shop air to the HPT ACC impingement manifold. The impingement pressure was increased from the design level of 144.8 kPa (21 psia) up to 227.5 kPa (33 psia). The impingement pressure drop was increased a maximum value of 20.7 kPa (3 psi) with the fan air supply to 93.1 kPa (13.5 psi). The shop air system had the capability of supplying

0.68 kg/sec (1.5 lb/sec) or about 1% $W_{25}$ at max power conditions. So that the LPT ACC cooling system would not be back pressured by the 3X increase in HPT ACC flow, a 7.62 cm (3 inch) diameter vent pipe was installed in the aft core cowl cavity. The purpose of the vent pipe was to dump the shop air overboard after it was used for HPT casing cooling. The design intent of the system was to allow the LPT ACC system to function normally while significantly increasing the flow to the HPT ACC cooling system.

## 3.9 SUMPS, DRIVES, CONFIGURATION, AND LUBE SYSTEM

### Sumps

The ICLS engine was a simply arranged, two-sump engine. It was a five-bearing machine with three bearings, a ball and two roller bearings, supporting the low pressure system. The high pressure system was supported by a forward thrust bearing and an aft intershaft roller bearing. The intershaft bearing mounted between the LP and HP system eliminated the need for a "hot" frame with its cooling air requirements.

### Forward Sump

The forward sump design is shown in Figure 81. Included in this sump were both the LP and HP system thrust bearings whose loads were reacted by the stiff fan frame. The No. 2 roller bearing, which added support to the long LP system shafting, was also located in the forward sump, just ahead of the power takeoff (PTO) drive gear.

The PTO gearbox was driven directly from the compressor stub shaft and drove radially outward through the bottom strut in the fan frame. The radial drive shaft, because of its length, was supported by a midspan bearing located in the fan frame.

The thrust bearing for the HP system was mounted in a housing which featured a centering spring. The bearing was fluid damped with a multishim arrangement that was end sealed by piston rings.

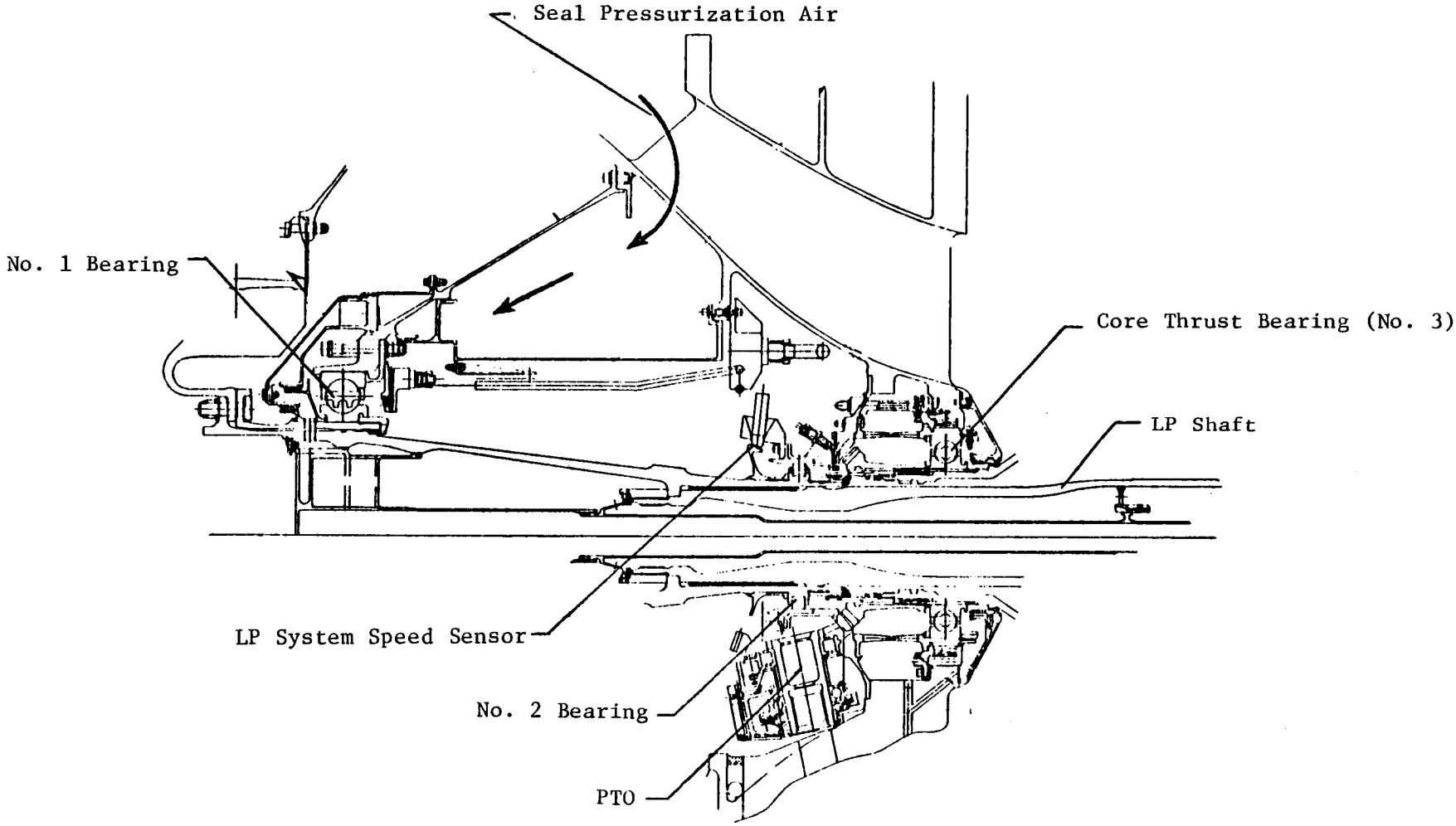


**Figure 81. Forward Sump Design.**

The main shaft and PTO bearings were either jet lubricated or underrace cooled. Oil was supplied from a common manifold with the oil for the fluid damper being supplied from its own manifold.

The forward sump sealing system consisted of labyrinth seals pressurized by fan discharge air. The sump was vented through the LP fan shaft, with the vent air being exhausted out the aft center vent tube.

Also included in the forward sump was an LP rotor speed pickup. A "cogged" wheel was mounted to the LP shaft just forward of the No. 2 bearing which was sensed by a stationary pickup mounted to the No. 2 bearing housing.

The core thrust bearing, its mounting hardware, and the PTO hardware had been successfully run on the Core test engine.

Aft Sump

The aft sump configuration is shown in Figure 82. This sump included the No. 4 and No. 5 roller bearings. The No. 4 bearing was an intershaft roller bearing with its outer race mounted in a housing with a controlled spring rate attached to the LP shaft and its inner ring mounted to the aft HP stub shaft. The No. 5 bearing, supporting both the HP and LP rotor system, was mounted to the aft turbine frame. Both the No. 4 and No. 5 bearings were underrace cooled, supplied by a jet mounted to the No. 5 bearing housing.

The aft sump sealing system featured labyrinth seals pressurized by fan discharge air obtained from the forward sump flowing to the aft sump through an annulus formed by the outside diameter of the vent shaft and the inside diameter of the LP shaft.

Compressor rotor cooling air flowed around the aft sump through sealed cavities and was directed out the aft center vent tube. The rotor cooling and the seal pressurizaiton air cavities "blanketed" the sump with cooler air protecting it from the higher turbine cavity temperatures.

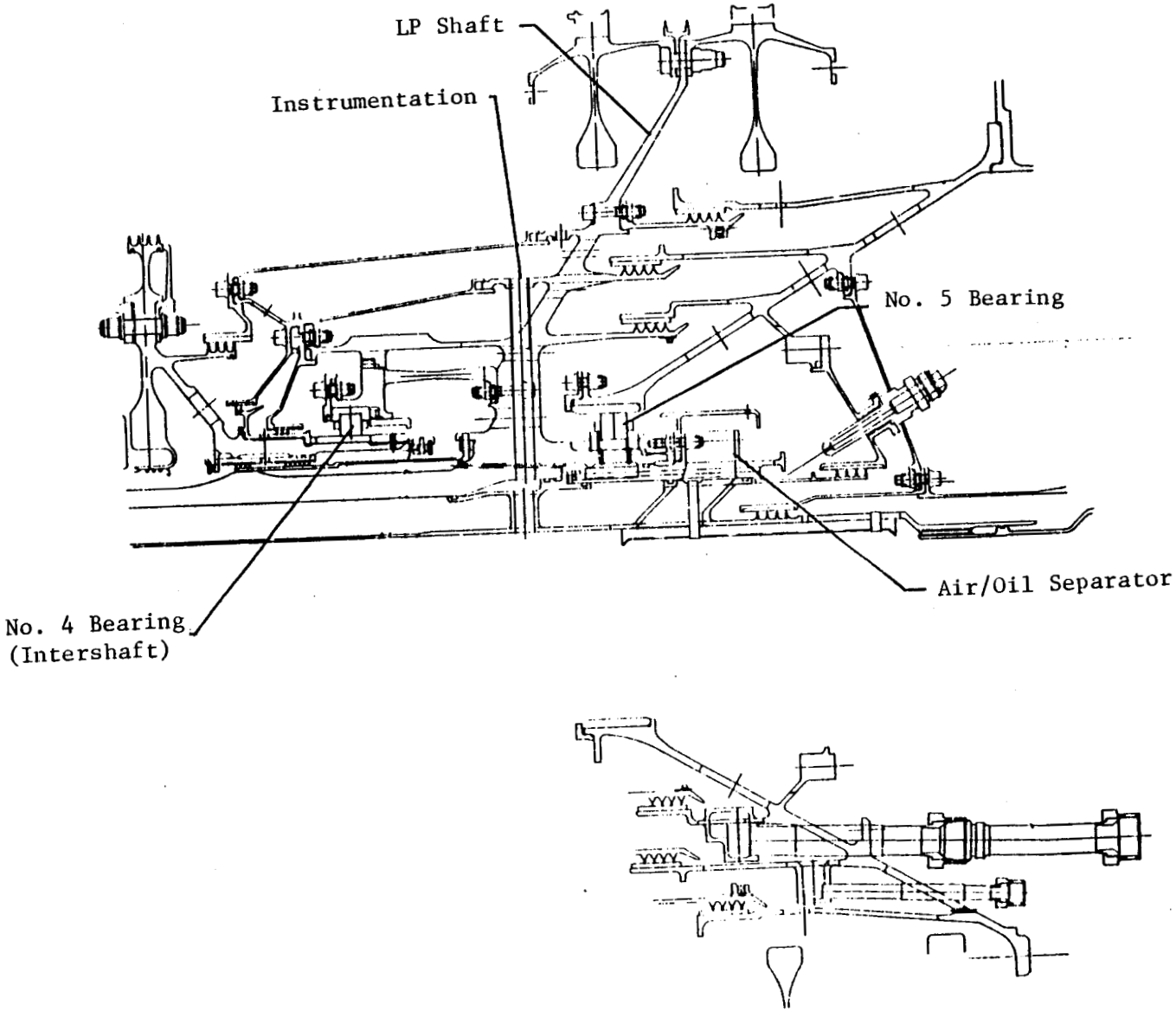


Figure 82. Afl Sump Design.

The aft sump was vented through an air/oil separator which was mounted on the end of the LP shaft. Aft sump vent air mixed with the vent air from the forward sump and was exhausted through the aft center vent tube.

Just behind the aft sump was mounted the LP system instrumentation slip ring assembly.

Accessory Drive System

Figure 83 shows a cross section of the ICLS accessory drive system. The accessory drive system hardware was the same used on the core engine test with the exception of the radial drive shafting. The radial drive shafting consisted of two shafts splined together, connected to the PTO and the accessory gearbox (AGB), and supported in the middle by a midspan bearing. The midspan bearing was required to have "critical" speed margin over the maximum operating speeds.

The AGB provided drive pads for the following accessories:

- Lube and scavenge pump
- Two air starters
- Control alternator
- Fuel pump and control.

The AGB was designed for a maximum combined torque from the starters of 1084.6 Nm (800 ft-lb). The maximum accessory horsepower requirement for the ICLS engine was 53.69 kw (72 hp). Figure 84 shows a cross section of the AGB.

Configuration

The configuration encompasses the following areas:

- Pneumatic piping for the compressor and turbine active clearance control and turbine cooling.
- All external lube and fuel lines.

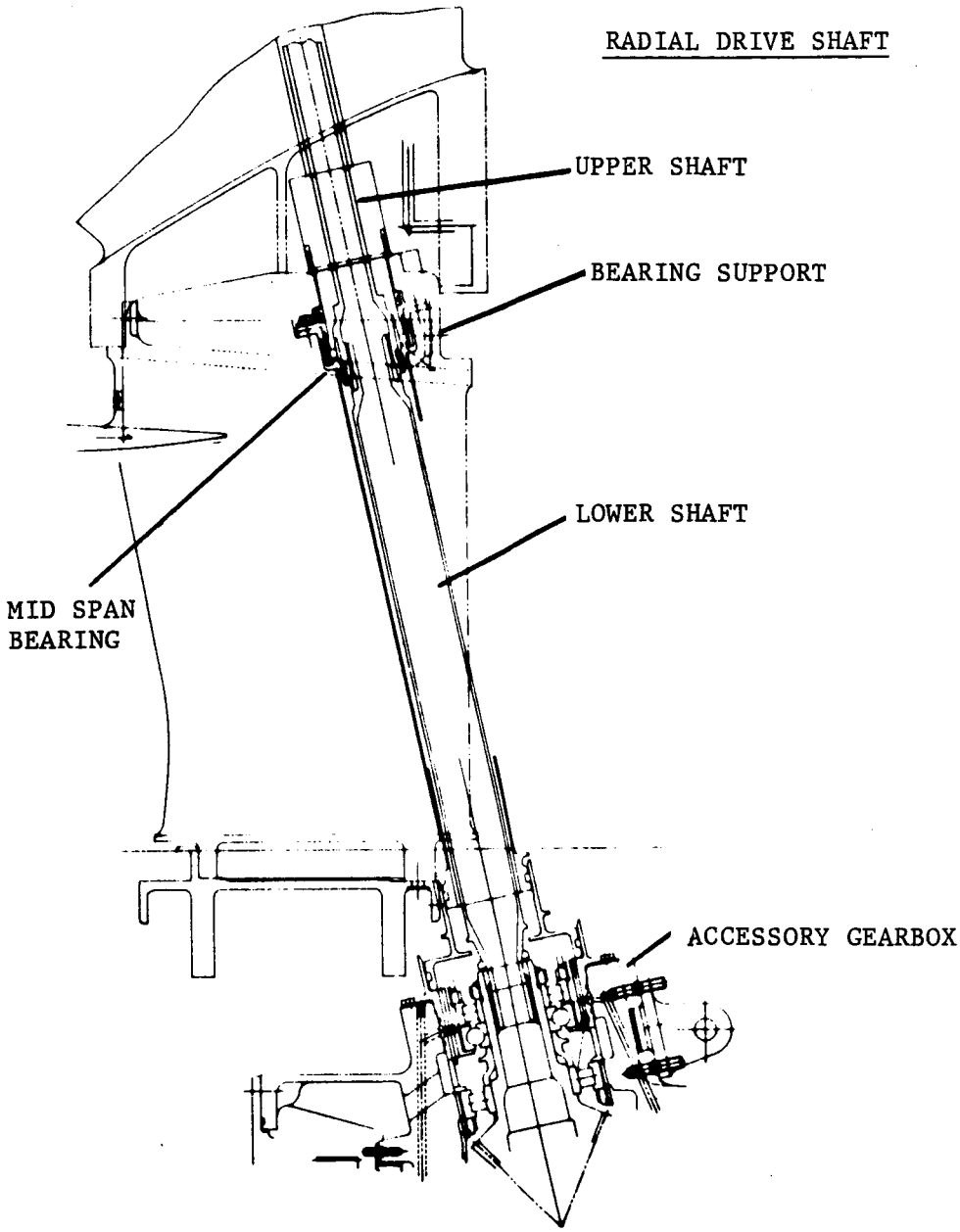


Figure 83. Accessory Drive System.

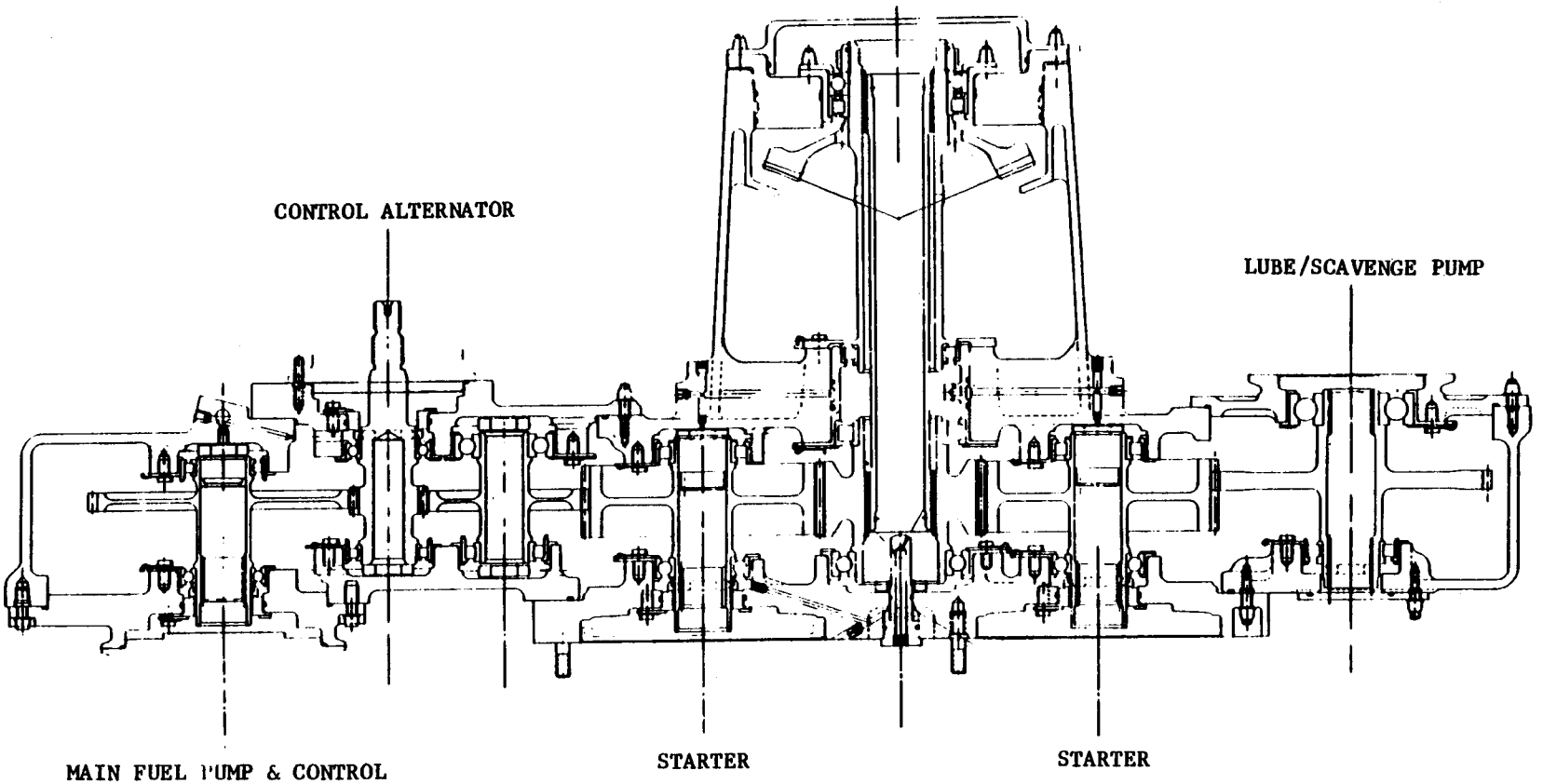


Figure 84. Accessory Gearbox Cross Section.

- All electrical harnesses.
- The pressure bulkhead.

Fan discharge air plus fifth and seventh stages of the compressor were bled to accomplish the pneumatic functions.

Fifth stage air was used to control the clearance in the aft stages of the compressor. This was accomplished by the use of a valve which allowed air to pass over the casing of these stages to reduce clearance or bypass this cooling function in varying degrees. The discharge air from this system was then utilized to cool the LPT vanes. Seventh stage air was used to cool the HPT second stage nozzles. Fan air was used to control the clearance of both the HP and LP turbine.

The fuel lines were used to supply fuel to the pilot and main burners. In addition, fuel was used to hydraulically power all of the control valves in the system.

The electrical harnesses primarily transmitted signals from the Full Authority Digital Electronic Control (FADEC) to the various valves in the system.

A six sector curved pressure bulkhead was used to create a low pressure region around the turbines' outer casings to provide a "sink" for the turbine clearance control cooling air. It was designed for radial temperature gradients of 389°C (700°F) and an axial pressue gradient of 48 kPa (7 psid). The design also included metal bellows to minimize air leakage where piping penetrations were required.

Lube System

The lube system schematic for the ICLS engine is shown in Figure 85 and is typical of other GE high bypass fan engines.

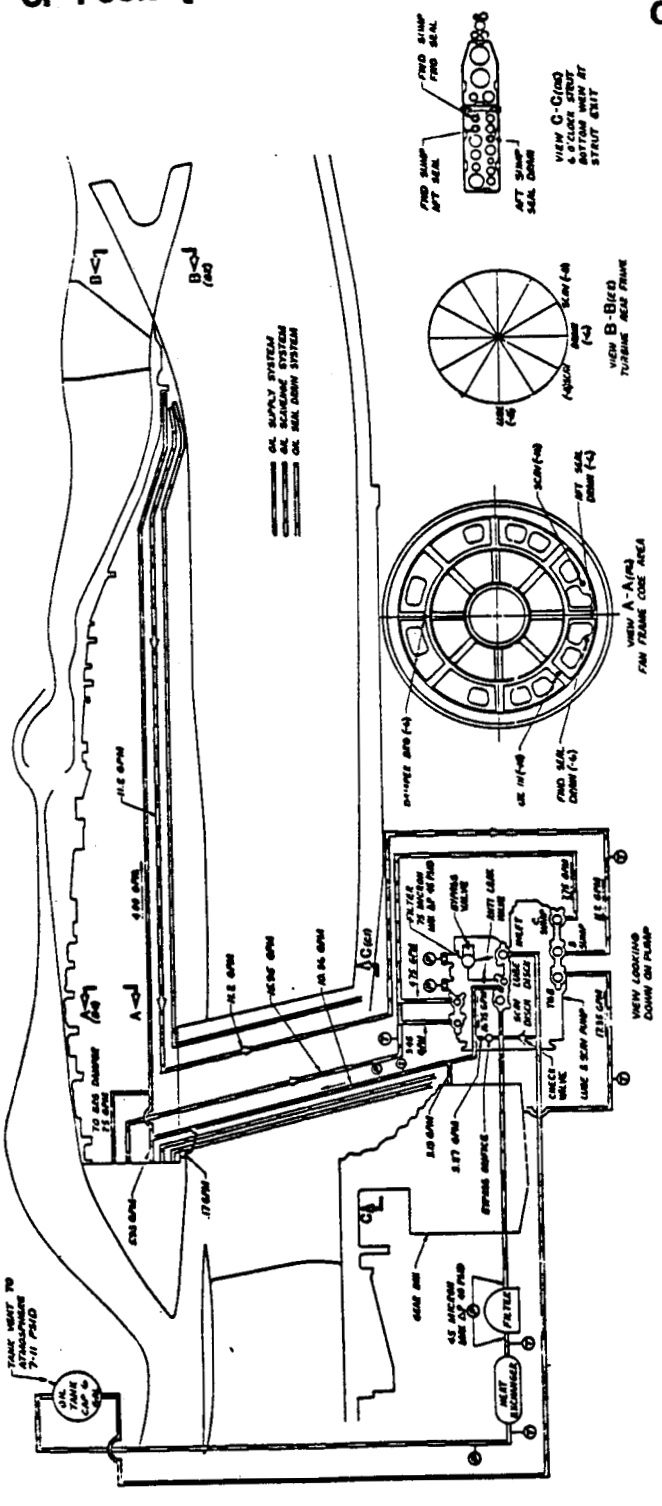

Figure 85. Lube System Schematic.

Lubrication and cooling oil was supplied to each sump and to the gearbox by a single supply pumping element, then scavenged by utilizing separate scavenge pumping elements.

Oil filters were used on both the supply and scavenge side of the lube system. The supply filter protected the sumps and gearbox from contamination, and the scavenge filter protected the heat exhanger and the lube tank. Each scavenge element had an inlet screen to protect the pumping elements from larger debris.

The lube tank was mounted to the fan frame; it was protected from overpressuring by a ΔP valve which also served to pressurize the supply pump inlet slightly above atmospheric pressure. Check valves were located in the lube supply side to prevent back-flow of oil into the engine sumps, which could cause flooding at engine shutdown.

The lube pump used in the ICLS engine was from another engine program and has excessive flow capacity for the ICLS engine. To provide the proper quantity of oil to each component, a bypass orifice was used to return excess oil to the lube pump inlet.

The sump systems and gearbox were center vented aft to the exhaust nozzle of the engine.

Rotor Thrust

A complex computer model of the secondary air systems, which is pertinent to the calculation of the fan and core thrust bearings axial loads, was completed as part of the design analysis of the ICLS engine system. This computer modeling was used during the design process to evaluate (1) various labyrinth air seal diameters throughout the engine and (2) their effect on the thrust bearing loads.

## 3.10 DYNAMIC SYSTEM DESIGN

### 3.10.1 Design Concept

A high load squeeze film damper has been designed as an integral part of the engine system. This damper was configured to provide effective vibration control over a broad unbalance range that included low-to-abusive unbalance levels. The design incorporated a tuned core rotor bearing support arrangement combined with a multiple film squeeze film damper located at the core rotor forward bearing (No. 3 bearing). The damper-suspension system reduces the dynamic response levels by driving the bending strain energy associated with core rotor bending into the tuned bearing supports allowing the squeeze film damper that is in parallel with the forward tuned bearing support to provide an efficient energy sink to dissipate the energy of vibration through the action of viscous damping. Figure 86 shows the bearing support system and the damper. The bearing supports were "squirrel cage" structures that provide relatively soft load paths via spring elements machined integral with the cylindrical structural portions. It was established that a $5.254 \times 10^7$ N/m ($3 \times 10^5$ lb/in) spring rate for each "squirrel cage" would provide the required rotor centering action for maneuver loads (based on requirements for the flight propulsion system configuration) and also permit the squeeze film damper to provide the desired vibration control. As shown in Figure 86 and in greater detail in Figure 87, the damper consisted of a sealed squeeze film damper with sleeves or shims inserted in the damper annulus. The insertion of sleeves into the squeeze film resulted in small clearance annuli and the sum of the individual clearances provided a relatively large overall clearance. The combination of small clearance annuli and circumferential flow results in high damping and the large overall clearance allows large deflections to occur with a low spring rate.

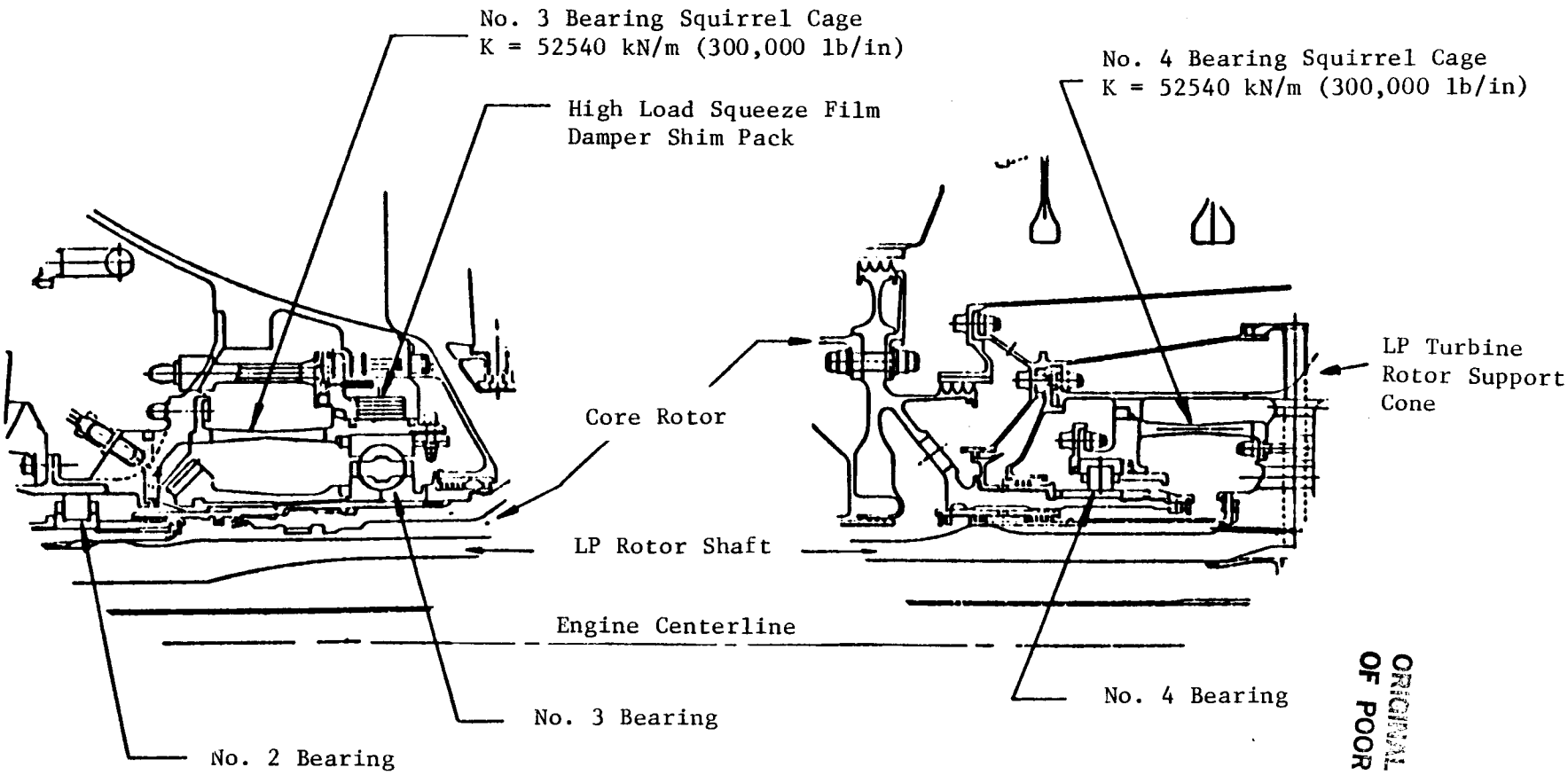




**Figure 86. Core Rotor Soft Support and Squeeze-**

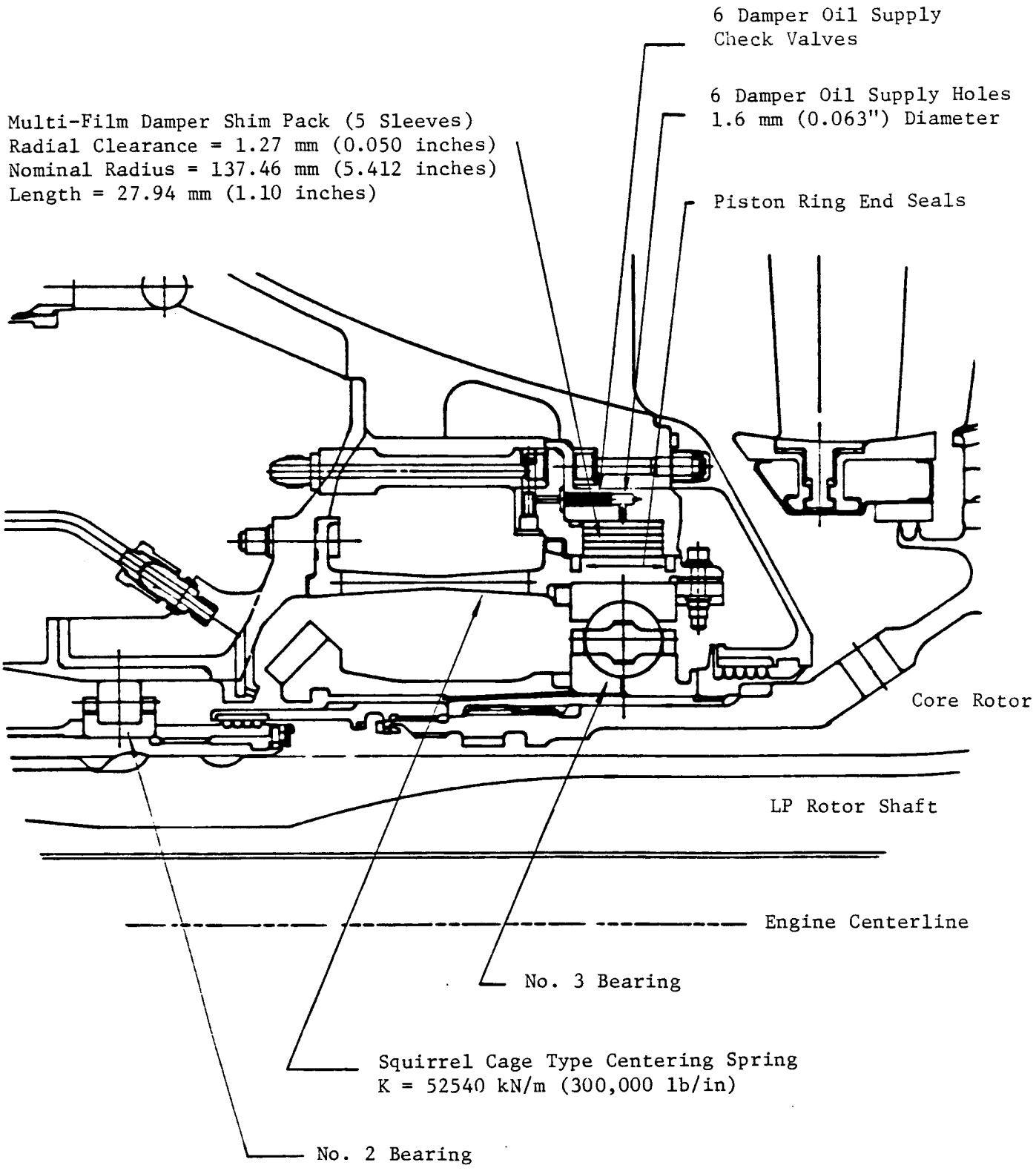


Figure 87. Number 3 Bearing Soft Support and High Load Damper.

### 3.10.2 System Vibration Analysis

#### 3.10.2.1 Background

System vibration analysis for both the flight propulsion and ICLS systems indicated that for a hard mounted core rotor a high strain energy condition existed in both the core rotor and the low pressure shaft. This condition resulted in prohibitively high dynamic loads in the bearings and supporting structures for the core rotor unbalance levels expected in normal commercial service.

#### 3.10.2.2 Design Goals for Engine Sensitivity to Unbalance

Relative to smaller levels of rotor unbalance, two design goals were established that were derived from a base of experience obtained with engines in commercial airline service. The first design goal was to provide the ability to maintain clearance with a high pressure compressor unbalance level of 0.00381 kg-m (150 g-in). It is expected that this level of unbalance could exist in engines with long service time due to minor FOD, erosion, slipped bolt joints, etc. The second design goal was to achieve an 18,000 hour bearing life with a high pressure compressor unbalance level of 0.00762 kg-m (300 g-in). This level of unbalance could result from moderate FOD.

In addition to these requirements for low-to-moderate unbalance levels, a capability to withstand high unbalance without severe secondary damage was established as a requirement. The high unbalance condition selected was 0.0381 kg-m (1,500 g-in) of high pressure turbine unbalance. This high level of unbalance corresponds to approximately the loss of two high pressure turbine Stage 2 blade airfoils.

In order to meet the design objectives, the design concept outlined in Section 3.10.1 was utilized; that is, a soft-mounted core rotor in conjunction with a static housing high load damper was used instead of a hard-mounted core rotor.

### 3.10.2.3 System Vibration Modeling

Figure 88 shows a schematic of the $E^3$/ICLS system vibration model. This model has over 1,000 degrees-of-freedom and is an assemblage of segmented beam and generalized spring-type elements. The former element type, represented by solid lines, is called a span and includes both stiffness and mass properties. The latter element, represented pictorially by the springs shown in Figure 88 models strain energy load paths and includes fully coupled action. A similar system vibration model was constructed for the flight propulsion engine system and the dynamic characteristics predicted with this model were quite similar to those of the ICLS. The primary differences between the FPS and the ICLS were a flight weight frame for the FPS instead of the steel frame for the ICLS and the presence of a nacelle structure for the FPS.

### 3.10.2.4 Fan Synchronous Modes

The mode shapes for the significant fan excited modes which reflect a soft-mounted core rotor are shown in Figure 89. The mode at 3,098 rpm involves bouncing of the core rotor off of the soft supports at the No. 3 and 4 bearings. The modal displacements shown in Figure 89 indicate that this mode can be excited primarily by unbalance in the low pressure shaft and turbine. The mode at 6,678 rpm is characteristic of high bypass turbofan engines and involves nodding of the fan rotor off of the No. 1 bearing and support and the fan frame. This mode would be highly sensitive to fan rotor unbalance; however, it is significantly above the maximum fan speed of 3,311 rpm with a margin equal to 100%.

Figure 90 shows the frequency response characteristics associated with low rotor unbalance. The mode at 3,098 rpm results in relatively low displacement response at the No. 3 bearing. The low speed peak at approximately 700 rpm corresponds to a rigid body mode of the engine off of the engine mounts and is associated with very low bearing loads. The only significant bearing loads are associated with operating speeds in proximity to

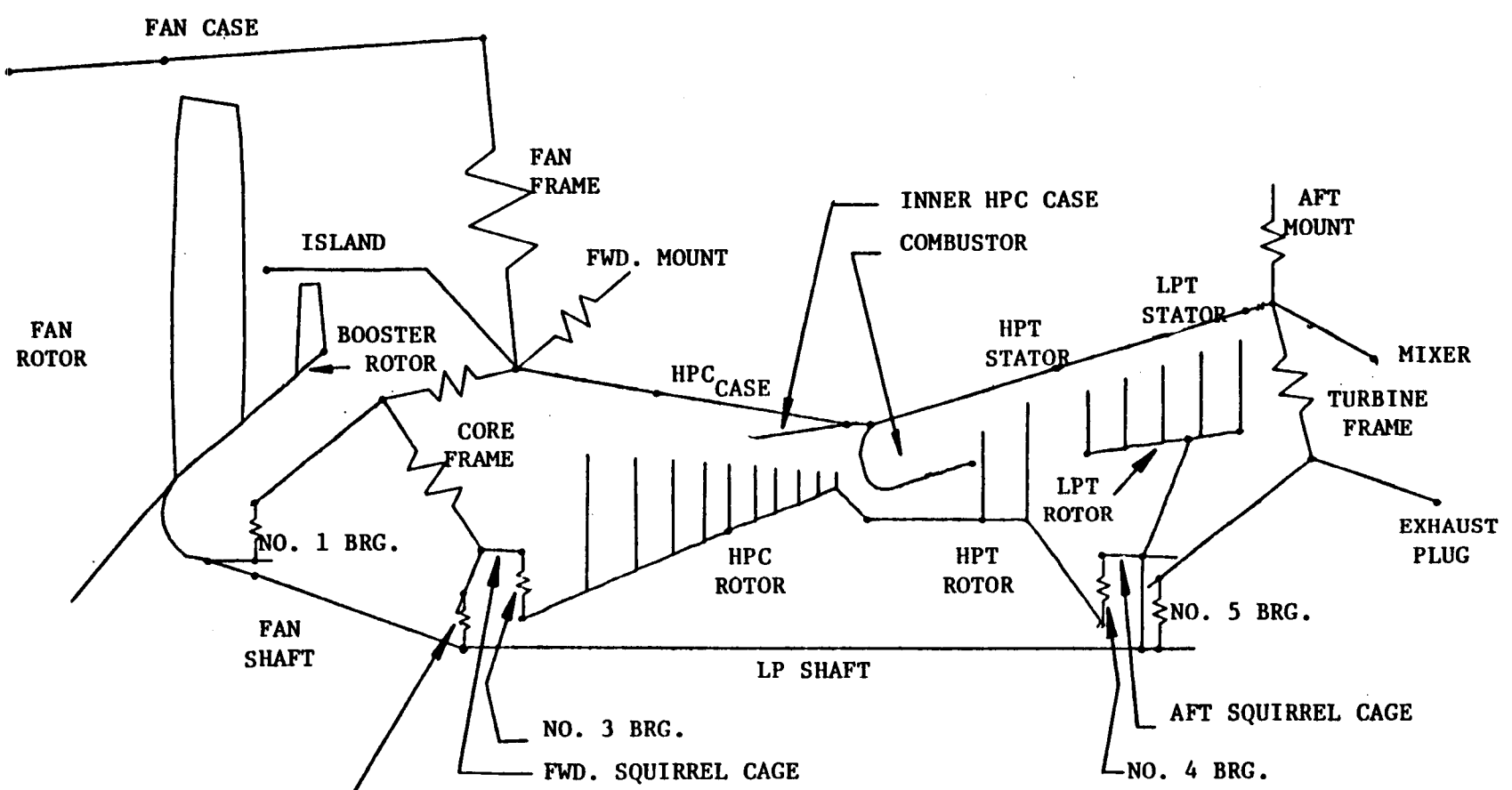


Figure 88. ICLS System Dynamics Computer Model Schematic.

SOLID LINE = UNDEFLECTED
BROKEN LINE = DEFLECTED

P = PE = POTENTIAL (STRAIN) ENERGY
K = KE = KINETIC ENERGY

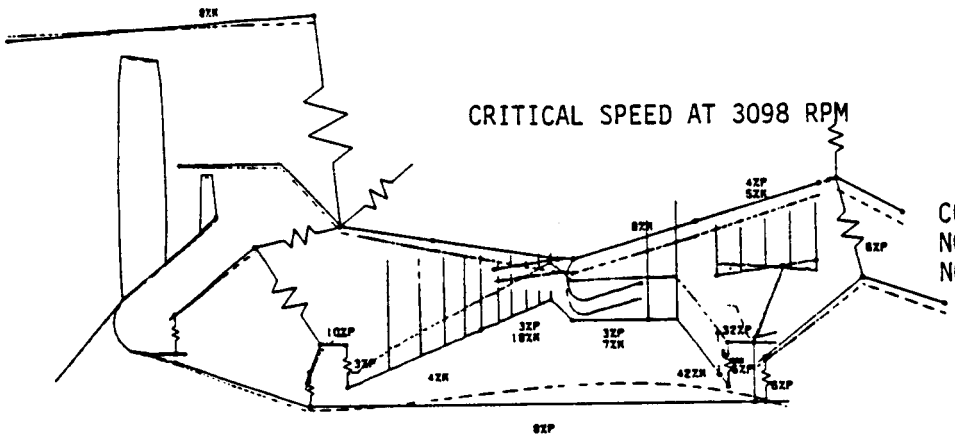


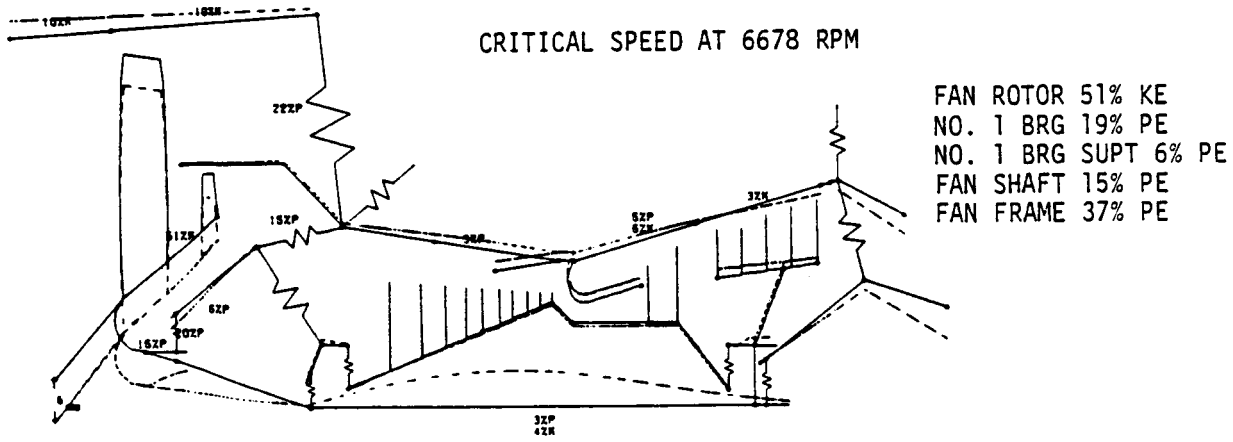


**Figure 89. Fan Synchronous Modes.**

A - $1.270 \times 10^{-2}$ kg-m (500 GM-IN) FAN UNBALANCE
B - $5.080 \times 10^{-3}$ kg-m (200 GM-IN) LPT STG. 1 UNBALANCE
C - $5.080 \times 10^{-3}$ kg-m (200 GM-IN) LPT STG. 5 UNBALANCE

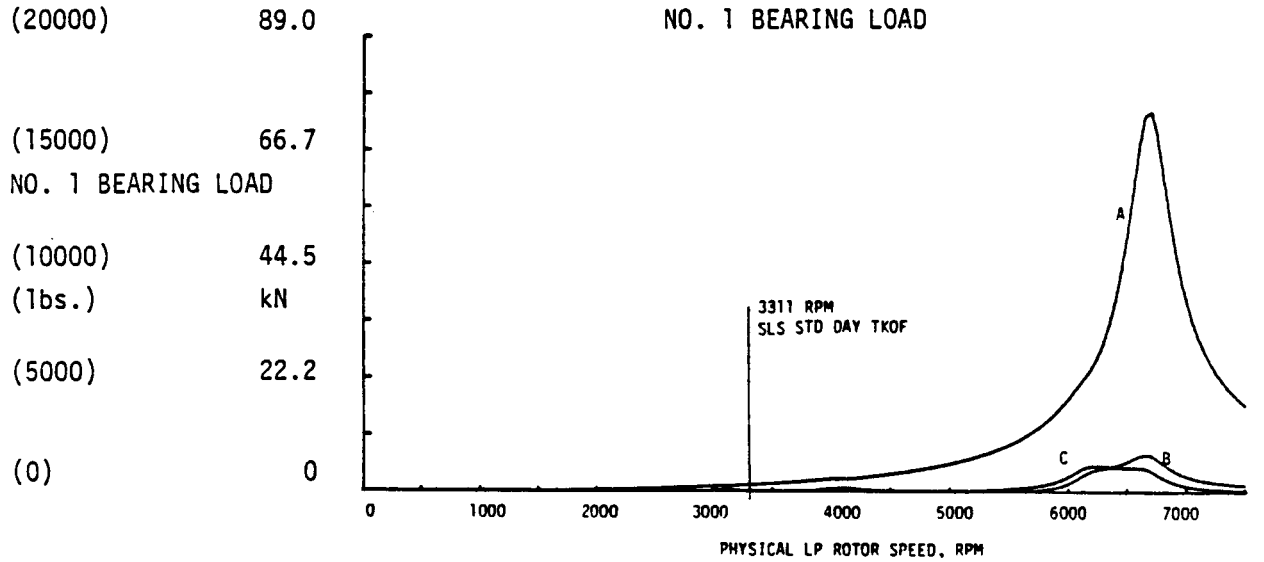


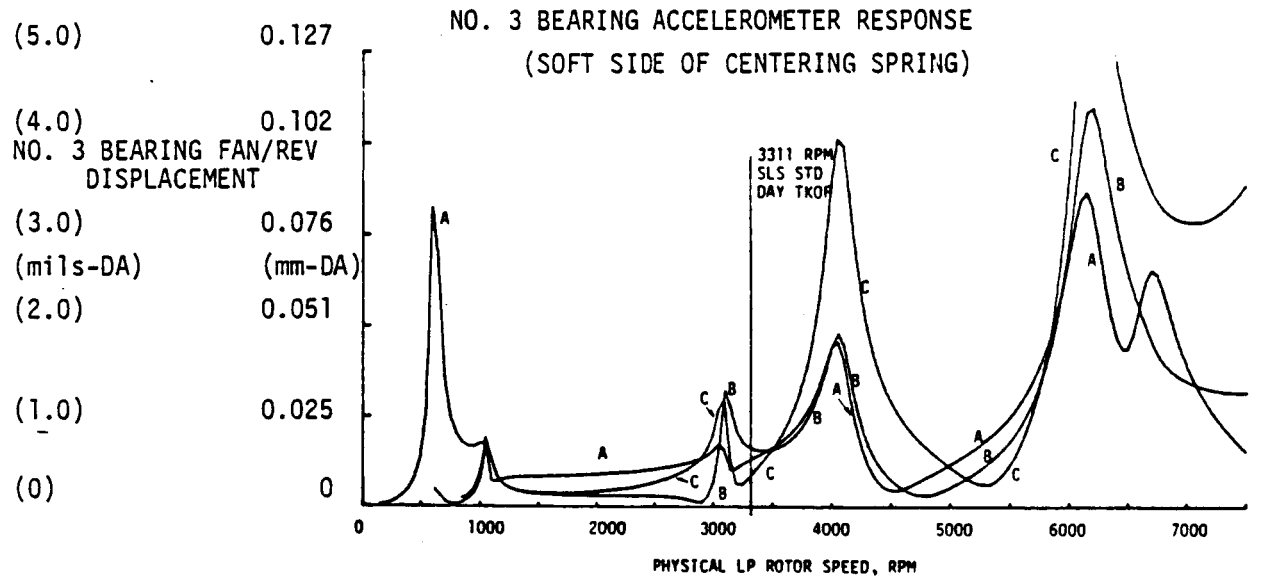


**Figure 90. LP Synchronous Combined Modes Frequency Response.**

the 6,678 rpm fan nodding mode. In the operating speed range, the load build-up associated with this mode is not large. From the above, it can be seen that the engine is not predicted to be responsive to low rotor unbalance.

3.10.2.5 Core Synchronous Modes

Figure 91 shows the significant core excited modes which reflect a soft-mounted core rotor. The low speed mode at 2,647 rpm involves bending of the low pressue shaft. The modes at 5,993 and 7,391 rpm involve basically rigid body motion of the core rotor, with coupling of the forward squirrel cage in the former case and coupling of both squirrel cages in the latter case. The participation (percent strain energy) by forward (No. 3 bearing) squirrel cage for the 5,993 and 7,391 rpm modes indicates that a squeeze film damper at the No. 3 bearing will be effective in controlling the vibration response. The mode at 2,647 rpm does not involve significant activity at the forward squirrel cage and hence will not be damped by the squeeze film. However, this mode does not present a problem because it lies in the very low sub-idle speed range where steady state operation is not required.

For comparison with the soft-mounted core rotor modes, Figure 92 shows the significant modes for a hard-mounted configuration. In this case, a low pressure shaft bending mode occurs at 10,648 rpm and core rotor bending modes occur at 7,587 and at 13,728 rpm. In addition, a relatively responsive mode involving coupled action between the core rotor and case occurs at 12,442 rpm.

From the above, it can be seen that high strain energy modes exist in and close to the operating speed range for a hard-mounted core rotor. However, the soft-mounted damped design results in excellent vibration characteristics which will substantially reduce the unbalance response sensitivity.

3.10.2.6 Damper-System Analysis

A component mode approach was used to calculate the damper-system response characteristics and to optimize the damper design. This was

SOLID LINE = UNDEFLECTED
BROKEN LINE = DEFLECTED

P = PE = POTENTIAL (STRAIN) ENERGY
K = KE = KINETIC ENERGY

CRITICAL SPEED AT 2647 RPM

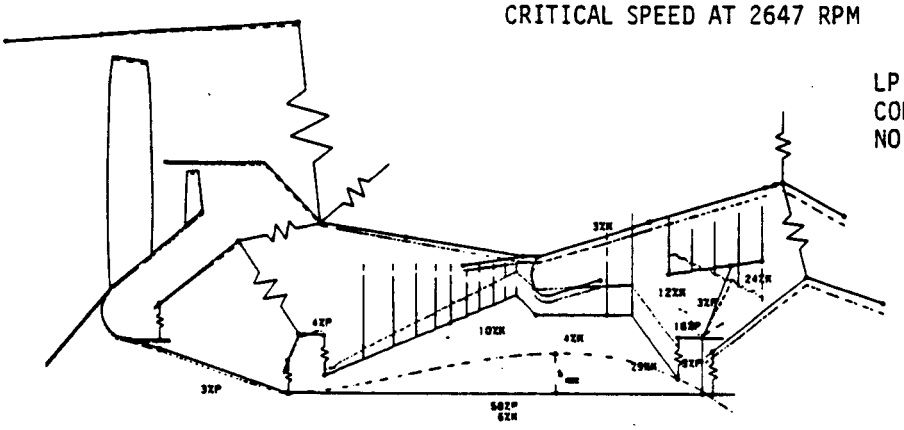

LP ROTOR SHAFT 58% PE
CORE ROTOR 5% PE & 44% KE
NO. 4 BRG SOFT SUPT 16% PE

CRITICAL SPEED AT 5993 RPM

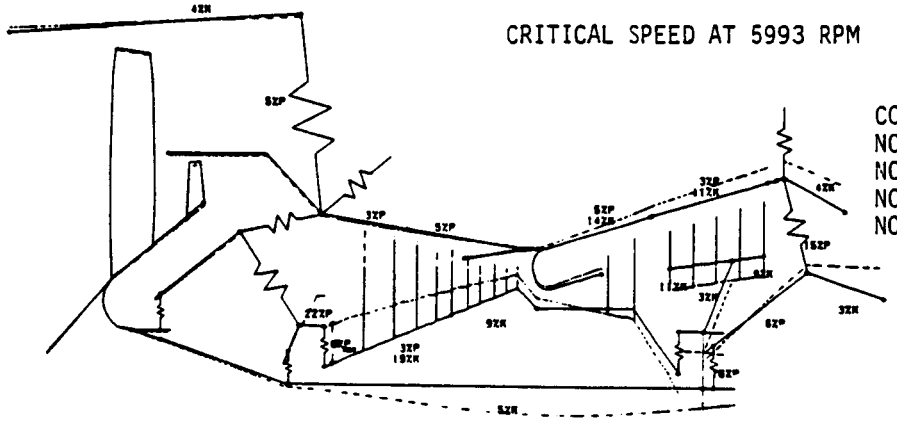

CORE ROTOR 5% PE & 29% KE
NO. 3 BRG SOFT SUPT 24% PE
NO. 4 BRG SOFT SUPT 32% PE
NO. 3 BRG 6% PE
NO. 4 BRG 6% PE

CRITICAL SPEED AT 7391 RPM

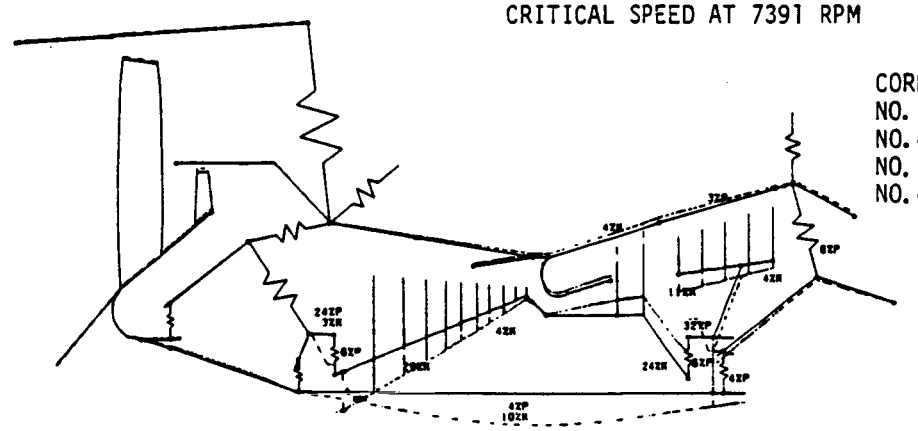

CORE ROTOR 7% PE & 58% KE
NO. 3 BRG SOFT SUPT 24% PE
NO. 4 BRG SOFT SUPT 32% PE
NO. 3 BRG 6% PE
NO. 4 BRG 6% PE

Figure 91. Core Synchronous Modes.

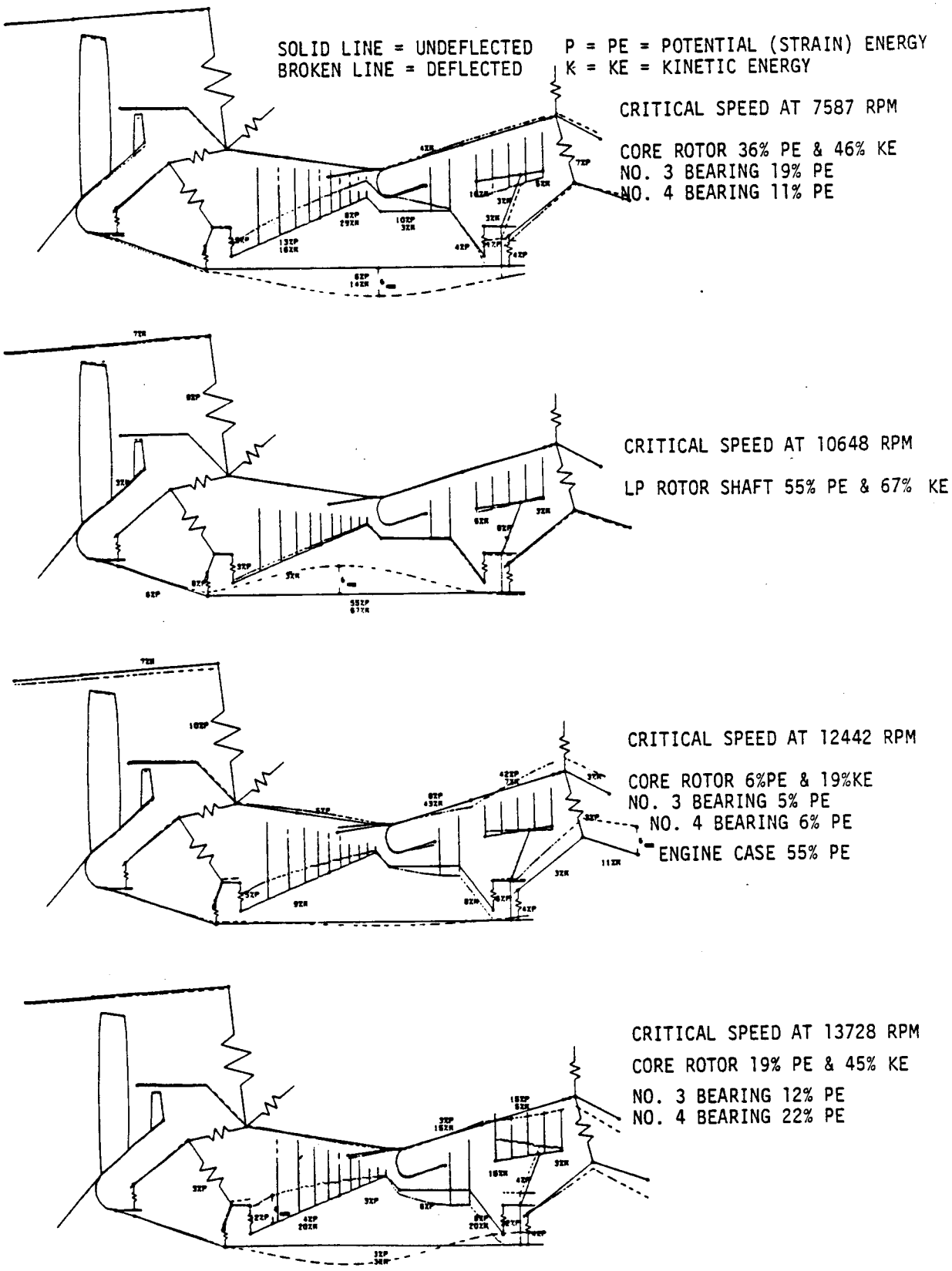


Figure 92. Hard-Mounted Core Rotor Synchronous Mode Shapes.

accomplished by subdividing the system vibration model of the engine shown in Figure 88 into the subsystems shown in Figure 93. The subsystems consisted of the reference (core) rotor and the remaining structure (the static structures and the low pressure rotor). The subsystems were mathematically represented with a reduced set of differential equations obtained through transformation from physical to generalized (modal) space. The damper was modeled as a nonlinear physical connecting element and the other connections (bearings) were modeled as linear connecting elements. The equations of motion for the subsystems and the connecting elements were assembled and solved through iteration at each forcing frequency as depicted in Figure 94.

Preparatory to performing the damper-system design studies, a modal truncation study was performed to verify the adequacy of the selected subsystem modes to represent the engine system. This was accomplished by comparing the linear solution for the assembled system to that of the direct solution for the original physical system. For the core rotor, subsystem modes extending up to 15X the maximum core rotor speed were used while for the subsystem consisting of the static structures and the low pressure rotor, modes extending up to 2.7X the maximum core rotor speed were used. Figure 95 shows that an acceptable modal truncation error is obtained as demonstrated by the relative frequencies and amplitudes of the peak response levels for the direct and component mode solutions. The peak level in both cases corresponds to the 7,391 rpm core rotor bounce mode and the frequency shift for this mode obtained with the component mode solution is caused by the residual flexibility contributed from the higher modes which are included in the direct solution.

The damper parameters shown in Figure 87 were found to satisfy the design goals discussed in Section 3.10.2.2 for engine sensitivity to unbalance. These damper parameters were optimized for the blade out condition. Figure 96 demonstrates how the number of shims was selected. This figure shows that the lowest core rotor bearing loads are obtained when 5 shims are used. Figure 97 shows comparisons between the unbalance response characteristics for the damped, soft-mounted undamped, and the hard-mounted

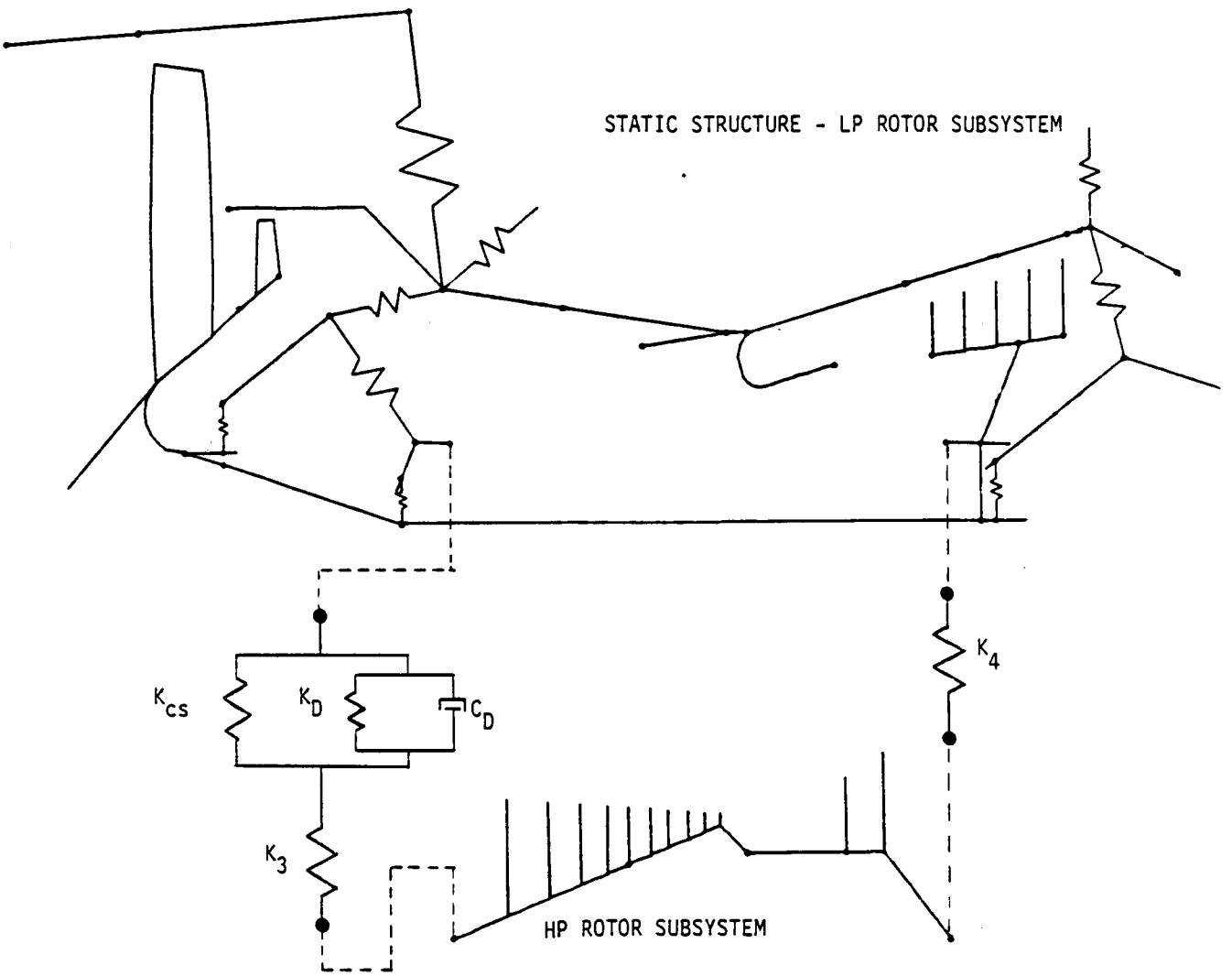


FORWARD CONNECTING ELEMENT

$K_3$ = No. 3 Bearing

$K_{cs}$ = Centering Spring

$K_D$ = Squeeze Film Spring Rate

$C_D$ = Squeeze Film Damping

AFT CONNECTING ELEMENT

$K_4$ = No. 4 Bearing and Centering Spring

**Figure 93. Subsystem and Connecting Elements for Component Mode Analysis.**

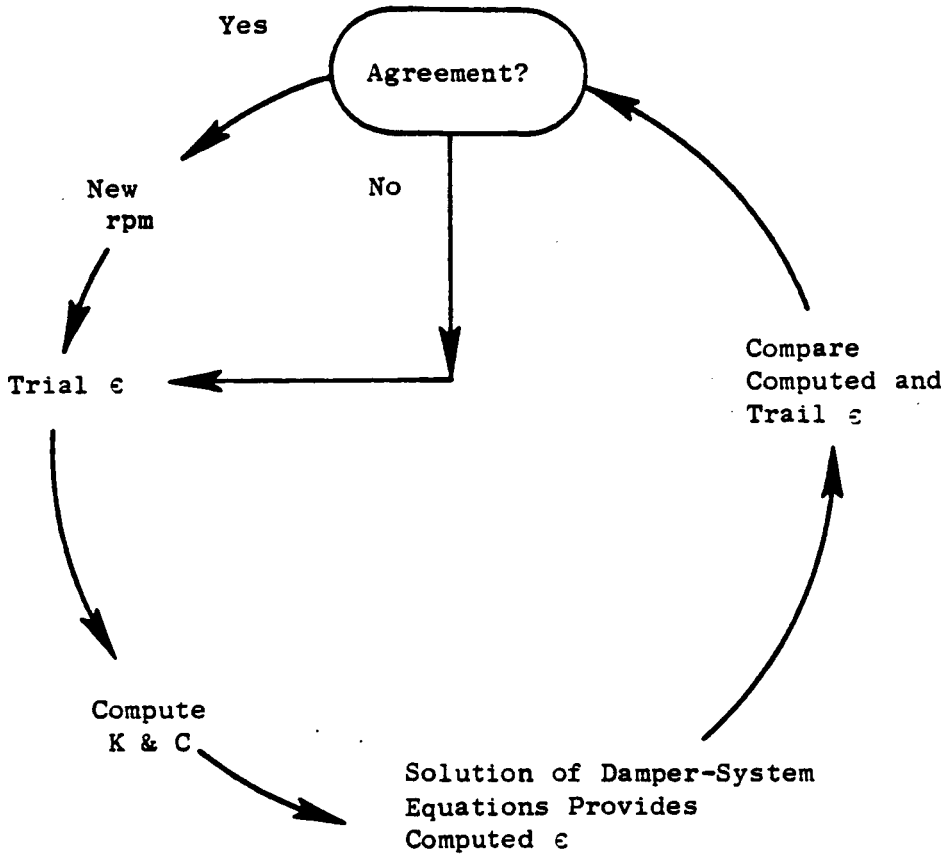


- A Damper-System Solution is Obtained in the Frequency Domain Through Iteration.

- ϵ = Eccentricity Ratio
- K & C are the Squeeze-Film Spring and Damping Coefficients

Figure 94. Damper-System Analysis.

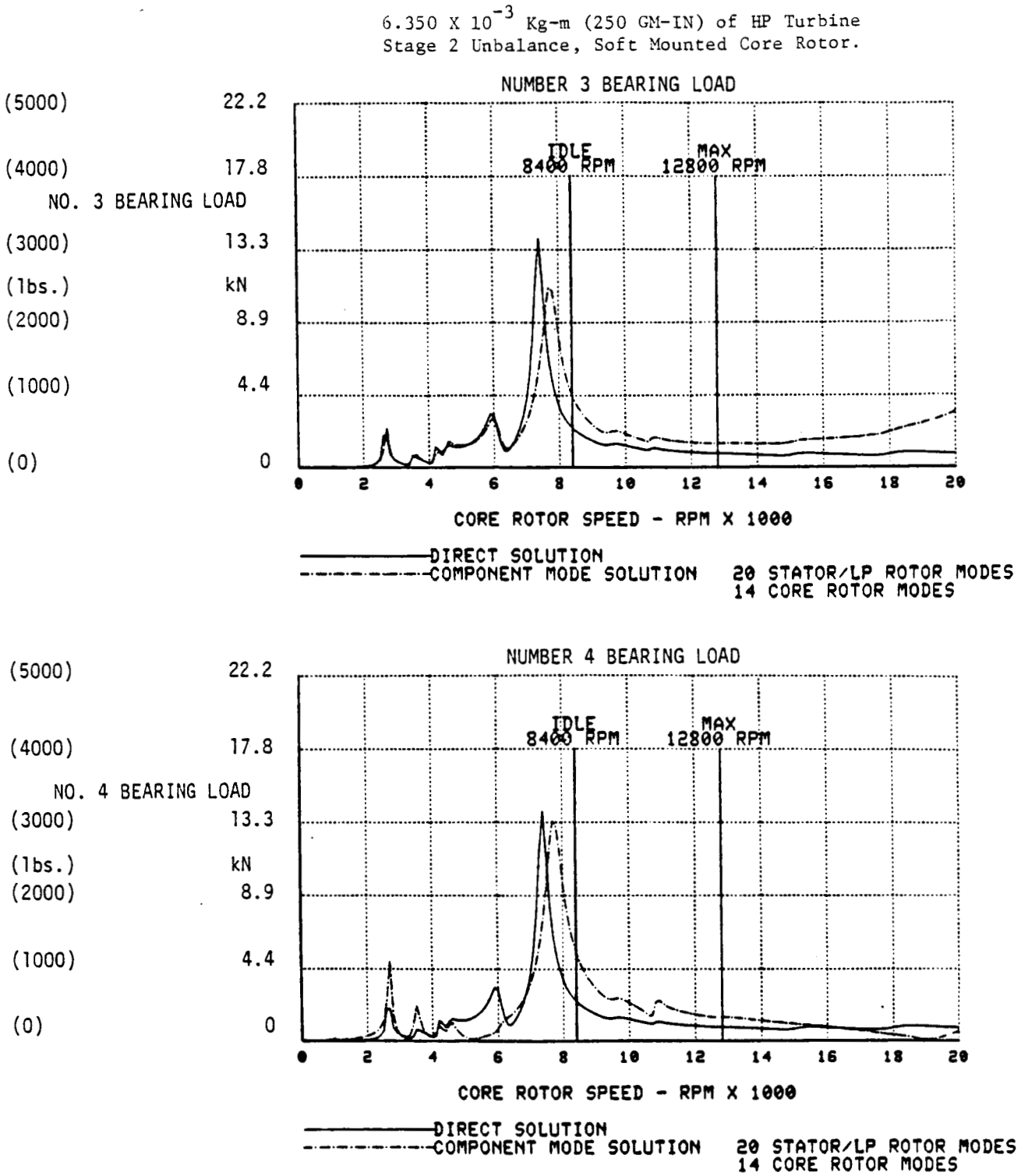


**Figure 95. Core Synchronous Combined Modes Linear Frequency Response Component Mode Truncation Error.**

No. 3 and No. 4 Bearing Loads Versus Number of Shims

$3.81 \times 10^{-2}$ kg-m (1500 GM-IN) HP Turbine Stage 2 Unbalance

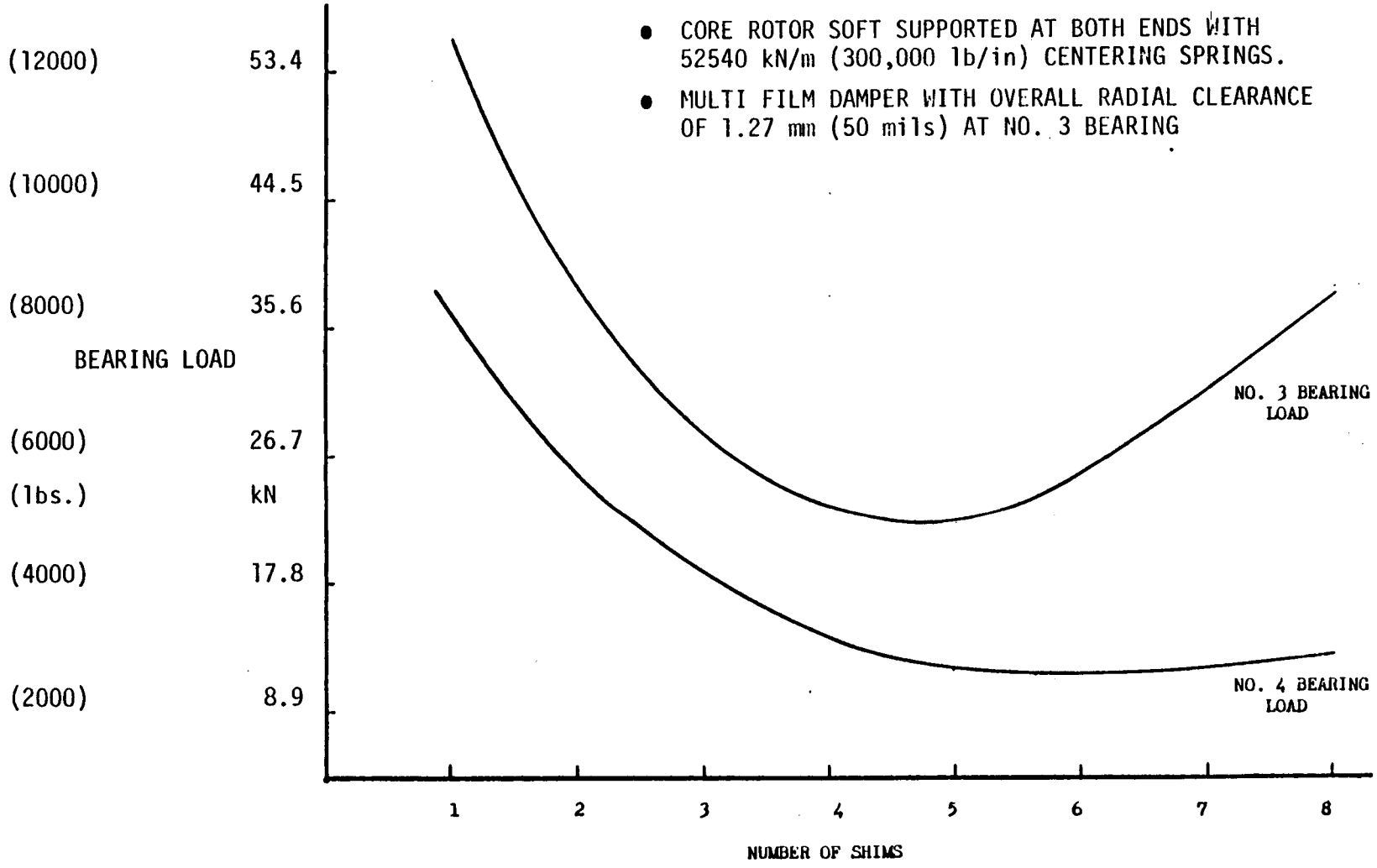


**Figure 96. High Load Squeeze Film Damper Optimization.**

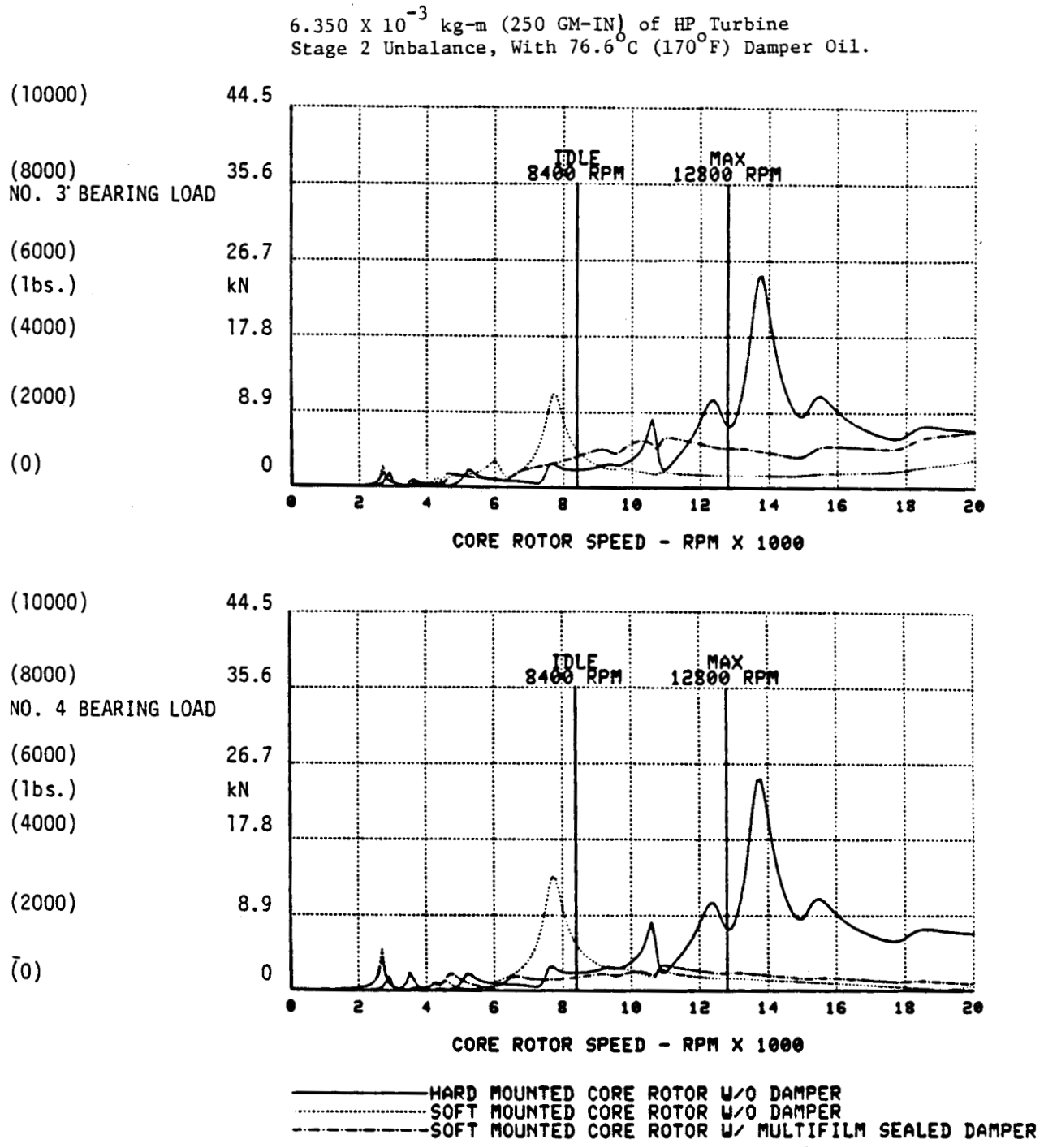


Figure 97. Core Synchronous Combined Modes Frequency Response Component Mode Solution.

configurations. The damped configuration provides superior vibration characteristics with basically a flat response curve over the operating speed range.

## 3.11 CONTROL DESCRIPTION

The ICLS engine control system is shown schematically in Figure 98. A Full Authority Digital Electronic Control (FADEC) was the central element in the system. The air-cooled, engine-mounted FADEC-controlled fuel flow, fuel flow split to the double annular combustor, compressor stators, and clearance control air valves on the compressor, HPT, and LPT. The FADEC was also designed to control starting bleed valves and a start range turbine cooling function but testing of the core engine proved these functions to be unnecessary and they were not used on the ICLS engine. Figure 99 is a photograph of the $E^3$ FADEC.

The FADEC received inputs from a variety of sources as outlined below:

- Command Inputs - Command data was provide through a serial, multiplexed digital link which simulated an aircraft interface connection. The primary command input was the position of the engine operator's power lever but the data link was also used to transmit adjustments and selector switch positions from the control room to provide experimental flexibility for engine testing.

- Temperature Inputs - Seven temperatures were sensed. Thermocouples provided temperature measurements from the compressor discharge, the HP turbine discharge, and the three engine casings where active clearance control was provided. Resistance temperature detectors were used for sensing fan and compressor inlet temperatures.

- Electrical Power Inputs - A control alternator on the core-driven accessory gearbox served as the primary source of electrical power for the FADEC with power also provided from an external 28 volt dc source for backup in the event of an alternator failure and for use during starts and control checkout when the engine was not running.

- RPM Inputs - Core rpm was sensed by detecting the frequency of the input from the control alternator, and fan rpm was sensed by means of a magnetic pick-up and a toothed wheel mounted on the fan shaft.

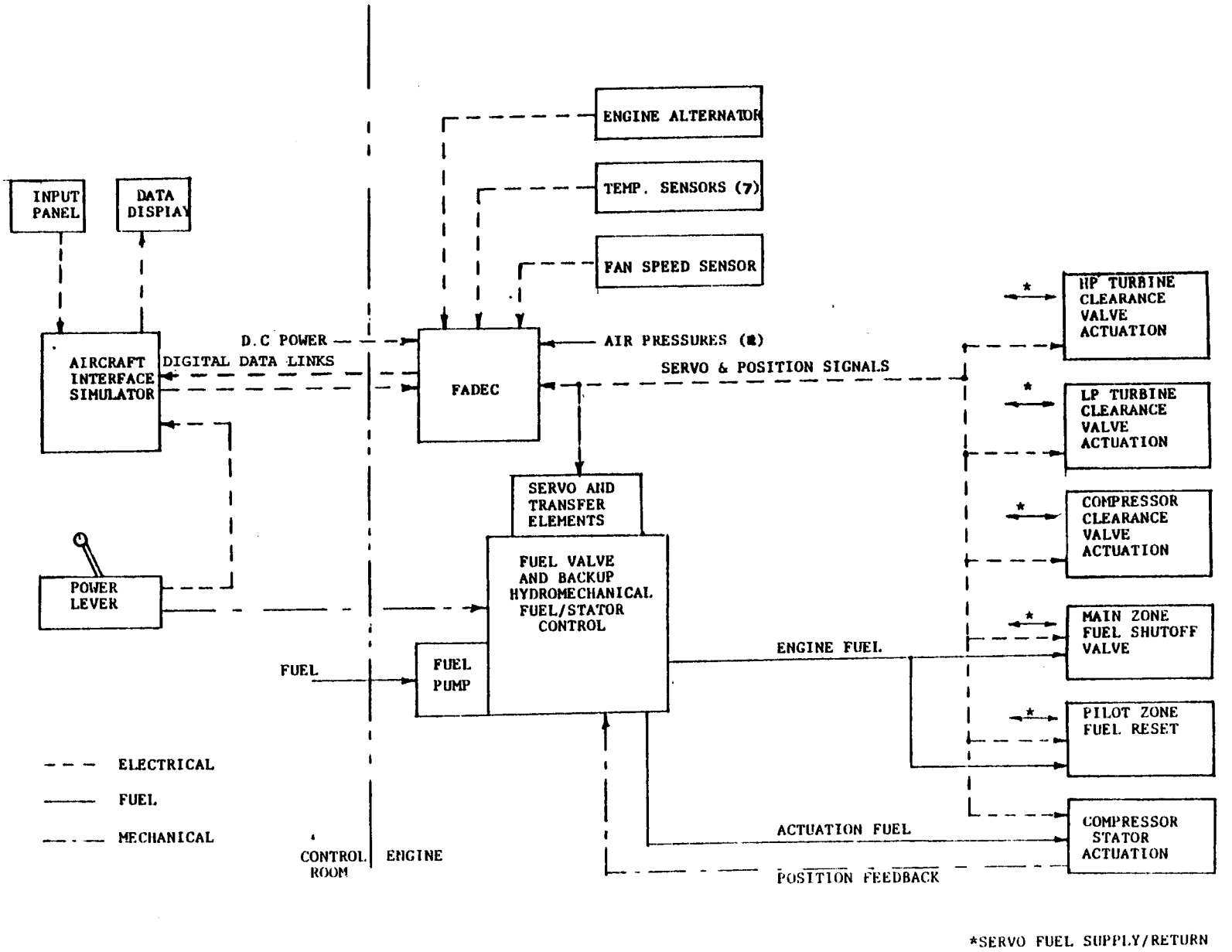


Figure 98. Engine Control System Schematic.

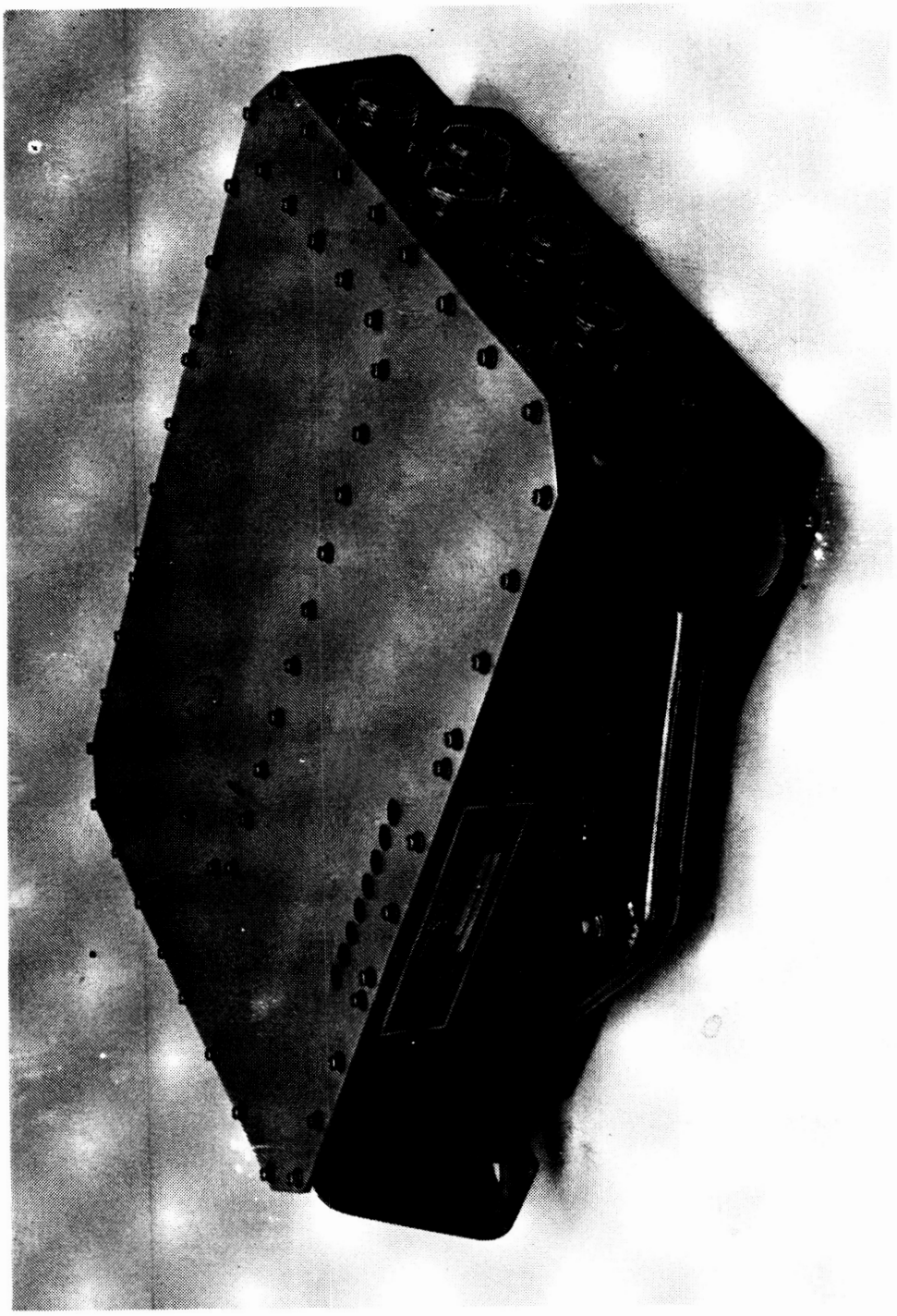

Figure 99. Full Authority Digital Electronic Control (FADEC).

- Pressure Inputs - Two pressure transducers were included in the FADEC, one sensing ambient pressure and the other sensing compressor discharge pressure.

- Position Feedbacks - Position indications from each of the actuators controlled by the FADEC were sensed by means of linear variable phase transducers (LVPT) located in or near each actuator.

The primary outputs of the FADEC were electrical signals to electro-hydraulic servovalves that control the flow of high pressure fuel to actuators for each of the controlled variables. The servovalves that control fuel flow, main zone fuel shutoff, and compressor stators were of a new, fail-safe design whereas the other servovalves (pilot zone fuel reset and the three clearance control valves) were of conventional design. Loss of the electrical signal to any servovalve would have caused the corresponding actuator to go to the safe extreme of travel which is closed for the fuel metering valve and pilot zone fuel reset valve, open for the main zone fuel shutoff, maximum available closure for the stators, and the minimum casing cooling position (maximum clearance) for each clearance control air valve. The actuators controlled by the fail-safe servovalves would have also gone to these safe extremes if their electrical signal failed hard-over (i.e., to an extreme level) in either direction. The FADEC also provided engine and control system data outputs over a multiplexed digital data link to the control room for display and recording.

The control strategy employed for the various controlled variables was as follows:

- Fuel Flow - Fuel flow was modulated to control engine rpm in response to the power lever angle (PLA) set by the engine operator. PLA schedules provided core rpm governing at low power settings and fan rpm governing at high power settings. Limits were imposed to prevent excessive engine temperatures and pressure. In addition, transient fuel schedules and rate-of-change limits were included to prevent compressor stalls, combustor blow-outs, and excessive thermal shocks during starts and thrust transients. A selectable manual fuel control mode was also included to allow exploration of engine characteristics, particularly in the starting region.

- Fuel Flow Split - During starts and at ground idle power, the control established single annular combustion by shutting off main zone fuel so that only the pilot zone received fuel. At flight idle and above, both zones were in operation. The transition between combustor modes was made as a function of corrected core rpm with hysteresis added deliberately to prevent cycling at the switchover point. During transition into double annular operation, main zone fuel flow was temporarily held low to prevent pilot zone starvation as the main zone fuel system fills and subsequently, the pilot zone fuel flow was temporarily reduced to enrich the main zone for improved light-off. A manual control mode was also available to allow experimentation with fuel flow split between combustor zones.

- Compressor Stator Control - Stator angle was scheduled in the conventional manner as a function of corrected core speed. Selectable resets were included to allow exploration of the potential for using off-design stator positions to improve transients response and compensate for unusual engine operating conditions.

- Active Clearance Control - Both manual and automatic control modes were provided for each of the active clearance control valves. In the automatic mode, the air valves modulated to schedule casing temperature as a function of rotor speed and engine internal air temperatures. The schedules were designed to provide the desired steady state clearance characteristics. A rapid deceleration would cause the valves to close until the casings reach their normal steady state temperatures. This was done to achieve the maximum casing diameter immediately after a deceleration to minimize the chance of a rub if the engine was reaccelerated before the rotor cools. The compressor clearance control had an additional feature to maximize clearance during accelerations. When the calculated temperature of the clearance control air (Stage 5 bleed) exceeded the aft compressor casing temperature, as it temporarily will during an acceleration, the valve was positioned to cause the air to pass over the casing and promote rapid heating. In the manual mode, the air valves were positioned in response to potentiometer inputs from the control room. The deceleration override was also active in the manual mode and, once triggered, had to be manually reset.

A hydromechanical control was included in the control system to serve as a backup for the single-channel FADEC in controlling fuel flow and compressor stators. In the backup mode, the other controlled variables were electrically de-energized and hydromechanically biased to go to safe

positions, the main zone shutoff valve opening, the pilot zone reset valve closing, and the clearance control air valves going to the maximum clearance positions.

The system would automatically revert to the backup mode if all FADEC power was lost, if the self-test routines in the FADEC detected a fault, or if the hydromechanical control detected a core overspeed. The backup mode could also be manually selected from the control room.

Another protective feature in the control system was the Failure Indication and Corrective Action (FICA) sensor failure protection strategy. The basic FICA concept involved the incorporation of a simplified engine model in the FADEC software along with sensor failure detection logic which monitored sensor signals and replaced failed signals with model-generated substitutes. A mathematical filter technique (extended Kalman filter) was used to continuously update the engine model using data from all unfailed sensors.

The ICLS control system was representative of the design envisioned for the production FPS engine in many respects such as :

- On-engine digital electronic computation used for all control functions.
- Control laws stored as software in the computer's memory.
- FICA sensor failure protection included in software.
- Air-cooled, engine-mounted FADEC.
- Advanced technology, multilayer ceramic module mounting of electrical elements.

Dual computer redundancy, proposed for the initial FPS to enhance operational reliability, was not included in the ICLS system because the extra engineering effort and hardware costs involved were considered beyond the scope of the program. With a dual channel system, operation is unaffected by any single failure in the electronic control and the probability of completing any single flight without operational faults is quiet high. This

characteristic was not necessary for the demonstrator program, and the limited hydromechanical backup described above provided ample engine protection, allowing continued safe operation and orderly shutdown in the event of an electronic control failure.

## 3.12 INSTRUMENTATION DESCRIPTION

The ICLS test vehicle was instrumented to investigate the following areas:

- Safety
- Aero-performance
- Speeds
- Thrust
- Fuel Flow
- Dynamic strains and temperatures on static hardware and the low pressure rotor
- Operating pressures and temperatures
- Blade tip clearances in the compressor and high pressure turbine
- Vibrational displacements and accelerations
- Secondary flow system flow rates
- Acoustics

The quantity of instrumentation exceeded the site read-out capability. Therefore, not all performance instrumentation was read during mechanical checkout, and not all mechanical instrumentation was read during performance testing.

Instrumentation is specified in the following series of tables and figures:

| | |
|---|---|
| Safety Instrumentation | Table VI |
| Aero-performance Instrumentation | Figure 100 |
| Fan Instrumentation | Figure 101 |
| Compressor Instrumentation | Figure 102 |

Table VI. Safety Instrumentation.

- UNDERCOWL (FIRE DETECTION) THERMOCOUPLES
- SUMP PRESSURES AND TEMPERATURES
- BEARING THERMOCOUPLES
- ACCELEROMETERS ON BEARING SUPPORTS AND FRAMES
- PARASITIC PRESSURES, TEMPERATURES AND FLOWS
- CONTROL PARAMETERS
- FUEL FLOWS
- LP AND HP ROTOR SPEEDS
- THRUST

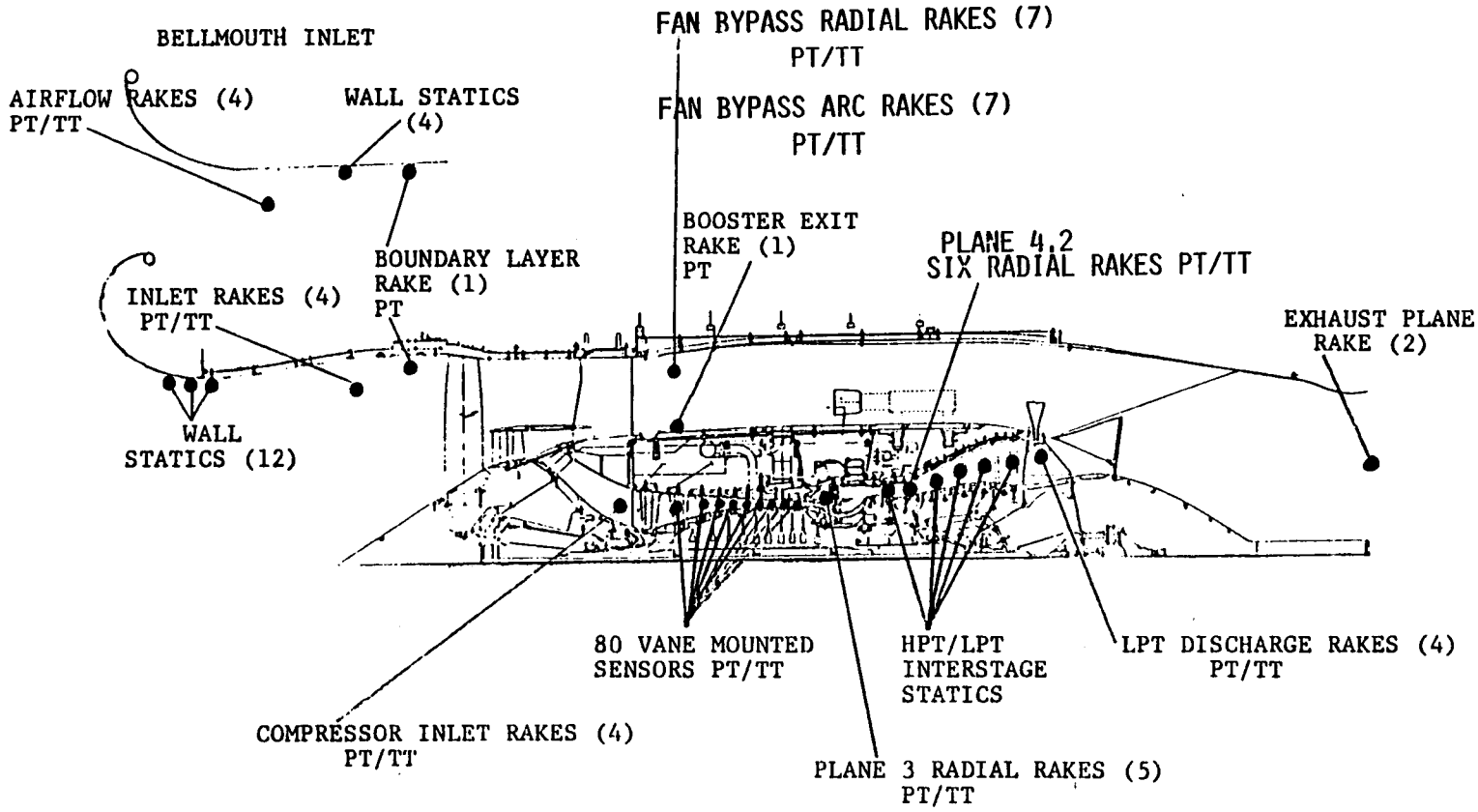


Figure 100. Aero-Performance Instrumentation.

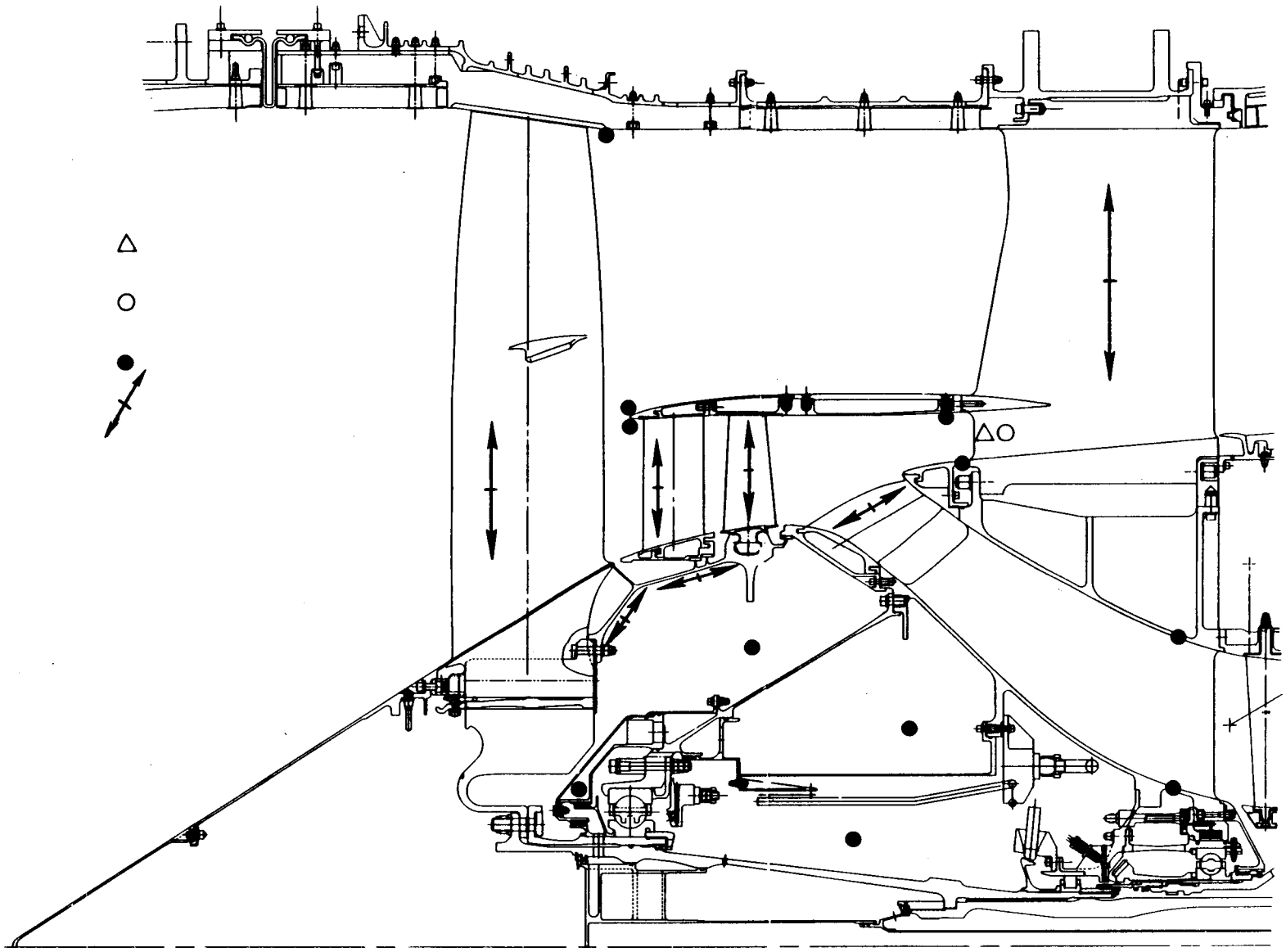

Figure 101. Fan Instrumentation.

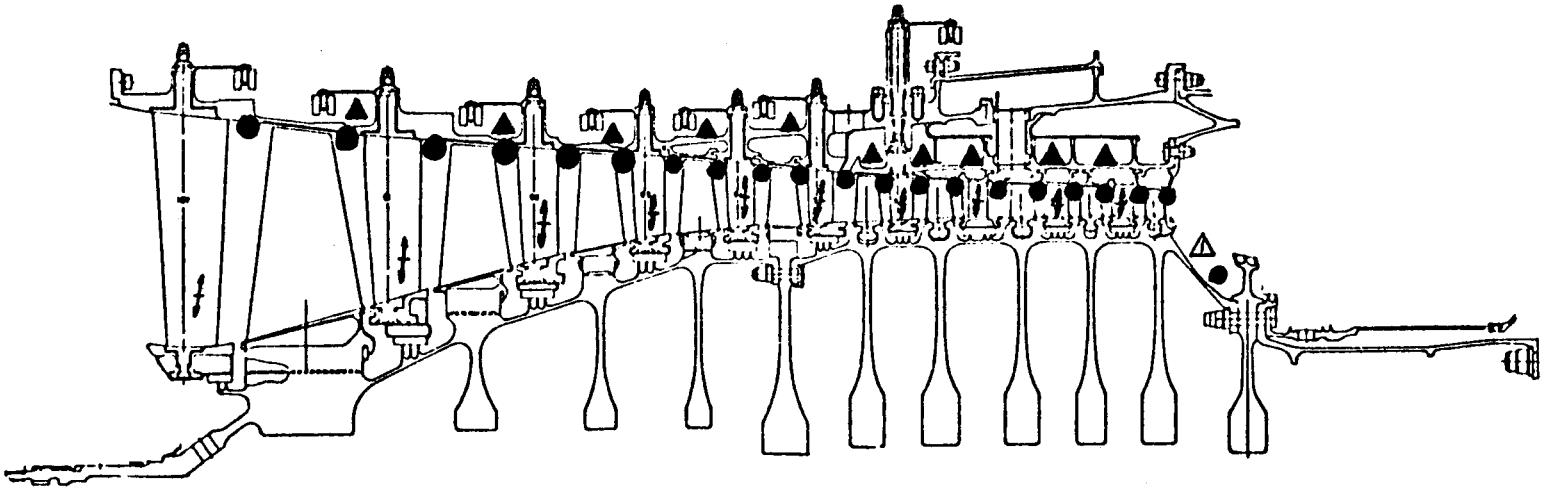


- INTERSTAGE STATIC PRESSURES
- CASING TEMPERATURES
- STATOR STRAIN GAGES
- CLEARANCEOMETERS - STAGES 3, 5 & 10
- STATIONARY INSTRUMENTATION - SIMILAR TO CORE
- ROTATING INSTRUMENTATION - ALL REMOVED FROM CORE

**Figure 102. Compressor Instrumentation.**

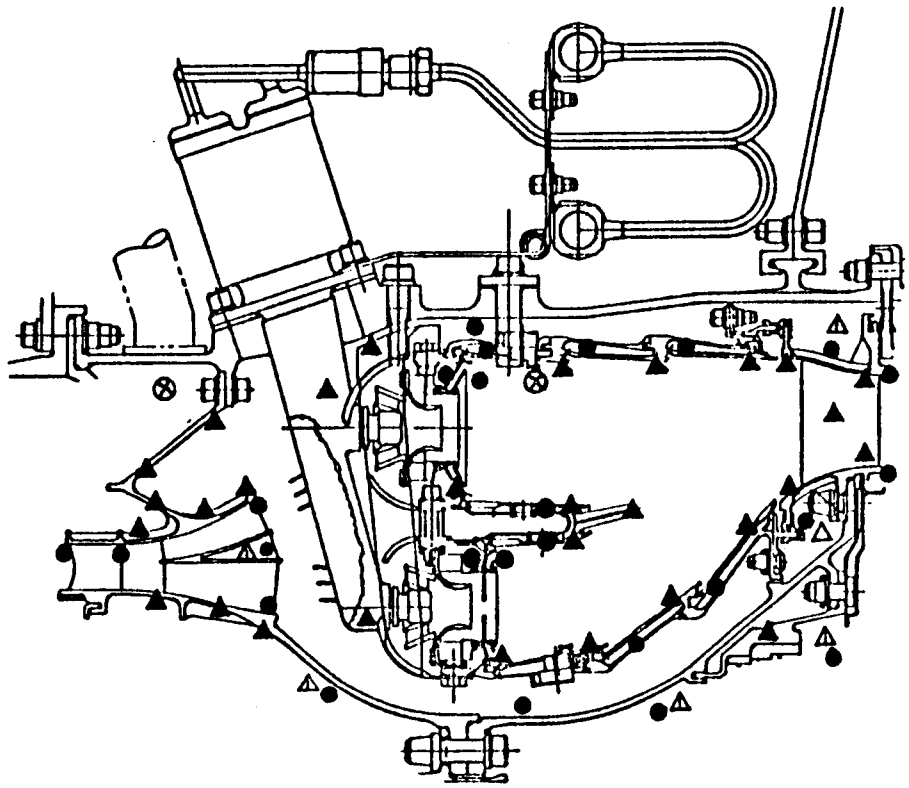


- DYNAMIC PRESSURE PROBES
- AIR AND SKIN THERMOCOUPLES
- WALL STATIC PRESSURES
- COMPRESSOR DISCHARGE RAKES ($P_T/T_T$)
- SIMILAR TO CORE

Figure 103. Diffuser and Compressor Instrumentation.

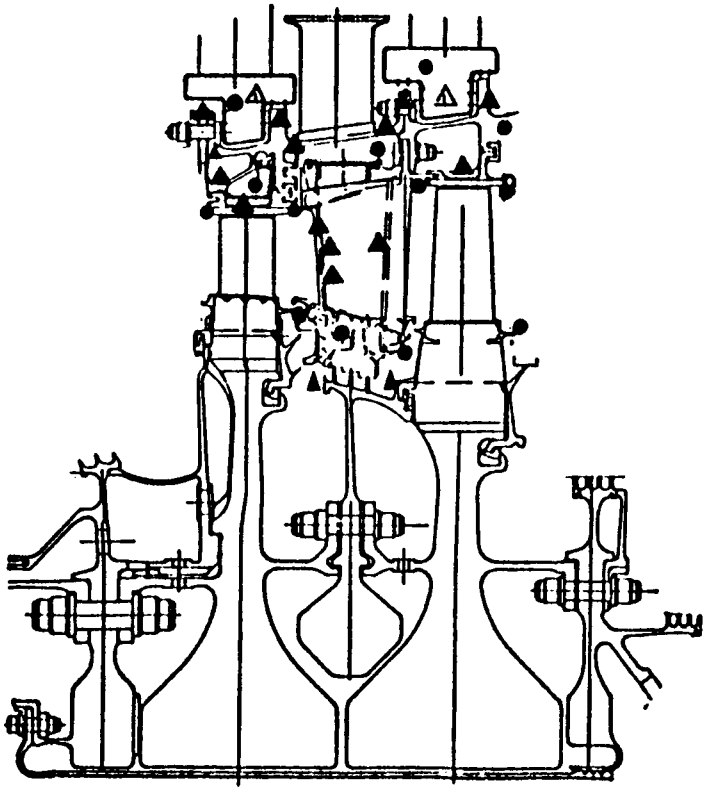

- ● STATIC PRESSURES
- ▲ SKIN TEMPERATURES
- △ AIR TEMPERATURES

- ● Skin Thermocouples
- ● Air Thermocouples
- ● Static Pressures
- ● Optical Clearance Probes

- ● Stationary Instrumentation-Similar to Core
- ● Rotating Instrumentation-All Removed From Core

**Figure 104. High Pressure Turbine Instrumentation.**

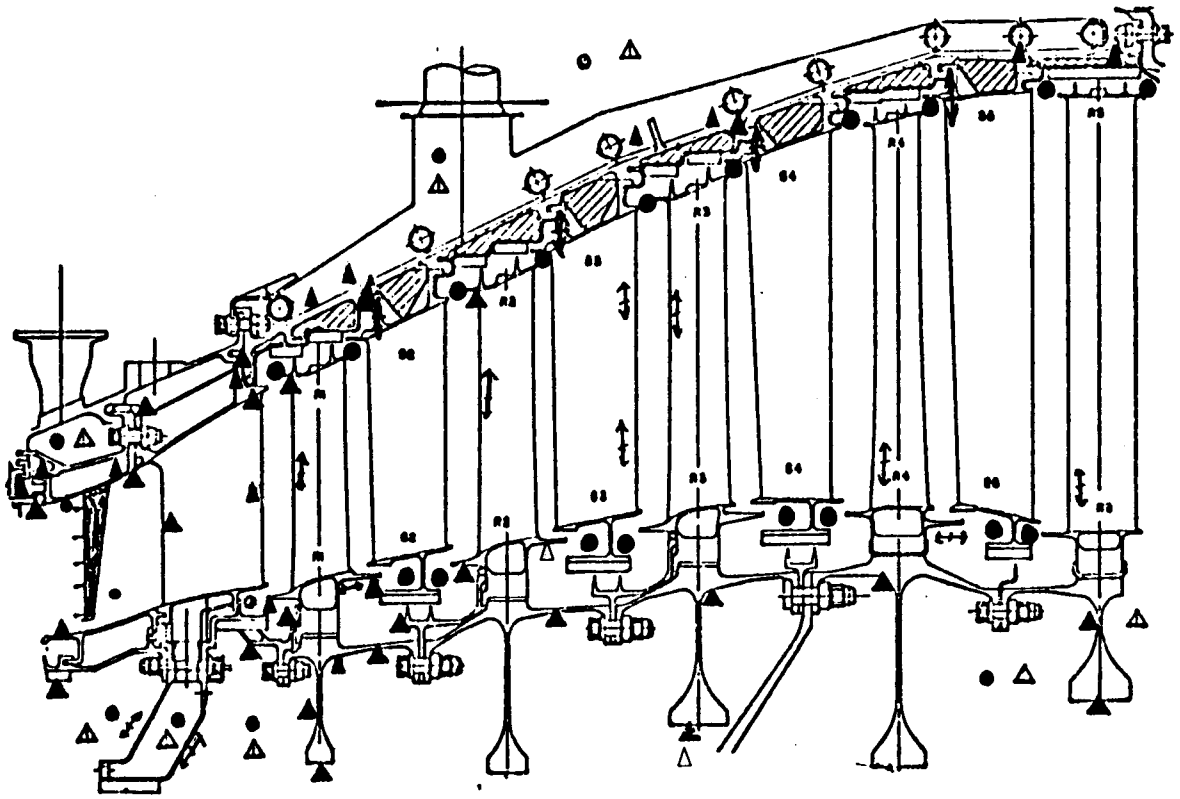


- HPT Total Temperature Discharge Rakes
- HPT Total Pressure Discharge Rakes
- Skin Thermocouples
- Air Thermocouples
- Static Pressures
- Dynamic Strain Gages

Figure 105. Low Pressure Turbine Instrumentation.

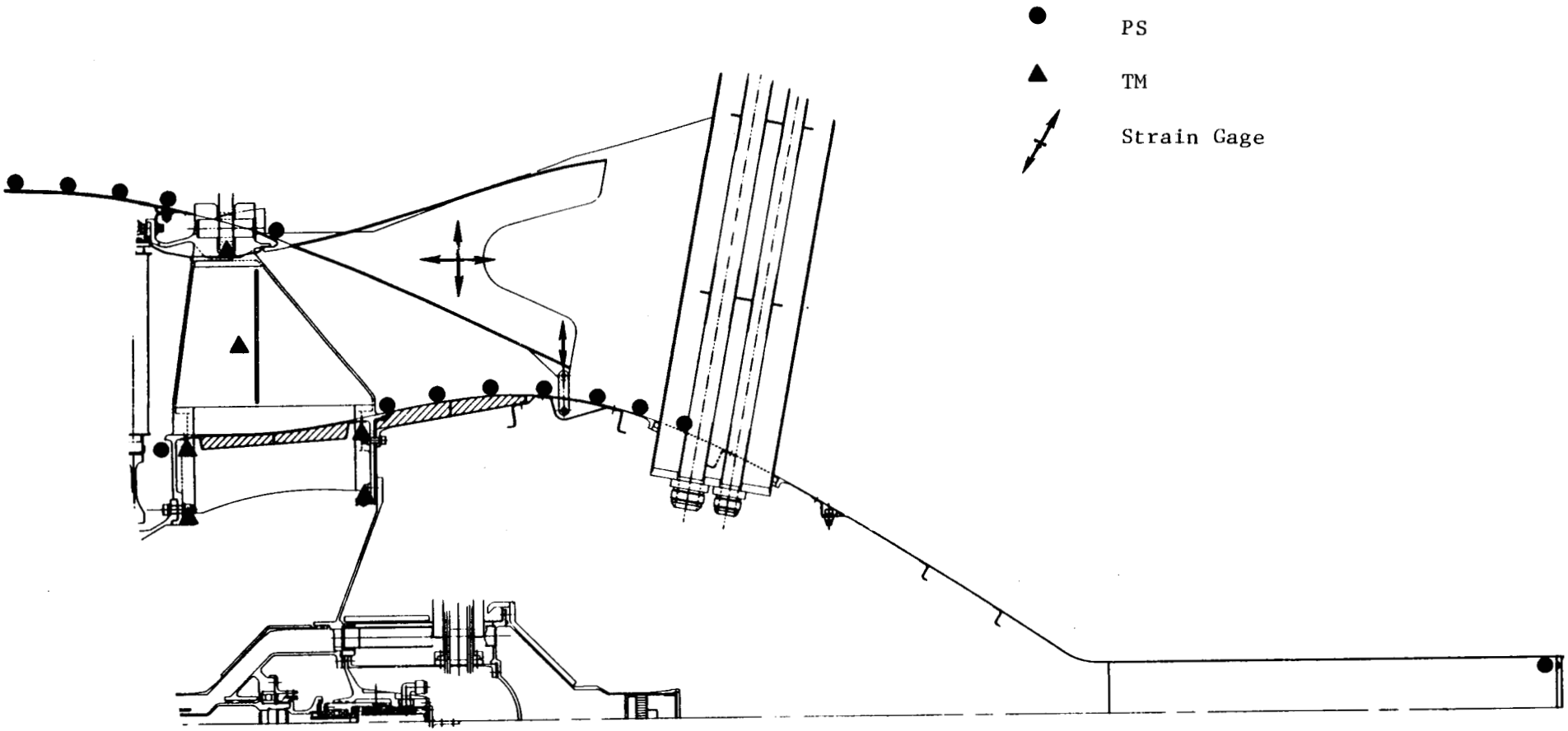


**Figure 106. Turbine Frame and Exhaust System Instrumentation.**

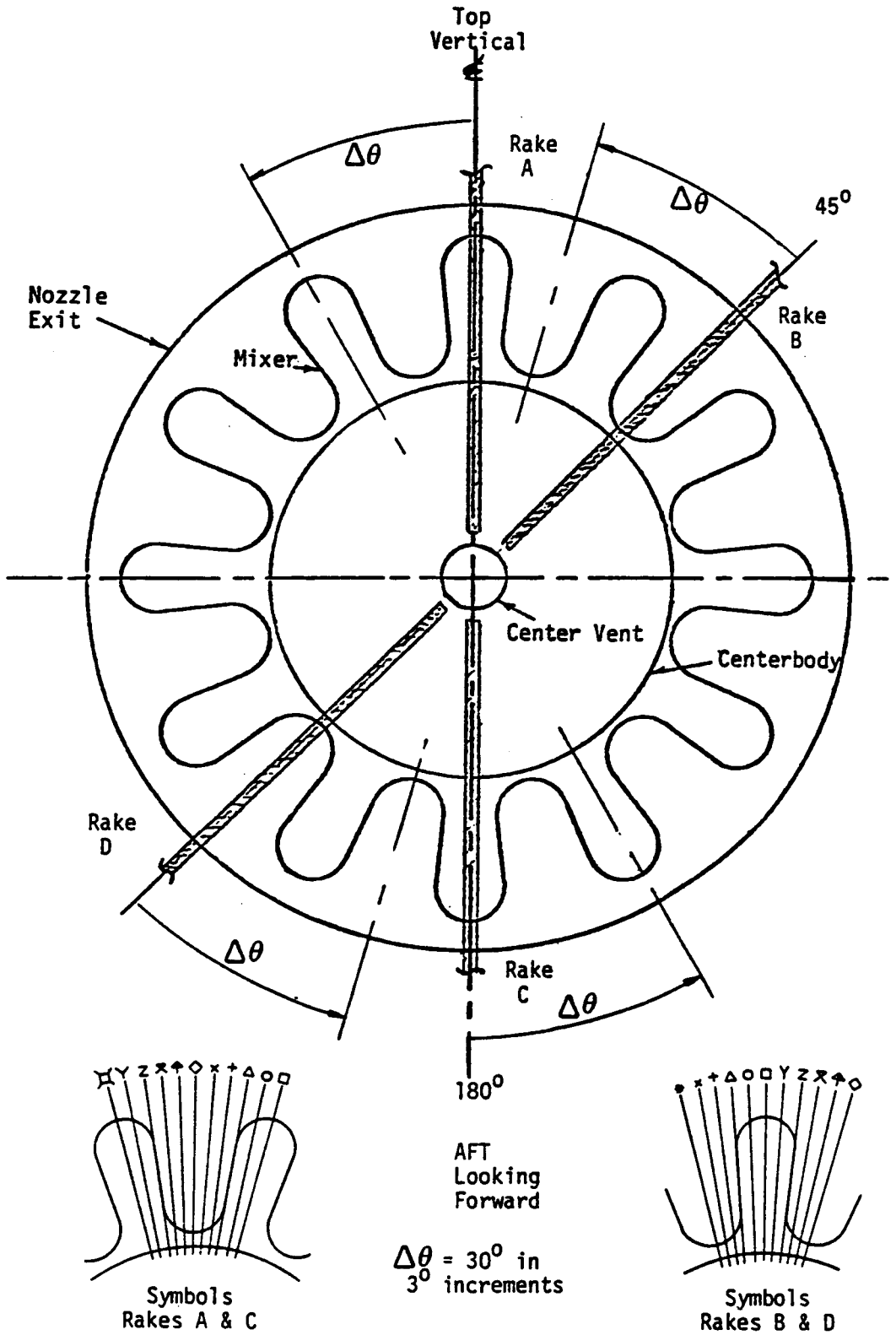


Figure 107. Exhaust Nozzle Exit Survey Rake Position.

Table VII. Secondary Flow Measurements.

| Parameter, Source | Method |
|---|---|
| LPT Purge Air, Stage 5 | Calibrate Piping |
| S2 HPTN Cooling, Stage 7 | Calibrate Piping |
| Compressor ACC Air, Stage 5 | Calibrate Piping |
| Center Vent Tube | Calibrate Vent Tube |
| Turbine ACC Air | Calibrate Manifold |

Table VIII. Acoustic Instrumentation.

| INSTRUMENTATION | OBJECTIVE |
|---|---|
| Farfield Microphones | • Overall Engine Noise Levels |
| Nearfield Microphones | • Overall Treatment Effectiveness |
| Inlet Wall Kulites | • In-Duct Treatment Effectiveness |
| | • Source Characteristics |

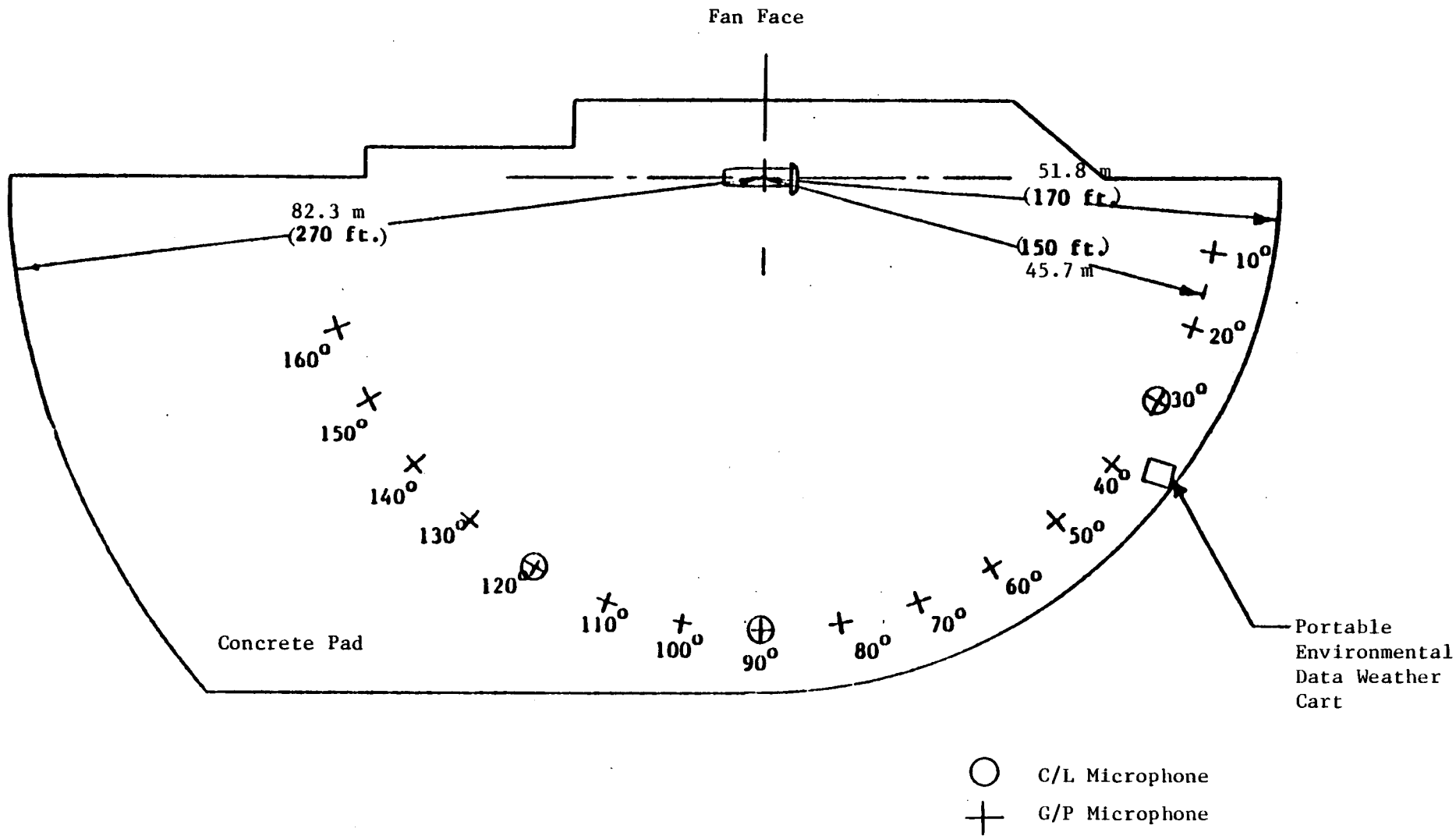


**Figure 108. Microphone Location.**

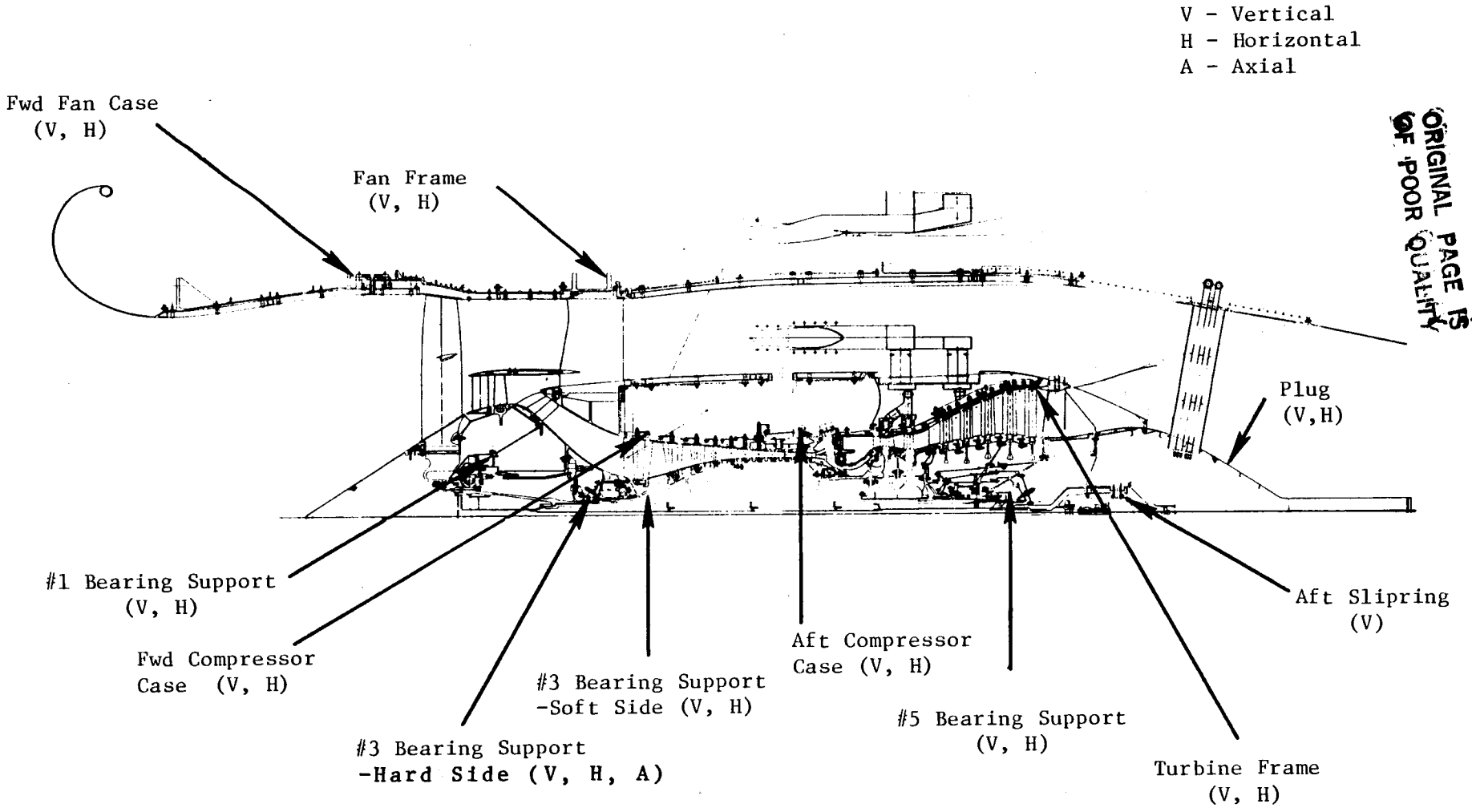




**Figure 109. Vibration Instrumentation.**

## 4.0 TEST FACILITY DESCRIPTION

The ICLS engine was tested at Site IV D at the General Electric Peebles test facility, located near Peebles, Ohio. Site IV D is an outdoors test facility with acoustic test capability. The engine was suspended from a thrust frame, over a large concrete pad. The engine installation in Site IV D is pictured in Figure 110.

The facility load table and engine mount structure, with phantomed fan cowling, are shown in Figure 111. The inlet was supported from the facility rather than from the fan case.

A one-story building, about 300 m (1,000 ft) from the engine, housed the control, computational and monitor stations. Critical engineering parameters were displayed in real time and recorded by oscilloscopes, Sanborn strip charts and tape recorders. Engineering test data was independently processed by the Data Management System (DMS).

The DMS linked all GE-Evendale and Peebles engine test sites with a central data processing facility. It operated independently of the real-time systems described above and performed a number of functions, such as data acquisition, processing, distribution, and graphic presentation of engine test data. It consisted of three functional subsystems: Cell Unit, Site Unit, and Communications Controller (C-Con).

The Cell Unit functional subsystem is illustrated in Figure 112 and consisted of two minicomputers, analog-to-digital conversion units, a control console, and a hard-copy printer. Its primary functions were data acquisition, system calibration, sample averaging, and engineering units conversion. It interfaced only with the site unit for data transfer.

The site unit, shown in Figure 113 received data from the cell unit. It duplicated some cell unit calculations and then performed average and error rejection calculations, data quality checks, and engineering calculations. It

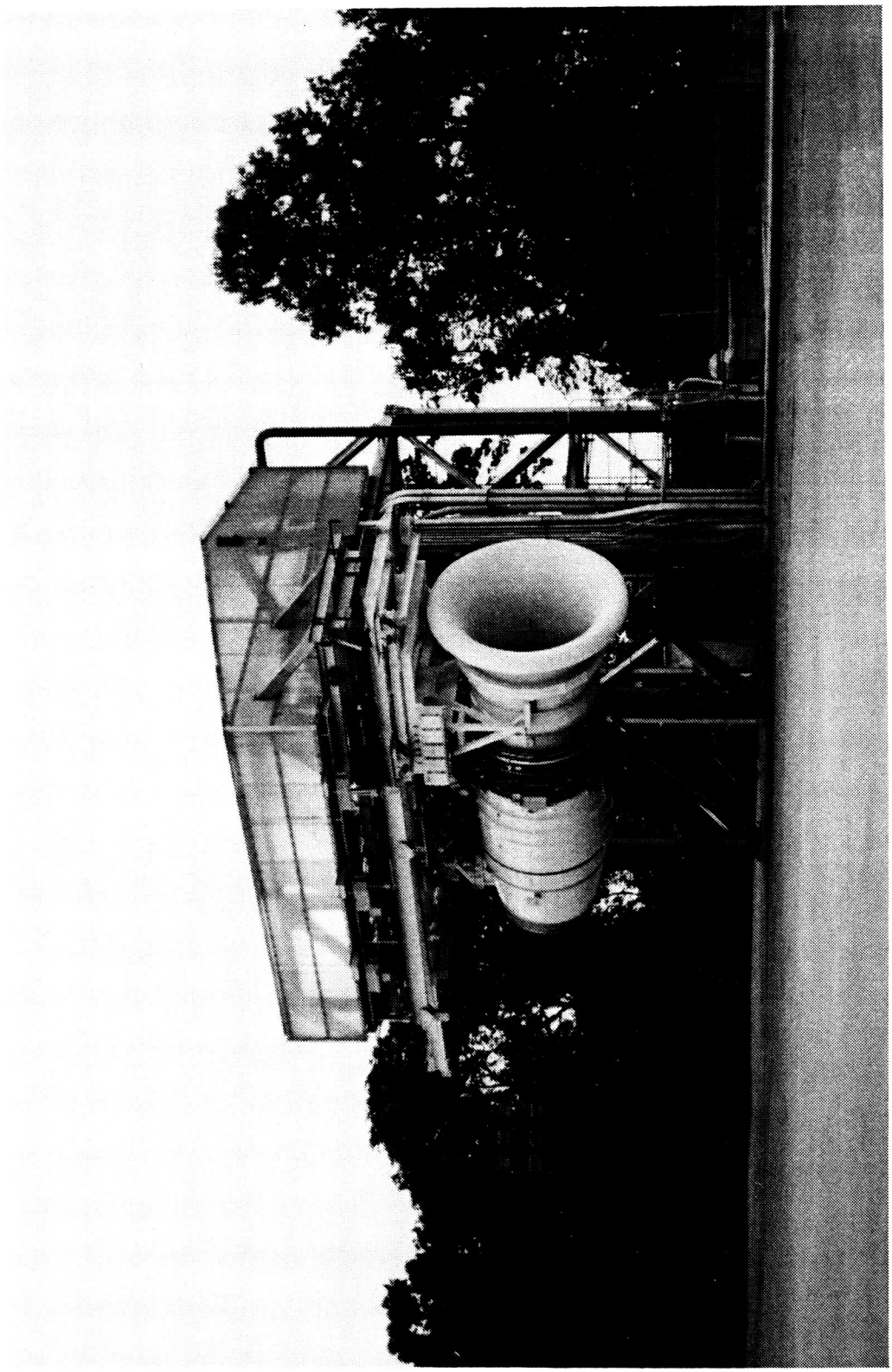

Figure 110. ICLS Installed at Peebles Test Site, IV D.

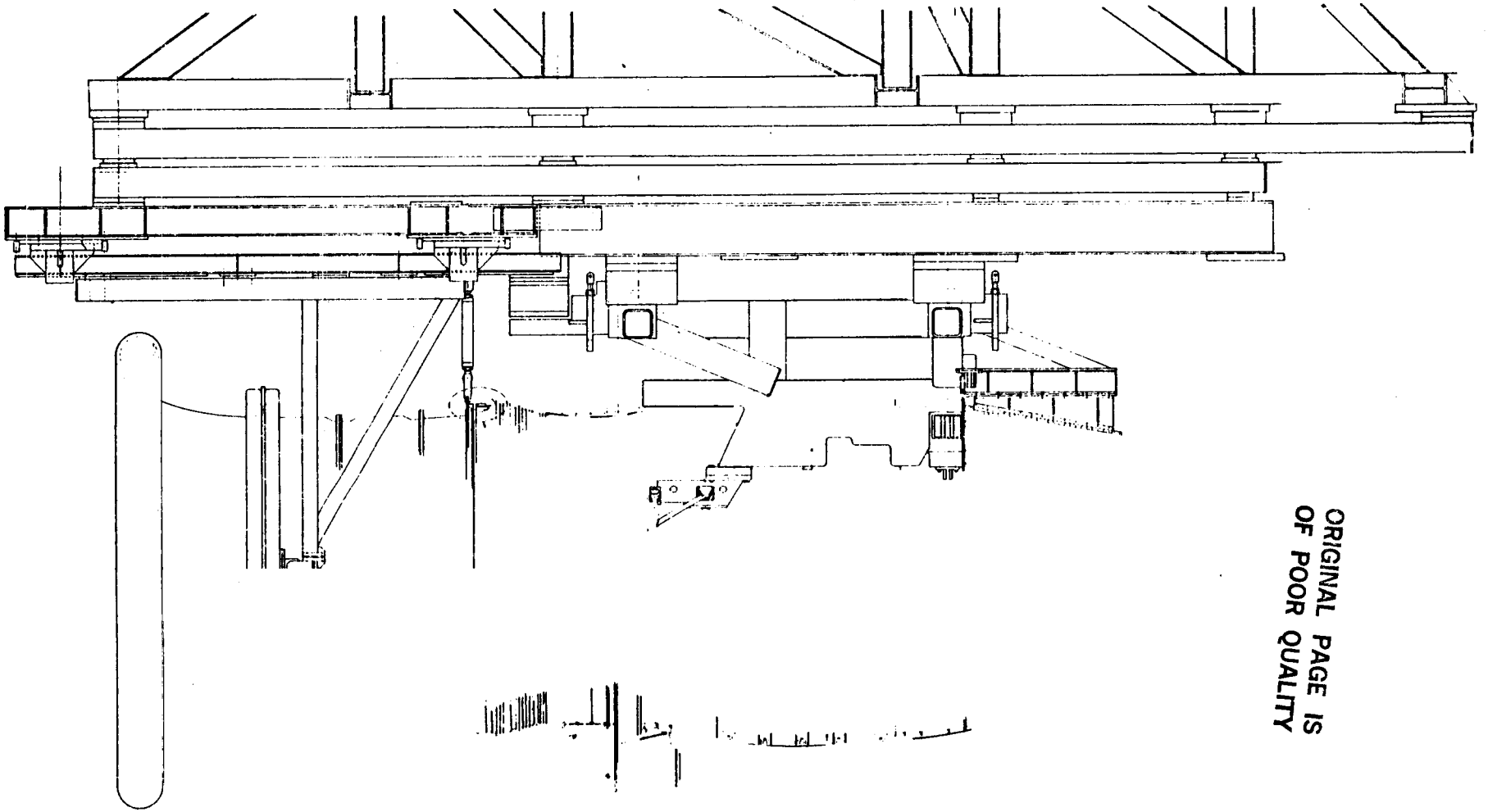



Figure 111. Site IV D Installation Drawing.

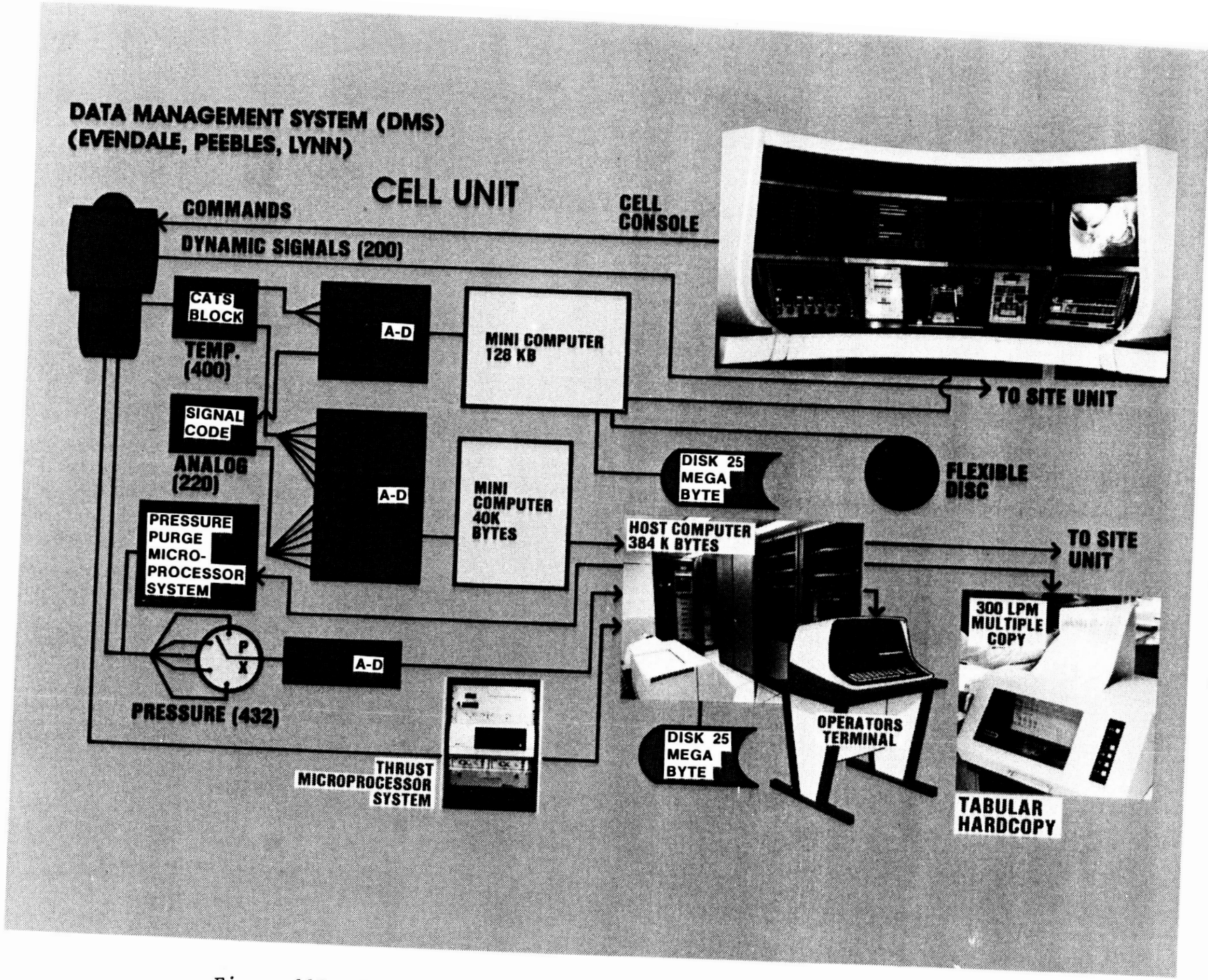


Figure 112. Data Management System - Cell Functional Unit

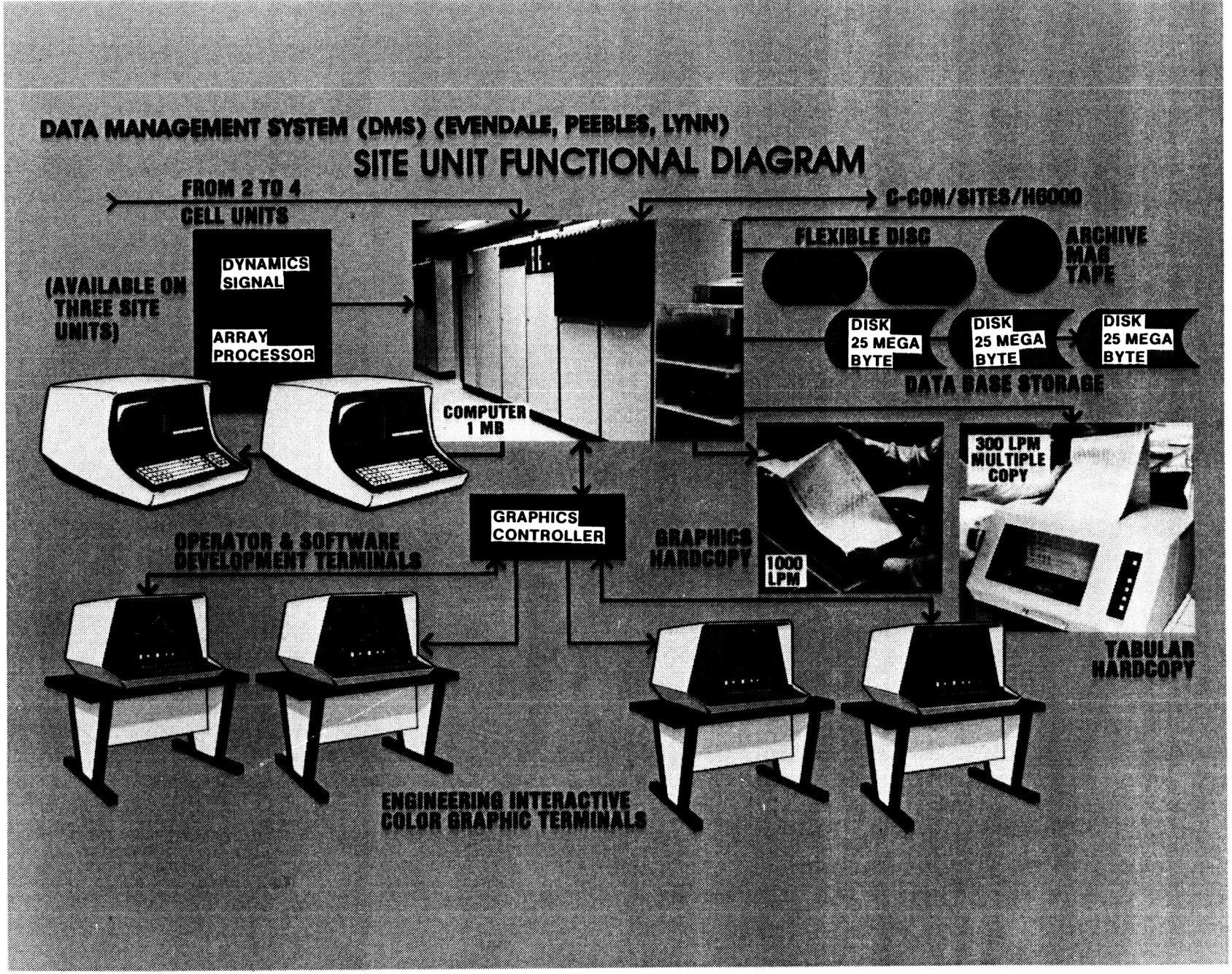


Figure 113. Data Management System - Site Unit Functional Diagram

had a data base storage system and color interactive graphics capability with three consoles.

The C-Con was the coordination unit for data transfer from the site unit to a central Honeywell 6000 computer. A flow chart of the DMS system in Site IV D is shown in Figure 114.

The cell and site units at Peebles were used during the ICLS engine test; they provided on-line performance calculations. All data were stored on the site unit data base and simultaneously transferred to the Honeywell 6000 computer at Evendale, Ohio. Further re-processing (if needed) and subsequent post-test analysis were performed at Evendale.

The interactive graphics system at the Peebles test site permitted an on-line (near real time) comparison of the test data with the pretest data stored in the site computer. The system provided hard copies of the selected data plots, as well as data printouts for each data reading. A dynamic capability of the system also provided transient data of the starting, accelerating, and decelerating characteristics of the engine.

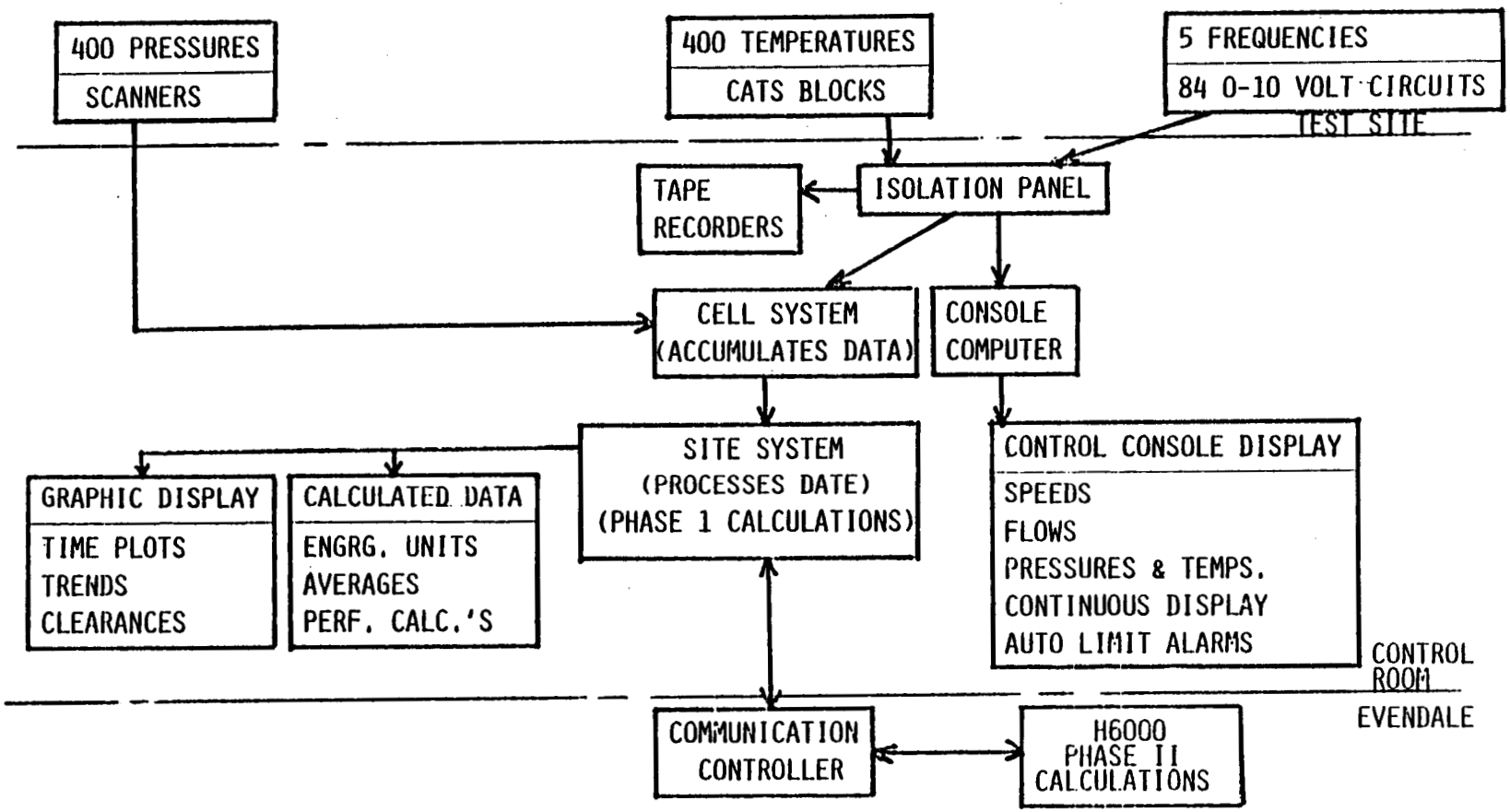


Figure 114. Site IV D Data Acquisition.

## 5.0 TEST OPERATIONS SUMMARY

This section provides a detailed history of the test activities. It covers configuration changes, test conditions, and details of test cell operations.

The $E^3$ ICLS engine completed assembly on March 22, 1983, in Evendale, Ohio, and was transported to the prep-to-test building at the Peebles Test Operation, Peebles, Ohio. Final preparations were completed and installation in test pad IV D was initiated on April 22, 1983. Testing began April 26, 1983, and was completed on the morning of June 15, 1983. Testing occupied 64 hours and 50 minutes of fired rotating time.

The first portion of testing comprised a checkout of the engine and facility. Then, mechanical integrity was evaluated in a series of tests. Performance and acoustic testing followed. Control testing was included in these as was expedient. For instance, control tests could be conducted while waiting for acceptable weather for performance testing. Inlets, exhaust nozzles and acoustic treatment were changed during the test series. The instrumentation varied, depending on the purpose of the test. A summary of the tests is given in Table IX. The configuration changes are further detailed in Table X.

For compactness, abbreviations and performance nomenclature are used in the tables in this section without definitions. These are defined in the LIST OF SYMBOLS, ABBREVIATIONS, AND ENGINE STATION DESIGNATIONS. Fuel schedule terminology is explained below. Fuel flow was scheduled using the parameter $W_f$/PS3. Normally, the control set fuel flow equals to $W_f$/PS3 times measured PS3. During some testing, fuel scheduling was manipulated using three separate parameters. A fuel schedule of "nominal plus 20% + 5 Phi + 13.8 kPa (2 psia) PS3" would have been the nominal schedule programmed into the control, increased by 20% (1.2 multiplier), then further increased by an adder of 5 pph/psia, and then multiplied by [PS3 plus 13.8 kPa (2 psia)]. This system allowed fuel schedule slopes and levels to be manipulated.

Table IX. Summary of $E^3$ ICLS Test Runs.

| | Run Date and Test | Instrumentation Configuration | Inlet | Nozzle | Laser Probes | ACC HPC | ACC HPT | ACC LPT | Steady State DMS Rdg. No. |
|---|---|---|---|---|---|---|---|---|---|
| 1. | 4/26/83 Dry and Wet Motor | Mechanical C/O | B/M | Perf. | 6 | Off | Off | Off | 1-2 |
| 2. | 4/27/83 Initial Start | Mechanical C/O | B/M | Perf. | 6 | Off | Off | Off | 3-8 |
| 3. | 4/29/83 Mechanical Checkout | Mechanical C/O | B/M | Perf. | 6 | Off | Off | Off | 9-21 |
| 4. | 5/6/83 Mechanical Checkout | Mechanical C/O | B/M | Perf. | 6 | Off | Shop Air | Off /On | 22-52 |
| 5. | 5/9/83 Mechanical Checkout | Mechanical C/O | B/M | Perf. | 6 | Off | Shop Air | On | 53-77 |
| 6. | 5/10/83 Fan Mapping | Mechanical C/O | B/M | Perf. | 6 | Off | Shop Air | On | 78-106 |
| 7. | 5/17/83 Performance | Performance | B/M | Perf. | 6 | Off /On | Shop/Air Fan/Air | On | 107-138 |
| 8. | 5/24/83 Mixer Perf. | Mixer Perf. | B/M | Survey | 6 | On | Shop Air | On | 140-149 |
| 9. | 5/25/83 | Mixer Perf. | B/M | Survey | 6 | On | Shop Air | On | 150-159 |
| 10. | 5/26/83 Mixer Perf./ 2nd Operating Line | Mixer Perf. | B/M | Survey | 6 | On | Shop Air | On | 160-208 |
| 11. | 6/1/83 Perf. W/O P1 4.2 rakes/FICA | Mixer Perf. | B/M | Survey | 0 | On | Shop Air | On | 210-229 |
| 12. | 6/7/83 Acoustic Test, Fully Suppressed | Acoustic | A/A | Survey | 0 | On | Shop Air | On | 231-260 |
| 13. | 6/8/83 Acoustic Test, Short Inlet | Acoustic | A/A | Survey | 0 | Off | Shop Air | On | 261-293 |
| 14. | 6/9/83 Acoustic Test, Fully Taped Inlet | Acoustic | A/A | Survey | 0 | Off | Shop Air | On | 294-318 |
| 15. | 6/14/83 Acoustic Test, Baseline | Acoustic | B/M | Survey | 0 | Off | Shop Air | On | 320-358 |

Table X. ICLS Test Configuration Changes.

For Run No. 1 - Initial Set Up Included

- Instrumentation - mechanical checkout configuration
- Six laser probes and 4 clearanceometers installed
- Bellmouth offset - 0.24 cm (0.094 in.) higher than engine
- Performance exhaust nozzle

For Run No. 2

- Replaced Marotta valve on stall dump system
- Replaced IGV rotary position pot

For Run No. 3

- Installed orifice plate in LPT ACC valve system
- Recalibrated throttle control
- Installed new $T_3$ probe

For Run No. 4

- Installed "porky pig" filter
- Blanked-off HPT ACC manifolds at 135° and 225°
- Installed insulation around HPT case and combustor
- Installed oil drain plug in mixer

For Run No. 5

- Changed to back-up reference temperature on slipring

For Run No. 6

- Replaced bad scanner valve
- Removed "porky pig" filter

For Run No. 7

- Changed to performance instrumentation configuration
- Installed new oil level sensor
- Recalibrated Stage 1 rotary position pot
- Replaced broken LPT borescope plug
- Replaced acoustic panels with hardwall panels
- Installed bellmouth position pots

For Run No. 8

- Replaced damaged bellmouth position pots
- Installed survey exhaust nozzle
- Installed exhaust plane rakes
- Changed to mixer performance instrumentaion configuration

Table X. ICLS Test Configuration Changes (Concluded).

For Run No. 9

- None

For Run No. 10

- Removed exhaust plane rakes
- Adjusted bellmouth to 1.0 cm (0.40 in.) up and 0.38 cm (0.15 in.) left

For Run No. 11

- Removed 3 plane 42 rakes and all laser probes

For Run No. 12

- Installed aero-acoustic inlet
- Changed to acoustic instrumentation configuration
- Removed all fan stream rakes

For Run No. 13

- Taped forward half of inlet

For Run No. 14

- Taped complete inlet

For Run No. 15

- Removed acoustic panels; reinstalled hardwall panels
- Replaced aero-acoustic inlet with bellmouth
- Reinstalled performance instrumentation

The following is a history of the test activities from an operational standpoint. The test parameters are engine control console data, which may not exactly match the DMS performance data. The term "Run" refers to a specific time period of testing. The term "Test" refers to a specific test activity or test objective.

$E^3$ ICLS Test No. 1 - Initial Dry and Wet Motors

Run No. 1

Date: April 26, 1983

DMS Readings: Steady State 1 and 2, Transient 7002

Test Conditions:

Weather: Clear 17°C (63°F)
Inlet: Bellmouth
Nozzle: Performance
Instrumentation:
- Mechanical Checkout Configuration
- Clearanceometer - 1 Stg 3, 1 Stg 5, 2 Stg 10 in HPC
- 4 Laser Probes on Stg 1 HPT
- 2 Laser Probes on Stg 2 HPT

The engine and facility checklists were completed. Starter air pressure was slowly brought up to 228 kPa (33 lbf/in.$^2$). Air pressure was then shutoff due to a system fault on console. No indication of core rotation was noted. After clearing fault, starter air was brought up to 331 kPa (48 lbf/in.$^2$). Still there was evidence of core rotation. Air was shut off, the cover plate was removed from the second starter pad on the gearbox, and an attempt was made to rotate core manually. The core finally broke free under approximately 1100 mn (800 ft-lb) torque. A third attempt to air motor was successful. A core speed of 3875 rpm was obtained with a starter air pressure of 350 kPa (51 lbf/in.$^2$). Fan speed was 180 rpm. A steady state DMS

reading was taken at these conditions and the fuel actuated ACC valves were exercised. No mechanical or lube system problems were encountered. Maximum starter oil temperature was 72°C (161°F) and core coast downtime was 3 minutes and 15 seconds. Postrun inspections revealed no leakage problems and the engine was immediately prepared for a wet motor.

Starter air pressure was set at 379 kPa (55 lbf/in.$^2$) to initiate engine rotation. The stopcock was opened and a 4 minute wet motor performed. The stopcock was closed and air turned off and a 3 minute coastdown from 3750 rpm was monitored with no problems seen. The engine was inspected and no fuel leaks were observed. The only facility problem encountered was a faulty stall dump system. This was traced to a faulty Marotta valve, which was replaced. The vehicle was then prepared for an idle leak check run.

RUN NO. 1

| DMS | Core Speed | PCN25R | Starter Air Pressure kPa | Starter Air Pressure (lbf/in.$^2$) |
|---|---|---|---|---|
| 1 | 0 | 0 | 0 | (0) |
| 2 | 3838 | 31% | 350 | (51) |
| 7002 | 0-3750 | --- | 379 | (55) |

$E^3$ ICLS Test No. 2 - Initial Start

Run No. 2

Date: April 27, 1983

DMS Readings: Steady State 3-8; Transient 7004-7007
Run Time: 29 Minutes

Test Conditions:

Weather: Clear, 26°C (78°F)

Inlet: Bellmouth

Nozzle: Performance

Instrumentation:
- Mechanical Checkout Configuration
- 4 Laser Probes on Stg 1 HPT
- 2 Laser Probes on Stg 2 HPT
- Clearanceometers - 1 Stg 3, 1 Stg 5, 2 Stg 10 in HPC

All starts were made with manual fuel control. Engine light-off speed was approximately 30% core speed with a starting fuel flow of 181 kg/hr (400 lbm/hr). First start attempt was unsuccessful. Stopcock was opened for 53 seconds without a light before start was aborted. Second attempt achieved a partial light 4 seconds after stopcock was opened. However, air to starter was cut off prematurely causing core speed to drop and the start to be aborted. Start No. 1 was successfully made on the third attempt. Light was achieved 41 seconds after stopcock was opened. The engine reached idle in 3 minutes and 08 seconds with a max EGT of 474°C (885°F). Two steady state DMS readings were taken before the engine was stopcocked due to an indicated loss of argon header pressure. Start No. 2 was made after the argon fault was cleared. The engine reached idle in 150 seconds with a maximum EGT of 524°C (975°F). The engine was at idle for 17 minutes. Three DMS readings were taken, with the LPT ACC valve opened to 11° for the latter two readings. No abnormalities were noted and all vibration levels were low.

Post-test engine inspections revealed that the kiss-me seal on the LPT ACC valve had shifted partially off the pylon fan duct allowing fan air to leak to ambient. This was repaired by fabricating an orifice plate which was inserted between the kiss-me seal and the fan duct. The magnetic plugs were pulled and found to be full of what appeared to be metal machining chips. Chips were sent to the lab for evaluation. No fluid leakages were observed. Several instrumentation faults were identified and corrected, and the engine was prepared for the mechanical checkout run.

RUN NO. 2

| DMS | Start No. | Time to Light | Time to Idle | Core Speed | PLN25R | LPT ACC |
|---|---|---|---|---|---|---|
| 3 | --- | --- | --- | 0 | 0 | Off |
| 7004 | 1 | No Light | --- | --- | --- | Off |
| 7005 | 1 | Partial | --- | --- | --- | Off |
| 7006 | 1 | 41 sec. | 3 min. 8 secs. | --- | --- | Off |
| 4 | --- | --- | --- | 8410 | 62.0 | Off |
| 5 | --- | --- | --- | 8400 | 62.0 | Off |
| 7007 | 2 | 16 sec. | 2 min. 30 secs. | --- | --- | Off |
| 6 | --- | --- | --- | 8519 | 68.0 | Off |
| 7 | --- | --- | --- | 8500 | 68.0 | 11° |
| 8 | --- | --- | --- | 8479 | 68.0 | 11° |

$E^3$ ICLS Test No. 3 - Mechanical Checkout

Run No. 3

Date: April 29, 1983

DMS Readings: Steady State 9-21; Transient 7009-7015

Run Time: 2 Hours and 20 Minutes

Test Conditions:

Weather: Cloudy, 16°C (60°F), Wind 3 km/hr (2 mi/hr) @ - 79° Inlet
Inlet: Bellmouth
Nozzle: Performance
Instrumentation: - Mechanical Checkout Configuration
- 4 Clearanceometers - HPCR
- 6 Laser Probes - HPTR

Starts were made with manual fuel control. Engine lightoff speed was approximately 30% core speed. After three unsuccessful start attempts (no light), a successful start was made on the fourth attempt after increasing

starting fuel flow from 181 kg/hr (400 lbm/hr) to 195 kg/hr (430 lbm/hr). The engine reached idle in 3 minutes 28 seconds with a maximum start EGT of 465°C (869°F). Two steady state DMS readings were taken before a red fault on the No. 5 bearing vertical vib forced a stopcock of the engine. The vibration problem was traced to a faulty signal due to a bad charge amplifier. In order to resume testing, the vertical vibration signal was replaced on the console by the No. 5 bearing horizontal vibration signal. Mechanical checkout then resumed with start No. 4. Steady state DMS readings were taken at 68% and 76.5% corrected core speed with the engine on single annular (S/A) burning. The engine was then successfully transitioned to double annular (D/A) burning and steady state DMS readings were taken. An idle leak check was made; no leaks were found. The engine was accelerated to 40% PCN12R and DMS readings were taken. The engine was then returned to 76.5% corrected core speed and an attempt was made to switch to hydromechanical backup control. Upon switching, engine speed began to drop off and the engine was switched back to FADEC control and stabilized. The engine was accelerated to 50% PCN12R and steady state DMS readings taken. An attempt was then made to accelerate 60% PCN12R. During acceleration a red fault showing a fan overspeed forced an engine stopcock. Engine was air motored till cool and then shut down.

The fan overspeed problem was traced to a faulty signal to the console and was repaired. Magnetic plugs were pulled and found to once again be full of chips. It was believed that problem was due to residue in forward sump from fan frame machining. The forward sump was completely flushed and no more chips were found. Because of indications of an HPTR blade rub at 6 o'clock, it was decided to blank-off cooling manifolds on lower half of case. The aft core cowl was removed, the HPT and LPT borescoped, manifolds on lower half of engine blanked off (135° and 225°), additional insulation was packed around lower half of HPT, and CDN cases and cowling were replaced. Also, Stages 9 and 10 of the compressor were borescoped. No problems were discovered in any of the borescoping. However, it was discovered that the LPT ACC actuator motor was deflecting on the pylon cover plate and not allowing the valve to open. The pylon rib was reworked to correct this problem. Instrumentation faults, including recalibration of the Stage 4 compressor vane angle pot, were corrected and the engine was prepared for continuation of mechanical checkout.

RUN NO. 3

| DMS | Start No. | PCN25R | PCN12R | Combustor Mode | LPT ACC | Remarks |
|---|---|---|---|---|---|---|
| 0 | --- | 0 | 0 | S/A | --- | Zero Reading |
| 7009 | 3 | --- | --- | S/A | 11° | No Light |
| 7010 | 3 | --- | --- | S/A | 11° | No Light |
| 7011 | 3 | --- | --- | S/A | 11° | Partial Light |
| 7012 | 3 | 0-620 | --- | S/A | 11° | Fuel Flow 195 kg/hr (430 lbm/hr) |
| 10 | --- | 68.5 | --- | | | |
| 11 | --- | 68.5 | | | | Stopcock No. 5 bearing fault |
| 7013 | 4 | 0-68.5 | --- | S/A | 11° | |
| 12 | --- | 68.5 | --- | S/A | 11° | |
| 13 | --- | 68.5 | --- | S/A | 11° | |
| 14 | --- | 76.5 | 33.5 | S/A | 11° | |
| 15 | --- | 76.5 | 33.5 | S/A | 11° | |
| 7014 | --- | 76.5 | 33.5 | D/A | 11° | |
| 16 | --- | 76.5 | 33.5 | D/A | 11° | |
| 17 | --- | 76.5 | 33.5 | D/A | 11° | |
| 18 | --- | ---- | 40 | D/A | 11° | |
| 19 | --- | ---- | 40 | D/A | 11° | |
| 7015 | --- | ---- | 33.5 | D/A | 11° | Switch to H/M backup |
| 20 | --- | ---- | 50 | D/A | 11° | |
| 21 | --- | ---- | 50 | D/A | 11° | Stopcock fan overspeed |

$E^3$ ICLS Test No. 3 - Mechanical Checkout

Run No. 4

Date: May 6, 1983

DMS Readings: Steady State 22-52; Transient 7016

Run Time: 4 hours, 21 minutes

Total Engine Run Time: 7 hours 10 minutes

Test Conditions:

Weather: Clear, 23°C (74°F), Wind, 11 km/hr (7 mi/hr) @ 0° inlet
Inlet: Bellmouth
Nozzle: Performance
Instrumentation: - Mechanical Checkout Configuration
- 4 Clearanceometers - HPCR
- 6 Laser Probes - HPTR

Start No. 5 was a pretest run to idle to verify that the fan speed fault and LPT ACC actuation problems had been corrected. Start No. 6 resulted in a shutdown after reaching idle due to the console computer not being able to read console parameters. After the console computer problem was corrected, Start No. 7 was made and the engine successfully transitioned to double annular burning. All three starts were made with manual fuel control and a starting fuel flow of 195 kg/hr (430 lbm/hr). After transition to D/A, shop air was introduced to the upper manifolds of the HPT ACC in an attempt to round up the case and avoid rubs at 6 o'clock. Several settings were made and DMS readings taken with the maximum setting being 7 kPa (1 lbf/in.$^2$) across the manifolds. The engine was then accelerated and DMS readings taken at 40%, 50%, and 60% corrected fan speed. The HPT ACC manifold delta remained at 7 kPa (1 lbf/in$^2$) and the LPT ACC valve was set at varying positions from 11° to 21° depending on speed. After reaching 60% PCN12R a yellow fault appeared on the No. 4 bearing temperature. The engine was returned to flight idle when the bearing temperature continued to rise. The engine was stopcocked to investigate the problem. The problem was found to be a bad slipring reference temperature. A switch to the backup reference temperature was made and engine was again prepared for further mechanical checkout.

RUN NO. 4

| DMS | PCN25R | PCN12R | Combustor Mode | HPT ACC kPa (lbf/in.$^2$) | LPT ACC | Remarks |
|---|---|---|---|---|---|---|
| 22 | 0 | 0 | S/A | Off (Off) | Off | Zero reading |
| 23 | --- | --- | S/A | Off (Off) | Off | Air motor |

| | | | | | | |
|---|---|---|---|---|---|---|
| 24 | 68.5 | --- | S/A | Off (Off) | Off | Start No. 5 |
| 25 | 68.5 | --- | S/A | Off (Off) | Off | |
| 26 | 0 | 0 | S/A | Off (Off) | Off | |
| 27 | 0 | 0 | S/A | Off (Off) | 11° | Zero reading |
| 28 | 68.5 | --- | S/A | Off (Off) | 11° | Start No. 6 |
| 29 | 68.5 | --- | S/A | Off (Off) | 11° | |
| 30 | 68.5 | --- | S/A | Off (Off) | 11° | |
| 31 | 68.5 | --- | S/A | Off (Off) | 11° | Shutdown console computer |
| 32 | 0 | 0 | S/A | Off (Off) | Off | Zero reading |
| 33 | 68.5 | --- | S/A | Off (Off) | 11° | Start No. 7 |
| 34 | 68.5 | --- | S/A | Off (Off) | 11° | |
| 35 | 68.5 | --- | S/A | Off (Off) | 11° | |
| 36 | 76.5 | 33.5 | S/A | Off (Off) | 11° | |
| 7016 | 76.5 | 33.5 | D/A | Off (Off) | 11° | Transition to D/A |
| 37 | 76.5 | 33.5 | D/A | Off (Off) | 11° | |
| 38 | 76.5 | 33.5 | D/A | Off (Off) | 11° | |
| 39 | 76.5 | 33.5 | D/A | Off (Off) | 11° | |
| 40 | 76.5 | 33.5 | D/A | 2. (0.3) | 11° | |
| 41 | 76.5 | 33.5 | D/A | 3. (0.5) | 11° | |
| 42 | 76.5 | 33% | D/A | 6. (0.9) | 11° | |
| 43 | --- | 40% | D/A | 7. (1.0) | 11° | |
| 44 | --- | 50% | D/A | 7. (1.0) | 11° | |
| 45 | --- | 50% | D/A | 7. (1.0) | 21° | |
| 46 | --- | 50% | D/A | 7. (1.0) | 16° | |
| 47 | --- | 67% | D/A | 7. (1.0) | 16° | |
| 48 | --- | 60% | D/A | 7. (1.0) | 16° | |
| 49 | --- | 60% | D/A | 7. (1.0) | 16° | DMS calibrating reading no good |
| 50 | --- | 60% | D/A | 7. (1.0) | 16° | No. 4 bearing temperature fault |
| 51 | 0 | 0 | D/A | Off (Off) | Off | |
| 52 | 0 | 0 | D/A | Off (Off) | Off | |

$E^3$ ICLS Test No. 3 - Mechanical Checkout

Run No. 5

Date: May 9, 1983

DMS Readings: Steady State 53-77; Transient 7017, 7018

Run Time: 6 hours 05 minutes

Total Engine Run Time: 13 hours 15 minutes

Test Conditions:

Weather: Clear, 13°C (56°F), Wind 16 km/hr (10 mi/hr) @ 160° Inlet
Inlet: Bellmouth
Nozzle: Performance
Instrumentation: - Mechanical Checkout Configuration
- 4 Clearanceometers - HPTR
- 6 Laser Probes - HPTR

Start No. 8 was manual start with fuel flow of 195 kg/hr (430 lbm/hr). DMS readings were taken and a leak check made at idle and the engine was transitioned to D/A. The LPT ACC valve was set at 16° for the entire test. Experimentation continued with shop air supplied to the HPT ACC. It was set at 14., 34., and 69. kPa (2.0, 5.0, and 10.0 $lbf/in^2$). The engine was successfully accelerated to 60%, 70%, 80%, and 85% corrected fan speed and DMS readings were taken at these points. The top speed reached for DMS readings 72 and 73 was 88.5% PCN12R. EGT at this point was 911°C (1670°F) and thrust approximately 166 Kn (37,300 lbf). This test successfully achieved all data points for completion of mechanical checkout. Unfortunately, a blown transducer on a pressure scanner valve caused a loss of some fan rake performance data required for sizing of the survey nozzle. At the completion of mechanical checkout, Start No. 9, the first automatic start, was attempted. The engine took 53 seconds to light and 1 minute 53 seconds to reach idle. The engine was then shut down and work to repair the scanner valve began in preparation for a final mechanical checkout (fan mapping) run to obtain the missing fan performance data.

## RUN NO. 5

| DMS | PCN25R | PCN12R | Combustor Mode | HPT ACC kPa (lbf/in.$^2$) | LPT ACC | Remarks |
|---|---|---|---|---|---|---|
| 53 | 0 | 0 | S/A | Off | 16° | Zero reading |
| 54 | 68.5 | --- | S/A | Off | 16° | Start No. 8 |
| 55 | 68.5 | --- | S/A | Off | 16° | |
| 56 | 76.5 | 33.5 | S/A | Off | 16° | |
| 7017 | 76.5 | 33.5 | D/A | Off | 16° | |
| 57 | 76.5 | 33.5 | D/A | 7. ( 1.0) | 16° | |
| 58 | 76.5 | 33.5 | D/A | 14. ( 2.0) | 16° | |
| 59 | --- | 60.0 | D/A | 14. ( 2.0) | 16° | |
| 60 | --- | 70.0 | D/A | 17. ( 2.4) | 16° | |
| 61 | --- | 70.0 | D/A | 17. ( 2.4) | 16° | |
| 62 | --- | 70.0 | D/A | 34. ( 5.0) | 16° | |
| 63 | --- | 70.0 | D/A | 34. ( 5.0) | 16° | Trimmed stator schedule |
| 64 | --- | 80.0 | D/A | 34. ( 5.0) | 16° | Open 1° |
| 65 | --- | 80.0 | D/A | 34. ( 5.0) | 16° | |
| 66 | --- | 80.0 | D/A | 69. (10.0) | 16° | |
| 67 | --- | 80.0 | D/A | 69. (10.0) | 16° | Closed stators 1° |
| 68 | --- | 60.0 | D/A | 38. ( 5.5) | 16° | |
| 69 | --- | 85.8 | D/A | 70. (10.1) | 16° | Maximum EGT |
| 70 | --- | 85.4 | D/A | 70. (10.1) | 16° | |
| 71 | --- | 88.0 | D/A | 70. (10.1) | 16° | DMS reading no good |
| 72 | --- | 88.5 | D/A | 16. ( 9.8) | 16° | Max power reached on test |
| 73 | --- | 88.5 | D/A | 70. (10.1) | 16° | |
| 74 | 76.5 | 33.5 | D/A | 72. (10.4) | 16° | |
| 75 | 68.5 | --- | --- | Off (Off) | 16° | |
| 76 | 60.0 | --- | D/A | Off (Off) | 16° | |
| 77 | 50.0 | --- | D/A | Off (Off) | 16° | |
| 7018 | 0 | 0 | D/A | Off (Off) | 16° | Start No. 9 |

$E^3$ ICLS Test No. 3 - Mechanical Checkout

Run No. 6

Date: May 10, 1983

DMS Readings: Steady State: 78-106; Transient 7019

Run Time: 6 hours 12 minutes

Total Engine Run Time: 19 hours 27 minutes

Test Conditions:

Weather: Clear, 17°C (62°F), Wind 8 km/hr (5 mi/hr) @ 170° inlet
Inlet: Bellmouth
Nozzle: Performance
Instrumentation: - Mechanical Checkout Configuration
- 4 Clearanceometers - HPCR
- 6 Laser Probes - HPTR

Start No. 10 was an automatic start with an acceleration schedule of nominal plus Phi. After idle leak check, the engine was transitioned to D/A and DMS readings were taken at 60%, 70%, 80%, 82.5%, and 85% corrected fan speed to obtain the fan performance points lost when a scanner valve failed in the previous mechanical checkout run. The HPC ACC was exercised from closed to full open at each point. The HPT ACC was set at 70 kPa (10 lbf/in.$^2$) for all points and the LPT ACC was set by a predetermined schedule depending on speed point. This run completed mechanical checkout and work was begun to convert to performance instrumentation. Magnetic plugs were inspected with nothing more found. It was discovered that LPT borescope plugs were incorrectly reinstalled after last borescope operation. One broken plug was replaced and the remainder were installed in correct positions. Cracks were also discovered in acoustic panels forward of the Stage 1 fan blades. The cracked panels were removed for repair and replaced with hardwall panels for the next test. The lube level indicator was changed and a new calibration made for the next test.

## RUN NO. 6

| DMS | PCN25R | PCN12R | Compressor Mode | HPC ACC | HPT ACC kPa (lbf/in.$^2$) | LPT ACC | Remarks |
|---|---|---|---|---|---|---|---|
| 78 | 0 | 0 | S/A | Off | Off (Off) | 16° | Zero reading |
| 7019 | 0-68.5 | --- | S/A | Off | Off (Off) | 16° | Start No. 10 |
| 79 | 76.9 | 33.5 | S/A | Off | Off (Off) | 16° | |
| 80 | 76.5 | 33.5 | D/A | Off | Off (Off) | 16° | |
| 81 | 76.5 | 33.5 | D/A | Off | Off (Off) | 16° | |
| 82 | --- | 60.0 | D/A | Off | 70. (10.1) | 16° | |
| 83 | --- | 70.0 | D/A | Off | 70. (10.1) | 16° | |
| 84 | --- | 70.0 | D/A | Off | 70. (10.1) | 16° | |
| 85 | --- | 70.0 | D/A | 50% Open | 70. (10.1) | 16° | |
| 86 | --- | 70.0 | D/A | 100% Open | 70. (10.1) | 16° | |
| 87 | --- | 70.0 | D/A | 100% Open | 70. (10.1) | 21° | |
| 88 | --- | 70.0 | D/A | 100% Open | 70. (10.1) | 31° | |
| 89 | --- | 70.0 | D/A | 100% Open | 70. (10.1) | 41° | |
| 90 | --- | 70.0 | D/A | Off | 70. (10.1) | 41° | |
| 91 | --- | 70.0 | D/A | Off | 70. (10.1) | 16° | |
| 92 | --- | 70.0 | D/A | Off | 70. (10.1) | 16° | |
| 93 | --- | 70.0 | D/A | 50% Open | 70. (10.1) | 16° | |
| 94 | --- | 70.0 | D/A | 100% Open | 70. (10.1) | 16° | |
| 95 | --- | 70.0 | D/A | 100% Open | 70. (10.1) | 21° | |
| 96 | --- | 80.0 | D/A | 100% Open | 70. (10.1) | 28° | |
| 97 | --- | 80.0 | D/A | Off | 70. (10.1) | 16° | |
| 98 | --- | 82.4 | D/A | Off | 70. (10.1) | 16° | |
| 99 | --- | 85.7 | D/A | Off | 70. (10.1) | 16° | |
| 100 | --- | 85.7 | D/A | 100% Open | 70. (10.1) | 16° | |
| 101 | --- | 85.7 | D/A | 100% Open | 70. (10.1) | 20° | |
| 102 | --- | 85.7 | D/A | Off | 70. (10.1) | 16° | |
| 103 | --- | 82.5 | D/A | Off | 70. (10.1) | 16° | |
| 104 | --- | 50.0 | D/A | Off | 70. (10.1) | 16° | |
| 105 | --- | 50.0 | D/A | 100% Open | 70. (10.1) | 16° | |
| 106 | --- | 50.0 | D/A | Off | 7. ( 1.0) | 16° | HPT ACC on fan air |
| 7020 | 0 | 0 | D/A | Off | Off (Off) | 16° | Shutdown |

$E^3$ ICLS Test No. 4 - Engine Performance

Run No. 7

Date: May 17, 1983

DMS Readings: Steady State: 107-138; Transient 7021, 7022

Run Time: 6 hours 51 minutes

Total Engine Run Time: 26 hours 18 minutes

Test Conditions:

Weather: Clear, 19°C (66°F), Wind 11 km/hr (7 mi/hr) @ 65° inlet
Inlet: Bellmouth
Nozzle: Performance
Instrumentation: Performance Configuration

Start No. 11 was an automatic start with a fuel schedule of nominal plus 1 Phi DMS readings were taken at 4% Gidle and 6% Gidle. The engine was then transitioned to D/A. While waiting for winds to calm for performance testing, readings were then taken at 40%, 50%, 60%, and 70% PCN12R with fan air supplying the HPT ACC cooling manifolds. HPT ACC was then returned to the shop air supply system. Next, a demonstration was made of the Auto ACC control of the FADEC. A switch was made to automatic on the HPC and LPT ACC. Target casing temperature was maintained by the FADEC on the HPC. About a ±3°C (±5°F) oscillation occurred on the LPT. The reference temperature was changed on both cases and the FADEC responded, though with still a slight oscillation in the LPT. Performance testing was then begun with DMS readings taken at 50%, 60%, 70%, 80%, 85%, and 87.17% PCN12R. At the end of performance testing, the Auto ACC was demonstrated once again. At the start, the compressor case was at 432°C (810°F) and the FADEC adjusted the case temperature to the target temperature of 398°C (748°F). LPT case temperature at start was at 454°C (850°F). The FADEC adjusted case temperature to near the target temperature of 431°C (807°F) but the temperature was not steady and wavered ±6°C (±10°F).

After the test, the LPT was borescoped revealing a slight rub on Stages 4 and 5. Also, bellmouth pots were found to be damaged. The inlet separated axially from engine at high speed more than anticipated and caused the pots to slip off their target plates. Survey nozzle and exhaust plane rakes as well as

new bellmouth pots were installed and the engine was prepared for mixer performance test.

RUN NO. 7

| DMS | PCN35R | PCN12R | HPC ACC | HPT ACC kPa (lbf/in.$^2$) | LPT ACC | Remarks |
|---|---|---|---|---|---|---|
| 107 | 0 | 0 | Off | Off (Off) | 11° | Zero reading |
| 7021 | 62% | --- | Off | Off (Off) | 11° | Start No. 11 |
| 108 | 62% | --- | Off | Off (Off) | 11° | |
| 109 | 62% | --- | Off | Off (Off) | 11° | |
| 110 | 68.5% | --- | Off | Off (Off) | 11° | |
| 7022 | 76.5% | 33.5 | Off | Off (Off) | 11° | |
| 111 | 76.5% | 33.5 | Off | 70. (10.1) | 11° | |
| 112 | --- | 40% | Off | 5. ( 0.7) | 11° | HPT ACC valve 100% open |
| 113 | --- | 50% | Off | 8. ( 1.1) | 11° | |
| 114 | --- | 60% | Off | 11. ( 1.6) | 11° | |
| 115 | --- | 70% | Off | 16. ( 2.3) | 11° | Open HPT ACC shop air |
| 116 | --- | 50% | Off | 72. (10.4) | 11° | HPT ACC valve closed |
| 117 | --- | 60% | Off | 72. (10.4) | 11° | Auto ACC testing |
| 118 | --- | 70% | Off | 72. (10.4) | 11° | Performance testing |
| 119 | --- | 70% | 50% Open | 72. (10.4) | 11° | |
| 120 | --- | 70% | 100% Open | 72. (10.4) | 11° | |
| 121 | --- | 70% | Over stroke | 72. (10.4) | 11° | |
| 122 | --- | 70% | Over stroke | 72. (10.4) | 41° | |
| 123 | --- | 70% | Off | 72. (10.4) | 11° | |
| 124 | --- | 80% | Off | 72. (10.4) | 16° | |
| 125 | --- | 80% | Over stroke | 72. (10.4) | 16° | |
| 126 | --- | 80% | Over stroke | 72. (10.4) | 26° | |
| 127 | --- | 80% | Off | 72. (10.4) | 16° | |
| 128 | --- | 80% | Off | 72. (10.4) | 22° | |
| 129 | --- | 85% | Off | 72. (10.4) | 22° | |
| 130 | --- | 87.1% | Off | 72. (10.4) | 22° | |
| 131 | --- | 87.1% | Over stroke | 72. (10.4) | 22° | |
| 132 | --- | 85% | Over stroke | 72. (10.4) | 22° | |
| 133 | --- | 82.5% | Over stroke | 70. (10.2) | 22° | |
| 134 | --- | 80% | Over stroke | 70. (10.2) | 26° | |
| 135 | --- | 70% | Over stroke | 70. (10.2) | 41° | Auto ACC testing |
| 136 | --- | 40% | Closed | 70. (10.2) | 41° | |
| 137 | --- | 40% | Over stroke | 70. (10.2) | 41° | |
| 138 | 0 | 0 | Closed | Off (Off) | 41° | |

$E^3$ ICLS Test No. 5 - Mixer Performance and Second Operating Line

Run No. 8

Date: May 24, 1983

DMS Readings: Steady State: 140-149; Transient 7023

Run Time: 2 hours 14 minutes

Total Engine Run Time: 28 hours 32 minutes

Test Conditions:

Weather: Clear, 21°C (70°F), Wind 6 km/hr (4 mi/hr) @ 0° inlet
Nozzle: Survey
Instrumentation: Mixer Performance Configuration

Start No. 12 was an automatic start with fuel schedule of nominal plus 1 Phi. The engine was transitioned to D/A and accelerated to 75% PCN12R for fast mixer performance speed point. After setting 5 angular points of the exhaust rake, it was realized that one set of pressures was not hooked up correctly. In addition, an "argon on" indication was seen on the laser probe cart. The engine was shut down to correct the pressure hookup and repair a blown gasket found on the laser cart.

RUN NO. 8

| DMS | PCN25R | PCN12R | HPC ACC | HPT ACC kPa (lbf/in.$^2$) | LPT ACC | Remarks |
|---|---|---|---|---|---|---|
| 140 | 0 | 0 | Off | --- | 11° | Zero reading |
| 7023 | 0-62.0 | --- | Off | Off (Off) | 11° | Start No. 12 |
| 141 | 62.0 | --- | Off | Off (Off) | 11° | |
| 142 | 76.5 | 33.5 | Off | Off (Off) | 11° | |
| 143 | 76.5% | 33.5 | Off | 70. (10.1) | 11° | Double Annular |
| 144 | --- | 75.0 | Over stroke | 70. (10.1) | 11° | |

| | | | | | | |
|---|---|---|---|---|---|---|
| 145 | --- | 75.0 | Over stroke | 70. (10.1) | 11° | |
| 146 | --- | 75.0 | Over stroke | 72. (10.4) | 26° | |
| 147 | --- | 75.0 | Over stroke | 72. (10.4) | 26° | |
| 148 | --- | 75.0 | Over stroke | 72. (10.4) | 26° | |
| 149 | --- | 75.0 | Over stroke | 72. (10.4) | 26° | Decel to Fidle and shutdown |

$E^3$ ICLS Test No. 5 - Mixer Performance and Second Operating Line

Run No. 9

Date: May 25, 1983

DMS Readings: Steady State: 150-159; Transient 7024

Run Time: 2 hours 05 minutes

Total Engine Run Time: 30 hours 37 minutes

Test Conditions:

Weather: Overcast 16°C (60°F), Wind 6 km/hr (4 mi/hr) @ 73° inlet
Inlet: Bellmouth
Nozzle: Survey
Instrumentation: Mixer Performance Configuration

Start No. 13 was an automatic start with a fuel schedule of nominal plus 1 Phi. The engine was transitioned to D/A and accelerated to 65% PCN12R for the first mixer performance speed point. Readings were successfully taken at 0°, 3°, 6°, 9°, 12°, and 15° when the "argon on" indicator again faulted on the laser probe cart. The engine was shut down in order to troubleshoot the cart. The problem was traced to a bad transducer in the argon backup system. The transducer was replaced and the engine was set up again to run the main performance test.

## RUN NO. 9

| DMS | PCN25R | PCN12R | HPC ACC | HPT ACC kPa (lbf/in.$^2$) | LPT ACC | Exhaust Rake | Remarks |
|---|---|---|---|---|---|---|---|
| 150 | 0 | --- | Off | Off (Off) | 11° | --- | Zero reading |
| 7024 | 0-62.0 | --- | Off | Off (Off) | 11° | --- | Start No. 13 |
| 151 | 62.0 | --- | Off | Off (Off) | 11° | --- | |
| 152 | 76.5 | 33.5 | Off | Off (Off) | 11° | --- | |
| 153 | 76.5 | 33.5 | Off | 72. (10.4) | 11° | --- | D/A |
| 154 | --- | 65.0 | Over stroke | 72. (10.4) | 26° | 0° | |
| 155 | --- | 65.0 | Over stroke | 71. (10.3) | 26° | 3° | |
| 156 | --- | 65.0 | Over stroke | 71. (10.3) | 26° | 6° | |
| 157 | --- | 65.0 | Over stroke | 71. (10.3) | 26° | 9° | |
| 158 | --- | 65.0 | Over stroke | 71. (10.3) | 26° | 12° | |
| 159 | --- | 65.0 | Over stroke | 71. (10.3) | 26° | 15° | Argon fault Engine shut-down |

$E^3$ ICLS Test No. 5 - Mixer Performance and Second Operating Line

Run No. 10

Date: May 26, 1983

DMS Readings: Steady State: 160-208; Transient 7025-7031

Run Time: 7 hours 14 minutes

Total Engine Run Time: 37 hours 51 minutes

Test Conditions:

Weather: Partly cloudy, 11°C (51°F), Wind 13 km/hr (8 mi/hr) @ 125° inlet
Inlet: Bellmouth
Nozzle: Survey
Instrumentation: Mixer Performance Configuration

Start No. 14 was an automatic start with a fuel schedule of nominal plus a 2 Phi. The engine was transitioned to D/A and accelerated to 65% PCN12R. The exhaust plane rake was rotated from 15° to 30° with DMS readings in 3° increments. The engine was acceled to 75% and 85% PCN12R and 11 DMS readings were taken at each point as the exhaust plane rake was rotated from 0° to 30°. This successfully completed the mixer testing and the engine was shut down. A hot restart, No. 15, was then performed with a fuel schedule of nominal plus 12%. The exhaust plane rake was then removed and the bellmouth adjusted in preparation for a second performance line run. A bellmouth setting of 1.0 cm (0.40 in.) up and 0.38 cm (0.15 in.) left was based on bellmouth pot measurements made at full speed. Start No. 16 was an automatic start with a fuel schedule of nominal plus 12%. The engine was transitioned to D/A and performance DMS readings were taken at 40%, 50%, 60%, 70%, 80%, 82.5%, 85%, and 87.5% PCN12R. After completion of performance testing, a demonstration was made of the FADEC's ability to limit fan speed based on a preset limit for T42. The same test was then successfully performed with a limit on PS3 and T41C. The final test on this run was the switch to hydromechanical control. On the first attempt, the control did not hold speed. Control was returned to FADEC. On a second attempt, made at higher speed, the hydromechanical control held speed acceptably stable, although not completely. The engine was returned to FADEC control, deceled to FIDLE and shutdown.

After completion of test five, the plane 42 rakes and all laser probes were removed and the engine was prepared for a performance run without the plane 42 rakes to determine their effect.

RUN NO. 10

| DMS | PCN25R | PCN12R | HPC ACC | HPT ACC kPa (lbf/in.$^2$) | LPT ACC | Exhaust Rake | Remarks |
|---|---|---|---|---|---|---|---|
| 160 | 0 | 0 | Off | Off (Off) | 11° | --- | Zero reading |
| 161 | 62.0 | --- | Off | Off (Off) | 11° | --- | |
| 162 | 76.5 | 33.5 | Off | 69. (10.0) | 11° | --- | D/A |
| 163 | --- | 65.0 | Over stroke | 69. (10.0) | 26° | 15° | HPT ACC shop air |

| | | | | | | | |
|---|---|---|---|---|---|---|---|
| 164 | --- | 65.0 | Over stroke | 69. (10.0) | 26° | 18° | |
| 165 | --- | 65.0 | Over stroke | 69. (10.0) | 26° | 21° | |
| 166 | --- | 65.0 | Over stroke | 69. (10.0) | 26° | 24° | |
| 167 | --- | 65.0 | Over stroke | 69. (10.0) | 26° | 27° | |
| 168 | --- | 65.0 | Over stroke | 69. (10.0) | 26° | 30° | |
| 169 | --- | 85.0 | Over stroke | 69. (10.0) | 22° | 30° | |
| 170 | --- | 85.0 | Over stroke | 69. (10.0) | 22° | 27° | |
| 171 | --- | 85.0 | Over stroke | 69. (10.0) | 22° | 24° | |
| 172 | --- | 85.0 | Over stroke | 69. (10.0) | 22° | 21° | |
| 173 | --- | 85.0 | Over stroke | 69. (10.0) | 22° | 18° | |
| 174 | --- | 85.0 | Over stroke | 69. (10.0) | 22° | 15° | |
| 175 | --- | 85.0 | Over stroke | 69. (10.0) | 22° | 12° | |
| 176 | --- | 85.0 | Over stroke | 69. (10.0) | 22° | 9° | |
| 177 | --- | 85.0 | Over stroke | 69. (10.0) | 22° | 6° | |
| 178 | --- | 85.0 | Over stroke | 69. (10.0) | 22° | 3° | |
| 179 | --- | 85.0 | Over stroke | 69. (10.0) | 22° | 0° | |
| 180 | --- | 76.5 | Over stroke | 69. (10.0) | 26° | 0° | |
| 181 | --- | 76.5 | Over stroke | 69. (10.0) | 26° | 3° | |
| 182 | --- | 76.5 | Over stroke | 69. (10.0) | 26° | 6° | |
| 183 | --- | 76.5 | Over stroke | 69. (10.0) | 26° | 9° | |
| 184 | --- | 76.5 | Over stroke | 69. (10.0) | 26° | 12° | |
| 185 | --- | 76.5 | Over stroke | 69. (10.0) | 26° | 15° | |
| 186 | --- | 76.5 | Over stroke | 69. (10.0) | 26° | 18° | |
| 187 | --- | 76.5 | Over stroke | 74. (10.7) | 26° | 21° | |
| 188 | --- | 76.5 | Over stroke | 74. (10.7) | 26° | 24° | |
| 189 | --- | 76.5 | Over stroke | 74. (10.7) | 26° | 27° | |
| 190 | --- | 76.5 | Over stroke | 74. (10.7) | 26° | 30° | |
| | | Shut ACC valves, return to FIDLE and shutdown | | | | | |
| 7025 | 0-62.0 | --- | | hot restart, transient DMS on | | | |
| 7026 | 62.0-0 | --- | | start and on coastdown | | | |
| 191 | 0 | 0 | Off | Off (Off) | 11° | --- | Zero reading |
| 7027 | 0-62.0 | --- | Off | Off (Off) | 11° | --- | Start No. 16 |
| 192 | 62.0 | --- | Off | Off (Off) | 11° | --- | |
| 193 | 76.5 | 33.5 | Off | 69. (10.0) | 11° | --- | D/A |
| 194 | --- | 40.0 | Off | 69. (10.0) | 11° | --- | |
| 195 | --- | 50.0 | Off | 69. (10.0) | 11° | --- | |
| 196 | --- | 60.0 | Off | 69. (10.0) | 11° | --- | |
| 197 | --- | 70.0 | Over stroke | 69. (10.0) | 41° | --- | |
| 198 | --- | 80.0 | Over stroke | 69. (10.0) | 26° | --- | |
| 199 | --- | 80.0 | Over stroke | 69. (10.0) | 26° | --- | |
| 200 | --- | 82.5 | Over stroke | 69. (10.0) | 22° | --- | |
| 201 | --- | 85.0 | Over stroke | 69. (10.0) | 22° | --- | |
| 202 | --- | 87.3 | Over stroke | 69. (10.0) | 22° | --- | |
| 203 | --- | 85.0 | Over stroke | 69. (10.0) | 22° | --- | |
| 204 | --- | 82.5 | Over stroke | 69. (10.0) | 22° | --- | |
| 205 | --- | --- | Over stroke | 69. (10.0) | 22° | --- | DMS 205 no good |
| 206 | --- | 80.0 | Over stroke | 69. (10.0) | 22° | --- | |
| 207 | --- | 70.0 | Over stroke | 69. (10.0) | 41° | --- | |
| 7028 | --- | 70.0-80.0 | Off | 69. (10.0) | 22° | --- | Set T42 limit on FADEC |

| | | | | | | | |
|---|---|---|---|---|---|---|---|
| 7029 | --- | 70.0-80.0 | Off | 69. (10.0) | 22° | --- | Dry PS3 limit on FADEC |
| 7030 | --- | 70.0-80.0 | Off | 69. (10.0) | 22° | --- | Set T41C limit on FADEC |
| 7031 | --- | 50.0 | Off | 69. (10.0) | 22° | --- | Switch to H/M back-up |
| 208 | 76.5 | 33.5 | Off | 69. (10.0) | 11° | --- | |

$E^3$ ICLS Test No. 6 - Plane 42 Rake Performance Effect Test
- FICA Single Substitution Test

Run No. 11

Date: June 1, 1983

DMS Readings: Steady State: 210-229; Transient 7032-7040

Run Time: 4 hours 49 minutes

Total Engine Run Time: 42 hours 40 minutes

Test Conditions:

Weather: Overcast, 17°C (63°F), Wind 6 km/hr (4 mi/hr) @ 45° inlet
Inlet: Bellmouth
Nozzle: Survey
Instrumentation: - Mixer Performance Configuration with
- 6 Laser Probes
- 5 Plane
- 42 Rakes Removed

Start No. 17 was an automatic start with a fuel schedule of nominal +10% +2 Phi. The engine was transitioned to D/A and DMS readings were taken at 40%, 50%, 60%, 70%, 80%, 82.5%, 85%, and 87.2% PCN12R. After completion of

performance testing, a demonstration was made of the FADEC Failure Indication Correction Action (FICA) system. The T3 sensor, T42 sensor, T25 sensor and fan speed sensor signals were individually failed and moderate accelerations and decelerations performed with transient DMS. FADEC substitutions were successful., An attempt was then made to fail the core speed sensor. A substitution was not made and engine began to lose speed rapidly. An unsuccessful attempt was made to fix the core speed signal and the engine was then stopcocked. Preparations were then begun for acoustic testing. All fan stream rakes were removed and acoustic instrumentation hooked up. The aero-acoustic inlet was installed in place of the bellmouth.

RUN NO. 11

| DMS | PCN25R | PCN12R | HPC ACC | HPT ACC kPa (lbf/in.$^2$) | LPT ACC | Remarks |
|---|---|---|---|---|---|---|
| 210 | 0 | 0 | Off | Off (Off) | 11° | Zero reading |
| 7032 | 0-62% | --- | Off | Off (Off) | 11° | Start No. 17 |
| 211 | 62.0% | --- | Off | Off (Off) | 11° | |
| 212 | 76.5 | 33.5 | Off | 70. (10.1) | 11° | D/A |
| 213 | --- | 40.0 | Off | 70. (10.1) | 11° | |
| 214 | --- | 50.0 | Off | 70. (10.1) | 11° | |
| 215 | --- | 60.0 | Off | 70. (10.1) | 11° | |
| 216 | --- | 70.0 | Over stroke | 70. (10.1) | 41° | |
| 217 | --- | 80.0 | Over stroke | 70. (10.1) | 26° | |
| 218 | --- | 82.5 | Over stroke | 70. (10.1) | 22° | |
| 219 | --- | 85.0 | Over stroke | 70. (10.1) | 22° | |
| 220 | --- | 87.3 | Over stroke | 70. (10.1) | 22° | |
| 221 | --- | 85.0 | Over stroke | 70. (10.1) | 22° | |
| 222 | --- | 82.5 | Over stroke | 70. (10.1) | 22° | |
| 223 | --- | 80.0 | Over stroke | 70. (10.1) | 26° | |
| 224 | --- | 70.0 | Over stroke | 70 (10.1) | 41° | |
| 225 | --- | 82.5 | Over stroke | 70. (10.1) | 27° | |
| 226 | --- | 82.5 | Over stroke | 70. (10.1) | 27° | |
| 227 | --- | 40.0 | Off | 70. (10.1) | 22° | Armed FICA |
| 228 | --- | 40.0 | Off | 70. (10.1) | 22° | Failed T3 sensor |
| 229 | --- | 87.0 | Off | 70. (10.1) | 22° | |
| 7033 | --- | 40.0-85.0 | Off | 70. (10.1) | 22° | Accel with failed T3 sensor |
| 7034 | --- | 85.0-40.0 | Off | 70. (10.1) | 22° | Decel with failed T3 sensor |
| 7035 | --- | 40.0-85.0 | Off | 70. (10.1) | 22° | Accel with failed T42 sensor |
| 7036 | --- | 85.0-40.0 | Off | 70. (10.1) | 22° | Decel with failed T42 sensor |

| | | | | | | |
|---|---|---|---|---|---|---|
| 7037 | --- | 40.0-85.0 | Off | 70. (10.1) | 22° | Accel with failed T25 sensor |
| 7038 | --- | 85.0-40.0 | Off | 70. (10.1) | 22° | Decel with failed T25 sensor |
| 7039 | --- | 40.0-85.0 | Off | 70. (10.1) | 22° | Accel with failed fan speed sensor |
| 7040 | --- | 86.0-40.0 | Off | 70. (10.1) | 22° | Decel with failed fan speed sensor; Engine stopcock-core speed substitution not made |

$E^3$ ICLS Test No. 7 - Acoustic Test, Fully Suppressed
Test No. 8B - FICA Double Substitution

Run No. 12

Date: June 7, 1983

DMS Readings: Steady State: 231-260; Transient 7041-7043

Run Time: 5 hours 47 minutes

Total Engine Run Time: 48 hours 27 minutes

Test Conditions:

Weather: Clear, 20°C (68°F), Wind 5 km/hr (3 mi/hr) @ 40° inlet
Inlet: Aero-Acoustic
Nozzle: Survey
Instrumentation: - Acoustic Configuration
- Fully Suppressed Acoustics

Start No. 18 was an automatic start with a fuel schedule of nominal plus 10% plus 4 Phi. The engine was transitioned to D/A and accelerated to 40% PCN12R. The engine was put on fan speed control in preparation for FICA

Double Substitution Testing. The core speed sensor signal was failed. Core speed began varying up to ±1200 rpm. The engine was returned to core speed control and was accelerated to 50% PCN12R. Speed was a bit more stable at this point. An attempt was then made to accelerate to 60% PCN12R. At this point high vibrations indicated were in the No. 3 bearing, vertical, and an overspeed red fault was indicated on core speed. The FICA was deactivated and the engine returned to FIDLE. The engine flamed out and was stopcocked. The vibration problem was traced to a bad signal. The problem was repaired. A decision was made to delay further FICA testing. The engine was prepared for the fully suppressed acoustic test. Start No. 19 was an automatic start with a fuel schedule of nominal plus 5 Phi. The engine was transitioned to D/A and acoustic and DMS readings were taken. The engine was then prepared for the 1/2 inlet taped testing. A two minute acceleration from 48.7 PCN12R to maximum fan speed and a two minute deceleration were recorded. The engine was returned to FIDLE and then shut down.

RUN NO. 12

| DMS | PCN25R | PCN12R | HPC ACC | HPT ACC kPa (lbf/in.$^2$) | LPT ACC | Remarks |
|---|---|---|---|---|---|---|
| 231 | 0 | 0 | Off | Off (Off) | 11° | Zero reading |
| 7041 | 0-62.0 | --- | Off | Off (Off) | 11° | Start No. 18 |
| 232 | 62.0 | --- | Off | Off (Off) | 11° | |
| 233 | 76.5 | 33.5 | Off | 69. (10.) | 11° | D/A |
| 7042 | --- | 40.0 | Off | 69. (10.) | 11° | Fail core speed sensor |
| 234 | 0 | 0 | Off | 69. (10.) | 11° | Zero reading |
| 7043 | 62.0 | --- | Off | 69. (10.) | 11° | Start No. 19 |
| 235 | 62.0 | --- | Off | 69. (10.) | 11° | |
| 236 | 76.5 | 33.5 | Off | 69. (10.) | 11° | D/A |
| 237 | --- | 48.7 | Off | 69. (10.) | 11° | |
| 238 | --- | 54.3 | Off | 69. (10.) | 11° | |
| 239 | --- | 58.3 | Off | 69. (10.) | 11° | |
| 240 | --- | 62.1 | Off | 69. (10.) | 11° | |
| 241 | --- | 66.9 | Off | 69. (10.) | 11° | |
| 242 | --- | 75.0 | Off | 69. (10.) | 11° | |
| 243 | --- | 82.9 | Off | 69. (10.) | 11° | |
| 244 | --- | 86.0 | Off | 69. (10.) | 11° | Max EGT |
| 245 | --- | 82.9 | Off | 69. (10.) | 11° | |
| 246 | --- | 75.1 | Off | 69. (10.) | 11° | |
| 247 | --- | 66.9 | Off | 69. (10.) | 22° | |

| | | | | | |
|---|---|---|---|---|---|
| 248 | --- | 62.1 | Off | 69. (10.) | 22° |
| 249 | --- | 58.3 | Off | 69. (10.) | 22° |
| 250 | --- | 54.3 | Off | 69. (10.) | 22° |
| 251 | --- | 48.5 | Over stroke | 69. (10.) | 22° |
| 252 | --- | 54.3 | Over stroke | 69. (10.) | 22° |
| 253 | --- | 58.3 | Over stroke | 69. (10.) | 22° |
| 254 | --- | 62.1 | Over stroke | 69. (10.) | 22° |
| 255 | --- | 66.9 | Over stroke | 69. (10.) | 22° |
| 256 | --- | 75.0 | Over stroke | 69. (10.) | 22° |
| 257 | --- | 86.0 | Over stroke | 69. (10.) | 22° |
| 258 | --- | 86.0 | Over stroke | 69. (10.) | 22° |
| 259 | --- | 82.9 | Over stroke | 69. (10.) | 22° |
| 260 | --- | 48.7 | Off | 69. (10.) | 22° |

$E^3$ Test No. 9 - Acoustic Test - Short Inlet Simulation
Test No. 8a - Auto Clearance Control

Run No. 13

Date: June 8, 1983

DMS Readings: Steady State: 261-293; Transient 7044-7050

Run Time: 4 hours 13 minutes

Total Engine Run Time: 52 hours 40 minutes

Test Conditions:

Weather: Clear, 24°C (75°F), Wind 6 km/hr (4 mi/hr) @ 100° inlet
Inlet: Aero-Acoustic
Nozzle: Survey
Instrumentation: - Acoustic Configuration
- Short-Inlet Taping

At the beginning of this run, five starts were made in order to evaluate engine starting characteristics. A wet motor was performed before

the initial start in order to ensure that the fuel manifold was full. The five starts were as follows:

| Start No. | Fuel Schedule | Transient DMS | Max EGT °C | Max EGT (°F) |
|---|---|---|---|---|
| 20 | Nominal + 0 Phi + 17% | 7044 | 577 | (1070) |
| 21 | Nominal + 0 Phi + 17% | 7045 | 588 | (1091) |
| 22 | Nominal + 2 Phi + 20% | 7046 | 620 | (1148) |
| 23 | Nominal + 4 Phi + 20% | 7047 | 654 | (1210) |
| 24 | Nominal + 5 Phi + 20% | 7048 | 639 | (1182) |

Start No. 23 took approximately 47 seconds from air motor to idle. After Start No. 24, the engine was transitioned to D/A and each acoustic speed point was set three times with steady state DMS readings taken at each point. After completion of acoustic testing, a demonstration of the auto clearance control was made. FADEC successfully adjusted casing temperature during a deceleration from 80% to 60% PCN12R and an acceleration back to 80% PCN12R with the qualification that the LPT case temperature tended to oscillate ±6°C (10°F). The engine was then returned to FIDLE and shut down. The engine inlet was completely taped and preparations begun for the next run.

RUN NO. 13

| DMS | PCN25R | PCN12R | HPC ACC | HPT ACC kPa (lbf/in.$^2$) | LPT ACC | Remarks |
|---|---|---|---|---|---|---|
| 261 | 0 | 0 | Off | Off (Off) | 11° | Zero reading |
| 262 | 0 | 0 | Off | Off (Off) | 11° | Zero reading |
| 263 | 0 | 0 | Off | Off (Off) | 11° | Zero reading |
| 264 | 62.0 | --- | Off | Off (Off) | 11° | |
| 265 | 76.5 | 33.5 | Off | 69. (10.) | 11° | D/A |
| 266 | --- | 48.7 | Off | 69. (10.) | 22° | |
| 267 | --- | 54.3 | Off | 69. (10.) | 22° | |
| 268 | --- | 58.3 | Off | 69. (10.) | 22° | |
| 269 | --- | 62.1 | Off | 69. (10.) | 22° | |
| 270 | --- | 66.9 | Off | 69. (10.) | 22° | |
| 271 | --- | 75.0 | Off | 69. (10.) | 22° | |
| 272 | --- | 82.9 | Off | 69. (10.) | 22° | |
| 273 | --- | 85.7 | Off | 69. (10.) | 22° | |
| 274 | --- | 82.9 | Off | 69. (10.) | 22° | |
| 275 | --- | 75.0 | Off | 69. (10.) | 22° | |
| 276 | --- | 66.9 | Off | 69. (10.) | 22° | |
| 277 | --- | 62.1 | Off | 69. (10.) | 22° | |

| | | | | | | |
|---|---|---|---|---|---|---|
| 278 | --- | 58.3 | Off | 69. (10.) | 22° | |
| 279 | --- | 54.3 | Off | 69. (10.) | 22° | |
| 280 | --- | 48.7 | Off | 69. (10.) | 22° | |
| 281 | --- | 54.3 | Off | 69. (10.) | 22° | |
| 282 | --- | 58.3 | Off | 69. (10.) | 22° | |
| 283 | --- | 62.1 | Off | 69. (10.) | 22° | |
| 284 | --- | 62.1 | Off | 69. (10.) | 22° | |
| 285 | --- | 66.9 | Off | 69. (10.) | 22° | |
| 286 | --- | 75.0 | Off | 69. (10.) | 22° | |
| 287 | --- | 86.3 | Off | 69. (10.) | 22° | Max EGT |
| 288 | --- | 82.9 | Off | 69. (10.) | 22° | |
| 289 | --- | 86.7 | Off | 69. (10.) | 22° | |
| 290 | --- | 48.6 | Off | 69. (10.) | 22° | |
| 291 | --- | 80.0 | Off | 69. (10.) | 22° | |
| 292 | --- | 80.0 | Off | 69. (10.) | 22° | Auto ACC |
| 7049 | --- | 80.0-60.0 | Off | 69. (10.) | 22° | |
| 293 | --- | 60.0 | Off | 69. (10.) | 22° | |
| 7050 | --- | 60.0-80.0 | Off | 69. (10.) | 22° | |

$E^3$ ICLS Test 9A - Acoustic Test - Fully Taped Inlet

Run No. 14

Date: June 9, 1983

DMS Readings: Steady State 294-318; Transient 7051-7052

Run Time: 3 hours 08 minutes

Total Engine Run Time: 55 hours 48 minutes

Test Conditions:

Weather: Clear, 21°C (70°F), Wind 10 km/hr (6 mi/hr) @ 60° inlet
Inlet: Aero-Acoustic
Nozzle: Survey
Instrumentation: - Acoustic Configuration
- Fully Taped Inlet

Starts 25 and 26 were automatic starts with a fuel enrichment schedule of nominal plus 17% + 2 Phi. The engine had to be shut down after Start No. 25 due to a PLA fault on FADEC, thus a second start was made. The same speed points were set as on previous acoustic tests with simultaneous sound and steady state DMS readings taken at each point. After completion of testing, it was discovered that a large portion of the inlet acoustic treatment face sheets were debonded and bubbling up into the flowpath. The aero-acoustic inlet was, therefore, removed and the bellmouth reinstalled. In addition, unbonding was found on the acoustic panels in front of the fan frame again and these were replaced with the hardwall panels. The acoustic treatment in the fan and core cowl doors was then taped in preparation for the baseline acoustic test.

RUN NO. 14

| DMS | PCN25R | PCN12R | HPC ACC | HPT ACC kPa (lbf/in.$^2$) | LPT ACC | Remarks |
|---|---|---|---|---|---|---|
| 294 | 0 | 0 | Off | Off (Off) | 11° | Zero reading |
| 7051 | 0-62.0 | --- | Off | Off (Off) | 11° | Start No. 25 |
| 295 | 0 | 0 | Off | Off (Off) | 11° | Zero reading |
| 7052 | 0-62.0 | --- | Off | Off (Off) | 11° | Start No. 26 |
| 296 | 62.0 | --- | Off | Off (Off) | 22° | |
| 297 | 76.5 | 33.5 | Off | 69. (10.) | 22° | D/A |
| 298 | --- | 48.7 | Off | 69. (10.) | 22° | |
| 299 | --- | 54.3 | Off | 69. (10.) | 22° | |
| 300 | --- | 58.3 | Off | 69. (10.) | 22° | |
| 301 | --- | 62.1 | Off | 69. (10.) | 22° | |
| 302 | --- | 66.5 | Off | 69. (10.) | 22° | |
| 303 | --- | 75.0 | Off | 69. (10.) | 22° | |
| 304 | --- | 82.9 | Off | 69. (10.) | 22° | |
| 305 | --- | 75.0 | Off | 69. (10.) | 22° | |
| 306 | --- | 82.9 | Off | 69. (10.) | 22° | |
| 307 | --- | 66.9 | Off | 69. (10.) | 22° | |
| 308 | --- | 62.1 | Off | 69. (10.) | 22° | |
| 309 | --- | 58.3 | Off | 69. (10.) | 22° | |
| 310 | --- | 54.3 | Off | 69. (10.) | 22° | |
| 311 | --- | 48.7 | Off | 69. (10.) | 22° | |
| 312 | --- | 54.3 | Off | 69. (10.) | 22° | |
| 313 | --- | 58.3 | Off | 69. (10.) | 22° | |
| 314 | --- | 62.1 | Off | 69. (10.) | 22° | |
| 315 | --- | 66.9 | Off | 69. (10.) | 22° | |
| 316 | --- | 75.0 | Off | 69. (10.) | 22° | |
| 317 | --- | 83.3 | Off | 69. (10.) | 22° | |
| 318 | --- | 48.7 | Off | 69. (10.) | 22° | |

$E^3$ ICLS Test No. 10 - Acoustic Test Baseline
No. 11 - Engine Transients
No. 8B - FICA Substitutions

Run No. 15

Date: June 14, 1983

DMS Readings: Steady State: 320-358; Transient 7054-7085

Run Time: 9 hours 02 minutes

Total Engine Run Time: 64 hours 50 minutes

Test Conditions:

Weather: Clear, 24°C (75°F), Wind 10 km/hr (6 mi/hr) @ 30° inlet
Inlet: Bellmouth
Nozzle: Survey
Instrumentation: - Acoustic Configuration
- All Tape Removed

Start No. 27 was an automatic start with a fuel enrichment schedule of nominal + 20% + 5 Phi + 14 kPa (2 lbf/in.$^2$) PS3. Maximum EGT was 660°C (1220°F). The engine was transitioned to D/A and the same acoustic points were set as in previous acoustic tests. Each point was set three times, sound and DMS readings were taken at each point. The engine was shut down and all tape was removed from the exhaust to obtain an acoustic baseline with the bellmouth inlet. Start No. 28 was an automatic start with a fuel enrichment schedule of nominal + 20% + 5 Phi + 28. kPa (4 lbf/in.$^2$) PS3. For this run acoustic points were set only once, sound and DMS readings were subsequently taken. After completion of acoustic testing, engine bursts and chops were made. Several bursts and chops were made from FIDLE to 50%, 70%, and 85% PCN12R and back using transient DMS on each one. The final test was FICA

substitutions, single and double. For double substitution, fan speed and T3, fan speed and T42 and fan speed and T25 signals were successfully failed. For single substitution, fan speed signal, PS3 and core speed signals were successfully failed while on fan speed control. An attempt to fail the core speed while on core speed control was still unsuccessful. The engine was then returned to FIDLE and shut down. Steady state DMS readings 359-369 were taken at 10 minute intervals after shutdown.

RUN NO. 15

| DMS | PCN25R | PCN12R | HPC ACC | HPT ACC kPa (lbf/in.$^2$) | LPT ACC | Remarks |
|---|---|---|---|---|---|---|
| 320 | --- | --- | Off | Off (Off) | 11° | Zero reading |
| 7054 | 0-62.0 | --- | --- | Off (Off) | 11° | Start No. 27 |
| 321 | 62.0 | --- | --- | Off (Off) | 11° | |
| 322 | 76.5 | 33.5 | Off | 69. (10.) | 22° | D/A |
| 323 | --- | 48.7 | Off | 69. (10.) | 22° | |
| 324 | --- | 54.3 | Off | 69. (10.) | 22° | |
| 325 | --- | 58.3 | Off | 69. (10.) | 22° | |
| 326 | --- | 62.5 | Off | 69. (10.) | 22° | |
| 327 | --- | 66.9 | Off | 69. (10.) | 22° | |
| 328 | --- | 75.0 | Off | 69. (10.) | 22° | |
| 329 | --- | 82.75 | Off | 69. (10.) | 22° | |
| 330 | --- | 75.1 | Off | 69. (10.) | 22° | |
| 331 | --- | 82.75 | Off | 69. (10.) | 22° | |
| 332 | --- | 66.9 | Off | 69. (10.) | 22° | |
| 333 | --- | 62.1 | Off | 69. (10.) | 22° | |
| 334 | --- | 58.3 | Off | 69. (10.) | 22° | |
| 335 | --- | 54.3 | Off | 69. (10.) | 22° | |
| 336 | --- | 48.7 | Off | 69. (10.) | 22° | |
| 337 | --- | 54.3 | Off | 69. (10.) | 22° | |
| 338 | --- | 58.3 | Off | 69. (10.) | 22° | |
| 339 | --- | 62.1 | Off | 69. (10.) | 22° | |
| 340 | --- | 66.1 | Off | 69. (10.) | 22° | |
| 341 | --- | 75.0 | Off | 69. (10.) | 22° | |
| 342 | --- | 82.5 | Off | 69. (10.) | 22° | |
| 343 | --- | 82.4 | Off | 69. (10.) | 22° | |
| 344 | --- | 48.7 | Off | 69. (10.) | 22° | |
| 345 | 0 | 0 | Off | Off (Off) | 11° | Shutdown |
| 346 | 0 | 0 | Off | Off (Off) | --- | Zero reading |
| 7055 | 0-62.0 | --- | Off | Off (Off) | 11° | Start No. 28 |
| 347 | 62.0 | --- | Off | Off (Off) | --- | |
| 348 | 76.5 | 33.5 | Off | 70. (10.2) | 20° | D/A |
| 349 | --- | 48.7 | Off | 70. (10.2) | 20° | |
| 350 | --- | 54.3 | Off | 70. (10.2) | 20° | |

| | | | | | | |
|---|---|---|---|---|---|---|
| 351 | --- | 58.3 | Off | 70. (10.2) | 20° | |
| 352 | --- | 62.1 | Off | 70. (10.2) | 20° | |
| 353 | --- | 66.9 | Off | 70. (10.2) | 20° | |
| 354 | --- | 75.0 | Off | 70. (10.2) | 20° | |
| 355 | --- | 82.0 | Off | 70. (10.2) | 20° | Set core speed limit 12,650 |
| 356 | --- | 60.2 | Off | 70. (10.2) | 20° | |
| 7056 | --- | 33.5-50.0 | Off | 70. (10.2) | 20° | Burst to 50% |
| 7057 | --- | 50.0-33.5 | Off | 70. (10.2) | --- | Chop to FIDLE |
| 7058 | | 33.5-70.0 | Off | 70. (10.2) | 20° | Burst to 70° |
| 7059 | --- | 70.0-33.5 | Off | 70. (10.2) | 20° | Chop to FIDLE |
| 7060 | --- | 33.5-70.0 | Off | 70. (10.2) | 20° | 10 sec accel |
| 7061 | --- | 70.0-33.5 | Off | 70. (10.2) | 20° | 10 sec decel |
| 7062 | --- | 33.5-85.0 | Off | 70. (10.2) | 20° | Burst to 85% |
| 7063 | --- | 85.0-70.0 | Off | 70. (10.2) | 20° | Chop to 70% |
| 7064 | --- | 70.0-33.5 | Off | 70. (10.2) | 20° | Chop to 33.5% |
| 7065 | --- | 33.5-85.0 | Off | 70. (10.2) | 20° | Burst to 33.5% |
| 7066 | --- | 85.0-33.5 | Off | 70. (10.2) | 20° | Chop to 33.5% |
| 7067 | --- | 33.5-85.0 | Off | 70. (10.2) | 20° | Burst to 85% |
| 7068 | --- | 33.5-85.0 | Off | 70. (10.2) | 20° | Burst to 85% |
| 7069 | --- | 33.5-85.0 | Off | 70. (10.2) | 20° | Burst to 85% |
| 7070 | --- | 33.5-85.0-33.5 | Off | 70. (10.2) | 20° | Burst to 85% then chop to FIDLE |
| 7071 | --- | 33.5-85.0-33.5 | Off | 70. (10.2) | 20° | 2 minutes accel to 85% then 2 minute decel to FIDLE |
| 7072 | --- | 33.5-85.0 | Off | 70. (10.2) | 20° | Burst to 85% |
| 358 | --- | 83.0 | Off | 70. (10.2) | 20° | 81.87% PCN12R limit on FADEC |
| 7073 | --- | 40% | Off | 70. (10.2) | 20° | Failed T3 and fan speed |
| 7074 | --- | 40.0-80.0-40.0 | Off | 70. (10.2) | 22° | 30 sec accel and decel w/failed sensors |
| 7075 | --- | 40.0 | Off | 70. (10.2) | 22° | Failed T42 and fan speed sensor |
| 7076 | --- | 40.0-80.0-40.0 | Off | 70. (10.2) | 22° | 30 sec accel and decel w/failed sensors |
| 7077 | --- | 40.0 | Off | 70. (10.2) | 22° | Failed T25 and fan speed sensor |
| 7078 | --- | 40.0-80.0-40.0 | Off | 70. (10.2) | 22° | 30 sec accel and decel w/failed sensors |
| 7079 | --- | 50.0 | Off | 70. (10.2) | 22° | Failed fan speed sensor |
| 7080 | --- | 50.0 | Off | 70. (10.2) | 22° | Failed PS3 sensor |

| | | | | | | |
|---|---|---|---|---|---|---|
| 7081 | --- | 50.0 | Off | 70. (10.2) | 22° | Failed core speed sensor on fan speed control |
| 7082 | --- | 50.0 | Off | 70. (10.2) | 22° | 15 sec transient with fan and core speed sensor |
| 7083 | --- | 60.0 | Off | 70. (10.2) | 22° | 15 sec transient with failed core speed sensor |
| 7084 | --- | 60.0-40.0 | Off | 70. (10.2) | 22° | Decel to 40% with core speed sensor failed |
| 7085 | --- | 40.0 | Off | 70. (10.2) | 22° | Switch to core speed control with failed core speed sensor |
| 359 thru 369 | | Readings at 10 minute intervals after shutdown | | | | |

After completion of testing the engine was removed from the test stand and returned to the prep building. All engine cowling was removed and compressor, HPT, and LPT were borescoped with no apparent problems discovered. Drop checks of HPT blade clearance were also taken. Oil was drained from the AGB and forward and aft sumps. The engine was loaded into a dolly and returned to the Evendale assembly area on June 30, 1983.

# 6.0 TEST RESULTS

Mechanical and thermodynamic performance were analyzed in detail during and following ICLS testing. The results of those analyses are presented here. Section 6.1 presents overall engine thermodynamic performance. This is based on the establishment of component performance levels to achieve a balanced engine cycle which best matches all test measurements. Subsequent sections present the detailed mechanical and thermodynamic performance of each component. Performance of the remaining engine systems are then presented.

## 6.1 TURBOFAN SYSTEM THERMODYNAMIC PERFORMANCE

Overall performance results from the ICLS test were compared with pretest predictions from the ICLS thermodynamic cycle model. This model was developed from the results of the component rig tests, model tests, the core engine test and analytical predictions. Since the high pressure (HP) turbine clearances during the test differed substantially from expectations, the pretest prediction data for performance comparisons used the clearances as determined by the mechanical analysis of test results.

In addition to the evaluation of absolute performance levels, the component performance relative to the cycle model was examined over the full range of engine operation in order to evaluate the off-design modeling of the component performance trends. This was a significant factor in establishing the validity of the model for subsequent performance predictions outside the range of ICLS test operation.

### 6.1.1 Data Use for Performance Analysis

Seven different major instrumentation and hardware configurations were used during the test as shown in Table XI. Utilization of the test data for performance analysis differed with each configuration. Figures 115 through 121 describe the configuration and instrumentation changes which affected the performance analysis of the engine.

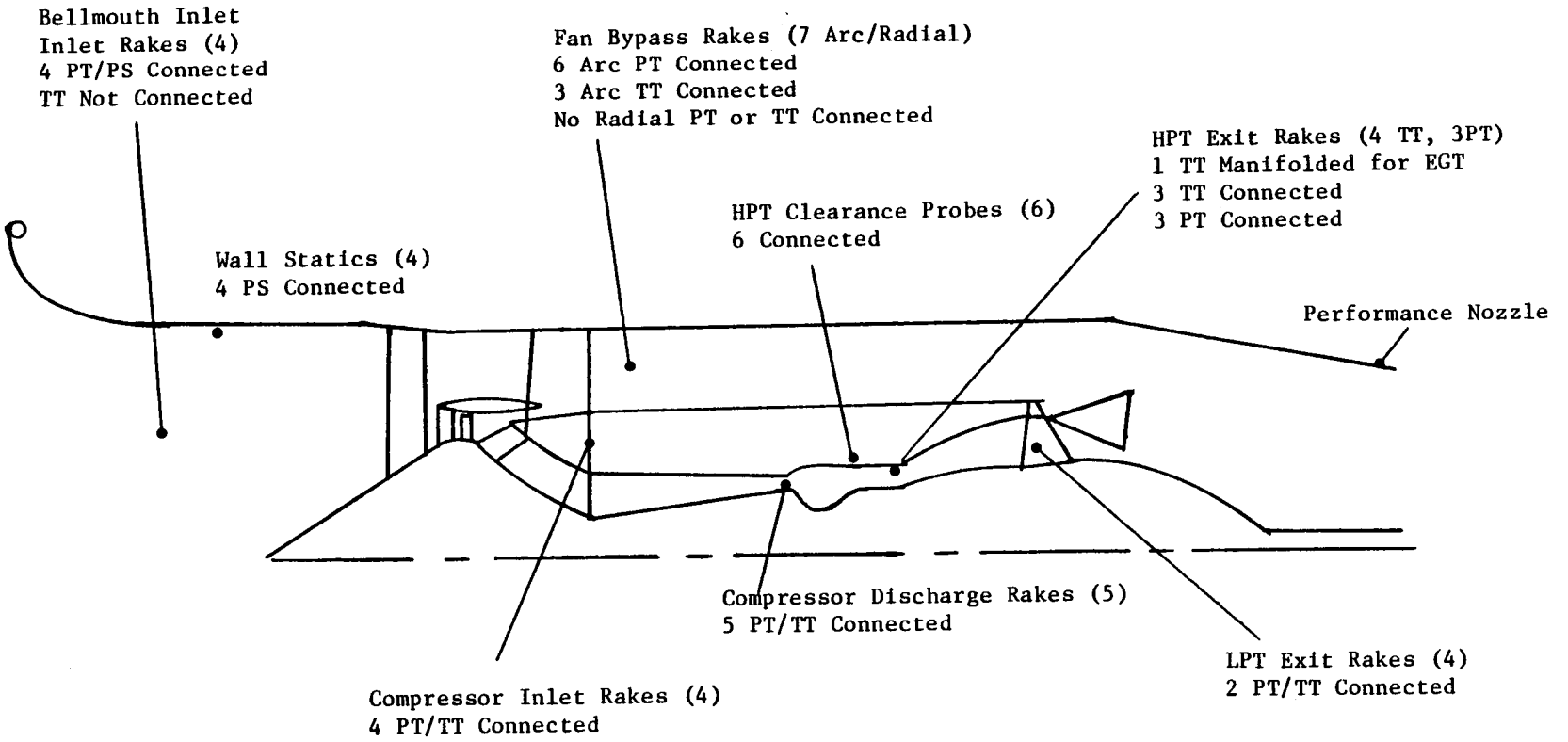


Figure 115. Mechanical Checkout Instrumentation for Performance Analysis.

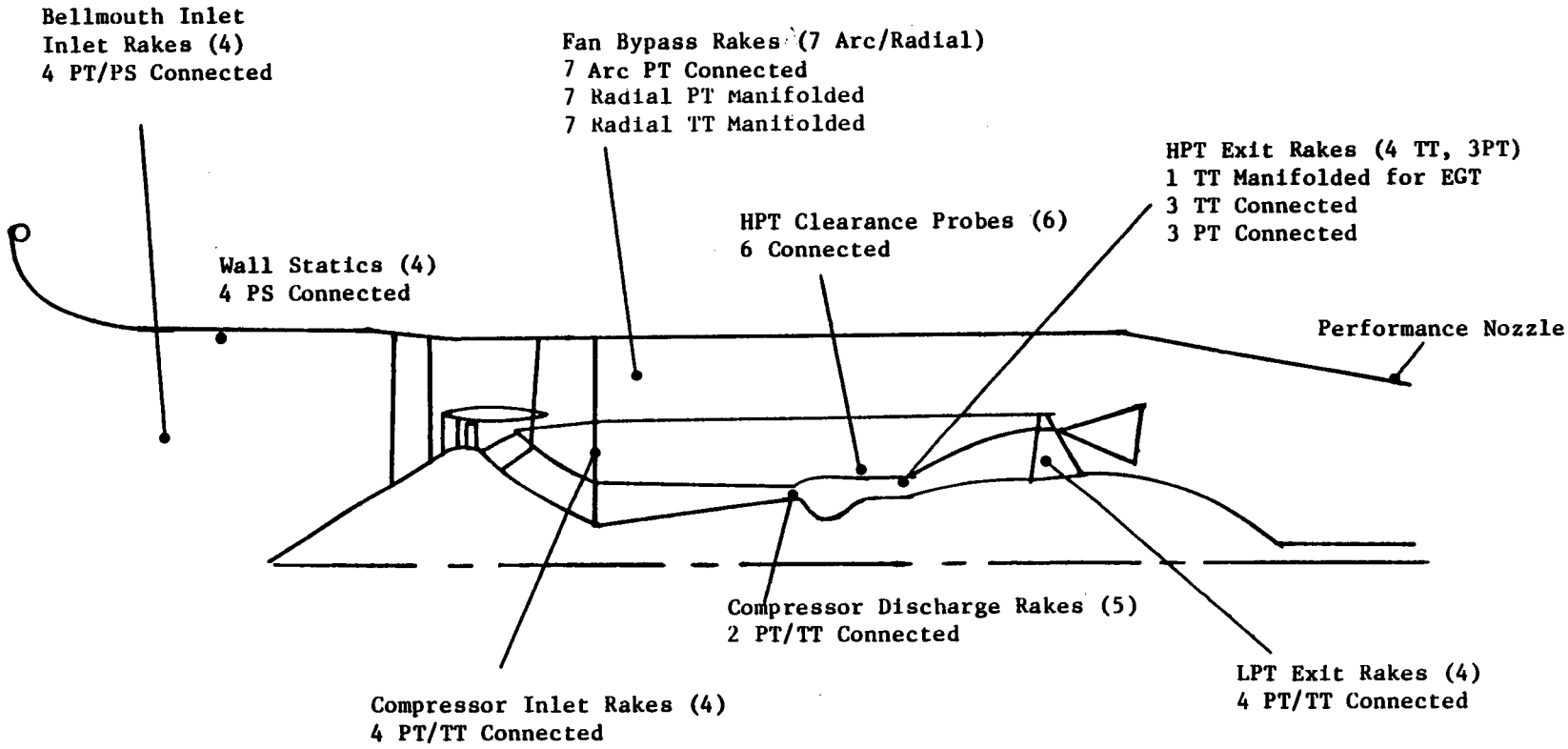


Figure 116. Performance Run Instrumentation for Performance Analysis.

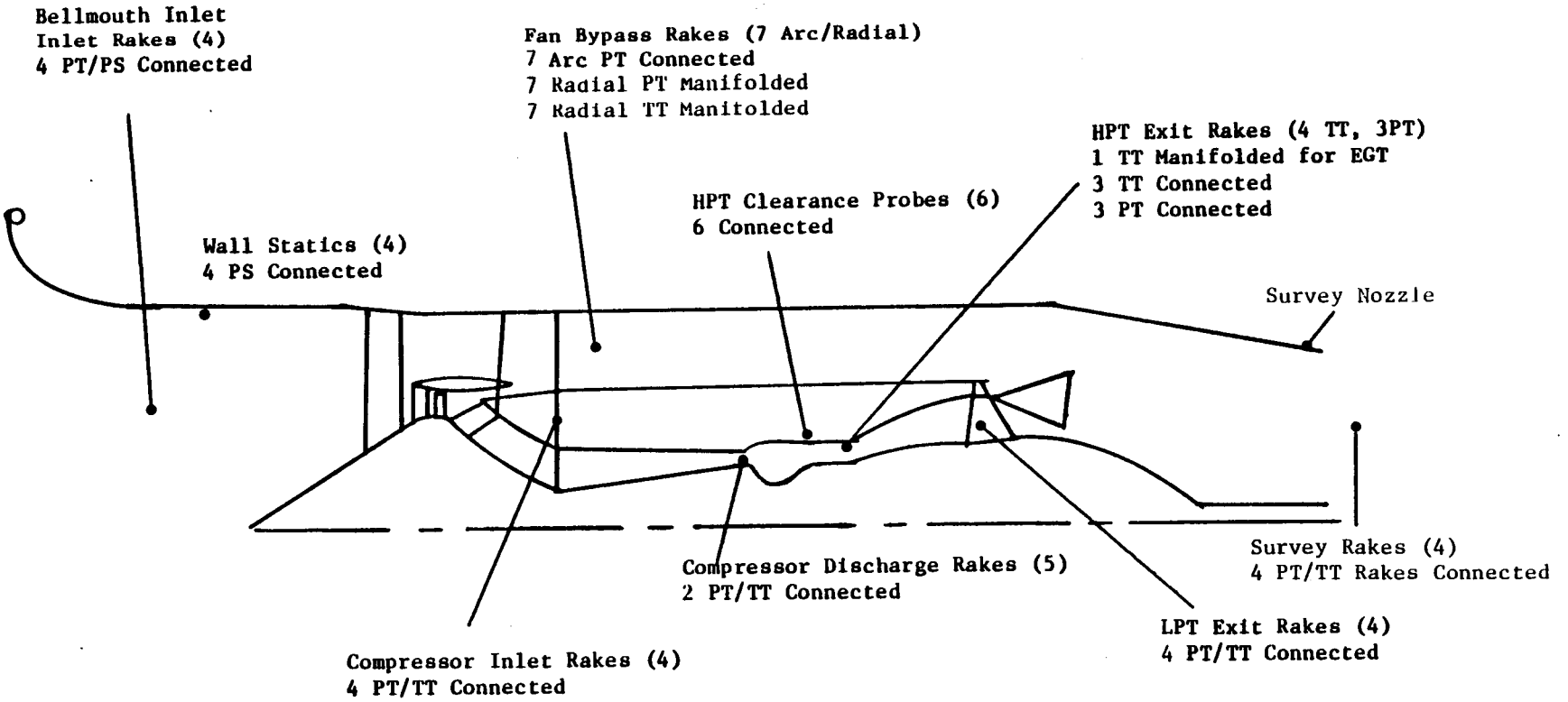


Figure 117. Exhaust Survey Instrumentation for Performance Analysis.

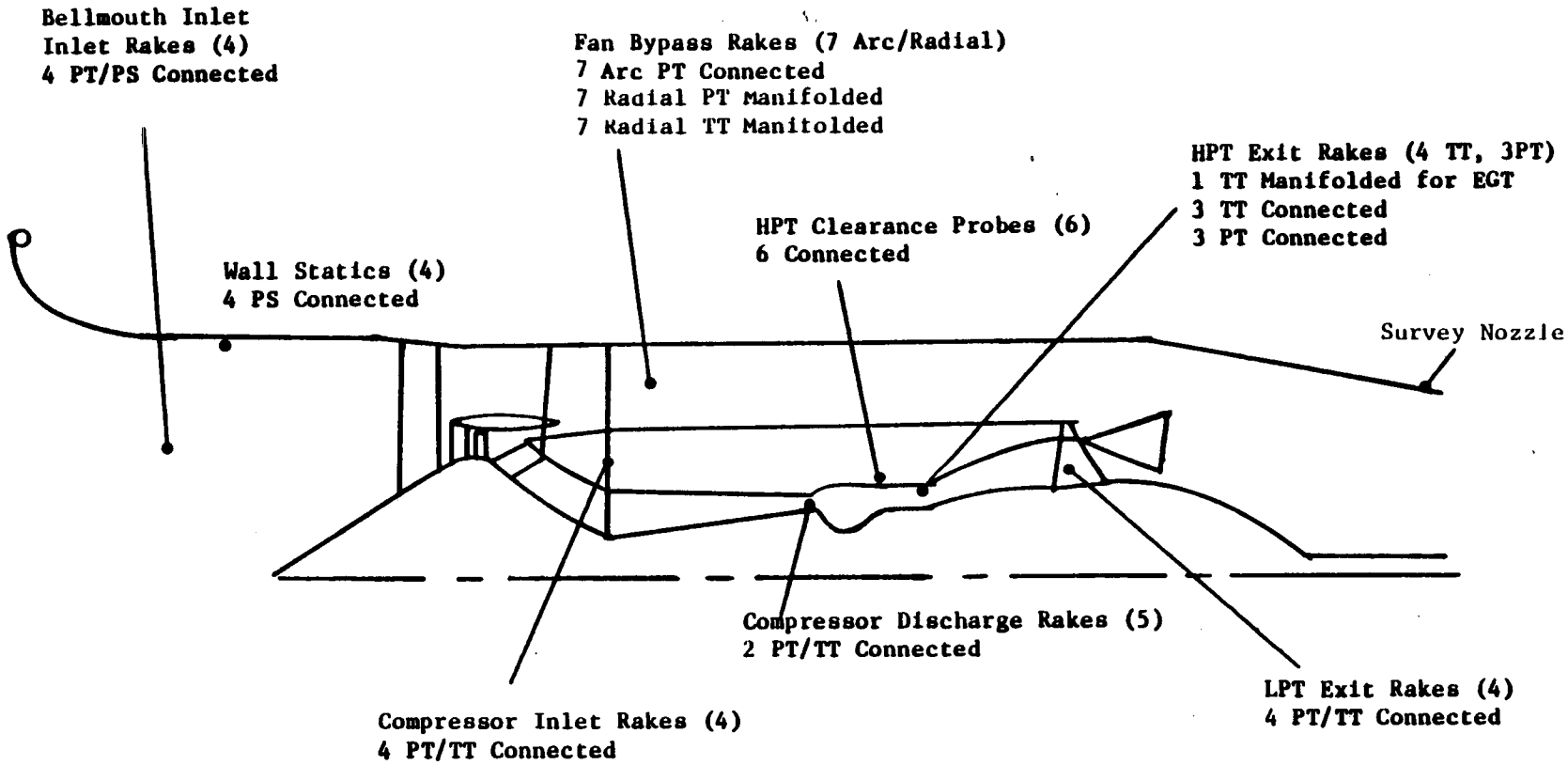


Figure 118. Survey Nozzle Baseline Run Instrumentation for Performance Analysis.

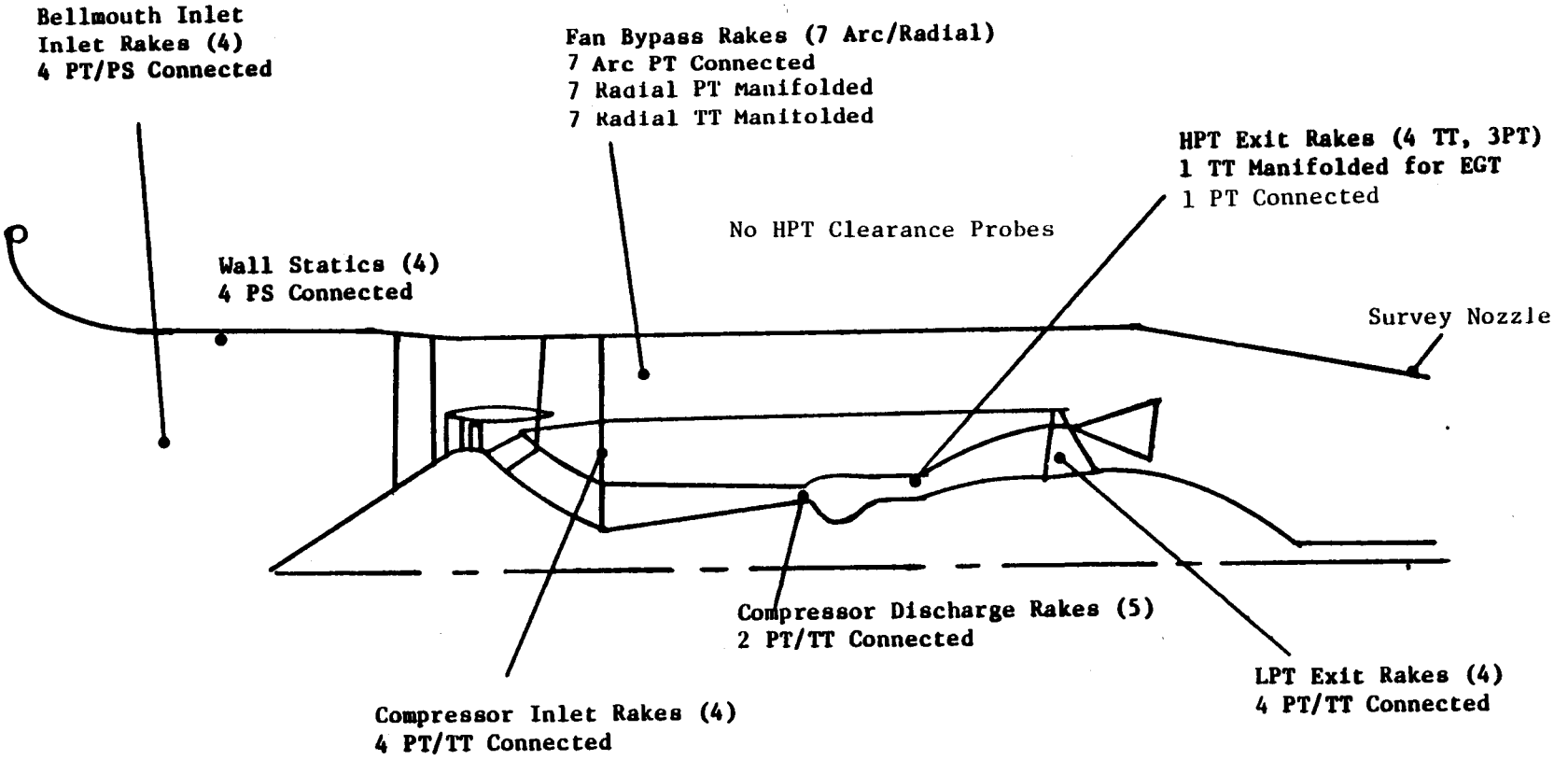


Figure 119. Plane 41 Rake Removal Run Instrumentation for Performance Analysis.

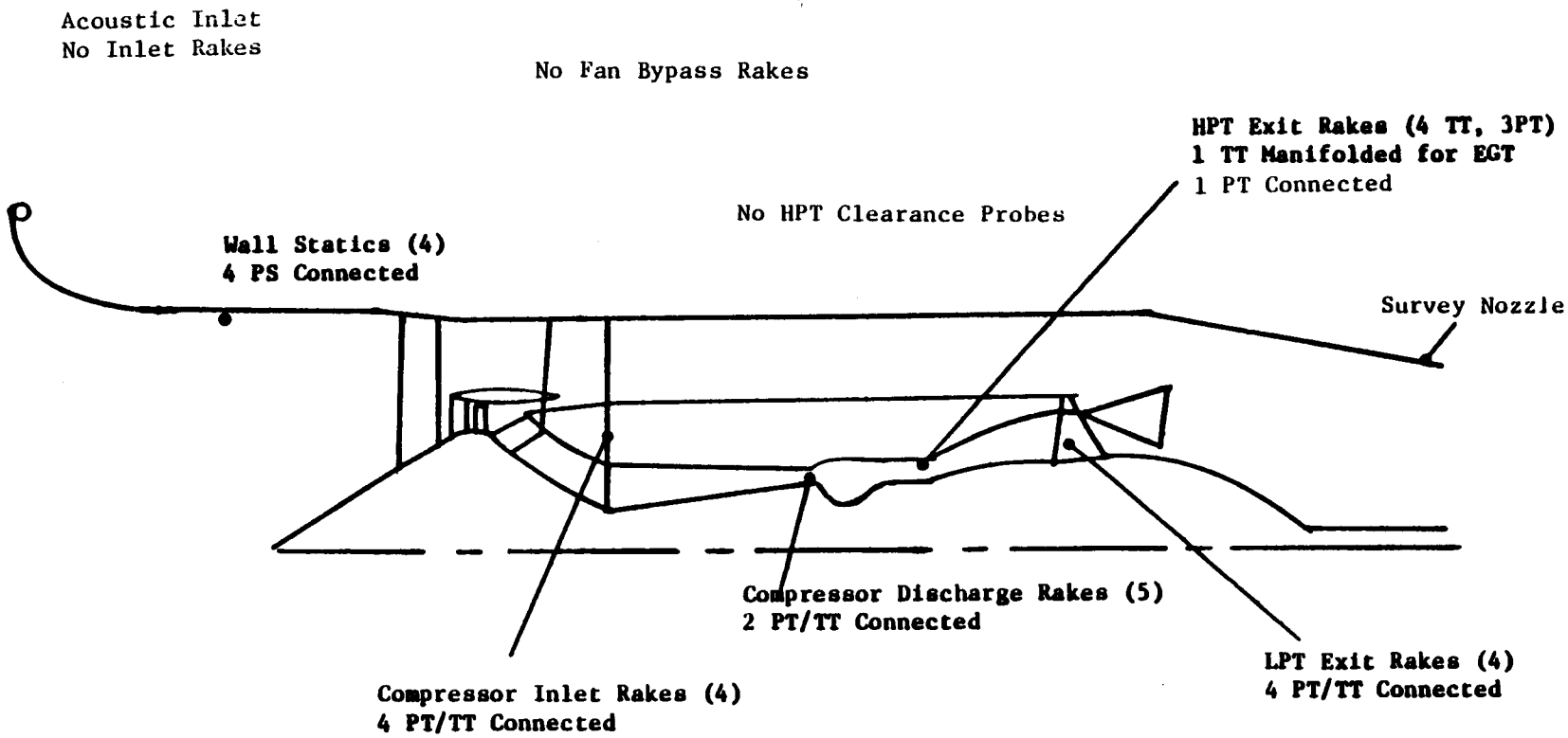


Figure 120. Acoustic Inlet Runs Instrumentation for Performance Analysis.

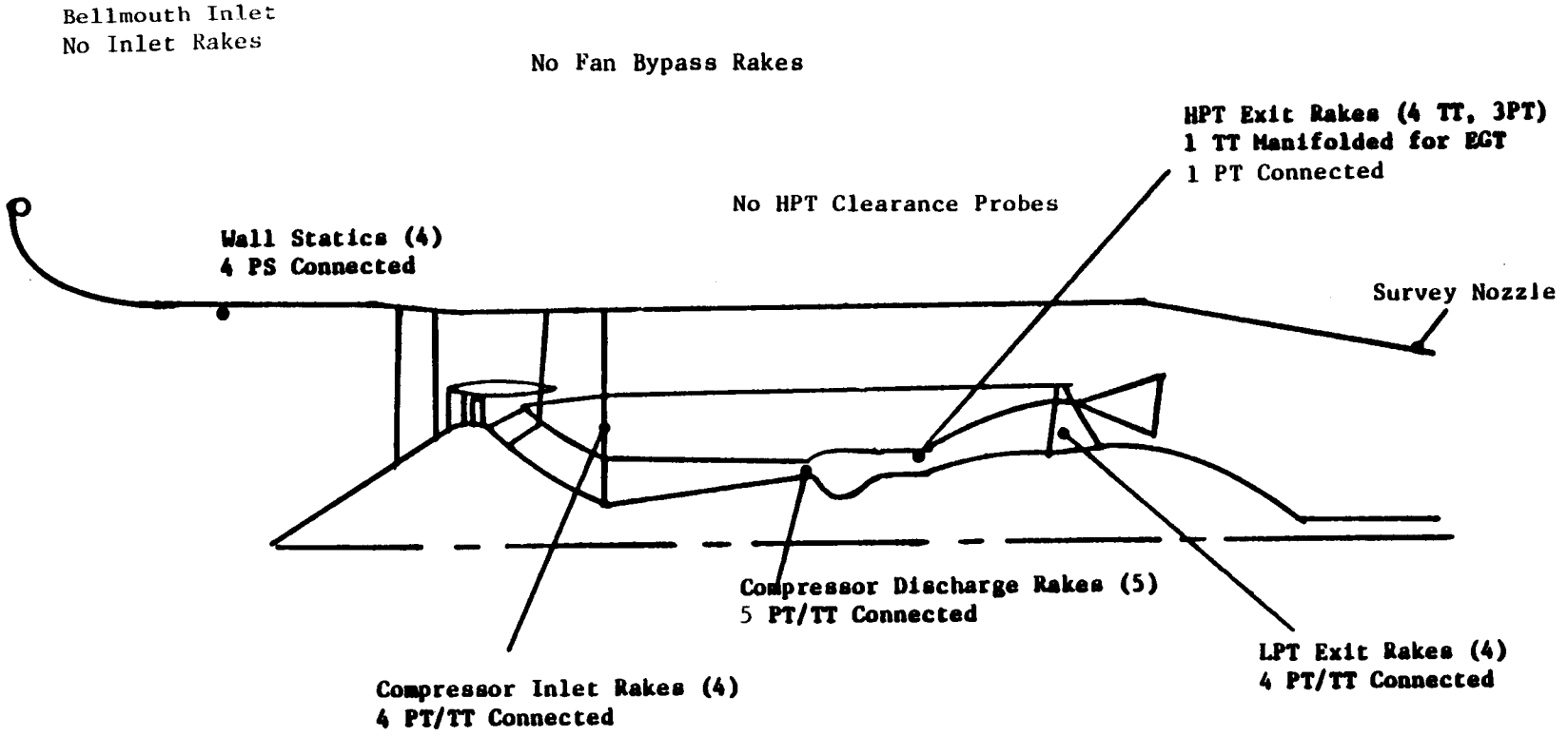


Figure 121. Bellmouth Inlet Acoustic Run Instrumentation for Performance Analysis.

Table XI. Instrumentation and Hardware Configurations.

Mechanical Checkout
Performance
Exhaust Survey
Survey Nozzle Baseline
Plane 42 Rake Removal
Acoustic Inlet
Bellmouth Inlet Acoustic Test

Mechanical Checkout Test data were used for analysis of the individual core components and the overall core performance.

The Performance Test provided data for assessment of the overall core performance; the fan, low pressure turbine (LPT), and exhaust component performance, and the overall engine performance. Ambient conditions for this test were acceptable for performance evaluation. Wind velocities were low, inlet temperature profiles showed no temperature distortion, and temperature levels permitted operation to over 87% corrected fan speed.

The Mixer Survey Test provided data for evaluation of the fan along a high operating line. The survey nozzle effective area was about 2% smaller than the performance nozzle, and the exhaust traverse rake produced an additional 4% blockage of nozzle effective area.

The baseline calibration run with the survey nozzle installed and the exhaust traverse rakes removed provided data along a third fan operating line with an effective exhaust nozzle area approximately 2% smaller than the performance nozzle. Data from this run were also used in the evaluation of the overall engine, fan, LPT, overall core, and exhaust system performance. This run also was the baseline for evaluation of the effects of the HP turbine discharge rakes on LPT performance. During this run some inlet temperature distortion was encountered. Figure 122 shows the inlet

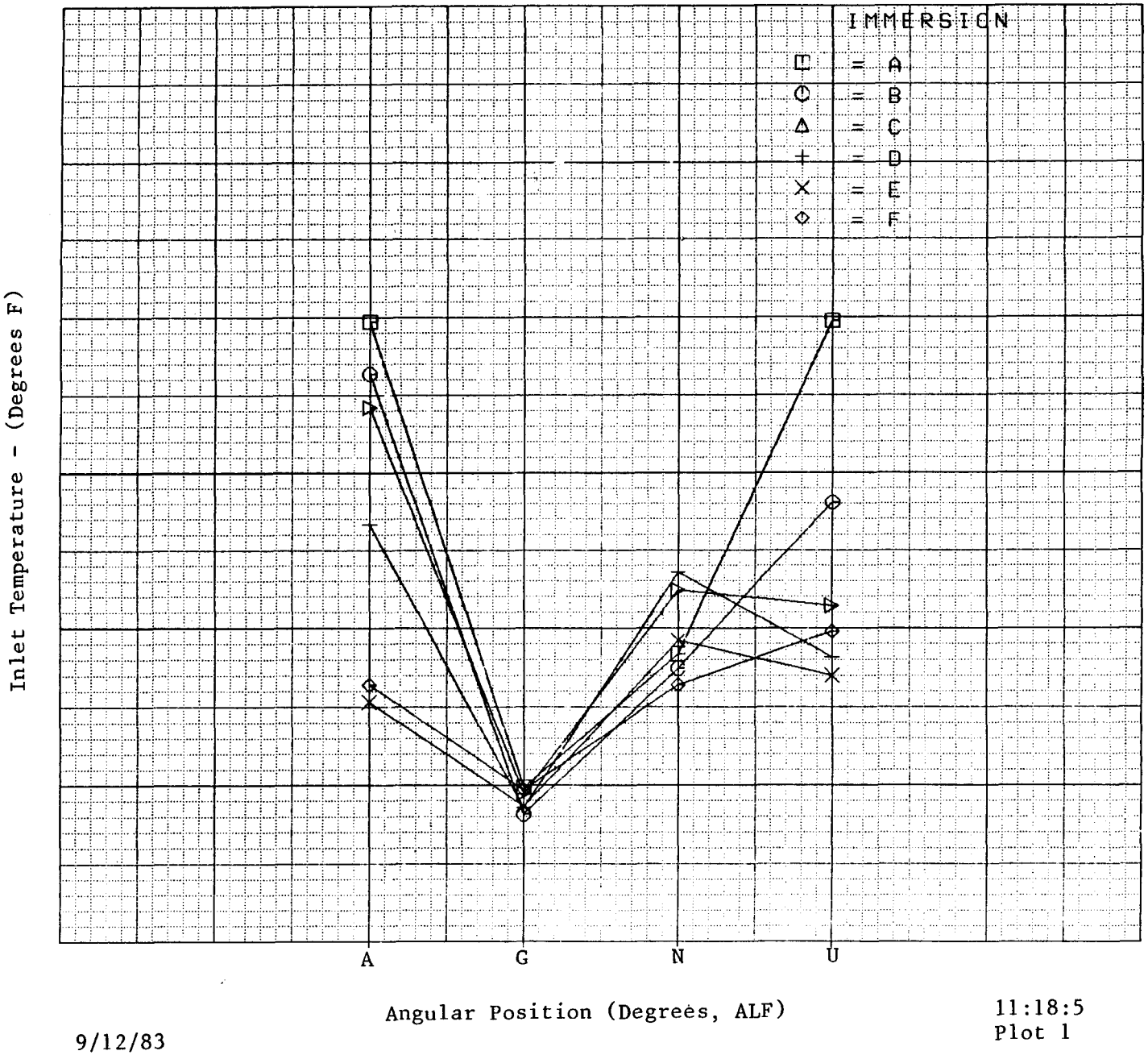


**Figure 122. Inlet Temperature Profile, Reading 200.**

temperature profile for a typical reading. Inlet rake temperatures indicated a range of temperature variation of as much as 2.2°C (4°F) on some readings. Average inlet temperature from the rakes was 0.55 to 1.1°C (1 to 2°F) higher than the ambient temperature measurement. A post-test recalibration of the inlet rake verified that the rake was reading correctly. An investigation of the source of the temperature distortion indicated that inlet air may have been affected by the exhaust from an engine operating on a nearby test stand.

Because of this temperature distortion the uncertainty in the fan, LP turbine, and overall performance was greater than in the performance run. The survey nozzle baseline readings were, therefore, used more to verify general trends in performance than to establish absolute levels.

The primary purpose of the next run was to evaluate the LPT performance loss caused by the high pressure turbine (HPT) discharge/LPT inlet rakes. The data were also used to verify fan and overall performance trends. Since only a single exit pressure rake was left, the applicability of the data for core and LPT performance assessment is limited by the accuracy of the correlation between the single rake pressure and the average HPT discharge pressure. As with the previous run, a significant level of inlet temperature distortion was evident and, thus, caused higher uncertainty in the absolute performance levels.

For the remainder of the test the fan inlet and discharge rakes were removed. The individual component performance levels could only be inferred from an evaluation of sfc versus thrust and some core path parameters. Taping of the exhaust system acoustic treatment panels produced some unexpected performance results that were used to evaluate exhaust system performance. One factor in the use of the acoustic data for performance analysis is that the acoustic measurements did not require a long engine stabilization time prior to the data acquisition. Thus, some of the acoustic readings have shorter stabilization times than readings taken specifically for performance evaluation.

### 6.1.2 Analysis Methods

#### Data Reduction Computer Program

Post-test analysis of the performance data utilized a computer simulation of the thermodynamic cycle referred to as a Phase II data reduction program. The Phase II program adjusted the cycle model for each reading analyzed such that the measured data were matched by the computer model. At the same time the cycle was balanced to satisfy conservation of mass, momentum, and energy throughout with appropriate accounting of the gas properties. The resulting adjustments to the cycle model were then examined to determine how each component performed relative to its expected performance.

#### Analysis Path Selection

With the extensive instrumentation available on the ICLS, alternate methods were available to evaluate several key parameters. The method used for any given set of test data depended on the instrumentation connected for that test. The preferred method for each parameter was that which was expected to provide the most reliable measurement. Where appropriate, the results from the alternate methods were compared to verify the consistency of the measurements.

#### Inlet Flow

Inlet flow was determined from the inlet rake total pressures and the wall static pressures in the plane of the rake. Results were compared with the flows determined from the rake total and static pressures and were found to be in good agreement (Figure 123). Comparison of the measured fan flow versus speed with the predicted characteristic (Figure 124) provided further substantiation of the inlet flow measurement.

With the inlet rakes removed for the acoustic tests, it was necessary to use the fan flow versus speed from the fan map to determine inlet flow.

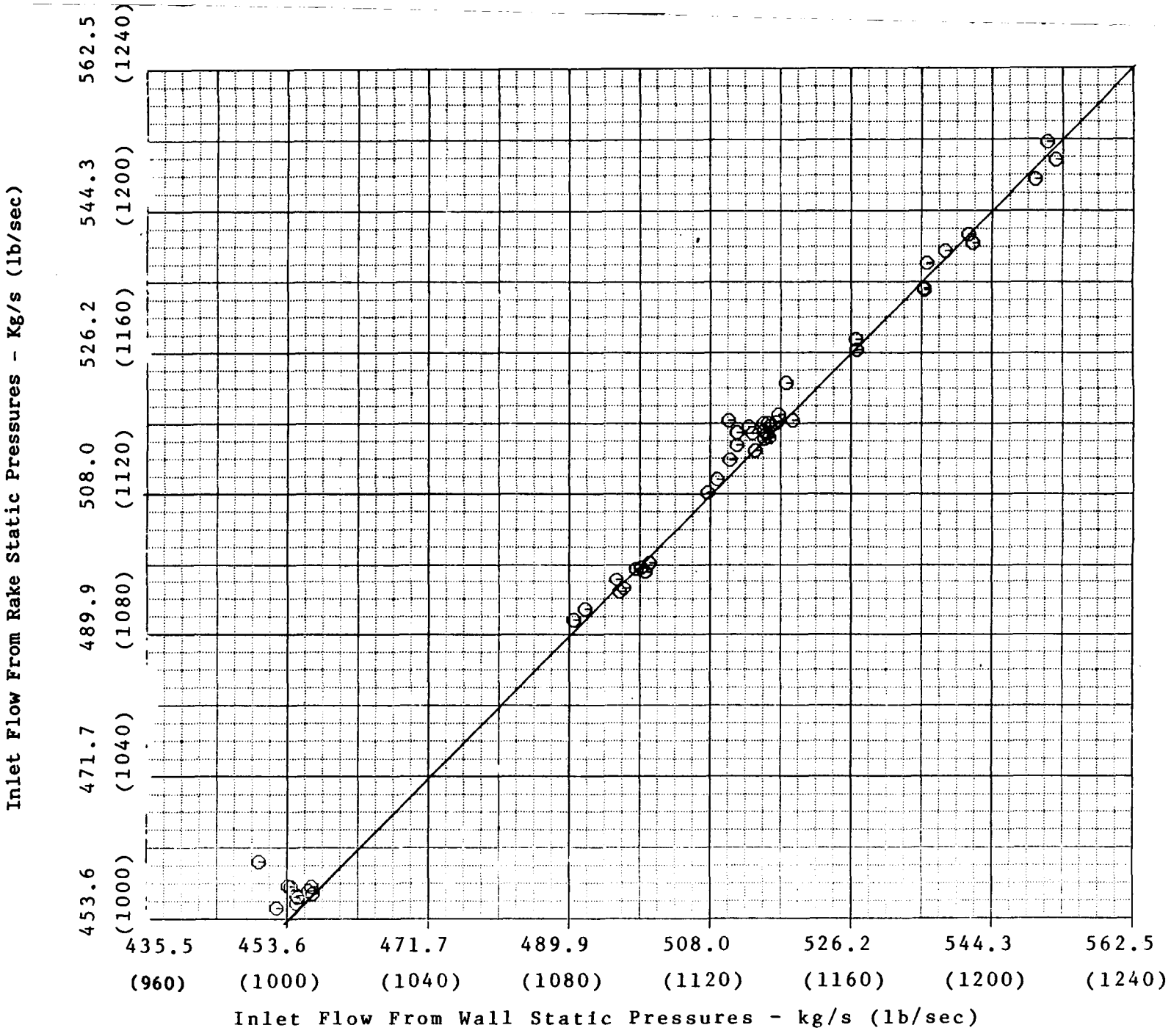


Figure 123. Inlet Flow Measurement Comparison.

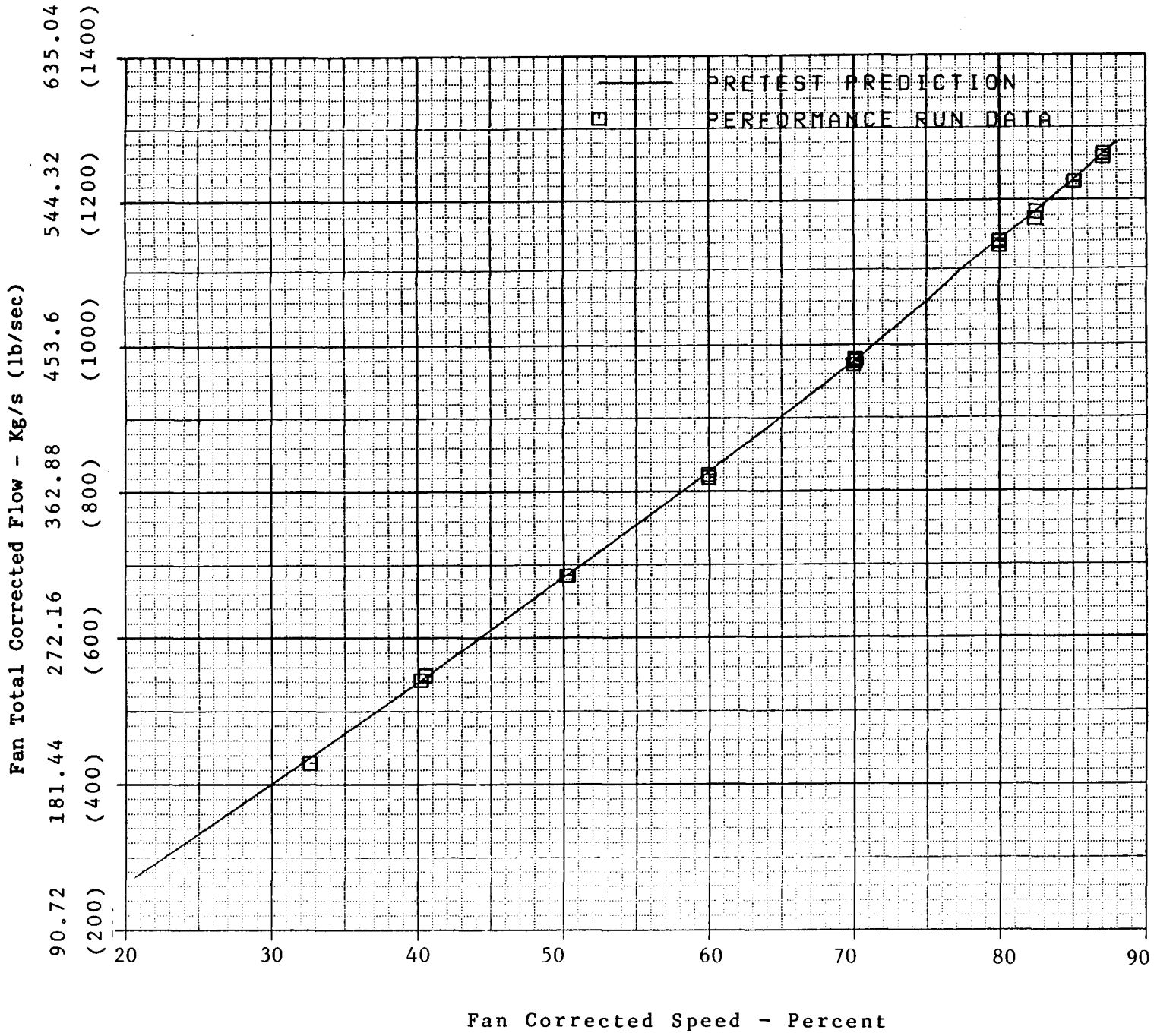


Figure 124. Fan Corrected Flow vs. Corrected Speed.

## Core Flow

The core airflow was determined from the HPT flow function characteristic which was defined by the core engine test. Comparison of the resulting compressor corrected flow versus corrected speed (Figure 125) and the LP turbine flow function (Figure 126) with predictions verified that the three available methods would produce consistent results.

## Fan and Low Pressure Turbine Work

The energy provided to the fan by the LPT was determined from the fan temperature rise measured by the inlet and discharge rakes. For the acoustic test data where no fan rakes were installed, a correlation of measured to cycle average LPT discharge temperature was established from the performance data and the LPT temperature drop was used to determine the fan and LPT work.

## Other Factors in Phase II Analysis

Several items affecting engine performance were evaluated in preparation for the Phase II analysis. Results were used to establish fixed inputs to the Phase II program.

## Parasitic Flows

Parasitic flows were evaluated prior to the Phase II data reduction using the results from the on-line data analysis program. This program determined flows from pretest calibrations and measured pressures and temperatures. The 5th stage and compressor discharge (CDP) parasitic bleeds agreed well with predicted levels as shown in Figures 127 and 128. The 7th stage parasitic bleed indicated by the calibration was higher than expected (Figure 129); however, the calibration of the pipe was suspect due to alterations in the pipe shape during assembly and the installation of the downstream pressure taps. Post-test analysis by the heat transfer designers indicated that the actual bleed flow was a constant 4% of compressor inlet

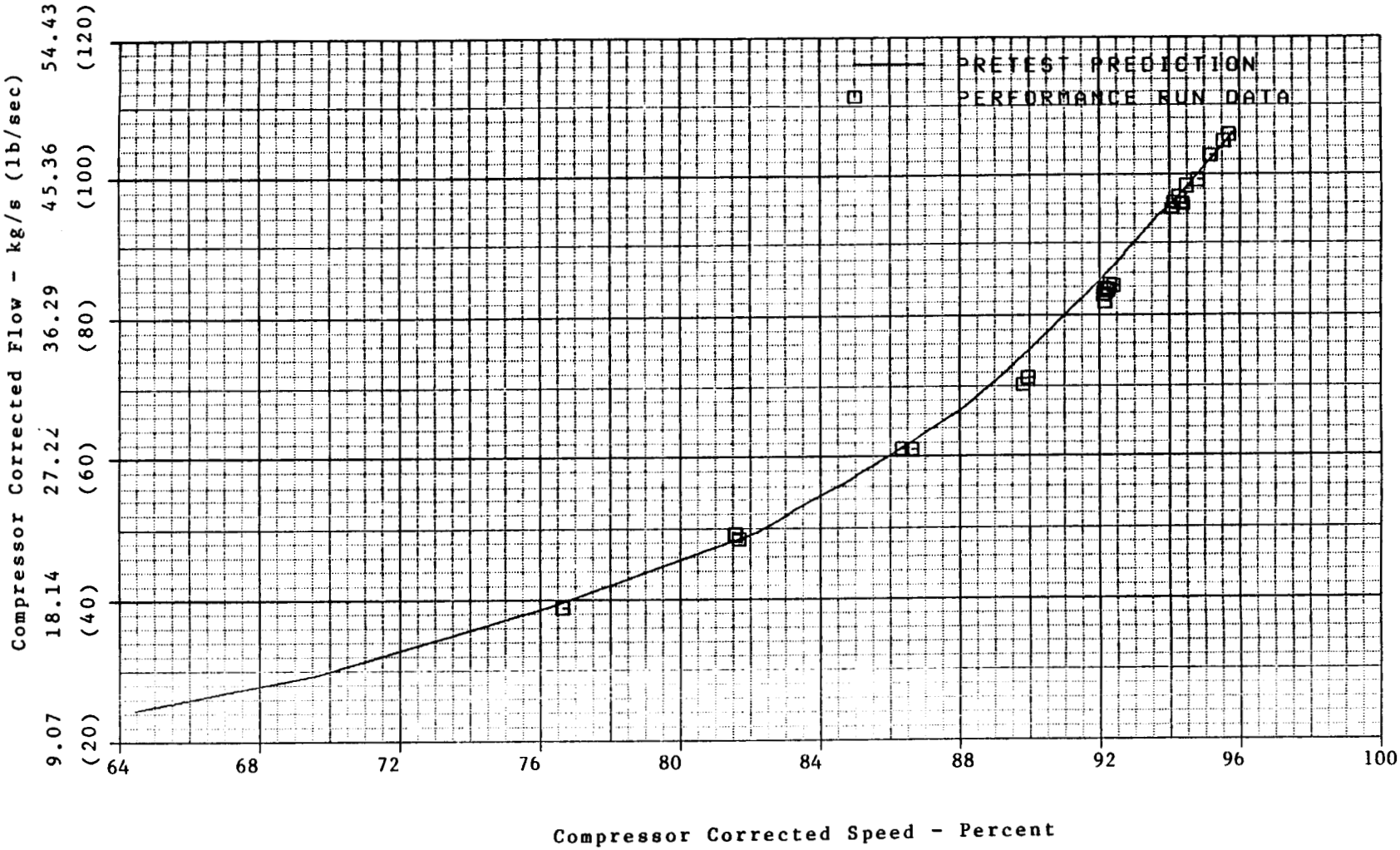


Figure 125. Compressor Corrected Flow vs. Corrected Speed.

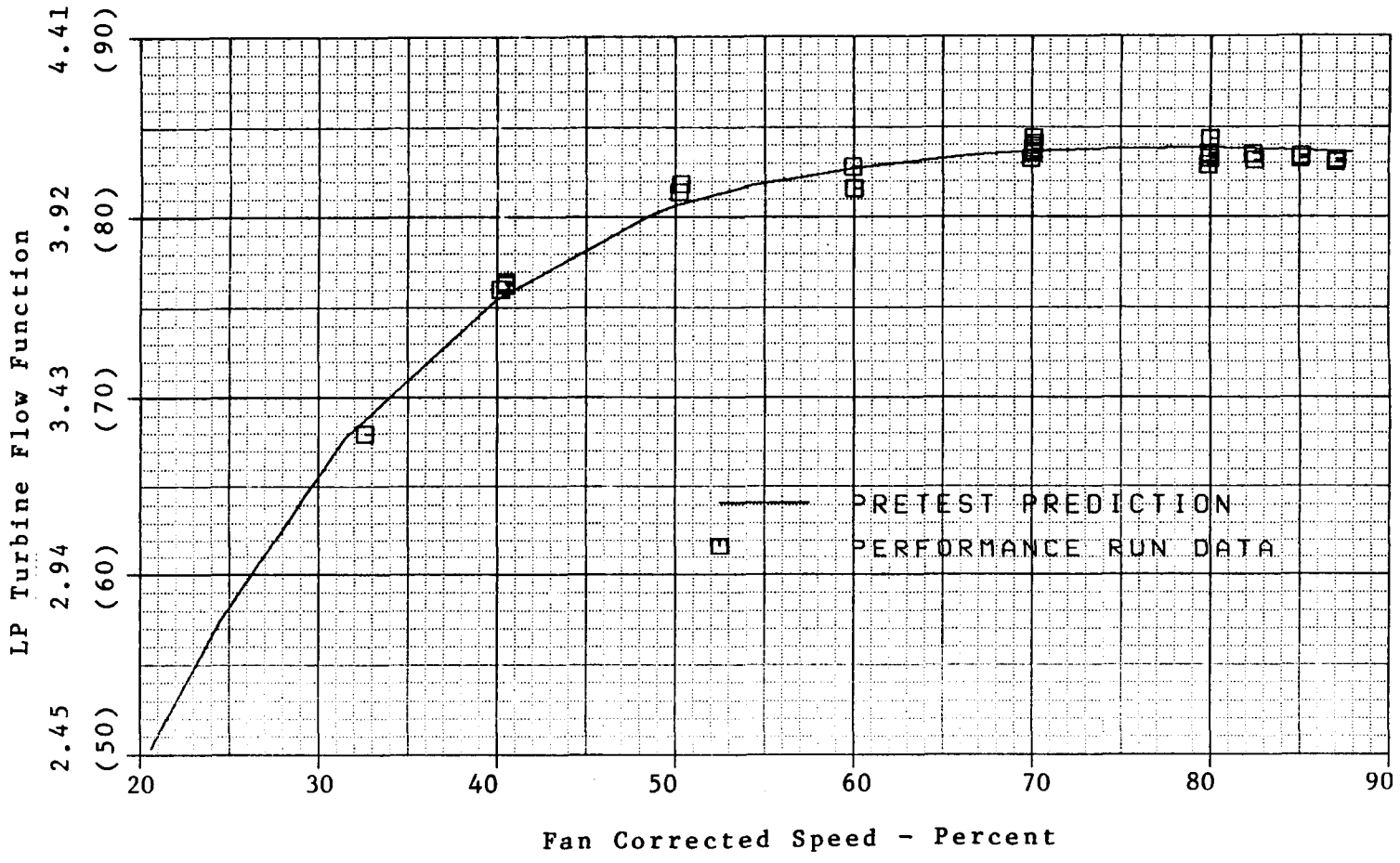


**Figure 126. Low Pressure Turbine Flow Function.**

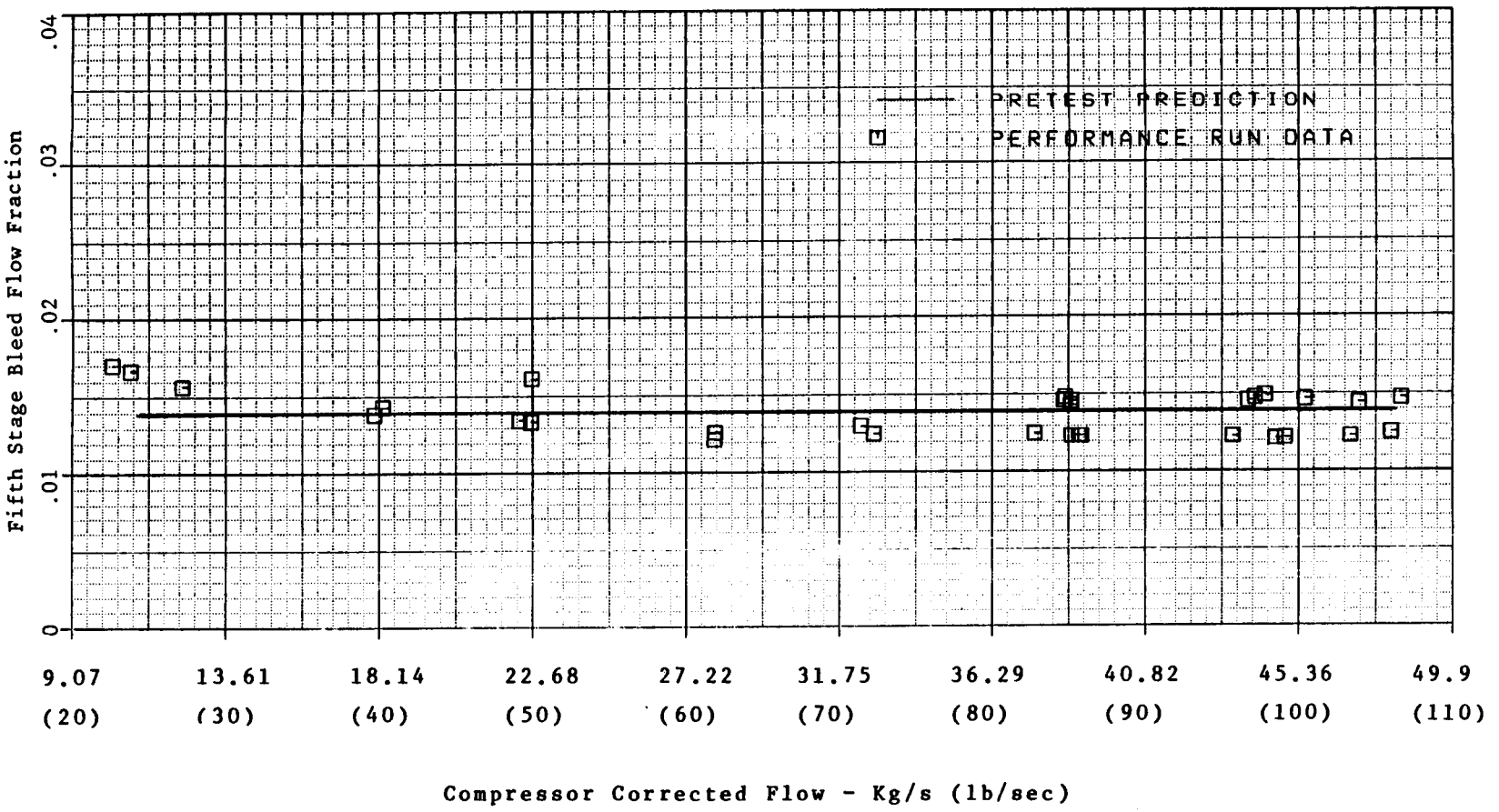


Figure 127. Fifth Stage Bleed Flow Fraction.

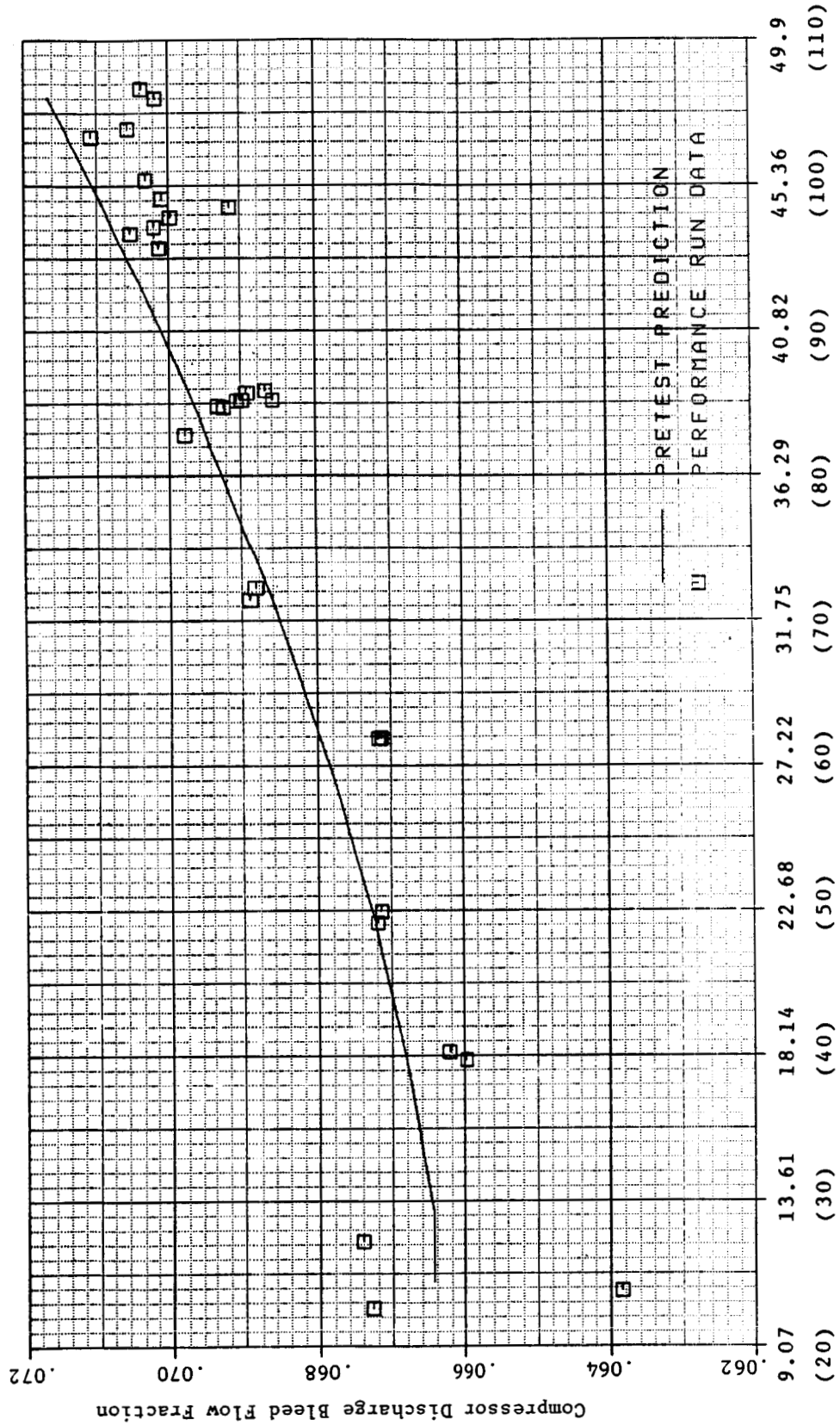


Figure 128. Compressor Discharge Bleed From Calibration.

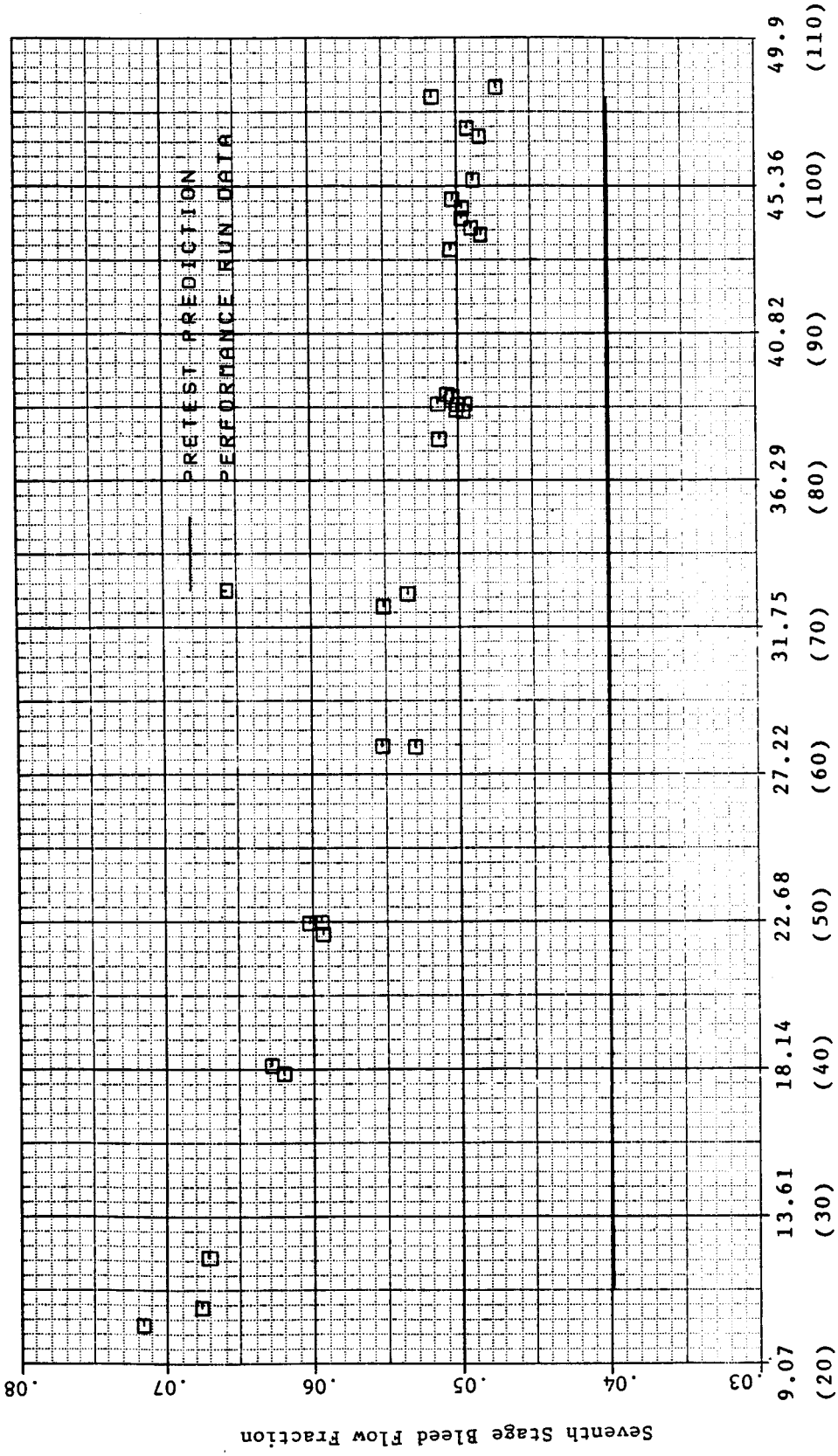


Figure 129. Seventh Stage Bleed From Calibration.

flow as predicted prior to the test. Average curves of 5th stage and CDP bleed and a constant 7th stage bleed of 4% were input to the Phase II program for initial data analysis. The CDP bleed was subsequently re-evaluated using the Phase II program. Results are discussed later with the component performance results.

Compressor Clearance

Since the measurement of compressor 10th stage clearance on ICLS was unreliable, the compressor performance was analyzed using the clearances predicted by the simplified clearance model incorporated in the engine cycle deck.

High Pressure Turbine Clearance

HPT clearances were determined from six laser clearance probes. The Stage 1 and 2 average clearances versus core corrected speed were input to the Phase II program for analysis of the HPT performance.

Since Stage 2 clearances were derived from only two probes, there was uncertainty in these results. The Phase II program was used to cross check the mechanical assessment by assuming that HPT performance was as predicted and determining the Stage 2 clearance required to match the measured performance. Results of this analysis are discussed in Section 6.1.4 along with other HPT performance results.

Low Pressure Turbine Clearances

LPT clearances were not measured during the test. Performance of the LPT was compared with that predicted from rig test results without isolating the effects of clearances.

## Correlation of Measurements to Average Plane Conditions

At most major measurement planes in the engine, it was necessary to adjust the measured values of pressure and temperature to determine the average conditions at the component inlet or exit. These adjustments corrected for various typical sampling effects.

### Fan Inlet Pressures

Fan tip inlet pressure was determined by adjusting the inlet rake measurement of total pressure for the inlet recovery (boundary layer losses) and the analytically predicted inlet rake loss. The fan hub inlet total pressure was determined from the inlet rake measured pressure and the inlet rake loss.

Inlet recovery of the bellmouth inlet was analyzed using inlet boundary layer rake data as discussed in Section 6.4. The resulting inlet recovery for the ICLS was about 0.08% lower at takeoff conditions than predicted as shown in Figure 130. This lower recovery was used for the Phase II analysis.

### Fan Discharge Pressure and Temperature

The measured total pressures and temperatures at the fan bypass discharge were adjusted for the effects of radial and circumferential profiles to determine average fan bypass exit conditions. The momentum weighting, which corrects for the mixing losses due to the radial pressure gradients, was used as calculated in the on-line data reduction program during the test. The corrections for circumferential variations in pressure and temperature were incorporated in the Phase II program.

### Other Correlations

Correlations for other measurements were determined during rig tests or core engine tests. The appropriate adjustments were applied to the ICLS data

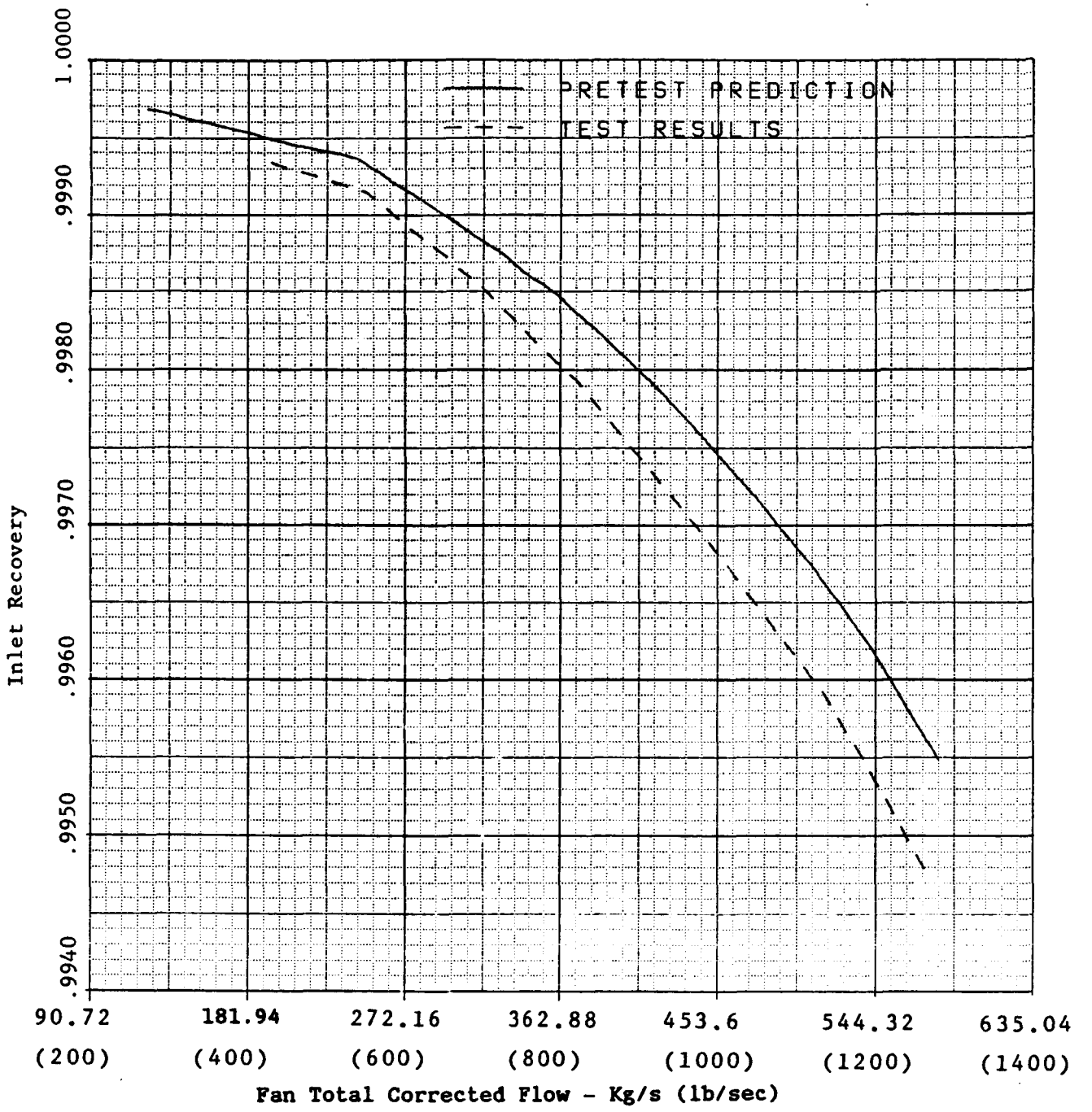


**Figure 130. Inlet Recovery Including Rake Loss.**

to determine fan hub exit pressure and compressor inlet pressure from the compressor inlet rakes, HPT exit pressure and LPT inlet pressure from three HPT exit radial rakes and the compressor OGV exit pressure from the diffuser exit rakes.

### 6.1.3 Overall Performance Accuracy

Figure 131 shows the measured specific fuel consumption (sfc) versus thrust for the performance run. Using a least squares curve fit with 95% confidence bands, it was found that the repeatability of the sfc at maximum thrust was about $\pm$0.6%.

A similar evaluation was made for the exhaust survey run data. Since a large number of readings were taken at each speed point and since they were taken sequentially with only a change in the exhaust rake angular position, these data provided a good indication of the best repeatability which could be expected. As can be seen in Figure 132, the repeatability in this data was also about $\pm$0.6%.

### 6.1.4 Core Performance

Overall core performance throughout the ICLS test was consistent with the performance demonstrated during the core engine test. Overall pumping (Figure 133) agreed well at high power with the level expected for the compressor and HPT clearances encountered during the test. Pumping was somewhat lower at low power.

#### Compressor

#### Efficiency

Compressor efficiency levels in the ICLS were generally lower than those measured in the core engine test; however, the results agreed well with the performance expected at the clearances predicted for the ICLS. Figure 134

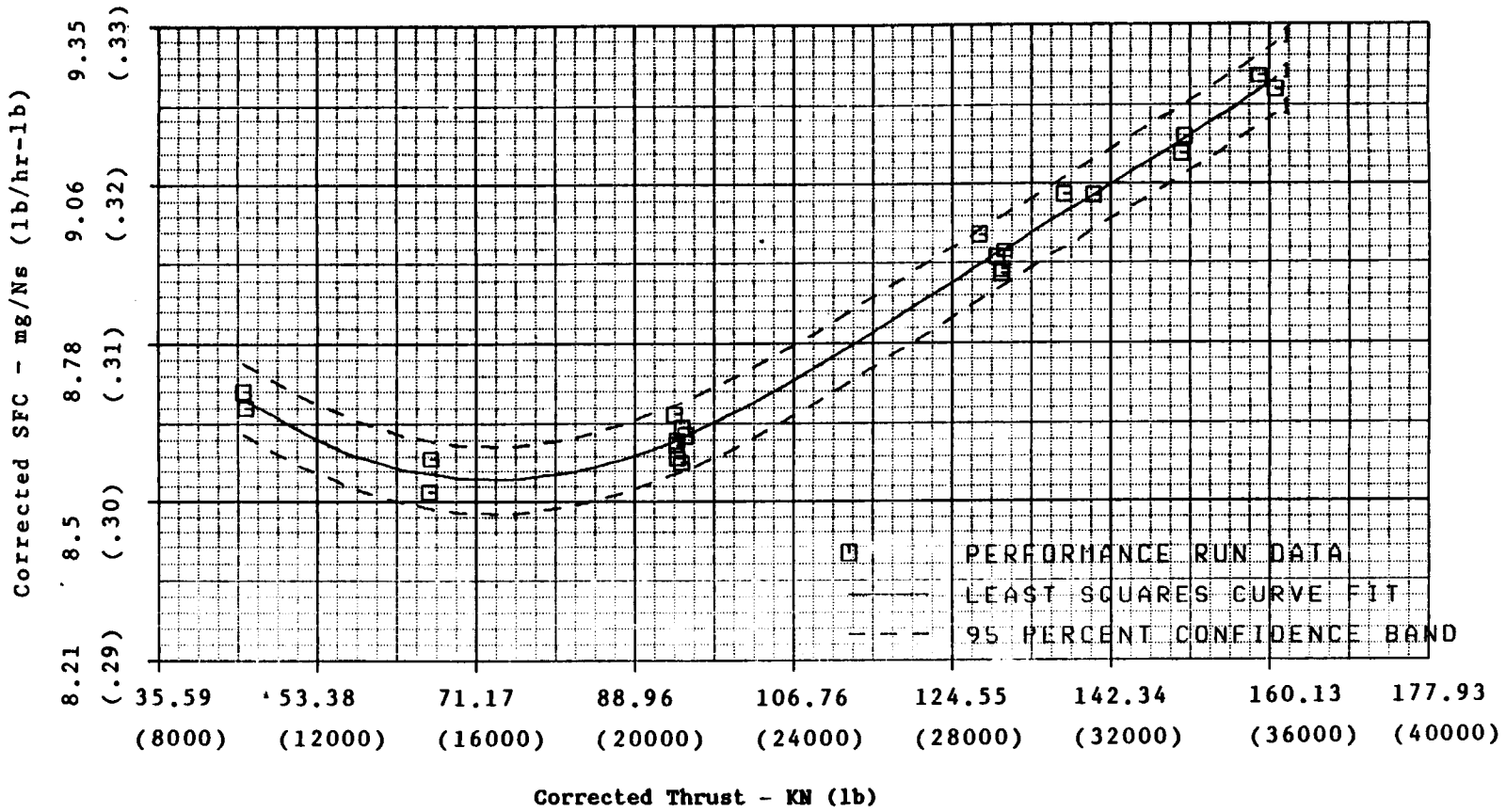


Figure 131. Corrected SFC vs. Corrected Thrust.

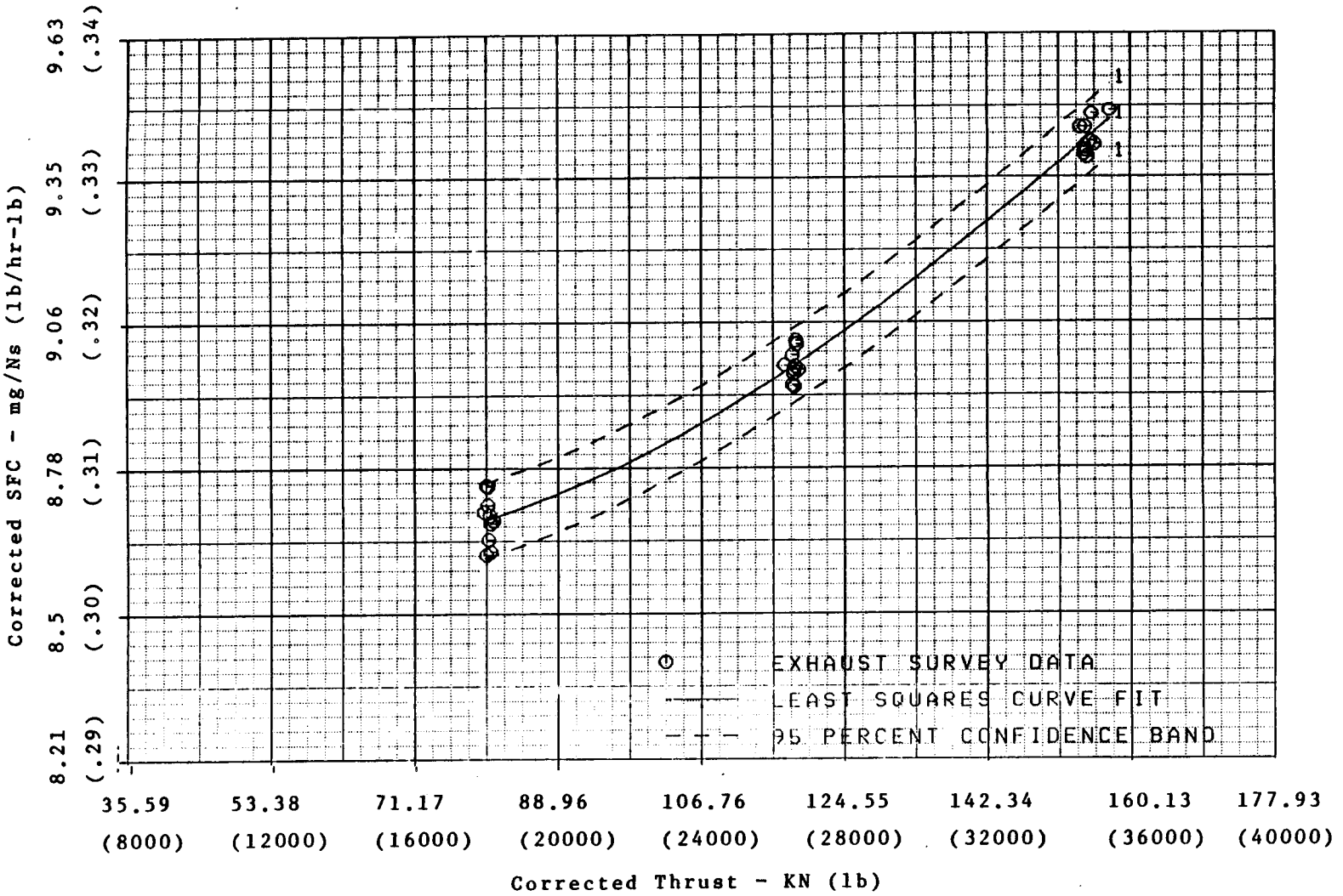


Figure 132. Corrected SFC vs. Corrected Thrust.

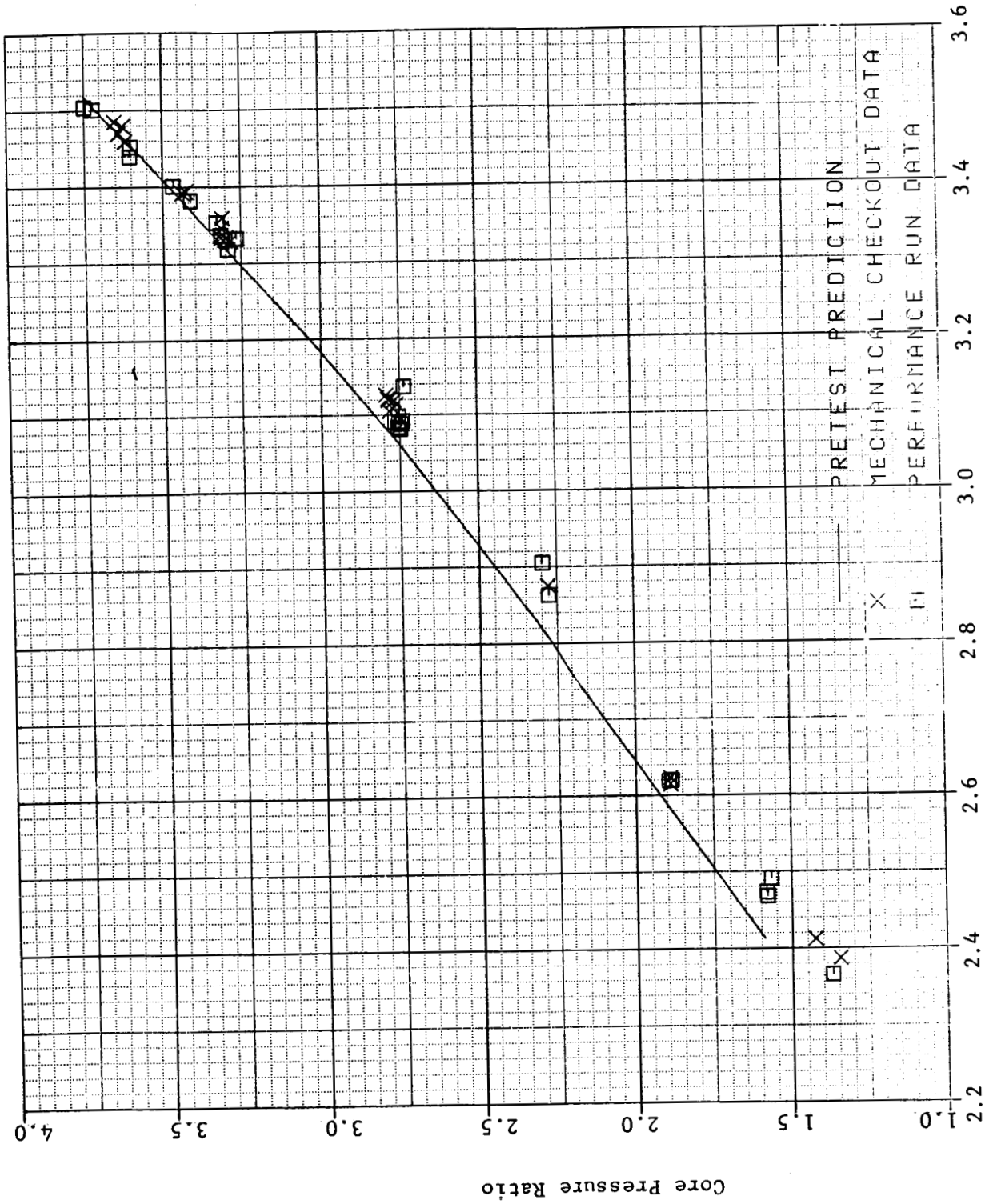


**Figure 133. Core Pumping.**

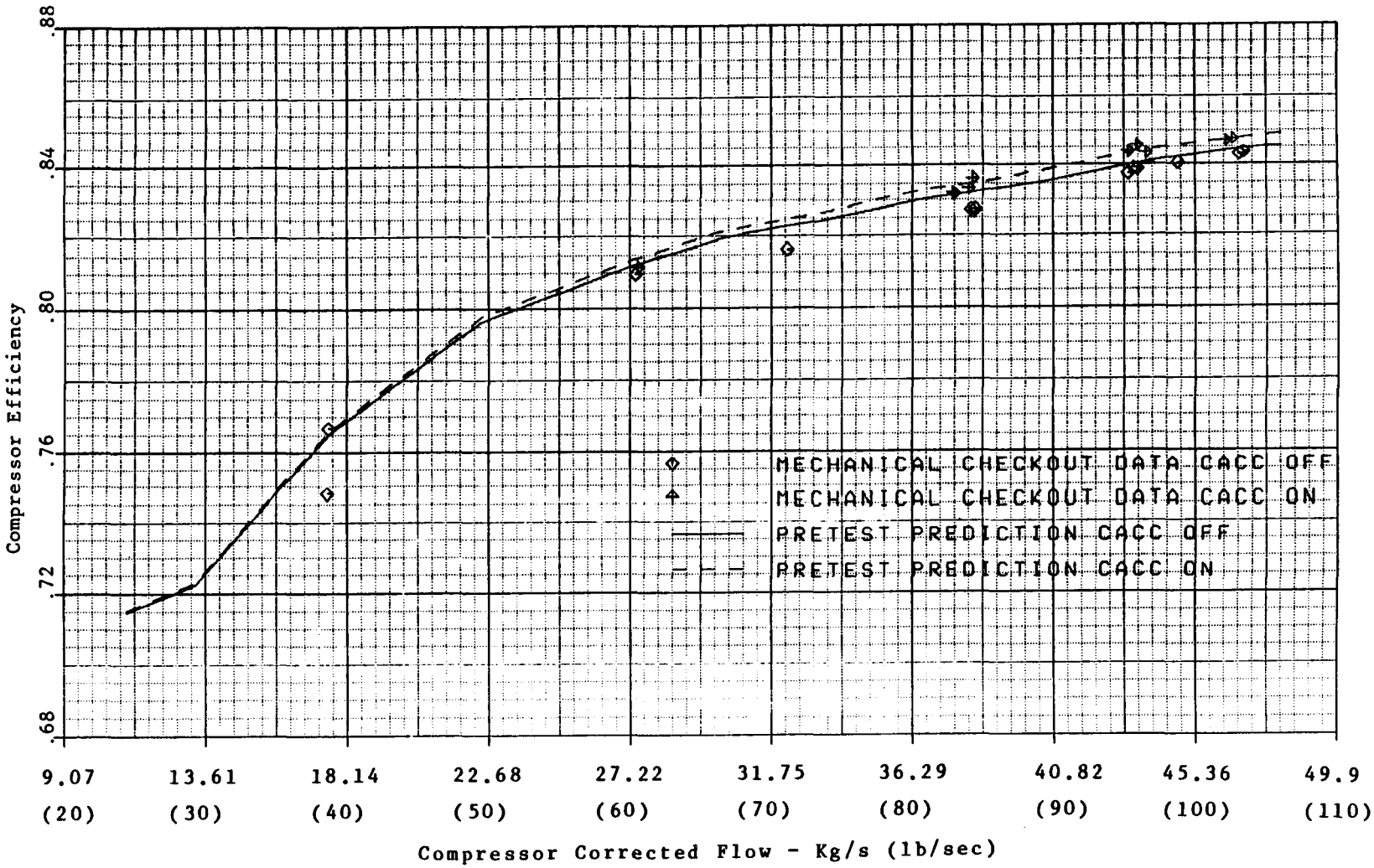


Figure 134. Compressor Efficiency.

shows the comparison of measured and predicted efficiencies for data with compressor active clearance control off and fully on.

Corrected Flow

Compressor corrected flow versus corrected speed is shown in Figure 135 for the mechanical checkout data. Results indicated that the cycle model needed some revision between speeds of 88 to 93% but that flow at takeoff conditions closely matched predictions. The region of greatest mismatch occurred at speeds where the inlet guide vane schedule changed slope rapidly with speed. This is inherently a more difficult region to match with the cycle model.

Combustor

Combustor performance was essentially unchanged from the core test.

HP Turbine

The most significant factor affecting the HPT performance in the ICLS engine was the blade tip clearance. In order to evaluate the turbine performance, the measured efficiency was compared with the predicted efficiency at the clearances determined from the mechanical analysis. These results indicated that efficiency was lower than expected as shown in Figure 136.

Since there was some uncertainty in the second stage clearances due to the use of only two clearance probes, the data were also analyzed to determine the stage two clearances required to match measured efficiency with predicted efficiency. The required change in clearance from the mechanical evaluation was found to be larger than reasonable (Figure 137). In addition, the trend of clearance with speed was contrary to the core test experience and the measured ICLS Stage 1 trend.

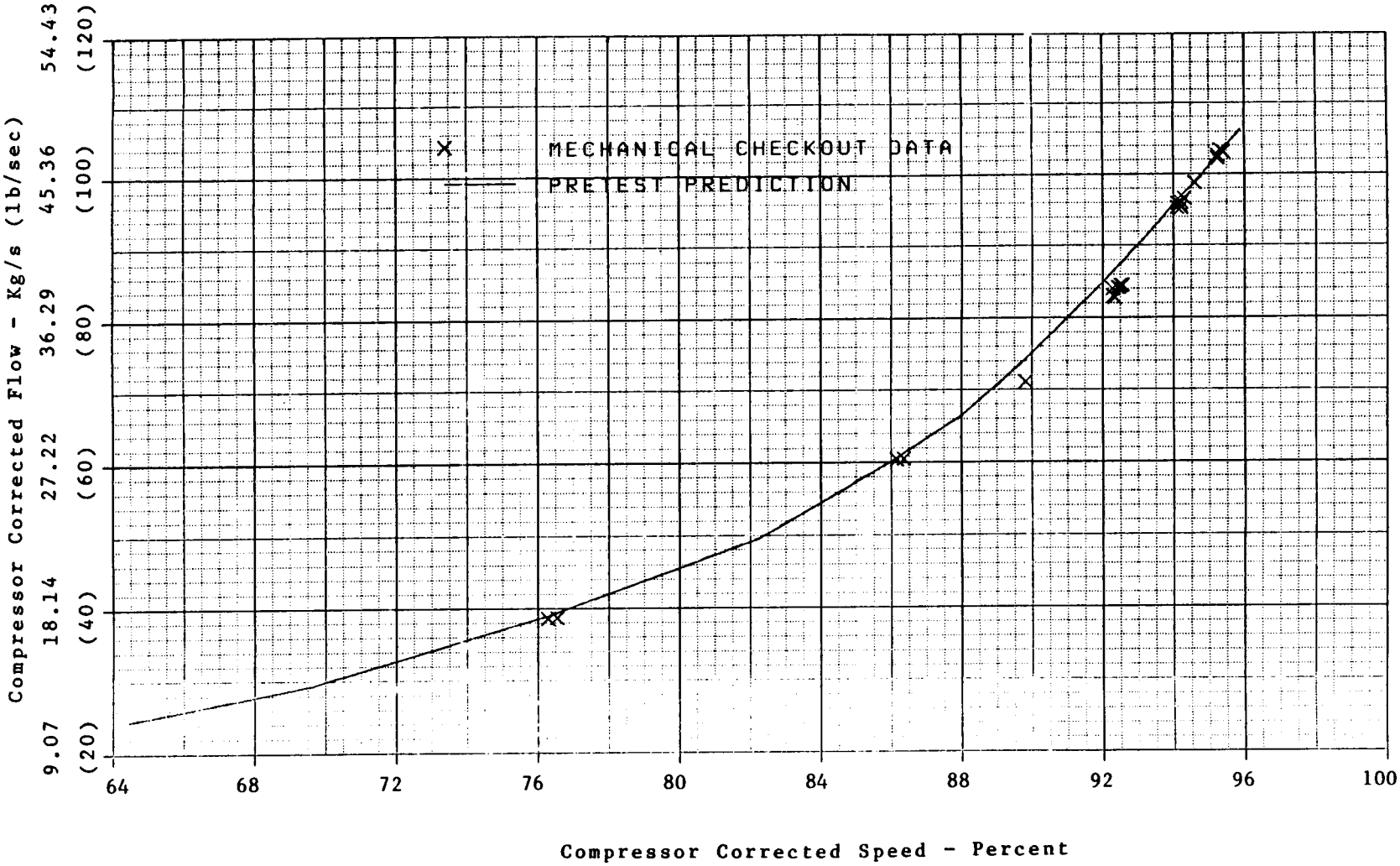


Figure 135. Compressor Corrected Flow.

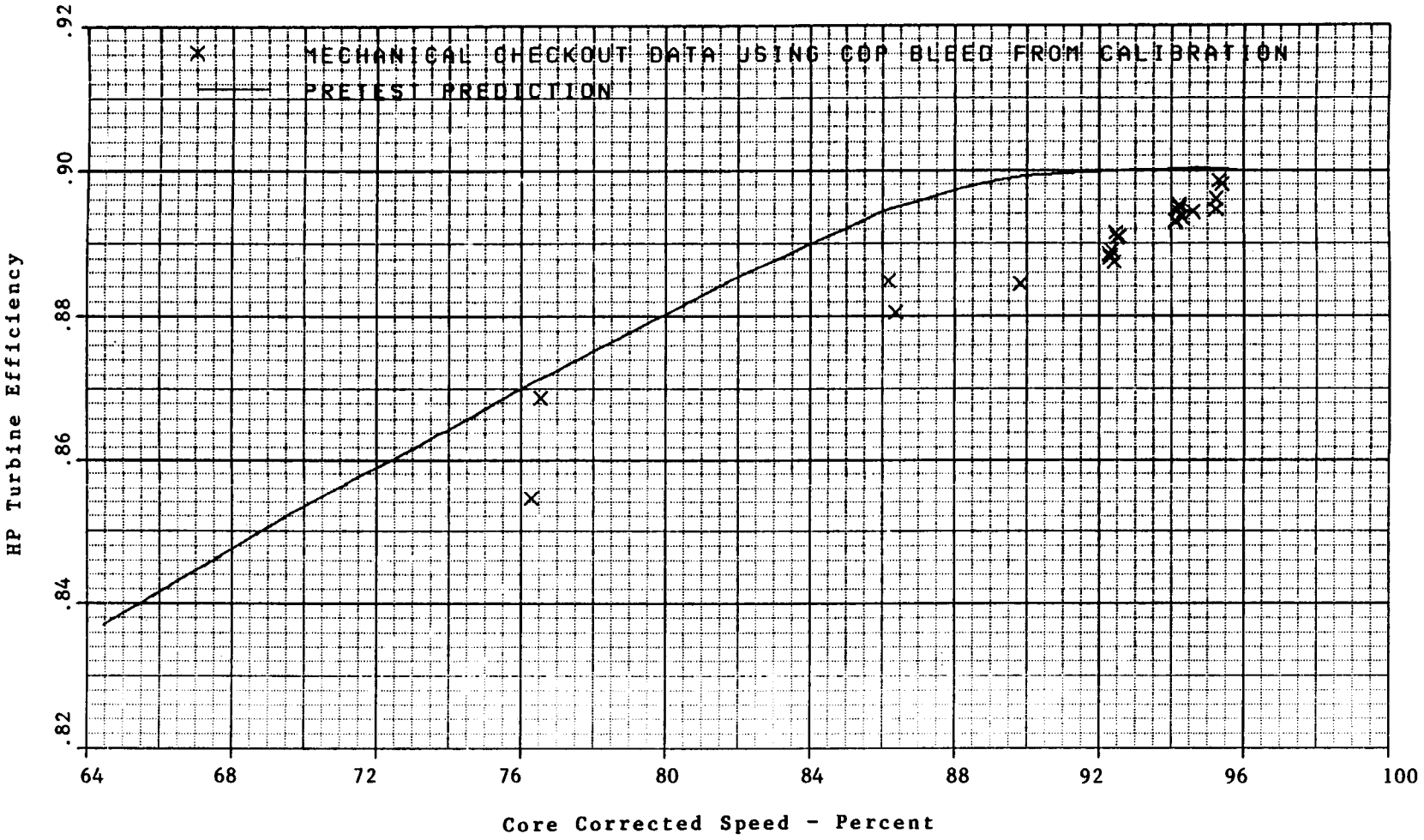


Figure 136. Initial High Pressure Turbine Efficiency.

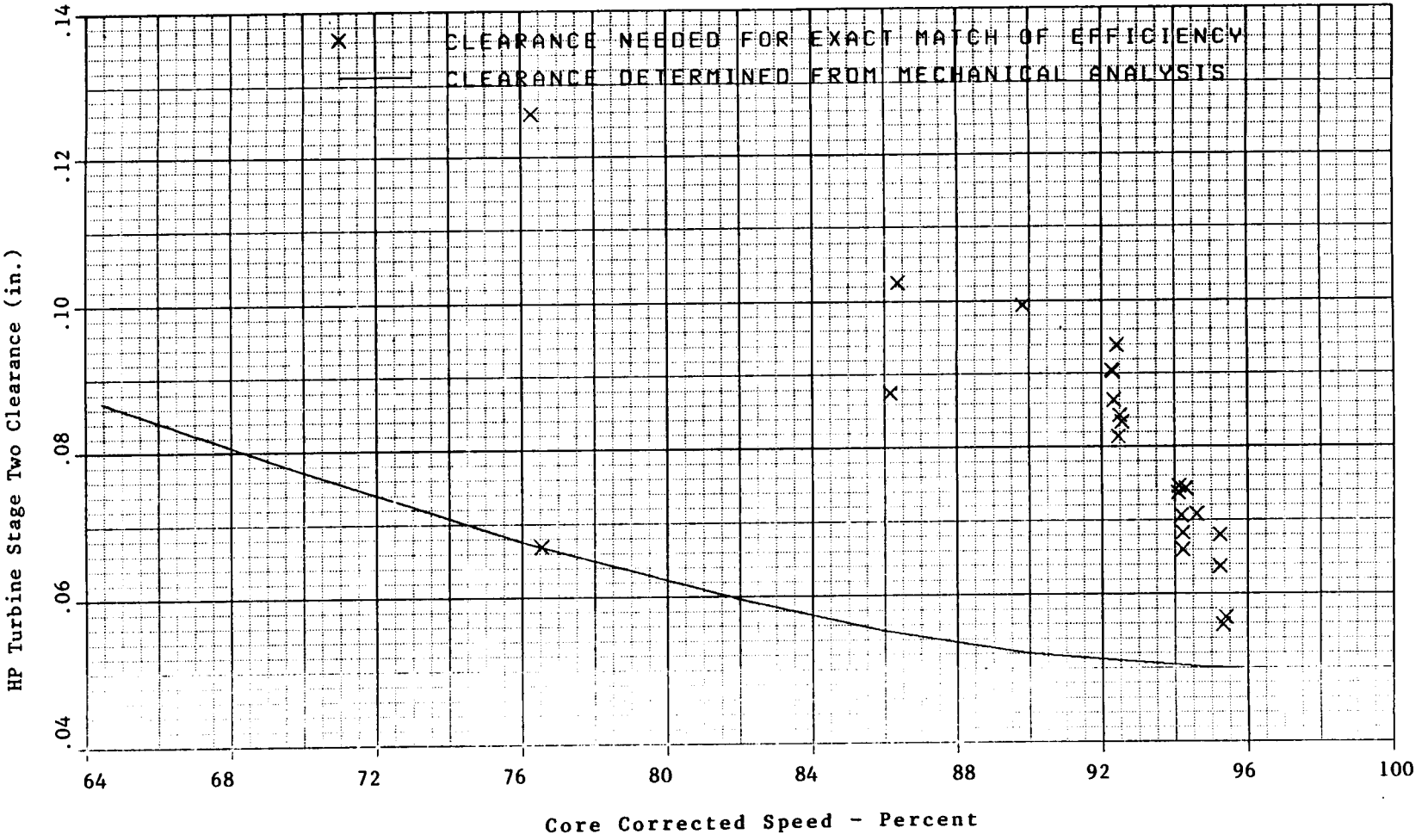


Figure 137. High Pressure Turbine Stage Two Clearance.

Subsequent evaluation showed that higher parasitic bleeds from either 7th stage or compressor discharge would improve the match of measured and predicted HPT efficiency using the clearances determined by the mechanical analysis. Further analysis of the bleeds verified that CDP bleed was higher than initial estimates. The HPT efficiency results using the final CDP bleed levels are shown in Figure 138. This illustrates that HPT performance agreed well with the cycle model prediction at high power and verified the mechanical assessment of Stage 2 average clearance. The difference in efficiency at low power indicates that some uncertainty remains in the parasitic flows and HPT clearances at low power.

Parasitic Flows

The compressor discharge (CDP) bleed was evaluated in conjunction with the HPT analysis since its efficiency is affected by the level of CDP bleed used.

Using the balanced cycle model, it was possible to determine the total CDP bleed flow which would produce an exact match of measured and predicted turbine efficiency. At takeoff conditions the required bleed was higher than the bleed calibration data from the on-line analysis results by 0.3 to 0.4% of compressor flow. The inducer seal flow which is a part of the CDP bleed was evaluated independently by the heat transfer designers and was found to be higher than the calibration results by about 0.35% of compressor flow at takeoff and by about 0.5% at idle. The total CDP bleed was, therefore, increased as shown in Figure 139. When these results were applied to the Phase II cycle analysis, it was found to improve agreement between predicted and measured compressor flow vs. speed and LPT flow function as well as the HPT efficiency.

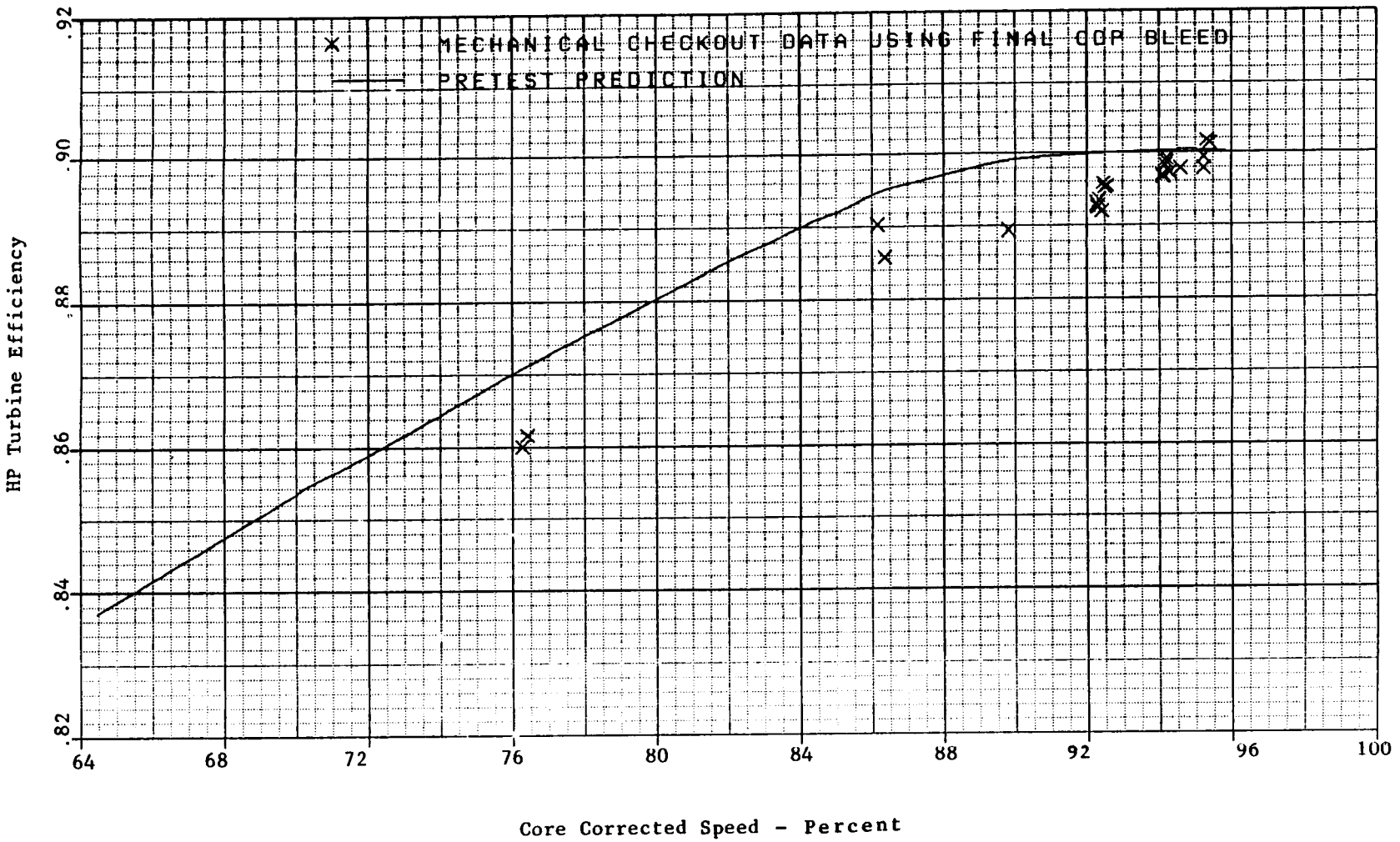


Figure 138. Final High Pressure Turbine Efficiency.

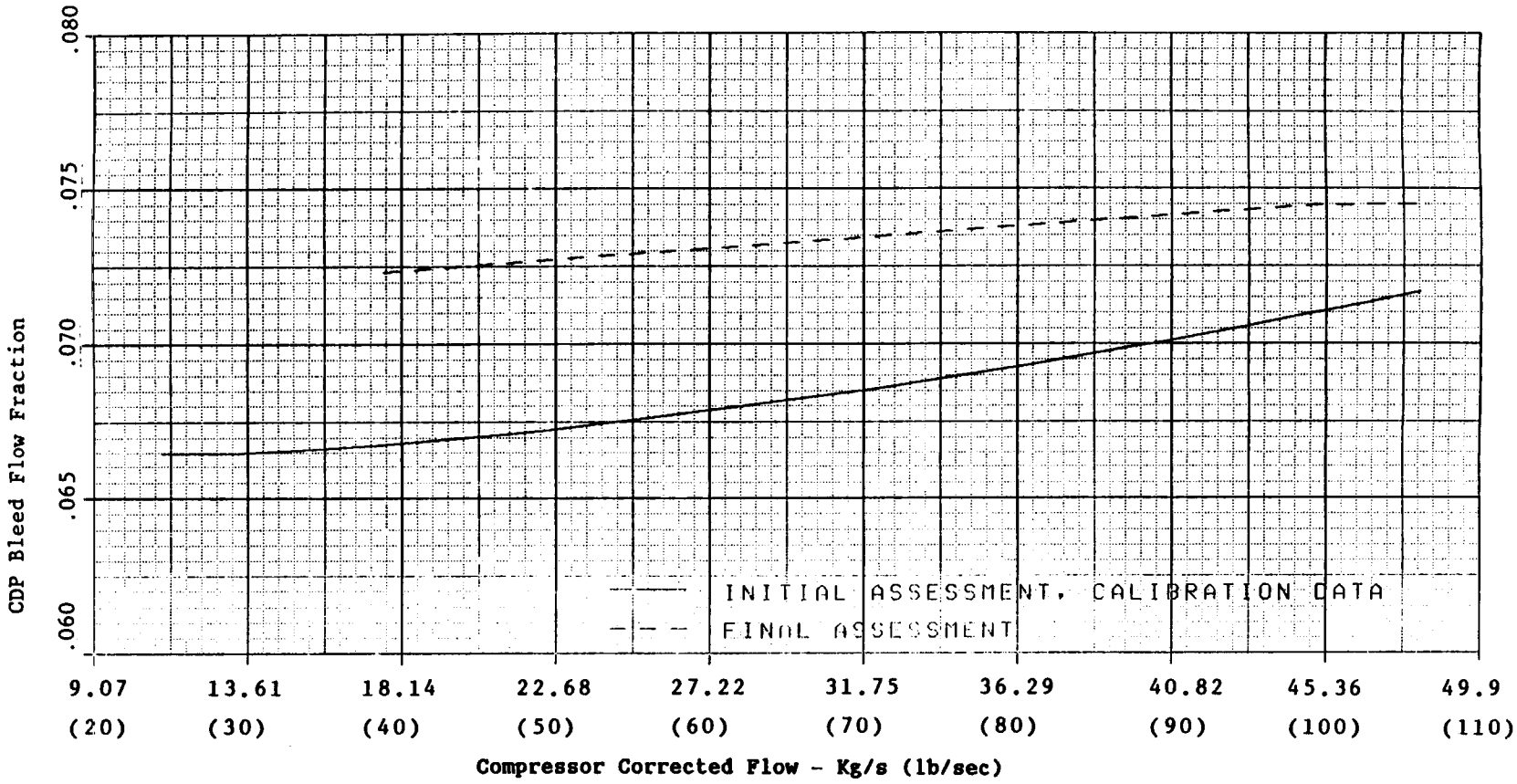


Figure 139. CDP Bleed, Initial and Final Assessment.

### 6.1.5 Fan Bypass Stream Performance

#### Efficiency

Fan efficiency was evaluated for three different operating lines (Figure 140). The performance run data along the lowest operating line were considered the most reliable since inlet temperatures were more uniform than on other runs. Efficiency along this operating line is compared with predicted levels in Figure 141. Near takeoff conditions the efficiency was about 0.6 points lower than predicted and at lower flows it was about 1.0 point lower.

Efficiencies along the two higher operating lines (Figures 142 and 143) were 1.0 to 1.5 points lower than expected levels; however, the inlet temperature distortion observed during these runs created some additional uncertainty in the average inlet temperatures used to determine the efficiency. An error in inlet temperature of 0.5°F would have caused an error in fan efficiency of 0.5 to 1.0 points because of the low temperature rise across the fan. It was concluded that the performance run data provided a better indication of the average fan performance.

#### Corrected Flow Versus Corrected Speed

Fan total corrected flow versus corrected speed is shown in Figures 144, 145, and 146 for the three operating lines. Test results closely followed the predictions.

#### Fan Effect on Overall Performance

At takeoff speed, the fan efficiency difference from prediction was responsible for about an 0.5% difference in specific fuel consumption.

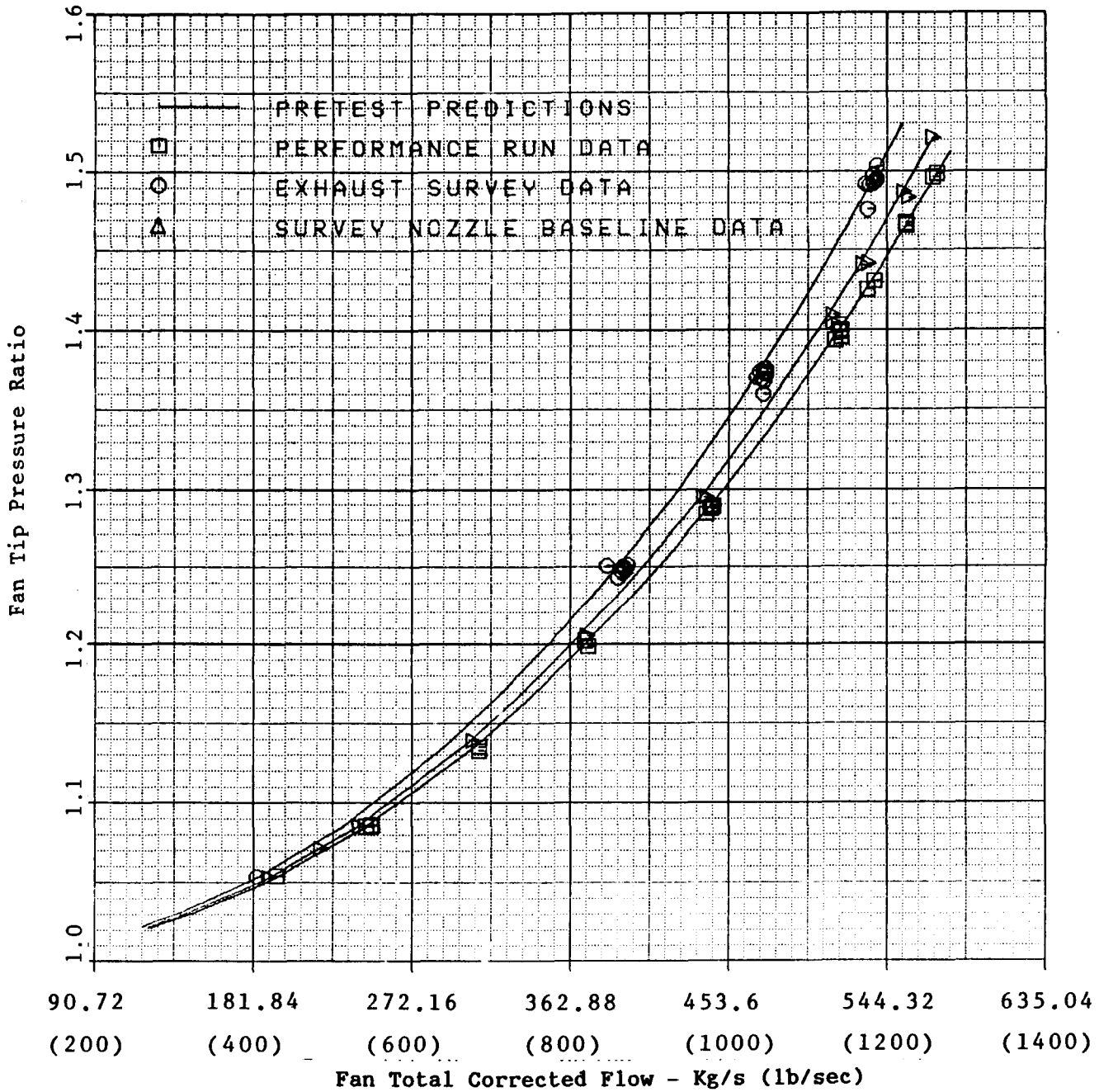


Figure 140. Fan Operating Line.

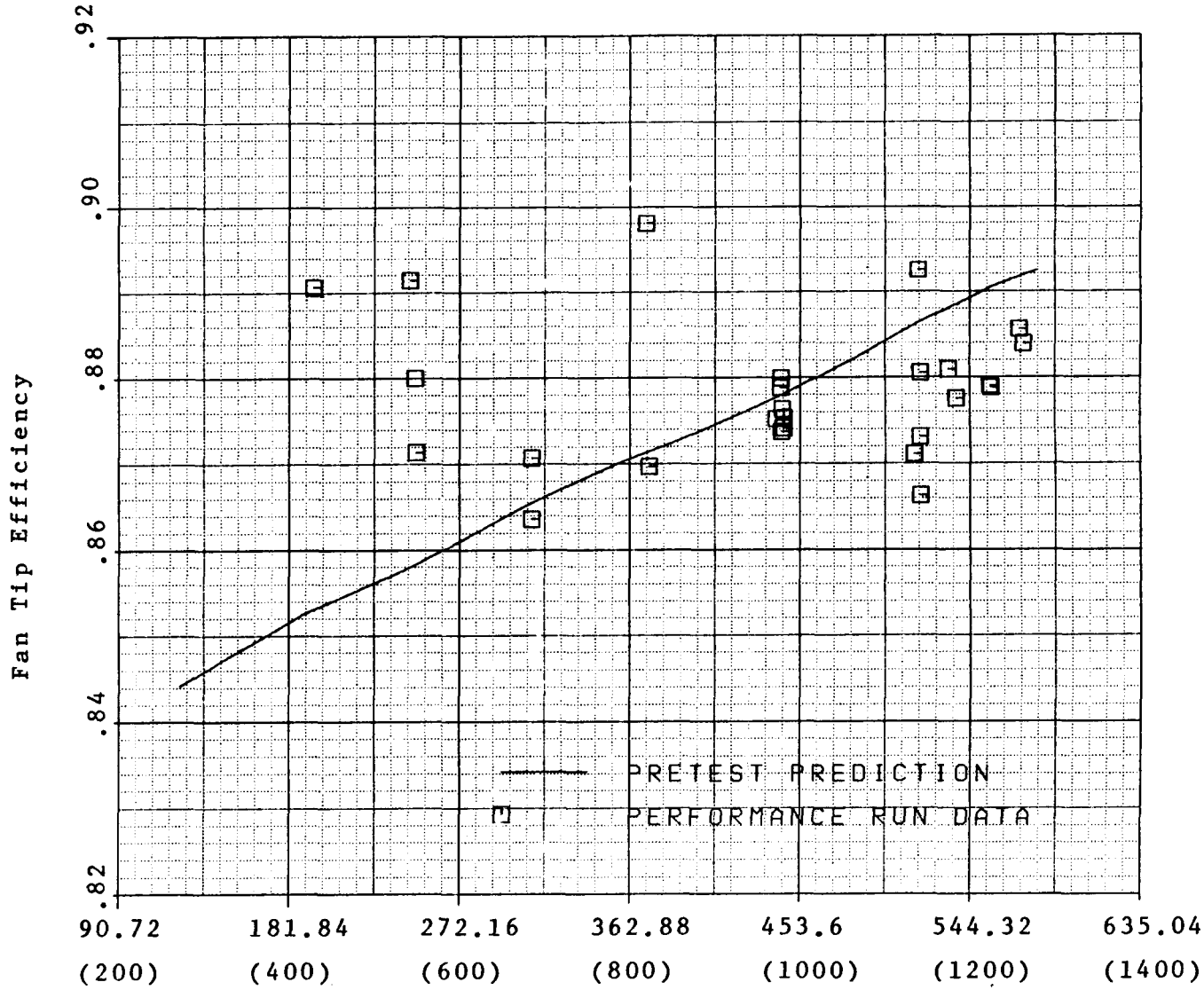


**Figure 141. Fan Tip Efficiency, Performance Data.**

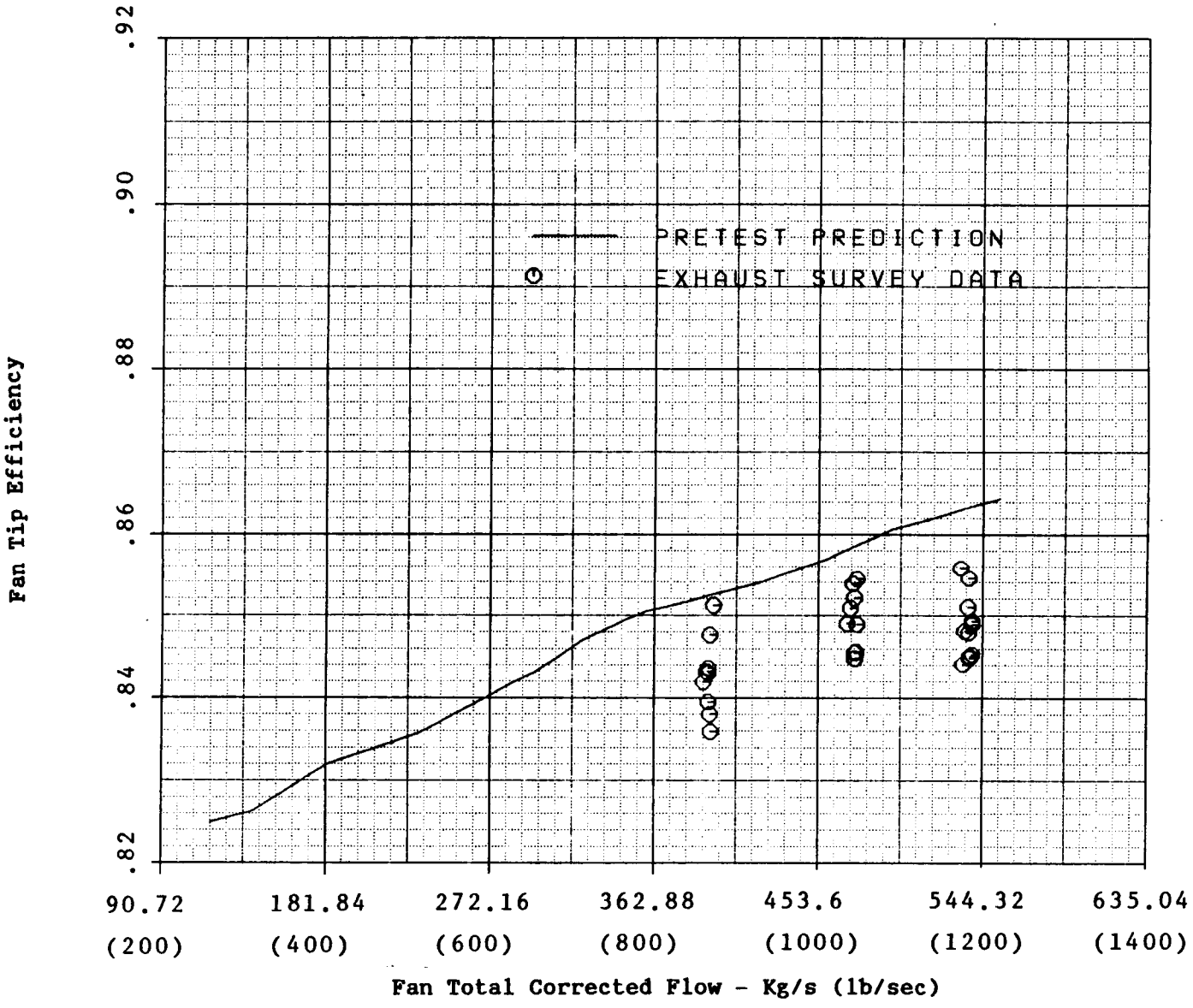


**Figure 142. Fan Tip Efficiency, Exhaust Survey.**

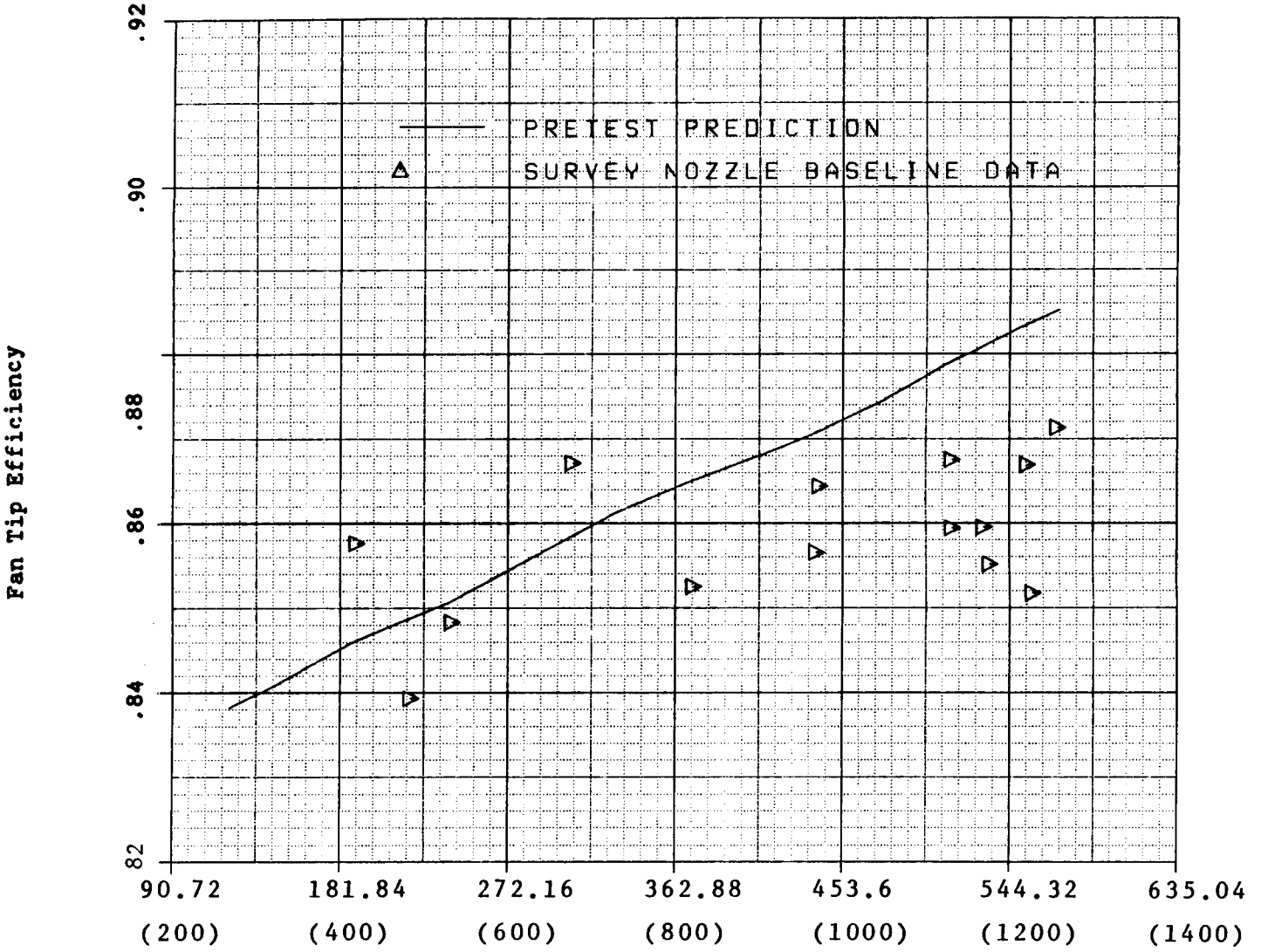


Figure 143. Fan Tip Efficiency, Survey Nozzle Baseline.

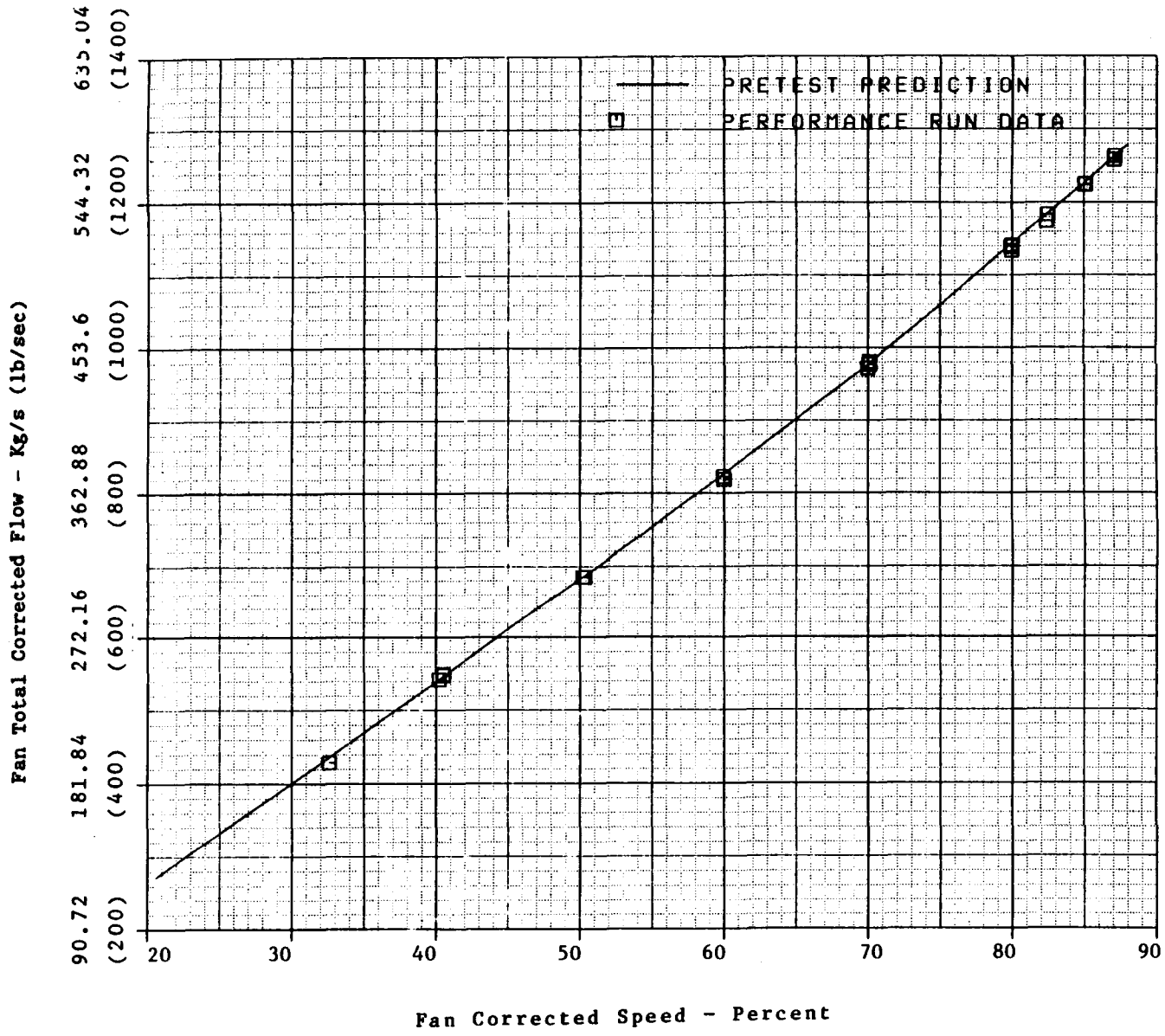


Figure 144. Fan Corrected Flow, Performance Data.

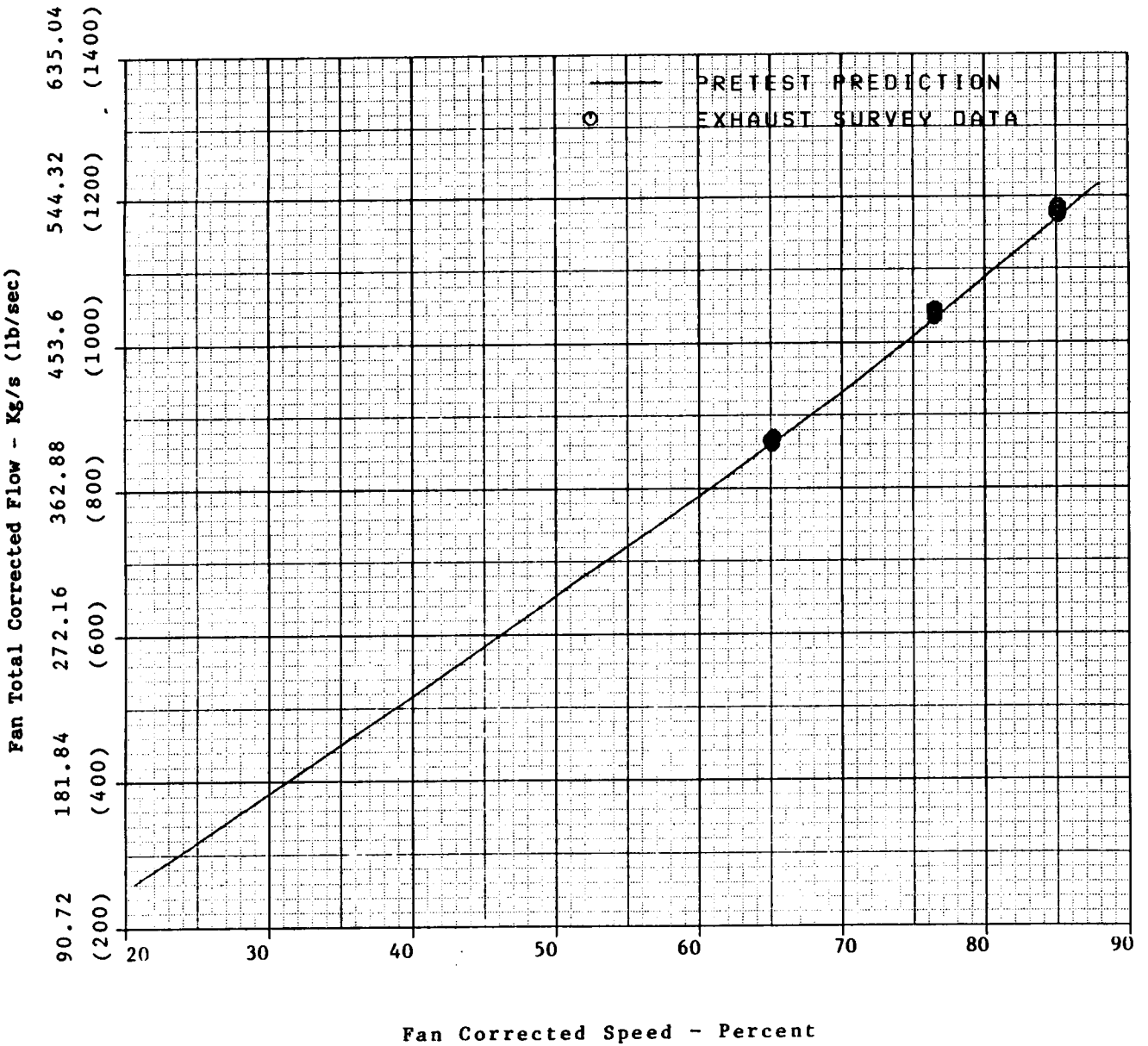


Figure 145. Fan Corrected Flow, Exhaust Study.

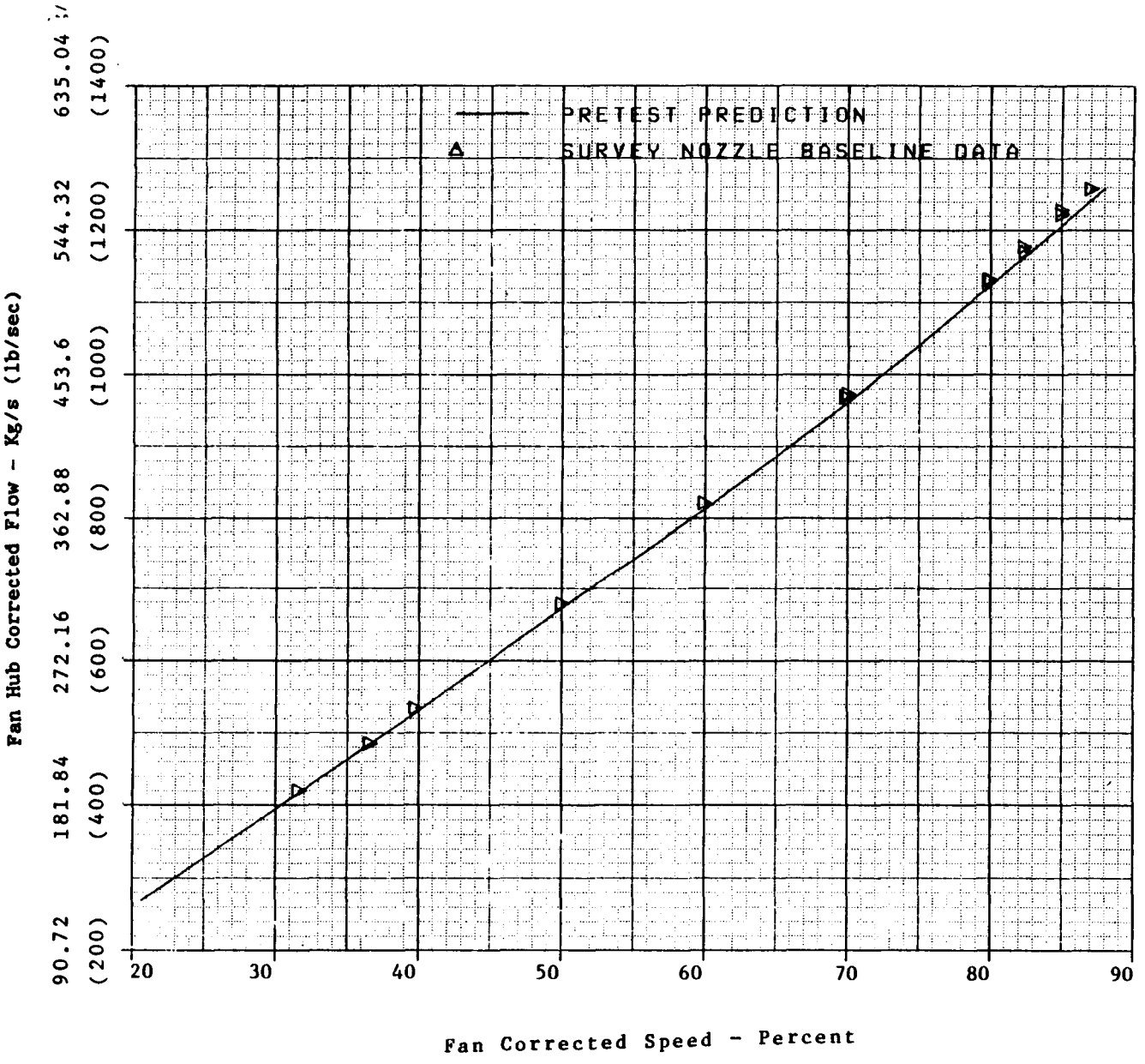


Figure 146. Fan Corrected Flow, Survey Nozzle Baseline.

### 6.1.6 Fan Hub and Quarter Stage

#### Efficiency

The efficiency of the fan hub and quarter stage was about 1.0 point higher than prediction over the full range of operation (Figure 147).

#### Corrected Flow

Corrected flow through the hub was slightly higher than predicted (Figure 148). This was partially due to the change in required core flow resulting from other component performance variations. A single adjustment in the cycle model of hub and quarter stage losses brought both the efficiency and flow/speed into close agreement with the test data.

#### Effect on Overall Performance

The higher than predicted efficiency of the fan hub and quarter stage was worth about an 0.2% improvement in specific fuel consumption.

### 6.1.7 Low Pressure Turbine Performance

#### Efficiency

Low pressure turbine efficiency results are shown in Figure 149 for the data taken during the performance run. Figure 150 shows the data from all runs which could be used to evaluate LPT performance. The general level of efficiency was 1 to 1.5 points lower than expected over most of the operating range.

Because of the lower than expected efficiency indicated by the performance test, an investigation was made into the effects of the HPT discharge/LPT inlet (Plane 42) rakes on LP turbine performance.

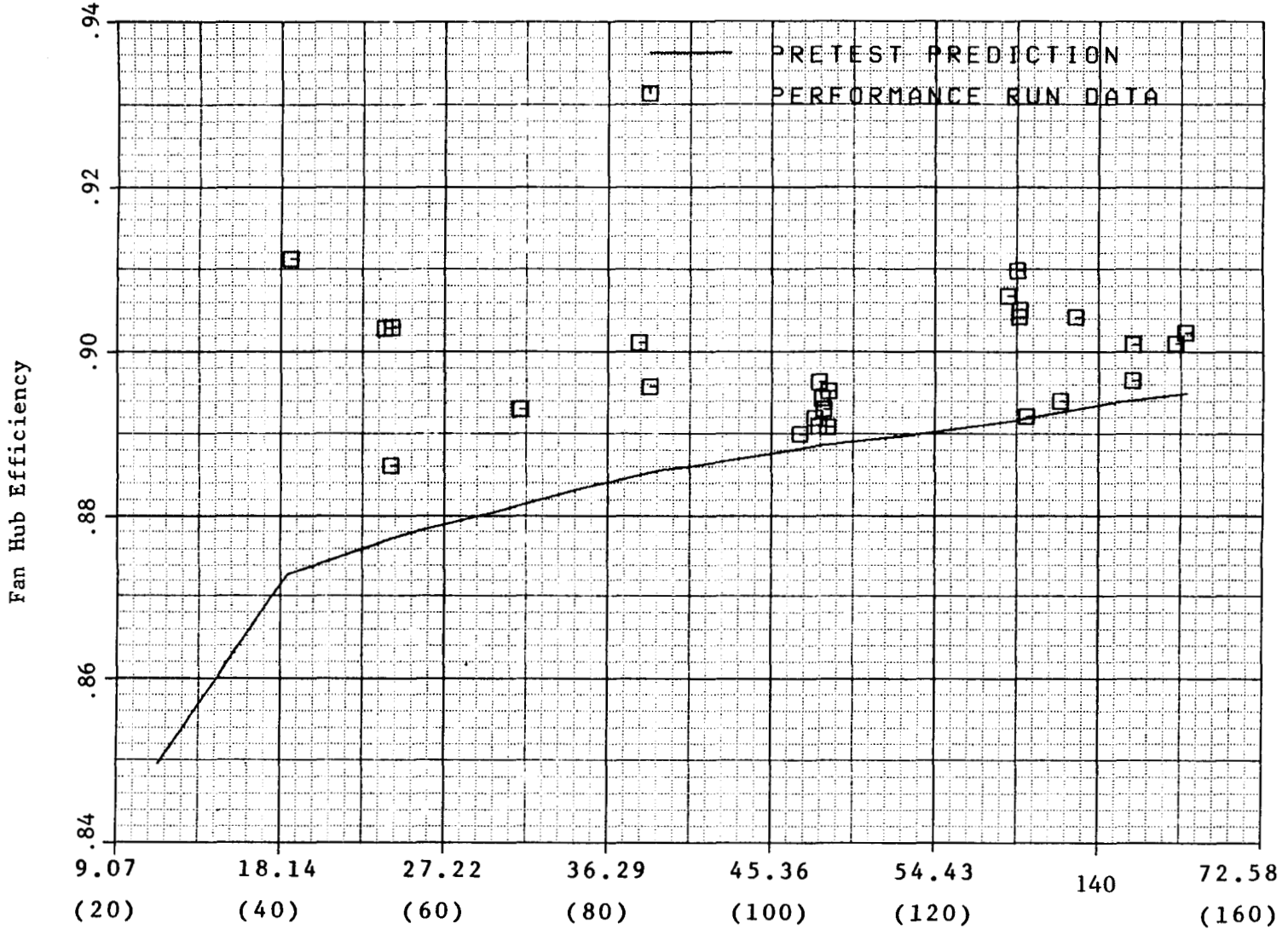


Figure 147. Fan Hub Efficiency.

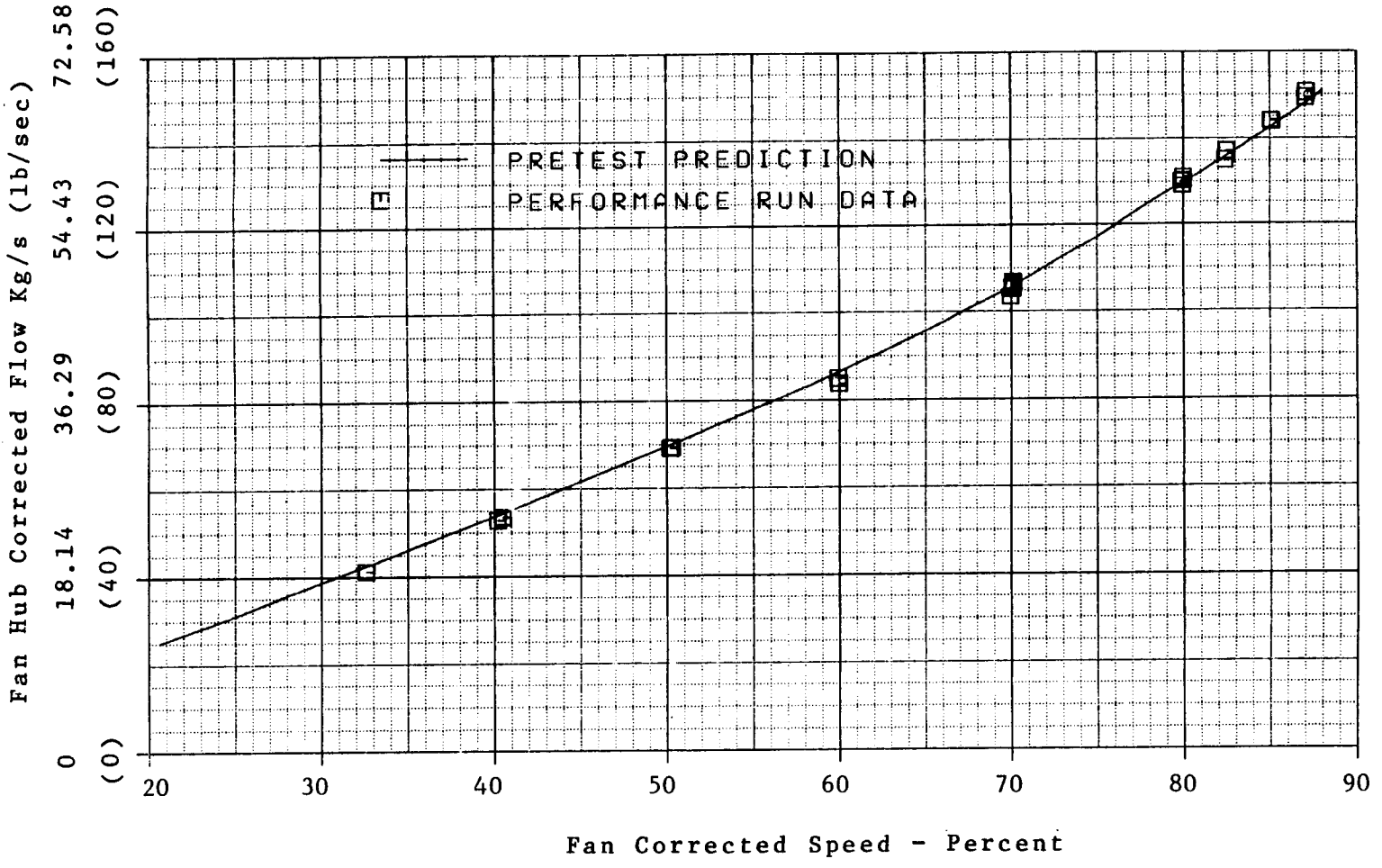


**Figure 148. Fan Hub Corrected Flow.**

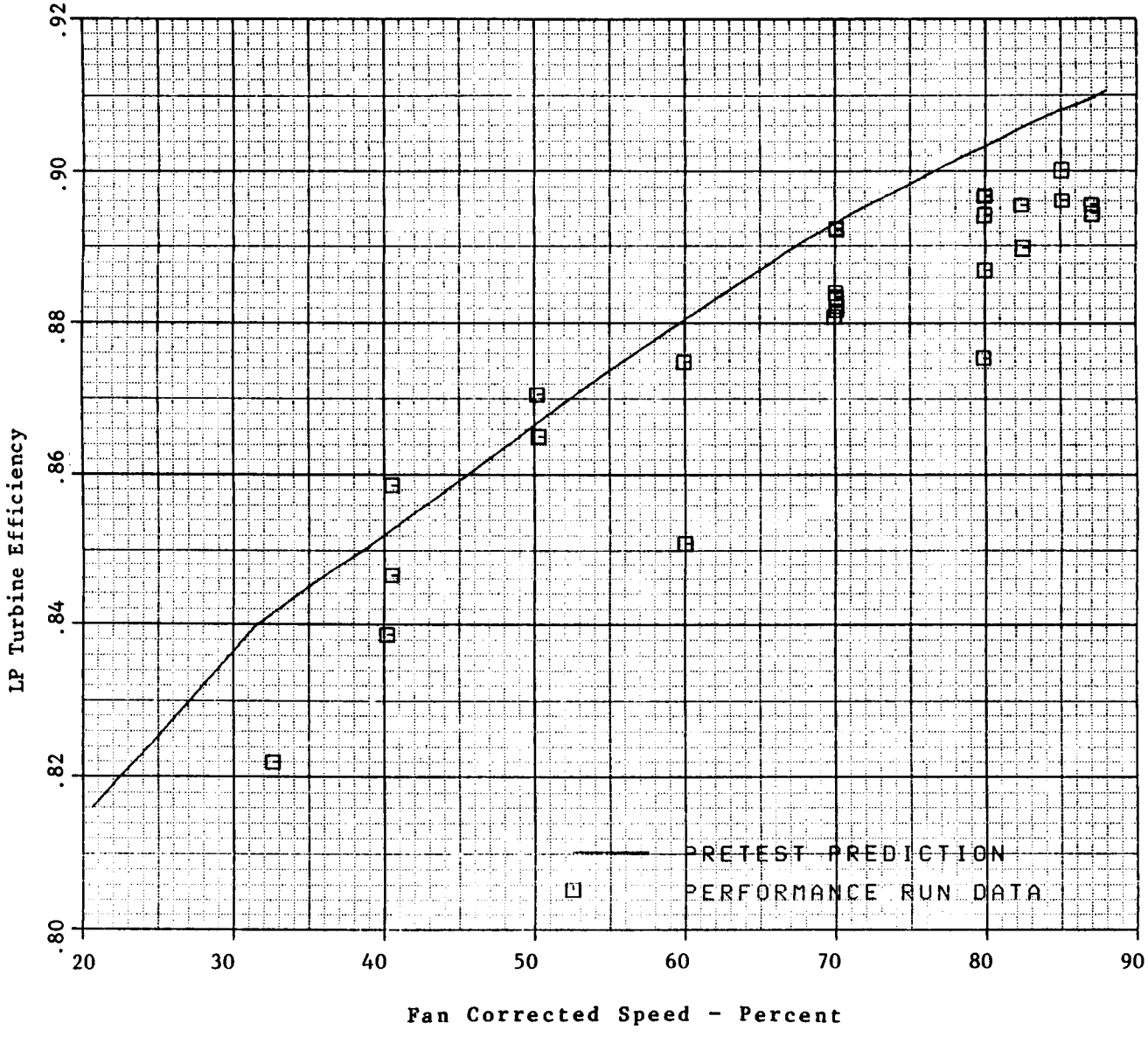


Figure 149. Low Pressure Turbine Efficiency.

ORIGINAL PAGE IS
OF POOR QUALITY

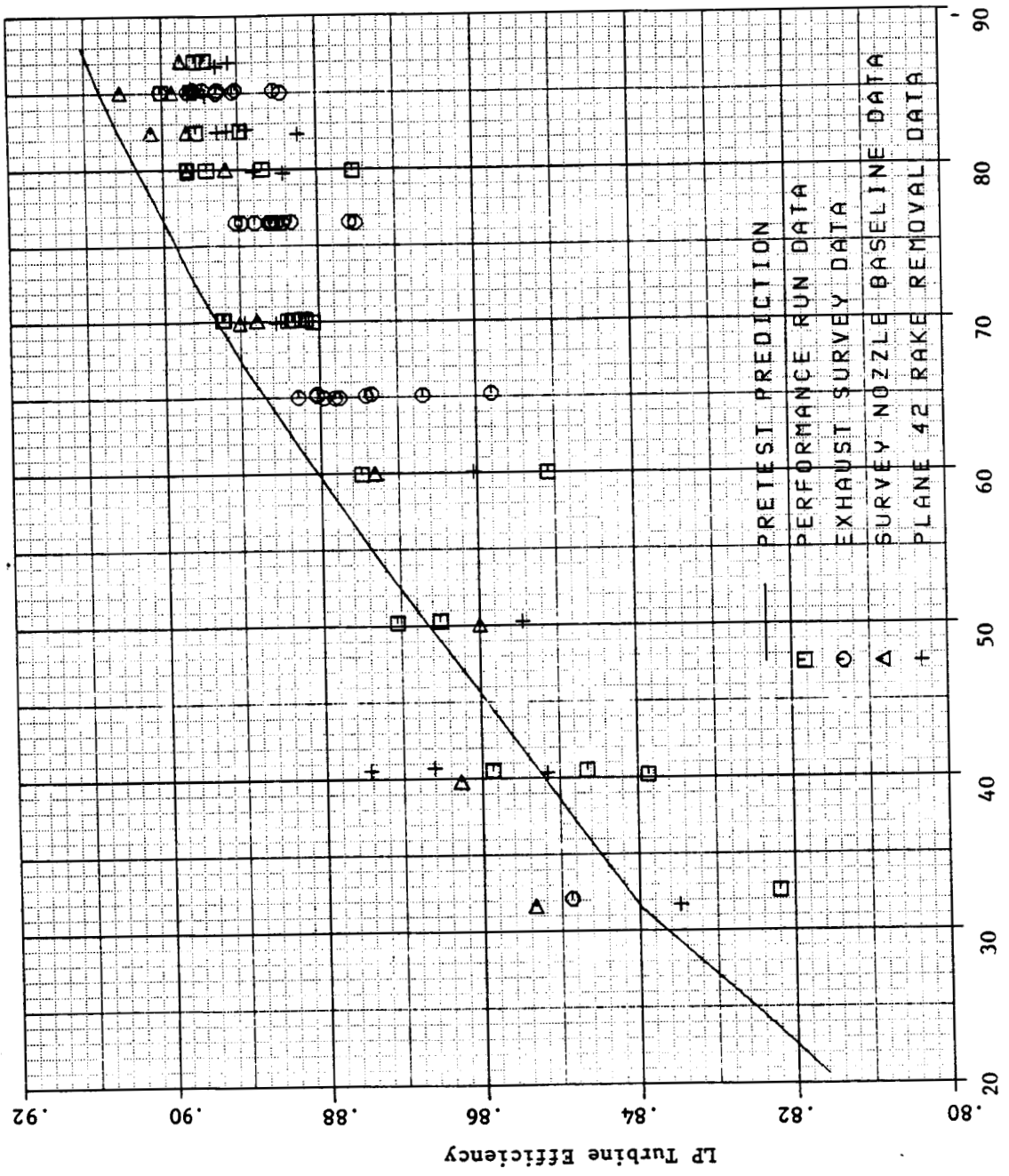


Figure 150. Low Pressure Turbine Efficiency.

Five of the seven rakes were removed after a baseline operating line was run. (The HPT laser clearance probes were also removed at this time which eliminated some CDP bleed used for cooling the probes.) Figure 151 shows the expected performance change along with the test data. No significant change was seen in overall performance which suggested that the losses for the Plane 42 rakes were essentially as expected and that losses due to the CDP bleed for the laser probes may have been lower than expected.

Flow Function

LPT flow function agreed well with expected level as shown in Figure 152. The general trend was within ±1% of prediction across the full range of engine operation.

Effect on Overall Performance

The LPT efficiency difference of 1.0 to 1.5 points was responsible for 0.9 to 1.3% in specific fuel consumption increase above predictions.

### 6.1.8 Exhaust System

It was not possible from direct measurement to isolate individual exhaust system performance parameters since the only internal measurements were at the fan and LPT discharge. The exhaust system parameters which affected overall performance were:

- Overboard leakage
- Fan duct pressure loss
- Core duct pressure loss
- Mixing effectiveness
- Nozzle pressure loss
- Nozzle velocity coefficient
- Nozzle flow coefficient

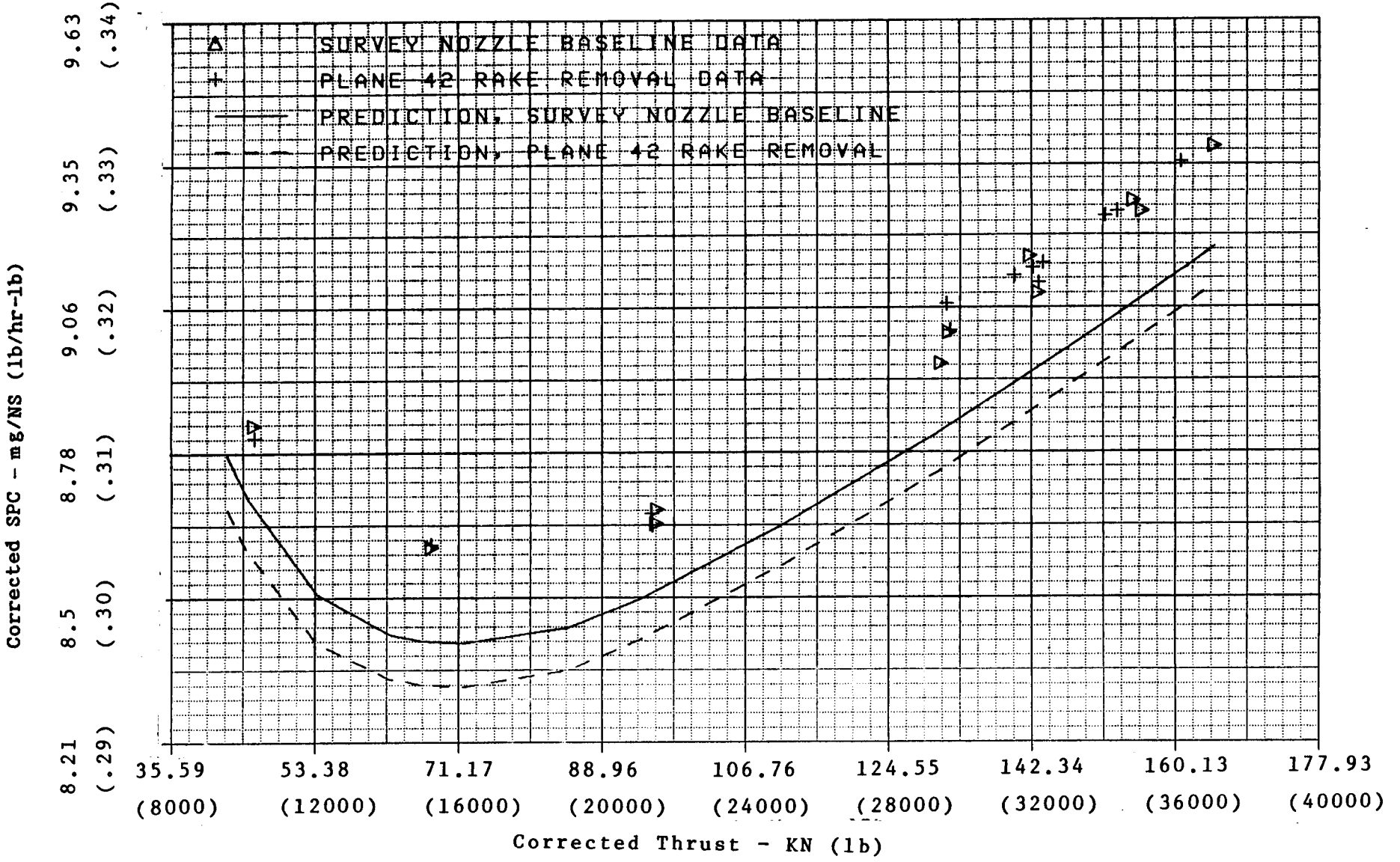


Figure 151. Back to Back Plane 42 Rake Removal.

ORIGINAL PAGE IS
OF POOR QUALITY

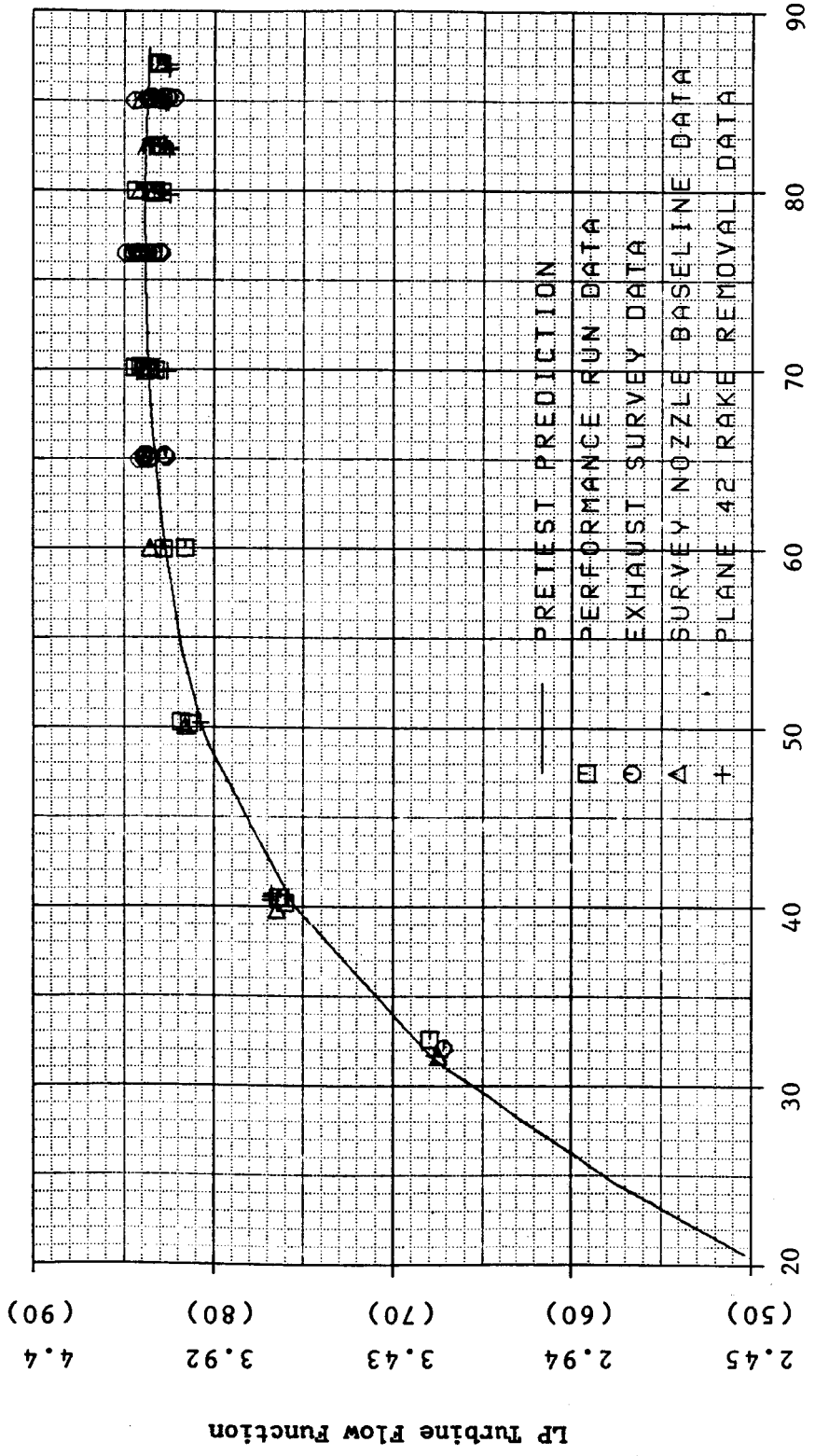


Figure 152. Low Pressure Turbine Flow Function.

In order to complete a balanced cycle match of the test data, it was necessary to adjust two of the exhaust system performance parameters.

The mixing effectiveness results from the exhaust survey were incorporated as input to the Phase II analysis and were not varied in the post-test studies.

An overboard leakage area of 0.00645 $m^2$ (10 $in^2$) was determined from the pretest leak check; however, the number of instrumentation and hardware changes which occurred during the test could have resulted in additional leakage. Since overall performance was relatively sensitive to overboard leakage, the total leakage area was varied to satisfy the data match.

The fan duct pressure loss also had a large effect on overall performance so it was selected as the other variable in the analysis. Since the nozzle was a simple conic design, its coefficients were considered reasonably predictable. Core duct pressure losses required to match the data would have been much larger than predictions, which was considered unlikely. Core duct losses were, therefore, left at predicted levels.

Another factor affecting the selection of leakage and fan duct losses as the exhaust system variables was the unexpected change in specific fuel consumption with the taping of the exhaust acoustic panels during acoustic testing. Since the taping was only in the fan duct, it indicated that leakage and/or fan duct pressure losses were different from predictions.

Leakage Area

The resulting leakage area required to match test data is shown in Figure 153 for the performance run data. An average leakage area of about 0.0193 $m^2$ (30 $in^2$) at high power was indicated by these results. At low power the area agreed more closely with the leak check results.

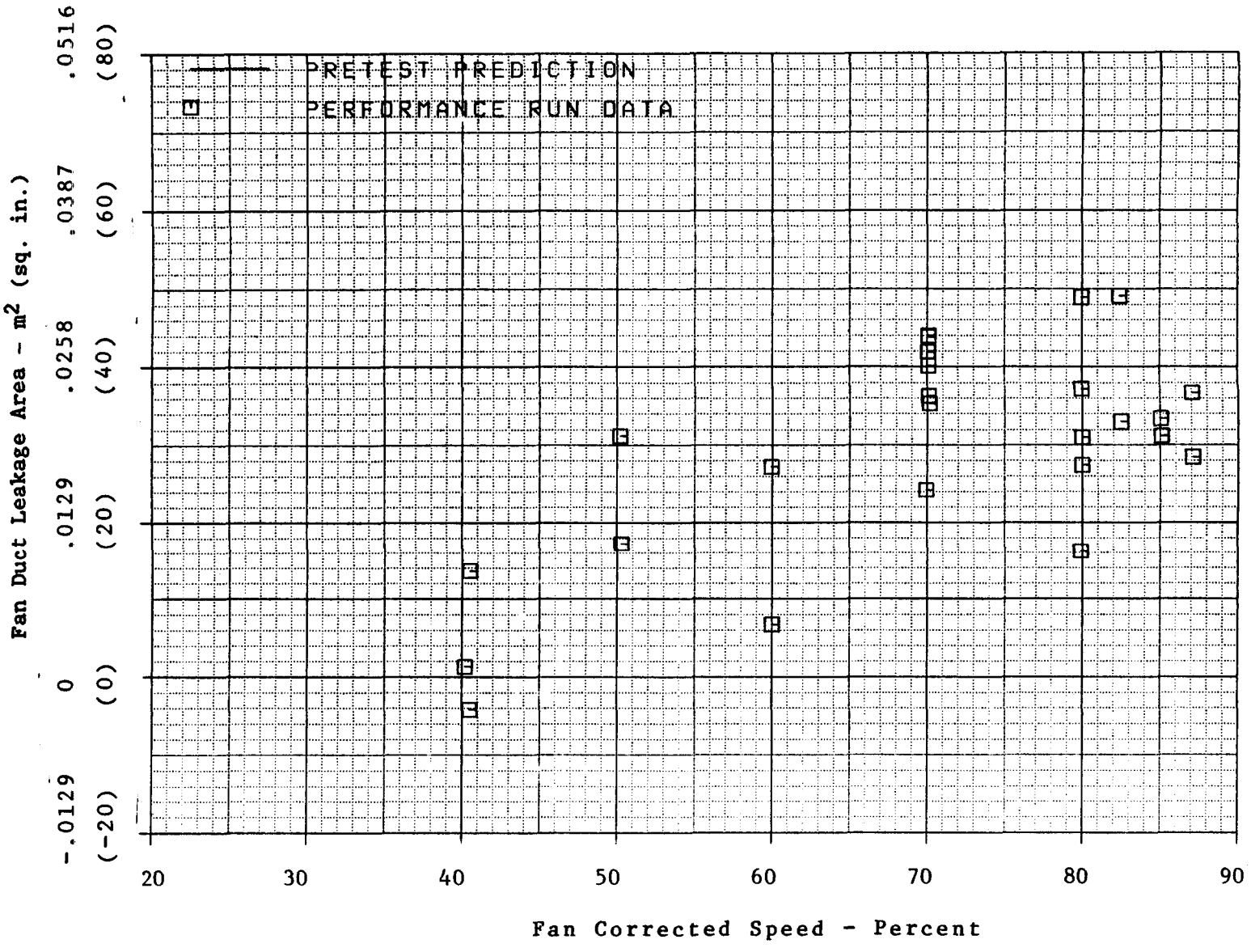


**Figure 153. Fan Duct Leakage Area.**

## Fan Duct Pressure Loss

The overall fan duct pressure loss compared to prediction is shown in Figure 154 as a percent of total pressure. The lower pressure ratio at high power indicated that duct pressure loss could have been about 0.3% higher than expected.

## Acoustic Test Performance Results

The final two runs during the acoustic test were examined in order to determine possible causes for the shift in sfc with the taping of the exhaust acoustic panels (Figure 155). These two runs provided a back-to-back comparison. The exhaust was taped for the next to last run, and for the final run the tape was removed. No other change to the hardware was made between the runs, and the runs were made within a few hours of each other during the final night of testing.

Those parameters which could be directly evaluated with the remaining instrumentation were fuel flow, thrust, core speed, fan speed, engine pressure ratio, fan hub pressure ratio, and LPT pressure ratio. Comparisons at constant fan corrected speed showed that, with the taped exhaust, fuel flow, core corrected, engine pressure ratio, fan hub pressure ratio, and LPT pressure ratio were all unchanged (Figures 156 through 160). Only thrust showed a significant change with the taped exhaust (Figure 161). The only component changes which would produce this type of change were fan duct pressure loss or overboard leakage.

The magnitude of change in either parameter required to produce the thrust change, however, was somewhat larger than reasonable. A leakage area change of 0.0645 $m^2$ (100 $in^2$) or a pressure loss change of 1% was necessary to produce the thrust change. It is most likely that the change was due to a combination of reduced leakage and reduced pressure loss with the exhaust taping. While it was not possible to determine a specific combination of leakage and pressure loss from the acoustic data, the results did support the conclusions from other data that the leakage and pressure loss were higher than predicted.

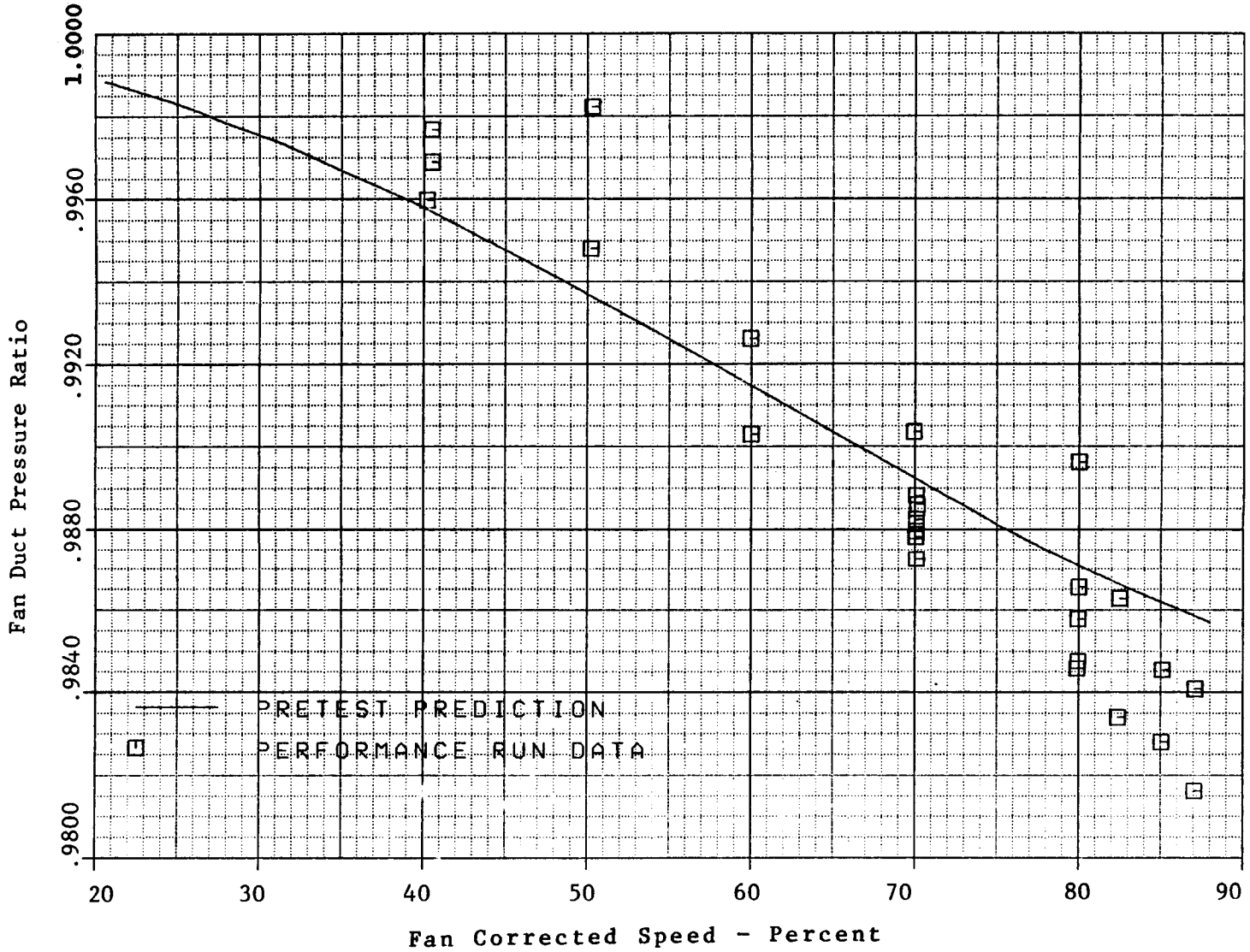


**Figure 154. Fan Duct Pressure Ratio.**

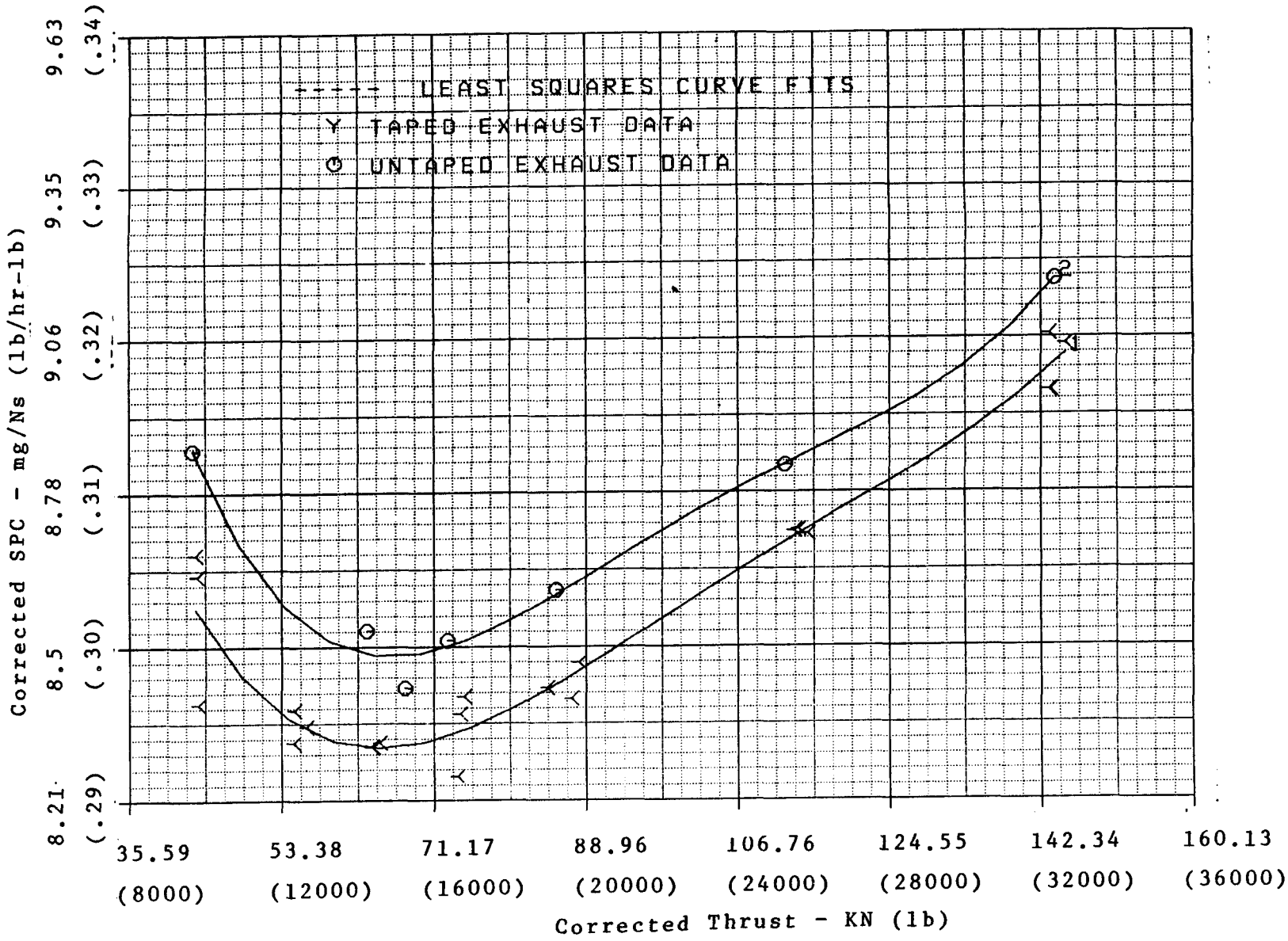


Figure 155. Specific Fuel Consumption, Acoustic Data.

ORIGINAL PAGE IS
OF POOR QUALITY

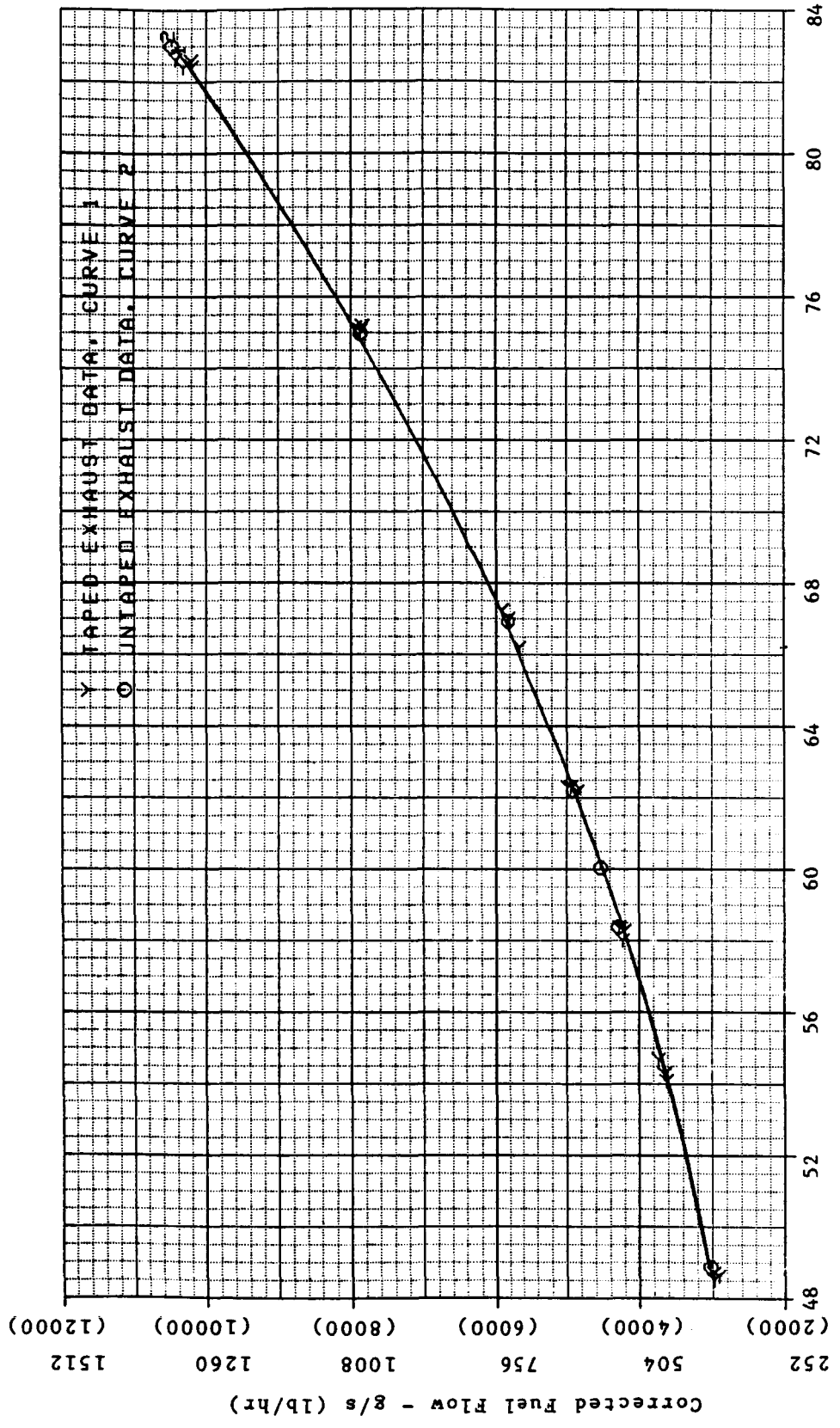


Figure 156. Corrected Fuel Flow, Acoustic Data.

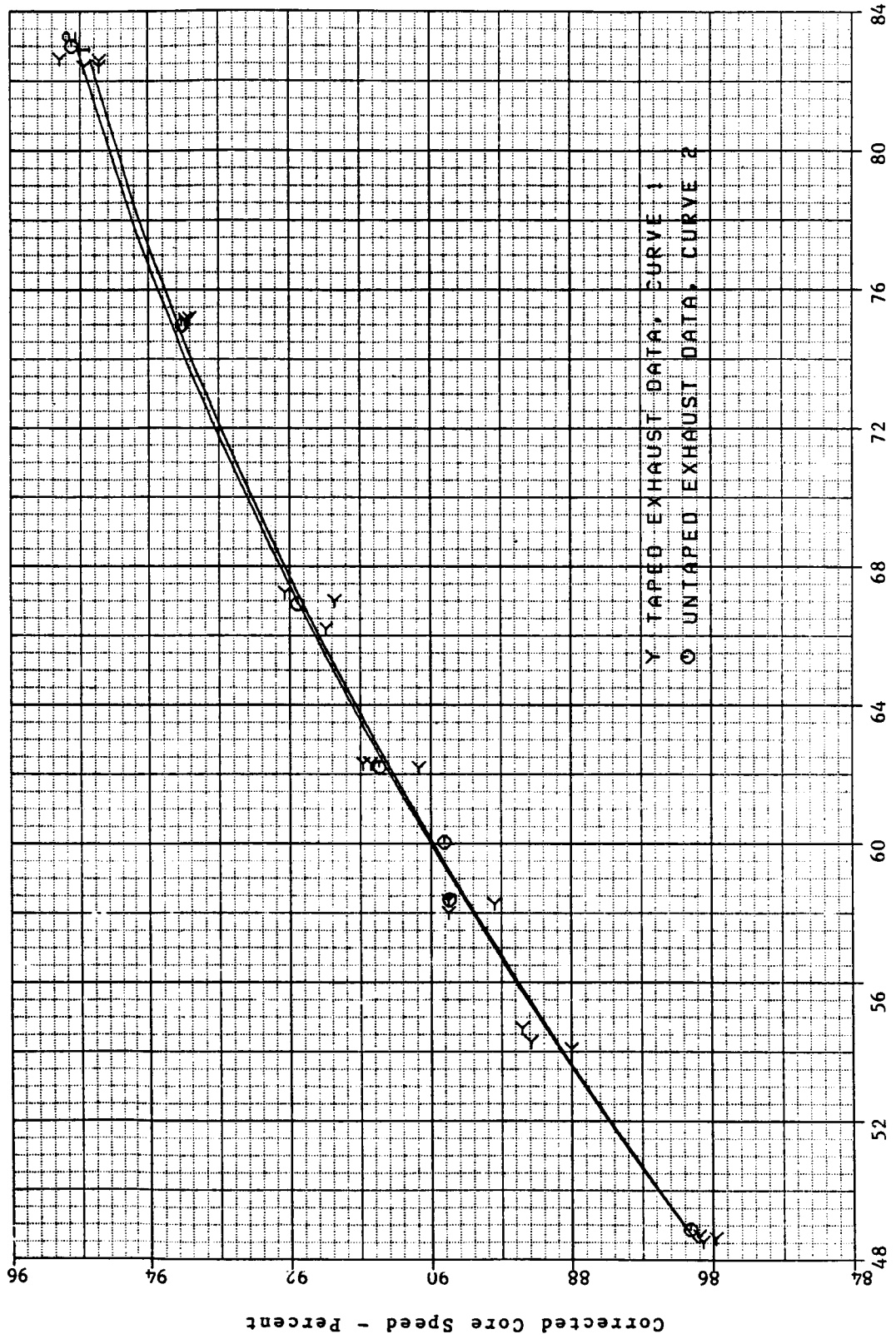


Figure 157. Corrected Core Speed, Acoustic Data.

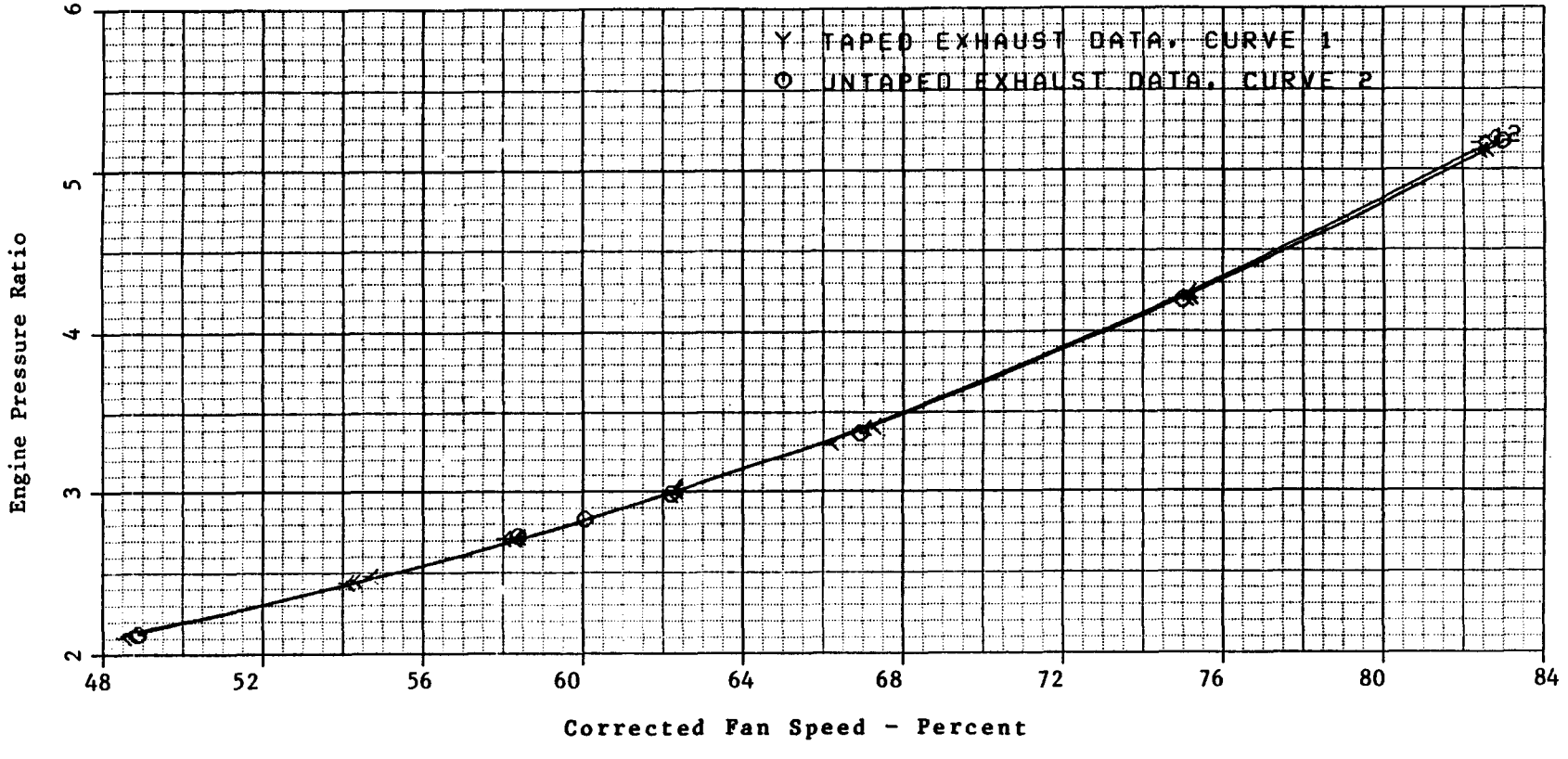


Figure 158. Engine Pressure Ratio, Acoustic Data.

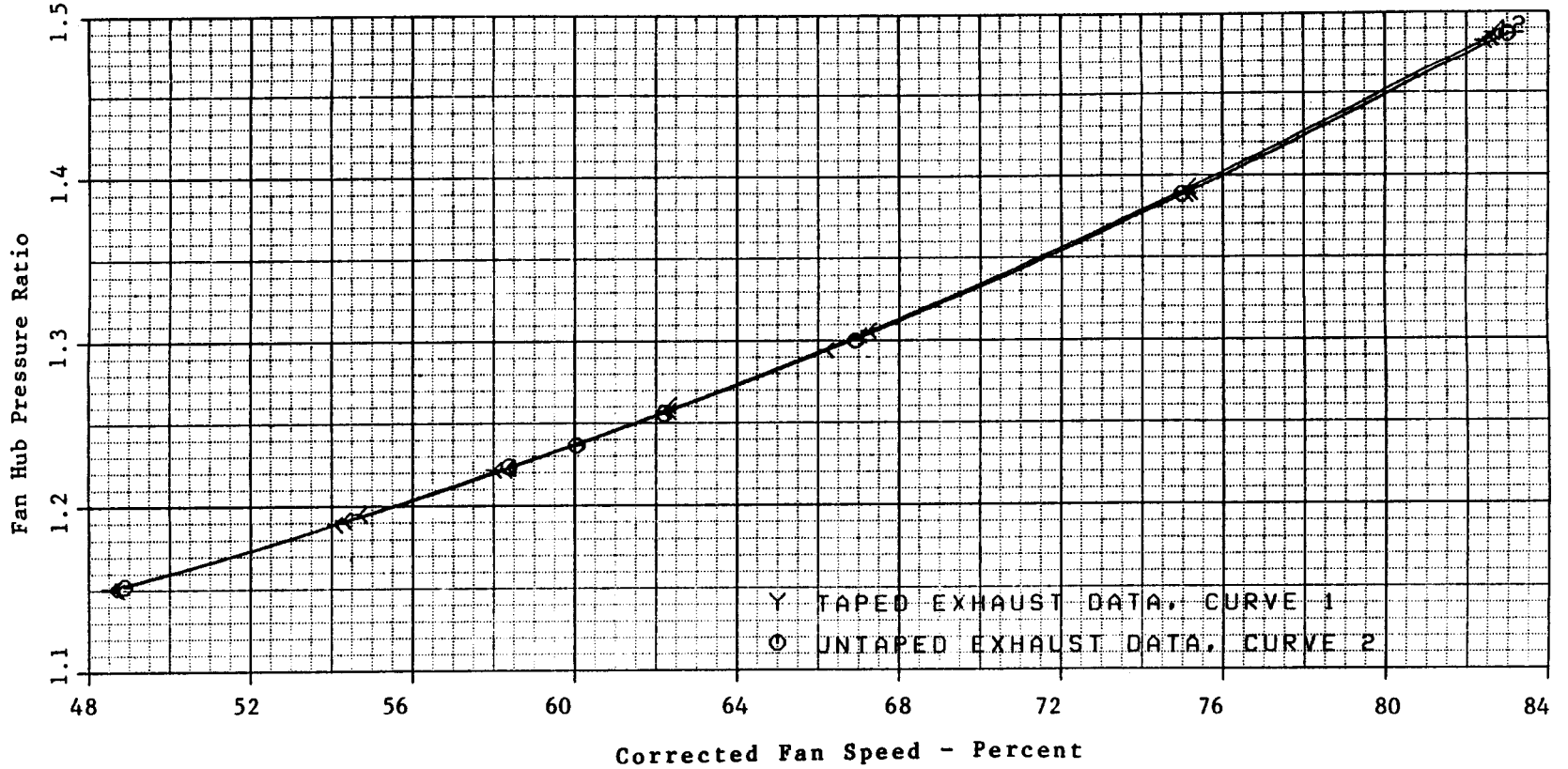


Figure 159. Fan Hub Pressure Ratio, Acoustic Data.

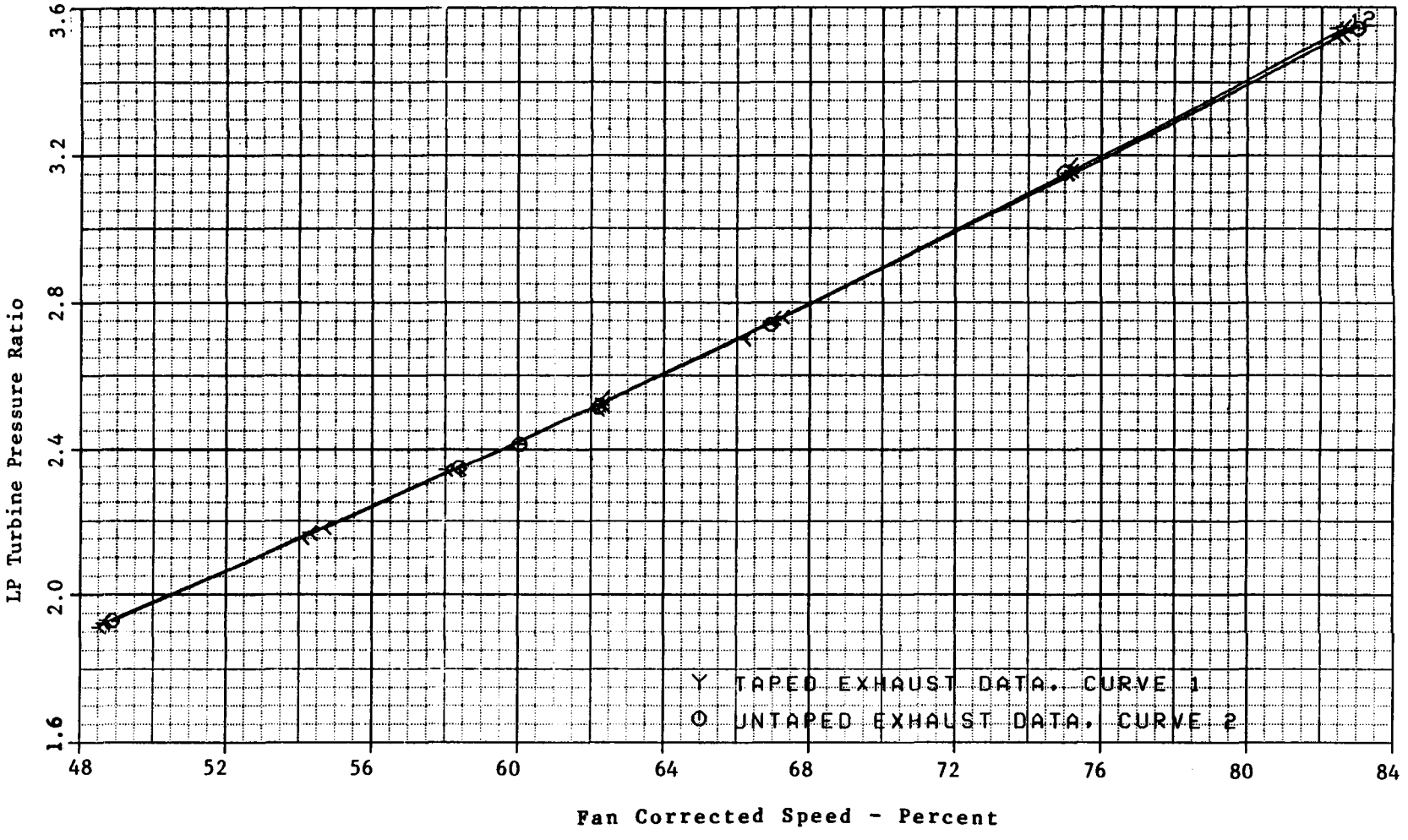


Figure 160. LP Turbine Pressure Ratio, Acoustic Data.

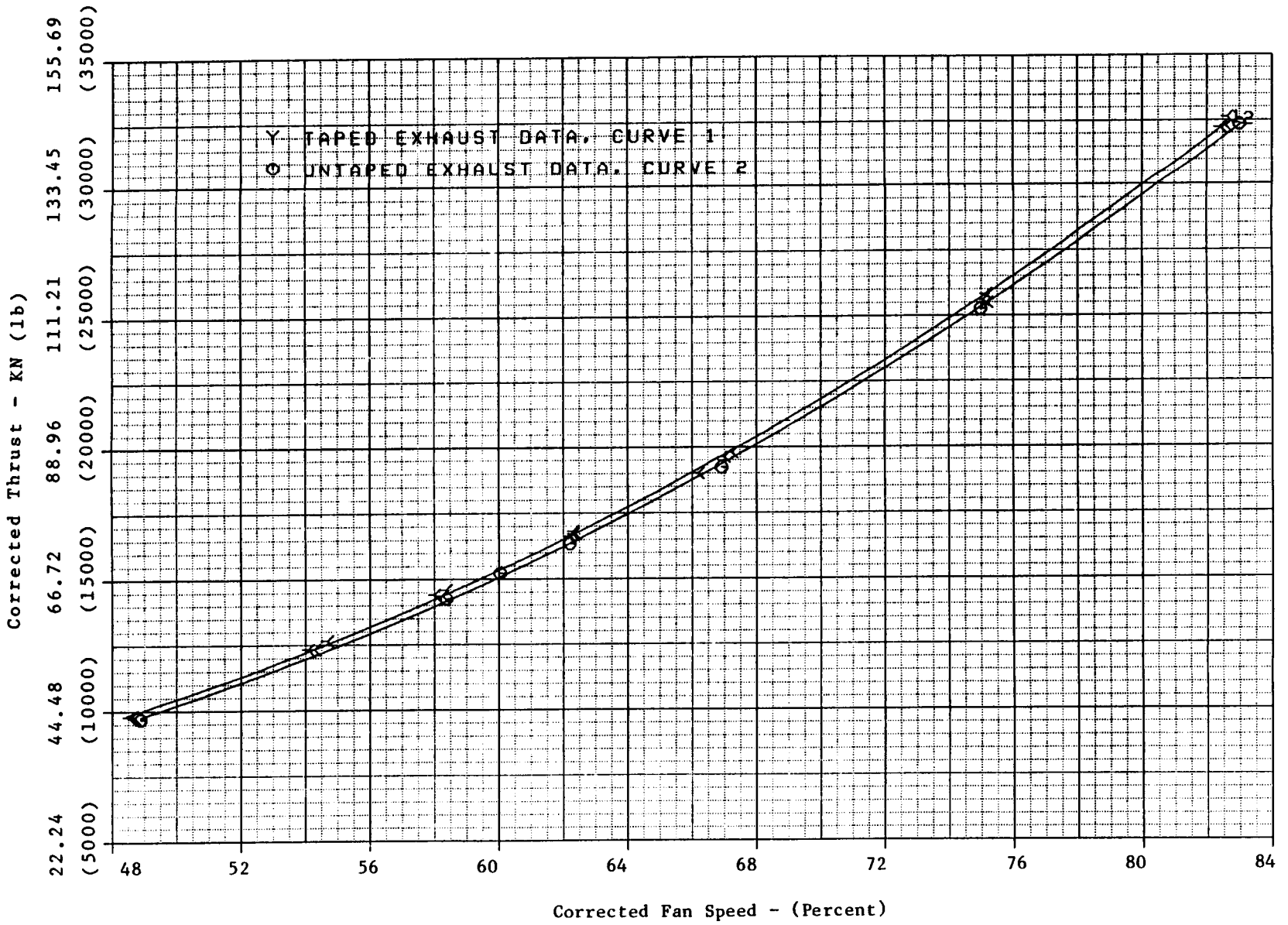


Figure 161. Corrected Thrust, Acoustic Data.

Effect on Overall Performance

While there was some uncertainty in the distribution of losses, it was concluded that the overall effect of the exhaust system and overboard leakage was to increase sfc by about 1.0%.

### 6.1.9 Overall Performance Results

Engine Pressure Ratio, Bypass Ratio, and Fan Versus Core Speed

Figures 162 through 164 show the engine pressure ratio (EPR), bypass ratio (BPR), and core versus fan speed for the performance data. The variations from prediction are consistent with the component performance differences.

Specific Fuel Consumption

Specific fuel consumption for the performance run is shown in Figure 165. All data were corrected to sea level, static, standard day conditions. At the takeoff thrust of 162.36 kN (36,500 lb) the measured sfc of 9.234 mg/N-sec (0.326 lb/hr-lb) was about 2.5% above the predicted sfc of 9.008 mg/N-sec (0.318 lb/hr-lb). At the takeoff condition the sfc difference was attributed to the component performance differences as shown in Table XII.

In order to compare the performance directly with the ICLS goal, appropriate adjustments were made for instrumentation losses and other test peculiar items (see Table XIII). With these adjustments the projected takeoff sfc was 8.781 mg/N-sec (0.310 lb/hr-lb).

At the 10.67 km (35,000 ft)/0.8 Mach/standard day/maximum cruise thrust condition, the projected uninstalled sfc was 15.579 mg/N-sec (0.550 lb/hr-lb) which was a 12.1% improvement from the reference CF6-50C performance. With the installed performance improvements for nacelle drag and an integral oil cooler, the installed performance improvement was 13.2%. The ICLS objective was a 12% improvement in installed performance.

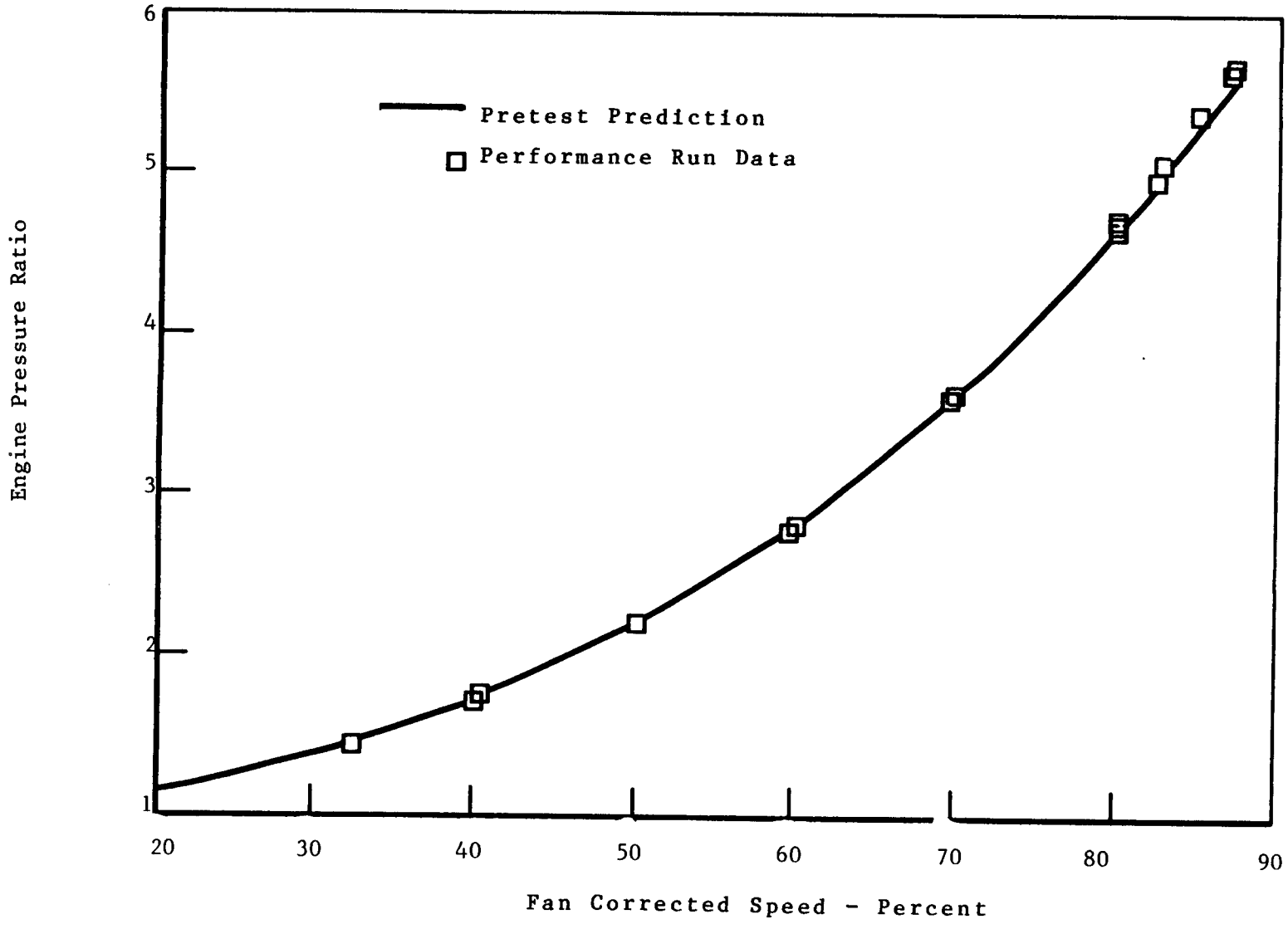


Figure 162. Engine Pressure Ratio.

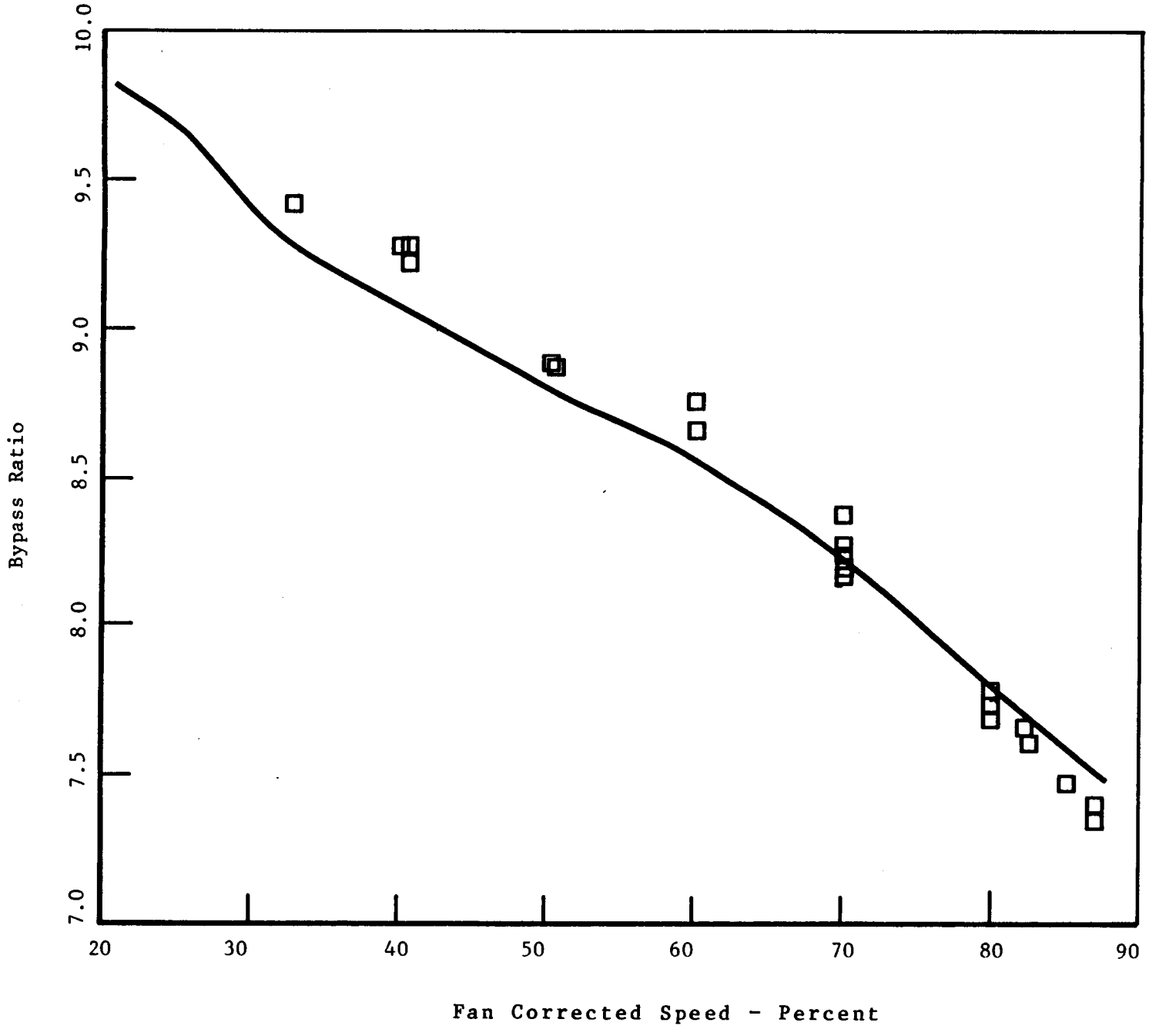


Figure 163. Bypass Ratio.

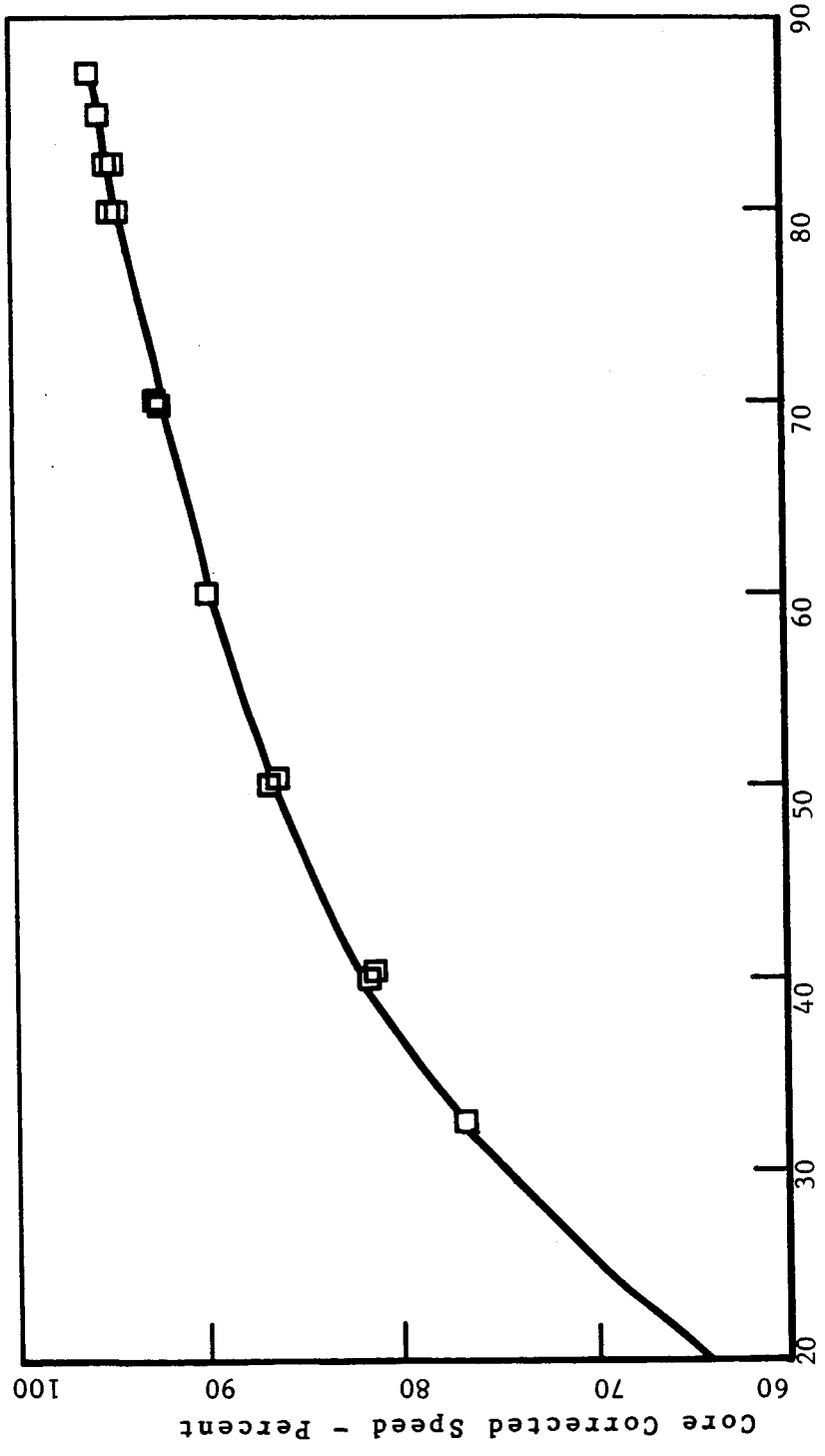


Figure 164. Core Speed Versus Fan Speed.

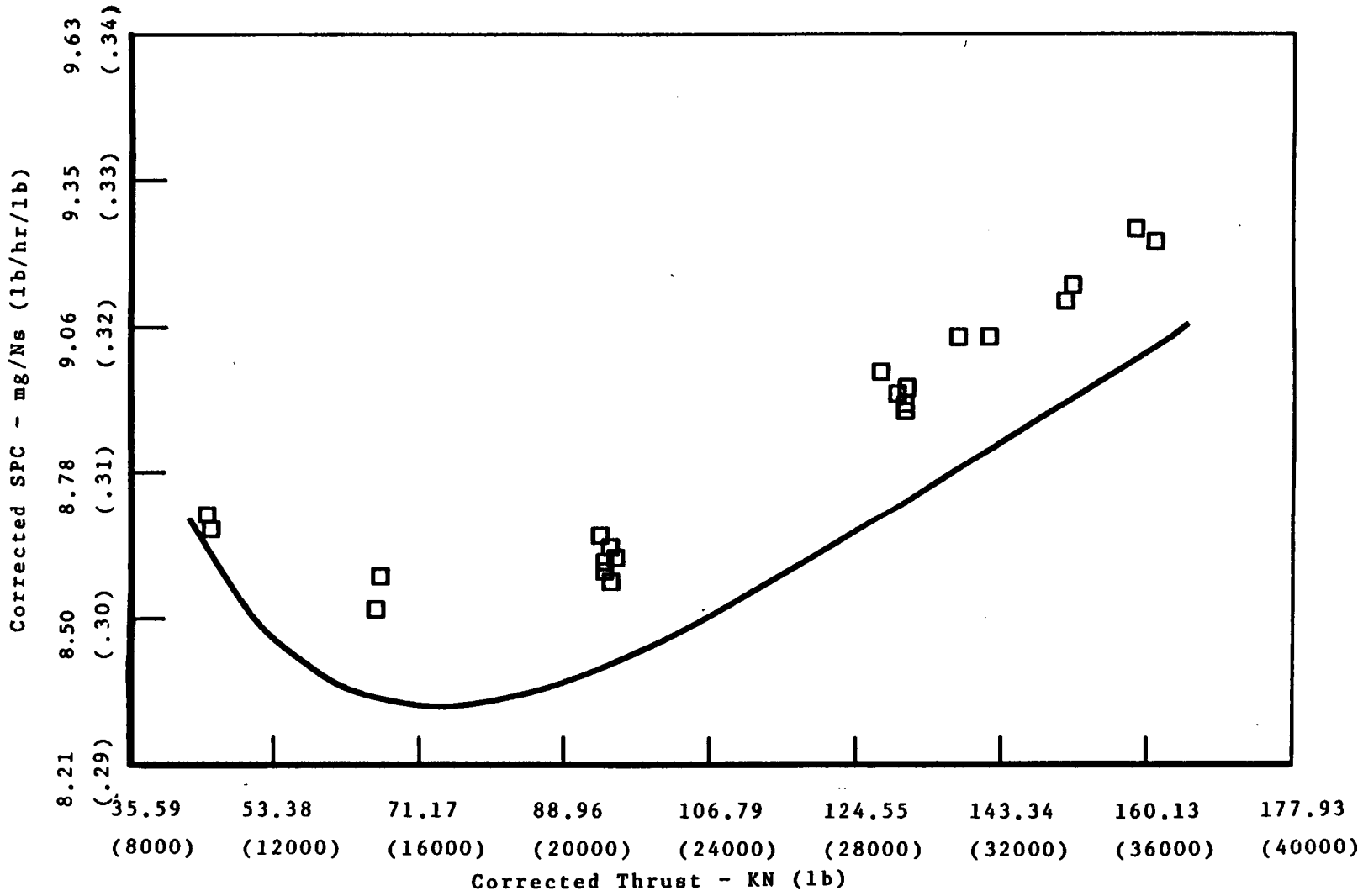


Figure 165. Specific Fuel Consumption - Performance Run.

Table XII. Overall Performance Stackup.

| Component | Variation from Prediction | SFC (Percent) |
|---|---|---|
| Inlet | -0.8 Percent Recovery | +0.2 |
| Fan | -0.6 Percent Efficiency | +0.4 |
| Fan Hub | +1.0 Percent Efficiency | -0.2 |
| LP Turbine | -1.0 Percent Efficiency | +0.9 |
| Exhaust | Leakage, Pressure Loss | +1.0 |
| CDP Bleed | +0.35 Percent | +0.2 |

Table XIII. Adjustments for ICLS Cruise Performance Forecast

Ideal Inlet
No Instrumentation
Flight Type Nacelle with Reverser
Reduced Cooling Flows
Rematched Turbine and Exhaust Areas
Flight Type Exhaust Nozzle
Operating Clearances

### 6.1.10 Conclusions

From the analysis of the ICLS component performance, it was concluded that the off-design modeling of the component performance trends was satisfactory for reliable prediction of cruise performance. It was determined from the measured ICLS performance and the projection for cruise installed performance that the ICLS objective for performance improvement was exceeded by 1.2%.

## 6.2 ACOUSTIC SYSTEM PERFORMANCE

### 6.2.1 Test Instrumentation and Objectives

Nineteen 45.7 meter (150 ft) arc microphones and four in-duct dynamic pressure transducers were recorded on a 28 track FM tape recorder, along with fan speed, core speed, time code, and a reference oscillator. Sixteen of the 45.7 meter arc microphones were positioned at 10° increments (10°-160°), pointing towards the ground, 6.35 millimeters (0.25 inch) above the center of a metal plate which was glued to the concrete test pad. The other three microphones were pointing upwards 3.96 meters (13 ft) above the concrete surface at 30°, 90°, and 120° (reference Figure 107). The dynamic pressure transducers were located at the positions defined in Table XIV.

Table XIV. Dynamic Pressure Transducers.

| Approximate Station No. | Approximate Circumferential Position (°ALF) | Transducer Type | Description |
|---|---|---|---|
| 114 | 30 | Kulite XCS-190-15 | 10-32 bolt |
| 151.8 | 30 | Endevco 8507-15 | Panel Bolt Probe |
| 204.8 | 84 | Kulite XCS-190-15 | 10-32 bolt |
| 286.7 | 84 | Kulite XCS-190-15 | 10-32 bolt |

Five suppressed and unsuppressed configurations were tested as defined in Table XV.

Table XV. ICLS Acoustic Test Configurations.

| Configuration | Nacelle Treatment | | Inlet Type |
|---|---|---|---|
| | Inlet | Exhaust | |
| 1 | Suppressed | Suppressed | Aero-acoustic |
| 2 | Partially suppressed | Suppressed | Aero-acoustic |
| 3 | Unsuppressed | Suppressed | Aero-acoustic |
| 4 | Unsuppressed | Unsuppressed | Perf. Bellmouth |
| 5 | Unsuppressed | Suppressed | Perf. Bellmouth |

Treatment panels were rendered "unsuppressed" by covering the facesheets with 0.0127 cm (0.005 inch) thick aluminum tape. The partially suppressed inlet configuration was run with aluminum tape covering up the leading 48.3 cm (19 in) of acoustic treatment.

Three acoustic fan speed operating lines were tested for the first four acoustic test configurations. Each operating line consisted of at least seven stabilized speed points (eight on configurations 1 and 2), selected to be within 50 rpm of the FPS operating speeds (reference Table XVI). The last acoustic test configuration was tested for only one operating line.

Table XVI. Acoustic Testing - Fan Speed Operating Line.

| Point No. | NIK |
|---|---|
| 1 | 1820 |
| 2 | 2030 |
| 3 | 2180 |
| 4 | 2320 |
| 5 | 2500 |
| 6 | 2800 |
| 7 | 3100 |
| (8)* | 3270 |

*This point was not reached on Configurations 3, 4, and 5 due to the exhaust gas temperature limit.

The objective of testing five different suppresion configurations was to deduce the treatment effectivity for the inlet and exhaust nacelles independently.

### 6.2.2 Test Results

Figures 166 through 173 give the measured, freefield tone-corrected perceived noise level (PNLT) directivity for the five configurations tested. Example spectra from which these PNLT directivities were deduced are shown in Figures 174 through 177. The high power data is given for 305 m (1,000 ft) altitude, corresponding to takeoff. Lower power data is given for 122 m (400 ft) altitude, corresponding to approach.

The static, one-third octave, freefield data were projected to an engine alone level flyover to determine the relative benefits of the inlet and exhaust treatment. Corrections were made for a doppler shift of frequency, spherical divergence and atmospheric absorption. No corrections were made to the data for cycle differences and nearfield jet noise measurement effects (source location correction). The reductions in noise level due to inlet treatment and exhaust treatment are given in Table XVII.

### 6.2.3 Projected Aircraft Performance

The projected margins based on ICLS test results are given in Figure 178, with scaling performed using the procedures in Figure 179.

First, the individual static 45.7 meter measured data was corrected to freefield and averaged. Static jet and combustor noise was predicted and then subtracted from the freefield 45.7 meter averaged data. Using static 45.7 meter narrowband data, the effect of turbine and booster tone levels were computed for one-third octave bands and removed from the data, leaving only fan-related noise data.

The fan spectra was scaled to flight FPS cycle conditions correcting for differences in fan weight flow and tip speed. The flight FPS jet and

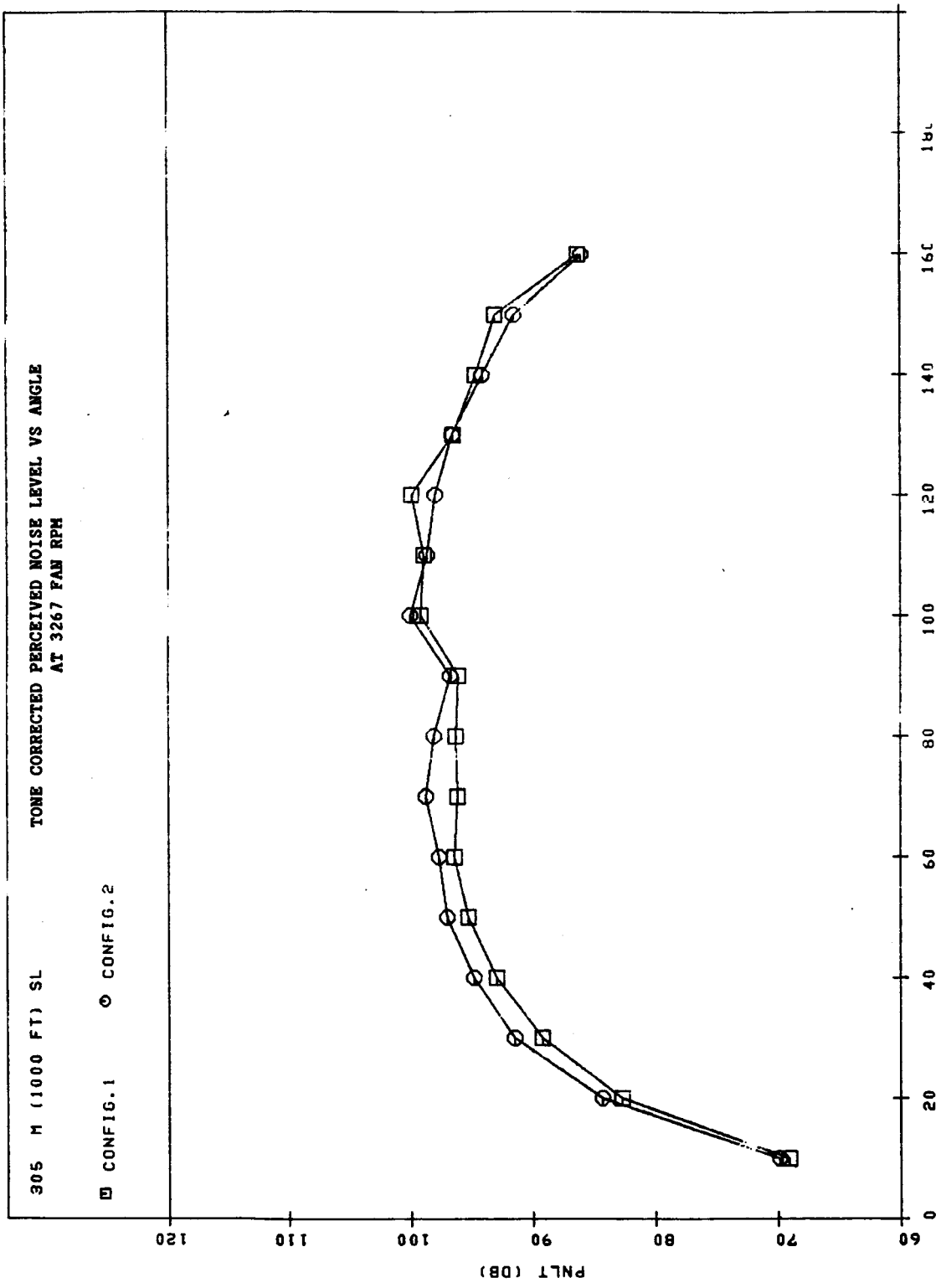


Figure 166. Tone Corrected Perceived Noise Level Versus Angle - 3,267 RPM.

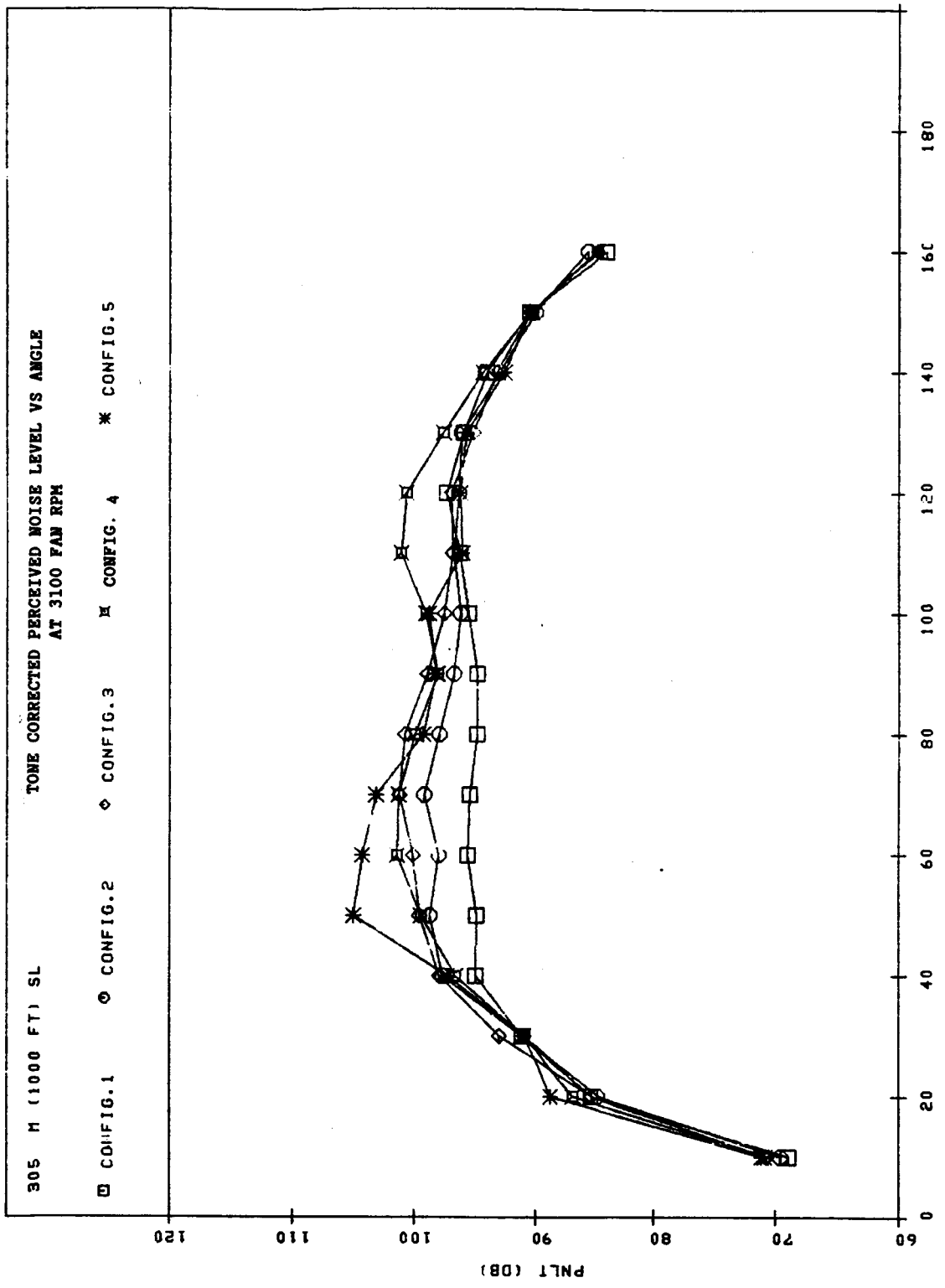


Figure 167. Tone Corrected Perceived Noise Level Versus Angle - 3,100 RPM.

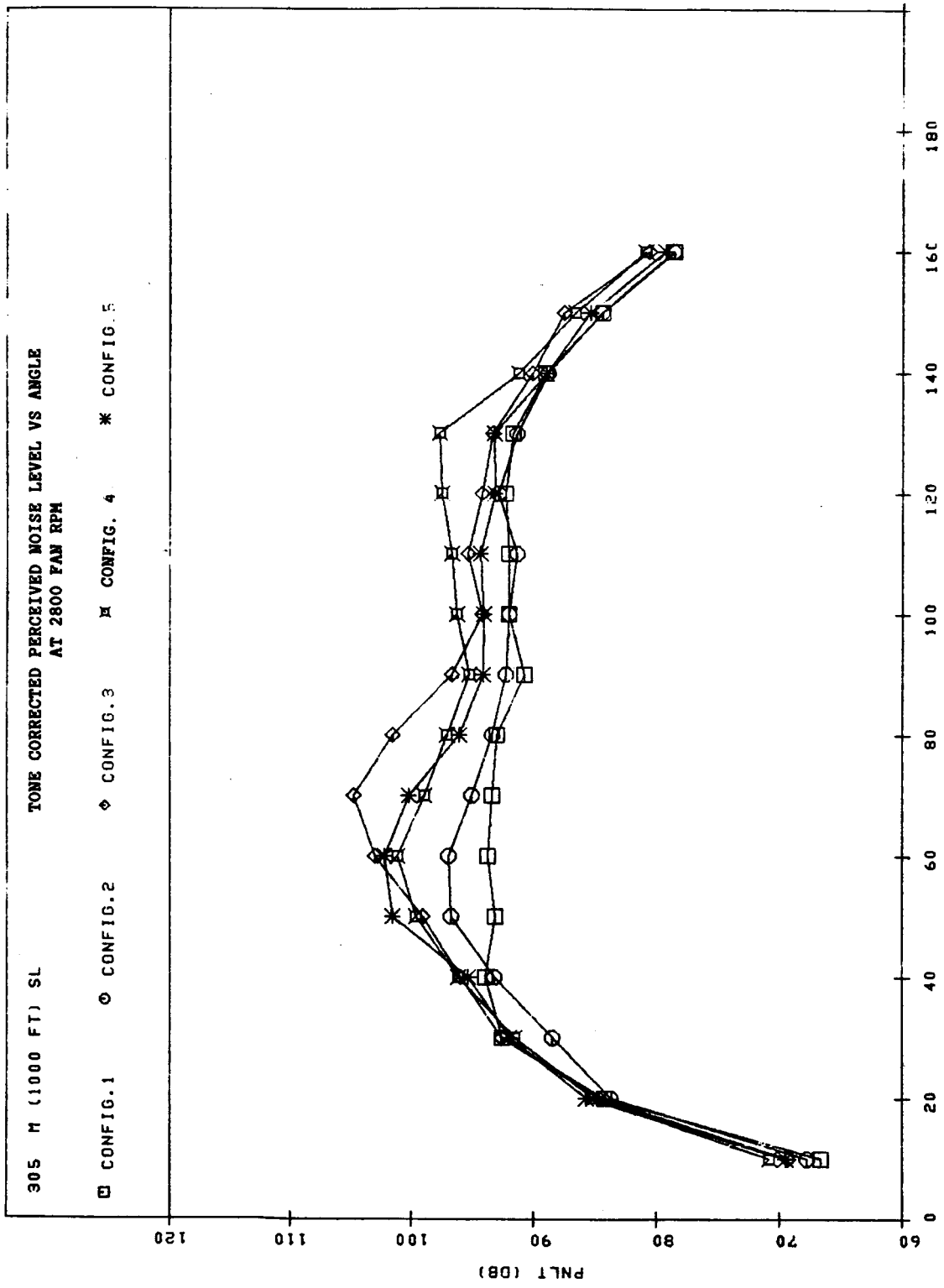


Figure 168. Tone Corrected Perceived Noise Level Versus Angle - 2,800 RPM

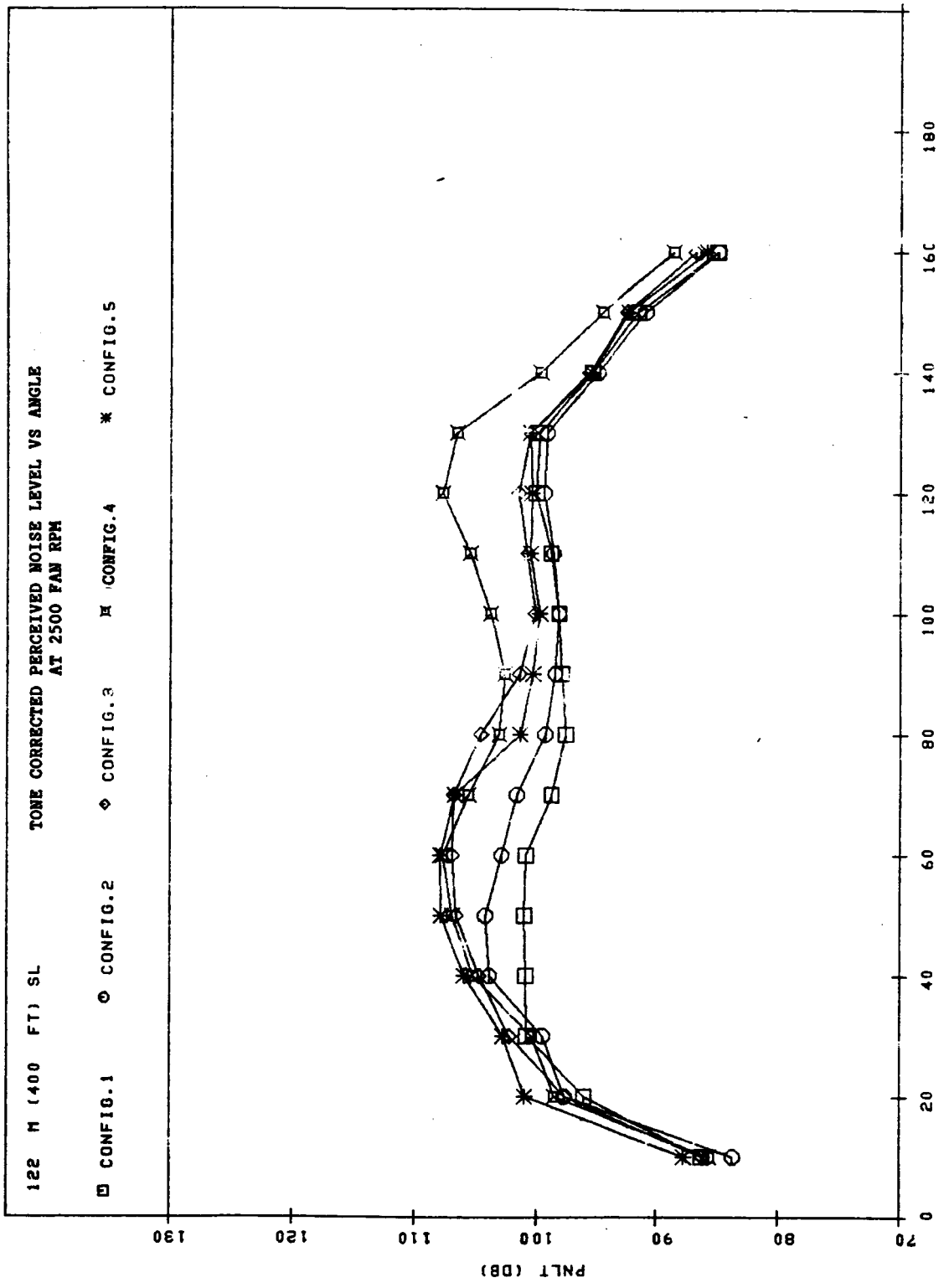


Figure 169. Tone Corrected Perceived Noise Level Versus Angle - 2,500 RPM.

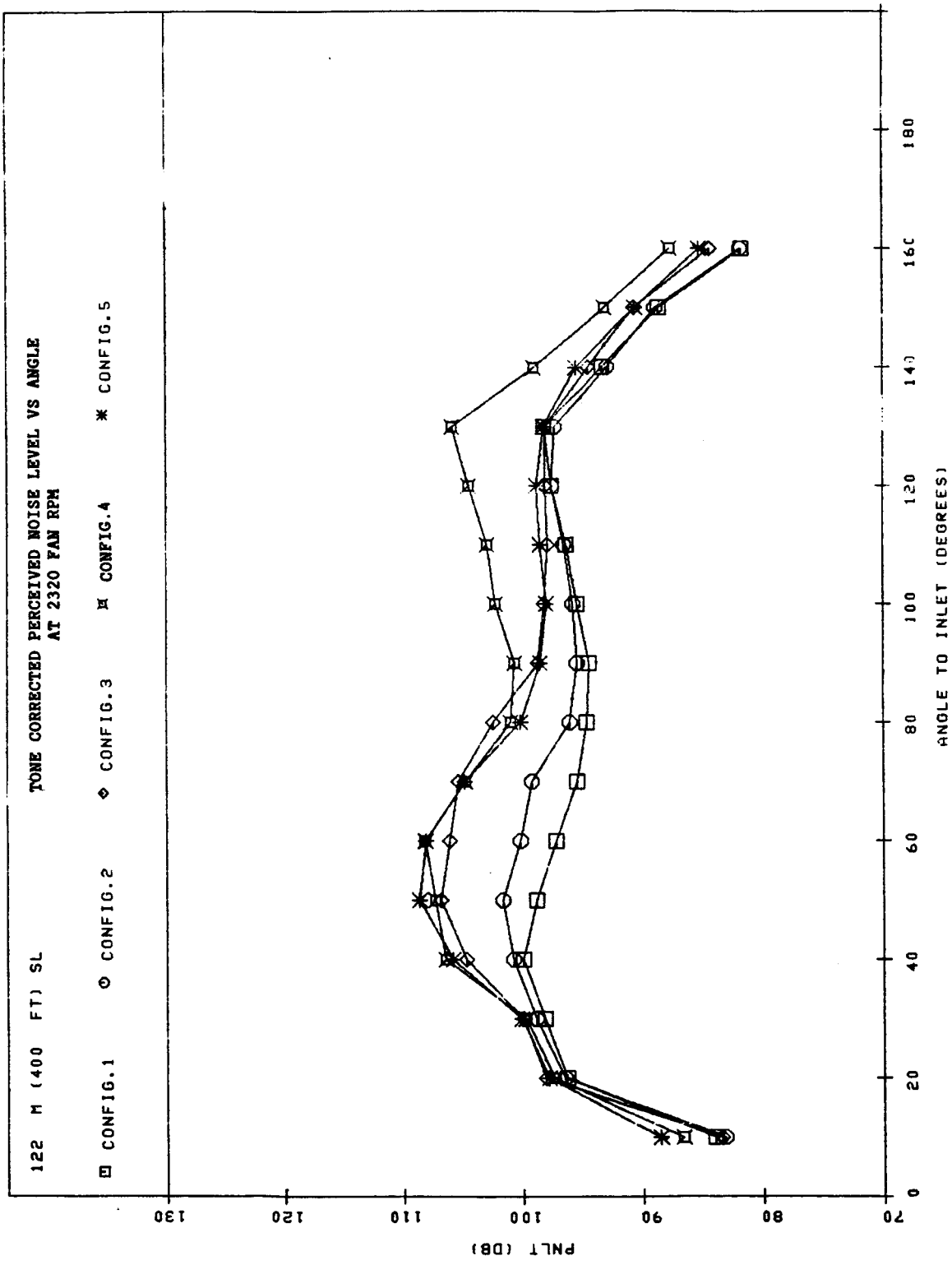


Figure 170. Tone Corrected Perceived Noise Level Versus Angle - 2,320 RPM.

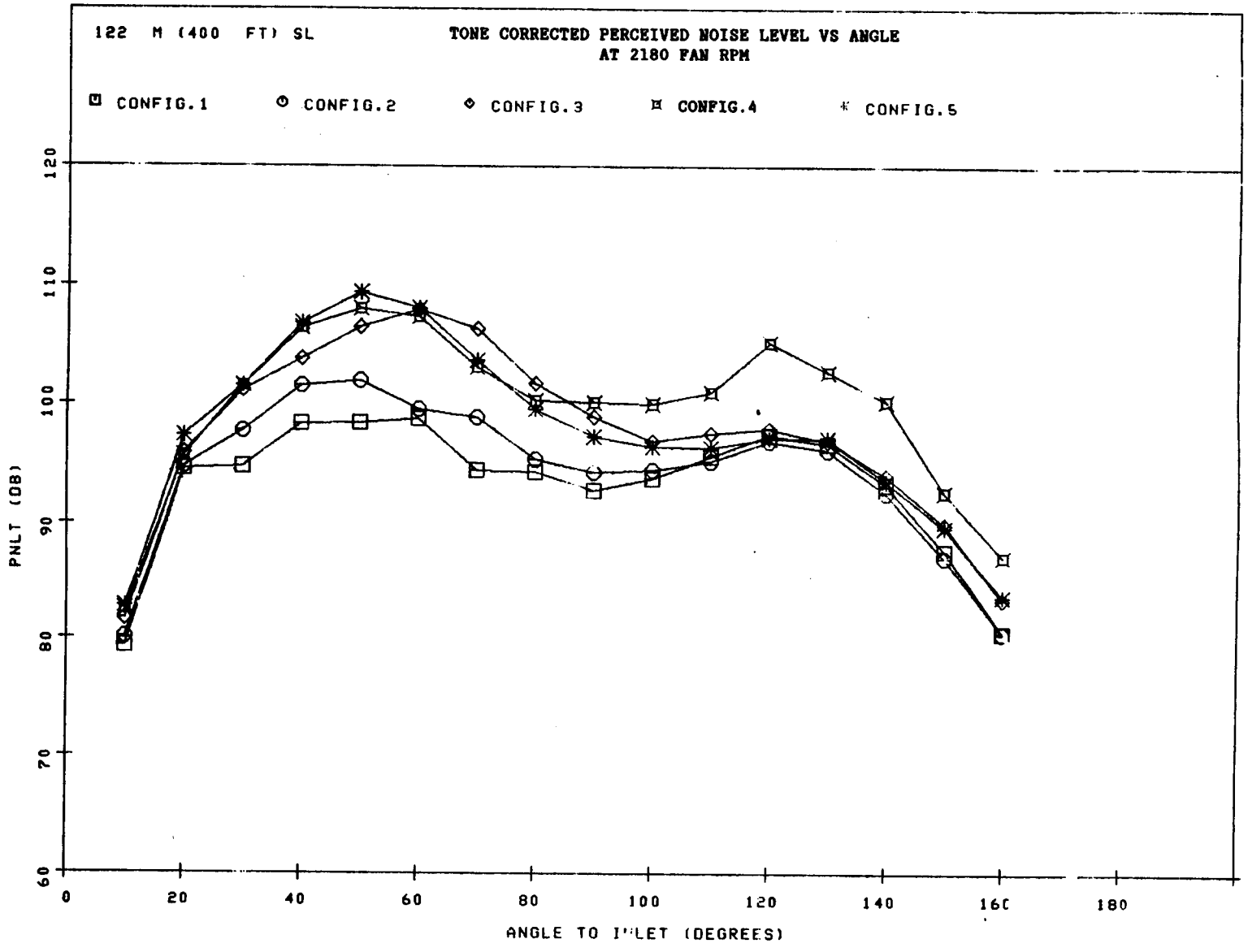


Figure 171. Tone Corrected Perceived Noise Level Versus Angle - 2,180 RPM.

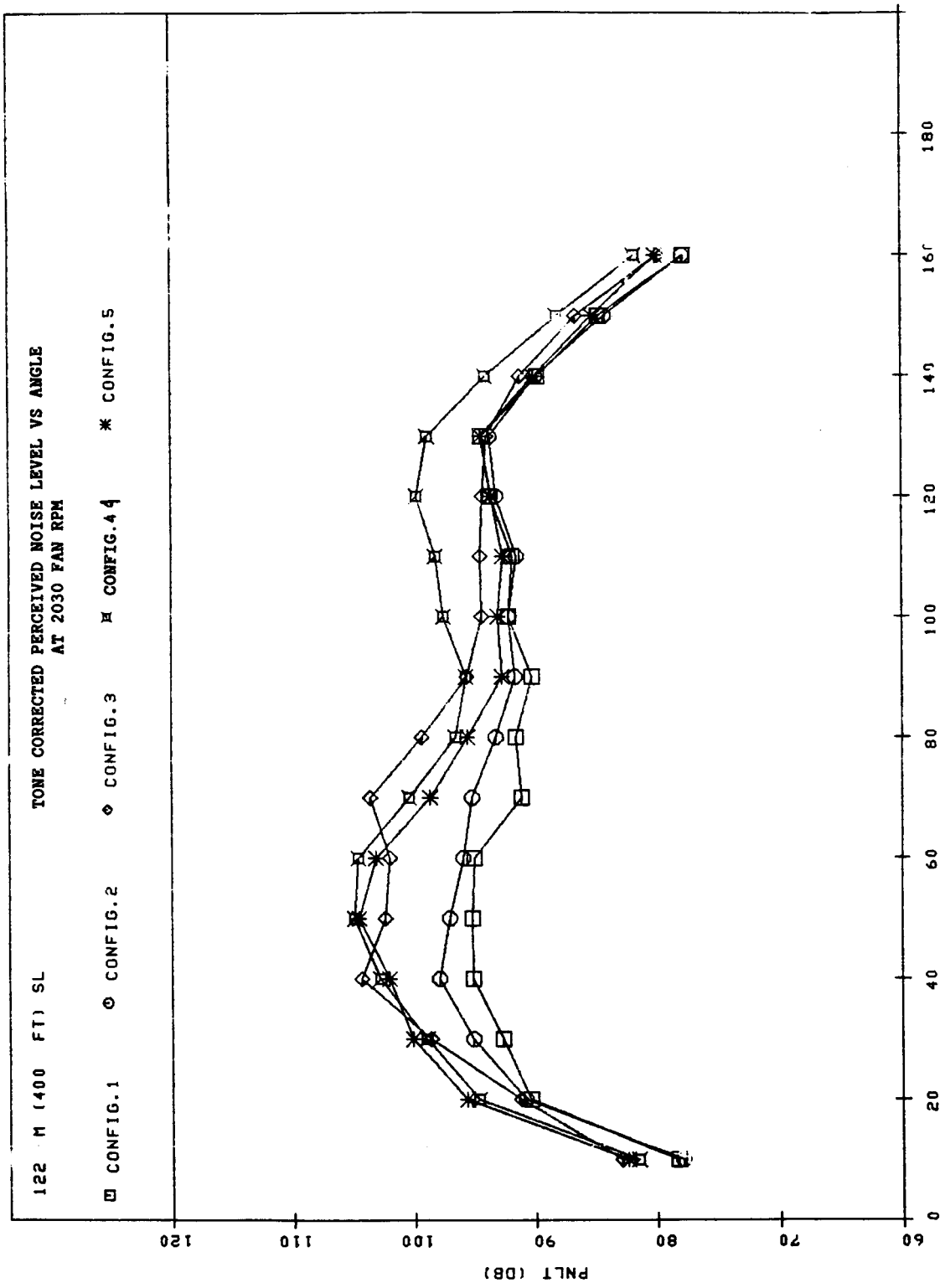


Figure 172. Tone Corrected Perceived Noise Level Versus Angle - 2,030 RPM.

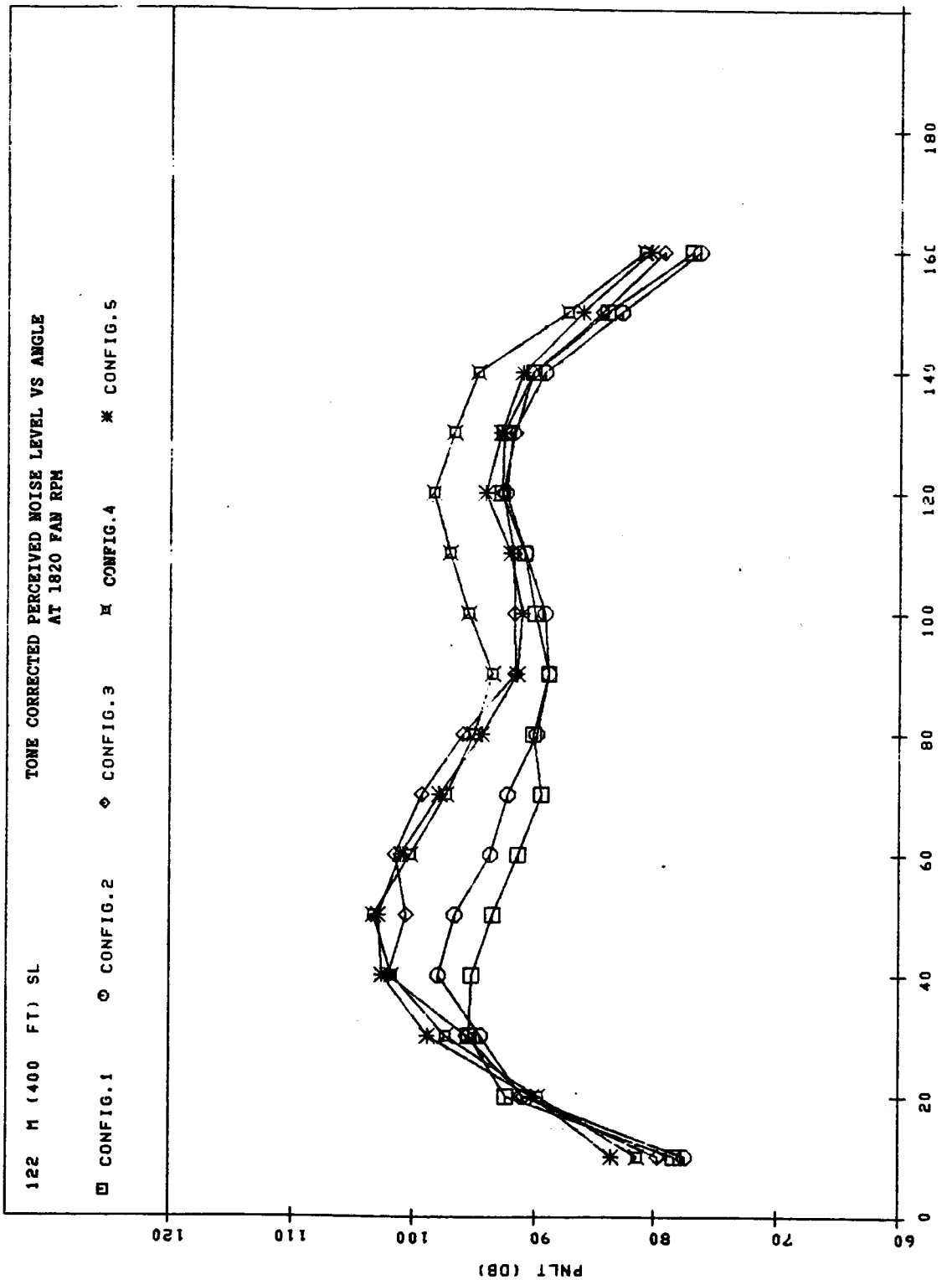


Figure 173. Tone Corrected Perceived Noise Level Versus Angle - 1,820 RPM.

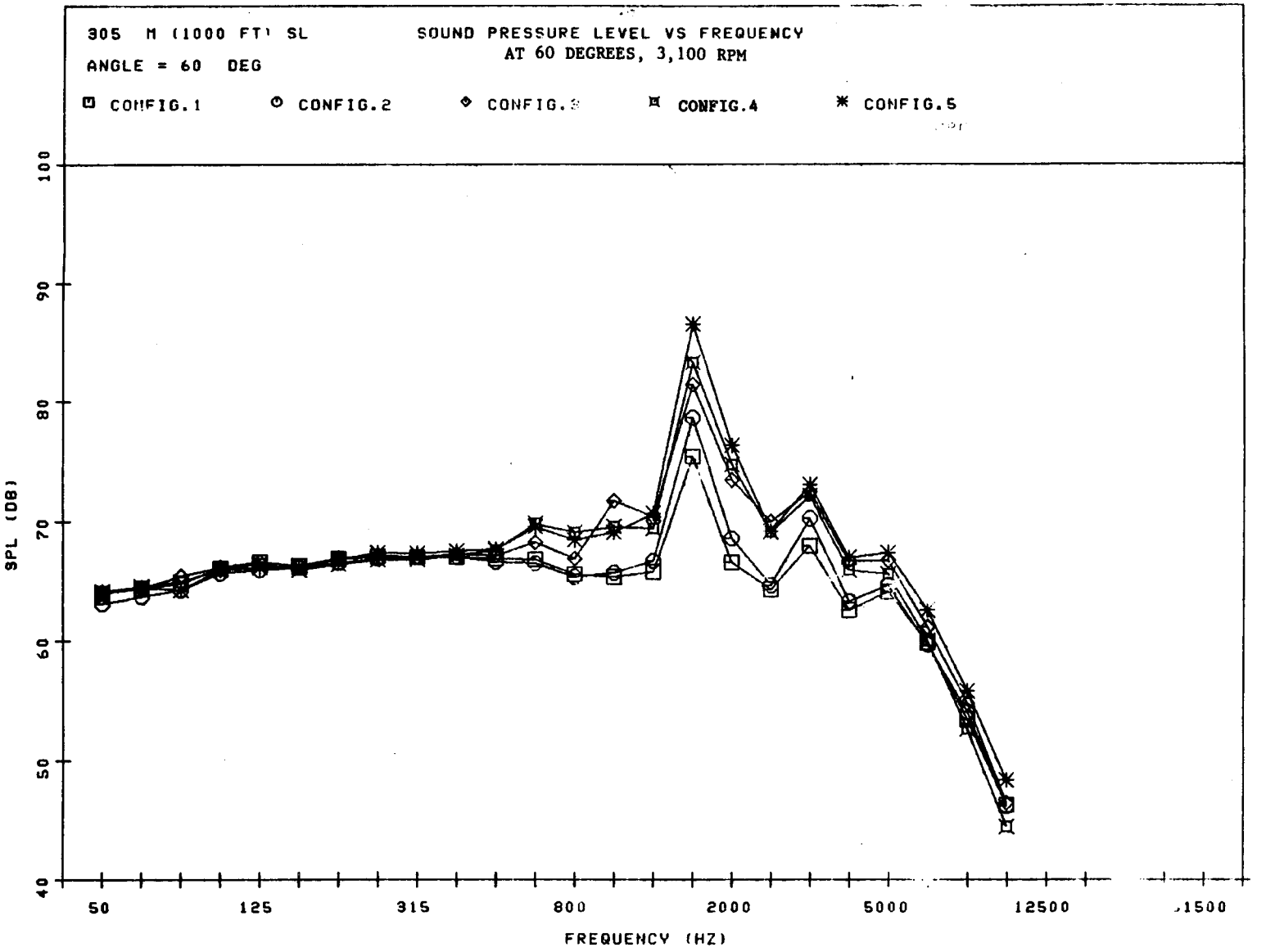


Figure 174. Sound Pressure Level Versus Frequency - 3,100 RPM at 60 Degrees.

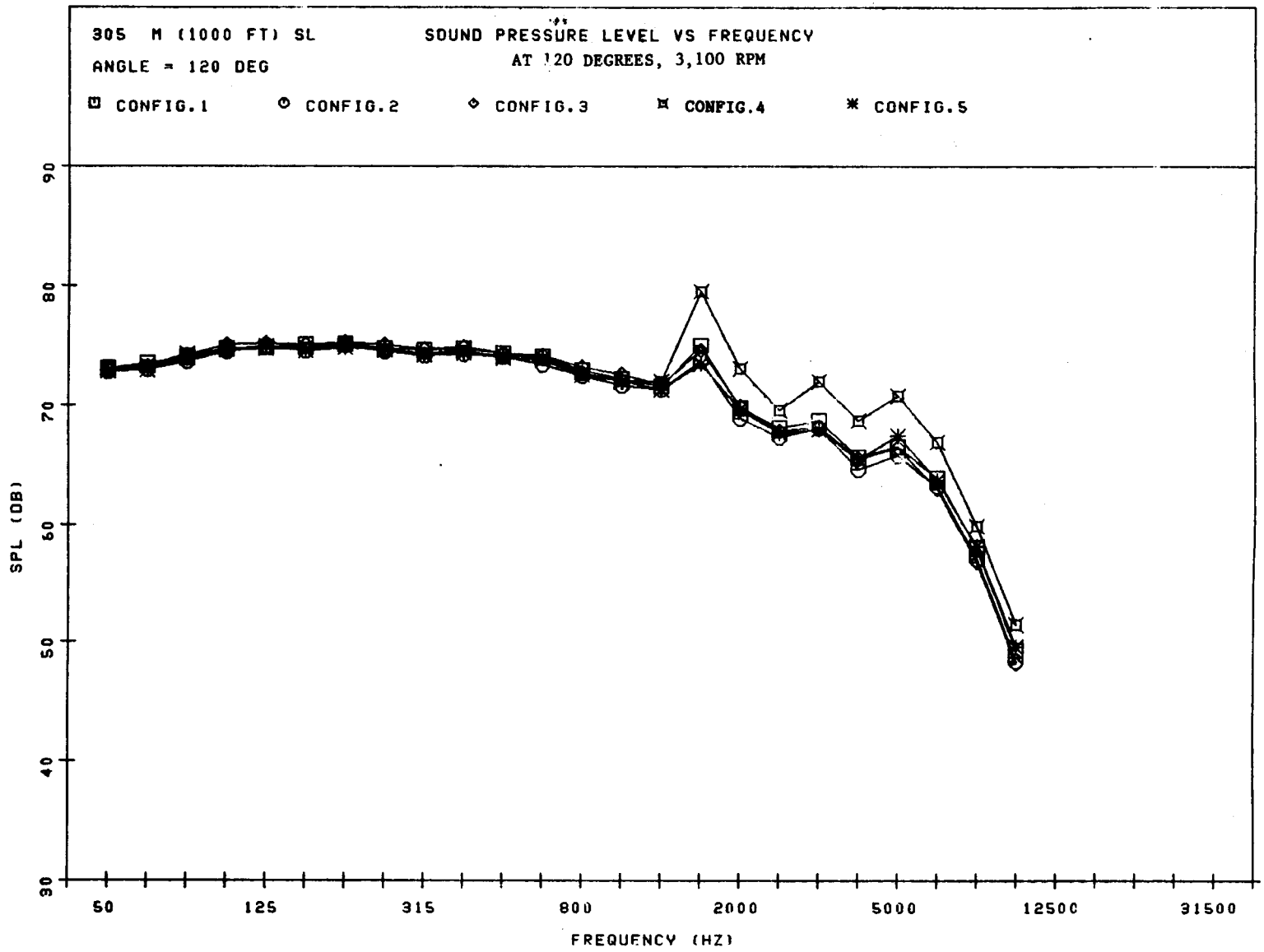


Figure 175. Sound Pressure Level Versus Frequency - 3,100 RPM at 120 Degrees.

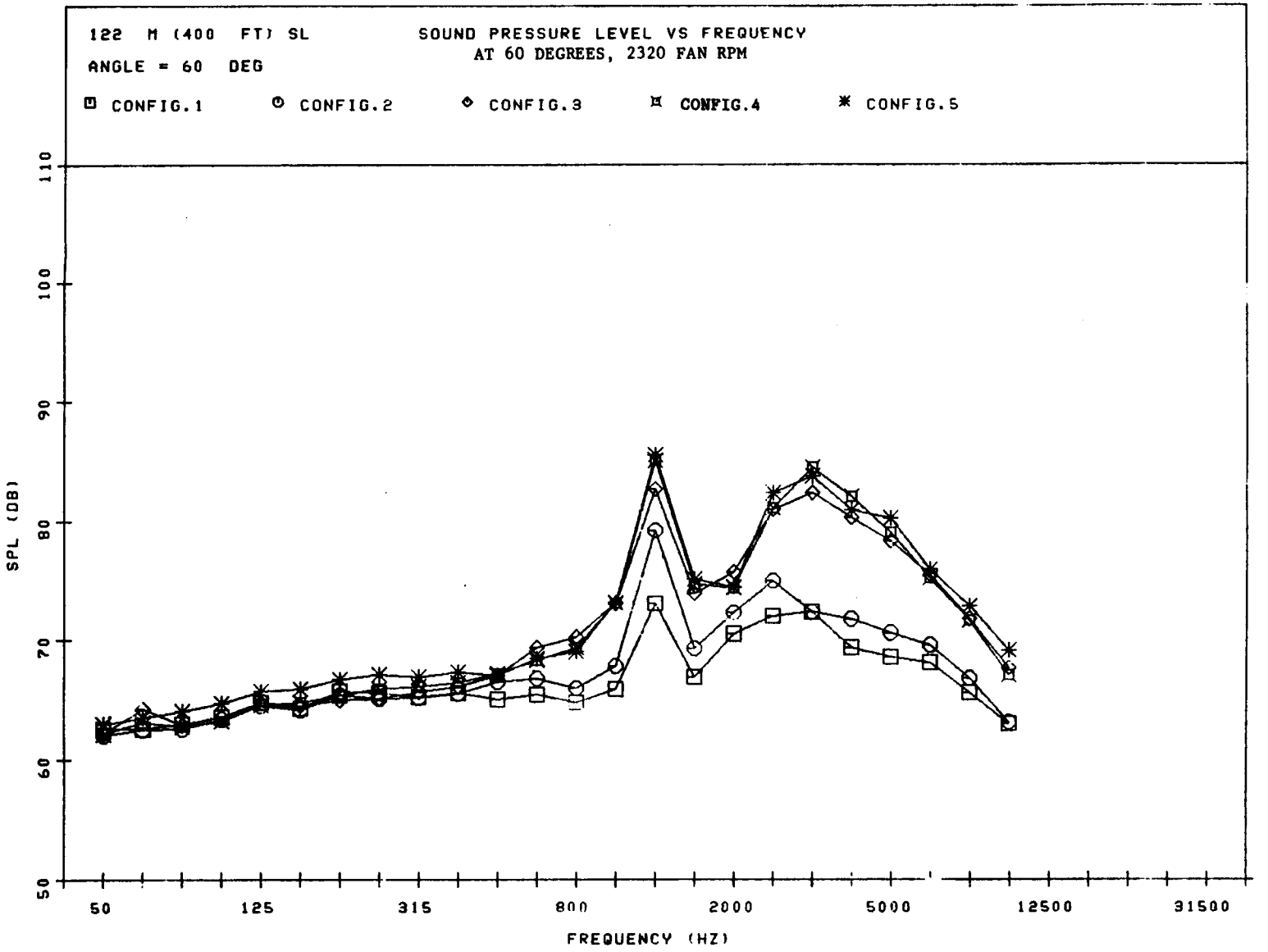


Figure 176. Sound Pressure Level Versus Frequency - 2,320 RPM at 60 Degrees.

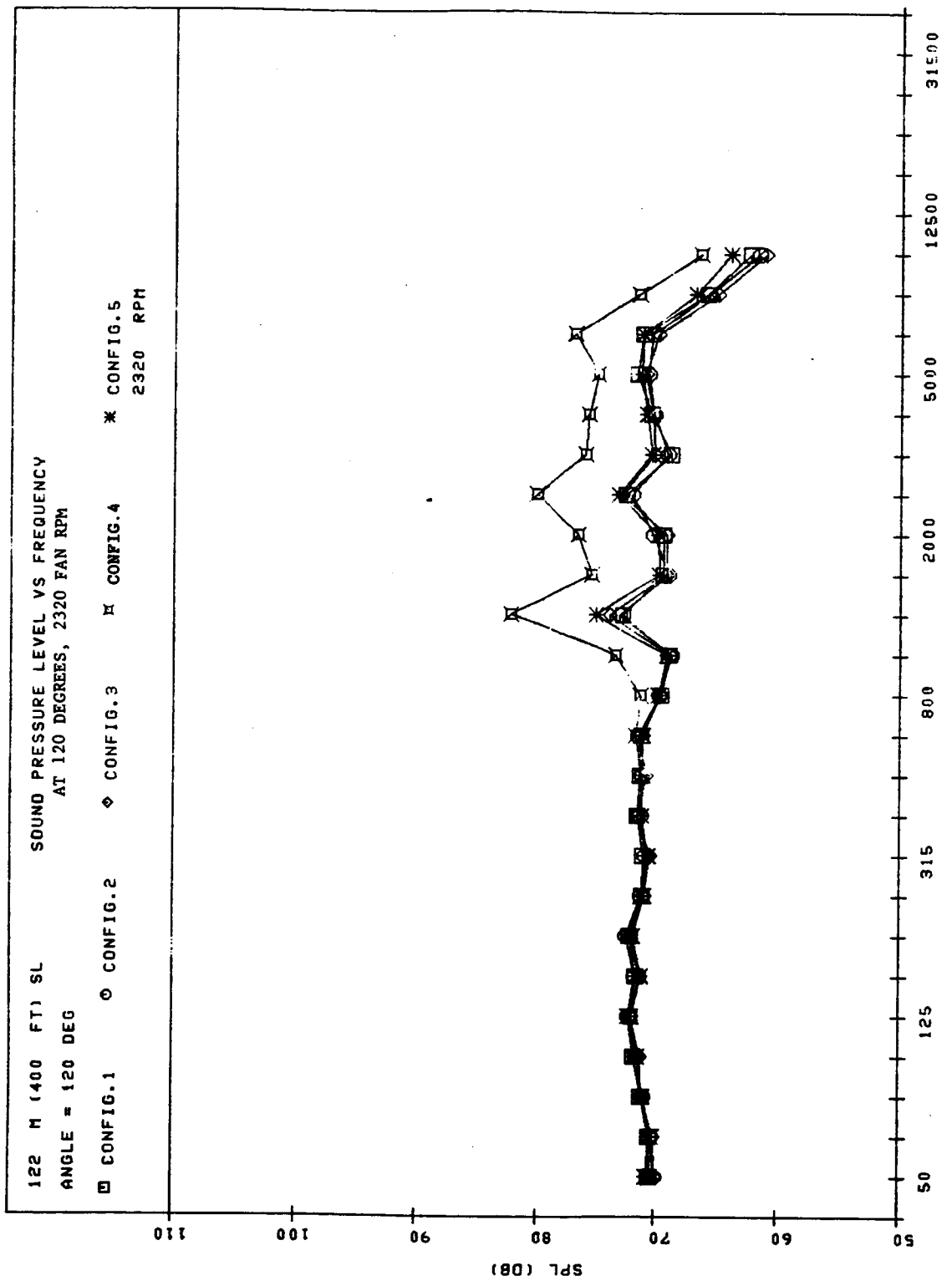


Figure 177. Sound Pressure Level Versus Frequency - 2,320 RPM at 120 Degrees.

Table XVII. Noise Reductions Due to Nacelle Noise Suppression Treatment.

Approach

Level Flyover
Alt. 122 m. (400 ft.)
$V_{ac}$ 68.9 m./sec. (226 ft./sec.)

| Fan RPM | 1820 | 2030 | 2180 | 2320 |
|---|---|---|---|---|
| Reduction in EPNdB Due to Inlet Treatment | 2.9 | 5.6 | 4.9 | 3.9 |
| Reduction in EPNdB Due to Exhaust Treatment* | 0.8 | 1.2 | 0.8 | 1.4 |

Takeoff

Level Flyover
Alt. 304.9 m (1,000 ft)
$V_{ac}$ 77.7 m/sec (225 ft/sec)

| Fan RPM | 3100 | 2800 |
|---|---|---|
| Reduction in EPNdB Due to Inlet Treatment | 2.2 | 4.6 |
| Reduction in EPNdB Due to Exhaust Treatment* | -0.5** | 0.5** |

*Evaluated with hardwall inlet.

**Inlet noise dominated the noise field, making exhaust measurements at this condition less significant.

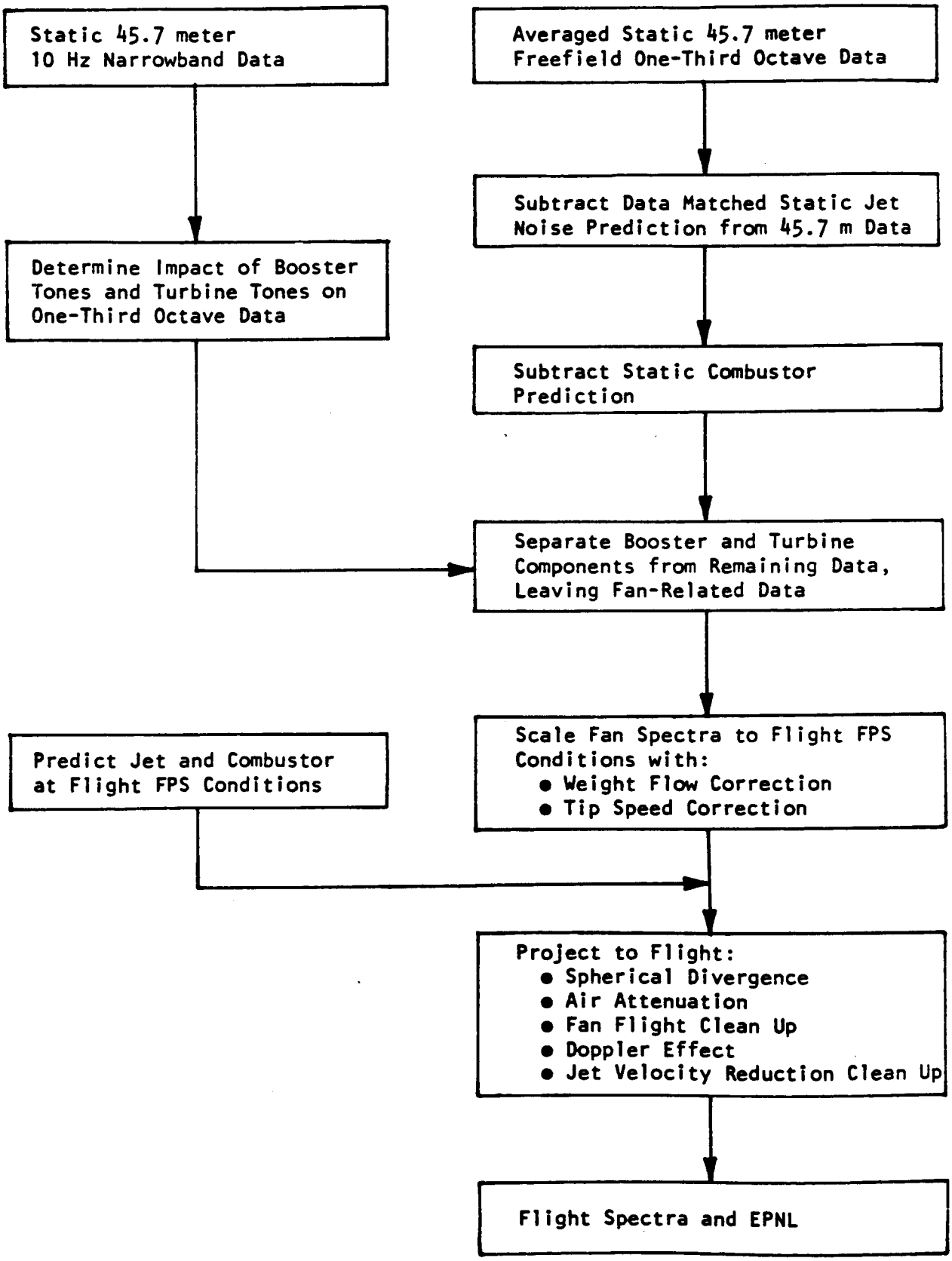


Figure 178. Static-to-Flight Acoustic Projection Flowchart.

| | Boeing Twinjet<br>SLS $F_n$ = 37,710 lb.<br>TOGW = 243,660 lb. | Douglas Trijet<br>SLS $F_n$ = 41,230 lb.<br>TOGW = 497,000 lb. | Lockheed Trijet<br>SLS $F_n$ = 40,757 lb.<br>TOGW = 462,857 lb. | Lockheed Quadjet<br>SLS $F_n$ = 37,767 lb.<br>TOGW = 626,841 lb. |
|---|---|---|---|---|
| Takeoff Level | 90.9 | 96.5 | 94.8 | 99.1 |
| Margin re: FAR36 (1978) | 2.9 | 4.4 | 5.6 | 5.1 |
| Sideline Level | 91.6 | 94.4 | 92.8 | 93.6 |
| Margin re: FAR36 (1978) | 5.6 | 6.5 | 7.7 | 8.1 |
| Approach Level | 100.2 | 100.5 | 99.9 | 99.7 |
| Margin re: FAR36 (1978) | -1.7 | 3.8 | 4.1 | 5.3 |
| Airframer Supplied Aircraft Noise | 93.2 | 92.3 | 95.9 | 96.0 |

Figure 179. Flight Noise Estimates EPNdB.

combustor noise was predicted and projected to flight with the fan, turbine, and booster component data.

Each component was projected to flight using corrections for spherical divergence, air attenuation, doppler shifting, and dynamic amplitude effects. The static data was then re-evaluated using enhanced waveform and probability density techniques to determine the effect of rotor-turbulence interaction on fan tone levels. As rotor-turbulence levels are reduced in flight, a "clean-up" condition is applied to the static fan tone levels to deduce the appropriate flight levels.

The flight-projected components are then combined and an Effective Perceived Noise Level (EPNL) is calculated.

### 6.2.4 Conclusions

The $E^3$ FPS, mounted in the reference aircraft shown in Figure 179, exceeds the acoustics goals of the $E^3$ program.

## 6.3 INLET MECHANICAL PERFORMANCE

The performance inlet was used for all mechanical checkout testing and performance testing. The aero-acoustic inlet was then installed for the acoustic test portion of the program. The fully suppressed and short inlet simulation (partially taped) aero-acoustic inlet testing was performed without event. At the end of the fully taped inlet test, it was found that the acoustic facesheet (perforated aluminum) was badly distorted and bulged out into the flowpath. It is most likely that the taping, since it closed all of the holes in the facesheet, did not allow the facing to "breathe," thus creating a small pressure differential across the facing. Since the unsupported area of the facesheets is rather large and the facing sheets thin and, due to the acoustic perforations, relatively weak, the facesheets could be readily deformed in the manner noted. This situation should not occur in a flight design where the acoustic treatment holes would not be blocked over

large areas. The performance inlet was reinstalled for the few remaining tests and no further inlet problems were encountered.

## 6.4 INLET AERODYNAMIC PERFORMANCE

A detailed analytical study of the performance bellmouth shown in Figure 8 was conducted prior to the ICLS test to define the bellmouth flow coefficient. The prime method for inlet airflow determination was subsequently established based on this analysis. The resulting inlet flow coefficient curve, shown in Figure 180, uses the wall static and rake total pressures to determine the inlet pressure ratio and airflow.

An analysis of the inlet pressure data was performed to check the measured flowfield characteristics against the analytical study used to derive the flow coefficient. Measured wall static and pitot static pressure distributions from the ICLS performance bellmouth are shown in Figure 181 for two corrected inlet flow conditions. The test results depict the static pressure curve shapes and scatter/accuracy for the four pitot static rakes and four wall statics. Comparison of the measured data with the analytical prediction indicates excellent agreement in both absolute level and shape. Thus, the ICLS test results verify the analytical flow coefficient prediction and establish inlet airflow calculation accuracy to within $\pm$1/2%.

A second parameter of interest in the inlet aerodynamic performance is the inlet recovery at the fan face. The recovery includes both the boundary layer loss and the pressure loss due to the four inlet $P_T/T_T$ rakes. A boundary layer rake installed at the fan face in the fan component rig test defined that portion of the inlet recovery. Combined with an analytical calculation of the rake drag, the inlet recovery was established as shown by the curve labeled Rig Recovery Curve in Figure 182. An analytical study of the bellmouth boundary layer loss showed excellent agreement with the boundary layer rake data as shown by the dashed line in Figure 182.

However, because of structural limitations on the ICLS vehicle, the bellmouth could not be direct-connected to the fan face and had to be mounted

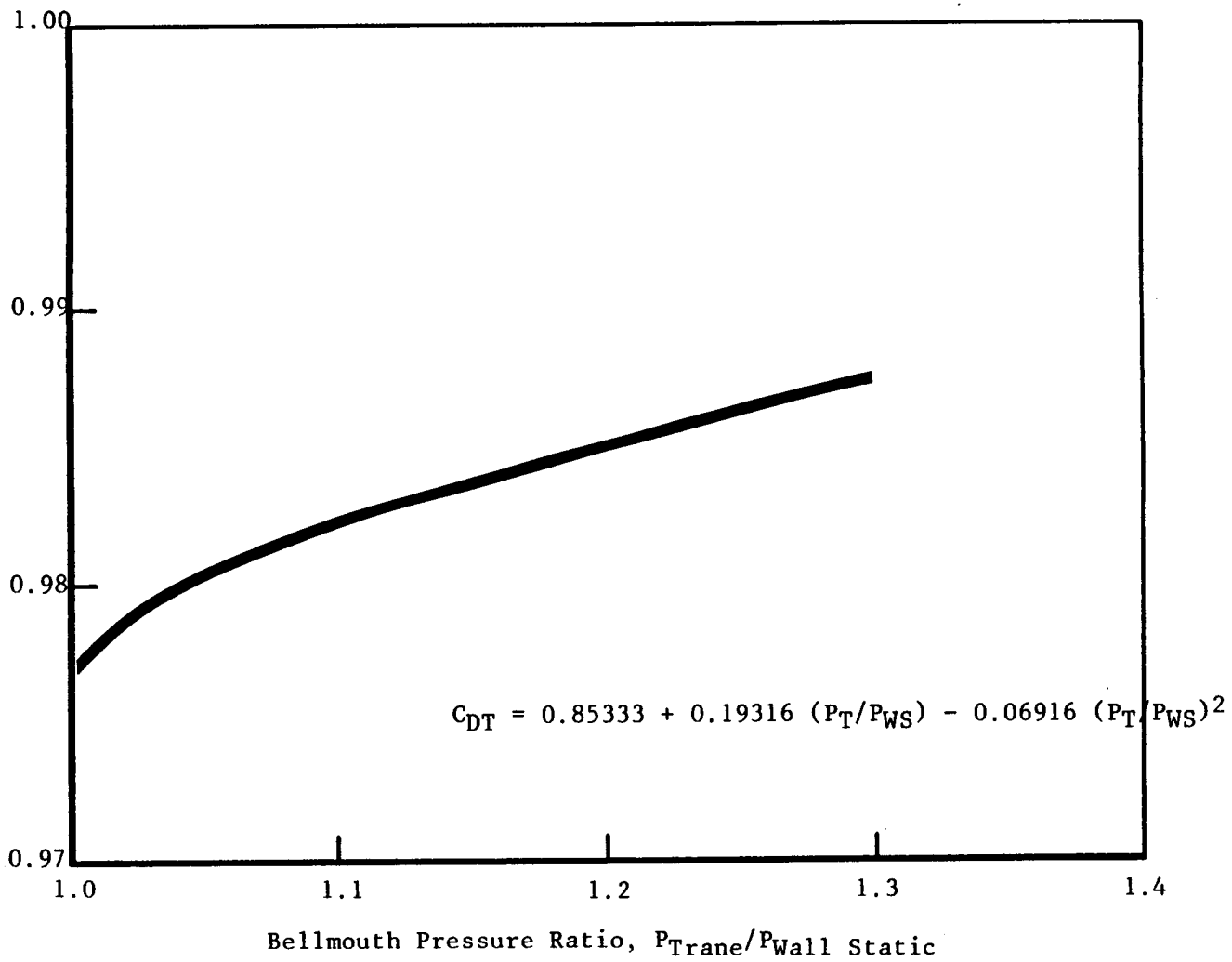


Figure 180. Performance Bellmouth Flow Coefficient.

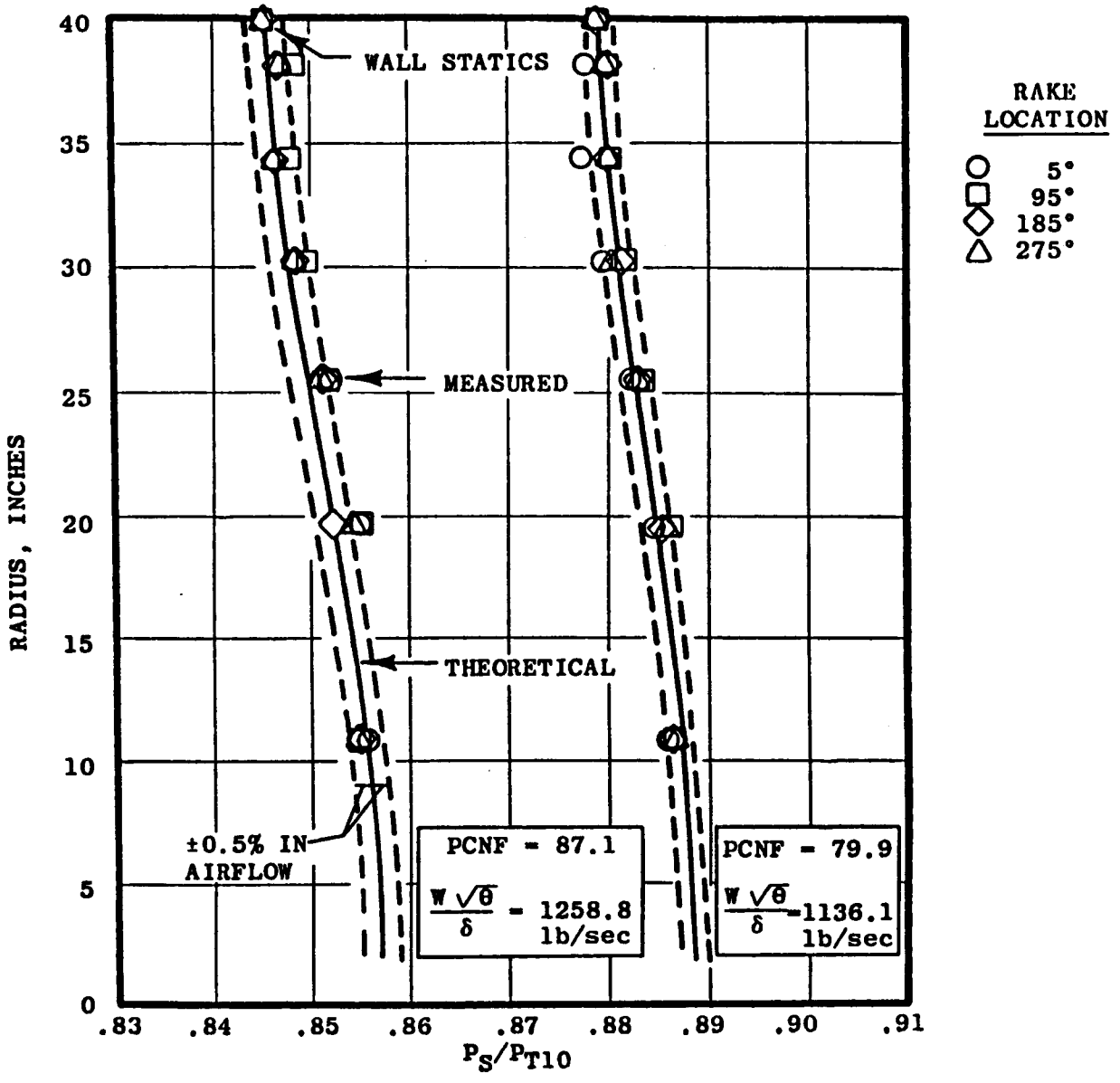


Figure 181. Measured Bellmouth Throat Pressure Profiles.

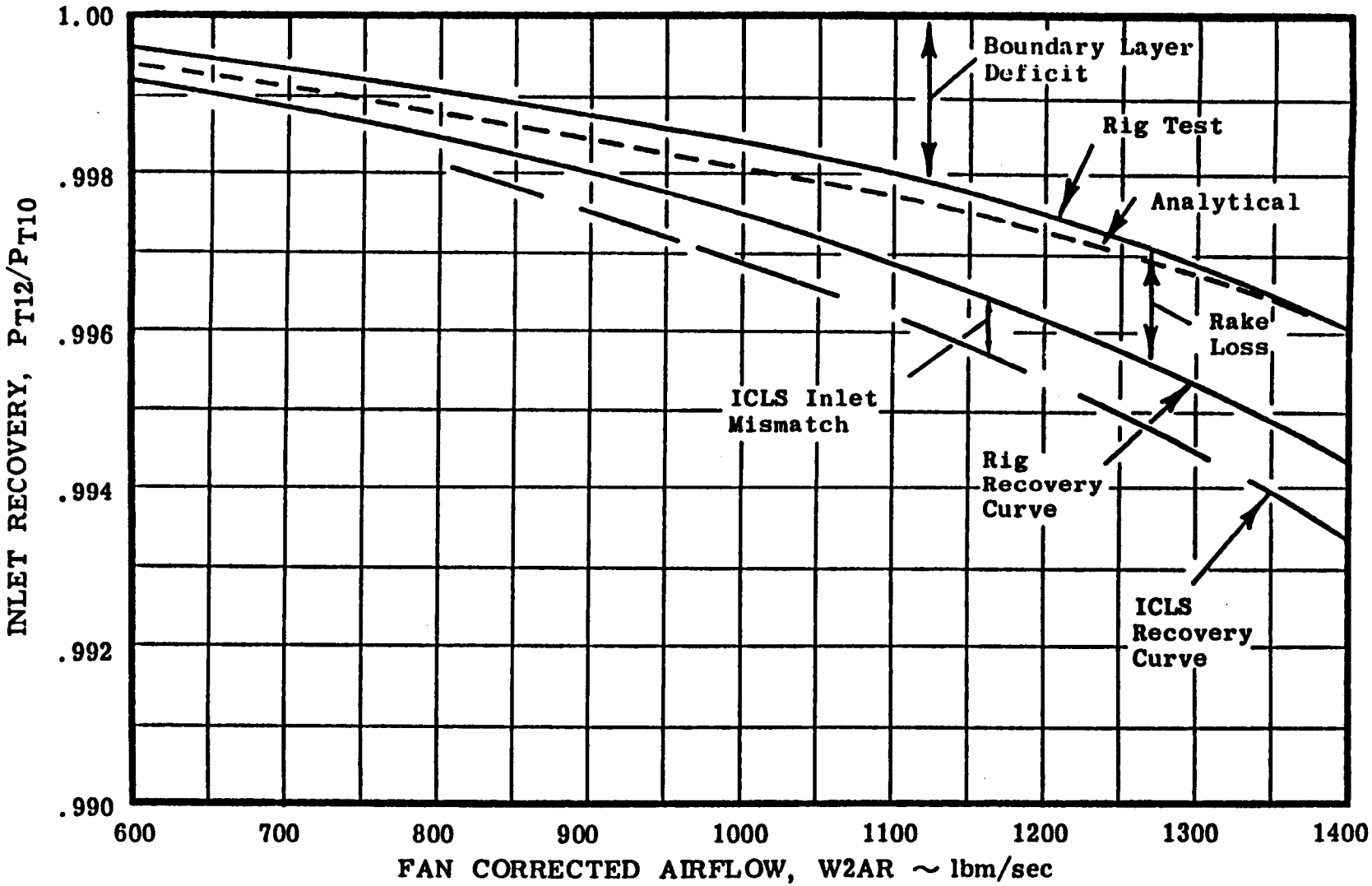


Figure 182. Performance Bellmouth Recovery.

to the facility test stand. A rubber seal between the bellmouth and fan frame as shown in Figure 183 prevented air leakage into the bellmouth. As a result of this mounting, an axial gap existed between the fan frame and the inlet. Additionally, the varying thrust and load forces on both the bellmouth and the engine caused the gap size to vary on test and caused a varying radial misalignment between the bellmouth and engine. The net result was a combination axial gap and step, both of which varied and had an effect on inlet recovery.

The boundary layer rake used to define the recovery from the rig test was also installed on ICLS. Comparison of the boundary layer profiles in Figure 184 shows the effect of the inlet-fan face mismatch. This boundary layer deficiency was integrated for a range of inlet airflows to define an adjustment to the inlet recovery curve and is represented as the ICLS Recovery Curve in Figure 182. The ICLS curve was used for the overall engine and fan component performance evaluation.

Only one boundary layer rake was available to define the mismatch effect, and potentiometer measurements indicate that the rake was in a region which may have had a less than average step height. An analytical calculation of the potential pressure loss due to the step resulted in a 0.15% $\Delta P_T$ loss compared to the 0.08% measured by the single rake at the max engine speed condition [~572 kg/sec (~1260 lb/sec)]. Thus, although it is possible that the exact ICLS Recovery Curve may have been slightly lower than shown in Figure 182, the Figure 182 curve is concluded to be within 0.1% of the true value.

## 6.5 MOUNT SYSTEM MECHANICAL PERFORMANCE

The engine mount system performed without any problems during the entire ICLS engine test program.

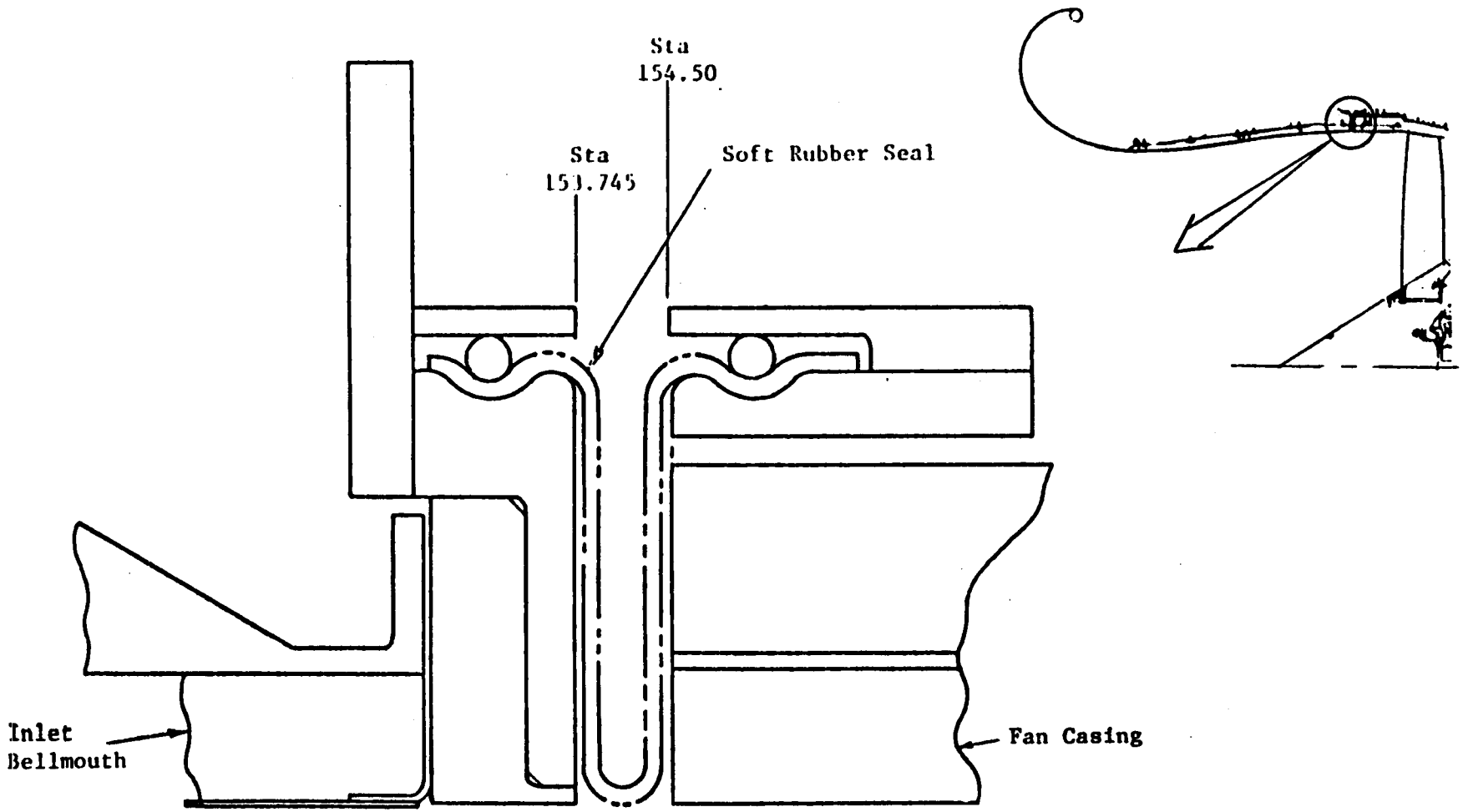


Figure 183. ICLS Inlet Bellmouth - Fan Frame Interface.

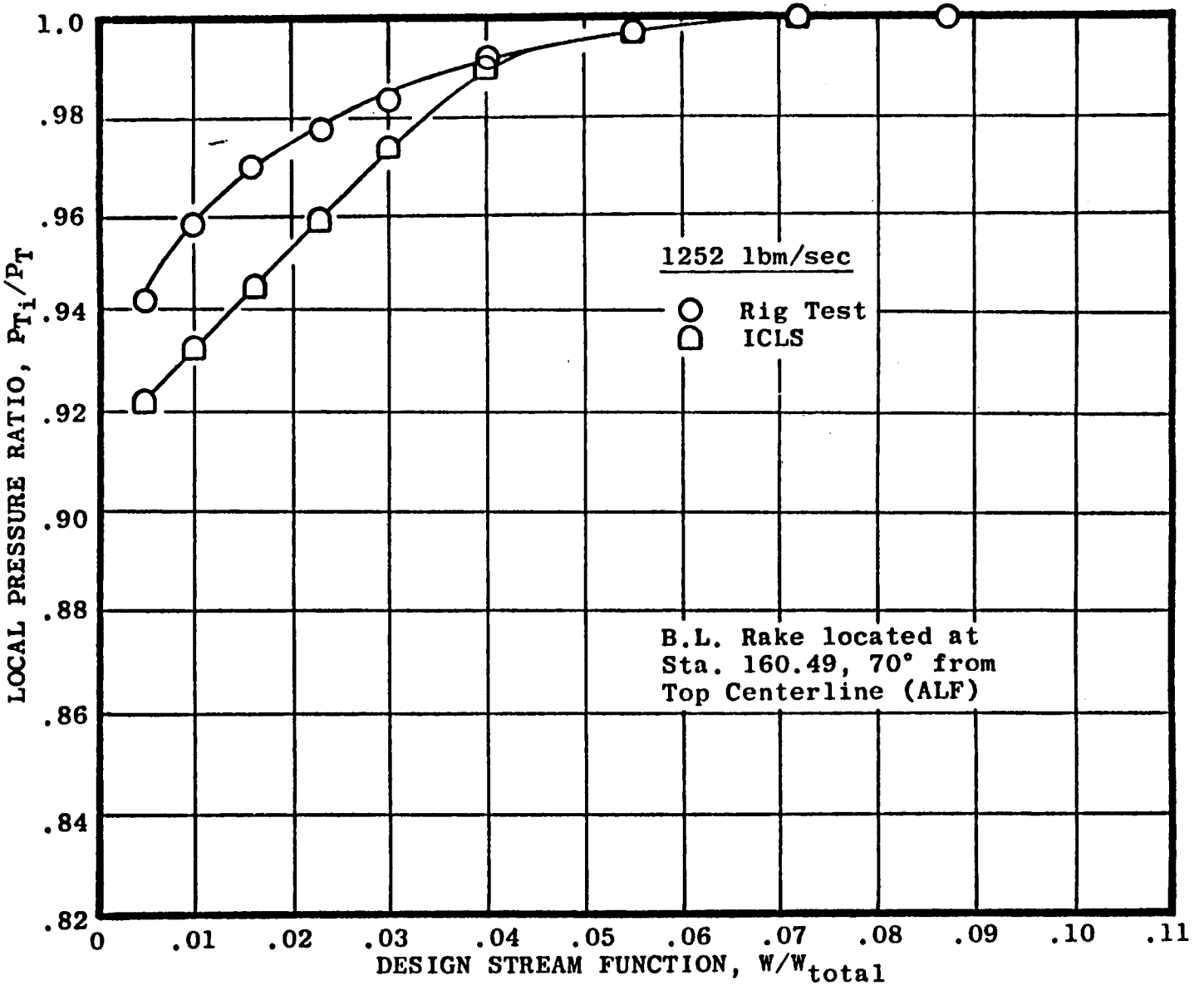


Figure 184. Inlet Boundary Layer Shape Comparison.

## 6.6 FAN MECHANICAL PERFORMANCE

### 6.6.1 Fan Rotor Mechanical Performance

The Stage 1 fan and quarter stage blade vibratory characteristics were as predicted and well within limits. The max stress noted on the Stage 1 blade was 11% limits at 58% Nf where the first flexure mode crosses 3/rev. The maximum stress noted on the quarter stage was 29% limits at 88% Nf where the first flexure mode crosses 5/rev. Campbell diagrams in Figures 185 and 186 show the airfoil frequencies versus rotor speed. No system modes were encountered.

### 6.6.2 Fan Stator Mechanical Performance

As in the Full Scale Fan Test program, the vibratory response of the Stage 1 vanes was well-behaved during the ICLS engine test program. The primary response was again the 32/rev/excitation crossing of the first torsional vane mode at around 2,600 fan rpm. The noted response level during the mechanical checkout portion of the test program was less than 30% of limits. No other mode produced any significant vibratory response.

For the core OGV's, the strong resonance of the first torsion mode with the fan blade passing 32/rev stimulus that was present in the 3,500-3,700 fan rpm range during the fan component test was not present during the ICLS engine test. As anticipated, the maximum physical fan speed for the ICLS engine was well below the 3,500-3,700 rpm range. Other responses of the core OGV's were very minor with observed response levels below 10% of allowable limits.

The fan frame bypass vanes again exhibited only minor responses at any fan speed. The solid 17-4PH steel bypass vanes, procured to expedite the timing and reduce cost, were geometrically shaped as the proposed FSP bypass vanes would be but were structurally much more massive than the proposed hollow composite vanes for the FPS configuration. Therefore, the vibratory modes and response levels for the FPS bypass vanes will likely be different

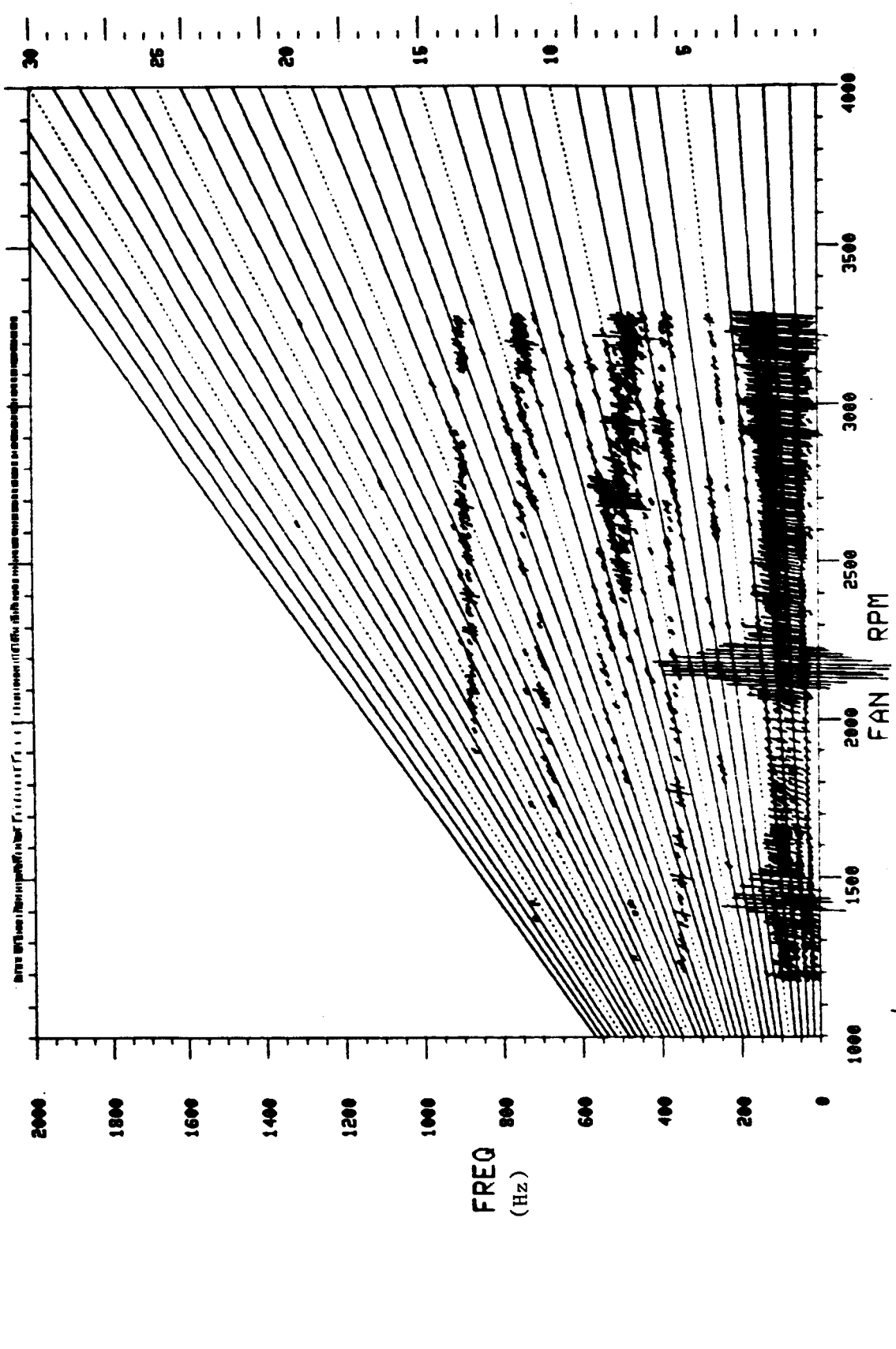


Figure 185. Campbell Diagram - Stage 1 Fan Blade.

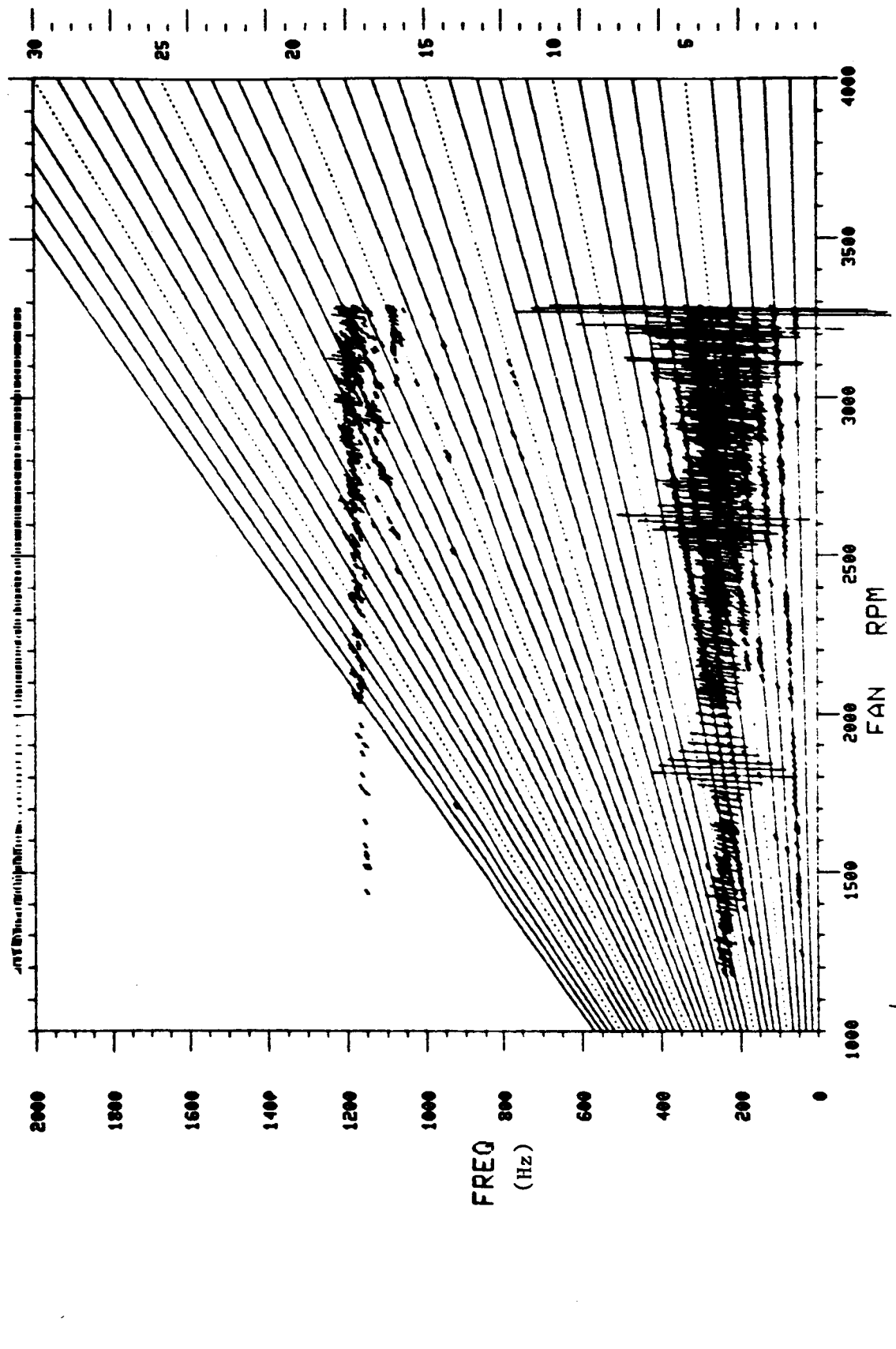


Figure 186. Campbell Diagram - Quarter Stage Fan Blade.

than the modes and response levels of the FSFT and ICLS fan bypass vane configurations. Recent GE experience in the design of hollow composite vanes (used for the $E^3$ FPS) has demonstrated prototype vanes that exhibit weight and cost benefits over existing metal vane designs while satisfying all the mechanical design requirements for stress, deflection, fatigue, impact, erosion, etc. This experience would be utilized to develop the hollow composite fan bypass vane for the $E^3$ FPS configuration.

The only problems encountered by any fan stator components during the ICLS engine test program were associated with the acoustic suppression panels located forward of the fan in the fan containment casing. Figure 15 shows the ICLS fan stator assembly and the location of the acoustic suppresion panels. A cross section of the design of the panels is shown in Figure 187. A fiberglass carrier was filled with acoustic suppression material, Kevlar 29. An aluminum facesheet, perforated to provide 30% open area to the acoustic suppression material, was bonded to the fiberglass carrier. Each panel was bolted to the fan containment case. During a post-test inspection following the completion of the mechanical checkout tests, cracks were discovered in the aluminum perforated facesheet. The cracking appeared to initiate in the perforated facesheet at the location where the facesheet was bonded to the fiberglass carrier (see Figure 187). The cracking was more severe on the bonded edge nearest the fan blade. Five of the six panels that make up a complete assembly were cracked on the edge nearest the fan blade while only three showed cracking on the edge farthest from the fan blade. The most severely cracked panel had approximately 50% of the circumferential length cracked on the edge nearest the fan blade. No material was lost from any panel. None of the other acoustic panels in the fan stator assembly, those in the midcase or in the flow splitter island (Figure 19), exhibited this cracking problem during the entire test program.

The damaged acoustic panels were removed from the fan stator assembly for repair. A stainless steel facesheet was used to replace the damaged aluminum facesheet. The panels were repaired and returned to the engine test program. The performance testing and the fully suppressed acoustic testing

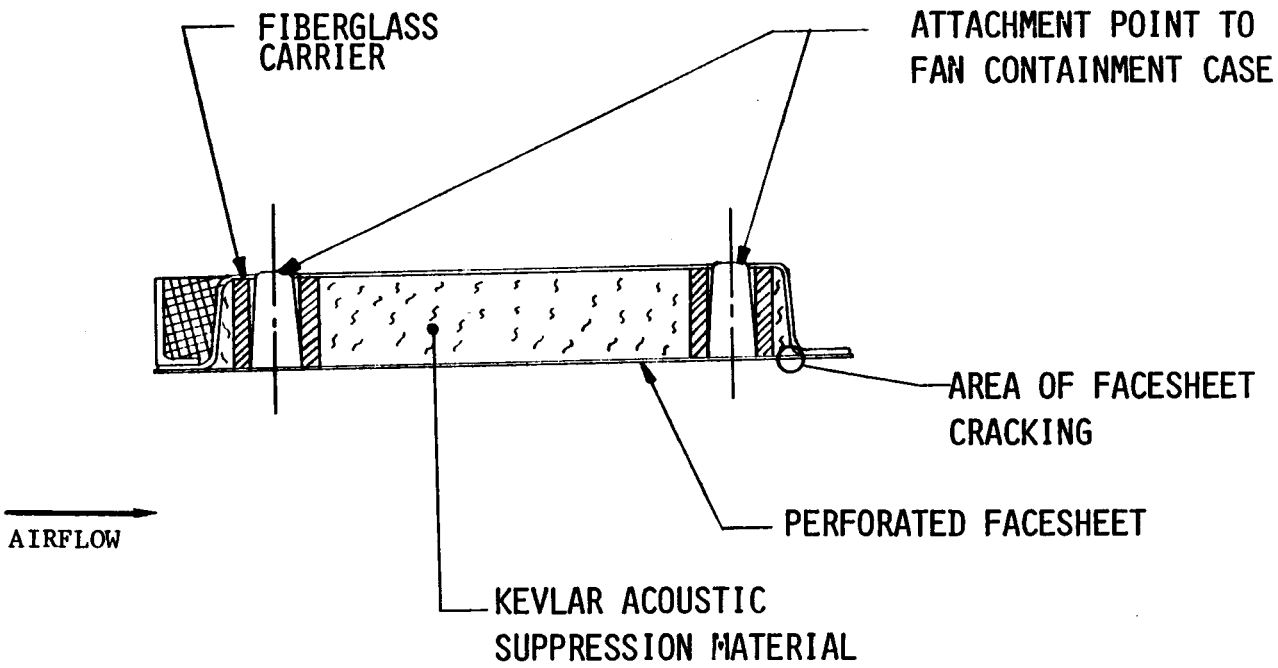


Figure 187. Acoustic Suppression Panel - Cross Section.

were completed with the repaired panels without any problems. However, routine hardware inspections during additional acoustic testing showed some unbonding of the repaired panel facesheet from the fiberglass carrier. The repaired acoustic suppression panels were removed and replaced with nonacoustic (hardwall) panels used during the Full Scale Fan Test program which did not require acoustic testing. An inspection of the repaired acoustic suppression panels revealed no cracking of the stainless steel facesheet.

While completing the engine test program with the hardwall panels, an inspection showed some apparent internal damage to one of the six panels. The hardwall panel construction utilized a fiberglass carrier with a solid fiberglass facesheet and flexcore aluminum honeycomb as the internal structure bonded to the carrier and the facesheet. The suspect hardwall panel was removed and disassembly revealed the internal honeycomb was beginning to disintegrate, but no damage had occurred to the fiberglass carrier or facesheet. Figure 188 shows the hardwall panel with the fiberglass facesheet removed. Following completion of the test program an inspection of the hardwall panels still assembled in the fan stator assembly indicated similar internal damage was present in other hardwall panels.

The damage to the acoustic panel facesheet and the hardwall panel honeycomb was due to fatigue. The acoustic panel facesheet was basically unsupported over the panel width. Circumferential ribs and a softer transition of the facesheet to the fiberglass carrier support areas at the edges would stiffen the panel and improve the stress gradient for the facesheet supports at the panel edges. The material change to the stainless steel facesheet as part of the acoustic panel repair provided sufficient improvement in fatigue strength to eliminate the cracking for the remainder of the test program. Configuration changes and/or material changes would need to be evaluated for the acoustic panels just forward of the fan blade to establish an acceptable design for the FPS engine configuration. In the case of the hardwall panel damage, the construction utilized a lightweight aluminum honeycomb. Improvements in honeycomb compressive strength, crush strength,

- Construction: Fiberglass Carrier and Facesheet (.027" thick) Bonded to Honeycomb Core (Flexcore: 5052 Alum, 40 Cells/Ft., .0013 Foil Thick, 2.1 #/$Ft^3$, .99" thick)

- Honeycomb Disintegration in Damaged Areas
  No Damage to Fiberglass Carrier or Facesheet



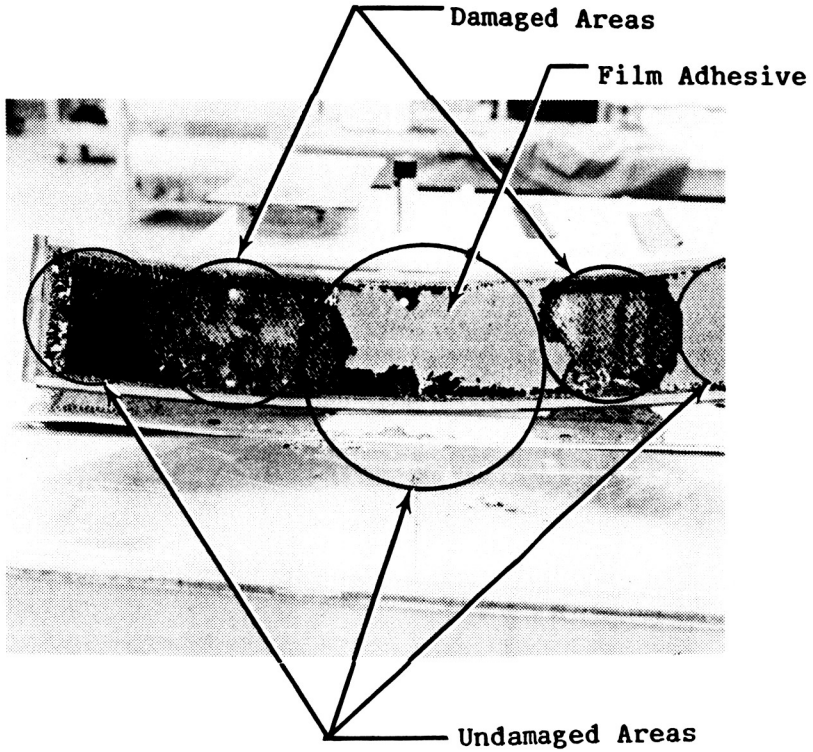


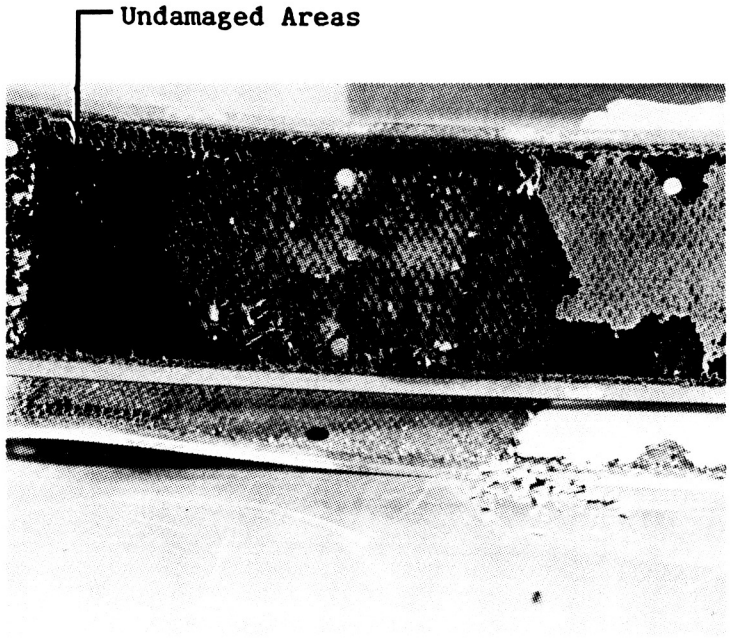


Close-up of Damaged Areas



Figure 188. Fan Casing Hardwall Panel Damage.

stiffness, etc., can be realized by changes to the honeycomb material, the foil thickness and the cell spacing.

## 6.7 FAN AERODYNAMIC PERFORMANCE

The ICLS engine fan and quarter-stage configuration is shown in Figure 15, and the aerodynamic instrumentation is shown in Figure 100. The fan component was built from the same hardware used in the full-scale fan test (FSFT), except that acoustic panels were installed in the casing forward and aft of the fan rotor and on the upper surface of the quarter-stage island. Instrumentation set-up and rakes at major measurement planes were identical to the FSFT, except that the seven bypass exit radial rakes were manifolded at each immersion and the Plane 23 arc rakes were removed. Vane-mounted instrumentation was not recorded except at Plane 23, the inner bypass OGV leading edge.

Fan and quarter-stage performance data points were taken at various fan speeds on three operating lines as determined by a performance nozzle (A8A), an exhaust plane survey nozzle (A8A-2%), and the survey nozzle with survey rakes (A8A-6%). The highest fan speed data points were taken near takeoff conditions at 87.1% corrected fan speed.

The main instrumentation planes used for defining the overall fan performance are:

1. Inlet Plane (PL10) - Four, six-element pitot-static rakes with 6-TT elements on each rake, located at the bellmouth throat.

2. Bypass OGV Exit (PL14) - Seven, 10-element PT/TT arc rakes and seven, seven-element radial rakes located ~1/2 OGV chord length behind bypass OGV's. Arc rakes were used to define fan bypass performance with the radial rake measurements used to adjust for circumferential variations.

3. Core Duct Exit (PL25) - Four, five-element PT/TT radial rakes located at the core duct exit.

Other instrumentation was located on the portion of the bypass OGV leading edge that is below the island (PL93) and on the flowpath walls. A boundary layer rake at the fan rotor inlet (Plane 12) was used to measure the total-pressure gradient near the outer wall and to determine the total-pressure loss in the duct between Plane 10 and Plane 12.

Fan Bypass Performance

The preliminary performance of the fan bypass region from the ICLS engine test is presented on the performance map in Figure 189. Speed lines and stall points from the FSFT data (solid lines and symbols) are shown for reference. The predicted pressure ratio versus flow and efficiency versus flow operating lines are also shown. The ICLS operating line data are momentum-averaged and adjusted for Plane 14 circumferential variations as well as inlet losses. The fan bypass momentum-averaged efficiency data are shown for the performance nozzle operating line. The adjusted efficiency near the sea level takeoff power setting is 0.6 point below the FSFT demonstrated level. Poor casing boundary layer flow conditions, created by an inlet-bellmouth flowpath mismatch, were measured at the fan inlet. Only one boundary layer rake, located at 70° (ALF-CW) and just ahead of the fan rotor, was available to determine the average Plane 12 total pressure. With the engine/bellmouth mismatch being the greatest at the top of the engine, the position of this rake was not suitable for obtaining a true average inlet total pressure. Furthermore, the "A" immersion arc rake at Plane 14 was located in the same circumferential sector as the forward facing step at the inlet. These two factors contributed significantly to the poorer bypass performance relative to the FSFT vehicle. Additionally, the presence of the acoustic panels in the duct at the casing and island flowpaths between the fan rotor and OGV could adversely affect the bypass performance. The bypass efficiency level and adjustments at the takeoff data point are presented in Table XVIII.

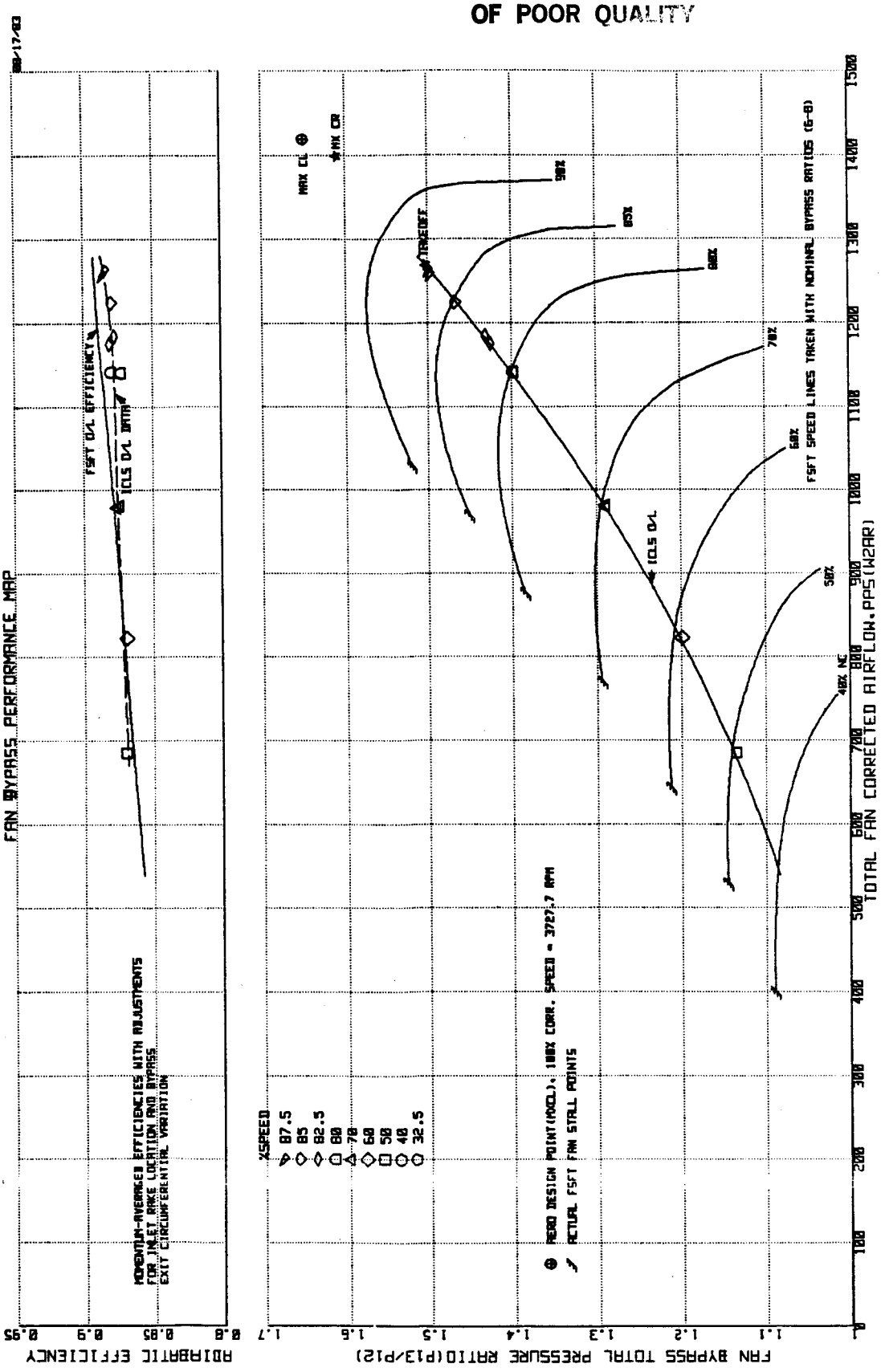


Figure 189. Fan Bypass Performance Map.

Table XVIII. Fan Aerodynamic Performance at Takeoff.

| | Measured[1] | Adjusted[2] | ICLS Pred. Adjusted[3] | (FSFT) |
|---|---|---|---|---|
| Total Fan Inlet Corrected Flow (lbm/sec) | 1253.5 | 1254.7 | 1258.0 | 1258.0 |
| Bypass Total Pressure Ratio | 1.489 | 1.493 | 1.497 | 1.497 |
| Adiabatic Efficiency | 0.874 | 0.880 | 0.886 | 0.892 |

(1) Measured data at Plane 10 and Plane 14; mass-averaged efficiency.

(2) Adjustments to Plane 14 data for momentum-averaging and circumferential variation; Plane 10 total pressure adjusted for predicted inlet duct loss based on FSFT data. (These are same adjustments made to FSFT measured data.)

(3) Adjusted for additional inlet duct loss as indicated by boundary layer rake measurements.

The momentum-averaged efficiency at Plane 14 is less than the mass-averaged value by approximately 0.4 point. The adjustment for circumferential variation effects on the Plane 14 pressures and temperatures, when applied in a manner consistent with the FSFT data adjustment, is about 0.2 point in efficiency. The initial inlet loss adjustment (assumed from the FSFT data) accounts for 0.6 efficiency point. An additional adjustment of 0.6 point is made as a result of the ICLS measured boundary layer being larger than that of the FSFT configuration.

The flow versus speed characteristic (Figure 190) for the performance nozzle test configuration shows that the fan is operating as predicted by the pretest cycle calculations.

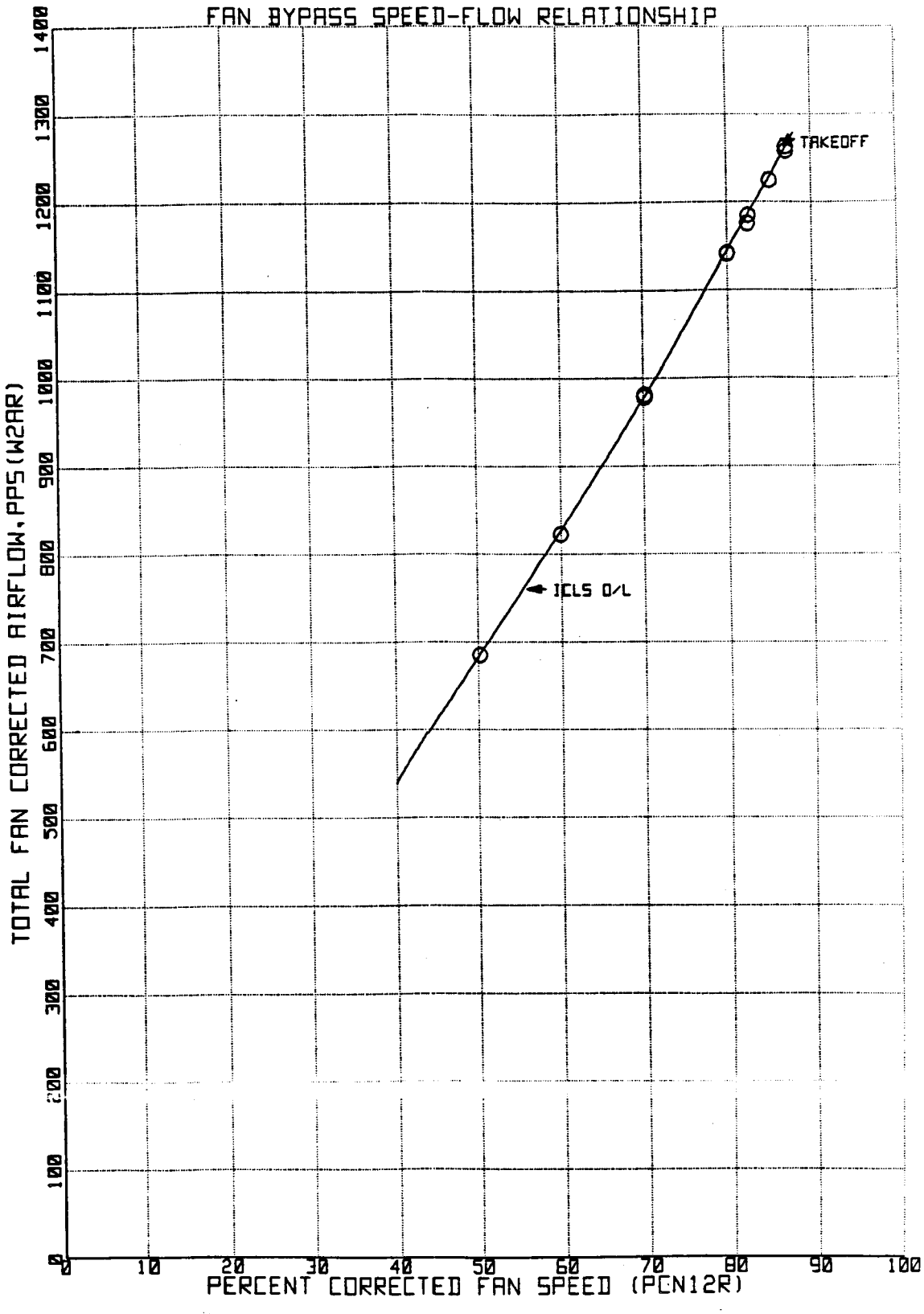


Figure 190. Fan Bypass Speed-Flow Relationship.

Radial distributions of the fan exit (Plane 14) total pressure ratio and total temperature ratio data from a test reading at 85% corrected speed are compared in Figures 191 and 192 with a FSFT reading at about the same operating condition. The ICLS data indicate a close agreement with the FSFT profiles except at the casing and near-island immersions. The adiabatic efficiency profiles are compared in Figure 193. The largest efficiency discrepancy occurs at the tip and island immersions where the acoustic panels and inlet mismatch adversely affect the performance.

Fan Hub and Quarter-Stage Performance

The core-stream corrected flow versus percent corrected fan speed relationship is shown in Figure 194. The solid line is the predicted operating line and the symbols represent the ICLS test data for the performance nozzle configuration; the test data agree very well with the predicted line.

The core-stream performance map is shown in Figure 195. The core-stream airflow, measured at Plane 25 and corrected to the fan inlet, is plotted on the abscissa. The total-pressure ratio, used for the ordinate, is the Plane 23 total-pressure as derived from the Plane 25 rake data and ratioed to the Plane 10 inlet total-pressure. The Plane 23 total-pressure was determined from an FSFT loss correlation of Plane 23 and 25 measured data. The background speed lines on the core-stream performance map represent the FSFT data which were taken at or near the nominal design bypass ratio of 6.8. The ICLS data were taken at the engine cycle bypass ratios which are somewhat higher as shown in Figure 196. The higher bypass ratio at speed tends to produce a lower core flow on the performance map. The adiabatic efficiencies shown are based on Plane 23 pressures and Plane 25 temperatures. Test data agree closely with the predicted pressure ratio versus flow operating line. Efficiency data is slightly higher (approximately 0.6 points) than the FSFT efficiency, which may be a result of the different engine environment and operating conditions. A comparison of performance with an FSFT data point near takeoff is presented in Table XIX.

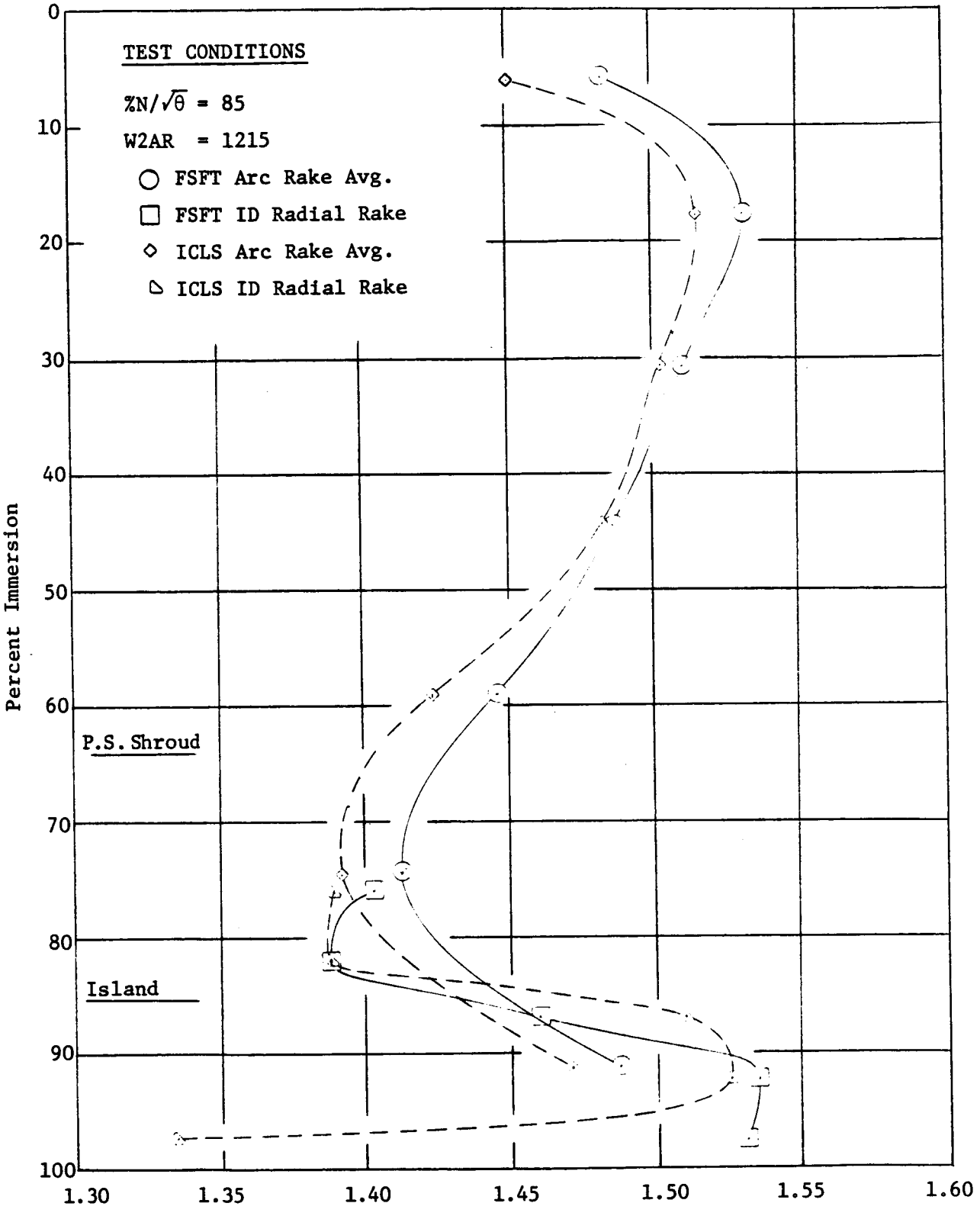


Figure 191. Fan Bypass OGV Exit (Plane 14) Radial Total Pressure Profiles.

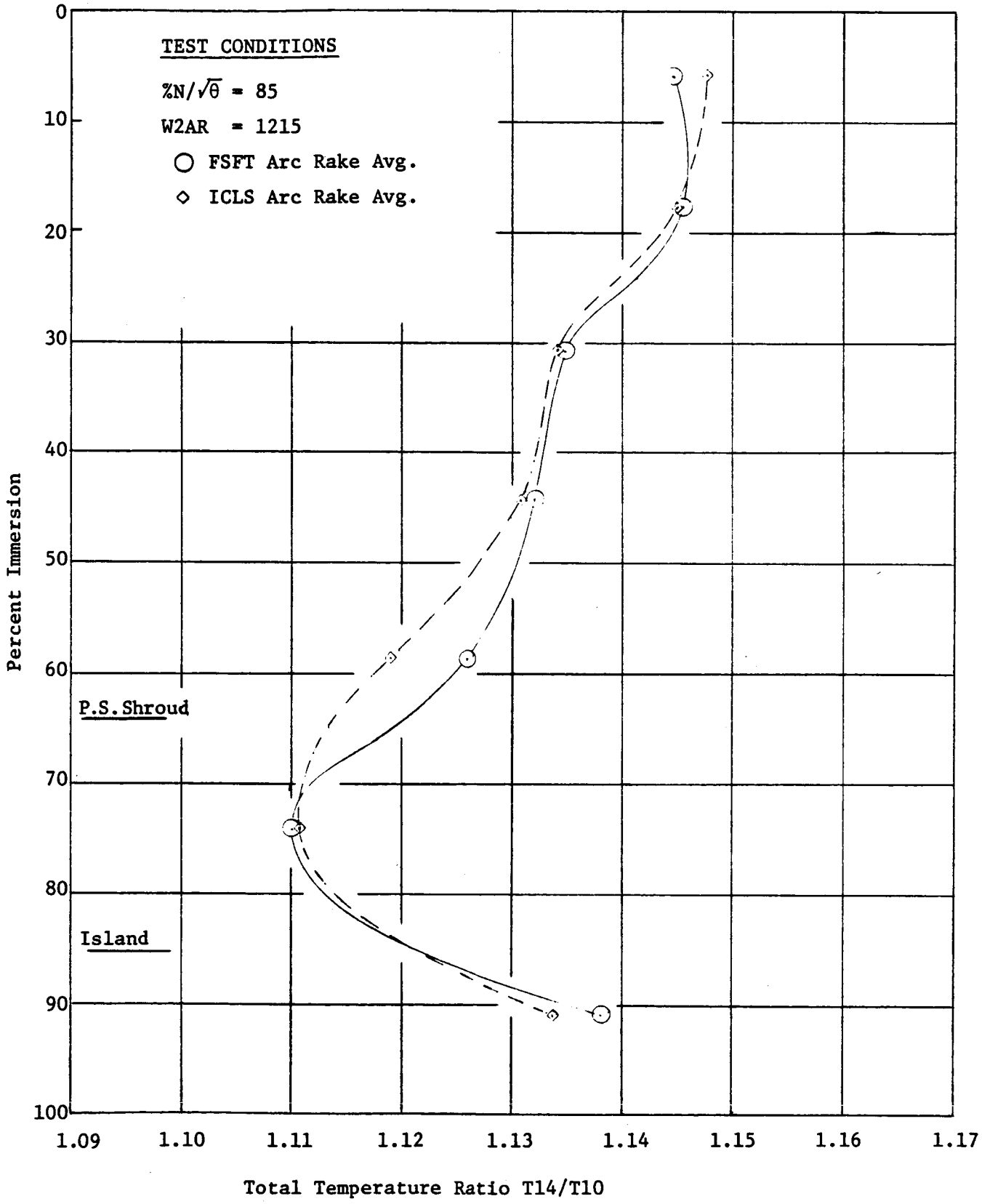


Figure 192. Fan Bypass OGV (Plane 14) Radial Total Temperature Profile.

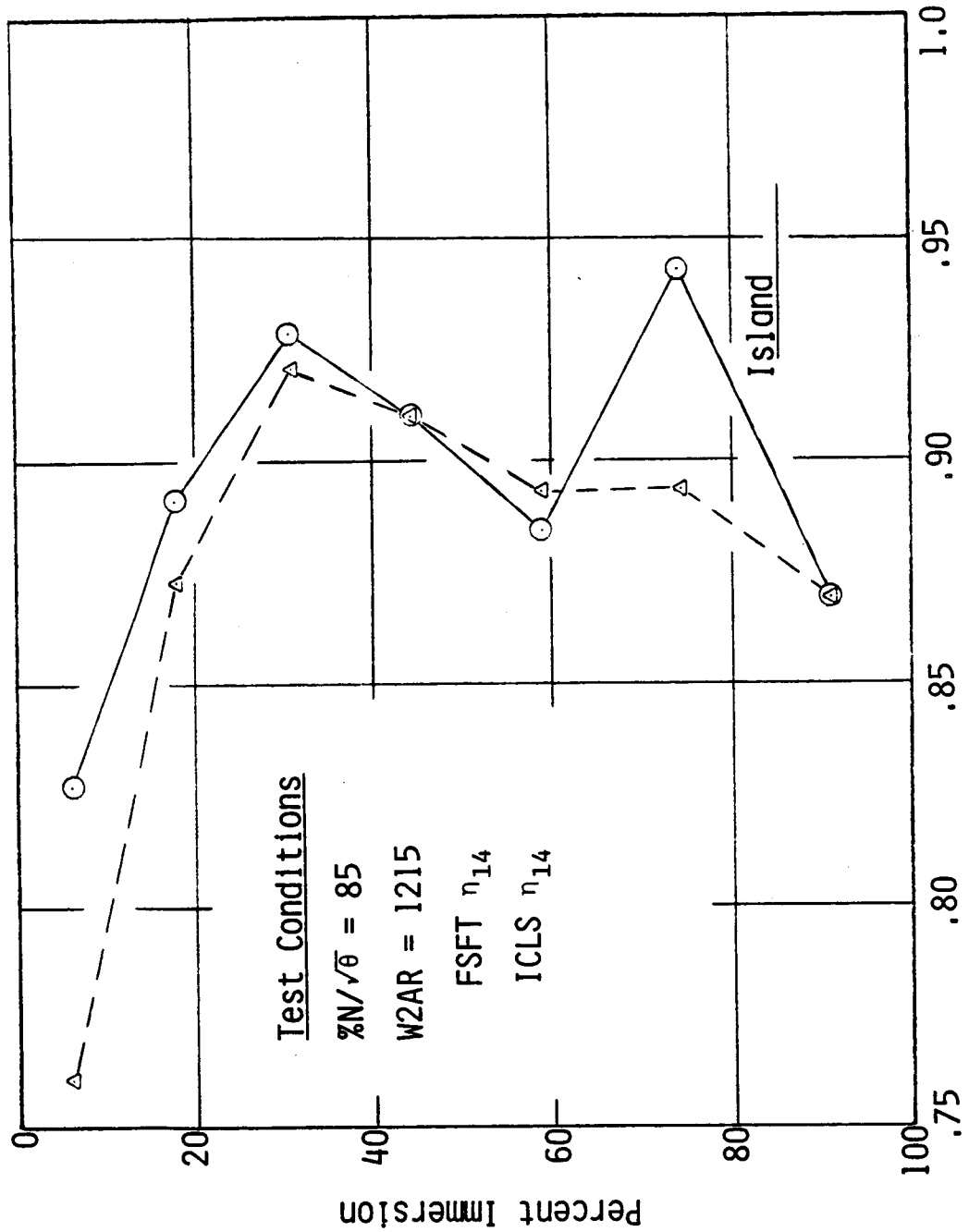


Figure 193. Fan Bypass OGV Exit (Plane 14) Radial Efficiency Profiles.

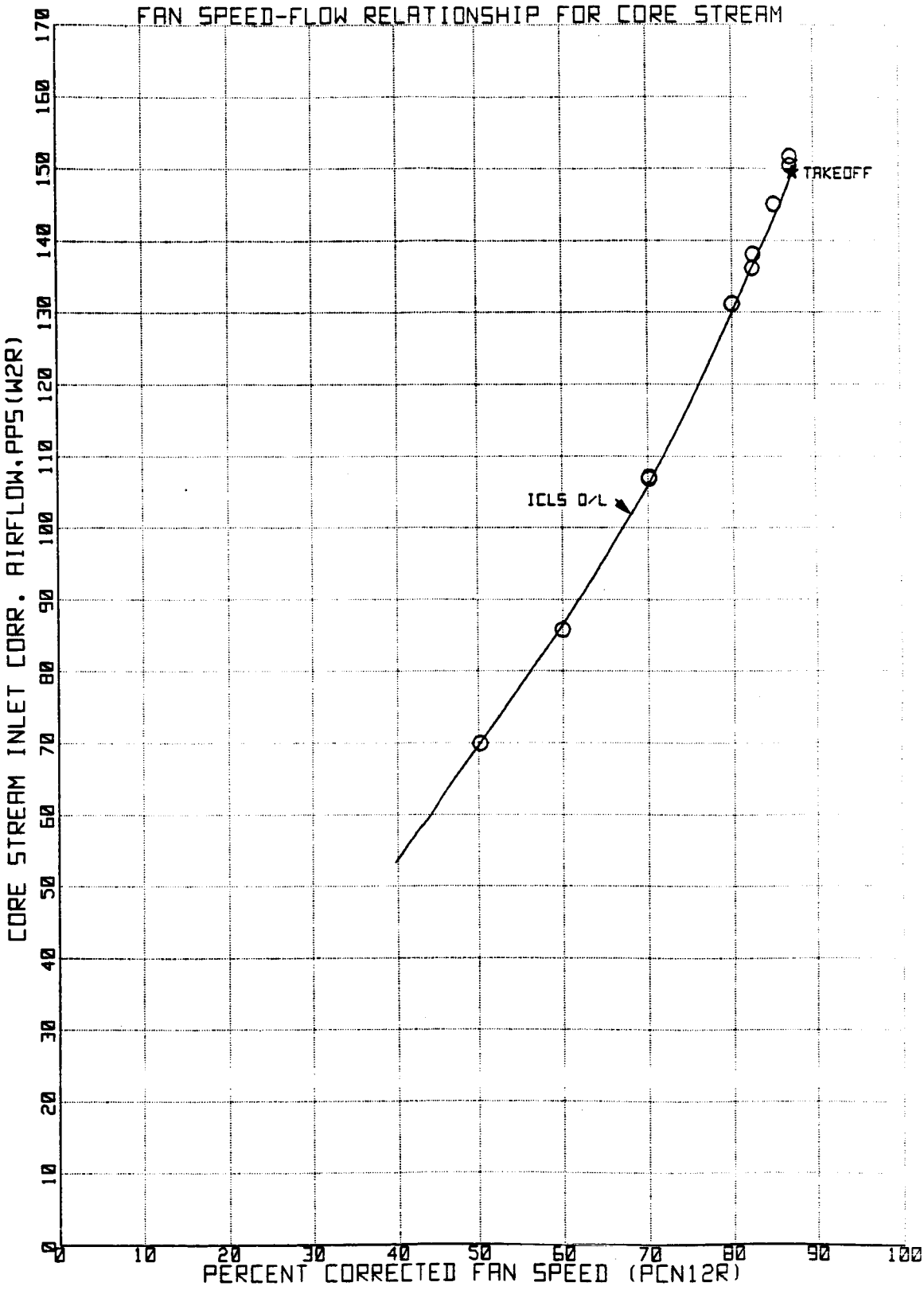


Figure 194. Fan Speed-Flow Relationship for Core Stream.

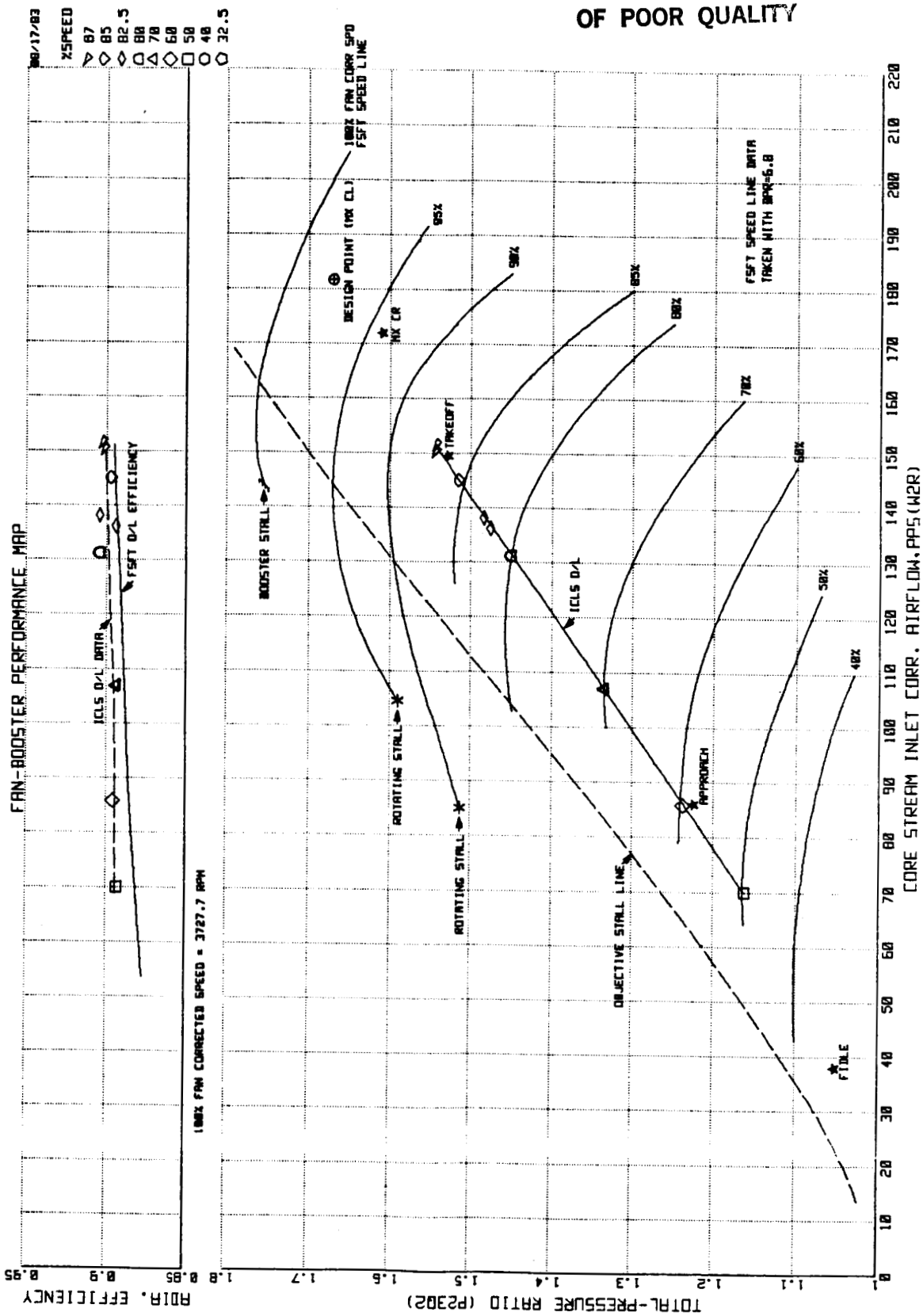


Figure 195. Fan-Booster Performance Map.

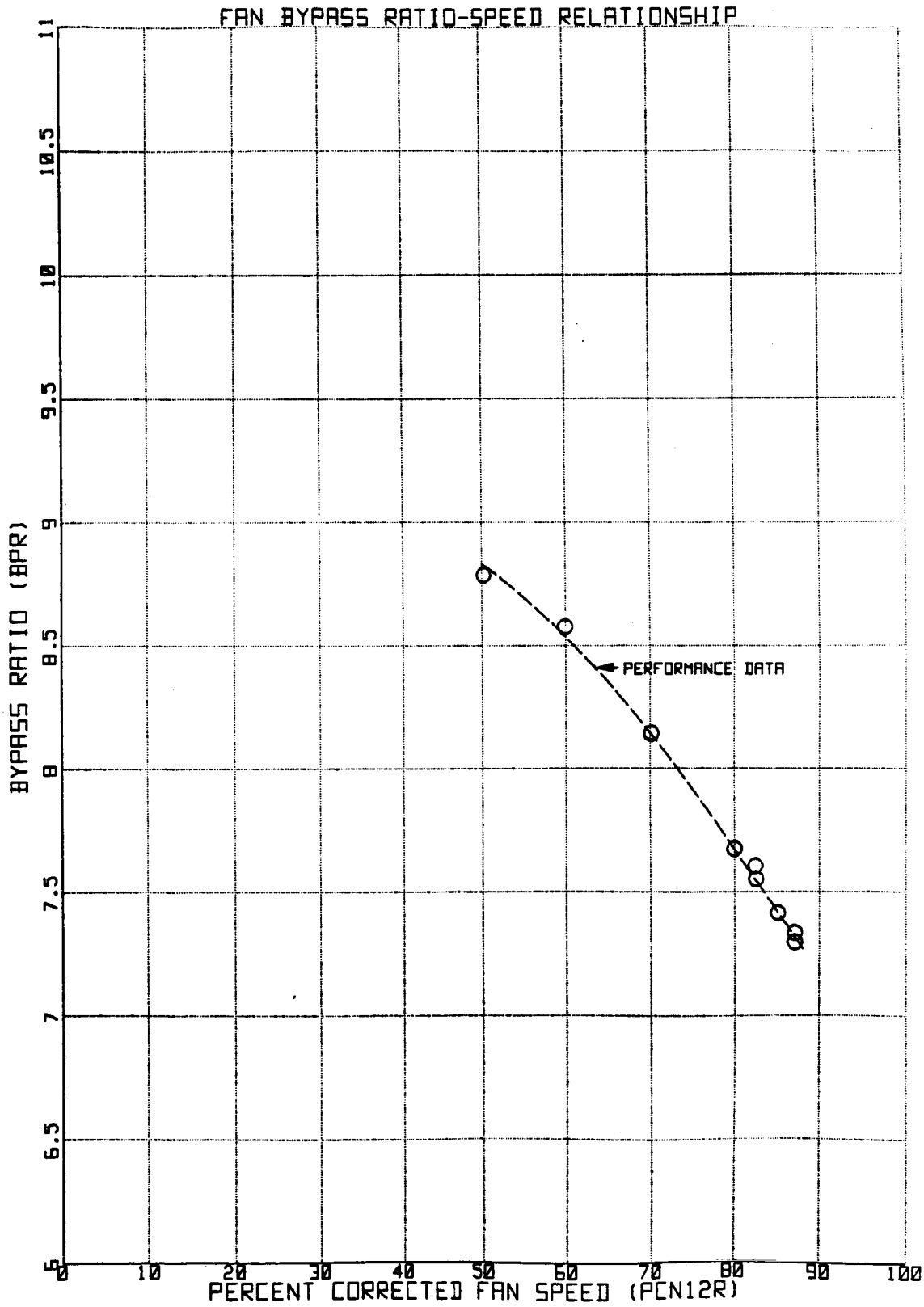


Figure 196. Fan Bypass Ratio-Speed Relationship.

Table XIX. Fan Core-Stream Performance Near Takeoff (No Inlet Adjustments).

| | ICLS | FSFT |
|---|---|---|
| Core-Stream Inlet Corrected Flow ~ WZR (lbm/sec) | 143.5 | 143.6 |
| Total Pressure Ratio (PT23/PT10) | 1.514 | 1.504 |
| Adiabatic Efficiency $\eta$23/10 | 0.901 | 0.894 |

Radial profiles of Plane 25 total pressure and total temperature ratioed to Plane 10 are shown in Figure 197 and the corresponding adiabatic efficiencies are shown in Figure 198. Solid lines represent data from an FSFT data point at 85% corrected fan speed near the performance operating line. The dashed line data were measured at similar operating conditions from the ICLS test. The data show slightly flatter PT and TT profiles near the outer wall which could indicate more favorable flow conditions in that region. The efficiency profile shape agrees closely with FSFT data while the level is slightly higher, as indicated on the performance map.

Summary and Conclusions

Preliminary performance test results indicate that the fan bypass and core stream are operating as predicted. The highest fan speed data was recorded during the performance test near takeoff condition at 87.1% corrected speed and a bypass pressure ratio of 1.497. The fan bypass adiabatic efficiency at this point is about 0.6 point below the FSFT demonstrated level; the core stream efficiency is about 0.6 point above the FSFT data.

## 6.8 CORE MECHANICAL PERFORMANCE

The mechanical performance of the core components was established in the core tests. Pressures, temperatures and strains were measured on the

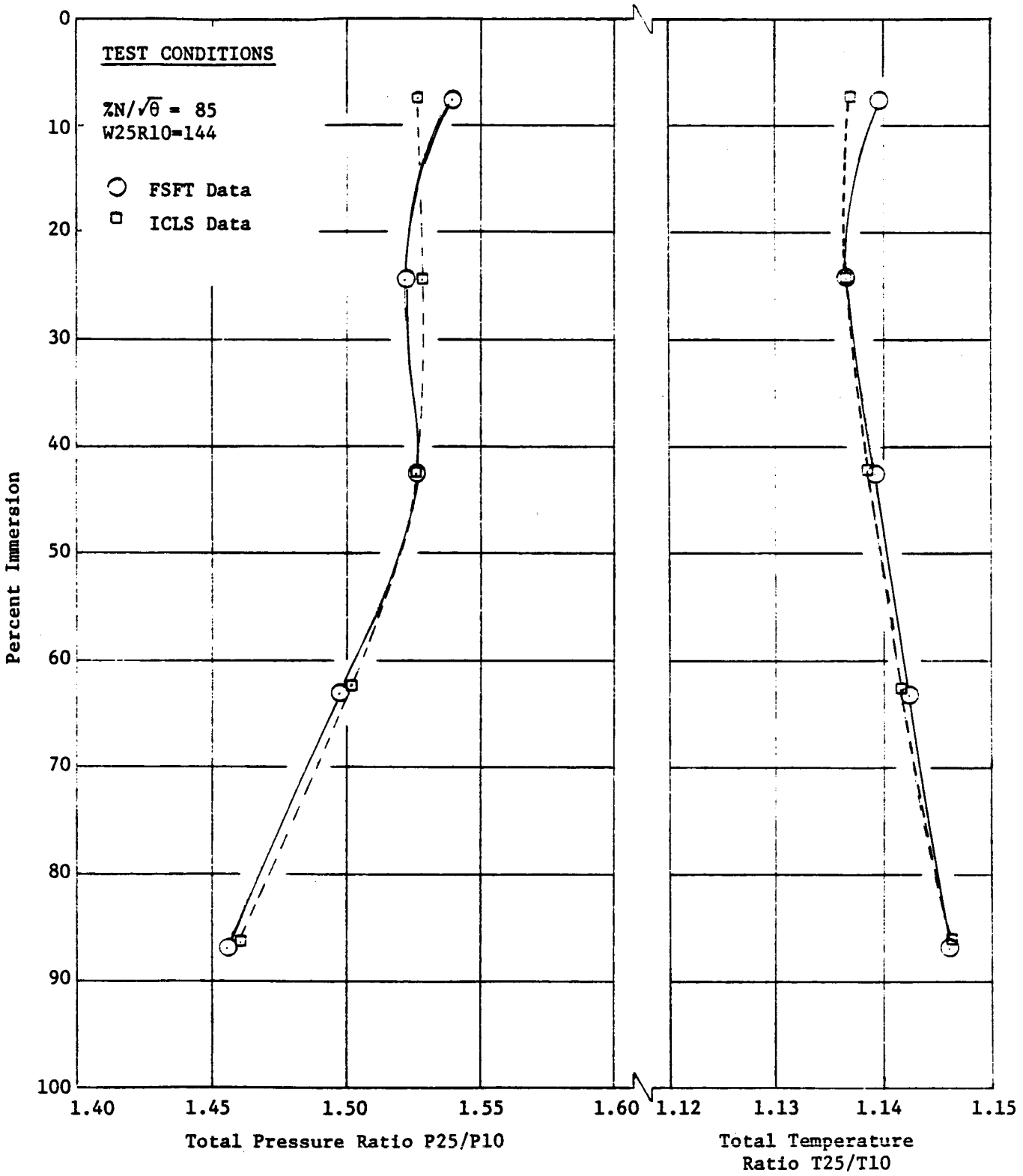


Figure 197. Fan Hub and Quarter Stage - Core Inlet (Plane 25) Radial Profiles.

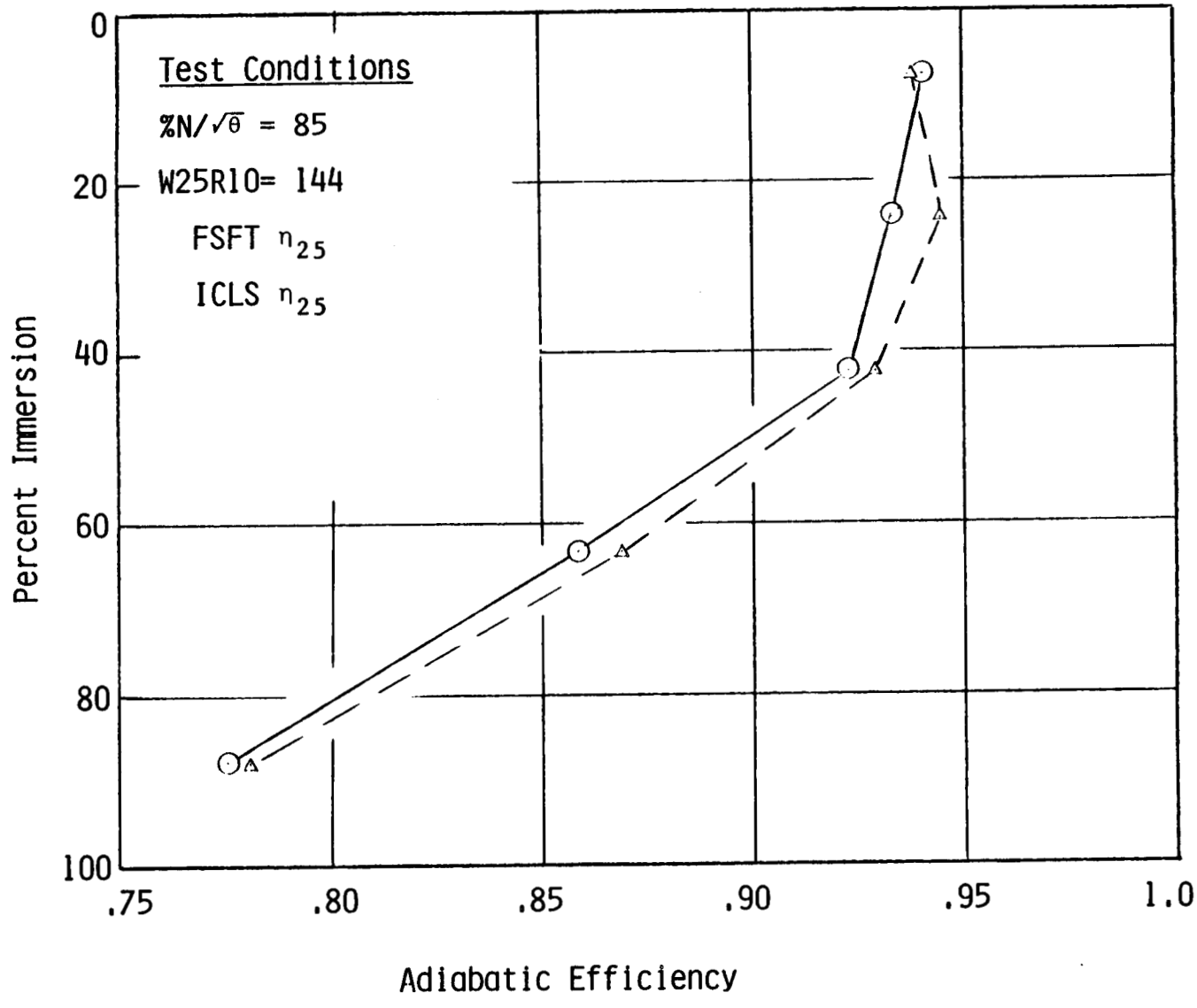


Figure 198. Fan Hub and Quarter Stage - Core Inlet (Plane 25) Radial Efficiency Profile.

rotor and more static instrumentation was available in the core than in ICLS. The reader is referred to Reference 3 for detailed information on the mechanical performance of the core components. This section provides the additional knowledge gained during ICLS testing.

### 6.8.1 Compressor Rotor Mechanical Performance

During turbofan operation, the core rotating instrumentation could not be read out, so rotor mechanical performance was not monitored. A mid- and post-test borescope inspection revealed no distress.

### 6.8.2 Compressor Stator Mechanical Performance

Stator vane vibratory frequencies were the same as observed during the core engine test of 1982. Vibratory stress responses of the seven stages of variable vanes (IGV - S6) were less than 40% of limits. Stators 7, 8, and 9 responded at higher levels with a maximum stress of 76% of limits. The only aeromechanical change from the core engine test occurred at 95% corrected core speed where the IGV responded at low stress level to the wake from the fan rotor quarter-stage blade (56/rev). The Campbell Diagram for the IGV is shown in Figure 199.

The VSV torsion bar actuation system performed very successfully during the ICLS test. IGV through Stator 4 vane angles tracked within $\pm$0.5 degree of the desired schedule throughout the test. Stators 5 and 6 were locked in place.

Radial tip clearances at rotor Stages 3, 5, and 10 were measured by clearanceometers during engine operation. The Stage 10 clearanceometers produced questionable data which is still being reviewed.

The minimum clearances measured at rotor Stages 3 and 5 are presented as a function of core corrected speed in Figures 200 and 201.

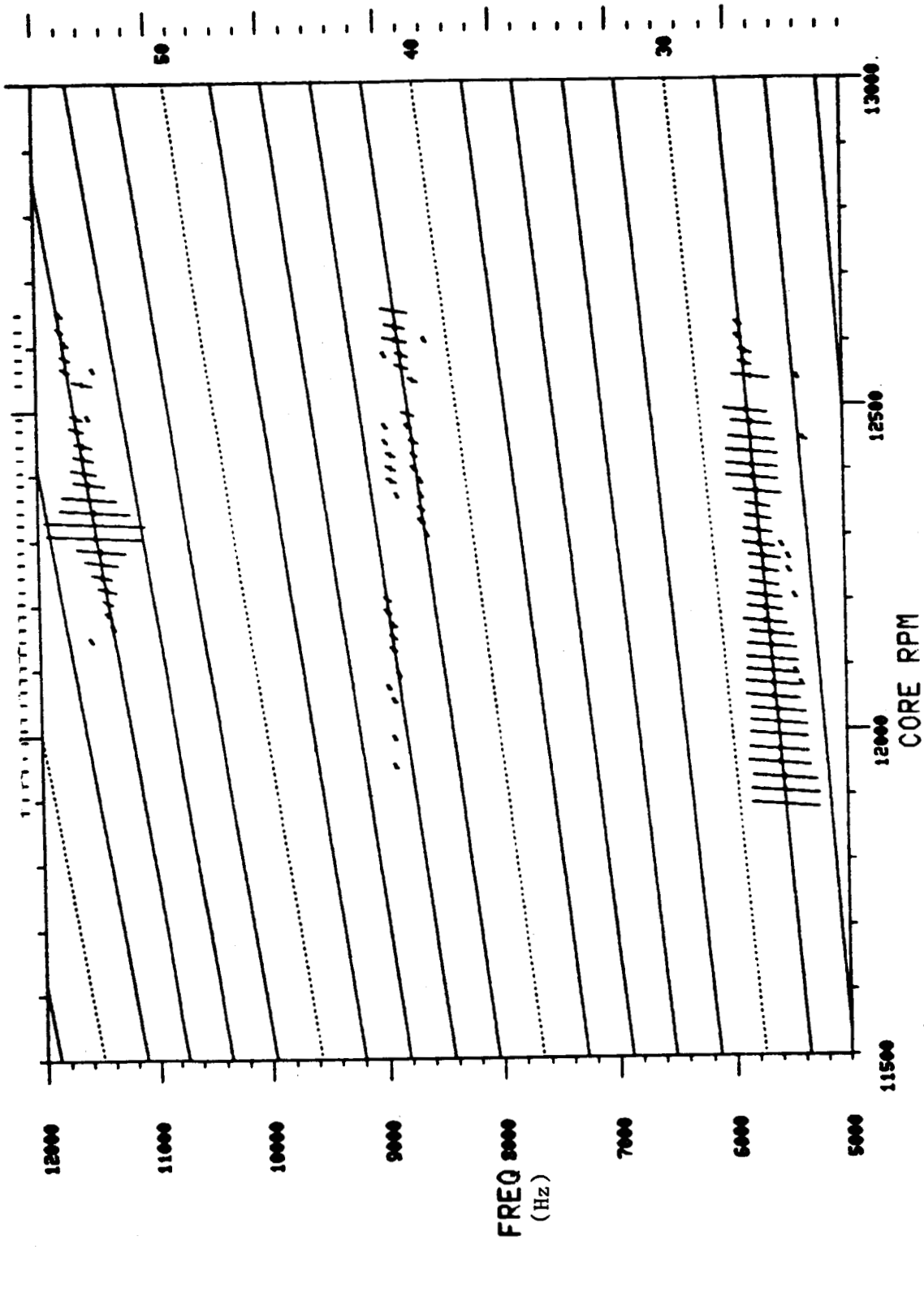


Figure 199. Campbell Diagram - Core IGV.

ORIGINAL PAGE IS
OF POOR QUALITY

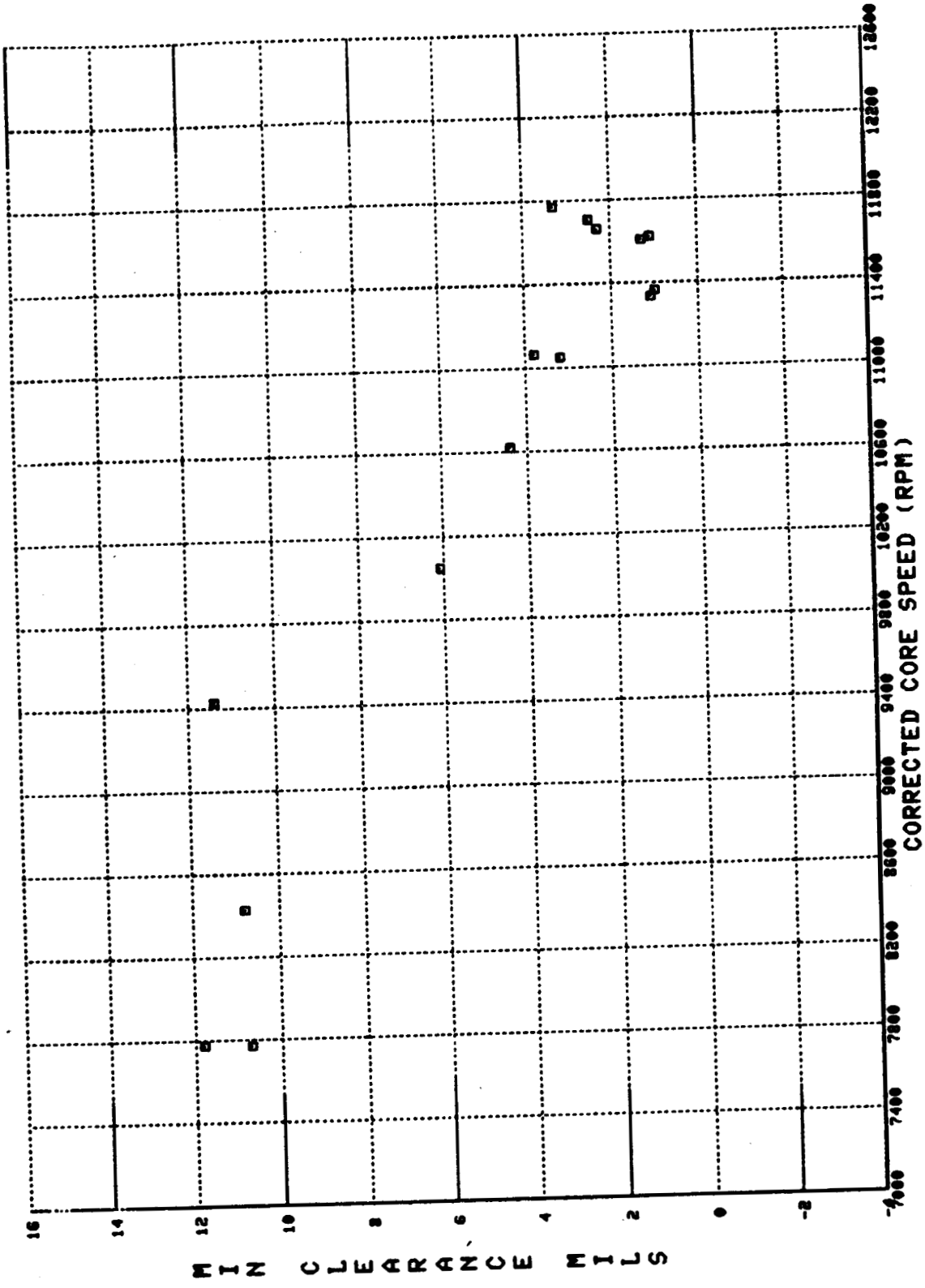


Figure 200. Rotor 3 Tip Clearances.

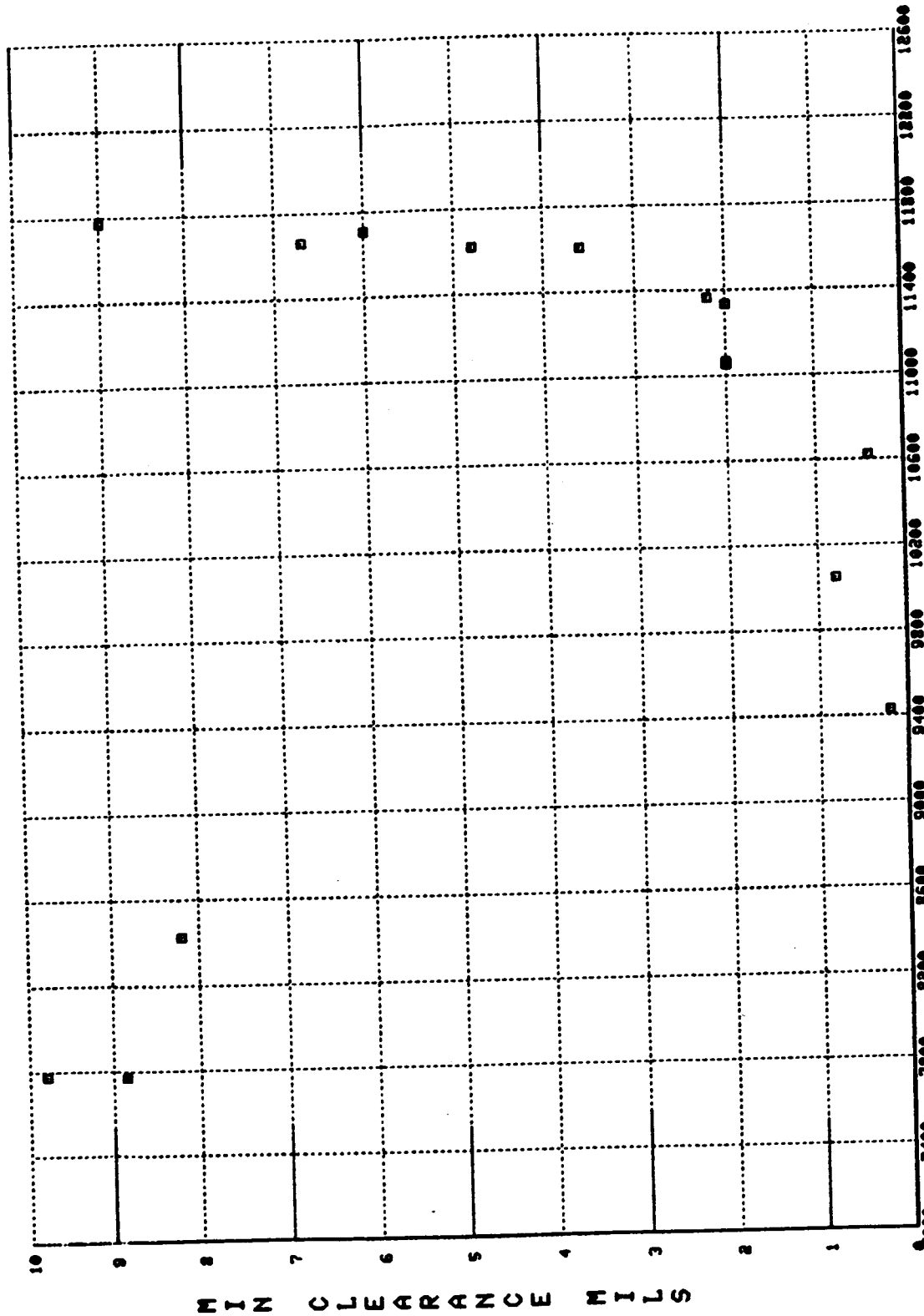


Figure 201. Rotor 5 Tip Clearances.

### 6.8.3 Combustor Mechanical Performance

The combustor performed well mechanically throughout the ICLS testing. Liner metal temperatures correlated well with core test results. No metal temperature limits were reached during the test.

Transient temperature measurements were obtained for rapid accelerations during the testing. Results for row 1 inner and outer shingles are shown in Figures 202 and 203. The data show no temperature overshoot during the acceleration. Past experience has shown that temperature overshoots during transients result in combustor liner and turbine vane distress occurring earlier than predicted, as a result of high transiently induced thermal stresses. The data show no such problem and indicate that the fuel scheduling has produced a smooth, fast acceleration.

The combustor was borescoped at the conclusion of the test and found to be in excellent condition. Temperature patterns indicated there were no severe local hot spots. Condition of the centerbody was excellent.

Spallation of the TBC of the pilot side of the centerbody (observed in previous rig and core testing) had continued during the ICLS test. The spalled areas increased in size circumferentially approximately 20% but remained constant axially. No new areas of spallation were observed and no parent metal distress or significant oxidation was evident. The dome and fuel nozzles looked clean with very little carboning. No progress in the minor oxidation of splashplate edges and sleeves (observed after previous testing) was noted.

### 6.8.4 High Pressure Turbine Mechanical Performance

#### Introduction and Summary

The maximum speed, temperature, and pressure experienced by the high pressure turbine during ICLS testing are listed in Table XX. Detailed HPT

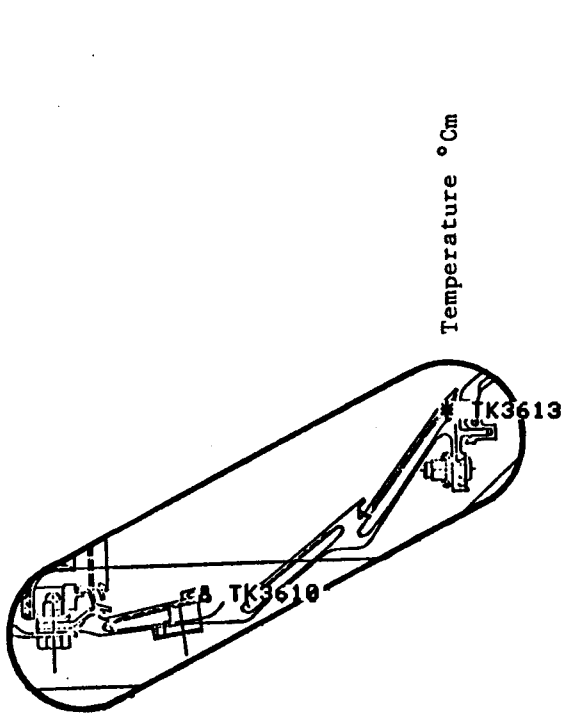


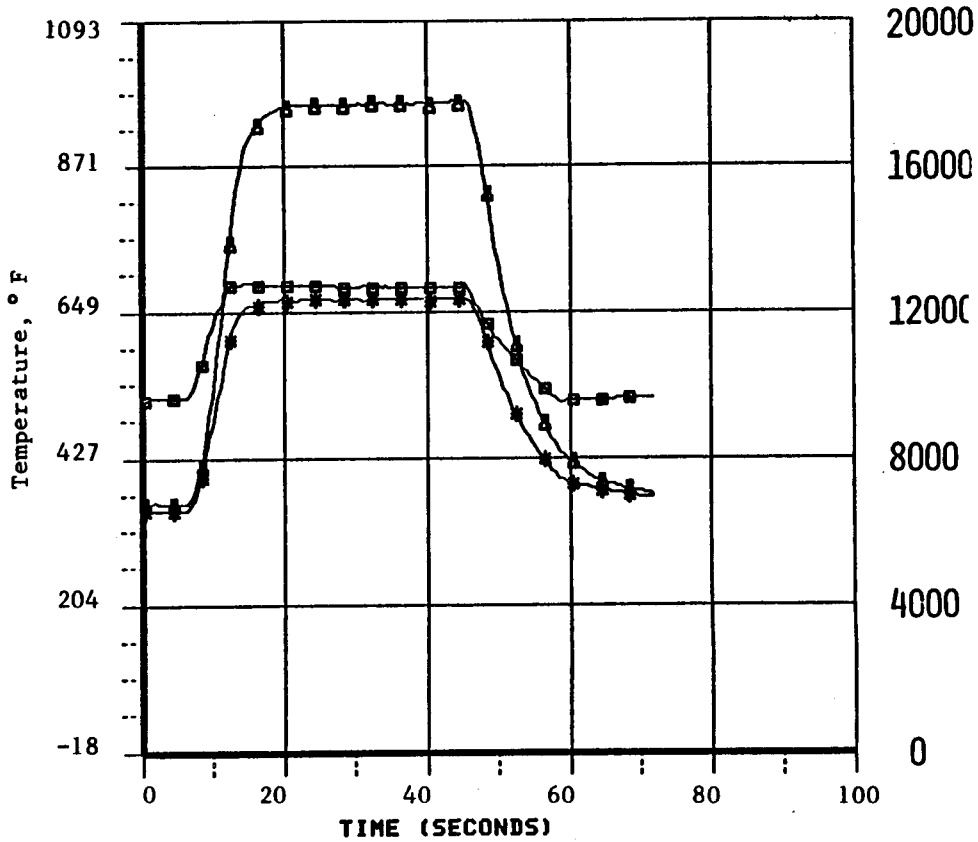




Figure 202. Combustor Inner Liner Transient Temperatures.

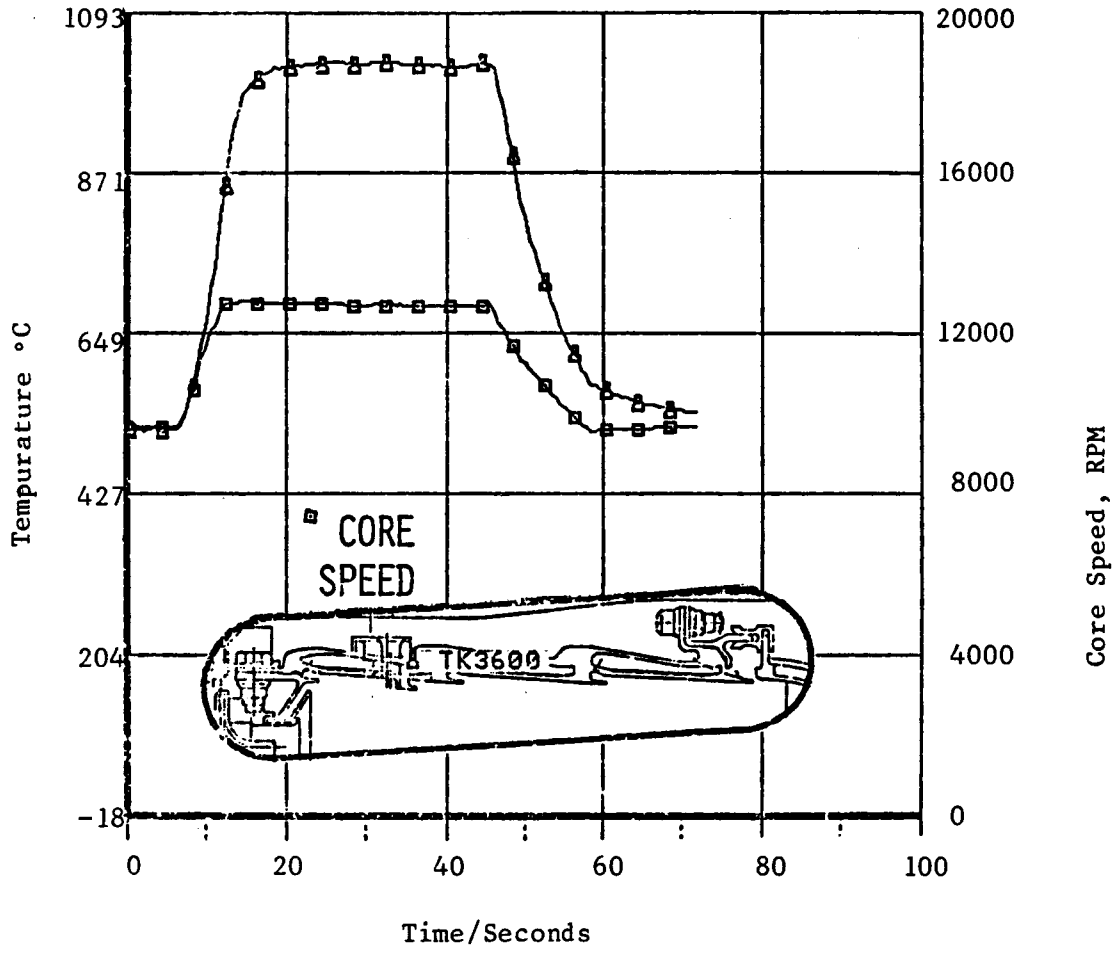


Figure 203. Combustor Outer Liner Transient Temperature.

temperature and pressure data for the high power point are illustrated in Figure 204.

Table XX. Most Extreme High Pressure Turbine Environment Achieved During ICLS Testing.

| Parameter | Max Level Obtained | Reading No. | ICLS Design (86° Day, SLS T/O) | FPS Design (122° Day, T/O MO.3) |
|---|---|---|---|---|
| Core Speed, rpm | 12597 | 102 | 13240 | 13287 |
| $P_3$, kPa (PSIA) | 2827 ( 410) | 75 | 2965 ( 430) | 2660 (385.8) |
| $T_{41}$ AVG, °C (°F) | 1386 (2527) | 72 | 1421 (2590) | 1421 ( 2590) |
| $T_3$, °C (°F) | 541 (1006) | 99 | 586 (1087) | 597 ( 1107) |

Rotor

No HPT rotor instrumentation was available during ICLS testing. To ensure that blade stresses and temperatures were within safe limits, the ICLS maximum speed was confined to that previously explored with the fully instrumented core. Gas path temperatures and pressures and data from the rotor cooling air delivery system gave no reason to expect that the HPT blading ran differently than it did during core testing.

Nozzles

The Stage 1 nozzle completed the ICLS test in excellent condition. Borescope inspections made during the test showed no significant distress and the recorded temperatures were all within the design limit of 1066°C (1950°F). The maximum recorded temperature was 1019°C (1866°F) at 60% span during DMS No. 72. Airfoil temperatures are shown in Figure 205 for the 60% airfoil height.

Stage 2 vane airfoil temperatures ran about 11° to 17°C (20° to 30°F) cooler than for comparable core test conditions and reached a maximum

| DMS READING | 131 | S1 |
|---|---|---|
| CORE SPEED | 12588 RPM | |
| % CORRECTED | 96.7% | |
| T25 | (134°F) | 57°C |
| P3 | (397 psi) | 2737 KPa |
| FAN SPEED | 3250 RPM) | |
| % CORRECTED | 87% | |
| $T_4$ | (2659°F) | 1459°C |
| $T_{41}$ | (2487°F) | 1364°C |
| $T_{42}$ | (1592°F) | 867°C |
| $T_3$ | (995°F) | 535°C |

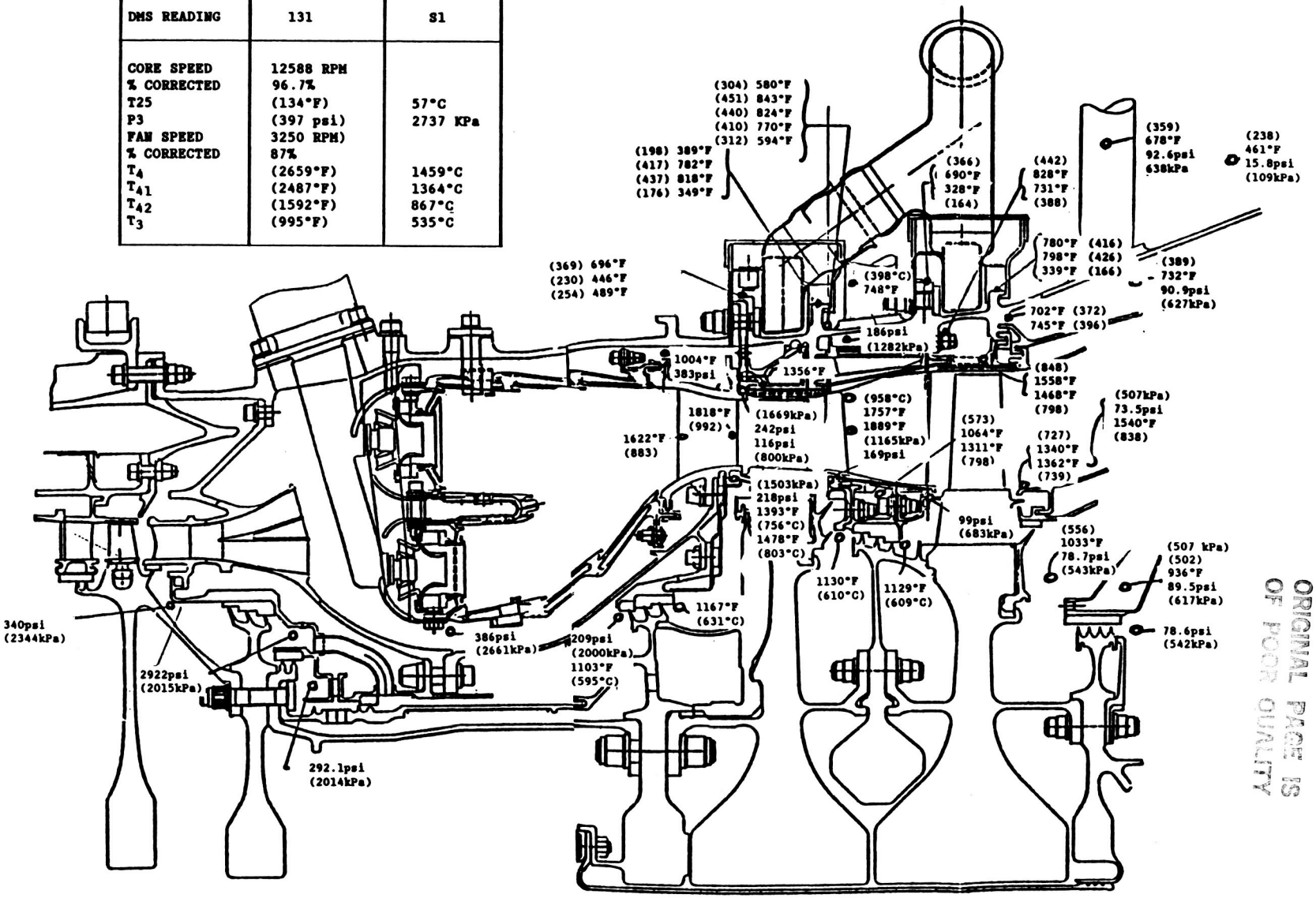




Figure 204. Temperatures and Pressures for HP Turbine.

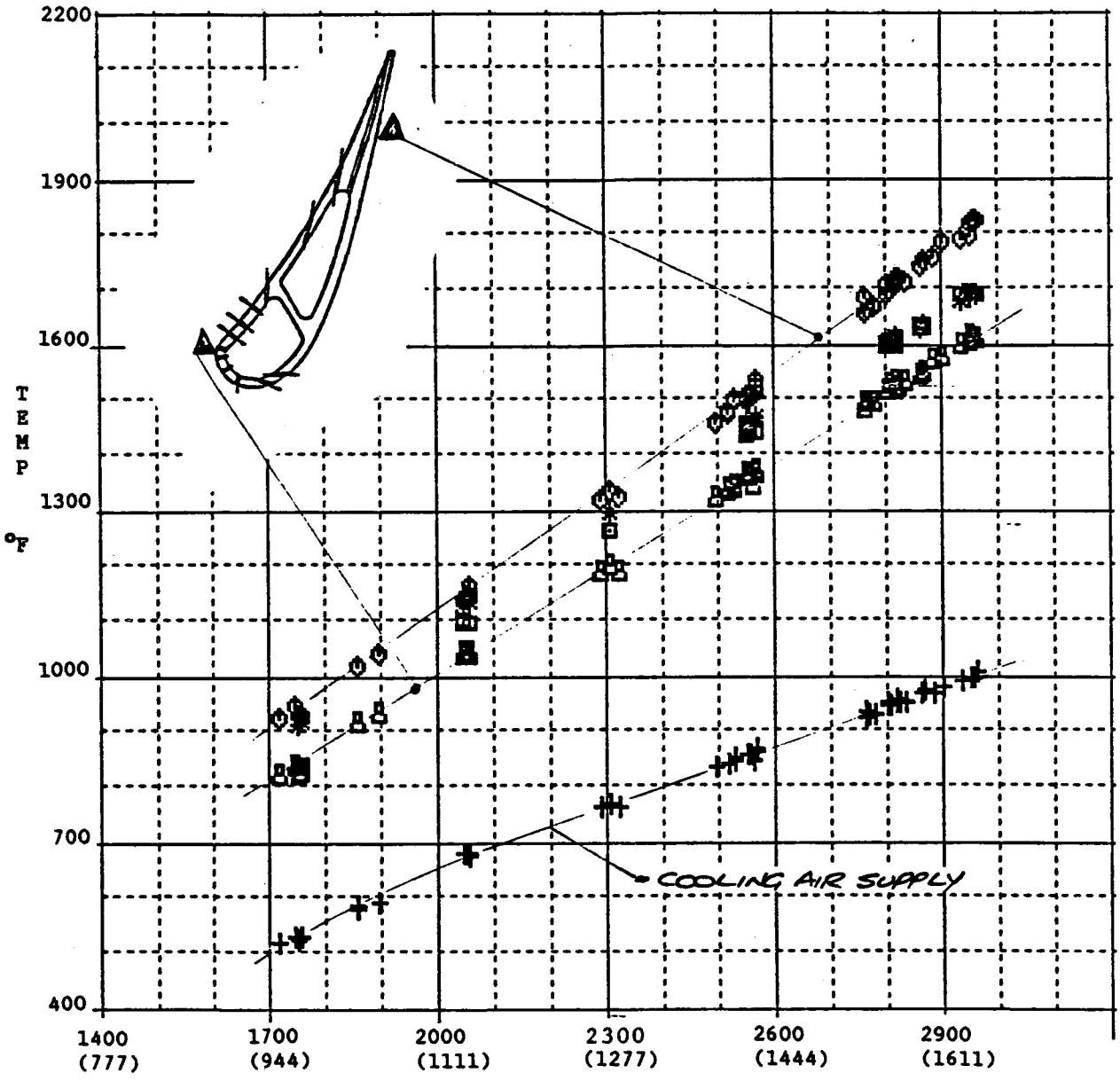


Figure 205. High Pressure Turbine Stage 1 Vane Temperatures.

temperature of 1039°C (1903°F) for DMS Reading 72, at the 60% span, leading edge location. Airfoil temperatures are shown in Figure 206. Stage 2 vane temperature did not limit ICLS testing.

Inducer and Inducer Seal

The inducer seal leakage airflow rate (GW 31S) is shown in Figure 207. This leakage flow increases from about 0.14 kg/sec (0.3 lbm/sec), to about 0.72 kg/sec (1.58 lbm/sec) over the operating speed range. The value is nearly constant when expressed as a percent of compressor flow, varying from 0.9 to 1.0% W25, as shown in Figure 208. The inducer seal leakage was 0.56% W25 during core testing. Inducer airflow rate for rotor cooling is also shown (GE31F) and may be compared to predicted design cruise flow of 4.6% W25.

Figure 209 shows the measured air temperatures for the inducer seal disk. The levels were as expected.

Wheelspace and Interstage Cavities

Figure 209 also shows the measured air temperatures for the flowpath cavity between the Stage 1 nozzle support and the rotor system. These were as expected. Air temperatures should decrease as transients break in the seals.

Figure 210 shows the 7th stage feed pressure to the Stage 2 nozzle, the interstage cavity pressure and the forward and aft wheelspace pressures. No discernible difference existed between the cavity pressure and the forward wheelspace pressure. Inspection of the numerical data indicates a range of pressure margins from 2.6 kPa (0.38 psi) to 4.4 kPa (0.64 psi) (0.39% to 1% ΔP). At no point during ICLS testing was a negative backflow margin indicated. Figure 211 shows the percent pressure margin.

The interstage cavity temperature received close scrutiny during the ICLS mechanical checkout to ensure that hot gas was not ingested through the seals. TA4A03, the hottest thermocouple, was monitored initially on a Sanborn

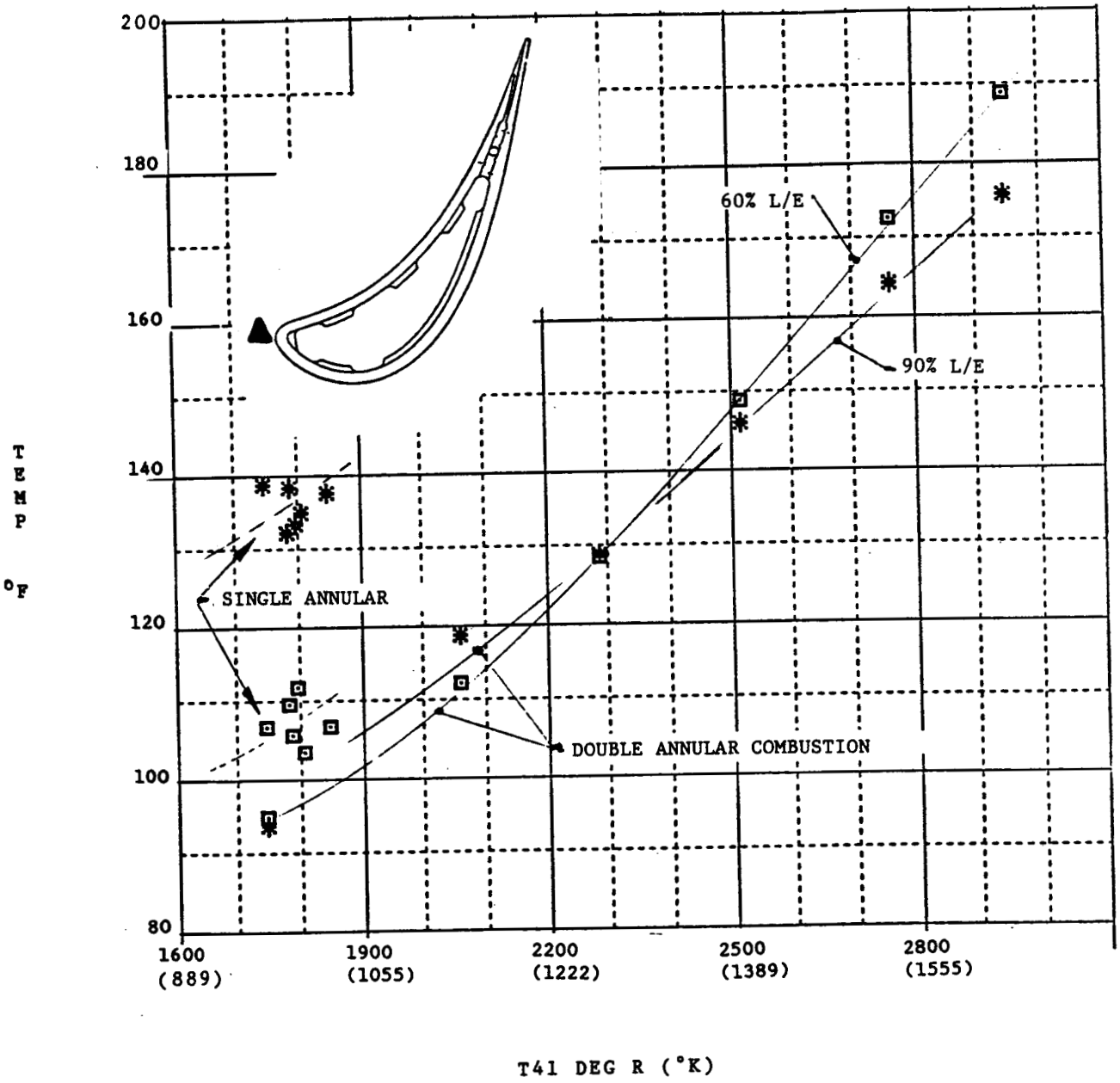


Figure 206. High Pressure Turbine Stage 2 Vane Temperatures.

CELL IVD ENGINE 531002 TEST 1332 LC
FIRST READING # 77 ACQ TIME 22:36:49 DATE 5/ 9/83
LAST READING # 138 ACQ TIME 0:44:53 DATE 5/18/83
RA:1/2/3/4

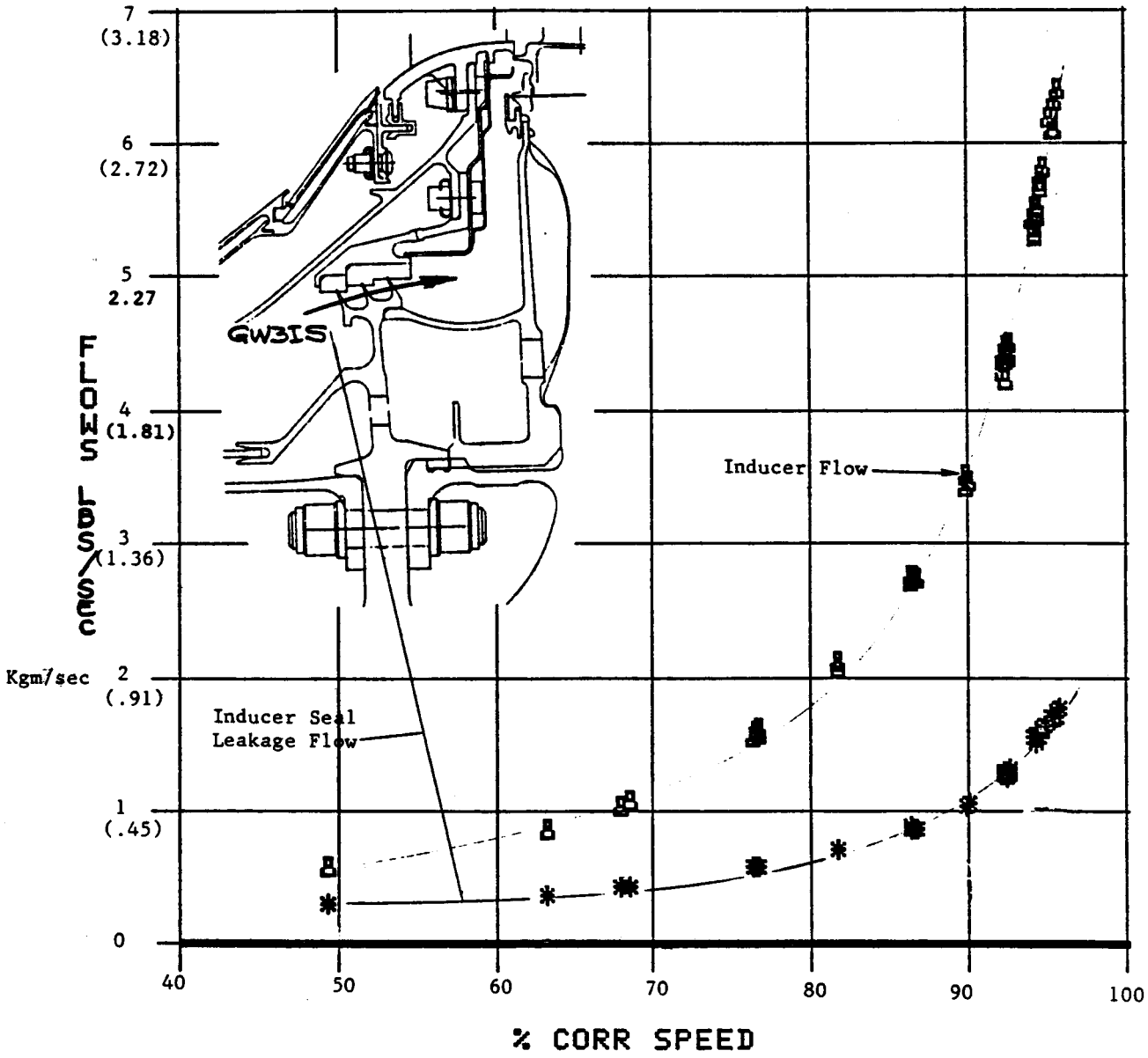


Figure 207. High Pressure Turbine Inducer Seal Flows.

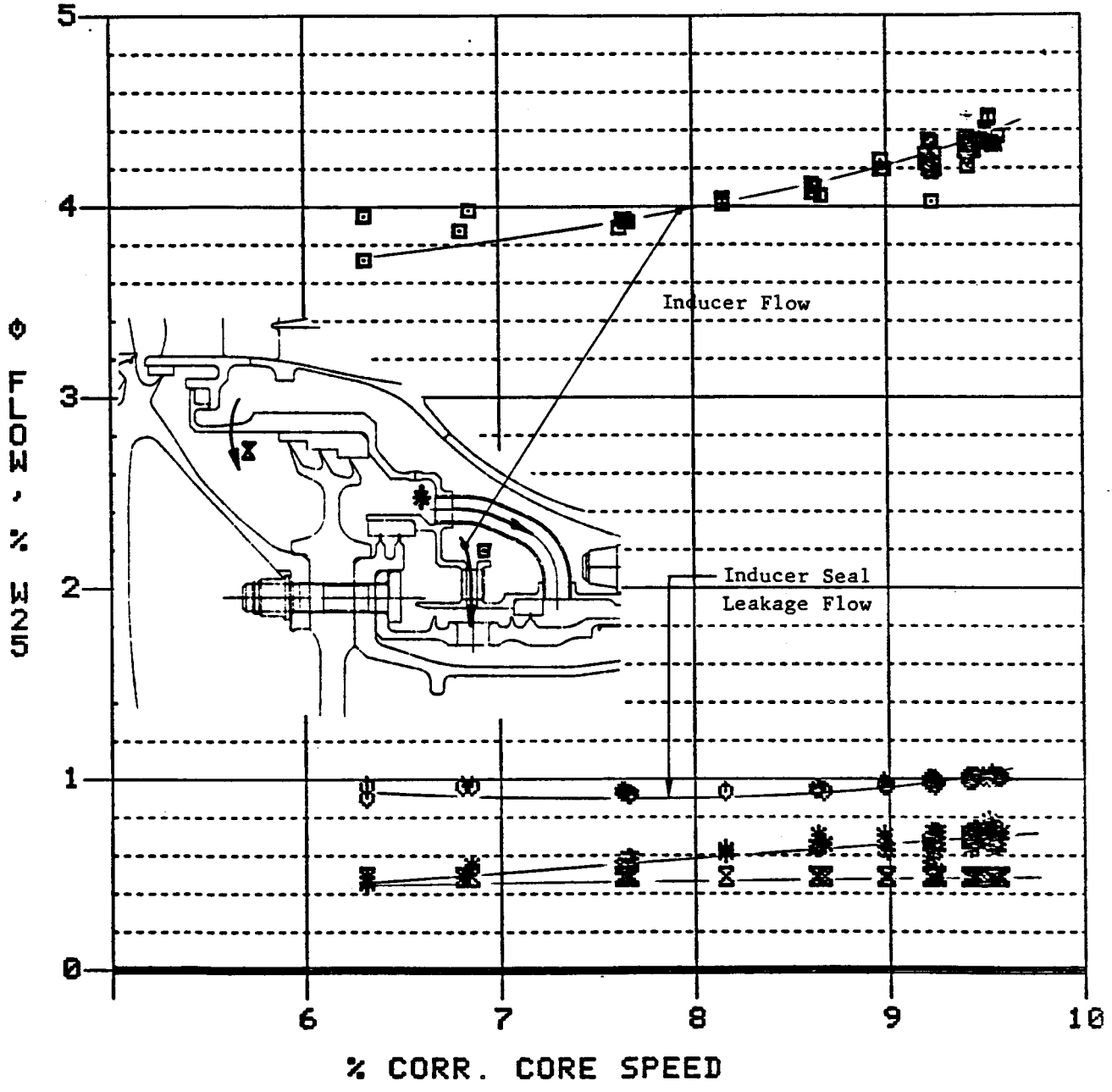


Figure 208. High Pressure Turbine Inducer Percent Flows.

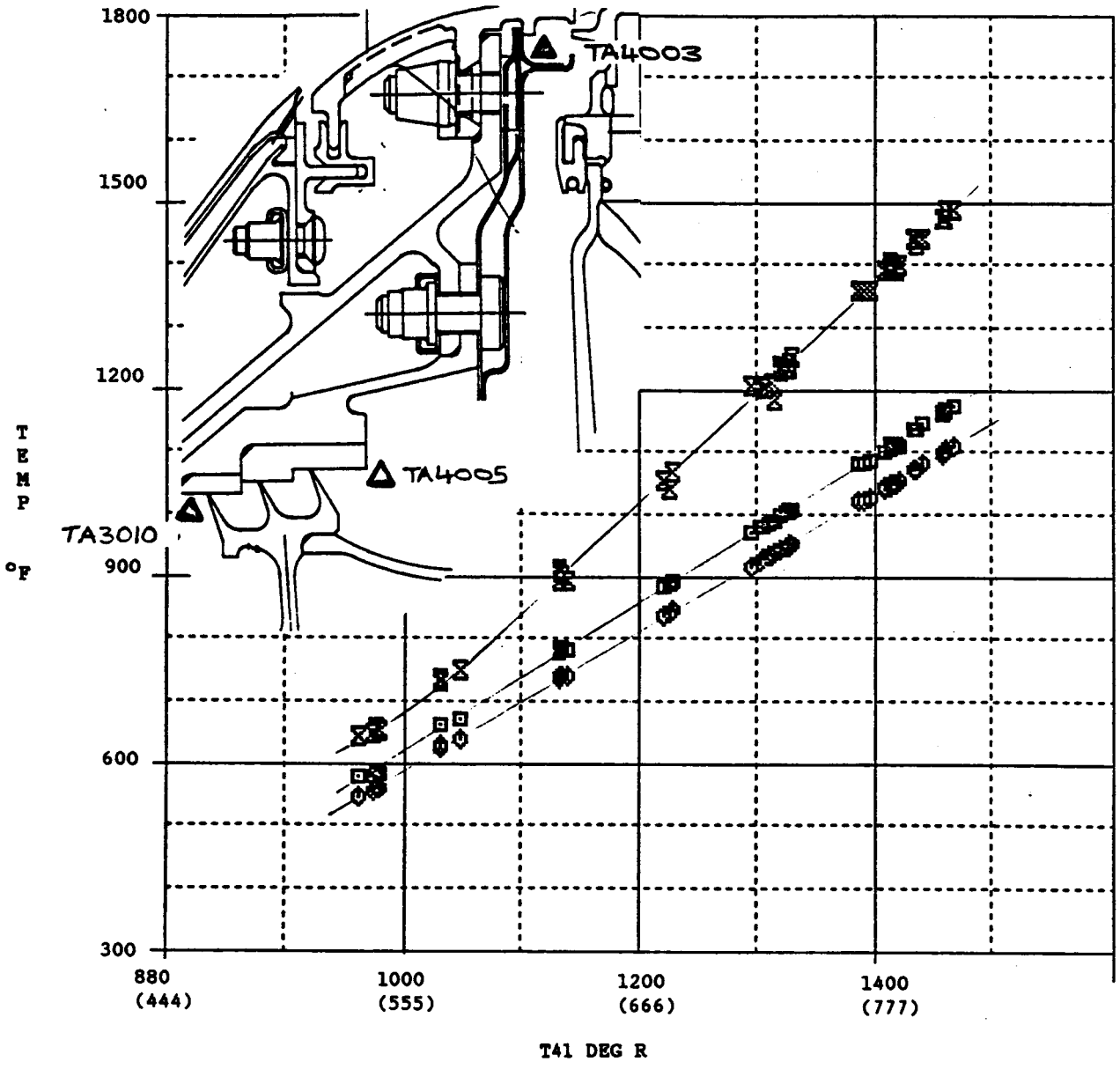


Figure 209. High Pressure Turbine Inducer Seal Air Temperature.

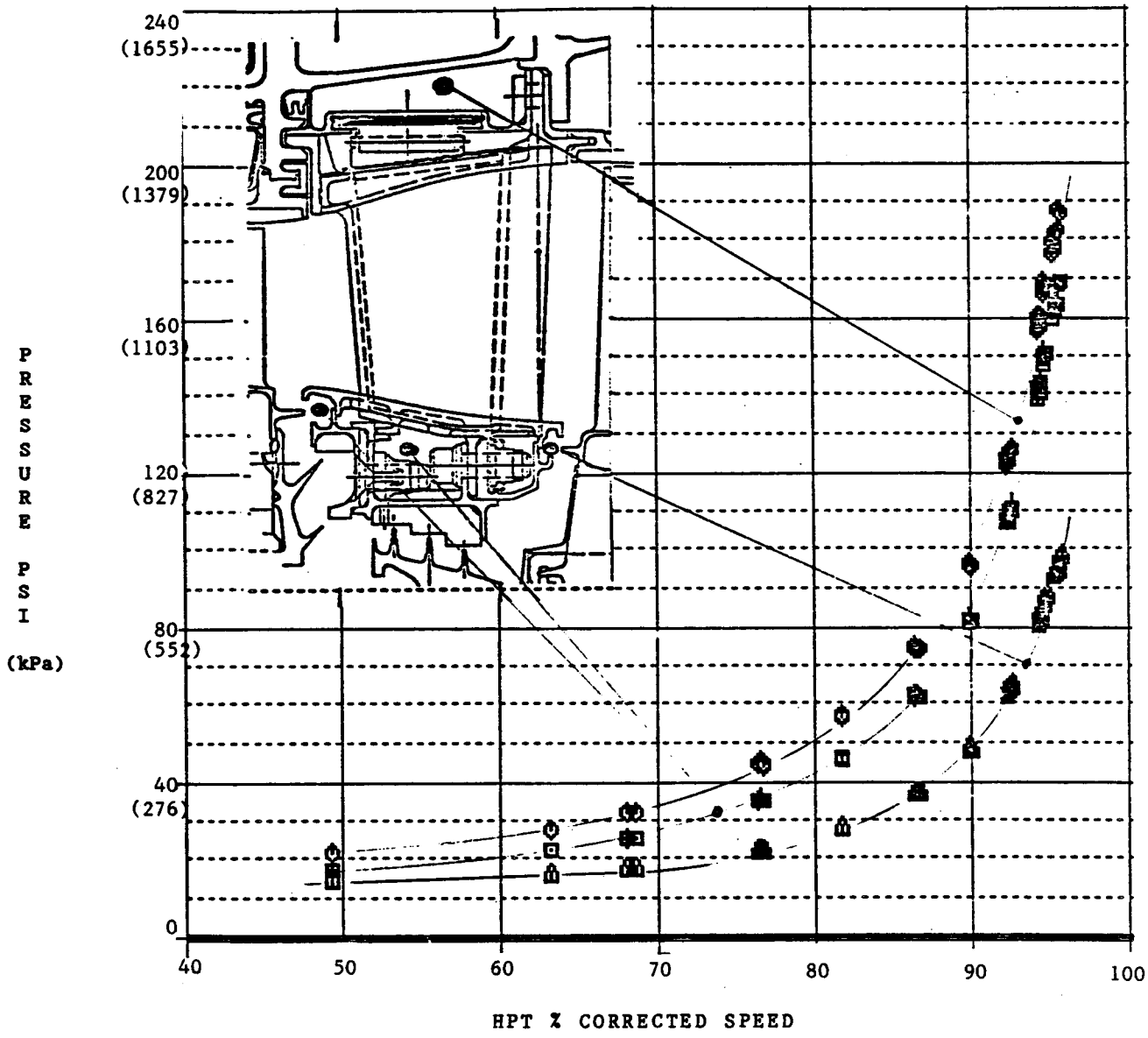


Figure 210. High Pressure Turbine Stage 2 Vane Cooling and Purge Pressures.

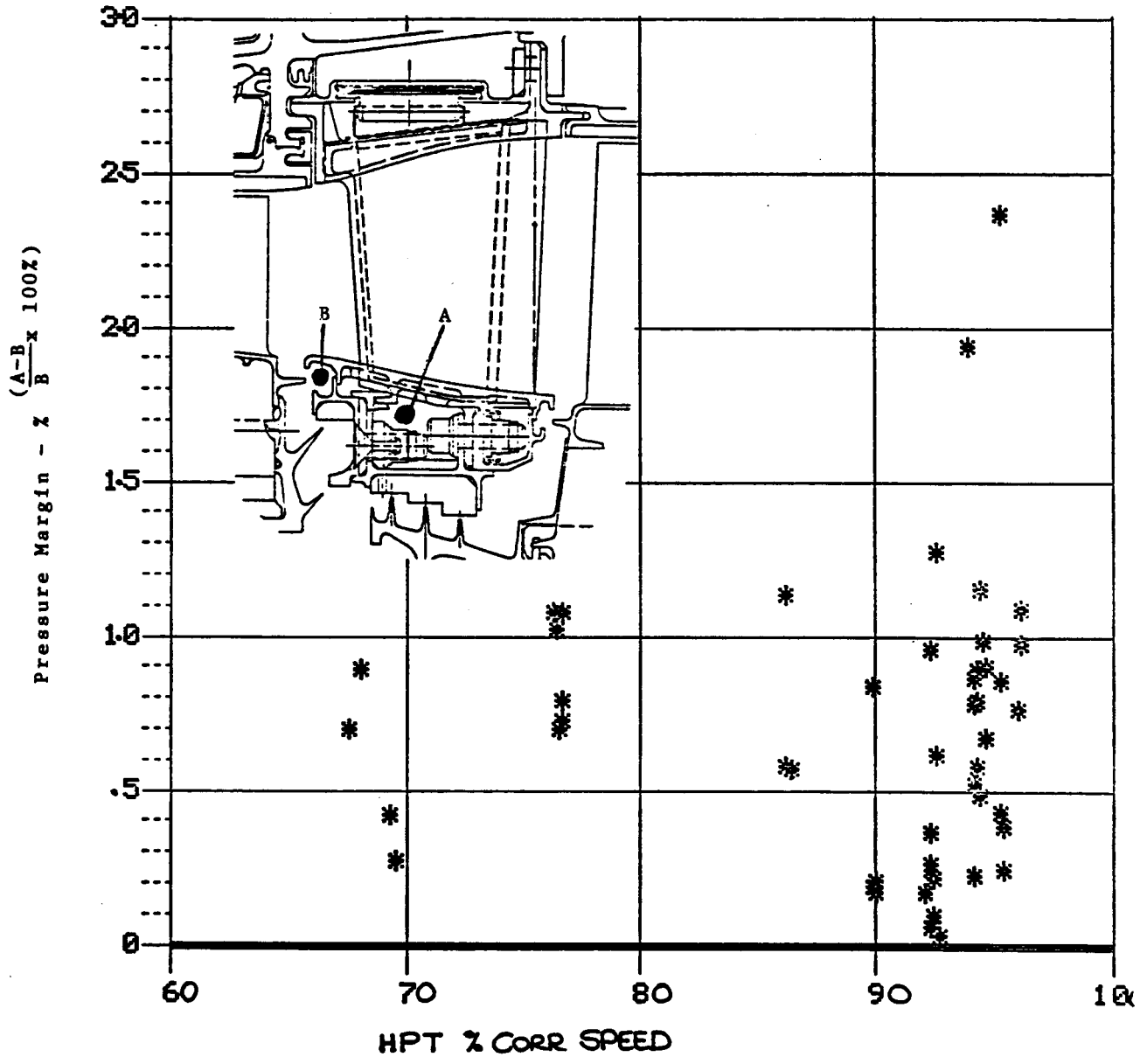


Figure 211. High Pressure Turbine Stage 2 Vane Interstage Pressure Margin.

and reached a maximum temperature of 611°C (1131°F) during DMS Reading 131. Figure 212 shows the response of TA4A03 and TA4A02 to compressor discharge temperature (T3). A temperature difference ranging from about 56°C (100°F) at idle to about 139°C (250°F) at maximum power existed. Seventh stage feed air temperature to the top of the Stage 2 nozzle is also plotted for reference.

Figure 213 shows the response of the aft wheelspace temperature. The air downstream of the interstage seal reached a maximum temperature of 609°C (1129°F). Figure 214 shows the forward wheelspace temperature measurements. These temperatures differ by 36° to 94°C (65° to 170°F). TA4A05 appears closer to the expected results than TA4A04, which tracks remarkably close to the aft wheelspace temperature, TA4A07, reaching a maximum temperature of 610°C (1130°F).

The air temperature surrounding the Stage 2 blade retainer was monitored closely and reached a maximum temperature of 571°C (1060°F) during DMS Reading 99. Comparison of the surrounding air temperature with the measured metal temperatures for the core test showed the two to be almost identical above 96% corrected core speed. This indicates that the retainer reached temperatures in excess of 566°C (1050°F) during the ICLS test, 56°C (100°F) hotter than projected prior to core testing, but cooler than those reached during the core tests (see Figure 215).

Casings and Shrouds

Additional instrumentation was placed on the HPT casings for the ICLS test (Figure 216). The purpose of these extra thermocouples was to obtain more detailed measurements on the circumferential variations of the casing ring temperatures and to gain a better understanding of the associated operating clearances between HPT rotor blade tips and shrouds. Instrumentation for the shrouds, however, was reduced compared to the core test engine configuration (Figure 217). This was necessary to make room for newly added monitoring sensors in other areas of the engine.

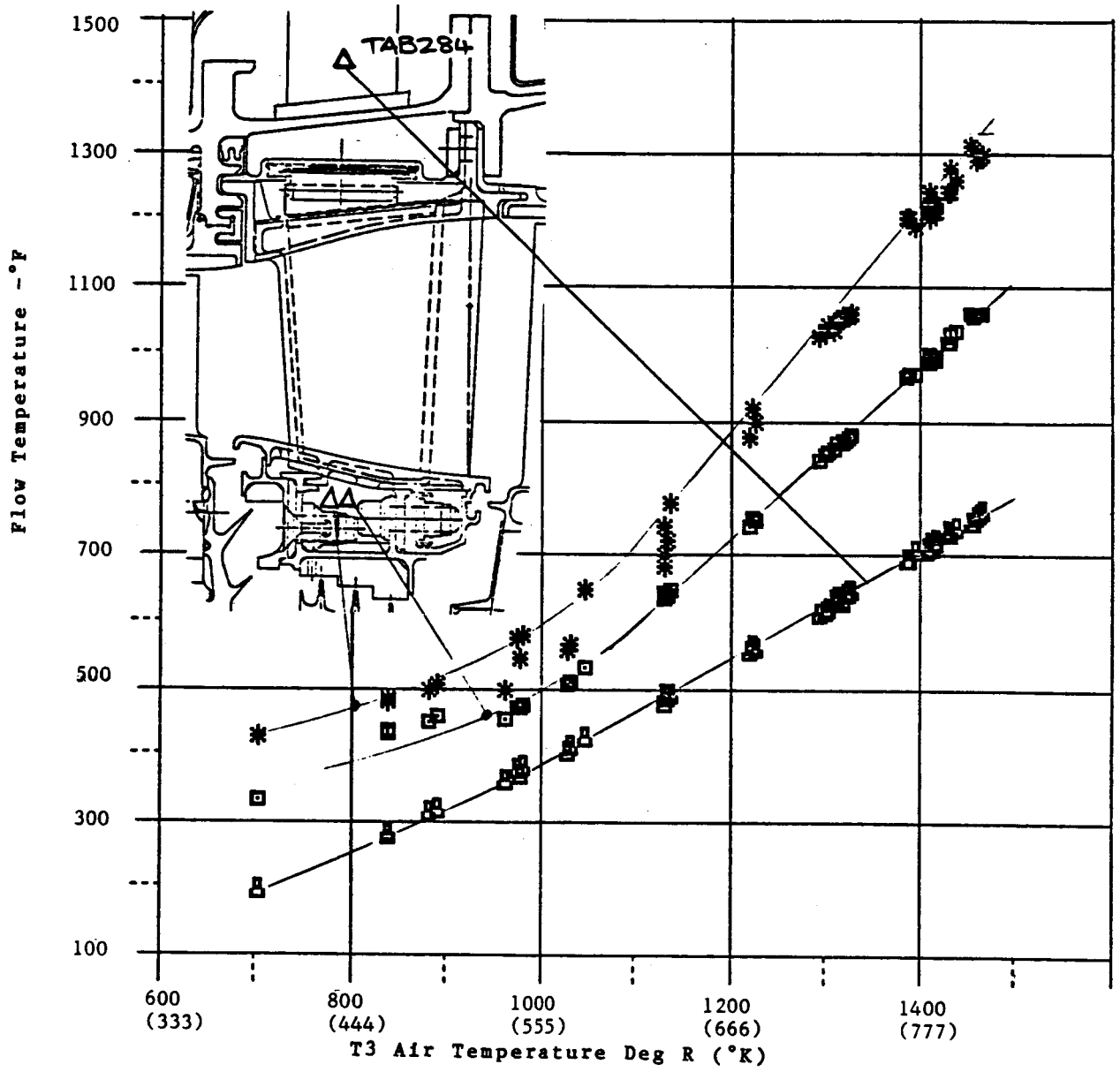


Figure 212. High Pressure Turbine Interstage Feed and Cavity Temperature.

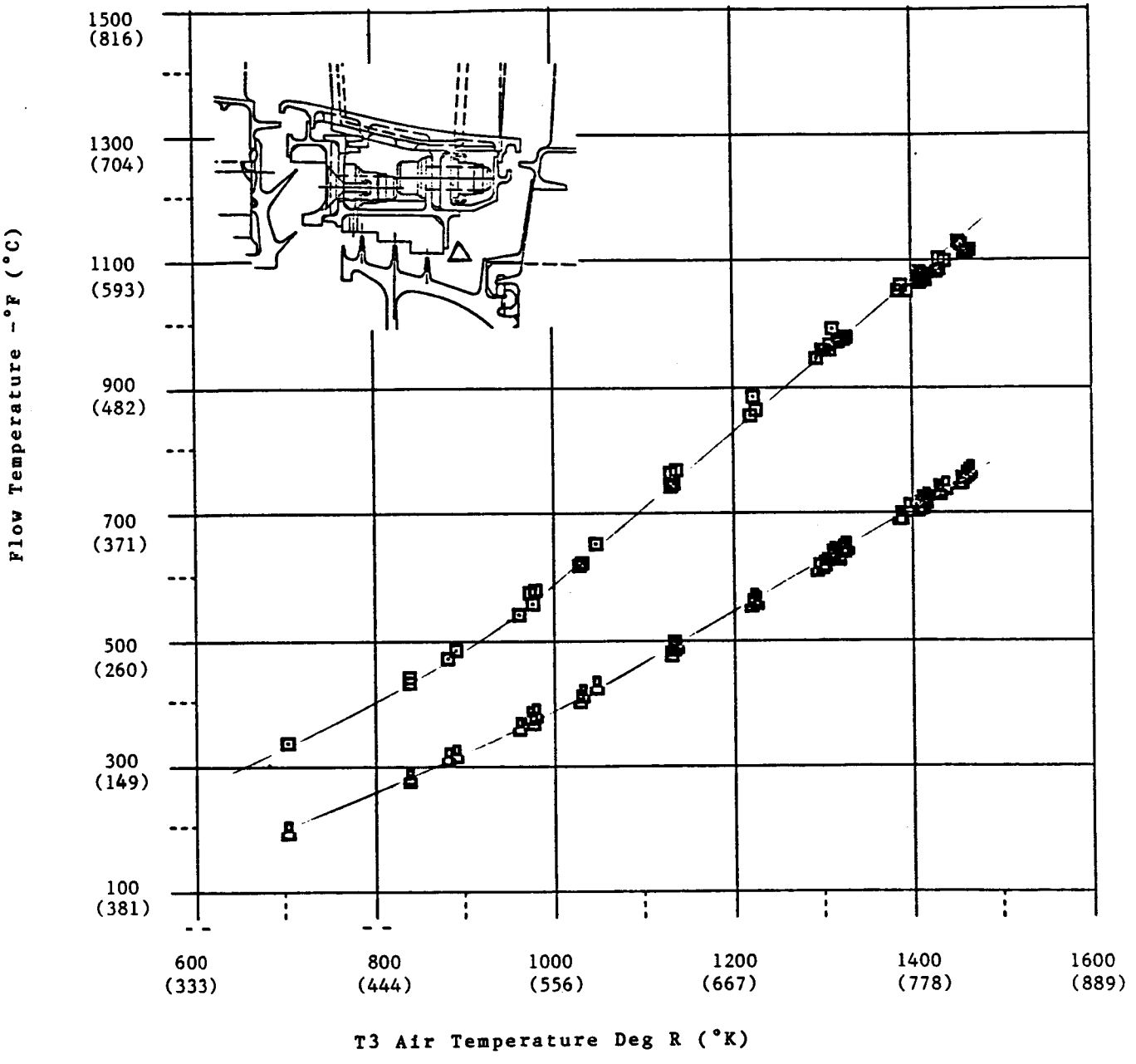


Figure 213. High Pressure Turbine Stage 2 Vane Aft Interstage Cavity Temperature.

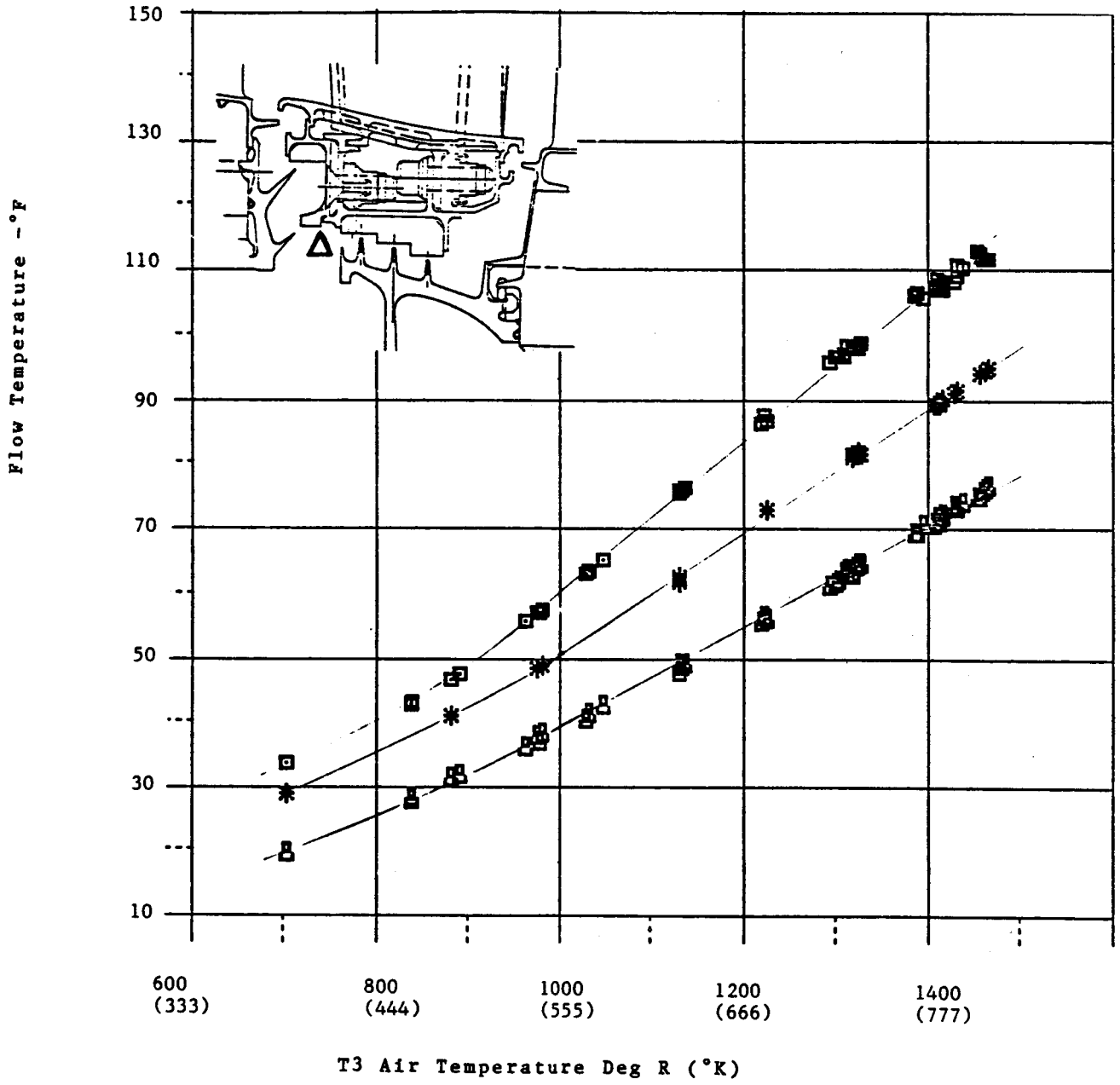


Figure 214. High Pressure Turbine Stage 2 Vane Forward Interstage Cavity.

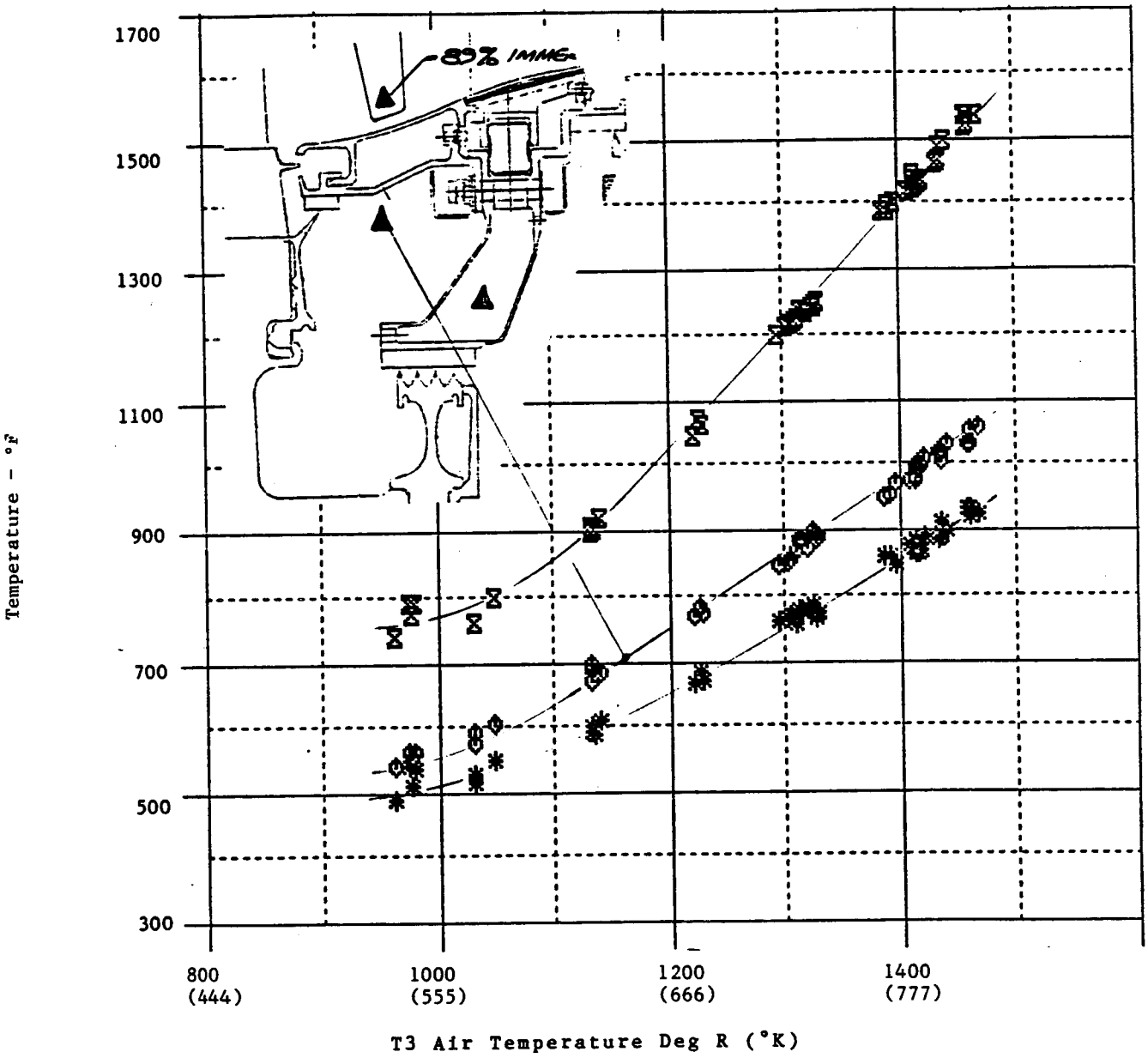


Figure 215. High Pressure Turbine Stage 2 Retainer Cavity Temperature.

(Thermocouple (T/C) Locations are AFT Looking FWD).

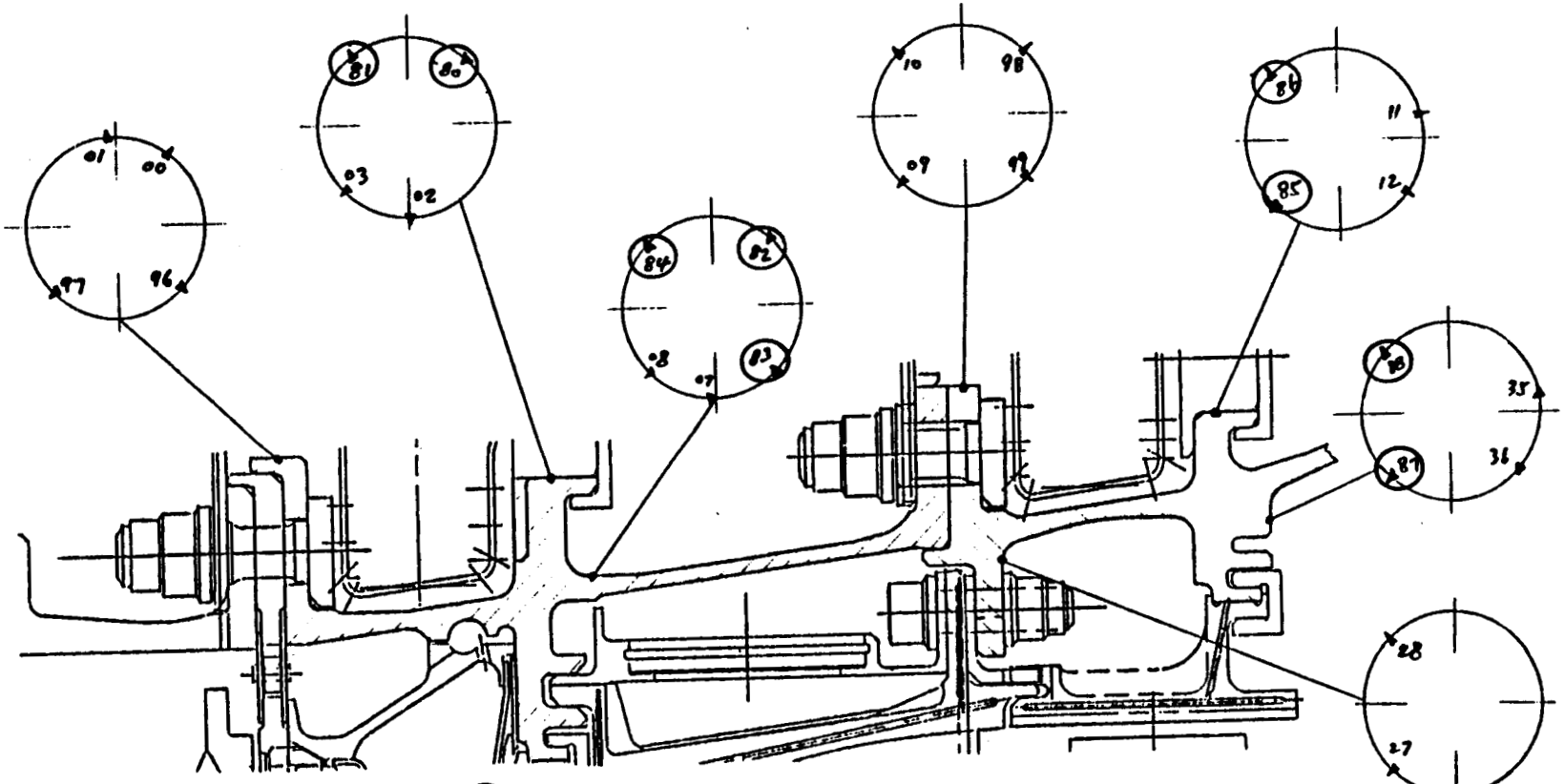


Legends: ○ = New T/C Additions After Core Test
An T/C Lead Out Identifications are Prefixed with "TK4F," e.g. TK4F 96, TK4F 97 etc.

Figure 216. High Pressure Turbine Casing Instrumentation.

(T/C Locations Are AFT Looking Forward)

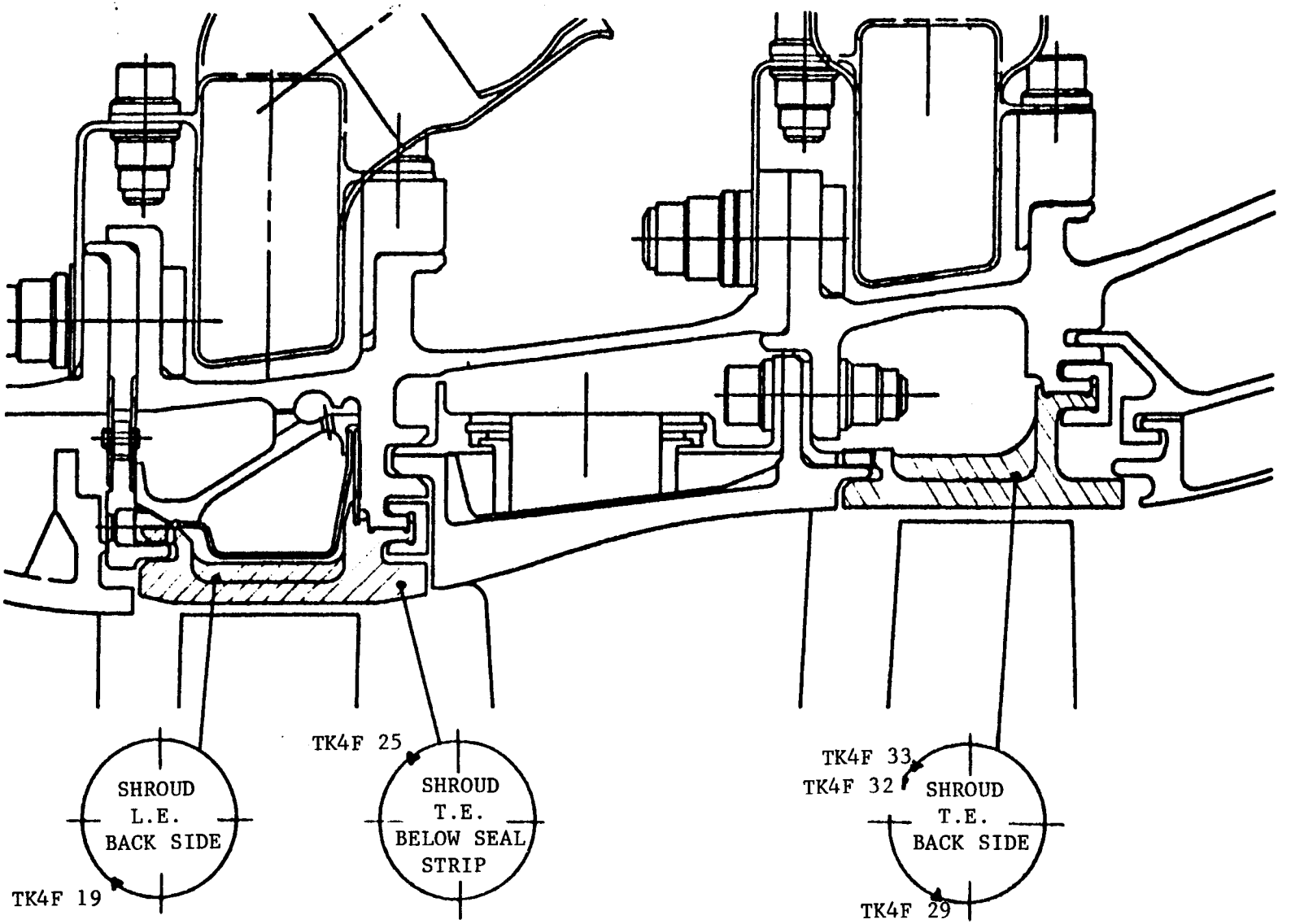


Figure 217. High Pressure Turbine Shroud Instrumentation.

The recorded temperatures for both Stage 1 and Stage 2 casings were well below the design limits of 649°C (1200°F) (Figures 218 and 219) and the shrouds completed the test in very good condition. Registered shroud temperatures were within the design limit of 871°C (1600°F) throughout the test (Figures 220 and 221).

Blade Tip Clearance and Active Clearance Control

During ICLS assembly, the rotor became eccentric with respect to the casing. Blade tip clearance measurements made through laser probe ports during assembly showed decreased clearances from core test levels at the bottom of the engine and increased clearances at the top. ICLS and core static clearances are shown in Figure 222.

Further eccentricity when at power was expected because, during core testing, the clearances closed more at the bottom of the engine than at the top.

To offset the expected eccentricity and to improve effectiveness of the HPT ACC, the following modifications were made:

- Material was trimmed from the ACC manifold support brackets to expose more casing flange area to cooling air.
- Three extra rows of impingement holes were added on all Stage 1 manifold segments (one row on the forward side and two rows on the inside of the segments).
- Orifice plates were inserted into the two inlets which fed all four bottom manifolds, plus the bottom two butterfly valves to Stage 1 were closed (the butterfly valves were so designed that even at the fully closed position they would still provide 12% of the open flow area).

During the early part of mechanical checkout without ACC air, the sanborn recordings as well as the CRT console indicated blade tip rubs. This occurred between DMS Readings 13 and 14, at the low core speed of 9579 rpm. The recorded clearance data showed that while the 6 o'clock clearance was

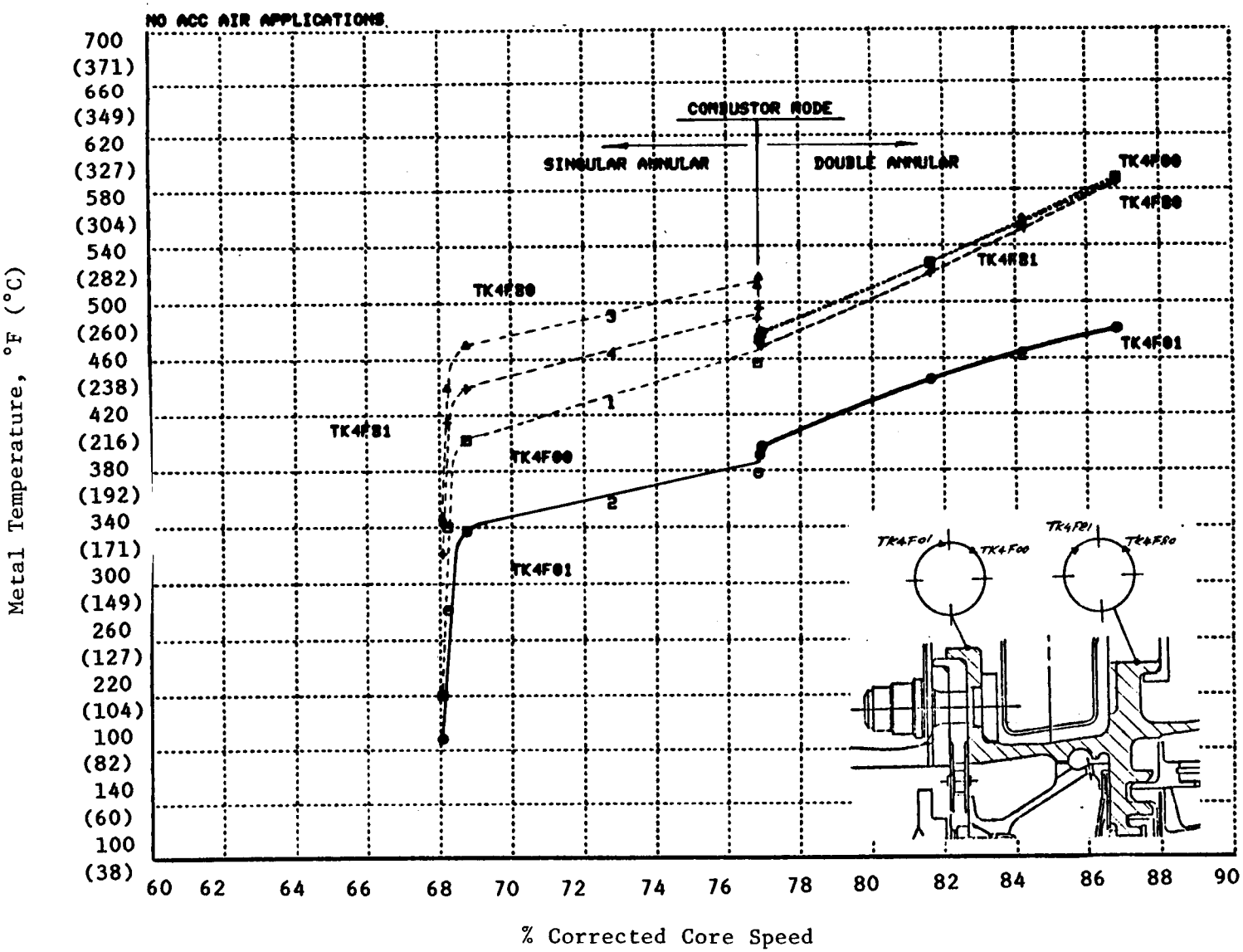


Figure 218. High Pressure Turbine Stage 1 Casing Flange Temperature.

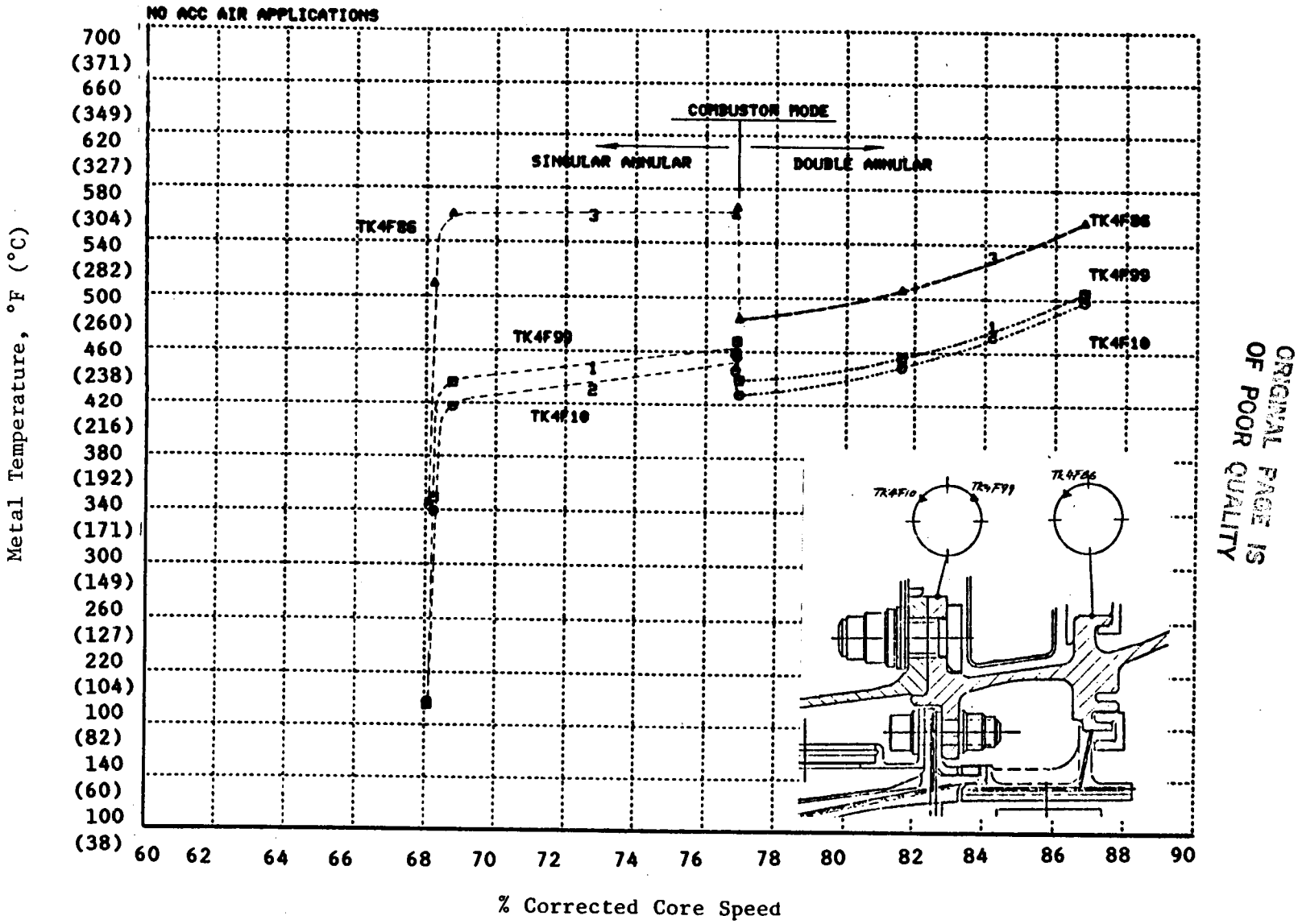


Figure 219. High Pressure Turbine Stage 2 Casing Flange Temperature.

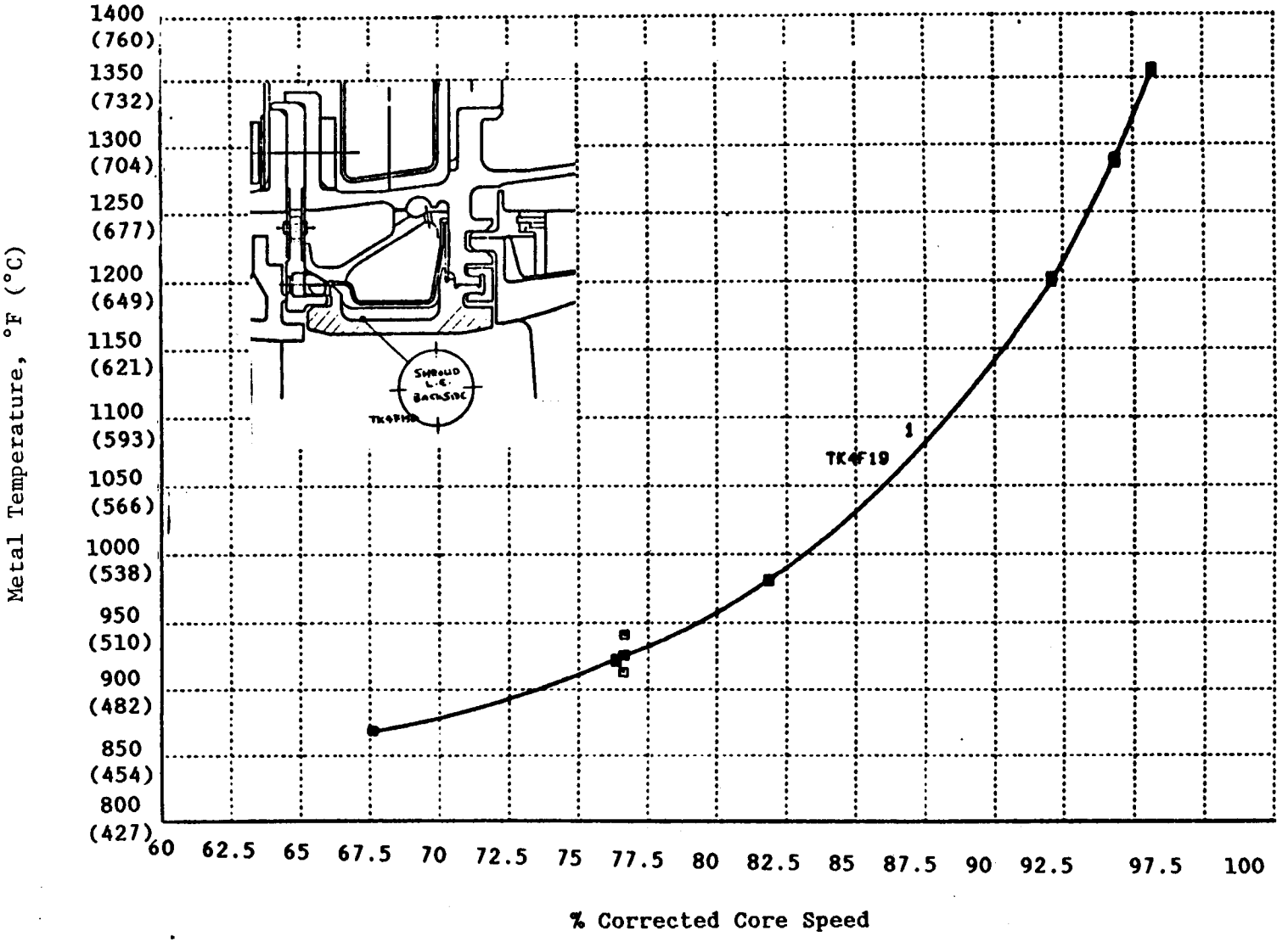


Figure 220. High Pressure Turbine Stage 1 Shroud Temperature.

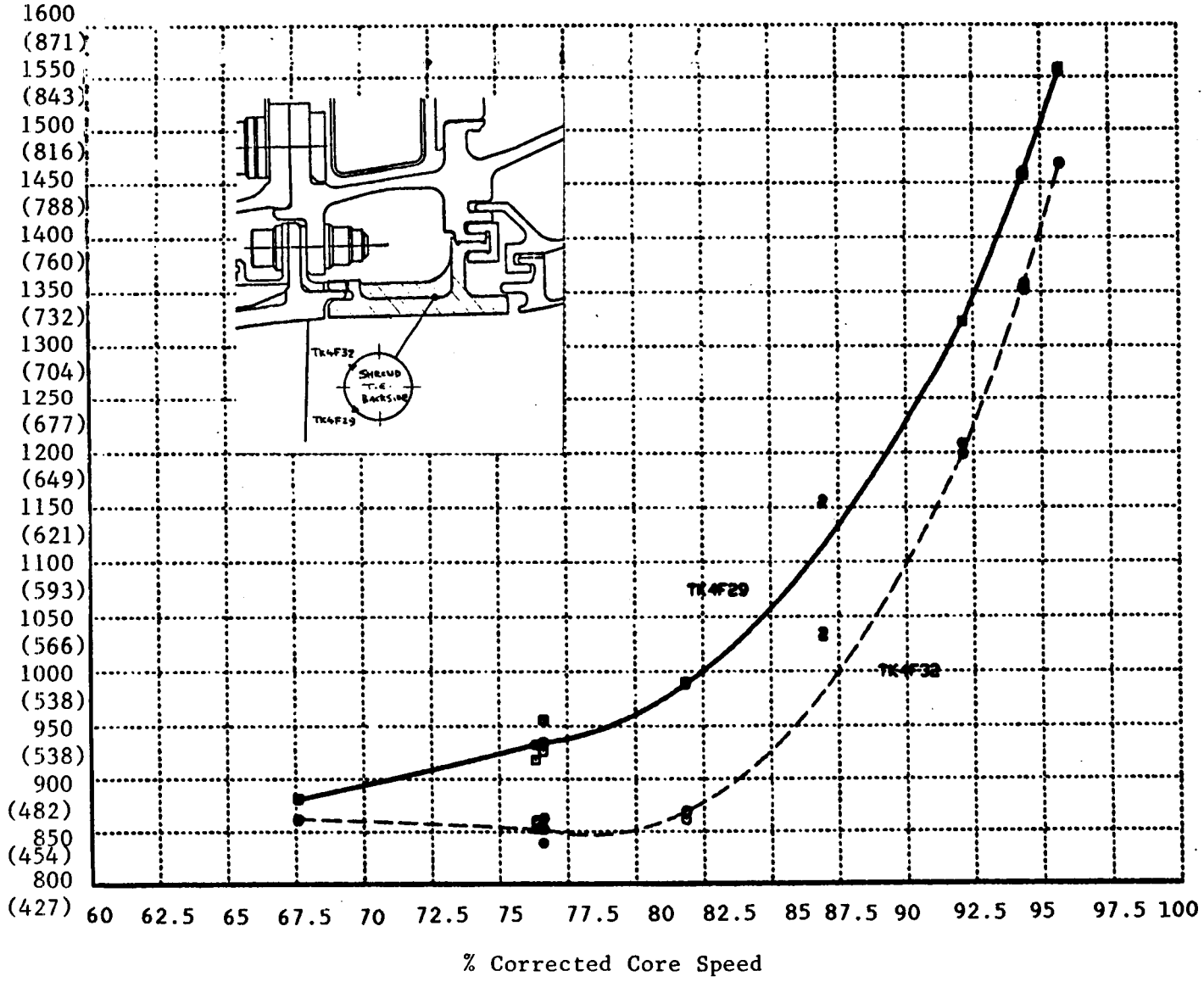


Figure 221. High Pressure Turbine Stage 2 Shroud Temperature.

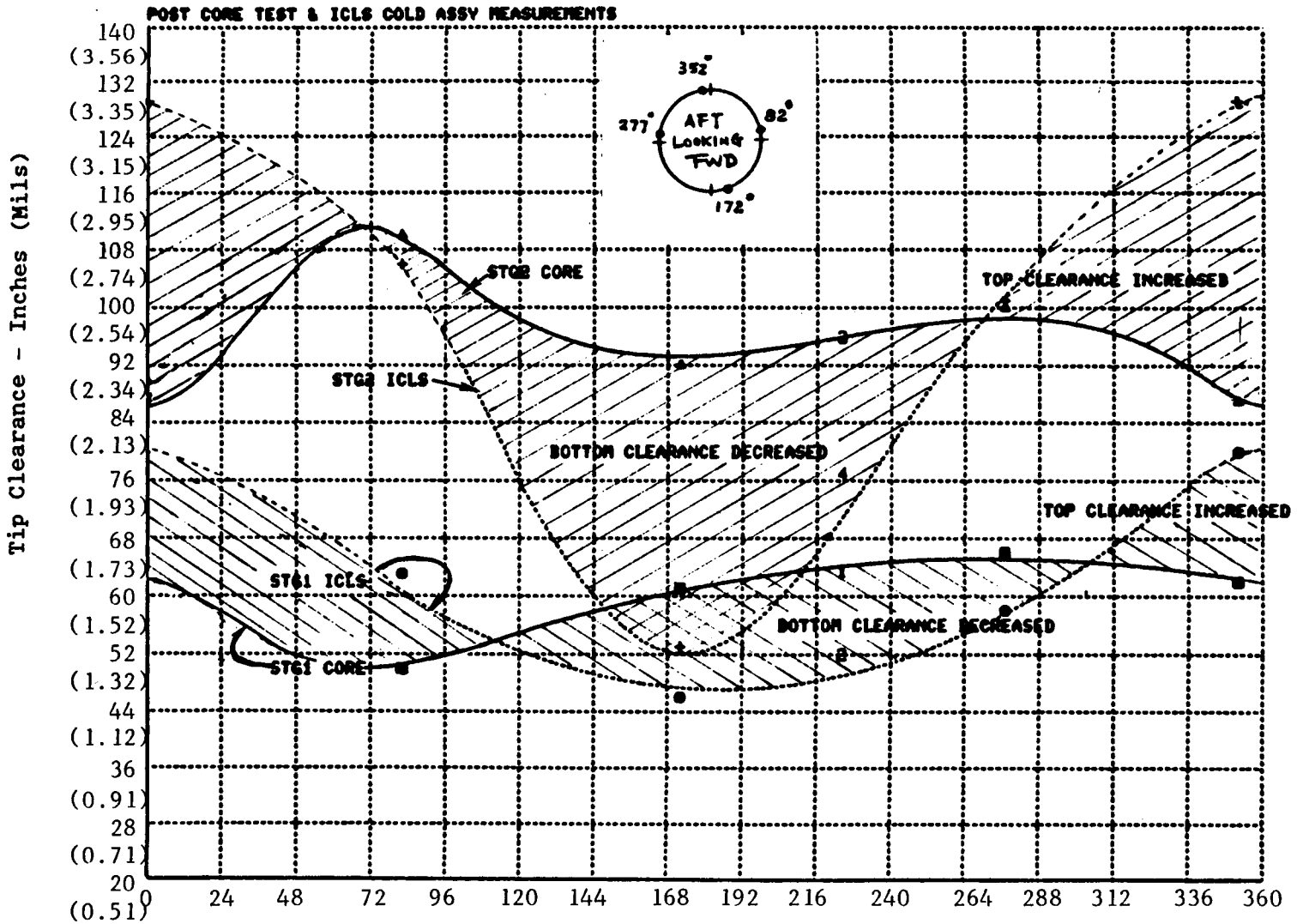


Figure 222. High Pressure Turbine Static Clearances.

approaching a rub, the 12 o'clock clearance was moderately increasing. The clearance changes with speed are shown in Figure 223. Subsequent borescope inspection and idle speed running revealed that about 0.43 mm (0.017 in) had been removed from the Stage 1 blade tips.

The local rub at low speed was not expected since the circumferential thermal gradients on the casing rings were within 33°C (60°F). The gradients are shown on Figures 224 and 225. Investigation after the initial tests revealed that air temperature in the adjacent core cowl cavity over the combuster region and the LPT casing metal temperature had similar circumferential thermal patterns, except that their magnitudes were more severe. Gradients in both areas were about 111°C (200°F).

To remedy the premature HPT clearance closure for subsequent tests, the lower half of the combuster and HPT casings were insulated and the lower two ACC manifold segments for both stages were sealed off completely; ACC cooling air was introduced into the two top manifold segments only of Stage 1 and Stage 2.

The arrangement proved to be successful and no further rubs were observed through the remainder of the test. Consequent temperature distributions on the casing rings were such that the upper-half regions were much cooler while the lower-half operated a little hotter (Figures 226 and 227). Most of the engine testing was conducted using shop air for ACC; a short test was also conducted up to about 92% corrected core speed using fan air.

The clearance behavior after the remedial actions for Stage 1 and Stage 2 are shown in Figures 228, through 231. The effectiveness of the ACC system in cooling only the top half casing is shown in Figures 232 and 233.

Running blade tip clearances at the high power performance points using shop air ACC, were 1.09 mm (0.043 in) over Stage 1 and 1.27 mm (0.050 in) over Stage 2. These are much larger than the design values of 0.41 mm (0.016 in.) for both stages. The reasons for the large clearance are a tip rub during

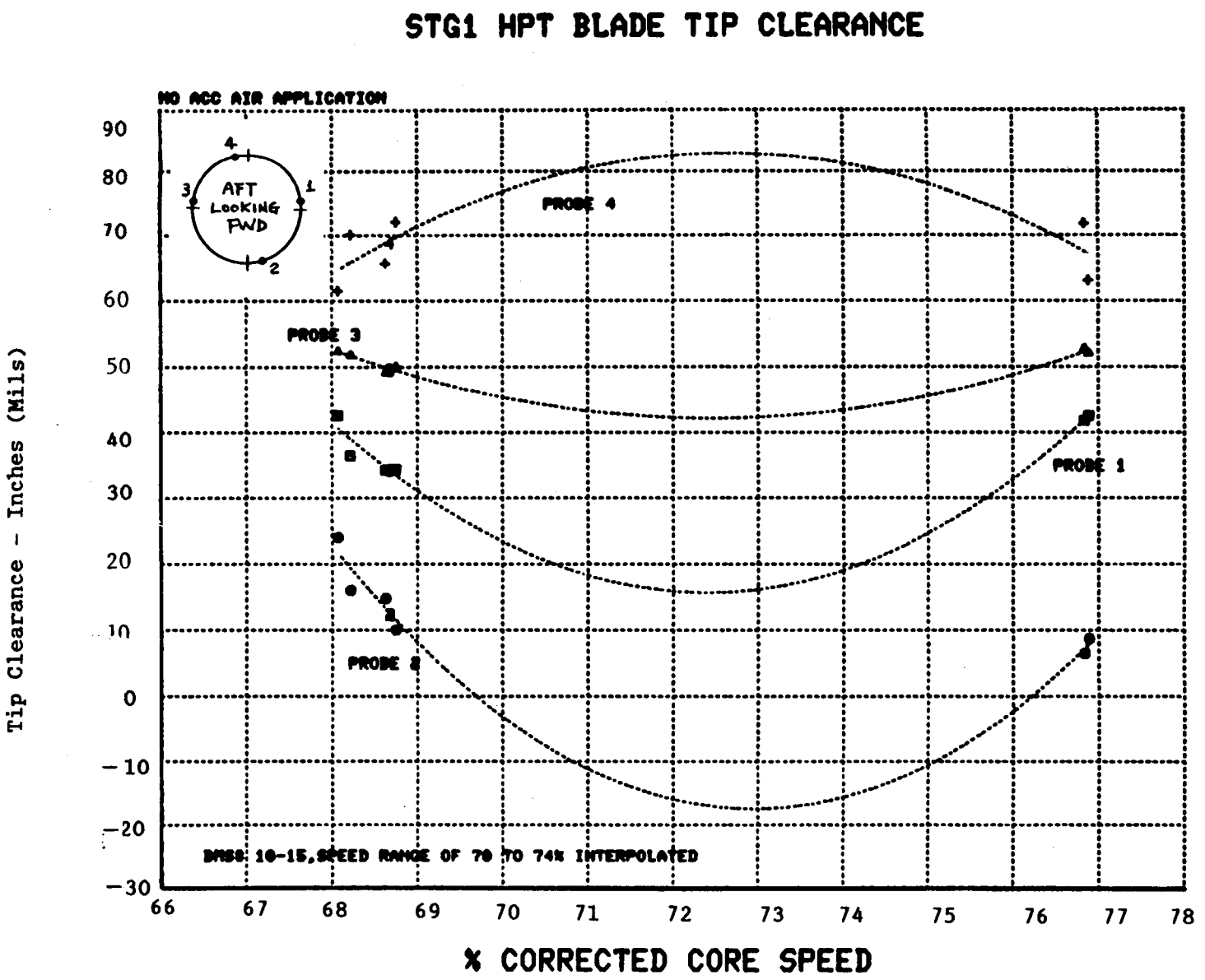


Figure 223. High Pressure Turbine Stage 1 Blade Tip Clearance Variation With Speed.

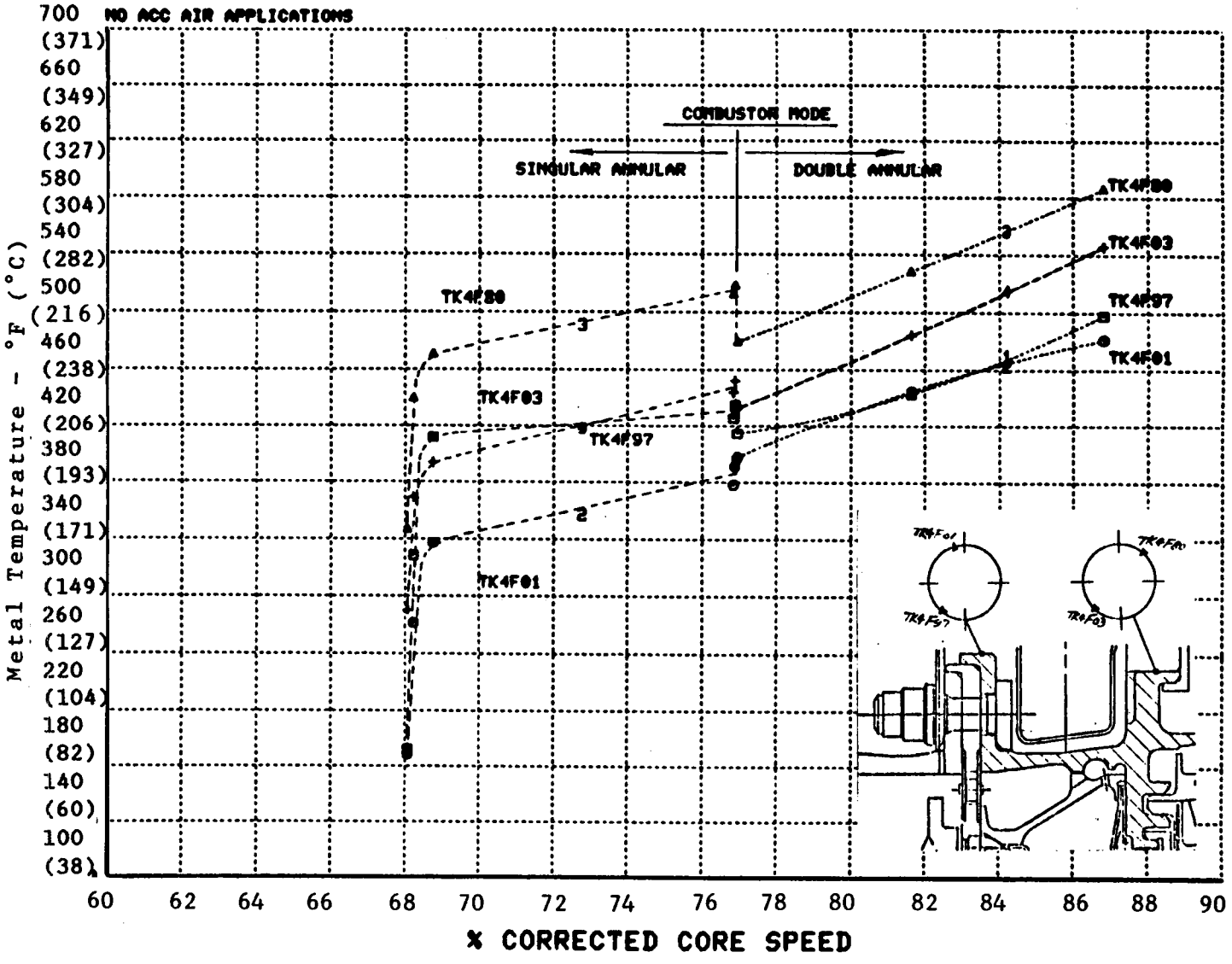


Figure 224. High Pressure Turbine Stage 1 Casing Flange Temperature.

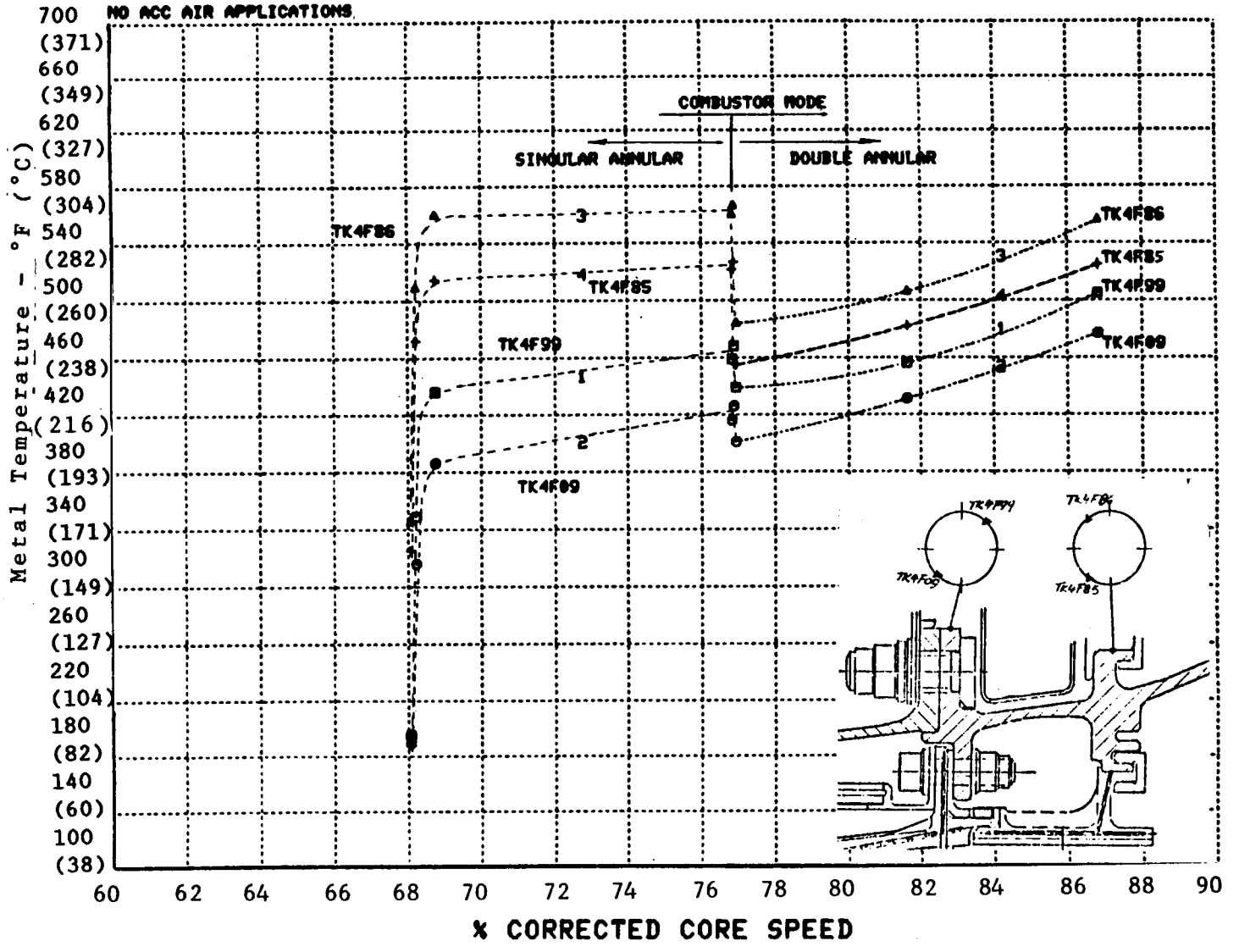


Figure 225. High Pressure Turbine Stage 2 Casing Flange Temperature.

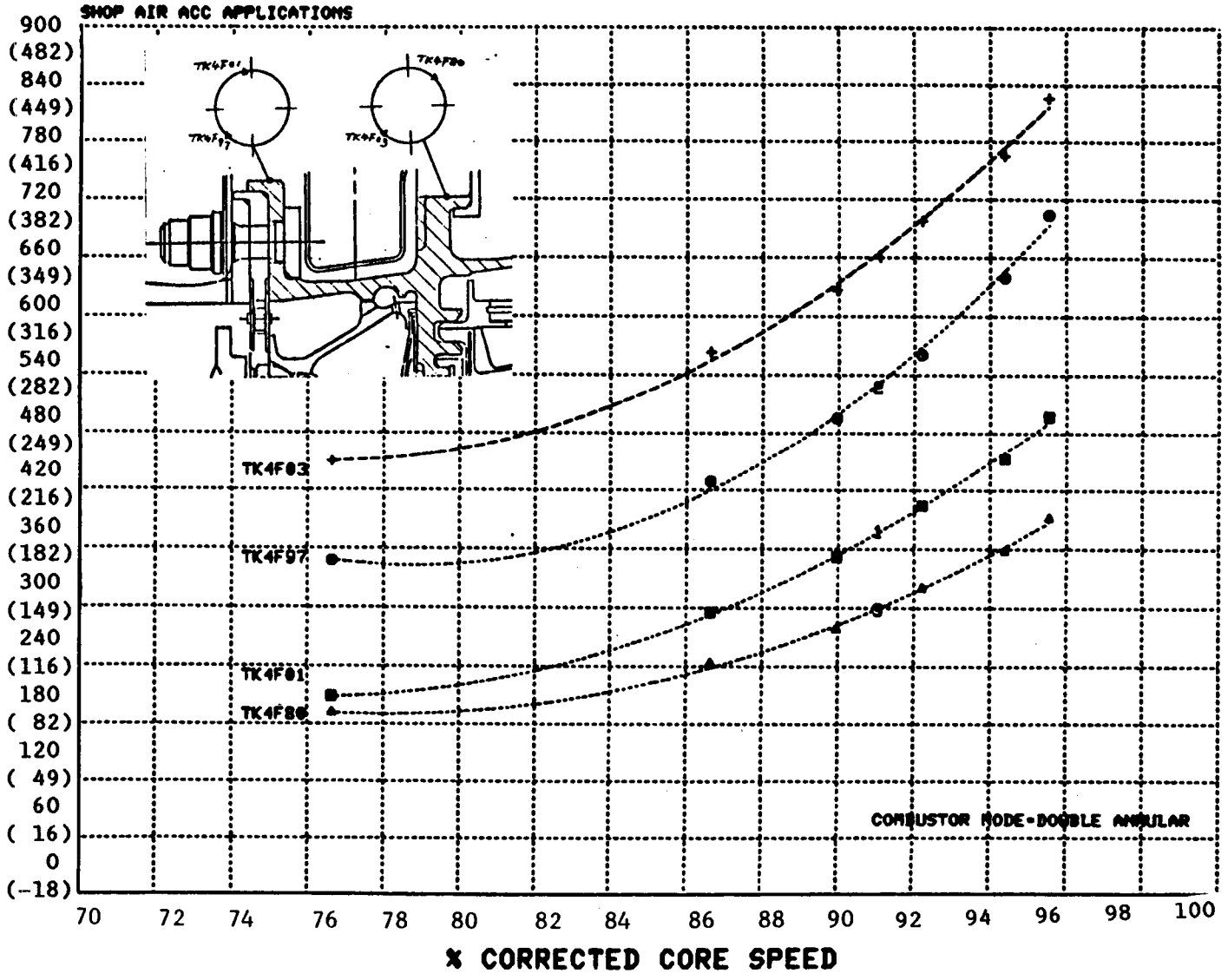




Figure 226. High Pressure Turbine Stage 1 Casing Flange Temperature After ACC Modification.

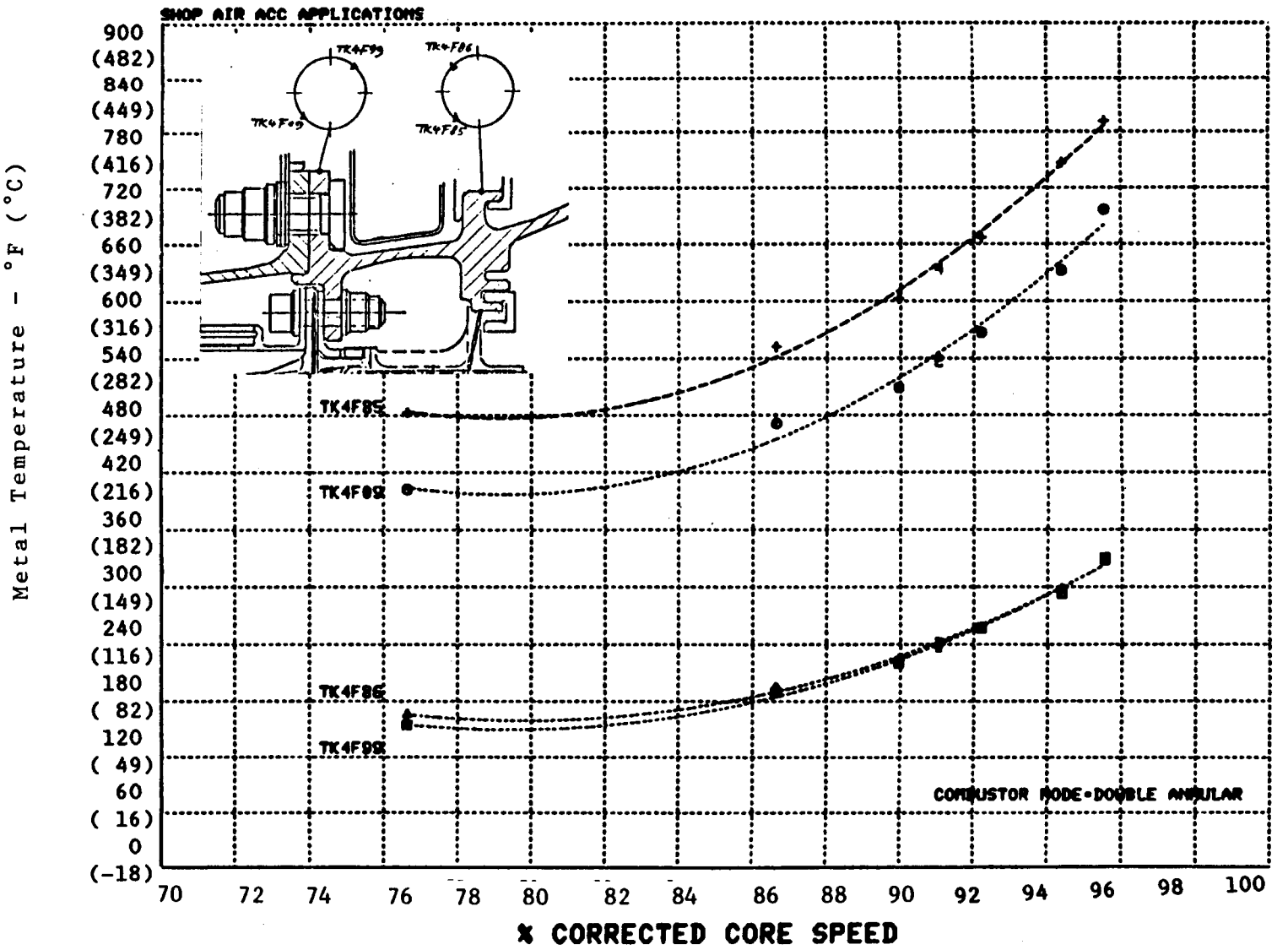


Figure 227. High Pressure Turbine Stage 2 Casing Flange Temperature After ACC Modification.

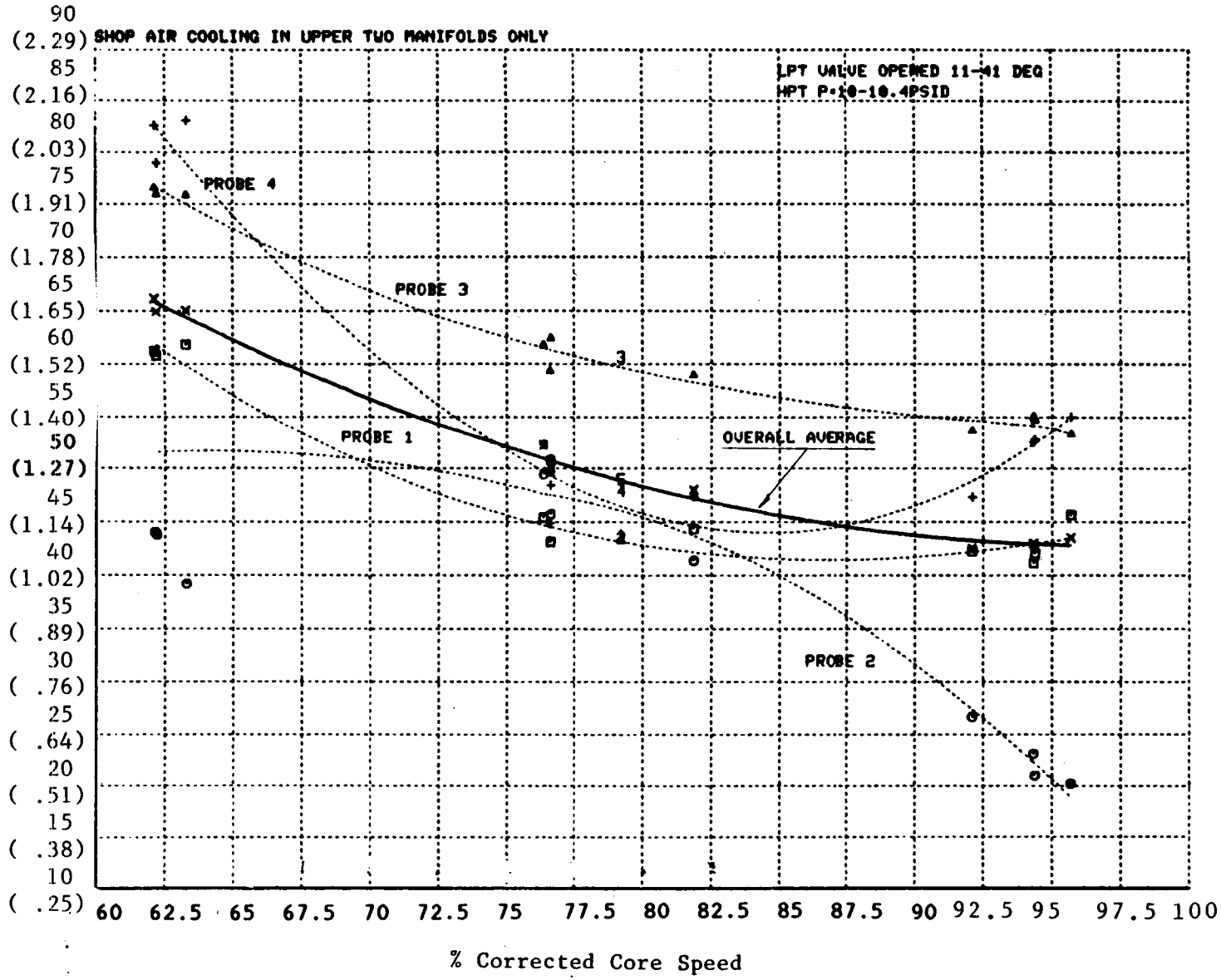




Figure 228. High Pressure Turbine Stage 1 Blade Tip Clearances with Shop Air ACC.

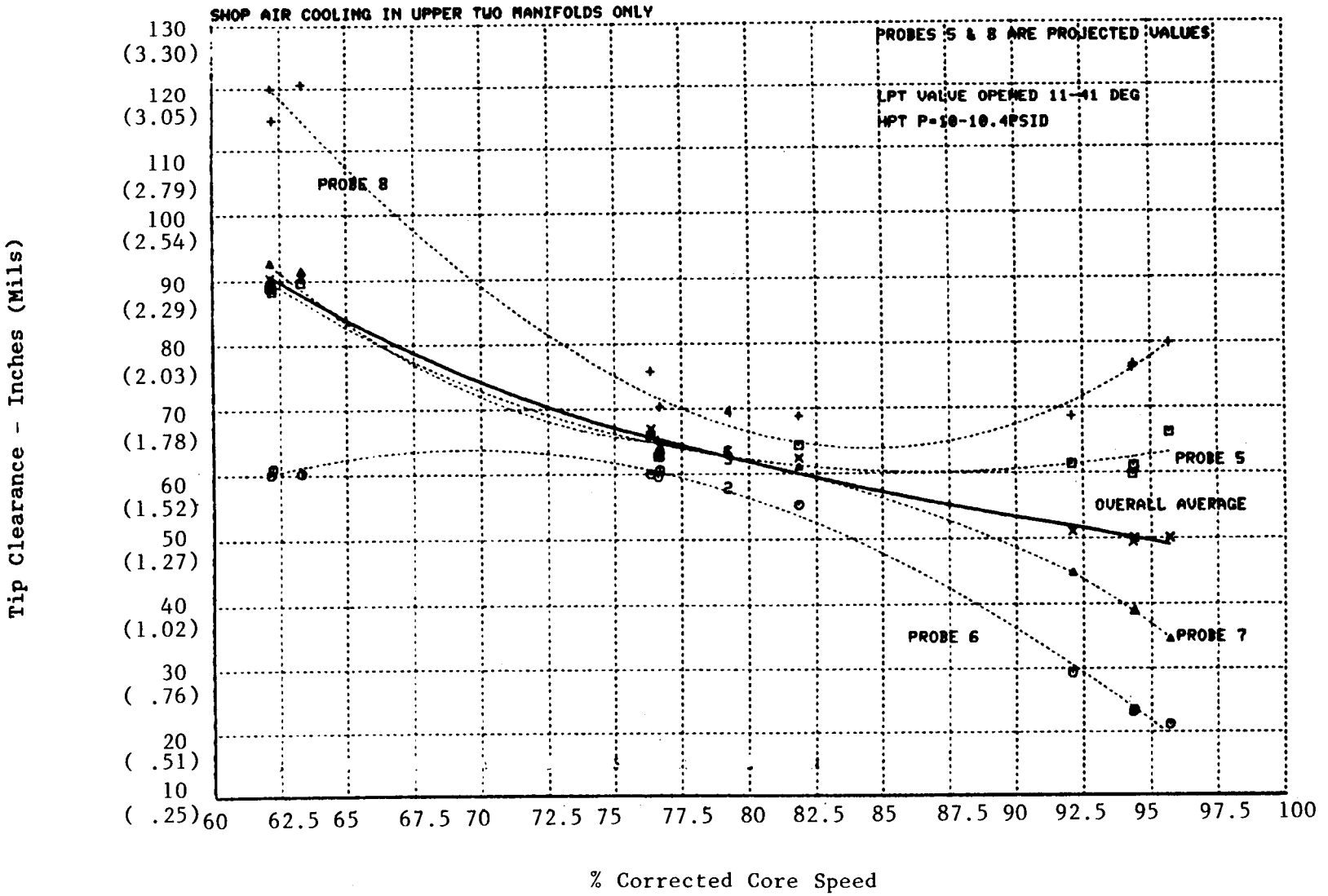


Figure 229. High Pressure Turbine Stage 2 Blade Tip Clearances with Shop Air ACC.

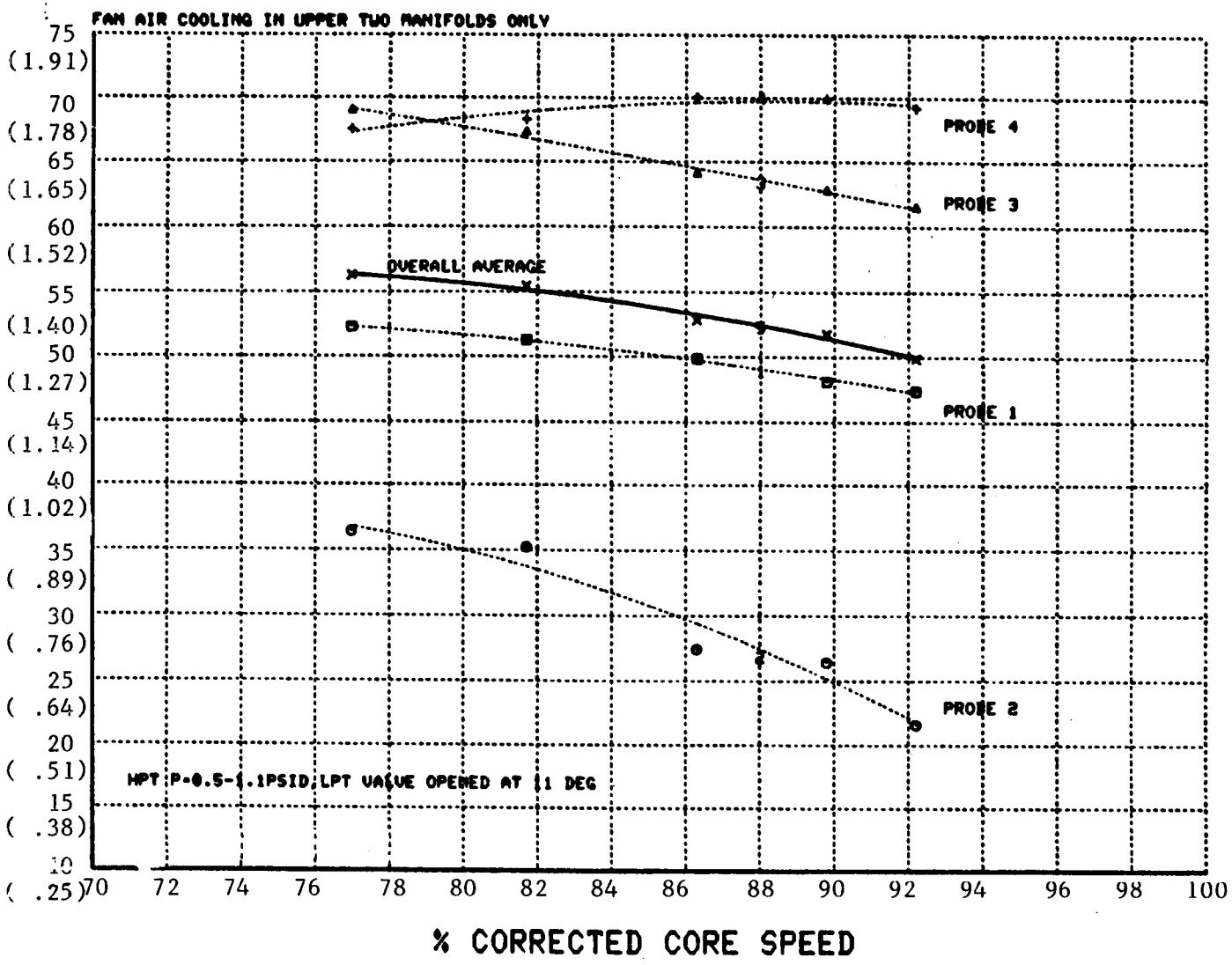


Figure 230. High Pressure Turbine Stage 1 Blade Tip Clearances with Fan Air ACC.

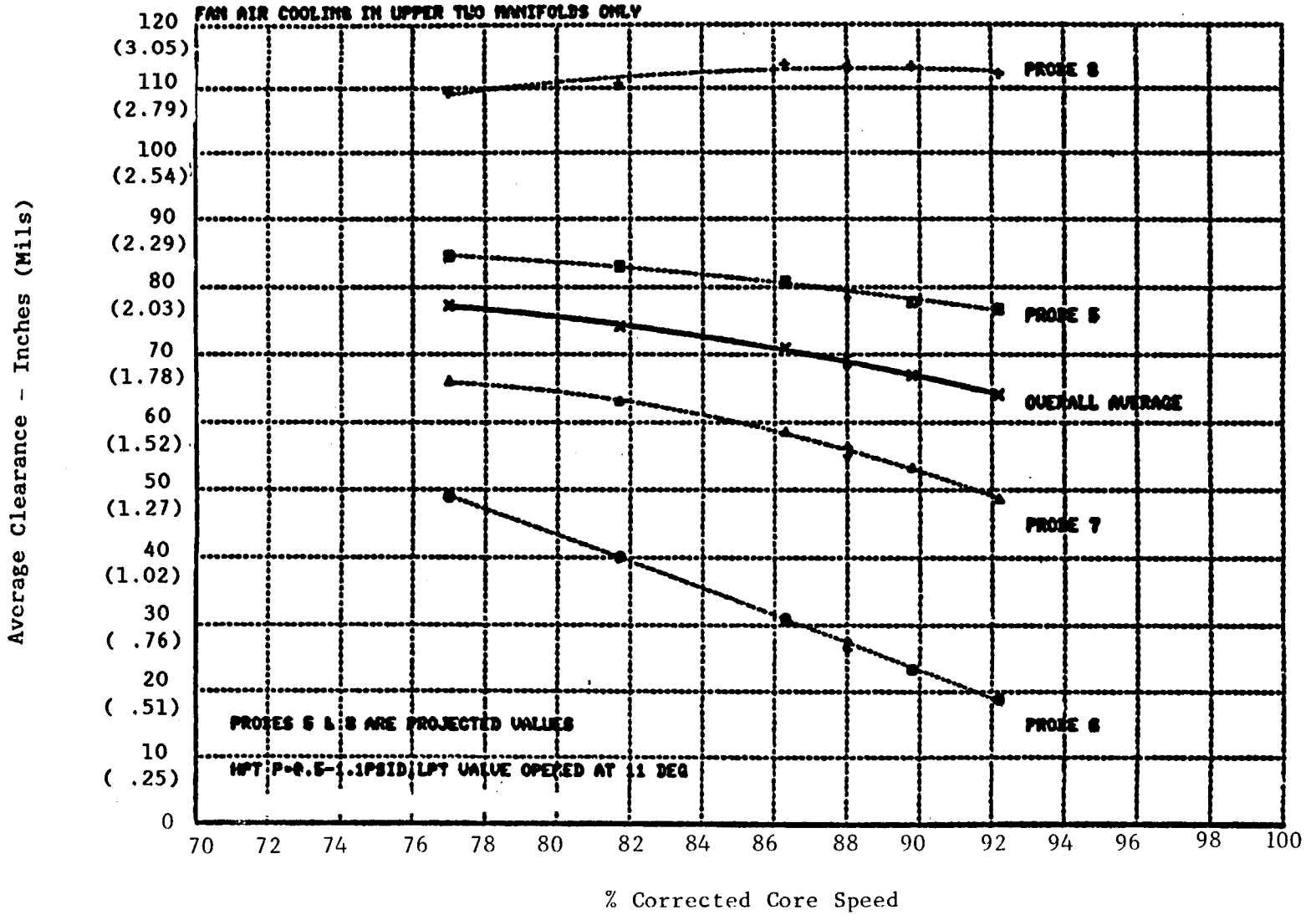




Figure 231. High Pressure Turbine Stage 2 Blade Tip Clearance with Fan Duct ACC.

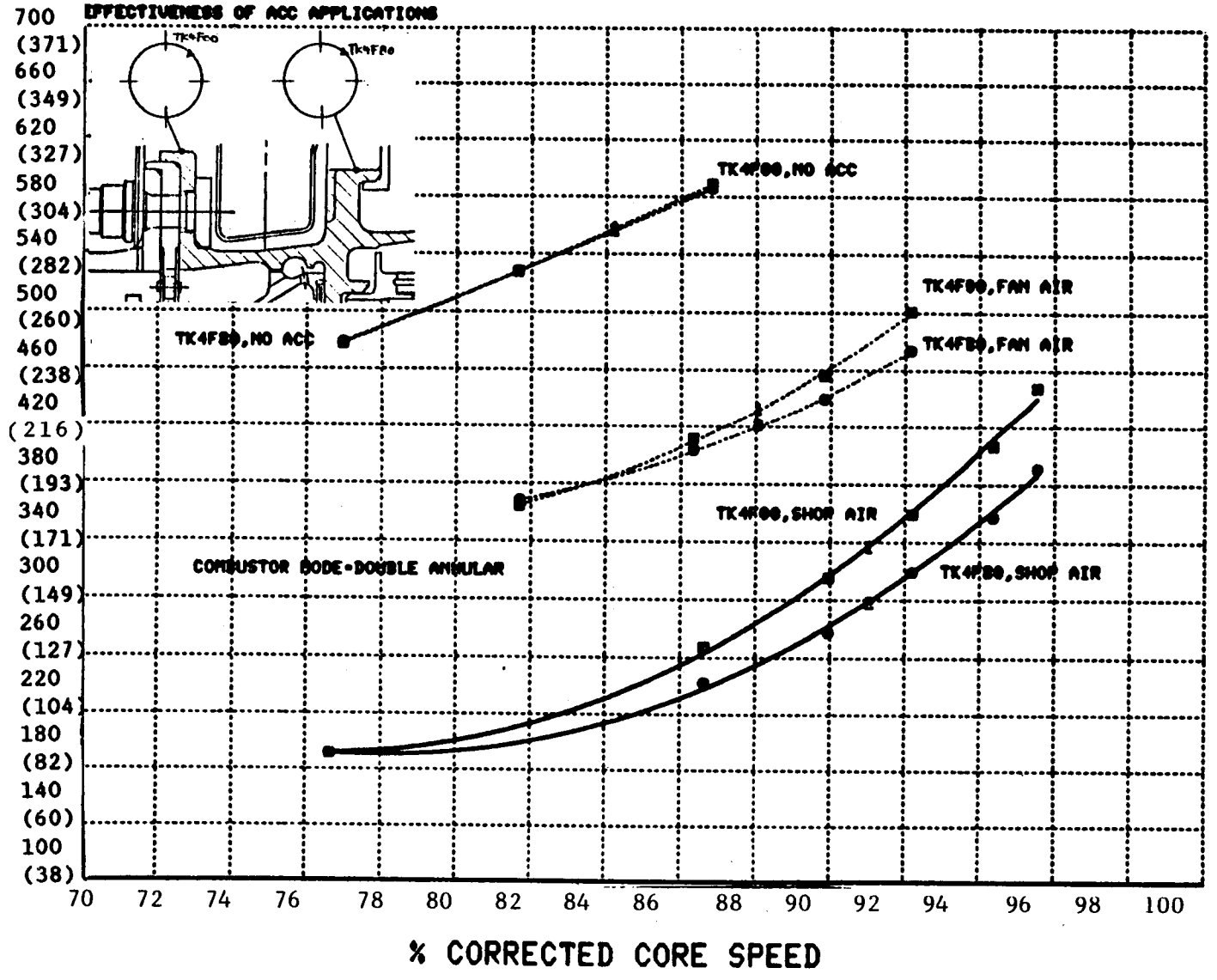




Figure 232. High Pressure Turbine Stage 1 Casing Flange Temperature After ACC Modification.

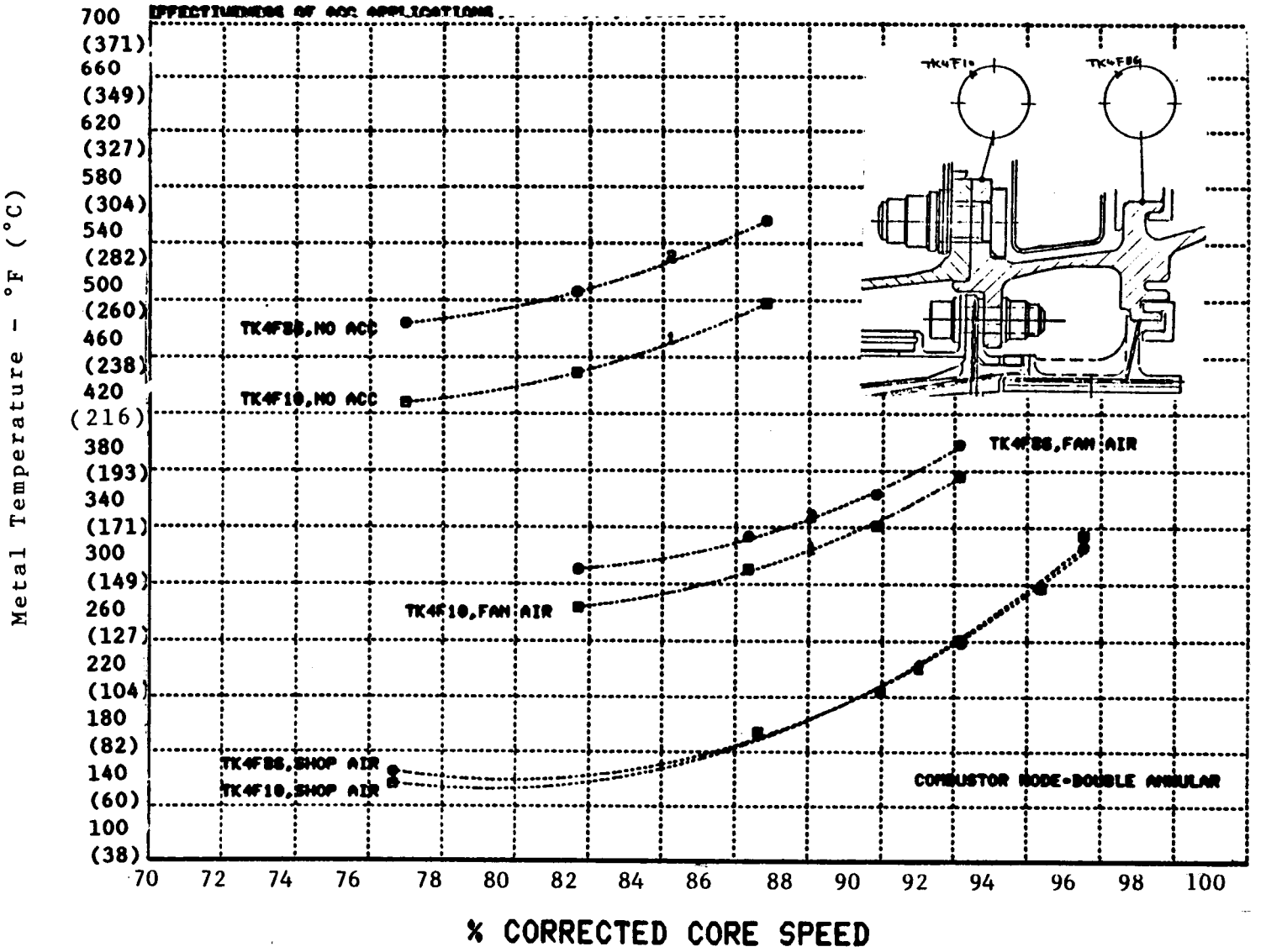




Figure 233. High Pressure Turbine Stage 2 Casing Flange Temperature After ACC Modification.

core testing, a tip rub during ICLS testing, and the modifications to the ACC system to correct an eccentricity.

Because the ACC system was modified to correct the eccentricity problem, ICLS testing did not fully evaluate the performance of the system. However, ACC was still effective and the fan air cooling system was successfully demonstrated.

The cause(s) of the premature rubs and the operating eccentric behavior of the HPT casing is the subject of extensive investigation. These areas have been identified as the probable source: (1) uneven airflow distribution around the core cowl which resulted in large thermal gradient on the adjacent structures, (2) bulk head reinforcements of the lower half of the fire wall next to the forward flange of Stage 1 casing, which created undue stiffness that might prevent natural thermal movements of the casing ring, and (3) initial assembly eccentricity which would magnify itself in the presence of elevated temperatures. There is no doubt that all three sources have contributed to the phenomenon. Analysis is now underway to unveil the most likely cause(s) or the biggest influence, so that lessons learned can be implemented into future designs and practice.

Transients

Rapid transient excursions were performed as part of the final test in the ICLS series. Figures 234 through 244 show the transient response of some HP turbine components during the above tests.

Figures 234 through 236 show the response of the Stage 1 nozzle metal temperature thermocouples at the leading edge (TK4010) and at the trailing edge suction side (TK4015) for the 60% span location. Plane 42, HPT discharge, gas temperatures are also shown together with the core speed responses for reference. Figure 234 shows transient 7070 which consists of a 7-1/2-second accel, 30-second hold time at maximum conditions and a 14-second decel. Figure 235 repeats the accel portion of Figure 234 to improve clarity

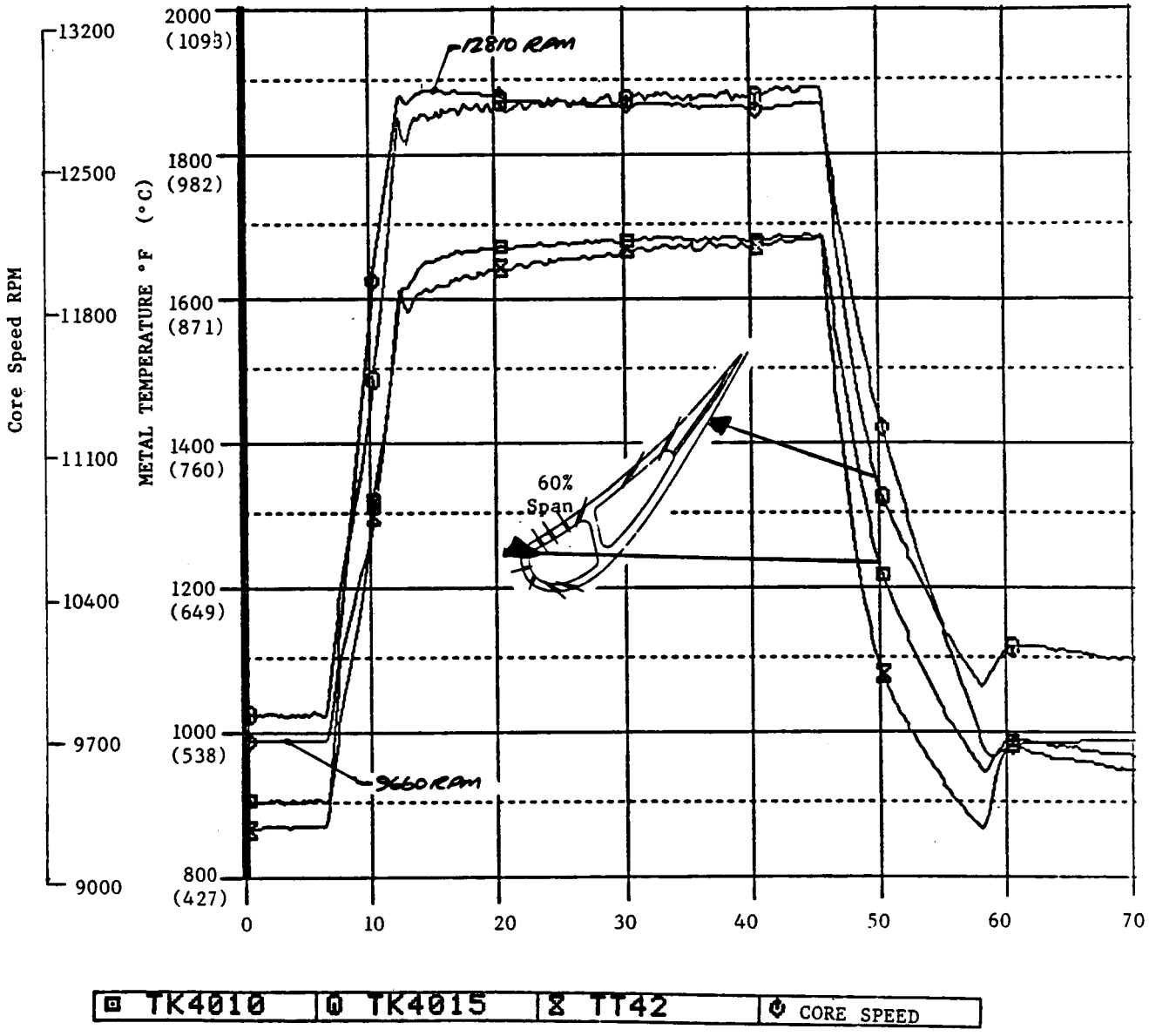


Figure 234. High Pressure Turbine Stage 1 Nozzle Transient Temperatures.

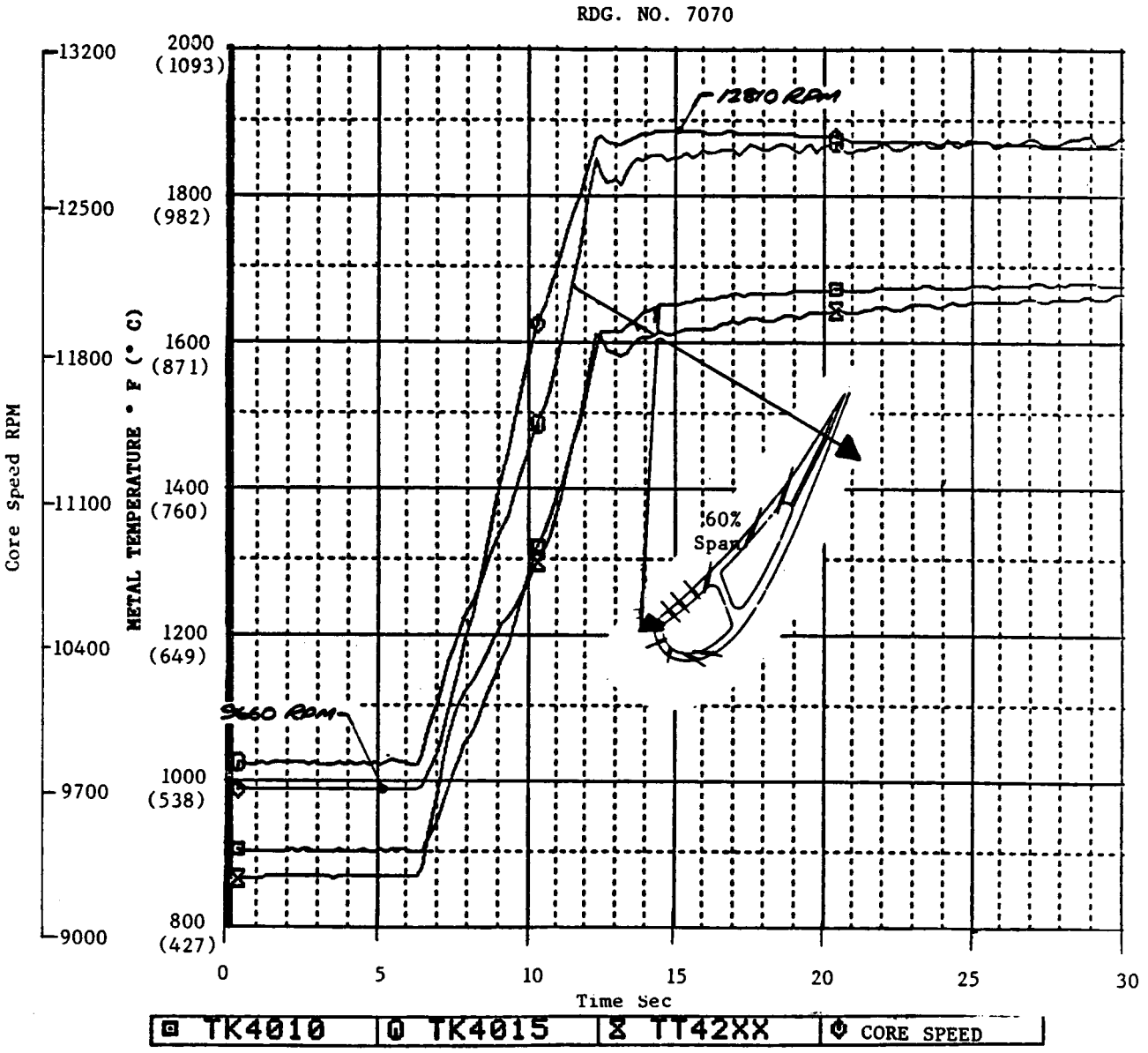


Figure 235. High Pressure Turbine Stage 1 Nozzle Transient Temperatures.

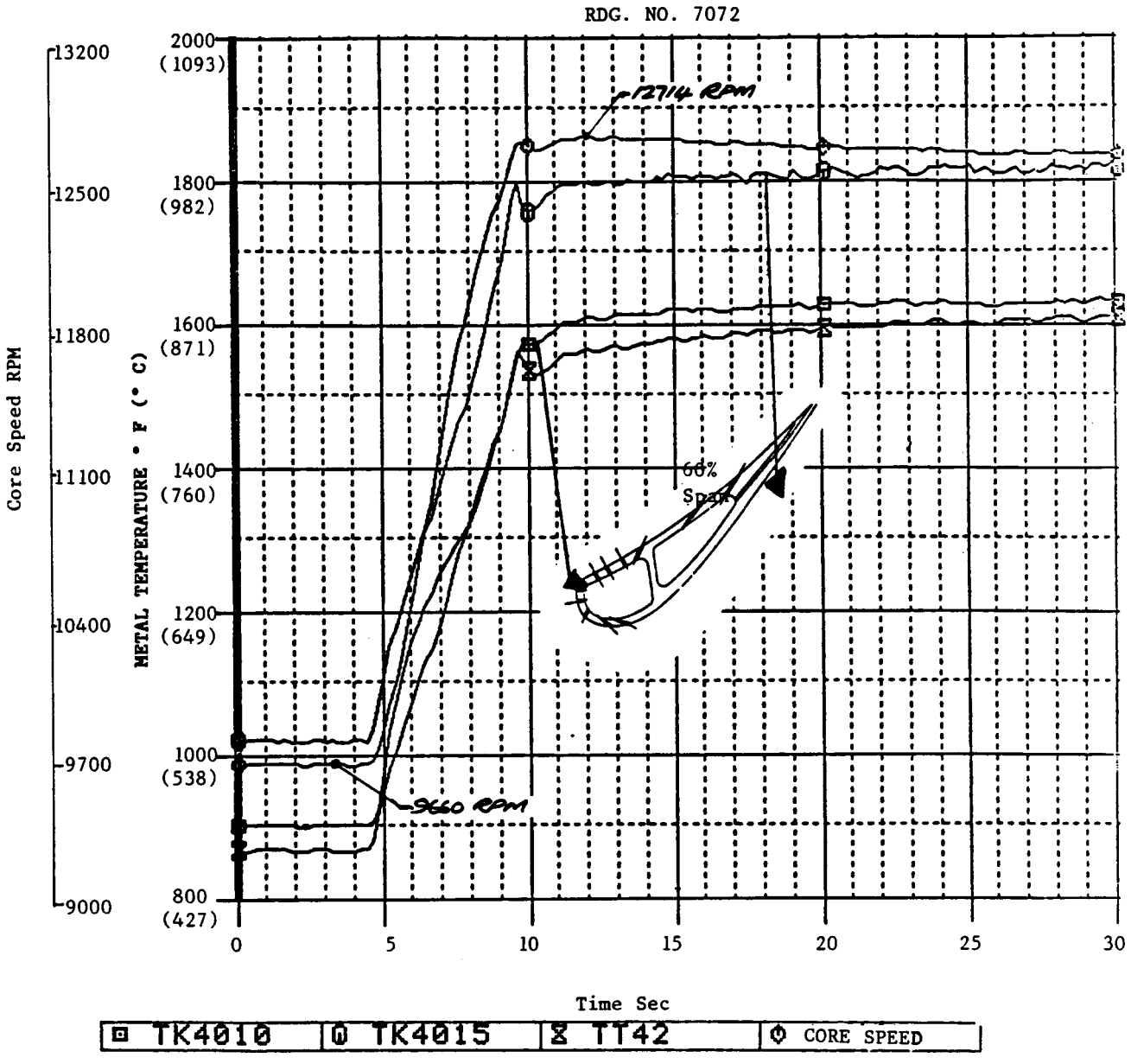


Figure 236. High Pressure Turbine Stage 1 Nozzle Transient Temperatures.

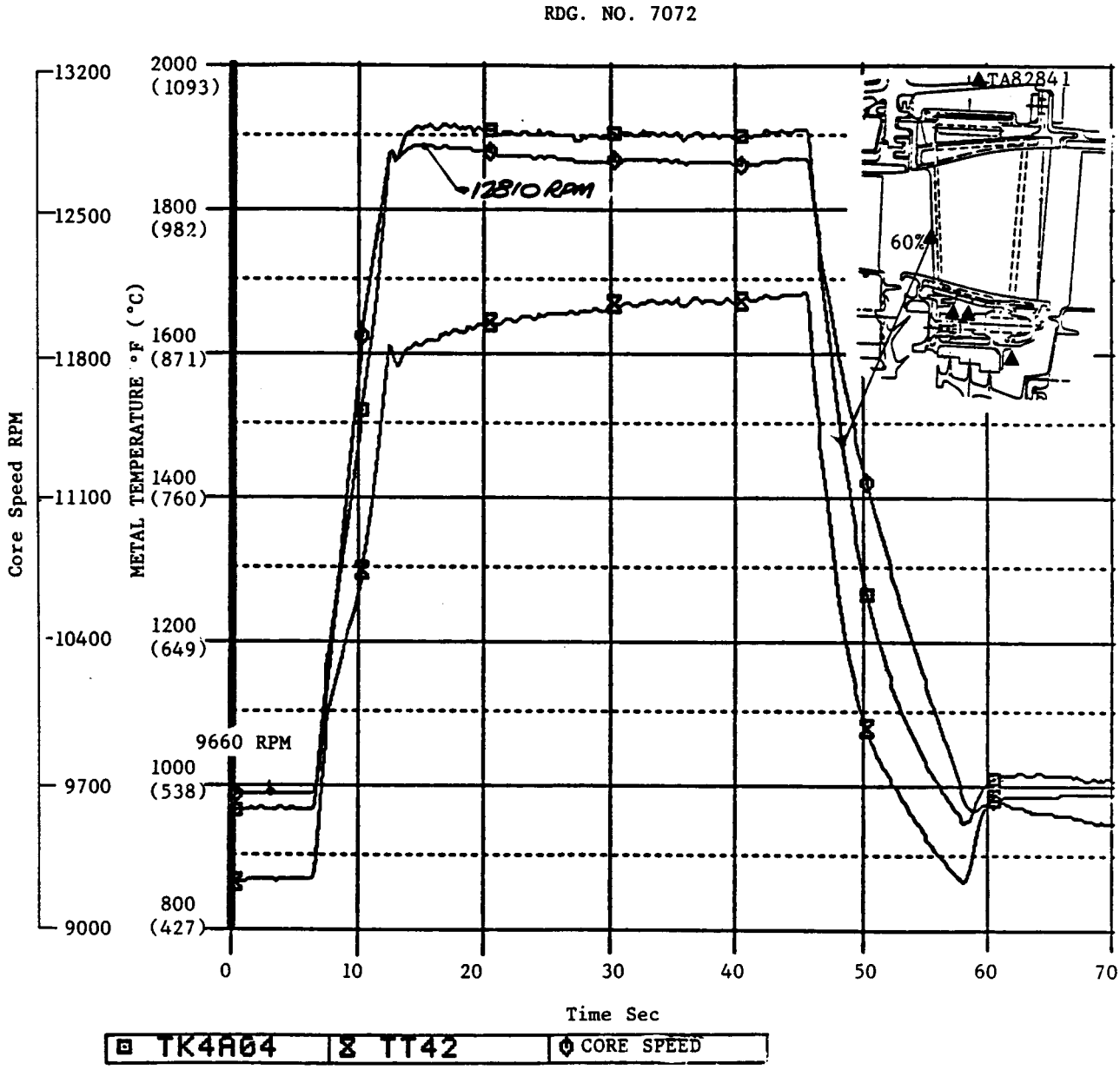


Figure 237. High Pressure Turbine Stage 2 Nozzle Transient Temperatures.

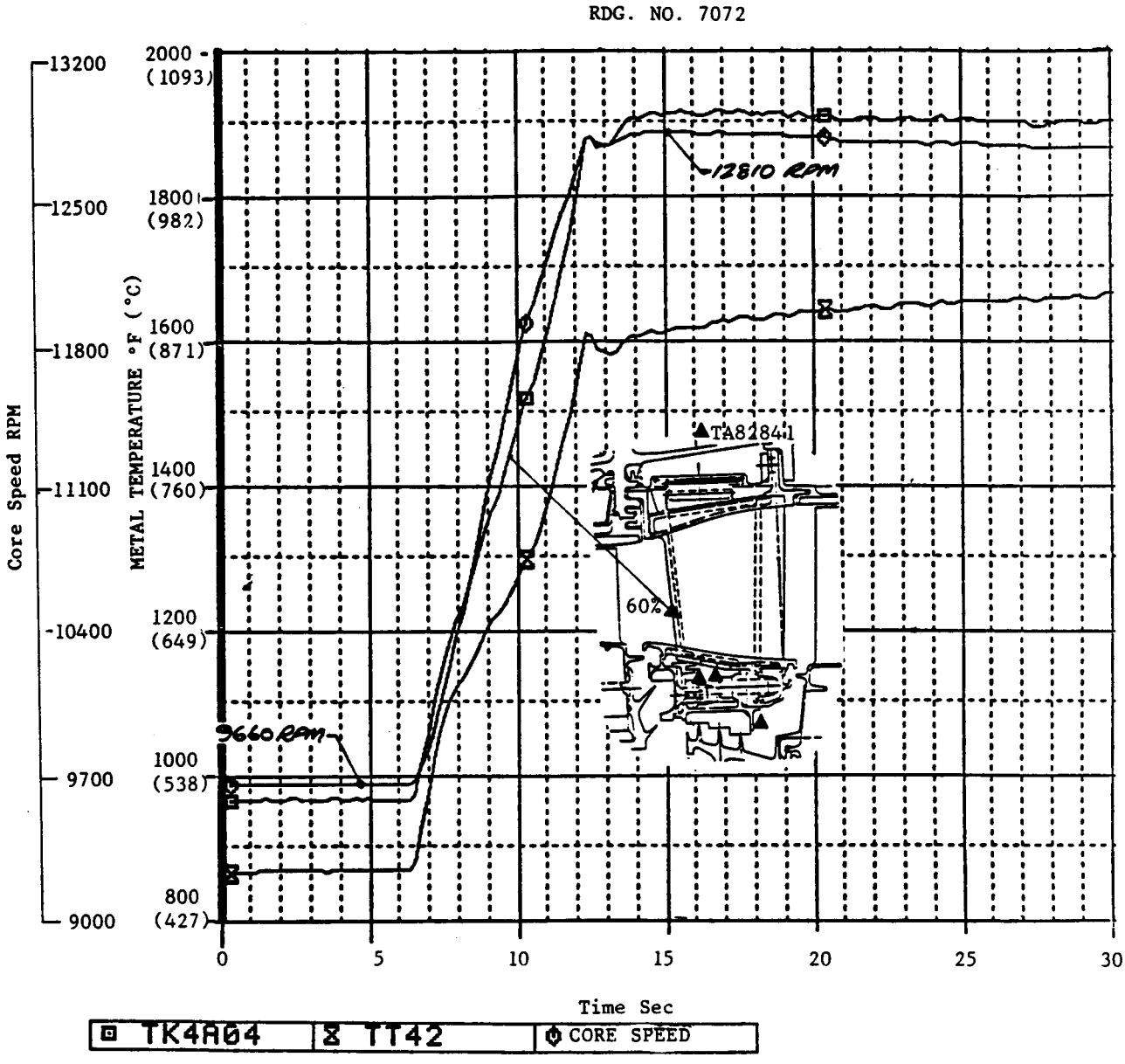


Figure 238. High Pressure Turbine Stage 2 Nozzle Transient Temperatures.

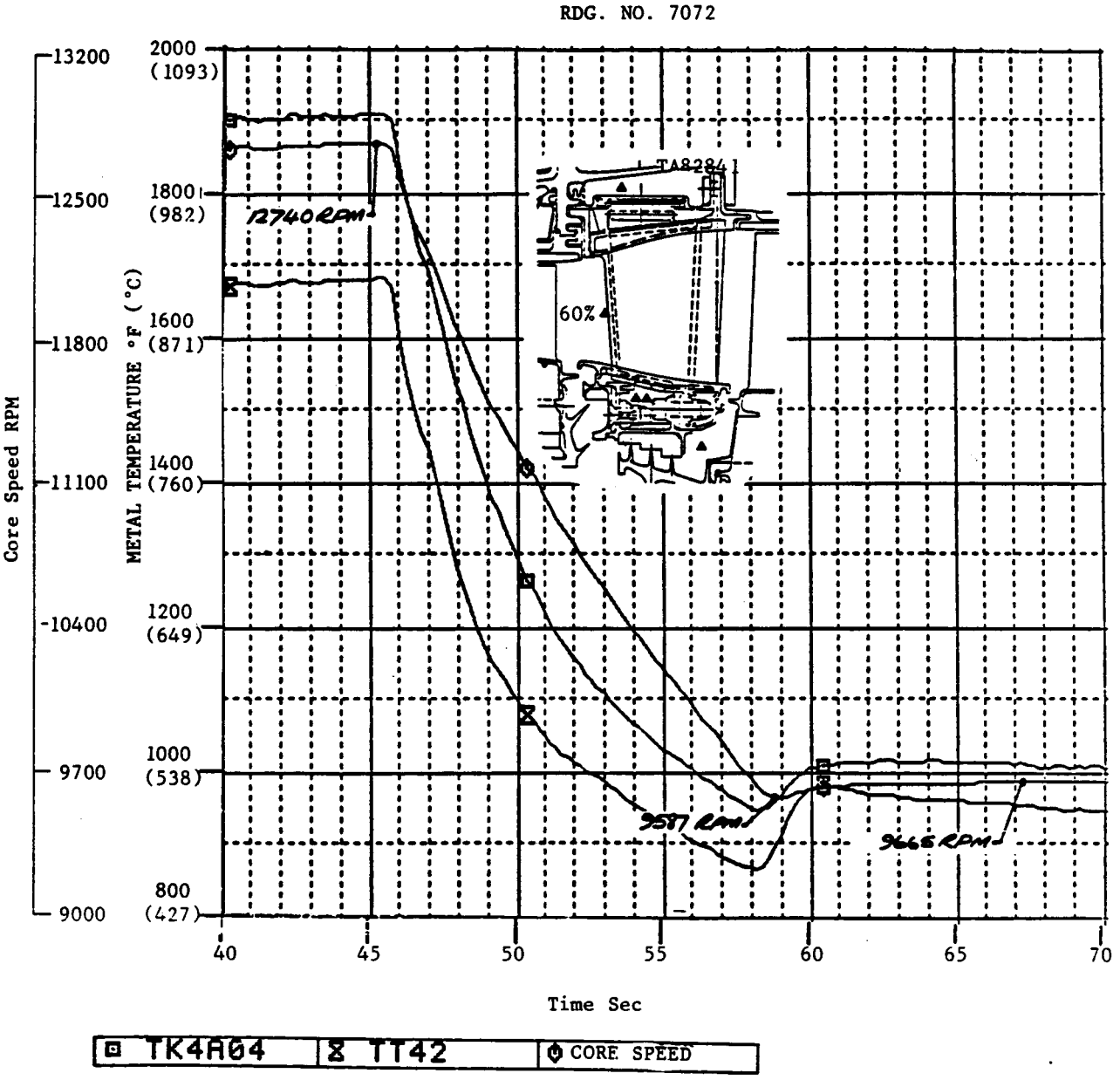


Figure 239. High Pressure Turbine Stage 2 Nozzle Transient Temperatures.

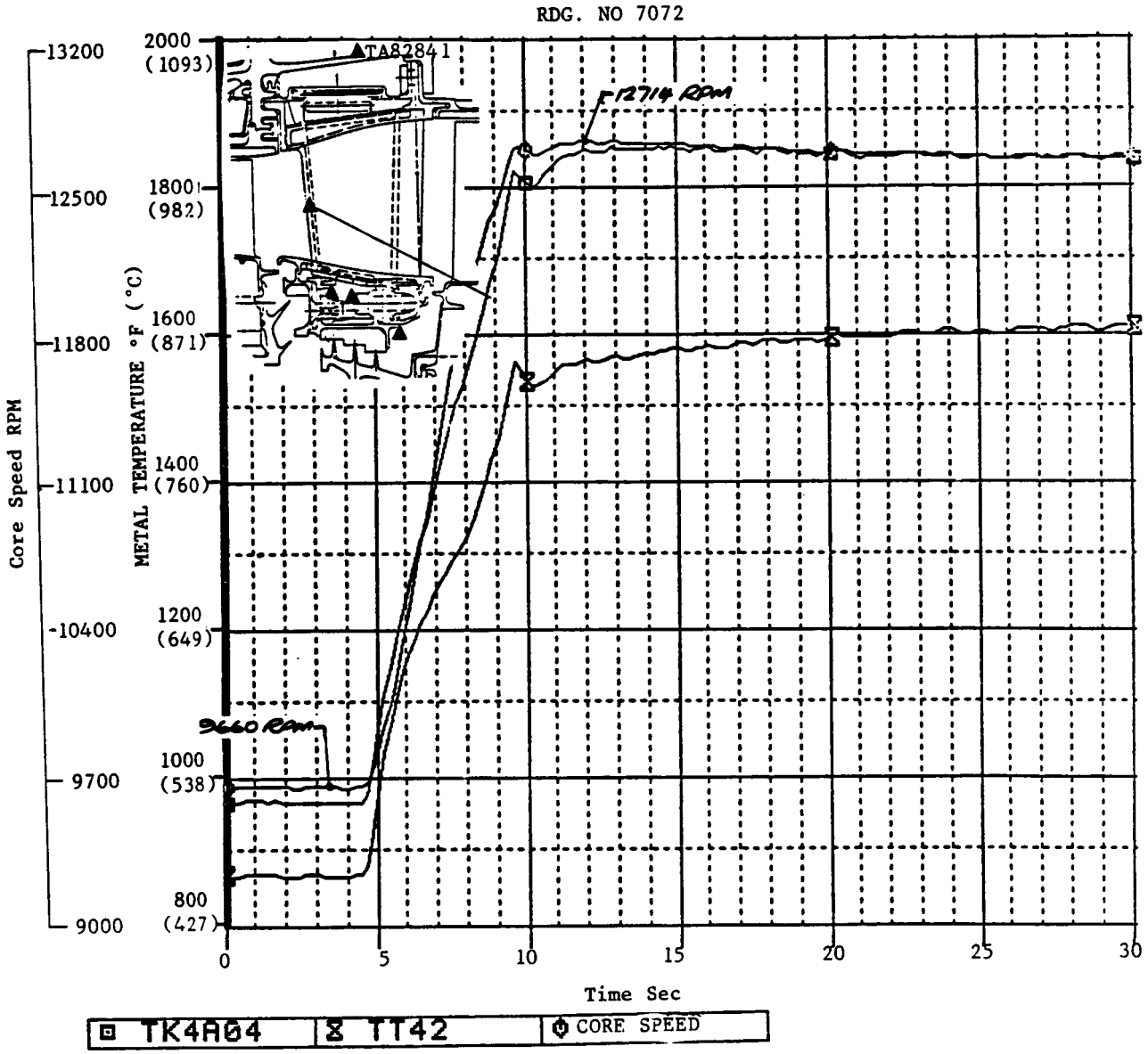


Figure 240. High Pressure Turbine Stage 2 Nozzle Transient Temperatures.

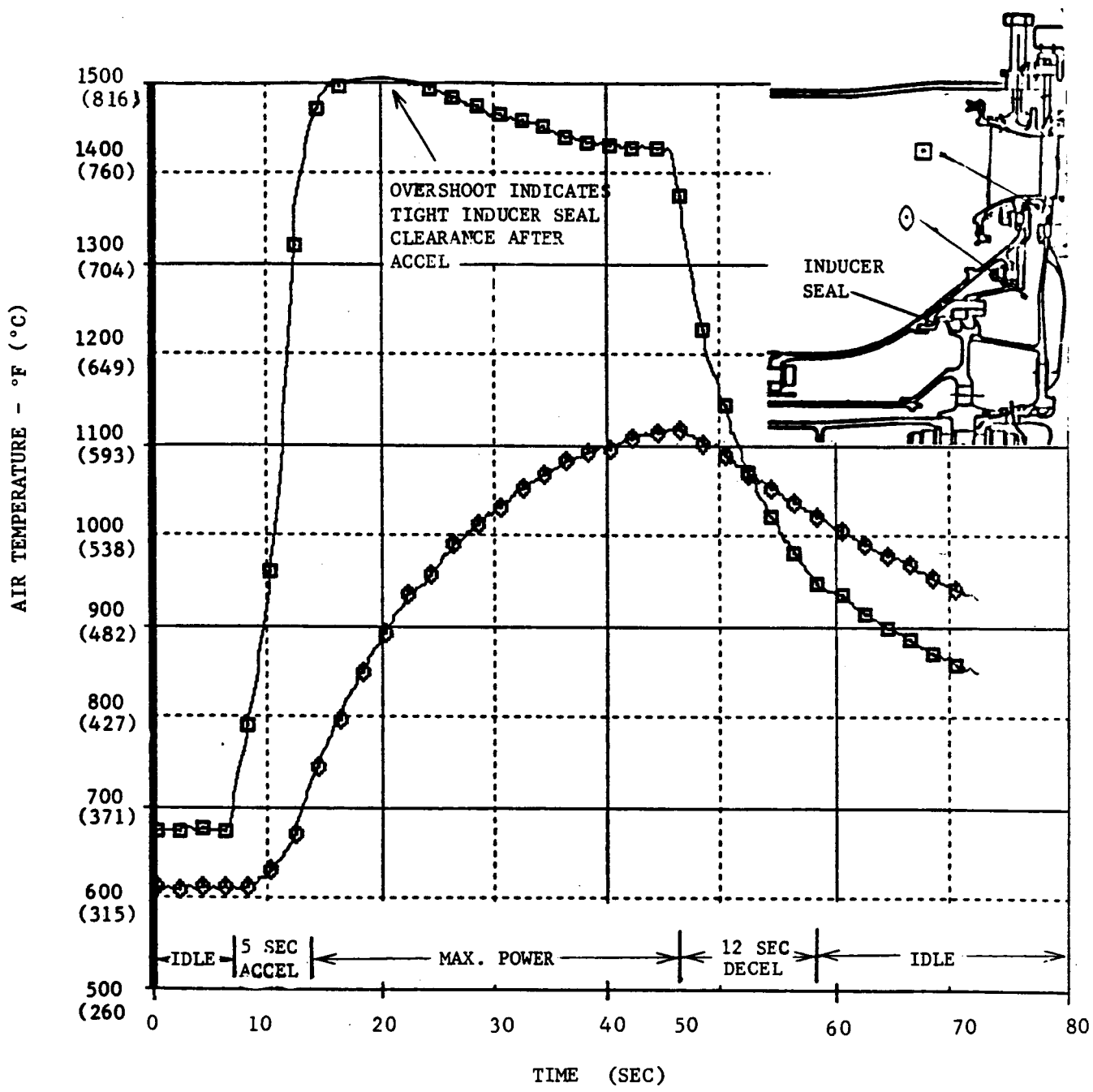


Figure 241. High Pressure Turbine Stage 1 Rotor Forward Cavity Transient Air Temperatures.

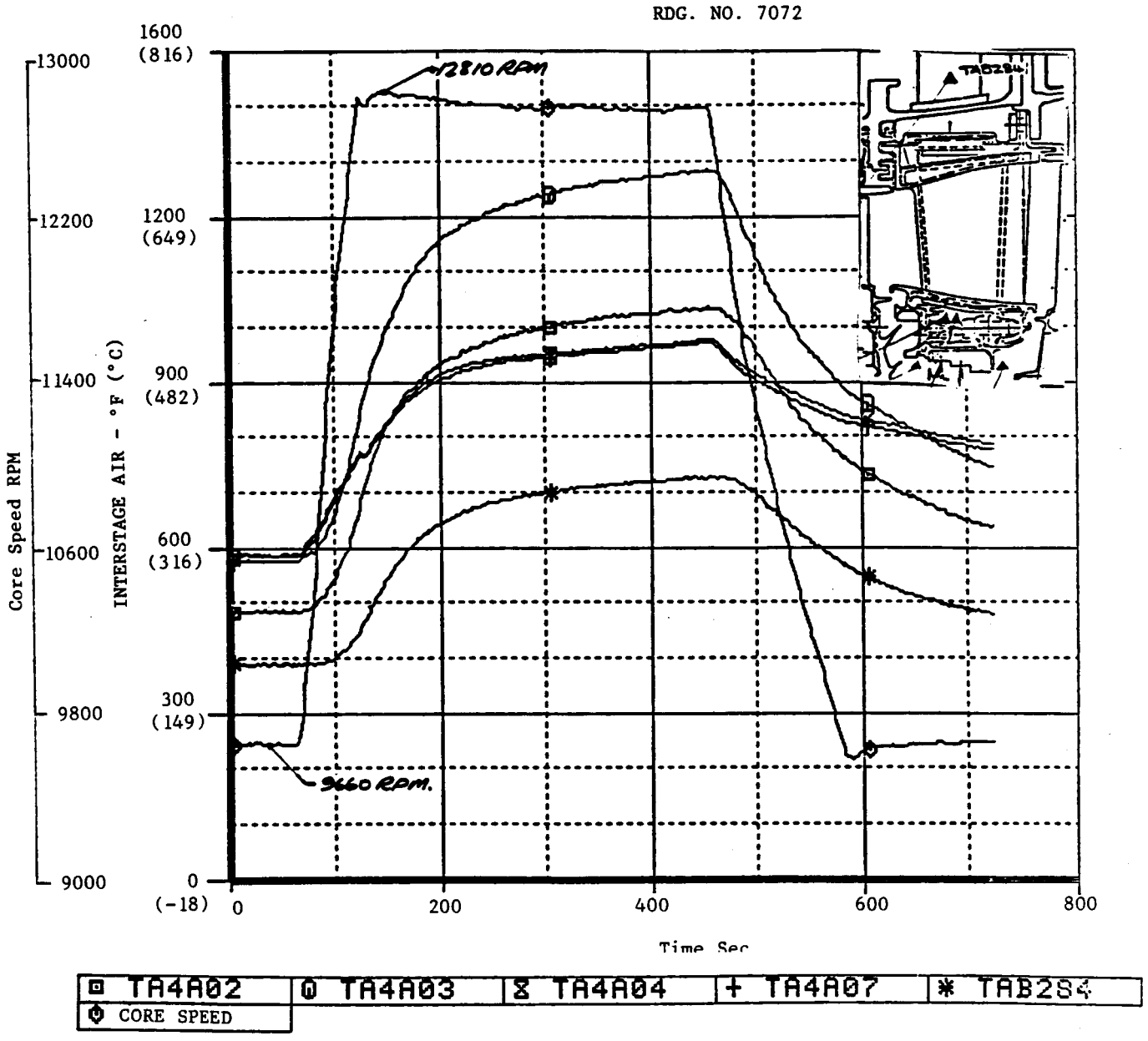


Figure 242. High Pressure Turbine Interstage Transient Temperature.

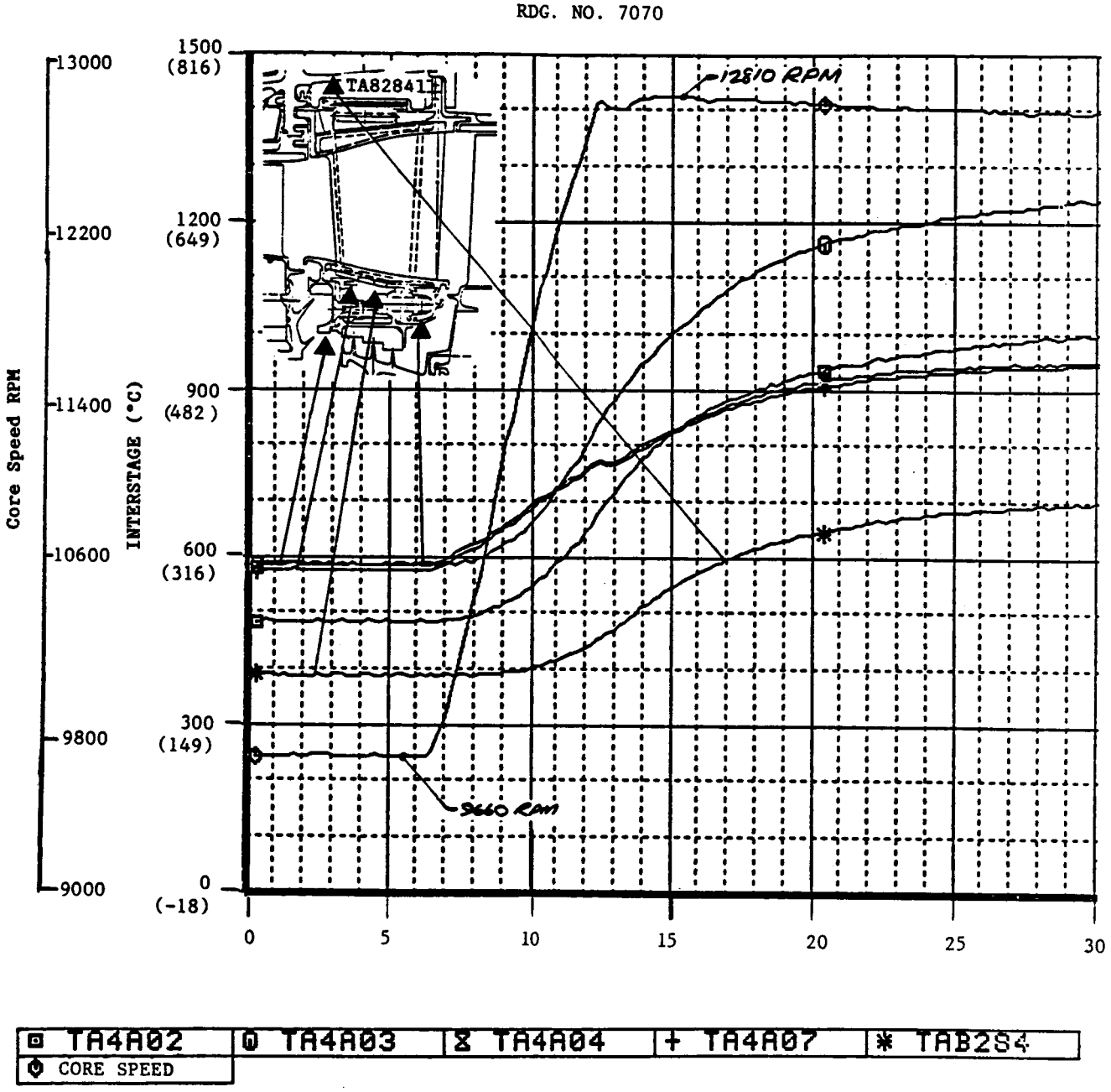


Figure 243. High Pressure Turbine Interstage Transient Temperature.

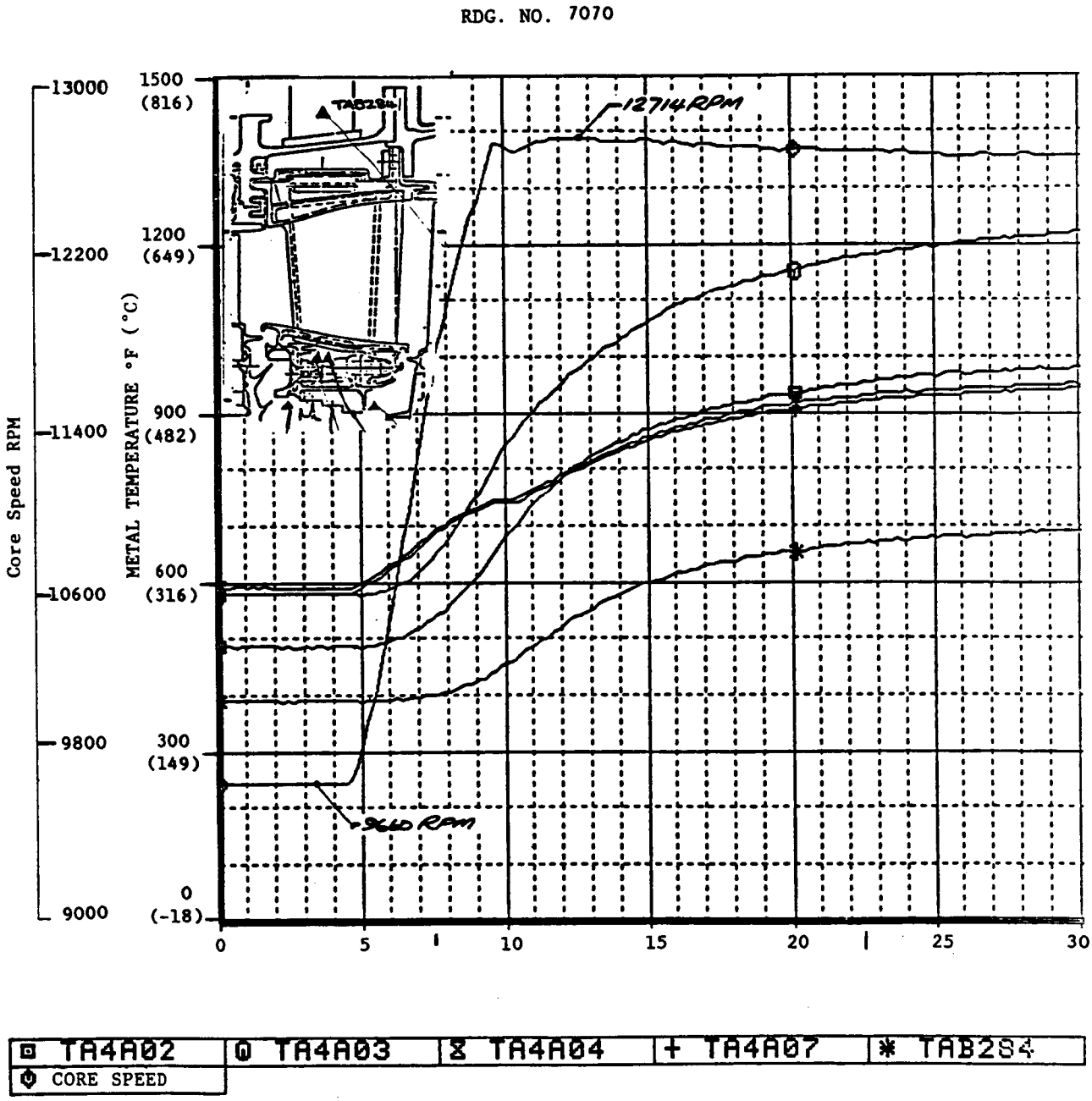


Figure 244. High Pressure Turbine Interstage Transient Temperature.

Figure 236 shows transient 7072, a 6 1/2 second accel with hold time at maximum conditions.

Figures 237 through 240 show the response of the thermocouple installed to measure metal temperature at the 60% span leading edge location on the Stage 2 nozzle. Transient 7070 is shown in Figures 237 through 239 while Figure 240 shows the response during transient 7072. The leading edge thermocouple indicated maximum temperatures of 1048°C (1918°F), 16.9 seconds into the accel portion of transient 7070 and 1012°C (1854°F), 14.8 seconds into accel 7072. These temperature levels can be compared with a steady-state maximum recorded temperature of 1039°C (1903°F) for the same location.

During the part of the test program where fast accelerations to maximum power were being conducted, one area of interest was the HPT Stage 1 disk forward rotor cavity purge flows. The inducer seal clearance during and shortly after the acceleration will close down and restrict the quantity of purge flow to the rotor cavity. The transient test measurements verified this. The air temperatures near the gas path climbed to 816°C (1500°F) shown in Figure 241 before dropping back to 774°C (1425°F) at steady-state takeoff. The air temperature at the discharge of the seal did not show this characteristic indicating that, while the flow to the cavity was restricted, there was no significant recirculation of the hotter gases.

The transient response of thermocouples measuring the interstage air temperatures is shown in Figures 242 through 244. Figure 242 shows the complete transient 7070. The accel portion is expanded and shown again in Figure 243 while Figure 244 plots the 7072 transient.

Cavity air thermocouples TA4A02 and TA4A03 are shown. The response characteristics of these two thermocouples match well; however, the maximum temperature levels reached differ by some 139°C (250°F) just prior to the initiation of the decel.

The response of thermocouples TA4A04 and TA4A07, located forward and aft of the interstage seal, respectively, differ from the cavity air

temperature response as expected. The two curves (TA4A04 and TA4A07) are, however, almost identical in every aspect which is not entirely expected in view of their different locations. Some doubt, during and after the core tests, about the correct installation/identification of these thermocouples has not been resolved. Careful post ICLS teardown may resolve the dilemma, but the transient response would tend to indicate that TA4A04 and TA4A07 are similarly located rather than on either side of the seal. Core speed together with 7th stage cooling air supply temperature are shown for reference.

There were many start transients during the ICLS test program. Because the engine was started on the pilot combustor dome only, there was some concern that the Stage 1 vane could be exposed to overly high gas temperatures. Presented in Figure 245 are the stage one vane metal temperatures measured during a cold engine start. The leading edge temperature did not exceed 850°F (454°C), while the trailing edge remained below 1100°F (593°C). Stage 1 vane temperatures during starts were not a problem.

Since the cooling effectiveness of the Stage 2 vane was lower and the work extraction in the turbine was also lower during the engine start, the metal temperatures were evaluated at this condition. The leading edge temperatures during start are presented in Figure 246. During the actual start the 60% span leading edge peaked out at a temperature of about 649°C (1200°F). The 90% span temperature continued to creep up in temperature even after the accel to idle was over. The steady-state idle temperature for the 90% span leading edge was over 704°C (1300°F). The reason for the time delay in the 90% span temperature achieving its steady-state idle temperature is due to the fact that the blade tip clearance is tight right after the engine reaches steady-state idle. The combuster liner and turbine outer flowpath structure heating may also slow the rate of response of the Stage 2 vane 90% span leading edge temperature. As with Stage 1, Stage 2 vane temperatures were not a problem during start transients.

Start transient casing temperature measurements were also made. Presented in Figure 247 are the Stage 1 shroud aft ring support structure

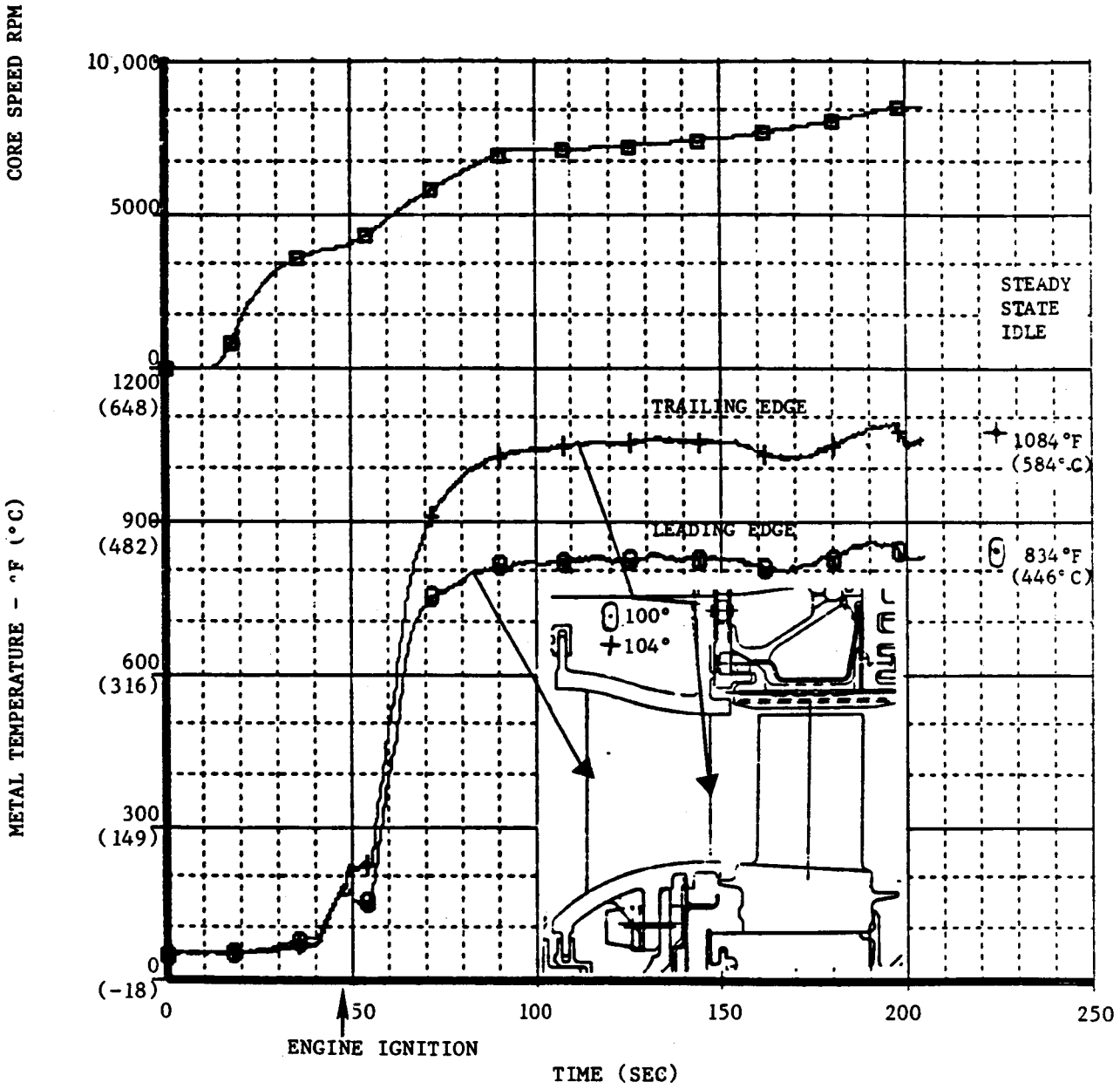


Figure 245. High Pressure Turbine Stage 1 Vane Start Transient Metal Temperatures.

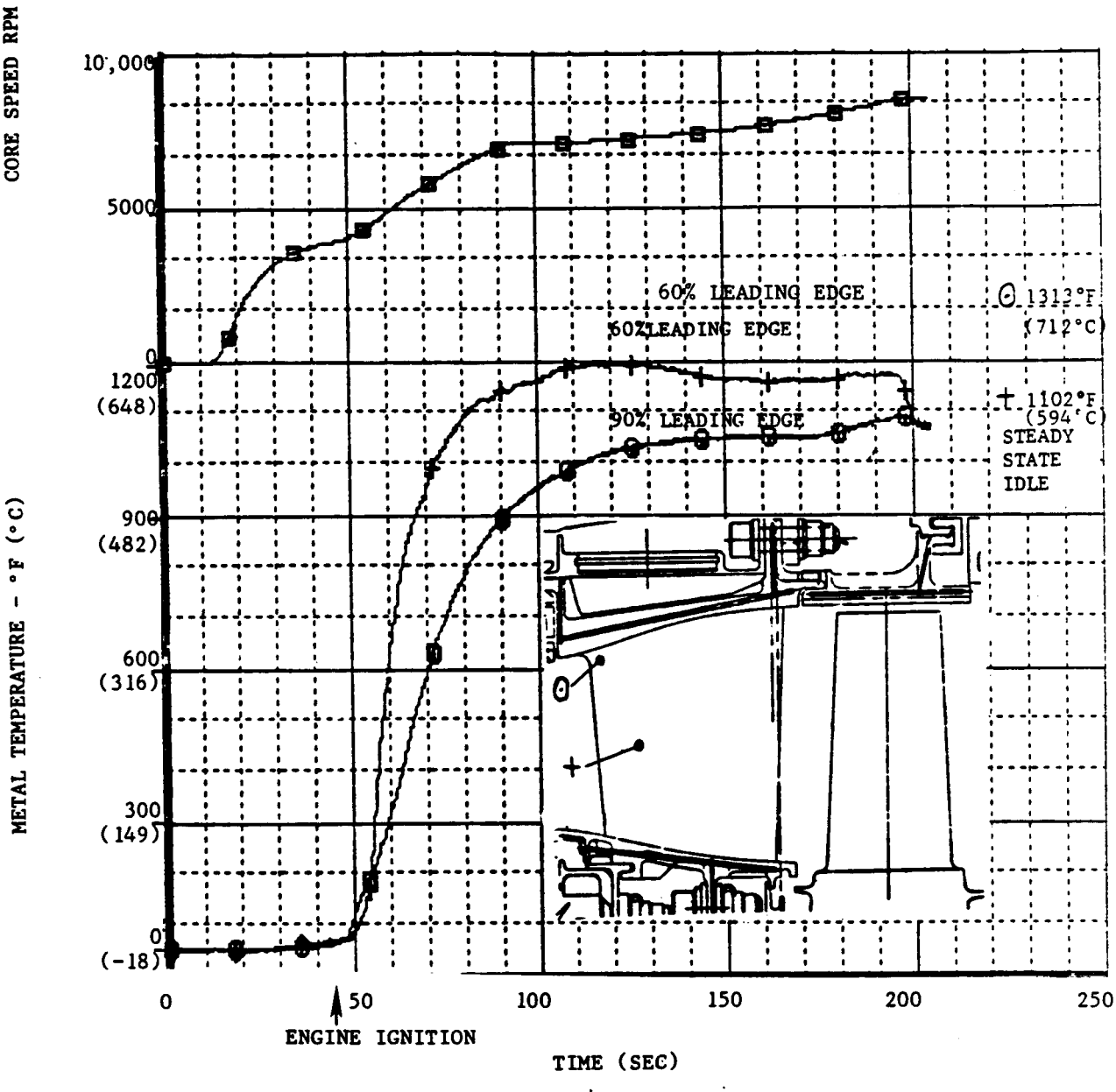


Figure 246. High Pressure Turbine Stage 2 Vane Start Transient Leading Edge Temperatures.

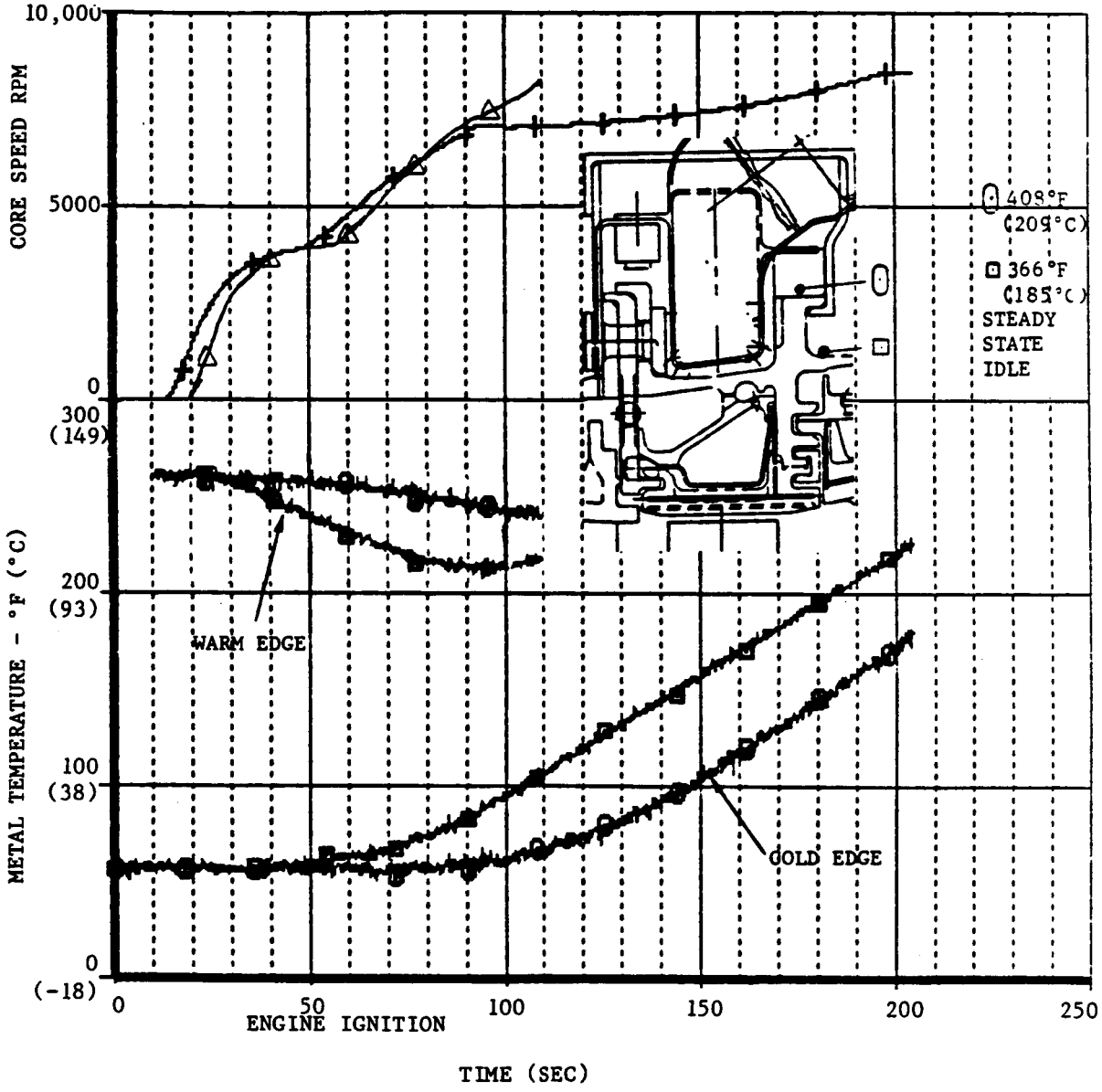


Figure 247. High Pressure Turbine Stage 1 Shroud Support Structure Start Transient Temperatures.

temperatures during start. A cold engine and a warm engine start transient are presented. As can be seen from the data, the casing of the warm engine actually cools down at first. The rate of response is very slow, as indicated by steady-state idle temperatures. A similar chart is presented in Figure 248 for the Stage 2 shroud support structure. The casing is actually warmer than the Stage 1 shroud support structure even though the steady-state idle values are cooler.

Warming of the LP system by the HP hardware after shutdown is of interest. Soak back temperature characteristics of the LP rotor were recorded for 100 minutes following shutdown. Presented in Figure 249 are temperatures of the LPT shaft under the HPT disk and the aft sump. As can be seen, the temperatures initially decreased after shutdown but then started to rise due to conduction and free convection from the HPT rotor.

## 6.9 CORE AERODYNAMIC PERFORMANCE

Core testing provided a more detailed and accurate evaluation of compressor, combustor, and turbine aerodynamic performance than could be obtained in testing of a complete turbofan engine. The aerodynamic performance of the core components is documented in Reference 3. The additional information learned in ICLS testing is presented in this section. For more detailed information, see Reference 3.

### 6.9.1 Compressor Aerodynamic Performance

Performance of the high pressure ratio compressor during the ICLS engine test was consistent with that of the core engine test. The ICLS engine compressor achieved the efficiency goal established for this test vehicle program at the engine takeoff power setting. The engine demonstrated a 44-second start time from zero speed to ground idle without indication of core compressor stall. The chop and burst fast transient tests were also smooth and stall free. In fact, there was no indication of any core compressor stall during the entire series of tests. The demonstrated stall-free operations at

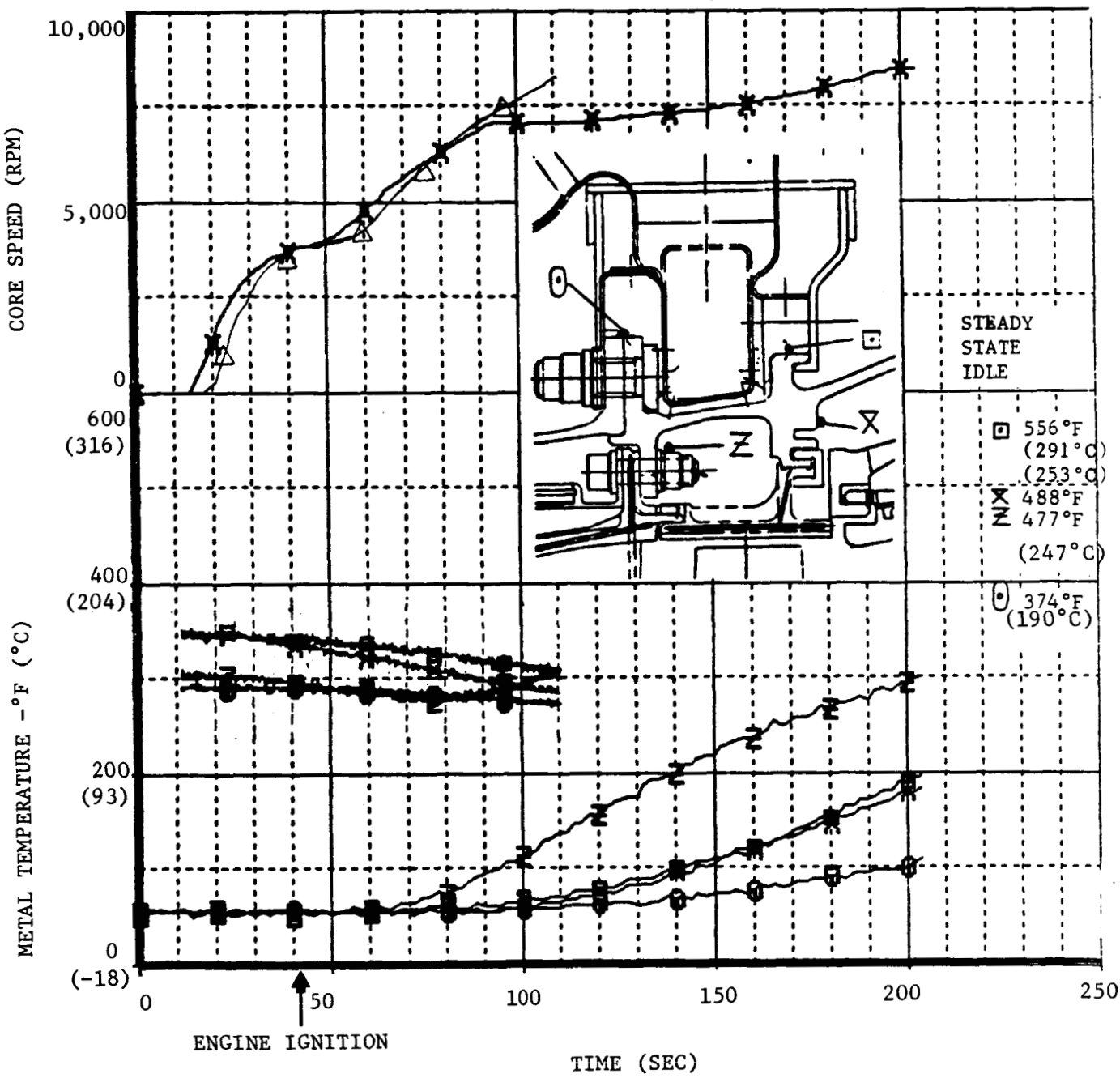


Figure 248. High Pressure Turbine Stage 2 Shroud Support Structure Start Transient Temperatures.

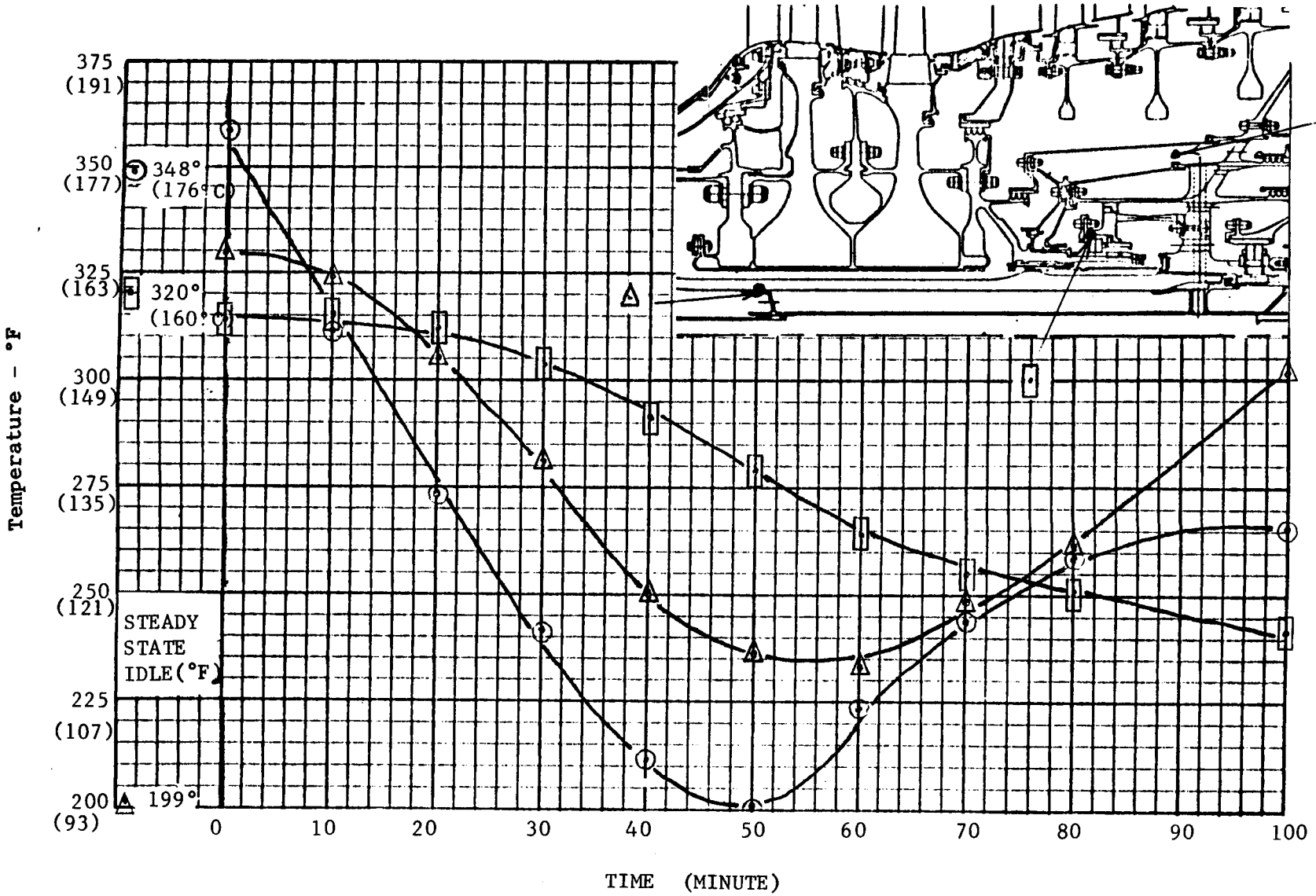




Figure 249. Low Pressure Shutdown Temperature Soak Back Characteristics.

starting and midspeed regions have important significance because they occurred in a real engine environment with a fully automated engine-type stator actuation system and controls.

The compressor overall performance along the ICLS engine operating line is compared with the core engine results in Figure 250. The predicted operating line performance was based on the core engine data. The speed lines shown were from the second 10-stage component tests. Data shown represent the measured compressor pressure ratios and efficiencies with the inlet pressure adjusted to the IGV leading edge and with the exit pressure adjusted to the OGV trailing edge, so that it is consistent with the definition used by the engine performance model. The open symbols represent compressor performance without using rear casing active clearance control (ACC) air; and the solid symbols are data points recorded with ACC air fully on. The core engine test data were taken with ACC on at speeds above flight idle and with ACC off at lower speeds. As shown in the map, the operating line of the ICLS engine compressor was very close to the cycle prediction over the entire speed range. The measured efficiencies shown are also close to the core engine level with a deficit of 0.5 point near the takeoff power setting. Since there were no hardware changes between the core engine and the ICLS engine tests for the core compressor, the deficiency is attributed to the different engine environment. No adjustments were made due to the lack of accurate casing skin temperature and rotor tip clearance measurements. A comparison of the core engine and ICLS turbofan engine test results at the takeoff power setting is given in Table XXI.

The ICLS core compressor was exposed to hotter fan bypass air in the front case than the core engine compressor and, therefore, the rotor tip clearances were predicted to be more open. The rear case temperature was controlled by the active clearance control airflow; however, the case cooling air available was lower than the core engine test due to a bleed valve restricton, whereas the compressor airflow was hotter due to high inlet temperature from the fan-booster exit. This resulted in larger rear rotor tip clearances.

Figure 250. ICLS Compressor Performance Map.

Table XXI. Compressor Sea Level Takeoff Performance.

| | Corrected Airflow ($W\sqrt{\theta}/S$) | | Pressure Ratio | Adiabatic Efficiency ($\eta_{ad}$), | Polytropic Efficiency ($\eta_p$), |
|---|---|---|---|---|---|
| | Kgm/sec | lbm/sec | (P3/P25) | % | % |
| ICLS as Measured | 48.7 | (107.4) | 18.83 | 84.3 | 89.2 |
| Fully Adjusted* | 49.4 | (109.0) | 19.10 | 85.6 | 90.1 |
| Core Engine as Measured | 48.7 | (107.4) | 19.10 | 84.8 | 89.5 |
| Fully Adjusted | 49.4 | (109.0) | 19.38 | 86.1 | 90.4 |

*Adjustments include: unsensed inlet duct, inlet rake and interstage instrumentation losses and variable stators 5 and 6.

The compressor inlet flow, fed by the fan-booster stage, had similar radial profiles of pressure and temperature as the full scale fan test data had indicated but exhibited more hub distortion than the core engine test. Comparisons of the compressor inlet pressure and temperature profiles with the core engine data are shown in Figure 251. It is seen that the total pressure near the hub region is lower for the ICLS compressor. The inlet temperature profile of the ICLS compressor shows a five degree rise near the hub compared with a uniform distribution for the core engine compressor. In summary, the $E^3$ core compressor performance demonstrated during the ICLS turbofan engine tests met the goals established for the ICLS demonstration engine program and showed good agreement with the core engine test results. The small efficiency difference between these two engine tests is explainable. Since the ICLS engine compressor did not reach speed above takeoff, the core engine test results above takeoff speed are recommended for component performance reference.

Rapid engine starts and transients were accomplished without the assistance of midstage bleed and with no indication of core compressor stall. The compressor operated smoothly and stall free under real engine environment with a fully-automated engine-type stator actuation system and controls. The

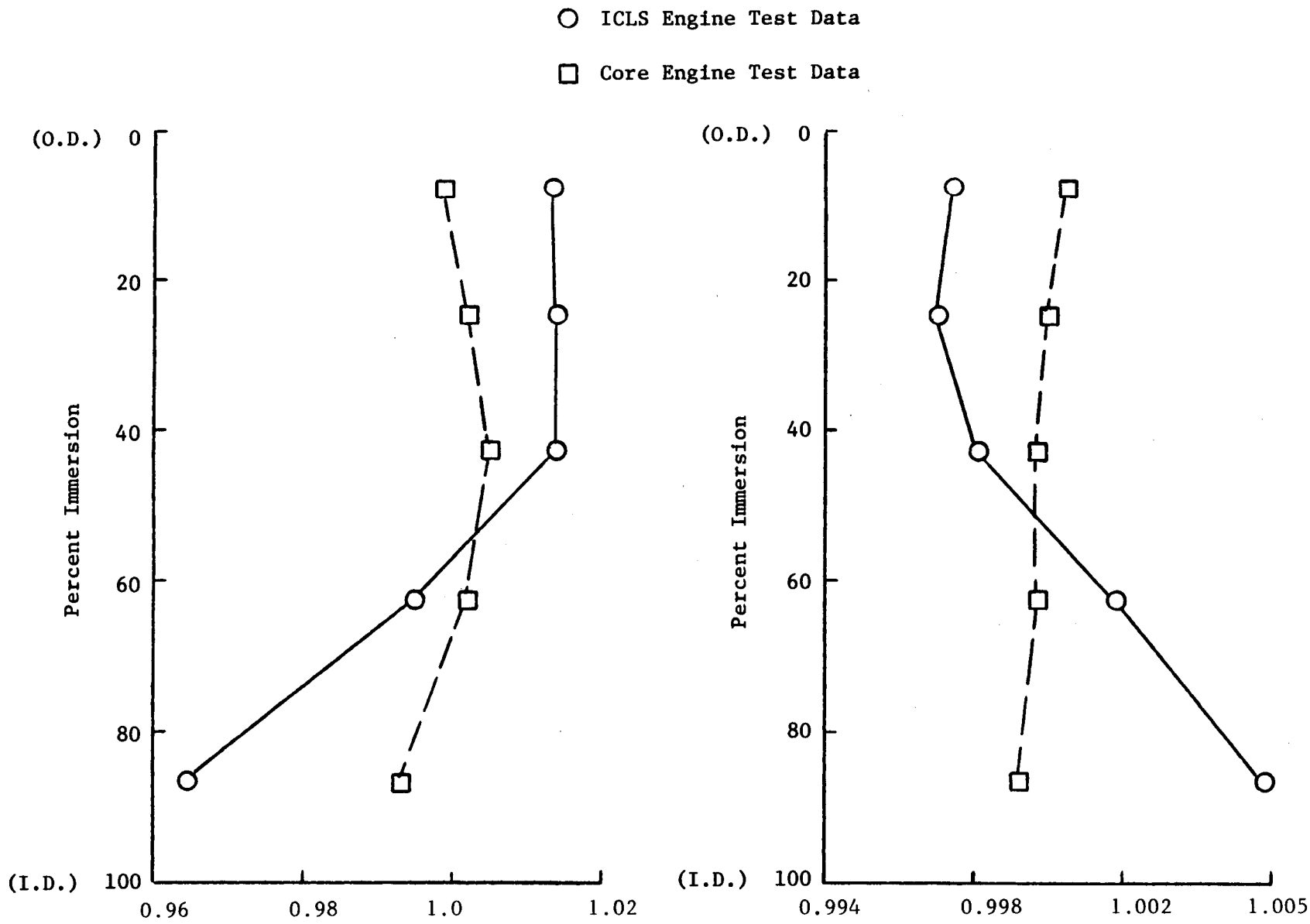


(a) Normalized Pressure

(b) Normalized Temperature

Figure 251. Comparisons of Compressor Inlet Pressure and Temperature Profile.

tests demonstrated that the final FPS compressor design could be significantly simplified by eliminating Stage 7 starting bleed and by fixing Stators 5 and 6.

### 6.9.2 Combustor Aerodynamic Performance

The core engine combustor and fuel system were incorporated, intact, into the ICLS vehicle. Performance remains essentially unchanged from that reported in Reference 3.

The only new information accrued concerns visible smoke. No measurements were taken during ICLS testing; however, visual observations of the engine exhaust plume during daylight hours and while at approximately 85% rated fan speed (88% was maximum) revealed the engine to be smoke-free.

Engine starting and staging were accomplished in a trouble-free manner, and acceleration times from idle to high speed were solely a function of fuel scheduling. Rapid accelerations and decelerations were successfully demonstrated.

### 6.9.3 High Pressure Turbine Aerodynamic Performance

Performance of the high pressure turbine during ICLS testing was consistent with that from core engine test. This was evidenced by comparison to a pretest cycle prediction, which was based on core test results. ICLS results are based on a balanced cycle calculation.

High pressure turbine pressure ratio is plotted as a function of percent corrected core speed in Figure 252, where ICLS data are compared to pretest prediction based on core test data. The excellent agreement in pressure ratio trend and level is indicative that the low pressure turbine Stage 1 nozzle area was properly sized.

High pressure turbine efficiency, corrected to design intent clearance of 0.041 cm (0.016 in) on both stages is presented in Figure 253. It is seen that test points agree with prediction within 0.13 points at all speeds.

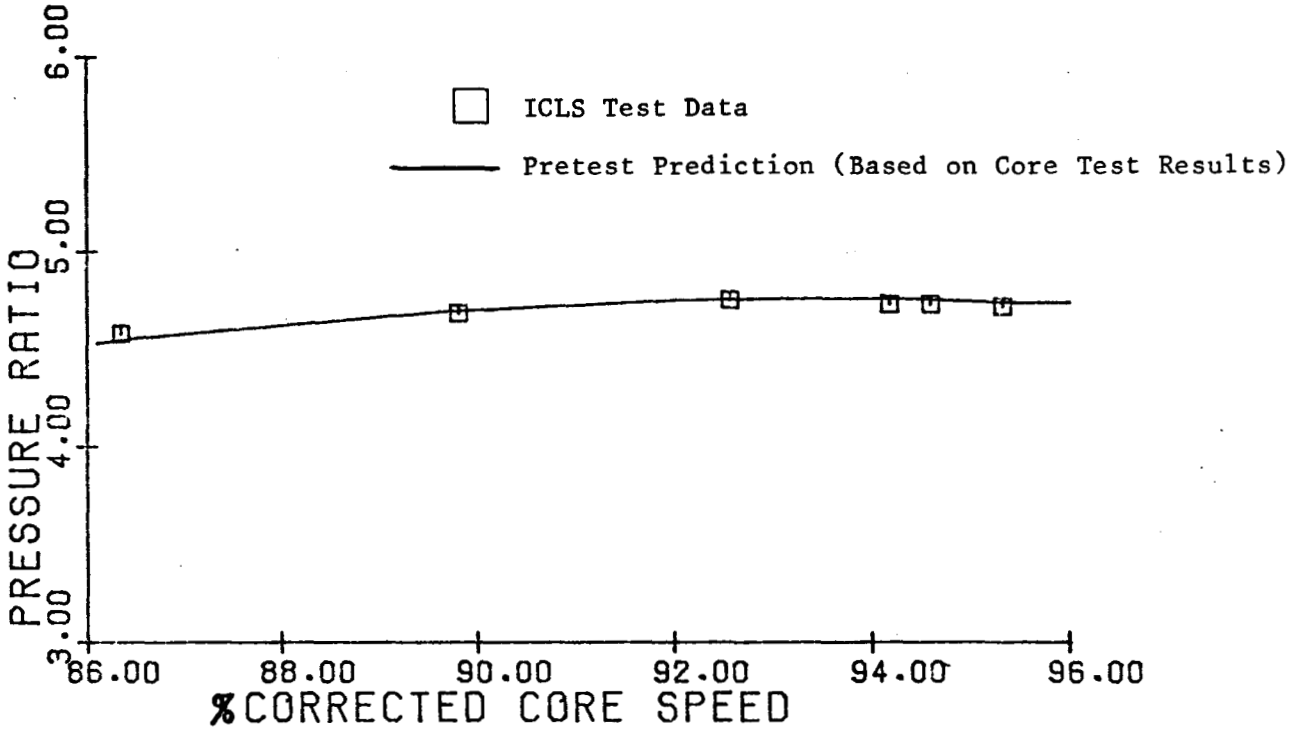


Figure 252. High Pressure Turbine Pressure Ratio Versus Percent Corrected Core Speed, ICLS Test Versus Prediction.

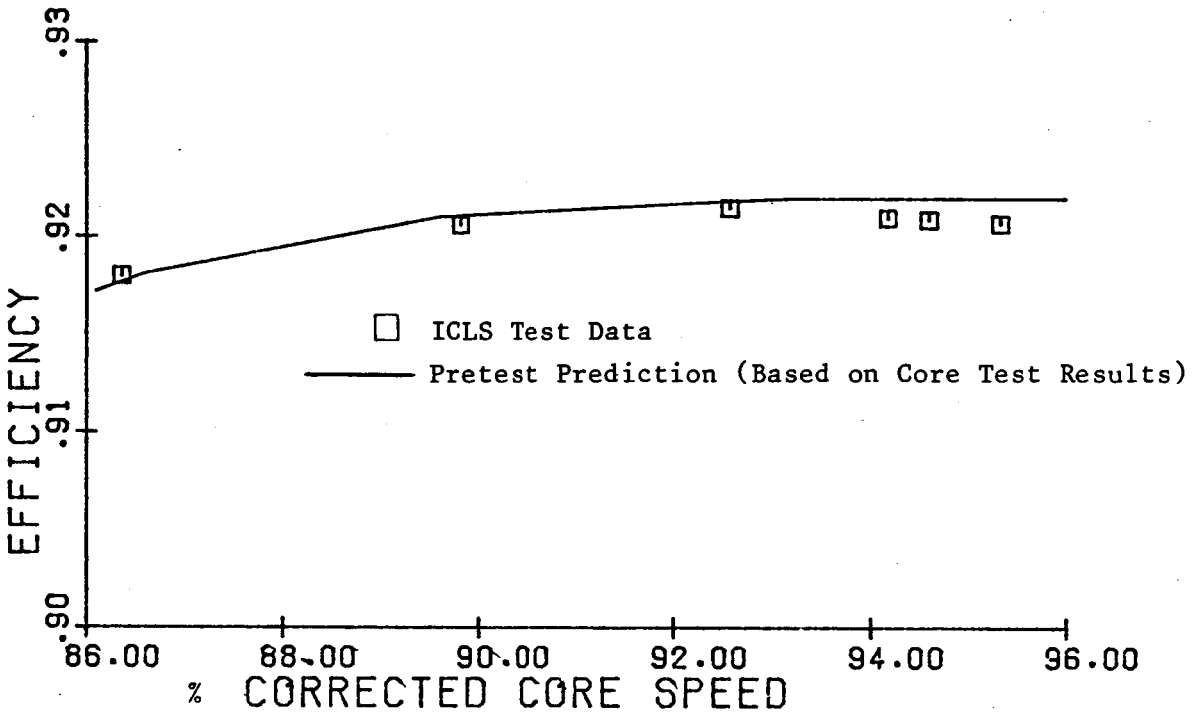


Figure 253. High Pressure Turbine Efficiency Versus Percent Corrected Core Speed, ICLS Test Versus Prediction.

Inner and outer flowpath static pressure distributions, normalized by turbine inlet total pressure, P4, are presented versus axial station in Figure 254. Agreement here is very good, indicating that power split and reaction levels in ICLS were identical to those of the core test. These comparisons are at 95.4% corrected core speed.

Equivalent max climb design point conditions and clearances achieved during core testing were not attained in the ICLS test. ICLS and core data agree with the turbine map based on component rig test. It is concluded from this, that if the ICLS turbine ran at design point conditions an efficiency of 92.5% would have been attained. This exceeds ICLS goals by 0.6 point and FPS goals by 0.1 point. Efficiency goals and results are related in Table XXII.

## 6.10 LOW PRESSURE TURBINE MECHANICAL PERFORMANCE

The mechanical performance of the $E^3$ LPT during ICLS testing was excellent and demonstrated three major points: (1) there were no mechanical problems, (2) the active clearance control (ACC) worked well, and (3) several innovative mechanical features were proved to be practical.

### 6.10.1 Low Pressure Turbine Instrumentation

The five stage, low pressure turbine with uncooled airfoils was instrumented with strain gages, thermocouples, pressure sensors, and air temperature sensors. The strain gages provided a quantitative validation of the mechanical integrity of the LPT by measuring vibratory stresses. The thermocouples monitored temperatures throughout the LPT to ensure no overtemperature condition and also provided information for evaluating performance and estimating clearances. The pressure sensors and air temperature sensors monitored the condition of the airflow and ensured that any excess leakage would be detected.

The low pressure turbine was initially instrumented with 64 strain gages, 102 thermocouples, 64 pressure sensors, and 18 air temperature sensors. The thermocouples had an excellent survival rate with only three

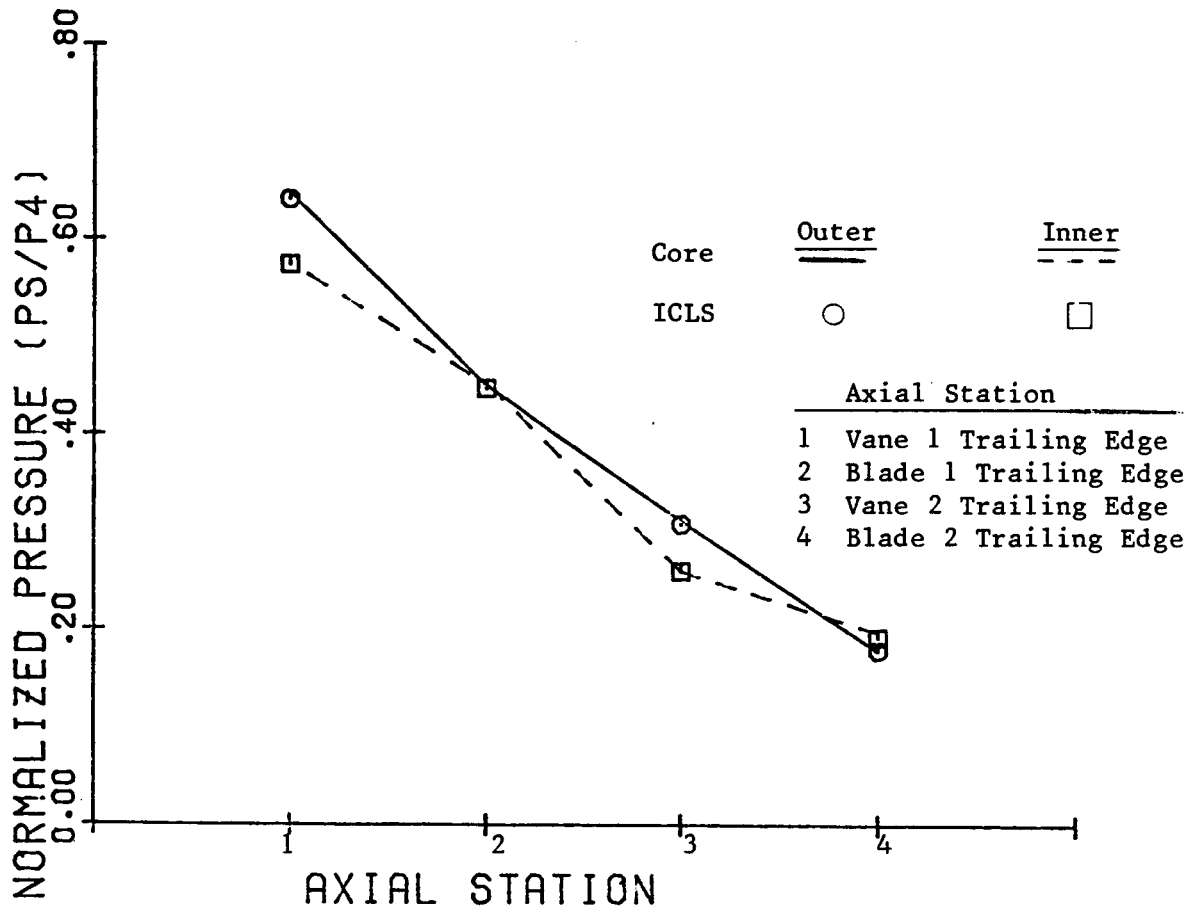


**Figure 254. High Pressure Turbine Interstage Static Pressure Distributions at 95.4% Corrected Core Speed, ICLS Versus Core Test.**

Table XXII. High Pressure Turbine Efficiency.

| | Maximum Climb |
|---|---|
| FPS Goal | 0.924 |
| Rig, Core and ICLS Goal | 0.919 |
| Rig Results | 0.925 |
| Core Results | 0.925 |
| ICLS Results | 0.925* |

*Altitude value based on sea level test points.

thermocouples being lost on the entire LPT rotor during testing. The strain gages had a higher mortality rate with 60% of the gages being lost. Yet, due to the selected layout of instrumentation, the data obtained from the functioning gages provided a thorough picture of the vibratory stresses within the range of interest. Figures 255 and 256 display the original instrumentation drawings. Any instrumentation which was lost during installation or testing has been crossed out on the drawing. The final quantity of functioning instrumentation consisted of 20 strain gages, 84 thermocouples, 59 pressure sensors, and 12 air temperature sensors.

In the sections which follow, a detailed description of quantity and location of instrumentation for each component for the LPT is presented.

## LPT Blade Instrumentation

The five stages of low pressure turbine blades were instrumented with thermocouples to obtain temperature measurements and with strain gages to obtain vibratory stresses and frequency measurements. Figure 257 shows four views of a representative LPT blade with the locations of instrumentation for all five stages. A tabulation is included with the figure to enumerate the instrumentation location by stage.

The strain gages within a given stage were all located at the same position on the blades to provide redundancy. The particular gage location for each stage was chosen in such a manner that the instrumentation would be responsive to all vibration modes of interest with emphasis on the more active modes anticipated. Having all gages within a given stage at identical locations aided in the statistical analysis of the data and minimized the difficulties of evaluating results when some instrumentation was lost.

## LPT Disk and Rotating Seal Instrumentation

The LPT Stage 1, 2, 3, and 5 disks were instrumented with thermocouples to obtain temperature information necessary to estimate clearances due to

ORIGINAL PAGE IS
OF POOR QUALITY

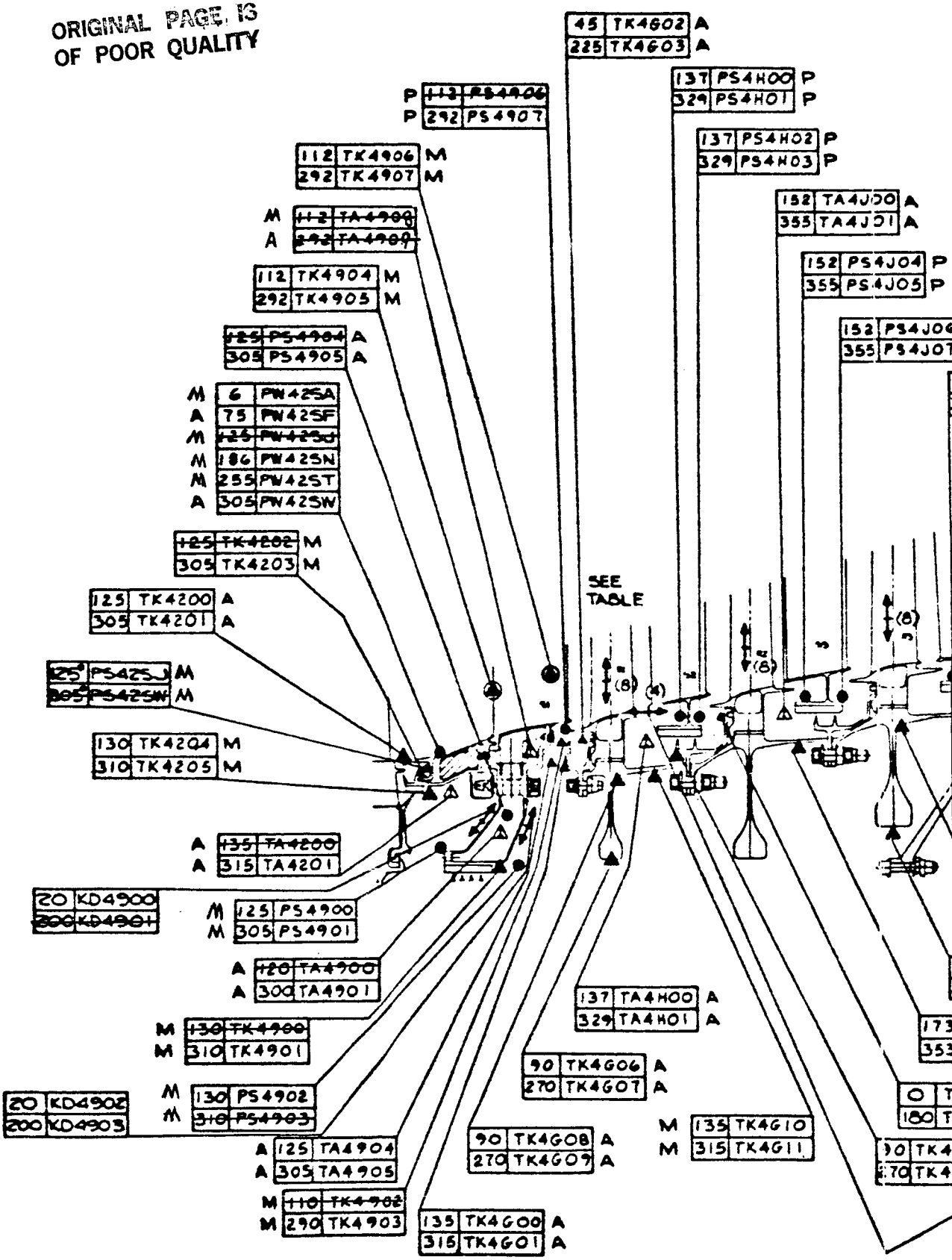


FOLDOUT FRAME

## LPT ROTOR BLADE STRAIN GAGES

| STAGE 1 | | STAGE 2 | | STAGE 3 | | STAGE 4 | | STAGE 5 | |
|---|---|---|---|---|---|---|---|---|---|
| ∠ | ITEM | ∠ | ITEM | ∠ | ITEM | ∠ | ITEM | ∠ | ITEM |
| 0 | ~~KD4G00~~ | 0 | ~~KD4J00~~ | 2 | ~~KD4L00~~ | 16 | ~~KD4N00~~ | 0 | ~~KD4Q00~~ |
| 45 | ~~KD4G01~~ | 47 | ~~KD4J01~~ | 50 | ~~KD4L01~~ | 60 | ~~KD4N01~~ | 46 | ~~KD4Q01~~ |
| 90 | ~~KD4G02~~ | 92 | KD4J02 | 94 | KD4L02 | 106 | ~~KD4N02~~ | 92 | ~~KD4Q02~~ |
| 135 | KD4G03 | 136 | ~~KD4J03~~ | 138 | ~~KD4L03~~ | 150 | KD4N03 | 137 | KD4Q03 |
| 180 | KD4G04 | 180 | KD4J04 | 183 | KD4L04 | 196 | KD4N04 | 180 | ~~KD4Q04~~ |
| 225 | ~~KD4G05~~ | 227 | ~~KD4J05~~ | 230 | ~~KD4L05~~ | 240 | KD4N05 | 226 | ~~KD4Q05~~ |
| 270 | KD4G06 | 272 | ~~KD4J06~~ | 274 | ~~KD4L06~~ | 286 | ~~KD4N06~~ | 272 | ~~KD4Q06~~ |
| 315 | ~~KD4G07~~ | 316 | ~~KD4J07~~ | 318 | ~~KD4L07~~ | 330 | ~~KD4N07~~ | 317 | ~~KD4Q07~~ |

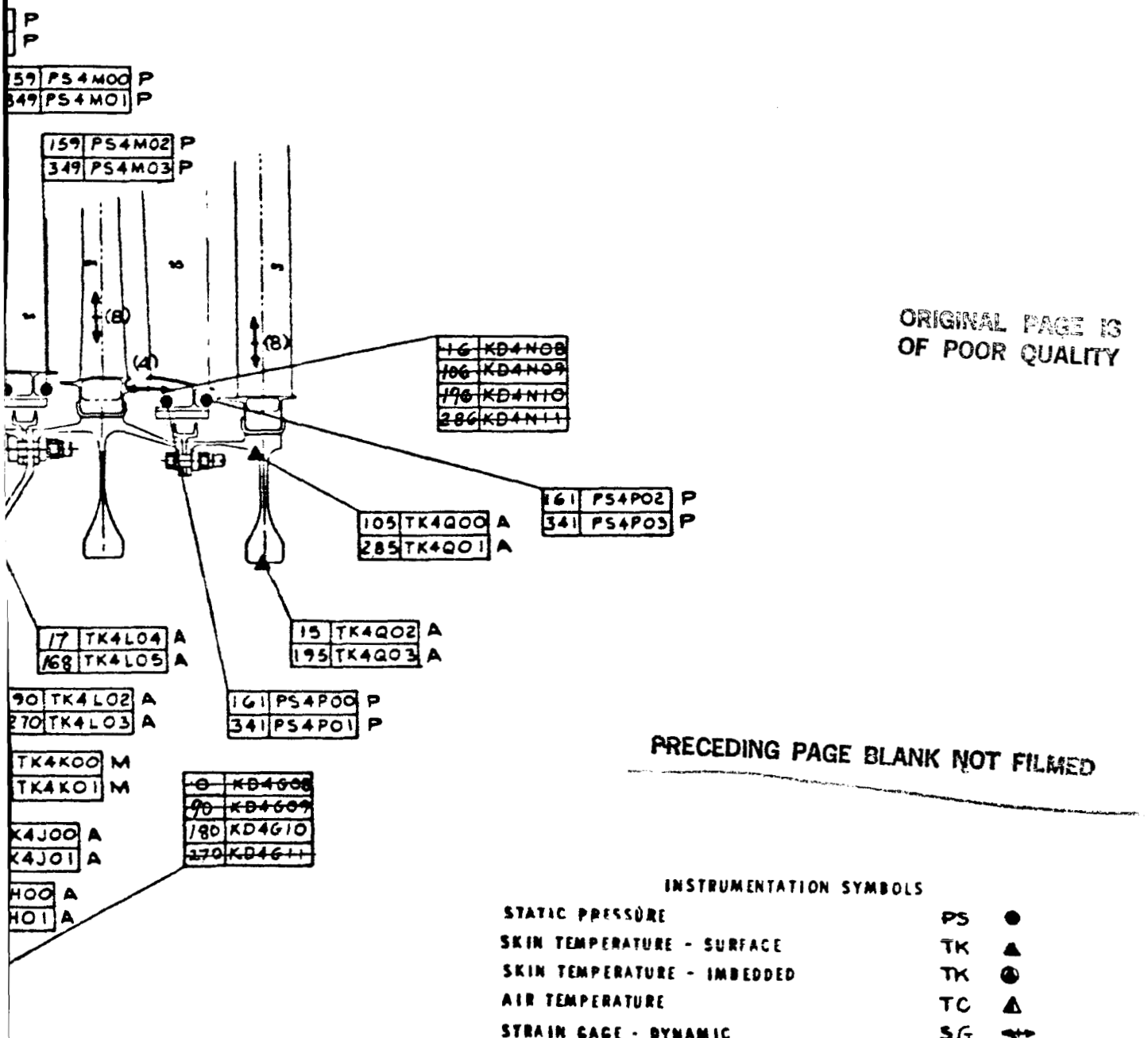


ORIGINAL PAGE IS
OF POOR QUALITY

PRECEDING PAGE BLANK NOT FILMED

INSTRUMENTATION SYMBOLS

| | | |
|---|---|---|
| STATIC PRESSURE | PS | ● |
| SKIN TEMPERATURE - SURFACE | TK | ▲ |
| SKIN TEMPERATURE - IMBEDDED | TK | ◉ |
| AIR TEMPERATURE | TC | ◭ |
| STRAIN GAGE - DYNAMIC | SG | ⟿ |

Figure 255. Low Pressure Turbine Instrumentation.



2 FOLDOUT FRAME

## LPT STATOR NOZZLE STRAIN GAGES

| STAGE 2 | | STAGE 3 | | STAGE 4 | | STAGE 5 | |
|---|---|---|---|---|---|---|---|
| ∠ | ITEM | ∠ | ITEM | ∠ | ITEM | ∠ | ITEM |
| 137 | KD4H00 | 152 | KD4K00 | 139 | ~~KD4M00~~ | 161 | ~~KD4P00~~ |
| 329 | KD4H01 | 355 | KD4K01 | 349 | ~~KD4M01~~ | 341 | ~~KD4P01~~ |
| | | 197 | ~~KD4K02~~ | | | | |
| | | 333 | KD4K03 | | | | |
| | | 197 | ~~KD4K04~~ | | | | |
| | | 333 | ~~KD4K05~~ | | | | |

ORIGINAL PAGE IS
OF POOR QUALITY

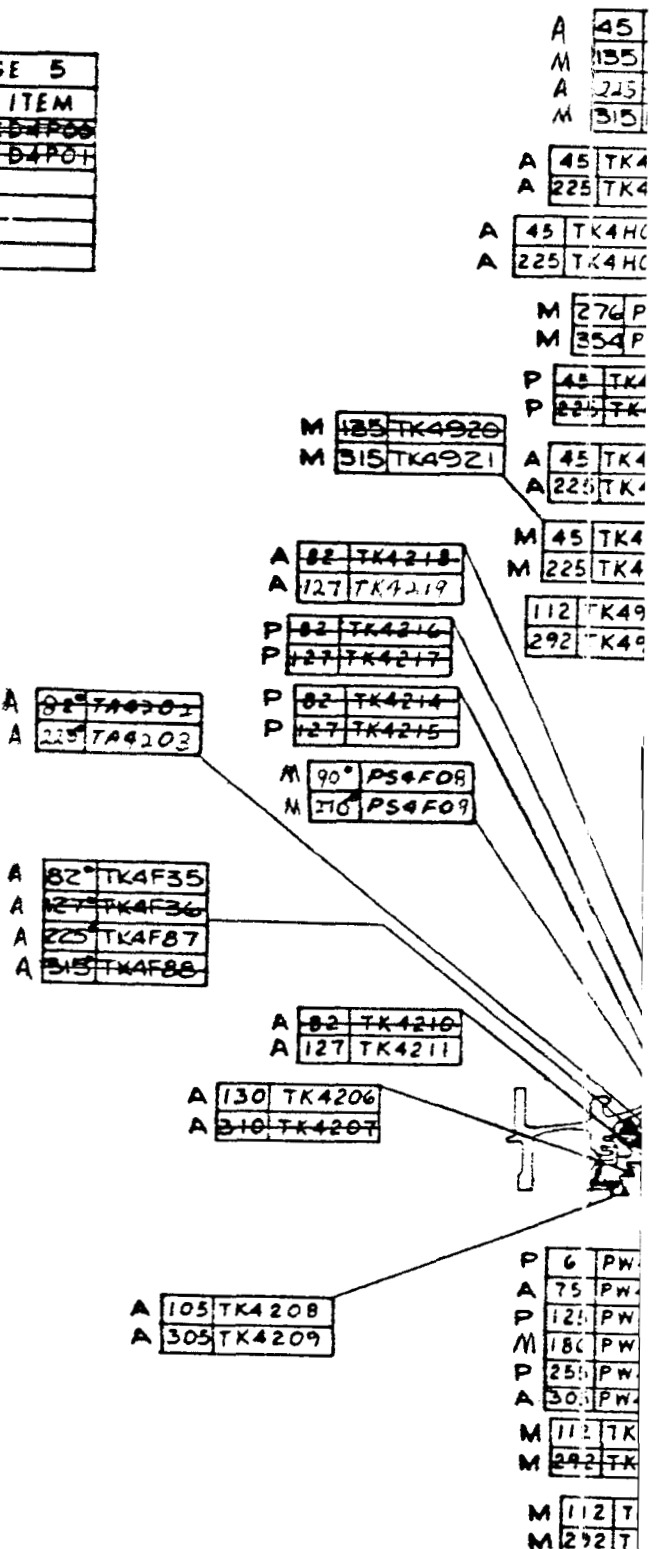


FOLDOUT FRAME

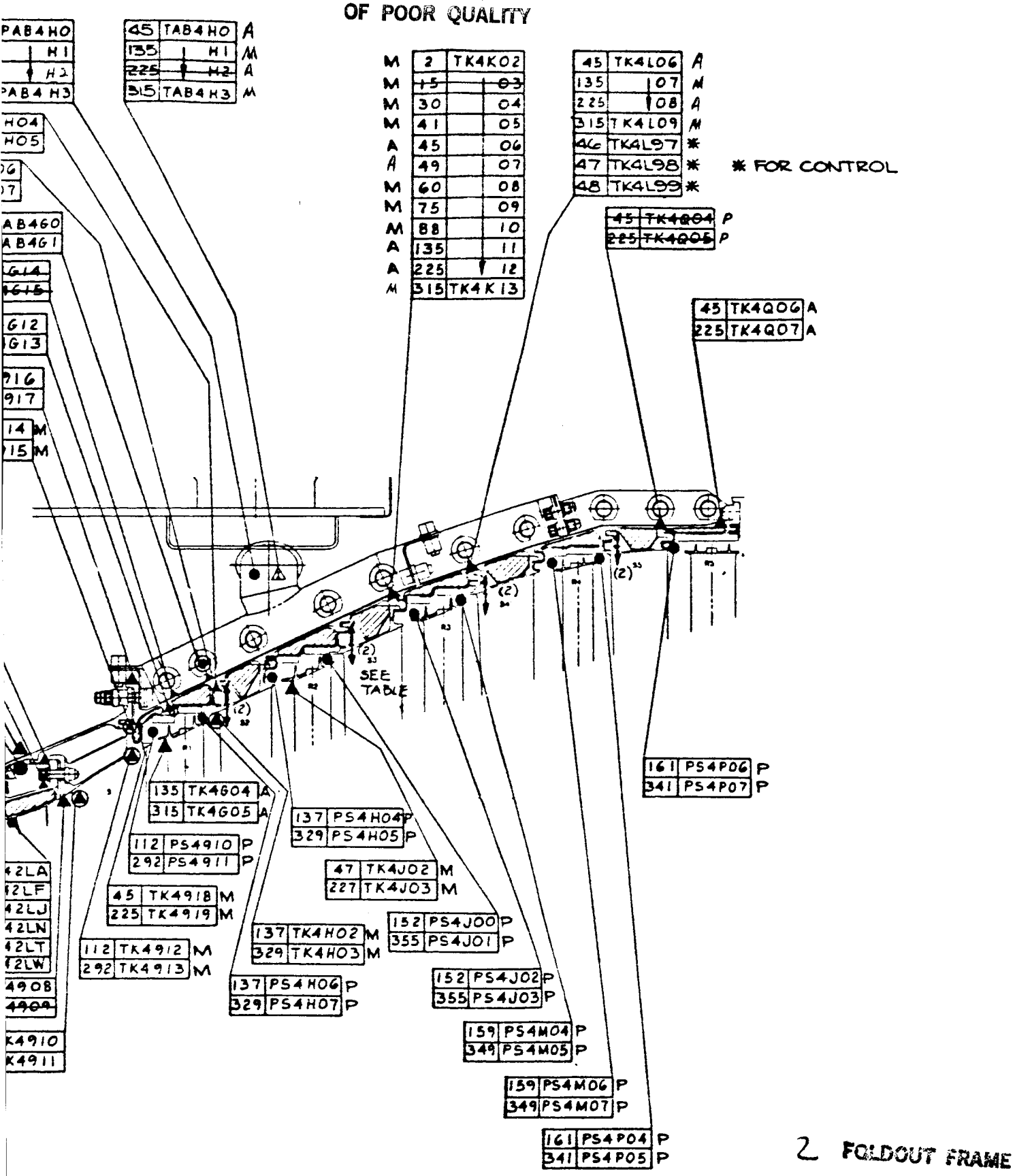


Figure 256. Low Pressure Turbine Instrumentation.

thermal growth. Because of the unavailability of enough instrumentation to instrument all five stages, the Stage 4 disk was not instrumented since it was very similar to the Stage 5 disk. A representative instrumented LPT disk is presented in Figure 258 along with a table which provides a detailed description of the instrumentation distribution.

Thermocouples were mounted on the Stage 1 and 2 rotating seals to ensure that any overtemperature condition would be detected. Figure 259 displays a representative instrumented seal along with a tabulation of thermocouple circumferential locations.

LPT Nozzle Instrumentation

The first stage LPT nozzle was instrumented with imbedded thermocouples to obtain a temperature profile of the nozzle for comparison with analytical predictions. Since the first stage nozzle was not a highly stressed part, the thermocouples could be imbedded in order to avoid perturbation of the airflow. Pressure and air temperature sensors were also included to evaluate the gas stream aerodynamic performance. Three views of the first stage nozzle along with a table detailing the instrumentation locations are shown in Figure 260.

The Stage 2 through 5 nozzles were instrumented with strain gages to monitor the vibratory stresses along the trailing edge of the nozzle and to ensure the mechanical integrity of the nozzle hook. Thermocouples were applied to monitor temperatures at critical, high stress locations. Pressure and air temperature sensors were again included to provide airflow data. Figure 261 summarizes the instrumentation locations with two views of a typical Stage 2 through 5 nozzle and a tabulation of circumferential locations.

AFT LPT Inner Seal Support Instrumentation

The sheet metal portions of the inner seal support were instrumented with strain gages to obtain measurements of any vibratory stresses in the component which are relatively difficult to predict. Thermocouples were

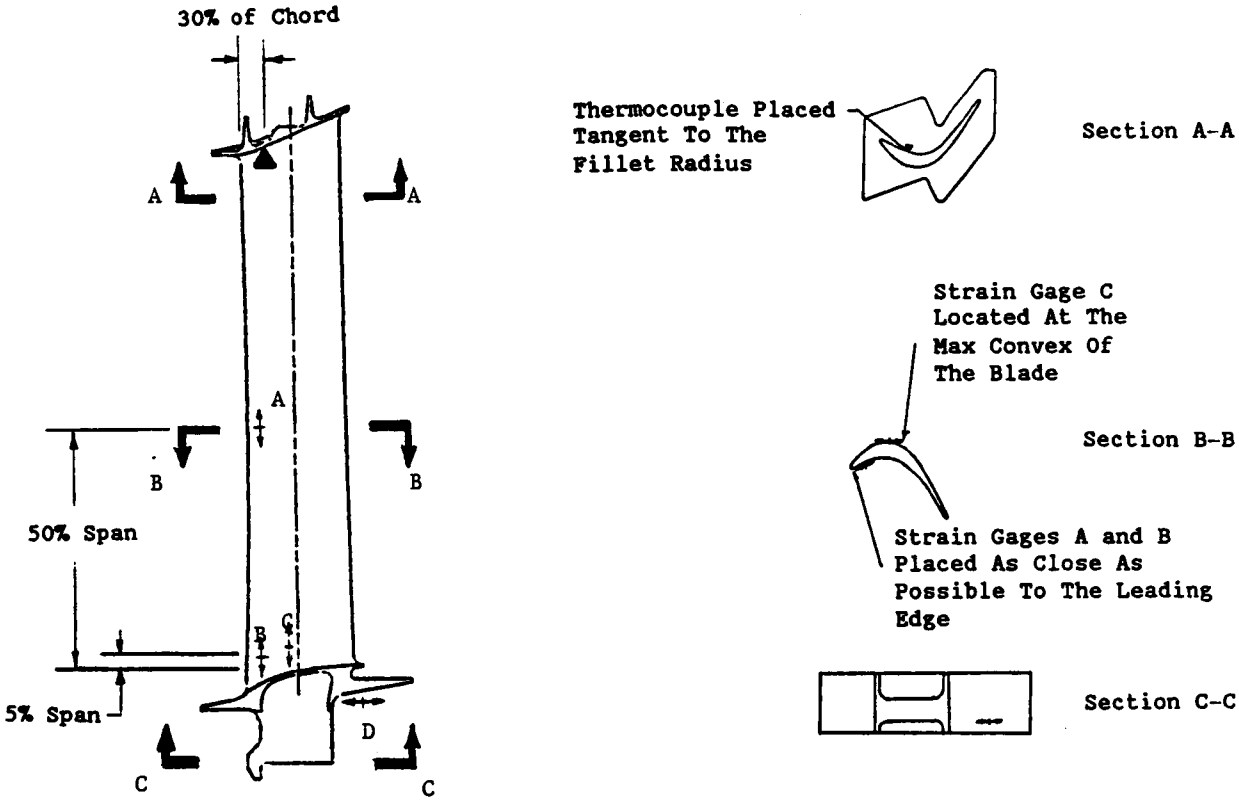


| STAGE | INSTRUMENTATION | Circumferential Angle in Rotor (Degrees) | | | | | | | |
|---|---|---|---|---|---|---|---|---|---|
| | | 0 | 45 | 90 | 135 | 180 | 225 | 270 | 315 |
| 1 | Strain Gage A | X | X | X | X | X | X | X | X |
| | Strain Gage D | X | | X | | X | | | X |
| | Thermocouple | | | | X | | | | X |
| | | 0 | 47 | 92 | 136 | 180 | 227 | 272 | 316 |
| 2 | Strain Gage A | X | X | X | X | X | X | X | X |
| | Thermocouple | | X | | | | X | | |
| | | 2 | 50 | 94 | 138 | 183 | 230 | 274 | 318 |
| 3 | Strain Gage A | X | X | X | X | X | X | X | X |
| | | 16 | 60 | 106 | 150 | 196 | 240 | 286 | 330 |
| 4 | Strain Gage B | X | X | X | X | X | X | X | X |
| | Strain Gage D | X | | X | | X | | X | |
| | | 0 | 46 | 92 | 137 | 180 | 226 | 272 | 317 |
| 5 | Strain Gage C | X | X | X | X | X | X | X | X |

Figure 257. Detail of LPT Blade Instrumentation.

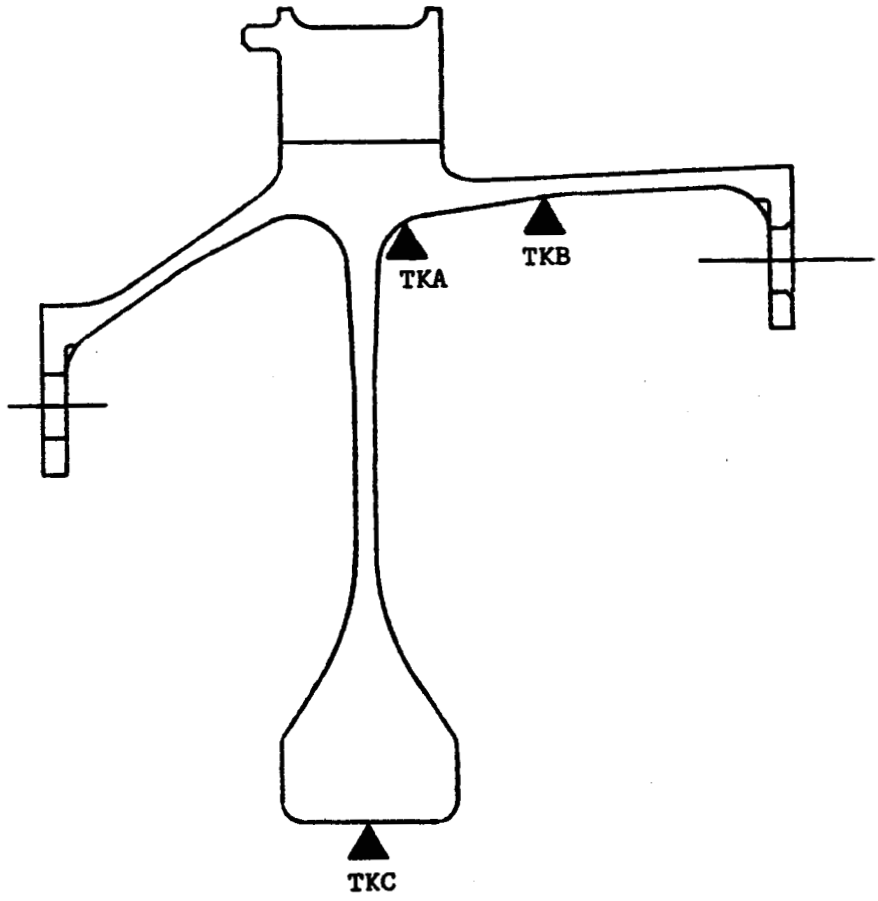


| STAGE | INSTRUMENTATION | Circumferential Angle in Rotor (°) | | | |
|---|---|---|---|---|---|
| | | 90 | 135 | 270 | 315 |
| 1 | Thermocouple A | X | | X | |
| | Thermocouple B | | X | | X |
| | Thermocouple C | X | | X | |
| | | 173 | 353 | | |
| 2 | Thermocouple B | X | X | | |
| | | 17 | 90 | 168 | 270 |
| 3 | Thermocouple A | X | | X | |
| | Thermocouple C | | X | | X |
| | | 15 | 105 | 195 | 285 |
| 5 | Thermocouple A | | X | | X |
| | Thermocouple C | X | | X | |

Figure 258. Low Pressure Turbine Disk Instrumentation.

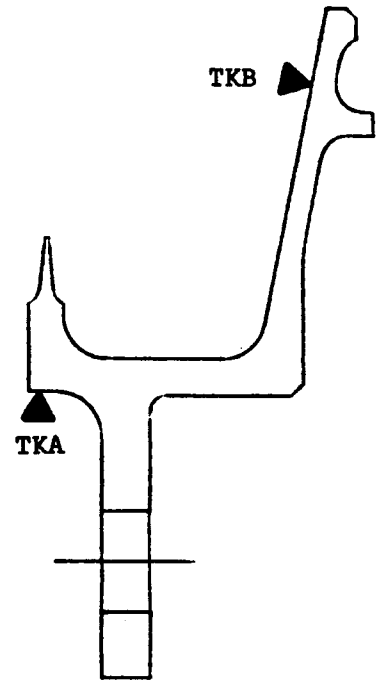


| STAGE | INSTRUMENTATION | Circumferential Angle In Rotor (Degrees) | | | |
|---|---|---|---|---|---|
| | | 45 | 135 | 225 | 315 |
| 1 | Thermocouple A | | X | | X |
| | Thermocouple B | X | | X | |
| | | 0 | 90 | 180 | 270 |
| 2 | Thermocouple A | | X | | X |
| | Thermocouple B | X | | X | |

**Figure 259. Instrumentation for LPT Rotating Seals.**

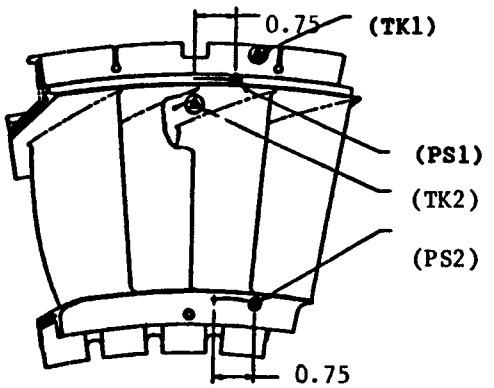


View A

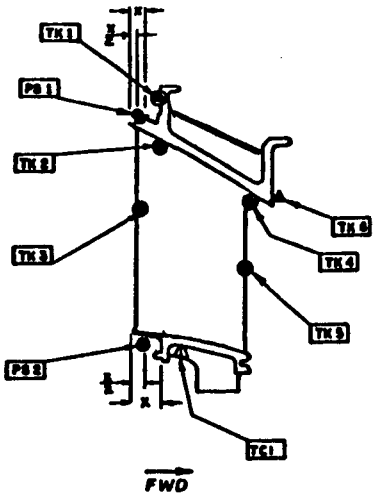


View B

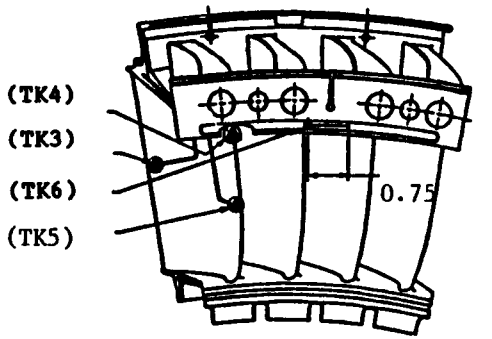


View C

| STAGE | CIRCUMFERENTIAL ANGLE IN ROTOR (DEGREES) | INSTRUMENTATION | | | | | | | | |
|---|---|---|---|---|---|---|---|---|---|---|
| | | TK1 | TK2 | TK3 | TK4 | TK5 | TK6 | PS1 | PS2 | TC1 |
| 1 | 112 | X | X | X | X | X | X | X | X | X |
| | 292 | X | X | X | X | X | X | X | X | X |

Figure 260. Distribution of LPT Stage Nozzle Instrumentation.

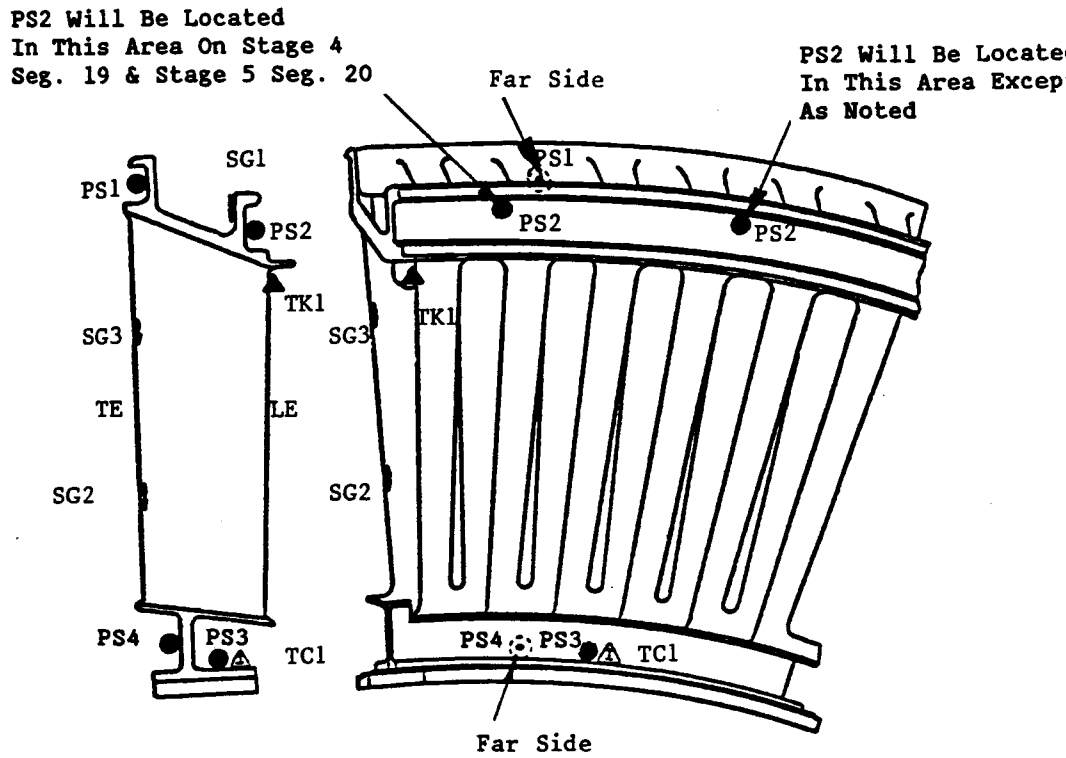


| STAGE | CIRCUMFERENTIAL ANGLE IN ROTOR (DEGREES) | INSTRUMENTATION | | | | | | | | |
|---|---|---|---|---|---|---|---|---|---|---|
| | | TK1 | PS1 | PS2 | PS3 | PS4 | TC1 | SG1 | SG2 | SG3 |
| 2 | 137 | X | X | X | X | X | X | X | | |
| | 329 | X | X | X | X | X | X | X | | |
| 3 | 152 | | X | X | X | X | X | X | | |
| | 197 | | | | | | | | X | X |
| | 333 | | | | | | | | X | X |
| | 355 | | X | X | X | X | X | X | | |
| 4 | 159 | | X | X | X | X | | X | | |
| | 349 | | X | X | X | X | | X | | |
| 5 | 161 | | X | X | X | X | | X | | |
| | 341 | | X | X | X | X | | X | | |

Figure 261. Stage 2 Through 5 Nozzle Instrumentation.

utilized to monitor the skin temperature at various locations along the part in order to compare temperatures on opposite sides of seals and to predict seal gaps which depend on thermal growth. Pressure sensors and air temperature sensors were used as diagnostic indicators for monitoring the purge air to ensure that neither the HPT or LPT rotor cavities became too hot. These sensors also provided airflow information. Figure 262 displays the instrumentation layout.

LPT Outer Nozzle Support Assembly Instrumentation

The outer nozzle support assembly was instrumented with thermocouples to obtain clearances between mating parts and as a safety precaution to detect any overtemperature condition. Pressure and temperature sensors were mounted in the cooling air inlet to provide data on the initial conditions of the LPT purge cooling air supplied from the Stage 5 compressor bleed. Figure 263 describes the location of the instrumentation.

LPT Casing and Manifold Instrumentation

The LPT casing was instrumented with thermocouples to assist in calculating radial clearances and to ensure detection of any localized overtemperature condition which would limit the casing life. Pressure and air temperature sensors were located on the manifold to monitor the airflow for aerodynamic performance purposes and to evaluate the effectiveness of the cooling air. Figure 264 displays the location of casing and manifold instrumentation and the table details their circumferential location.

### 6.10.2 LPT Vibratory Stresses

The objective of instrumenting the low pressure turbine with strain gages was to monitor blade vibratory stresses during engine operation. If a resonance occurred, these gages would determine if the engine could be operated safely without a high cycle fatigue failure. If a significant resonance occurred at a certain engine speed, that speed could be avoided in future testing.

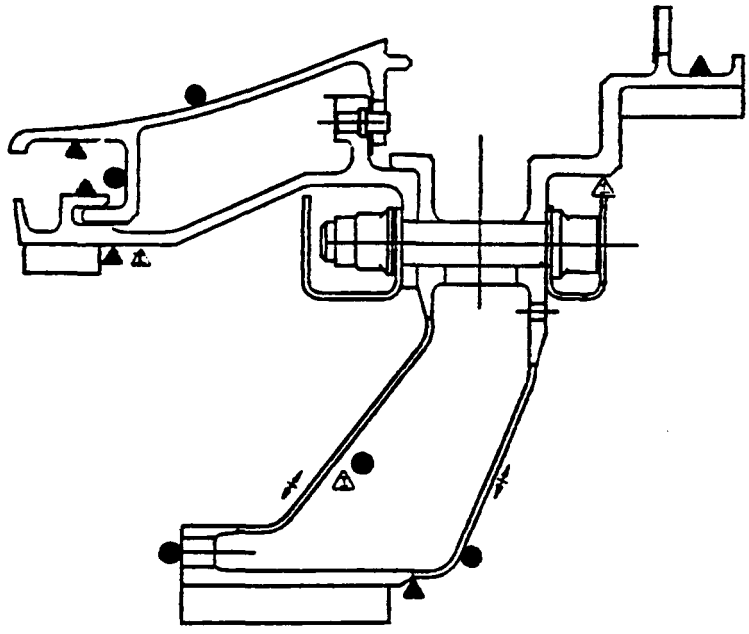

| INSTRUMENTATION | Circumferential Angle (Degrees) | | | | | | | | | | | | | | |
|---|---|---|---|---|---|---|---|---|---|---|---|---|---|---|---|
| | 6 | 20 | 75 | 110 | 120 | 125 | 130 | 135 | 186 | 200 | 255 | 290 | 300 | 305 | 310 | 315 |
| Thermocouple 1 | | | | | | X | | | | | | | | X | | |
| Thermocouple 2 | | | | | | X | | | | | | | | X | | |
| Thermocouple 3 | | | | | | | X | | | | | | | | X | |
| Thermocouple 4 | | | | | | | X | | | | | | | | X | |
| Thermocouple 5 | | | | X | | | | | | | | X | | | | |
| Pressure Sensor 1 | X | | X | | | X | | | X | | X | | | X | | |
| Pressure Sensor 2 | | | | | | X | | | | | | | | X | | |
| Pressure Sensor 3 | | | | | | X | | | | | | | | X | | |
| Pressure Sensor 4 | | | | | | X | | | | | | | | X | | |
| Pressure Sensor 5 | | | | | | | X | | | | | | | | X | |
| Strain Gage 1 | | X | | | | | | | | X | | | | | | |
| Strain Gage 2 | | X | | | | | | | | X | | | | | | |
| Air Temperature 1 | | | | | | | | X | | | | | | | | X |
| Air Temperature 2 | | | | | X | | | | | | | | X | | | |
| Air Temperature 3 | | | | | | X | | | | | | | | X | | |

Figure 262. Aft LPT Inner Seal Support Instrumentation.

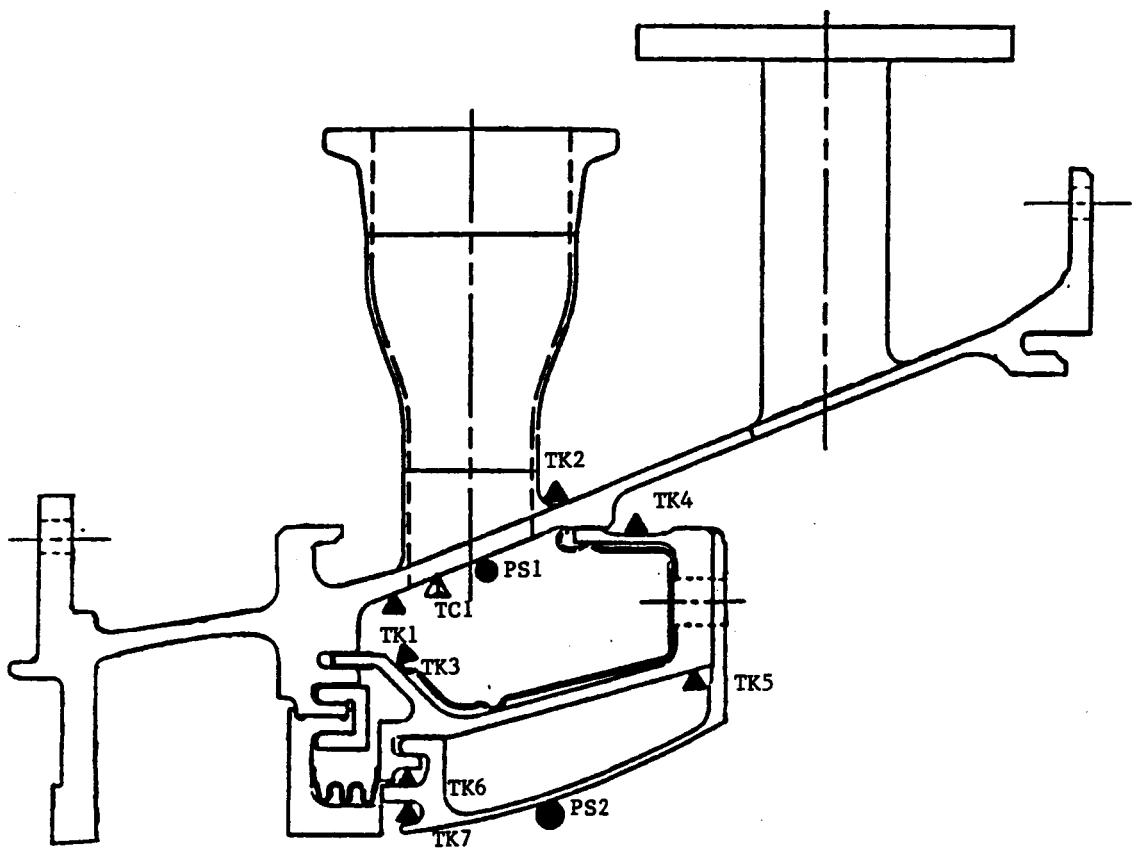


| PART | INSTRUMENTATION | Circumferential Angle (°) | | | | | | |
|---|---|---|---|---|---|---|---|---|
| | | 78 | 82 | 90 | 127 | 225 | 270 | 315 |
| Outer HPT Stator Support Nozzle | Thermocouple 1 | | X | | X | X | | X |
| | Thermocouple 2 | | X | | X | | | |
| | Pressure Sensor 1 | | | X | | | X | |
| | Air Temperature | | X | | | X | | |
| | | 82 | 127 | 130 | 310 | | | |
| LPT Outer Duct Support Ring | Thermocouple 3 | X | X | | | | | |
| | Thermocouple 4 | X | X | | | | | |
| | Thermocouple 5 | X | X | | | | | |
| | Thermocouple 6 | | | X | X | | | |
| | | 6 | 72 | 125 | 186 | 255 | 305 | |
| LPT Outer Duct | Thermocouple 7 | | | X | | | X | |
| | Pressure Sensor 2 | X | X | X | X | X | X | |

Figure 263. LPT Outer Nozzle Support Assembly Instrumentation.

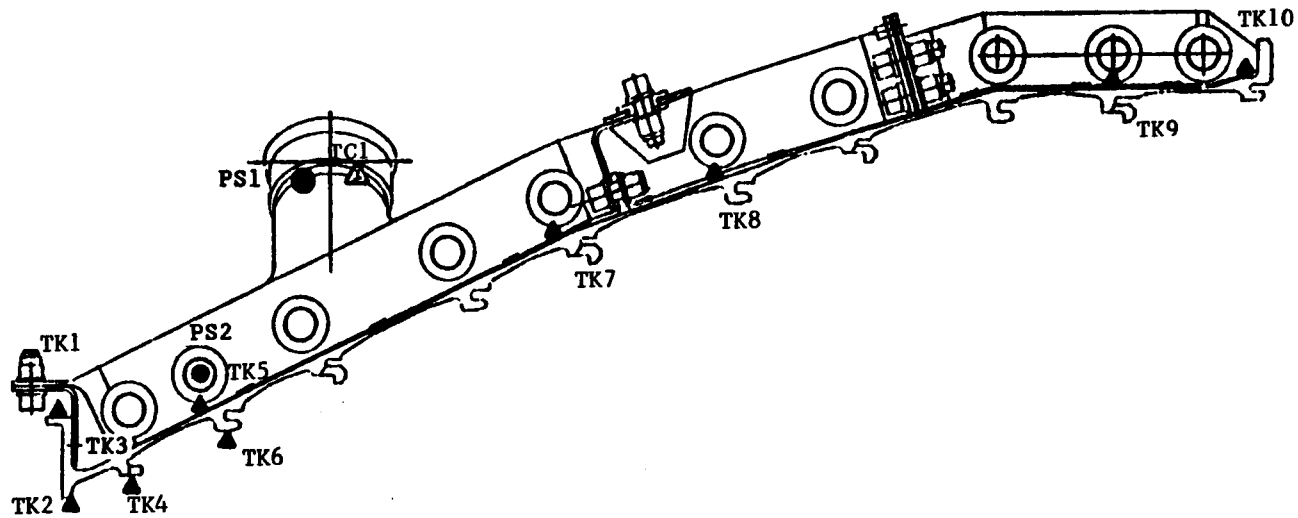


| CIRCUMFERENTIAL ANGLE (DEGREES) | INSTRUMENTATION | | | | | | | | | | | | |
|---|---|---|---|---|---|---|---|---|---|---|---|---|---|
| | TK1 | TK2 | TK3 | TK4 | TK5 | TK6 | TK7 | TK8 | TK9 | TK10 | TC1 | PS1 | PS2 |
| 2 | | | | | | | X | | | | | | |
| 15 | | | | | | | X | | | | | | |
| 30 | | | | | | | X | | | | | | |
| 41 | | | | | | | X | | | | | | |
| 45 | X | X | X | X | X | X | X | X | X | X | X | X | |
| 49 | | | | | | | X | | | | | | |
| 60 | | | | | | | X | | | | | | |
| 75 | | | | | | | X | | | | | | |
| 88 | | | | | | | X | | | | | | |
| 135 | X | | | | | | X | X | | X | X | | |
| 225 | X | X | X | X | X | X | X | X | X | X | X | | |
| 276 | | | | | | | | | | | | X | |
| 315 | X | | | | | | X | X | | X | X | | |
| 354 | | | | | | | | | | | | X | |

Figure 264. Instrumentation For The LPT Casing and Manifold.

All stages of blade airfoils were strain gaged per standard GE methods. Items of special interest were the aerodynamically extended platforms and tip shrouds, the nozzle support hooks (which were susceptible to vibration if interlocks were not tight), the Stage 3 nozzle (where little data exists) and the stationary seal (a unique structure).

Stage 1 Blade

The Stage 1 blade vibratory stresses, as measured by the airfoil strain gages, are shown in Figure 265. Predicted frequencies based on component testing are plotted on the same figure for reference. A resonant excitation was noted at 1100 rpm when the blade was driven in the first torsion (1T) tip free mode by the 72/rev Stage 1 vane passing frequency. The peak stress measured was only 18.6 mPa (2700 psi) double amplitude (DA), which corresponded to 9% of limits.

Vibratory stresses were also monitored on the Stage 1 blade aft angel wing. The vibration frequencies were slightly higher than predicted as shown in Figure 266. Two different angel wing modes occurred as expected, due to the two corners of the angel wing vibrating at slightly different frequencies. The measured vibratory stresses were very low, less than 5% of limits.

Stage 2 Blade

The Stage 2 blade measured vibratory stresses are shown in Figure 267. A first torsional tip-free resonance was encountered at 2900 rpm. It was being driven by a 6/rev vane difference (102/rev Vane 2 minus 96/rev Vane 3 = 6/rev) or by core plus fan. The peak stress was 10 mPa (1500 psi) DA (8% of limits) and, based on the Campbell diagram, the response would be expected to diminish at higher speeds.

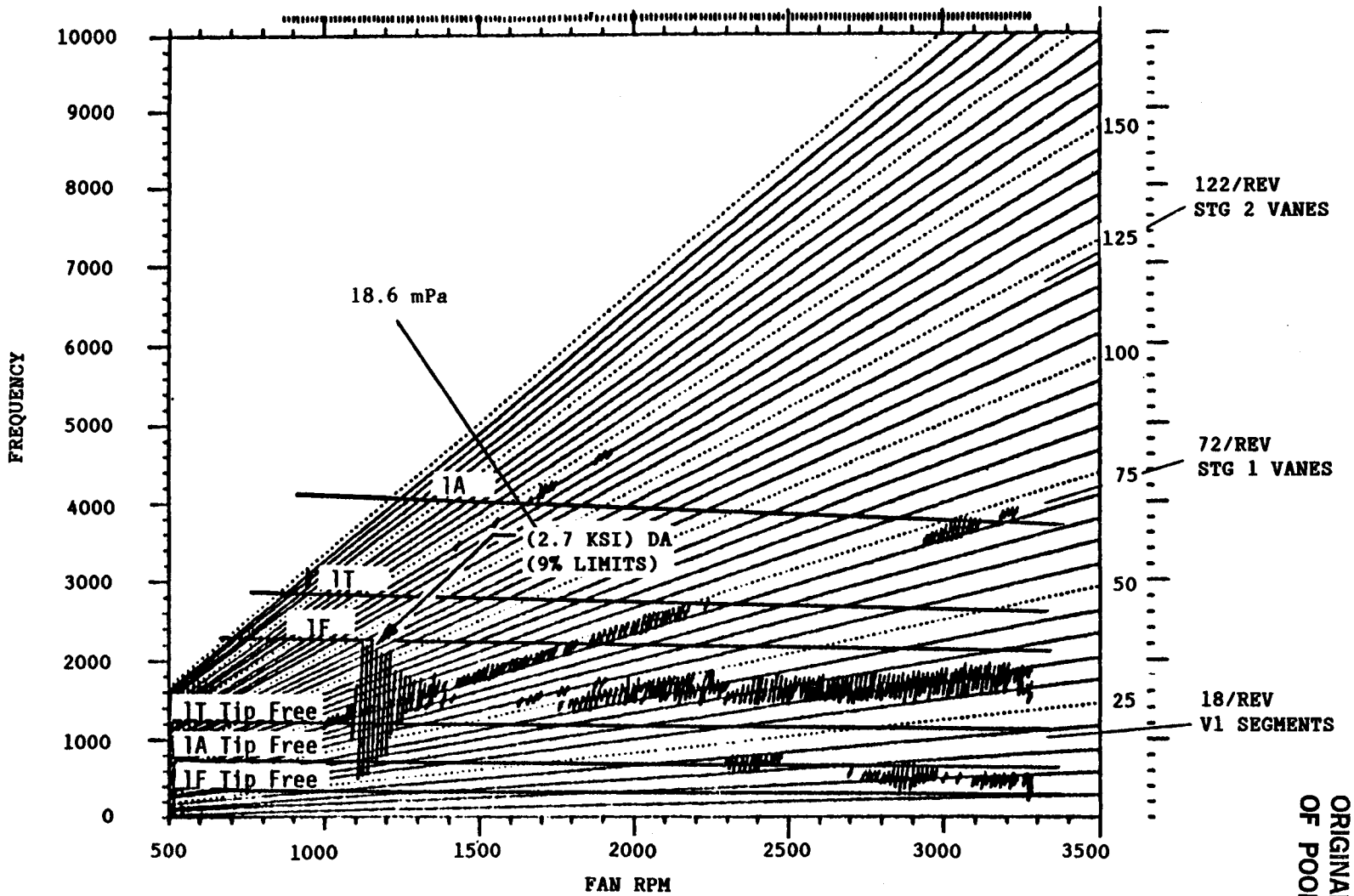


6.9 mPa (1.00 KPSI) DAS = *f*
Threshold = 0.20000

Figure 265. Low Pressure Turbine Stage 1 Blade Campbell Diagram.

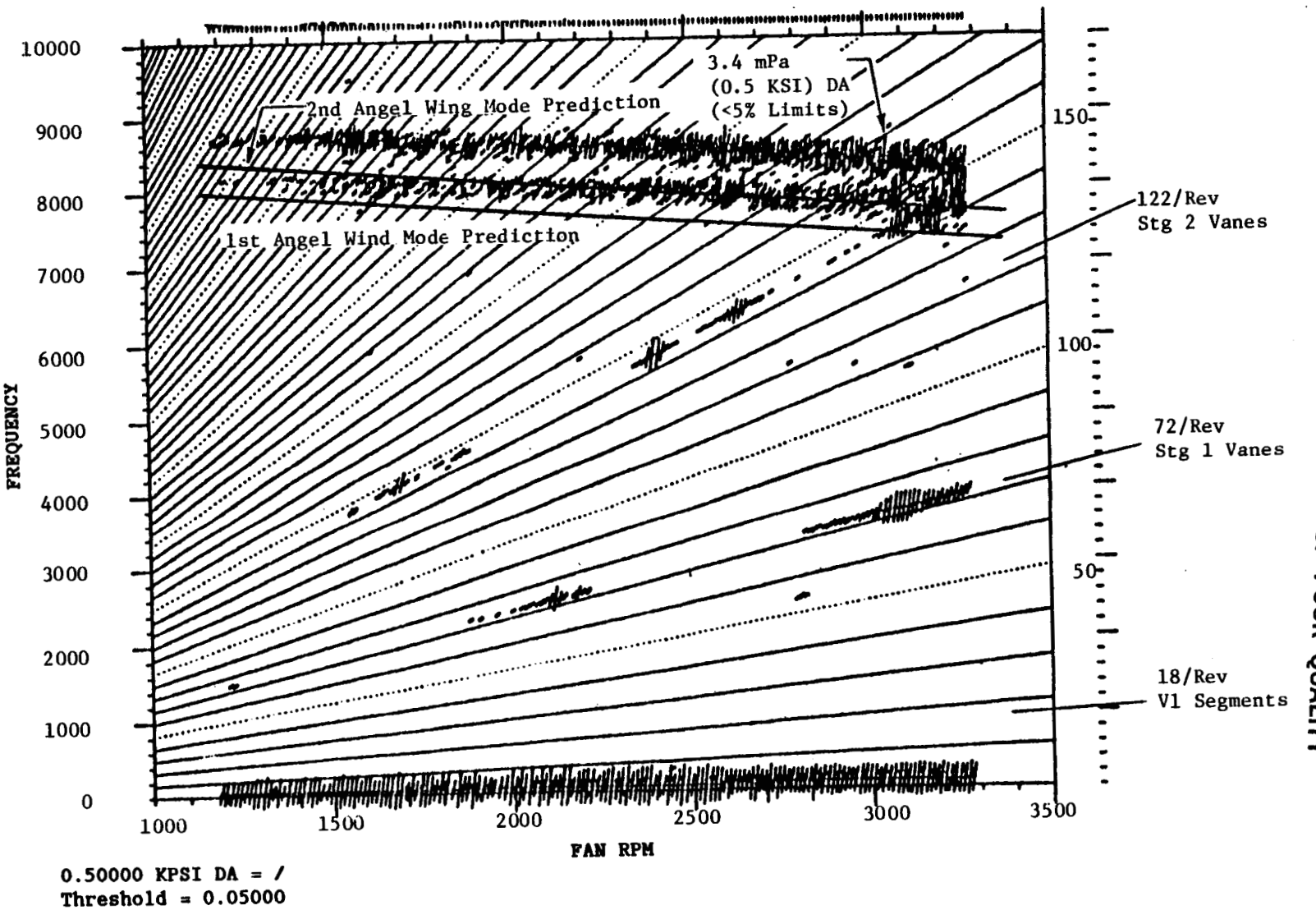




Figure 266. Low Pressure Turbine Stage 1 Blade Aft Angel Wing Campbell Diagram.

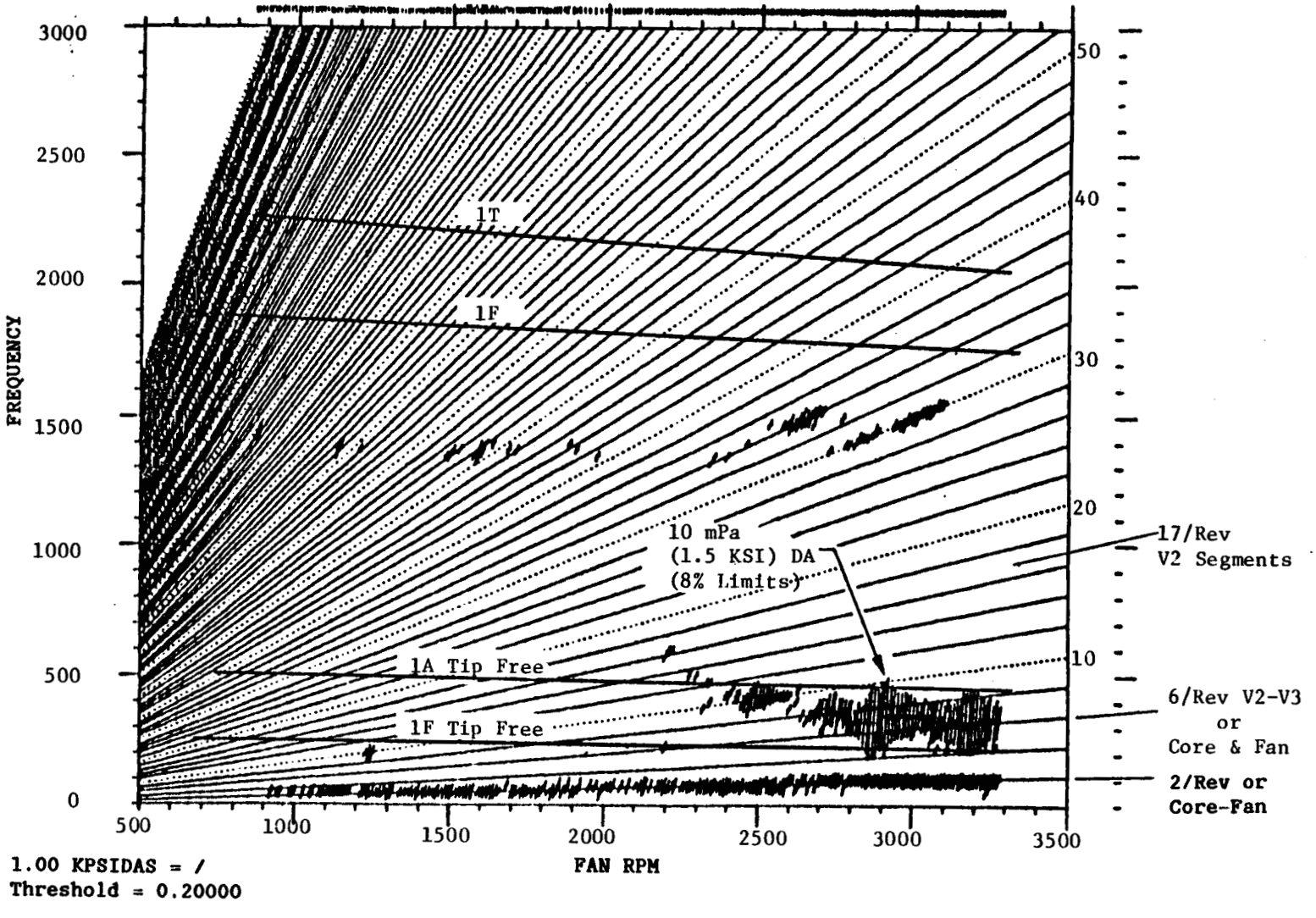


Figure 267. Low Pressure Turbine Stage 2 Blade Campbell Diagram.

Stage 3 Blade

The Stage 3 blade airfoil vibratory stresses are shown in Figure 268. No significant resonances of this stage were encountered during ICLS engine testing. The largest response seen was the first axial (1A) tip-free mode being driven by core plus fan. The peak stress was 5.5 mPa (800 psi) DA, 6% of limits.

Resonance frequency and nodal pattern component testing was conducted on the Stage 3 blade to investigate its tip shroud vibration modes. Since the Stage 3 tip shroud had the largest overhangs, thus the lowest natural frequencies, it was the one tested. The blade was clamped at the dovetail and damped on the airfoil to prevent excessive tip shroud motion so that the pure vibratory modes of the shroud could be determined. Bench test results are shown in Figure 269. Since no excitation forces are present in the engine at the high frequency of the shroud, even the lowest first mode would not be expected to be excited. No tip strain gage instrumentation was therefore required. The absence of excitations in the shroud frequency range was verified during engine testing. As shown by Figure 270, no resonances occurred between 5,000 Hz and 10,000 Hz.

Stage 4 Blade

The Stage 4 blade vibratory stresses as measured by the airfoil strain gages are shown in Figure 271. A resonance was seen at 2760 rpm due to the first axial (1A) tip-free mode being driven by a 6/rev vane difference. The peak stress was 16 mPa (2300 psi) DA, 21% limits. This long slender blade with an aspect ratio of 7.57 and first torsional flutter index of 3.06 at 3280 rpm, (3.27 index at max cruise speed) remained relatively quiet, providing new confidence for this acoustically desirable slim contour.

Strain gages were also placed on the Stage 4 blade angel wing. Unfortunately, by the time the engine reached the higher speed range, the gages were either open or noisy beyond use. However, no resonances were

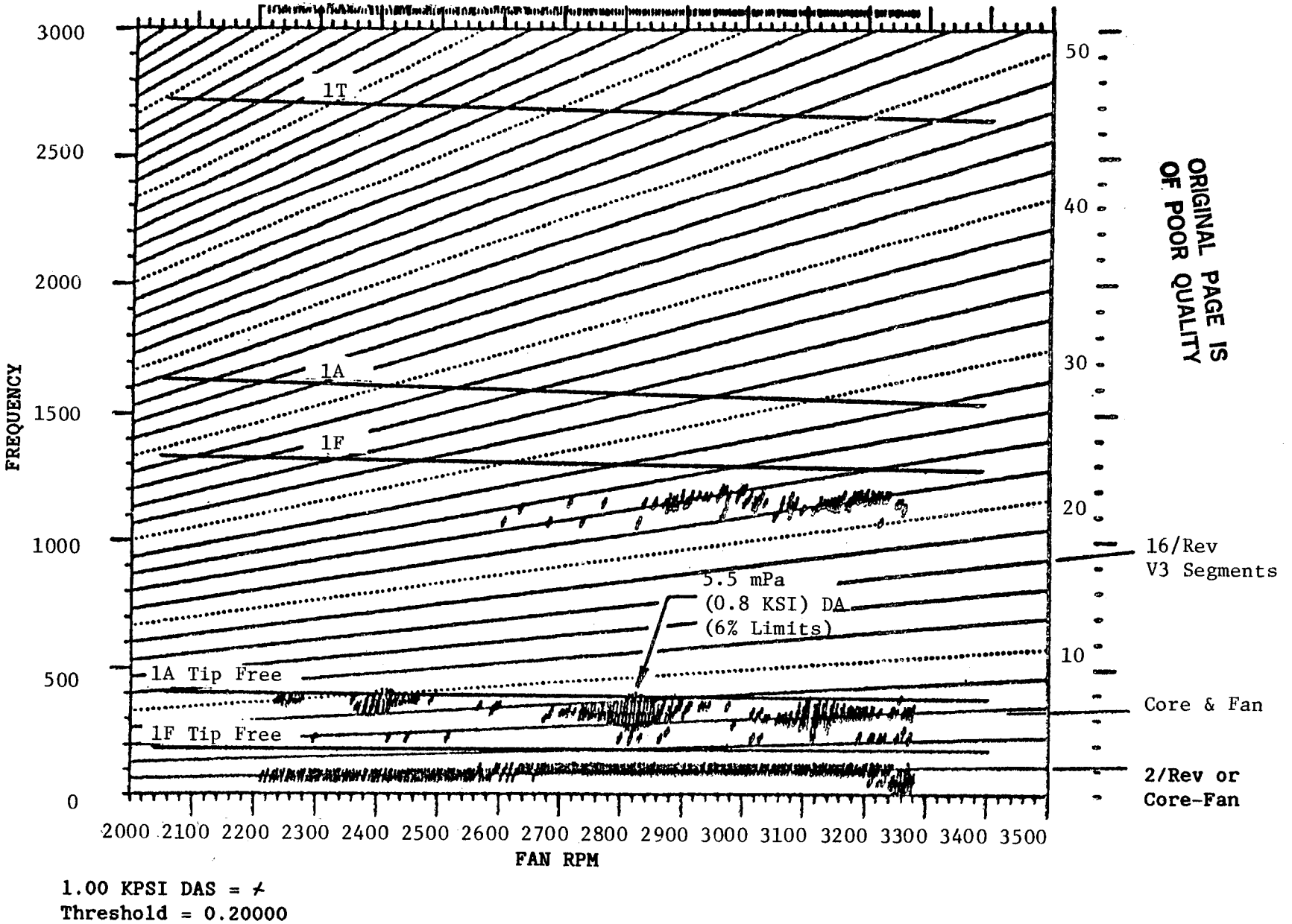


Figure 268. Low Pressure Turbine Stage 3 Blade Campbell Diagram

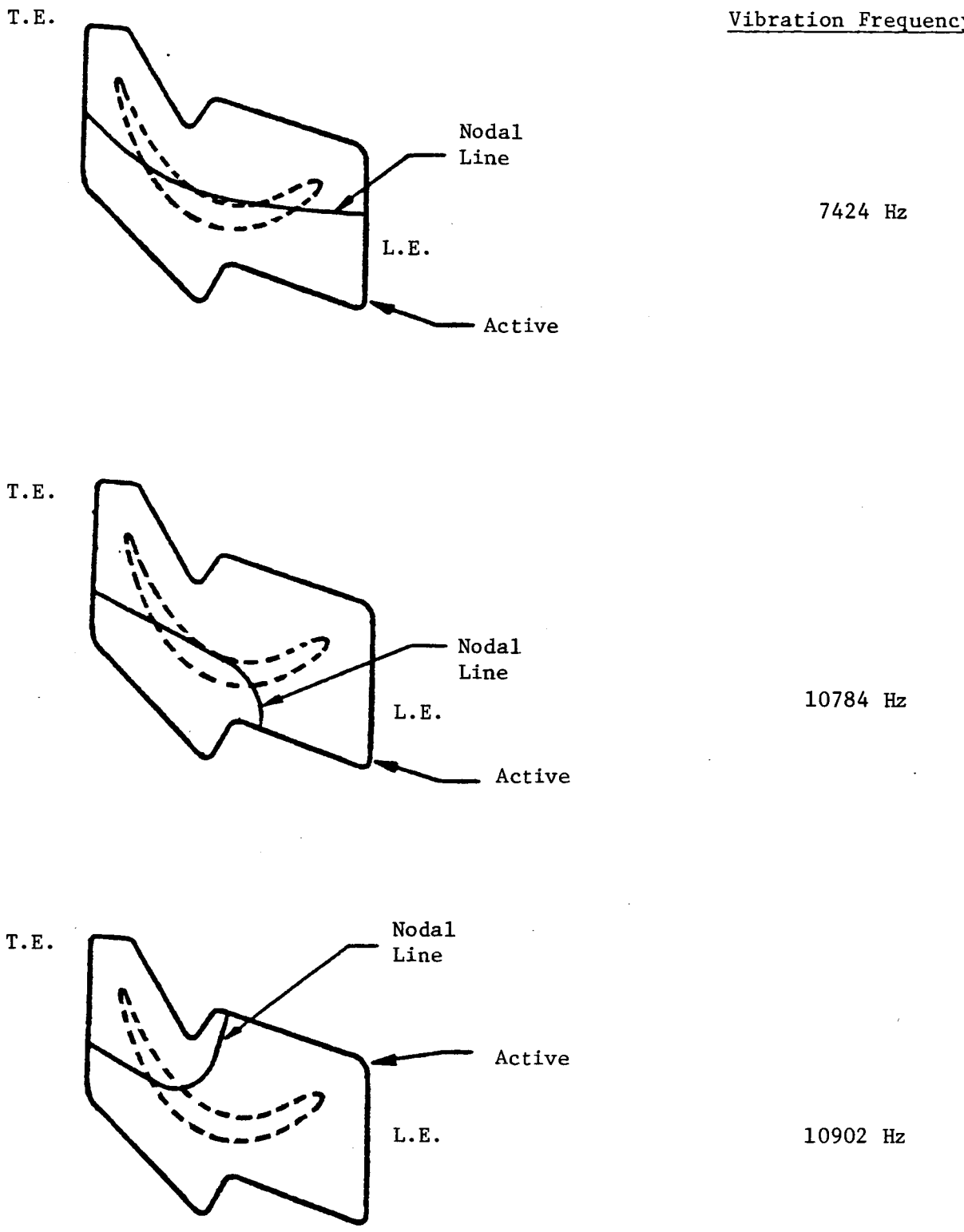


Figure 269. Low Pressure Turbine Stage 3 Blade Tip Shroud Bench Test Results.

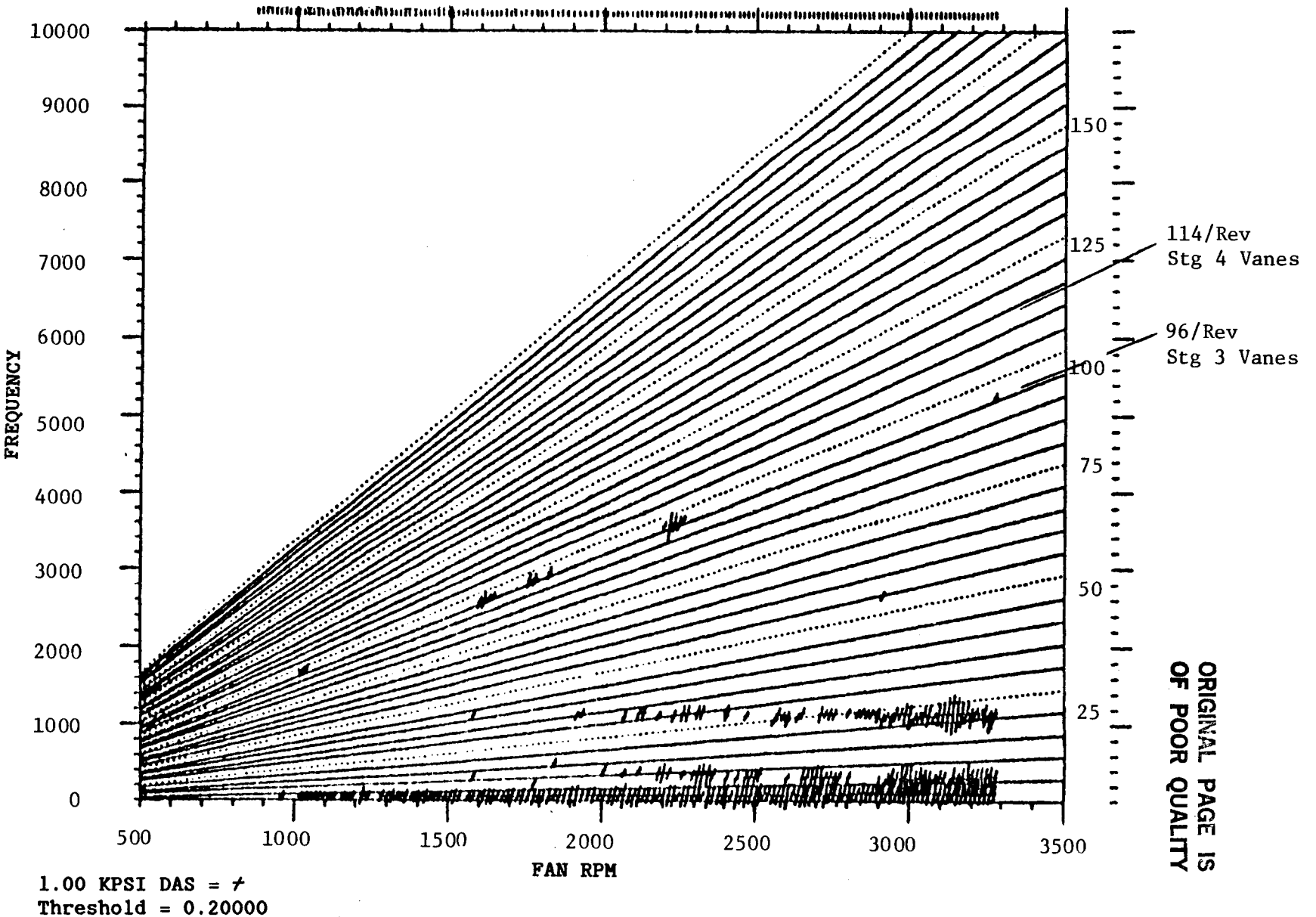




Figure 270. Low Pressure Turbine Stage 3 Blade Campbell Diagram

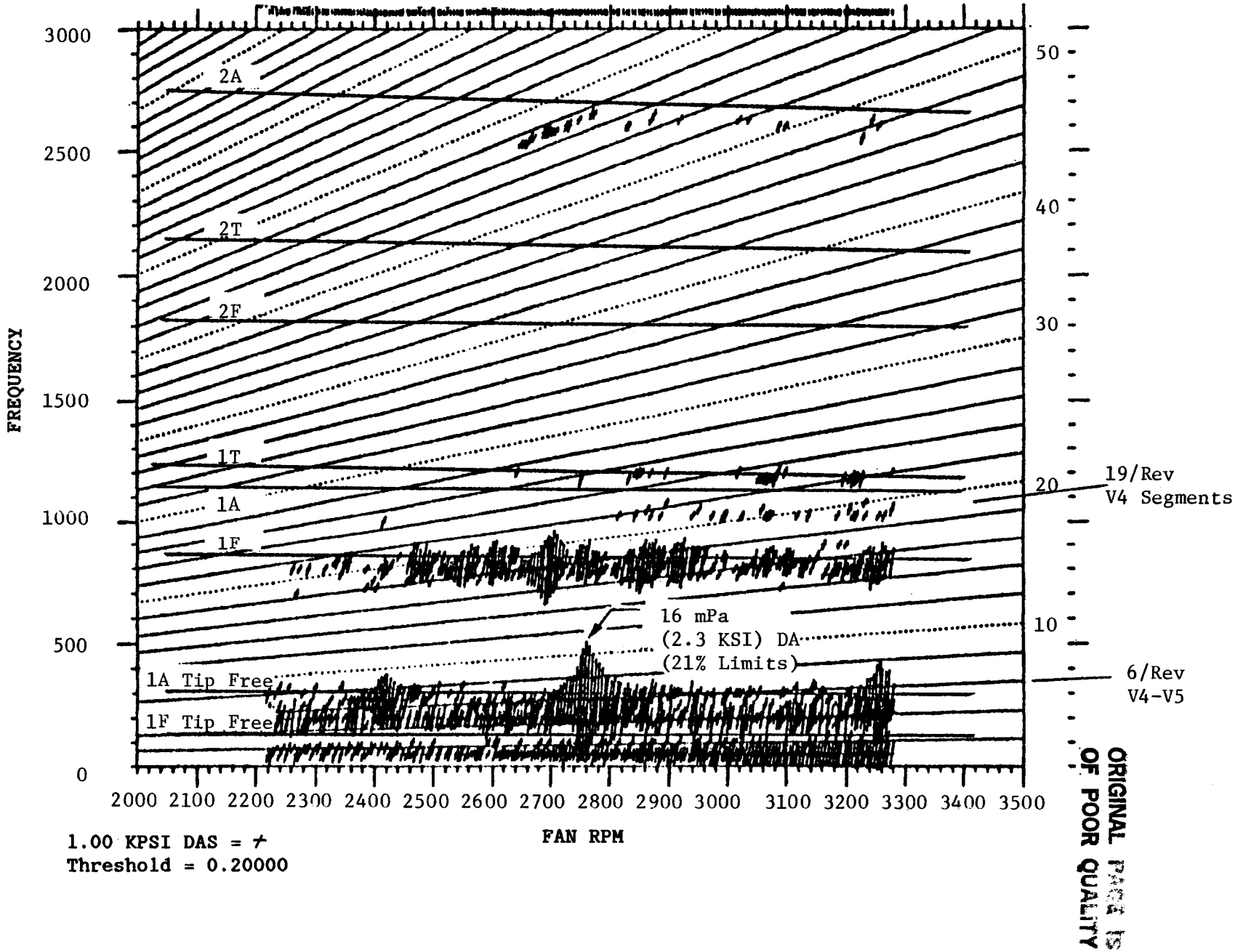




Figure 271. Low Pressure Turbine Stage 4 Blade Campbell Diagram

expected based on previous component test results since the angel wing primary mode frequency was more than 15% higher than the highest vane per rev.

Stage 5 Blade

Measured vibratory stresses for the Stage 5 blade are shown in Figure 272. The gage was noisy but the data was still readable. The maximum alternating stress was 21 mPa (3000 psi) DA, 10% of limits, with the blade driven in the first flexure mode by the 12/rev frame strut passing frequency. These low levels were realized in spite of the fact that the axial gap between the blade row and the rear frame was relatively close compared with prior GE experience.

Stage 1 Nozzle Inner Seal Support

The Stage 1 nozzle inner seal support was cantilevered from the ID of the Stage 1 nozzle. Strain gages were applied to the forward and aft sheet metal portions of the inner seal support in order to be able to monitor vibratory stresses during ICLS engine testing.

The vibratory stresses measured during mechanical checkout were very low and are shown in Figure 273. Maximum excitation was due to the sump rotating seal bolts which were located approximately 1.5 inches below the inner seal support. The bolts provided a 24/rev forcing frequency which caused a peak vibratory stress of 6 mPa (800 psi) DA, less than 5% of limits.

Stage 2 Nozzle Hook

The Stages 2-5 nozzles were supported at their OD by the low pressure turbine casing. Hooks fit into slots in the casing and transmitted the nozzle loads to the casing. These nozzle hooks were instrumented with strain gages to ensure that any significant vibrations could be monitored during ICLS engine testing. The Stage 2 nozzle hook vibratory stresses are shown in Figure 274. No significant resonances were recorded. The largest measured stress was 4 mPa (600 psi) DA, less than 10% of limits.

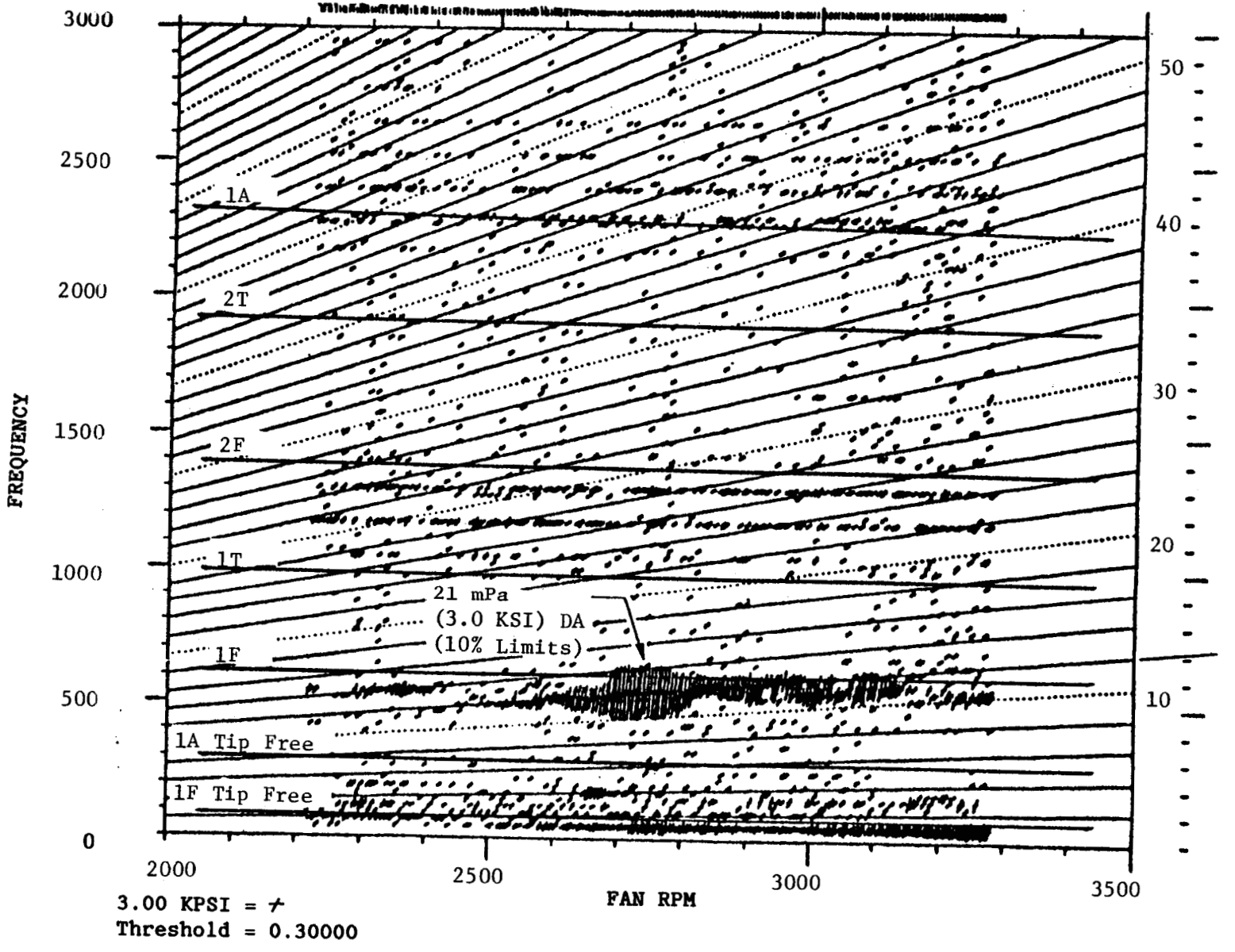




Figure 272. Low Pressure Turbine Stage 5 Blade Campbell Diagram

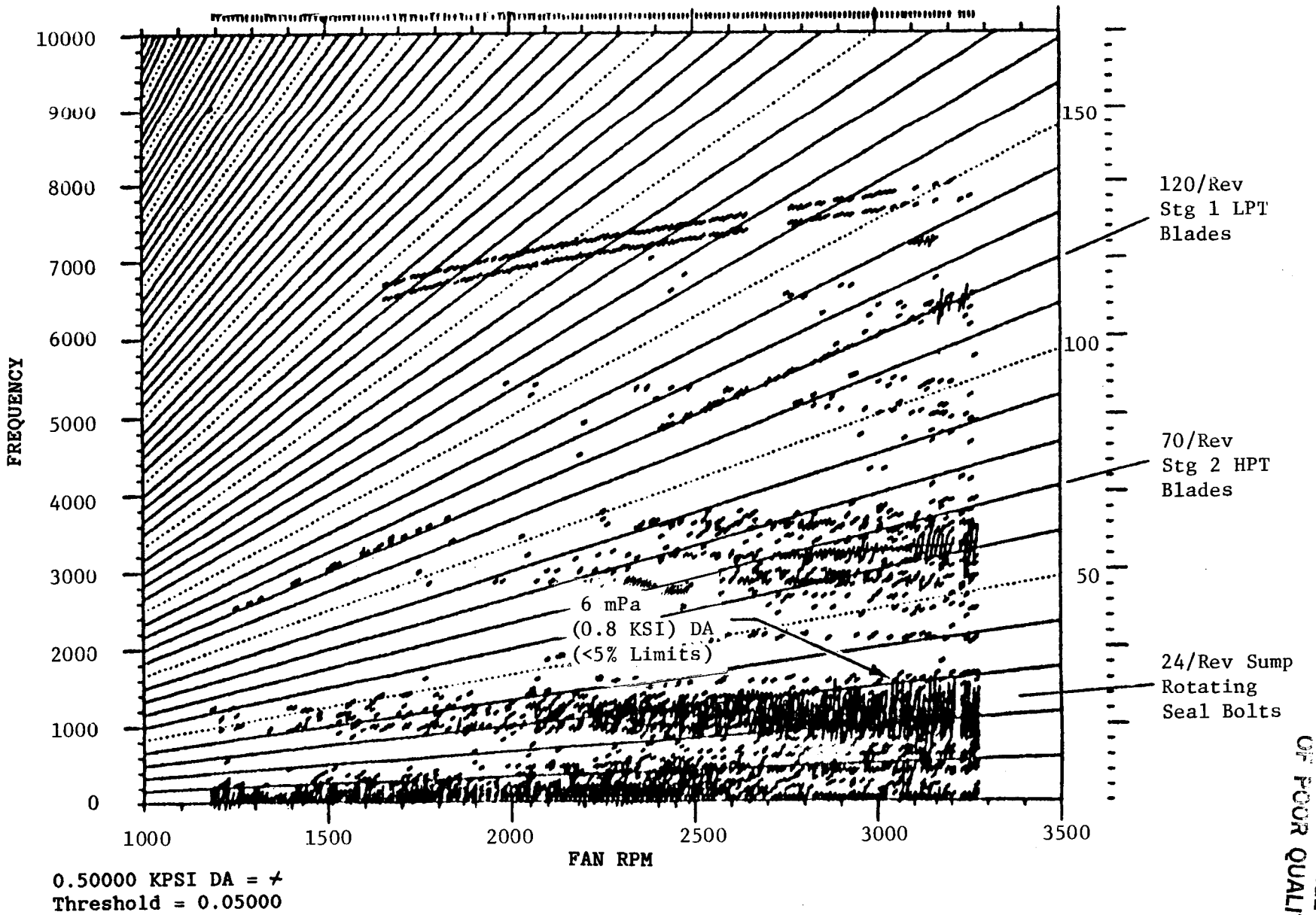


Figure 273. Low Pressure Turbine Stage 1 Nozzle Inner Seal Support Campbell Diagram ICLS Engine Test Measured Vibratory Stresses.

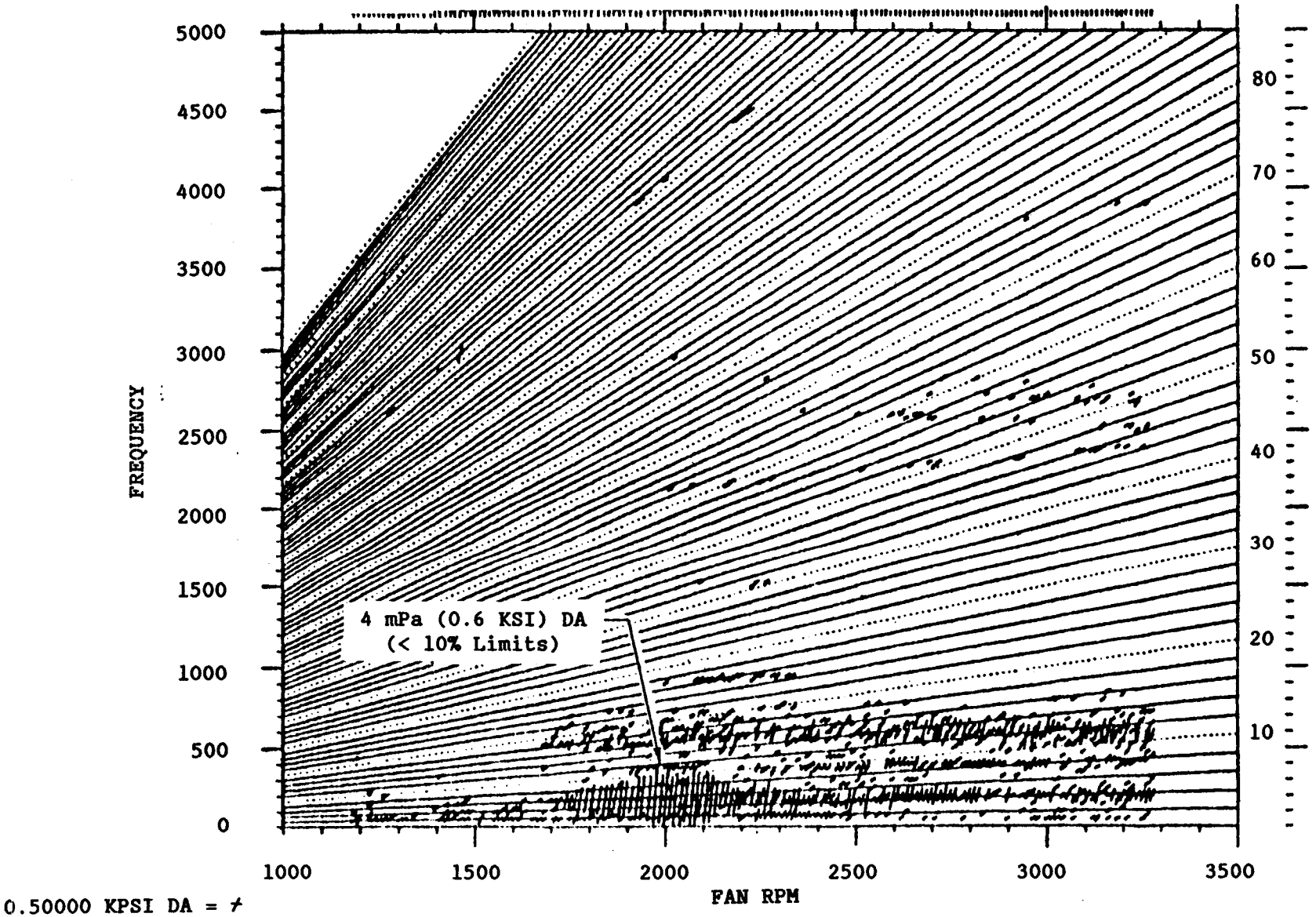




Figure 274. Low Pressure Turbine Stage 2 Nozzle Hook Campbell Diagram.

Stage 3 Nozzle Hook

The Stage 3 nozzle hook vibratory stresses are shown in Figure 275. No resonances were seen throughout the entire speed range. The two lines that cross the Campbell diagram at approximately 700 Hz are thought to be noise since the amplitude remains constant over a large speed range. The same pattern also occurred on the Stage 2 nozzle hook, the Stage 1 nozzle inner seal support, and Stage 3 nozzle.

Stage 4 and 5 Nozzle Hooks

The Stage 4 and 5 nozzle hook strain gages failed before the engine reached the higher speed range. The design of these nozzle hooks were similar to Stage 2 and 3 nozzle hooks, which experienced no vibratory problems whatsoever; therefore, the loss of the stain gages was not a major concern.

Stage 3 Nozzle Airfoil

Previous component testing identified the Stage 3 nozzle as the only nozzle with a potential resonance. A second flex calculated resonance with 122 per rev excitation was found when plotting the resonant frequency data on a Campbell diagram. There were 122 blades in Stage 1 and 122 blades in Stage 2. The other stages did not have significant excitation sources; therefore, only the Stage 3 nozzle airfoil was instrumented. No vibration problems were expected on the Stage 3 nozzle because of its rigid design and because General Electric experience indicates a history free of vibration problems on LPT nozzles. The ICLS engine test results proved this to be true. Figure 276 shows the Stage 3 nozzle measured vibratory stresses recorded during engine testing. No significant resonances occurred throughout the entire speed range.

Summary

ICLS mechanical checkout testing verified the excellent vibratory mechanical integrity of the LPT blades, nozzles and stationary seal. Strain

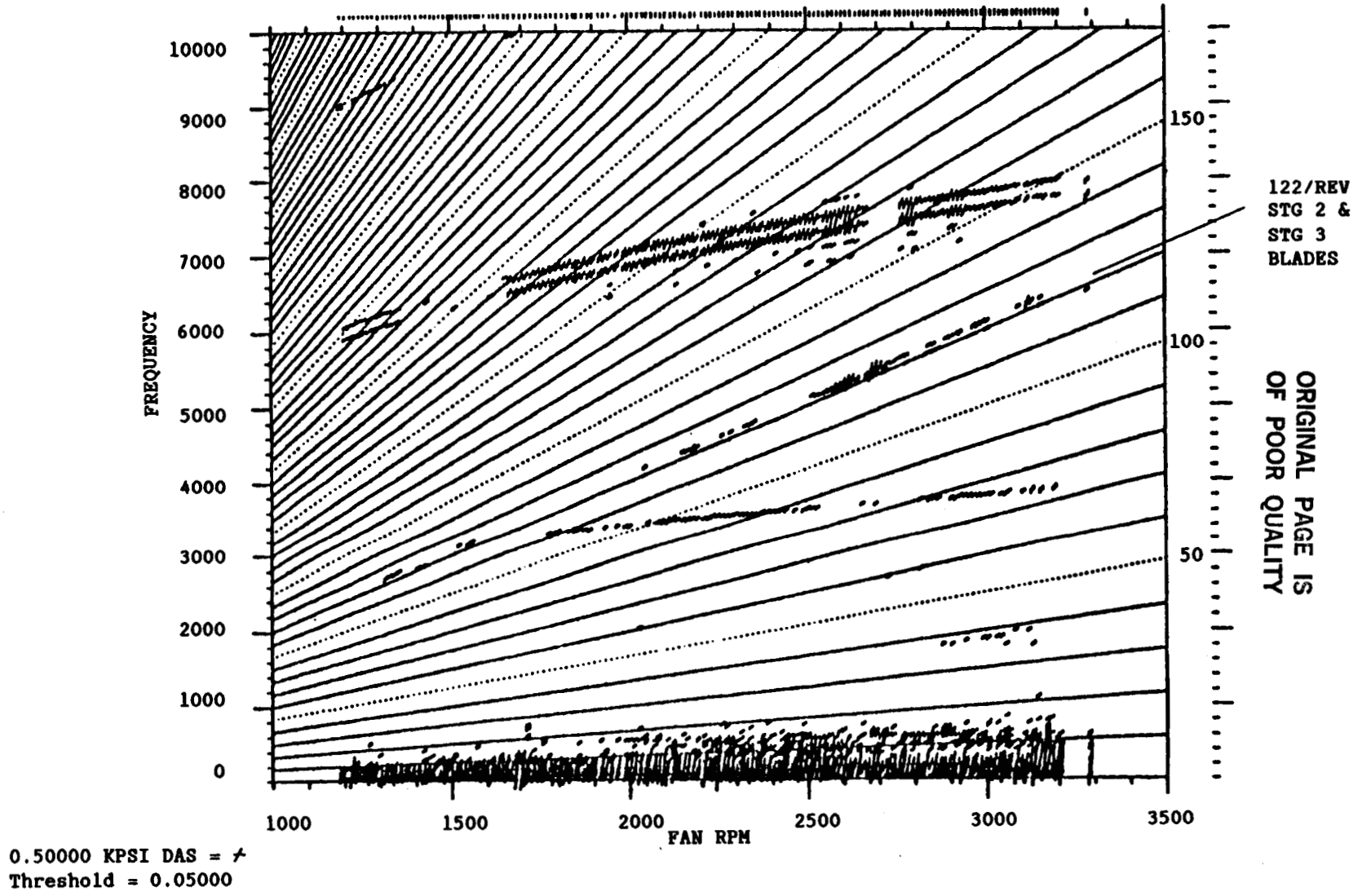


Figure 275. Low Pressure Turbine Stage 3 Nozzle Hook Campbell Diagram.

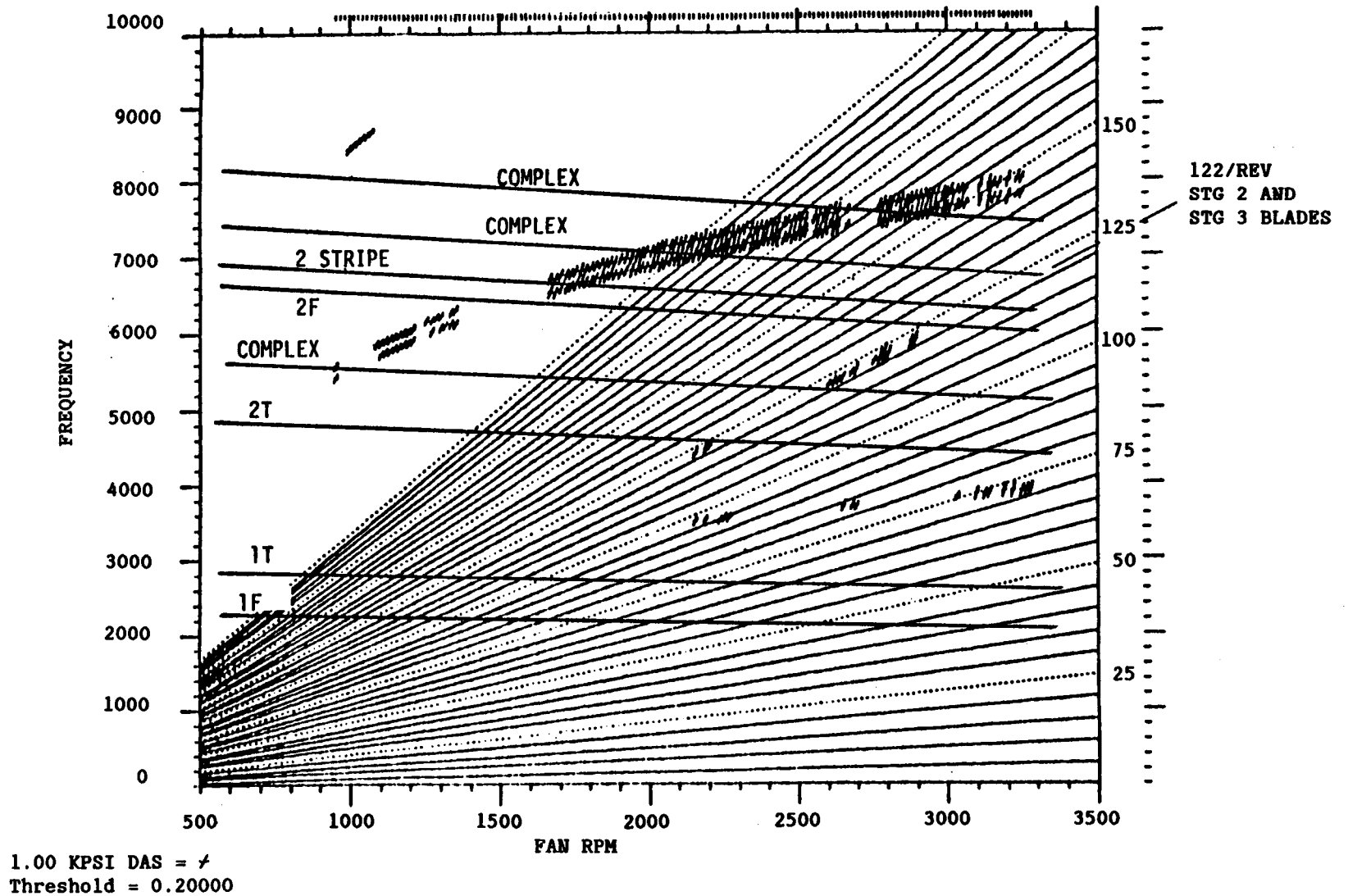


Figure 276. Low Pressure Turbine Stage 3 Nozzle Campbell Diagram.

gages on the blades and nozzles were monitored throughout mechanical checkout. Maximum fan speed attained was 3283 rpm. Strain gage loss throughout the entire test was relatively high (60% open or noisy beyond use). However, enough data was obtained to determine that the vibratory characteristics of the blades and nozzles were satisfactory. Vibratory stress levels remained very low over the speed range.

Based on the acceptable LPT vibration characteristics seen during ICLS engine testing, the following LPT design features were successful:

- Aerodynamically extended blade platforms
- Aerodynamically extended tip shrouds
- Aerodynamically decambered blade airfoils
- Interlocks integral with nozzle inner seals that are simpler, lighter, and less expensive than separate bolted seals
- Designing of vibration-free nozzles
- Designing of vibration-free stationary seals of light sheet metal construction
- Shortened axial flowpath from LPT blade exit to rear frame

### 6.10.3 Operating Seal Clearances and Active Clearance Control (ACC)

The Low Pressure Turbine module utilized 12 seals to ensure low leakage between rotating and stationary parts. Three of the seals were part of the Stage 1 nozzle assembly and were independent of ACC. Five outer seals were located at the blade tip-to-shroud regions, and the four remaining inner seals were located between the five stages of the LPT disks. Because turbine efficiency was directly affected by flowpath gas leakage across the seals, the use of ACC to reduce these leakages was an integral part of the ICLS test.

The three seals associated with the Stage 1 nozzle assembly were purged by 5th stage compressor bleed air, and though not affected by ACC, the amount of gas leaking across the seals due to operating clearances was still an important aspect of turbine performance. Verification of seal rubs could not be accomplished because of limited borescope port locations and limited

flexibility of the borescope instrument. However, using predicted hot day takeoff maximum operating conditions in conjunction with the available thermocouple data and measured hot flowpath gas data, post-test calculations were made of the three seals' radial gaps at the maximum operating test point. The results of these calculations along with measured cold radial gaps are tabulated in Figure 277.

The remaining nine seal clearances were directly affected by ACC. Both the calculated and measured cold radial gaps and the calculated hot running clearances with ACC at the maximum operating point are shown in Figure 278. In Figures 277 and 278, the calculated cold clearance was based on nominal stack-ups. The calculated clearances at ICLS maximum speeds is based on cold measured clearances.

Operating curves showing the radial clearance values have been plotted to show the characteristics due to speed and to the quantity of ACC air applied. Figures 279 and 280 for Stage 1 and 5 blades respectively show the range of response. Similarly, Figures 281 and 282 for Stage 1 and 2 and 4 and 5 inner seals, respectively, are representative of the range of all the main seals.

The operating gap at each seal must incorporate any prior rubs. For this reason, a supplementary ordinate scale has been added to the right side of each figure. Using the maximum rub point as the new zero seal gap, the resultant operting gaps for any other speed and ACC condition can be determined.

Borescope inspections agreed with the calculated clearance values of these two stages. As the figures indicate, and borescope inspections showed, there was very little or no rub between the Stage 1 blade tips and shrouds; and although visibility was limited, the inspection showed rubs estimated at 0.76 mm (0.030 in) or more between the Stage 5 blade tips and shrouds.

The results of the plots shown in Figures 279 and 280 have been incorporated into Table XXIII. This table summarizes the major engine

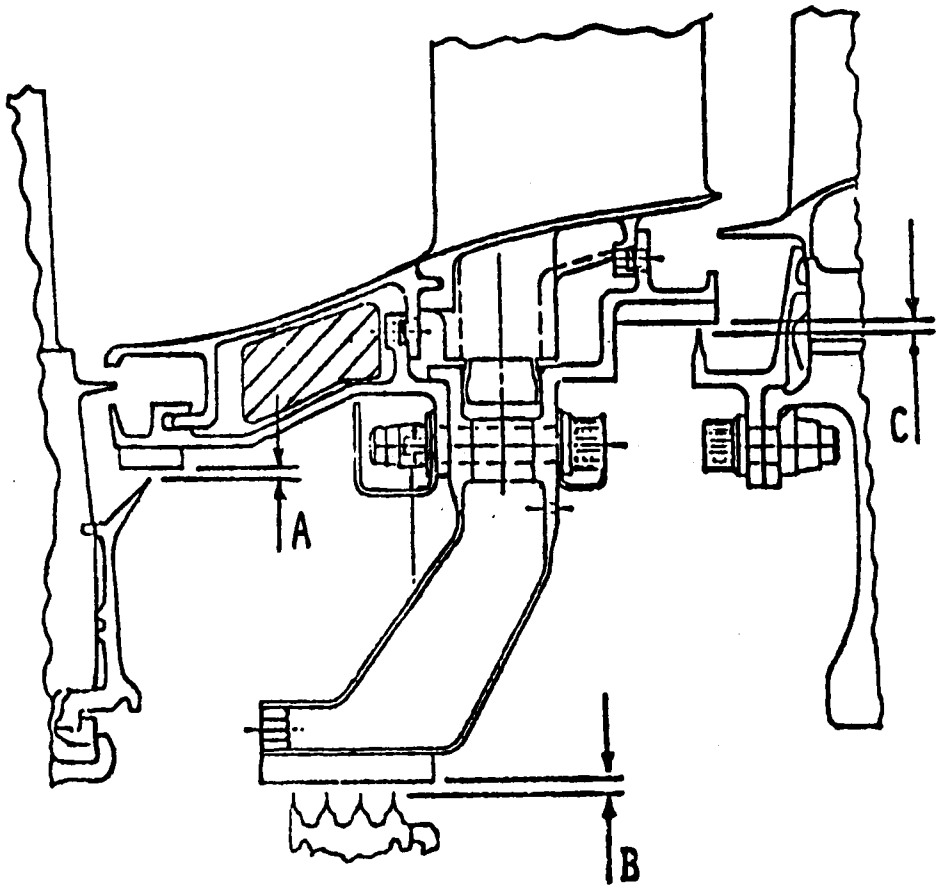


| | A | | B | | C | |
|---|---|---|---|---|---|---|
| | mm | in | mm | in | mm | in |
| Cold Assy. (Measured) | 0.50 | (0.0195) | 0.55 | (0.0215) | 0.03 | (0.001) |
| (Calculated) | 0.30 | (0.012) | 0.58 | (0.023) | 0.36 | (0.014) |
| Predicted, Hot Day Takeoff | 0.76 | (0.030) | 0.23 | (0.009) | -0.03 | (-0.001) |
| Calculated $E^3$ ICLS @ Max Operation | 0.81 | (0.032) | 0.25 | (0.010) | -0.03 | (-0.001) |

**Figure 277.** Low Pressure Turbine Stage 1 Nozzle Assembly Inner Seal Clearances.

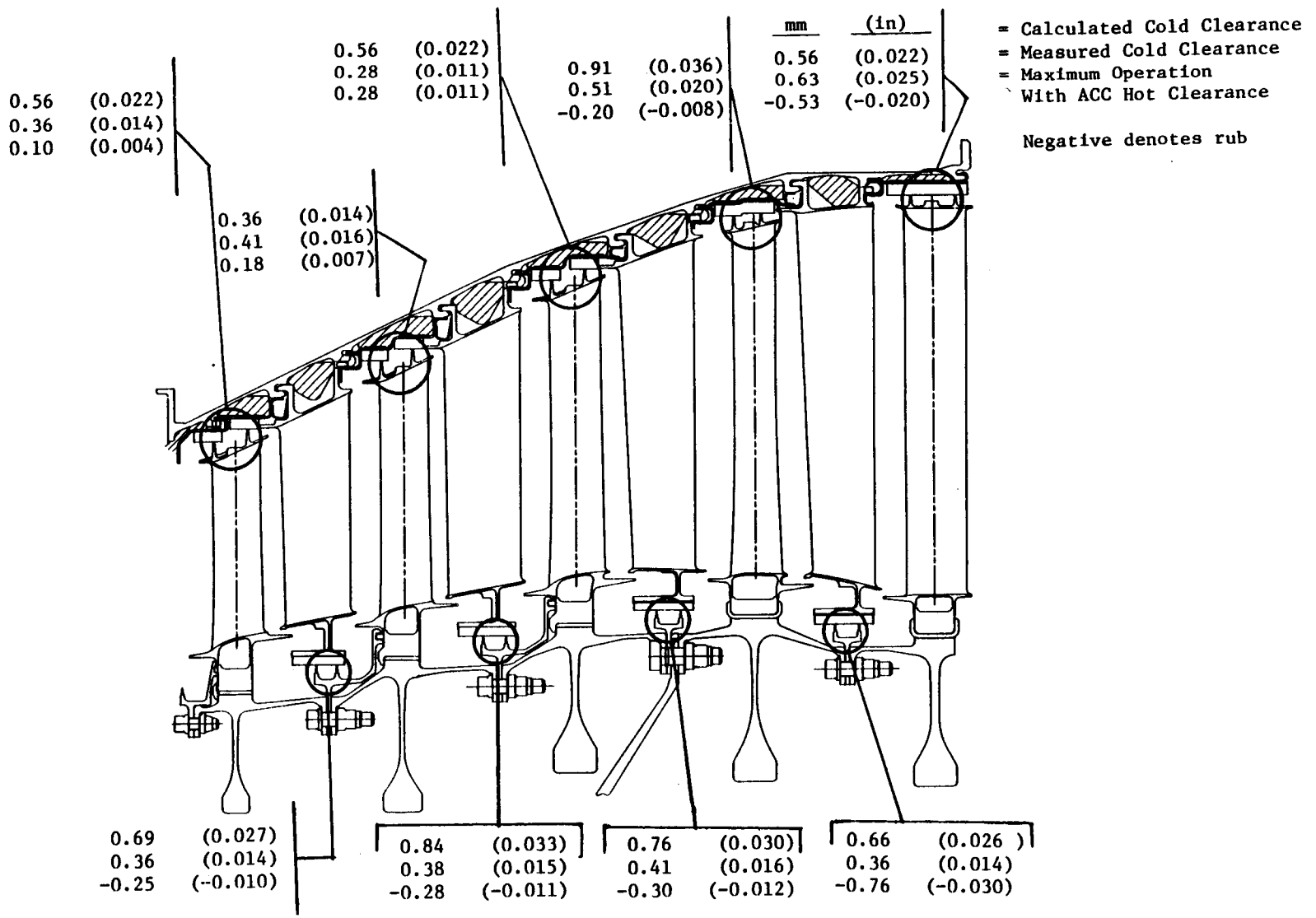


Figure 278. Low Pressure Turbine Blade Tip and Inner Stage Seal Clearances.

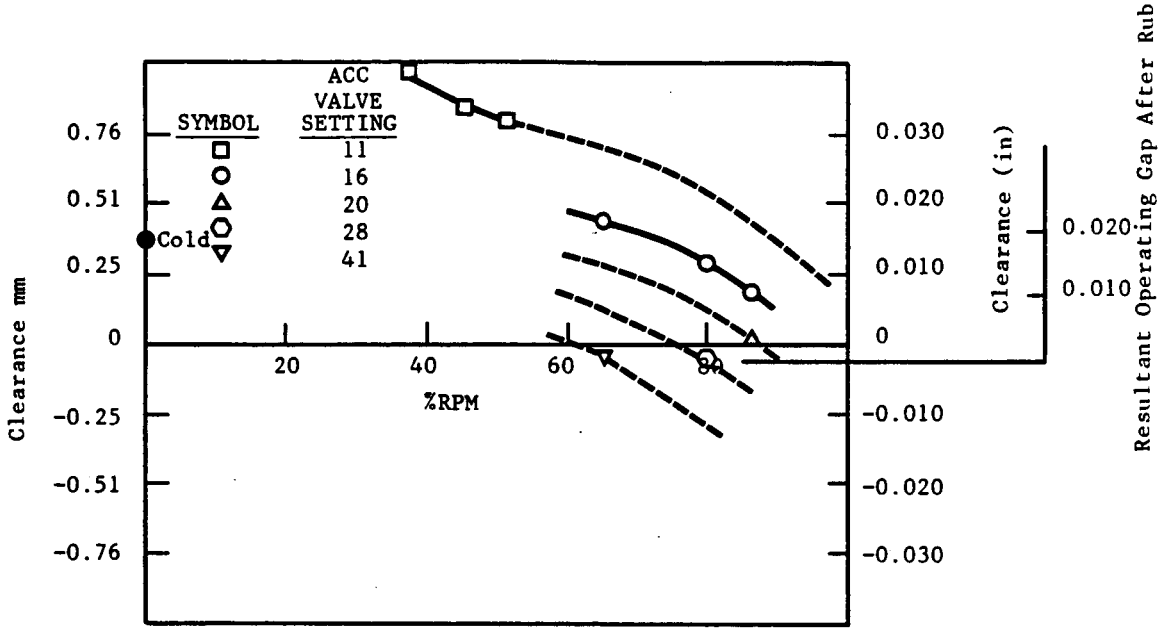


Figure 279. Actual Stage 1 LPT Blade Tip Clearance.

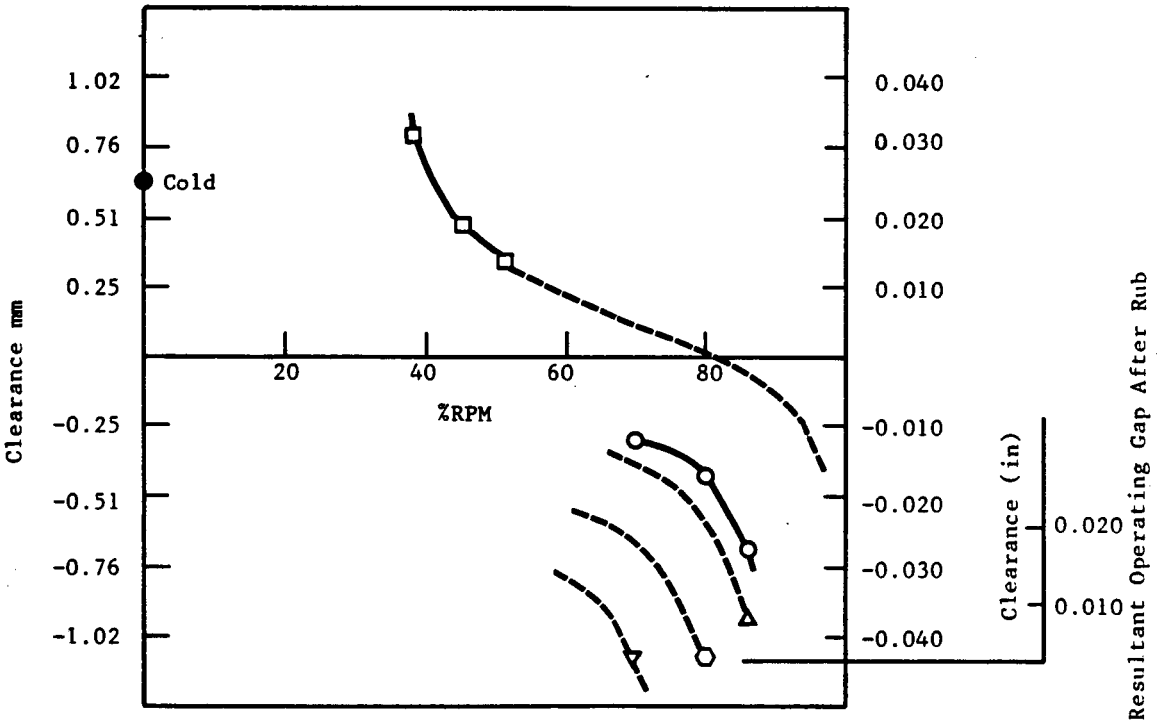


Figure 280. Actual Stage 5 LPT Blade Tip Clearance.

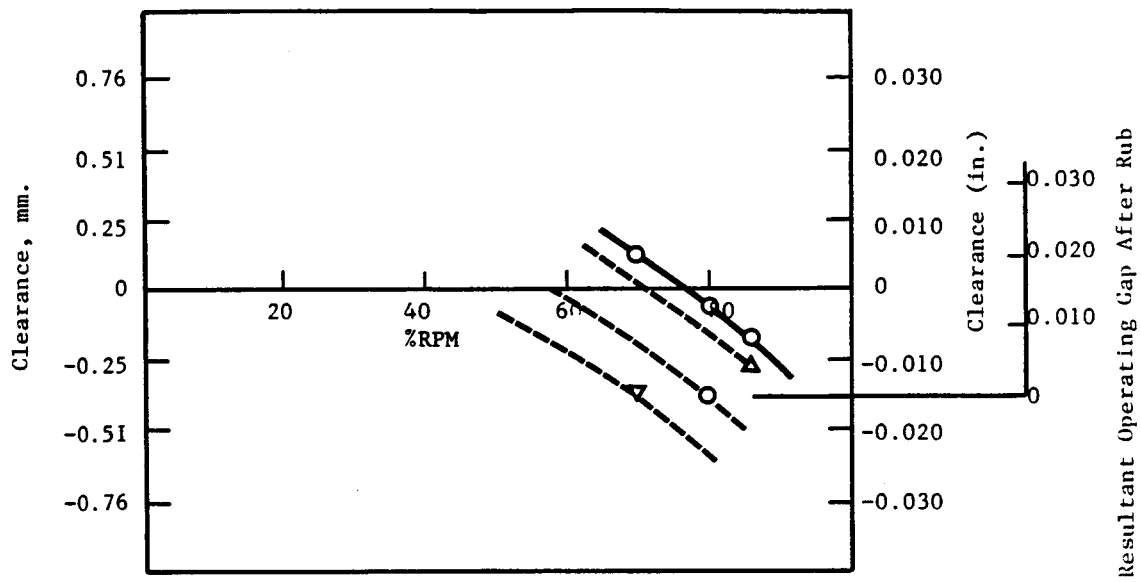


Figure 281. Actual Stage 1 - 2 LPT Inner Stage Seal Clearance.

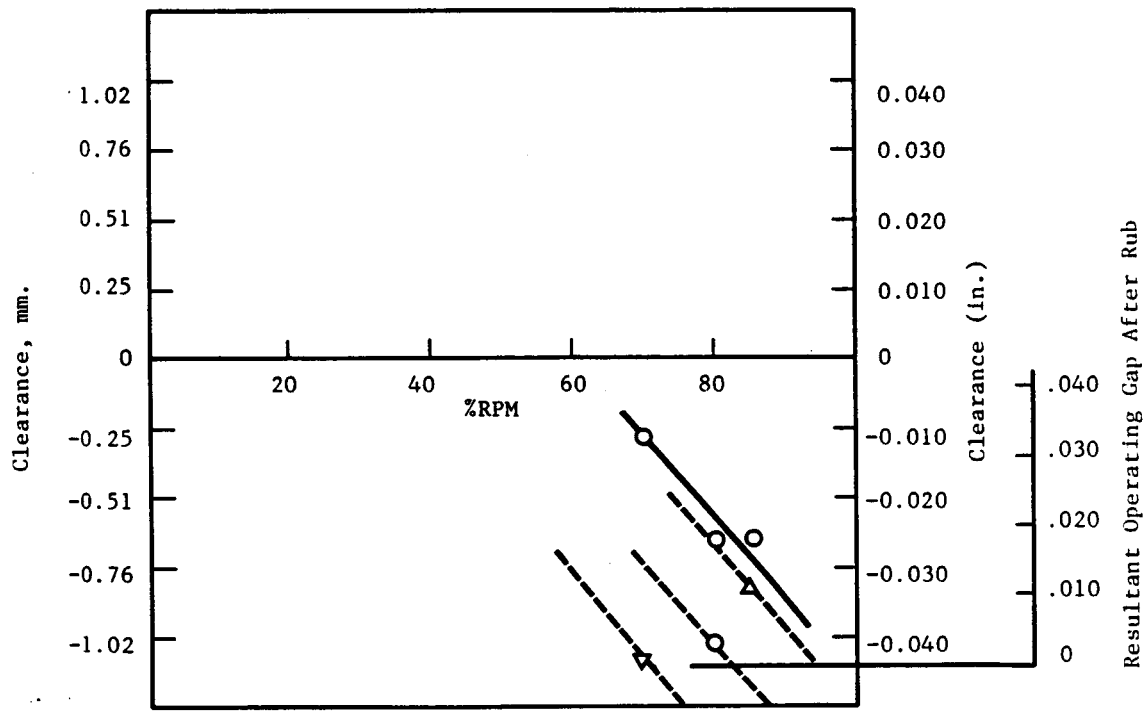


Figure 282. Actual Stage 4 - 5 LPT Inner Stage Seal Clearance.

## Table XXIII. Low Pressure Turbine Operating Clearances.

| DMS RDG. | Blade Tip Clearances mm (In.) 1 | 2 | 3 | 4 | 5 | Inner Stage Seals mm (In.) 1/2 | 2/3 | 3/4 | 4/5 | % Flow Speed | Valve Angle |
|---|---|---|---|---|---|---|---|---|---|---|---|
| | .035 | .044 | .054 | .044 | .044 | .040 | .046 | .045 | .042 | | |
| 116 | ( .889) | (1.118) | (1.372) | ( 1.118) | ( 1.118) | ( 1.016) | ( 1.168) | ( 1.143) | ( 1.067) | 50 | 11° |
| | .031 | .041 | .052 | .039 | .033 | .034 | .042 | .041 | .033 | | |
| 117 | ( .787) | (1.041) | (1.321) | ( .991) | ( .838) | ( .864) | ( 1.067) | ( 1.041) | ( .838) | 60 | 11° |
| | .027 | .037 | .049 | .033 | .020 | .027 | .039 | .034 | .023 | | |
| 118 | ( .686) | ( .940) | (1.245) | ( .838) | ( .508) | ( .686) | ( .991) | ( .864) | ( .584) | 70 | 11° |
| | .015 | .027 | .038 | .018 | .005 | .015 | .024 | .020 | .009 | | |
| 124 | ( .381) | ( .686) | ( .965) | ( .457) | ( .127) | ( .381) | ( .610) | ( .508) | ( .229) | 80 | 16° |
| | .009 | .017 | .028 | .008 | .002 | .000 | .013 | .004 | - .002 | | |
| 128 | ( .229) | ( .432) | ( .610) | ( .203) | ( .051) | ( .178) | ( .330) | ( .102) | (- .051) | 80 | 22° |
| | .004 | .010 | .015 | .001 | - .004 | - .001 | .006 | .009 | .003 | | |
| 126 | ( .102) | ( .254) | ( .381) | ( .025) | (- .102) | (- .025) | ( .152) | ( .229) | ( .076) | 80 | 26° |
| | .000 | .008 | .012 | - .003 | - .008 | .001 | .006 | - .001 | - .007 | | |
| 131 | ( .000) | ( .203) | ( .305) | (- .076) | (- .203) | ( . ) | ( .152) | (- .025) | (- .178) | 87 | 22° |
| | .001 | .008 | .016 | .005 | .007 | .002 | .007 | .006 | .006 | | |
| 134 | ( .025) | ( .203) | ( .406) | ( .127) | ( .178) | ( .051) | ( .178) | ( .152) | ( .152) | 80 | 26° |
| | - .001 | .000 | .002 | - .003 | .009 | .000 | .001 | - .001 | .005 | | |
| 135 | (- .025) | ( .000) | ( .051) | (- .076) | ( .229) | ( .000) | ( .025) | (- .025) | ( .127) | 70 | 41° |
| | .040 | .047 | .052 | .061 | .067 | .046 | .053 | .055 | .061 | | |
| 136 | ( 1.016) | (1.194) | (1.321) | ( 1.549) | ( 1.702) | ( 1.168) | ( 1.346) | ( 1.397) | ( 1.549) | 40 | 41° |

operating points, the maximum range of manifold valve settings, and the rotor speeds used to evaluate the ACC system. The tabulated results reiterate the observations made concerning the discussion of the maximum operating point (Figure 278), corroborates borescope inspections, and provides a total picture of how all nine radial seal gaps responded to ACC.

Little or no rub occurred on the Stage 1 blade tip while a significant rub occurred on Blade 5. Relative to Stage 1, the Stage 5 running clearance with minimum ACC was tighter than expected and the Stage 5 closure due to ACC was more than expected.

The effects of active clearance control cooling on the LPT casing are given in Figures 283 through 285. These show the thermal response of the Stage 1, 3, and 5 forward hooks. As shown in these figures, at 70% speed, increasing the value setting from 16° to 41° produced temperature drops of 28°C (50°F), 110°C (200°F), and 69°C (125°F) at Stages 1, 3, and 5, respectively.

One observation made during borescope inspections, as shown in Figure 286, was a rub between the trailing edge of the Stage 5 nozzle inner band and the Stage 5 blade angel wing. Prior to engine testing, based on heat transfer analyses and thermal growth calculations, the minimum operating clearance between the two components was estimated at 0.76 mm (0.030 in). Post-test analysis provides two reasons for the unexpected rub. First, the predicted cold radial gap between the nozzle inner band and blade angel wing was 3.0 mm (0.117 in), based on nominal dimensions. The actual measured cold gap was 2.0 mm (0.080 in). Second, blade casting drawings call for a contour tolerance on the angel wing of 0.38 mm (0.015 in), which means each angel wing can vary $\pm$0.191 mm ($\pm$0.0075 in) from the nominal position. However, the rubs that resulted were not severe and did not affect the mechanical integrity of the nozzles and blades, and all testing was completed as planned.

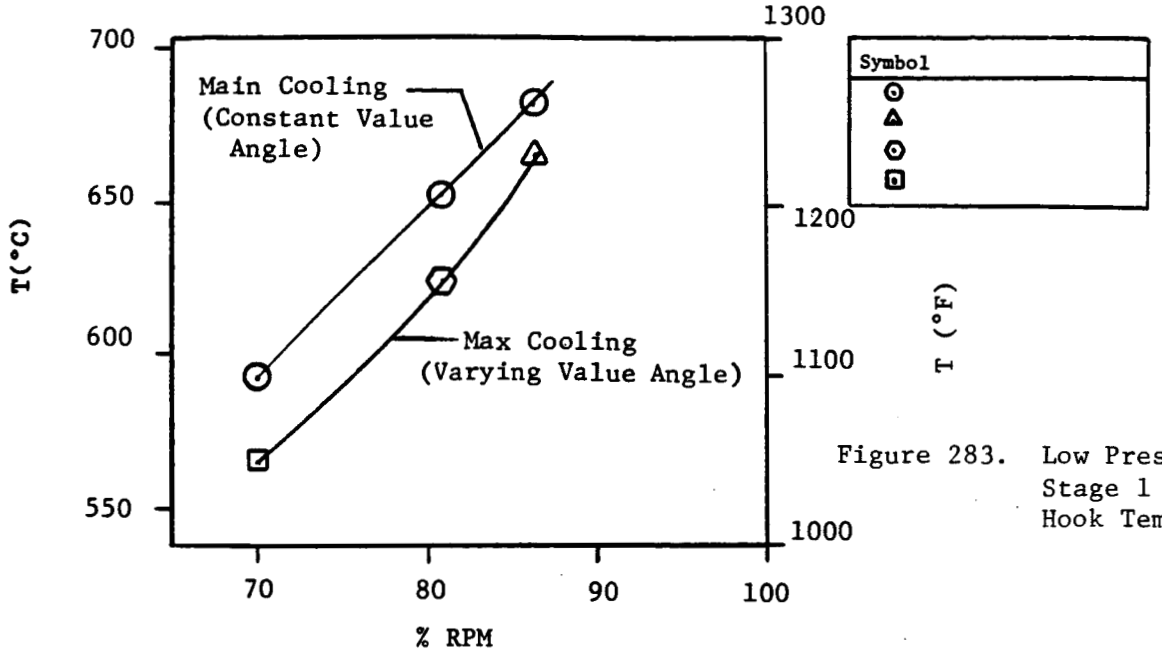


Figure 283. Low Pressure Turbine Stage 1 Casing Forward Hook Temperature.

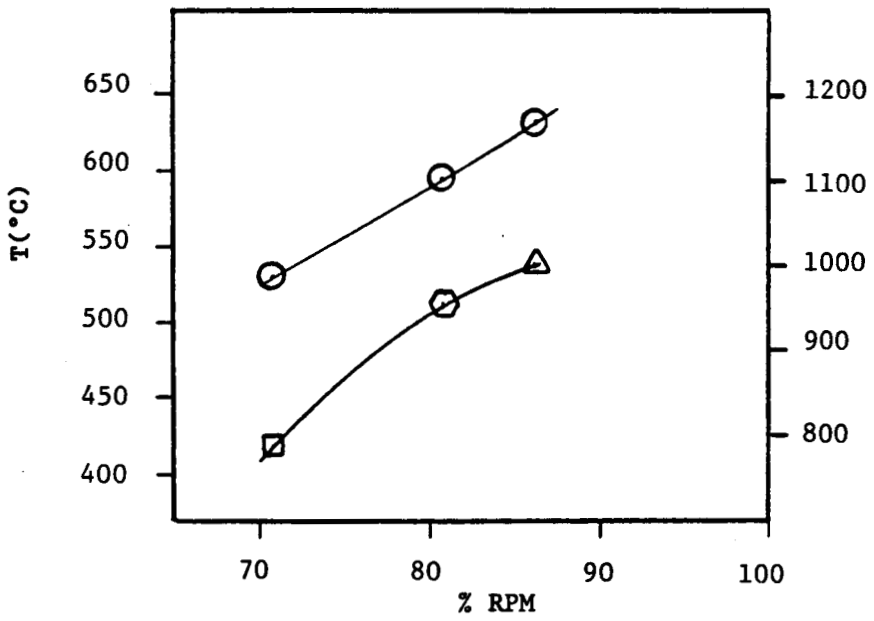


Figure 284. Low Pressure Turbin Stage 3 Casing Forward Hook Temperature.

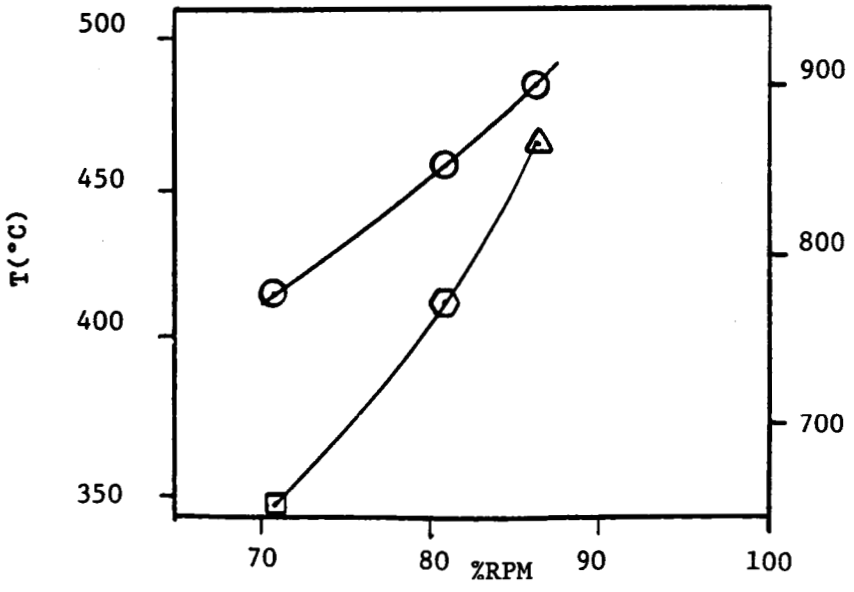


Figure 285. Low Pressure Turbine Stage 5 Casing Forward Hook Temperature.

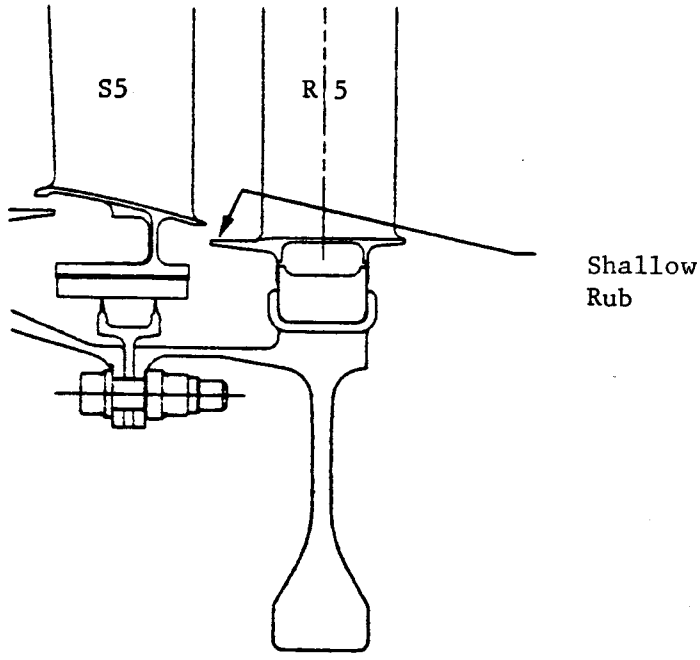


Figure 286. Rub Location on Low Pressure Turbine Stage 5 Blade Angel Wing.

## Conclusions

1. The $E^3$ ICLS test shows that impingement cooling on the LPT casing is a viable means of controlling seal clearances in the LPT.

2. Based on clearance calculations and borescope inspections, a more effective overall turbine clearance control is possible by blocking off cooling to casing of the 4th and 5th stages.

3. A complete engine teardown and investigation of seal rubs would provide valuable insight to predicting and maintaining tighter seals.

4. Additional thermocouples on the casing would provide a better understanding of circumferential thermal gradients and provide a more thorough understanding of the amount and rate of heat conduction from the casing hooks to the rest of the shell.

6.10.4 Post-Test Borescoping

Following completion of all ICLS engine testing, the core cowl was removed to give access to the LPT casing, the ACC manifolds, and the borescope plugs which were removed for internal viewing of the turbine.

Blue discoloration due to heating was noted on the casing outside diameter as shown below:

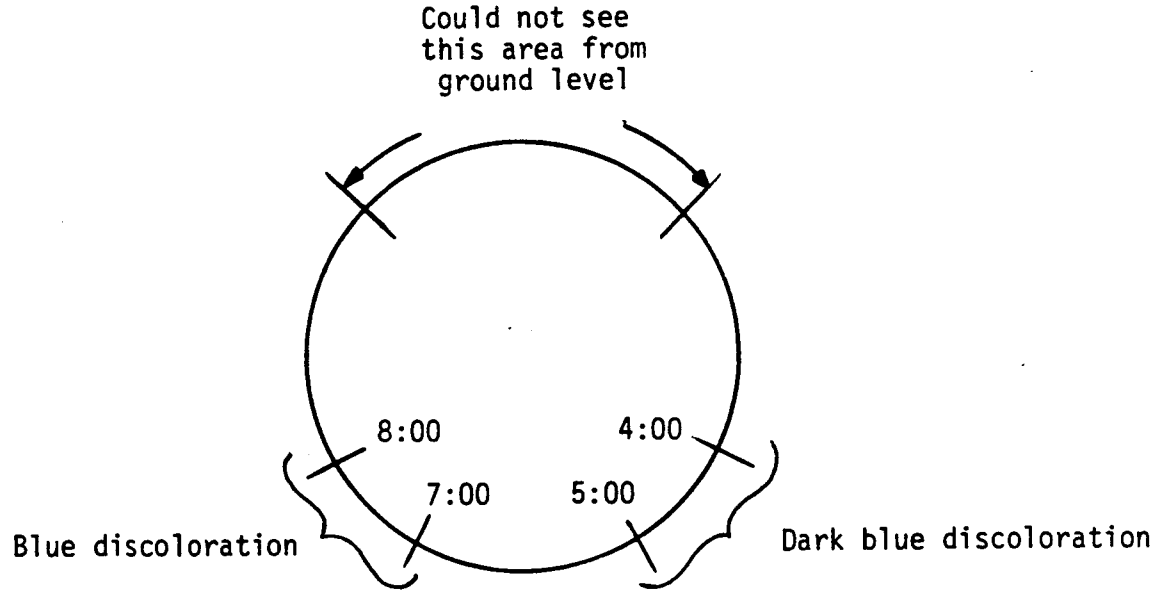


LPT Casing
Aft Looking Forward
Blue discoloration noted as shown above
in area of stages 1 and 2 LPT nozzles

The following observations were made from borescoping through the engine exhaust and through 4 borescope ports located at the Stages 2-5 nozzles at the 6:00 position:

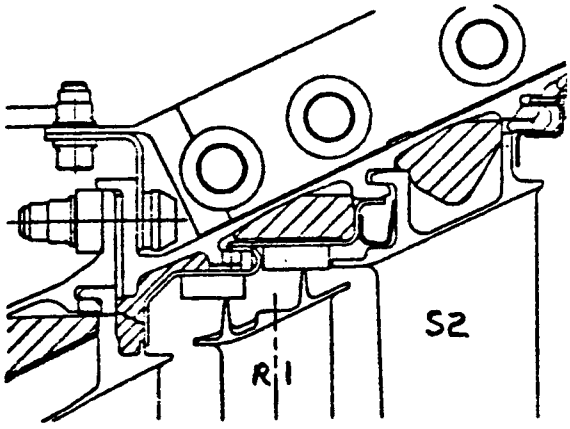


Stage 1 Blade Fwd. Tip Shroud
Tooth/Honeycomb
- not visible with borescope

Stage 1 Blade Aft Tip Shroud
Tooth/Honeycomb
- not much clearance between tip shroud and nozzle → difficult to see

- no rub in small area able to be seen

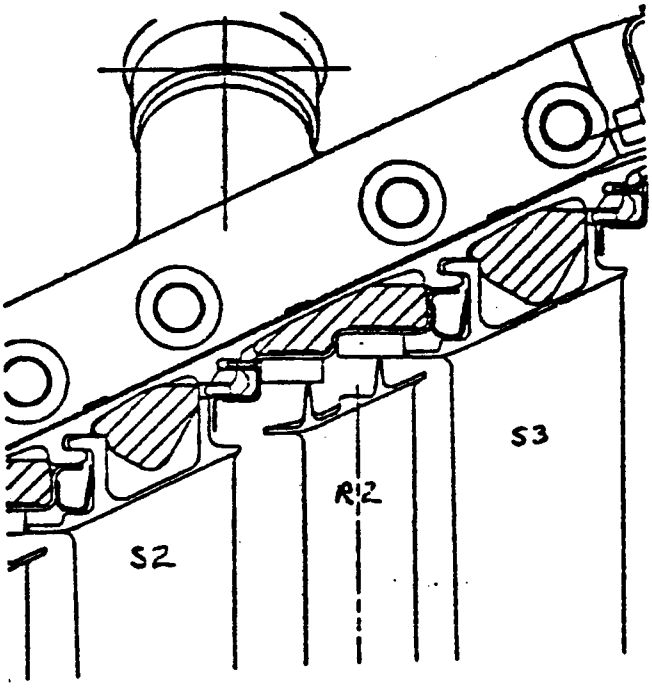


Stage 2 Blade Fwd. Tip Shroud
Tooth/Honeycomb
- not visible with borescope

Stage 2 Blade Aft Tip Shroud
Tooth/Honeycomb
- not much clearance between tip shroud and nozzle -- difficult to see

- no rub in area that can be seen (similar to Stage 1)

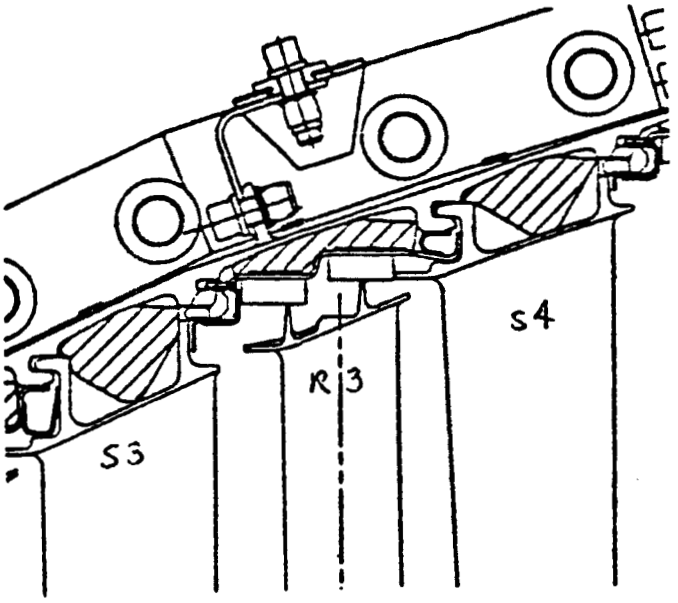


Stage 3 Blade Tip Shroud Tooth/Honeycomb

- same comments as for Stage 2 shown above

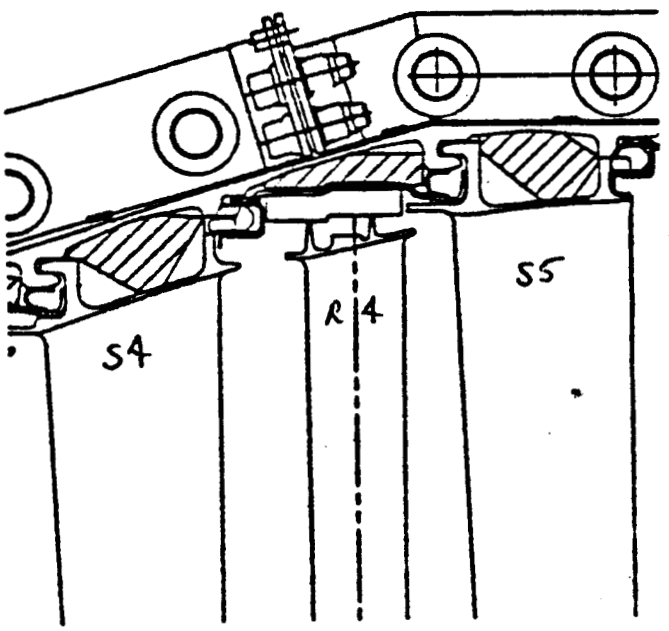


Stage 4 Blade Fwd Tip Shroud Tooth/Honeycomb

- rub seen

- not able to maneuver borescope into "trench" next to fwd tooth in order to get a photo

- rub estimated to be .015-.030 from previous borescoping

Stage 4 Blade Aft Tip Shroud Tooth/Honeycomb

- rub seen; however, the end of the rub is obscured by the blade tip

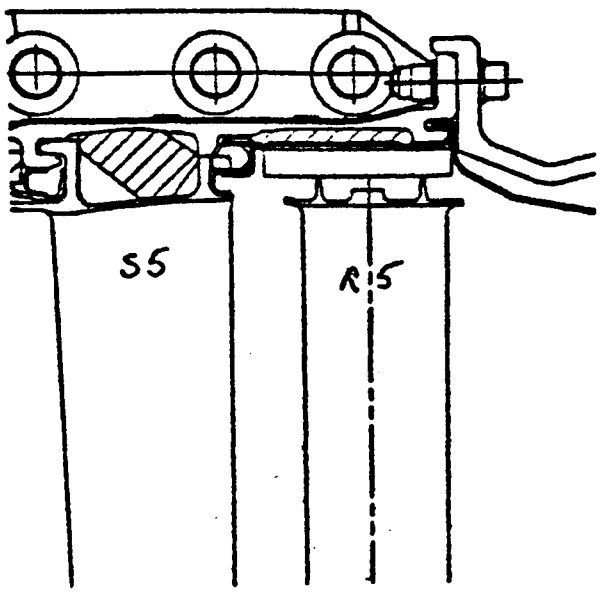


Stage 5 Blade Fwd Tip Shroud

Tooth/Honeycomb

- rub seen as in previous borescoping, starts approximately 3 1/2 honeycomb cells aft of fwd edge of honeycomb

Stage 5 Blade Aft Tip Shroud

Tooth/Honeycomb

- rub seen; however, the end of the rub is obscured by the blade tip making estimation of rub depth difficult

- rub estimated to be about 1 honeycomb cell deep from previous borescoping

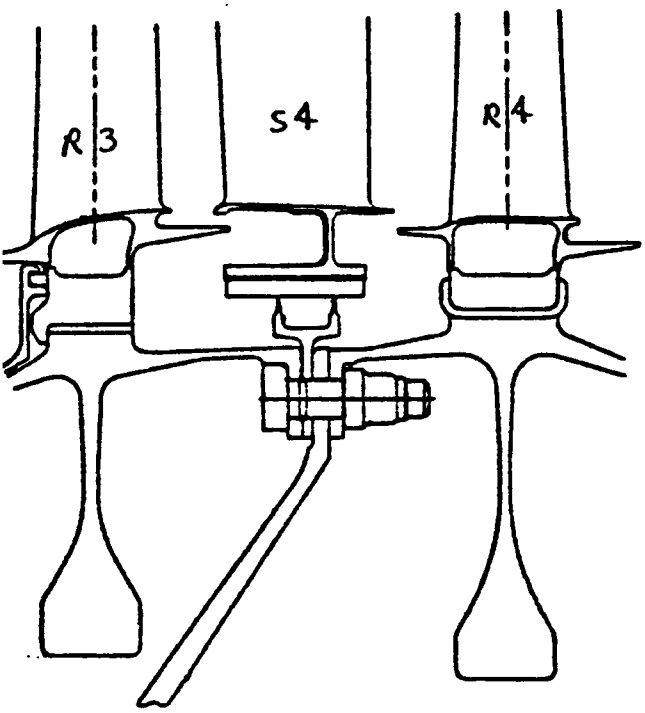


Stage 3 Blade Aft Angel Wing

- no rub with Stage 4 nozzle

Stage 4 Blade Fwd Angel Wing

- no rub with Stage 4 nozzle

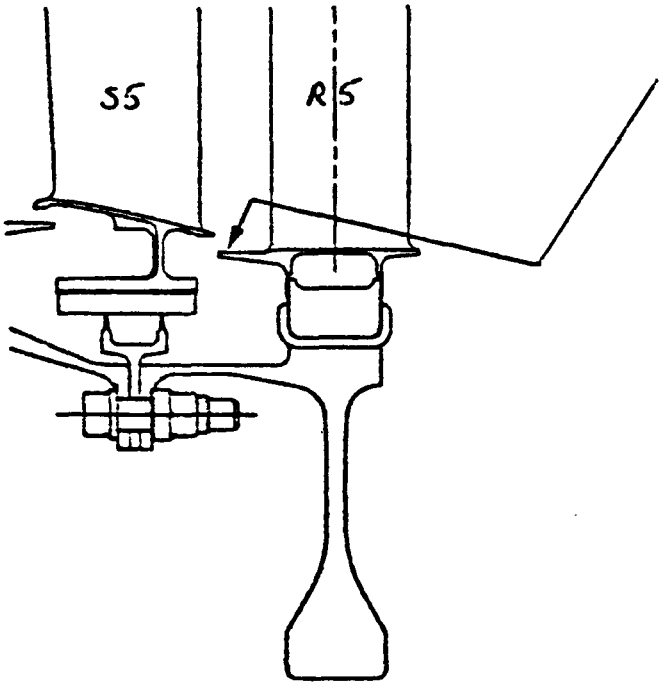


Stage 5 Blade Fwd Angle Wing
- shallow rub with Stage 5 nozzle as seen in previous borescoping

In summary, post-test borescoping of $E^3$ ICLS low pressure turbine shows no distress in regions visible, but full assessment can only be made from a full LPT teardown.

## 6.11 LOW PRESSURE TURBINE PURGE AND COOLING SYSTEM PERFORMANCE

### 6.11.1 LPT Design Conditions

The low pressure turbine heat transfer design has been established by the overall cycle parameters. The most severe temperature and pressure conditions occur at max power takeoff where the thrust requirements are maximum.

Presented in Table XXIV are the low pressure design parameters. Design cycle conditions was chosen as 50°C (122°F) day maximum power takeoff, at sea level, at Mach = 0.3. This represents the highest gas and coolant temperature condition that can be expected in engine service. Also presented in the table are the ICLS design conditions. The actual measured gas temperatures for reading #73 is also presented. Reading 73 was taken at the highest corrected fan speed that was obtained during ICLS test.

Table XXIV. Low Pressure Turbine
Heat Transfer Environment.

| | Heat Transfer Design Point 50°C (122°F) Day M-0.3 T/O | ICLS r Design Point 30°C (86°F) Day SLS T/O | Reading 73 |
|---|---|---|---|
| $T_{42}$ (Cycle) | 859°C (1578°F) | 897°C (1647°F) | 876°C (1609°F) |
| $T_{42}$ + Margin* | 9 0°C (1688°F) | 920°C (1688°F) | |
| $T_5$ (Cycle) | 578°C (1073°F) | 601°C (1113°F) | 604°C (1119°F) |
| $P_{42}$ | 509 kPa (73.88 psia) | 565 kPa (81.97 psia) | 571 kPa (82.87 psia) |
| $P_{42}/P_5$ | 3.589 | 3.782 | 3.788 |
| $T_{COOL}$ | 393°C (740°F) | 379°C (714°F) | 361°C (682°F) |
| $W_{COOL}$ | 1.40%$W_{25}$ | 1.40 | 1.20 |
| $P_{COOL}$ (TURB) | 522 kPa (75.80 psia) | 574 kPa (83.26 psia) | 599 kPa (86.86 psia) |
| RPM | 3289 | 3419 | 3280 |

*110°F (43°C) $T_{4.2}$ MARGIN

### 6.11.2 Cooling Air Supply System

The airflow that was used for cooling the low pressure turbine internal structure, Stage 1 nozzle and rotor, was extracted from the compressor at the 5th stage of the compressor. The location of the compressor bleed was defined as the most forward compressor extraction location that would still yield a satisfactory pressure at the LPT. Other restrictions such as the variable compressor vanes prevented moving the compressor bleed location to the fourth stage of the compressor. The extra pressure, associated with the one extra stage of compressor pumping, was used to flow the 5th stage bleed flow through compressor active clearance control cooling circuit. By the time the 5th stage compressor bleed air had been routed through the compressor active clearance control system, through the piping system, and into the low pressure casing manifold, the expected pressure was down to a level that was 3% above the gas stream total pressure at the LPT inlet. This pressure was high enough to cool and purge the rotor but not so high as to generate extra leakage that would be costly to the engine performance. The expected flow to the LPT was 1.4% $W_{25}$ but this depends on the anticipated leakage around the Stage 1 nozzle. The actual flow indicated by the calibrated pipe pressure measurements and LPT nozzle hub cavity inducer pressure measurements was 1.2% $W_{25}$. The LPT casing manifold pressure was 4.8% above the LPT inlet gas pressure. This was 1.8% higher than the design level of 3% and was consistent with the reduced flow to the LPT. The reason for the reduced flow was the reduced leakage around the LPT Stage 1 nozzle. A comparison of the LPT design flows and measured flows is presented in Figure 287.

The LPT casing was cooled with fan air which was extracted from the fan bypass duct. The air entered a scoop on the side of the pylon. After entering the scoop, the air was diffused before entering a 270° plenum surrounding the LPT. From this plenum, the fan air entered an array of impingement tubes. The air then impinged on the outside of the LPT casing to cool the structure. The LPT active clearance control system was also combined with the primary casing cooling system. This was done by incorporating a casing cooling flow modulation valve between the fan duct scoop and the 270° manifold that surrounds the LPT.

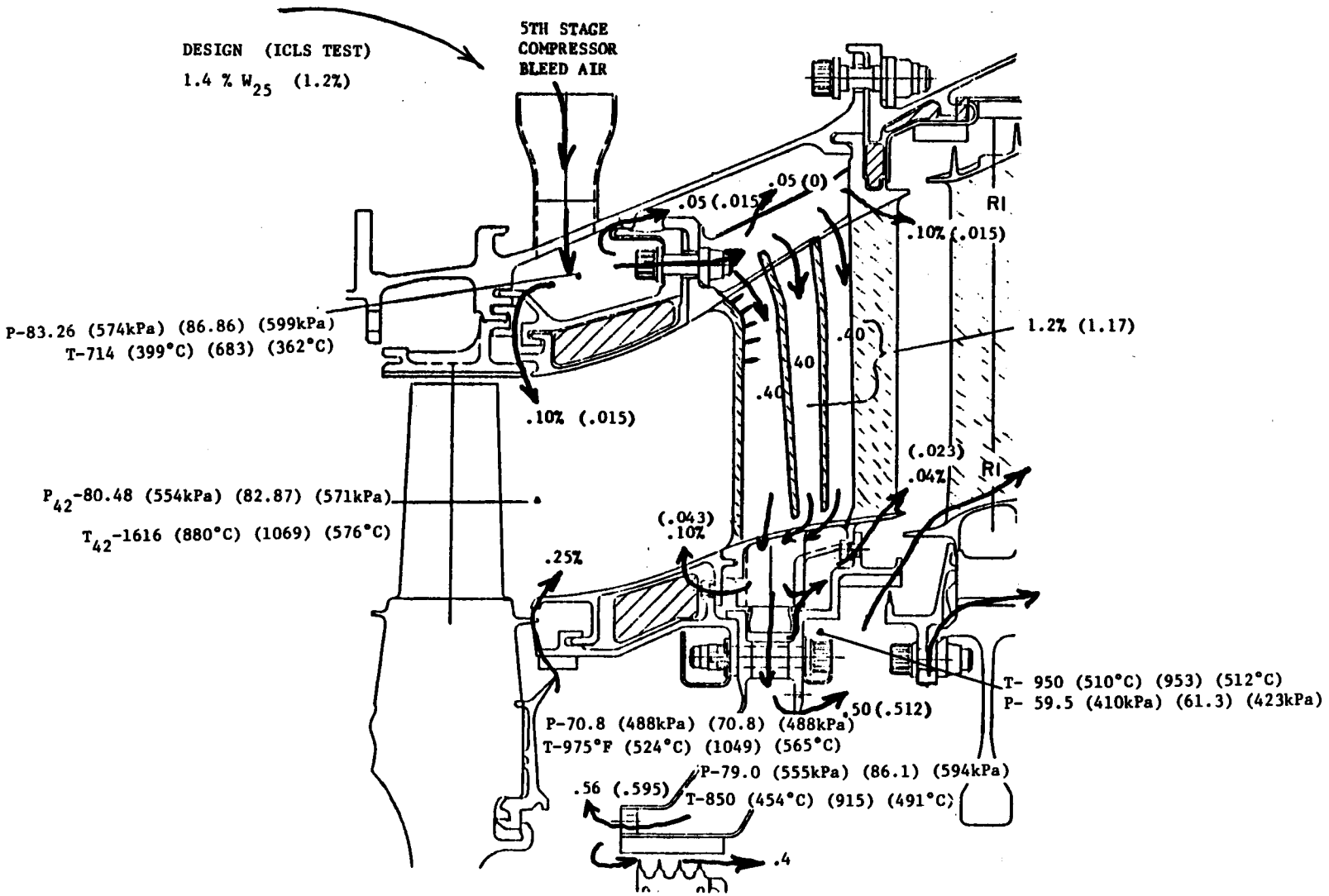


Figure 287. Low Pressure Turbine Cooling Flow.

The prime source of air for cooling the interior of the LPT was the Stage 5 compressor bleed which was delivered to the turbine through six pipes, equally spaced around the Stage 1 LP nozzle cooling supply manifold. This manifold, which was integral with the casing and outer transition duct hanger, allowed the cooling air to distribute itself uniformly around the inside of the casing. The total flow to the LPT amounted to 1.2% $W_{25}$ as compared to the design value of 1.4%. The cooling air then was fed into the 72 nozzle vanes and across the flowpath to the inner nozzle support structure. The cooling air warmed up 112°C (232°F) rather than the design value of 54°C (130°F) while flowing through the vanes. Most of the nozzle cooling was done near the leading edge where the highest stresses occur. Once the cooling air reached the nozzle hub it was delivered into the wheelspace supply plenum by 72 spoolies. The total cooling air passing through the nozzle was 1.17% $W_{25}$. Of this amount, 0.066% was then used to help purge the nozzle inner flowpath structure. Of the remaining 1.11% that entered the 360° wheelspace supply plenum, 0.59% was supplied to the forward wheelspace cavity and 0.511% was supplied to the aft wheelspace cavity. The plenum supply pressure was 599 kPa (86.1 psia) while the forward wheelspace cavity pressure was 521 kPa (75.6 psi) as shown in Figure 287. This yielded a 1.14 pressure ratio across the wheelspace injection holes. The holes were angled 60° from the circumferential direction which yields a tangential velocity. This tangential velocity that was imparted to the air by the inducer reduced the amount of boundary layer pumping that the HPT rotor had to do. Since the aft cavity, the low pressure rotor cavity, was at a pressure of 410 kPa (59.5 psia) the cooling air injection pressure ratio was higher and, thus, a higher tangential velocity was achievable. The low pressure rotor was rotating at less than 30% of the high pressure rotor speed and thus, the tangential velocity leaving the injection holes was better than twice the LP rotor wheel speed. With this system a substantial amount of work was obtained from the injected air as it boarded the rotor.

Of the 0.59% $W_{25}$ that was injected into the forward wheelspace cavity, 0.4% leaked back through the interturbine seal into the low pressure rotor cavity. Extensive seal clearance studies were conducted on the interturbine seal to assure the proper quantity of blockage air.

The LP rotor cooling/purge air supply consisted of the interturbine seal leakage air and the air that was injected tangentially into the rotor cavity from the wheelspace cooling supply plenum. The total cooling air supply to the rotor cavity was 0.91% $W_{25}$ for the ICLS engine. The temperatures that were measured indicated that all rotor heat transfer objectives were met. The test results do indicate that the cooling air temperature was warmer than expected.

The temperature rise of the cooling air in traversing the gas path through the LPT Stage 1 vane was approximately 56°C (100°F) higher than expected. This is shown in Figure 287 where the LPT inlet cooling air temperature is 18°C (31°F) cooler than the ICLS design temperature. By the time the cooling air had arrived at the hub inducer, the cooling air was 36°C (65°F) hotter than ICLS design. This resulted in the HPT Stage 2 disk aft cavity being approximately 56°C (100°F) warmer than expected as shown in Figure 288. The cavity was cooler than the core test but still hotter than the FPS design. The reson for the 70% increased temperature rise was partially due to the low flow but mainly due to the underestimation of the heat transfer to the cooling air. The heat flux to the cooling air was based on only the flowpath airfoil heat transfer. If the outer flowpath and inner flowpath structure heat flux is factored in, the temperature rise is more closely matched.

The measured LPT rotor cavity temperature was actually cooler than the HPT Stage 2 rotor aft cavity but still hotter than prediction by 20°C (36°F). This resulted in warmer disk bores. Presented in Figure 289 are the measured disk temperatures and the projected temperatures at the FPS design point. The design temperatures are also included as references.

In general, the measured metal temperatures matched up favorably with the design value. The Stage 1 disk rim and forward blade retainer temperatures were close to predictions. The bore temperatures were 44°C (79°F) hotter than prediction on Stage 1, 16°C (29°F) hotter than prediction on Stage 2 and 41°C (74°F) cooler than prediction on Stage 5. The fourth and

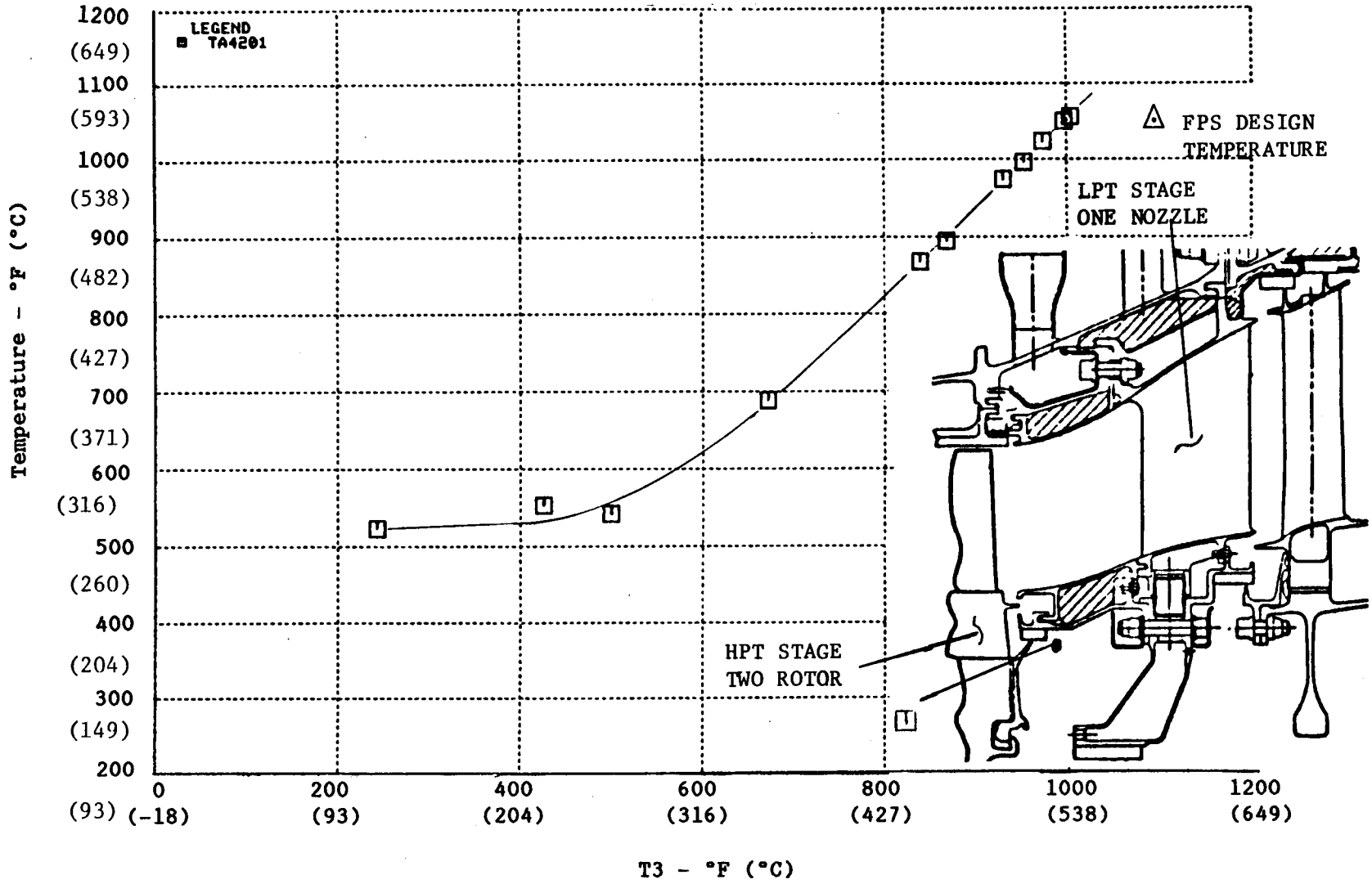


Figure 288. High Pressure Turbine Stage 2 Disk Aft Cavity Purge Temperature Vs. T3.

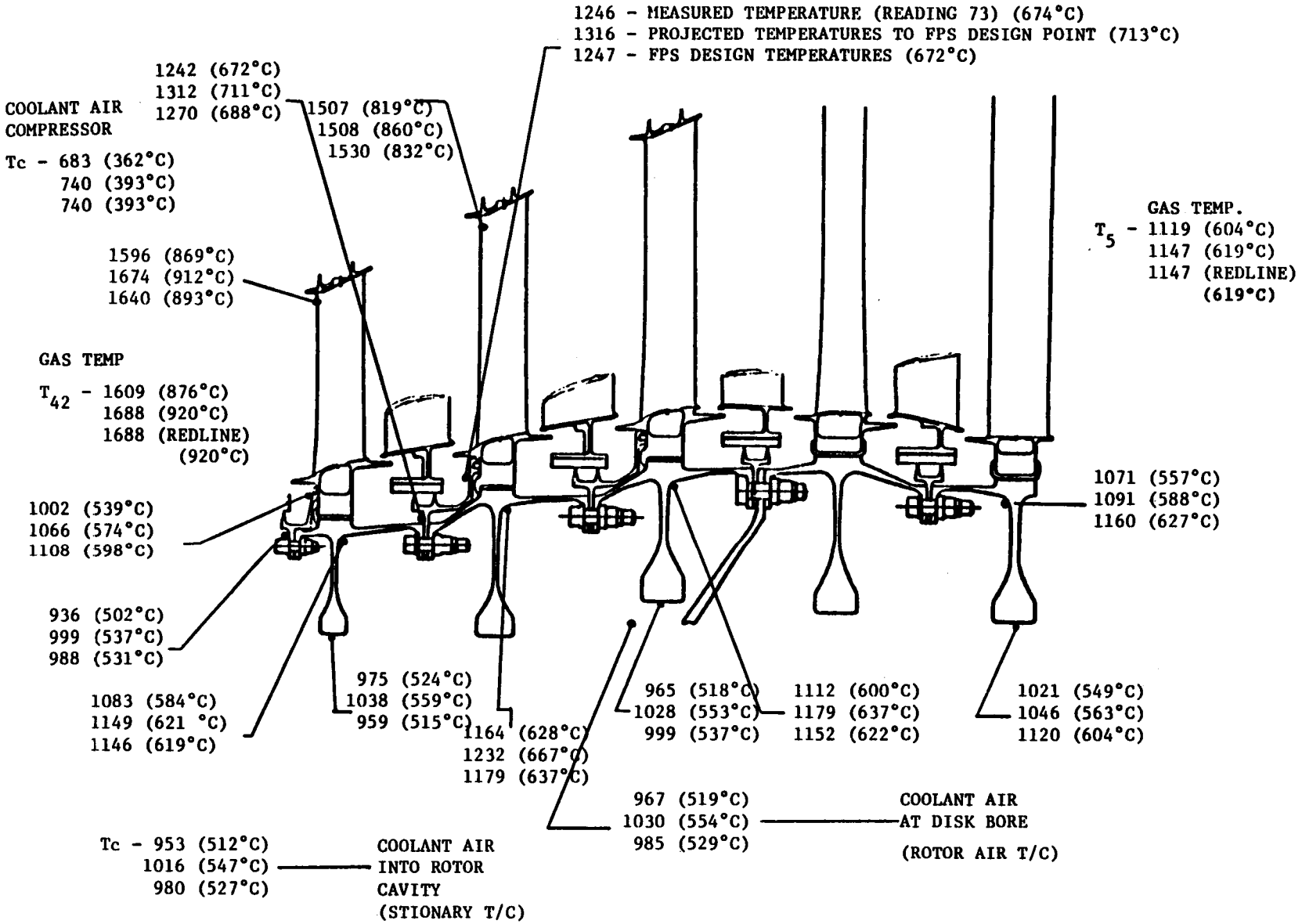


Figure 289. Low Pressure Turbine Maximum Power Temperature - Measured vs. Design.

fifth stage turbine bore rotor cavity was not purged with cool air but rather by LPT discharge gas. The fifth stage disk rim metal temperatures were close to the level of the gas temperature leaving the LPT. The bore was cooler and indicates that it may have felt the effects of either radiation to the sump or there may have been some leakage from the forward rotor cavity around instrumentation that may have diluted the gas down to a lower temperature. Instrumentation lead out leakage paths will be investiaged during tear down, if possible.

The rotor blade tip metal temperatures were hotter than prediction by 19°C (34°F) and 28°C (50°F) on Stage 1 and Stage 2, respectively. This can be explained by the LPT exit temperature profiles which indicate a radial outward skew in Figure 290. The LPT inlet temperatures profile also shows a similar amount of skewing as shown in Figure 291. Significantly less data were obtained at the LPT inlet and thus the average gas temperature as indicated by the LPT work extraction does not match up well with the measurements.

The radial outward skewing of the profile not only resulted in hotter blade tip temperatures but also in hotter than expected casing temperatures as shown in Figure 292. Along with the measured values are the design values. The actual measured values were all above the expected levels. Besides the gas temperatures being higher along the outer casing, the back side cooling was not doing an efficient job at low flow conditions, 0.08% $W_{25}$. The data indicate that the fan cooling air had risen in temperature significantly between the time it left the fan duct and when it arrived at the inlet to the impingement manifold. This is shown in Figure 293. On the bottom half of the engine, the cooling air temperature had risen as much as 111°C (200°F) at max power conditions. This in itself would cause approximately 42°C (75°F) of the metal temperature increase. This problem can be further enhanced if the air continues to rise in temperature in the impingement manifold before impingement.

At the higher cooling flow quantities, as shown in Figure 294, the active clearance control system became more effective. Outer casing

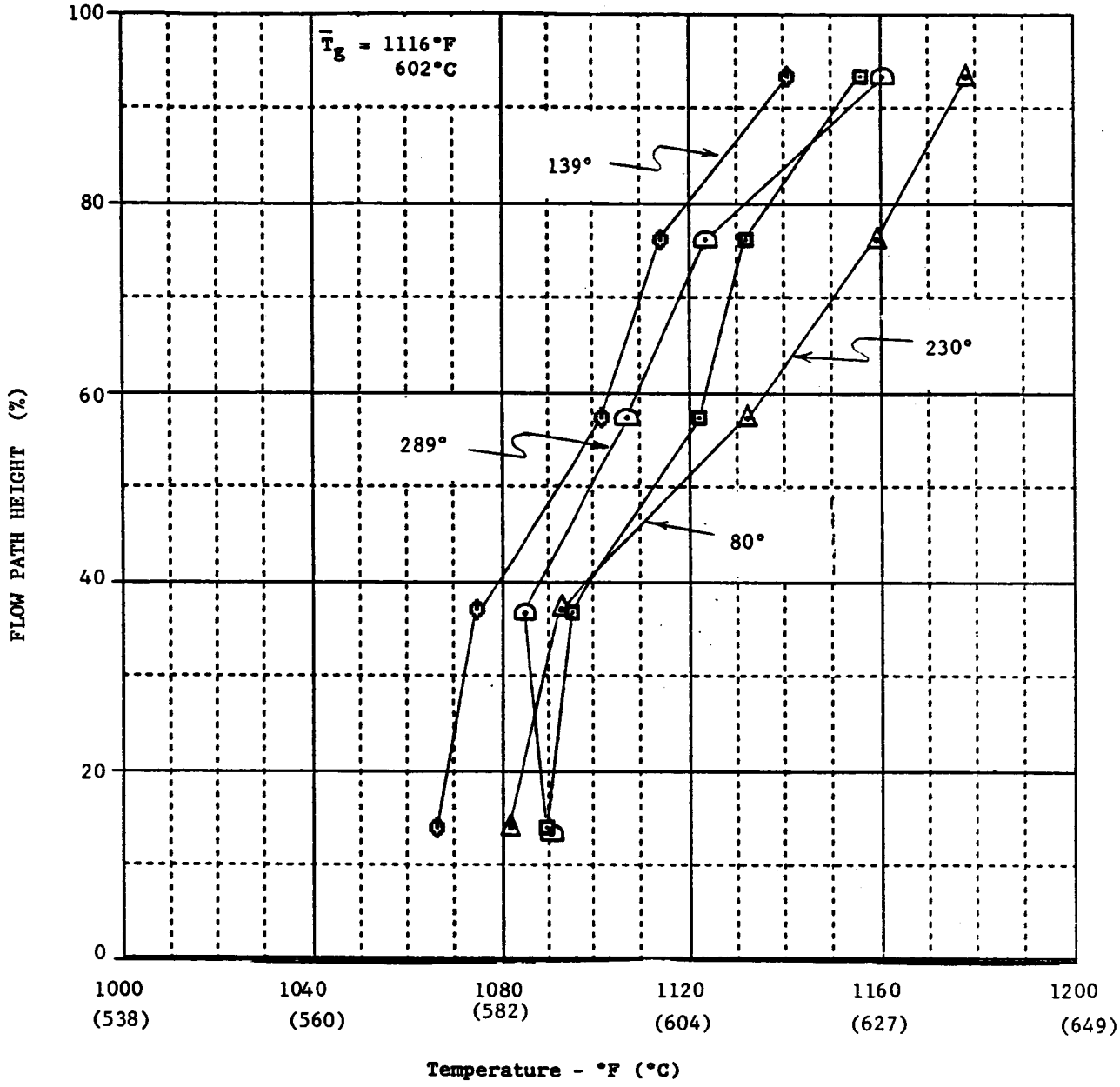


Figure 290. Low Pressure Turbine Exit Temperature Profile.



C-6

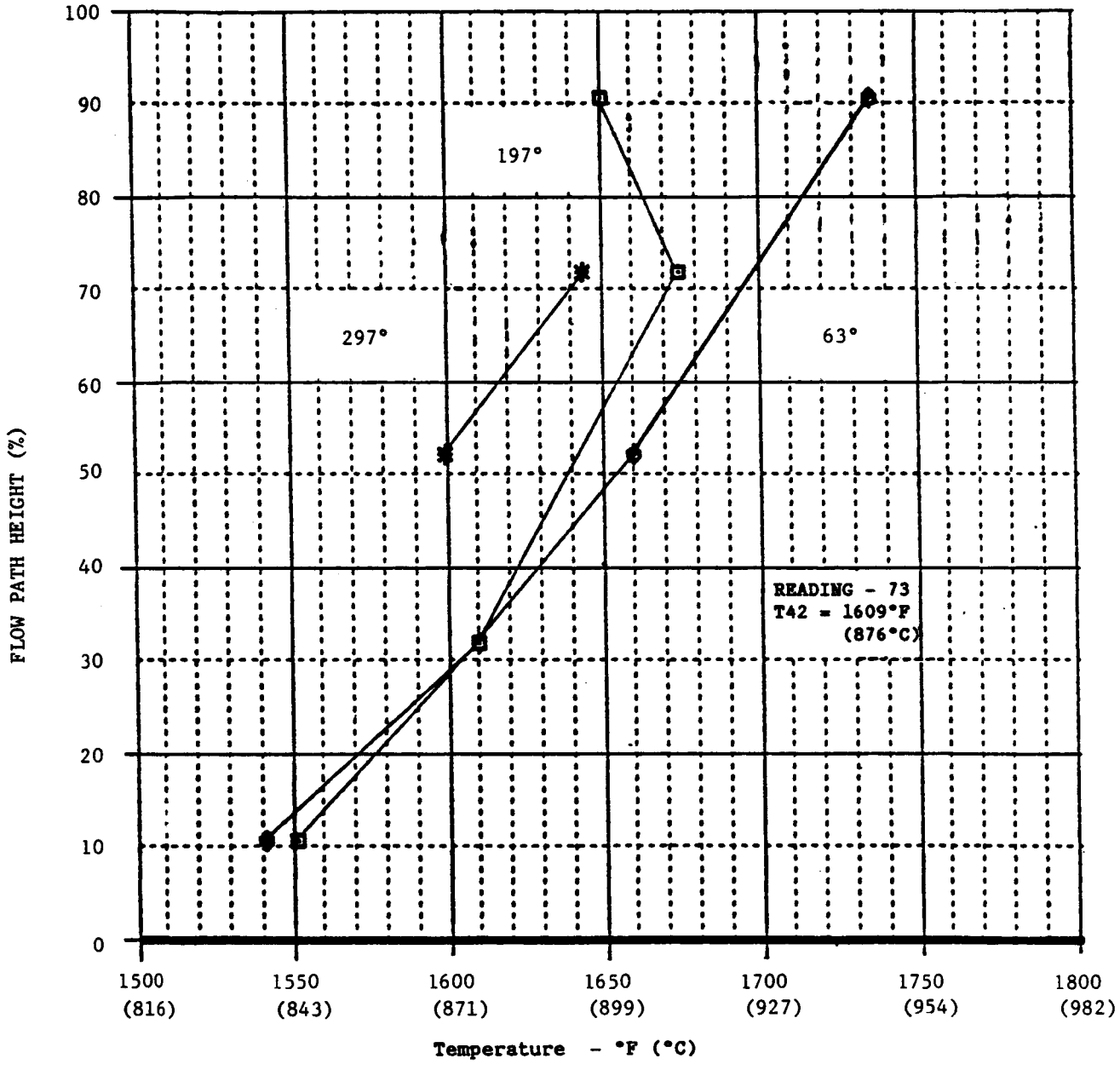


Figure 291. Low Pressure Turbine Inlet Measured Gas Temperature at Maximum Power Take-off,

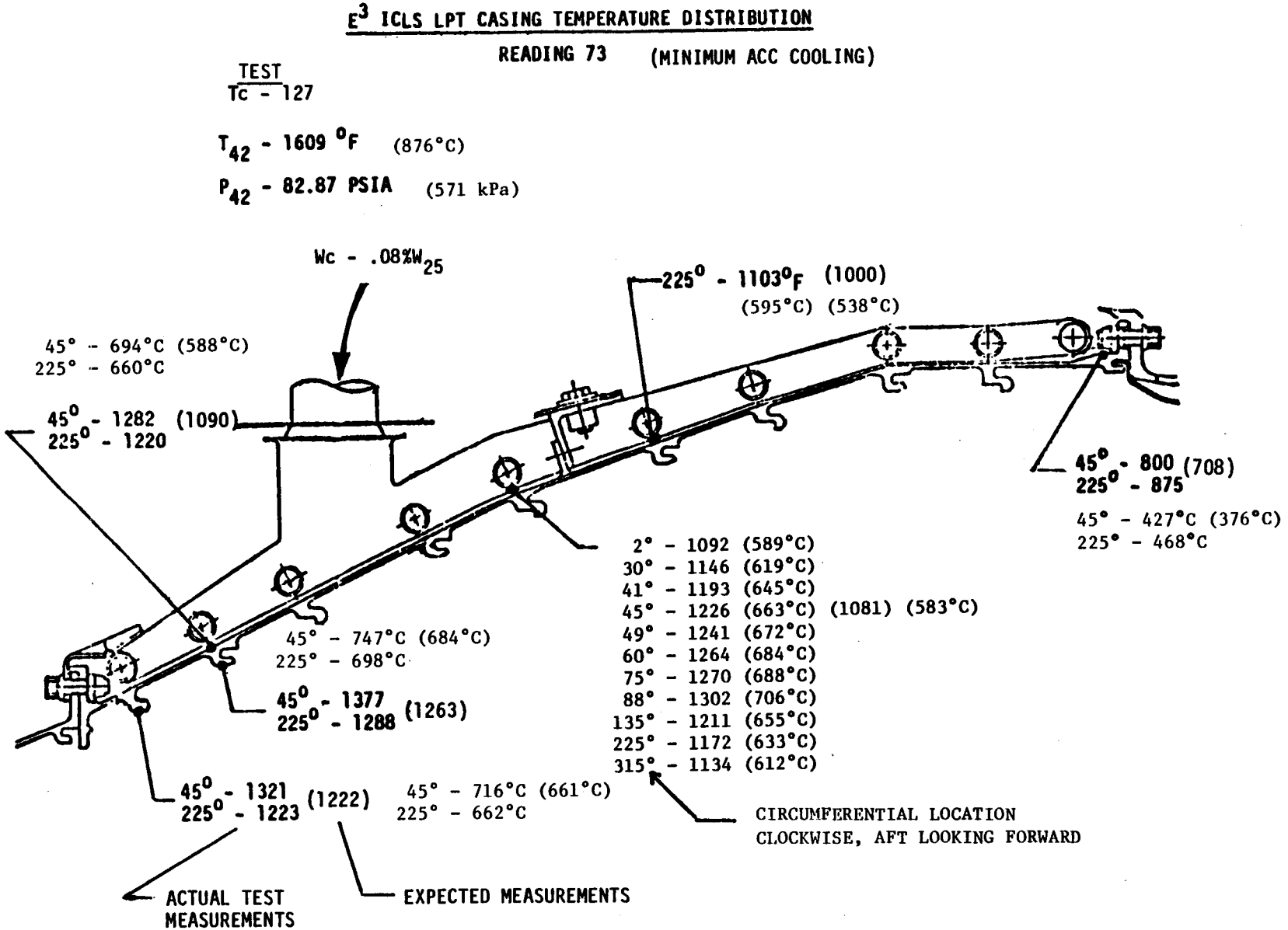


Figure 292. Low Pressure Turbine Casing Temperature Distribution.

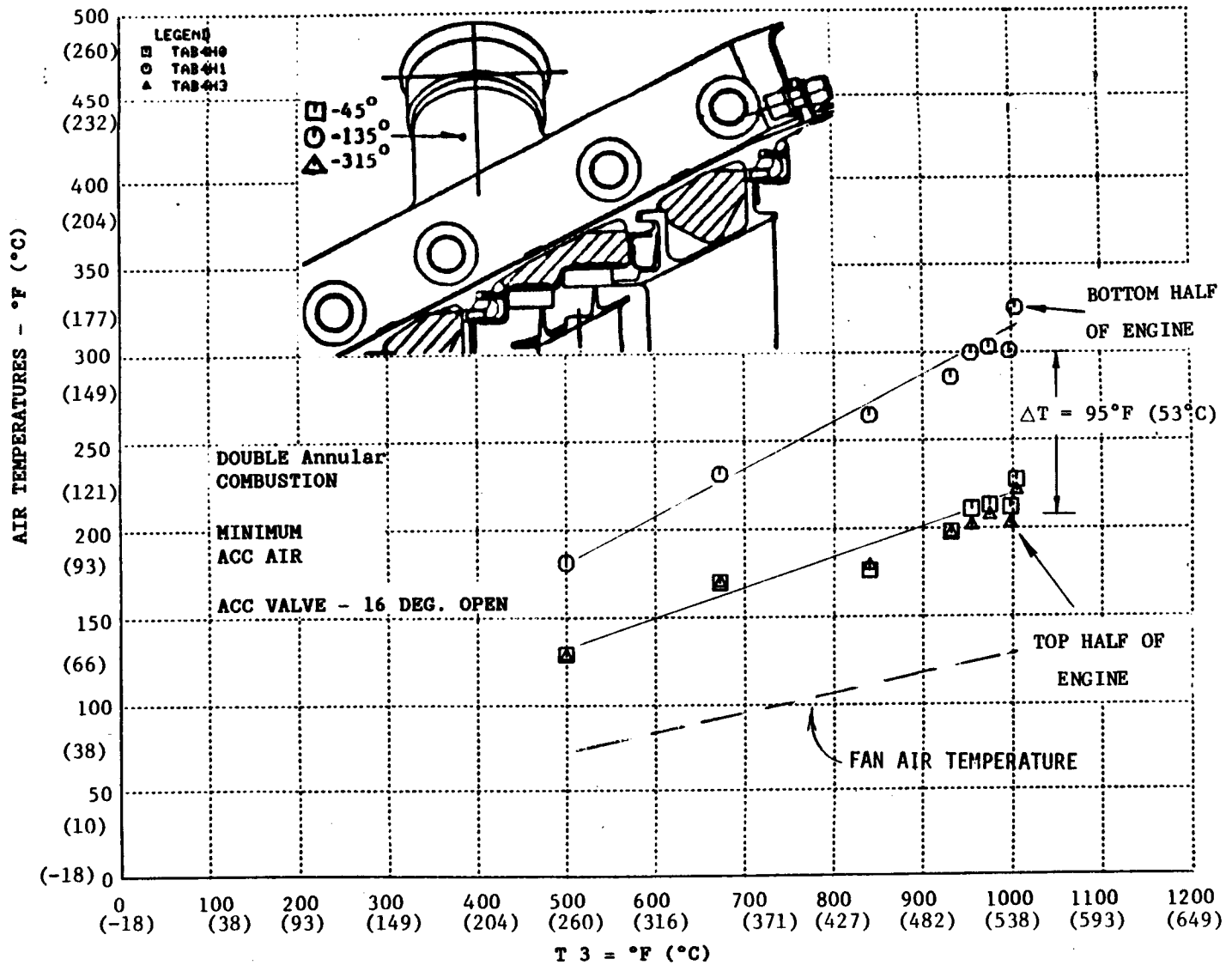


Figure 293. Low Pressure Turbine ACC Liner Air Temperature vs. $T_3$.

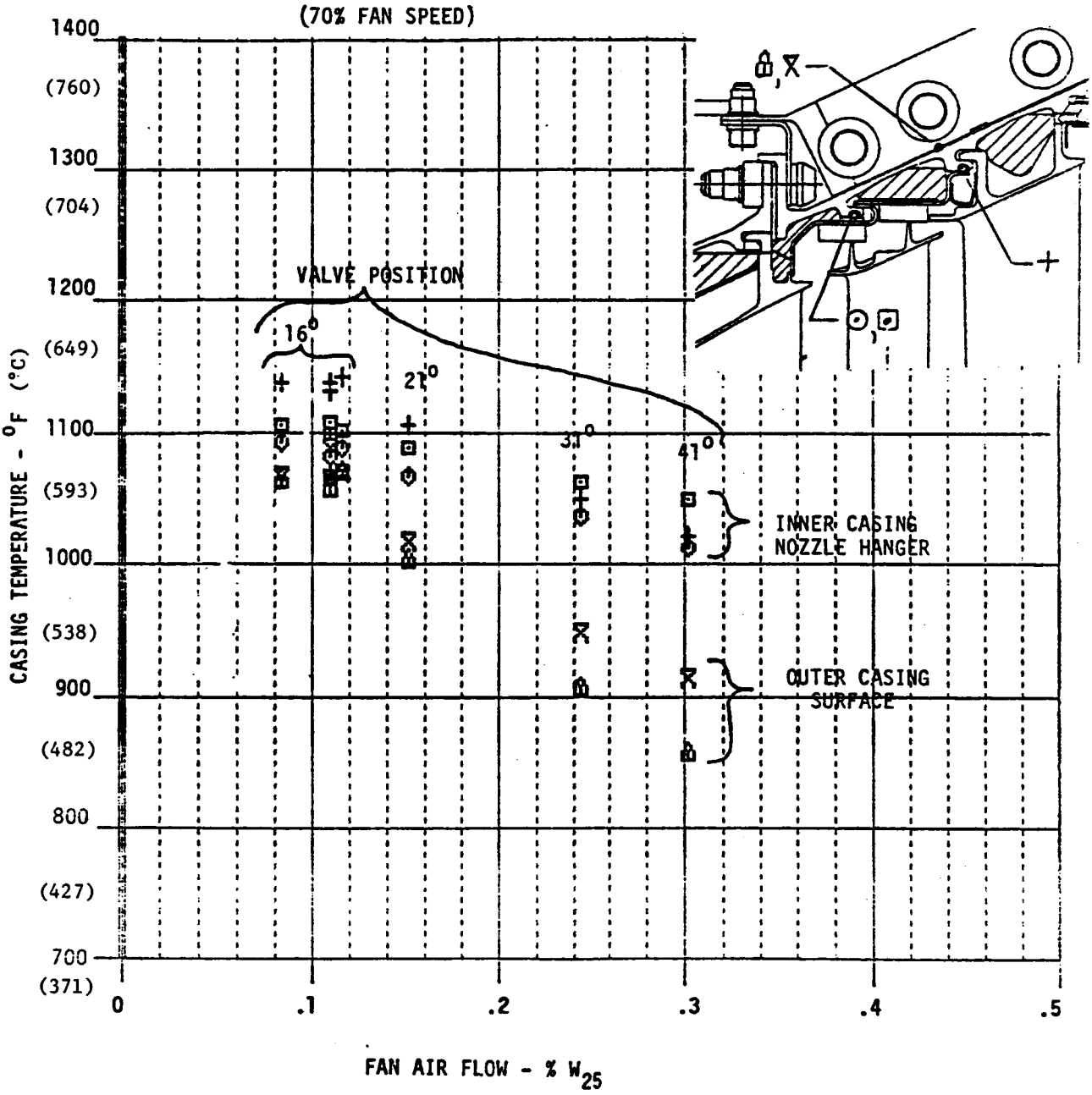


Figure 294. Low Pressure Turbine Stage One Casing Temperature vs. Cooling Flow.

temperatures were reduced from a level of 577°C (1070°F) at minimum flow conditions to 460°C (860°F) at 0.3% $W_{25}$. The valve was open 41° which corresponded to approximately 70%. This 117°C (210°F) casing temperature reduction occurred at 70% fan speed. The ACC valve could not be opened more than 22° at max power or excessive blade angle wing rubs would have occurred on the fifth stage rotor blade platforms. At 22°, the casing temperatures were brought down to a level where all measured metal temperatures were below the design limit of 704°C (1,300°F).

The Stage 1 nozzle was cooled only around the leading edge outer band to a significant degree. The purpose in cooling this region is to keep the material properties of the R'77 at an acceptable level so that the high gas bending loads can be withstood. The design objective was to keep the outer band leading edge below 918°C (1684°F). The maximum temperature that was recorded in this area was 815°C (1499°F), as shown in Figure 295. The results of the test indicate that the cooling in the passageways may be reduced. This will also help reduce the rotor purge cooling air temperature.

The maximum temperature that any part of the nozzle achieved was 891°C (1635°F) which was at the pitch line section trailing edge. The gas bending loads are down and the material properties are sufficient to handle the stress.

Another concern in the design of the nozzle was the engine start transient. The engine had to be started and acceled to idle power on the pilot combustor. LPT inlet and exit gas temperatures were measured to see how hot they would get. The results of these measurements are presented in Figures 296 and 297. The Stage 1 vane metal temperatures during the start transient are presented in Figure 298. The maximum temperature occurred at the pitch and did not exceed 677°C (1250°F). The temperature difference between the outer band and inner band shows the significant temperature profile coming out of the HPT. This was due in total to starting the engine and acceling to idle on the pilot combustor only.

The Stage 1 blade tip was also an item of concern. The blade was not cooled and thus would not feel the complete effect of the skewed combustor

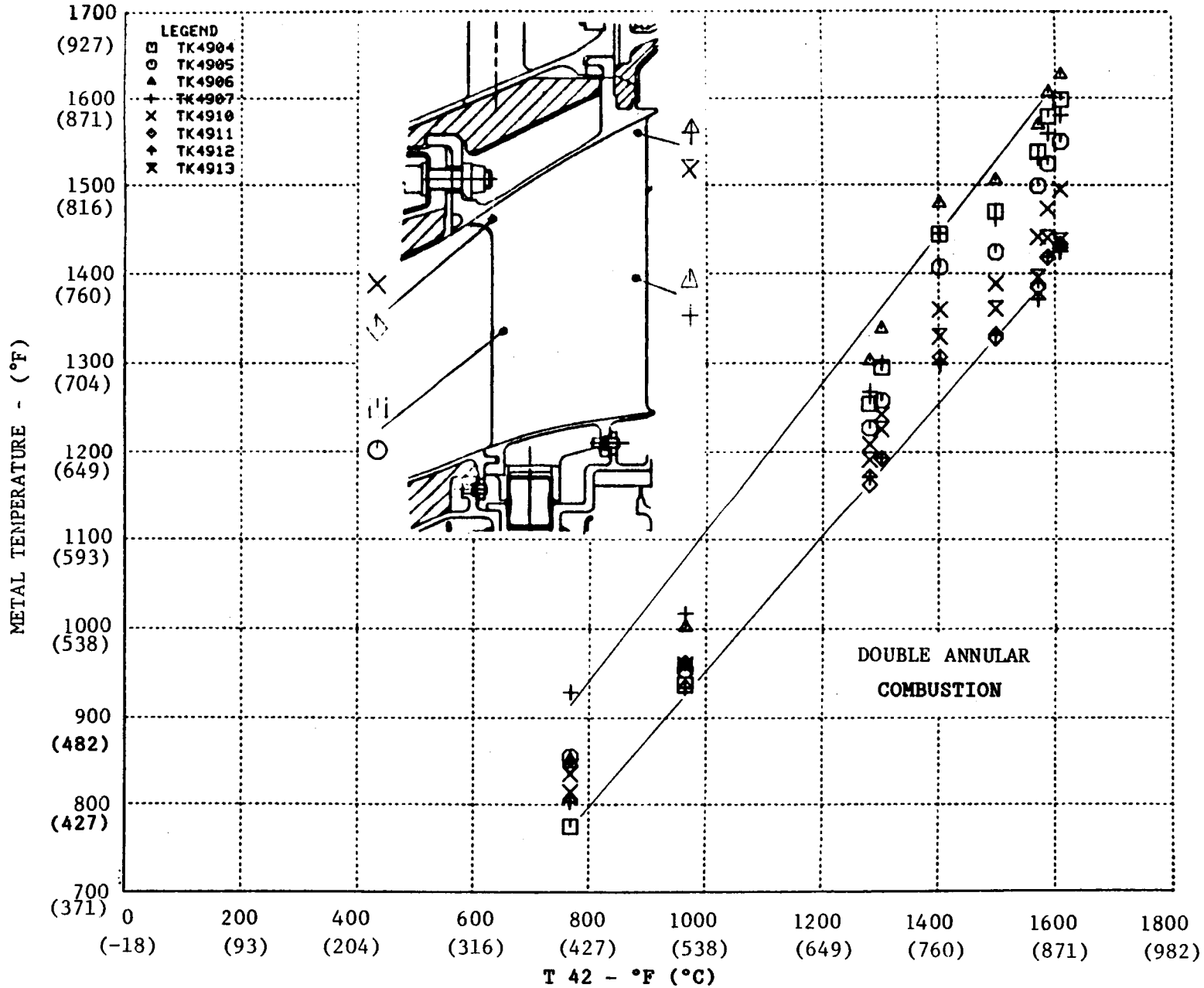




Figure 295. Low Pressure Turbine Stage 1 Stator Surface Temperature vs $T_{42}$.

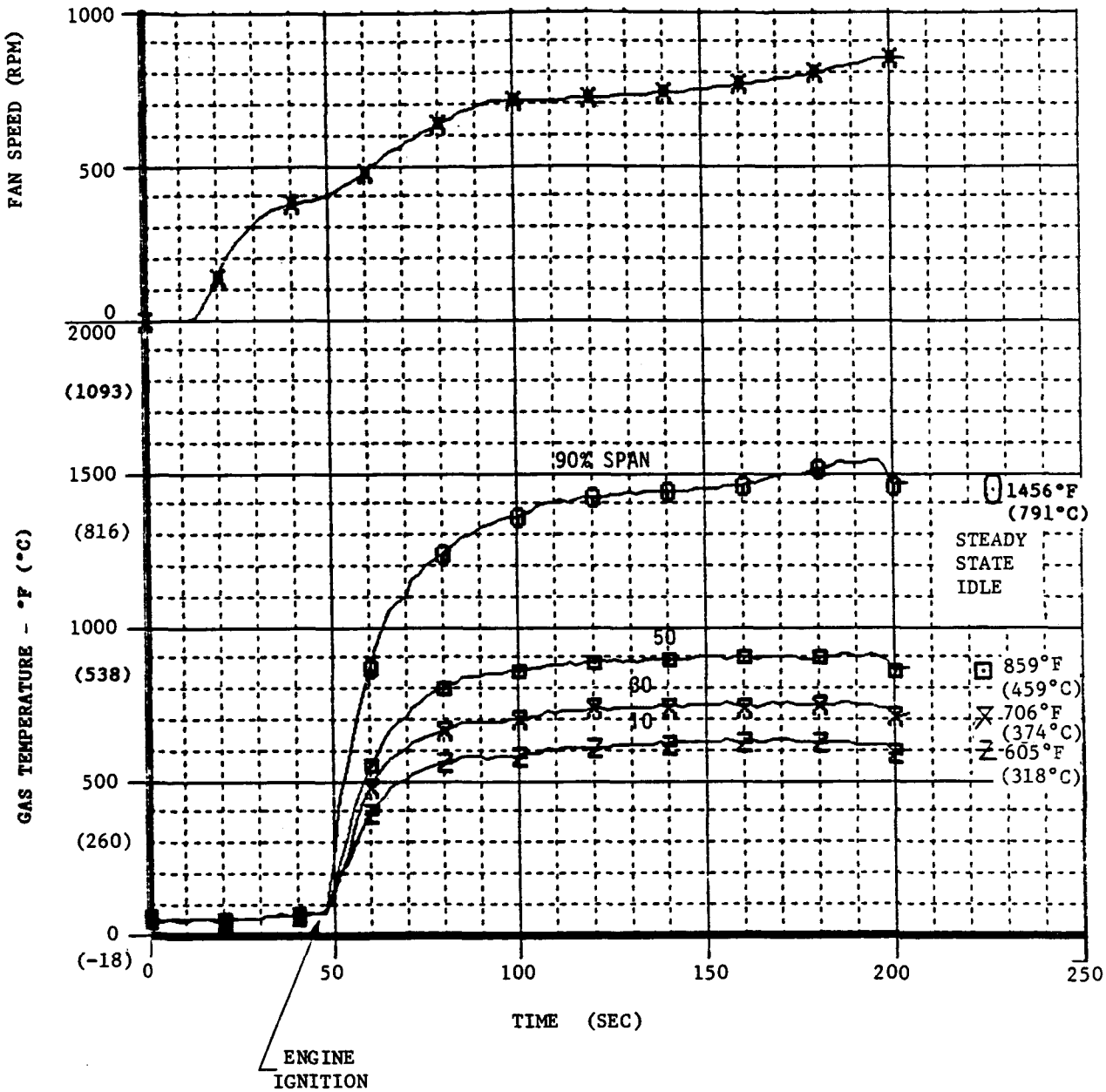


Figure 296. Low Pressure Turbine Inlet Gas Temperature During Cold Engine Start.

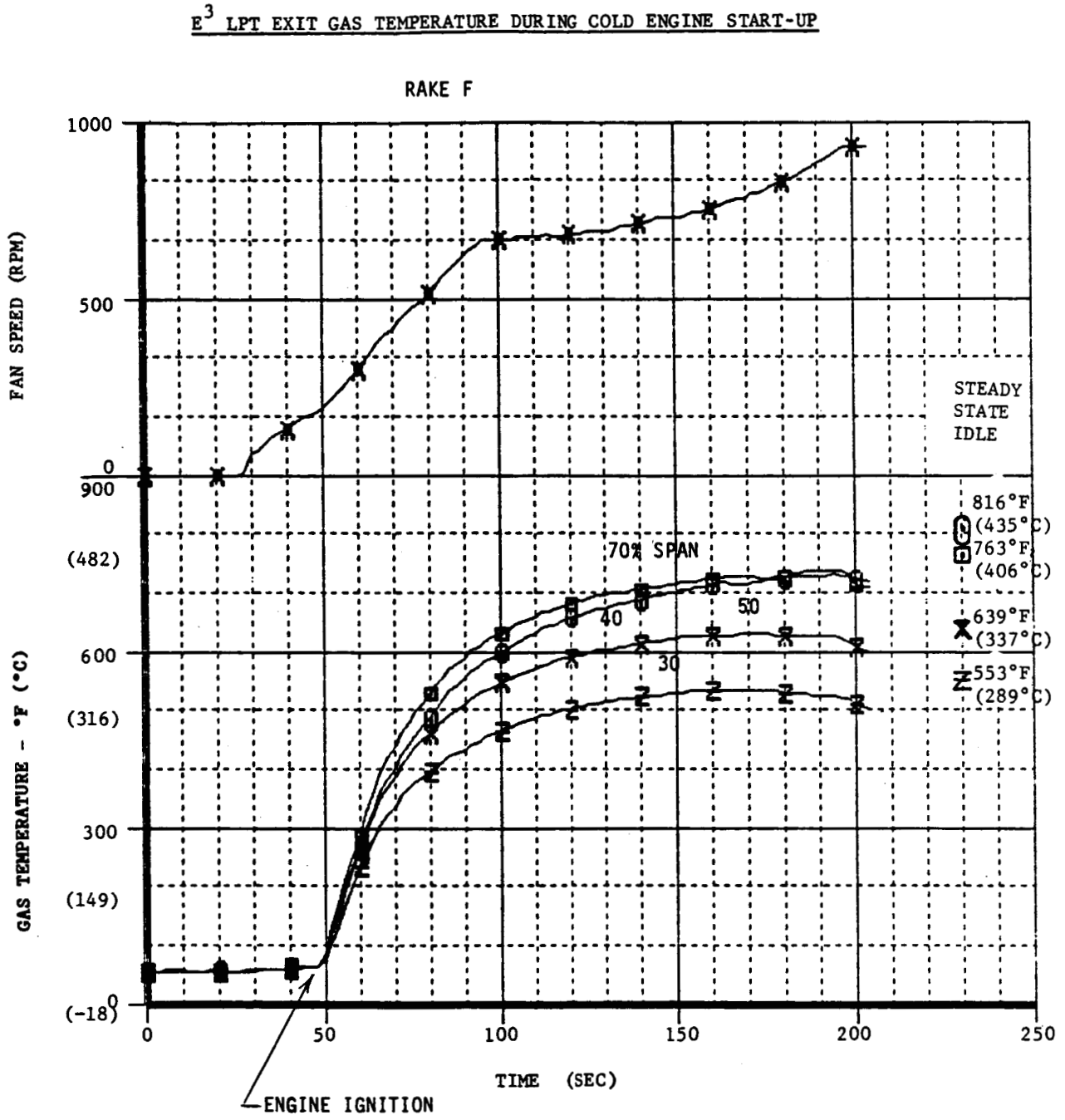


Figure 297. Low Pressure Turbine Exit Gas Temperature During Cold Engine Start.

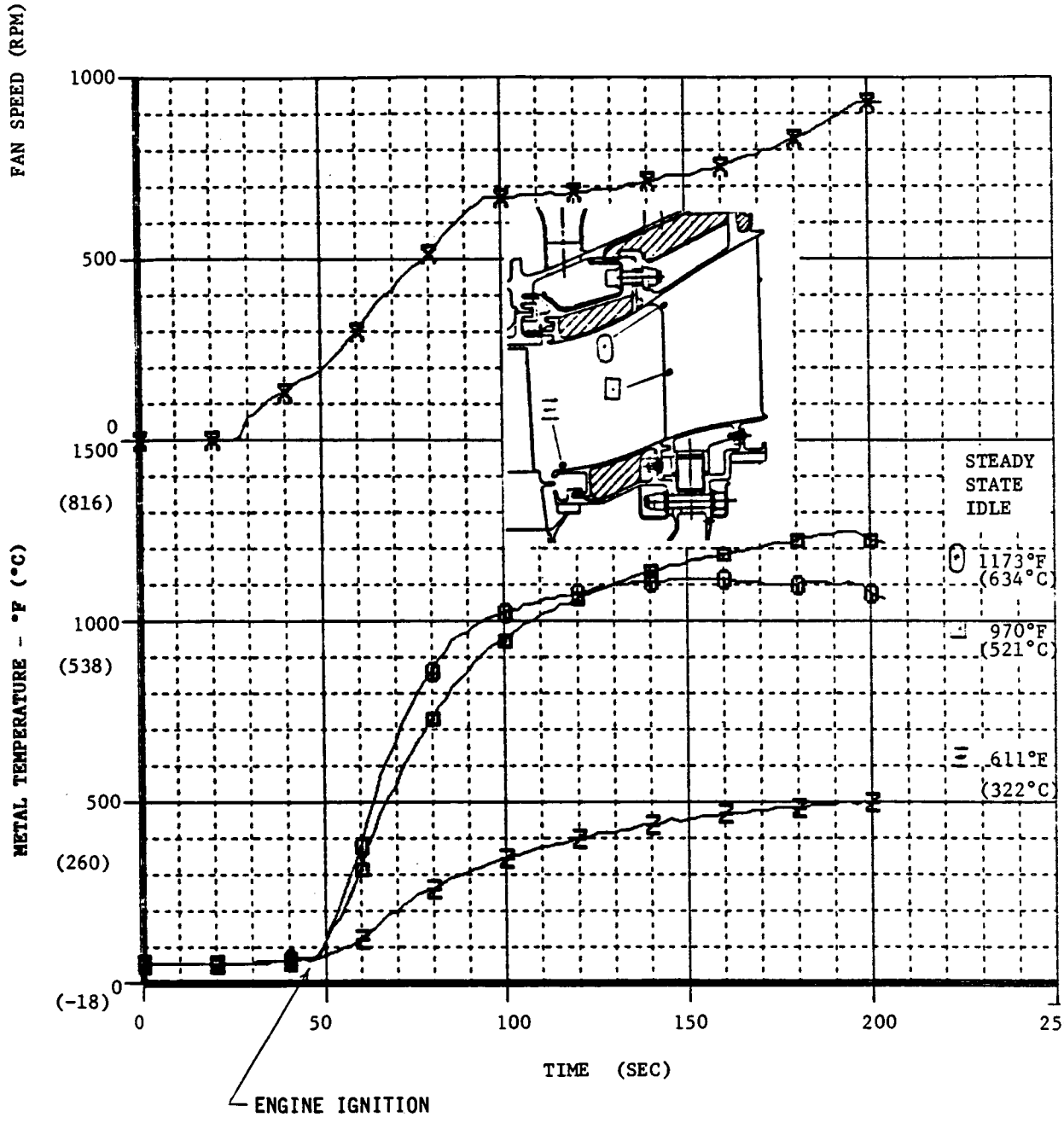


Figure 298. Low Pressure Turbine Stage One Vane Cold Start Transient Temperatures.

exit profile due to starting on the pilot combustor only. Blade tip transient temperatures were measured during start and indicated that the blade tip did not go over 760°C (1400°F) as shown on Figure 299. The steady-state blade tip temperature was approximately 83°C (150°F) cooler than the start transient max value.

Several other start transient temperatures were measured but the most significant data was obtained on those components that do not have a fast thermal response rate. Most of these included the rotor and rotor air supply system. Two transients were evaluated, No. 7018, a warm engine start and No. 7019, a cold engine start. For the warm engine start, the engine was shut down from idle power for 10 minutes before restarting. Figure 300 compares the LPT Stage 1 disk temperatures for the warm and cold engine starts. As can be seen, there was a 204° to 260°C difference (400° to 500°F) in the disk temperatures. This can have a significant impact on the blade tip clearances and is one of the reasons for shutting off ACC air during shutdown, thus allowing a tip clearance that will not be rubbed out by the warm disks upon restart. The Stage 5 disk showed a similar difference in temperature as shown in Figure 301.

### 6.11.3 Conclusions

The preliminary results of the test indicate that all LPT heat transfer objectives were met. The primary heat transfer objectives were:

- Purge the forward rotor cavities
- Purge the HPT Stage 2 disk cavity
- Demonstrate the 5th stage compressor bleed air supply to LPT along with the compressor ACC systems
- Demonstrate the LPT active clearance control fan air supply system
- Show the feasibility of the LPT exit gas purge aft rotor cavity
- Cool the LPT Stage 1 nozzle leading edge at the outer band
- Keep the casing temperatures within the material limits of INCO-718.

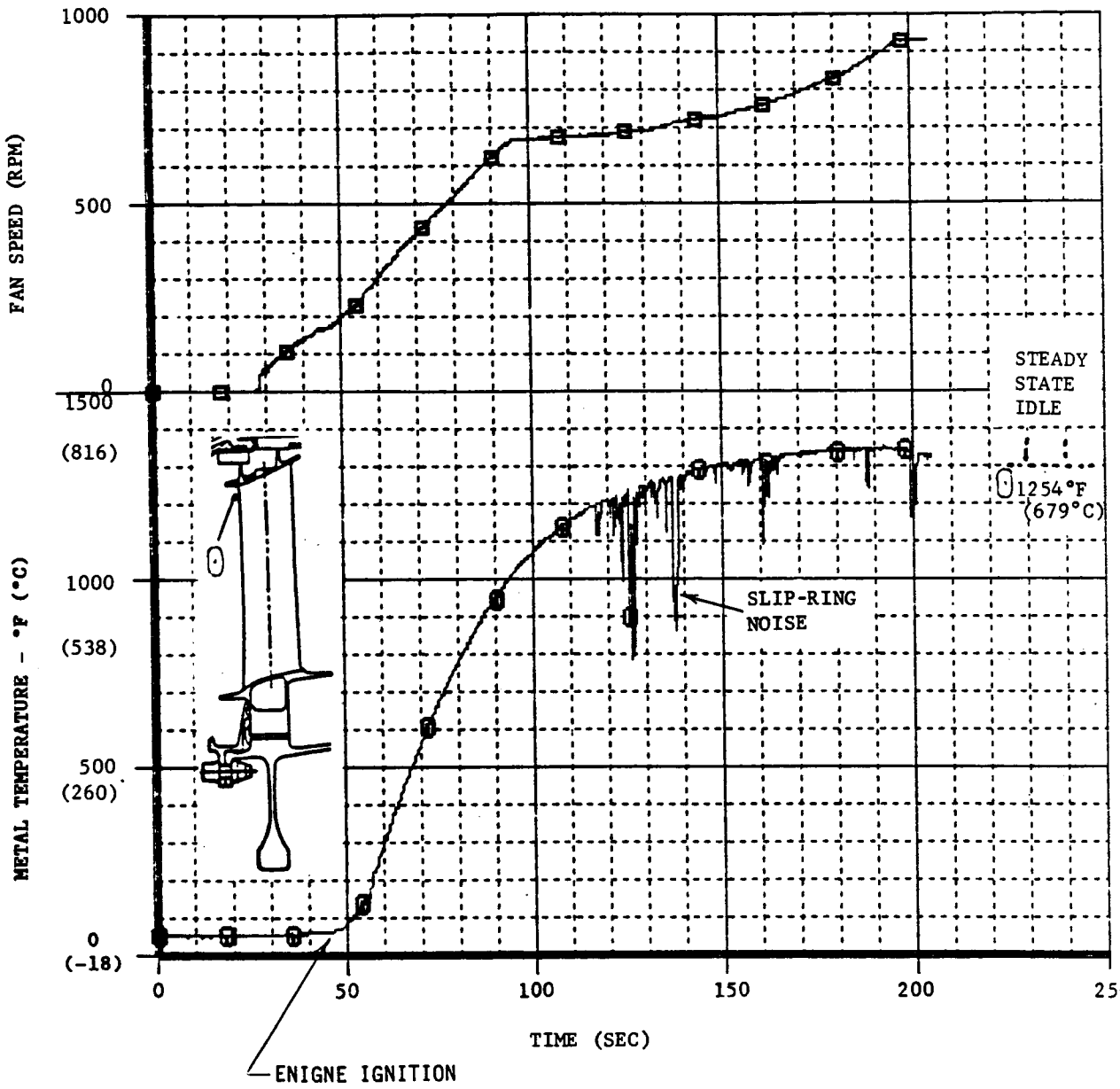


Figure 299. Low Pressure Turbine Stage 1 Forward Rotor Tip Temperature During Cold Engine Start-Up.

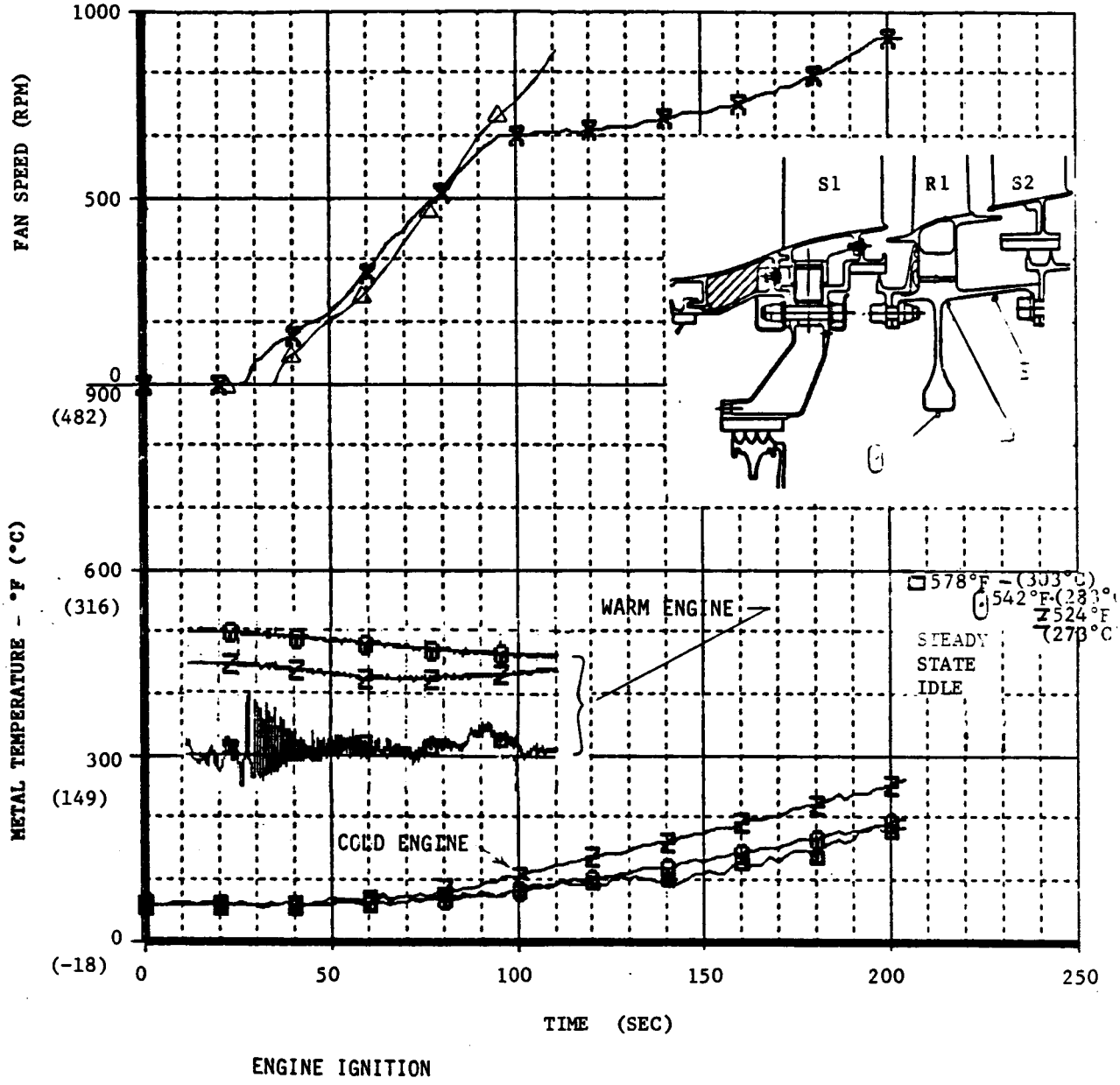


Figure 300. Low Pressure Turbine Stage One Disk Start Transient Temperatures.

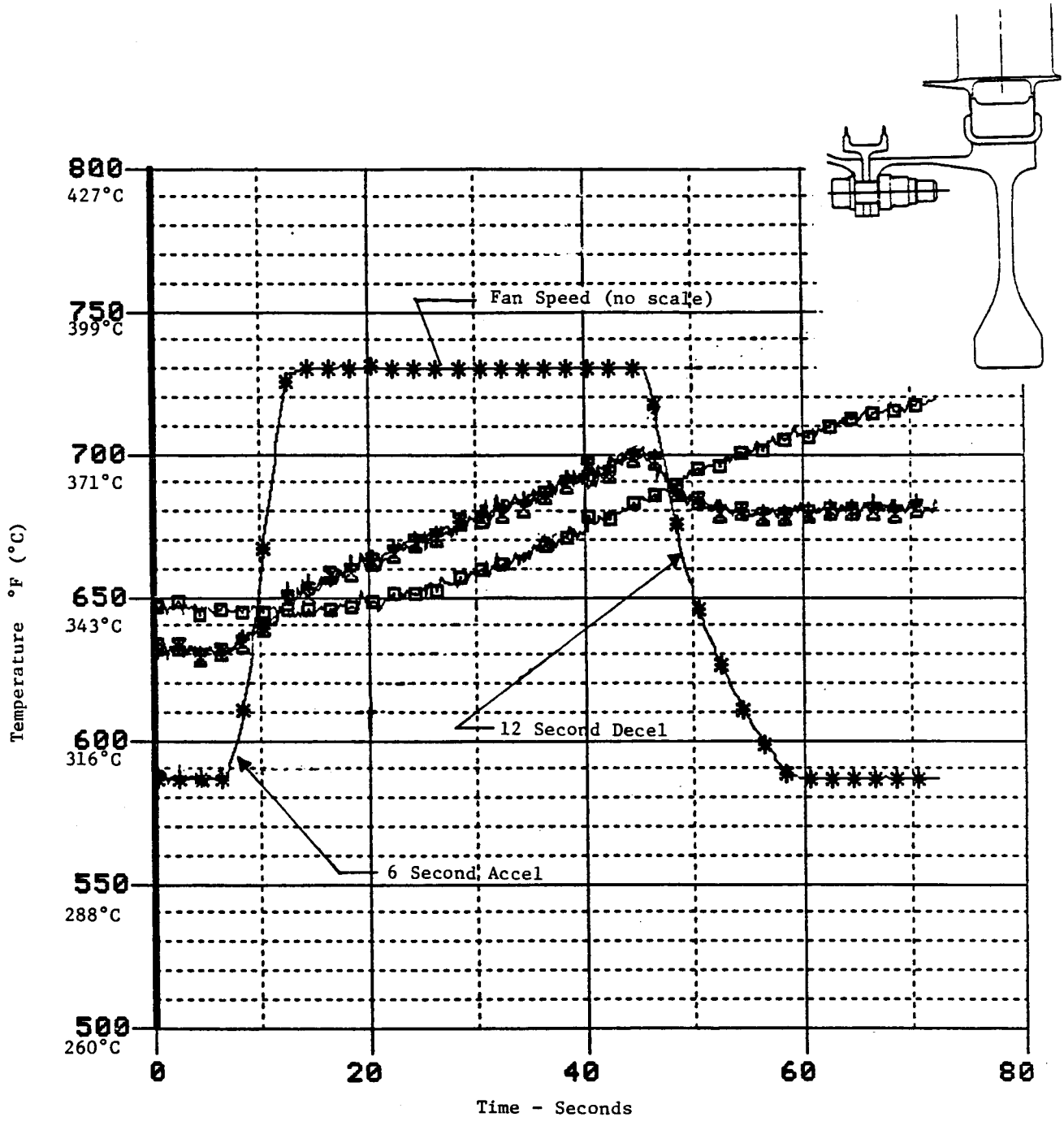


Figure 301. Low Pressure Turbine Rotor Stage Five Disk Transient Metal Temperatures.

## 6.12 LOW PRESSURE TURBINE AERODYNAMIC PERFORMANCE

The aerodynamic design point for the LPT was the M 0.8/10.67 km (35,000 ft) max climb condition. Design point aero parameters are compared to those for the max power point predicted for the ICLS static testing in the table below:

| Item | Symbol | Design Point, M0.8/10.67 km (35,000 ft.) | ICLS Max Thrust Predicted for Static Test |
|---|---|---|---|
| Low Function | $W\sqrt{T}/P$ | 83.40 | 83.53 |
| Extraction | $\Delta h/T$ | 0.0760 | 0.0714 |
| Corrected Speed | $N/\sqrt{T}$ | 78.50 | 72.68 |
| Pressure Ratio | P/P | 4.22 | 3.77 |
| Loading | $gJ\Delta/2U^2$ | 1.292 | 1.401 |

Note from this comparison that the LPT runs somewhat more highly loaded for the max power (or takeoff) condition that for the altitude climb design point. Note further that design values of pressure ratio and corrected speed are never attained for near sea level operation.

ICLS hardware discrepancies were minimal and consisted mainly of deviations in actual vs. design intent bladerow throat areas. These variations were usually less than 2%.

Performance instrumentation for the ICLS was a follows:

| Plane | Location | Measurment | Number and Type |
|---|---|---|---|
| 42 | HPT Exit | $P_T$ | 3 radial probes, 5 each |
| 42 | HPT Exit | $T_T$ | 3 radial probes, 5 each |
| 50 | LPT Exit | $P_T$ | 4 radial probes, 5 each |
| 50 | LPT Exit | $T_T$ | 4 radial probes, 5 each |

Plane 42 rakes were located nominally 3.55 cm (1.4 in) downstream of the HPT Stage 2 blade exit. Plane 50 rakes were loacted circumferentially between the turbine rear frame struts.

Interstage static pressure measurement was provided by static pressure taps located in the wheelspace before and after each LPT rotor. There were two taps each on the inner and outer wall at each axial location.

Results from the performance run are presented in Figures 302 through 307. Figure 302 presents ICLS LPT flow function and pressure ratio (total-to-total) as a function of percent corrected fan speed, PCN12R, compared to pretest prediction. Note that these data track prediction nicely, even into the Flight idle range (PCN12R≈30%). This is an important consideration since it is the pressure ratio, together with inlet flow and temperature levels, which set the idle (or available) level of LPT power, the denominator in the expression for efficiency.

It should be noted that all pretest predictions are based on five-stage rig test results.

Figure 303 presents ICLS LPT efficiency as a function of PCN12R compared to pretest prediction. The efficiency plotted is that determined from measured fan power, which is based on flow and temperature rise for the bypass and fan hub/booster streams. A redundant measure of power supplied to the fan was provided by measured LPT temperature drop (Plane 42 to Plane 50); however, circumferential variations in temperature measured at both planes precluded any accurate determination of LPT temperature drop. This is discussed briefly later in this section.

Note from Figure 303 that, in spite of the relatively large amount of scatter, the preliminary level of LPT efficiency is down from 1.0 to 1.5 points from predictions based on rig test results. Generally the data does show that the trend of efficiency versus fan speed matched predictions.

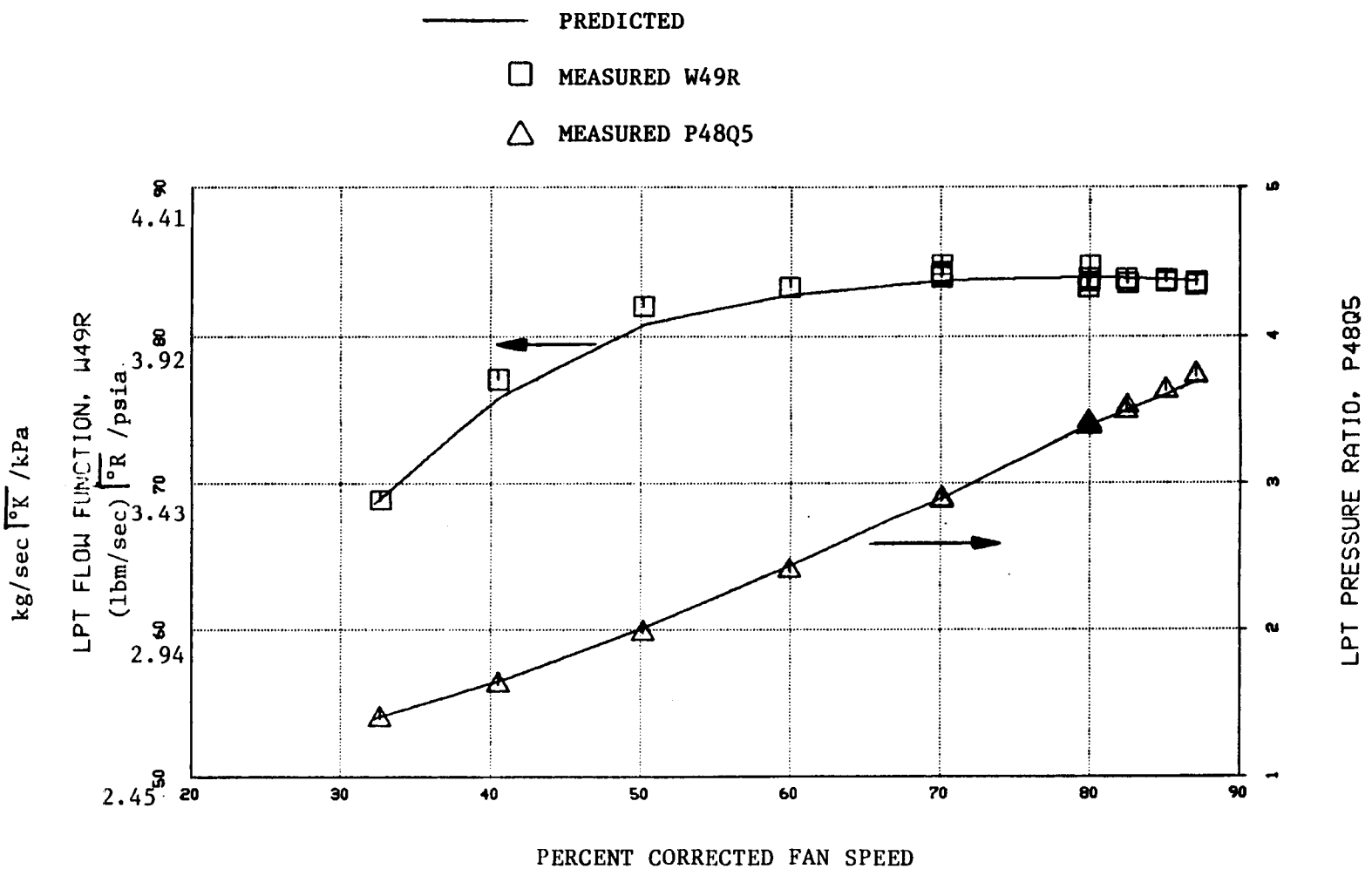


Figure 302. Low Pressure Turbine Function and Pressure Ratio vs Percent Corrected Fan Speed.

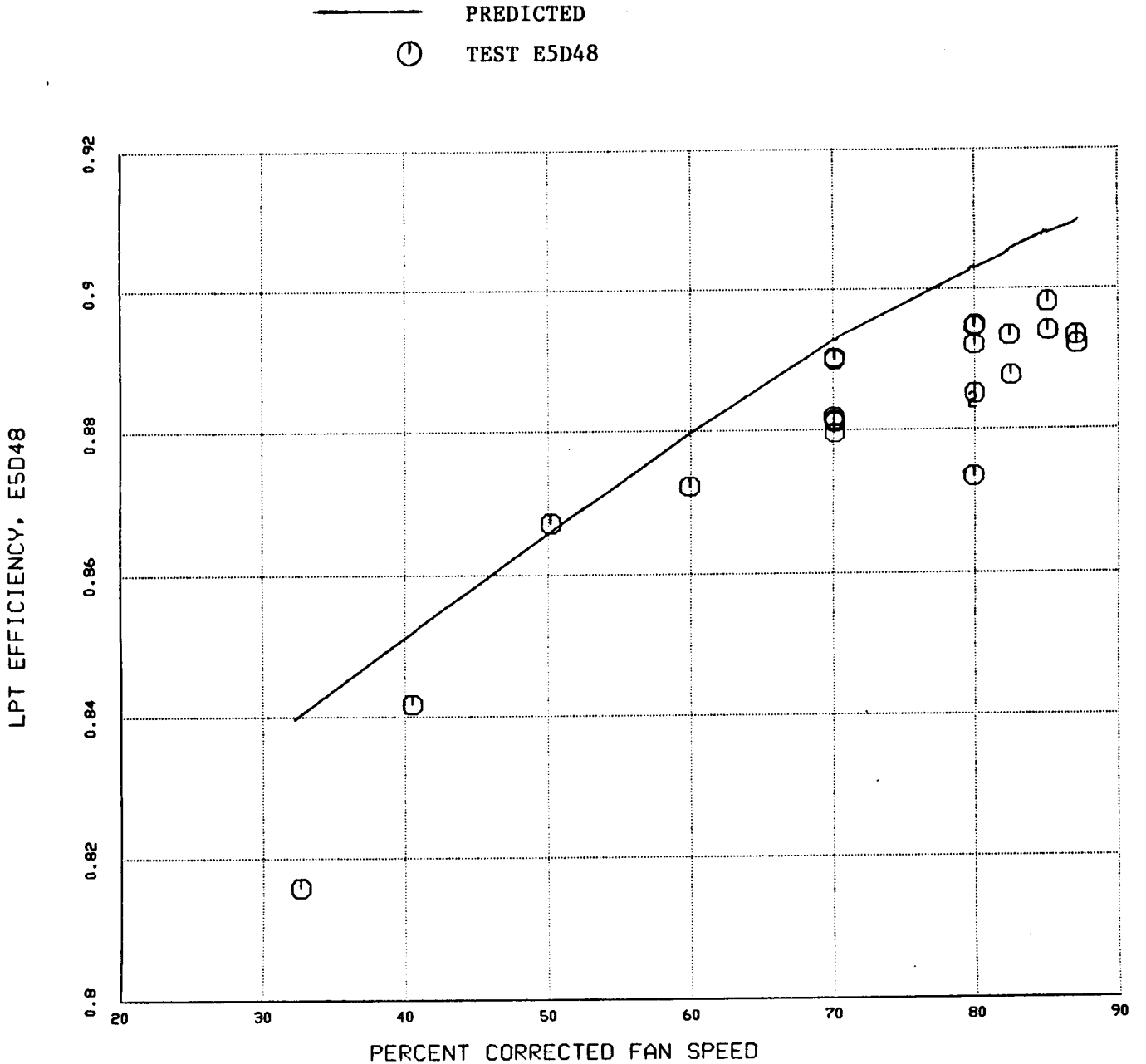


Figure 303. Low Pressure Turbine Efficiency vs Percent Corrected Fan Speed.

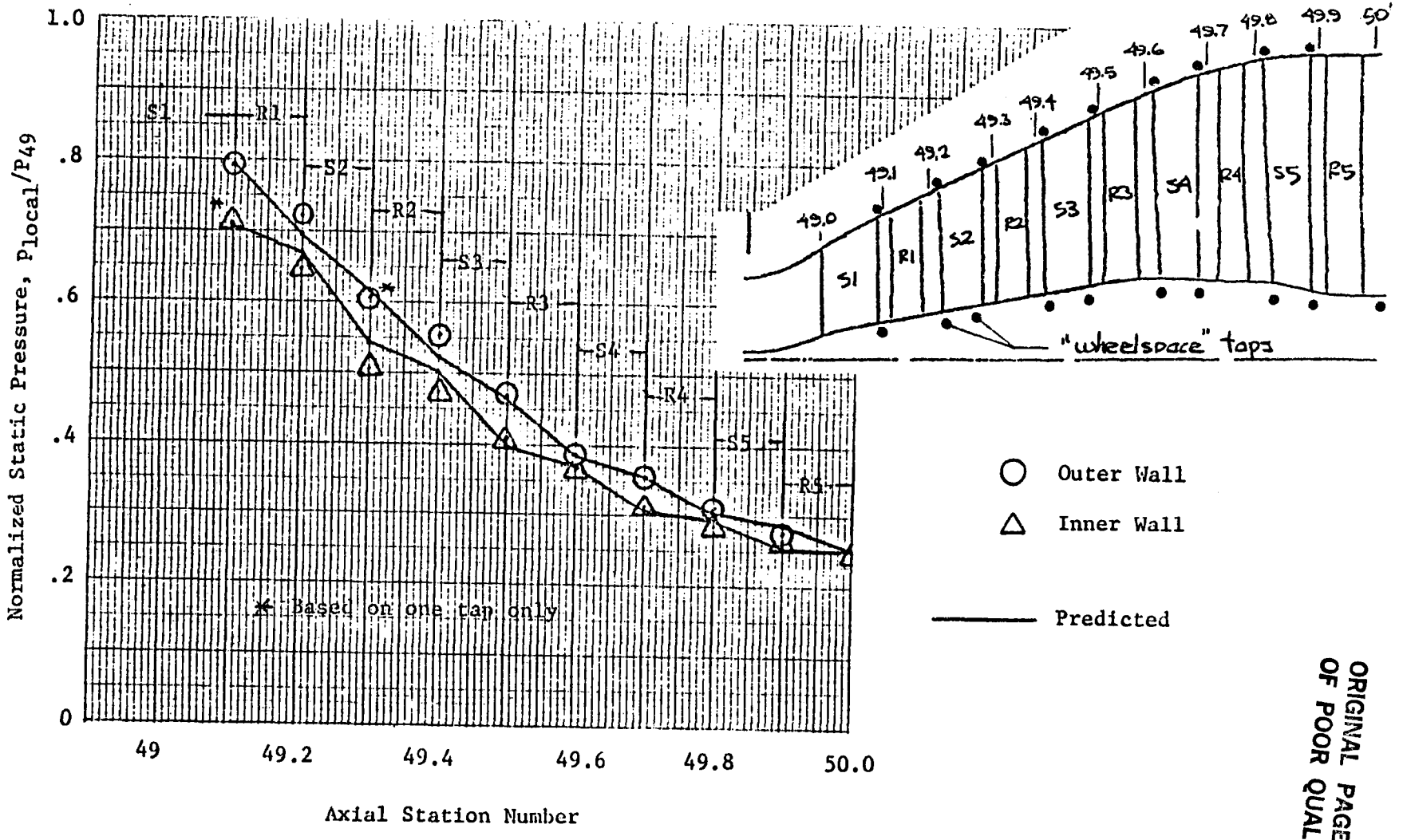


ORIGINAL PAGE IS OF POOR QUALITY

Figure 304. Low Pressure Turbine Interstage Static Pressures.

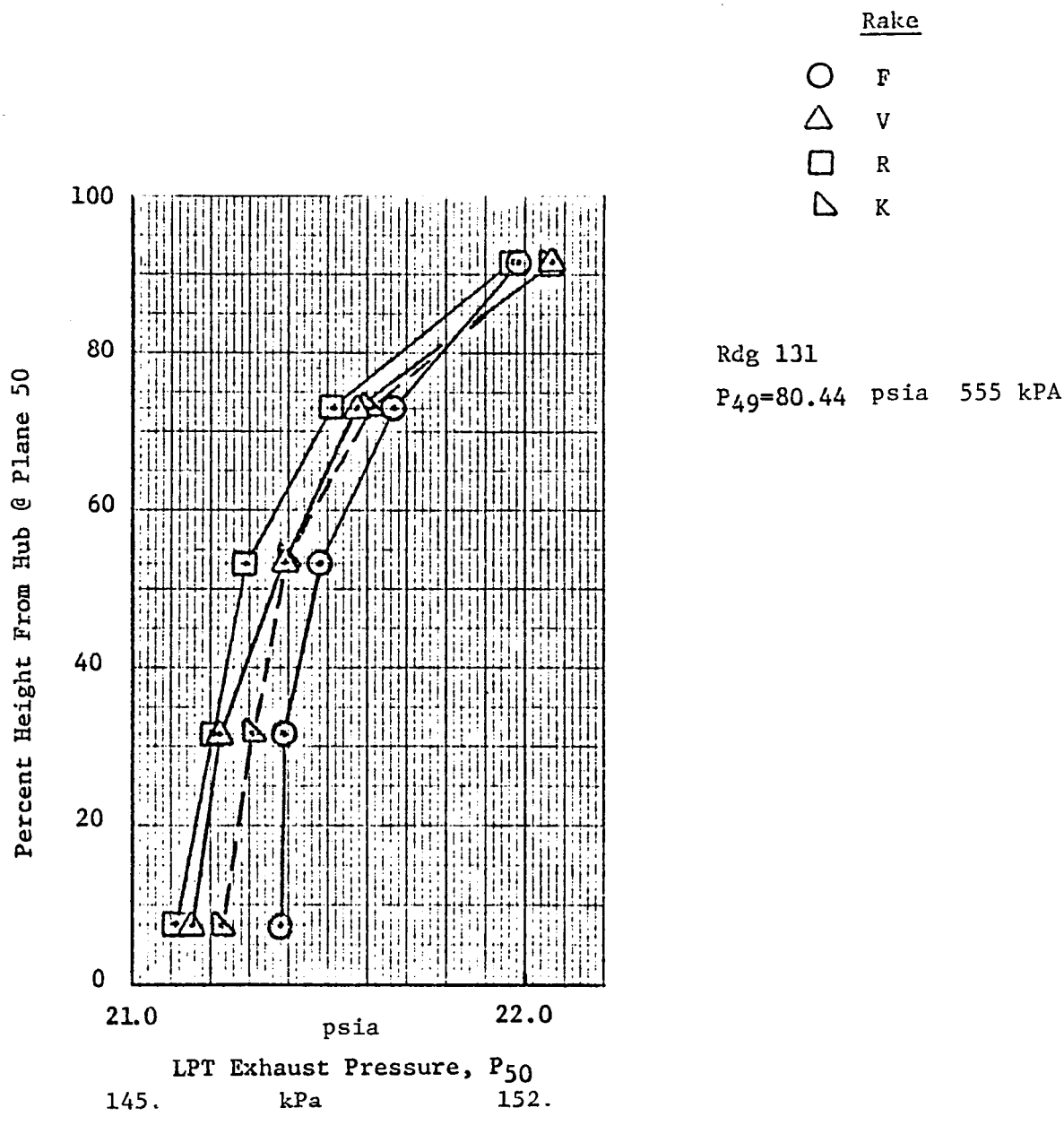


Figure 305. Low Pressure Turbine Exhaust Pressure Profile.

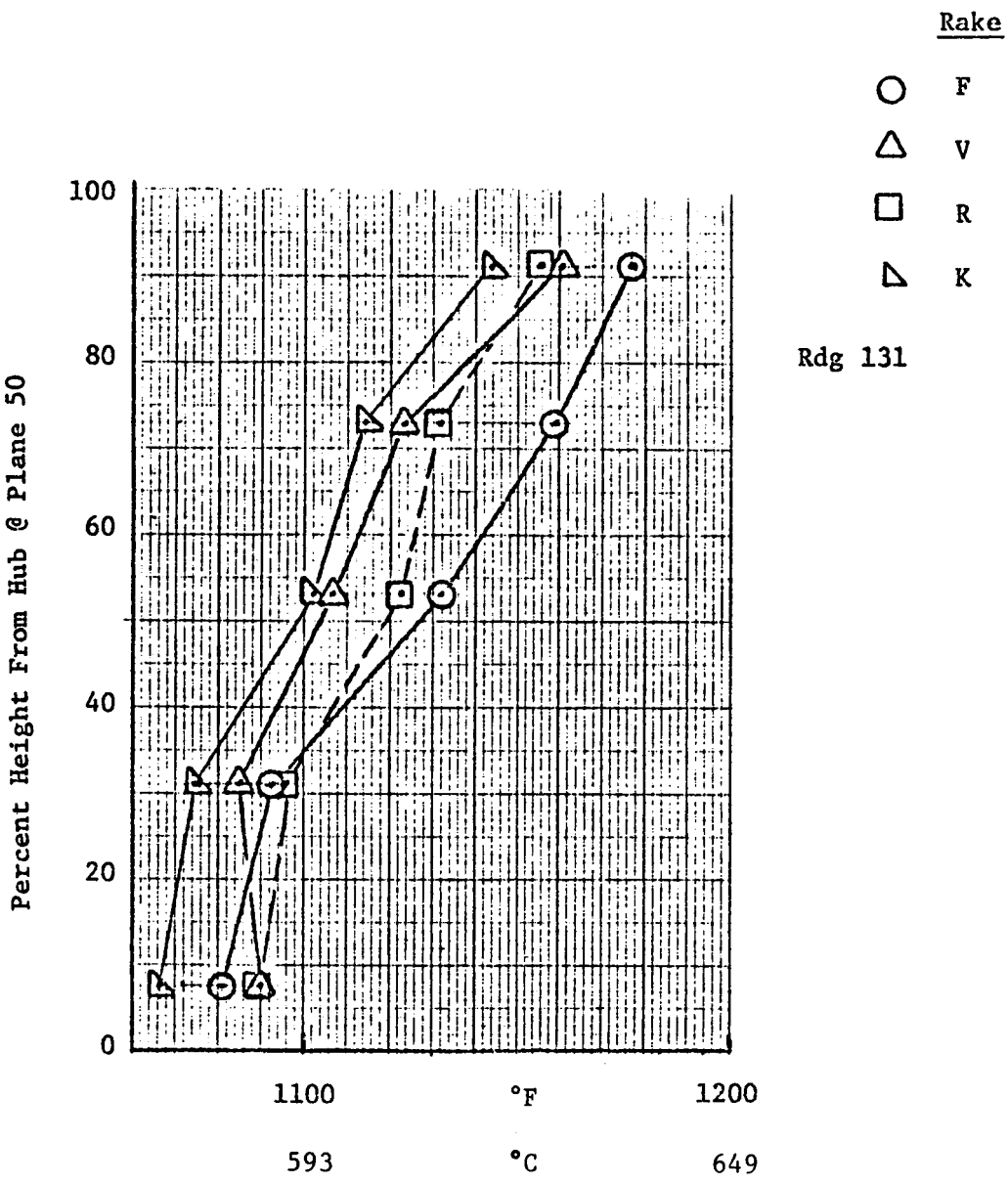


Figure 306. Low Pressure Turbine Exhaust Temperature.

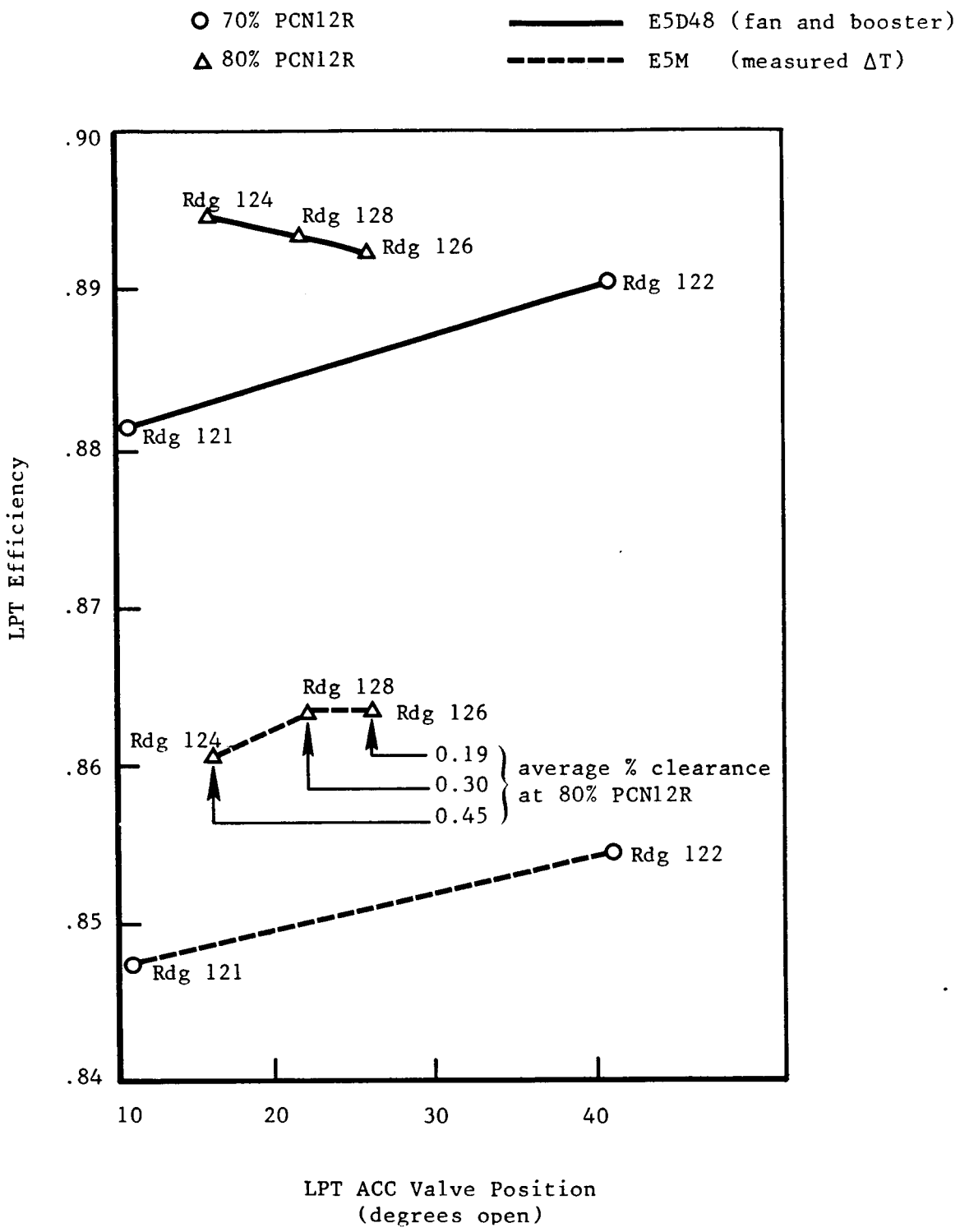


Figure 307. Effect of LPT Active Clearance Control (ACC).

The Plane 42 (HP exit) instrumentation was a possible source of the performance deficiency. The LPT is credited for an instrumentation loss for the seven radial probes based on data from a two-stage build of the rig. The loss measured in the two-stage rig was converted directly into five-stage loss for use in the ICLS Phase I program assuming that no further performance decrement due to the probes is incurred after the second stage. Since the probe effects were not simulated in the five-stage rig, this was only an assumption. Subsequent back-to-back runs of the engine with and without the probes in place, however, verified that the assigned loss was about right, as no net improvement in performance was noted with 5 of 7 Plane 42 rakes removed. Details of the Plane 42 rake performance effects evaluation are presented in Section 6.1, Overall Performance.

Interstage static pressures taken from Reading 131 (87% PNC12R) are presented in Figure 304 compared to pretest prediction. The conclusion from Figure 304 is that, on the average, there are no significant deviations from predicted row-by-row behavior in the LPT which would explain the performance deficiency.

Profiles from the Plane 50 pressure and temperature rakes are presented for Reading 131 in Figures 305 and 306, respectively. Circumferential scatter in the LPT exit pressure rakes, Figure 305, is minimal and the distribution looks reasonable. Exit temperature rakes, Figure 306, show quite a bit of circumferential variation; however, this has been traced to similar variations at Plane 42 and is not attributable to the LPT.

Figure 307 presents performance change in the LPT as a function of active clearance control (ACC) valve position for two valves of PCN12R. Note that LPT efficiency derived from measured temperature drop, E5M, gives a more consistent trend for both speed than does E5D48 (derived from fan power), which shows an apparently erroneous trend at 80% PCN12R. An average clearance for the five blades, expressed as average clearance/average blade height, is spotted on the line for 80% fan speed.

## 6.13 REAR FRAME MECHANICAL PERFORMANCE

The turbine frame struts at location 12, 1, and 2 had an engine mount located at their ends. An orientation view is provided in Figure 308. The other nine struts provided flow area for the spent Active Clearance Control air. Thermal analysis of the frame was performed with the General Electric finite element Transient Heat Transfer computer program. The results of this analysis are shown in Figure 309. These curves represent an engine start and warm-up to a nonstabilized ground idle with a subsequent 2 minute accel to takeoff power.

Figures 310 through 312 show the temperatures of the number 1, 10, and 12 struts relative to T5 average from the engine test. It can be seen that the number 1 and 12 struts ran approximately 19°C (35°F) higher in temperature than the number 10 strut which had spent ACC flowing through it. At maximum T5 average the highest strut temperature was 565.6°C (1050°F) for the ACC air-cooled strut, which compares to a maximum strut temperature of 540.6°C (1005°F) from Figure 309 as used in the design.

In order to reduce the thermal stress in the radially deep rings of the turbine frame hub, hot core gas was routed down over the rings to heat them. Temperatures were measured on the forward hub OD and ID. These temperatures are shown in Figure 313 and Figure 314 versus T5 average. The maximum radial $\Delta T$ measured on test was approximately 60°C (140°F) (OD temperature greatest) which is compatible with the predicted stress level.

Casing measured temperatures are shown in Figures 315 and 316. The sector at the top of the turbine frame under the pylon and between the engine mounts was exposed to fan airflow since the engine mounts penetrated the core cowl. The casing temperature measured in this area was found to be approximately 167°C (300°F) cooler than a similar area on the casing not exposed to fan air.

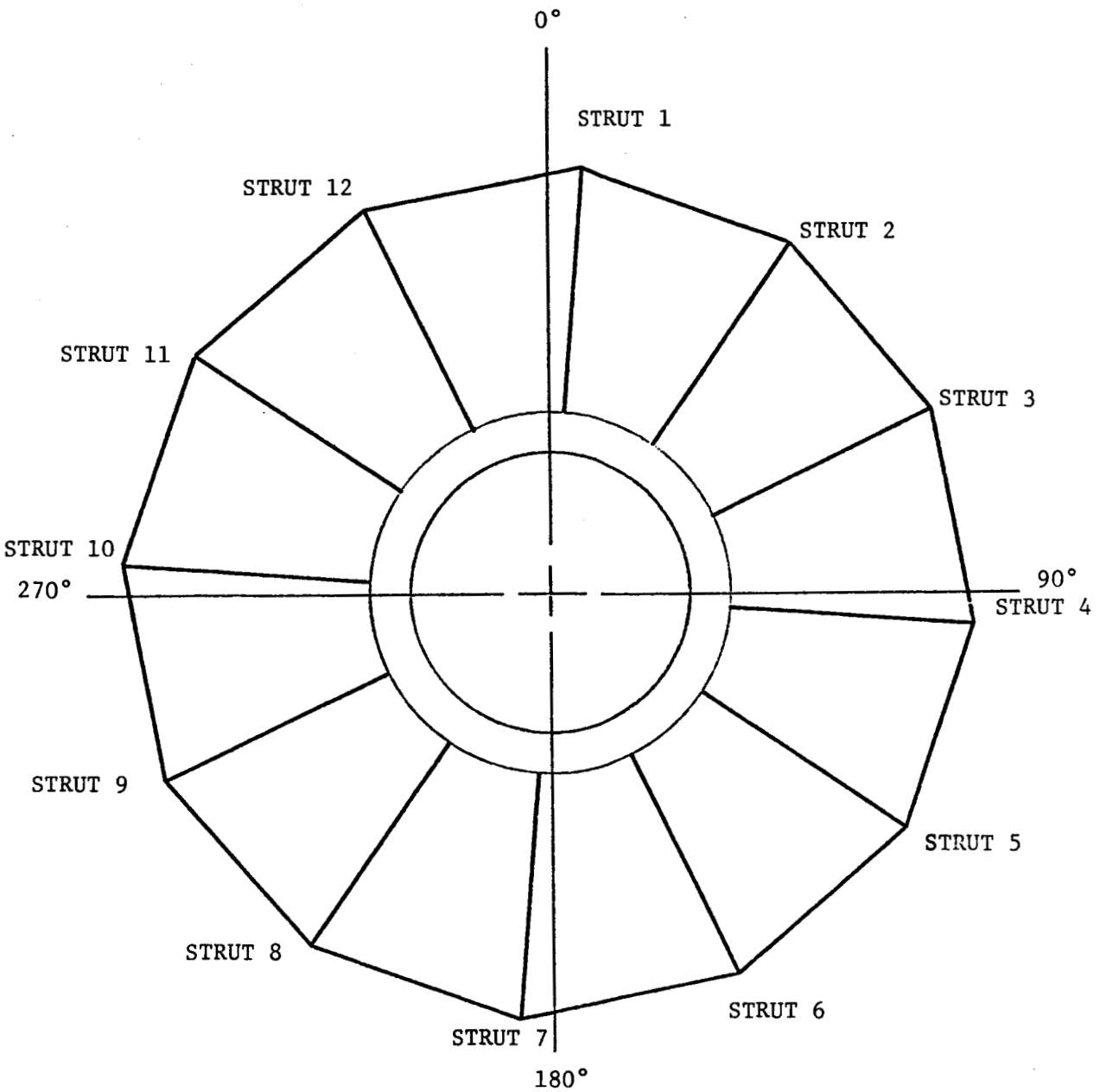


Figure 308. Turbine Frame Orientation-Aft Looking Forward.

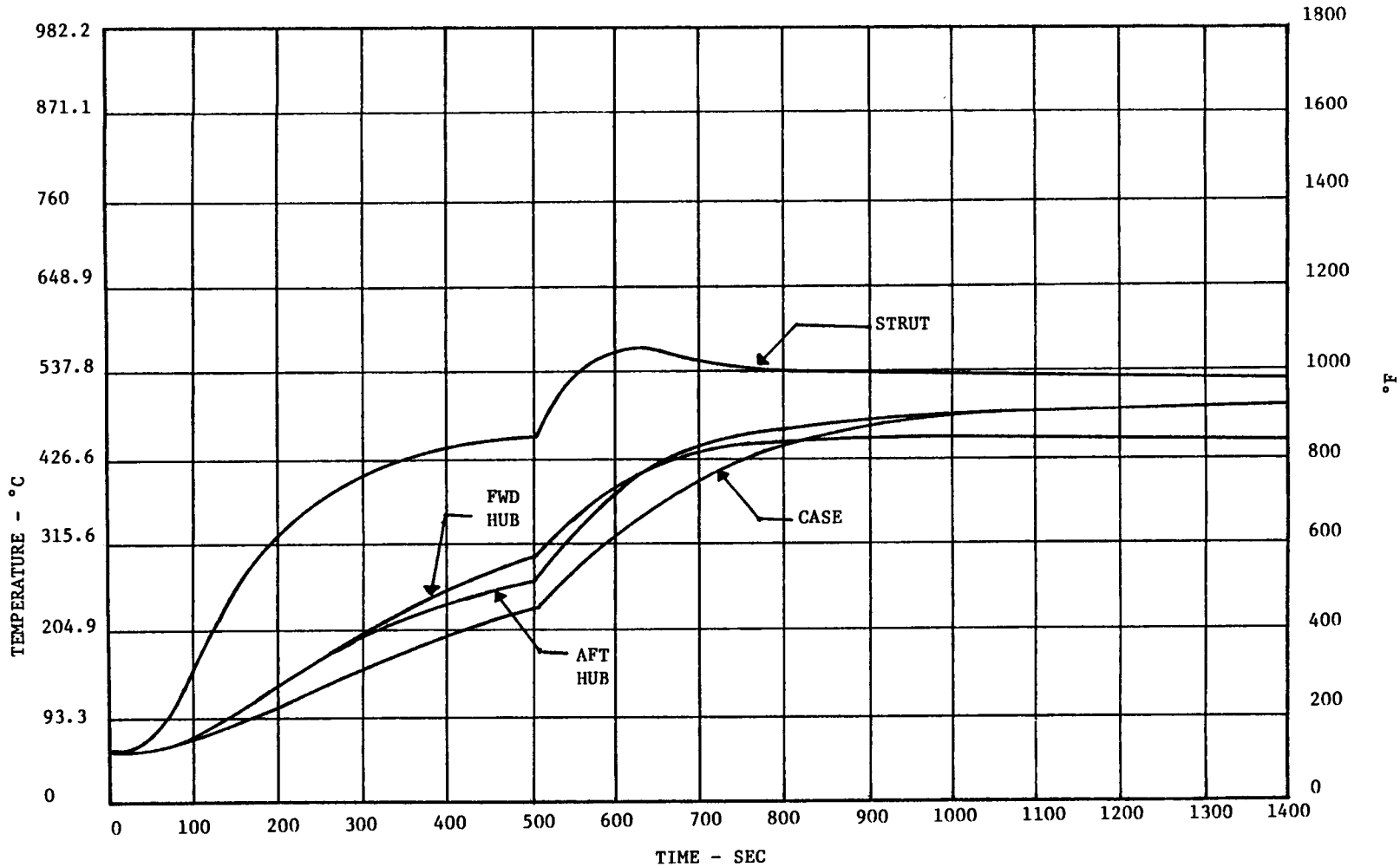


Figure 309. Turbine Frame Predicted Transient Temperature.

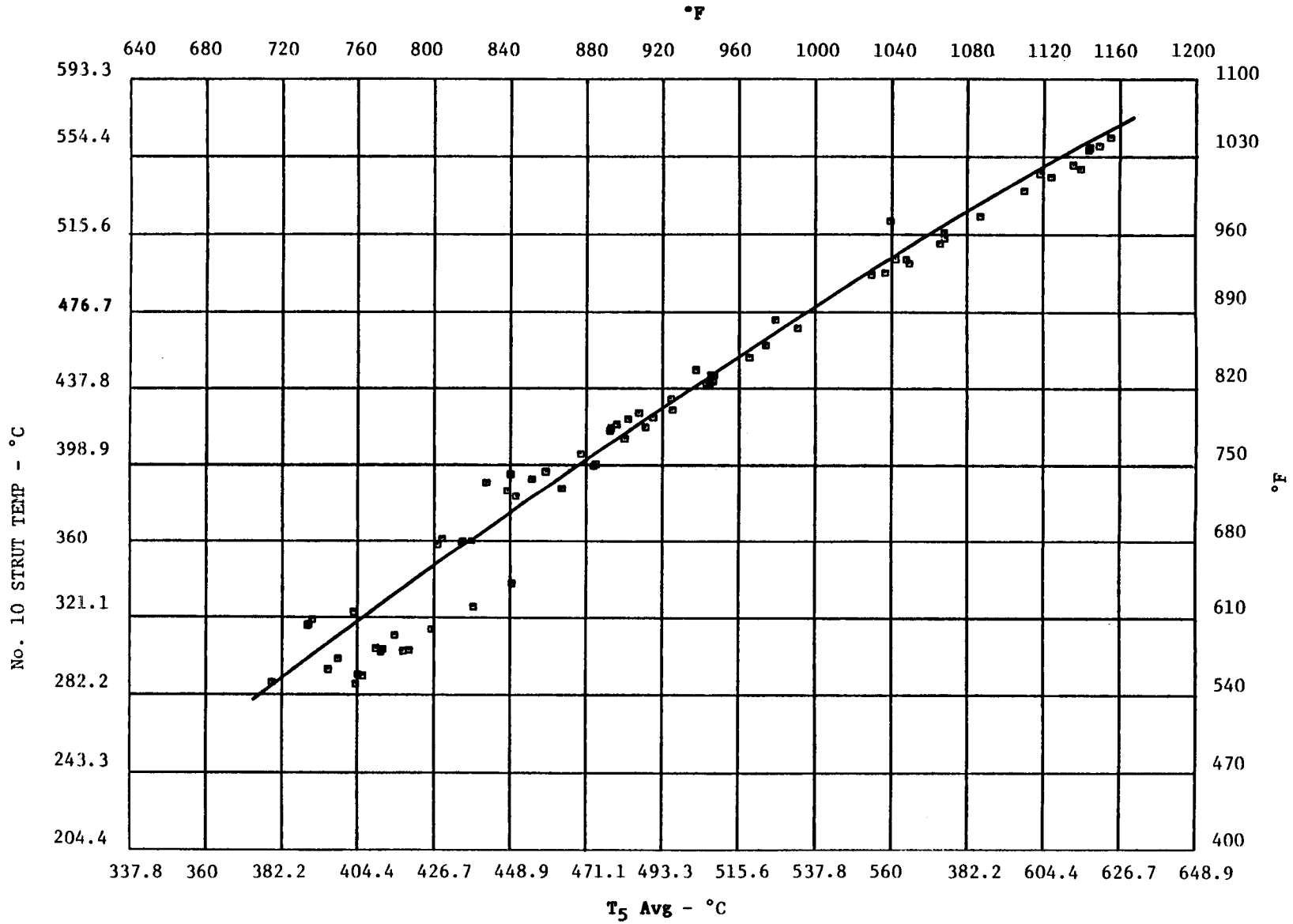


Figure 310. Turbine Frame Number 10 Strut Temperature vs. $T_5$ Average.

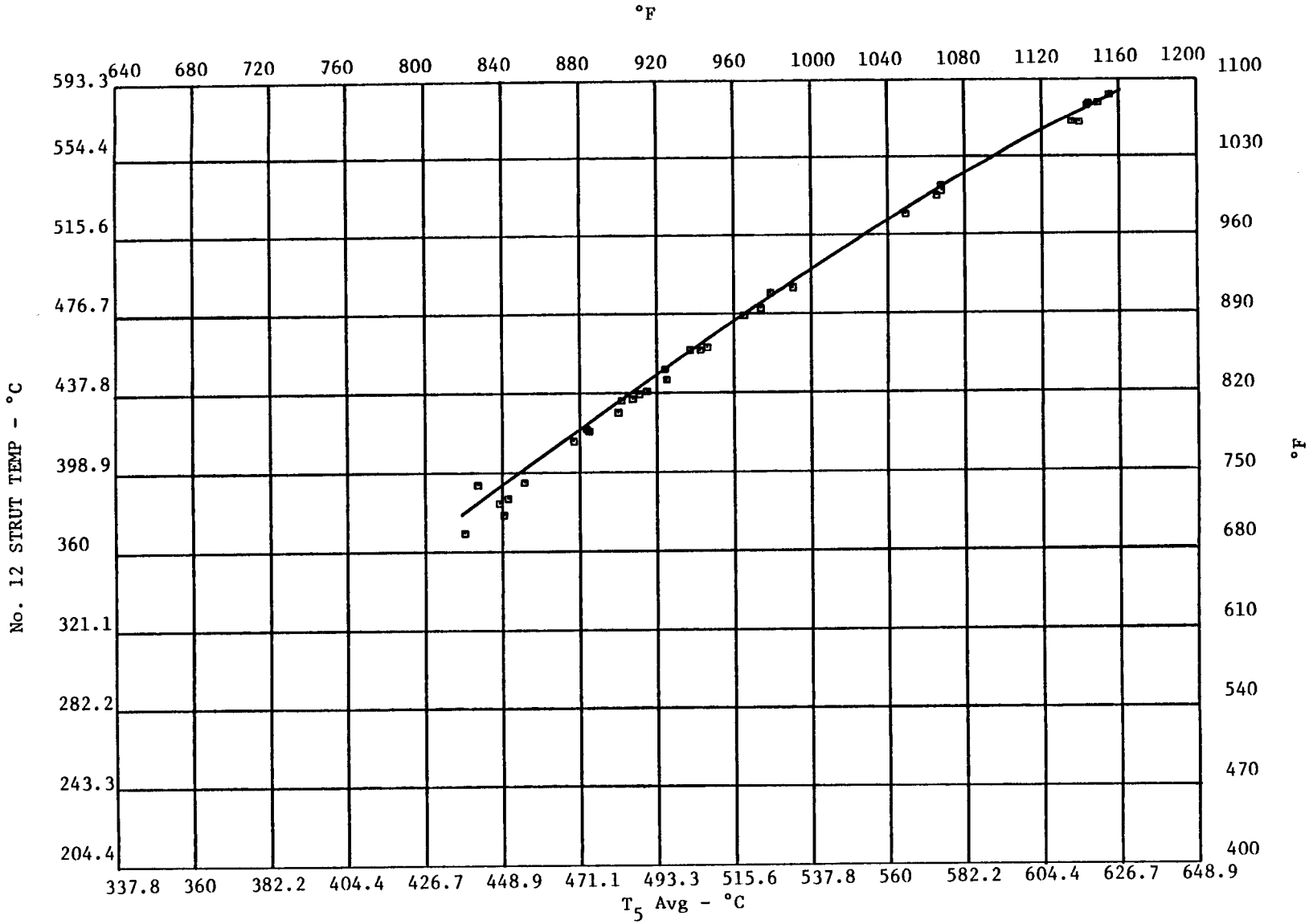


Figure 311. Turbine Frame Number 12 Strut Temperature vs. $T_5$ Average.

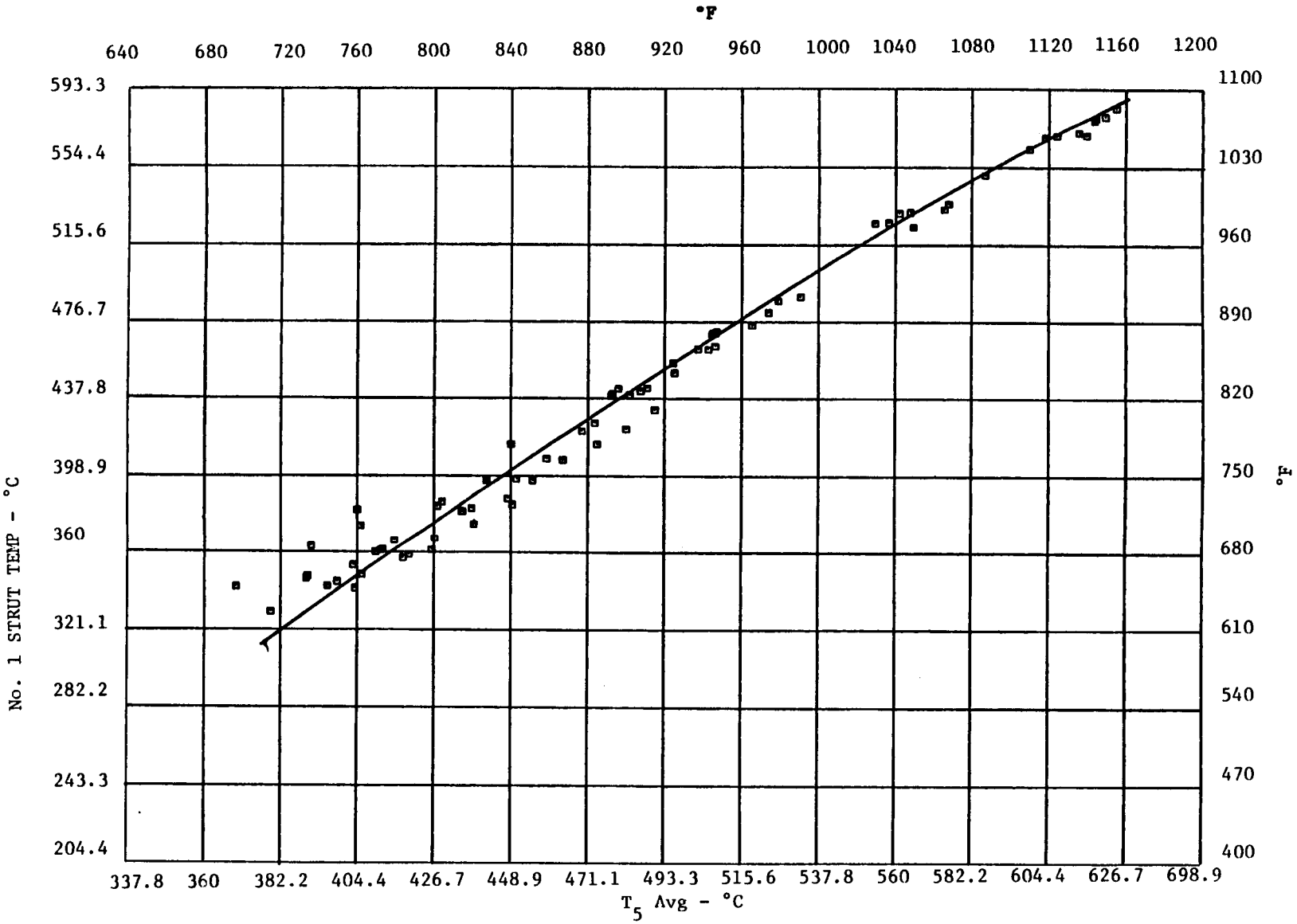


Figure 312. Turbine Frame Number 1 Strut Temperature vs. $T_5$ Average.

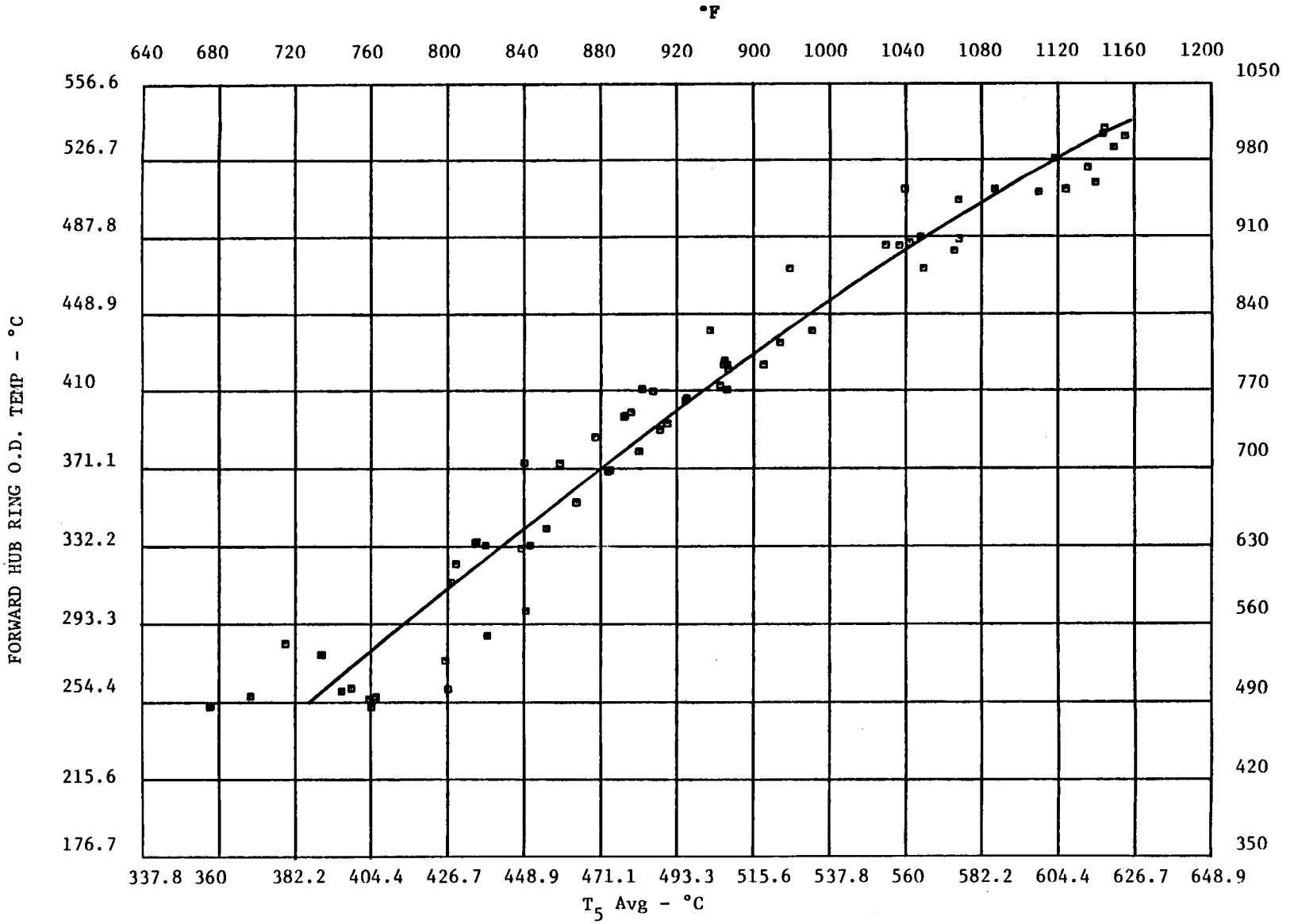


Figure 313. Turbine Frame Forward Hub Ring O.D. Temperature vs. $T_5$ Average.

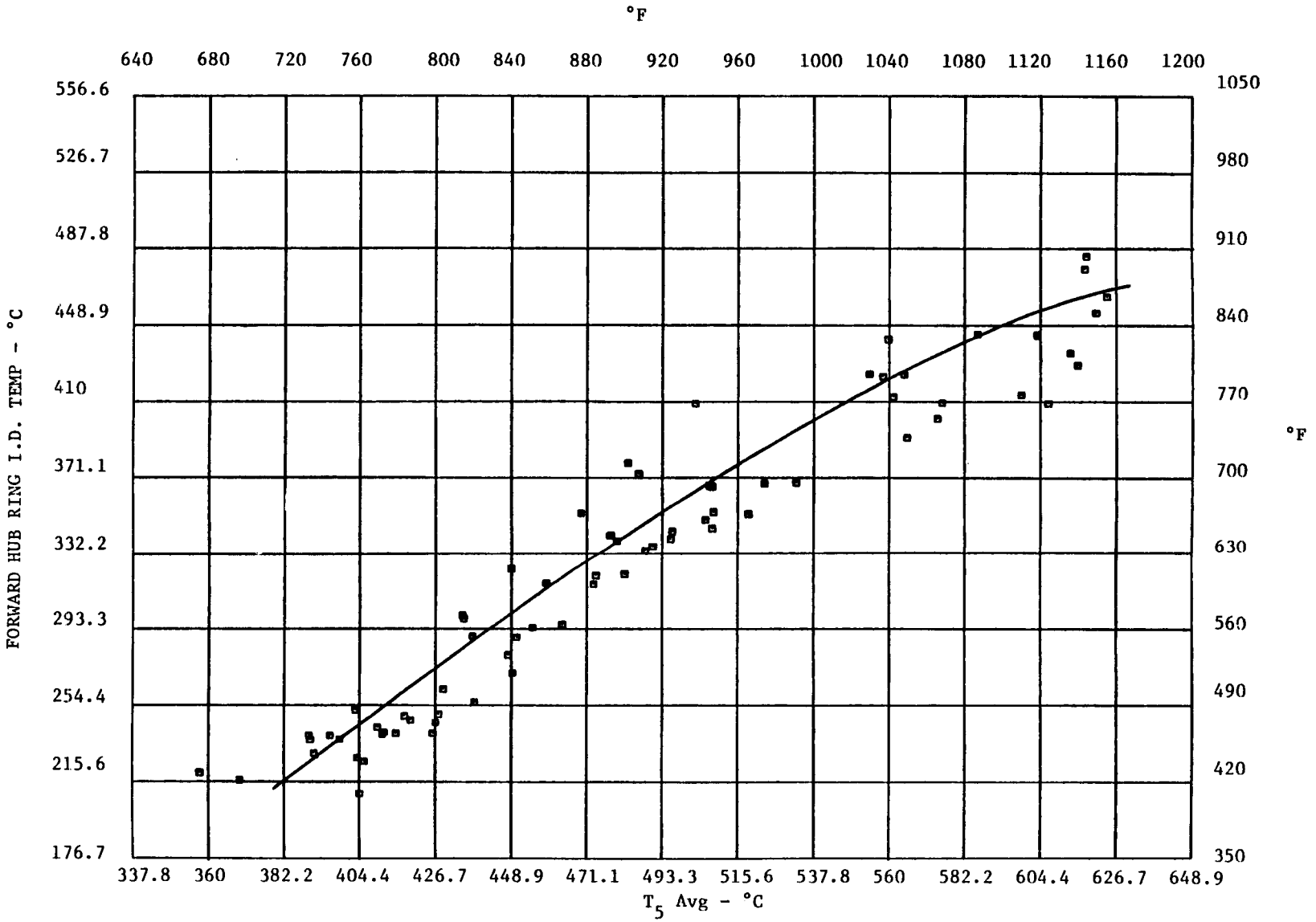


Figure 314. Turbine Frame Forward Hub Ring I.D. Temperature vs. $T_5$ Average.

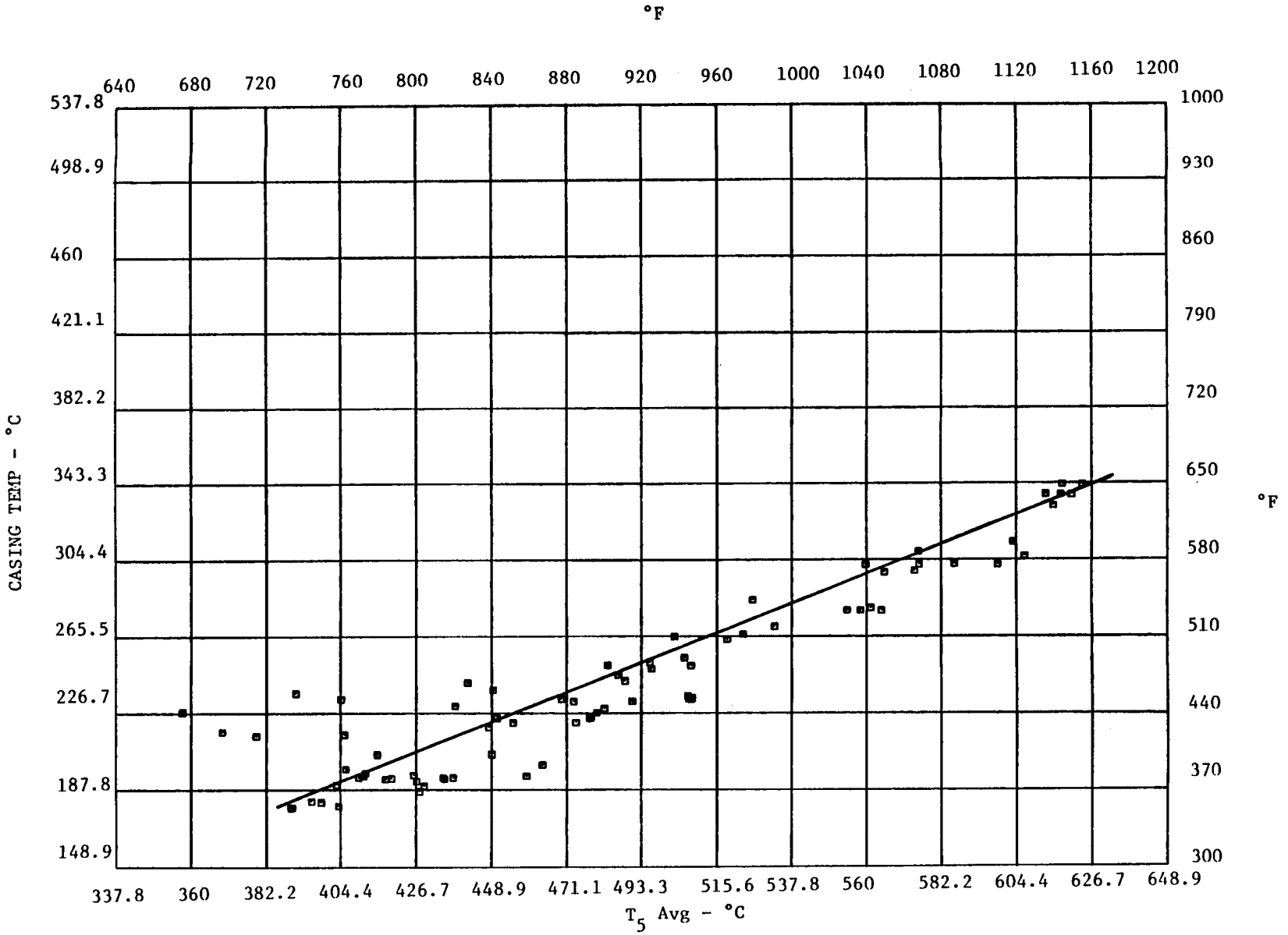


Figure 315. Turbine Frame Casing Temperature at $\Theta = 19°$ vs. $T_5$ Average.

## 6.14 EXHAUST SYSTEM HARDWARE PERFORMANCE

The mixer, core cowl and centerbody performed very well throughout the testing. There were no detectable vibration problems, and an examination of the hardware on conclusion of testing indicated no distress in any of the exhaust system parts. There was no instrumentation on the core cowl and centerbody. Strain gages were used on the mixer, as shown in Figure 107, to monitor chute vibration during testing. This is a concern with this type flow mixer due to a characteristic absence of structural stiffness in the design. The mixer support design did its job well. Only negligible levels of stress and thus vibration were observed during the testing.

## 6.15 EXHAUST SYSTEM MECHANICAL PERFORMANCE

No significant mechanical problems related to the exhaust system hardware were encountered during the ICLS testing. Post-test analysis indicates that the fan cowl and core cowl sealing may have deteriorated somewhat over the course of the testing, thus increasing the amount of fan duct leakage, but this cannot be quantified since no post-test leak check was performed.

## 6.16 MIXER AND EXHAUST SYSTEM AERODYNAMIC PERFORMANCE

### Mixer

Exhaust system mixing effectiveness was determined from an integration of the nozzle exit total pressure and temperature profiles. The pressure and temperature data were recorded for three engine speeds on four remotely controlled indexing rakes. A schematic of the rake locations is shown in Figure 317 along with a symbol guide for each rake position.

Figures 318 through 321 present the nozzle exit temperature profiles for the max speed condition. The temperatures are presented on a normalized basis relative to fan and core discharge temperatures and are plotted versus

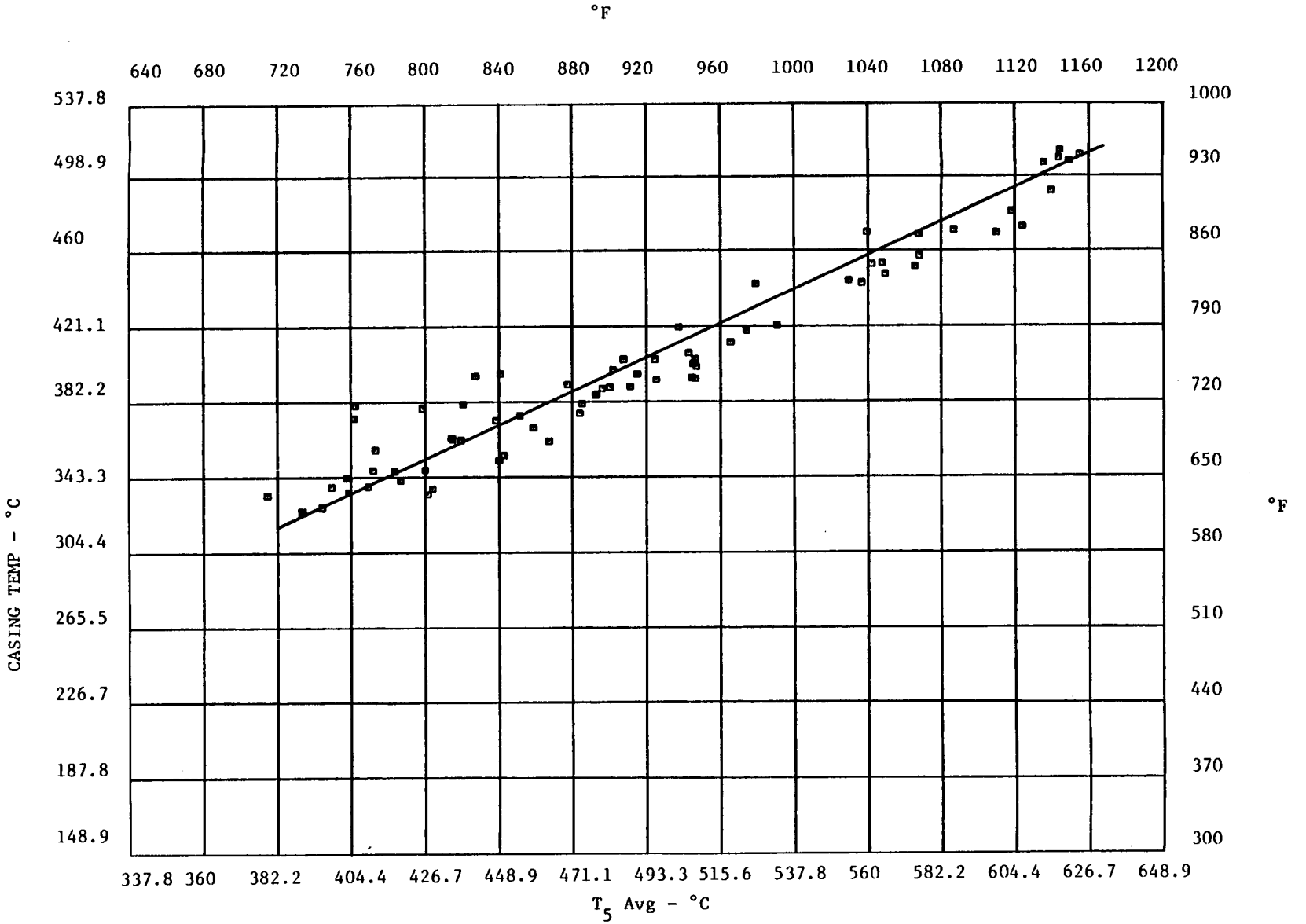


Figure 316. Turbine Frame Casing Temperature at $\Theta = 260°$ vs. $T_5$ Average.

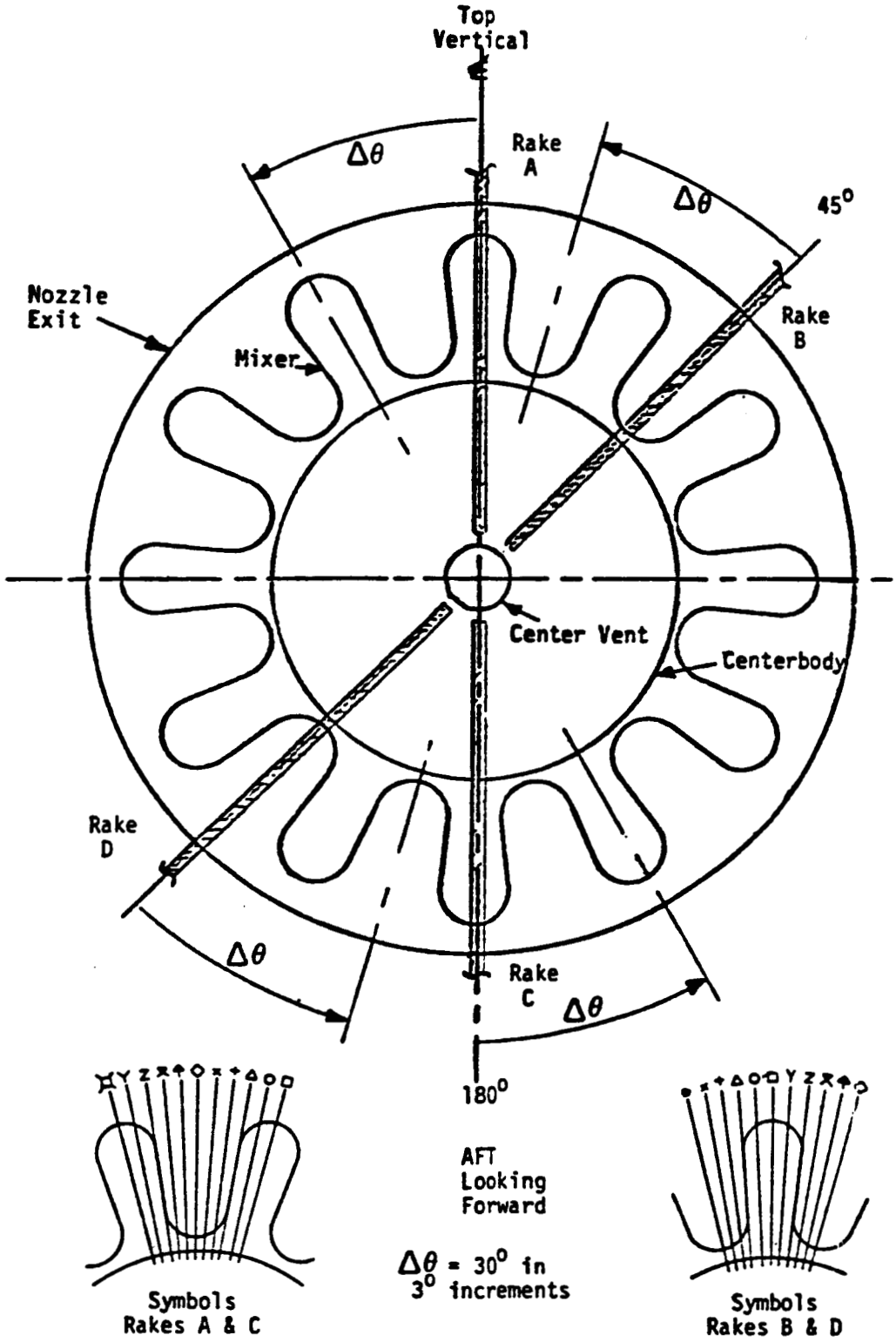


Figure 317. Nozzle Exit Survey Rake Description.

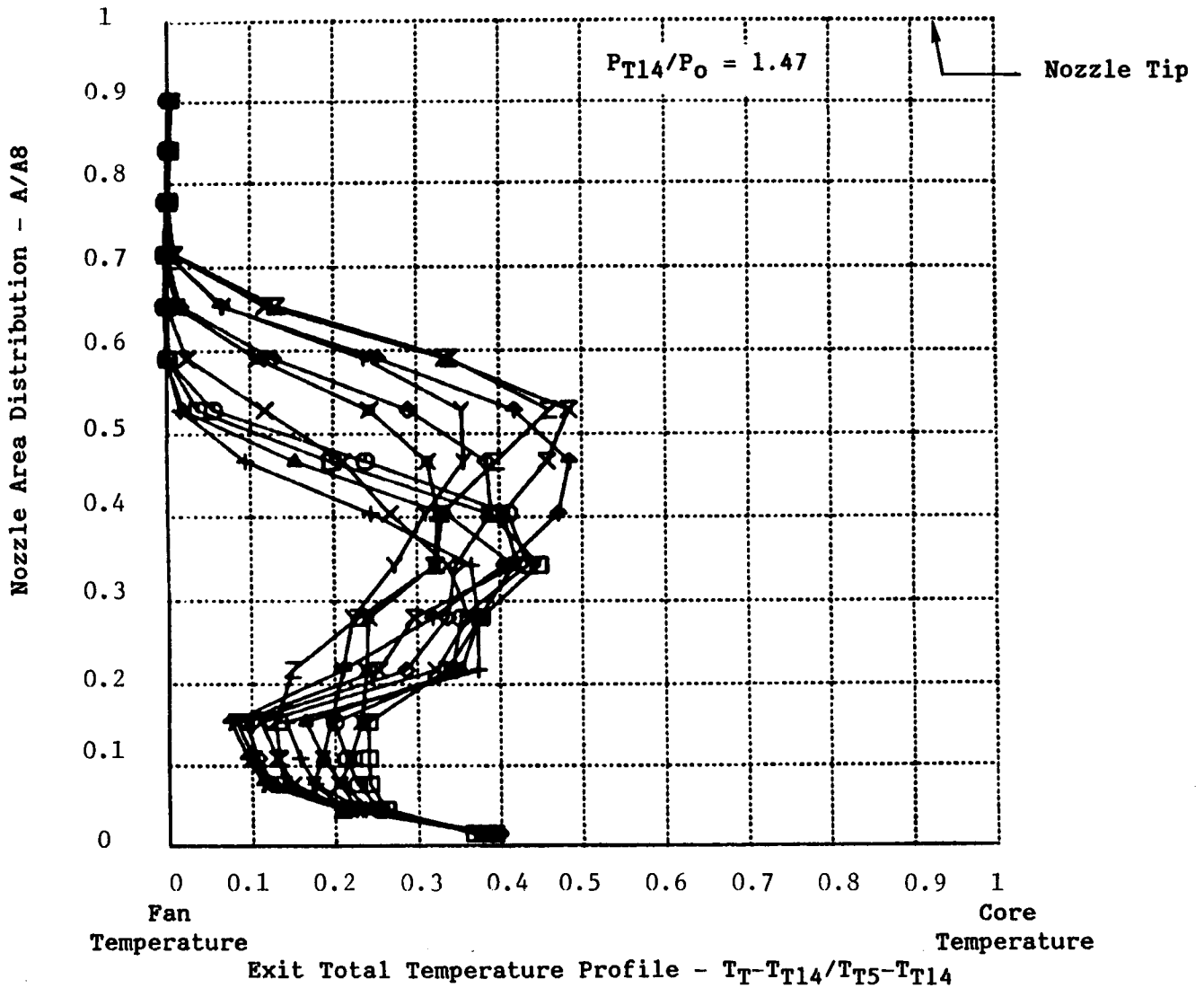


Figure 318. Nozzle Exit Temperature Profile, Rake A.

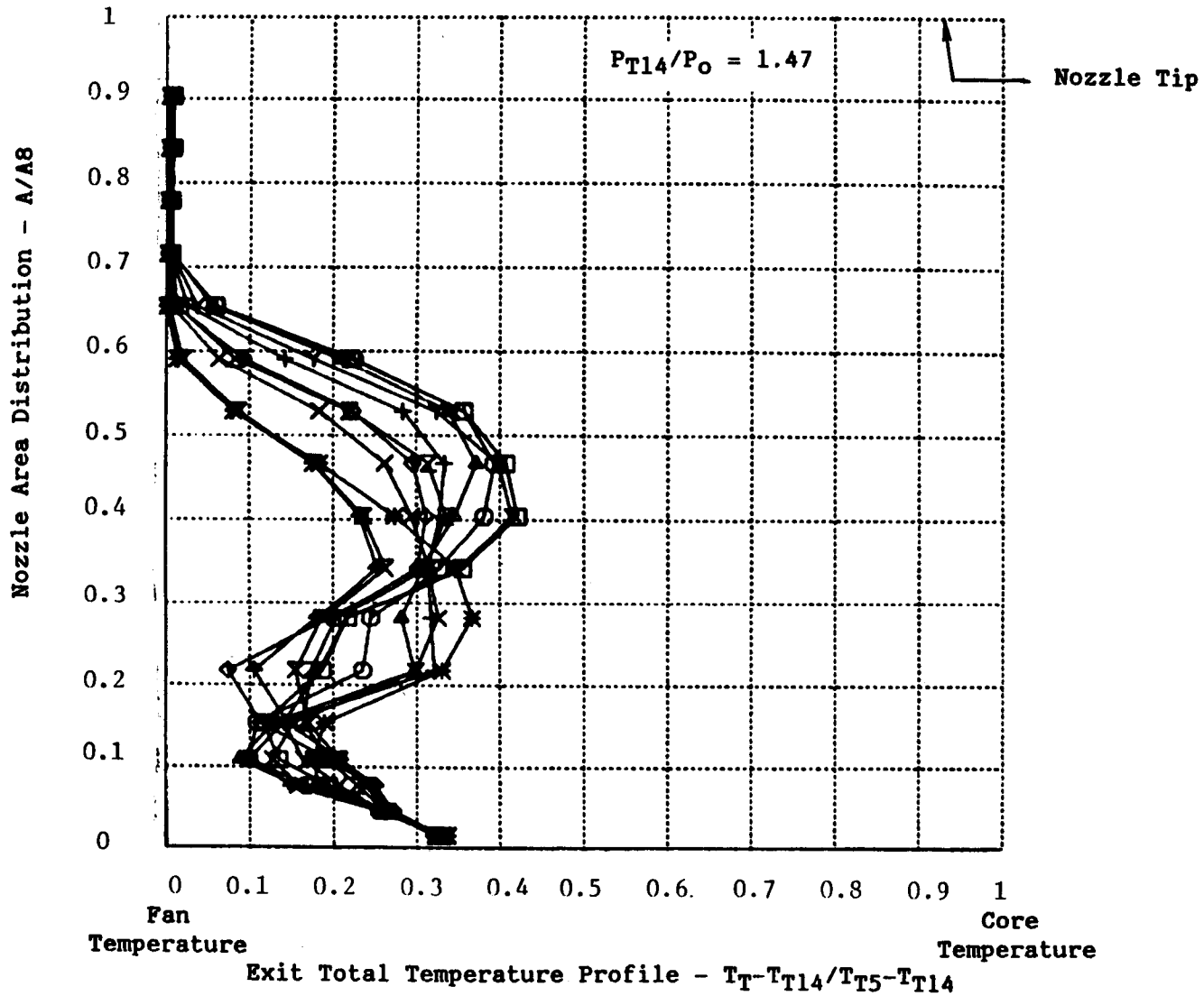


Figure 319. Nozzle Exit Temperature Profile, Rake B.

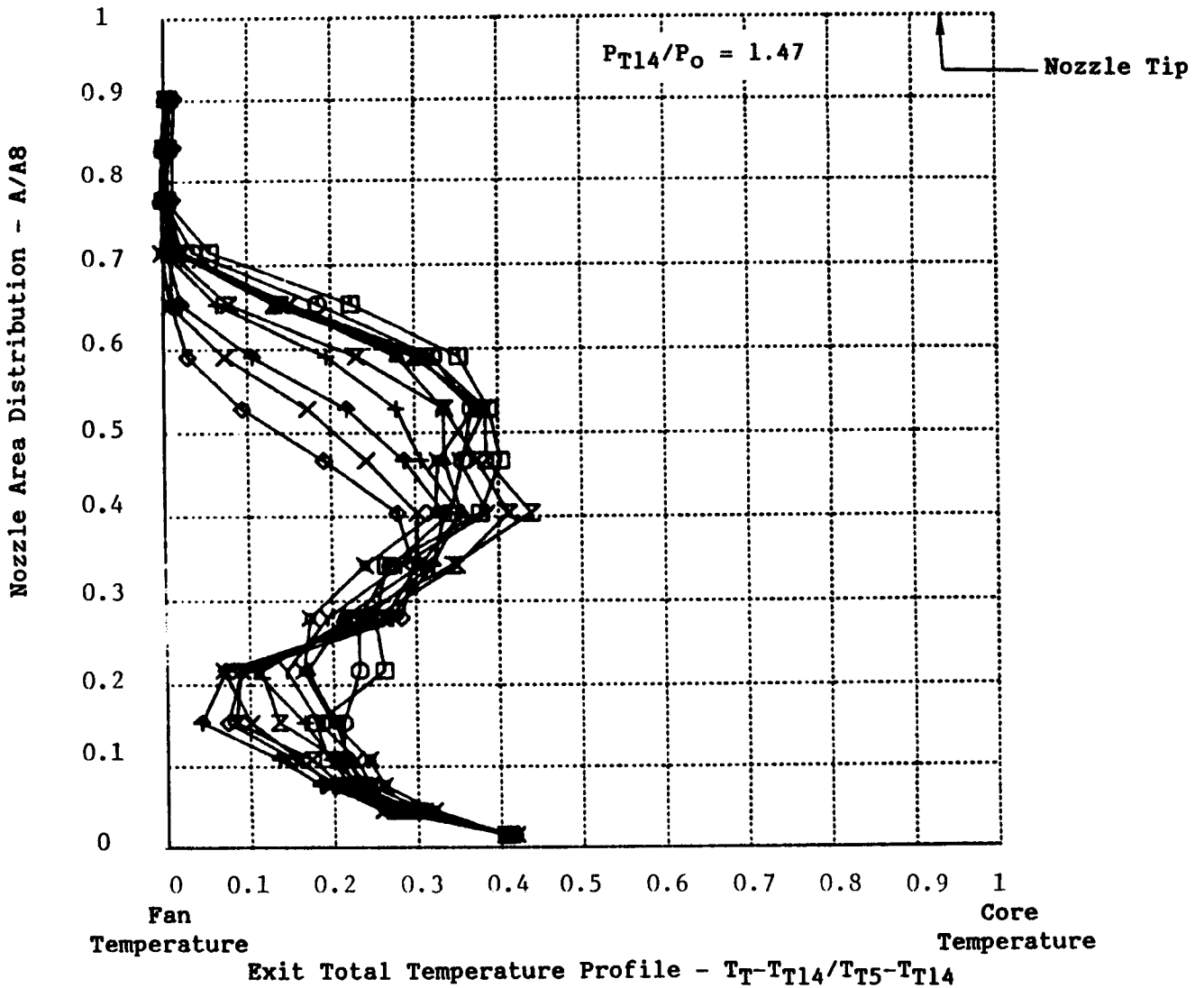


Figure 320. Nozzle Exit Temperature Profile, Rake C.

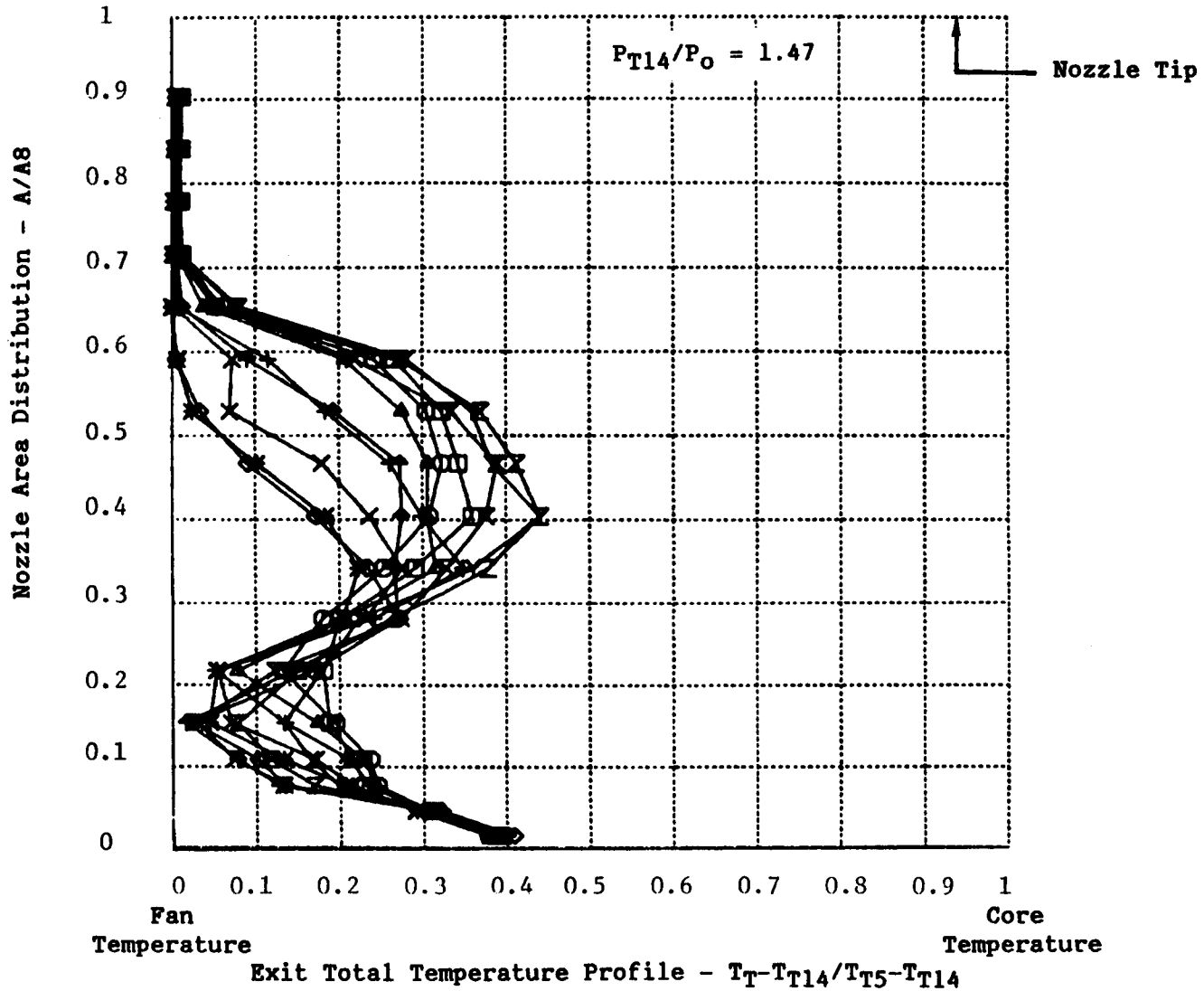


Figure 321. Nozzle Exit Temperature Profile, Rake D.

nozzle area distribution, $(R_{probe}/R_{nozzle})^2$. For comparative purposes, the corresponding temperature distributions recorded in Phase III of the scale model test program for the simulated ICLS mixer configuration are presented in Figures 322 and 323 for the two circumferential positions measured on the scale model.

There are three basic differences between the scale model and full scale temperature profiles, all of which indicate better mixing in the ICLS tests. First, the hot flow spike observed near the nozzle centerline is significantly reduced in the ICLS tests. This reduction was not unexpected. The large center vent tube shown in Figure 67 was not simulated on the scale model, and analytical studies using the Spalding mixing analysis program indicate that the turbulence generated along the surface of the center vent would have enhanced mixing. The temperature level of the spike measured on ICLS was superimposed on the scale model profiles, and the scale model mixing effectiveness was recalculated. From this analysis, it was determined that the reduction in the hot flow spike from model to full scale increased mixing effectiveness by ~3%. The second major difference between the scale model and ICLS profiles is the apparent improved circumferential mixing for ICLS as manifested by less temperature variation, on the average, at any given radial (percent nozzle area) position. Although it cannot be supported analytically, this improvement is concluded to be the result of higher turbulence levels in the ICLS flowfield relative to the scale model. This will be discussed further in subsequent paragraphs. The third major difference is that the ICLS hot flow penetrates radially outward approximately 10% more than the scale model (70+ % of the nozzle area versus 60+ %). It has been concluded that this higher flow penetration is due to a higher core-to-fan mixing plane velocity ratio achieved on ICLS versus the scale model. This effect, which will also be discussed further in subsequent paragraphs, is concluded to have increased mixing effectiveness by about 2.5%.

One further conclusion was reached from a qualitative analysis of the exit temperature profiles. Detailed comparison of the individual profiles for each rake indicated that the influence of the pylon at the top centerline was

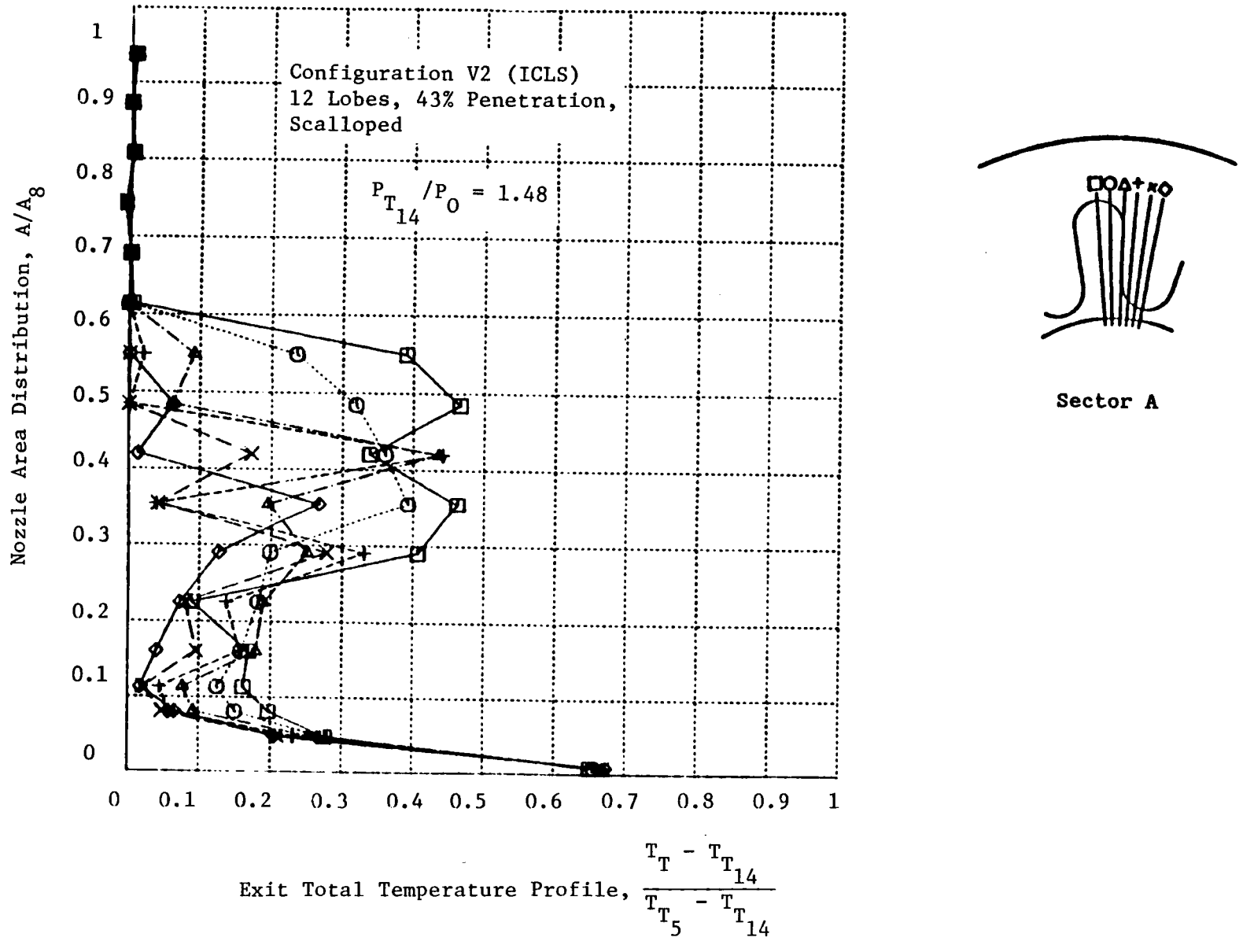




**Figure 322.** Phase III Scale Model Exit Survey Rake Total Temperature Profile.

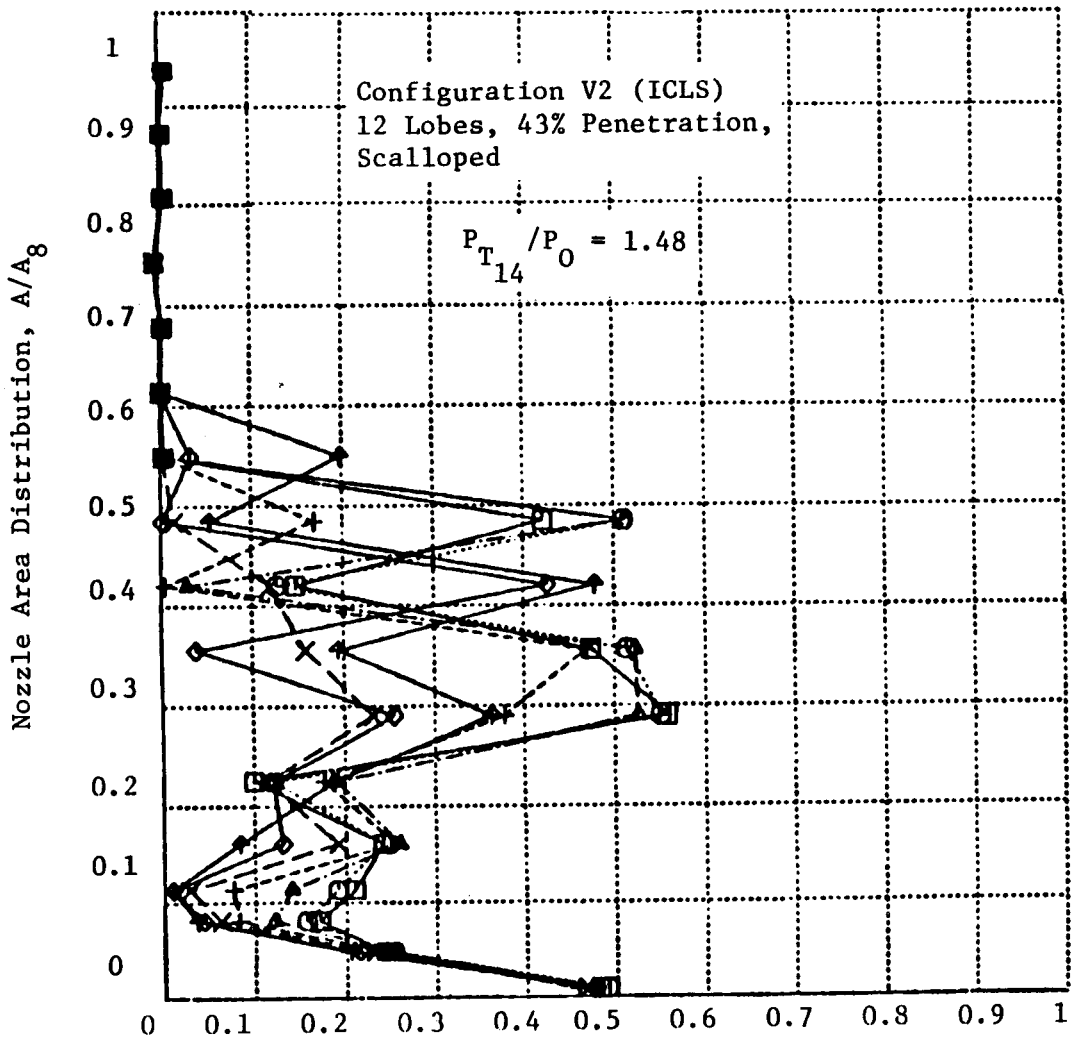


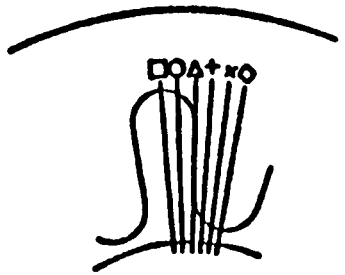

Sector B

**Figure 323.** Phase III Scale Model Exit Survey Rake Total Temperature Profile.

minimal and extended over a small portion (perhaps 10%) of the mixing region circumference. Indirectly, this suggests that the pylon imparted little disturbance to the overall flowfield and was aerodynamically clean and efficiently integrated with the mixer.

The exit survey data was integrated to determine mixing effectiveness using a data reduction procedure identical to that used in the scale model test program. Results are presented in Figure 324 versus nozzle pressure ratio for the three engine speeds. Also included in the figure are the results of the scale model exit survey integration for mixing effectiveness including the max cruise design point. Comparison of the two sets of data indicates the ICLS mixer to be ~8% higher than the scale model.

A detailed analysis was subsequently conducted to determine the reasons for the increased mixing effectiveness. When the scale model data was originally evaluated, the trend shown in Figure 324, particularly at the low pressure ratio, was concluded to be insignificant (data accuracy/scatter). Substantial full scale mixer test data obtained on a TF34 engine in 1980 in the NASA Lewis Cell 3 altitude test chamber as part of the Propulsion Engine Technology (PET) Program supported this conclusion. However, the similarity between the ICLS and the scale model data prompted a reassessment of all existing data to determine if there was a second-order effect of operating condition on mixing effectiveness. It was ultimately concluded from the reassessment that the velocity ratio of the two streams at the mixing plane does, in fact, impact mixing effectiveness. This correlation, shown in Figure 325, is intuitive; a higher velocity difference between the two streams should promote mixing.

The significant difference in velocity ratio between ICLS and the scale model at the max power condition (P14/Po = 1.47) is due in part to differences in fan-to-core pressure and temperature ratios. The pressure ratio, P14/P56, in the scale model was ~1.03 whereas on ICLS it was ~0.97. Part of the reason for this lower value on ICLS was due to the blockage of the rakes (~7%). For the performance tests without the rakes, the ICLS pressure ratio

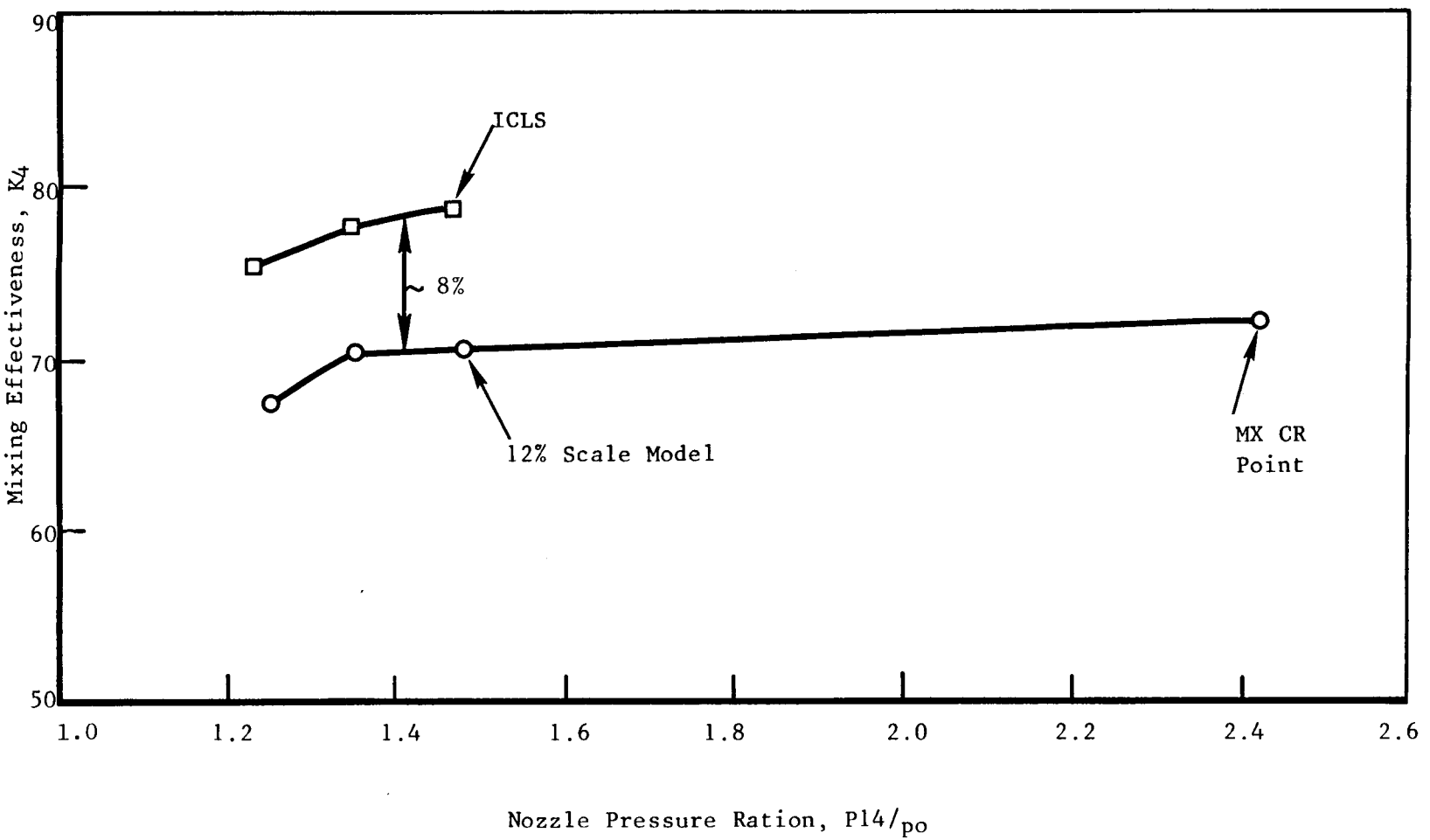


Figure 324. Calculated Mixing Effectiveness.

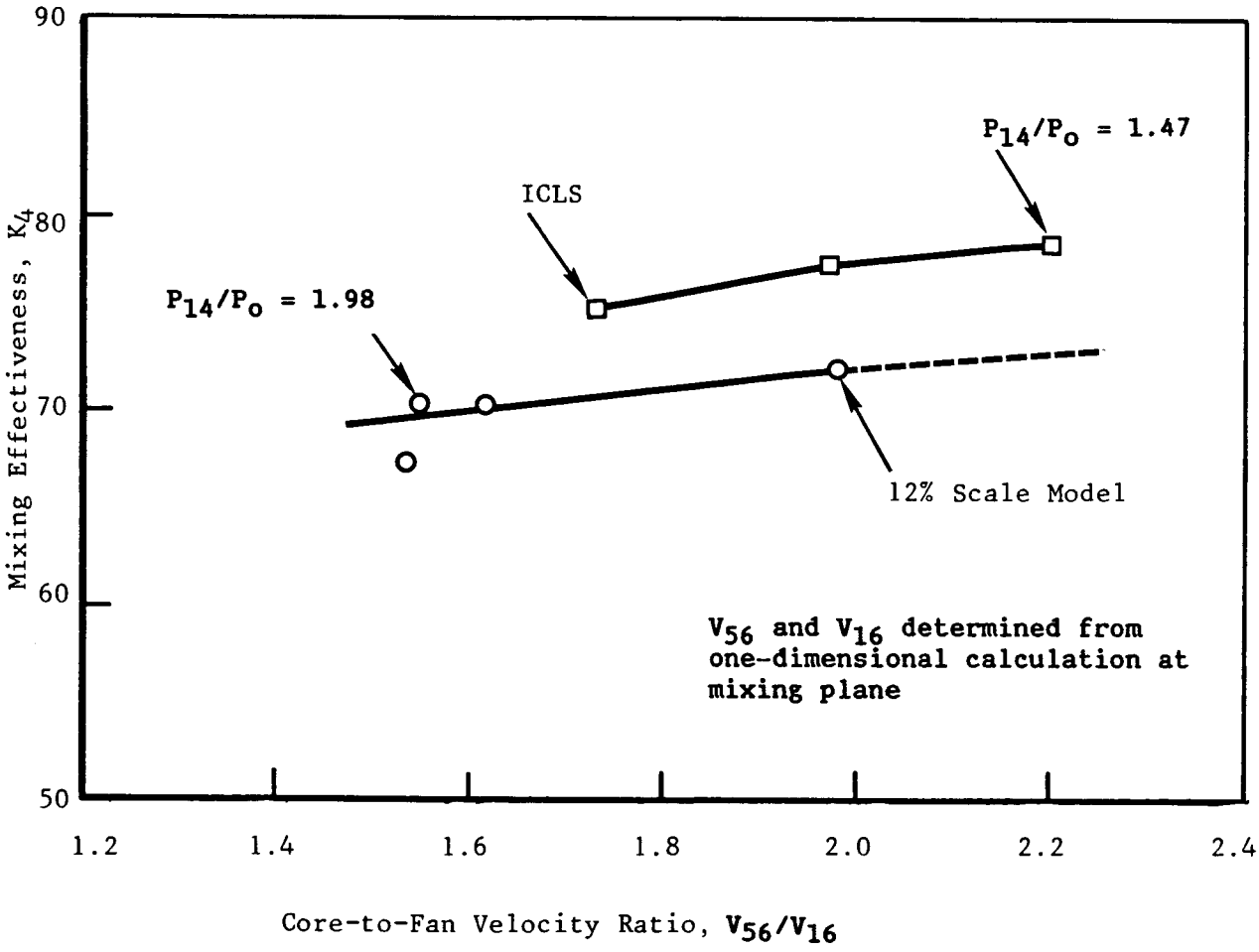


Figure 325. Mixing Effectiveness Dependency on Mixing Plane Velocity Ratio.

was 0.996. Thus, the lower fan-to-core pressure ratio for the ICLS survey tests effectively decreased the bypass ratio and increased the velocity ratio. Additionally, the ICLS core-to-fan temperature ratio, T56/T16, was higher than the scale model (2.6 versus 2.4) which would also increase the velocity ratio. Based upon the correlation in Figure 325, if the scale model at P14/Po = 1.48 were run at the same velocity ratio as ICLS, it would have been ~2.5% higher in mixing effectiveness. As previously mentioned, the higher velocity ratio for the ICLS test was concluded to be the reason for the increased hot flow penetration.

A stackup which explains the differences in mixing effectiveness shown in Figure 324 was formulated from these analyses and is summarized in Figure 326. An increase in mixing of 2.5% is due to the higher velocity ratio. Since the magnitude of the hot flow spike near the nozzle centerline remained essentially unchanged with pressure ratio for both the scale model and ICLS, the 3% increase in mixing due to the center vent would be essentially constant. Finally, the remaining 2.5% is concluded to be due to a higher level of turbulence likely for the ICLS flowfield versus the scale model. Increased turbulence levels should be expected in full scale engine flows due to the upstream rotating turbomachinery in both streams, the combustion process (unstready entropy) in the core stream, and the acoustic/noise level in the two streams. Industry research has shown that acoustic fields imposed on mixing streams can enhance the degree of mixing. While this phenomenon cannot be analyzed to quantify the effects on mixing, it is concluded that a 2 to 3% increase in mixing effectiveness for the turbulence associated phenomena is not unreasonable and represents a valid adjustment of model data to full scale. Thus, while scale model testing is a valid mixer aerodynamic development tool, model performance results may be slightly conservative.

The previous analyses leads to the characterization of the ICLS mixing effectivness as shown by the curves in Figure 327. Since the performance nozzle was 13.46 cm (5.3 inches) shorter than the survey nozzle, its mixing effectiveness would be lower because of the reduced mixing length. Parametric scale model test data were used to estimate the reduction in mixing (4.5%) for

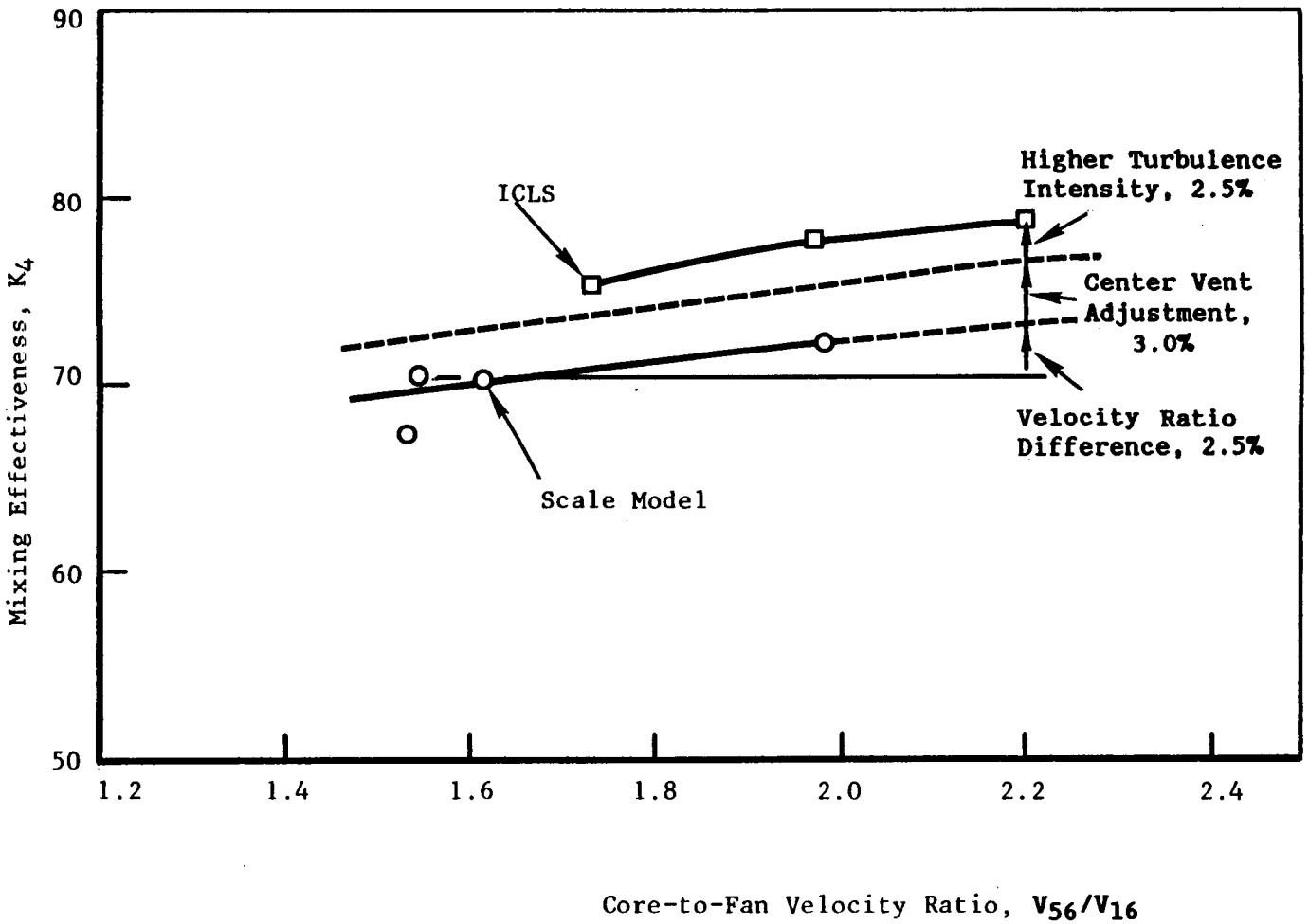


Figure 326. Model-to-Full Scale Mixing Effectiveness Stackup.

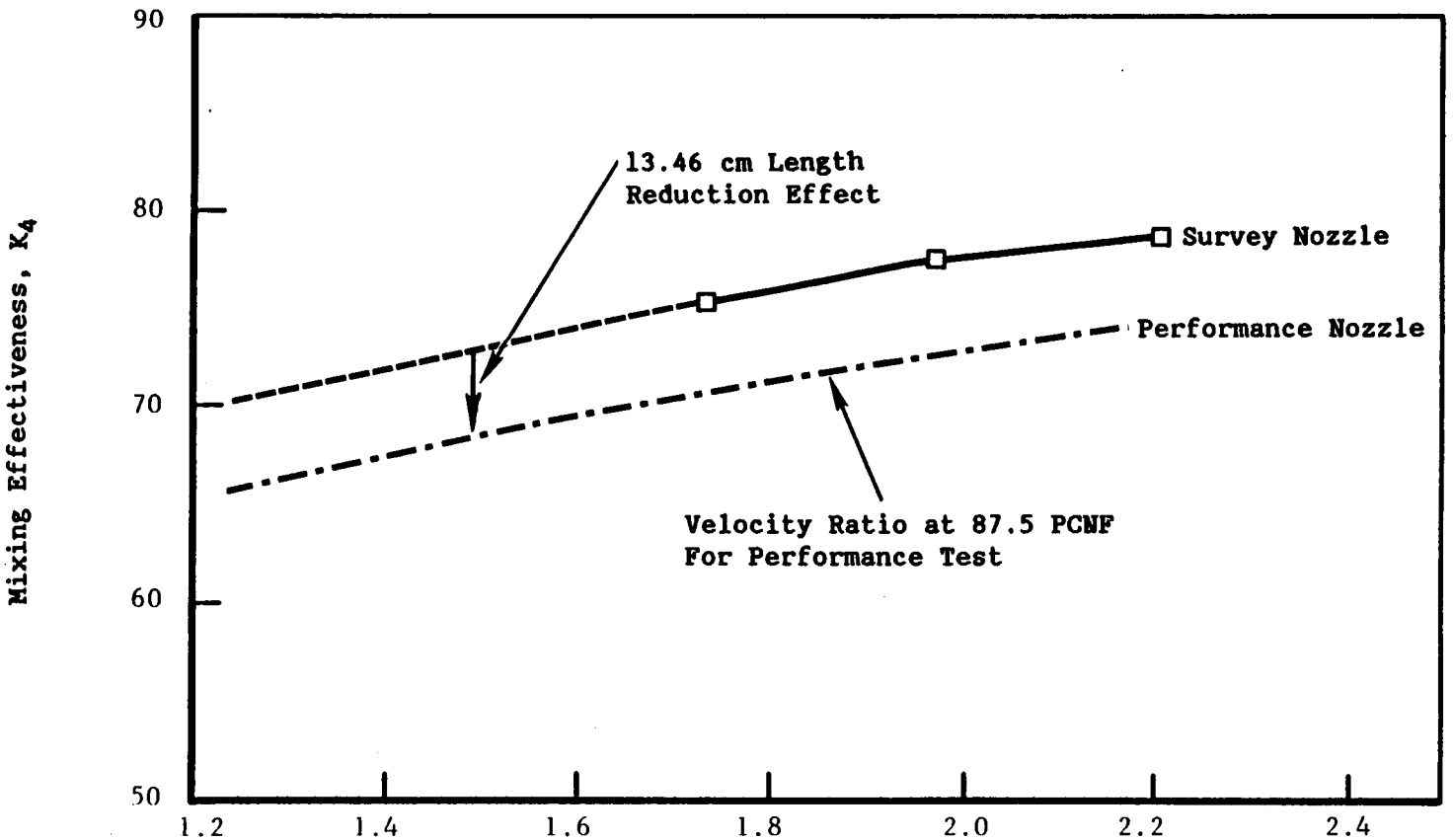


Figure 327. ICLS Mixing Effectiveness Characteristic.

the performance nozzle. The resulting curves, shown in Figure 327, required some extrapolation to cover lower power setting ranges and would have to be included as part of the engine cycle deck modeling to represent the mixer aerodynamic performance properly. Thus, at the actual velocity ratio with the performance nozzle (no rake blockage), the ICLS mixing effectiveness at the max speed point (87.5 PCNF) was 72% versus the 78.8% indicated by the data in Figure 324. For the survey nozzle which was the same length as the scale model test, the mixing effectiveness was 76.5%.

These results were used to project the mixing effectiveness for the FPS configuration. The best mixer configuration tested in the scale model program was shown in Figure 327 and had a mixing effectiveness of 79.2% at a velocity ratio of 1.87%. Two adjustments to this data point are valid based on the ICLS data and the foregoing analysis. It can be expected that the mixing effectiveness will increase due to better mixing at the nozzle centerline because of the center vent tube. In this case, the FPS scale model mixer had a smaller hot flow spike than the ICLS scale model mixer, and the gain was calculated to be 2%. Adding the 2.5% model-to-full scale flowfield turbulence intensity adjustment results in a mixing effectiveness of 83.7%. This point along with the slope of the ICLS characteristic shown in Figure 327 was used to estimate the mixing effectiveness characteristic for the best FPS mixer tested in the scale model program. This characteristic is presented in Figure 328. As a result of the scale model test development program, it was concluded that, with additional work, an improvement in mixing effectiveness of the best FPS scale model mixer from 79% to 85% could be achieved through some combination of lobe shape change, increased penetration, and increased number of lobes. Part of the 6% improvement would have come from an elimination of the hot flow spike at the nozzle centerline. Since this has already been accounted for in Figure 328 (2%), it can be concluded that further improvements in design amounting to 4% in mixing effectiveness are achievable. Adding this to the best FPS mixer tested, results in the FPS mixer projection in Figure 328. The velocity ratio expected for FPS will be in the 1.5 to 1.6% range at the M0.8/10.67 km (35,000 ft) point, and the resulting mixing effectiveness would be ~85%.

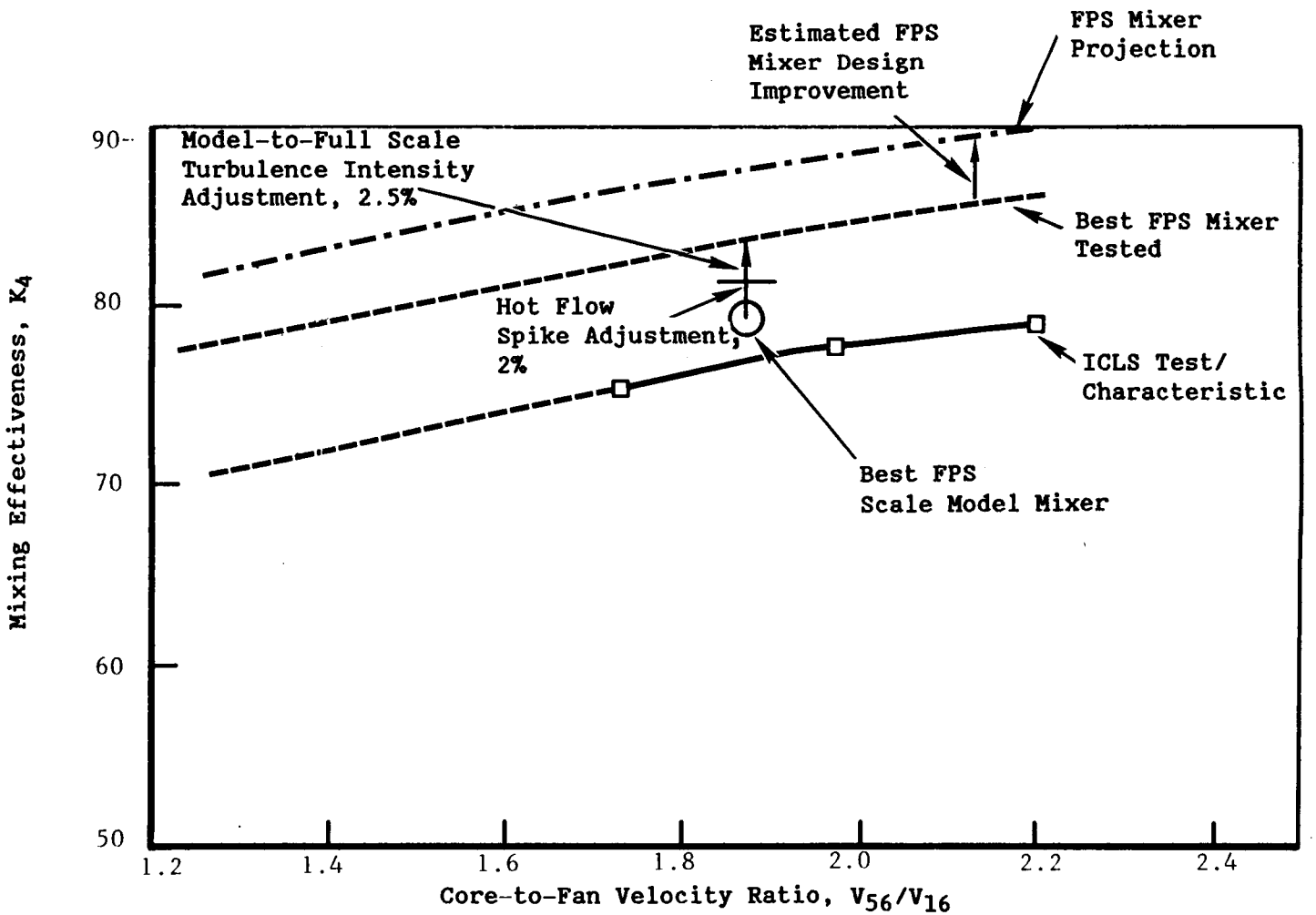


Figure 328. FPS Mixing Effectiveness Projection.

In summary, the results of the ICLS test in terms of mixing effectiveness were favorable from two aspects. First, the mixing effectiveness achieved was more than 5% higher than expected due to flow quality effects and geometry (center vent) differences. And second, the test data established the effect of mixing plane velocity ratio on performance and the need for its inclusion in cycle deck modeling of mixer performance. Results were also used to project the estimated mixer performance for the FPS design. The mixer performance including sfc benefit at MX cruise is summarized in the following table and Figure 329. Thus, the sfc goal can be essentially achieved but with a different combination of mixing effectiveness and pressure loss.

| | Mixing[1] Effectiveness, K4 | Mixer Pressure Loss, $\%\Delta P_T$ | SFC[2] Improvement, % |
|---|---|---|---|
| Program Goal | 75 | 0.2 | 2.9 |
| ICLS Test | 74 | 0.66[3] | 2.3 |
| Best FPS Mixer | 81 | 0.57[4] | 2.7 |
| FPS Projection | 85 | 0.57 | 2.9 |

1 At M0.85/7.6 km (25,000 ft) MXCR mixing plane velocity raito

2 Determined at M0.8/10.67 km (35,000 ft) MXCR relative to no mixing

3 For design intent geometry (survey nozzle)

4 Based on scale model test

Overall exhaust system aerodynamic performance was assessed by comparing the measured exhaust system coefficients with the cycle deck predictions. These include the overall thrust coefficient and overall flow coefficient defined as follows:

$$\text{Overall Thrust Coefficient} = C_{TOA} = \frac{F_{gmeasured}}{F_{gi_{fan}} + F_{gi_{core}}}$$

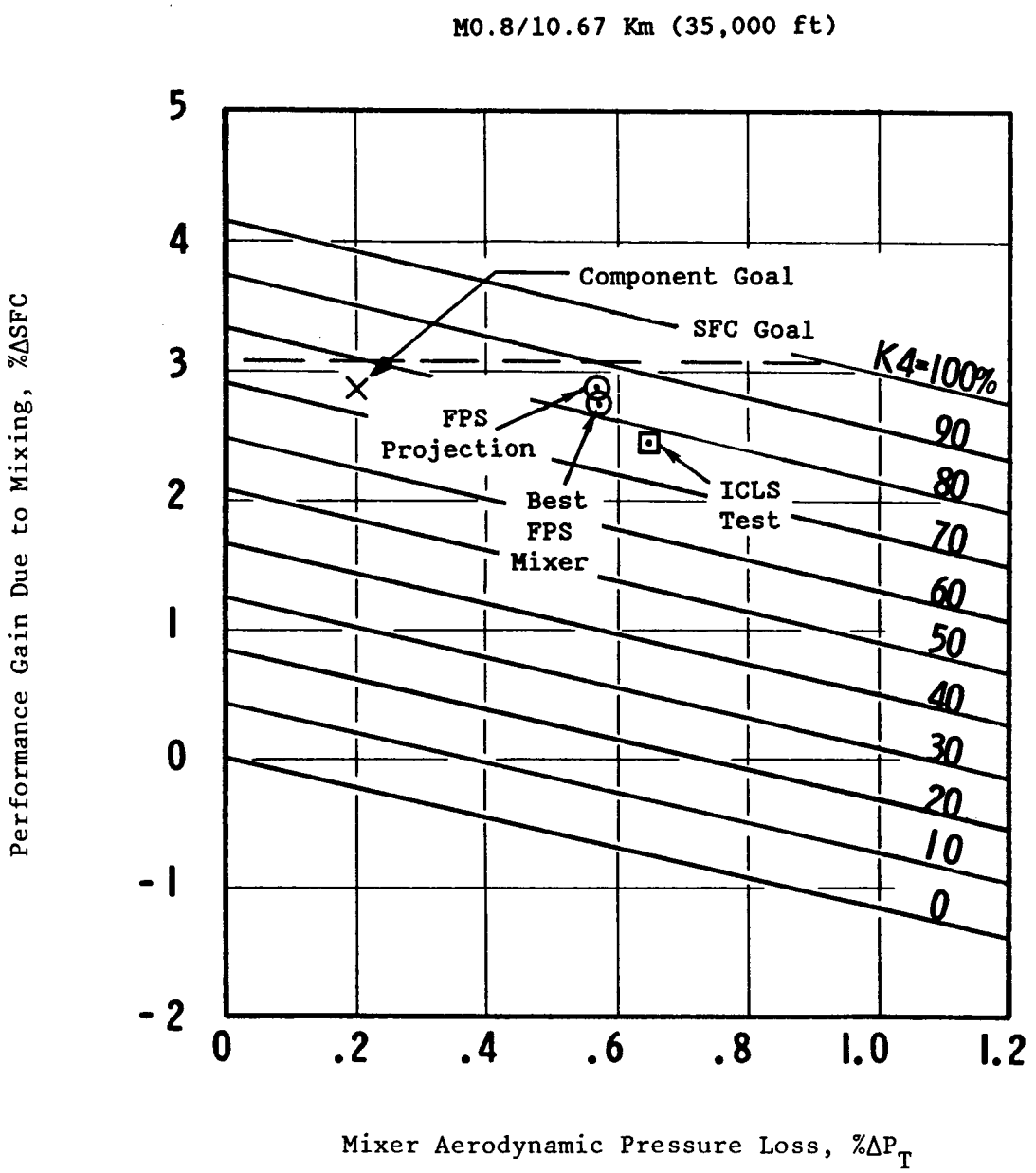


Figure 329. Mixer Performance Gain Summary.

where:

$F_{gmeasured}$ = measured nozzle gross thrust,

$F_{gi_{fan}}$ = ideal, unmixed fan flow thrust based on fan discharge flow, pressure, and temperature expanded to ambient pressure,

$F_{gi_{core}}$ = ideal, unmixed core flow thrust based on LPT discharge flow, pressure, and temperature expanded to ambient pressure,

$$\text{Overall Flow Coefficient} = C_{F8_{0A}} = \frac{A_{efan} + A_{ecore}}{A_{8nozzle}}$$

where:

$A_{efan}$ = effective area required to ideally expand the fan discharge flow to ambient pressure,

$A_{ecore}$ = effective area required to ideally expand the core discharge flow to ambient pressure,

$A_{8nozzle}$ = physical exit area of the exhaust nozzle.

Thus, the overall coefficients reflect all the elements of the exhaust system performance including fan and core duct pressure losses, mixer pressure loss, mixing effectiveness, exhaust nozzle pressure loss, and exhaust nozzle exit coefficients. Only the mixing effectiveness as previously discussed can be isolated from the total system performance.

The overall exhaust system coefficients from the performance test are presented in Figure 330 along with the predicted curves. The predictions include the effects of 64.5 $cm^2$ (10 $in^2$) of nacelle leakage area as determined from a pretest leak check of the nacelle and the actual mixing effectiveness as determined from the nozzle exit survey data. Comparison of test versus prediction indicates the thrust coefficients are approximately 1% below the expected values and the flow coefficients are 0 to 0.25% above the prediction.

Several factors, however, must be considered in the exhaust system performance data analysis. It had been noted during the course of the test

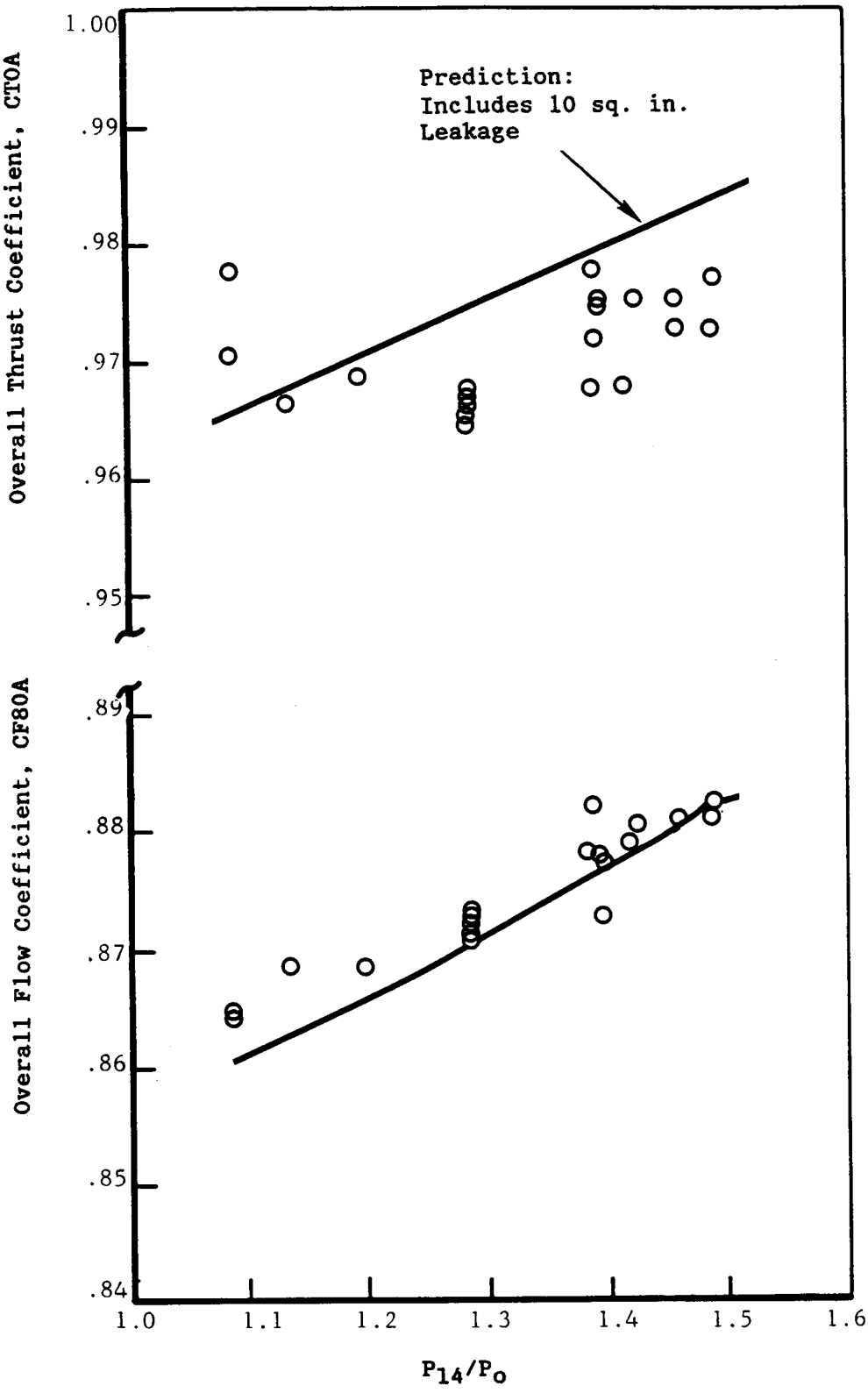


Figure 330. Overall Exhaust System Performance.

program that the fan duct outer nacelle doors opened and closed much more easily than at the beginning of the testing. Additionally, back-to-back test runs at the end of the program with the exhaust system taped and untaped for acoustic tests indicated a significant shift in engine performance (sfc). Because of these occurrences, it is suspected that the nacelle leakage may have significantly increased above the pretest leak test results. If additional leakage were considered in the predictions, the effects would be as shown in Figure 331.

The difference between the measured data and the predictions can be converted to a fan duct total pressure loss from either the flow or thrust coefficient parameters. This has been done for the 64.5 and 258.0 $cm^2$ (10 and 40 $in^2$) prediction curves as presented in Figure 332. If the leakage area were 64.5 $cm^2$ (10 $in^2$), the test data implies that the excess fan duct pressure loss at the high speed condition ($P_{14}/P_o$ = ~1.47) was approximately 0.75% and zero as derived from the thrust coefficient and flow coefficient data, respectively. Since these two results do not agree, the data indicates that the nacelle leakage area was larger than 64.5 $cm^2$ (10 $in^2$) Assuming 258.0 $cm^2$ (40 $in^2$) leakage area, the inferred fan duct pressure loss increase is in much closer agreement from the two coefficients. Thus, an inferred fan duct pressure loss increase and nacelle leakage area can be determined from a unique solution of the thrust and flow coefficient data versus predictions. This solution, shown for the high speed condition in Figure 333, implies that nacelle leakage was over 193.5 $cm^2$ (30 $in^2$) and the fan duct pressure loss was ~0.3% higher than expected.

Another consideration in this evaluation is the absolute level of accuracy of fan discharge total pressure measurement. It is very possible that this pressure may have been measured 0.3% higher than the true value, rather than the duct loss being higher. This is a recognized problem associated with the radial fan discharge pressure profiles of high bypass ratio turbofan engines.

A final consideration is data accuracy/repeatability. Following the exit survey tests with the survey nozzle shown in Figure 335, the survey

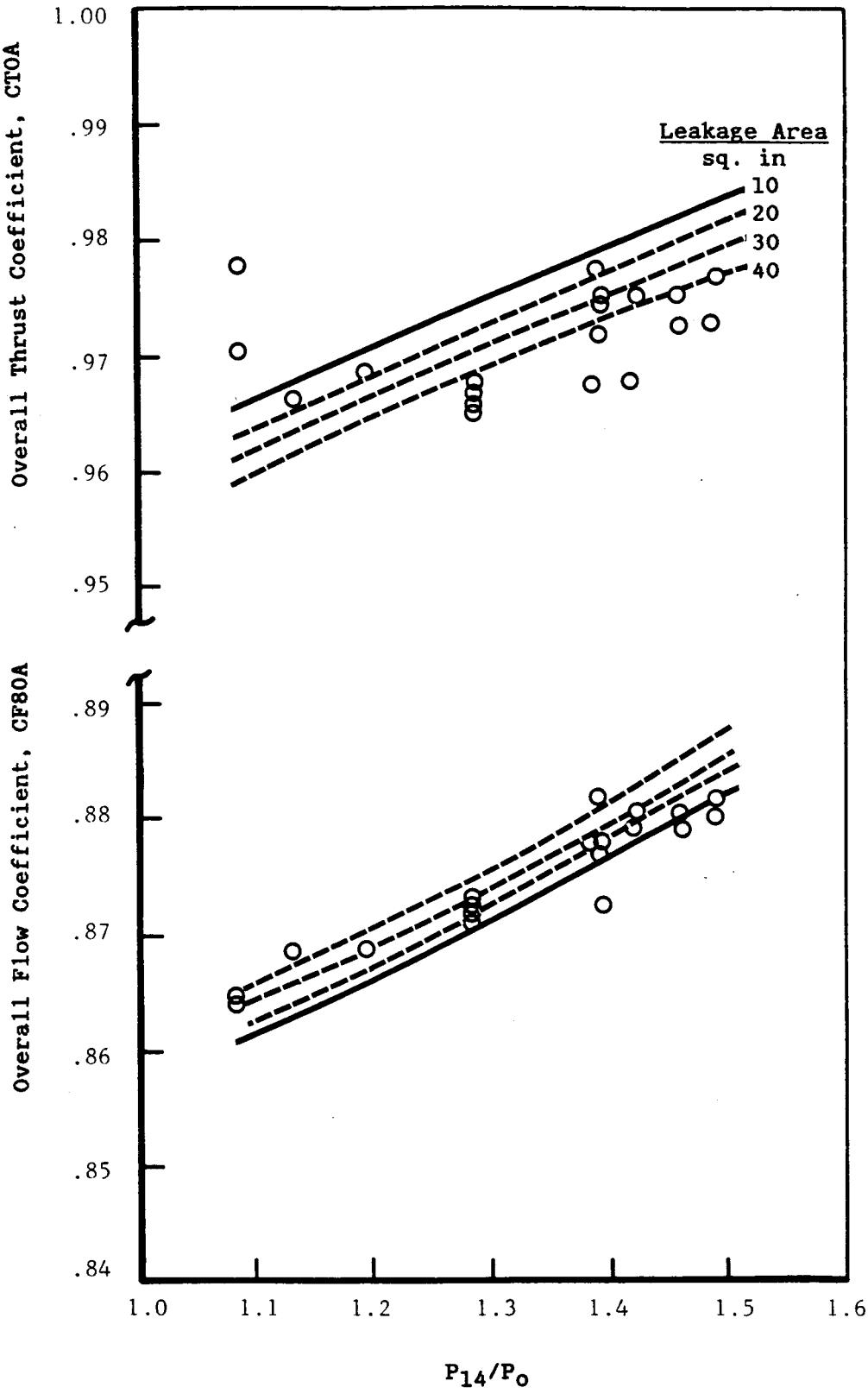


Figure 331. Nacelle Leakage Variation Effects on Overall Exhaust System Performance.

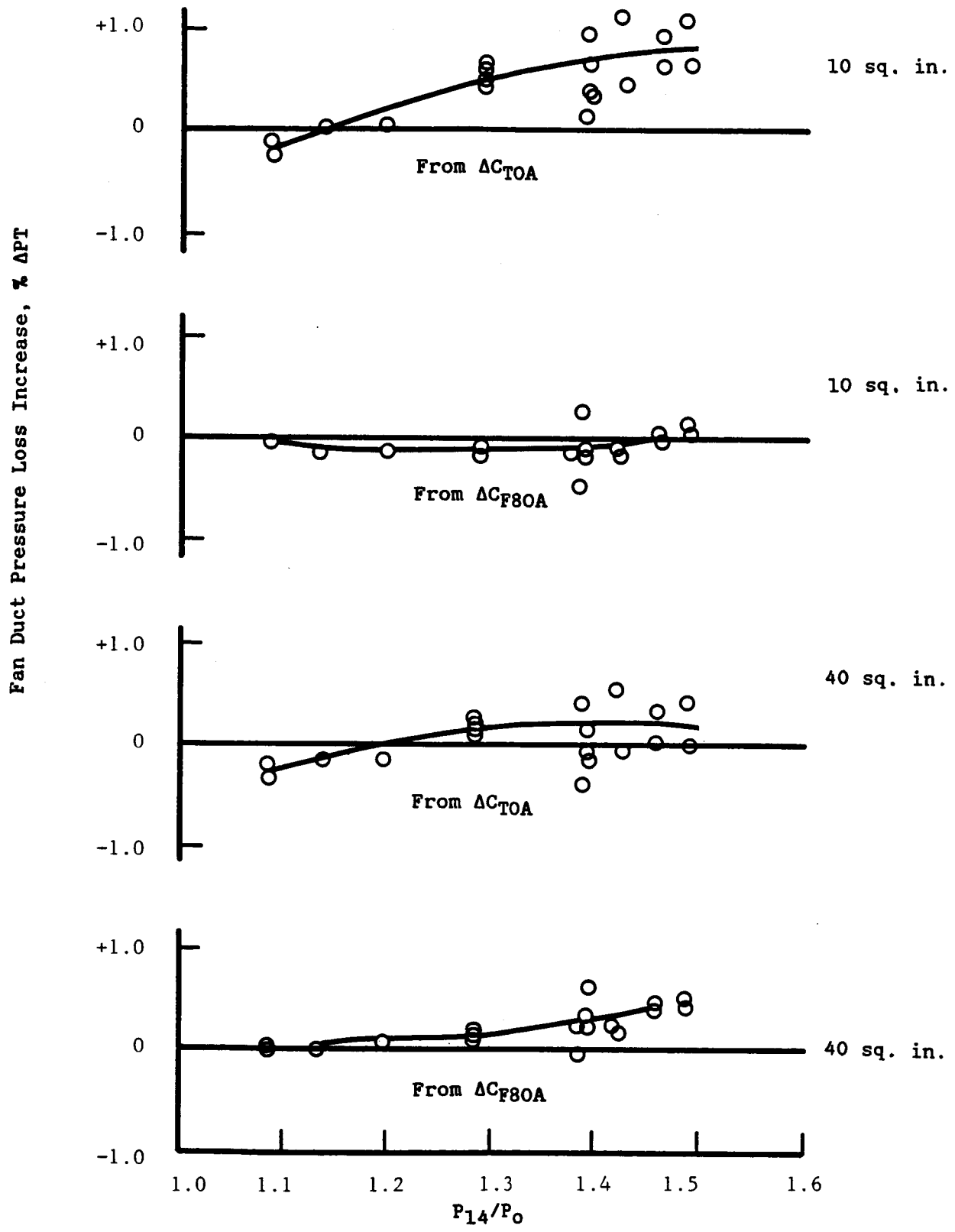


Figure 332. Fan Duct Pressure Loss Increase Derived From Exhaust System Coefficients.

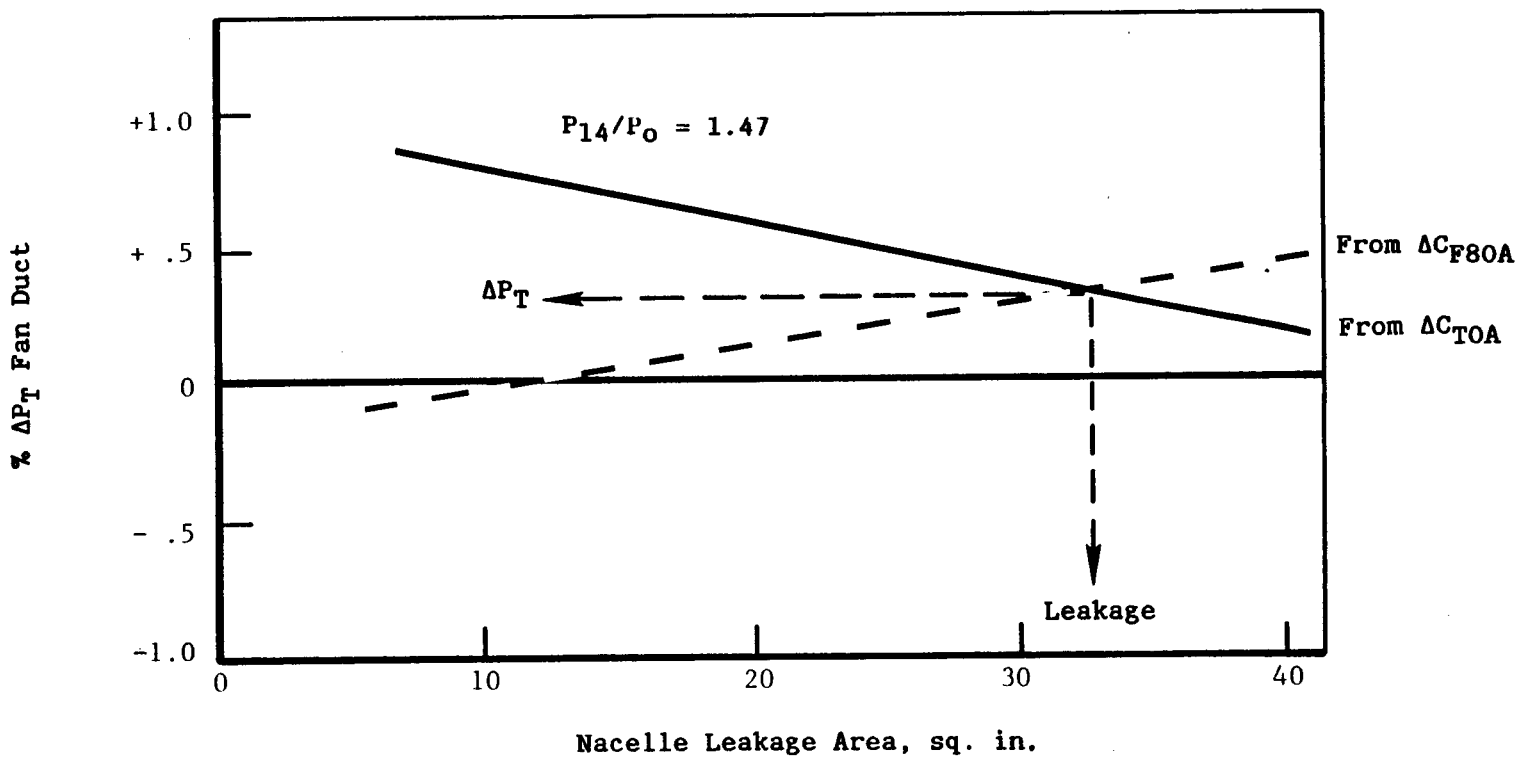


Figure 333. Fan Duct Pressure Loss Increase and Nacelle Leakage Inferred from Exhaust System Coefficients.

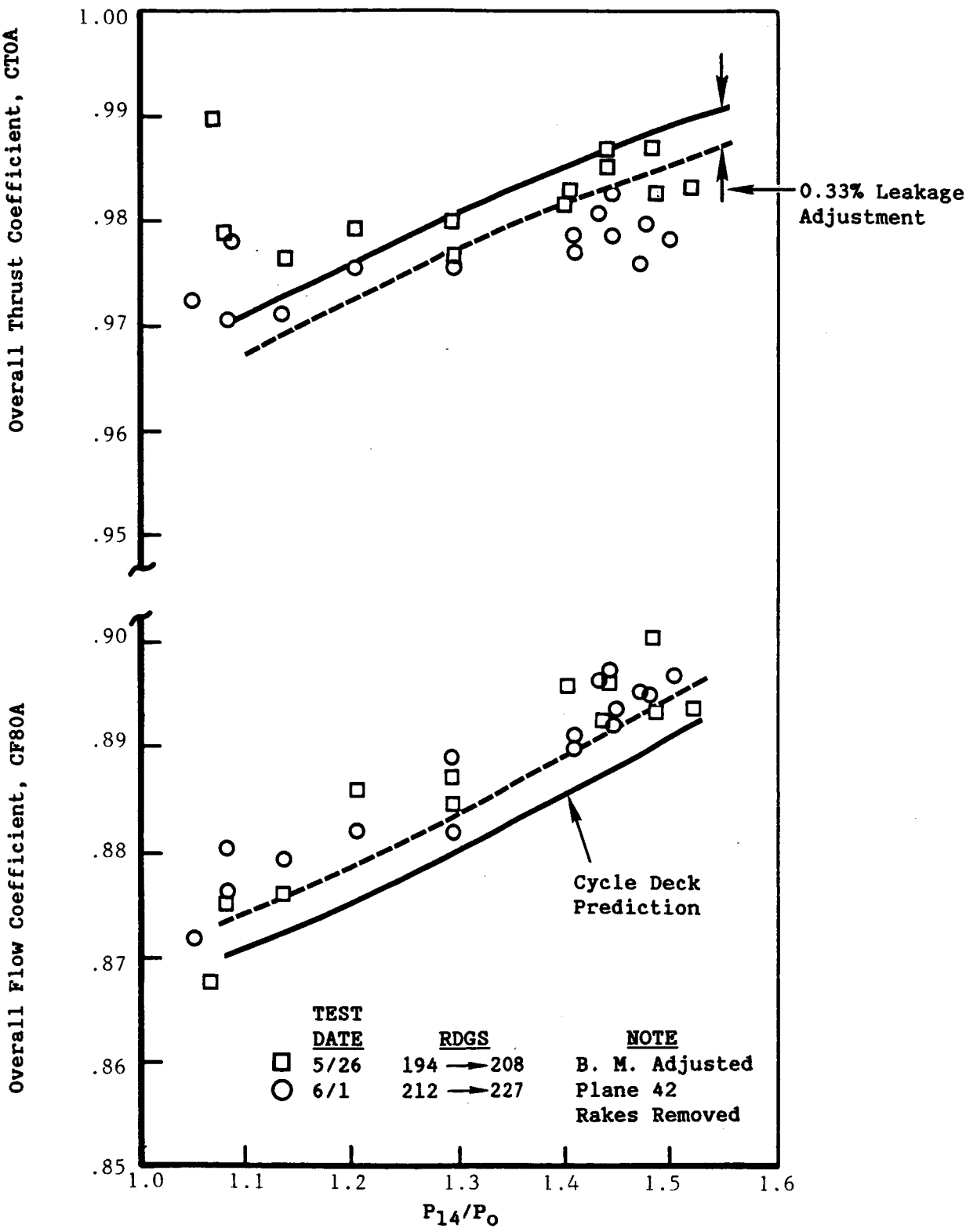


Figure 334. Overall Exhaust System Performance Repeatability.

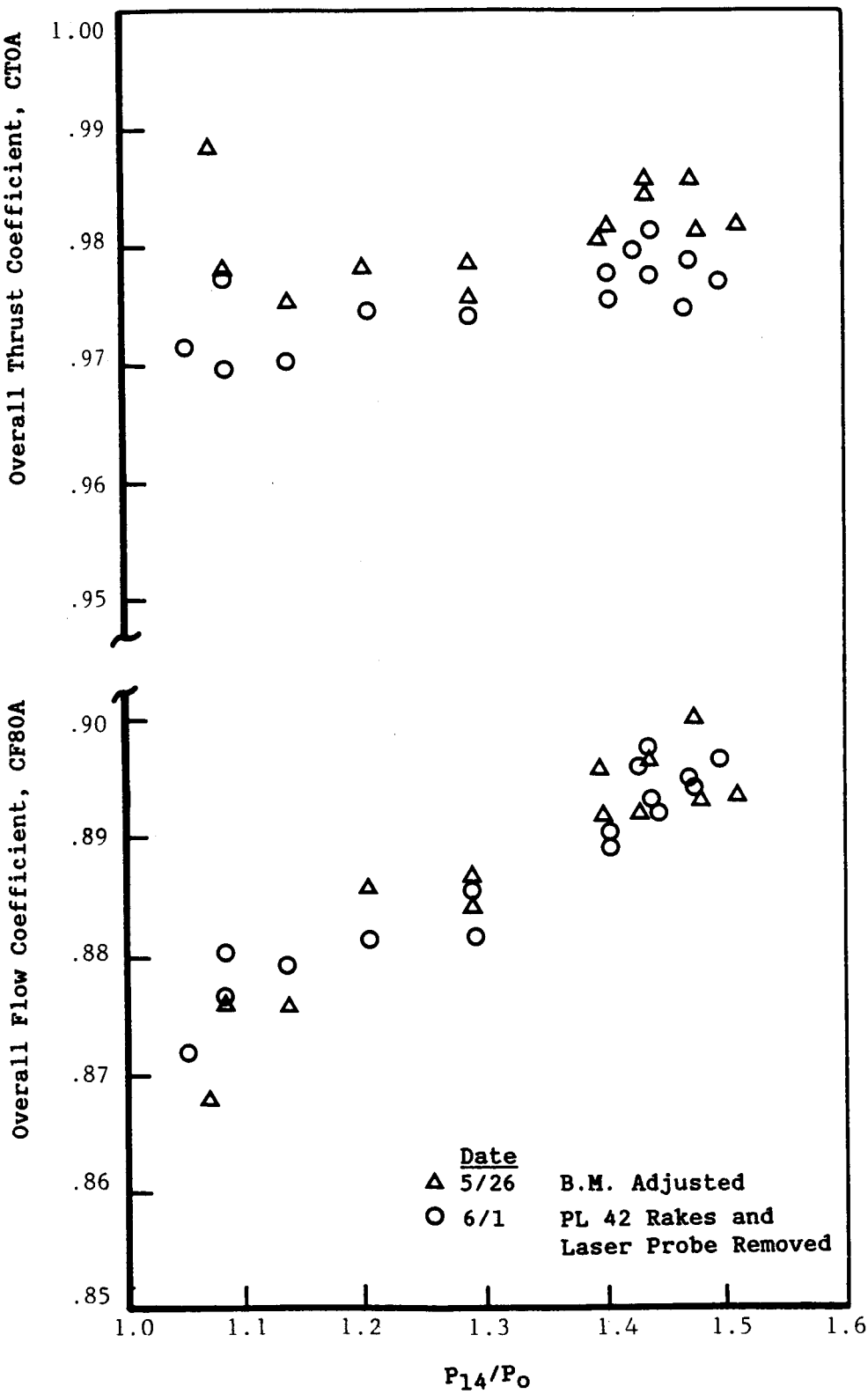


Figure 335. Overall Nozzle Performance Data Repeatability.

nozzle was tested without the exit rakes in two separate runs. The nozzle performance data from these two runs are shown in Figure 335. While no difference in flow coefficient can be discerned between the two runs, a shift of 0.5% in the thrust coefficient is clearly evident; thus, any difference between test and prediction less than 0.5% could very well be the limit of the data system measurement accuracy/repeatability.

Based on the foregoing analysis, it has been concluded that: (1) the actual exhaust system leakage area was probably between 64.5 $cm^2$ (10 $in^2$) (pretest measured value) and 193.5 $cm^2$ (30 $in^2$) and (2) the exhaust system performance was within 0.25% of predictions considering thrust data accuracy and P14 measurement capability. From this and a qualitative assessment of the nozzle exit total pressure profiles, it has also been concluded that the mixer pressure loss was essentially as predicted (0.66% $\Delta P_T$) from the mixer scale model tests.

## 6.17 SUMPS, DRIVES, CONFIGURATION, AND LUBE SYSTEMS PERFORMANCE

All components in the sumps, drive, piping, and lube systems functioned well during all testing of the ICLS engine. No test limits were exceeded in any of these components. Each area will be considered separately in the following paragraphs. The ICLS engine contains two sumps whose performance will be described individually.

### 6.17.1 Forward Sump

Figures 336, 337, and 338 show the temperature performance characteristics of the No. 1, No. 2, and No. 3 bearings, respectively. Shown in these figures is the bearing outer race $\Delta T$ (bearing outer race - oil in temperature) versus fan speed for the No. 1 and No. 2 bearings and core speed for the No. 3 bearing. The measured $\Delta T$ of these bearings is in line with previous engine experience.

The maximum outer race temperatures for the forward sump bearings are shown in Table XXV.

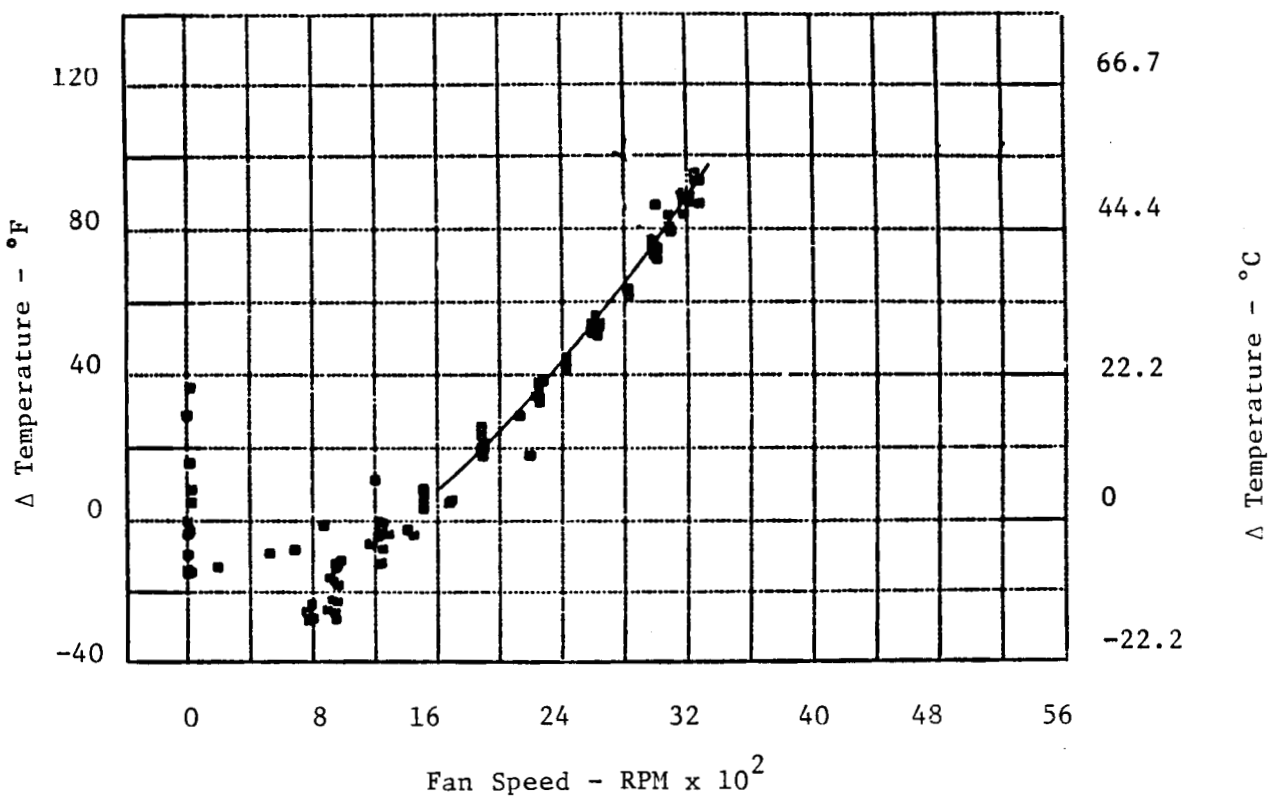


**Figure 336. Number 1 Bearing ΔT vs. Fan Speed.**

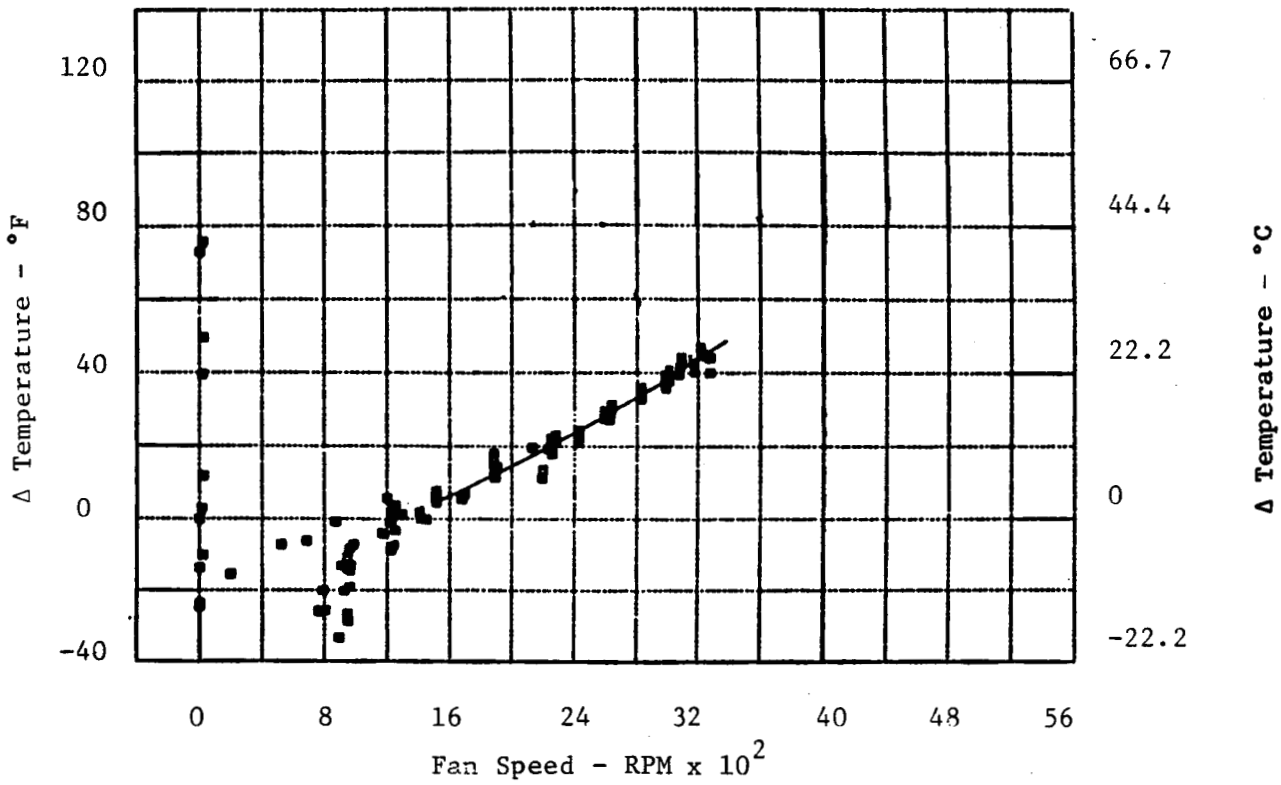


Figure 337. Number 2 Bearing ΔT vs Fan Speed.

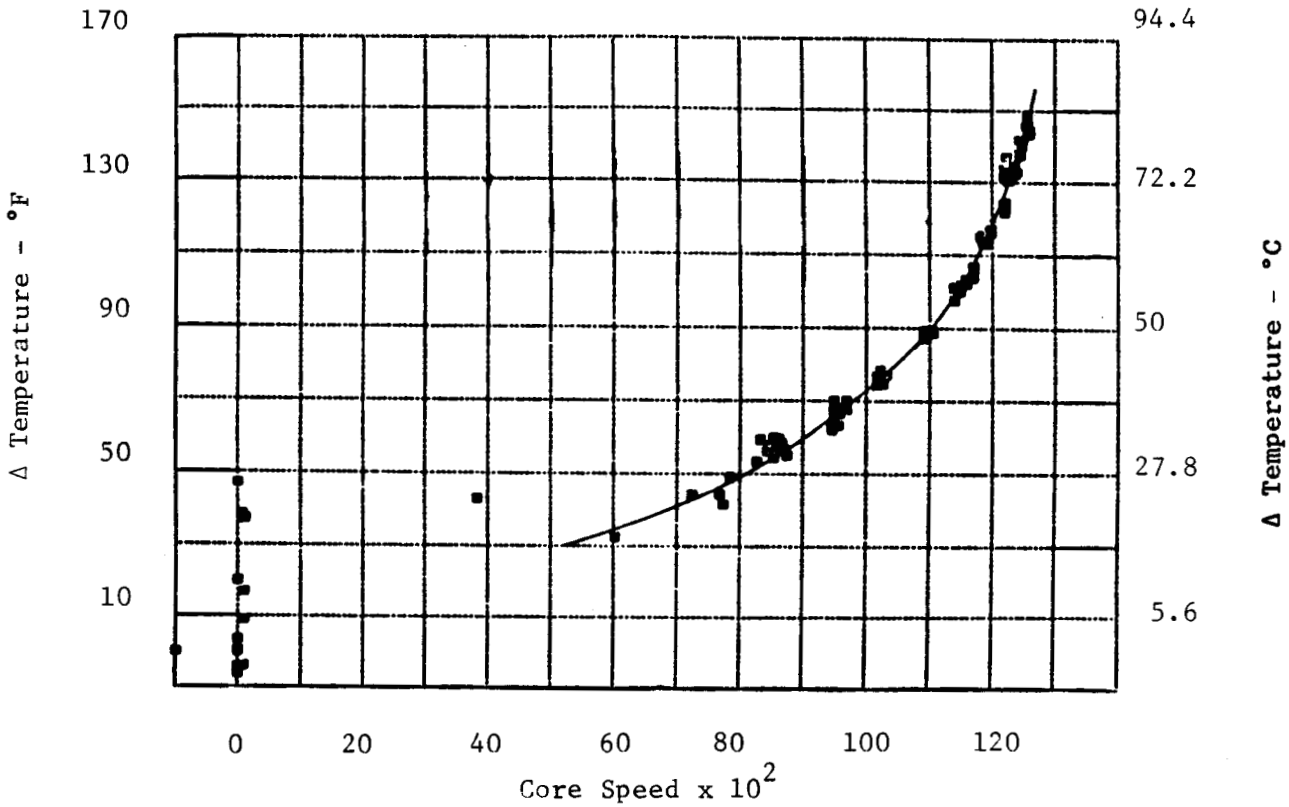


Figure 338. Number 3 Bearing ΔT vs Fan Speed.

Table XXV. Maximum Forward Sump Bearing Outer Race Temperatures.

| Bearing Position | Maximum Temperature |
|---|---|
| 1 | 126.1°C (259°F) |
| 2 | 85°C (185°F) |
| 3 | 152.2°C (306°F) |

The maximum allowable outer race temperature of 204.4°C (400°F) was not exceeded at any test point. The outer race temperatures of the No. 1 and No. 2 bearing were representative of low DN (bearing bore diameter, MM x shaft rpm) bearings. The core thrust bearing (No. 3) operated 14.4°C (26°F) hotter at maximum speed in the ICLS engine than it did in the Core engine. The difference between the thrust load and speed relationship of the two builds is the probable reason for the difference. The No. 3 bearing was the same bearing that was used in the Core engine.

The forward sump labyrinth seals were pressurized with fan discharge pressure. The seal pressure as a function of fan speed is shown in Figure 339. At maximum speed the sump seal ΔP was 38.0 kPa (5.51 psid) which was more than adequate to prevent oil leakage. At idle speed the seal ΔP, although lower, was still adequate to prevent leakage of oil.

Both the low pressure and high pressure system thrust bearings were located in the forward sump. Figures 340 and 341 show the "on line" calculation of the HP (No. 3) and LP (No. 1) thrust bearing axial load. Pretest predictions of the axial loads were made by using computer techniques developed for engine rotor thrust analysis. As part of substantiating these calculations, the bearing thrust loads were calculated for each DMS reading using preprogrammed equations and actual test data. Predicted loads and loads calculated during the test corresponded very well as can be seen in Figures 340 and 341. Positive thrust is in the forward direction.

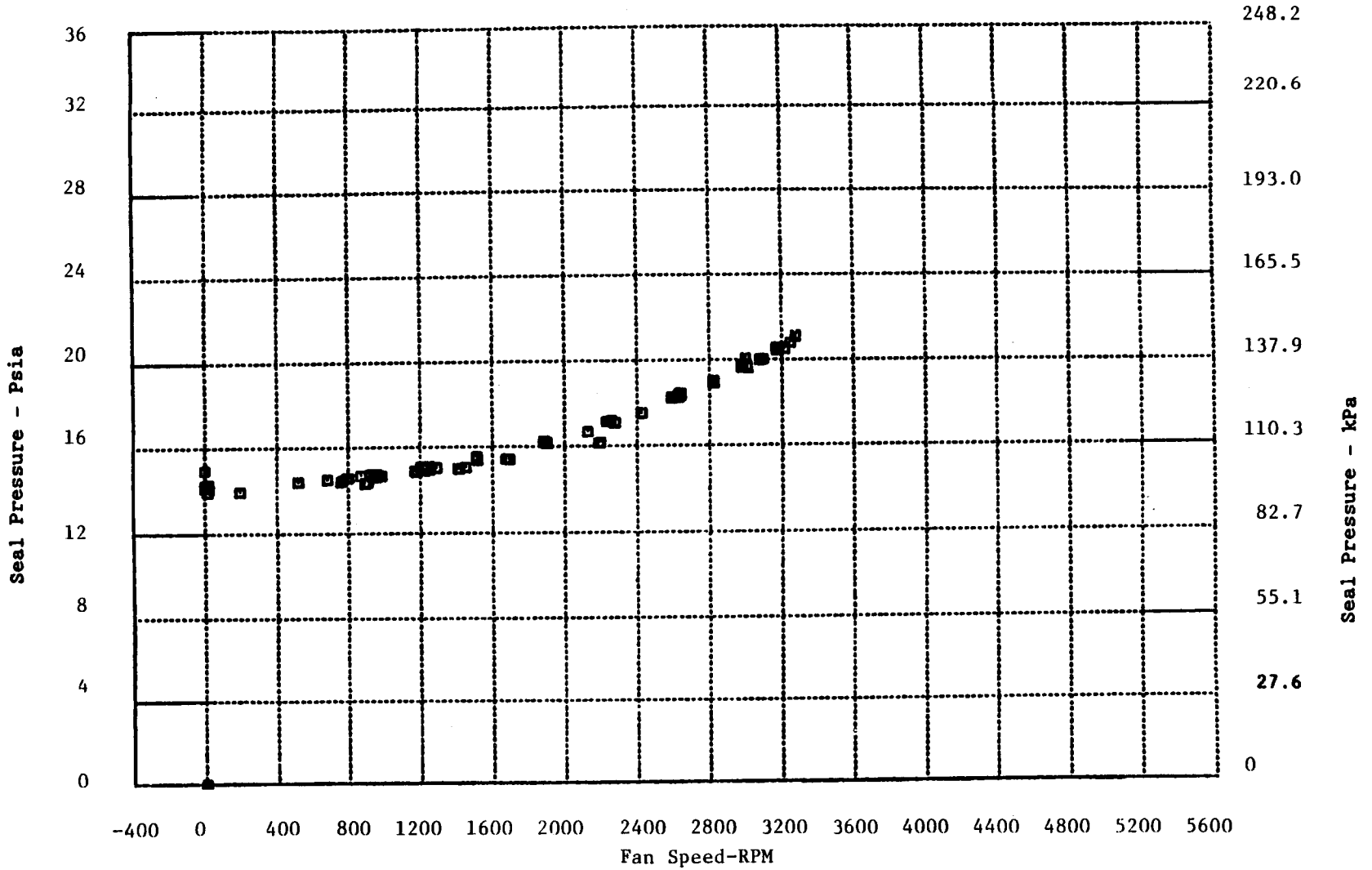


Figure 339. Forward Sumps Seal Pressure Versus Fan Speed.

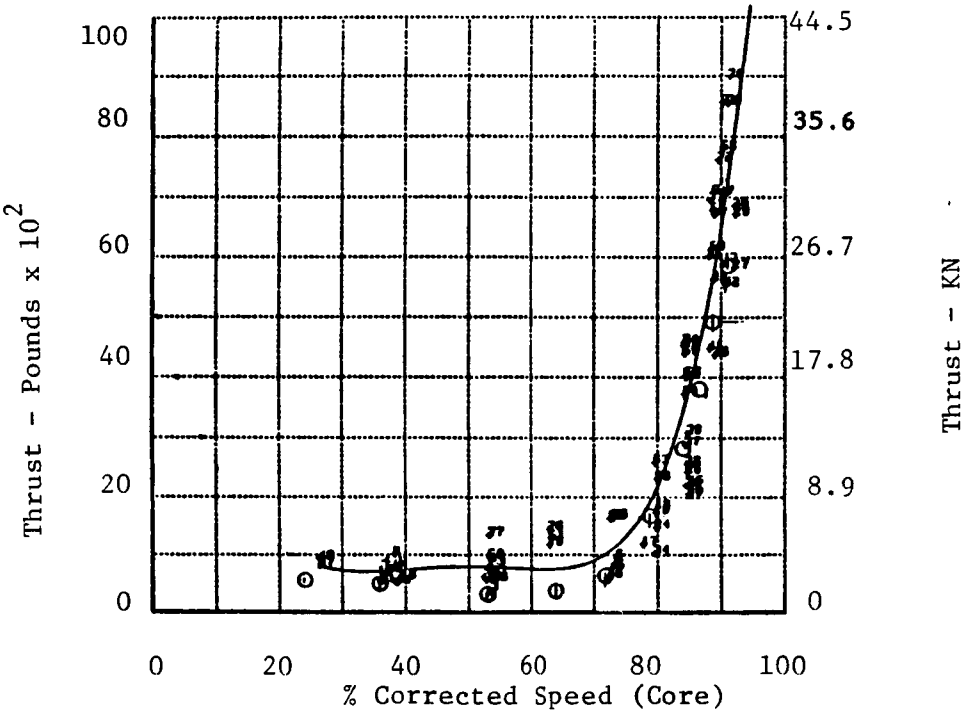


Figure 340. HP Bearing (Number 3) Thrust Load Versus Percent Corrected Core Speed.

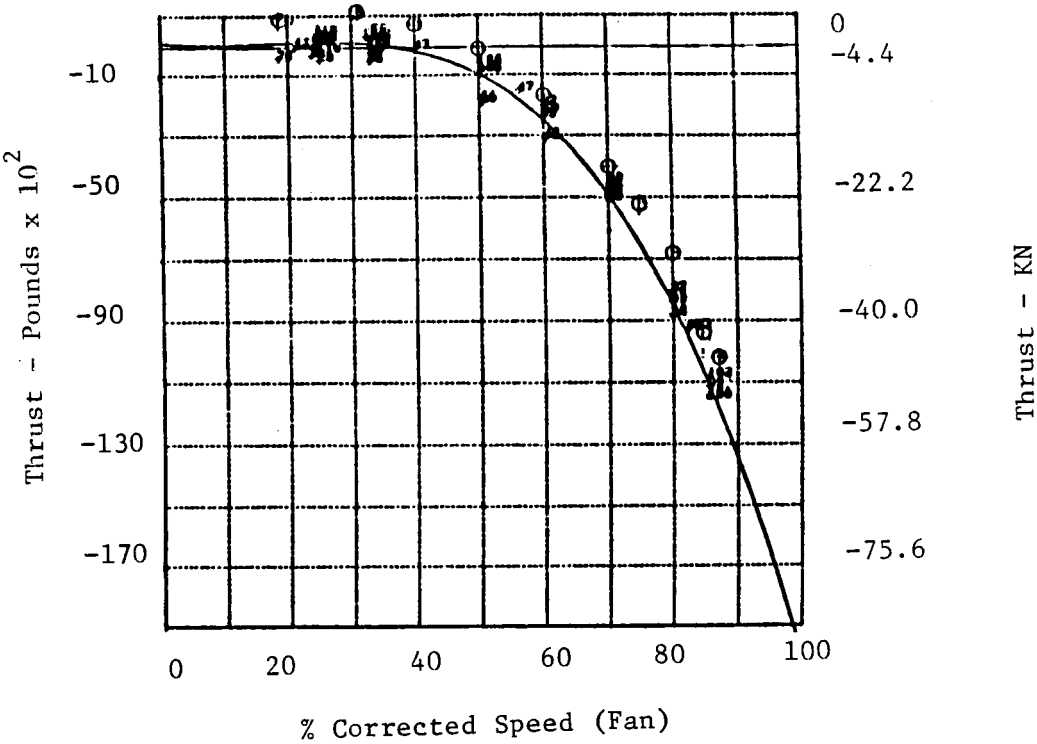


Figure 341. LP Bearing (Number 1) Thrust Load Versus Percent Corrected Fan Speed.

6.17.2 Aft Sump

The No. 4 and No. 5 bearing temperature performance is shown in Figures 342 and 343. Shown are the bearing ΔT (bearing outer race - oil in temperature) versus the difference in the Core and Fan speed for the No. 4 bearing and the fan speed for the No. 5 bearing. The measured ΔT's of these bearings are in line with previous engine experience. No problems were encountered with the No. 4 differential bearing which functioned as anticipated throughout the test.

Table XXVI shows the maximum outer race temperature for the aft sump bearings.

Table XXVI. Maximum Aft Sump Bearing Outer Race Temperature.

| Bearing Position | Maximum Temperature |
|---|---|
| 4 | 179.4°C (355°F) |
| 5 | 112.2°C (234°F) |

The maximum temperature of the aft roller bearing in the Core engine (No. 4 bearing in the ICLS engine) was 190.0°C (374°F) which occurred at the maximum speed. The maximum temperature of the No. 4 bearing during the ICLS test occurred approximately 1,800 rpm fan speed and decreased to about 148.9°C (300°F) at maximum speed. The lower temperature at maximum speed is due to the lower oil supply temperature at maximum speed and the co-rotating differential action of the bearing.

The operating temperature of the No. 5 bearing, because of its low operating speed, was low as would be expected.

The outer race temperature of the aft sump bearings never exceeded the test limit of 204.4°C (400°F) and were stable at each speed point.

The performance of the aft co-rotating differential bearing (No. 4) was of particular interest during the ICLS test. Important to the successful

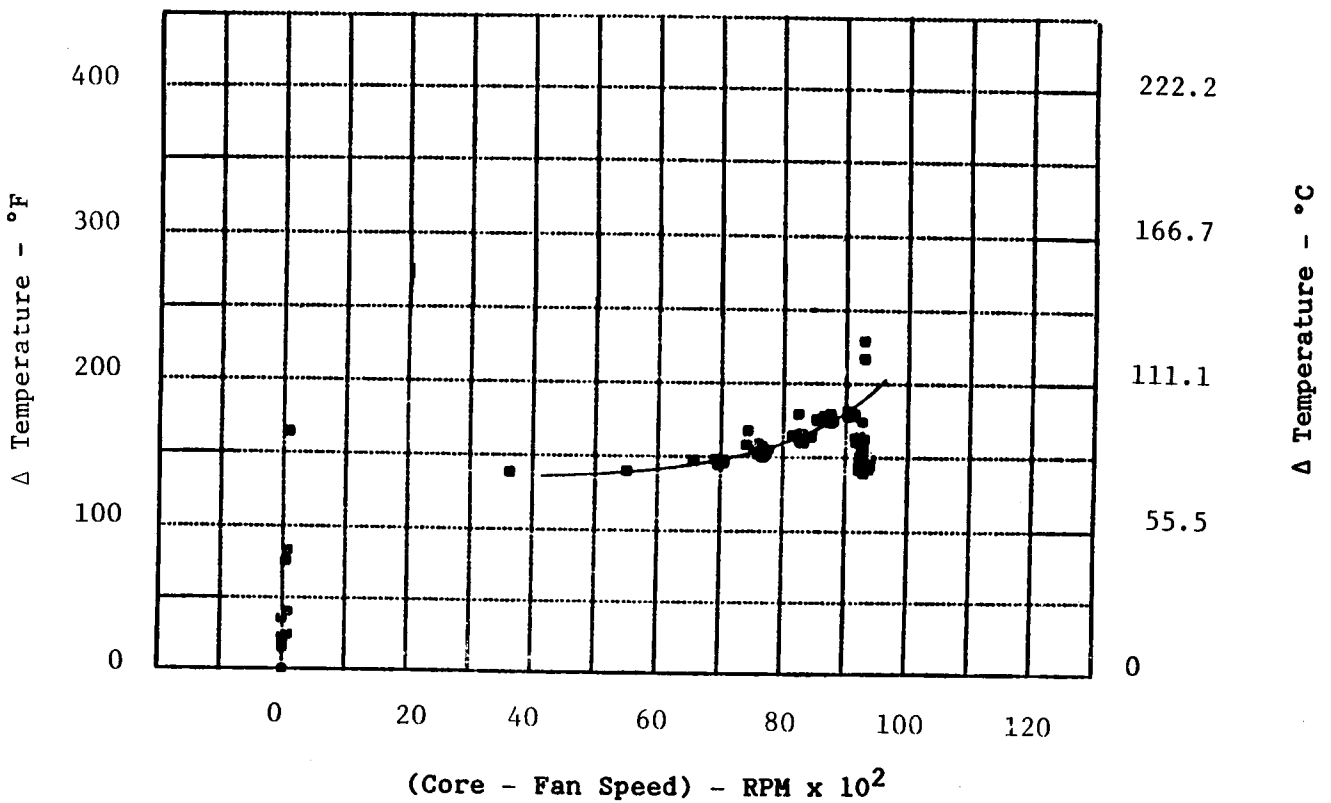


Figure 342. Number 4 Bearing ΔT Versus (Core - Fan) Speed.

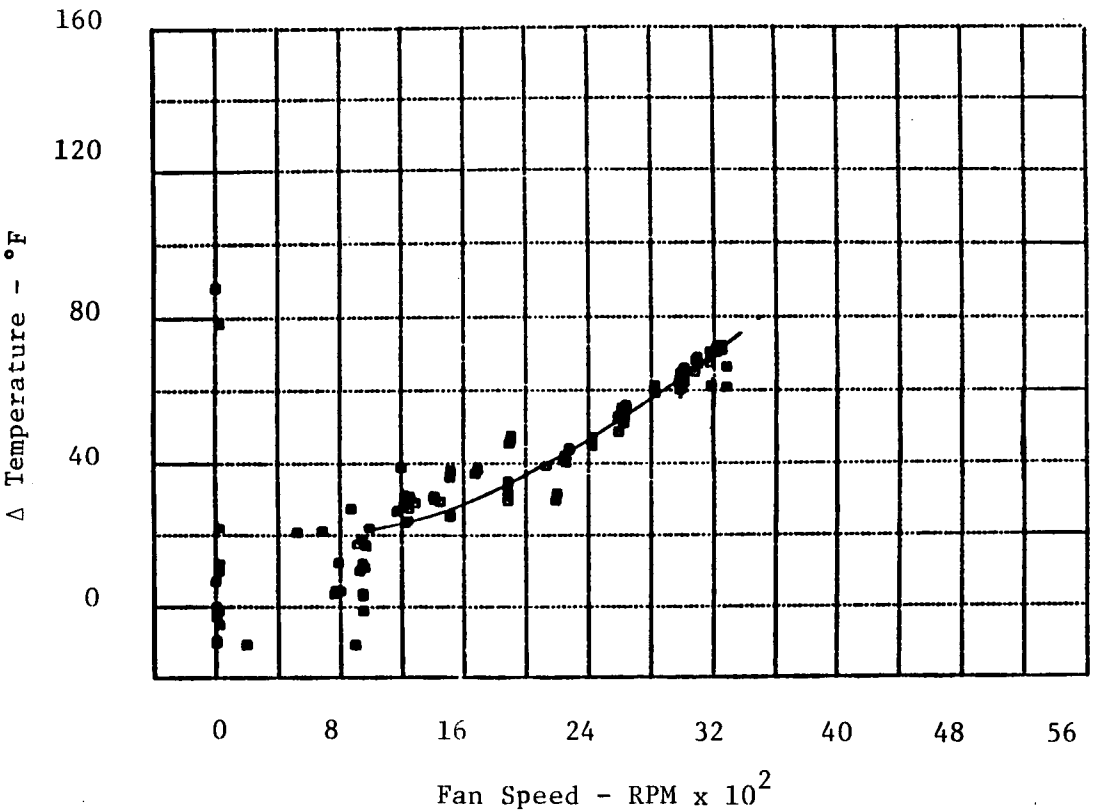


Figure 343. Number 5 Bearing ΔT Versus Fan Speed.

operation of this type of bearing is minimizing roller skidding due to high operating speeds and low external loads. To reduce the possibility of skidding, the internal fitup of the bearing was designed to run slightly tight at maximum speed.

To monitor the bearing for roller skidding, a previously developed method was used to measure roller passing frequency. Slots are produced in the outer race of the bearing which are wide enough that deflections, generated as the rollers pass under it, can be measured as elastic strain by strain gages. The output of the strain gage gives a dynamic readout of roller passing frequency. If the rollers are not skidding, they will pass the strain gages at a passing frequency corresponding to the cage epicyclic speed. Skidding occurs when the rollers are passing at less than or more than the theoretical epicyclic speed. The roller passing frequency is given by the following equation:

$$f_t = \frac{Z}{120} \times [1 - \alpha] \times [N_i - N_o] \text{ (peaks/second or cycles/second)}$$

where

D = Roller
dm = Pitch
Z = Number of roller
$N_i$ = Core shaft speed
$N_o$ = Fan shaft speed
$\alpha$ = D/dm

For the ICLS engine

$$f_t = .2167 [N_i - N_o]$$

Figure 344 shows the output of the No. 4 bearing outer race strain gages from 8,200 to 12,600 Core rpm. The vertical lines would have indicated a magnitude of stress if the strain gages had been calibrated, which they were

ORIGINAL PAGE IS
OF POOR QUALITY

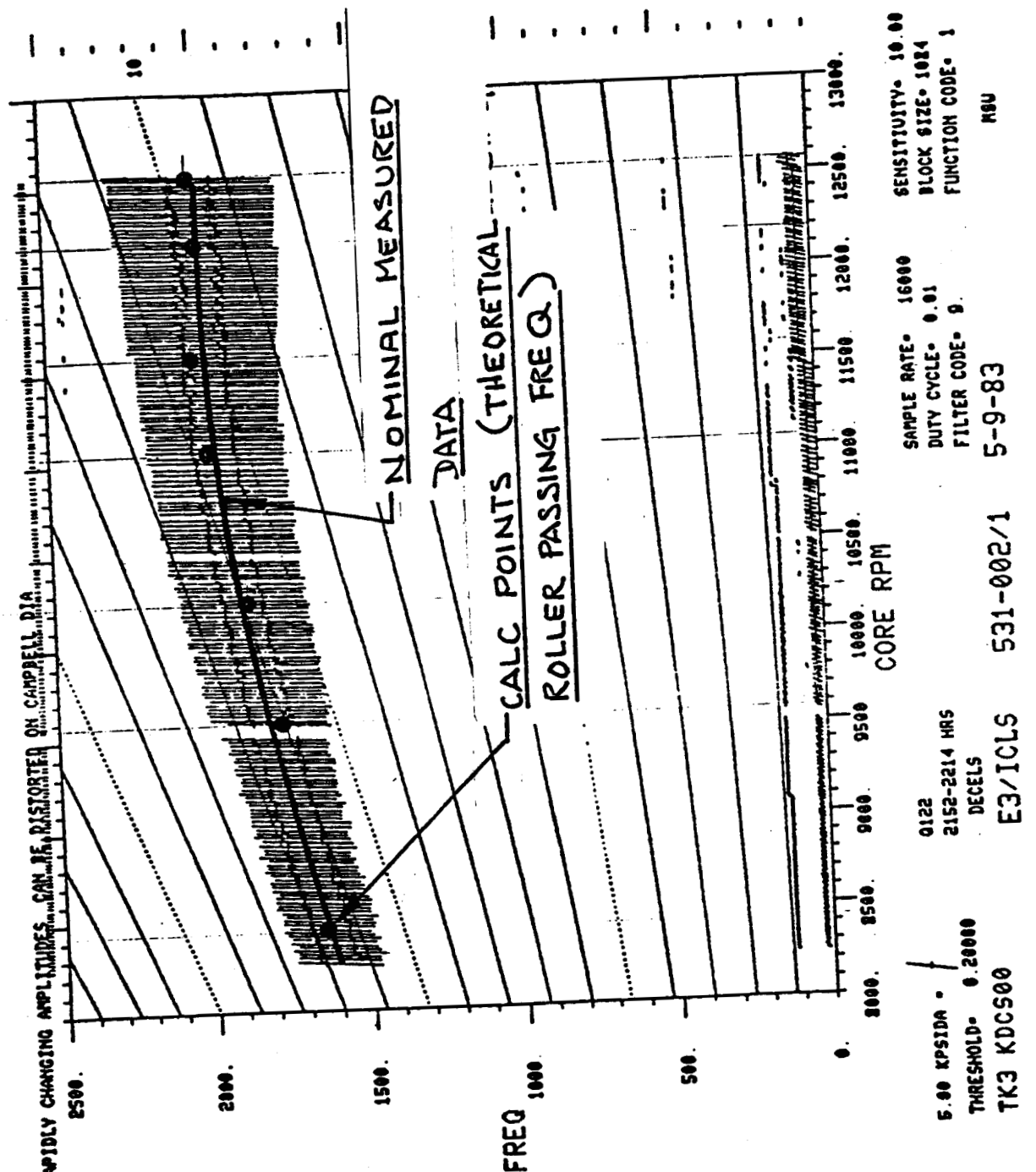


Figure 344. Number 4 Bearing Roller Passing Frequency.

not since frequency was the area of interest. The points shown on Figure 345 represent calculations of the theoretical roller passing frequency with no skidding. Measurements during the test indicate there was no skidding problem with the ICLS intershaft bearing.

The aft sump labyrinth seals were pressurized with fan discharge pressure. This seal pressurization air was obtained from the forward sump area through an annulus formed by the outside diameter of the center vent pipe and the inside diameter of the LP shaft. The aft seal pressure as a function of fan speed is shown in Figure 345. The pressure drop at maximum speed between the forward and aft sump is approximately 15.30 kPa (2.22 psid) as can be seen by comparing Figures 339 and 345. More than adequate pressure was available to prevent oil leakage from the aft sump at all speed conditions including idle speed.

### 6.17.3 Accessory Drives

All aspects of the drive system functioned well throughout the testing. The PTO and AGB were the same hardware that was used in the core engine test. The radial shafting was unique to the ICLS engine and no problems were encountered. Thermocouples on the midspan bearing housing did not indicate any unstable temperature conditions.

### 6.17.4 Configuration

The configuration system consisting of the pneumatic piping for the compressor and turbine active clearance control and turbine cooling, the external lube and fuel lines, all electrical harnesses, and the pressure bulkhead, did not experience any problems during test. The design limits of radial temperature gradient and $\Delta P$ on the pressure bulkhead were not exceeded during the test.

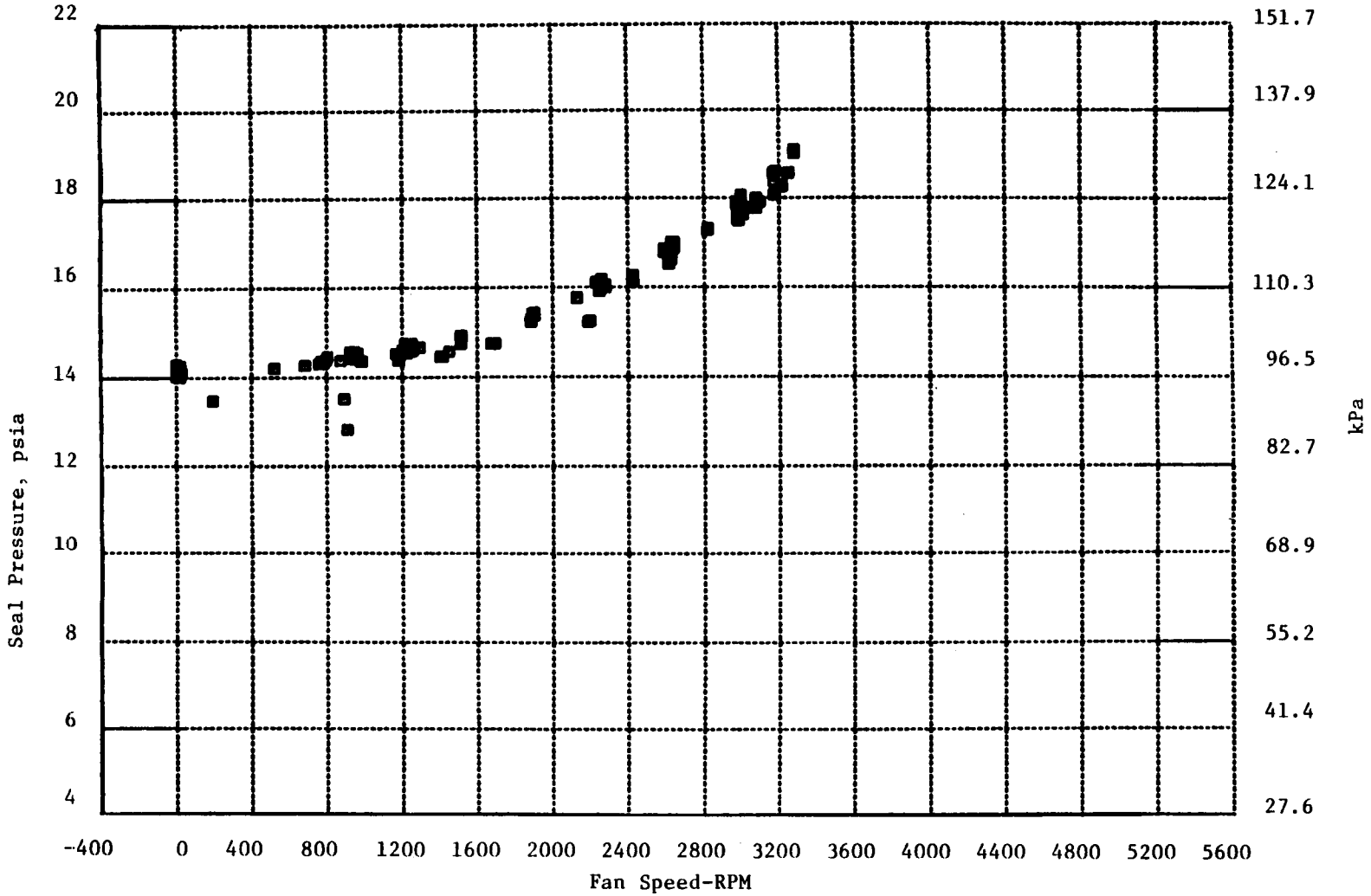


Figure 345. Aft Sump Seal Pressure Versus Fan Speed.

6.17.5 Lube System

All lube system parameters functioned well throughout the test. Figure 346 shows lube supply temperature to the engine as a function of fan speed. The maximum supply temperature was 82.8°C (181°F) which occurred at about 1200 rpm fan speed. The scavenge temperatures of the forward sump, the aft sump, and the accessory gearbox are shown in Figures 347, 348, and 349, respectively. The maximum lube temperature rise in these components shown in Table XXVII were representative of current engines.

Table XXVII. Lube Temperature Rise in Major Components of ICLS Engine.

| Component | Temperature Rise |
|---|---|
| Forward Sump | 41.6°C (74.8°F) |
| Aft Sump | 58.2°C (104.8°F) |
| Accessory Gearbox | 24.6°C (44.2°F) |

Figure 350 shows the combined scavenge temperature as it entered the heat exchanger.

Oil loss during testing was low. During one phase of testing, consisting of a 6 hour run, the average oil usage was 0.12 gal/hr which is consistent with current high bypass commercial engines.

To determine the heat generated in the lube system, the amount of heat added to the fuel at the heat exchanger was calculated using the following relationship:

$$Q = WC\ (TD - TU)$$

where

Q = Heat generated in fuel
W = Corrected measured fuel flow
C = Specific heat of fuel as a function of temperature
TD = Temperature of fuel leaving heat exchanger
TU = Temperature of fuel entering heat exchanger

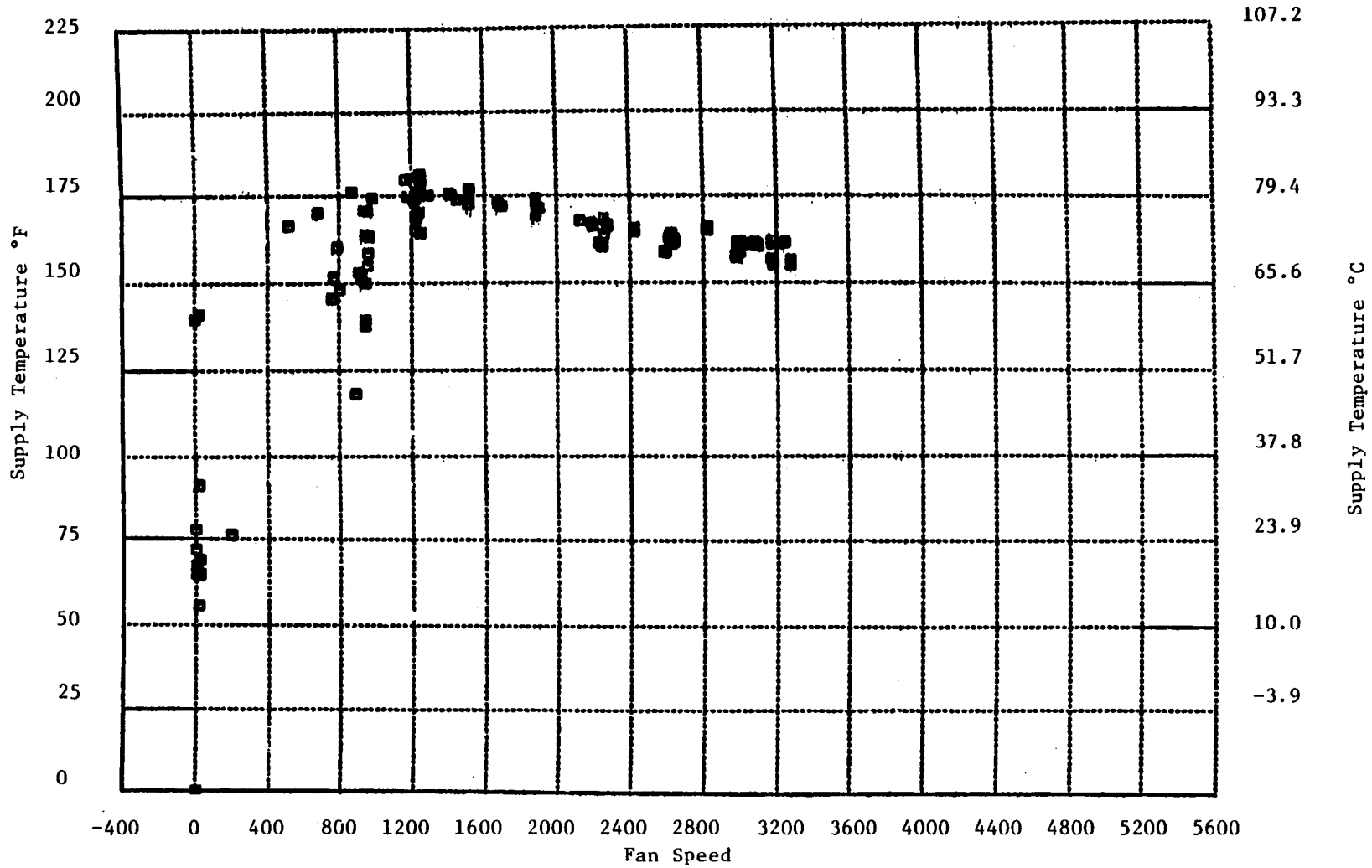


Figure 346. Lube Supply Temperature to Engine Versus Fan Speed.

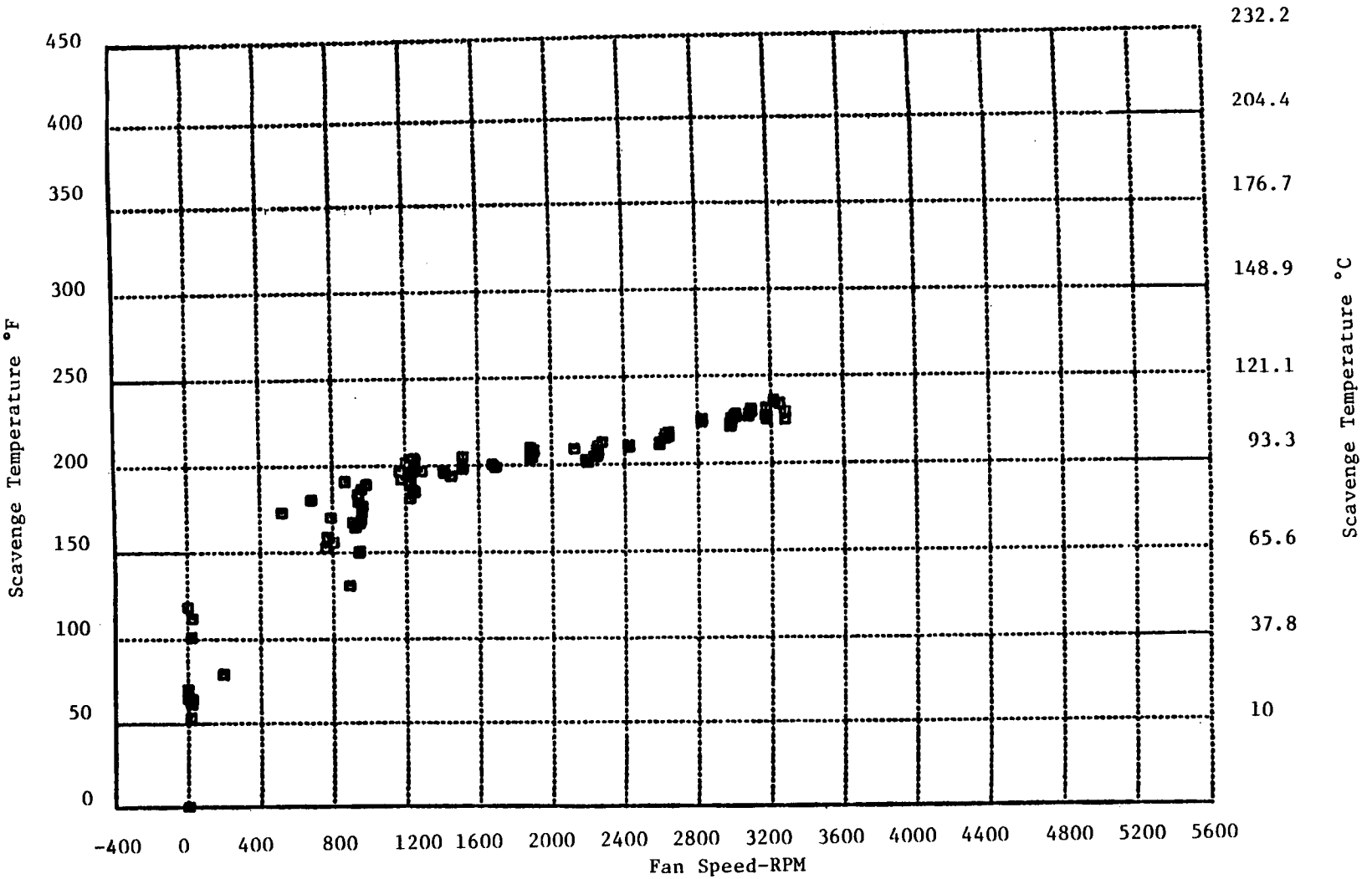


Figure 347. Forward Sump Scavenge Temperature Versus Fan Speed.

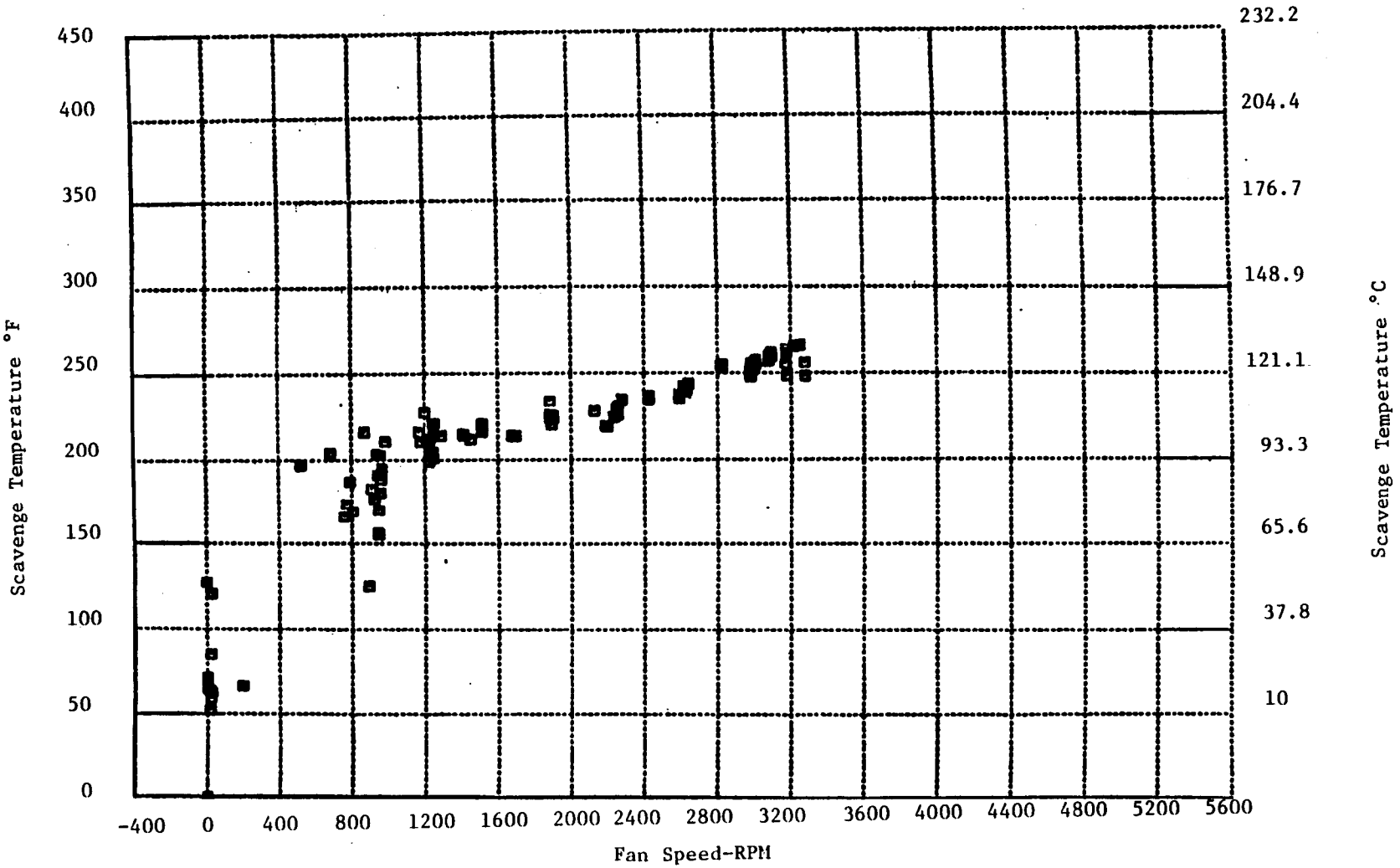


Figure 348. Aft Sump Scavenge Temperature Versus Fan Speed.

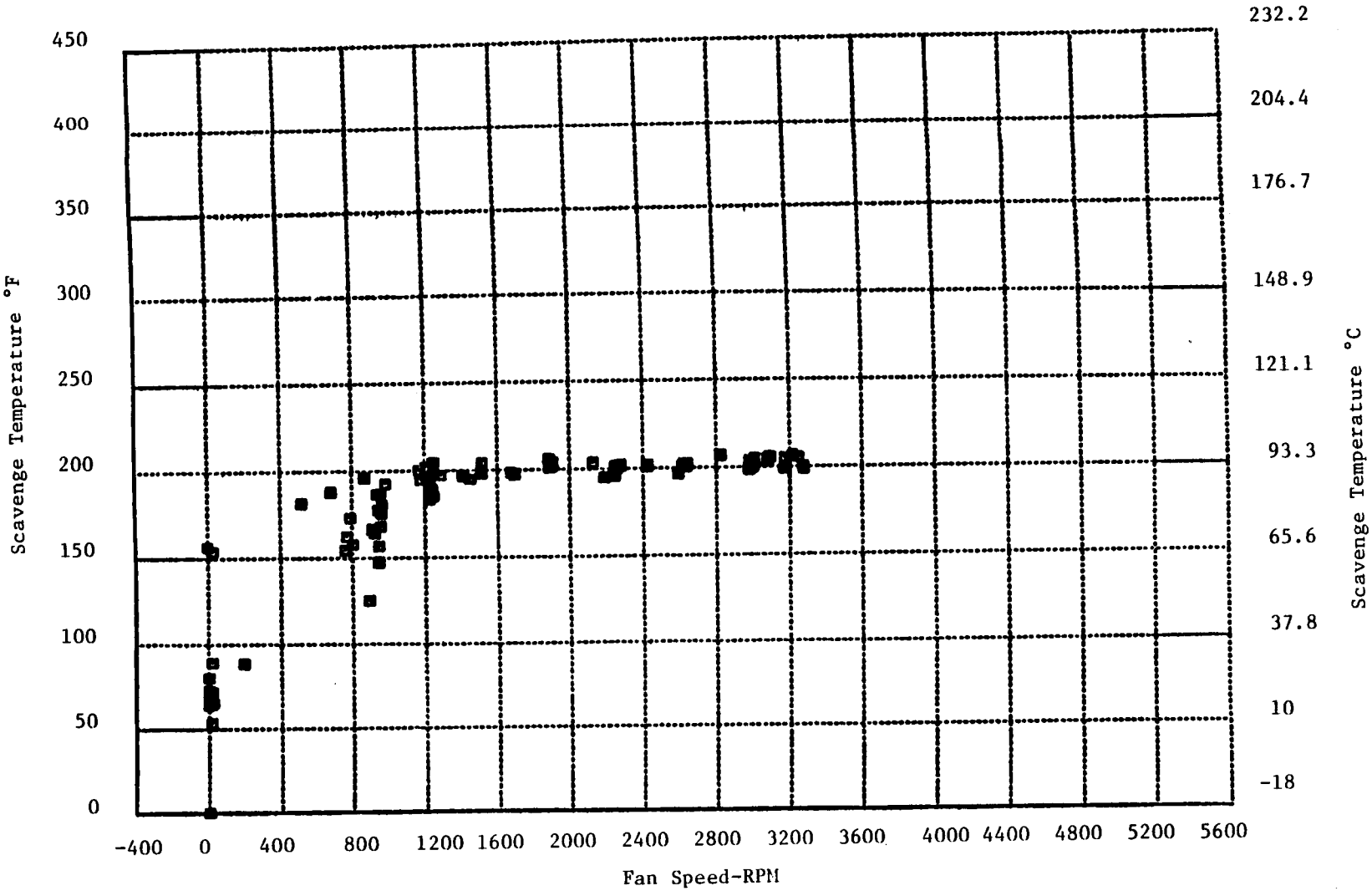


Figure 349. Accessory Gearbox Scavenge Temperature Versus Fan Speed.

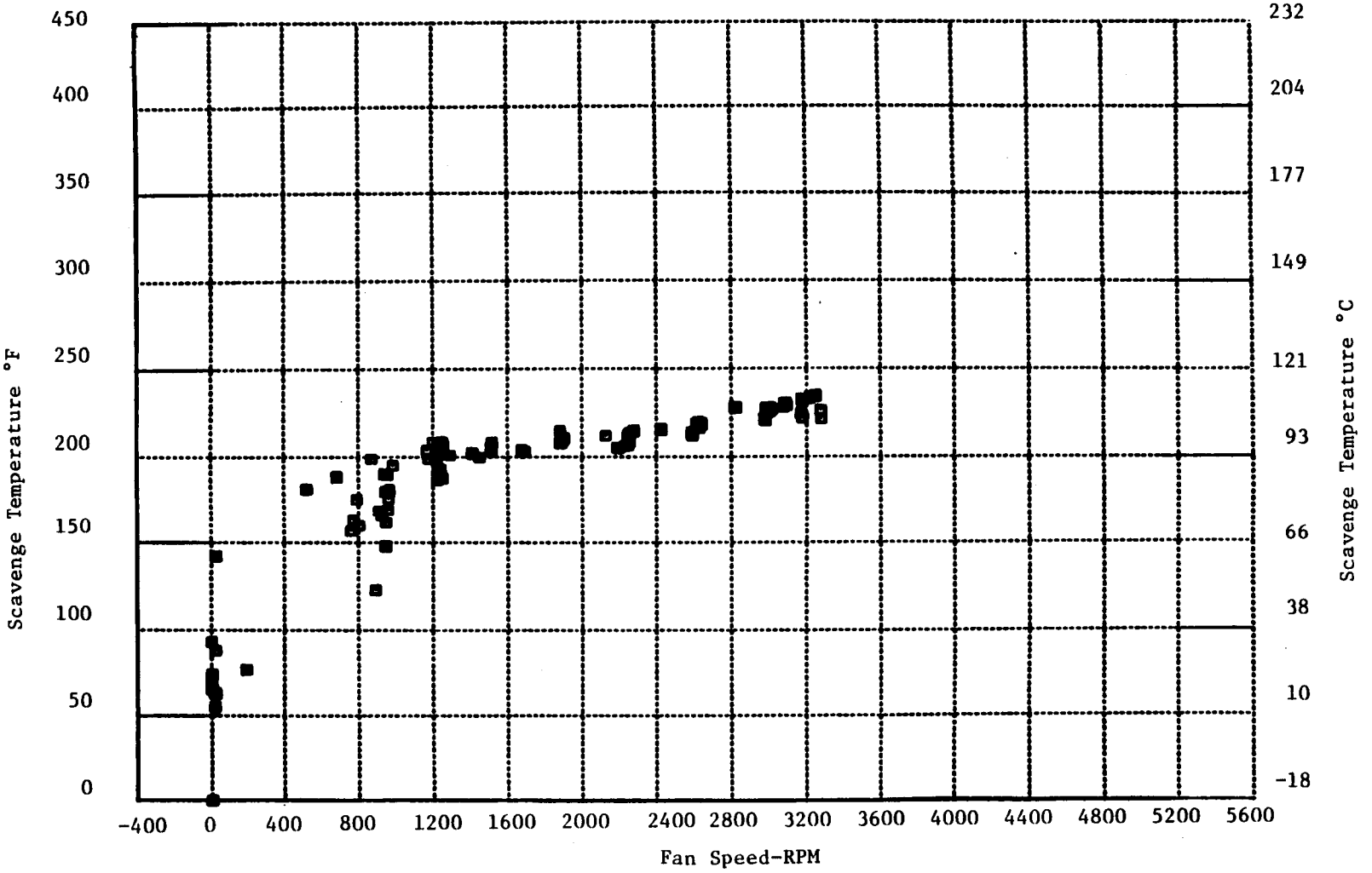


Figure 350. Combined Scavenge Temperature Versus Fan Speed.

Figure 351 shows this calculated heat load as a function of core speed. The maximum heat generated was 65.9 kw (3750 btu/minute). The core engine maximum heat load was 40.4 kw (2300 btu/minute) which indicates adding the LP system adds 63% to the heat load.

Calculations indicate the distribution of lube system heat load is as shown in Table XXVIII.

Table XXVIII. Distribution of Lube System Heat Load at Maximum Speed.

| Major Component | % of Heat Load |
|---|---|
| Forward Sump | 43.4 |
| Aft Sump | 40.6 |
| Accessory Gearbox | 16.0 |

## 6.18 TURBOFAN SYSTEM DYNAMICS PERFORMANCE

### 6.18.1 Summary

Test results for the ICLS engine demonstrated excellent system vibration characteristics with an absence of speed avoidance zones over the complete operating range. Engine vibration levels were well behaved and the vibration response characteristics showed good agreement with pretest calculations. Maximum synchronous vibration levels were recorded at the No. 3 bearing accelerometer located on the soft side (rotor side) of the forward squirrel cage; 0.104 mm-DA (4.1 mils-DA) 1/core at 3,200 rpm $N_F$/12,420 rpm $N_C$ and 0.127 mm-DA (5 mils-DA) 1/fan at 2,600 rpm $N_F$/11,900 $N_C$. As predicted, the core synchronous response levels indicated very highly damped behavior characterized by a basically flat response curve over the core operating speed range. The No. 3 bearing high load damper (multifilm sealed configuration) in conjunction with the soft-mounted core rotor provided this expected vibration control. It will be noted that in addition to a static squirrel cage spring support at the forward core rotor bearing, this engine employs a unique rotating squirrel cage spring support at the aft core rotor

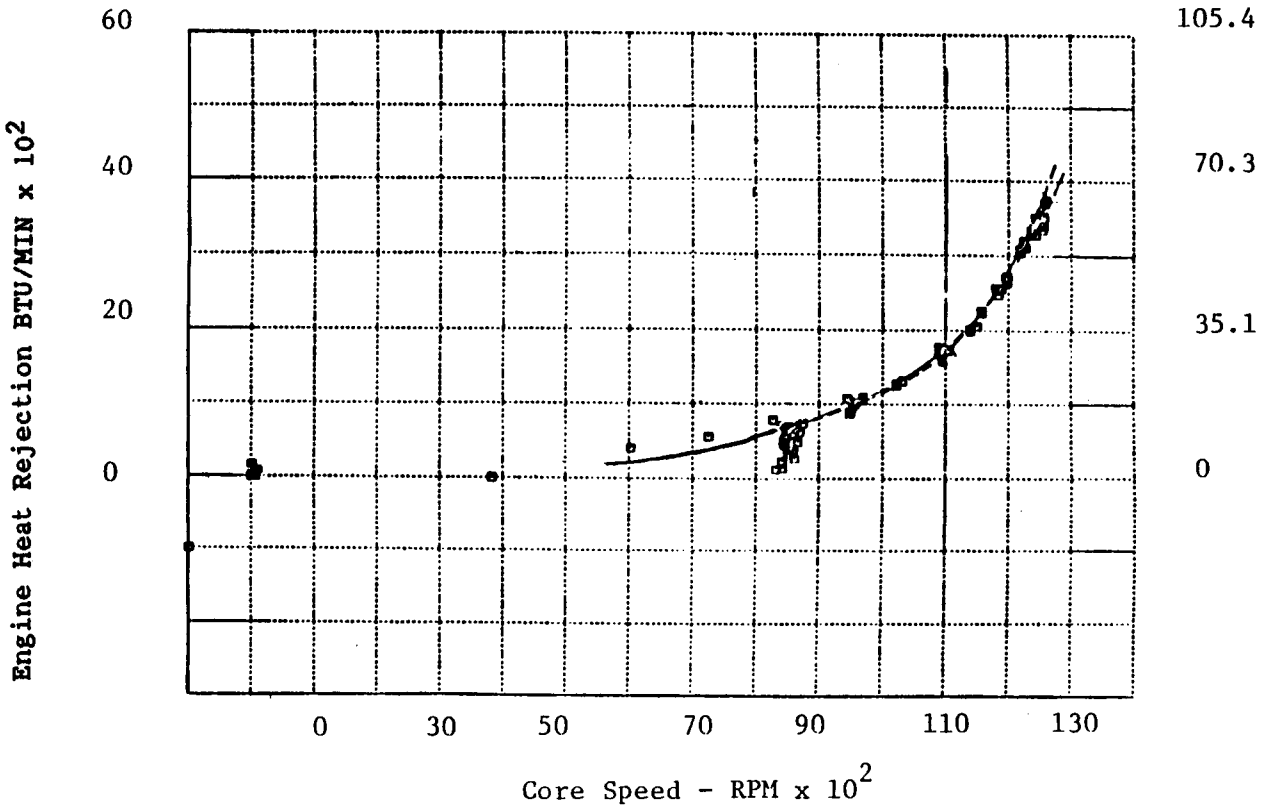


**Figure 351. Engine Heat Rejection Measured on Fuel Side of Heat Exchanger as a Function of Core Speed.**

bearing. Fan synchronous vibration response was associated with rigid body motion of the core rotor off of the soft suspension system. No trace of the fan nodding mode (coupled fan rotor/fan frame) was detected in the fan operating speed range. This was consistent with the pretest analysis which predicted the fan nodding mode to be well above the operating speed range. As expected, there was no evidence of whirl instability which was consistent with the highly damped core rotor mounting.

### 6.18.2 Test Results

#### 6.18.2.1 Assessment of the Vibration Characteristics

Both core and fan synchronous vibration response characteristics were associated with rigid body motion of the core rotor off of the soft suspension system shown in Figure 86. The design consisted of a soft-mounted core rotor via squirrel cage centering springs at the No. 3 bearing and No. 4 bearing, along with a high load multishim squeeze film damper at the No. 3 bearing. The soft mount suspension system provided for core rotor vibration isolation and the squeeze film damper was utilized to dissipate the vibration energy associated with the core rotor rigid body modes. Details of the damper configuration are illustrated in Figure 87. The system was designed to operate super-critical to the core rotor rigid body modes, and the soft mounts allowed the core rotor to run in a dynamically stiff configuration; i.e., core rotor bending did not occur over the operating speed range. The combined effect of the soft suspension system and the squeeze film damper resulted in a rotor that had a very low sensitivity to unbalance, as intended.

The core rotor support and damper system design was optimized to limit secondary damage due to unbalance associated with the loss of two HP turbine Stage 2 airfoils for the Flight Propulsion System (FPS). However, because of the similarity between the ICLS and the FPS, the core rotor damped suspension system was close to optimum for the ICLS configuration.

### 6.18.2.2 Vibration Instrumentation and Data Analysis

Accelerometers, proximity (inductance) probes, and dynamic strain gages were used to monitor and analyze the system vibration characteristics during the test program. Table XXIX defines this instrumentation. As indicated, the instrumentation was oriented in both the vertical plane (0°, 180°, 360°) and the horizontal plane (90°, 270°). However, the No. 3 bearing damper proximity probes were oriented 51° and 38° from vertical and horizontal respectively due to assembly and space considerations. Response characteristics of the proximity probes were of key interest because they represented the actual clearance change across the centering spring and damper. The No. 3 bearing accelerometers were located on the soft side or rotor side of the No. 3 bearing squirrel cage and therefore measured the actual rotor motion relative to an inertial reference.

Post-test data analysis was conducted by both digital and analog processing of magnetic tape data that was continuously recorded during the test program. Digital data analysis (Fast Fourier Transform - FFT) produced Campbell diagrams and first order plots. A Campbell diagram is a three-dimensional plot showing the relationship between speed, frequency, and amplitude. First order plots show 1/rev amplitudes versus speed. Analog data50nalysis consisted of plotting 1/rev amplitude and speed versus time.

### 6.18.2.3 Overall Vibration Signature

Figures 352 through 368 summarize the vibration characteristics for the decel from takeoff to ground-idle. This was a slow two part decel which took approximately four minutes to reach flight-idle (1,215 rpm, $N_F$/9,452 rpm, $N_c$) from takeoff (3,282 rpm, $N_F$/12,576 rpm, $N_c$) and an additional minute to reach ground-idle (891 rpm, $N_F$/8,371 rpm, $N_c$). These data represent the typical engine vibration response characteristics observed and recorded throughout the test program. Core synchronous vibration response levels were highest at the No. 3 bearing accelerometers. As illustrated in Figures 357 and 361, there was a gradual buildup to 0.112 mm-DA (4.4 mils-DA) at 11,500 rpm and 0.094 mm-DA (3.7 mils-DA) at 12,000 rpm at the horizontal and vertical No. 3 bearing accelerometers. The gradual vibration level buildup and broad

Table XXIX. Engine Vibration Monitoring Instrumentation.

DYNAMIC STRAIN GAGES

No. 3 Bearing Squirrel Cage - Vertical (356°)

No. 4 Bearing Squirrel Cage - Vertical (0°) and Horizontal (90°)

PROXIMITY PROBES

No 3 Bearing Damper - Vertical (231°) and Horizontal (71°)

ACCELEROMETERS

| | |
|---|---|
| Accessory Gear Box | - Vertical |
| No. 1 Bearing | - Horizontal (90°) |
| No. 2 Bearing | - Vertical (19°) and Horizontal (308°) |
| No. 3 Bearing Rotor Side of Squirrel Cage | - Vertical (350°) and Horizontal (80°) |
| No. 5 Bearing | - Horizontal (90°) |
| Forward Fan Case | - Horizontal (90°) |
| Fan Frame | - Vertical (0°) and Horizontal (90°) |
| Forward Compressor Case | - Vertical (0°) |
| Forward Combustor Case | - Horizontal (90°) |
| Turbine Frame | - Vertical (355°) |
| Exhaust Centerbody | - Vertical (0°) |
| Slip Ring | - Vertical (0°) |

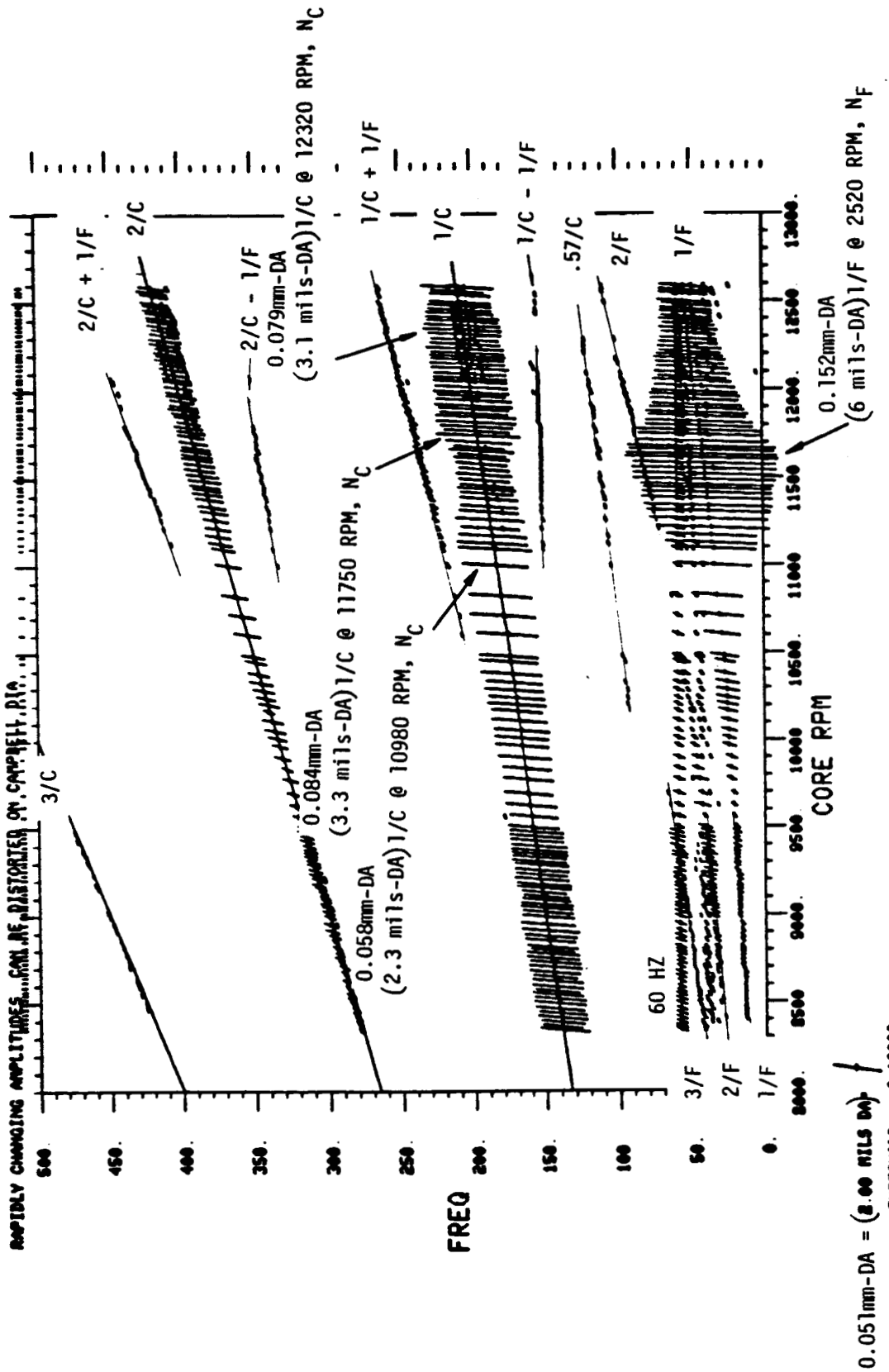


Figure 352. Number 3 Bearing Proximity Probe at 231° Measuring Change in Clearance Across Number 3 Bearing Centering Spring.

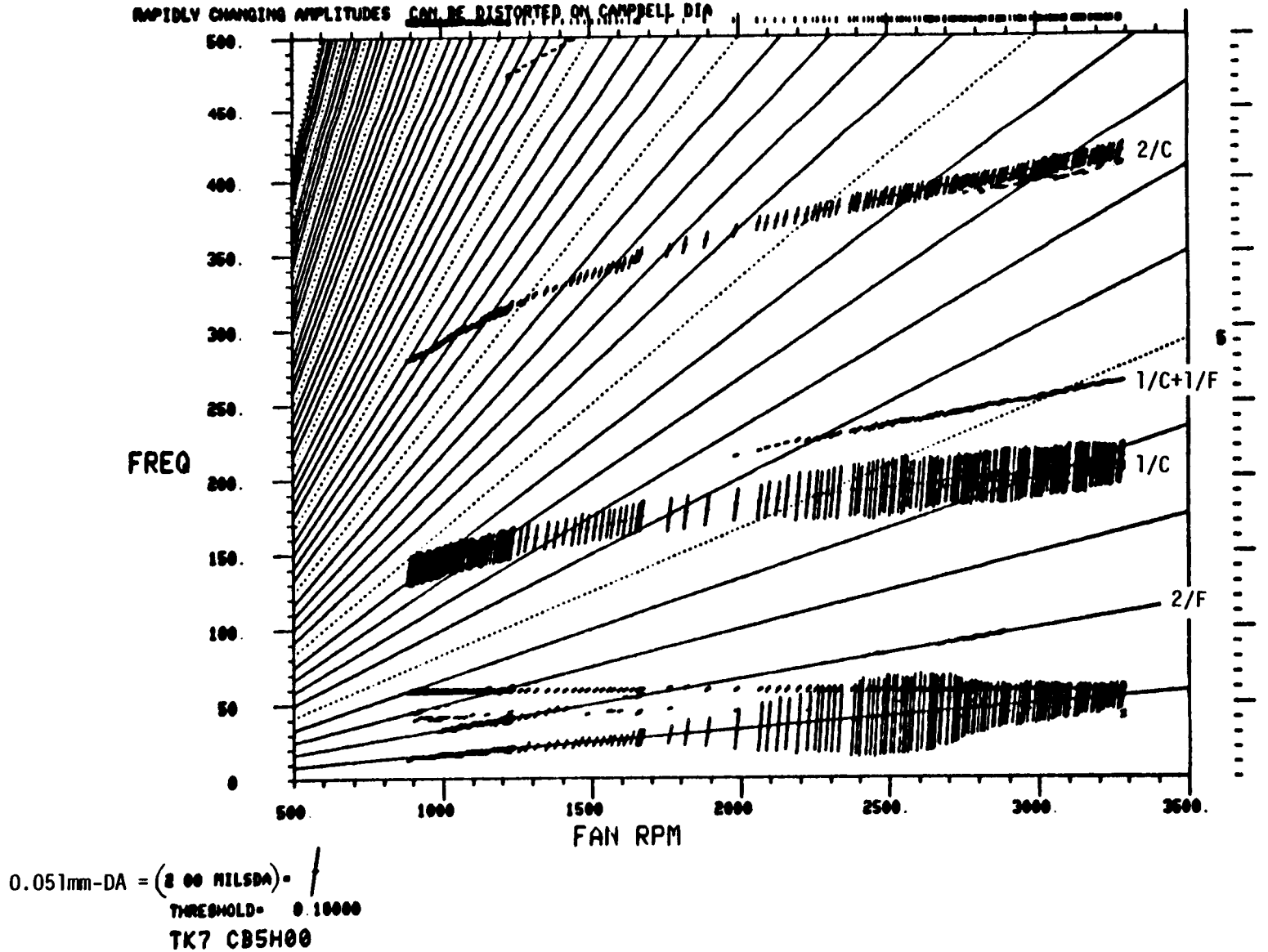


Figure 353. Number 3 Bearing Proximity Probe at 308° Measuring Change in Clearance Across Number 3 Bearing Centering Spring.

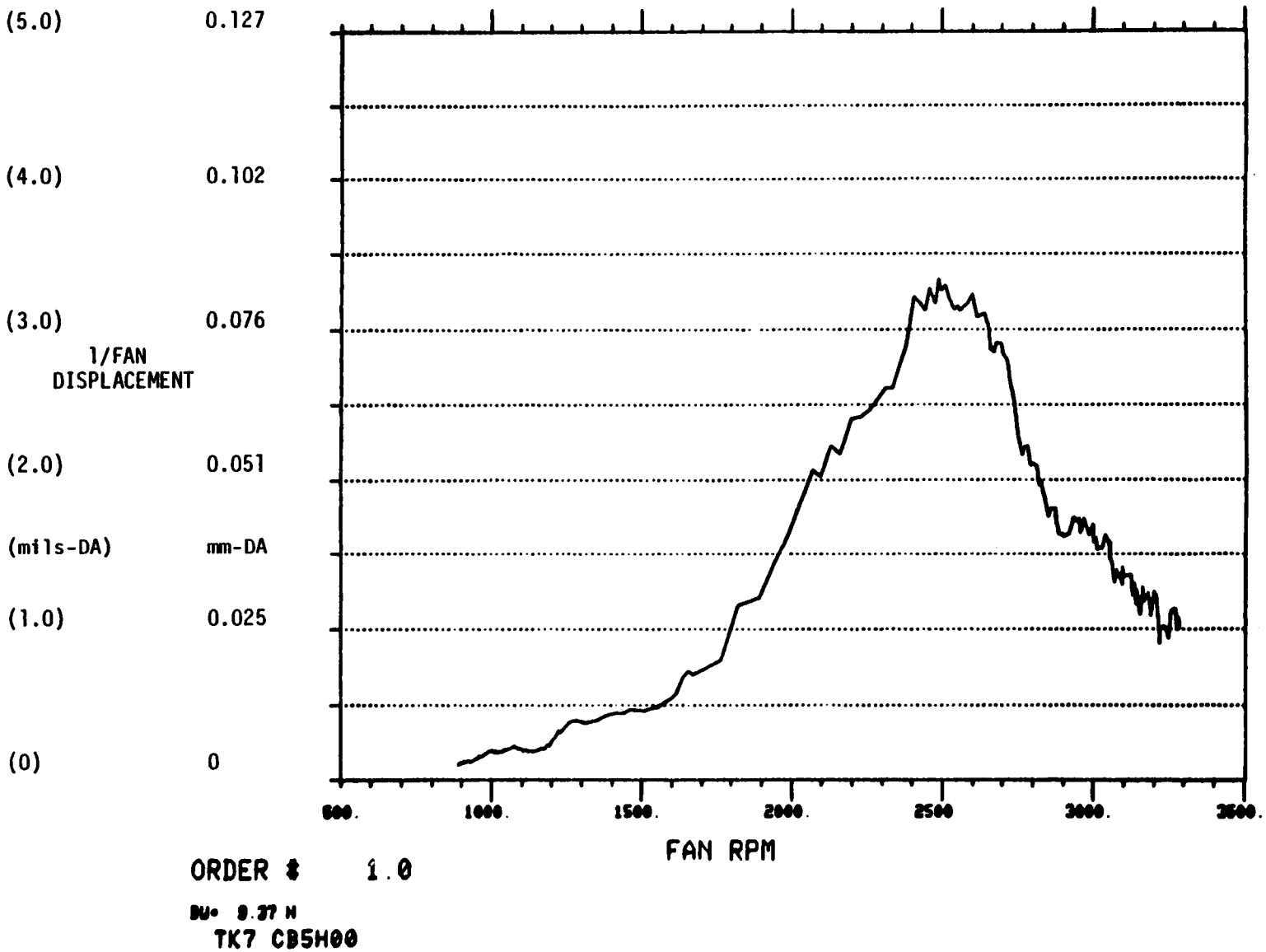


Figure 354. Number 3 Bearing Proximity Probe at 308° Measuring Change in Clearance Across Number 3 Bearing Centering Spring.

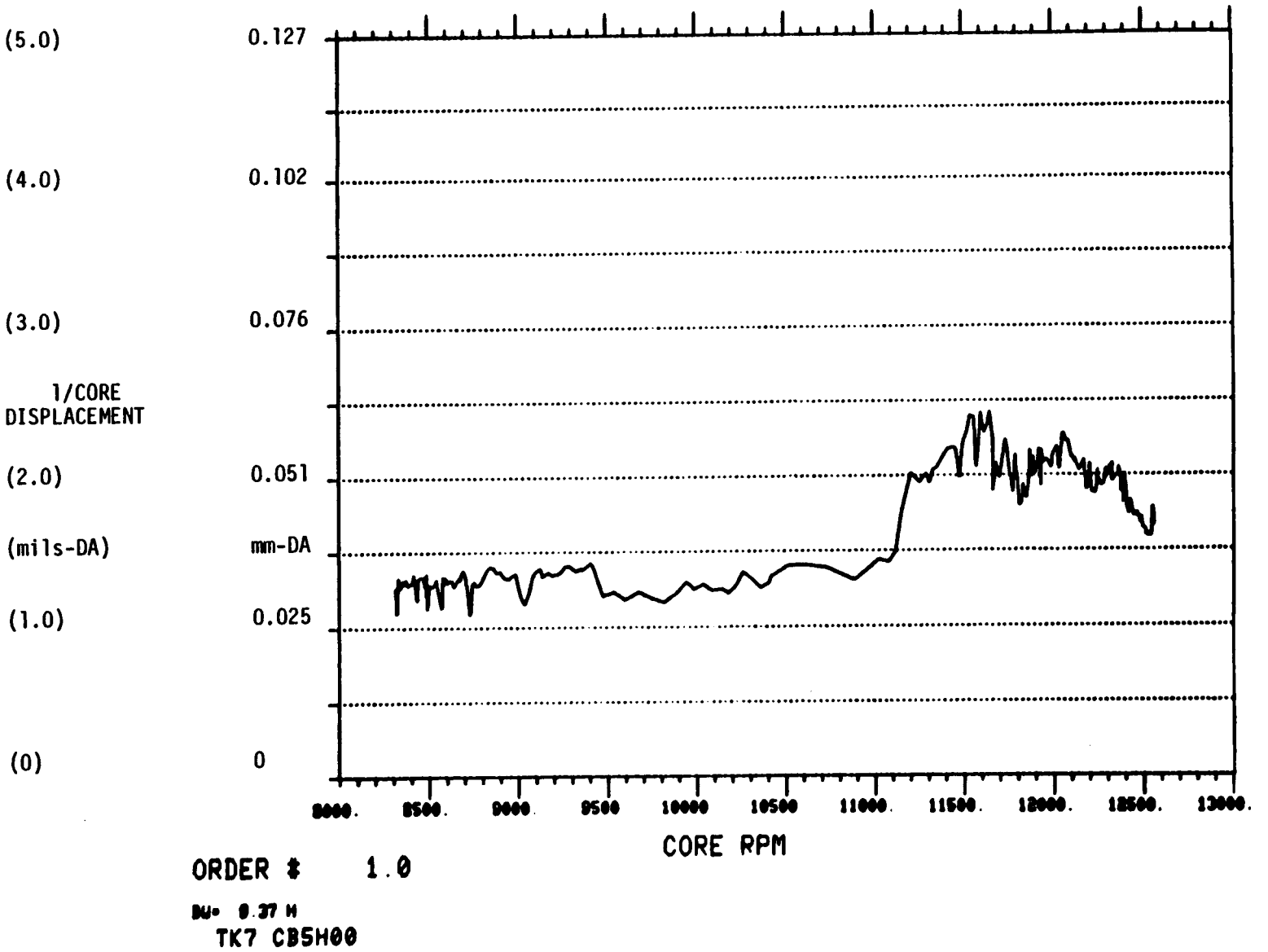


Figure 355. Number 3 Bearing Proximity Probe at 308° Measuring Change in Clearance Across Number 3 Bearing Centering Spring.

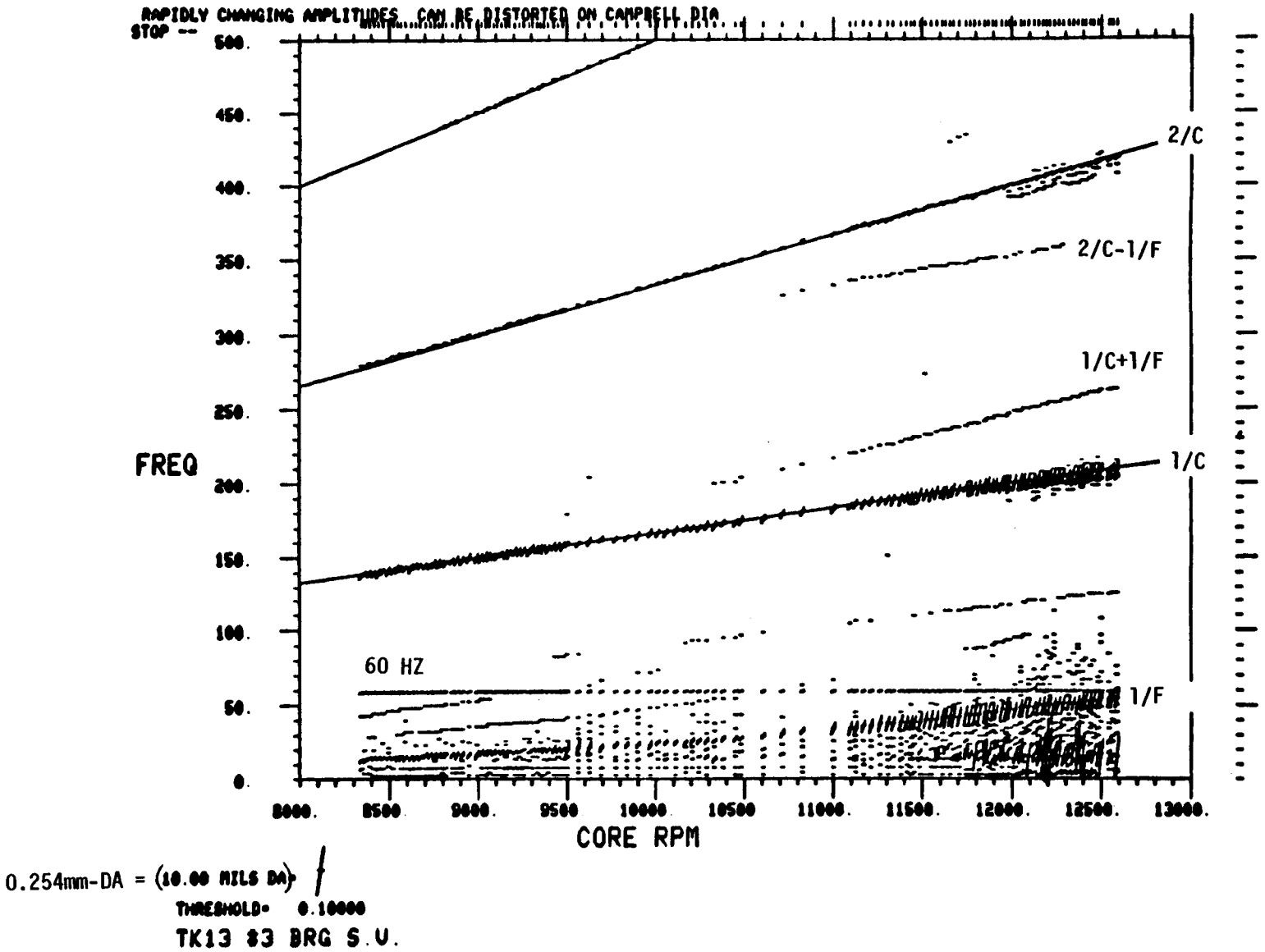


ORIGINAL PAGE IS
OF POOR QUALITY

Figure 356. Number 3 Bearing Vertical (350°) Accelerometer Located on Soft Side (Rotor Side) of Number 3 Bearing Centering Spring.

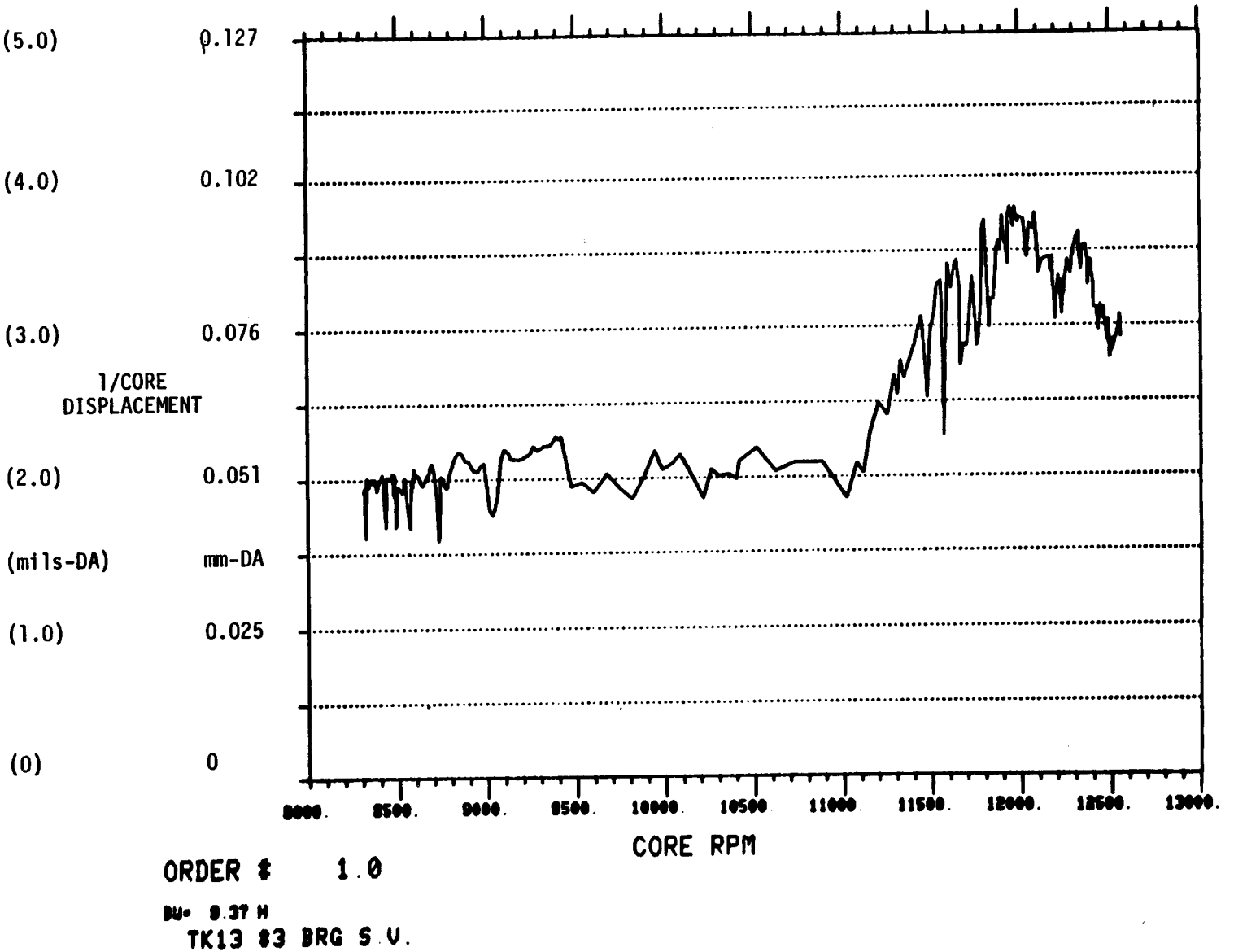


Figure 357. Number 3 Bearing Vertical (350°) Accelerometer Located on Soft Side (Rotor Side) of Number 3 Bearing Centering Spring.

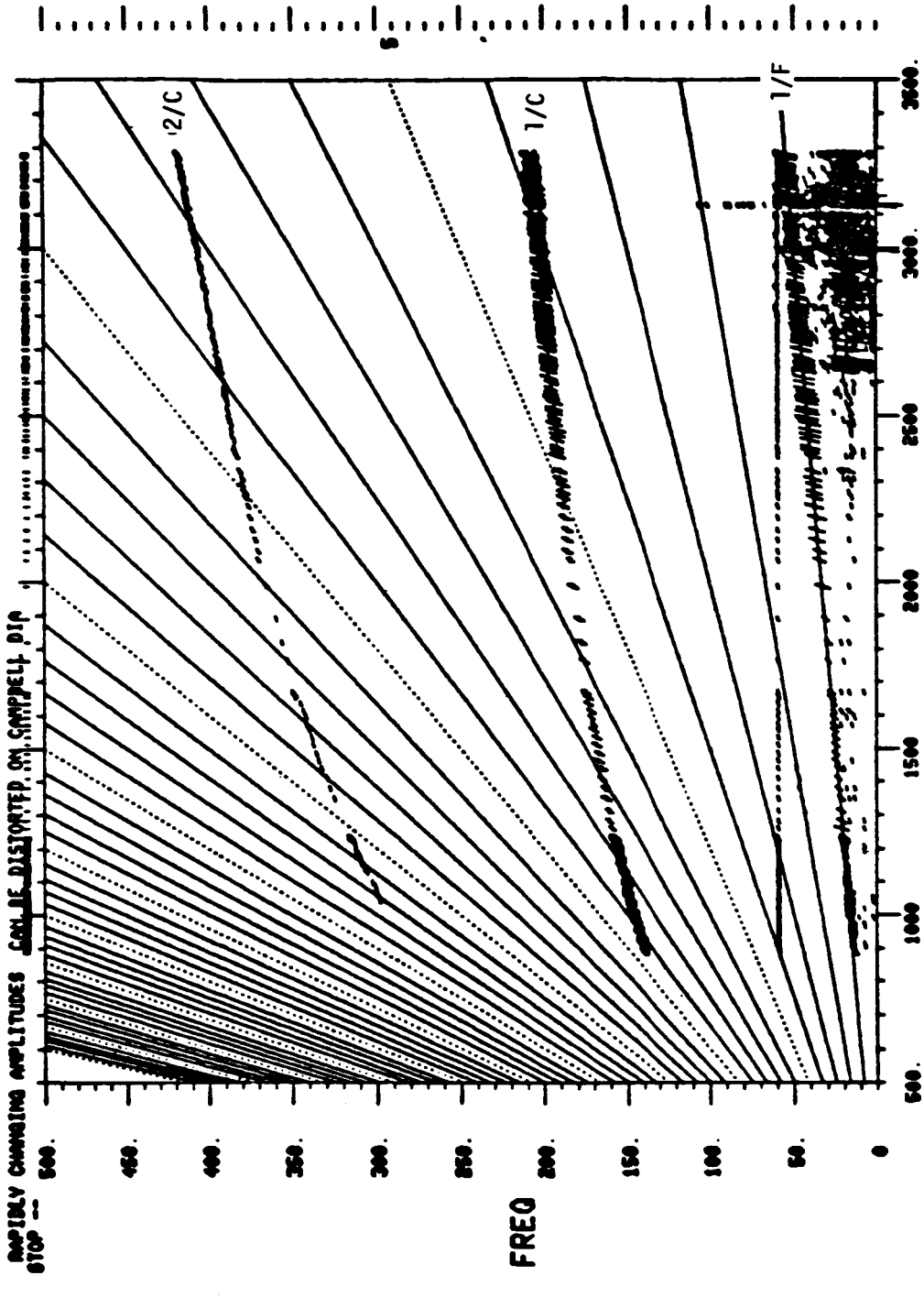


Figure 358. Number 3 Bearing Vertical (350°) Accelerometer Located on Soft Side (Rotor Side) of Number 3 Bearing Centering Spring.

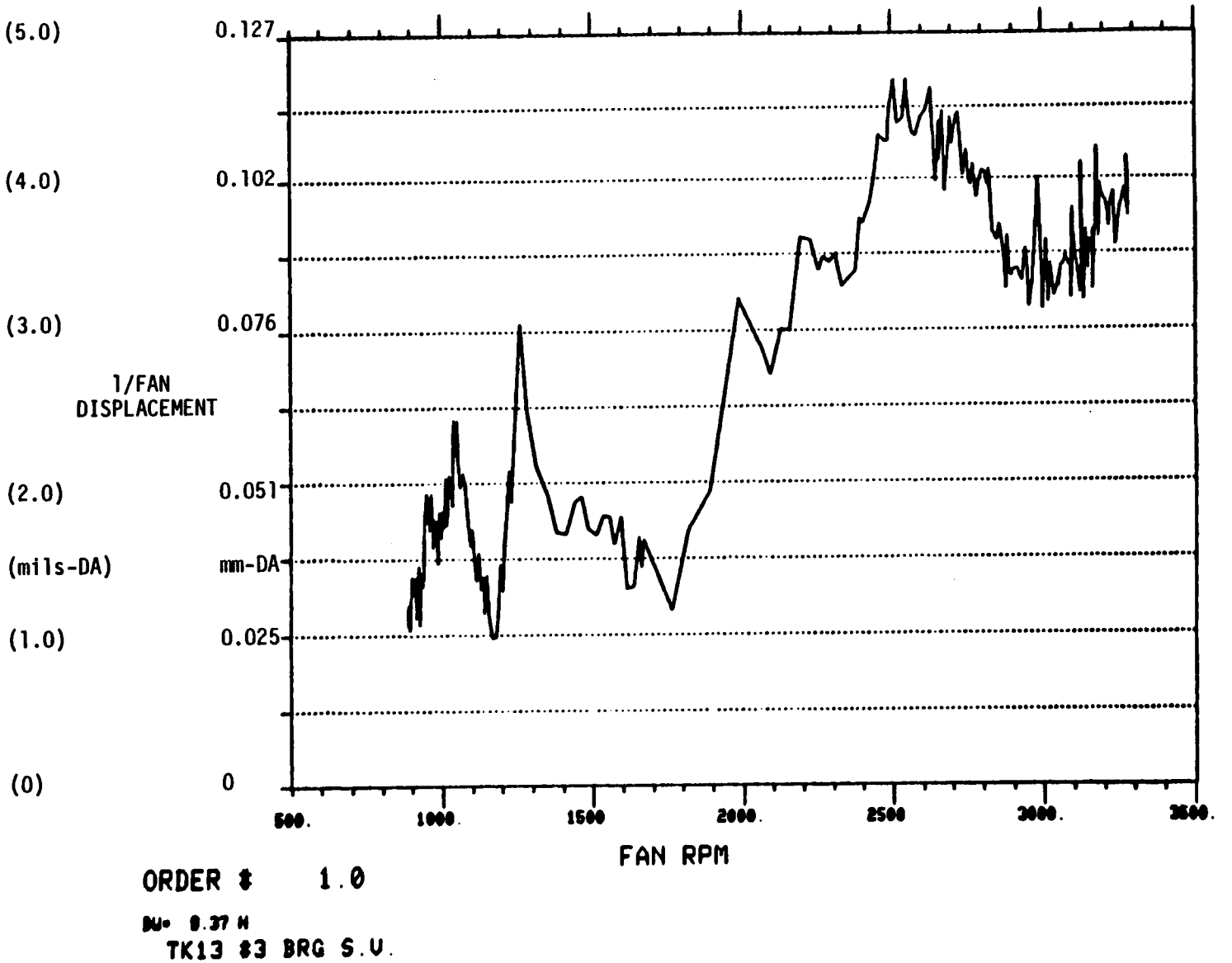


Figure 359. Number 3 Bearing Vertical (350°) Accelerometer Located on Soft Side (Rotor Side) of Number 3 Bearing Centering Spring.

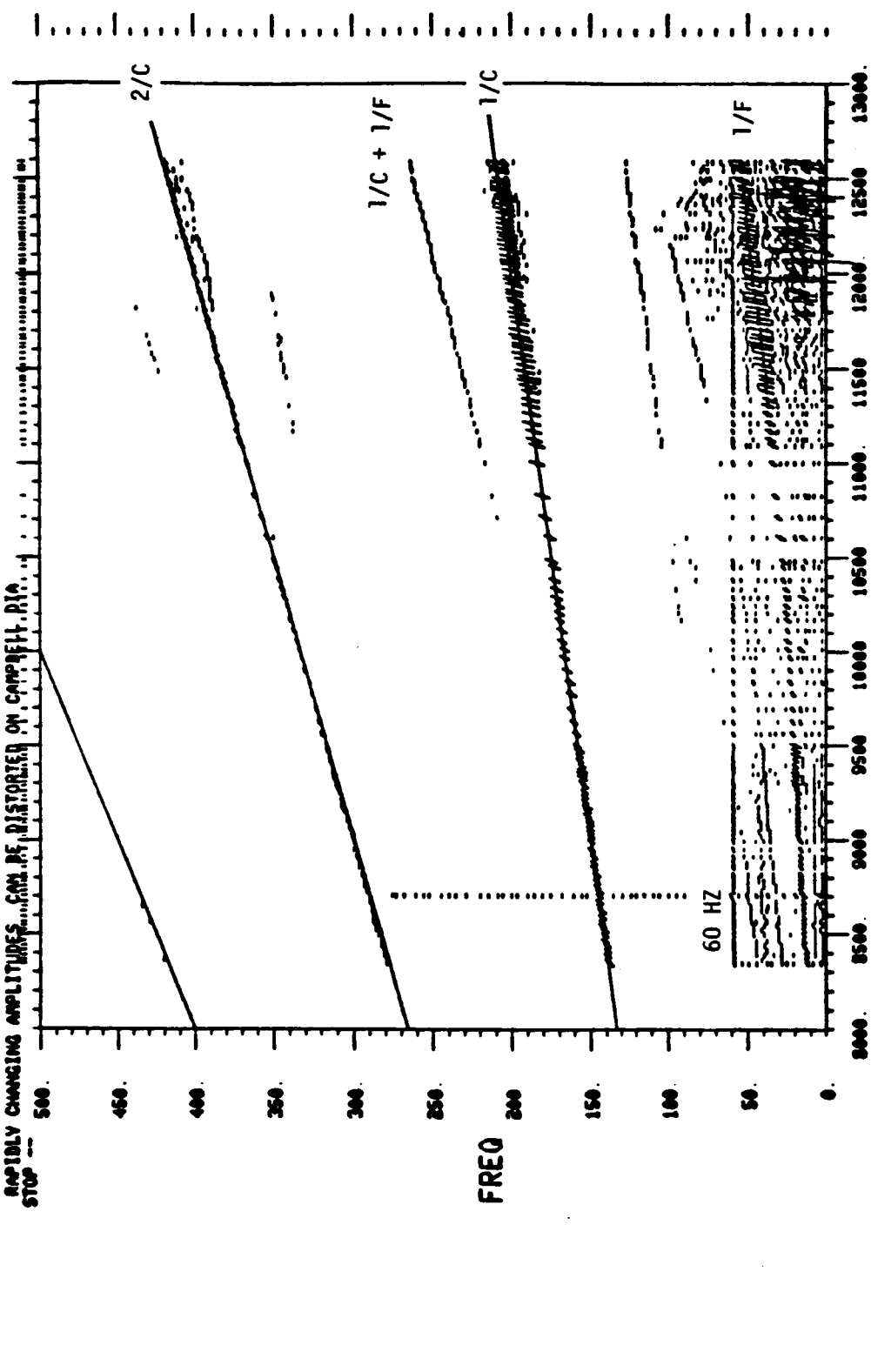


Figure 360. Number 3 Bearing Horizontal (80°) Accelerometer Located on Soft Side (Rotor Side) of Number 3 Bearing Centering Spring.

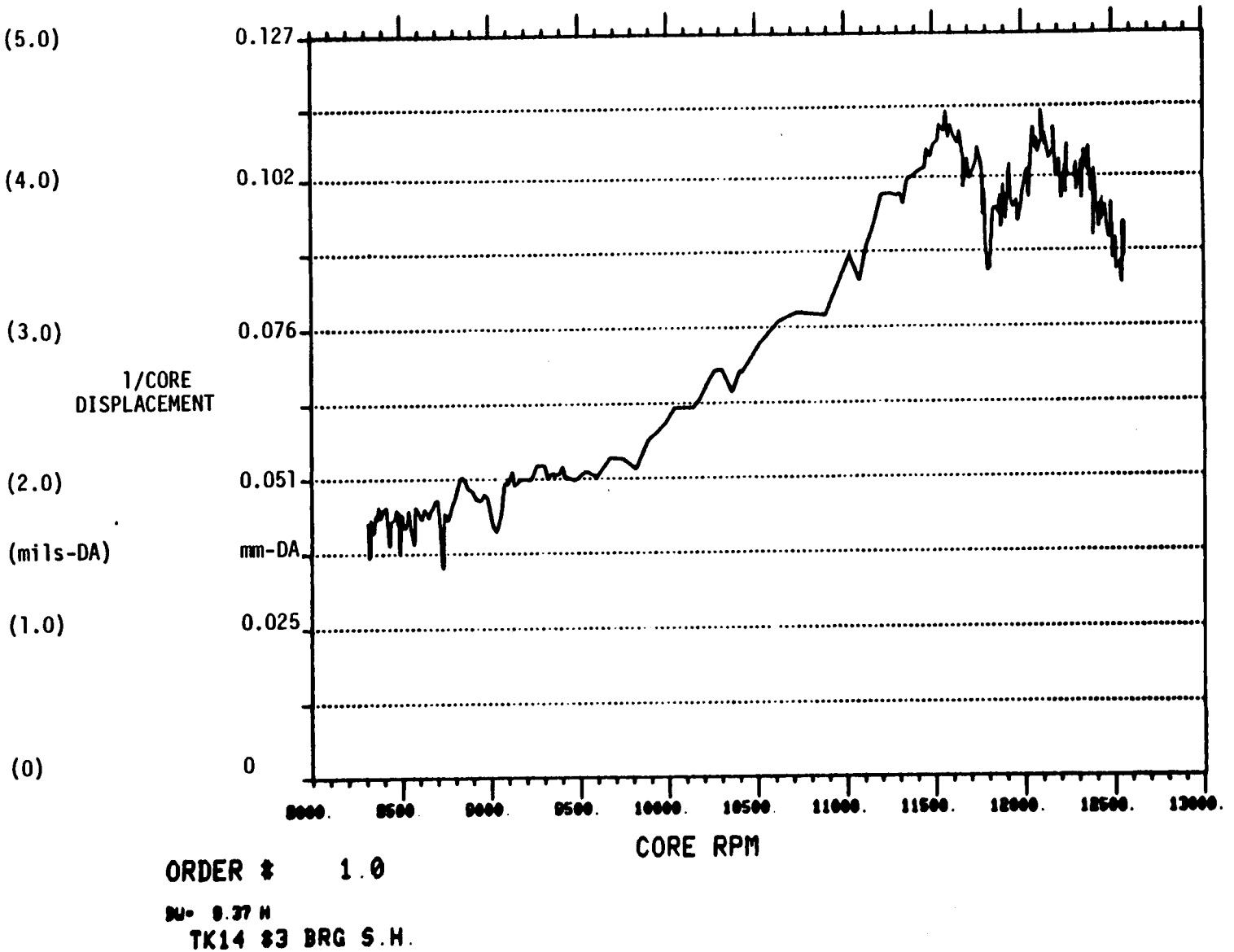


Figure 361. Number 3 Bearing Horizontal (80°) Accelerometer Located on Soft Side (Rotor Side) of Number 3 Bearing Centering Spring.

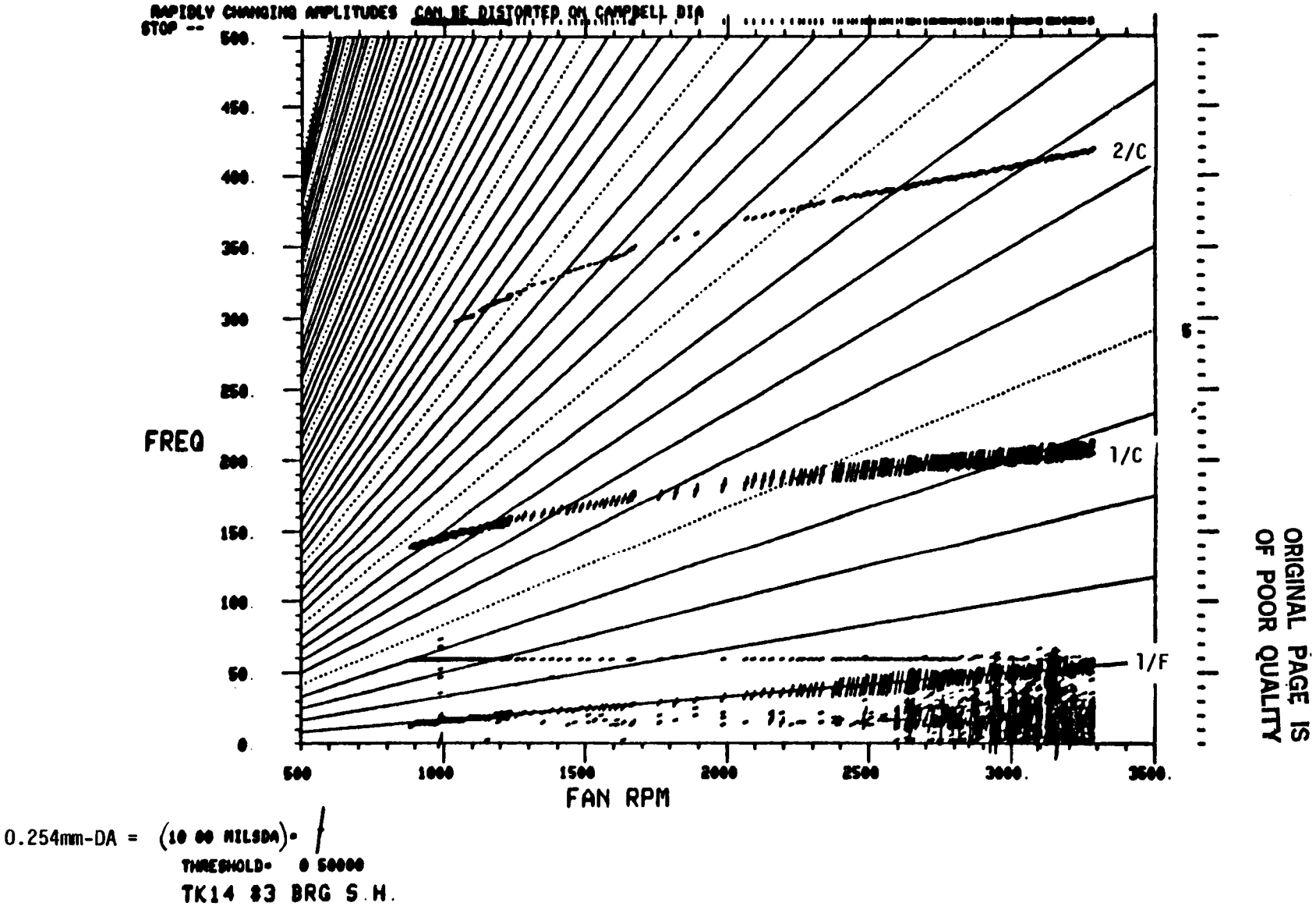




Figure 362. Number 3 Bearing Horizontal (80°) Accelerometer Located on Soft Side (Rotor Side) of Number 3 Bearing Centering Spring.

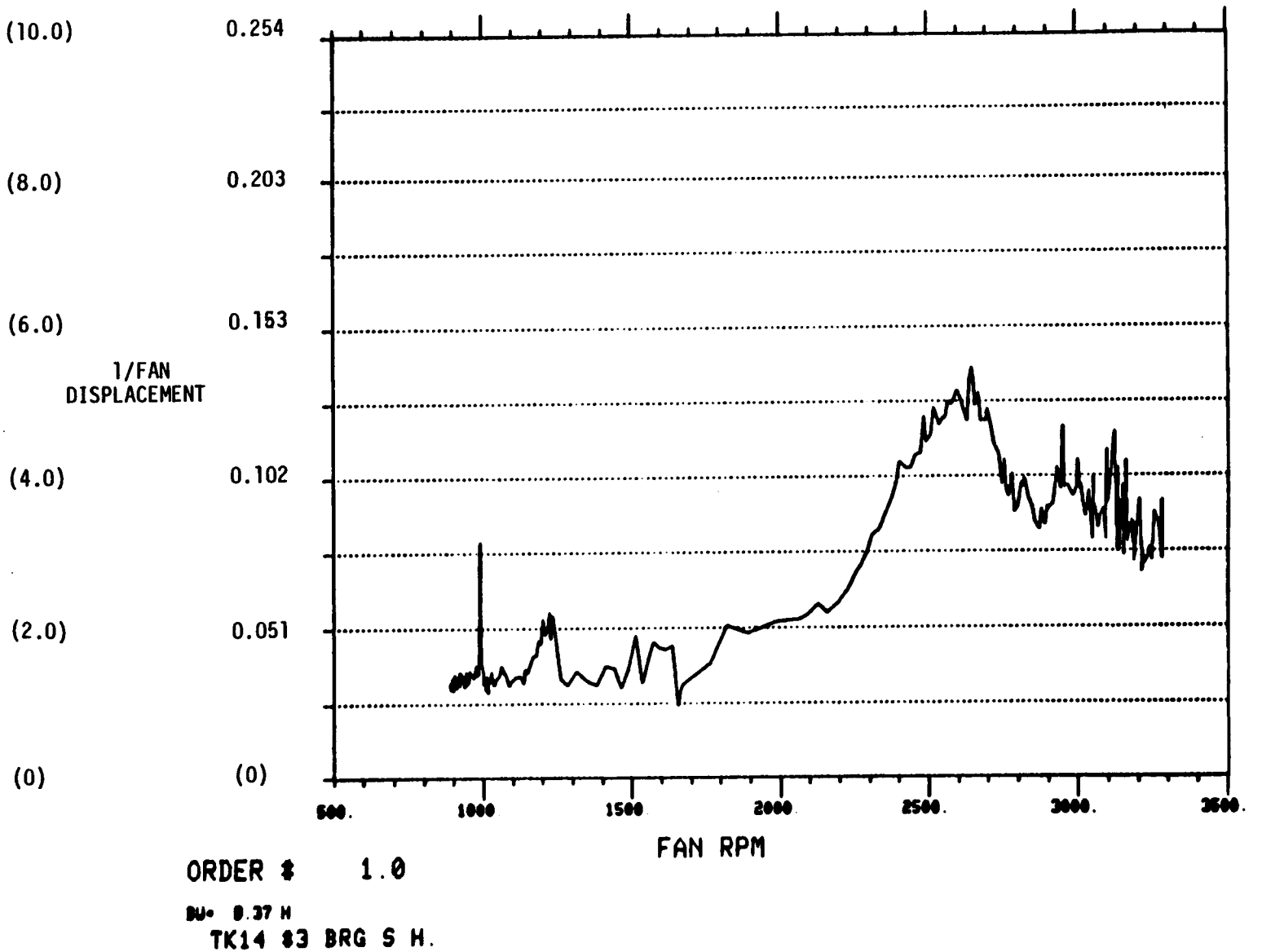


Figure 363. Number 3 Bearing Horizontal (80°) Accelerometer Located on Soft Side (Rotor Side) of Number 3 Bearing Centering Spring.

ORIGINAL PAGE IS
OF POOR QUALITY

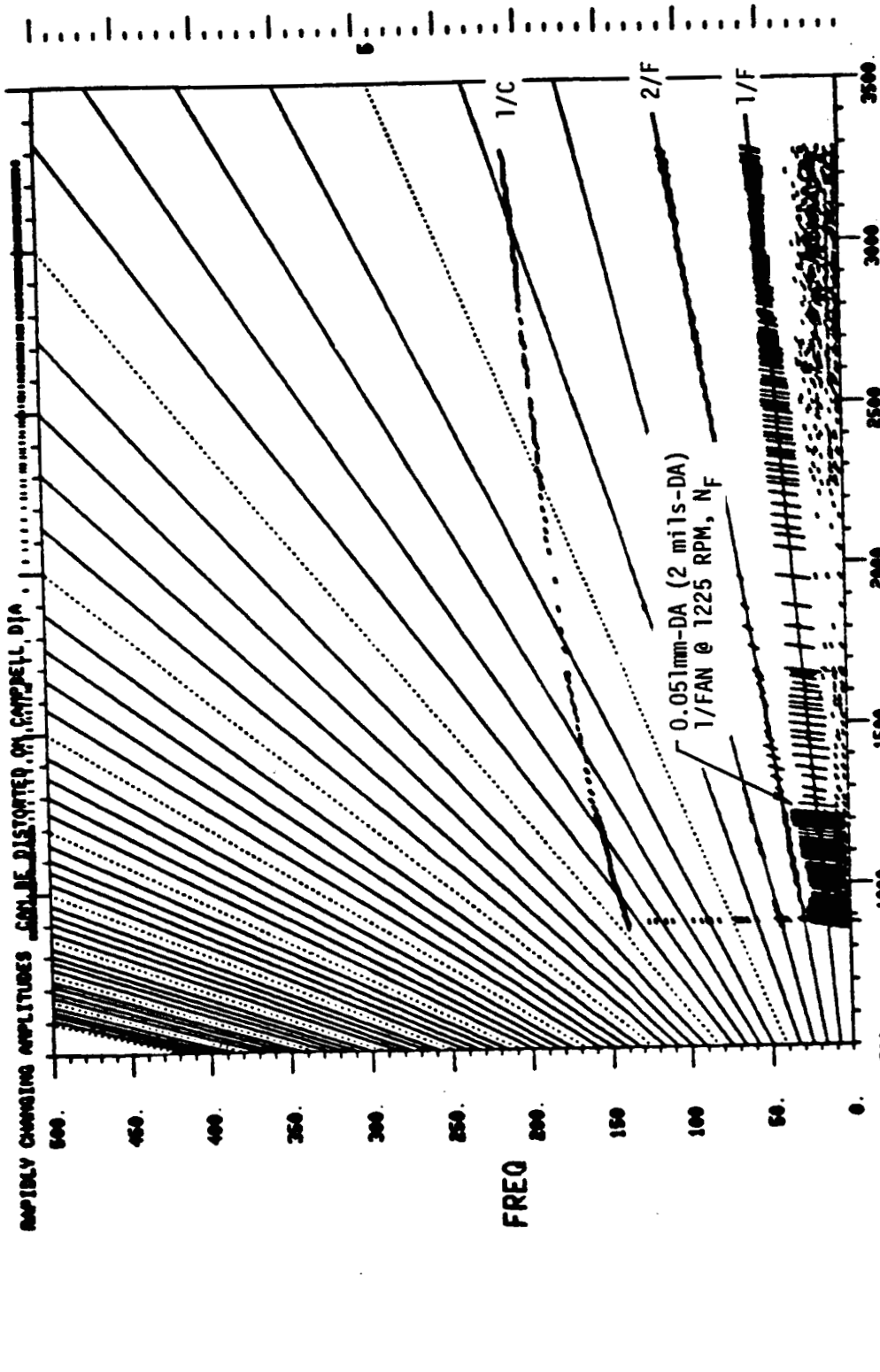


Figure 364. Number 1 Bearing Horizontal.

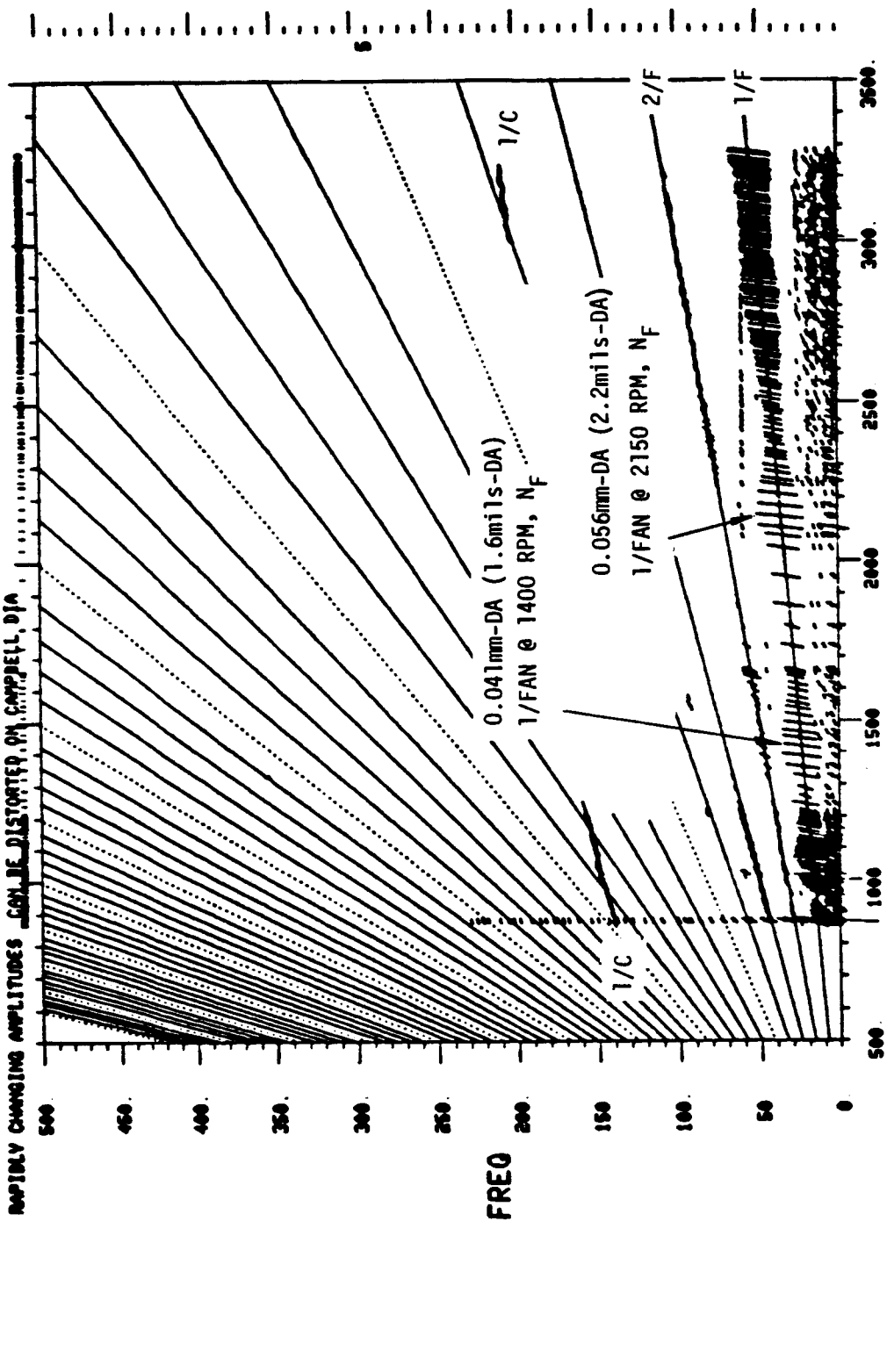


Figure 365. Number 5 Bearing Horizontal.

ORIGINAL PAGE IS
OF POOR QUALITY

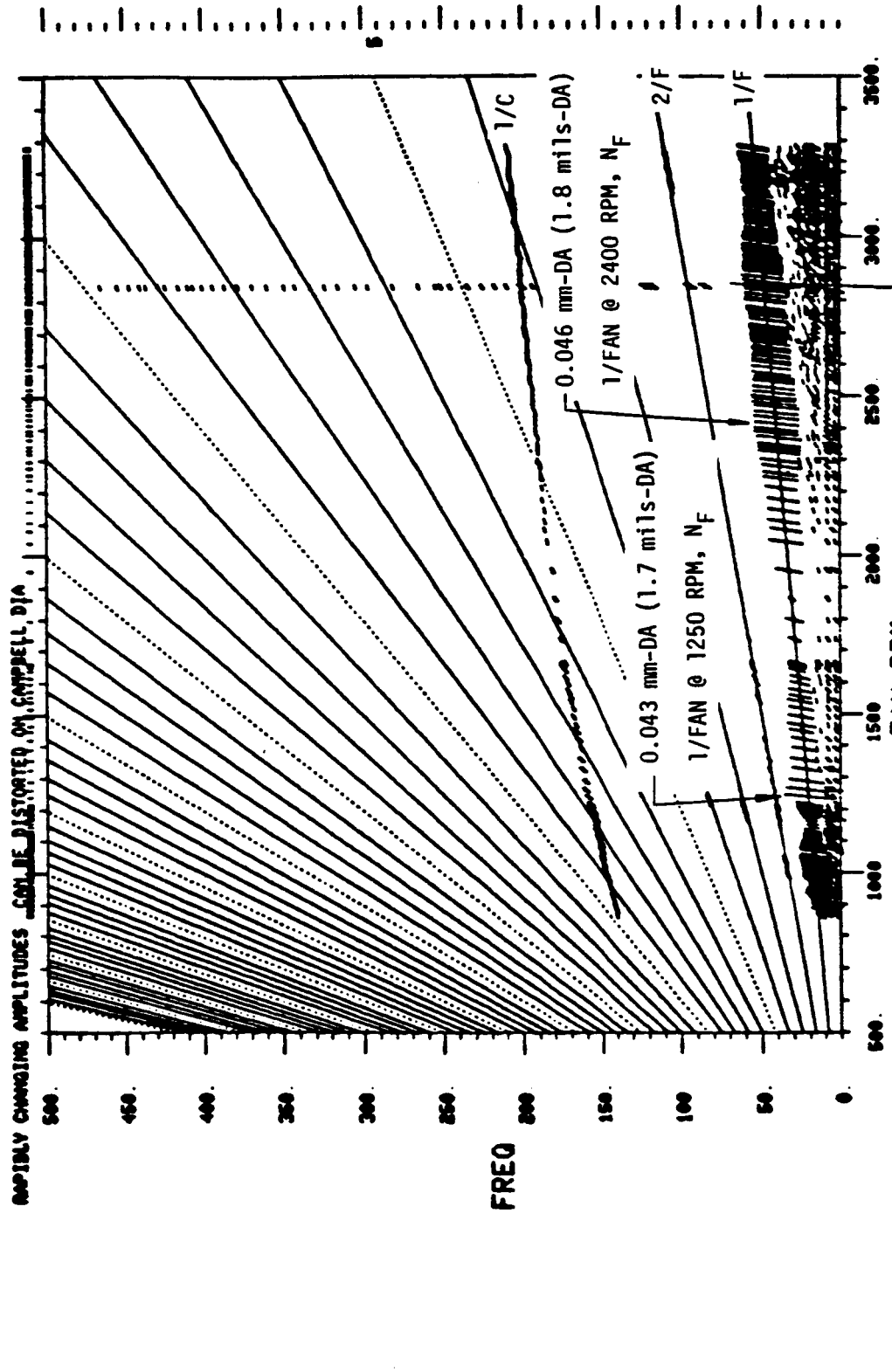


Figure 366. Fan Frame Vertical.

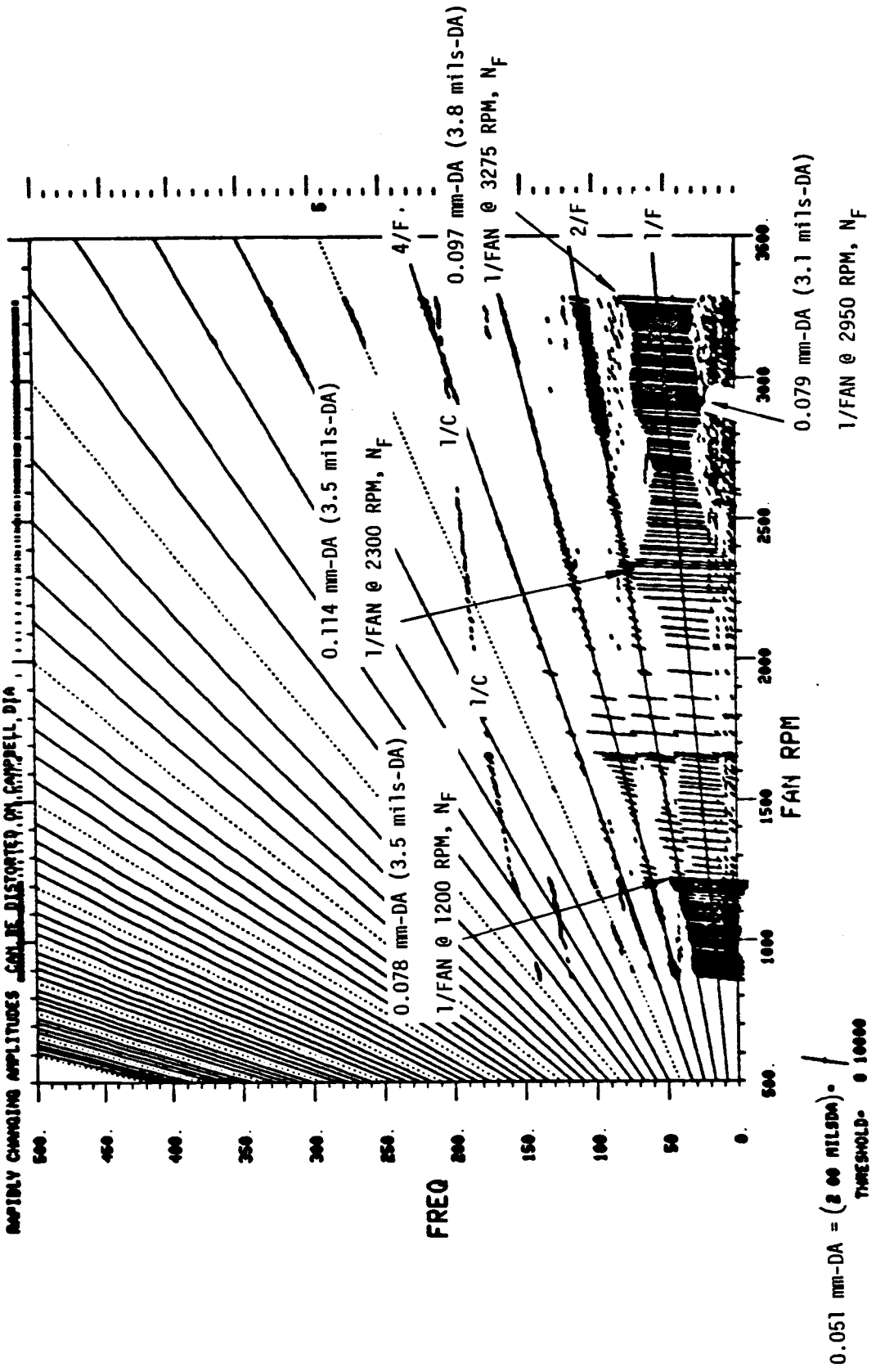


Figure 367. Fan Case Forward Flange Horizontal.

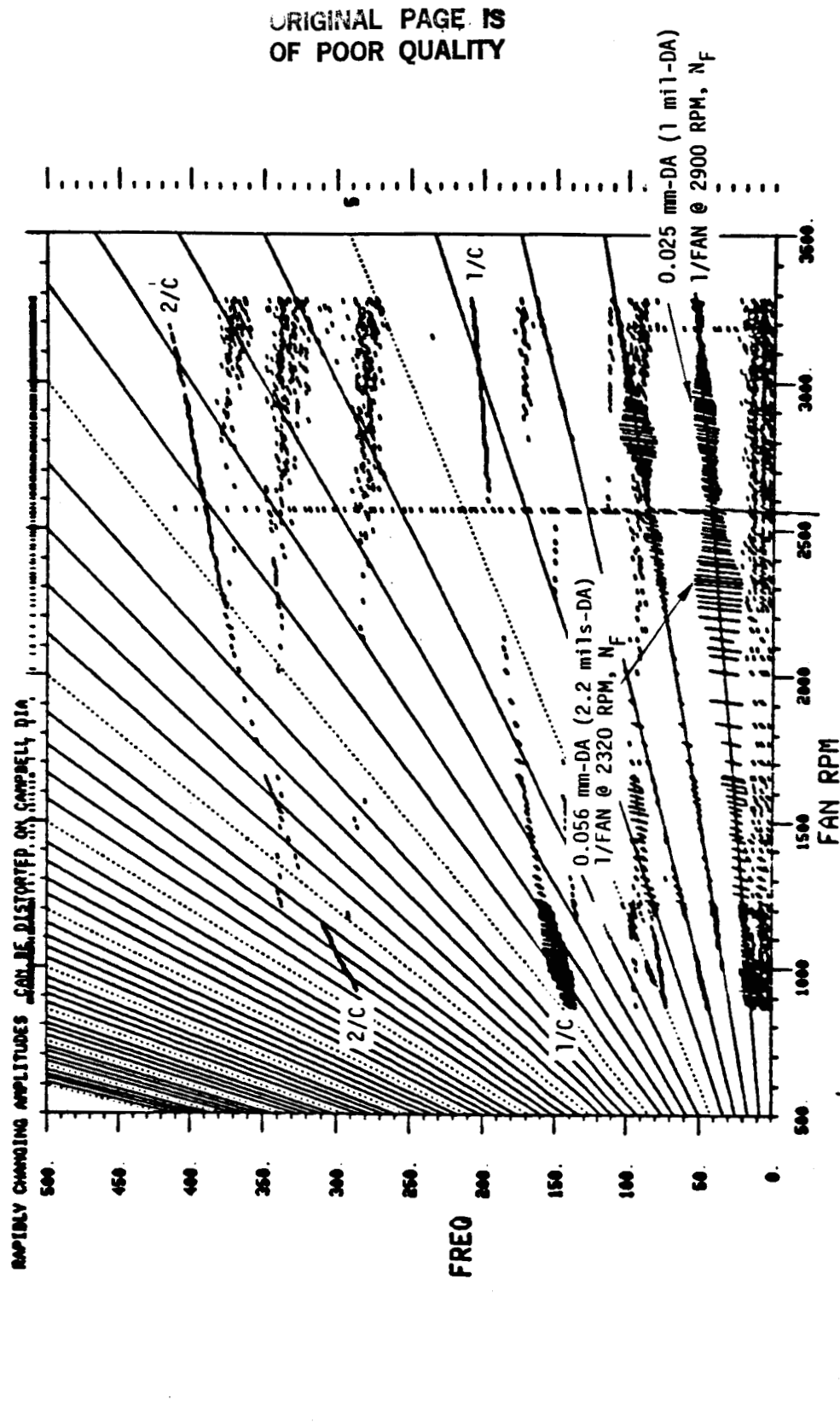


Figure 368. Exhaust Centerbody Vertical.

speed range at which the peak amplitudes exist indicate that the system was highly damped, as intended. Figures 352, 353, and 355 illustrate the No. 3 bearing damper proximity probe vibration response characteristics which verify the No. 3 bearing accelerometer response signature. The No. 3 bearing accelerometer and proximity probe response amplitudes were similar but not exactly the same. This was expected since the proximity probe directly measured the clearance across the centering spring, whereas the accelerometer measured absolute vibration response relative to an inertial reference. Also, as referenced in Table XXIX, the circumferential position of the proximity probes was different than the accelerometers, resulting in a measurement of different components of the rotor orbit. Core synchronous vibration levels at all other (bearings, frames, and casings) accelerometers were less than 0.013 mm-DA (0.5 mils-DA), indicating that core rotor excited vibration was successfully isolated, as intended. Fan synchronous vibration levels were highest at the No. 3 bearing proximity probes and accelerometers. As illustrated in Figures 352, 353, and 354, fan/rev vibration peaked between 0.089 mm-DA (3.5 mils-DA) and 0.152 mm-DA (6.0 mils-DA) at the No. 3 bearing proximity probes at a fan speed of 2,500 rpm. No. 3 bearing accelerometer fan/rev response levels were similar as shown in Figures 358, 359, 362, and 363, with peak amplitudes between 0.114 mm-DA (4.5 mils-DA) and 0.127 mm-DA (5.0 mils-DA) at 2,500 rpm, $N_F$. Fan case forward flange fan/rev levels were 0.089 mm-DA (3.5 mils-DA) at 12,000 rpm, $N_c$ and 2,300 rpm, $N_F$ and 0.097 mm-DA (3.8 mils-DA) at 3,275 rpm, $N_F$ (Figure 367). All other fan/rev amplitudes were less than 0.064 mm-DA (2.5 mils-DA).

6.18.2.4 Asynchronous Vibration

In addition to synchronous vibration components, the vibration signature was characterized by nonsynchronous components as shown in Figure 352. The nonsynchronous components were primarily associated with base frequencies which were harmonics of the core and fan 1/rev frequencies and with combination frequencies which are sums and differences of the harmonics. The higher harmonics of the core and fan 1/rev frequencies were associated with aerodynamic excitation and the sum and difference combination frequencies

result from engine system structural nonlinearities. Inspection of Figure 352 shows that all nonsynchronous response levels were low, well controlled, and tracked with speed. As expeced, there was no evidence of whirl instability which is consistent with the high damped core rotor mounting.

6.18.2.5 Low Speed Vibration Characteristics

Sub-idle and idle fan and core synchronous vibration levels are illustrated in Figures 369 through 373 for start No. 7 which occurred at 19:44 hours on May 6, 1983. This analog data shows 1/fan and 1/core amplitudes plotted versus time, with fan core speed versus time for reference. The highest sub-idle 1/core vibration level was 0.114 mm-DA (4.5 mils-DA) at 6000 rpm, $N_c$ at the exhaust centerbody (Figure 373). Maximum sub-idle No. 3 bearing accelerometer response levels were 0.071 mm-DA (2.8 mils-DA) and 0.056 mm-DA (2.2 mils-DA) vertical and horizontal, respectively, at 1000 rpm, $N_c$ (Figure 370). The highest 1/fan response was at the forward fan case (fan case forward flange), 0.033 mm-DA (1.3 mils-DA) at idle, 950 rpm, $N_F$ (Figure 372). Sub-idle 1/fan vibration levels were very low at all locations and were characterized only by a small buildup to idle response amplitudes starting at 700 rpm, $N_F$. All 1/core and 1/fan sub-idle and idle vibration characteristics were well controlled and consistent throughout the test program.

6.18.2.6 FADEC Vibration

The vibration environment for the FADEC was similar to the fan frame response. Figure 366 illustrates the vibration response characteristics between ground idle and takeoff. This figure shows that the maximum 1/fan vibration response was 0.046 mm-DA (1.8 mils-DA) at 2400 rpm, $N_F$. The 1/core vibration response levels were less than 0.013 mm-DA (0.5 mils-DA) throughout speed range. Figure 371 shows maximum sub-idle and idle 1/fan and 1/core vibration amplitudes at 0.015 mm-DA (0.6 mils-DA) at idle 960 rpm, $N_F$ and 0.015 mm-DA (0.6 mils-DA) at 2500 rpm, $N_c$, respectively. This indicates that vibration levels at the FADEC base were very low.

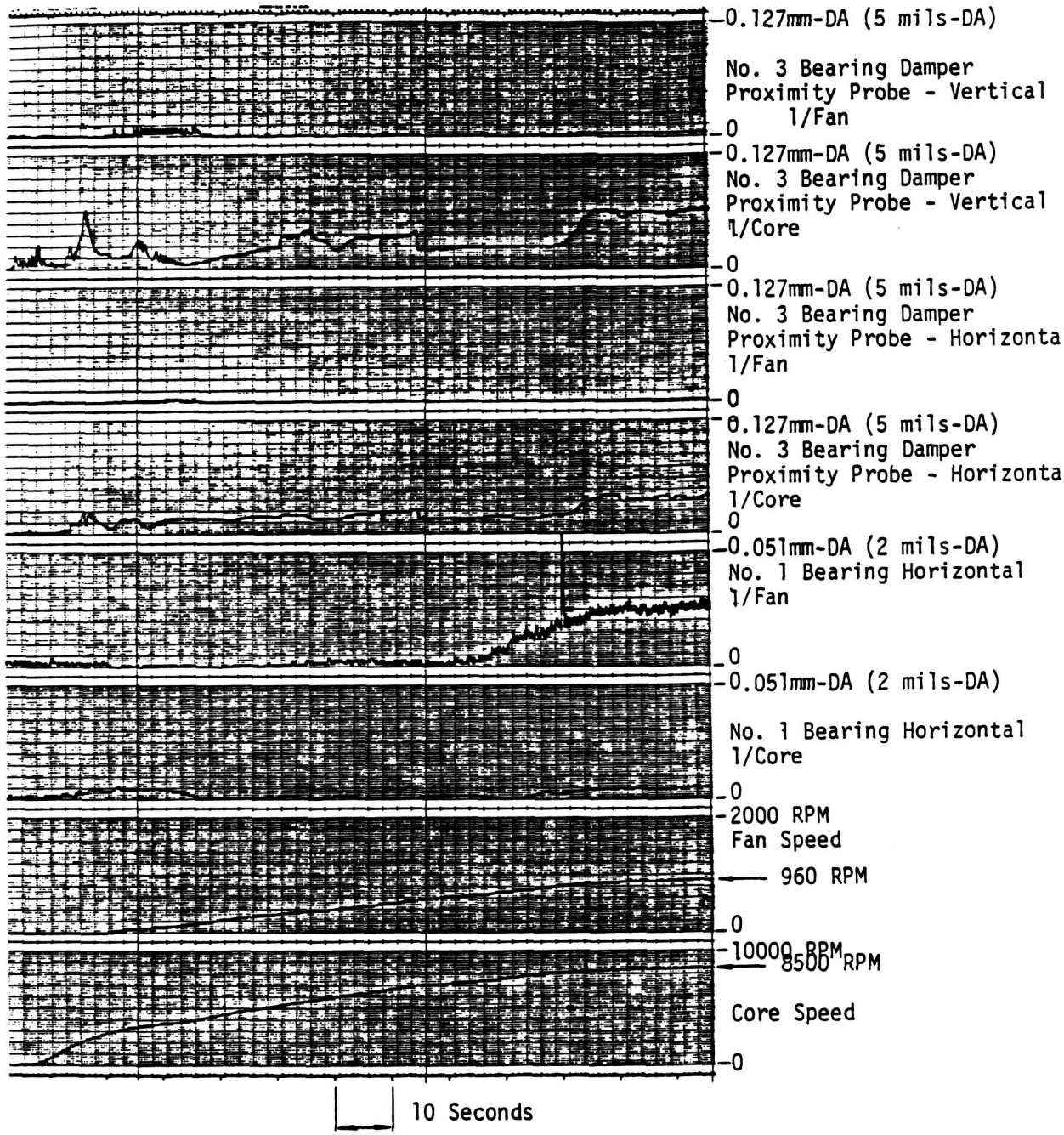


Figure 369. Sub-Idle and Idle Fan Synchronous (1/Fan) and Core Synchronous (1/Core) Engine Vibration Response Levels.

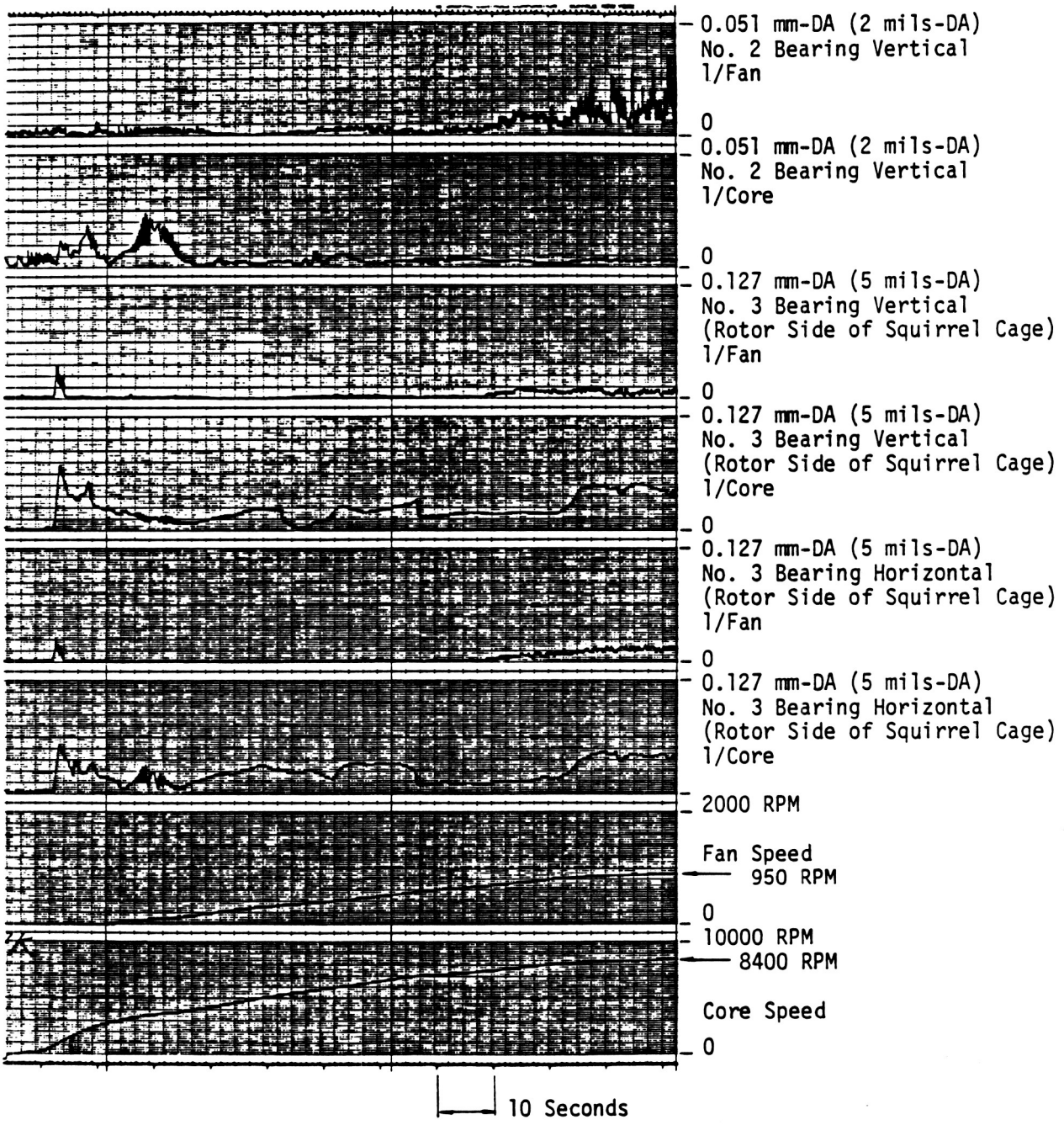


Figure 370. Sub-Idle and Idle Fan Synchronous (1/Fan) and Core Synchronous (1/Core) Engine Vibration Response Levels.

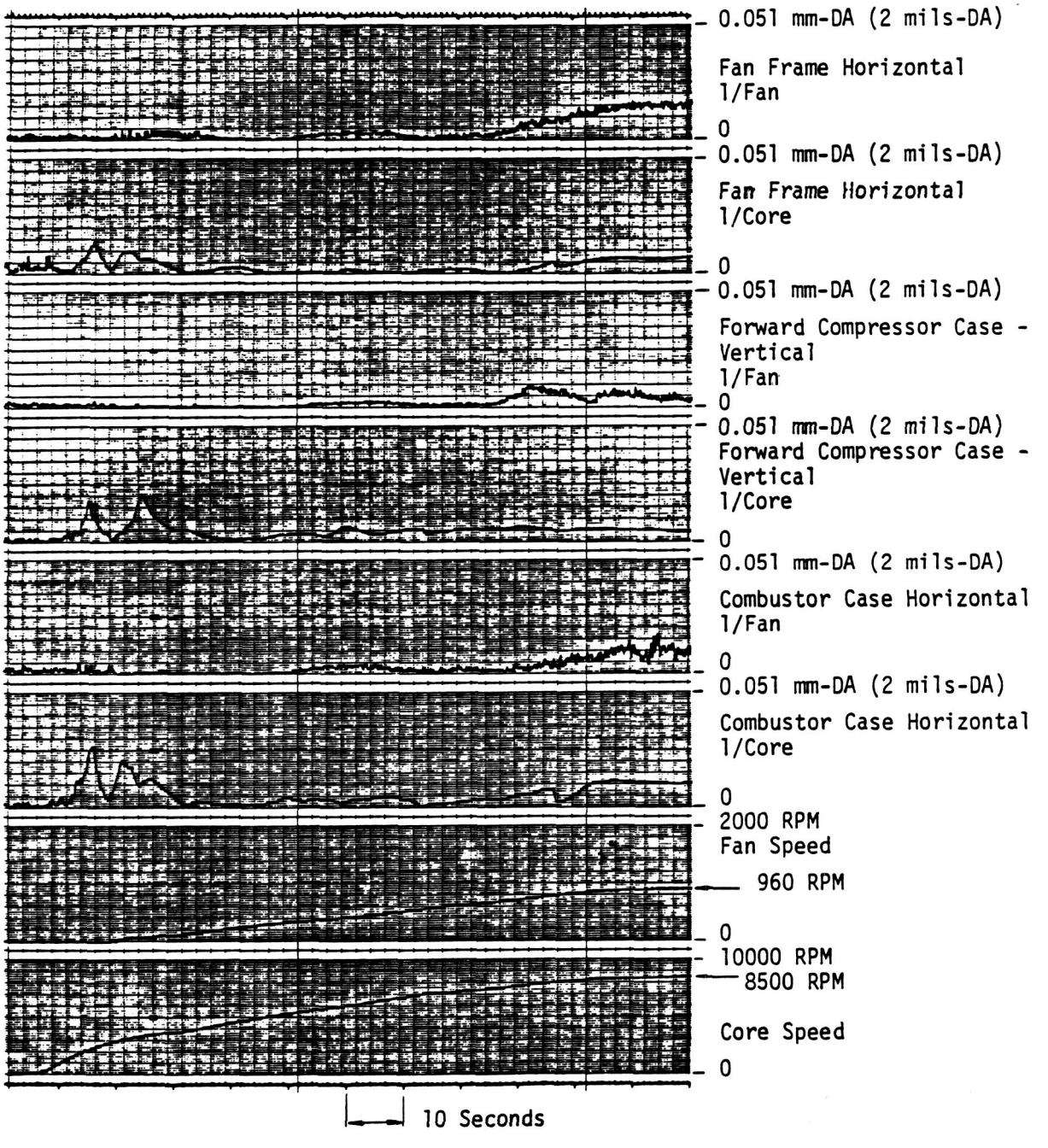


Figure 371. Sub-Idle and Idle Fan Synchronous (1/Fan) and Core Synchronous (1/Core) Engine Vibration Response Levels.

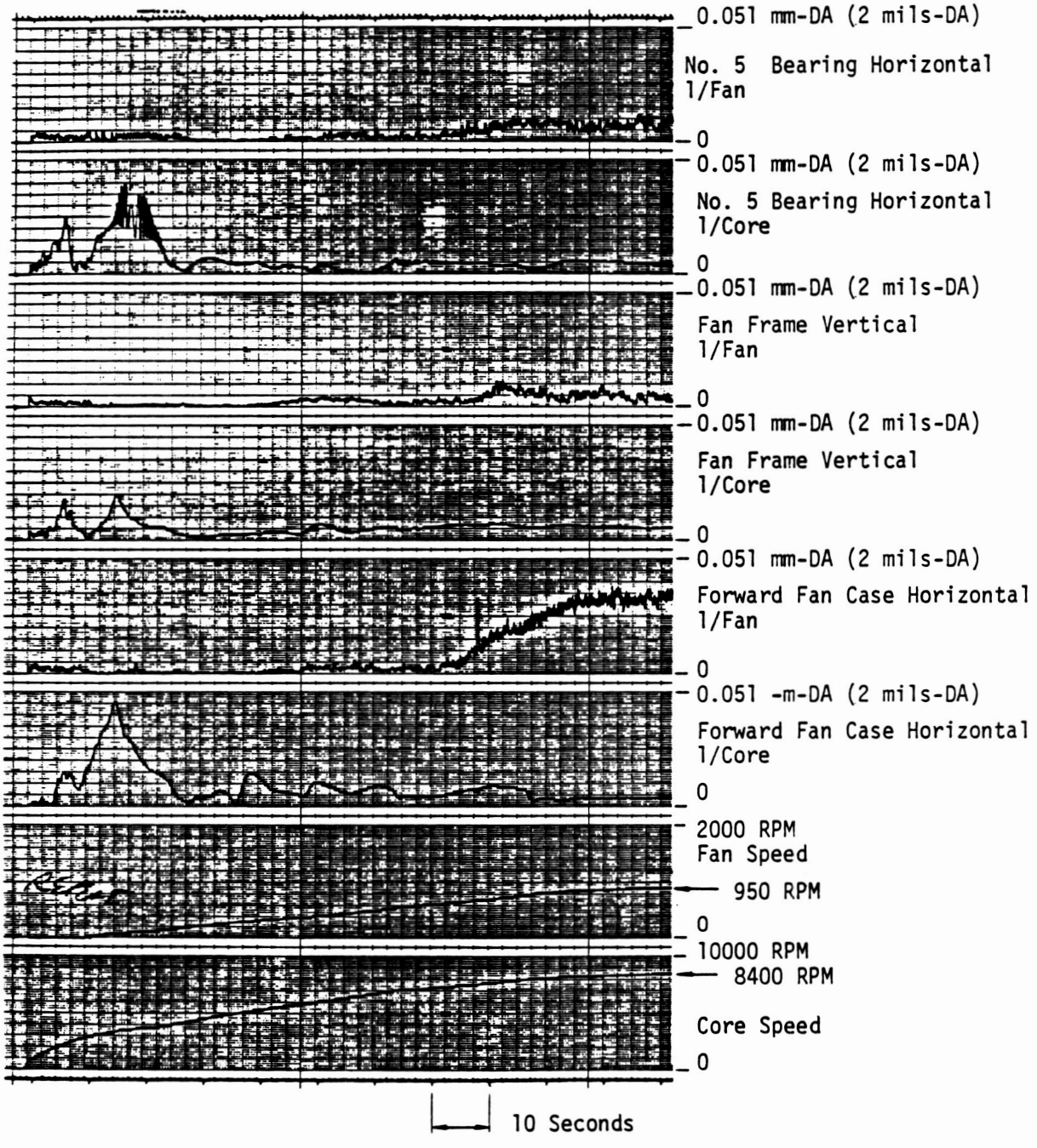


Figure 372. Sub-Idle and Idle Fan Synchronous (1/Fan) and Core Synchronous (1/Core) Engine Vibration Response Levels.

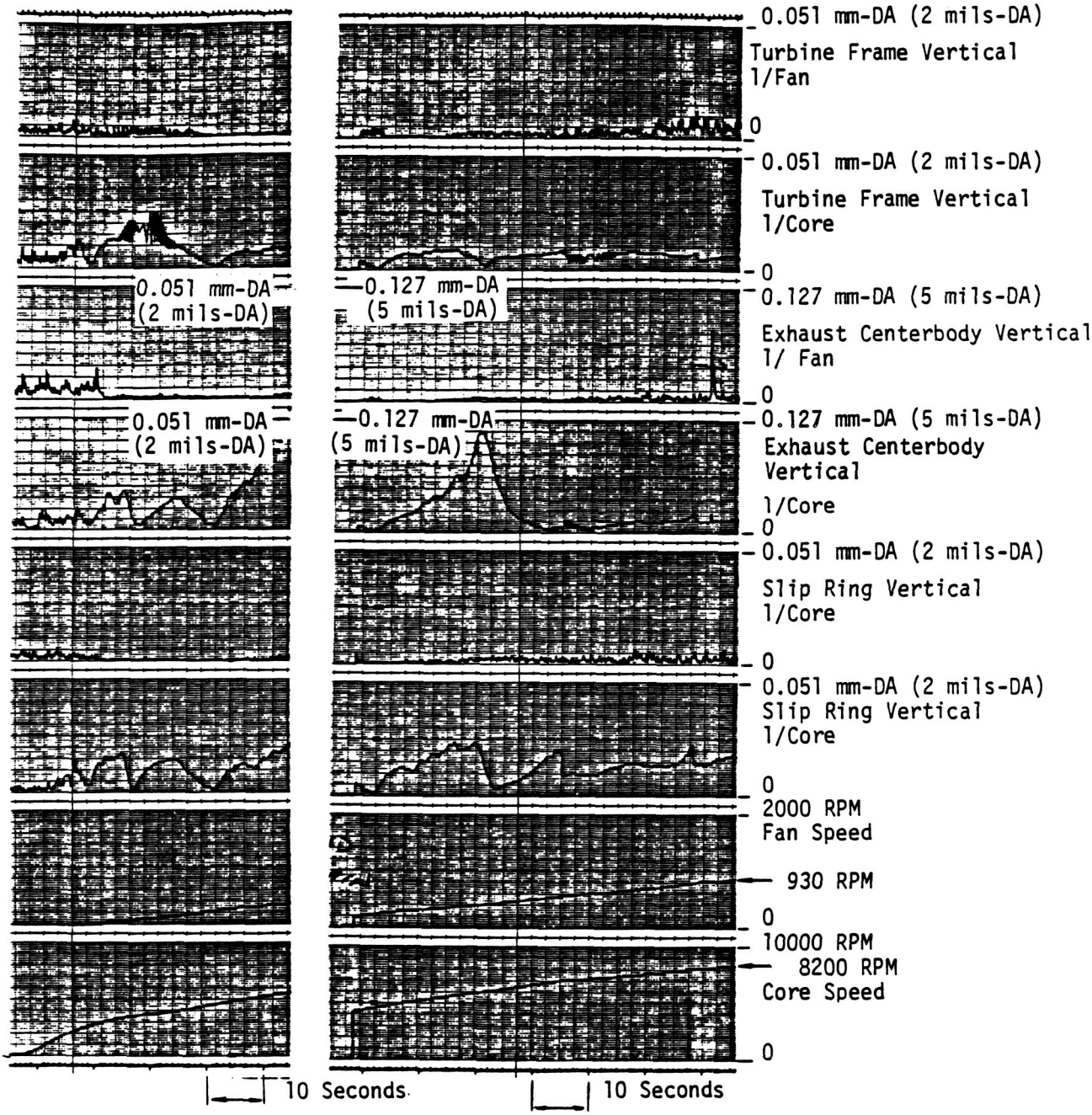


Figure 373. Sub-Idle and Idle Fan Synchronous (1/Fan) and Core Synchronous (1/Core) Engine Vibration Response Levels.

6.18.3 Test Correlation

Figure 374 shows a comparison of the predicted and measured core synchronous relative displacement response at the squeeze film damper. The measured data was obtained from a proximity probe located at the No. 3 bearing centering spring. This probe measured the clearance change across the centering spring and thus the clearance change across the damper oil film. Damper-system analysis indicated that the measured relative displacement characteristics at the damper could be analytically duplicated with an unbalance of $6.35 \times 10^{-3}$ kg-m (250 g-in) at the second stage of the HPT. Figure 375 shows the computed energy dissipated by the damper and the computed eccentricity ratio (relative displacement across the damper divided by the radial clearance) and the governing energy relationship relating oil flow to temperature rise. This governing relationship is arrived at by equating the power associated with damper work (left side of the equation) to the power associated with an increase in oil energy (right side of the equation). The HPT unbalance response calculation is based on an oil viscosity corresponding to 76.7°C (170°F) oil. From the energy equation, this results in a temperature rise of 4.6°C (8°F) above the measured 72.7°C (162°F) oil supply temperature and a damper oil flow of $2.21 \times 10^{-5}$ $m^3$/sec (0.35 gpm). Based on damper oil flow requirements for other damper applications at GE, this is a reasonable oil flow

For fan synchronous vibration, it was predicted that the maximum vibration levels would be associated with a rigid body bounce mode of the core rotor off of the soft suspension system at 3098 rpm fan speed. The test data, as indicated by the measurements at the No. 3 bearing accelerometer located on the soft side of the forward squirrel cage, showed that the maximum fan synchronous levels occurred at 2600 rpm fan speed. Although there is a difference in the predicted and measured critical speeds for this mode, the response characteristics are similar to those predicted.

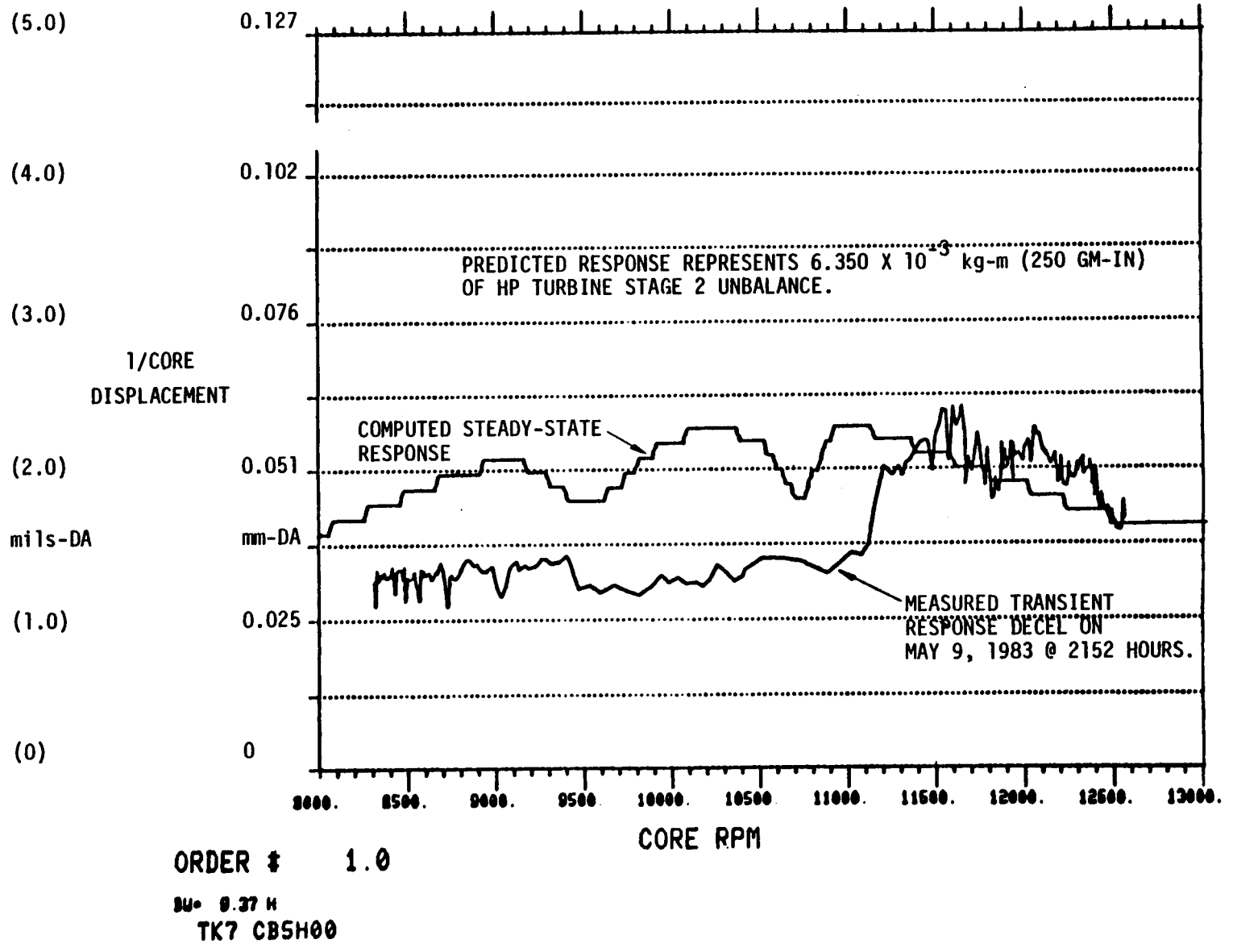


Figure 374. Core Synchronous Vibration Response Comparison of Measured and Predicted Displacement Across the Number 3 Bearing Centering Spring.

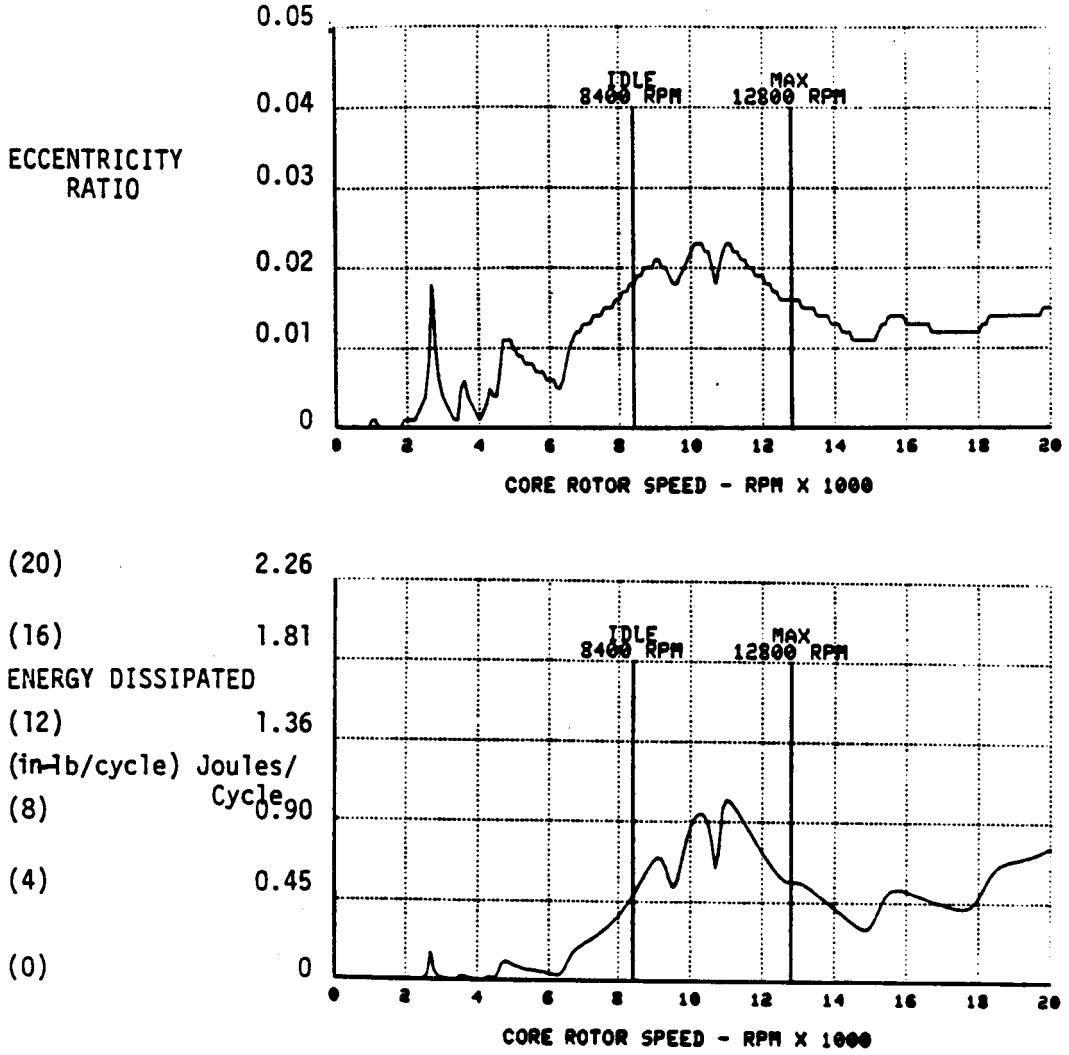


$$\left[\frac{E \times RPM}{12 \times 778}\right] \frac{BTU}{MIN} = \left[\dot{m} \times C_p \times \Delta T\right] \frac{BTU}{MIN}$$

E = ENERGY/CYCLE DISSIPATED BY DAMPER
RPM = ROTOR SPEED
$\dot{m}$ = OIL MASS FLOW THROUGH DAMPER
$C_p$ = OIL SPECIFIC HEAT
$\Delta T$ = OIL TEMPERATURE RISE IN DAMPER

PEAK ECCENTRICITY RATIO OF 0.023 AT 11025 RPM CORRESPONDS TO:
E = 1.03 JOULES/CYCLE (9.10 IN-LB/CYCLE) FOR A OIL FILM TEMPERATURE OF 76.7°C (170°F).
WITH THE OIL SUPPLY TEMPERATURE = 72.2°C (162°F), $\Delta T$ = 4.5°C (8°F)

THEREFORE: $\dot{m} = 2.21 \times 10^{-5}$ $m^3$/second (0.35 gpm)

CORRESPONDING POWER: 189 WATTS (10.7 BTU/MIN, 0.253 HP)

Figure 375. Core Synchronous Vibration Energy Dissipated by Damper and Corresponding Oil Flow Requirements of HP Turbine Stage 2 Unbalance.

### 6.18.4 Conclusions

Engine vibration response characteristics for the ICLS turbofan were well behaved for the entire speed range throughout the test program and showed good agreement with the pretest analysis. The soft-mounted core rotor and high load damper system was very effective, resulting in highly damped core vibration characteristics which were low in amplitude. Fan synchronous vibration levels were low with no trace of the characteristic fan nodding mode. The test program verified that this two-frame, five-bearing, high-bypass turbofan engine would operate with low core and fan synchronous vibration response throughout the entire speed range.

## 6.19 CONTROL SYSTEM PERFORMANCE

The ICLS control system with its new, engine-mounted FADEC performed very well throughout the entire test program. Accurate, predictable, responsive control of all controlled variables was provided and flexibility incorporated in the system served well in accommodating unexpected differences from pretest predictions relative to transient fuel flow requirements and active clearance control system characteristics. There were no control system component failures.

Highlights of the control system operation are given below.

### Starting

The first eight starts were made by motoring to maximum motoring speed (i.e., setting starter air pressure at 55 psia and holding until core speed stabilized), opening the stopcock until ignition occurred, and then manually increasing fuel flow until idle speed was achieved. Figure 376 shows a typical manual start.

All subsequent starts (9 through 28) were made with automatic scheduling of fuel flow. Automatic starts were made with progressive fuel

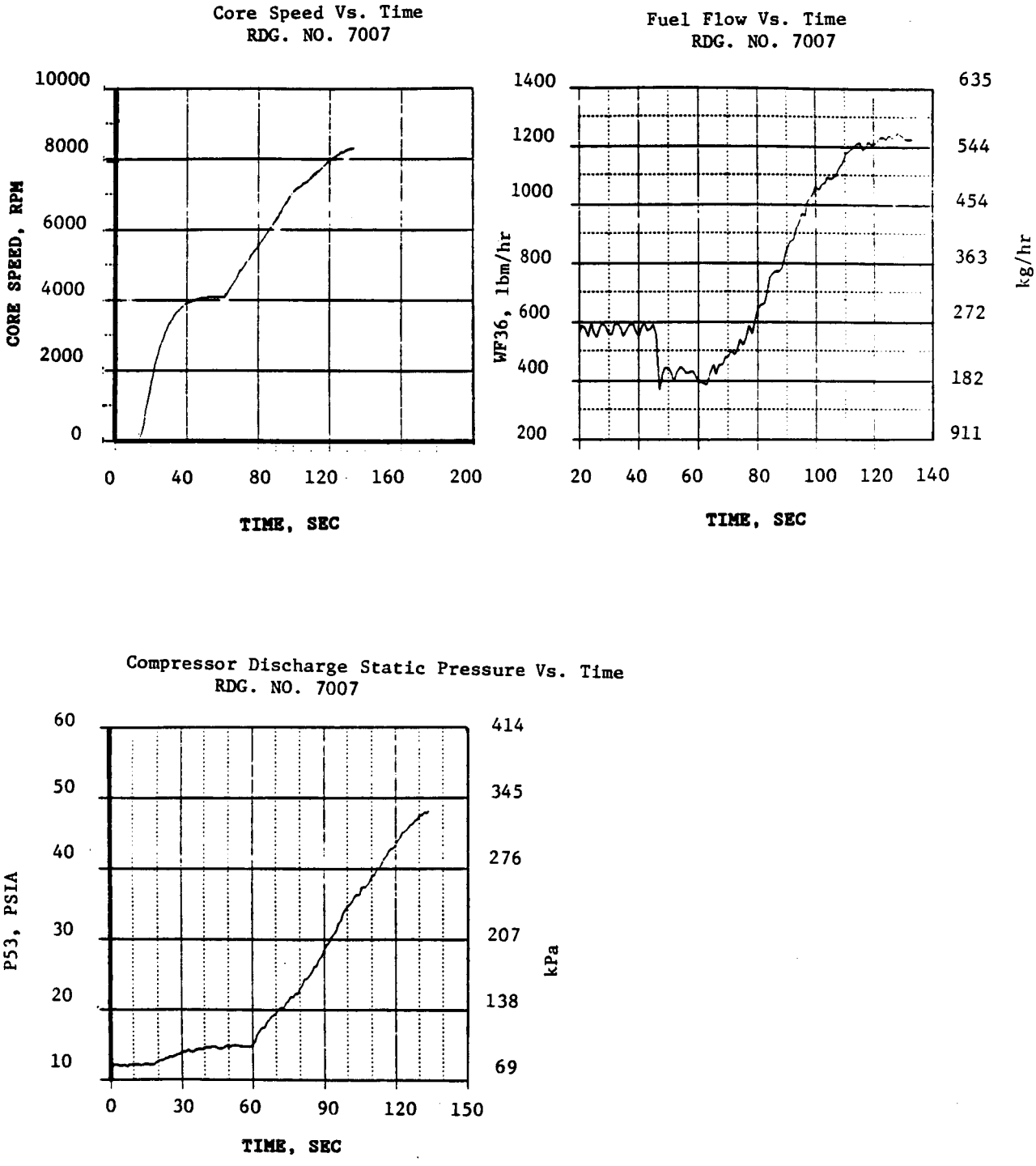


Figure 376. Typical Manual Start.

enrichment, ultimately using a schedule that was higher than the design schedule by approximately 70% at cranking speed and by 50% near ground idle. There was no evidence of compressor stall during any engine start.

Figures 377 and 378 are two successive starts which demonstrate the potential for a 44-second start. Figure 377 is a start with normal stopcock opening (20% PCNHR - approximately 2500 rpm at these inlet conditions). Figure 378 is the maximum enriched start. Stopcock opening was delayed here because of a false indication of high engine vibrations but if it had been opened at 20% PCNHR, time for the start would have been 44 seconds.

Data from these starts were combined with engine motoring data and post-test starter calibration data to define the general characteristics of the engine in the start range. Figure 379 is both a corrected and uncorrected plot of torque characteristics for the two enriched starts of Figures 377 and 378. Figure 379 also shows calculated torque at the highest steady-state speed attained while motoring the engine with the stater as well as the torque calculated from an engine coastdown. The difference between the indicated coastdown torque and the other torque data is attributed mainly to the fact that the engine was warm during the coastdown with lower viscosity oil and different internal clearances. Figure 380 also illustrates these torque differences. Note the difference in time required to start a hot engine and cold engine. Start No. 15 was made immediately after a shutdown and start No. 16 was made after a 4-hour shutdown. Both starts were made using the same accel schedule enrichment.

Speed Governing (Core and Fan)

For most ICLS testing, the power lever angle (PLA) schedules for fan speed and core speed were adjusted so that the core speed schedule was in effect from idle to approximately 30% thrust and the fan speed schedule was in effect above that. Figure 381 shows steady state operation at low power and Figure 382 shows steady-state operation on fan speed control at high power. Figure 383 is a steady-state plot of switching from core speed to fan speed

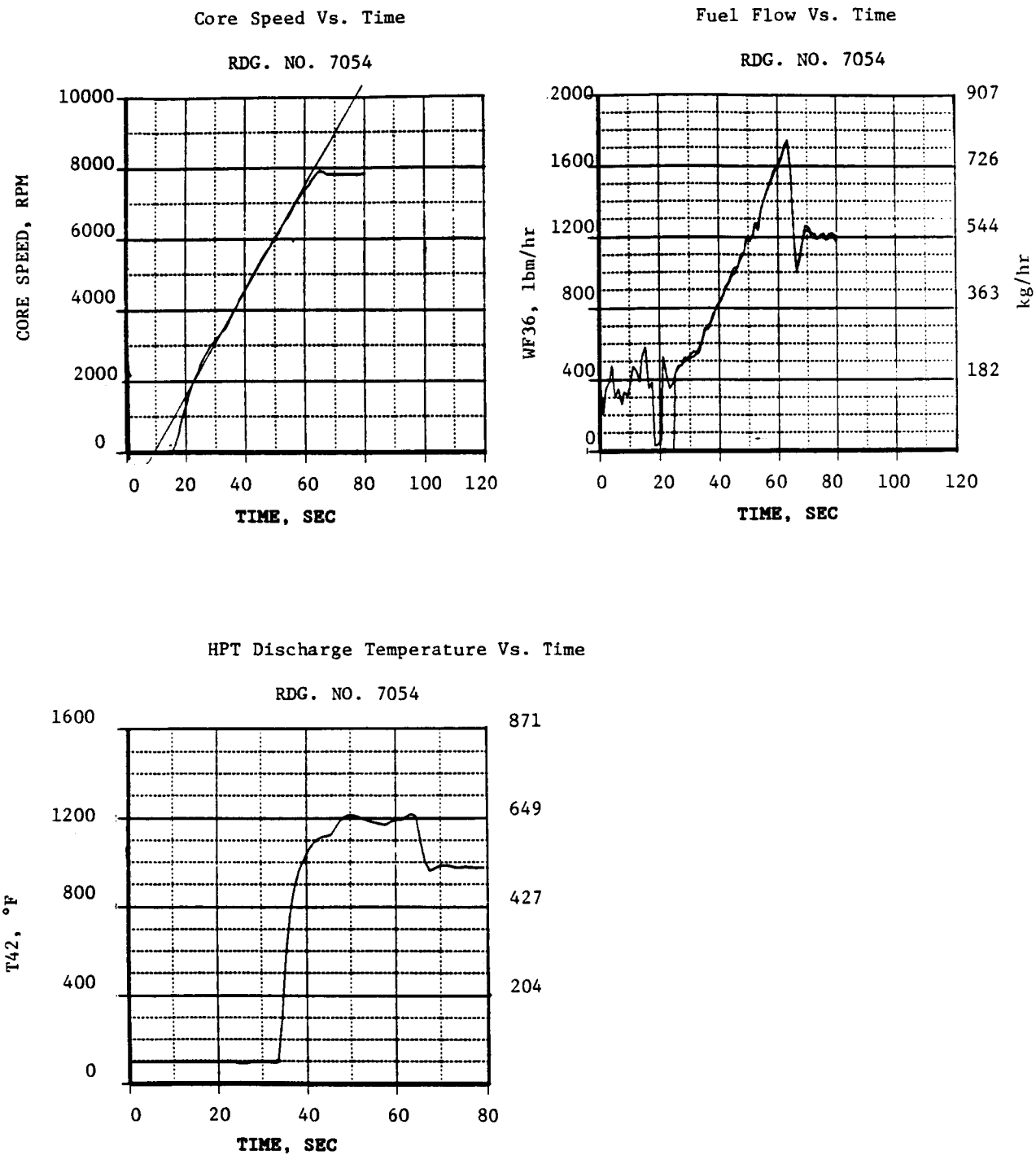


Figure 377. Start With Normal Stopcock Opening.

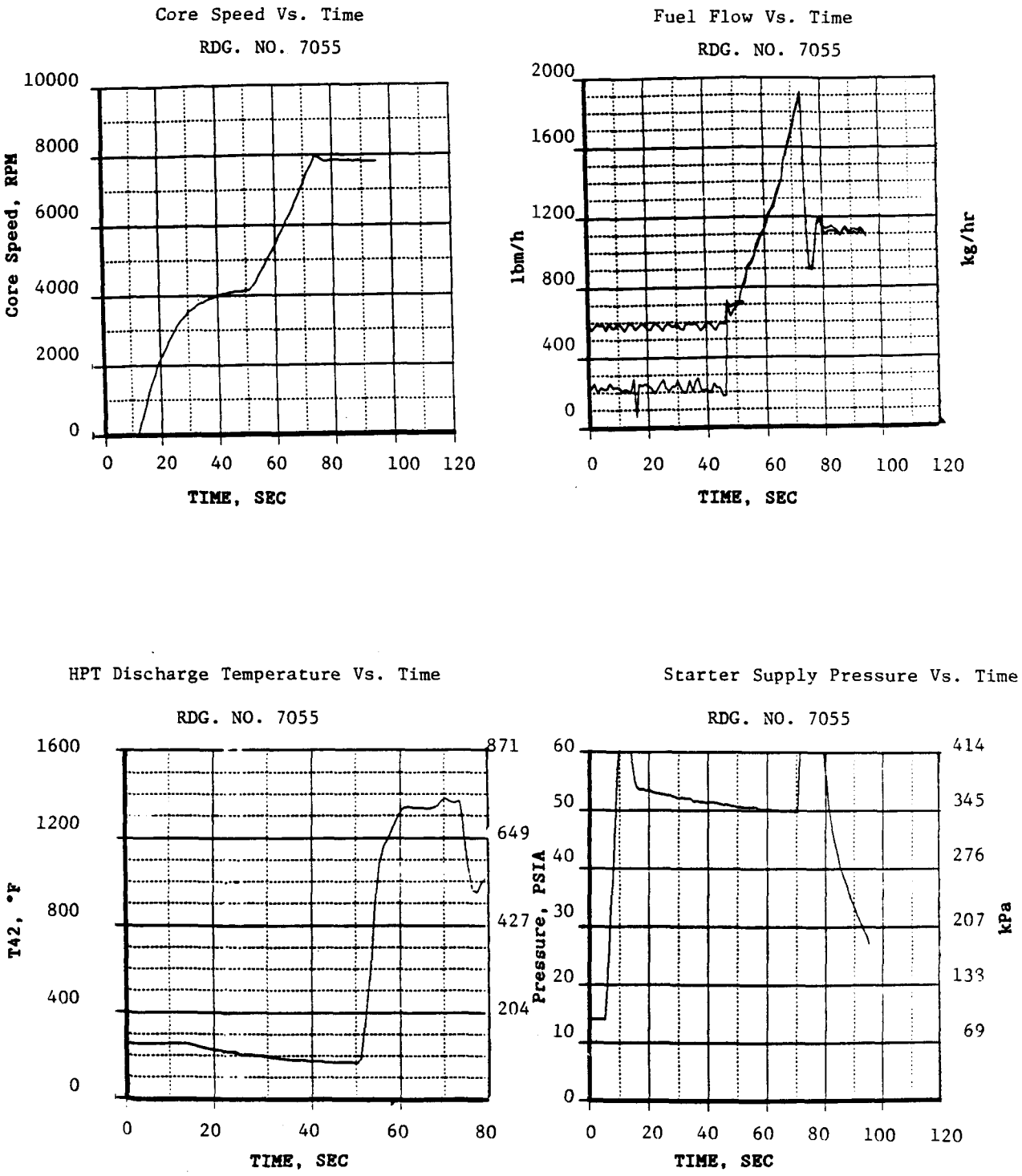


Figure 378. Maximum Enriched Fuel Schedule Start (Delayed Stopcock Opening).

Net Torque - Calaulated from Measured Acceleration Rate and Calculated HP Rotor Polar Moment of Intertia
Starter Torque - Calculated from Measured Starter Inlet Conditions and Calibrated Starter Data Defined by Hamilton Standard on the Starter Used (8/5/83)
Engine Torque - Calculated by Subtracting Starter Torque from Net Torque

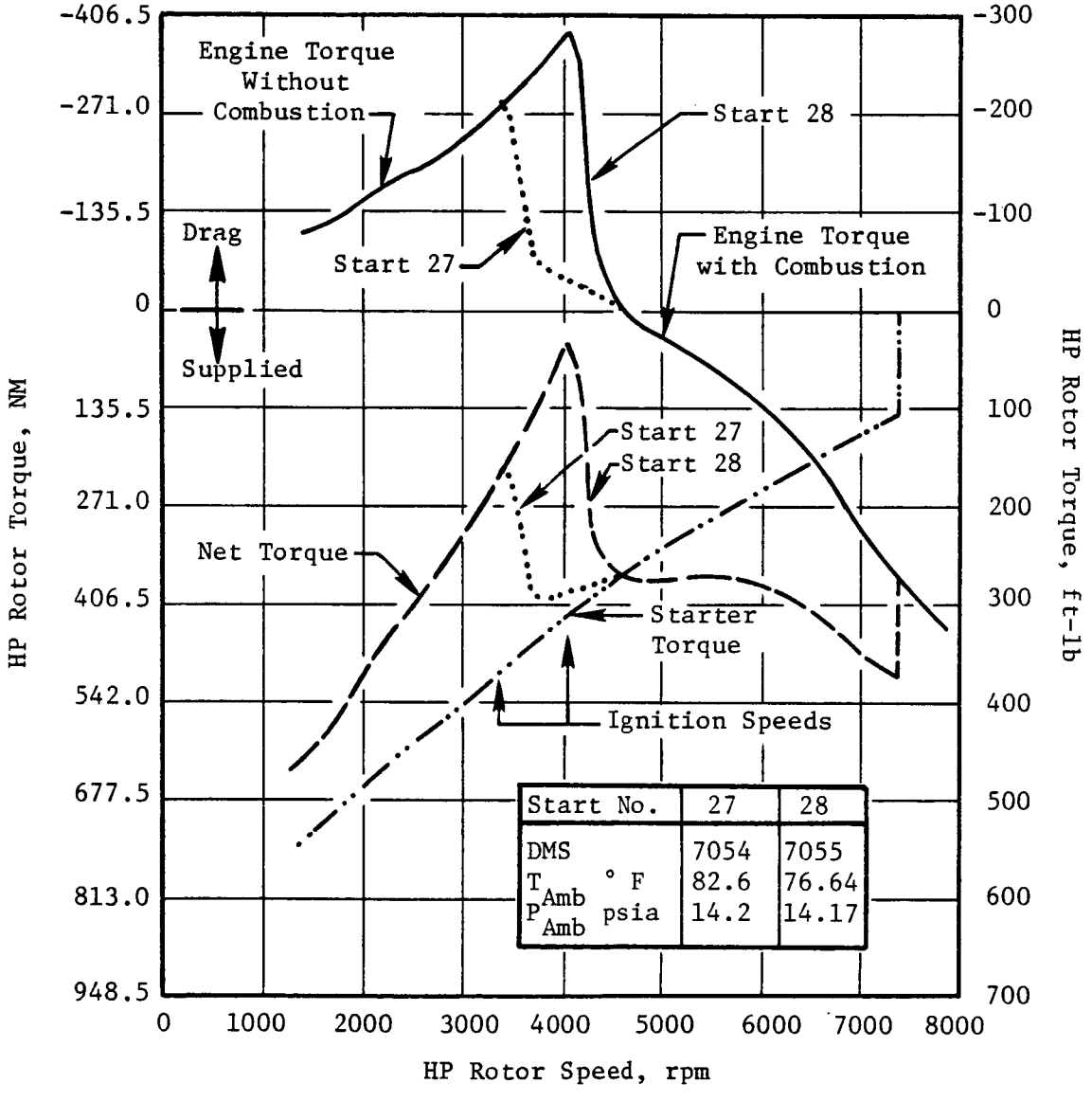


Figure 379. Engine Torque Data Maximum Enrichment.

Ⓐ Start No. 28 (Ambient Engine) DMS 7055-Engine Shutdown Approximately 3 Hours Prior to Start No. 28

Ⓑ Stabilized Maximum Motoring Speed Point (Ambient Engine) DMS 23 Maximum Motoring Made Prior to the First Start of the Day (Calibrated Starter Data Used for A and B and D Calculations)

Ⓒ Engine Coastdown from Idle After Fuel Shut-Off (Hot Engine) (DMS 7026)

Ⓓ Start No. 27 (Ambient Engine) DMS 7054 First Start of the Day

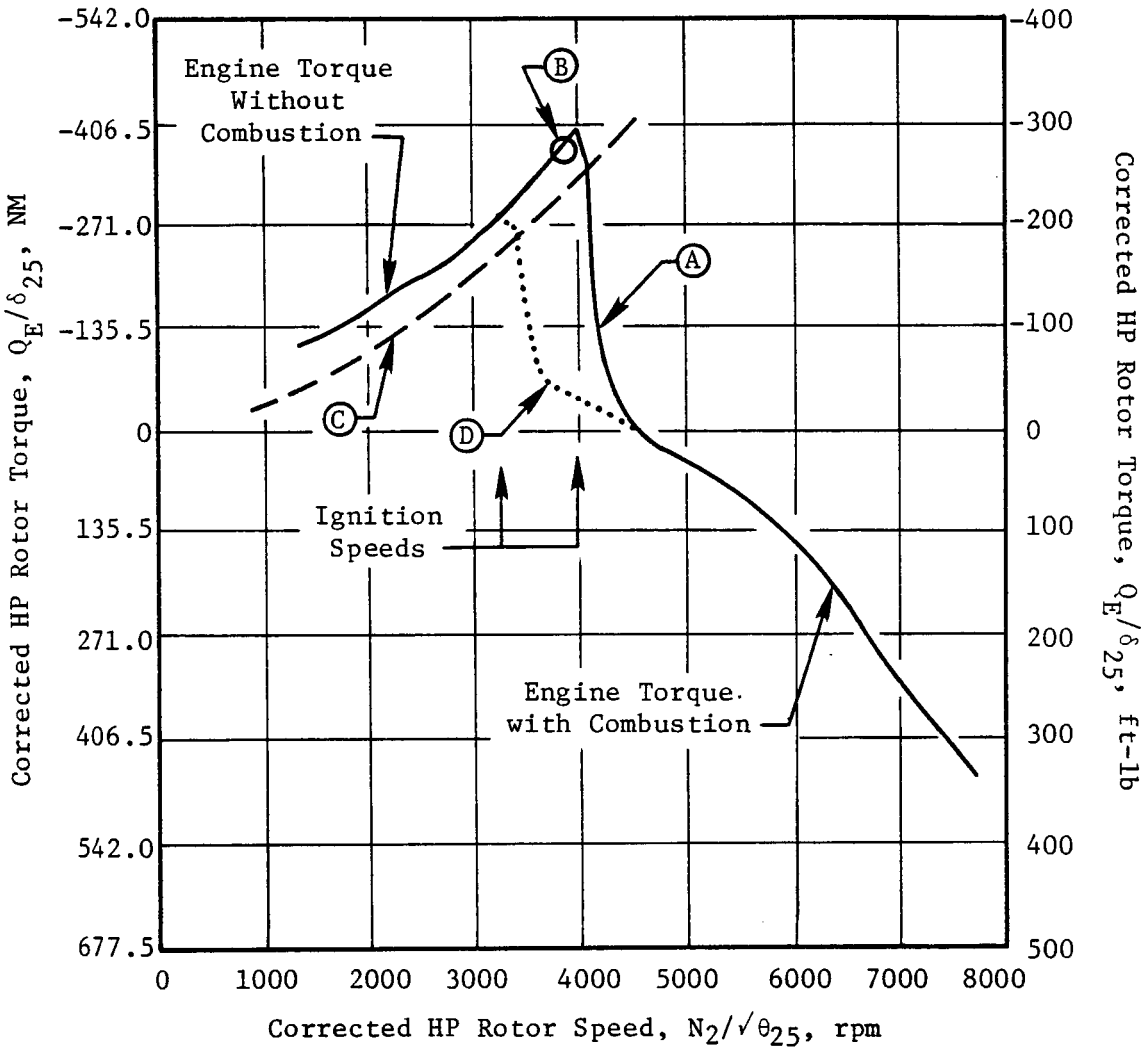


Figure 379. Engine Torque Data Maximum Enrichment (Concluded).

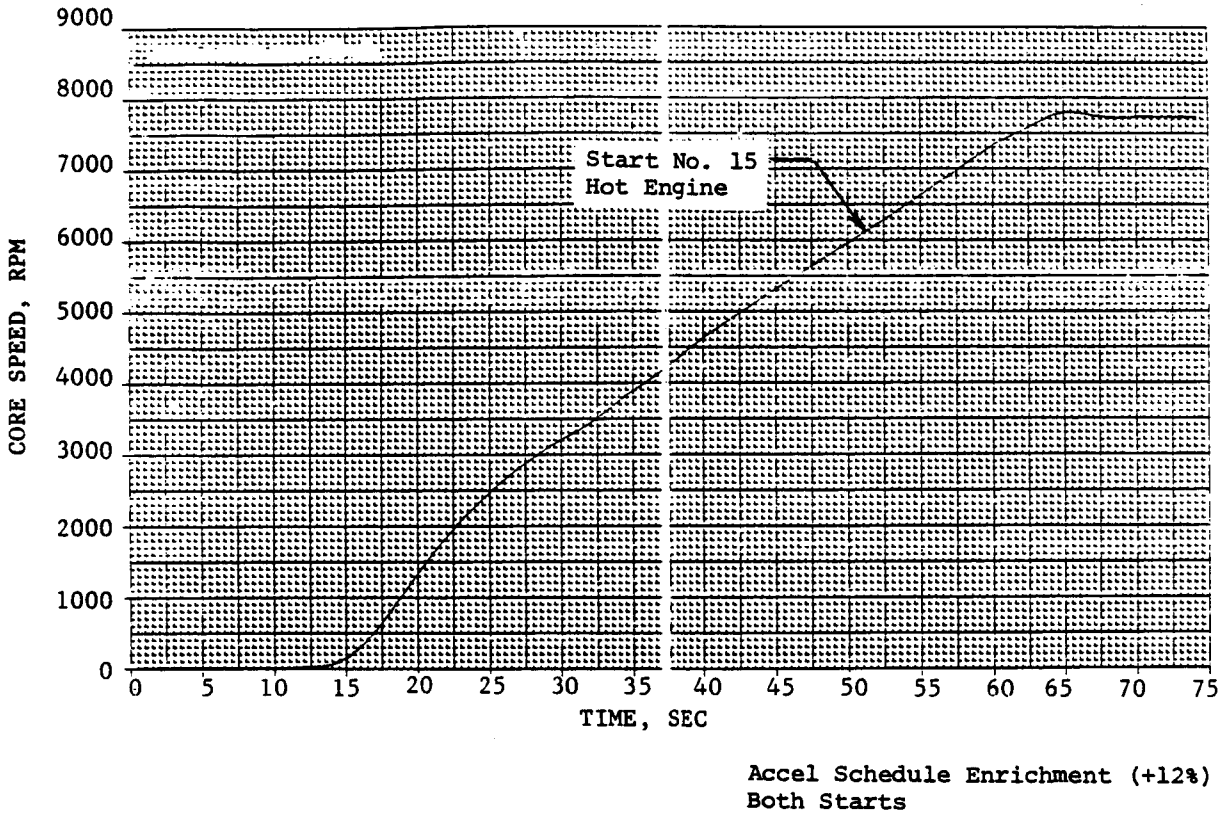


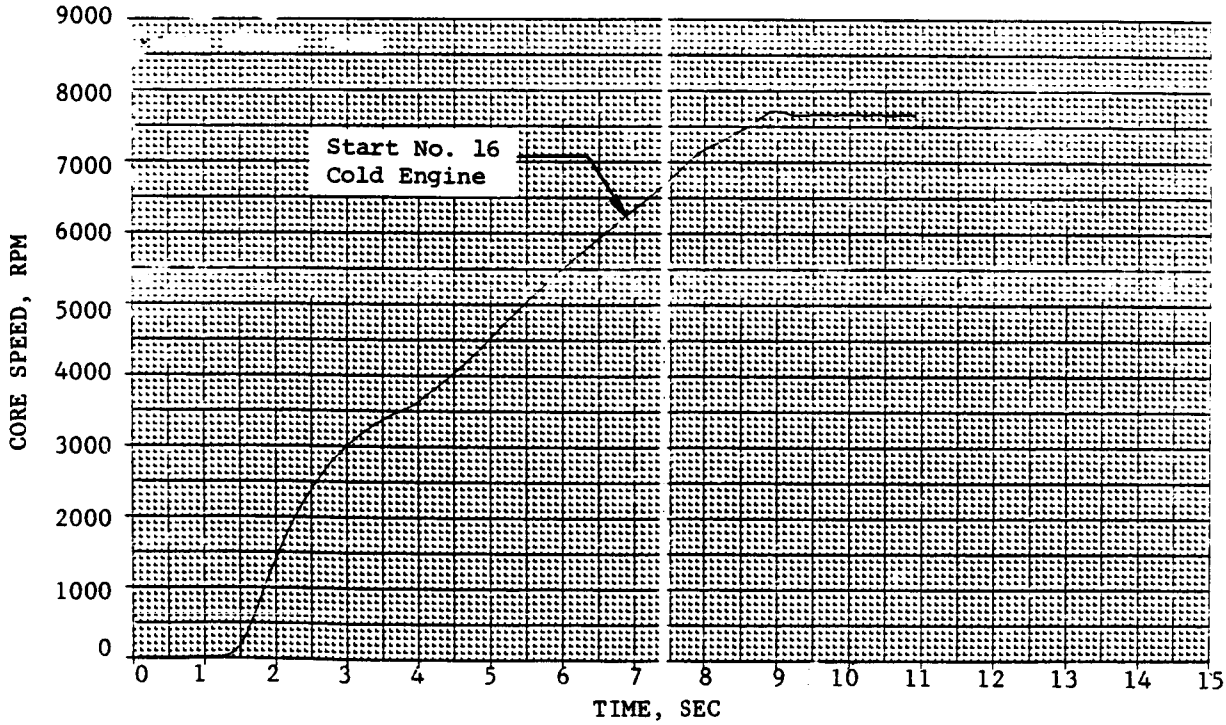


Figure 380. Starting - Hot Engine vs. Cold Engine.

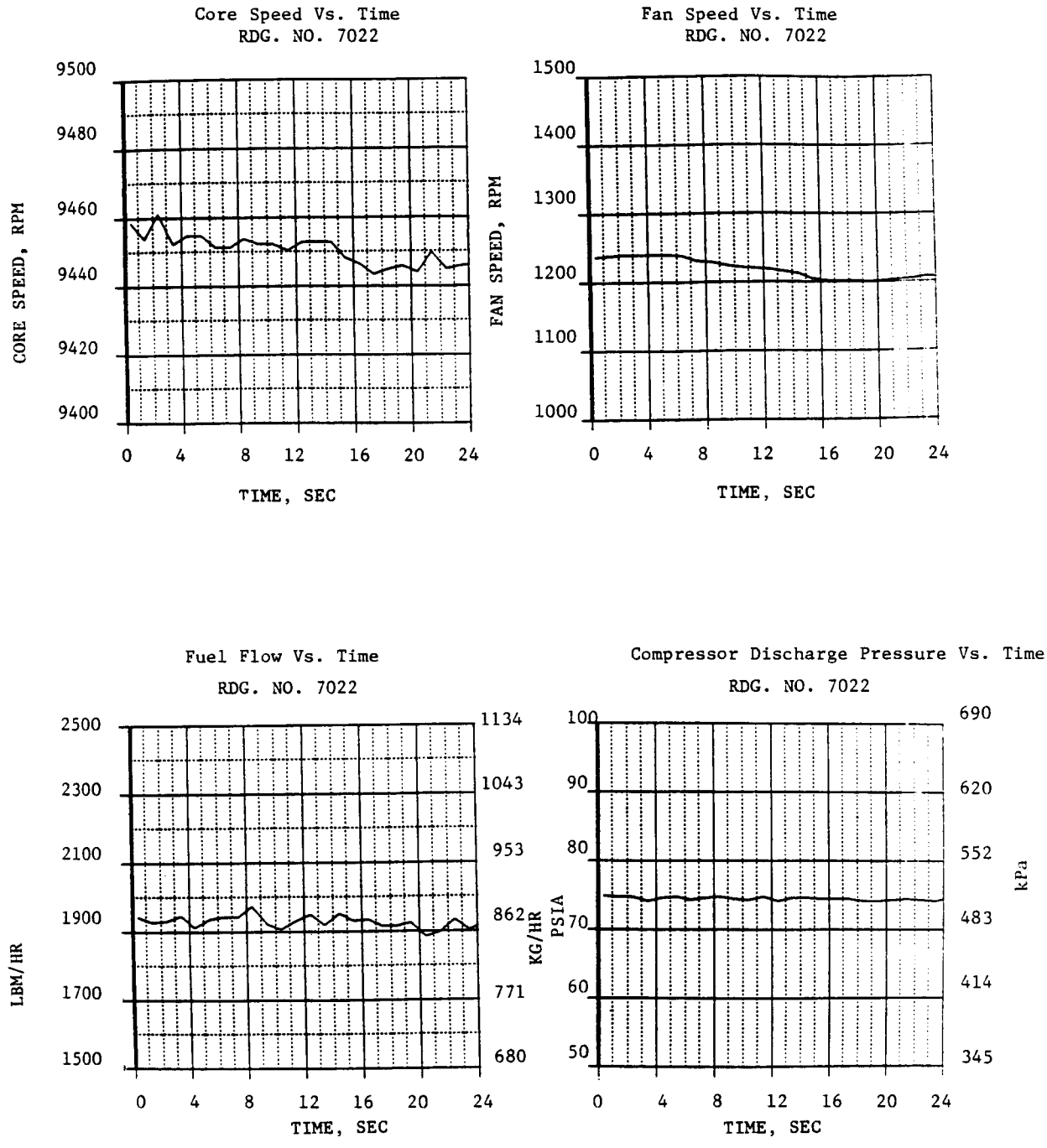


Figure 381. Core Rotor Speed Control at Low Power.

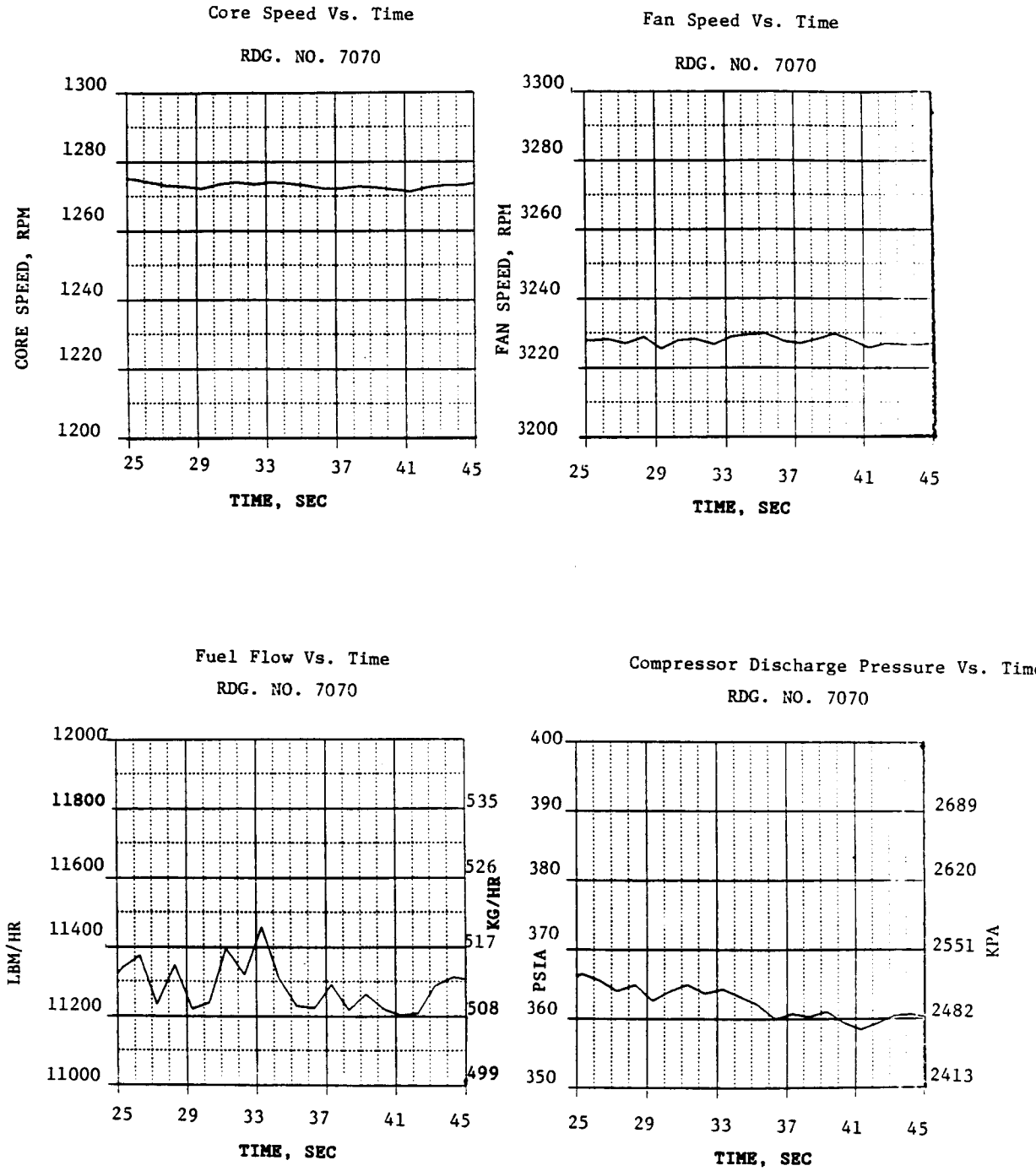


Figure 382. Fan Speed Control at High Power.

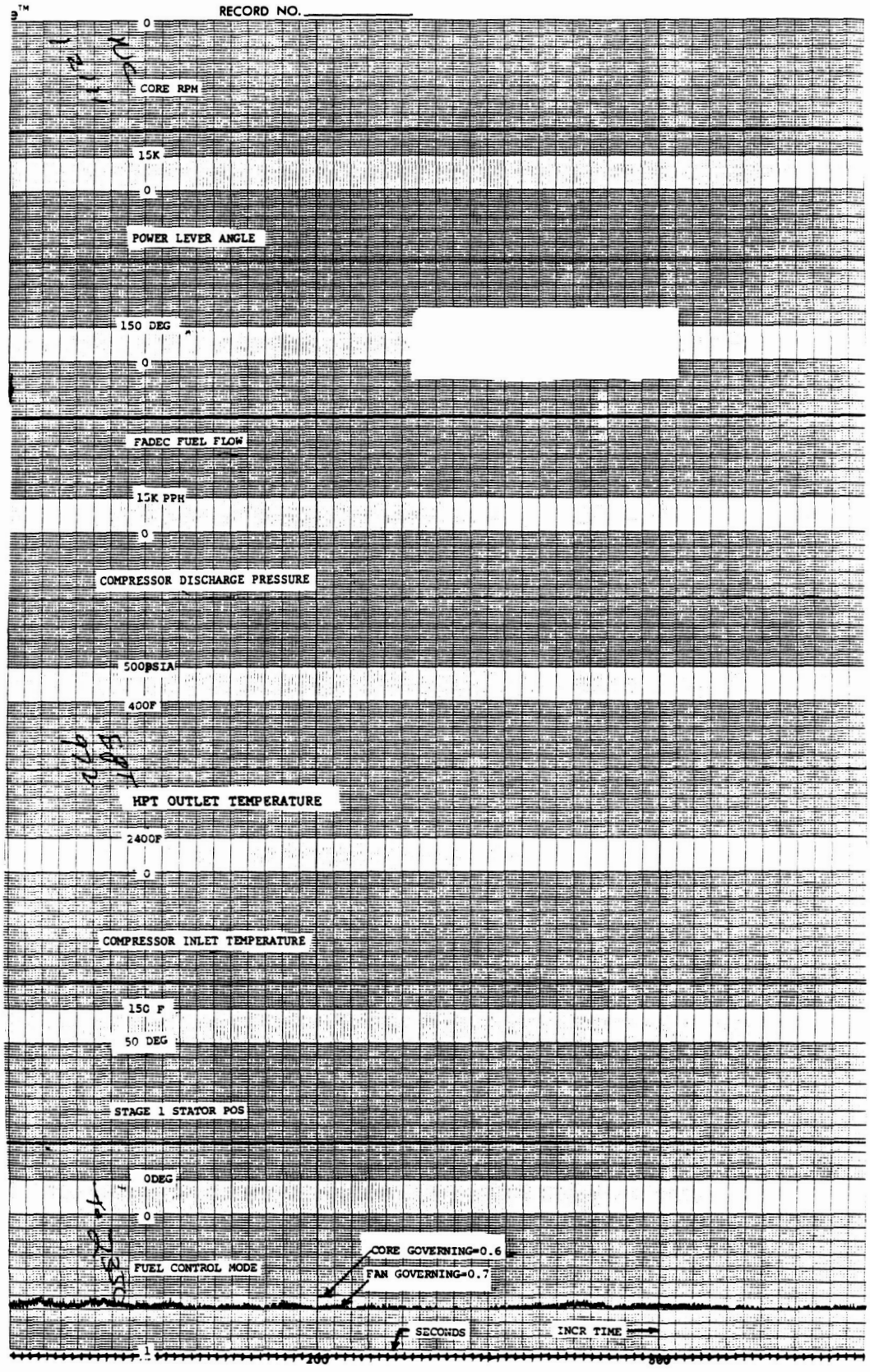


Figure 383. Steady State Operation at Fan/Core Governing Transition Point.

ORIGINAL PAGE IS
OF POOR QUALITY

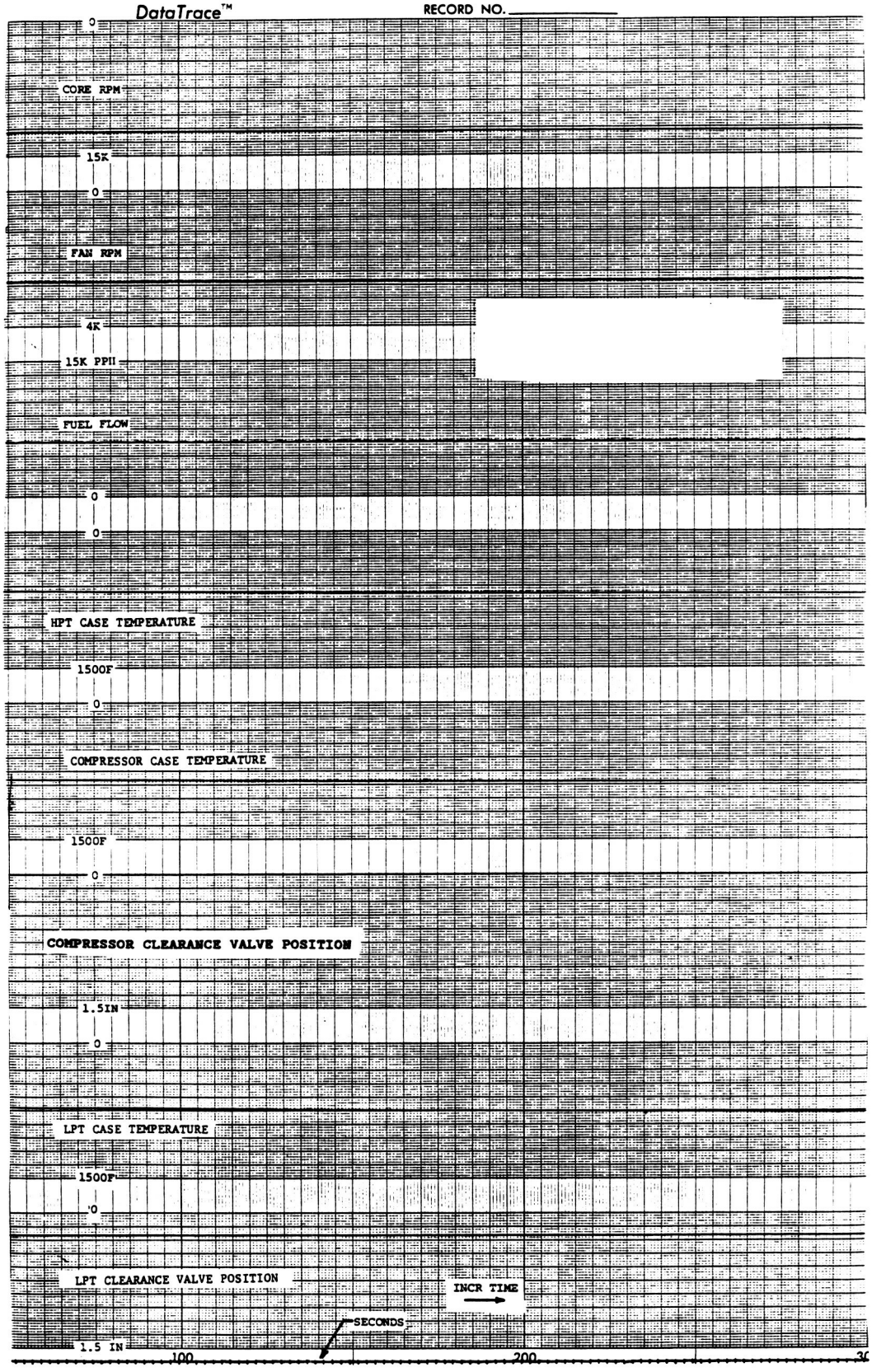


Figure 383. Steady State Operation at Fan/Core Governing Transition Point (Concluded).

control. The trace of the mode signal is obscured because signal excursions were limited by recorder response.

These plots demonstrate the excellent speed holding capability of the FADEC and also verify that switchover between speed control modes was smooth.

Fuel Flow Limits

Limits are imposed on the basic core rotor and fan speed schedules to prevent excessive HPT inlet temperature (calculated), excessive LPT inlet temperature (T42), and excessive compressor discharge pressure (PS3). These limits were combined in a selection network which established priorities and assured smooth transition between control modes.

A slow accel was made onto each limit to demonstrate transition onto the limit and steady-state operation on the limits. Figures 384, 385, and 386 are slow accelerations from fan speed control onto the T42, PS3, and T41C (calculated HPT inlet temperature) limits, respectively. Operation was satisfactory on each limit. (Note: T41C was not recorded transiently but the PS3 and fuel flow traces shown on Figure 386 are equivalent because these are the two main factors in the T41C calculation.)

T3 Sensing Error

Early in the ICLS test it was discovered that the compressor discharge temperature (T3) signal to the FADEC was erroneously low by increasing amounts as ambient temperature in the core cowl area increased. Limited investigation on the engine indicated the presence of an extra thermocouple junction at the T3 sensing lead connection in the core cowl area, suggesting the use of incorrect material in the lead and/or the connector pins. Because this lead passed through a crowded fan frame vane and was difficult to remove and reinstall, it was not replaced and steps were taken to minimize the effect of the error. By routing some instrumentation cooling water near the suspect connector and making FADEC adjustments, it was possible to use the T3 signal.

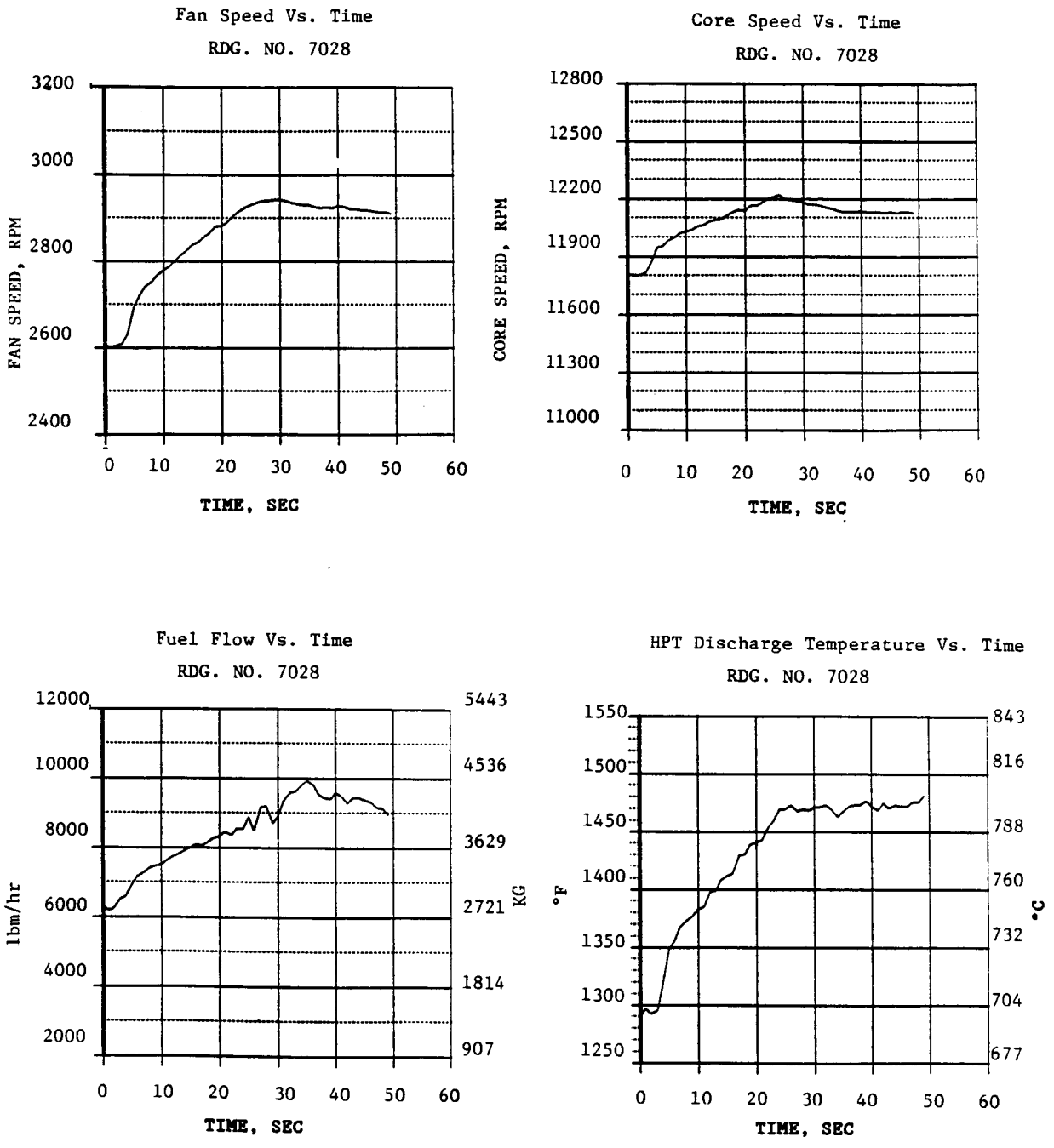


Figure 384. Acceleration to $T_{42}$ Limit.

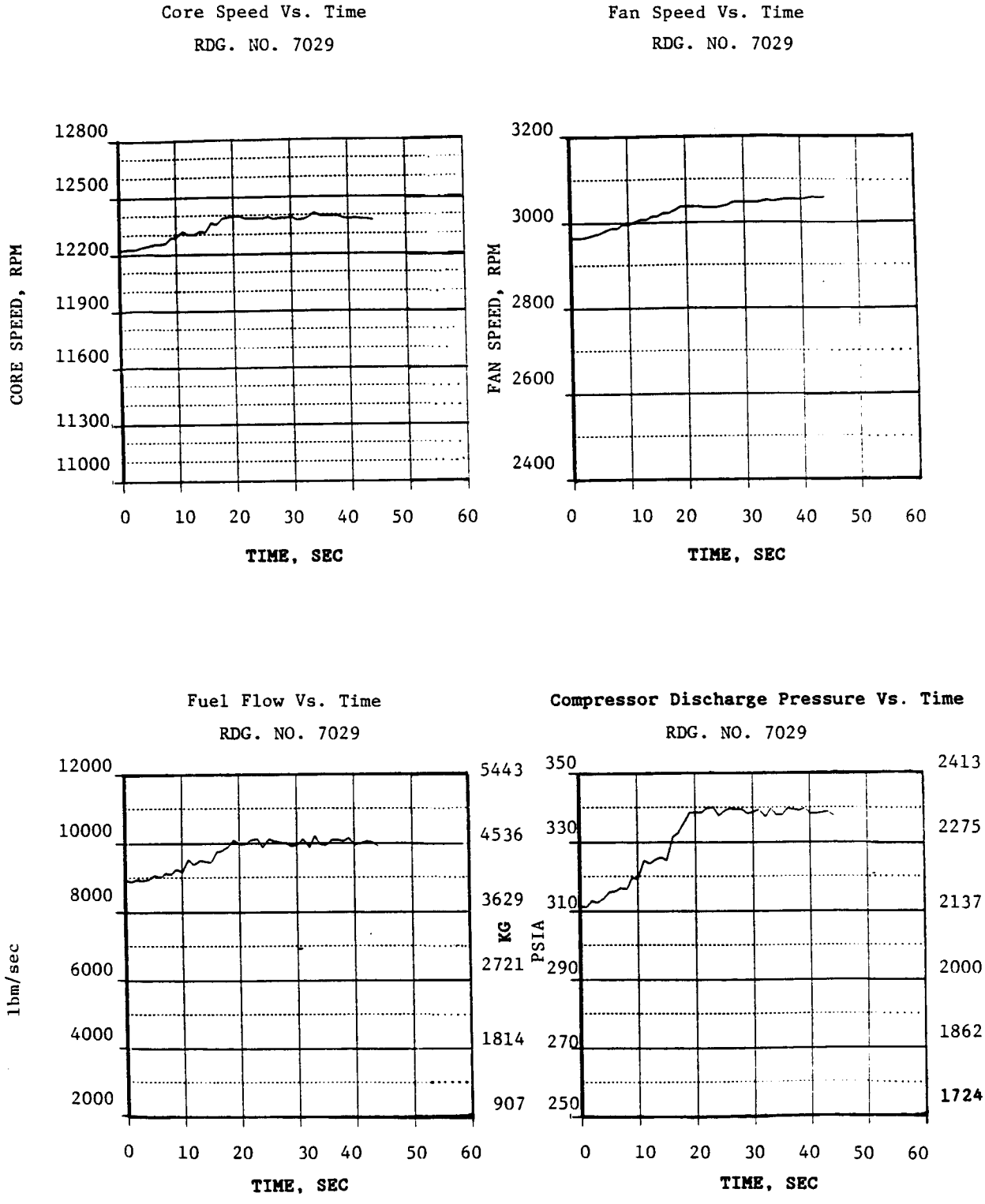


Figure 385. Acceleration to $P_{S3}$ Limit.

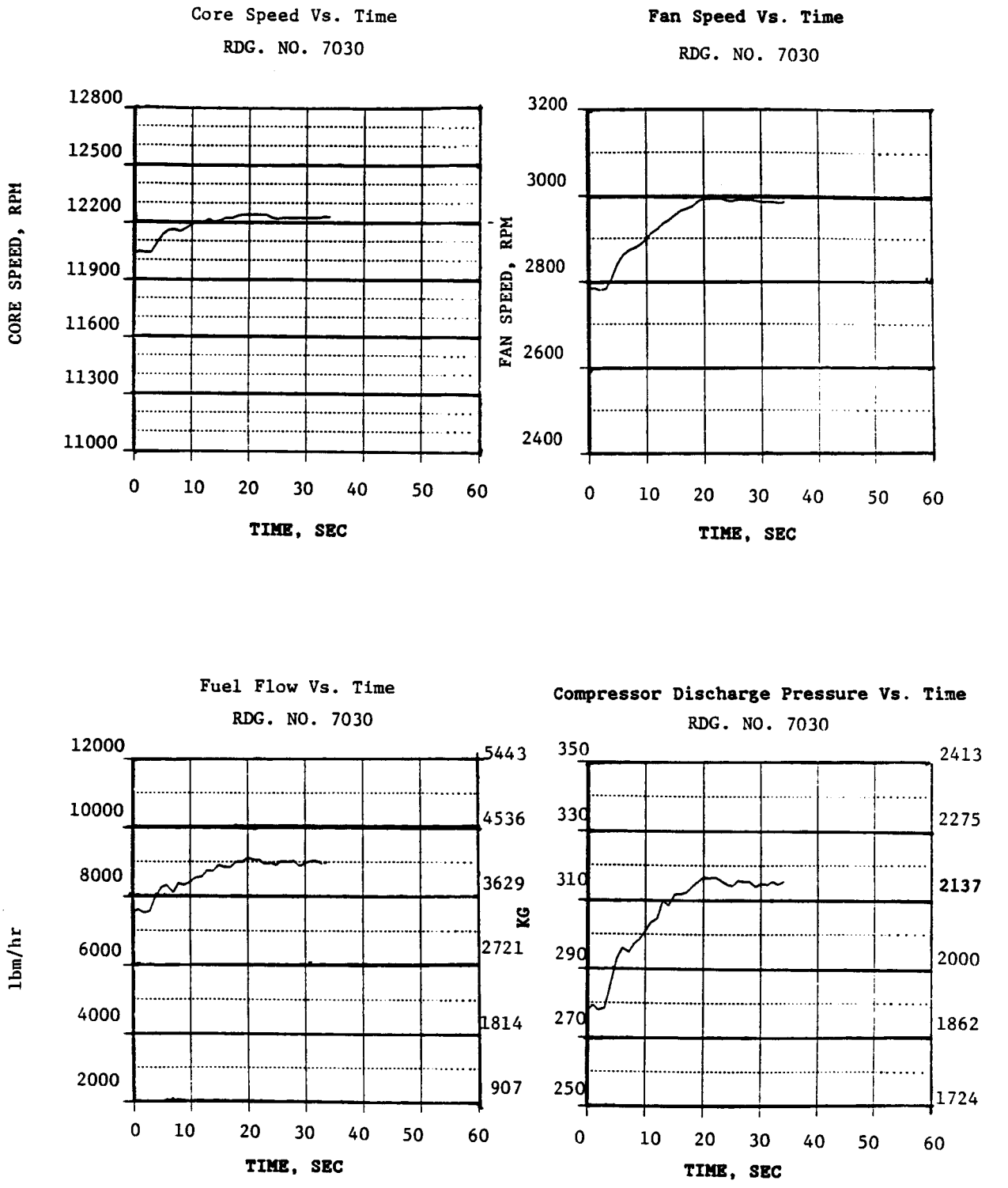


Figure 386. Acceleration to $T_{41C}$ Limit.

T3 is a factor in the T41C limit, the compressor clearance control automatic control strategy, and the sensor failure indicator and corrective action (FICA) feature.

A resistance test of the T3 lead after test completion revealed that the Chromel and Alumel wires were reversed. This created extra sensing junctions at both ends of the lead and explains why the T3 signal decreased as the temperature in the core cowl area increased.

Stator Scheduling

The conventional practice of scheduling compressor stator angles as a function of rpm and inlet temperature was used for ICLS testing. Steady state stator positioning accuracy and stability was excellent throughout the test. Figure 387 is a plot of steady state DMS data points of Stage 1 angle versus corrected core speed with the schedule line shown for reference purposes.

Transient stator accuracy is difficult to assess precisely because of the transient lag inherent in measuring compressor inlet temperature. A fairly good assessment is possible, however, by comparing the slow and fast accel/decel transients shown in Figures 388 and 389. This comparison indicates a maximum deviation of $\pm 0.5°$ for the fast transient as compared to the slow, essentially steady-state, transients.

Active Clearance Control

The active clearance control concept which uses closed-loop control of casing temperatures was demonstrated for the first time on the ICLS engine. Air valve modulation in both the compressor and LPT clearance control systems was successfully used to set casing temperatures as a function of rotor speeds and inlet temperatures. The casing temperature control mode was not demonstrated on the HPT because an unexpected out-of-roundness condition on the engine made it necessary to shut off the clearance control air manifold in the vicinity of the casing thermocouple used for control feedback.

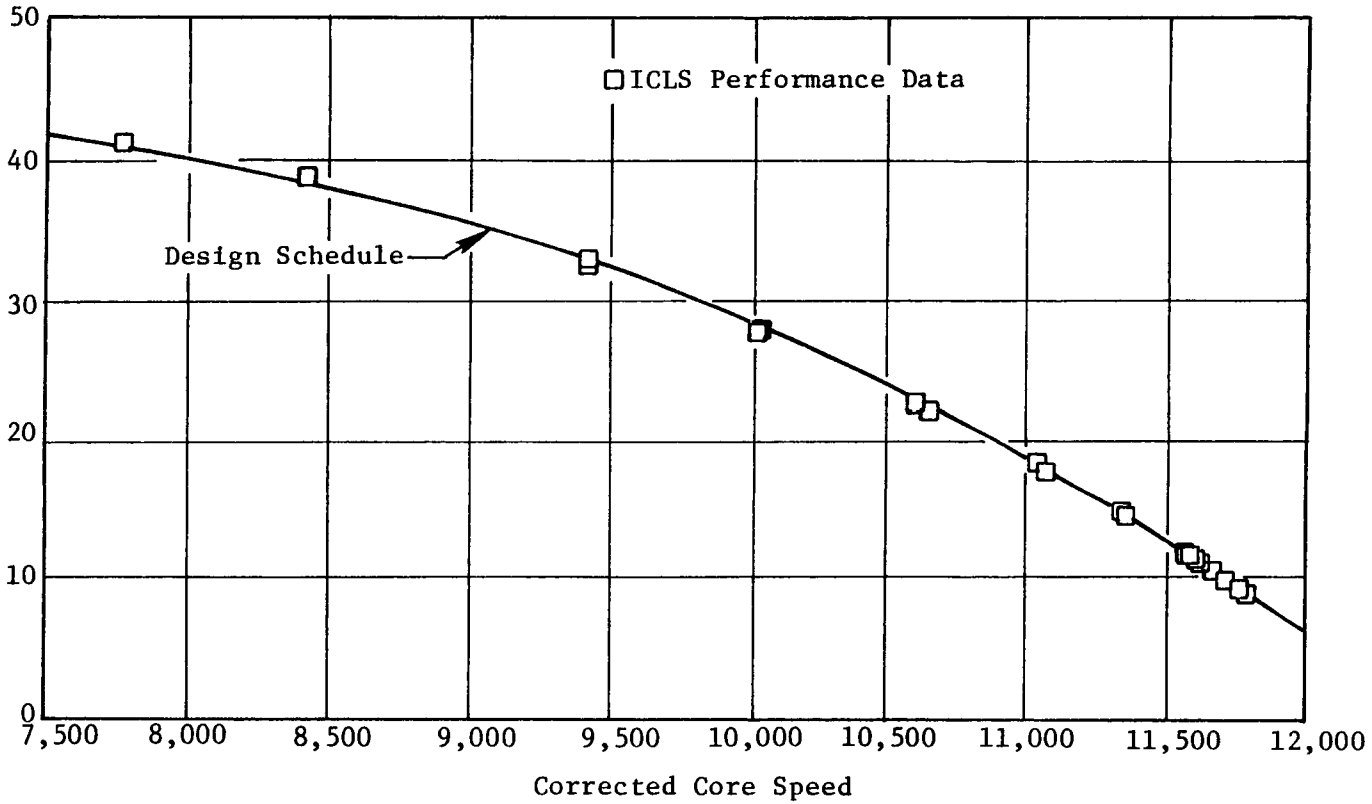


Figure 387. Steady State Stator Tracking.

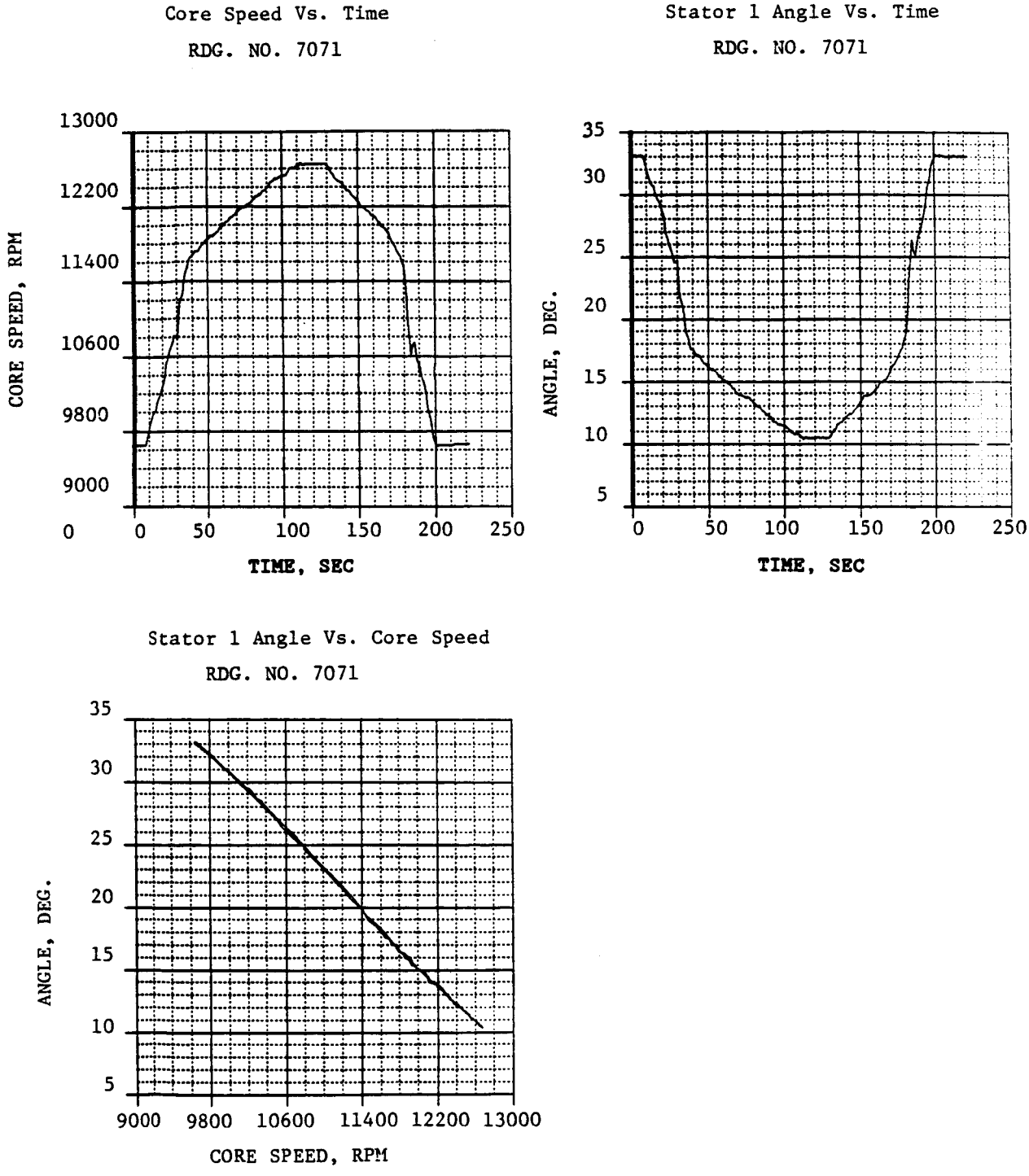


Figure 388. Slow Acceleration and Deceleration Stator Tracking.

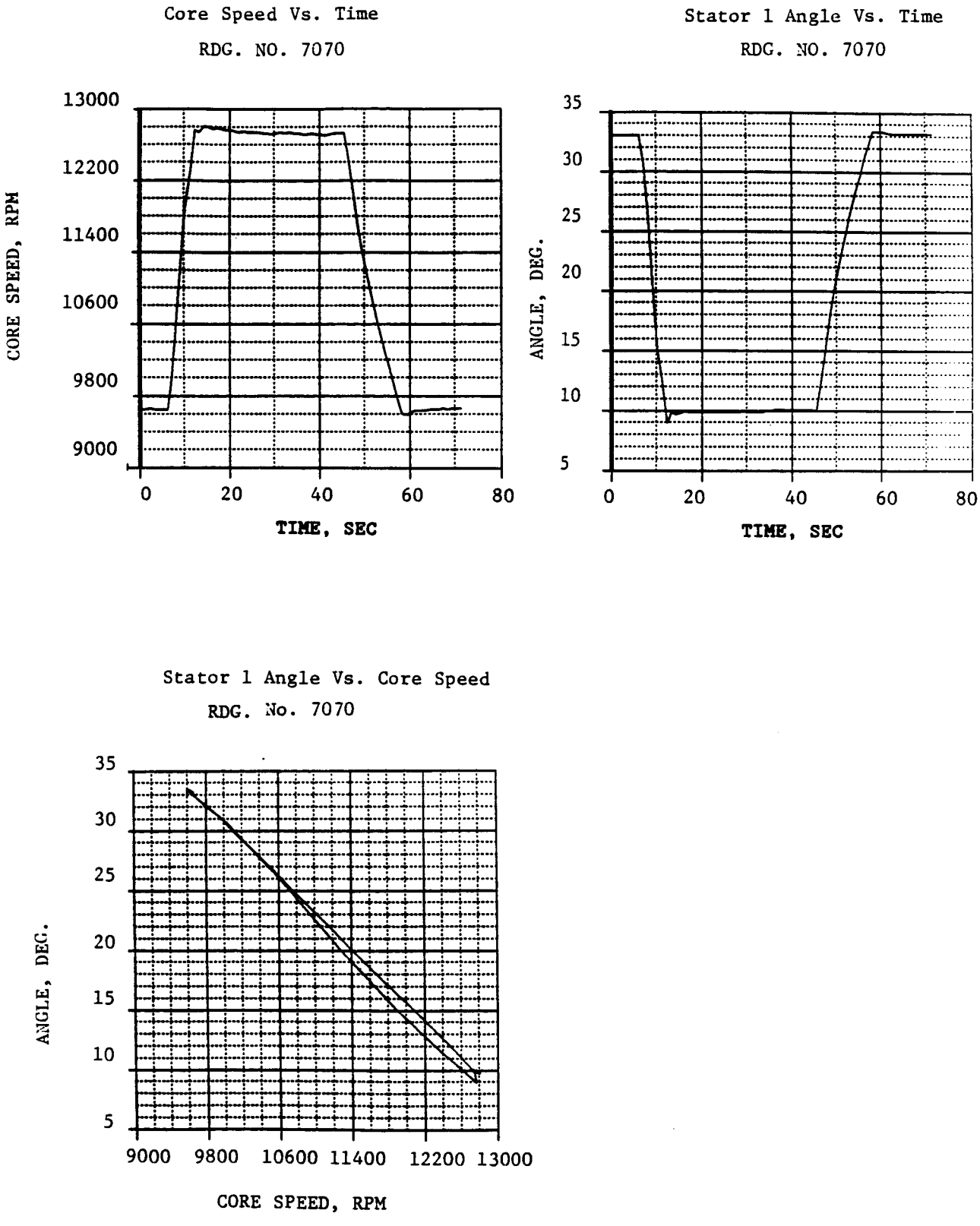


Figure 389. Rapid Acceleration and Deceleration Stator Tracking.

Figure 390 is a data trace showing compressor and LPT clearance control mode changes from manual to automatic at 80% fan corrected speed. The compressor system mode change was made first and it was done from a condition at which the compressor clearance control valve was in the minimum casing cooling position and casing temperature was higher than the schedule. The valve first moved to the high cooling region, then gradually moved to the midstroke region as casing temperature decreased to the schedule, and finally began modulating in that region to maintain the scheduled temperature. The response and stability during and after the transition into the automatic mode are considered to be quite satisfactory.

The LPT system mode change was made with the air valve partially open in the manual mode and casing temperature near the scheduled level. The system becomes somewhat unstable with casing temperature oscillating approximately 50°F at 0.25 Hertz. This amount of oscillation is undesirable but the unexpectedly high frequency of the oscillation suggests that the casing thermocouple response is faster than anticipated. This was primarily due to the thermocuple responding to cooling airflow rather than casing temperature. A standard instrumentation-type thermocouple was used here and it was attached to the casing using an electrically nonconductive, ceramic-based cement which reduced casing-to-thermocouple thermal conductivity. For any future application a study probe or set of probes would be designed that would provide a better measure of the casing temperature.

Figure 391 shows a deceleration to 40% corrected fan speed from the condition shown in the previous figure at a rate below that which would trigger the air valve decel shutoff function. The casing temperature characteristics proved to be such that both casings became hotter than scheduled during the decel but the compressor casings later dropped below the schedule and remained there even with no cooling while the LPT returned to the temperature modulating condition.

Figure 392 is a similar deceleration except that the deceleration rate was increased enough near the end of it to cause the air valve decel shutoff

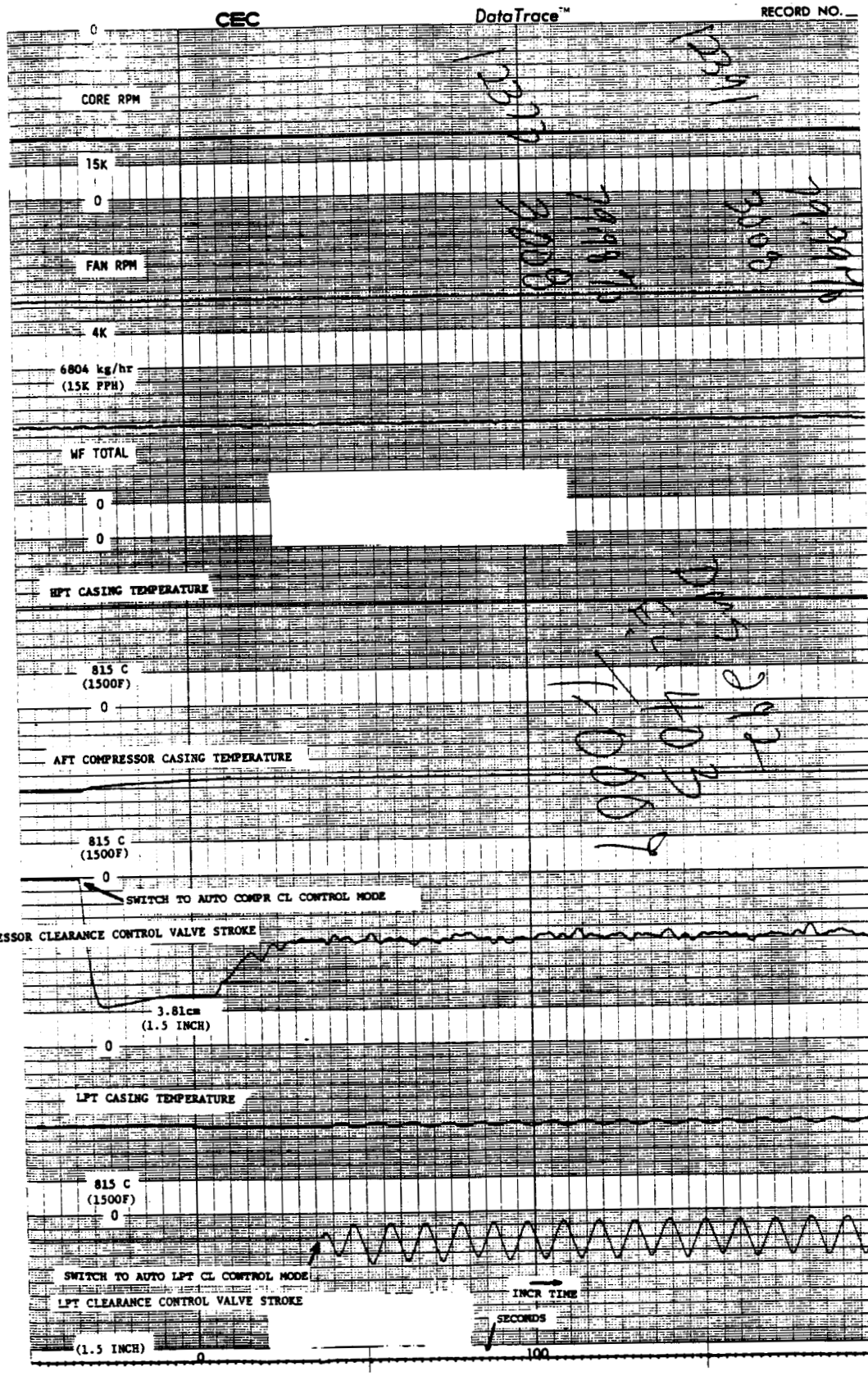


Figure 390. Auto Clearance Control Mode Initiation.

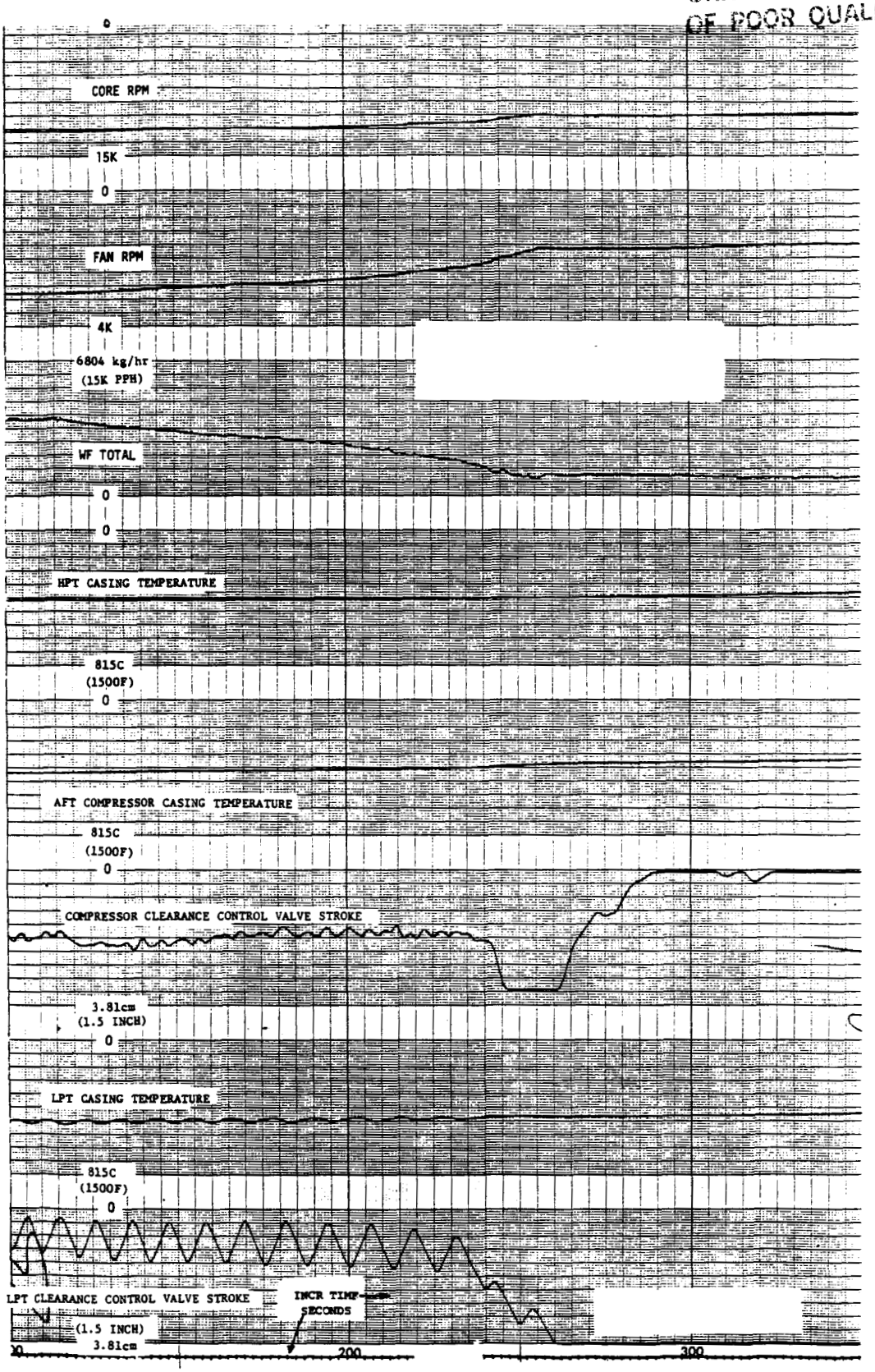


Figure 391. Slow Decel in Auto Clearance Control Mode.

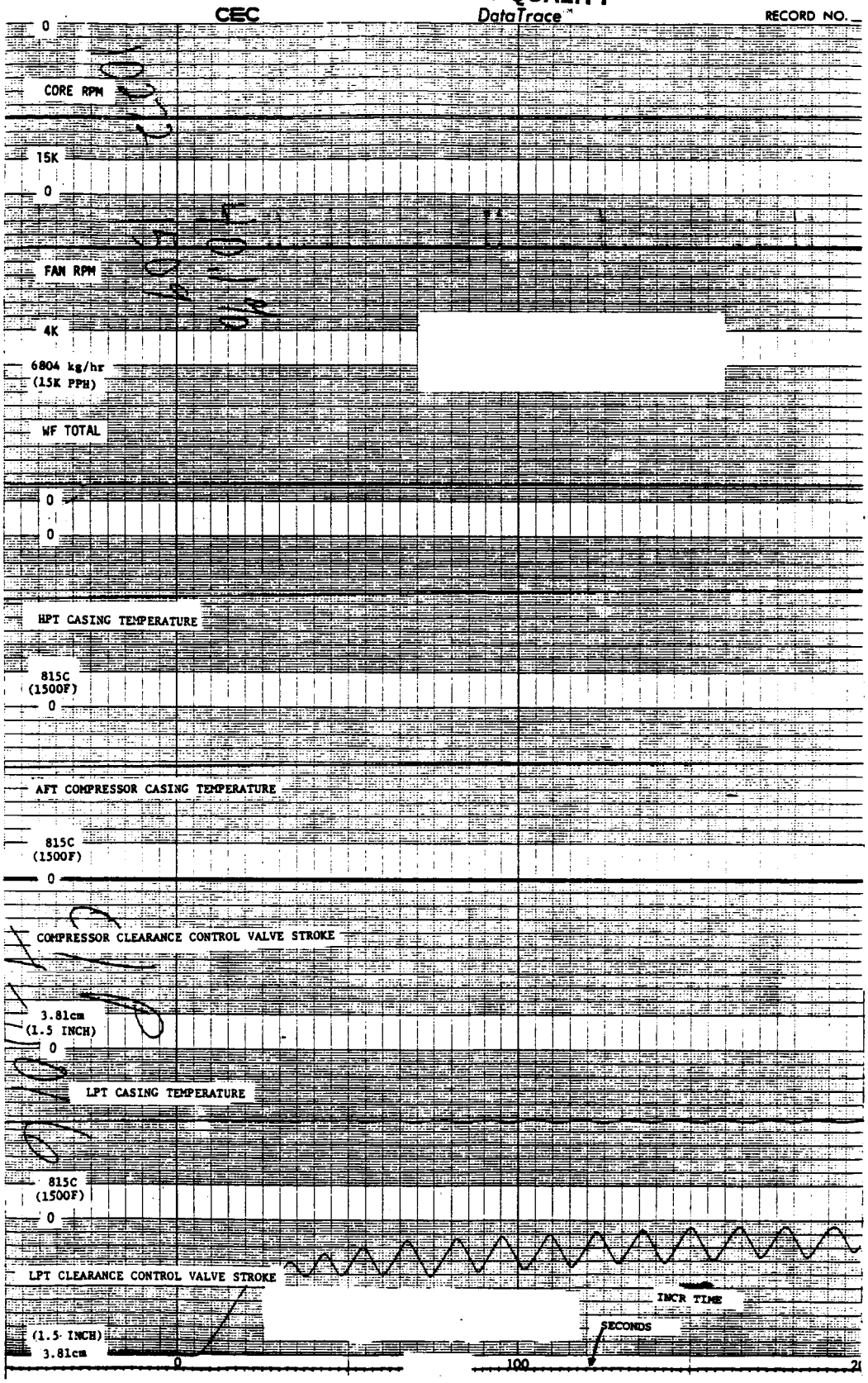


Figure 391. Slow Decel in Auto Clearance Control Mode (Concluded).

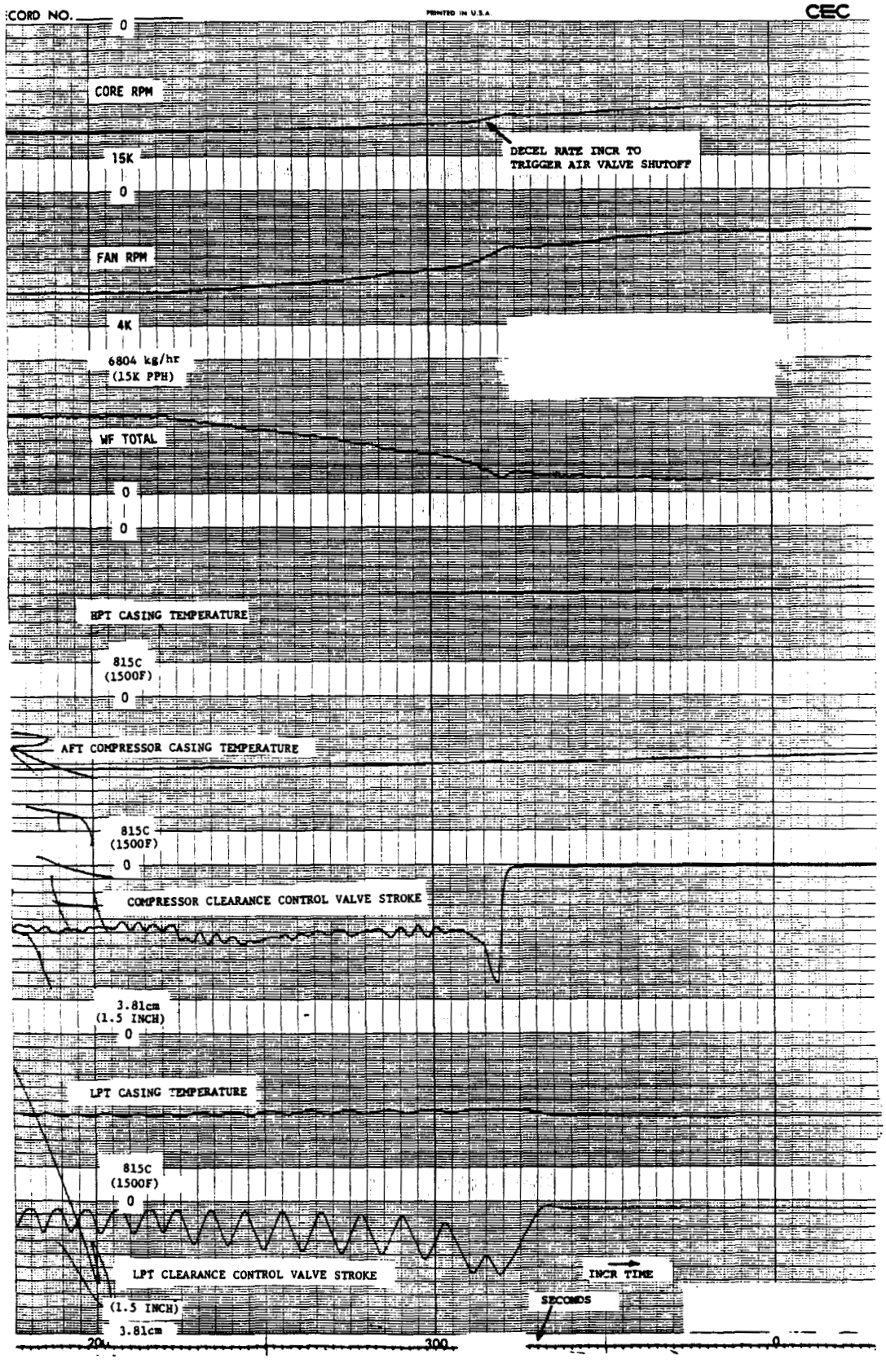


Figure 392. Deceleration Shutoff of Clearance Control Valves in Auto Mode.

function to operate. Both of the active clearance control valves closed as they should under these conditions.

The manual clearance control modes were used to explore the steady-state characteristics of the clearance control systems. The resulting data are plotted on Figure 393 in terms of the directly controlled parameters (casing temperatures). Corresponding clearance characteristics are discussed in sections of this report that relate to compressor and turbine mechanical performance.

Combustor Transition

Initial transitions from a single annular to double annular combustion were made in the manual mode to determine the necessary FADEC adjustment settings for fill volume (flow area set during main zone manifold filling) and fill time (time required to fill main zone manifold). These settings were then made on the engineering operator panel and all subsequent transitions were made in the automatic mode. Figure 394 is a slow accel showing the action of the main zone and pilot zone valves in the automatic mode during transition. To successfully transition from single annular to double annular burning, it was necessary to:

1. Fill the main zone manifold and nozzles. For this, the fill volume adjustment was set so that the engine did not decelerate during filling and the fill time was set at 30 seconds.

2. Close the pilot zone reset to enrich the main zone to allow the main burner to light. Note that the pilot zone reset valve is signaled closed 1.75 seconds before the main zone goes fully open. This is a slow (0.25 gpm servovalve) system and takes that long to close.

3. Open the main zone as the pilot zone reset is going fully closed.

4. Reopen the pilot zone reset after transition to double annular.

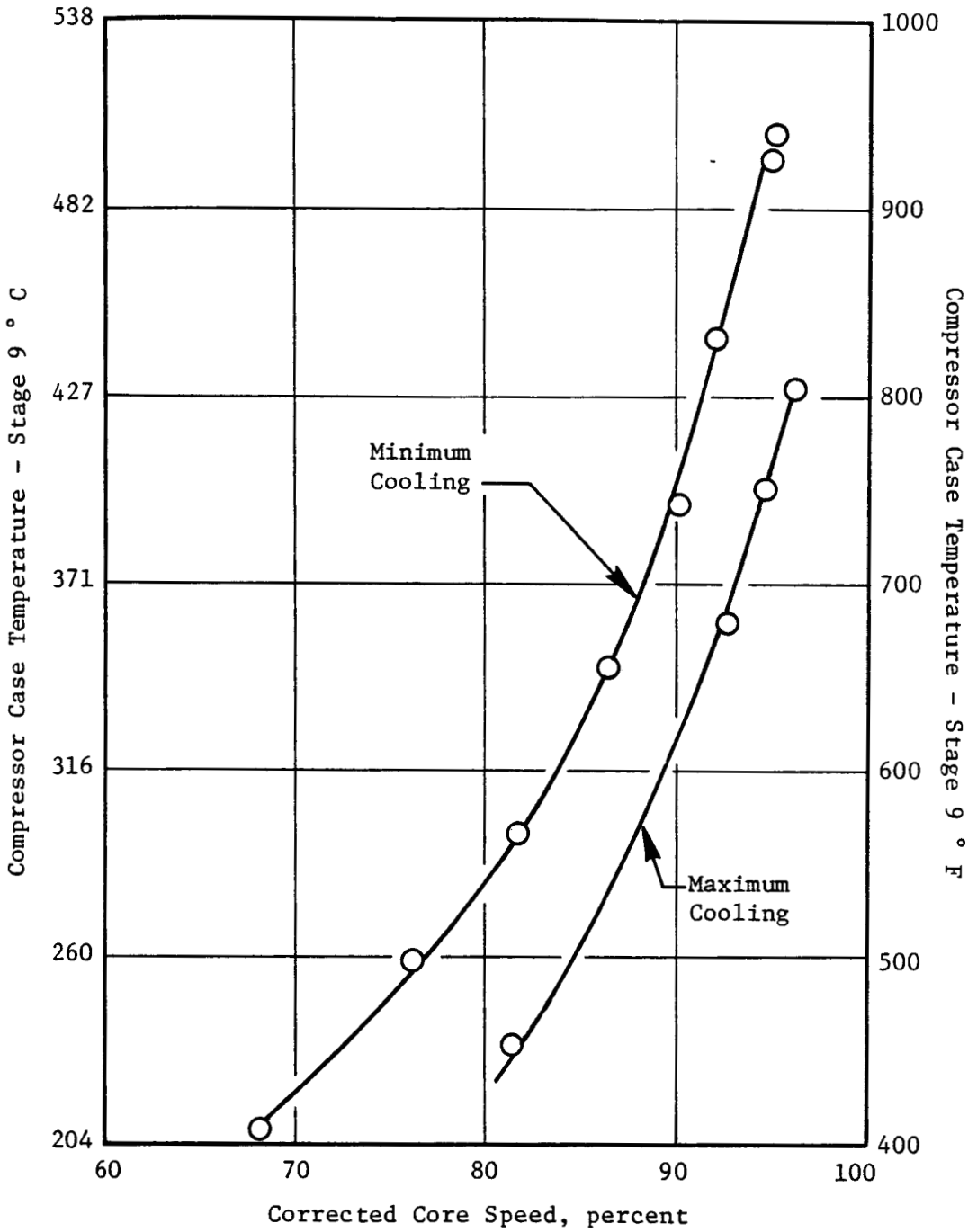


Figure 393. Steady State Casing Temperature.

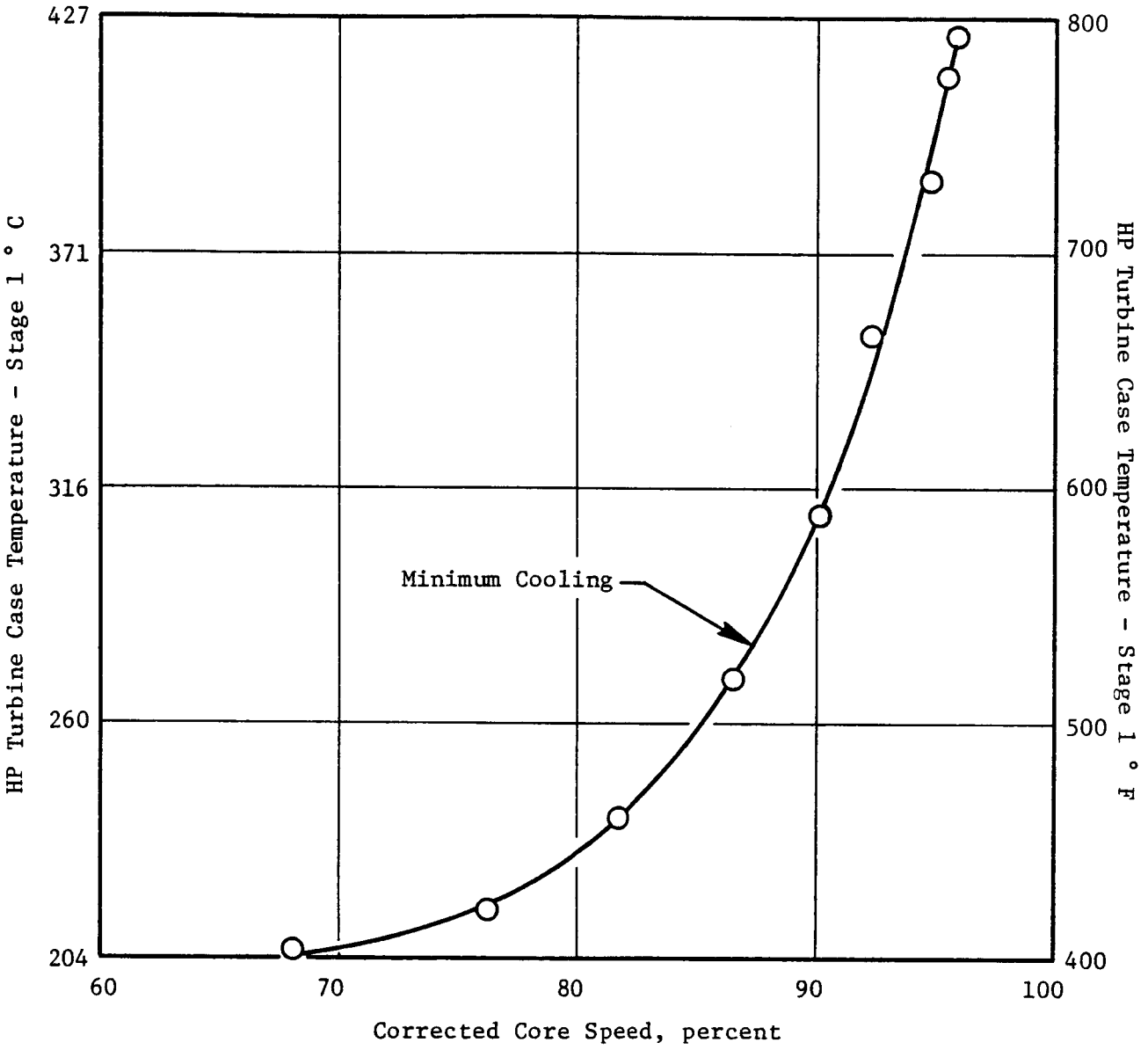


Figure 393. Steady State Casing Temperature (Continued).

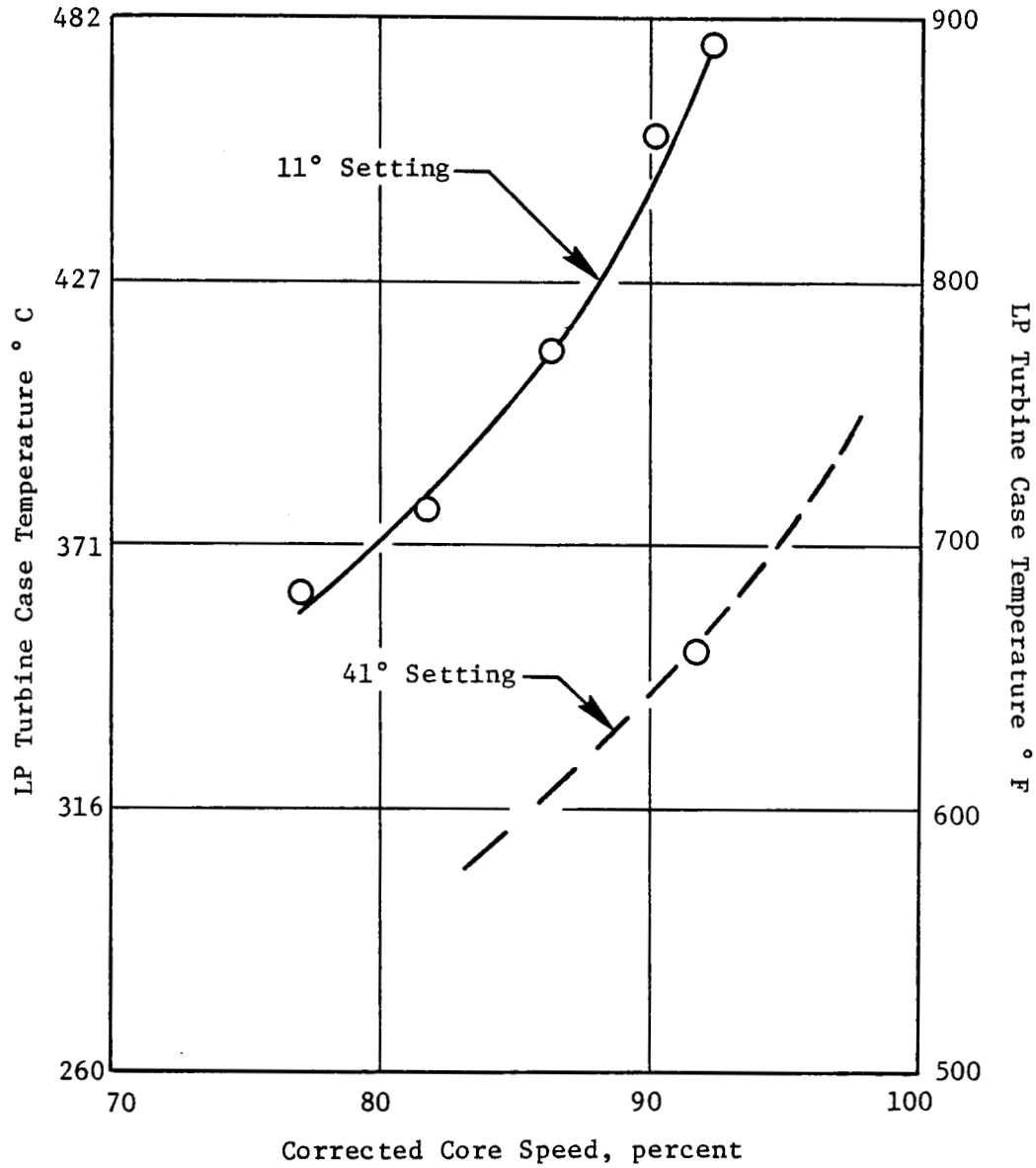


Figure 393. Steady State Casing Temperature (Concluded).

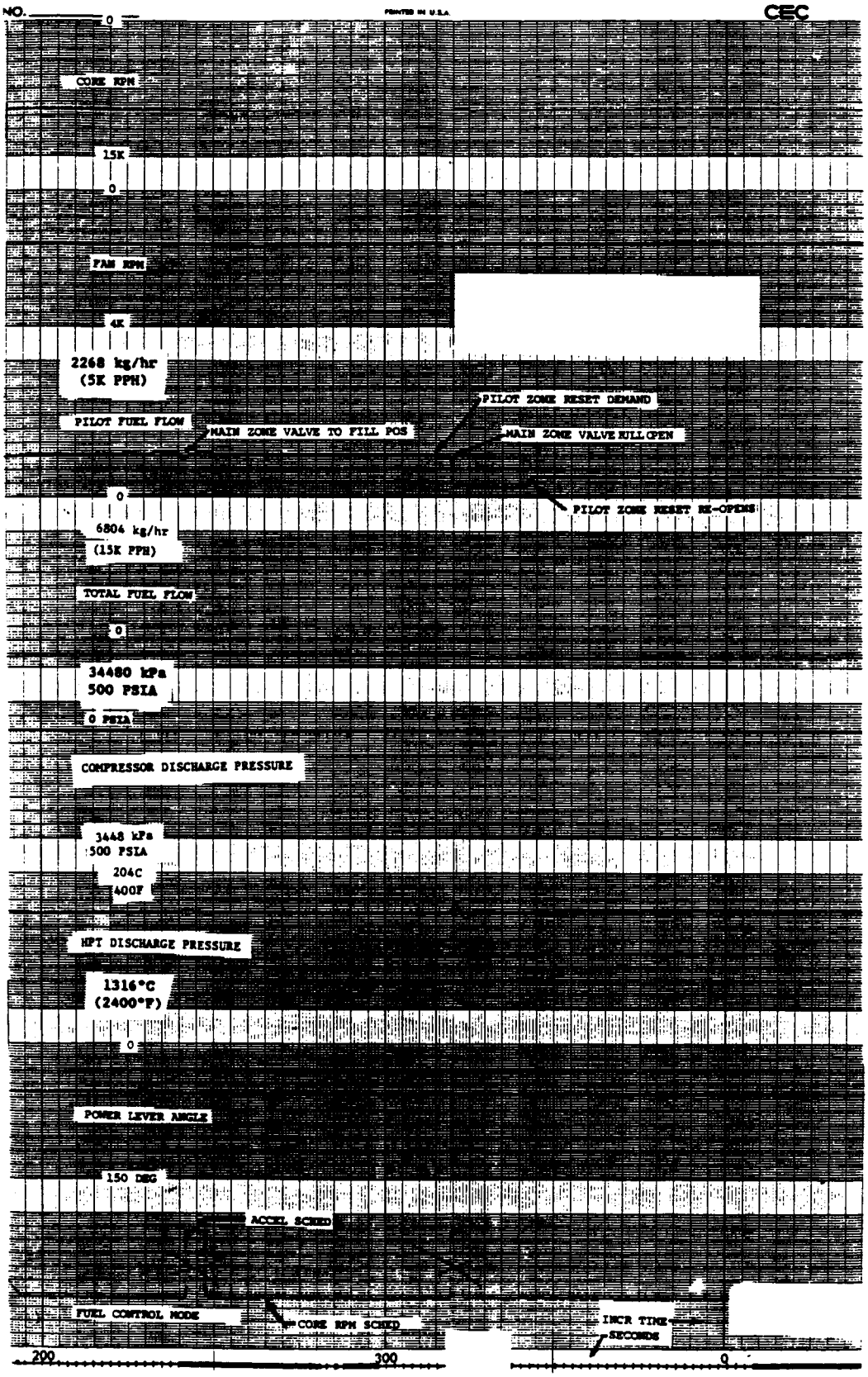


Figure 394. Combustion Transition - Main and Pilot Zone Valves During Slow Acceleration.

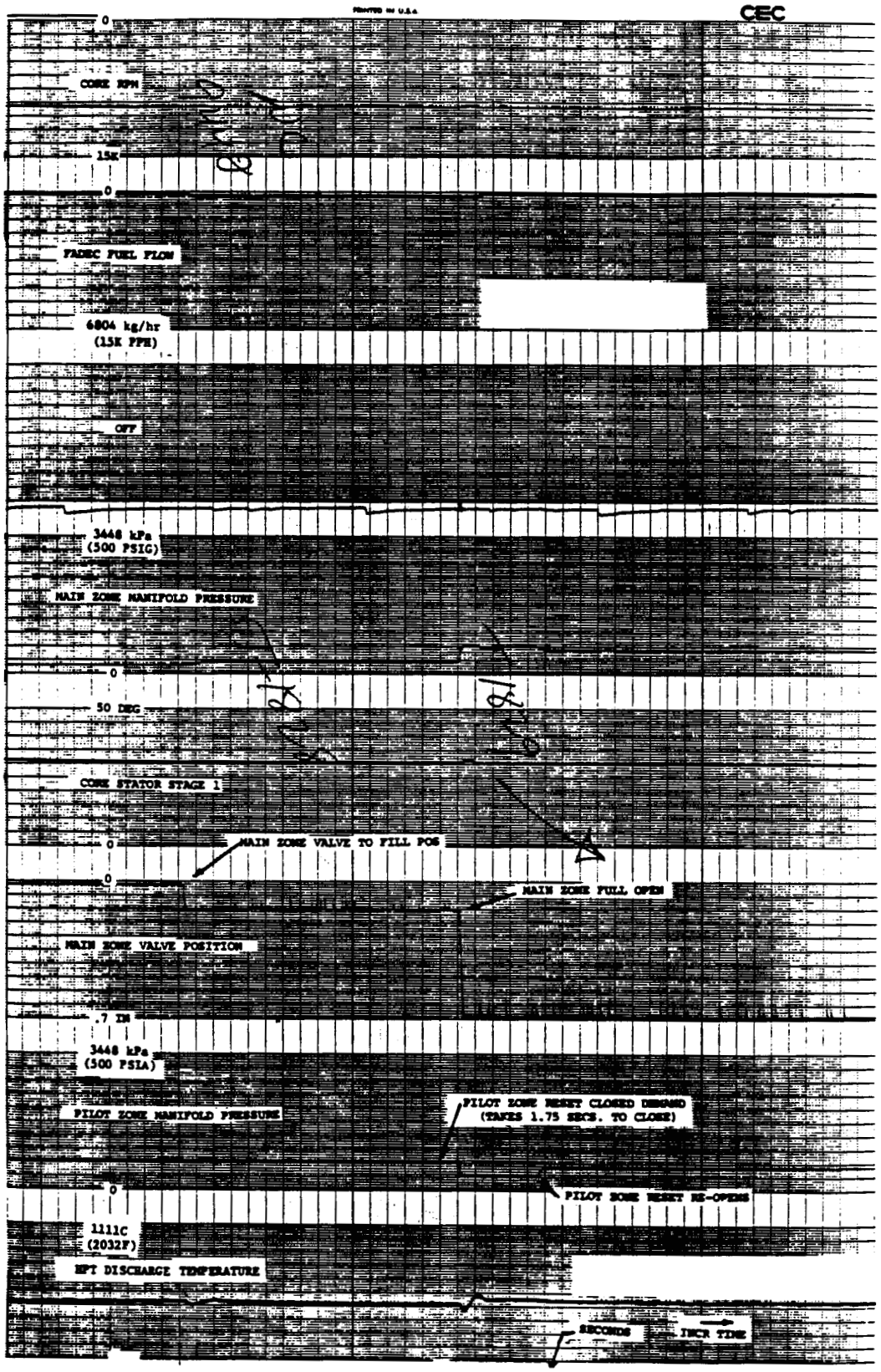


Figure 394. Combustion Transition - Main and Pilot Zone Valves During Slow Acceleration (Concluded).

Transition to single annular from double annular was accomplished simply by closing the main zone valve.

Accel/Decel Transients

A series of throttle bursts were made, first with the nominal accel schedule and then with gradually enriched schedules. Minimum demonstrated time from Flight Idle at 90% net thrust was approximately 5.5 seconds, where core physical rpm limits (based on the maximum speed proven safe in core testing) were reached. The maximum design core rpm was not reached because lack of airfoil instrumentation during ICLS testing made it prudent not to run "blind" at unexplored speeds. Figure 395 is a plot of core speed, fan speed, fuel flow, and Stage 1 core stator angle versus time for accel.

Figure 396 shows a 12-second chop from 90% net thrust to a 12% net thrust.

No stalls or blowout were encountered during the transient testing.

Failure Indication and Corrective Action (FICA)

For FICA demonstration purposes, the ICLS control strategy incorporated a feature to simulate sensor failures for each FICA substituted variable (fan speed XNL, core speed XNH, compressor inlet temperature T25, HPT discharge temperature T42, and compressor discharge pressure PS3). Each sensor was multiplied by an engineering operator panel potentiometer which was scaled from 0.5 to 1.5 (nominal value is 1.0). A switch on the engineering operator panel was used to enable the multipliers.

To induce a simulated sensor failure, the potentiometer associated with the sensor to be failed was adjusted to a value beyond the FICA tolerance and the switch was then activated to create a step change in the sensor value as seen by the control strategy. The FICA then substituted the estimated value for the sensed value. This method was used to demonstrate single and double sensor failures.

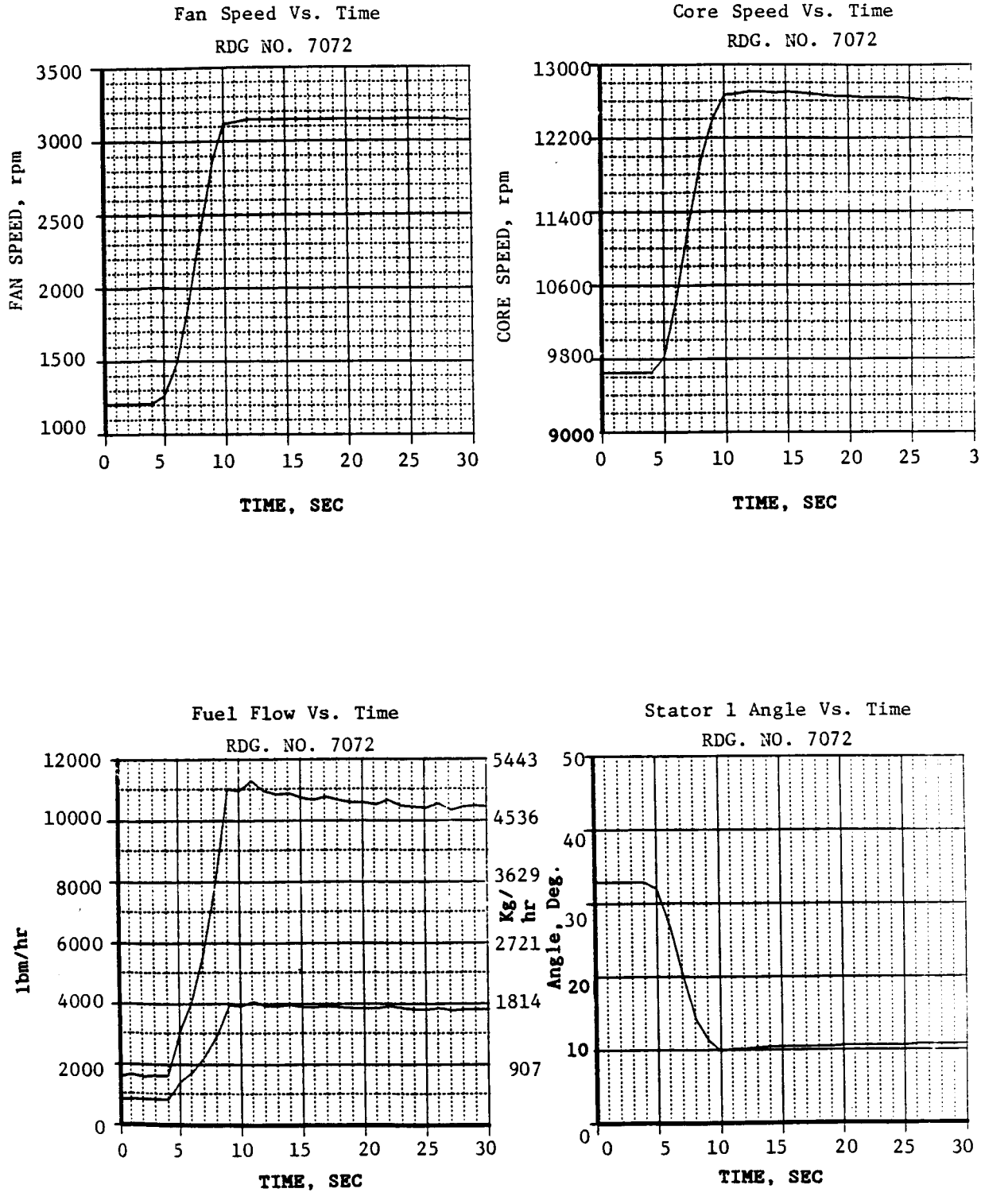


Figure 395. Throttle Burst - Maximum Fuel Schedule.

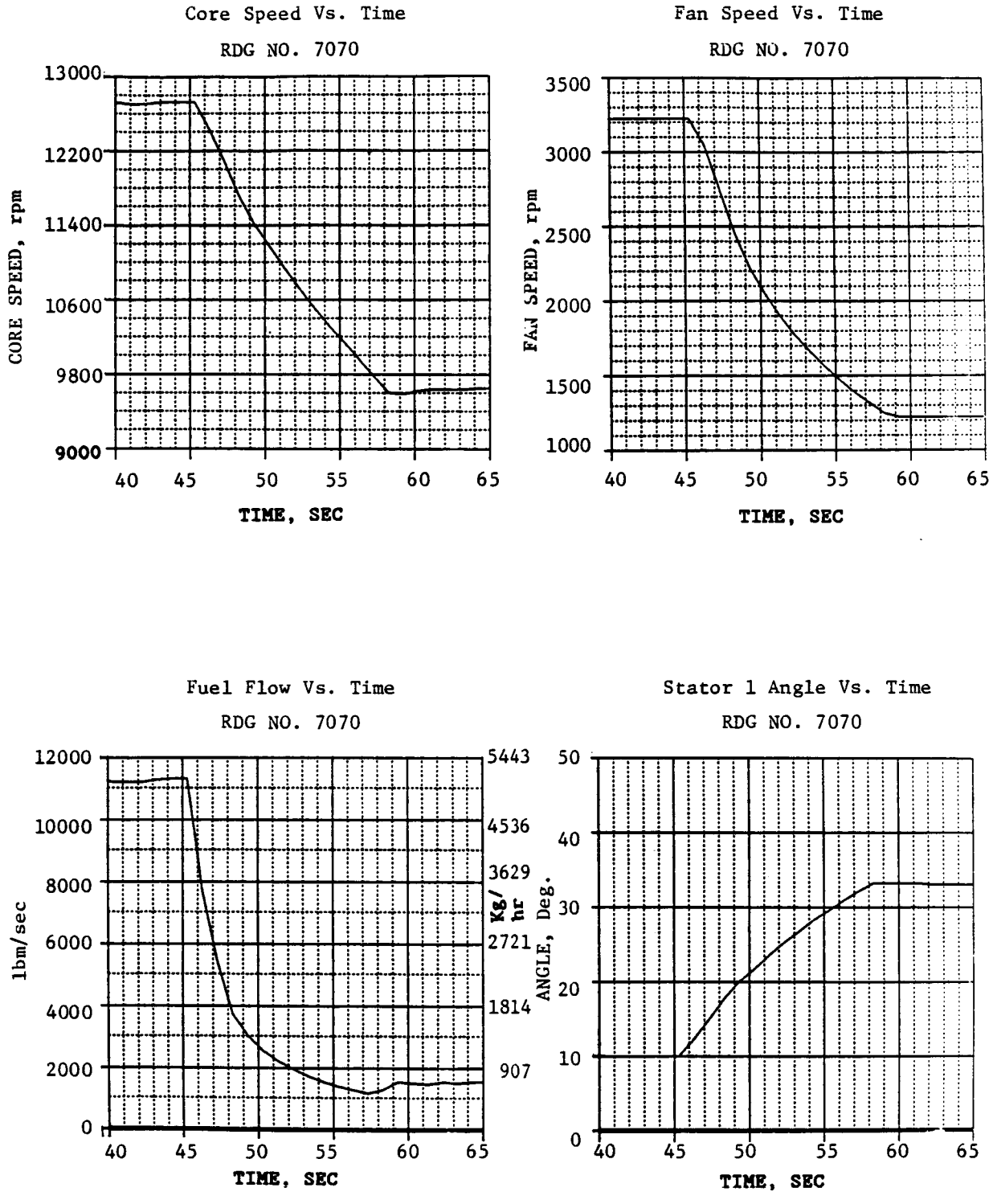


Figure 396. Typical Deceleration Transient.

The table below summarizes the simulated sensor failures demonstrated.

| Simulated Sensor Failure(s) | Range Tested | Comments |
|---|---|---|
| Compressor Discharge Temperature (T3) | 40% PCNLR* to Max T42 | Normal system operation |
| HPT Discharge Temperature (T42) | 40% PCNLR to Max T42 | Normal system operation |
| Compressor Inlet Temperature (T25) | 40% PCNLR to Max T42 | Normal system operation |
| Fan Speed (XNL) | 40% PCNLR to Max T42 | Normal system operation |
| Core Speed (XNH) | 40% PCNLR to 60% PCNLR | Marginally acceptable system operation |
| Compressor Discharge Static Pressure (PS3) | 40% PCNLR | Normal system operation |

*PCNLR - percent fan corrected speed.

| | | |
|---|---|---|
| XNL & T3 | 40% PCNLR to Max T42 | Normal system operation |
| XNL & T42 | 40% PCNLR to Max T42 | Normal system operation |
| XNL & T25 | 40% PCNLR to Max T42 | Normal system operation |

All simulated sensor failures except core speed produced normal operation both steady state and transiently. A typical transient with one simulated sensor failure is shown on Figure 397 and a simulated transient with two simulated sensor failures is shown on Figure 398.

Simulation of a core speed sensor failure produced marginally stable results. The first attempt was made with the engine on core speed control at just under 20% thrust. An instant after the simulated failure, substituted core speed from the FICA model jumped to a level above actual core speed causing the control to reduce fuel flow and open the core stators a small amount. The combined effect was a fuel-air ratio reduction of sufficient magnitude to cause loss of combustion and engine shutdown.

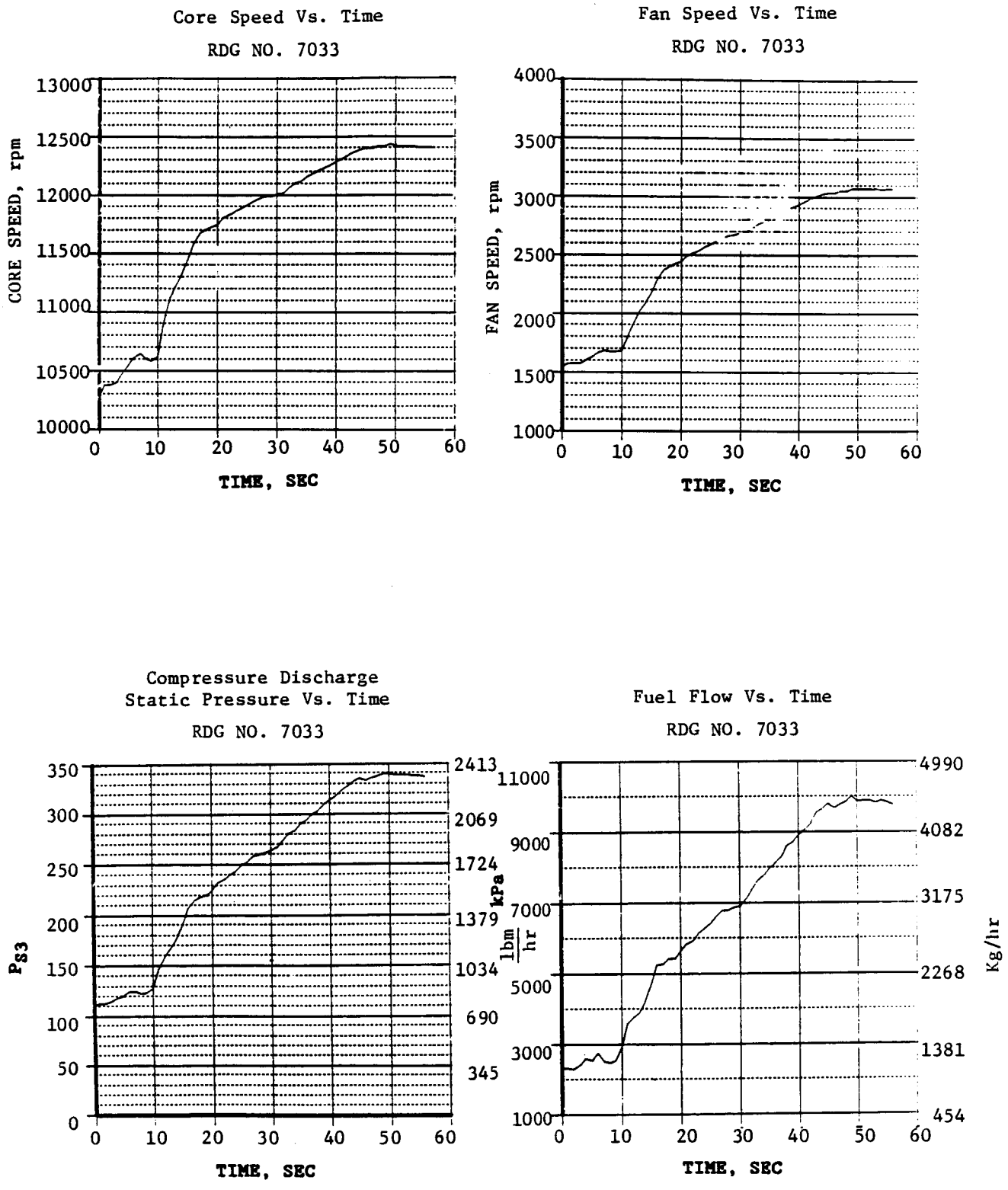


Figure 397. FICA Acceleration and Deceleration with $T_3$ Failed.

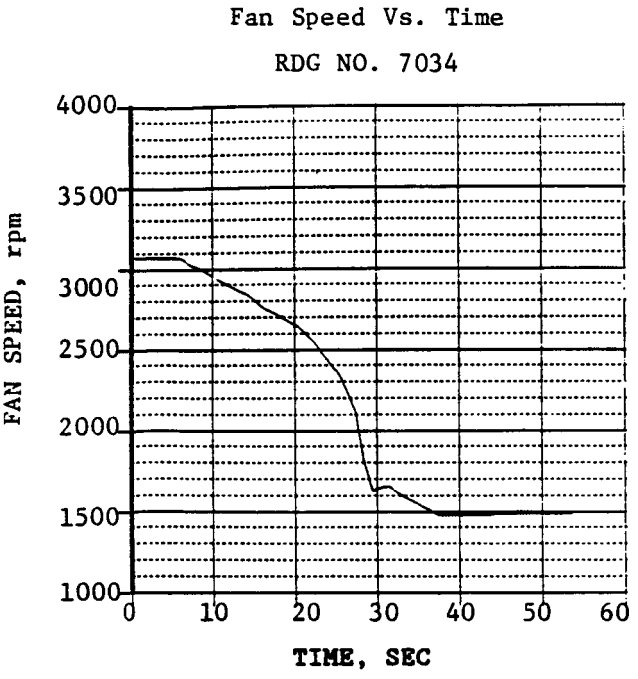


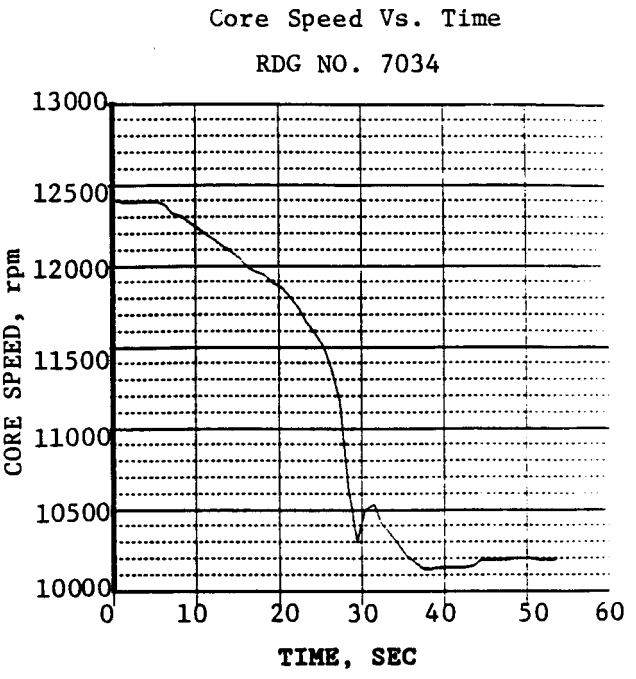


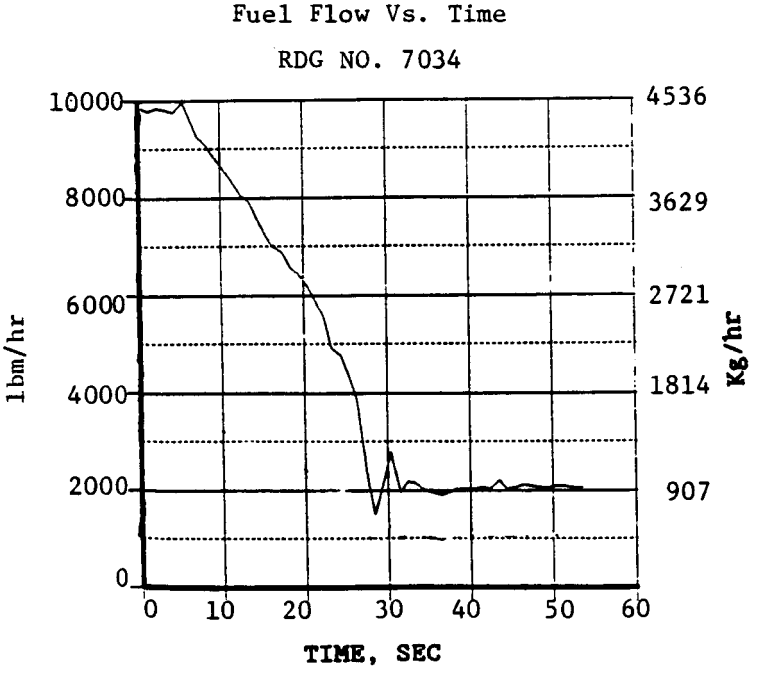


Figure 397. FICA Acceleration and Deceleration with $T_3$ Failed (Concluded).

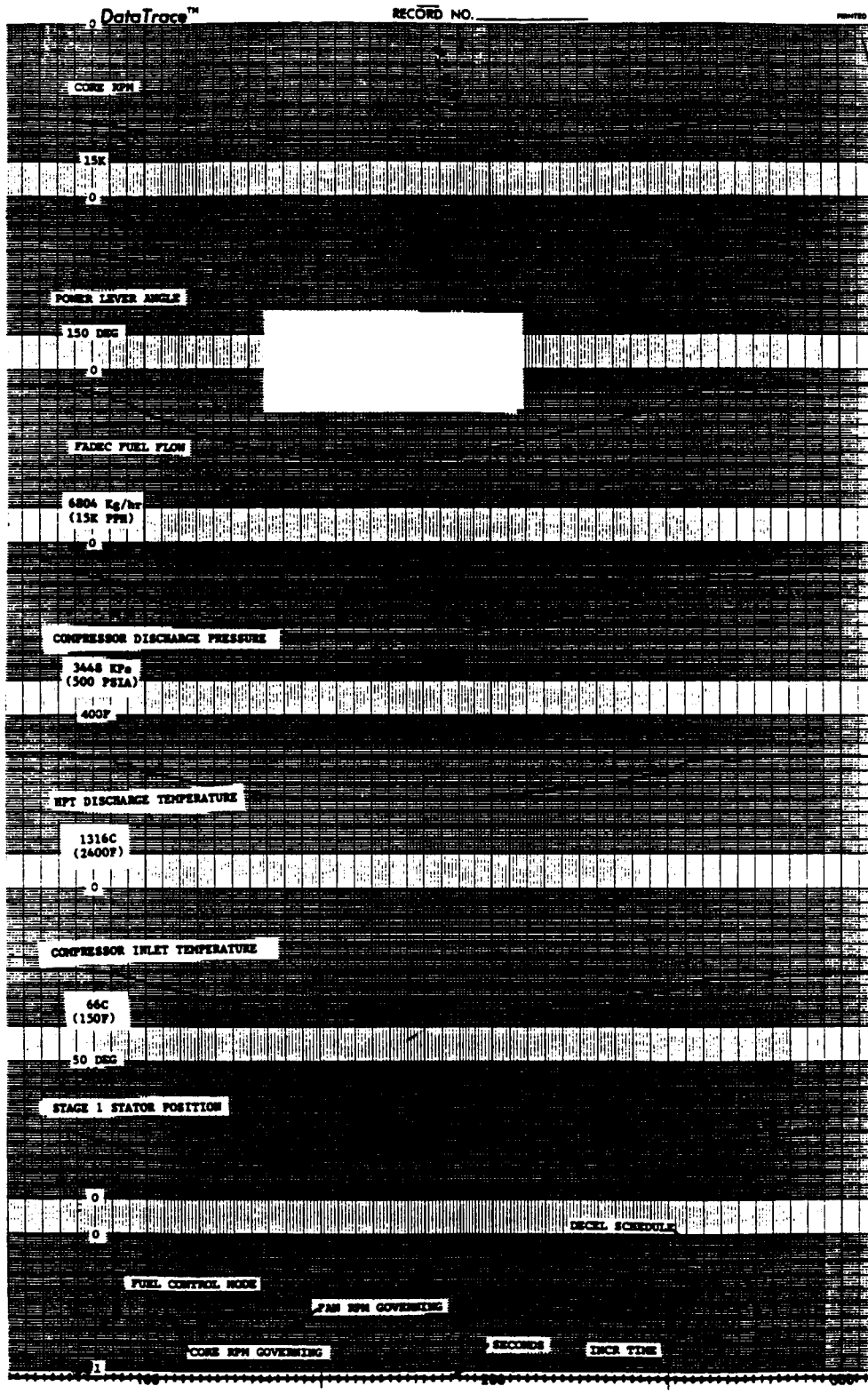


Figure 398. FICA Acceleration and Deceleration with Simulated Failure of Two Sensors (Fan RPM and Compressor Inlet Temperature).

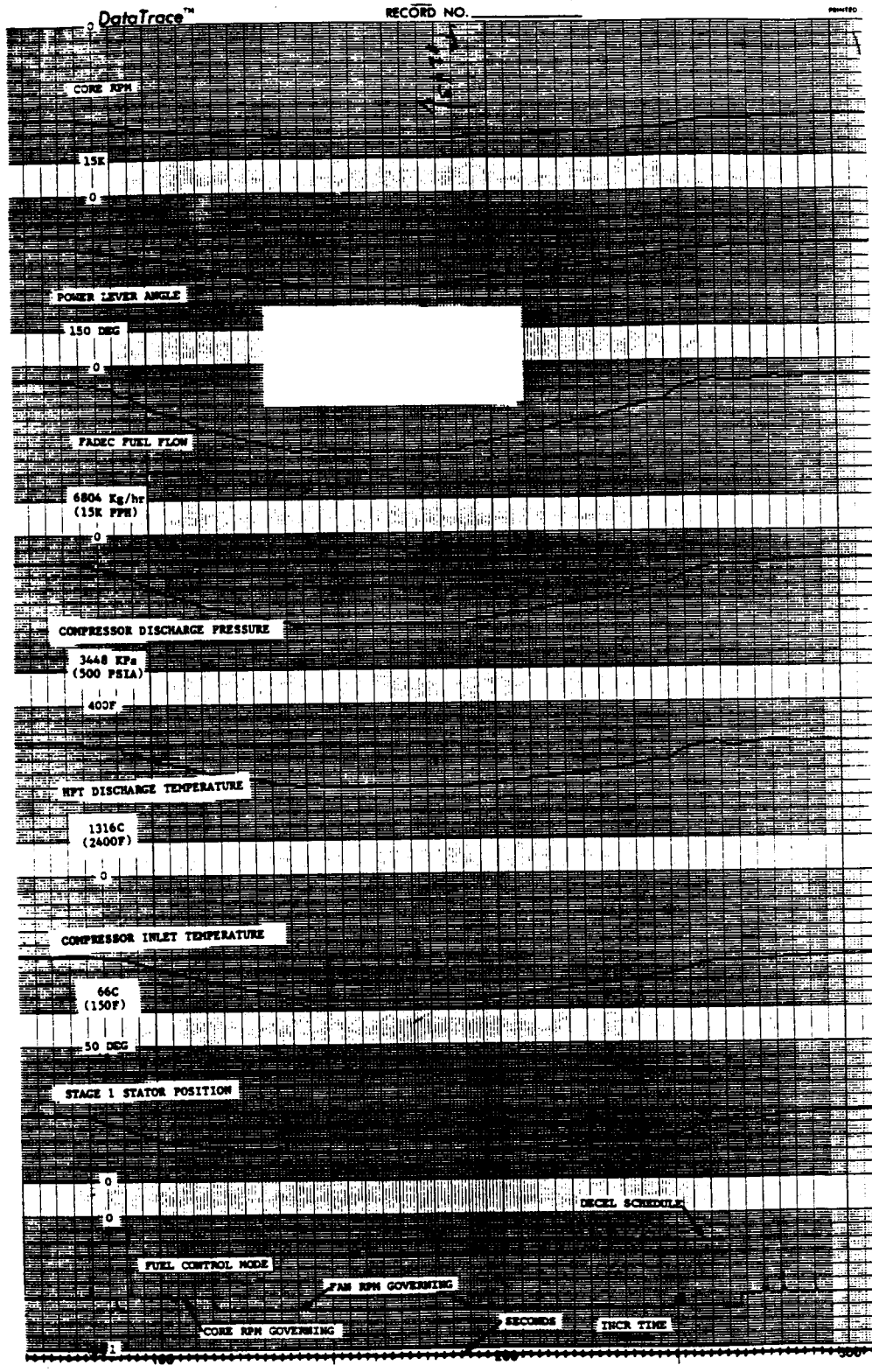


Figure 398. FICA Acceleration and Decelaration with Simulated Failure of Two Sensors (Fan RPM and Compressor Inlet Temperature) (Concluded).

A second attempt was made at the same thrust level but with the PLA schedule adjusted so that fuel flow was under fan speed rather than core speed control. Simulation of a core speed sensor failure caused the engine to break into an oscillation as shown on Figure 399. Adjustment of the PLA schedule to reestablish core speed control of fuel flow caused the amplitude of the oscillations to increase.

Preliminary analysis of this second attempt indicated that the oscillation was aggravated by the core stator effect on airflow through fan and core speed. In an attempt to reduce this effect, the servovalve null shift compensation in the stator control loop was deleted and a third simulation of a core speed sensor failure was made at the same conditions as in the previous attempt. As shown on Figure 400, this again produced an oscillation but it was smaller in amplitude than in the previous case. A slow acceleration to 40% thrust caused no increase in the oscillation, but an attempt to reestablish core speed control of fuel flow by PLA schedule adjustment had to be abandoned because it produced excessive oscillation amplitude.

Time did not permit more extensive investigation relative to FICA core speed sensing substitution. A future investigation should evaluate potential improvements such as the incorporation of core stator effects in the FICA model and the modification of Update Matrix coefficients after sensor substitution.

Overall, the ICLS FICA testing was a worthwhile step forward in the evolution of this promising concept for improving future engine control system operational reliability without added hardware. Simpler FICA implementations have been tested in the past, but the ICLS FICA brought together an engine model based on component equations and a multiple-element Model Update Matrix that, in combination, offer improved potential for full flight map suitability. The ICLS testing showed this combustion to be generally satisfactory and identified potential improvements for future evaluation as noted above.

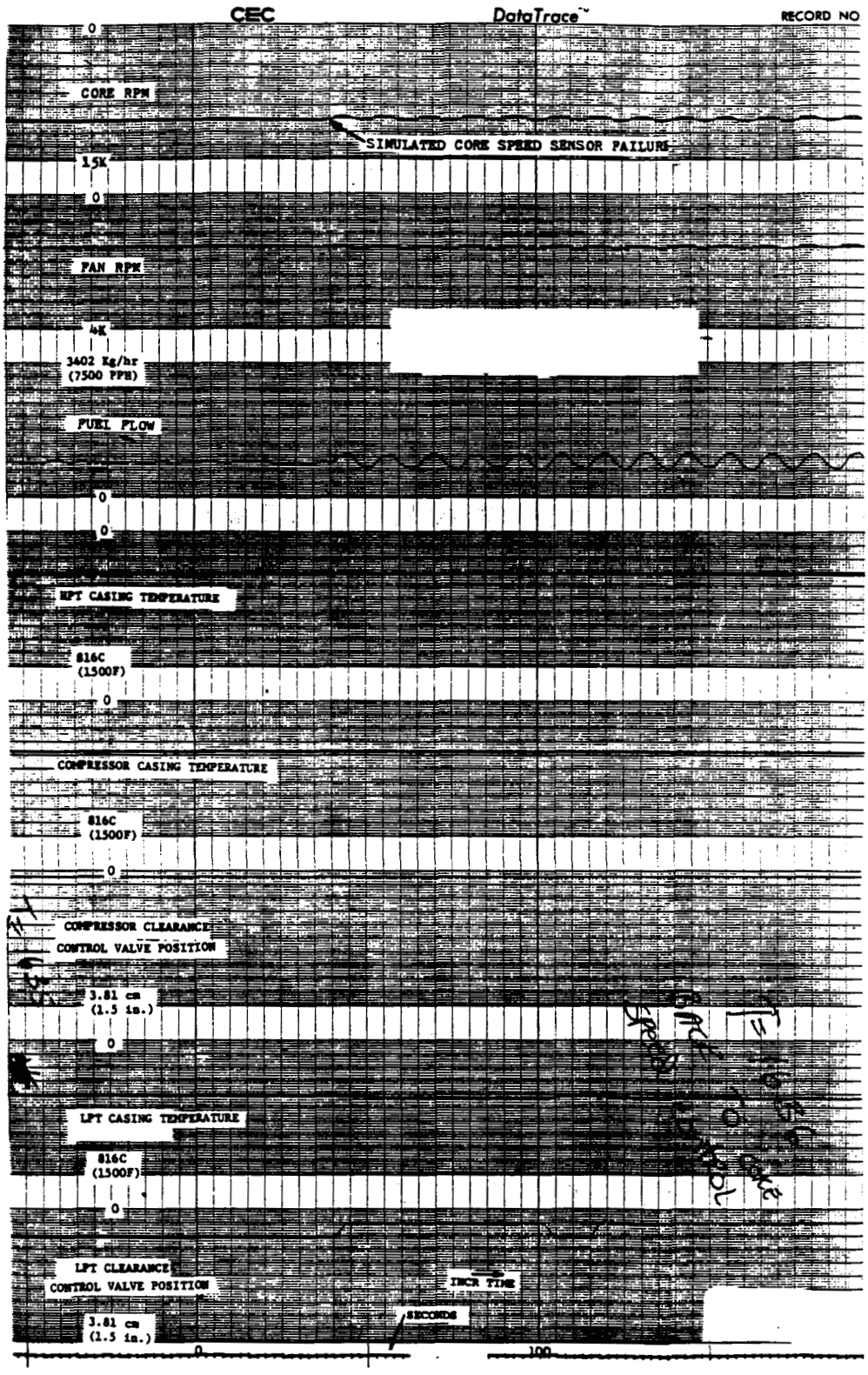


Figure 399. Simulated Core RPM Sensor Failure (Fan RPM Governing Mode).

ORIGINAL PAGE IS
OF POOR QUALITY

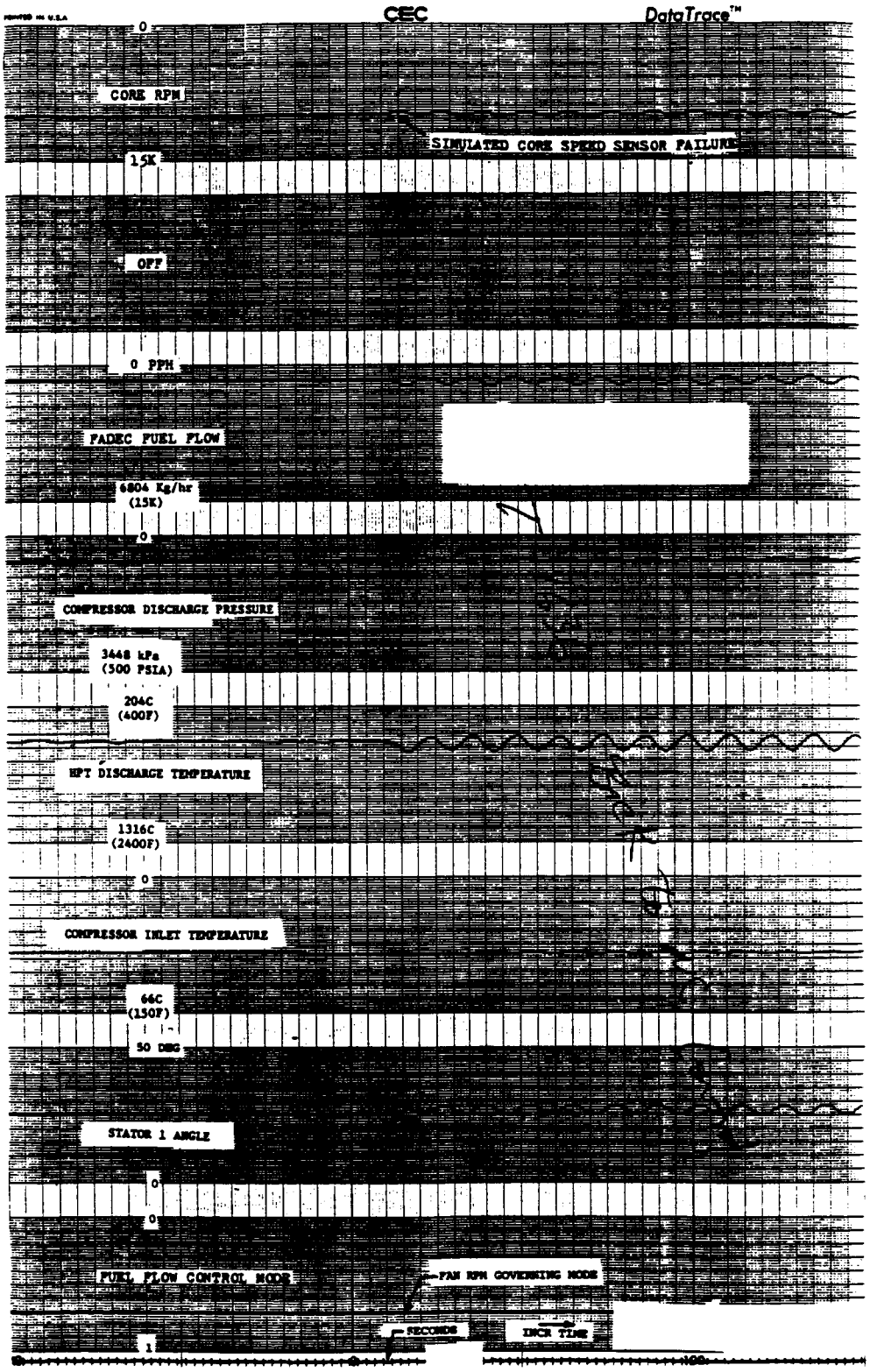


Figure 399. Simulated Core RPM Sensor Failure (Fan RPM Governing Mode) (Concluded).

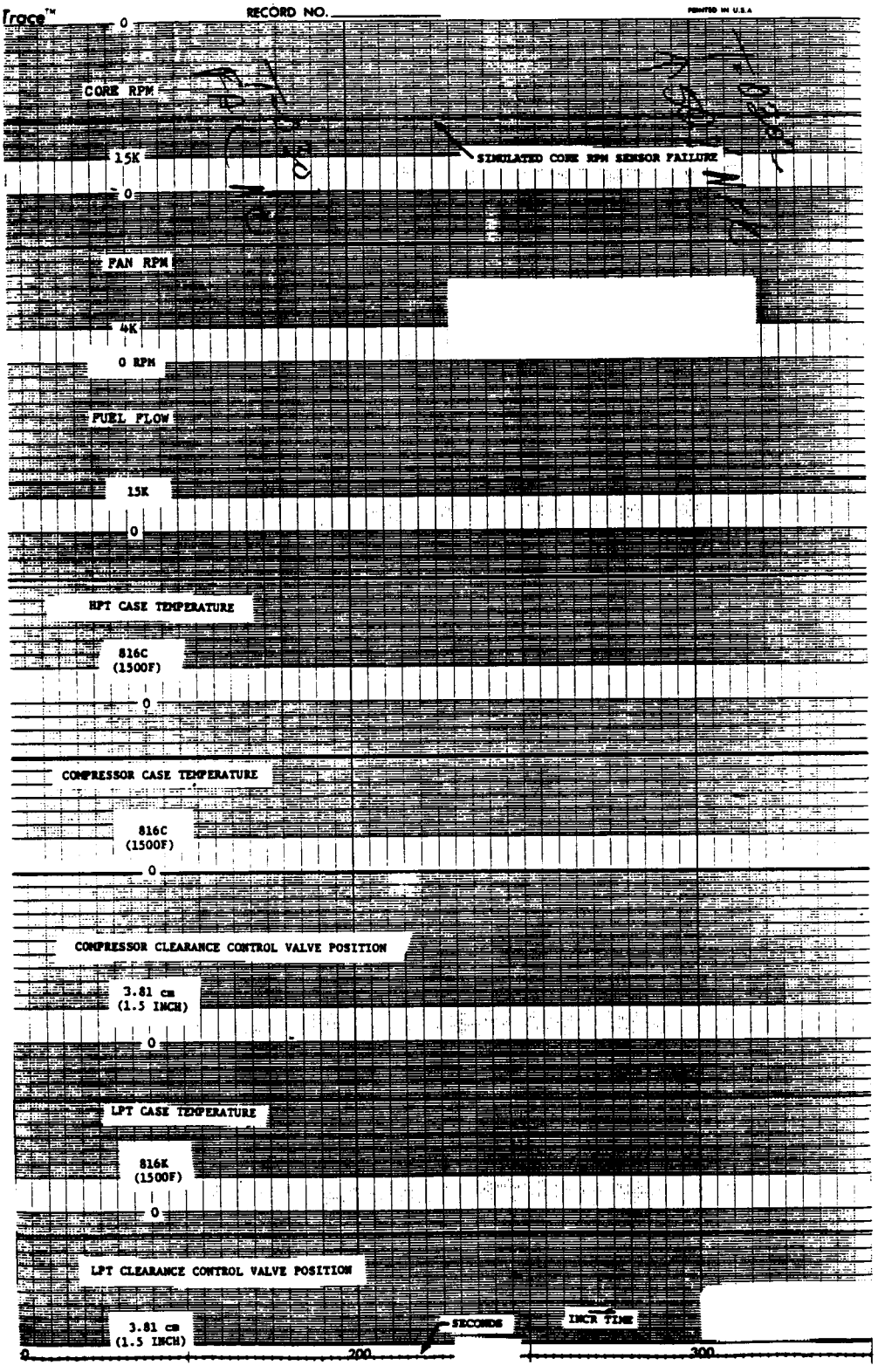


Figure 400. Simulated Core RPM Sensor Failure - Stator Null Shift Compensation Out.

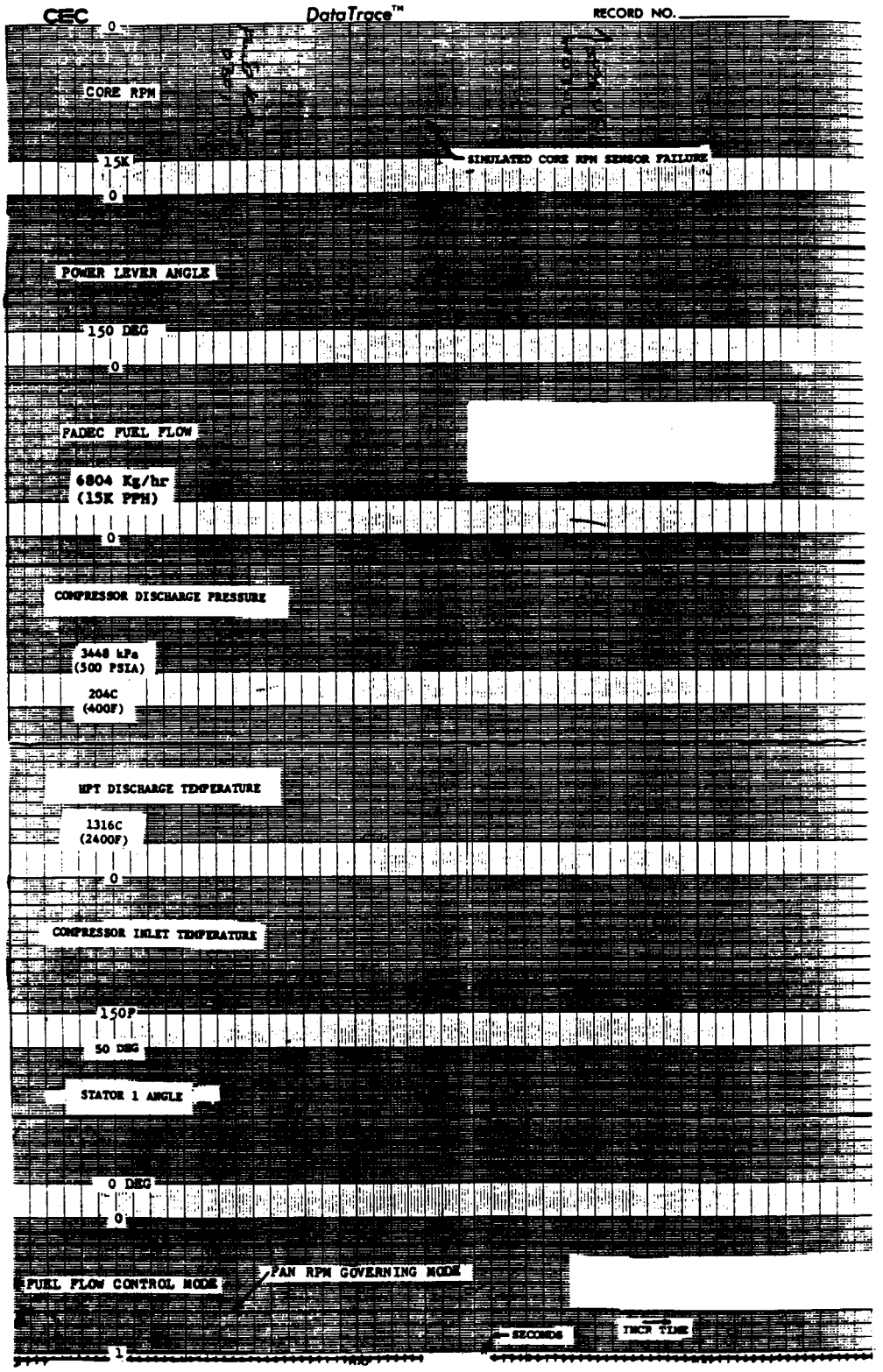


Figure 400. Simulated Core RPM Sensor Failure - Stator Null Shift Compensation Out (Concluded).

FADEC Operating Conditions

The on-engine FADEC operated satisfactorily throughout the ICLS test. It was mounted on the outside of the fan frame at the 3 o'clock position (aft looking forward) using four soft isolation mount elements. Vibration characteristics in this vicinity were recorded and are discussed in the Engine Dynamics section of this report.

FADEC cooling air was supplied from the test facility at approximately 17.2 $N/cm^2$ (25 psia) and at essentially ambient temperature. Calculated airflow at these conditions is 0.011 kg/sec (0.024 lb/sec) as limited by the 3/8 inch inlet fitting on the FADEC cooling manifold. Internal temperature of the FADEC ran 6°C to 11°C (10°F to 20°F) above ambient temperature with the maximum differential when the FADEC was in direct sunlight and the minimum differential at night.

Switch to Backup

For safety reasons, an F101 hydromechanical fuel control was included as a fuel and stator backup for the single-channel FADEC. Because of excellent FADEC operation, the backup was not needed at any point in the test program, but an intentional switchover to the backup mode proved the suitability of this design as shown in Figure 401.

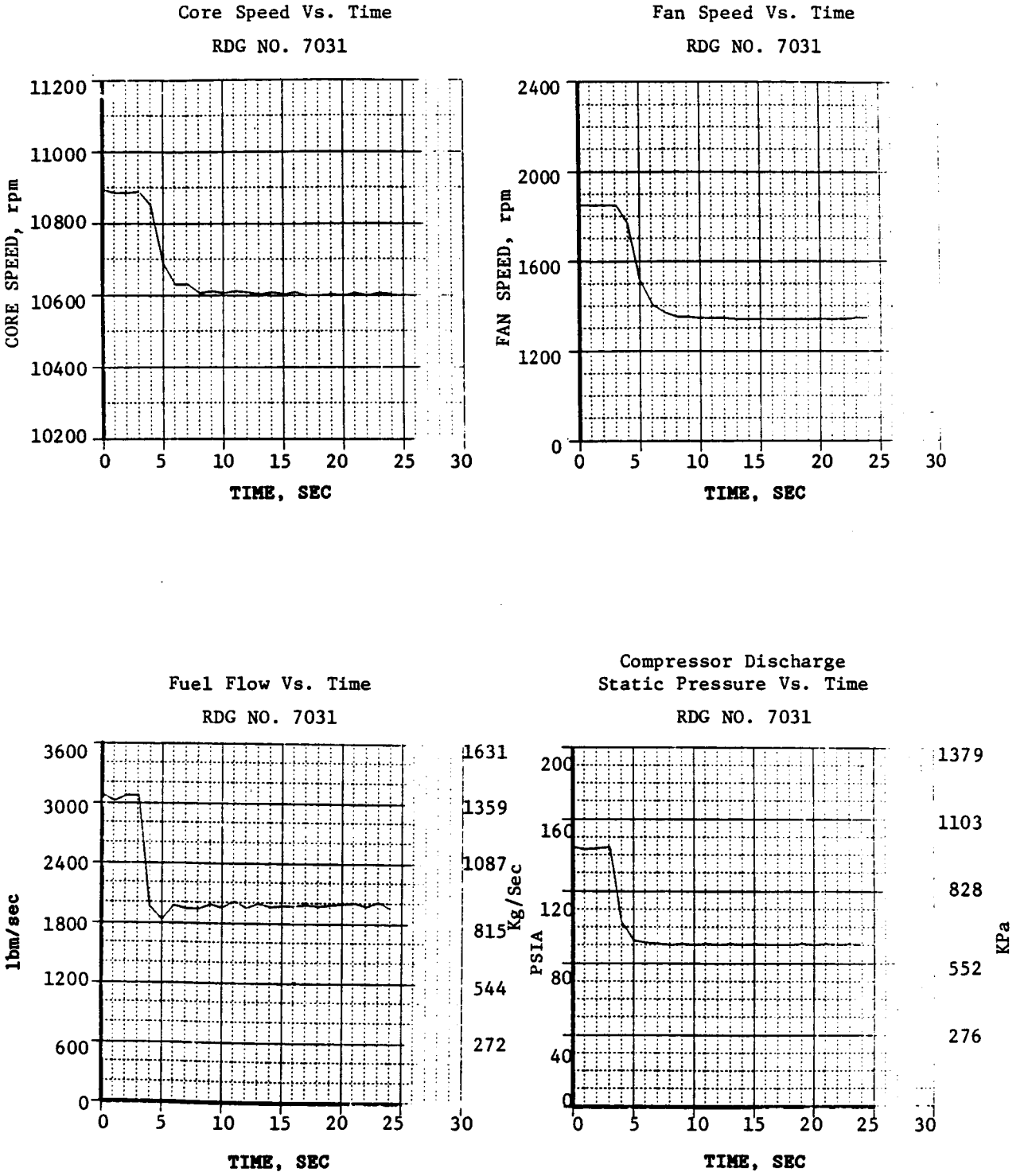


Figure 401. Trip to Backup Control.

## 7.0 CONCLUSIONS

The $E^3$ Integrated Core/Low Spool (ICLS) test vehicle was a ground test engine of the $E^3$ Flight Propulsion System (FPS) design. The purpose of ICLS testing was to evaluate the operation of the engine, measure performance, and demonstrate $E^3$ technology.

ICLS testing demonstrated the practicality and performance of the FPS design. No significant mechanical or operational problems were encountered. Design thrust was achieved. And, a sea level standard day specific fuel consumption of 0.332 kg/hr N (0.326 lbm/hr-lbf) was demonstrated. As far as is known, this was a record low fuel consumption for a turbofan engine.

Based on ICLS and preceding $E^3$ analysis and test, the FPS will meet or exceed $E^3$ program goals.

### Test Results

Throughout the engine, all temperatures were at acceptable levels. Aeromechanical performance was nearly perfect. All blade vibration characteristics were within desired limits over the entire speed range.

### Thermodynamic Performance

From the ICLS component performance results, it was concluded that the off-design modeling was satisfactory for reliable prediction of cruise performance. The measured performance and projection for cruise installed performance indicated that the objective performance improvement was exceeded by 1.2%.

### Acoustics

Test results showed the $E^3$ FPS exceeded the acoustic goals of the program.

Fan

Some acoustic panels deteriorated during testing and were replaced. This can be corrected for FPS by a design revision.

Fan bypass stream efficiency was 0.886 and fan hub and booster core stream efficiency was 0.901 at max cruise. These exceeded the respective goals by 0.4% and 1.1%.

Compressor

The $E^3$ core compressor performance demonstrated during the ICLS turbo-fan engine tests met the goals established for the program and showed good agreement with the core engine test results.

Combustor

As in the core engine tests, ignition, staging, and operational characteristics were trouble free. No smoke was visible.

High Pressure Turbine

The rotor was assembled eccentric from the casing and became more eccentric during operation. The active clearance control system was modified to partially restore concentricity. Because of this, clearance control could not be fully utilized. However, active clearance control, including the use of fan air, was demonstrated. Eccentricity would not be a problem in a production engine.

Efficiency matched the high level demonstrated in rig and core testing, 92.5% compared to a goal of 91.9%.

Low Pressure Turbine

The active clearance control system operated successfully. The use of turbine discharge gas to purge the aft rotor cavity was successful.

Efficiency was 1.0 to 1.5 points below that achieved in rig testing. As yet, the cause has not been determined.

Mixer

The mixer was over 5% more effective than expected from model tests. The causes, flow quality differences and the center vent tube, have since been incorporated into mixer modeling.

Engine Dynamics

Engine system vibrations were well behaved throughout the test program, demonstrating the effectiveness of the unique spring mounted and squeeze film damped core bearing arrangement.

Control

The on-engine Full Authority Digital Electronic Control (FADEC) performed very successfully. The control functioned properly, Failure Indication and Corrective Action (FICA) was demonstrated, and the control provided a very helpful experimental test operation flexibility.

Starting characteristics were excellent. Starting had been a concern area early in the program. Without the benefit of a start development program, the capability of a 44-second start was demonstrated. No stalls were encountered.

## 8.0 REFERENCES


1. Johnston, R.P., et al., "Energy Efficient Engine - Flight Propulsion System Preliminary Analysis and Design," NASA-Lewis Research Center, NASA CR-159583, November 1979.

2. Stearns, E.M., "Energy Efficient Engine - Flight Propulsion System Preliminary Analysis and Design Update," NASA-Lewis Research Center, NASA CR-167980, July 1982.

3. Stearns, E.M., et al., "Energy Efficient Engine Core Design and Performance Report," NASA-Lewis Research Center, NASA CR-168069, December 1983.

| 1. Report No. | 2. Government Accession No. | 3. Recipient's Catalog No. |
|---|---|---|
| NASA CR-168211 | | |

| 4. Title and Subtitle | 5. Report Date |
|---|---|
| Energy Efficient Engine<br>Integrated Core/Low Spool<br>Design and Performance Report | February 1985 |
| | 6. Performing Organization Code |
| 7. Author(s) | 8. Performing Organization Report No. |
| E.M. Stearns, et al. | R83AEB503 |
| | 10. Work Unit No. |
| 9. Performing Organization Name and Address | 11. Contract or Grant No. |
| General Electric Company<br>Aircraft Engine Business Group<br>Evendale, Ohio 45215 | NAS3-20643 |
| | 13. Type of Report and Period Covered |
| 12. Sponsoring Agency Name and Address | Topical<br>Jan 1978 - Aug 1983 |
| National Aeronautics and Space Administration<br>Lewis Research Center<br>21000 Brookpark Road<br>Cleveland, Ohio 44135 | 14. Sponsoring Agency Code |

15. Supplementary Notes
NASA Project: Mr. C. C. Ciepluch
NASA Project Engineer: Mr. R. Chamberlin
G.E. Project Manager: Mr. D. Y. Davis

16. Abstract
The Energy Efficient Engine ($E^3$) is a NASA program to create fuel saving technology for future transport aircraft engines. The $E^3$ technology advancements were demonstrated to operate reliably and achieve goal performance in tests of the Integrated Core/Low Spool vehicle. The first build of this undeveloped technology research engine set a record for low fuel consumption. Its design and detailed test results are herein presented.

17. Key Words (Suggested by Author(s))
Energy Conservation
Subsonic Transport Turbine Engine
Aircraft Turbine Engine
Energy Efficient Engine
ICLS Engine

[redacted]

| 19. Security Classif. (of this report) | 20. Security Classif. (of this page) | 21. No. of Pages | 22. Price* |
|---|---|---|---|
| Unclassified | Unclassified | 623 | |

[redacted]